ISSN 1580-3155

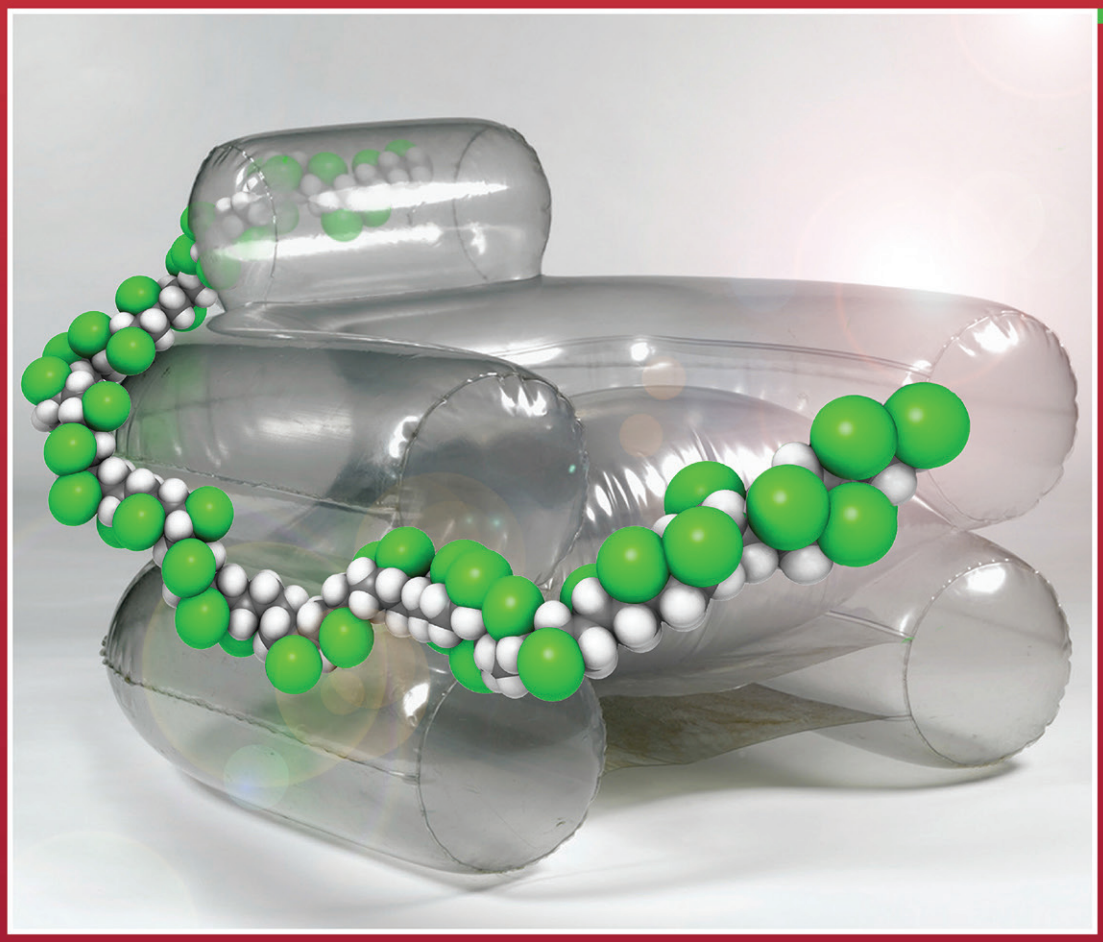
Pages 993–1314 ■ Year 2020, Vol. 67, No. 4

Slovensko kemijsko društvo
Slovenian Chemical Society

Acta Chimica Slovenica

4

67/2020



http://acta.chem-soc.si

EDITOR-IN-CHIEF

KSENIJA KOGEJ
University of Ljubjana, Facuty of Chemstry and Chemical Technology, Večna pot 113, SI-1000 Ljubljana, Slovenija
E-mail: ACSi@fkkt.uni-lj.si, Telephone: (+386)-1-479-8538

ASSOCIATE EDITORS

Alen Albreht, *National Institute of Chemistry, Slovenia*
Aleš Berlec, *Jožef Stefan Institute, Slovenia*
Janez Cerkovnik, *University of Ljubljana, Slovenia*
Mirela Dragomir, *Jožef Stefan Institute, Slovenia*
Ksenija Kogej, *University of Ljubljana, Slovenia*
Krištof Kranjc, *University of Ljubljana, Slovenia*
Matjaž Kristl, *University of Maribor, Slovenia*
Franc Perdih, *University of Ljubljana, Slovenia*
Aleš Podgornik, *University of Ljubljana, Slovenia*
Helena Prosen, *University of Ljubljana, Slovenia*
Irena Vovk, *National Institute of Chemistry, Slovenia*

ADMINISTRATIVE ASSISTANT

Marjana Gantar Albreht, *National Institute of Chemistry, Slovenia*

EDITORIAL BOARD

Wolfgang Buchberger, *Johannes Kepler University, Austria*
Alojz Demšar, *University of Ljubljana, Slovenia*
Stanislav Gobec, *University of Ljubljana, Slovenia*
Marko Goličnik, *University of Ljubljana, Slovenia*
Günter Grampp, *Graz University of Technology, Austria*
Wojciech Grochala, *University of Warsaw, Poland*
Danijel Kikelj, *University of Ljubljana*
Janez Košmrlj, *University of Ljubljana, Slovenia*
Blaž Likozar, *National Institute of Chemistry, Slovenia*
Mahesh K. Lakshman, *The City College and The City University of New York, USA*
Janez Mavri, *National Institute of Chemistry, Slovenia*
Friedrich Srienc, *University of Minnesota, USA*
Walter Steiner, *Graz University of Technology, Austria*
Jurij Svete, *University of Ljubljana, Slovenia*
Ivan Švancara, *University of Pardubice, Czech Republic*
Jiri Pinkas, *Masaryk University Brno, Czech Republic*
Gašper Tavčar, *Jožef Stefan Institute, Slovenia*
Christine Wandrey, *EPFL Lausanne, Switzerland*
Ennio Zangrando, *University of Trieste, Italy*

ADVISORY EDITORIAL BOARD

Chairman
Branko Stanovnik, Slovenia

Members
Udo A. Th. Brinkman, The Netherlands
Attilio Cesaro, Italy
Vida Hudnik, Slovenia
Venčeslav Kaučič, Slovenia
Željko Knez, Slovenia
Radovan Komel, Slovenia
Stane Pejovnik, Slovenia
Anton Perdih, Slovenia
Slavko Pečar, Slovenia
Andrej Petrič, Slovenia
Boris Pihlar, Slovenia
Milan Randić, Des Moines, USA
Jože Škerjanc, Slovenia
Miha Tišler, Slovenia
Đurđa Vasić-Rački, Croatia
Marjan Veber, Slovenia
Gorazd Vesnaver, Slovenia
Jure Zupan, Slovenia
Boris Žemva, Slovenia
Majda Žigon, Slovenia

Acta Chimica Slovenica is indexed in: *Academic Search Complete, Central & Eastern European Academic Source, Chemical Abstracts Plus, Chemical Engineering Collection (India), Chemistry Citation Index Expanded, Current Contents (Physical, Chemical and Earth Sciences), Digitalna knjižnica Slovenije (dLib.si), DOAJ, ISI Alerting Services, PubMed, Science Citation Index Expanded, SciFinder (CAS), Scopus and Web of Science.* Impact factor for 2019 is IF = 1.263.

Articles in this journal are published under the Creative Commons Attribution 4.0 International License

Izdaja – Published by:
SLOVENSKO KEMIJSKO DRUŠTVO – SLOVENIAN CHEMICAL SOCIETY
Naslov redakcije in uprave – Address of the Editorial Board and Administration
Hajdrihova 19, SI-1000 Ljubljana, Slovenija
Tel.: (+386)-1-476-0252; Fax: (+386)-1-476-0300; E-mail: chem.soc@ki.si

Slovensko kemijsko društvo
Slovenian Chemical Society

Izdajanje sofinancirajo – Financially supported by:
Slovenian Research Agency, Ljubljana, Slovenia
National Institute of Chemistry, Ljubljana, Slovenia
Jožef Stefan Institute, Ljubljana, Slovenia
Faculty of Chemistry and Chemical Technology, University of Ljubljana, Slovenia
Faculty of Chemistry and Chemical Engineering, University of Maribor, Slovenia
University of Nova Gorica, Nova Gorica, Slovenia

Acta Chimica Slovenica izhaja štirikrat letno v elektronski obliki na spletni strani http://*acta.chem-soc.si*. V primeru posvečenih številk izhaja revija tudi v tiskani obliki v omejenem številu izvodov.
Acta Chimica Slovenica appears quarterly in electronic form on the web site *http://acta.chem-soc.si*. In case of dedicated issues, a limited number of printed copies are issued as well.
Transakcijski račun: 02053-0013322846 Bank Account No.: SI56020530013322846-Nova Ljubljanska banka d. d., Trg republike 2, SI-1520 Ljubljana, Slovenia, SWIFT Code: LJBA SI 2X
Oblikovanje ovitka – Design cover: KULT, oblikovalski studio, Simon KAJTNA, s. p. Grafična priprava za tisk: OSITO, Laura Jankovič, s.p.

Graphical Contents



Acta Chimica Slovenica

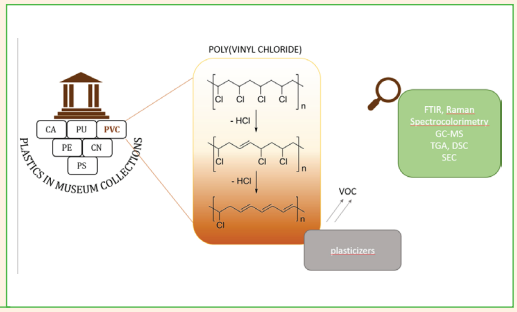
Year 2020, Vol. 67, No. 4

FEATURE ARTICLE

993–1013 Feature Article

Plastics in Heritage Collections: Poly(vinyl chloride) Degradation and Characterization

Tjaša Rijavec, Matija Strlič and Irena Kralj Cigić

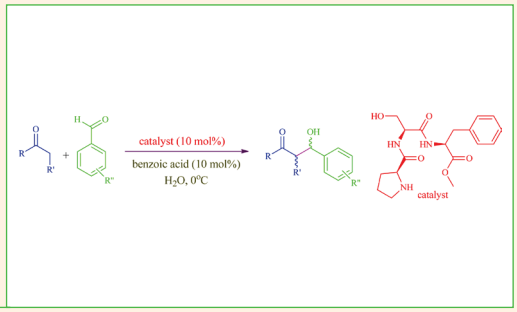


SCIENTIFIC PAPER

1014–1023 Organic chemistry

Synthesis of New Di- and Triamides as Potential Organocatalysts for Asymmetric Aldol Reaction in Water

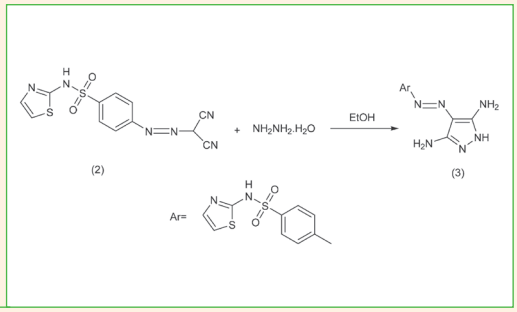
Elif Keskin, Cigdem Yolacan and Feray Aydogan



1024–1034 Organic chemistry

Synthesis and Antimicrobial Evaluation of Some New Pyrazolo[1,5-a]pyrimidine and Pyrazolo[1,5-c]triazine Derivatives Containing Sulfathiazole Moiety

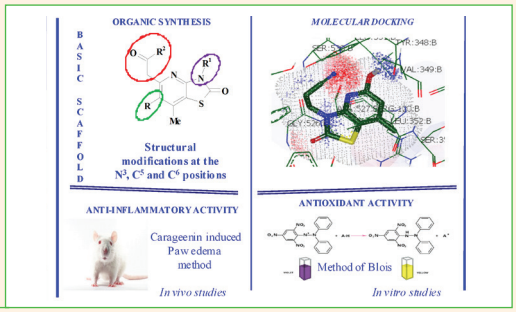
Elsherbiny Hamdy El-Sayed, Ahmed Ali Fadda and Ahmed Mohamed El-Saadaney



1035–1043 Organic chemistry

Synthesis, Molecular Docking and Biological Properties of Novel Thiazolo[4,5-b]pyridine Derivatives

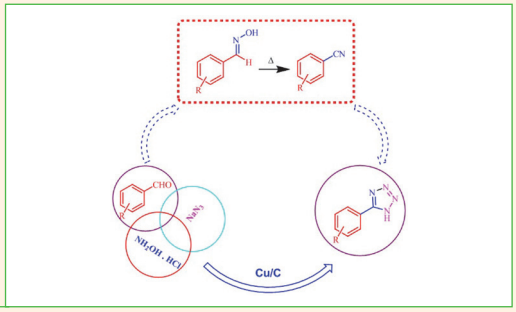
Taras I. Chaban, Yulia E. Matiichuk, Olga Ya. Shyyka, Ihor G. Chaban, Volodymyr V. Ogurtsov, Ihor A. Nektegayev and Vasyl S. Matiychuk



1044–1052 Organic chemistry

Highly Active and Reusable Cu/C Catalyst for Synthesis of 5-Substituted 1H-Tetrazoles Starting from Aromatic Aldehydes

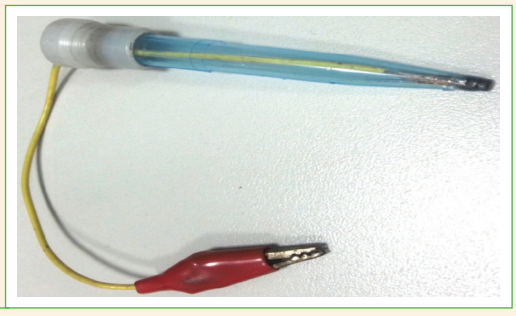
Reza Khalifeh, Najme Rastegar and Dariush Khalili



1053–1060 Analytical chemistry

Differential Pulse Anodic Voltammetric Determination of Chlorzoxazone in Pharmaceutical Formulation using Carbon Paste Electrode

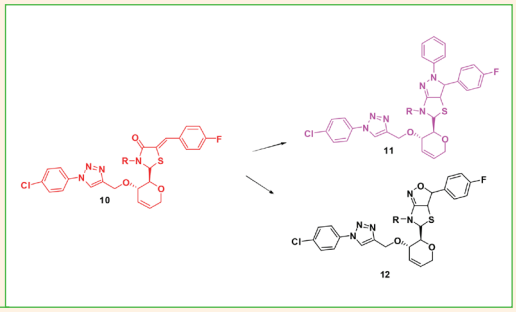
Sayed I. M. Zayed and Yousry M. Issa



1061–1071 Organic chemistry

Synthesis and Biological Evaluation of Novel Pyrane Glycosides

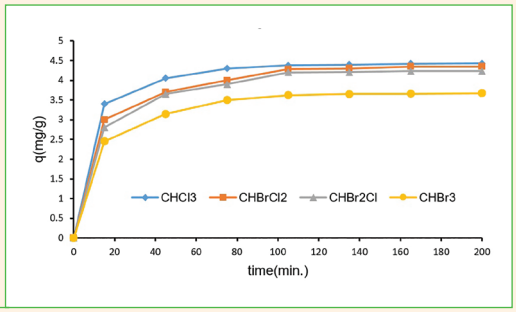
Avula Srinivas, Malladi Sunitha and Sriramoju Shamili



1072–1081 Analytical chemistry

Removal of Trihalomethanes from Water using Modified Montmorillonite

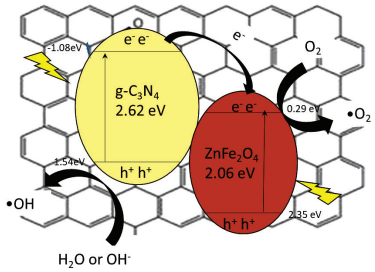
Majid Hamouni Haghighat and Ali Mohammad-Khah



1082–1091 Materials science

Visible Light-Driven Photocatalytic Activity of Magnetic Recoverable Ternary $ZnFe_2O_4$/rGO/g-C_3N_4 Nanocomposites

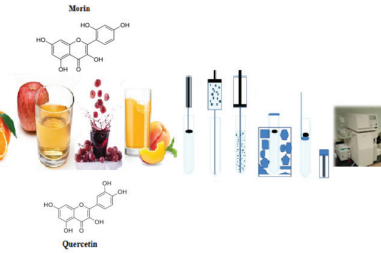
Martin Tsvetkov, Elzhana Encheva, Albin Pintar, and Maria Milanova



1092–1099 Analytical chemistry

Determination of Morin and Quercetin in Fruit Juice Samples using Air-Assisted Liquid-Liquid Microextraction Based on Solidification of Floating Organic Droplet and HPLC-UV

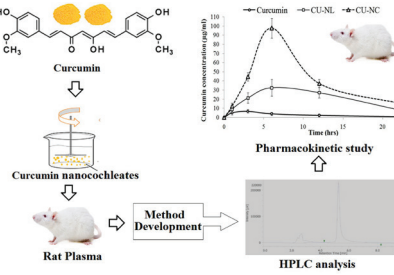
Armin Fallah and Mohammad Reza Hadjmohammadi



1100–1110 Analytical chemistry

Development and Validation of RP–HPLC Method for Estimation of Curcumin from Nanocochleates and Its Application in *in–vivo* Pharmacokinetic Study

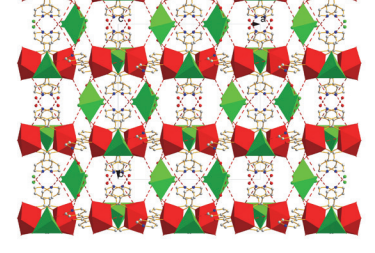
Sameer Nadaf and Suresh Killedar



1111–1117 Inorganic chemistry

Crystal Structure and Photophysical Properties of a Novel Dy-Hg Isonicotinic Acid Compound with One-Dimensional Chain-Like Cations

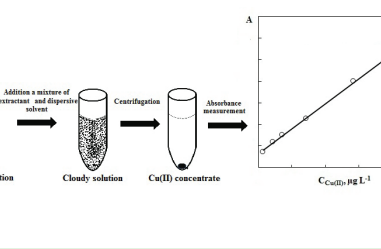
Wen-Tong Chen



1118–1123 Analytical chemistry

Dispersive Liquid-Liquid Semi-Microextraction of Cu(II) with 6,7-dihydroxy-2,4-diphenylbenzopyrylium Chloride for its Spectrophotometric Determination

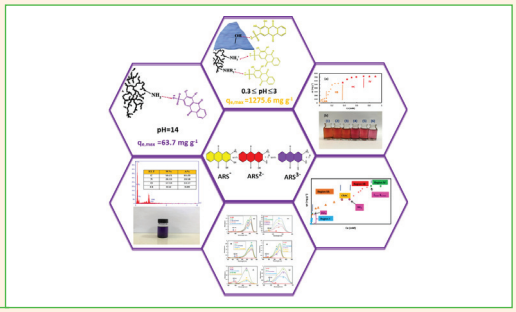
Alexander Chebotarev, Anastasiia Klochkova, Vitaliy Dubovyi and Denys Snigur



1124–1138 Chemical, biochemical and environmental engineering

GO/PAMAM as a High Capacity Adsorbent for Removal of Alizarin Red S: Selective Separation of Dyes

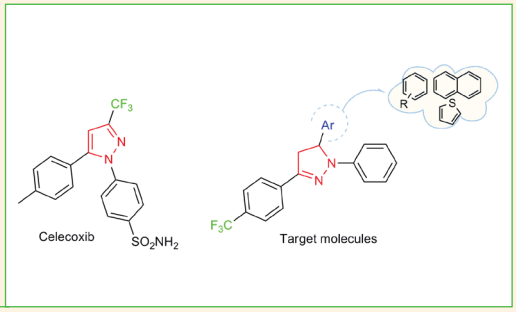
Mohammad Rafi, Babak Samiey and Chil-Hung Cheng



1139–1147 Organic chemistry

Design, Synthesis and Biological Screening of Novel 1,5-Diphenyl-3-(4-(trifluoromethyl)phenyl)-2-pyrazoline Derivatives

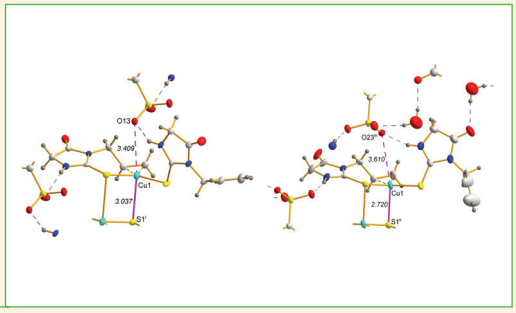
Fatih Tok and Bedia Koçyiğit-Kaymakçıoğlu



1148–1154 Inorganic chemistry

Cu(I) Arylsulfonate π-Complexes with 3-Allyl-2-thiohydantoin: The Role of the Weak Interactions in Structural Organization

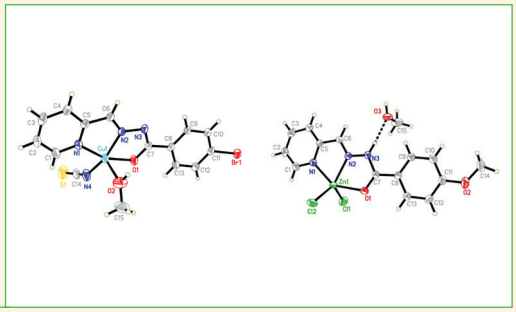
Andrii Fedorchuk, Evgeny Goreshnik, Yurii Slyvka and Marian Mys'kiv



1155–1162 Inorganic chemistry

Synthesis, Characterization, Crystal Structures, and Urease Inhibition of Copper(II) and Zinc(II) Complexes Derived from Benzohydrazones

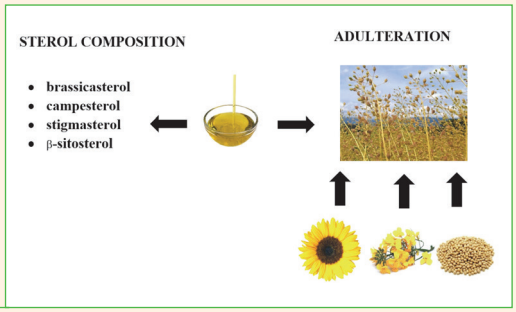
Fu-Ming Wang, Li-Jie Li, Guo-Wei Zang, Tong-Tong Deng and Zhong-Lu You



1163–1171 Analytical chemistry

Determination of Camelina Oil Sterol Composition and Its Application for Authenticity Studies

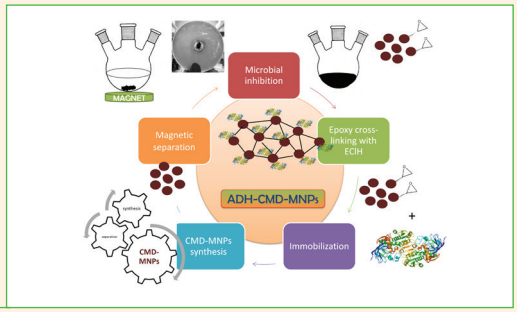
Zala Kolenc, Tanja Potočnik, Urban Bren and Iztok Jože Košir



1172–1179 Chemical, biochemical and environmental engineering

Epoxy Functionalized Carboxymethyl Dextran Magnetic Nanoparticles for Immobilization of Alcohol Dehydrogenase

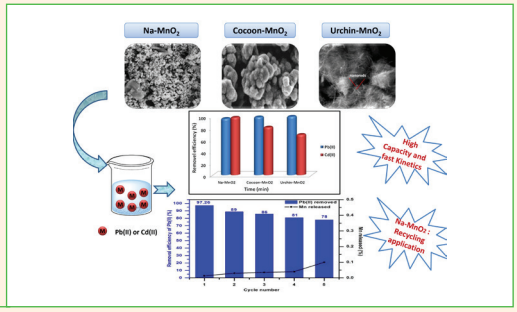
Katja Vasić, Željko Knez, Sanjay Kumar, Jitendra K. Pandey and Maja Leitgeb



1180–1195 General chemistry

Elaboration of Lamellar and Nanostructured Materials Based on Manganese: Efficient Adsorbents for Removing Heavy Metals

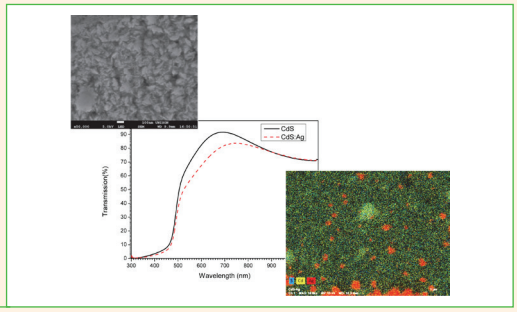
Amina Amarray, Sanae El Ghachtouli, Mohammed Ait Himi, Mohamed Aqil, Khaoula Khaless, Younes Brahmi, Mouad Dahbi and Mohammed Azzi



1196–1201 Materials science

Study of Selected Morphologic, Structural and Optical Effects of Silver Coated CBD-CdS Thin Films

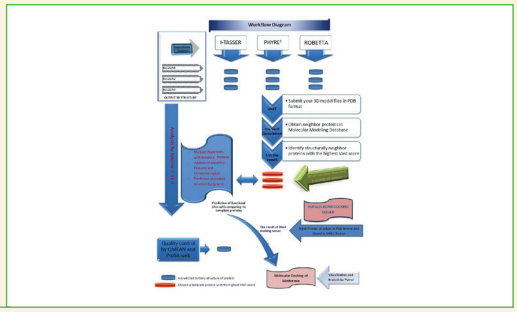
Angel Roberto Torres-Duarte, Horacio Antolín Pineda-Leon, Aned de Leon, Ramón Ochoa-Landín and Santos Jesús Castillo



1202–1215 Biochemistry and molecular biology

Assessment of Interaction of Human OCT 1-3 Proteins and Metformin Using Silico Analyses

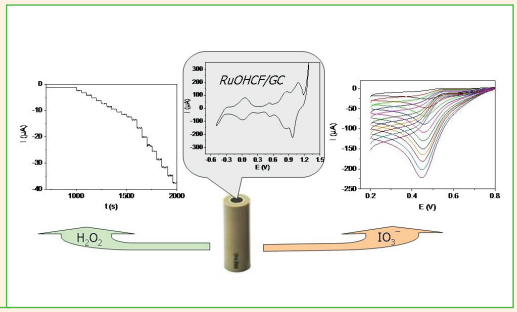
Faruk Berat Akçeşme, Nail Beşli, Jorge Peña-García and Horacio Pérez-Sánchez



1216–1226 Applied chemistry

Ruthenium Oxide Hexacyanoferrate as an Effective Electrode Modifier for Amperometric Detection of Iodate and Hydrogen Peroxide

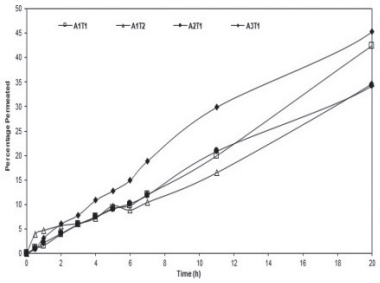
Totka Dodevska, Ivan Shterev, Yanna Lazarova and Dobrin Hadzhiev



1227–1232 Applied chemistry

Influence of TiO_2 on Mucosal Permeation of Aceclofenac: Analysis of Crystal Strain and Dislocation Density

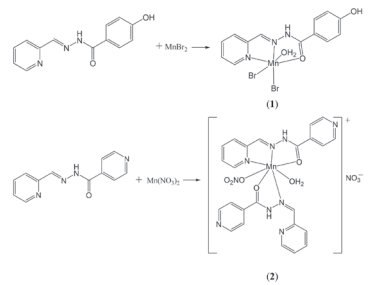
Souvik Nandi, Satyaki Aparajit Mishra, Rudra Narayan Sahoo, Rakesh Swain and Subrata Mallick



1233–1238 Inorganic chemistry

Synthesis, Crystal Structures, Characterization and Catalytic Property of Manganese(II) Complexes Derived from Hydrazone Ligands

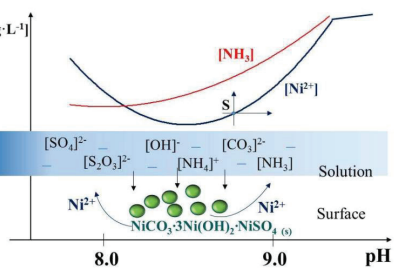
Yao Tan



1239–1249 Applied chemistry

Ammoniacal Carbonate Leaching: Effect of Dissolved Sulfur in the Distillation Operation Armando Rojas

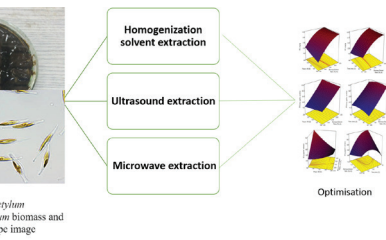
Armando Rojas Vargas, María Elena Trujillo Nieves and Yudith González Diaz



1250–1261 Chemical, biochemical and environmental engineering

Effects of Extraction Methods and Conditions on Bioactive Compounds Extracted from *Phaeodactylum tricornutum*

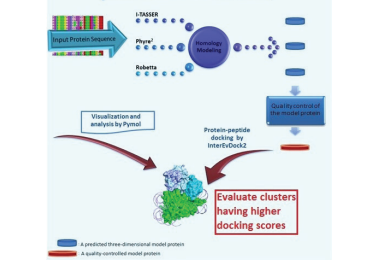
Saniye Akyıl, Işıl İlter, Mehmet Koç, Zeliha Demirel, Ayşegül Erdoğan, Meltem Conk Dalay and Figen Kaymak Ertekin



1262–1272 Biochemistry and molecular biology

Assessment of the Interaction of Aggregatin Protein with Amyloid-Beta (Aβ) at the Molecular Level via In Silico Analysis

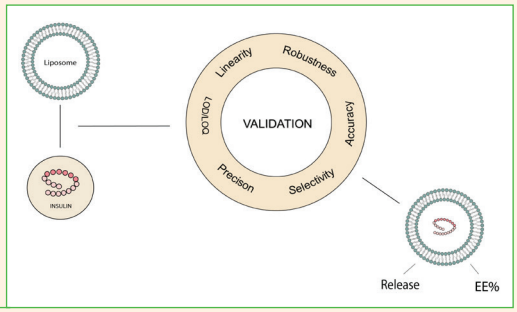
Nail Besli and Guven Yenmis



1273–1280 Analytical chemistry

Rapid and Sensitive Analytical Method for the Determination of Insulin in Liposomes by Reversed-Phase HPLC

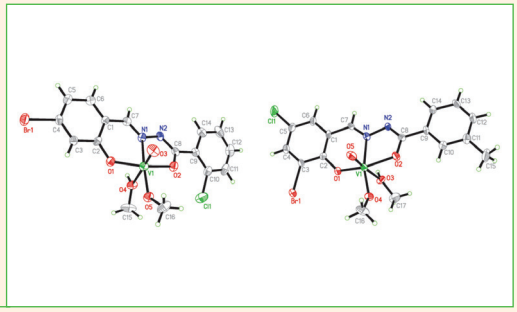
Eliete de Souza Von Zuben, Josimar Oliveira Eloy, Victor Hugo Sousa Araujo, Maria Palmira Daflon Gremião and Marlus Chorilli



1281–1289 Inorganic chemistry

Two Vanadium(V) Complexes Derived from Bromo and Chloro-Substituted Hydrazone Ligands: Syntheses, Crystal Structures and Antimicrobial Property

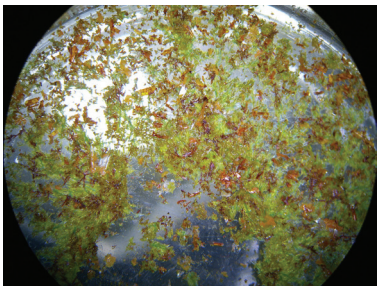
Zi-Qiang Sun, Shun-Feng Yu, Xin-Lan Xu, Xiao-Yang Qiu and Shu-Juan Liu



1290–1300 Inorganic chemistry

Four Different Crystalline Products from One Reaction: Unexpected Diversity of Products of the $CuCl_2$ Reaction with N-(2-Pyridyl)thiourea

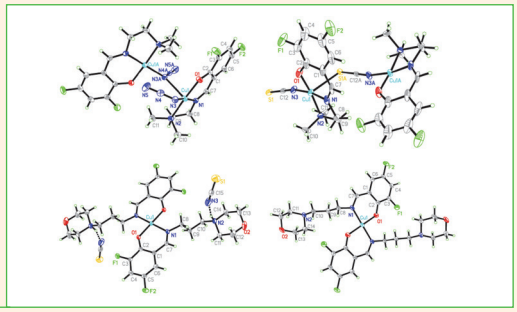
Sara Tomšič, Janez Košmrlj and Andrej Pevec



1301–1308 Inorganic chemistry

Syntheses, Crystal Structures and Antimicrobial Property of Schiff Base Copper(II) Complexes

Shun-Feng Yu, Xiao-Yang Qiu and Shu-Juan Liu

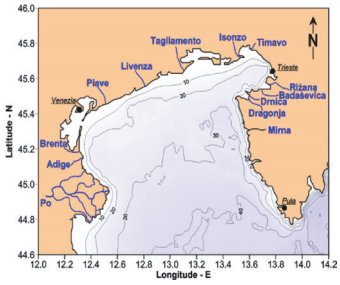


DRUŠTVENE VESTI

S91–S97 Chemical education

Obalni ekosistemi na prehodu: Primerjalna analiza severnega Jadrana in Zaliva Chesapeake

Jadran Faganeli, Alenka Malej



S98–S105 Chemical education

Obiski Rosalind Franklin v Sloveniji

Marko Dolinar



Feature Article

Plastics in Heritage Collections: Poly(vinyl chloride) Degradation and Characterization

Tjaša Rijavec[1], Matija Strlič[1,2,3] and Irena Kralj Cigić[1,4,*]

[1] *Faculty of Chemistry and Chemical Technology, University of Ljubljana, Ljubljana, Slovenia*

[2] *Institute for Sustainable Heritage, University College London, London, UK*

[3] *Museum Conservation Institute, Smithsonian Institution, Suitland MD, USA*

[4] *Department of Chemical and Pharmaceutical Sciences, University of Trieste, Trieste, Italy*

** Corresponding author: E-mail: irena.kralj-cigic@fkkt.uni-lj.si*

Received: 11-01-2020

Abstract

Museums and galleries house increasingly large collections of objects and contemporary art made of plastic materials, many of which undergo rapid material change. The main degradation processes of poly(vinyl chloride) (PVC) are elimination of HCl and plasticizer migration or leaching. This results in visible discolouration, stickiness and cracking. Degradation is known to be a multi-stage process that includes HCl elimination, formation of conjugated polyenes and cross-linking. Elimination of HCl begins due to structural irregularities (allylic and tertiary chlorides) and results in the formation of polyenes. When at least 7 conjugated double bonds are present, discolouration of PVC becomes visible.

Non-invasive techniques, such as IR and Raman spectroscopy are used for polymer identification and plasticizer quantification. Plasticizer degradation and particularly the late stages of PVC degradation can be investigated using SEC, GC-MS, TGA and DSC. Studies in heritage collections have revealed that, apart from HCl, PVC objects emit 2-ethylhexanol and other volatile degradation products, however, there is currently no indication that HCl is emitted at usual indoor conditions. There seems to be a general lack of systematic research into PVC degradation at the conditions of storage and display, which could result in the development of dose-response functions and in the development of preventive conservation guidelines for the management of PVC collections.

Keywords: poly(vinyl chloride); plastics; non-destructive characterization; heritage collections; accelerated degradation

1. Introduction

In the 20th century, poly(vinyl chloride) (PVC) and other plastics have achieved widespread use in daily life[1], with more than 5 M tonnes of PVC produced in Europe in 2018 alone, representing 10% of all plastic.[2] The evolution of artform has gone hand in hand with the discovery and invention of new materials, and plastics were no exception.[3,4] Many museums have significant collections of plastic objects from the late 19th and 20th century, as well as art made from plastic materials (Figure 1).[5–7]



Figure 1: Examples of PVC art and design objects. Left: Essuie-mains / Hygiène de l'art, 1971 (inv. no. AM 2006-114) by Hervé Fischer, middle: Fauteuil Blow, 1967 (inv. no. AM 2007-1-38), by de Pas, D'Urbino, Lomazzi, right: Plafonnier, 1968 (inv. no. AM 2007-1-5) by Quasar (Nguyen Manh Khan'h). Reproduced with permission of MNAM, Centre Pompidou, Paris, France.

A survey of museum collections in France, Netherlands and the United Kingdom was carried out in the scope of the project POPART during 2008–2012.[5] The results showed that PVC was present in all collections and represented 13% of all plastic objects. The degradation state was also assessed and 68% of objects in the collection were in a good or fair state, 25% were in a state of significant decay and 7% were severely damaged. Cellulose acetate (CA), cellulose nitrate (CN) and PVC represented 40% of all objects in poor state.[5] Plasticized PVC was a major commodity plastic found in the collection of the Museé d'art moderne et d'art contemporain (MAMAC) in Nice, France, and in the Musée d'art moderne de Saint-Etienne Métropole (MAM). The surveys had also exposed the problem of museums having a lack of reliable information regarding the identity of the polymers before the FTIR and Py-GC-MS analysis was carried out .[8]

Pure PVC is a solid brittle material, which makes it difficult to process and mould. It has poor thermal properties, as is prone to distorting when exposed to temperatures above 60 °C. Its discovery in 1872 by Eugen Baumann was not immediately followed by commercialization due to the difficulties with processing of this rigid and brittle pure polymer.[9] However, PVC's mechanical and thermal properties, such as density, tensile strength, electrical resistance and elastic properties can be modified with additives. In 1926, Waldo Semon and the B.F. Goodrich Company introduced additives to soften the PVC, making it easier to process, which led to worldwide commercial usage. Heat stabilizers, UV stabilizers, plasticizers, fillers, pigments, thermal modifiers, flame retardants, biocides and other modifiers are used to produce items for specific purposes. Additives are used to improve technological processing, the plastic's final characteristics and performance. Fillers, such as carbonates and silicates, are used to reduce the production costs and increase impact resistance.[10] Plasticizers act as softeners and reduce the viscosity of the polymer. They can make up to 50% of the final formulation in flexible PVC.[3,11,12] Heat stabilizers are included in most commercial PVC formulations to prevent thermal degradation, neutralize the emitted HCl, replace labile chlorine in PVC and prevent oxidation. Light stabilizers protect the material from thermal and UV degradation, while antioxidants prevent oxidation. Pigments are added to change the colour of the plastic. Unplasticized PVC is the material of choice for making electrical insulation boxes, pipes and electric cables, windows and flooring. Plasticized PVC is used to form clothing, tubes in healthcare, toys, vinyl records, food packaging, greenhouse windows and shower curtains.[1,12,13]

The aim of this review is to address what appears to be a significant lack of attention to PVC as a collection material. We will briefly discuss the mechanisms of thermal degradation of PVC, describe the determination of the material state of PVC with a particular focus on analytical techniques that provide useful information to make informed conservation decisions, and review the research on PVC degradation in heritage and museum collections. Many researchers studying commodity plastics focus on early-stage degradation and not on the advanced degradation relevant to museum objects. Early-stage degradation of commodity plastics in the first few years since production is important in the plastic industry to provide the guaranteed lifetime of the object. However, objects can become part of museum collections and retain their value as cultural heritage long after their useful lifetime as consumer products, defined by industrial standards, has ended.[3] Tackling advanced stages of degradation is thus important for preserving such objects.

We focus specifically on research into PVC and its degradation at moderate temperatures, as this could form the basis for modelling of degradation at environmental conditions of storage and display. There are numerous monographs and reviews approaching the problem from different angles of interest. Shashoua's seminal volume on the conservation of plastics in museum collections discusses the history of technology development, properties of plastics and their degradation.[3] The production and application of PVC are addressed in a volume by Patrick.[1] Wypych's book thoroughly addresses degradation and stabilization of PVC with a focus on industrial stabilizers,[12] while the mechanistical aspects of degradation are covered by Starnes in detail.[14–16]A review on volatile organic compounds (VOCs) emitted from plastics and rubbers in conservation, heritage science, construction and polymer science demonstrates examples of degradation markers for certain polymers.[17] Current trends and challenges in investigating the plasticizer loss mechanism and rates in heritage collections have been reviewed by King.[18] It is also well known how recycling affects the thermal degradation of PVC.[19] The decomposition of PVC by microorganisms appears to be an emerging area of interest.[20]

Classical art collections contain traditional materials such as ceramics, stone, metals, paper and textiles, and conservation issues related to such objects have been studied for long, they are therefore relatively well understood, and guidelines are available to extend their lifetimes.[21–26] For many plastic objects, especially those made of cellulose nitrate, cellulose acetate, poly(vinyl chloride) or polyurethane, which are frequent in collections and prone to deterioration, the lifetime can be orders of magnitude shorter than for traditional organic materials such as paper, oil paint or parchment.[3,24,25,27,28] In addition, the degradation of plastics in museums does not result only in the loss of integrity and value of the objects themselves but can lead to the deterioration of objects in their vicinity due to the formation of harmful substances e.g. acidic gasses.[29]

2. Plasticization of Poly(vinyl Chloride)

Most PVC objects in heritage collections are made of plasticized PVC. The physical and chemical degradation of

the plasticizer itself also directly dictates the current state and the degradation of PVC objects. Migration of plasticizers makes the surface sticky and hydrolysis of certain plasticizers may lead to the formation of white crystals on the surface, which changes the object's appearance. It also leads to warping and cracking, all of which negatively impacts the state of the object.

Commodity plastics, such as PVC, are plasticized externally, where the plasticizer is not chemically bonded and acts as a solvent for the polymer. Internal plasticizers are chemically bonded to the polymer by modification of the polymer backbone or by bonding to the backbone. Such engineering plastics are rare and formed during manufacture. Primary external plasticizers are highly compatible with the polymer and can be added in large quantities, while secondary plasticizers have high volatility or only limited compatibility with the polymer and are used in combination with primary plasticizers.[11,30] Plasticizers must solvate the polymer and cannot be prone to self-association, which makes esters appropriate compounds. Ideally, plasticizers should be stable, non-toxic, non-volatile, odourless, colourless liquids.

2. 1. Types of Plasticizers

More than 90% of all plasticizers are used in the PVC industry.[31] PVC is the only commercial polymer that can retain large concentrations of plasticizers. A major group of traditional and current plasticizers are ortho-phthalate esters. Low molecular weight ortho-phthalates (C_4 – C_7 alcohols) were historically used in many PVC formulations. They have been classified as substances of very high concern in Europe and United States of America[32] and are being replaced with high molecular weight ortho-phthalates, terephthalates and benzoate plasticizers.

Primary common PVC plasticizers are long-chain esters of phthalic acid, of which 75% represent di(2-ethylhexyl) phthalate (DEHP or DOP), diisononyl phthalate (DINP) and diisodecyl phthalate (DIDP) (Figure 2).[11,33] DEHP had been accepted as the standard all-purpose plasticizer until it was labelled as a reproductive toxicant in Europe.[34] It was replaced with DINP, DIDP, dipropylheptyl phthalate (DPHP) and its terephthalate analogue di(2-ethylhexyl) terephthalate (DEHT or DOTP).[31] In the USA, manufacturers of children's toys are prohibited from using 8 ortho-phthalates.[35] Diesters of terephthalic acid have replaced DEHP in many applications, including sensitive products such as toys, medical and food products.[30] Hydrogenation of ortho-phthalates produces 1,2-cyclohexane dicarboxylates which are also used as plasticizers. Mono- and di-benzoates of branched C_8 – C_{10} alcohols are often used as secondary plasticizers due to their high compatibility and high solvating power. Dibenzoate plasticizers have high viscosity so they are used in combination with primary plasticizers DINP, DIDP, DPHP and DEHT. Alkyl adipate esters have low intrinsic viscosity and good flexibility properties. Di(2-ethylhexyl) adipate (DEHA) is widely used in PVC clingfilm for food storage. Trimellitate esters have very low volatility and are resistant to extraction.[36] Tris(2-ethylhexyl) trimellitate (TOTM or TEHTM) is the most common, as it is approved for use in medical devices. Other commonly used plasticizers are citrates, such as acetyl tributyl citrate (ATBC), adipates (e.g. diisononyl adipade DINA), and sebacates (e.g. dibutyl sebacate DBS).

The most common secondary plasticizers are chlorinated hydrocarbons, isobutyrate esters and epoxidized oils. TXIB (2,2,4-trimethyl-1,3-pentandiol diisobutyrate) is a secondary plasticizer used in many PVC formulations to lower the cost of production and decrease the viscosity of plastisols. It is more volatile than long-chain phthalate esters, so the emissions of VOCs are increased.

Research and development of new plasticizers has recently focused on biobased plasticizers. A possible alternative is epoxidized soybean oil (ESBO), which is an efficient plasticizer and heat stabilizer for PVC.[13] It is used as a plasticizer in modern toys, as replacement for DEHP. Its cost is comparable to the traditional DEHP, but ESBO is also prone to migration. Acetylated and epoxidized cardanol was used to form plasticized PVC and investigate its tensile properties, UV and thermal degradation.[37] It had good mechanical properties and acted as a UV and heat stabilizer. The drawback is that it produced PVC darker in colour than traditional plasticizers. Epoxide groups in the structure of epoxidized plasticizers scavenge hydrochloric acid to form chlorohydrins and improve their thermal stability by reducing the rate of degradation. This inhibits thermal degradation by affecting the first

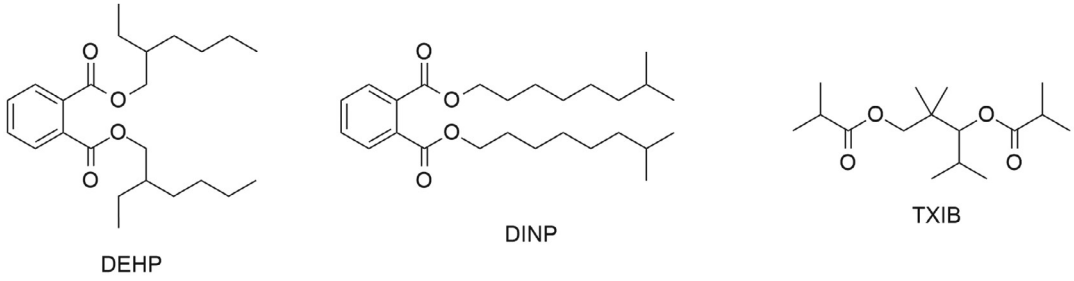


Figure 2: Common PVC plasticizers: di(2-ethylhexyl) phthalate (DEHP), diisononyl phthalate (DINP) and 2,2,4-trimethyl-1,3-pentandiol diisobutyrate (TXIB).

stage of degradation described in Section 2.3. A castor oil-based plasticizer has improved elongation and tensile properties of PVC.[38] A plasticizer based on epoxidized cottonseed oil (ECSO) has been shown to have comparable tensile and elongation properties to the traditional plasticizer DEHP.[39] The usual curing temperature of plastisols with phthalate esters is 160 °C, but ECSO requires higher temperatures up to 220 °C, where thermal degradation for PVC is significant. Cardanol is the main component of cashew nut oil, used to make epoxidized cardanol glycidyl ether.[40] It was tested as a plasticizer in making PVC films and demonstrated to have better thermal stability than films made with DEHP. Other plasticizers derived from raw materials, especially citrates, succinates, triglycerides, sugar derivatives and fatty acid esters have been synthesized and used as alternative plasticizers.[30,41]

New biobased plasticizers were tested in finished PVC formulation. Despite the accelerated degradation tests of emerging plasticizers, there are still uncertainties about the natural lifelong stability and performance of PVC products created with emerging plasticizers. As an example, a study of PVC plasticized with ESBO demonstrated that the presence of traditional stabilizers, such as calcium and zinc stearates, decreased the stability of PVC-ESBO system.[42]

To summarize, long-chain phthalates, terephthalates, trimellitates, adipates, sebacates and citrates are the most commonly used plasticizers in soft PVC. Sometimes secondary plasticizers, such as TXIB, are used to decrease the viscosity of plastisols and lower the production costs. DEHP was traditionally the most commonly used plasticizer and is likely currently the most prevalent in collections. However, it was prohibited for use in childcare articles and items in prolonged contact with skin. Recently, biobased plasticizers, such as ESBO, have been proposed as good alternatives.

2. 2. Mechanisms of Plasticization

Four different theories explaining the mechanism of plasticization have been developed.[11,43] The lubricity theory, developed by Kilpatrick, Clark and Houwink, explains that in the presence of plasticizers, the polymer chains can easily move over each other due to uneven attraction to different segments of the plasticizer molecules.[43] The polar segment of a plasticizer acts as a solvent for the polymer while the non-polar segment acts as a lubricant, allowing the polymer chains to move freely. The gel theory, developed by Aiken, proposes the formation of a gel structure by permanent intermolecular bonds or by the dynamic formation and breakage of bonds between the polymer chain and the plasticizer.[44] External plasticizers have more freedom to solvate and desolvate different polymer sites while internal plasticizers lack this option and soften less with increasing temperature. This theory also explains that secondary plasticizers can soften PVC by increasing the space between polymer chains and reducing the association of polymer chains. The free volume theory is used to explain the decrease in glass transition temperature with the addition of plasticizer.[11] Unplasticized PVC is hard and rigid because the motion of polymer chains is limited. The low free volume originates from limited motion of polymer end groups, motion of polymer side groups and internal polymer motions. Addition of plasticizers enables the motion of the plasticizer itself and increases the motion in polymer chains. Below the glass transition temperature such motions are limited, while above Tg the motions increase, which creates free volume. Kinetic and mechanistic theories view the associations between polymer and different plasticizers as transient.[45] The dominating associations depend on the polymer to plasticizer ratio.

Plasticization of PVC with phthalates is possible due to the polar bond between carbon and chlorine which interacts with phthalic ester polar groups and the polar aromatic ring, forming dipole–dipole interactions. Such polymer–plasticizer interactions need to be of comparable strength to plasticizer–plasticizer interactions, otherwise mixing would be unfavourable and lead to migration and leaching of plasticizer.

A decrease of glass-transition temperature from 80 °C to below room temperature can be achieved with the addition of plasticizers.[11] In general, the glass-transition temperature decreases with increasing weight fraction of the plasticizer (Table 1). The relationship is non-linear, but several simplistic functions have been used to predict the glass-transition temperature from known mass fractions and glass-transition temperatures of the starting polymer and plasticizer.[11] Better agreement was achieved by using two different equations, separated by critical plasticizer content. More advanced mathematical models predicting the glass-transition temperature of plasticized PVC have also been developed.[46] The critical plasticizer content is observed as a cusp in Tg vs. weight fraction of the plasticizer and indicates the most homogenous structure of plasticized PVC.[47] Polymer-plasticizer interactions dominate below the critical plasticizer content and plasticizer-plasticizer interactions predominate at higher plasticizer concentrations, which adds to the heterogeneity of the

Table 1: Glass-transition temperatures for PVC with different mass fraction of DEHP. Approximate values summarized from the literature.[11,47]

w (DEPH) [%]	100	60	50	40	35	30	25	20	10	0
Tg [°C]	–80	–60	–50	–20	–10	5	10	25	55	80

blend. In the case of PVC plasticized with DEHP, the critical plasticizer content is ~30 wt. % of DEHP.

Interestingly, an anti-plasticization effect can be observed with PVC mixtures containing less than 15 wt. % DEHP in PVC.[31,48] The small amount of plasticizer rearranges the PVC polymer chains and increases the crystallinity of PVC, which makes it more brittle than pure PVC. The plasticization effect becomes apparent with plasticizer content >15 wt. %. Plasticized PVC is in a rubbery state at room temperature, making it more flexible and ductile. Plasticization also decreases the tensile strength and the density of the plastic.[49]

Since most plasticizers are not chemically bonded to the polymer chain but only mixed with the polymer, the problem emerges due to their migration to the surface and leaching to materials in contact.[50,51] Such migration leads to a loss of flexibility, increased brittleness and eventual cracking.[52]

Migration of plasticizer can lead to physical distortion (shrinking and warping) or increased brittleness of the material.[49] The shrinkage of new PVC sheets decreases with increasing content of dioctyl phthalate plasticizer, because the plasticizer reduces polymer chain entanglements.[53] PVC membranes that experienced plasticizer loss had shrunk.[54] Warping is a result of ductile failure, while crazing and cracking result from brittle failure and are more common at advanced stages of degradation, when more rigid polyene segments are formed.[49]

The fact that the glass transition temperature of PVC decreases with increasing plasticizer content has bearing on the relevance of accelerated degradation experiments conducted at elevated temperatures. Since phase transitions significantly affect reaction kinetics, experiments need to be conducted in temperature intervals in which the examined PVC material is in the same phase as at the conditions of storage and display. This would require either sufficiently low temperatures during accelerated degradation experiments (e.g. <55 °C for PVC with 10% DEHP) or high enough concentrations of plasticizer. There is currently not enough information on how loss or migration of plasticizer affects the Tg, and whether this changes significantly during degradation of the PVC polymer itself.

2. 3. Degradation Processes Involving Plasticizers

Phthalate plasticizers are categorized as semi-volatile organic compounds and their loss depends on the diffusion from the bulk to the surface and evaporation. The rate-limiting process of plasticizer migration at room temperatures and in low air-flow conditions is evaporation from the surface while diffusion from the bulk becomes the rate-limiting step at higher temperatures, in high air flow environments or in vacuum. For PVC-DEHP systems this occurs at 110–120 °C.[55] The rate of evaporation for a given substance depends on the temperature of the substance, its concentration in the air (controlled by its volatility and air velocity) and the surface area.

In a study of PVC tubes exposed to a flow of nitrogen in an oven heated to 100 °C, mass loss became constant and diffusion controlled at flow rates higher than 75 mL/min.[51] At room temperatures and in low air velocity, the loss of plasticizer is controlled by evaporation, so a thin film of plasticizer is present on the object surface.[51,56,57] The layer is saturated with the plasticizer, which slows down the diffusion process from the bulk that is driven by a concentration gradient as described by Fick's law. The loss of plasticizers in such conditions is thought to be independent of plasticizer content and determined mostly by temperature, plasticizer polarity and volatility, flow-rate above the surface and volume of surrounding air.[58] In closed environments with stagnant air, the plasticizer vapour pressure builds up and the evaporation is slowed down.

In a study of accelerated degradation at 80 °C, this resulted in a 5% mass loss after 20 weeks in a closed environment and a 25% mass loss in an open environment.[59] This is in agreement with a study showing that the plasticizer loss rate is three-times higher in ventilated degradation conditions than in closed environments with stagnant air.[60] Accelerated degradation of model PVC sheets by Shashoua also confirmed these observations. The evaporation rate of DEHP was not affected by humidity in studies by Ekelund[51] and by Clausen[61]. Shashoua reported the mass loss was decreased in high-humidity environments, although this could result from water absorption.[57]

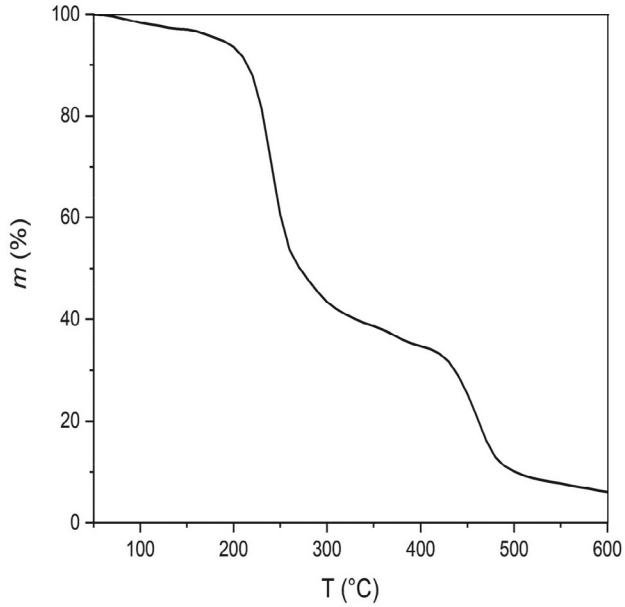


Figure 3: TGA thermogram of PVC. Degradation proceeds in two stages. From 190 to 350 °C elimination of HCl takes place and chlorine is completely removed from the polymer. In the second stage (350–550 °C) conjugated polyenes form benzene, alkylated benzene and crosslink and thermal cracking of PVC's backbone also takes place and a variety of hydrocarbon products are released. Adapted from literature [63,64].

The processes of plasticizer evaporation and elimination of HCl from PVC are difficult to investigate since they occur simultaneously and both result in a mass loss. Evaporation of pure phthalate plasticizer has been studied by thermogravimetric analysis, but it seemed to occur at lower temperatures then in plastisol mixtures with the polymer, due to a lack of plasticizer-polymer interactions and no diffusion present.[62] Many thermogravimetric studies of plasticized PVC are conducted at high temperatures (up to 250 °C), where the mechanisms may not be representative and characteristic for the degradation at room temperatures (Figure 3).

The role of plasticizers and their concentration on the stability of a PVC formulation cannot be overgeneralized. Dioctyl azelate, dioctyl adipate and DEHP were found to linearly increase the stability of PVC plastisols with increasing concentration, while benzyl butyl phthalate, dibutyl phthalate and diphenyl octyl phosphate linearly decreased the stability with increasing concentration.[11] Increasing the plasticizer content causes an increase of the dielectric constant of the material, which correlated to a loss of thermostability. The increased polarity of the medium could increase the elimination of hydrogen chloride. Contrary, plasticizers are believed to decrease the rate of dehydrochlorination due to dilution of the polymer and decreasing the probability of dehydrochlorination.[11] It should be noted that these studies were conducted on PVC plastisols. The effect of different plasticizers and plasticizer concentrations on the stability of PVC objects is unclear. This may be due to the high variety of heat stabilizers and other additives that influence the stability of the final product, which makes the comparison difficult.

Plasticizers are also prone to degradation, which can occur as hydrolysis or oxidation. Phthalate esters are prone to hydrolysis to phthalic acid and emission of alkyl alcohols, which are volatile organic compounds. The hydrolysis is catalysed by acidic conditions, such as the emission of HCl from the degradation of PVC. DEHP can hydrolyse to phthalic acid at acidic or alkaline conditions, which can be visible as white crystals on the surface.[3] In turn, phthalic acid also negatively affects the stability of PVC.[11]

An isothermal approach was taken to determine the loss of DEHP plasticizer from PVC and found it to be a first order kinetic process.[62] The rate constants of volatilization were determined for four different concentrations of plasticizer at different temperatures ranging from 120–150 °C. The rate of evaporation was largely dependent on the temperature. The activation energy and preexponential factor of the volatilization of DEHP were determined with the Arrhenius equation and were found to increase with increasing DEHP concentration in the polymer. Exposure to outdoor conditions can cause the top layer to be exposed to an increased rate of plasticizer evaporation at higher temperatures and photo-degradation, which causes the surface to have different elastic behaviour than the bulk and may cause surface cracking. The concentration dependency of evaporation of plasticizer led to some controversy, where Braun and et al. have shown the relationship not to be linear and having a minimal value based on the chosen plasticizer and possible interactions.[65,66] The highest compatibility of a plasticizer with polymer is designated as the critical concentration, but no studies were found to connect it with the lowest evaporation rate.

To briefly summarize, plasticizers are volatile and semi-volatile organic compounds that can migrate from the bulk and evaporate from the surface of plasticized PVC objects. Temperature, plasticizer volatility, air-low rate and the geometry of the object determine if the loss is controlled by evaporation or diffusion. Plasticizers are also prone to degradation. Phthalates degrade to phthalic acid and alkyl alcohols. The effect of plasticizers on the stability of PVC objects is unclear, as studies of thermal stability are rarely comparable due to vastly different PVC formulations, unknown identities and quantities of other additives, such as heat stabilizers. More studies are needed of the degradation products of stabilizers themselves in order to ensure that these do not represent a conservation risk.

2. 4. Evaluation of Migration of Phthalates

Determination of the total phthalate content in PVC is possible using extraction with hexane, methanol or diisopropyl ether, but migrated phthalates can also be removed from the surface with water solutions of surfactants.[3,11] Surface removal of phthalates can also take place in contact with adsorbent materials, such as polyester/polyamide cloths or low-density polyethylene (LDPE).[57]

FTIR analysis was used to quantify PVC and DEHP on the surface.[67] In the study, model PVC sheets were made from plastisol containing two types of phthalate plasticizers, DEHP and 2,2,4-trimethyl-1,3-pentanediol diisobutyrate (TXIB). Both plasticizers exhibited characteristic C=O bond stretching around 1725 cm^{-1}. For quantification, the concentration of DEHP was determined from a band characteristic for C-H stretching at 2860 cm^{-1}, while the concentration of PVC was determined from a band attributed to CH_2 wagging at 1426 cm^{-1}. The total DEHP concentration of samples was determined by Soxhlet extraction in diisopropyl ether. The results revealed that samples with different bulk concentrations had different surface concentrations.

Samples of PVC tube containing 45 wt.% DEHP were immersed in hexane. The tube was analysed by attenuated-total reflection (ATR) FTIR spectroscopy, which showed that DEHP was removed from the surface.[56] In addition, X-ray photoelectron spectroscopy (XPS) was used to determine characteristic bands in plasticized PVC and to monitor C, Cl and O ratios consistent with the removal of DEHP from PVC tube samples. The outermost surface of PVC tubing was free from plasticizer after 6 min of immersion in hexane.

Internal plasticization of PVC can supress the migration of the plasticizer. In one example, PVC was internally

plasticized with aminated tung oil methyl ester and exhibited no migration of plasticizer.[68] The drawback is that such PVC material is thermally less stable than pure PVC In a different study, di(2-ethylhexyl) 4-mercaptophthalate and di(2-ethylhexyl) 5-mercaptoisophthalate had been prepared an internal plasticizers and were used to substitute chlorine in the PVC chain.[69] Therefore, the migration was stopped entirely and no loss of plasticizer was observed by extraction with heptane in 5 h at room temperature. In addition, although the plasticizing efficiency was decreased when compared to conventional DEHP plasticizer, glass-transition temperatures below room temperature could be reached at higher concentrations of plasticizer. A simpler approach by using a one-pot procedure from trichlorotriazine was used to modify PVC by chlorine substitution. A wide range of glass-transition temperatures were achieved by modification, where long-chain ethers reached the lowest values. Other approaches such as crosslinking and surface grafting have been examined and found to be lacking in thermal stability.[70,71]

Further studies on plasticizer migration, plasticizer degradation and the influence of plasticizer degradation products on the degradation of PVC at room temperatures are needed. The migration of phthalate plasticizer had been observed by FTIR spectroscopy and XPS by observing the surface of PVC objects before and after exposure to different conditions that promote the migration. There seems to be an acute lack of systematic research on the conditions needed for plasticizers to accumulate on the surface of PVC, leading to conservation issues related to cleaning of sticky surfaces.

3. PVC Degradation Pathways

The carbon – chlorine bond in PVC is the principal source of its thermal instability. Due to naturally occurring irregularities in chain structure (such as tertiary or allylic chlorine atom positions) PVC is prone to elimination of HCl (Figure 4). An additional allylic chlorine is formed in the polymer chain, that is prone to further elimination, making it an autocatalytic process described in detail elsewhere.[72,73] Continuous removal of released HCl *in vacuum* can decrease the initial rate of PVC degradation considerably.[74] Due to HCl elimination, a polyene segment is formed in the PVC chain (Figure 4). When 7–11 conjugated bonds are formed, the absorption peak shifts from UV to visible region which is the reason why degraded PVC objects progressively appear yellow, orange, red, dark brown and then black. Conjugated C=C bonds have characteristic IR bands in the range 1585–1625 cm^{-1}.

3. 1. Thermal Degradation of PVC

The seemingly simple elimination process of hydrogen choride becomes quite complex once we attempt to determine at which labile structures the elimination of HCl begins, how these structures are formed, what the mechanism of propagation of polyene formation is and how elimination of HCl is terminated. The initial structural irregularities in the PVC chain form during polymer synthesis. Some characteristic unstable structures, such as allylic chloride, tertiary chloride, carbonyl allyl and head-to-head structures have been considered as possible initiation sites for HCl elimination and are explained in detail elsewhere.[14] Most researchers describe allylic chloride and tertiary chloride as the most important sites for thermal elimination of HCl.[74–76] Allylic chloride can be formed in head-to-head chain growth followed by addition of vinyl chloride monomer, 1,2-chlorine shift and chain-transfer reactions.[14,77] This amounts to an average value of one initial double bond per PVC chain which was confirmed with NMR studies.[14]

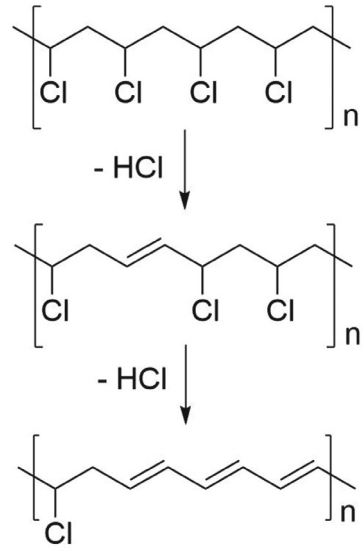


Figure 4: Scheme of elimination of HCl from PVC.

Tertiary chlorides occur at branching points in PVC chains. These can be formed by hydrogen abstraction and reactions with vinyl chloride monomers. An *n*-butyl branch is considered as the main structure containing chlorine bonded to a tertiary carbon. It can be formed by two additions of vinyl chloride monomer, which was confirmed by a ^{13}C NMR study of PVC dechlorinated with Bu_3SnD.[14] In ordinary conditions, the concentration of a butyl branch is 1.0 – 2.4 per thousand monomer units. Starnes et al. have proposed an equation predicting butyl branch concentration in polymers from the temperature and average monomer concentration during polymerization.[78] Certain branch points, such as ethyl branch are stable moieties present in commercial resins.[79]

Thermal elimination of HCl at allylic and tertiary chlorides proceeds in an ionic or quasi-ionic manner.[80–82] According to Bacaloglu, the elimination of HCl occurs in a single step, via a four-centre transition state (Figure 5).[83,84]

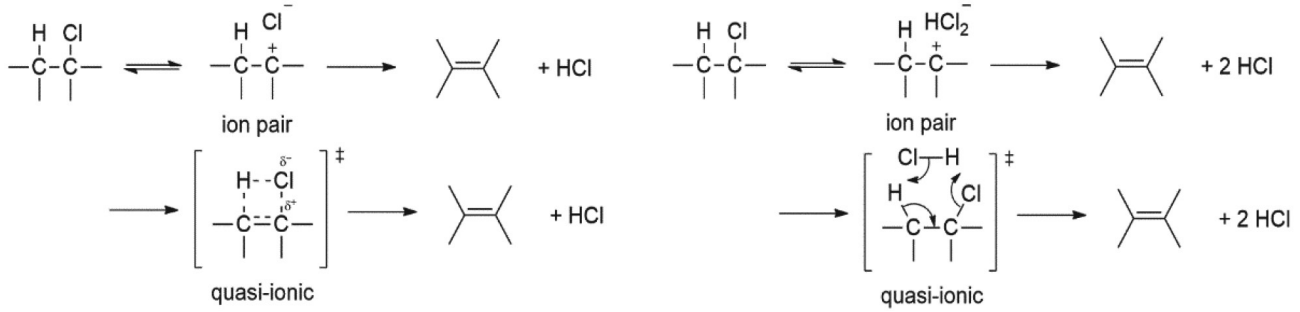


Figure 5: Elimination (the left schemes) and autocatalytic elimination (the right schemes) of HCl by an ion pair and quasi-ionic mechanism. Adapted from literature[14].

The evidence for the ionic manner of elimination of HCl at allylic and tertiary chlorides was gathered from determination of reaction rates of model compounds taking into account their structure and reaction conditions.[76] The C-Cl bond energy of allylic chlorides is 58 kcal/mol, while the bond energy of a tertiary chloride is 67 kcal/mol.[85] Investigation of reaction rates of allylic and tertiary chlorides at different concentrations of HCl demonstrated that allylic chlorides are more susceptible to HCl catalysis than tertiary chlorides, but the elimination of HCl from tertiary chlorides occurs at a higher rate than that of allylic chlorides at low concentrations of HCl.[86] The rate of HCl elimination increased linearly with the concentration of tertiary chlorides in PVC but had no correlation with the concentration of allylic sites.[87] Additionally, the ionic mechanism is supported by the increase of reaction rates with increasing solvent polarity.[88] During thermal reprocessing of waste polymer conjugated double bonds are formed, which further decreases the thermal stability.[89]

Bacaloglu and Fisch were investigating the degradation of unplasticized PVC by TGA, ^{1}H-NMR, ^{13}C NMR and UV/Vis spectroscopy.[83] Elimination of HCl was confirmed to be the main degradation pathway for temperatures up to 200 °C. Condensation of double bonds and crosslinking were only minor processes. Elimination of HCl was monitored continuously with a conductivity cell and proceeded as a two-stage process. First, a faster elimination of HCl occurred from structural irregularities (allylic and tertiary chlorine) with a lower activation energy for conversions under 0.1%. When those were exhausted, elimination of HCl occurred at random from regular monomer structural segments with up to 2–3% conversion.[83] Structural irregularities were found to be significant only for low conversions and the majority of HCl elimination occurred randomly from regular monomer units. UV/Vis spectra of PVC in THF analysed with empirical equations revealed that relatively short polyenes ($n < 8$) are the most common and the longest polyene was 25–30 double bonds long.

Simultaneous measurements of HCl emission by conductometry and the formation of polyenes by Raman spectroscopy were performed for the degradation studies of PVC films at 171 °C.[90] A polyene with 14 conjugated double bonds represented the formation of long polyene sequences and was chosen by selecting wavelength of Raman excitation. It was shown that the number of polyenes n=14 rapidly increased in the first 30 min, while the emission of HCl continued. At a degradation level of 0.1% HCl elimination, the number of polyenes n=14 reached a plateau value. The value was lower at higher degradation temperatures and higher oxygen pressure. During cooling, the number of polyenes doubled but no additional HCl was emitted. This suggested that longer polyenes may undergo consecutive reactions, oxidize or cross-link.

Other structures and mechanism have been proposed as possible reasons for PVC instability. Some research concluded that carbonyl allyls are responsible for the degradation of PVC by forming furanoid moieties.[91] There is no strong evidence for the presence of such structures in commercial PVC. The degradation of PVC involves free radicals, as shown by ESR spectroscopy.[92] The initial elimination of HCl does not proceed via a radical mechanism due to non-selective reactivity of a chlorine radical in hydrogen abstraction and high concentration of non-allylic hydrogens. The detected radicals are most likely degradation products. When the degradation reaches a point with sufficient levels of polyenes and HCl, polyenyl cation radicals are formed. They degrade autocatalytically by abstraction of a methylene hydrogen and β-scission to form new allylic chloride initiation sites.[15] A source of these radicals may be a residual initiator or excitation of polyenes. A six-centre mechanism involving isomerization and elimination of HCl from *cis* chloroallyl structures has been proposed by Bacaloglu but Starnes thought it improbable due to slow isomerization of allyl chlorides as shown in a reactivity study of model compounds.[83] Termination of continuous dehydrochlorination may include cyclization, leading to the formation of aromatic compounds and monoalkylcyclopentane structures, detectable by ^{13}C NMR.[14,77]

3. 1. 1. Influence of Isomerism and Crystallinity

Additionally, isomerism of PVC influences the mechanism of its degradation. A polymer can be organ-

ised into three configurational structures: isotactic, where all chlorine atoms are on the same side of the chain; syndiotactic, where the positions of chlorine atoms alternate; and atactic, where chlorine atoms are distributed randomly. The lower is the processing temperature of PVC formation, the higher is amount of syndiotactic sequences. Among these, the atactic form of PVC is amorphous, while isotactic and syndiotactic forms can crystallize. The syndiotactic sequences are usually short but enable strong forces between chains to induce crystallinity. They are also thought to cause the antiplasticization effect.[93] Bonding amongst chains is increased in syndiotactic segments, so free volume and chain mobility are decreased. Initially, it was thought that syndiotacticity increases the dehydrochlorination rate, but it was proven that tacticity does not directly affect dehydrochlorination.[94] Commercial PVC, polymerized at 50 °C, has about 30% syndiotactic sequences, that are 5–6 units long and around 5–10% crystallinity[95], so the majority of PVC objects in heritage collections are likely similar.

Chain length, branching, chain folding, and chain entanglement affect polymer properties, such as viscosity and shape memory, UV and thermal stability by affecting the crystallinity of the material. Chartoff identified three IR bands in the C-Cl stretching region, specifically 610(615), 635 and 690 cm^{-1} as useful for indicating crystallinity and the ratio of A_{635}/A_{610} was used for determination of crystallinity.[96] In more recent studies, bands at 604, 635 and 1427 cm^{-1} are considered to represent crystalline regions while bands at 615 and 1435 cm^{-1} are considered to represent amorphous regions.[97–99]

The presence of crystalline regions in the material can be observed by DSC as a sharp endothermic peak at temperatures 100–200 °C. Crystallinity affected the physical degradation of PVC.[100] The influence of plasticization on crystallinity is not clear.[101,102] It is believed that degradation at temperatures below the Tg affects only the amorphous regions.[103] Some studies show that the degree of crystallinity decreases with increasing plasticizer content.[104] Other studies imply that plasticizer does not change the crystalline domains because it cannot penetrate them and does not affect the crystallinity of the material.[105] The crystallinity regions in the material are dependent on the plastic's thermal history. During annealing the material is heated to elevated temperatures and cooled down to reduce moulded stress.

Heating and cooling rates influence the crystallinity of the material as slower cooling allows more time for PVC chains to reach an equilibrium state and crystallize. A study investigated the effect of thermal degradation temperature on the melting temperature of crystalline PVC in plasticized PVC.[106] The degradation was carried out at different temperatures below Tg (23, 40, 60 °C) or at 100 °C for up to 45 days. The melting temperature of crystalline PVC (a sharp endothermal peak at 100–200 °C) was observed after only 7 days of degradation at 40 °C and 60 °C, but not for degradation at 23 °C nor 100 °C. The melting temperature was increasing with the degradation time for degradation at 40 °C and 60 °C. This indicates that exposure to elevated temperature below Tg allows the chains in the amorphous region to reorganize and form crystalline domains, but the process is generally slow. Degradation above 100 °C is already in the region of melting crystalline PVC. The higher degree of crystallinity reduces the free volume and increases the specific density of the material.

Elimination of HCl creates sequences of polyenes, which may be subjected to geometrical *cis-trans* isomerism. The degradation of PVC by elimination of HCl leads to the eventual formation of all-*trans* polyenes.[107] In general, the *trans* form is thermally more stable than the *cis* form. A spectrophotometric investigation of *cis/trans* isomers of polyacetylene revealed that the *trans* form is red in colour, while the *cis* form is blue.[108,109] The degraded PVC first turns yellow and then red and brown, which is in agreement with the characteristic red colour of the *trans* form. The degraded all-*trans* isomer becomes more rigid and less flexible.

3. 1. 2. Impact of Heat Stabilizers and Object Geometry

Barium, calcium, cadmium and zinc salts of long-chain aliphatic acids, such as stearates, are commonly used as heat stabilizers in PVC material.[98,110] Organotin compounds and lead salts were historically used in great extent.[1,111] Heat stabilizers react with HCl and form metal chlorides. Calcium, barium and other alkaline metals form stable chloride salts, that do not accelerate the degradation of PVC even in the form of partially reacted calcium or barium stearates.[112] On the contrary, stearates of aluminium, cadmium, zinc and antimony were found to accelerate the elimination of hydrogen chloride.[113–115] Tin stabilizers can help reduce the rate of elimination by additionally forming stabilizing coordination complexes and chlorine exchange reactions[116], but $SnCl_4$ and $RSnCl_3$ were found to increase the elimination rate and cause the material to fail.[111]

It was demonstrated that the rate of HCl elimination decreases with an increase in the surface-area-to-volume ratio, because diffusion of the evolved HCl reduces its concentration in the polymer, and surface degradation is no more intensive than in the bulk.[72] PVC films of varying thicknesses were prepared and exposed to temperatures 150–190 °C. The HCl produced takes longer to diffuse through thicker samples, so that the dehydrochlorination rates are higher due to more effective autocatalysis. It was shown that the dehydrochlorination rate of previously degraded samples increased. The study was carried out at high temperatures, and it remains to be seen whether the observed increase of degradation in thicker samples is also valid for degradation at room temperatures.

3. 1. 3. Consequences of Thermal Degradation

Thermal degradation of plasticized PVC results in the emission of plasticizer and elimination of HCl. These processes do not occur in the same timeframes as is graphically presented in the Figure 6. The emissions of plasticiser are intensive immediately after the production of PVC and then remain more or less constant (depending on storage conditions). Degradation is not directly related only to the intensity of dehydrochlorination as suggested by the studies described in the previous Sections. Elimination of HCl gradually increases as new dehydrochlorination sites form, and reaches a maximum. During advanced stages of degradation the chlorine sites become exhausted and production rates of HCl decrease.

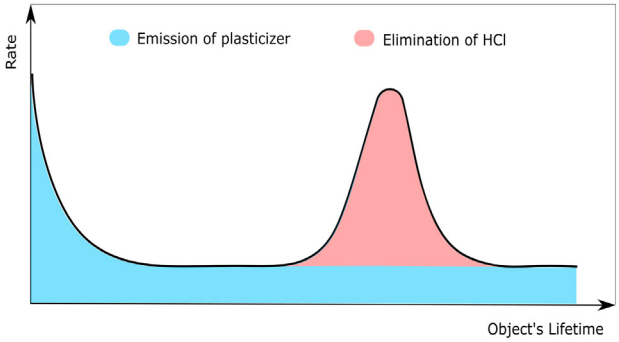


Figure 6: A schematic presentation of hypothetical emission and elimination rates during the lifetime of a PVC object.

Although experiments at elevated temperatures suggest that HCl evaporates from the material, it is not clear if this is significant at temperatures close to room temperatures. PVC has some affinity for water and may absorb up to 1% of water upon immersion.[117] With at least some water present in the material it is therefore possible to assume that HCl, being a strong acid, is mostly dissociated, or that weak acids are preferentially protonated and emitted from the material, e.g. plasticizer degradation products. This could explain why elimination of HCl has not yet been observed at room temperatures and may not be a significant conservation risk, as further discussed in Section 4.2. However, more research is needed to understand these processes better.

3. 2. Mechanical Instability of PVC

Plastic structures are exposed to continuous stress at joints, beams and hanging supports. Plastics under constant stress eventually permanently deform, which is described as creep deformation. Even if such stress is below the yield-point, localized molecular disentanglement can occur at stress-points.[118] Time and temperature act similarly and can lead to creep rapture as brittle or ductile failure. The time of failure can be predicted with dynamic mechanical analysis based on time-temperature equivalency.[119]

The effect of pollutants such as ozone, nitrous oxides and hydrocarbons on the degradation of PVC was also studied.[120] Exposure to atmospheric ozone for 15 months caused the biggest deteriorating effect. Initially, oxidation products were observed on the surface of samples with FTIR and UV/Vis spectroscopy, but the samples still retained their hardness. Further exposure to ozone caused chain scission and accelerated the elimination of HCl and formation of polyene sequences. The effect of NO and NO_2 was not as pronounced.

Ito and Nagai studied the degradation of plasticized PVC under accelerated degradation conditions.[121] PVC sheets were prepared by blending PVC with DEHP, carbon black, $CaCO_3$ and a stabilizer and moulding to 1 mm sheets. Weathering using exposure to xenon light, cyclic spraying with distilled water at elevated temperature of 63 °C, as well as thermal degradation (at 100 °C in a ventilated oven) were used. Degradation was followed by measuring mechanical properties (tensile strength and dynamic properties), SEC, pulsed NMR and DEHP content. The number average molecular weight M_n did not change under weathering conditions nor under thermal degradation. At weathering conditions, some inorganic additives were removed from the surface, creating voids that were visible under a microscope. Plasticizer concentration was determined by Soxhlet extraction and GC-MS analysis. A higher loss of plasticizer content was observed in the weathering test than during thermal degradation due to the plasticizer being washed out during spraying cycles. The decrease of DEHP content during the thermal degradation conditions was due to evaporation.

Some studies of PVC degradation involve SEC. Loss of mechanical properties of 10-year-old PVC exposed to sunlight was evaluated.[122] SEC measurements showed an obvious decrease of the weight average molecular weight M_w from M_w=91.702 g/mol and the polydispersity index, given as the ratio M_w/M_n, M_w/M_n=2.27 for the reference PVC to M_w=13.847 g/mol and M_w/M_n=15.7 for the degraded PVC. A study of high-dose gamma radiolysis of PVC showed a strong decrease in molecular weight of PVC dissolved in THF, reported as polystyrene equivalent.[123]

3. 3. Photodegradation of PVC

Thermal elimination of HCl and plasticizer migration are the major degradation pathways for PVC kept indoors at room temperature, although it may also degrade due to oxidation[124], photooxidation[125,126], or radiolysis[123]. Objects used outdoors are exposed to UV light causing photooxidation. Such degradation may not be directly relevant to degradation in museums, but understanding it is useful for preventing further damage.

Although the PVC structure contains C-H, C-C and C-Cl bonds, which are too strong to be broken directly, it is known that PVC does degrade on exposure to sun-

light.[127] Absorption of UV radiation can occur due to chromophore impurities (carbonyl groups), presence of sensitizers (benzophenones, hydroquinone, …), organometallic compounds, thermal stabilizers forming metal chlorides, metal oxides (TiO_2, Al_2O_3), and fillers.[128] Impurities catalyse photodegradation by forming radicals. Photooxidation causes the formation of conjugated double bonds, carbonyl compounds, and chain scission.[129] Monochromatic radiation was used to study the changes in absorption of rigid PVC from 280 nm to 500 nm.[130] It was shown that the sensitivity of PVC decreases with increasing wavelength. Wavelengths from 280 nm to 340 nm caused the samples to become yellow, but irradiation at 400 nm and 500 nm had a photobleaching effect.[131] Photooxidation causes short polyenes to form, which absorb light at wavelength below 400 nm. Exposure to sunlight caused yellowing to appear with a delay, if the objects were stored in the dark after irradiation. Short polyene segments underwent thermal isomerization and started to absorb wavelengths above 400 nm, giving them a yellow appearance. By exposing them to 400/500 nm, yellowing reversed as the polyene segments isomerized. Higher pressure of oxygen promotes oxidation which causes ozonolysis of double bonds with no yellowing. This is observed in older PVC formulation, but PVC intended for outdoor use contains TiO_2, which prominently decreases yellowing.[132]

4. Properties Relevant to Conservation

Research investigating the properties of PVC objects relevant to conservation has been organized in three subsections. Firstly, studies on the topic of colour change of PVC objects during ageing are discussed. Secondly, studies of emissions of hydrogen chloride and volatile organic compounds relevant to the conservation of heritage collections are gathered. Lastly, studies encompassing a broader variety of analytical techniques investigating natural and accelerated degradation are presented.

4. 1. Colour

The most common method for the determination of apparent colour change of objects is spectrocolorimetry. Colour coordinates using CIELab, XYZ or RGB colour systems can be calculated, either in transmission or reflectance mode. CIELab colour space uses L* for lightness (black to white), a* for green to red and b* for blue to yellow as the three coordinates to describe the perceived colour. It is more perceptually uniform than the XYZ colour space. The difference between two colours (CIELab ΔE_{2000}) can be calculated from the differences in the measured L*, a*, b* values. In general, $\Delta E_{2000} = 1.5$ is considered a threshold of perceptible change in colour.[133]

PVC discolouration is related to the formation of conjugated polyene segments in PVC chains. The degradation of PVC is apparent as objects become visibly yellow, brown or in some cases pink (Figure 7), if the formulation contains TiO_2 and lead stabilizers.[57,59,134,135]



Figure 7: Discolouration of PVC objects.

A systematic approach to examining absorption spectra of polyenes with increasing number of conjugated double bonds *n* was carried out by Daniels and Rees.[136] The values for absorption maxima and extinction coefficients were gathered and used as linear combinations to determine an approximate concentration of each polyene in a sample. A visible colouration appears when at least 7 conjugated double bonds are present. Since degradation leads to polyene segments varying in length, the absorption spectra of which contain multiple maxima, the cumulative absorption spectrum is broad. A study of conjugated alkenes with UV/Vis spectroscopy revealed that an average increase in the wavelength of the absorption maximum of 30 nm per each additional conjugated double bond is observed for up to 6 conjugated double bonds.[137] The Lewis-Calvin equation is based on empirical data and describes the square of the wavelength of the absorption maximum of polyenes being proportional to the number of conjugated bonds.[138] Additionally, it has been shown that the extinction coefficient of polyenes increases linearly with *n*. The shape of the absorption spectra is affected by the substituent effect, the solvent effect and *cis*/*trans* isomerism. In general, *trans* isomers absorb at longer wavelengths.

Describing the extent of PVC degradation based on apparent colour change as a simple 'colour scale' was designed in 1971 by Ocskay et al.[139] The scale had 11 levels and was based only on the darkening of the material evaluated by visual comparison, which is too imprecise and prone to human error for systematic studies of degradation. Hollande and Laurent used spectrophotometry to study the changes in absorption for plasticized and unplasticized PVC films during exposure to UV light.[140] Pure DOP and PVC films with or without DOP were prepared and degraded under a UV lamp at 50 °C. The

absorption bands between 250 and 500 nm kept increasing with exposure time. In addition, it was shown that plasticizer contributes to the increase of absorption and discolouration as well. In a different approach by Wijdekop et al., reflectance spectroscopy was examined as a tool for monitoring colour change of a PVC coated steel strip.[141] The intensity of HCl elimination was quantified by calculating the difference in surfaces of spectra taken before and after photodegradation. As the PVC samples continued to darken under UV light, the reflectance across the whole visible region 400–700 nm kept decreasing.

Apart from using spectroscopy and colour models for investigating changes during degradation, changes in optical density due to darkening are also of interest. Such an approach was used by Shashoua to determine the darkening of model PVC sheets.[57] A blue filter was used to determine yellowing from accelerated degradation. Sheets with lower DEHP concentration exhibited increased yellowing compared to sheets with higher DEHP concentrations. Additionally, the effect of different sorbents on the discolouration was tested. All sorbents had a significant effect on the discolouration. It was observed that silica and active charcoal initiated a more intensive change of colour.[57,67] It is important to remember that colour change is guided by many simultaneous processes driven by the composition of an item, as well as its exposure to heat, light and pollutants.

Pastorelli et al. investigated the colour change of 17 different polymeric materials at different conditions, with variables such as temperature, relative humidity, concentration of NO_2 and ozone being continuously measured.[134] PCA was used to determine the most important variable. NO_2 concentration and exposure to light had the most pronounced effect on discolouration. A previously mentioned study[120] found ozone to cause the most deterioration. The different conclusions are likely the result of different experimental set-ups. Pastorelli's study was carried out by monitoring the variables in sheltered conditions, while Belhaneche-Bensemra's study compared accelerated ageing to natural ageing at outdoor conditions without shelter.

Different approaches to quantifications of colour change have been used in studies of PVC degradation. Observing the degradation through a colour change is especially useful for objects of heritage value, because the technique is both non-destructive and fast.

4. 2. Emissions

Headspace analysis is a non-invasive sampling technique that enables identification of characteristic emissions from PVC objects. Hydrogen chloride is the main degradation product of PVC polymer, on the other hand emissions of VOCs are related to used additives, mainly plasticizers.

PVC degradation can be monitored by the determination of the amount of the released volatile HCl. Complete elimination of HCl would result in 58.3% mass loss for pure PVC. As a polar volatile compound, HCl, the main degradation product of PVC, can be trapped by silica gel and other molecular sieves, however, these are not suitable for sampling in high relative humidity.

There are different approaches to determination of the formed HCl. The ISO 182 standard prescribes a qualitative method using an oil bath at 180/200 °C to heat the investigated material in a glass tube and collect the acidic emissions on a wetted indicator paper.[142] This may be useful for identification, although not for objects of heritage value. Another approach is to heat the test material at 180/200 °C in a gas stream to absorb the formed HCl into a trapping solution. This can be demineralized water for potentiometric measurements or measurements of conductivity.

Most studies of hydrogen chloride emission from PVC have been carried out at high temperatures because such processes are relevant for incineration, pyrolysis and waste management. During this literature review no studies investigating the emission near room temperature were found. It is expected that the rate of dehydrochlorination at low temperatures is orders of magnitude lower than in studies discussed previously. Experimental limitations such as long sampling times and working with concentrations near detection limits occur. Long sampling times can lead to experimental error when using sorbents or liquid traps. Sorbents may contain impurities that make quantification difficult.

The degradation products of plasticizers are usually more volatile and categorized as semi-volatile organic compounds (SVOCs). The emissions of VOCs can be sampled actively or passively by using solid sorbents, e.g. solid phase microextraction (SPME) fibres, or liquid traps. Determination of characteristic VOC emissions from PVC objects is commonly carried out with headspace analysis followed by chromatographic separation, such as GC-MS analysis for the identification and/or quantification.

Determination of VOCs from newly produced commodity PVC is commonly performed in the course of emission testing, e.g. flooring materials and other products. Lundgren et al. determined the total VOC (TVOC) emissions rates from newly manufactured PVC flooring materials using a FLEC cell (Field and Laboratory Emission Cell), as used for emission testing on planar materials and coatings.[143] New PVC materials released hydrocarbons from pentane to octadecane, 2-(2-butoxyethoxy)ethanol, butoxyethanol, cyclohexanone, 2-ethylhexanol, 2-ethoxyhexanol, 2-ethylhexanoic acid, phenol, trimethylbenezene, diethylbenzene, toluene and *N*-methyl-2-pyrrolidone. The emission rates of PVC flooring were in the range of 100–500 μg TVOC/m^2h after 4 weeks since production and in the range of 50–200 μg TVOC/m^2h after 26 weeks since production. For many flooring

materials, the emission rate decreased to less than half in 4 to 26 weeks following production.

Carlsson et al. have exposed PVC to accelerated UV degradation.[144] Volatiles released during and after the experiment were identified. Using SEC, a decrease in the average molar mass of PVC was determined during the experiment, while the volatiles were collected on a series of two thermal desorption tubes. The first tube was packed with Carbotrap and the second one with Carbosieve S. The powdered samples were placed into Pyrex tubes and inserted into a modified inlet system at 80 (or 120) °C for 1 (or 3) min to desorb volatile compounds remaining after UV irradiation. Butan-1-ol, di-butyl ether and methyl methacrylate were present in non-degraded samples while UV exposure led to the formation of various chlorinated species, such as 1-chlorobutane, 1,2-dichlorobutane, 1-chloropentane and 1,1-dichloropropan-2-one. The obtained results were in accordance with investigations on outdoor-weathered PVC surfaces. The released HCl was continuously monitored using a conductivity cell and gravimetric determination after precipitation with $AgNO_3$. XPS analysis of the surface revealed that degraded samples were highly oxidised, with elevated oxygen and deficient chlorine levels.

VOCs released from a general collection of heritage plastics have been examined to determine their effect on the stability of other heritage objects by Mitchell et al. in 2013.[145] VOC and SVOC were collected from plastic objects using a micro-chamber/thermal extractor at 23 °C or 70 °C for 1 h to Tenax TA tubes and analysed using thermal desorption in combination with GC-MS (TD-GC-MS). The emissions from PVC samples at 23 °C were non-specific VOCs, present in many polymers and were not suitable to distinguish PVC from other plastics: dibutylhydroxytoluene, decanal, nonanal, benzaldehyde, styrene, 1,3-dimethylbenzene, ethylbenzene, TXIB plasticizer and diethyl hexanolacetophenone. After heating to 70 °C, the emissions were more intensive and benzene, toluene, nonanal, nananoic acid, decanal, decanoic acid and isopropylbenzene were detected in addition.

A study of VOCs from PVC films by headspace SPME-GC-MS identified 2-ethylhexanole, nonanal, hexanal, heptanal, m-xylene and chlorobutane as the main compounds.[146] Plasticized PVC sheets were heated and the emitted VOCs were trapped by Tenax GR sorbent before analysis by GC-MS to identify phenol, 2-ethylhexanol, octadecene, triphenyl phosphate and DEHP.[147]

A study by Curran et al. used VOC analysis to classify museum artefacts by type and extent of degradation.[148] SPME GC-MS analysis of samples made of PVC and other plastics found in collections was carried out following degradation at 80 °C and 65% relative humidity for up to 10 weeks. 2-ethylhexanol emission from PVC samples was shown to increase up to two weeks into the process of accelerated degradation and remained at that level for the following 8 weeks.

4. 3. Survey of PVC Degradation in Heritage Collections

Historic polymeric samples from a private collection were analysed by ATR-FTIR spectroscopy and identified successfully by band assignment, a suitable method for characterizing unknown polymers in heritage collections. Principal component analysis (PCA) was tested to classify unknown samples with moderate success.[149] Cellulose acetate, cellulose nitrate, polycarbonate and polyurethane foam samples were successfully recognised, while polystyrene, rubber, polyvinyl chloride, polyethylene and polypropylene were not. Terahertz time-domain spectroscopy (THz-TDS) is a novel spectroscopic technique that was used for characterization of historic plastics.[150] THz-TDS spectra could reflect long-chain vibrations and vary for different polymers but exhibited no features immediately useful for identification. THz-TDS could also not be used to detect plasticizers in PVC.

A study of PVC degradation included accelerated degradation and comparison of possible conservation methods for storage of PVC objects.[67] PVC model sheets were kept in different environments and degraded for 65 days at 70 °C, after which the mass loss was examined.[57] The mass loss was attributed to loss of DEHP plasticizer. The least amount of mass loss was observed in sheets degraded at high relative humidity, in a freezer at –20 °C or in a closed environment. It is possible that mass loss by accelerated degradation in high-humidity was deceivingly low due to simultaneous water uptake and DEHP loss, since studies have shown that DEHP loss is independent from humidity.[51,61] The highest loss of mass was observed when PVC sheets were degraded in an open environment or stored in LDPE bags, which are capable of absorbing DEHP from PVC sheets, making them observably stiffer. The highest DEHP loss was observed in the first 7–10 days of accelerated degradation in open environment and 14 days in closed environments. Accelerated degradation at high relative humidity environment caused the sheets to turn opaque. After returning them to normal conditions, the transparency was mostly recovered. No change in optical density was observed for degradation in a closed environment. Discolouration occurred during degradation in the presence of sorbents and for samples stored in a LDPE bag, and was the highest for sheets with lower concentrations of DEHP. Degradation with silica gel or activated carbon in the closed container led to higher discolouration and development of darker spots on the sheets. Low-vacuum SEM mapping of chlorine and oxygen allowed visualisation of PVC and DEHP on sheets. It appeared that a thin DEHP layer was present on all model sheets containing more than 33 wt. % of DEHP by bulk. Sheets with lower bulk concentrations were homogenous in composition.

An investigation into cold storage revealed that while the rate of chemical degradation (elimination of HCl) is reduced, physical change, such as shrinking and brittle-

ness may lead to degradation if the process of cooling is too rapid.[151] Gradual cooling and heating are essential to avoid degradation. In another study, dolls made of plasticized PVC were kept in cold museum storage for 10 years, with the average temperature of 11 °C and temperatures ranging from 7 °C to 16 °C during the year. After inspection, the dolls appeared to have a white waxy substance covering their plastic parts.[152] The bloom was identified as stearyl alcohol by ATR-FTIR, which is not a common additive for plasticized PVC. It was independent of the plasticizer and exuded due to reduced compatibility with PVC at low temperatures. The stearyl alcohol was reabsorbed into the dolls after keeping them at room temperature.

Yellowing and surface cracking of PVC due to photooxidation was investigated with spectrocolorimetry and microscopy.[153] During the degradation, PVC turned darker and more yellow. In addition, the scratch hardness of degraded PVC increased while indentation hardness had decreased according to micro- and nanoindentation tests. The indentation hardness may have decreased due to chemical changes in additives, such as the reaction of calcium carbonate with hydrochloric acid. Micro-scratching is relevant for assessing possible damages during an object's transportation. FTIR spectroscopy revealed that hydroperoxides and polyenes are formed during the photooxidation. This was in line with the observed surface embrittlement.

A more recent study by Royaux showed that the loss of plasticizer and yellowing of PVC can be slowed down significantly by keeping the item in a closed container, as demonstrated with TGA and ATR-FTIR measurements.[59] 30-year-old PVC samples, stored at museum conditions, were investigated. Accelerated degradation was carried out in a temperature cycle of 80 °C for 2 days and 25 °C for 1 day at 65% relative humidity in open and closed containers. Yellowing was measured as Δb^* and reached values of 10 and 14, after 12 weeks of degradation in closed and open environment, respectively. Degradation was also noticeable as an increase of absorbance by UV/Vis spectroscopy but ATR-FTIR could not be used to detect any changes. The study found that plasticizer migration proceeded in a diffusion-controlled manner. In addition, surface cleaning and removal of exuded plasticizer had no negative effect on the kinetics of PVC degradation, retaining its appearance.

A study compared naturally degraded 15- to 30-year old PVC samples to degradation in locations with hot or cold environment with accelerated photooxidative degradation.[154] TGA was used to determine the plasticizer content of samples by measuring the weight loss at 400 °C. The mass loss until 400 °C, due to the loss of DEHP plasticizer and dehydrochlorination, can be used for calibration to determine the plasticizer content of unknown PVC samples. Loss of plasticizer was found to be the main process for naturally degraded samples. An increase of porosity was observed as well. Upon exposure to water, lead salts were released from the cables. Photooxidative degradation was observed as an increase in absorption at 1720 cm^{-1} by IR spectroscopy. Accelerated degradation at 140 °C resulted in an increase of the molecular weight due to cross-linking reactions. The authors concluded that the exposure to different outdoor environments and conditions of use significantly affected PVC's properties, so there was no point in having a general kinetic equation describing the differentdegradation mechanisms.

The cross-infection effect of historic and heritage polymer artefacts was tested by measuring the degradation of cellulose reference test material.[29] Degrading polymers emit compounds, such as acetic acid from cellulose acetate[155], NO_2 from cellulose nitrate[156] and as often assumed, HCl from PVC, and these may cause degradation of materials kept nearby. The cross-infection effect of 14 polymer types was tested by exposing them to a reference paper of pure cellulose in a sealed vessel for 14 days at 80 °C. After the exposure, the impact of VOC emissions was determined by the change of the degree of polymerisation of cellulose. The headspace above plastic samples was also investigated by SPME-GC-MS analyses. Cellulose nitrate exhibited the most severe cross-infection effect, followed by specific samples of cellulose acetate, polyvinyl chloride and polyvinyl acetate copolymer, polyethylene and polypropylene. Polyvinyl chloride, polymethylmethacrylate and phenol formaldehyde had a neutral cross-infection effect. The main emissions of PVC were found to be 2-ethylhexanol, 2-ethyl acetate, 2-ethyl hexanal, methyl methacrylate and butyl 2-methyl-2-propenoate, which are degradation products of commonly used plasticizers, however, potential emissions of HCl were not measured.

Plastics are also popular construction materials for display cases, storage and transportation in museums. Oddy testing is an established method for evaluating the suitability of materials used in museums to assess risks to objects in collections due to emissions of VOC from materials on selected metals: silver, lead and copper.[157,158] Evolved gas analysis (EGA) coupled to GC-MS was used to detect VOC emitted from common polymeric materials.[159] 3-Nonene, p-ethyltoluene, α-methylstyrene, 2,3,6,7-tetramethyloctane, 2,6-dimethyloctane, 5-ethyl-2,2,3-trimethylheptane and 2-phenyl isopropanol were emitted from PVC powder. Plasticized PVC is generally not recommended for use in museums due to migration of plasticizer and HCl emission. Rigid unplasticized PVC boards, sometimes used in construction of gallery cases, pass the Oddy test as no signs of corrosion on metals are observed.[160] The previously-described study of cross-infection effect is in agreement with these results. EGA-GC-MS was proposed as a fast alternative to Oddy testing. The analysis reported the emission of 2-ethyhexanol, 4-chlorooctane and 2-ethylhexyl thioglyconate, which is a by-product of organotin heat stabilizer.[161] However, EGA-GC-MS detects VOCs emitted at high temperatures, and it may not be representative of normal conditions of use.

Heritage objects are sometimes stored by wrapping. Silk, LDPE and polyethylene terephthalate (PET) were tested as wrapping materials for the storage of old and model PVC films.[162,163] Bulk and surface properties were measured during accelerated degradation of PVC with different wrapping materials. Colour change was the most significant for PET, followed by LDPE. Silk paper affected neither discolouration nor the rate of degradation. Migration of DOP plasticizer from PVC sample to LDPE was observed as an increase of mass for LDPE and as the presence of characteristic absorption bands by FTIR spectroscopy on LDPE. PVC stored in PET showed a presence of phthalic acid from DOP degradation, not present in other cases of storage.[163]

Museum objects need regular care and maintenance to prevent the accumulation of soiling. Cleaning of PVC objects can be carried out using solvents or dry-cleaning methods. Water, detergent solutions, alkaline solutions, polar and non-polar organic solvents (ethanol, iso-propanol, heptane), aqueous-organic mixtures, detergents and alkaline solutions have all been used.[59,164–166] A study evaluated cleaning of undamaged and of photodegraded plasticized PVC objects by ATR-FTIR spectroscopy. Pure organic solvents were found to be unsuitable for cleaning undamaged and photo-degraded PVC objects, because of plasticizer extraction. Cleaning with deionized water, and mixtures with small proportions of organic solvents, a KOH solution and a commercial detergent was found suitable.[164] The study used FTIR spectroscopy, however, this may not be sensitive enough for the detection of small changes in the surface. Optical microscopy and non-contact profilometry were used to evaluate the cleaning efficiency and found aqueous solutions of KOH to be too aggressive for conservation and a commercial cleaning liquid was found more appropriate.[165] FTIR, colorimetry, profilometry and optical microscopy have been used for evaluating the efficiency of soiling removal using dry cleaning.[59,166] Cotton swabs were the least suitable for removal of dirt particles, because they changed surface topography by producing ridges, and caused the plasticizer to migrate to the surface.[166] PEL cloths from polyester/polyamide fibers created a slightly rougher surface but were considered the safest dry-cleaning materials, because dirt is removed due to static cling.

The degradation of plastic objects in museums does not result solely in the loss of integrity and value of the object itself but can lead to deterioration of objects in its vicinity due to the emission of harmful substances e.g. acidic gasses. Organisation of collections by plastic type may thus be a suitable strategy for successful preservation and storage of plastic objects.

Studies of the accelerated degradation of PVC below 100 °C are rare. So far, Shashoua's[57] study was carried out at 70 °C and Royaux[59,163] carried out two studies with a temperatures fluctuation at 65 °C for two days and at 25°C for 1 day. Investigations of natural degradation of PVC objects in different outdoor environments and comparison with accelerated degradation at higher temperatures can be problematic as processes of degradation can be different. Accelerated degradation is suitable with the assumption that the activation energy of the reaction remains the same when extrapolating to room temperature.[167] Difficulties arise, whether even studies performed at 50 °C cannot correctly describe the ongoing processes of degradation. Table 1 shows that the glass-transition temperature of PVC objects with 20 wt. % of DEHP is 25 °C, so a transition occurs above this temperature. Because it is accompanied by changes in physical properties, a change in the activation energy of the degradation is expected. A relatively well-understood example relevant to heritage is degradation of paper, where one reaction dominates at temperatures <100 °C, while the other predominates >100 °C. Therefore, the investigations of paper stability should be carried out at temperatures below 100 °C. [25,168] A similar understanding of the potential for phase transitions affecting the degradation behaviour of PVC is needed.

5. Conclusions

Plastic materials in collections often exhibit advanced stages of degradation that are rarely observed in commodity products and applications, such as discolouration, warping, cracking and surface exudation, which is undesirable in the context of long-term conservation. These processes may be difficult to manage because conservation guidelines are often not polymer-specific. Advanced degradation is often visible and thus aesthetically displeasing for conservators and museum visitors. This literature overview revealed the following gaps in the understanding of PVC degradation as relevant to conservation and collection management:

- Degradation at temperatures below Tg
- The role of plasticizers in the process of PVC degradation, the role of plasticizer compatibility and the influence of its migration
- Surface accumulation of plasticizer
- HCl elimination and emission at temperatures of storage and display
- Combined influence of temperature, relative humidity, pollutants and air velocity on the degradation of PVC (damage function).

Most of the published studies of PVC degradation have focused on HCl elimination kinetics, thermogravimetric analysis or degradation due to outdoor weathering. Studies of accelerated degradation have mostly been carried out at temperatures above 100 °C, which is higher than the glass transition temperature and melting temperature of crystalline PVC. Such research is relevant for reprocessing and combustion studies, but the resulting knowledge may not be directly applicable to museum conditions. Unfortunately, reasonable predictions are expect-

ed only from studies carried out by accelerated degradation at moderately elevated temperatures.

It is well known that the degradation of PVC involves elimination of hydrogen chloride with the formation of polyene sequences that cause discolouration of the object. In addition, plasticizers are major components of flexible PVC and they are prone to migration within the material, followed by evaporation or by extraction into materials in direct contact. The role of plasticizers on the stability and degradation of PVC cannot be easily generalized as it significantly depends on the plasticizer type, presence of thermal stabilizers and other additives. The loss of plasticizer depends on the temperature, plasticizer volatility and the airflow rate above the surface. Studies of accelerated degradation demonstrated that the degradation of plasticized PVC objects was higher in open environments when compared to closed environments, where loss of plasticizer was limited. Research has shown that the presence of sorbents negatively affected the state of PVC objects. Sorbents meant to remove harmful acidic emissions are not selective and increase the rate of plasticizer evaporation. In addition, the discolouration had also increased. There seems to be a lack of clear evidence on how temperature affects solubility of plasticizer in PVC and the increased rate of plasticizer migration with evaporation observed at elevated temperatures. Such research would be of tremendous help in selecting optimal storage conditions.

Degradation of three-dimensional art objects is especially concerning because their importance and value is often directly linked to their structural integrity. Different mechanisms of degradation are relevant for three-dimensional PVC objects based on their geometry, presence of specific plasticizers, stabilizers and other additives, and the history of previous storage conditions. For objects made of thin PVC with large and exposed surfaces, the main degradation pathway is likely to be loss of plasticizer due to evaporation. Objects from thick PVC are more likely to exhibit degradation by elimination of HCl, because the emitted gas remains in the matrix longer and acts autocatalytically.

Management of plastics collections requires guidelines for proper storage. The main degradation factors for many plastics are still unknown and may differ greatly. For example, storage of cellulose nitrate and cellulose acetate requires sorbents and high air circulation to avoid the autocatalytic degradation due to emission of NO_2 and acetic acid. The same conditions are inappropriate for PVC storage due to increased loss of plasticizer, exacerbating PVC degradation. Therefore, identification of the main degradation factors and their contribution to the overall rate of degradation of PVC is crucial for successful mitigation of long-term degradation. Dose-response functions need to be constructed to identify the relative contributions of the main degradation factors and thus aid collection managers in the decision-making process leading to the selection of appropriate storage conditions.

While the initial PVC degradation processes are relatively well-understood, being of industrial interest, plastic objects in museums are often past their intended lifetime as consumer plastics, from a polymer scientist's point of view. Unfortunately, this resulted in a lack of systematic research of advanced stages of material deterioration at indoor conditions. Such research is urgently needed in order to enable conservators and collection managers to make informed decisions regarding storage, display and cleaning of museum PVC objects.

So far, there have been very few studies on the PVC degradation at low temperatures. The mechanism of degradation, which can be different at the conditions of accelerated degradation at higher temperatures, has to be considered. For example, the degradation of museum PVC objects could be described by a dose-response function based on experiments carried out close to indoor conditions. On the other hand, the degradation of PVC objects intended for outdoor use should be studied by experiments involving weathering, including larger fluctuations of temperature and humidity and exposure to UV light.

Declaration of interest

The authors declare that they have no competing interests.

Acknowledgements

The work was financially supported by European Union's Horizon 2020 Research and In- novation Programme APACHE project (Grant Agreement ID: 814496), IPERION HS project (Grant Agreement ID: 871034) and the Slovenian Research Agency (Research Programme No. P1-0153) and was partly carried out in the frame of »Mobility of teachers at the University of Ljubljana 2018-2021«, co-financed by the Republic of Slovenia and EU European Social Fund. The authors are grateful to Véronique Sorano Stedman (Centre Pompidou, Paris, France) for her kind assistance.

6. References

1. S. Patrick: Practical Guide to Polyvinyl Chloride 1st ed., Smithers Rapra Technology, Shawbury, UK, 2005.
2. Plastics – the Facts 2019, PlasticsEurope, 14.10.2019.
3. Y. Shashoua: Conservation of Plastics: Materials science, degradation and preservation. 1st Ed., Butterworth-Heinemann, Oxford, UK, **2008**, pp. 113–222.
4. POPART (Preservation Of Plastic ARTefacts in museum collections), Introduction, C. Williamson: From blood and sawdust to lycra: 200 years of plastics in art & design, http://popart-highlights.mnhn.fr/index.html (accessed September 16, 2020).
5. POPART (Preservation Of Plastic ARTefacts in museum collections), Collection Survey, What is the condition of the

collection?, http://popart-highlights.mnhn.fr/index.html (accessed September 17, 2020).
6. B. Keneghan, *Museum Manag. Curatorsh.* **2001**, *19*, 321–331. **DOI:**10.1016/S0260-4779(01)00054-1
7. S. L. Molina, *Ge-Conservacion* **2017**, *1*, 278–285. **DOI:**10.37558/gec.v11i0.532
8. B. Lavédrine, A. Fournier, G. Martin: Collection Survey. In: CTHS Comité des travaux historiques et Scientifiques, ed. Preservation of Plastic Artefacts in Museum Collections., **2012**, pp. 107–151.
9. J. Leadbitter, J. A. Day, J. L. Ryan: PVC: Compounds, Processing and Applications, Smithers Rapra Technology, Shawbury, UK, **1994**.
10. I. D. Hounsham, W. V. Titow: Fillers in PVC, In: PVC Technology, Springer, Dordrecht, Netherlands, **1984**, pp. 215–254. **DOI:**10.1007/978-94-009-5614-8_8
11. G. Wypych: Handbook of Plasticizers 3rd Edition, ChemTec Publishing, Toronto, Canada, **2004**, pp. 33, 119–134, 442–462, 661–671.
12. G. Wypych: PVC Degradation and Stabilization 3rd ed., ChemTec Publishing, Toronto, Canada, **2015**. **DOI:**10.1016/B978-1-895198-85-0.50011-X
13. C. Bueno-Ferrer, M. C. Garrigós, A. Jiménez, *Polym. Degrad. Stab.* **2010**, *95*, 2207–2212. **DOI:**10.1016/j.polymdegradstab.2010.01.027
14. W. H. Starnes, Prog. *Polym. Sci*. **2002**, 27, 2133–2170. **DOI:**10.1016/S0079-6700(02)00063-1
15. W. H. Starnes, X. Ge, *Macromolecules* **2004**, 37, 352–359. **DOI:**10.1021/ma0352835
16. W. H. Starnes, B. Du, S. Kim, V. G. Zaikov, X. Ge, E. K. Culyba, *Thermochim. Acta* **2006**, 442, 78–80. **DOI:**10.1016/j.tca.2006.01.018
17. K. Curran, M. Strlič, *Stud. Conserv*. **2015**, 60, 1–14. **DOI:**10.1179/2047058413Y.0000000125
18. R. King, J. Grau-Bové, K. Curran, *Herit. Sci.* **2020**, 8, 123. **DOI:**10.1186/s40494-020-00466-0
19. J. Yu, L. Sun, C. Ma, Y. Qiao, H. Yao, *Waste Manag*. **2016**, 48, 300–314. **DOI:**10.1016/j.wasman.2015.11.041
20. F. Cappitelli, C. Sorlini, Appl. Environ. *Microbiol.* **2008**, 74, 564–569. **DOI:**10.1128/AEM.01768-07
21. S. Buys, V. Oakley: Conservation and Restoration of Ceramics (Conservation & Museology) 1st ed., Routledge, Abingdon, UK, **2014**. **DOI:**10.4324/9780080502892
22. M. Rule, A. E. Charola, R. J. Koestler, V. Daniels, P. Garside, P. Wyeth, R. Thomson, D. Barker, H. Romich, Y. Shashoua, R. Inkpen, E. May, K. Petersen, M. Jones, R. Eaton, D. Gregory, H. Matthiesen, in E. May, M. Jones (Eds.): Conservation Science: Heritage Materials, The Royal Society of Chemistry, Cambridge, UK, **2006**.
23. E. F. Doehne, C. A. Price: Stone Conservation : An Overview of Current Research 2nd ed., Getty Conservation Institute; Los Angeles, California, **2010**.
24. E. Menart, G. De Bruin, M. Strlič, *Polym. Degrad. Stab.* **2011**, *96*, 2029–2039. **DOI:**10.1016/j.polymdegradstab.2011.09.002
25. M. Strlič, C. M. Grossi, C. Dillon, N. Bell, K. Fouseki, P. Brimblecombe, E. Menart, K. Ntanos, W. Lindsay, D. Thickett, F. France, G. De Bruin, *Herit. Sci.* **2015**, 1–11. **DOI:**10.1186/s40494-015-0065-y
26. M. M. Brooks, D. D. Eastop (Eds.): Changing Views of Textile Conservation, Getty Conservation Institute, Los Angeles, California, **2011**.
27. Y. Shashoua: Inhibiting the inevitable; current approaches to slowing the deterioration of plastics: Macromolecular Symposia, Vol 238. John Wiley & Sons, Ltd; **2006**, pp. 67–77. **DOI:**10.1002/masy.200650610
28. A. Burnstock, K. J. van den Berg: Twentieth Century Oil Paint. The Interface Between Science and Conservation and the Challenges for Modern Oil Paint Research, in: Issues in Contemporary Oil Paint. Springer International Publishing, New York, **2014**, pp. 1–19. **DOI:**10.1007/978-3-319-10100-2_1
29. K. Curran, A. Možir, M. Underhill, L. T. Gibson, T. Fearn, M. Strlič, *Polym. Degrad. Stab.* **2014**, *107*, 294–306. **DOI:**10.1016/j.polymdegradstab.2013.12.019
30. S. N. Lakeev, I. O. Maydanova, R. F. Mullakhmetov, O. V. Davydova, **2016**, *89*, 1–15. **DOI:**10.1134/S1070427216010018
31. B. Pelzl, R. Wolf, B. L. Kaul: Plastics, Additives, in: Ullmann's Encyclopedia of Industrial Chemistry, Wiley-VCH, Weinheim, Germany, **2012**, pp. 619–671.
32. Phthalates ActionPlan, U.S. Environmental Protection Agency, 14.3.2012.
33. A. Wypych: Databook of Plasticizers 2nd Edition, ChemTec Publishing, Toronto, Canada, 2012, pp. 480–483, 506–508, 523–525.
34. S. S. S. Rowdhwal, J. Chen, *Biomed Res. Int.* **2018**, *2018*. **DOI:**10.1155/2018/1750368
35. USA's Consumer Product Safety Improvement Act of 2008 – Public Law 110-314-Aug. 14.8.2008.
36. E. Eckert, F. Münch, T. Göen, A. Purbojo, J. Müller, R. Cesnjevar, *Chemosphere* **2016**, 145, 10–16. **DOI:**10.1016/j.chemosphere.2015.11.067
37. A. Greco, F. Ferrari, A. Maffezzoli, *J. Clean. Prod.* **2017**, *164*, 757–764. **DOI:**10.1016/j.jclepro.2017.07.009
38. S. Mukherjee, M. Ghosh, *JAOCS, J. Am. Oil Chem. Soc.* **2020**, *97*, 187–199. **DOI:**10.1002/aocs.12294
39. A. Carbonell-verdu, D. Garcia-sanoguera, A. Jord, L. Sanchez-nacher, R. Balart, **2016**, *43642*, 1–10. **DOI:**10.1016/j.eurpolymj.2014.11.043
40. J. Chen, Z. Liu, J. Jiang, X. Nie, Y. Zhou, R. E. Murray, *RSC Adv.* **2015**, *5*, 56171–56180. **DOI:**10.1039/C5RA07096A
41. S. Kumar, *Ind. Eng. Chem. Res.* **2019**, *58*, 11659–11672. **DOI:**10.1021/acs.iecr.9b02080
42. P. Karmalm, T. Hjertberg, A. Jansson, R. Dahl, *Polym. Degrad. Stab.* **2009**, *94*, 2275–2281. **DOI:**10.1016/j.polymdegradstab.2009.07.019
43. P. H. Daniels, *J Vinyl Addit. Technol* **2009**, *21*, 129–133. **DOI:**10.1002/vnl.20211
44. W. Aiken, T. Alfrey, A. Janssen, H. Mark, *J. Polym. Sci.* **1947**, *2*, 178–198. **DOI:**10.1002/pol.1947.120020206
45. P. Walters, D. F. Cadogan, C. J. Howick: Plasticizers in: Ull-

mann's Encyclopedia of Industrial Chemistry, Wiley-VCH, Weinheim, Germany, **2020**, pp. 1–27. **DOI:**10.1002/14356007.a20_439.pub2
46. K. A. Mauritz, R. F. Storey, B. S. Wilson, *J. Vinyl Addit. Technol.* **1990**, *12*, 165–173. **DOI:**10.1002/vnl.730120309
47. T. Vilics, H. A. Schneider, V. Manoviciu, I. Manoviciu, *Polymer (Guildf).* **1997**, *38*, 1865–1870. **DOI:**10.1016/S0032-3861(96)00722-7
48. N. Kinjo, T. Nakagawa, *Polym. J.* **1973**, *4*, 143–153. **DOI:**10.1295/polymj.4.143
49. ASM International: Characterization and Failure Analysis of Plastics. (Lampman S, ed.). ASM International; **2003**.
50. M. Hakkarainen: Migration of monomeric and polymeric PVC plasticizers, in: Advances in Polymer Science Vol 211., **2008**, pp.159–185. **DOI:**10.1007/12_2008_140
51. M. Ekelund, B. Azhdar, U. W. Gedde, *Polym. Degrad. Stab.* **2010**, *95*, 1789–1793. **DOI:**10.1016/j.polymdegradstab.2010.05.007
52. L. Monney, M. Jamois-Tasserie, C. Dubois, P. Lallet, F. Villa, C. Renaud, *Polym. Degrad. Stab.* **2001**, *72*, 459–468. **DOI:**10.1016/S0141-3910(01)00047-7
53. P. Hadi, A. A. Babaluo, *J. Appl. Polym. Sci.* **2007**, *106*, 3967–3974. **DOI:**10.1002/app.27045
54. J. P. Giroud, *Geosynth. Int.* **1995**, *2*, 1099–1113. **DOI:**10.1680/gein.2.0047
55. L. Audouin, B. Dalle, G. Metzger, J. Verdu, *J. Appl. Polym. Sci.* **1992**, *45*, 2091–2096. **DOI:**10.1002/app.1992.070451204
56. C. Wang, D. Johnson, M. A. Suleman, M. A. Suleman, W. Zhang, D. Pestov, P. Ramsinghani, R. Wickham, K. J. Wynne, *Polymer (Guildf).* **2015**, *76*, 70–79. **DOI:**10.1016/j.polymer.2015.08.048
57. Y. R. Shashoua, *Polym. Degrad. Stab.* **2003**, *81*, 29–36. **DOI:**10.1016/S0141-3910(03)00059-4
58. X.-F. Wei, E. Linde, M. S. Hedenqvist, *npj Mater. Degrad.* **2019**, *3*, 1–8. **DOI:**10.1038/s41529-019-0080-7
59. A. Royaux, I. Fabre-Francke, N. Balcar, G. Barabant, C. Bollard, B. Lavédrine, S. Cantin, *Polym. Degrad. Stab.* **2017**, *137*, 109–121. **DOI:**10.1016/j.polymdegradstab.2017.01.011
60. E. Linde, U.W. Gedde, *Polym. Degrad. Stab.* **2014**, *101*, 24–31. **DOI:**10.1016/j.polymdegradstab.2014.01.021
61. P. A. Clausen, Y. Xu, V. Kofoed-Sørensen, J. C. Little, P. Wolkoff, *Atmos. Environ.* **2007**, *41*, 3217–3224. **DOI:**10.1016/j.atmosenv.2006.06.063
62. Ž. Mrklić, T. Kovačić, *Thermochim. Acta* **1998**, *322*, 129–135. **DOI:**10.1016/S0040-6031(98)00479-1
63. H. M. Zhu, X. G. Jiang, J. H. Yan, Y. Chi, K. F. Cen, *J. Anal. Appl. Pyrolysis* **2008**, *82*, 1–9. **DOI:**10.1016/j.jaap.2007.11.011
64. S. S. Suresh, S. Mohanty, S. K. Nayak, *Waste Manag.* **2017**, *60*, 100–111 **DOI:**10.1016/j.wasman.2016.08.033
65. D. Braun, *Pure Appl. Chem.* **1971**, 26, 173–192. **DOI:**10.1351/pac197126020173
66. D. Braun, B. Böhringer, W. Knoll, N. Eidam, W. Mao, *Angew. Makromol. Chemie* **1990**, 181, 23–40. **DOI:**10.1002/apmc.1990.051810102
67. Y. Shashoua: Inhibiting the deterioration of plasticized poly (vinyl chloride). Chem. Eng. **2001**, PhD thesis.
68. R. Navarro, M. Pérez Perrino, M. Gomez Tardajos, H. Reinecke, *Macromolecules*. **2010**, 43, 2377–2381. **DOI:**10.1021/ma902740t
69. R. Navarro, M. Pérez Perrino, C. García, C. Elvira, A. Gallardo, H. Reinecke, *Macromolecules* **2016**, *49*, 2224–2227. **DOI:**10.1021/acs.macromol.6b00214
70. P. M. R. Tendero, A. Jimenez, A. Greco, A. Maffezzoli, *Eur. Polym. J.* **2006**, 42, 961–969. **DOI:**10.1016/j.eurpolymj.2005.10.006
71. Y. Ma, S. Liao, Q. Li, Q. Guan, P. Jia, Y. Zhou, *React. Funct. Polym.* **2020**, *147*, 104458. **DOI:**10.1016/j.reactfunctpolym.2019.104458
72. K. Patel, A. Velazquez, H.S. Calderon, G.R. Brown, *J. Appl. Polym. Sci.* **1992**, *46*, 179–187. **DOI:**10.1002/app.1992.070460117
73. M. Carenza, Y. V. Moiseev, G. Palma, *J. Appl. Polym. Sci.* **1973**, *17*, 2685–2694. **DOI:**10.1002/app.1973.070170905
74. B. B. Troitskii, L. S. Troitskaya, V. N. Denisova, Z.B. Luzinova, *Polym. J.* **1978**, *10*, 377–385. **DOI:**10.1295/polymj.10.377
75. A. A. Yassin, M. W. Sabaa, *J. Macromol. Sci. Part C* **1990**, *30*, 491–558. **DOI:**10.1080/07366579008050916
76. W. H. Starnes Jr., S. Girois, in: R. A. Pethrick (Ed.).: Polymer Yearbook 1995 12th ed., Gordon & Breach, Boston, Massachusetts, **1995**.
77. J. Purmová, K. F. D. Pauwels, M. Agostini, M. Bruinsma, E. J. Vorenkamp, A. J. Schouten, M. L. Coote, *Macromolecules* **2008**, *41*, 5527–5539. **DOI:**10.1021/ma800583k
78. W. H. Starnes, B. J. Wojciechowski, H. Chung, G. M. Benedikt, G. S. Park, A. H. Saremi, *Macromolecules* **1995**, *28*, 945–949. **DOI:**10.1021/ma00108a023
79. W. H. Starnes, B. J. Wojciechowski, A. Velazques, G. M. Benedikt, *Macromolecules*. **1992**, *25,* 3638–3641. **DOI:**10.1021/ma00040a006
80. N. Boughdady, K. Chynoweth, D. Hewitt, *Aust. J. Chem.* **1991**, *44*, 567. **DOI:**10.1071/CH9910567
81. Z. Mayer, *J. Macromol. Sci. Part C* **1974**, *10*, 263–292. **DOI:**10.1080/15321797408076100
82. Z. Mayer, B. Obereigner, D. Lim, *J. Polym. Sci. Part C Polym. Symp.* **2007**, *33*, 289–305. **DOI:**10.1002/polc.5070330128
83. R. Bacaloglu, M. H. Fisch, *Polym Degrad Stab* **1994**, *45*, 301–313. **DOI:**10.1016/0141-3910(94)90200-3
84. M. H. Fisch, R. Bacaloglu, *J. Vinyl Addit. Technol.* **1995**, *1*, 233–240. **DOI:**10.1002/vnl.730010409
85. K. Endo, In: Progress in Polymer Science, Pergamon, Oxford, UK, **2002**, pp. 2021–2054. **DOI:**10.1016/S0079-6700(02)00066-7
86. W. H. Starnes Jr., *Polym. Mater. Sci. Eng.* **1988**, *58*, 220.
87. T. Y. Xie, A.E. Hamielec, M. Rogestedt, T. Hjertberg, *Polymer (Guildf).* **1994**, *35*, 1526–1534. **DOI:**10.1016/0032-3861(94)90354-9
88. W. H. Starnes, I. M. Plitz, D. C. Hische, D. J. Freed, F. C. Schilling, M.L. Schilling, *Macromolecules* **1978**, *11*, 373–382. **DOI:**10.1021/ma60062a019
89. G. Szarka, B. Iván, *J. Macromol. Sci. Part A Pure Appl. Chem.* **2013**, *50*, 208–214. **DOI:**10.1080/10601325.2013.742804

90. J. P. H. M. Hillemans, C. M. C. J. Colemonts, R. J. Meier, B. J. Kip, *Polym. Degrad. Stab.* **1993**, *42*, 323–333. **DOI:**10.1016/0141-3910(93)90228-B
91. K. S. Minsker, S. V. Kolesov, G. E. Zaikov: Degradation and stabilization of vinyl chloride-based polymers 1st Edition, Pergamon, Oxford, UK, **1988**.
92. B. B. Troitskii, L. S. Troitskaya, A. S. Yakhnov, M. A. Novikova, V. N. Denisova, V. K. Cherkasov, M.P. Bubnov, *Polym. Degrad. Stab.* **1997**, *58*, 83–89. **DOI:**10.1016/S0141-3910(97)00023-2
93. G. Martinez, C. Mijangos, J. Millan, *J. Appl. Polym. Sci.* **1983**, *28*, 33–43. **DOI:**10.1002/app.1983.070280104
94. B. B. Troitskii, A. S. Yakhnov, M. A. Novikova, T. G. Ganyukhina, V. N. Denisova, *Eur. Polym. J.* **1997**, 33, 505–511. **DOI:**10.1016/S0014-3057(96)00190-5
95. R. Flores, J. Perez, P. Cassagnau, A. Michel, J. Y. Cavaillé, *Polymer (Guildf).* **1994**, *35*, 2800–2807. **DOI:**10.1016/0032-3861(94)90309-3
96. R. P. Chartoff, T. S. K. Lo, E. R. J. Harrell, R. Joon Roe, *J. Macromol. Sci. Part B* **1981**, *20*, 287–303. **DOI:**10.1080/00222348108219443
97. G. A. Voyiatzis, K. S. Andrikopoulos, G. N. Papatheodorou, E. I. Kamitsos, G. D. Chryssikos, J. A. Kapoutsis, S. H. Anastasiadis, G. Fytas, *Macromolecules* **2000**, *33*, 5613–5623. **DOI:**10.1021/ma991772m
98. S. Ulutan, *J. Appl. Polym. Sci.* **2003**, *90*, 3994–3999. **DOI:**10.1002/app.13133
99. R. Chen, D. R. Tyler, *Macromolecules* **2004**, *37*, 5430–5436. **DOI:**10.1021/ma0496302
100. C. Tsitsilianis, M. Tsapatsis, C. Economou, *Polymer (Guildf).* **1989**, *30*, 1861–1866. **DOI:**10.1016/0032-3861(89)90359-5
101. A. Marcilla, M. Beltrán, *Polym. Degrad. Stab.* **1998**, *60*, 1–10. **DOI:**10.1016/S0141-3910(96)00124-3
102. R. Zorn, M. Monkenbusch, D. Richter, A. Alegría, J. Colmenero, B. Farago, *J. Chem. Phys.* **2006**, *125*, 154904. **DOI:**10.1063/1.2357738
103. V. K.-H. Illers, *Die Makromol. Chemie* **1969**, *127*, 1–33. **DOI:**10.1002/macp.1969.021270101
104. S. T. Bee, W. R. Mok, T. S. Lee, T. T. Tee, G. Issabayeva, A. R. Rahmat, *J. Polym. Eng.* **2014**, *34*, 521–529. **DOI:**10.1515/polyeng-2013-0324
105. M. Beltrán, J. C. García, A. Marcilla, *Eur. Polym. J.* **1997**, *33*, 453–462. **DOI:**10.1016/S0014-3057(96)00213-3
106. E. B. Rabinovitch, J. W. Summers, *J. Vinyl Technol.* **1992**, *14*, 126–130. **DOI:**10.1002/vnl.730140303
107. B. J. Kip, R. J. Meier, M. van Aaken, K. P. J. Williams, D. L. Gerrard, *Macromolecules* **1992**, *25*, 4290–4296. **DOI:**10.1021/ma00043a008
108. H. Shirakawa, T. Ito, S. Ikeda, *Die Makromol. Chemie* **1978**, *179*, 1565–1573. **DOI:**10.1002/macp.1978.021790615
109. T. Yamabe, K. Akagi, K. Ohzeki, K. Fukui, H. Shirakawa, *J. Phys. Chem. Solids* **1982**, *43*, 577–581. **DOI:**10.1016/0022-3697(82)90047-6
110. J. Lemaire, N. Siampiringue, N. Girod, P. Delprat, G. Parmeland, N. Macdonald, C. Spriet, *J. Vinyl Addit. Technol.* **2003**, *9*, 54–60. **DOI:**10.1002/vnl.10063
111. E. Arkiş, D. Balköse, *Polym. Degrad. Stab.* **2005**, *88*, 46–51. **DOI:**10.1016/j.polymdegradstab.2004.02.021
112. J. Oremusová, P. Šimon, L. Valko, P. Kovařík, *Chem. Pap.* **1989**, *43*, 721–731.
113. J. F. Rabek, J. Lucki, H. Kereszti, T. Hjertberg, Q.B. Jun, *J. Appl. Polym. Sci.* **1990**, *39*, 1569–1586. **DOI:**10.1002/app.1990.070390714
114. A. Michel, *J. Macromol. Sci. Part A – Chem.* **1978**, *12*, 361–371. **DOI:**10.1080/00222337808061385
115. A. H. Frye, R. W. Horst, *J. Polym. Sci.* **1959**, *40*, 419–431. **DOI:**10.1002/pol.1959.1204013712
116. V. H. Tran, A. Guyot, T. P. Nguyen, P. Molinié, *Polym. Degrad. Stab.* **1995**, *49*, 331–337. **DOI:**10.1016/0141-3910(95)00075-W
117. Omnexus, The material selection platform, Polymer Properties, Water Absorption 24 hours, https://omnexus.specialchem.com/polymer-properties/properties/water-absorption-24-hours, 14.9.2020.
118. Y. Hu, J. Summers, A. Hiltner, E. Baer, *J. Vinyl Addit. Technol.* **2002**, *8*, 251–258. **DOI:**10.1002/vnl.10371
119. L. Laiarinandrasana, E. Gaudichet, S. Oberti, C. Devilliers, *Int. J. Press. Vessel. Pip.* **2011**, *88*, 99–108. **DOI:**10.1016/j.ijpvp.2011.01.002
120. N. Belhaneche-Bensemra, *J. Vinyl Addit. Technol.* **2002**, *8*, 45–54. **DOI:**10.1002/vnl.10344
121. M. Ito, K. Nagai, *Polym. Degrad. Stab.* **2007**, *92*, 260–270. **DOI:**10.1016/j.polymdegradstab.2006.11.003
122. M. Lenartowicz, B. Swinarew, A. Swinarew, G. Rymarz, *Int. J. Polym. Anal. Charact.* **2014**, *19*, 611–624. **DOI:**10.1080/1023666X.2014.933071
123. J. Colombani, V. Labed, C. Joussot-Dubien, A. Périchaud, J. Raffi, J. Kister, C. Rossi, *Nucl. Instruments Methods Phys. Res. Sect. B Beam Interact. with Mater. Atoms* **2007**, *265*, 238–244. **DOI:**10.1016/j.nimb.2007.08.053
124. Z. Dobkowski, *Polym. Degrad. Stab.* **2006**, *91*, 488–493. **DOI:**10.1016/j.polymdegradstab.2005.01.051
125. J. Verdu, *J. Macromol. Sci. Part A – Chem.* **1978**, *12*, 551–567.
126. L. E. Pimentel Real, A. M. Ferraria, A. M. Botelho do Rego, *Polym. Test.* **2008**, *27*, 743–751. **DOI:**10.1016/j.polymertesting.2008.05.009
127. W. H. Starnes, In: S. Peter Pappas, F. H. Winslow (Eds.): Photodegradation of Polyvinyl Chloride, ACS Publications, Washington D, Washington, **1981**, pp. 197–215. **DOI:**10.1021/bk-1981-0151.ch014
128. U. Gesenhues, *Polym. Degrad. Stab.* **2000**, *68*, 185–196. **DOI:**10.1016/S0141-3910(99)00184-6
129. A. Torikai, H. Hasegawa, *Polym. Degrad. Stab.* **1999**, *63*, 441–445. **DOI:**10.1016/S0141-3910(98)00125-6
130. A. L. Andrady, K. Fueki, A. Torikai, *J. Appl. Polym. Sci.* **1990**, *39*, 763–766. **DOI:**10.1002/app.1990.070390325
131. J. L. Gardette, J. Lemaire, *J. Vinyl Addit. Technol.* **1997**, *3*, 107–111. **DOI:**10.1002/vnl.10175
132. A. L. Andrady, A. Torikai, K. Fueki, *J. Appl. Polym. Sci.* **1989**, *37*, 935–946.
133. J. Ashley-Smith, A. Derbyshire, B. Pretzel, I.C. for Conservation: The continuing development of a practical lighting

policy for works of art on paper and other object types at the Victoria and Albert Museum. 13th Triennial Meeting, Rio de Janiero, 22–27 September 2002, London, UK, **2002**, pp. 3–8.
134. G. Pastorelli, C. Cucci, O. Garcia, G. Piantanida, A. Elnaggar, M. Cassar, M. Strlič, *Polym. Degrad. Stab.* **2014**, *107*, 198–209. **DOI:**10.1016/j.polymdegradstab.2013.11.007
135. M. Edge, C. M. Liauw, N. S. Allen, R. Herrero, *Polym. Degrad. Stab.* **2010**, *95*, 2022–2040. **DOI:**10.1016/j.polymdegradstab.2010.07.006
136. V. D. Daniels, N. H. Rees, *J Polym Sci* **1974**, *12*, 2115–2122. **DOI:**10.1002/pol.1974.170120929
137. R. B. Woodward, *J. Am. Chem. Soc.* **1941**, *63*, 1123–1126. **DOI:**10.1021/ja01849a066
138. G. N. Lewis, M. Calvin, *Chem. Rev.* **1939**, *25*, 273–328. **DOI:**10.1021/cr60081a004
139. G. Ocskay, Z. Nyitraj, F. Varflavi, T. Wein, *Eur. Polym. J.* **1971**, *7*, 1135–1145. **DOI:**10.1016/0014-3057(71)90146-7
140. S. Hollande, J. L. Laurent, *Polym. Degrad. Stab.* **1997**, *55*, 141–145. **DOI:**10.1016/S0141-3910(96)00165-6
141. M. Wijdekop, J.C. Arnold, M. Evans, V. John, A. Lloyd, *Mater. Sci. Technol.* **2013**, *21,* 791–797. **DOI:**10.1179/174328405X47500
142. ISO 182 Plastics — Determination of the tendency of compounds and products based on vinyl chloride homopolymers and copolymers to evolve hydrogen chloride and any other acidic products at elevated temperatures.
143. B. Lundgren, *Indoor Air* **1999**, *9*, 202–208. **DOI:**10.1111/j.1600-0668.1999.t01-1-00007.x
144. D. J. Carlsson, M. Krzymien, D. J. Worsfold, M. Day, *J. Vinyl Addit. Technol.* **1997**, *3*, 100–106. **DOI:**10.1002/vnl.10174
145. G. Mitchell, C. Higgitt, L. T. Gibson, *Polym. Degrad. Stab.* **2014**, *107*, 328–340. **DOI:**10.1016/j.polymdegradstab.2013.12.003
146. S. Panseri, L. M. Chiesa, A. Zecconi, G. Soncini, I. De Noni, *Molecules* **2014**, *19*, 8707–8724. **DOI:**10.3390/molecules19078707
147. M. Noguchi, A. Yamasaki, *Heliyon* **2020**, *6*, e03314. **DOI:**10.1016/j.heliyon.2020.e03314
148. K. Curran, M. Underhill, J. Grau-Bové, T. Fearn, L. T. Gibson, M. Strlič, *Angew. Chemie – Int. Ed.* **2018**, *57*, 7336–7340. **DOI:**10.1002/anie.201712278
149. G. Mitchell, F. France, A. Nordon, P. L. Tang, L. T. Gibson, *Herit. Sci.* **2013**, *1*, 1–10. **DOI:**10.1186/2050-7445-1-28
150. G. Pastorelli, T. Trafela, P.F. Taday, A. Portieri, D. Lowe, K. Fukunaga, M. Strlič, *Anal. Bioanal. Chem.* **2012**, *403*, 1405–1414. **DOI:**10.1007/s00216-012-5931-9
151. Y. Shashoua, *Stud. Conserv.* **2004**, *49*, 91–95. **DOI:**10.1179/sic.2004.49.s2.020
152. C. B. Lauridsen, L. W. Hansen, T. Brock-Nannestad, J. Bendix, K. P. Simonsen, *Stud. Conserv.* **2017**, *62*, 445–455. **DOI:**10.1080/00393630.2016.1206651
153. D. Saviello, L. Andena, D. Gastaldi, L. Toniolo, S. Goidanich, *J. Appl. Polym. Sci.* **2018**, *135*, 1–12. **DOI:**10.1002/app.46194
154. K. Z. Gumargalieva, V. B. Ivanov, G. E. Zaikov, J. V. Moiseev, T. V. Pokholok, *Polym. Degrad. Stab.* **1996**, *52*, 73–79. **DOI:**10.1016/0141-3910(95)00209-X
155. J. Puls, S. A. Wilson, D. Hölter, *J. Polym. Environ.* **2011**, *19*, 152–165. **DOI:**10.1007/s10924-010-0258-0
156. Y. Shashoua, S. M. Bradley, V. D. Daniels, *Stud. Conserv.* **1992**, *37*, 113. **DOI:**10.2307/1506403
157. L. Robinet, D. Thickett, *Stud. Conserv.* **2004**, *48*, 263–268. **DOI:**10.1179/sic.2003.48.4.263
158. G. G. Beiner, M. Lavi, H. Seri, A. Rossin, O. Lev, J. Gun, R. Rabinovich, *Collect. Forum* **2015**, *29*, 22–36. **DOI:**10.14351/0831-4985-29.1.22
159. M. J. Samide, G. D. Smith, *J. Chromatogr. A* **2015**, *1426*, 201–208. **DOI:**10.1016/j.chroma.2015.11.066
160. E. Canosa, A. Wiman, S. Norrehed, M. Hacke, Characterization of Emissions from Display Case Materials – Tecnical Report June 2019, Swedish National Heritage Board, **2019**.
161. M. J. Samide, M. C. Liggett, J. Mill, G. D. Smith, *Herit. Sci.* **2018**, *6*, 1–10. **DOI:**10.1186/s40494-018-0213-2
162. A. Royaux, I. Fabre-Francke, N. Balcar, G. Barabant, C. Bollard, B. Lavédrine, S. Cantin, *Polym. Degrad. Stab.* **2018**, *155*, 183–193. **DOI:**10.1016/j.polymdegradstab.2018.07.016
163. A. Royaux, E. Apchain, I. Fabre-Francke, N. Balcar, G. Barabant, C. Bollard, B. Lavédrine, O. Fichet, S. Cantin, *J. Cult. Herit.* August **2020**. **DOI:**10.1016/j.culher.2020.07.002
164. C. M. Muñoz, H. Egsgaard, J. S. Landaluze, C. Dietz, *J. Am. Inst. Conserv.* **2014**, *53*, 236–251. **DOI:**10.1179/0197136014Z.00000000040
165. C. M. Muñoz, *J. Microsc.* **2011**, *243*, 257–266. **DOI:**10.1111/j.1365-2818.2011.03499.x
166. C. Morales Muñoz, *Appl. Surf. Sci.* **2010**, *256*, 3567–3572. **DOI:**10.1016/j.apsusc.2009.12.156
167. M. Strlič, D. Thickett, J. Taylor, M. Cassar, *Stud. Conserv*. **2013**, *58,* 80–87. **DOI:**10.1179/2047058412Y.0000000073
168. X. Zou, T. Uesaka, N. Gurnagul, *Cellulose* **1996**, *3,* 243–267. **DOI:**10.1007/BF02228805

Povzetek

V muzejih in galerijah so vse večje zbirke predmetov in sodobne umetnosti, ki so iz plastičnih materialov, ki se lahko hitro spreminjajo. Glavni procesi razgradnje polivinil klorida (PVC) so eliminacija HCl ter migracija ali izguba mehčal. Posledica teh procesov je opazna obarvanost, togost in krhkost. Znano je, da je razgradnja večstopenjski proces, ki vključuje eliminacijo HCl, nastanek konjugiranih polienov in zamreženje. Eliminacija HCl se začne zaradi strukturnih nepravilnosti (alilni in terciarni kloridi) in povzroči nastanek polienov. Spremembo barve PVC vidimo, ko nastane vsaj 7 konjugiranih dvojnih vezi.

Za identifikacijo polimerov in kvantifikacijo mehčal se uporabljajo neinvazivne tehnike, kot sta IR in Ramanska spektroskopija. Razgradnjo mehčal in zlasti pozne faze razgradnje PVC je mogoče raziskati s SEC, GC-MS, TGA in DSC. Študije v zbirkah dediščine so pokazale, da se poleg HCl iz PVC predmetov emitirajo tudi 2-etilheksanol in drugi hlapni razgradni produkti, vendar trenutno ni navedb, da se HCl emitira pri običajnih notranjih pogojih. Na splošno ni sistematičnih raziskav razgradnje PVC v pogojih skladiščenja in razstavljanja, kar bi omogočilo razvoj funkcije doza-odziv in oblikovanje smernic preventivnega konserviranja za upravljanje zbirk PVC.

Except when otherwise noted, articles in this journal are published under the terms and conditions of the Creative Commons Attribution 4.0 International License

DOI: 10.17344/acsi.2018.4748 *Acta Chim. Slov.* **2020,** *67,* 1014–1023
creative commons

Scientific paper

Synthesis of New Di- and Triamides as Potential Organocatalysts for Asymmetric Aldol Reaction in Water

Elif Keskin, Cigdem Yolacan and Feray Aydogan*

Department of Chemistry, Yildiz Technical University, Davutpasa Campus, 34010 Esenler, Istanbul, Turkey

** Corresponding author: E-mail: feray_aydogan@yahoo.com*
Tel: +90 212 383 42 15

Received: 09-27-2018

Abstract

New di- or triamide organocatalysts derived from (*L*)-proline were synthesized and successfully used in the direct asymmetric aldol reaction of aliphatic ketones and aromatic aldehydes in water at 0 °C in the presence of benzoic acid as co-catalyst. (*S*)-methyl-2-((*S*)-3-hydroxy-2-((*S*)-3-pyrrolidine-2-carboxamido)propanamido)-3-phenylpropanoate (**7c**) as organocatalyst showed best results under these reaction conditions, and good diastereoselectivities (up to 99%), enantioselectivities (up to 98%) and yields (up to 91%) were observed.

Keywords: Aldol reaction; organocatalysis; asymmetric synthesis; prolinamide

1. Introduction

The aldol reaction is an important tool in organic chemistry to synthesize attractive intermediates. This carbon-carbon bond formation reaction yields the β-hydroxyketones which are important precursors for pharmaceuticals and natural products. Especially, the asymmetric version of the reaction has been extensively studied and used for the synthesis of valuable intermediates, highly functionalized and complex molecules with important biological activities. The most considerable asymmetric method is the using of asymmetric organocatalysis which

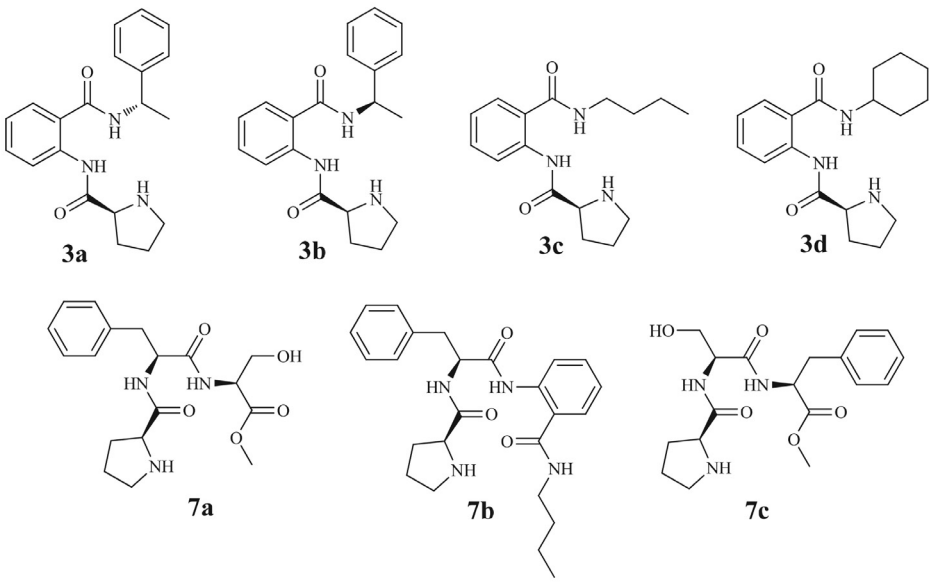


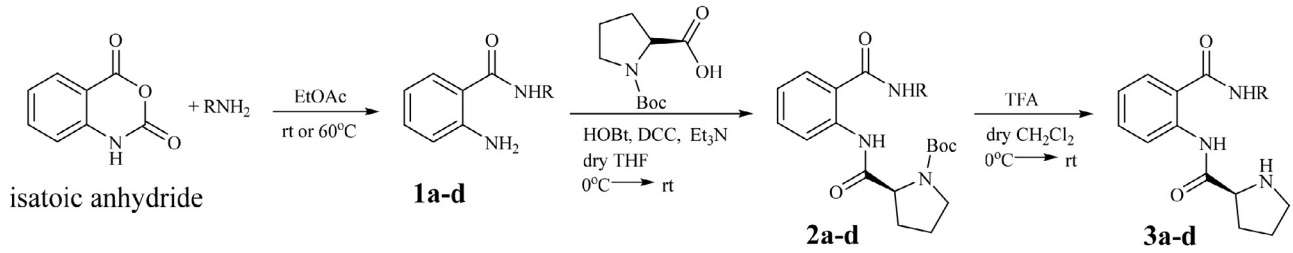
Figure 1. The structures of organocatalysts investigated in this study

are non-metal, small, easily synthesizable organic compounds with low toxicity and mostly natural products.[1–3] Among these natural organocatalysts, *L*-proline is the corner stone of natural amino acid organocatalysts and used successfully to catalyze various organic reactions.[4–7] But, this small organic compound has some drawbacks such as low solubility, low yields and low enantioselectivity with aromatic aldehydes as organocatalyst in asymmetric aldol condensation.[8] To overcome these drawbacks, some derivatives of proline had been succesfully synthesized and used in asymmetric aldol reaction and new modifications on proline are still under investigation.[9–24] Especially, proline based amides have been used succesfully for this reaction.[25–30] These derivatives have some advantages such as easy preperation, high stability and the presence of important functional groups. The catalytic effect of these catalysts based on secondary amine group on the pyrrolidine ring which form enamine to activate carbonyl group and the hyrogen bond donors which improve the activation of electrophile and selectivity. These advantages make them one of the most popular organocatalysts for organic synthesis and the design and investigation of new proline based amides as organocatalysts for various organic reactions is still under investigation by several research groups.[31,32]

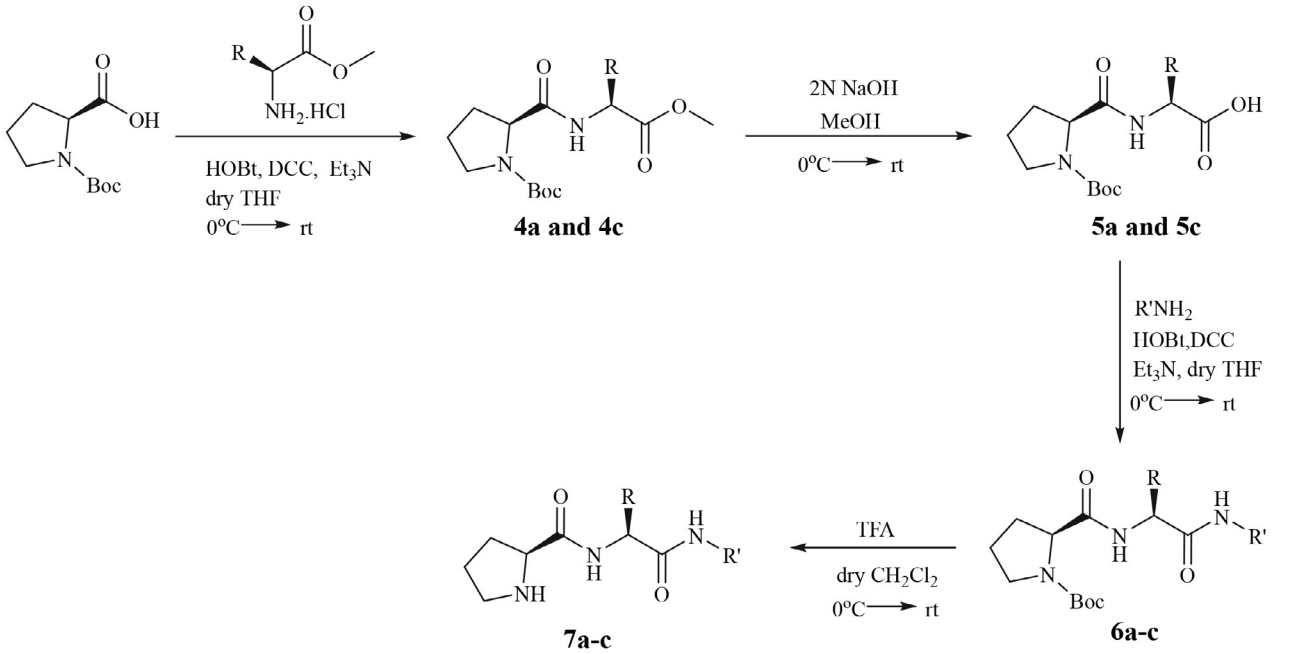
In our continuing research on the synthesis of chiral organocatalysts and their investigation in direct asymmetric aldol reaction, we have investigated the catalytic potential of some proline amide derivatives and also 1,2,3,4-tetrahydroisoquinoline and thiazolidine-4-carboxylic acid amide derivatives.[33–36] Now we herein report the synthesis of new proline based amides (**3a–d** and **7a–c**) (Figure 1) and their application in asymmetric direct aldol reaction.

2. Results and Discussion

The reaction of Boc-protected *L*-proline with aminobenzamide derivatives (**1a–d**) which were synthesized by the reaction of isatoic anhydride with some amines and subsequent deprotection of products (**2a–d**) gave new pro-



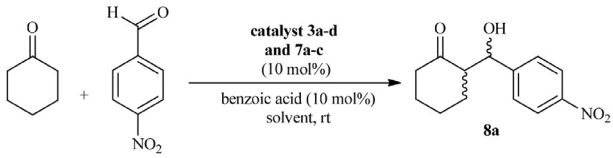
Scheme 1. The synthetic route for compounds **3a–d**.



Scheme 2. The synthetic route for compounds **7a–c.**

line based diamides (**3a–d**) (Scheme 1). Aminobenzamides (**1a–d**) were known in the literature[37,38] and the IR, ^{1}H NMR and MS data of the compounds **1a–d** were in accordance with those data. The characterization of unknown compounds **2a–d** and **3a–d** were performed from their spectral data.

Table 1. Catalytic activities of di- and tri-amides.



Catalyst (10 mol%)	Solvent	Reaction time (h)	dr[a] (syn/anti)	ee[a] (%) (anti)	Yield[b] (%)
3a	DCM	72	1/1.7	16.7	84.2
3a	H_2O	24	1/2.2	32.0	79.9
3a	none	48	1/1.5	32.4	77.7
3b	DCM	72	1/1.7	21.6	58.8
3b	H_2O	24	1/2.6	42.4	83.0
3c	DCM	72	1/2.3	24.7	58.4
3c	H_2O	72	1/1.8	34.5	75.7
3c	none	48	1/1.7	34.9	83.1
3d	DCM	72	1/2.1	28.8	80.6
3d	H_2O	24	1/1.9	45.9	95.8
3d	none	48	1/1.6	29.0	86.2
7a	DCM	72	1/2.7	47.9	86.9
7a	H_2O	24	1/3.9	65.5	70.3
7a	none	24	1/1.6	68.3	63.7
7b	DCM	72	1/3.5	50.7	76.0
7b	H_2O	24	1/2.5	32.0	91.0
7b	none	48	1/2.7	53.3	96.0
7c	DCM	72	1/3.9	78.5	52.0
7c	H_2O	48	1/9.3	90.6	89.4
7c	none	72	1/4.7	87.5	96.0
7c	H_2O/THF (2/1)	72	1/5.6	89.4	88.1

[a] Determined by chiral-phase HPLC analysis. [b] Combined yields of isolated diastereomers.

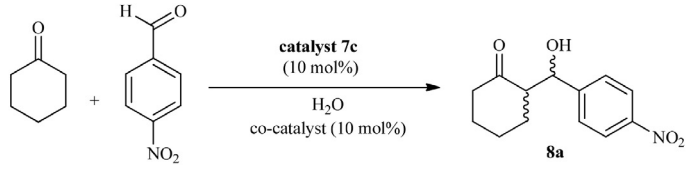
Compounds 7a–c were synthesized by a reaction sequence as amidation, hydrolysis, second amidation and deprotection reactions starting from Boc-protected proline and some amino acid esters and amine (Scheme 2). All new compounds were in accordance with their spectral data.

The reaction of *p*-nitrobenzaldehyde with cyclohexanone under diferent conditions was chosen as a model reaction to investigate the catalytic activities of amide compounds **3 a–d** and **7 a–c,** in direct asymmetric aldol reactions. First, the reaction was carried out with new amide compounds in water or dichloromethane (DCM), or without any solvent in the presence of benzoic acid (BA) as co-catalyst at room temperature. The results are shown in the Table 1. Compound **7c** showed the best catalytic activity with good diastereoselectivity (90%), enantioselectivity (91%) and yield (89%). The poor activities of **3 a–d** can be interpreted that the planar phenyl rings prevent the appropriate arrangement in the transition state due to the sterical effect and thus these compounds did not show good asymmetric induction. Compounds **7a** and **7b** also showed lower selectivities due to the steric effect of phenyl group. The best asymmetric induction was obtained with **7c**, which has less steric effect around proline NH and prolinamide NH. It is also thought that the OH group is effective in asymmetric induction through hydrogen bond formation.

Then, various co-catalysts containing 4-nitrobenzoic acid (4-NBA), (2*R*, 3*R*)-(+)-tartaric acid (2*R*, 3*R*-TA), acetic acid (AcOH) and benzoic acid (BA) were also tested at 0 °C and room temperature to determine the optimum conditions with the best organocatalyst **7c**. As it can be seen from the Table 2, the best results were obtained at 0 °C in the presence of BA as co-catalyst in water.

With these promising results, the substrates in the reaction were broadened with different aliphatic ketones and aromatic aldehydes in the presence of organocatalyst **7c** under the optimum conditions (Table 3). All aldol products are known in the literature, and their structures

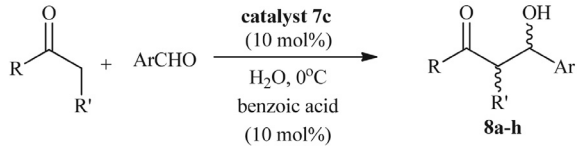
Table 2. Catalytic acitivity of organocatalyst **7c** under various conditions.



Catalyst (10 mol %)	Co-catayst (10 mol%)	Temperature time (h)	Reaction (syn/anti)	dr[a] (anti)	ee[a] (%) (%)	Yield[b]
7c	4-NBA	rt	72	1/4.5	90.1	79.6
7c	(2*R*-3*R*)-TA	rt	72	1/1.9	73.1	54.0
7c	AcOH	rt	48	1/5.6	92.2	77.6
7c	BA	rt	12	1/8.6	87.9	50.0
7c	BA	0 °C	72	1/12.7	95.4	91.3
7c (5% mol)	BA	0 °C	72	1/2.9	84.5	27.4
7c	4-NBA	0 °C	72	1/12.3	93.8	94.6

[a] Determined by chiral-phase HPLC analysis. [b] Combined yields of isolated diastereomers.

Table 3. Aldol reactions of different aldehydes and ketones catalyzed by **7c.**



Compound	Ketone	Aldehyde	Reaction time (h)	dr[a] (syn/anti)	ee[a] (%) (anti)	Yield[b] (%)
8a	Cyclohexanone	4-Nitrobenzaldehyde	72	1/12.7	95.4	91.3
8b	Cyclohexanone	2-Nitrobenzaldehyde	36	1/222.2	90.9	53.9
8c	Cyclohexanone	3-Nitrobenzaldehyde	72	1/39.5	93.4	66.5
8d	Cyclohexanone	4-Cyanobenzaldehyde	72	1/3.2	91.9	59.2
8e	Cyclohexanone	4-Bromobenzaldehyde	24	1/20.0	34.8	62.9
8f	Cyclohexanone	Trifluoromethylbenzaldehyde	24	1/19.6	94.0	64.5
8g	Cyclopentanone	4-Nitrobenzaldehyde	72	1/0.7	98.3[c]	73.4
8h	Acetone	4-Nitrobenzaldehyde	72	–	60.4	40.0

[a] Determined by chiral-phase HPLC analysis. [b] Combined yields of isolated diastereomers. [c] *syn* isomer.

are in agreement with the literature data.[39,40] The diastereomeric ratios and enantiomeric excesses were determined by chiral HPLC analysis of the products by using literature methods.[41–43]

3. Conclusion

In conclusion, we have designed and synthesized new di- or triamide organocatalysts derived from (*L*)-proline and successfully used in the direct asymmetric aldol reaction of aliphatic ketones and aromatic aldehydes in water. Among the catalysts investigated in this study, catalyst **7c** gave the best diastereoselectivities (up to 99%), enantioselectivities (up to 98%) and yields (up to 91%) when different aliphatic ketones and aromatic aldehydes with electron withdrawing groups were used. Furthermore, these catalysts showed their best catalytic activities in water which is also an important contribution to green chemistry requirements.

4. Experimental

General

All reagents were of commercial quality and reagent quality solvents were used without further purification. IR spectra were determined on a Perkin Elmer, Spectrum One FT-IR spectrometer and Bruker Tensor 27 spectrometer. NMR spectra were recorded on Bruker Avance III 500 MHz and Varian-INOVA 500 MHz NMR spectrometer. Chemical shifts δ are reported in ppm with TMS as internal standart and the solvents were $CDCl_3$ and CD_3OD. Column chromatography was conducted on silica gel 60 (40–63 μM). TLC was carried out on aluminum sheets precoated with silica gel $60F_{254}$ (Merck). GC-MS spectrum was recorded on Agilent 6890N-GC-System-5973 IMSD spectrometer. LC-MS (QTOF) spectra were obtained on Agilent G6530B model TOF/Q-TOF Mass Spectrometer. Optical rotations were measured with Bellingham Stanley ADP-410 Polarimeter. Chiral HPLC analyses were performed with Shimadzu HPLC (Daicel Chiralpak AD and AD-H columns) equipped with SPD-20A detector and isopropanol/hexane mixtures as the eluent. The protection of *L*-proline was carried out according to the literature procedure.[44] Spectroscopic data of this compound were in accordance with its structure.

General Procedure for the Synthesis of Aminobenzamid Derivatives (1a–d)

The corresponding amines (1.15 mmol) were added to isatoic anhydride (1.00 mmol), dissolved in ethyl acetate and stirred at room tempearature for 5 hours (for compound **1a** at 60 °C for 1.5 hours). The precipitates were filtered and the crude products were purified by crystallization or column chromatography.

General Procedure for Amidation Reactions

1-Hydroxy-1*H*-benzotriazole (HOBt, 1.00 mmol) was added to the stirred solution of Boc-protected acid (0.92 mmol) in dry THF. After 10 min stirring at 0 °C under nitrogen, dicyclohexylcarbodiimide (DCC) (1.00 mmol) was added. The mixture was stirred at 0 °C for 1 h, and the amine (1.02 mmol) was added. In the case of amino acid ester hydrochloride, to the suspension of amino acid ester hydrochloride in dry THF, triethylamine (0.5 mL) was added, and stirred at room temperature for 1 h. This solution was then added to the first mixture. The reaction mixture was then stirred at room temperature for 24 h, and the reaction monitored by TLC. The formed precipitate was removed by filtration, and filtrate evaporated under vacuum. The residue was dissolved in 50 mL of ethyl acetate, and resultant solution washed successively with

saturated aqueous solution of $NaHCO_3$ (30 mL × 3), 5% aqueous solution of $KHSO_4$ (30 mL × 3) and saturated aqueous solution of NaCl (30 mL × 3) and finally dried with anhydrous Na_2SO_4. After filtration, the mixture was evaporated under vacuum to give the crude products **2a–d, 4a, 4c** and **6a–c** which were purified by column chromatograpy on silica gel.

General Procedure for Hydrolysis to Synthesize 5a and 5c

To the solution of compounds **4a** and **4c** (1.00 mmol) in methanol (5 mL), 2 N aqueous NaOH was added at 0 °C to adjust to pH 11. The reaction mixture was stirred at 0 °C for 3 h, and at room temperature for 24 h, and then adjusted to pH 2 with aqueous solution of $KHSO_4$. The solution was evaporated under vacuum to remove methanol, and extracted with ethyl acetate (30 mL × 3). The combined organic layer was successively washed with brine (20 mL × 2) and dried with anhydrous Na_2SO_4. After filtration, the filtrate was evaporated to provide compounds **5a** and **5c** which was used without any further purification.

General Procedure for Deprotection and Synthesis of 3a–d and 7a–c

To the solution of *N*-Boc protected compounds **2a–d** and **6a–c** (1.00 mmol) in dry DCM (15 mL) at 0 °C, TFA (27.00 mmol) was added dropwise over 5 min with stirring. The reaction mixture was stirred at 0 °C for 1 h, and at room temperature for 2 h, then 2M K_2CO_3 was added to the reaction mixture to adjust basic pH. The organic phase was washed with water, dried over $MgSO_4$, filtered and evaporated to give the pure compounds **3a–d** and **7a–c**.

(*S*)-2-Amino-*N*-(1-phenylethyl)benzamide (1a)

White solid, yield 71 %, mp 132.4–133.2 °C, (mp 136–138 °C,[37]), $[\alpha]^{20}_D$ = −103.9 (c = 1.02, $CHCl_3$); ^{1}H NMR ($CDCl_3$, 500 MHz) δ 1.57 (d, *J* = 6.9 Hz, 3H, CH_3), 5.23–5.29 (m, 1H, C<u>H</u>CH_3), 6.29 (brs, 1H, NH), 5.49 (brs, 2H, NH_2), 6.61–6.66 (m, 2H, ArH), 7.17–7.20 (m, 1H, ArH), 7.25–7.28 (m, 1H, ArH), 7.31–7.38 (m, 5H, ArH) ppm; FTIR (ATR) ν 3418, 3299, 3083, 3057, 3029, 2984, 2971, 1618, 1531, 1493, 1447, 1156 cm^{-1}; GC-MS: *m/z* 240 (M^+), 136 ($C_7H_8N_2O$), 120 (C_7H_7NO-1), 105 (C_7H_6O-1), 92 (C_7H_8), 77 (C_6H_6-1).

(*R*)-2-Amino-*N*-(1-phenylethyl)benzamide (1b)

White solid, yield 95 %, mp 132.6–133.8 °C, $[\alpha]^{20}_D$ = + 82.0 (c = 1.00, $CHCl_3$), [30]. FTIR (ATR) ν 3417, 3298, 3084, 3057, 3028, 2984, 2927, 1618, 1531, 1493, 1447, 1346, 1156 cm^{-1}.

2-Amino-*N*-butylbenzamide (1c)

White solid, yield 95 %, mp 88.5–89.2 °C;[38] ^{1}H NMR ($CDCl_3$, 500 MHz) δ 0.93 (td, *J* = 7.3, 1.4 Hz, 3H, CH_3), 1.34–1.41 (m, 2H, CH_2), 1.52–1.58 (m, 2H, CH_2), 3.34–3.39 (m, 2H, CH_2), 5.34 (brs, 2H, NH_2), 6.20 (brs, 1H, NH), 6.59–6.62 (m, 1H, ArH), 6.65 (d, *J* = 8.2 Hz, 1H, ArH), 7.15–7.18 (m, 1H, ArH), 7.29 (d, *J* = 8.0 Hz, 1H, ArH) ppm; FTIR (ATR) ν 3421, 3303, 3076, 2958, 2931, 2872, 1633, 1531, 1488, 1448, 1367, 1155 cm^{-1}.

2-Amino-*N*-cyclohexylbenzamide (1d)

White solid, yield 82 %, mp 156.9 °C;[38] ^{1}H NMR ($CDCl_3$, 500 MHz) δ 1.17–1.23 (m, 1H, CH_2), 1.35–1.40 (m, 4H, 2 × CH_2), 1.64–1.66 (m, 1H, CH_2), 1.76–1.79 (m, 2H, CH_2), 1.95–1.96 (m, 2H, CH_2), 3.86–3.93 (m, 1H, C<u>H</u>NH), 6.19 (brs, 2H, NH_2), 6.49–6.52 (m, 1H, ArH), 6.74 (d, *J* = 8.1 Hz, 1H, ArH), 7.11–7.14 (m, 1H, ArH), 7.25 (brs, 1H, NH), 7.48 (d, *J* = 7.8 Hz, 1H, ArH) ppm; FTIR (ATR) ν 3462, 3355, 3279, 3056, 2930, 2849, 1616, 1538, 1494, 1463, 1447, 1151 cm^{-1}.

(*S*)-*tert*-Butyl 2-(2-((*S*)-1-phenylethylcarbamoyl)phenylcarbamoyl)pyrrolidine-1-carboxylate (2a)

Colorless oil, yield 73.1 %, $[\alpha]^{20}_D$ = −88.00 (c = 1.00, $CHCl_3$); ^{1}H NMR ($CDCl_3$, 500 MHz) δ 1.36 and 1.53 (s, 9H, 3 × CH_3, rotamers), 1.59 (d, *J* = 6.9 Hz, 3H, CH_3), 1.77–1.80 (m, 2H, pro-γ), 2.02–2.08 (m, 1H, pro-β), 2.11–2.13 (m, 1H, pro-β), 3.46–3.51 (m, 1H, pro-δ), 3.61–3.66 (m, 1H, pro-δ), 4.22–4.25 and 4.38–4.41 (m, 1H, pro-α, rotamers), 5.27–5.32 (m, 1H, PhCH), 6.55 (brd, *J*=6.7 Hz, 1H, NH), 7.05–7.11 (m, 1H, ArH), 7.29–7.32 (m, 1H, ArH), 7.35–7.38 (m, 4H, ArH), 7.42–7.51 (m, 2H, ArH), 8.61–8.63 (m, 1H, ArH), 11.40 and 11.43 (brs, 1H, NH, rotamers) ppm; ^{13}C NMR ($CDCl_3$, 125 MHz) δ 21.7 (CH_3), 23.7 (pro-γ), 28.2 (3xCH_3), 31.4 (pro-β), 46.6 (pro-δ), 49.2 (PhCH), 63.7 (pro-α), 80.1 ($C(CH_3)_3$), 120.8 ($C_{aro}H$), 121.1 ($C_{aro}H$), 122.9 ($C_{aro}H$), 126.1 ($C_{aro}H$), 126.4 ($C_{aro}H$), 127.5 ($C_{aro}H$), 128.7 ($C_{aro}H$), 132.6 (C_{aro}), 139.2 (C_{aro}), 142.9 (C_{aro}), 154.1 (C=O), 167.8 (C=O), 172.3 (C=O) ppm; LC-MS (ESI-QTOF) *m/z* $[M+H]^+$, found 438.2389. $C_{25}H_{31}N_3O_4$ requires 438.2393. FTIR (ATR) ν 3323, 3033, 2970, 2927, 1688, 1580, 1505, 1448, 1156 cm^{-1}.

(*S*)-*tert*-Butyl 2-(2-((*R*)-1-phenylethylcarbamoyl)phenylcarbamoyl)pyrrolidin-1-carboxylate (2b)

Pinkish solid, yield 27 %, mp 54.4 °C, $[\alpha]^{20}_D$ = −8.0 (c = 1.00, $CHCl_3$); ^{1}H NMR ($CDCl_3$, 500 MHz) δ 1.32 and 1.53 (s, 9H, 3 × CH_3, rotamers), 1.59 and 1.62 (d, *J* = 6.6 Hz, 3H, CH_3, rotamers), 1.86–1.91 (m, 1H, pro-γ), 1.93–2.02 (m, 1H, pro-γ), 2.08–2.16 and 2.21–2.29 (m, 2H, pro-β, rotamers), 3.41–3.47 and 3.51–3.56 (m, 1H, pro-δ, rotamers), 3.66–3.76 (m, 1H, pro-δ), 4.22–4.25 and 4.38–4.40 (dd, *J* = 8.5, 4.1 Hz, 1H, pro-α, rotamers), 5.27–5.33 (m, 1H, PhCH), 6.48 and 6.64 (brd, *J* = 7.5 Hz, 1H, NH, rotamers), 7.00–7.08 (m, 1H, ArH), 7.28–7.31 (m, 1H, ArH), 7.36–7.39 (m, 4H, ArH), 7.44–7.48 (m, 2H, ArH), 8.57–8.63 (m, 1H, ArH), 11.48 and 11.56 (brs, 1H, NH, rotamers) ppm; ^{13}C NMR ($CDCl_3$, 125 MHz) δ 19.1 (CH_3), 21.6 (pro-γ), 28.2 (3 × CH_3), 31.4 (pro-β), 46.7 (pro-δ), 49.1 (Ph<u>C</u>H), 62.4 (pro-α), 80.0 ($C(CH_3)_3$), 120.0 ($C_{aro}H$), 121.0 ($C_{aro}H$), 122.8 ($C_{aro}H$), 126.3 ($C_{aro}H$), 126.6 ($C_{aro}H$), 127.5 ($C_{aro}H$), 128.7 ($C_{aro}H$), 132.4 (C_{aro}), 139.2 (C_{aro}),

142.7 (C_{aro}), 154.1 (C=O), 167.8 (C=O), 172.2 (C=O) ppm; LC-MS (ESI-QTOF): *m/z* $[M+H]^+$, found 438.2389. $C_{25}H_{31}N_3O_4$ requires 438.2393; FTIR (ATR): ν= 3313, 3065, 2974, 2931, 1676, 1642, 1585, 1444, 1386, 1158 cm^{-1}.

(*S*)-*tert*-Butyl 2-(2-(butylcarbamoyl)phenylcarbamoyl) pyrrolidine-1-carboxylate (2c)

Yellow oil, yield 85 %, $[\alpha]^{20}_D$ = −64.0 (c = 1.00, $CHCl_3$); ^1H NMR ($CDCl_3$, 500 MHz) δ 0.87 (brs, 3H, CH_3), 1.26 and 1.41 (s, 9H, 3 × CH_3, rotamers), 1.29–1.32 (m, 2H, CH_2), 1.49–1.51 (m, 2H, CH_2), 1.79–1.81 (m, 1H, pro-γ), 1.86–1.90 (m, 1H, pro-γ), 2.00–2.09 and 2.16–2.20 (m, 2H, pro-β), 3.26–3.31 (m, 1H, NCH_2), 3.32–3.36 (m, 1H, NCH_2), 3.41–3.46 (m, 1H, pro-δ), 3.59–3.65 (m, 1H, pro-δ), 4.13–4.16 and 4.28–4.30 (m, 1H, pro-α, rotamers), 6.68 and 6.72 (brs, 1H, NH, rotamers), 6.90–7.00 (m, 1H, ArH), 7.26–7.46 (m, 2H, ArH), 8.48 and 8.52 (brd, 1H, ArH, rotamers), 11.51 (brs, 1H, NH) ppm; ^{13}C NMR ($CDCl_3$, 125 MHz) δ 13.8 (CH_3), 20.1 (CH_2), 23.7 (CH_2), 28.2 (3 × CH_3), 30.5 (pro-γ), 31.5 (pro-β), 39.6 ($NHCH_2$), 46.7 (pro-δ), 62.4 (pro-α), 80.0 ($\underline{C}(CH_3)_3$), 120.8 ($C_{aro}H$), 120.9 ($C_{aro}H$), 122.8 ($C_{aro}H$), 126.7 ($C_{aro}H$), 132.2 (C_{aro}), 139.0 (C_{aro}), 154.1 (C=O), 168.6 (C=O), 172.2 (C=O) ppm; LC-MS (ESI-QTOF) *m/z* $[M+H]^+$, found 390.2388. $C_{21}H_{31}N_3O_4$ requires 390.2393; FTIR (ATR) ν 3351, 3067, 2957, 2931, 2873, 1679, 1644, 1585, 1516, 1477, 1446 cm^{-1}.

(*S*)-*tert*-Butyl 2-(2-(cyclohexylcarbamoyl)phenylcarbamoyl)pyrrolidine-1-carboxylate (2d)

Yellow solid, yield 86 %, mp 139.2–140.1 °C, $[\alpha]^{20}_D$ = −76.0 (c = 1.00, $CHCl_3$); ^1H NMR ($CDCl_3$, 500 MHz) δ 1.19–1.26 (m, 3H, CH_2), 1.35 and 1.50 (s, 9H, 3 × CH_3, rotamers), 1.41–1.43 (m, 2H, CH_2), 1.64–1.67 (m, 1H, CH_2), 1.74–1.76 (m, 2H, CH_2), 1.87–1.92 (m, 1H, CH_2), 1.96–1.98 (m, 3H, CH_2 ve pro-γ), 2.08–2.11 (m, 1H, pro-β), 2.16–2.19 (m, 1H, pro-β), 3.41–3.47 and 3.51–3.56 (m, 1H, pro-δ), 3.67–3.75 (m, 1H, pro-δ), 3.91–3.95 (m, 1H, NH$\underline{CH}$), 4.22–4.25 and 4.39–4.42 (m, 1H, pro-α, rotamers), 6.11 and 6.17 (brd, *J* = 7.3 Hz, 1H, NH), 7.02–7.09 (m, 1H, ArH), 7.39–7.47 (m, 2H, ArH), 8.61–8.63 (m, 1H, ArH), 11.47 (brs, 1H, NH) ppm; ^{13}C NMR ($CDCl_3$, 125 MHz) δ 23.8 (CH_2), 24.8 (CH_2), 25.5 (CH_2), 28.2 (3xCH_3), 30.5 (CH_2), 31.5 (pro-γ), 32.9 (CH_2), 33.0 (pro-β), 47.7 (N-CH), 48.5 (pro-δ), 62.5 (pro-α), 80.0 ($\underline{C}(CH_3)_3$), 121.1 ($C_{aro}H$), 121.3 ($C_{aro}H$), 122.8 ($C_{aro}H$), 126.4 ($C_{aro}H$), 132.4 (C_{aro}), 139.1(C_{aro}), 154.1 (C=O), 167.7 (C=O), 172.2 (C=O) ppm; LC-MS (ESI-QTOF) *m/z* $[M+H]^+$, found 416.2545. $C_{23}H_{33}N_3O_4$ requires 416.2549; FTIR (ATR) ν 3326, 3064, 2957, 2930, 2873, 1683, 1641, 1586, 1446, 1366, 1160 cm^{-1}.

(2*S*)-*N*-(2-((1*S*)-1-phenylethylcarbamoyl)phenyl)pyrrolidin-2-carboxamide (3a)

White solid, yield 57 %, mp 161.2–162.1 °C, $[\alpha]^{20}_D$ = −40.9 (c = 1.27, $CHCl_3$); ^1H NMR ($CDCl_3$, 500 MHz) δ 1.53 (d, *J* = 6.9 Hz, 3H, CH_3), 1.55–1.60 (m, 2H, pro-γ), 1.85–1.91 (m, 1H, pro-β), 1.99 (brs, 1H, NH), 2.04–2.11 (m, 1H, pro-β), 2.74–2.79 (m, 1H, pro-δ), 2.90–2.94 (m, 1H, pro-δ) , 3.76–3.79 (m, 1H, pro-α), 5.22–5.27 (m, 1H, PhCH), 6.33 (brd, *J* = 6.5 Hz, 1H, NH), 6.97–7.00 (m, 1H, ArH), 7.18–7.21 (m, 1H, ArH), 7.25–7.30 (m, 4H, ArH), 7.34–7.39 (m, 2H, ArH), 8.44–8.46 (d, *J*=8.2 Hz, 1H, ArH), 11.62 (brs, 1H, NH) ppm; ^{13}C NMR ($CDCl_3$, 125 MHz) δ 21.8 (CH_3), 26.1 (pro-γ), 31.1 (pro-β), 47.2 (pro-δ), 49.1 (Ph$\underline{C}$H), 61.5 (pro-α), 121.7 ($C_{aro}H$), 122.9 ($C_{aro}H$), 123.0 ($C_{aro}H$), 126.1 ($C_{aro}H$), 126.5 ($C_{aro}H$), 127.4 ($C_{aro}H$), 128.7 ($C_{aro}H$), 132.0 (C_{aro}), 138.2 (C_{aro}), 143.0 (C_{aro}), 167.6 (C=O), 174.8 (C=O) ppm; LC-MS (ESI-QTOF) *m/z* $[M+H]^+$, found 338.1866. $C_{20}H_{23}N_3O_2$ requires 338.1869; FTIR (ATR) ν 3292, 3063, 3031, 2975, 2933, 1673, 1640, 1597, 1514, 1447, 1374 cm^{-1}.

(2*S*)-*N*-(2-((*R*)-1–phenylethylcarbamoyl)phenyl)pyrrolidine-2-carboxamide (3b)

White solid, yield 77 %, mp 161–161.9 °C, $[\alpha]^{20}_D$ = −5.8 (c = 2.43, $CHCl_3$); ^1H NMR ($CDCl_3$, 500 MHz) δ 1.51 (d, *J* = 6.9 Hz, 3H, CH_3), 1.61–1.70 (m, 2H, pro-γ), 1.89–1.95 (m, 1H, pro-β), 2.03 (brs, 1H, NH), 2.06–2.12 (m, 1H, pro-β), 2.95–3.01 (m, 2H, pro-δ), 3.73–3.76 (m, 1H, pro-α), 5.21–5.27 (m, 1H, PhCH), 6.35 (brd, *J* = 7.6 Hz, 1H, NH), 6.95–6.98 (m, 1H, ArH), 7.19–7.23 (m, 1H, ArH), 7.27–7.36 (m, 6H, ArH), 8.43 (brd, *J*=8.2 Hz, 1H, ArH), 11.56 (brs, 1H, NH) ppm; ^{13}C NMR ($CDCl_3$, 125 MHz) δ 21.5 (CH_3), 26.1 (pro-γ), 31.1 (pro-β), 47.3 (pro-δ), 49.1 (PhCH), 61.5 (pro-α), 121.6 ($C_{aro}H$), 122.9 ($C_{aro}H$), 123.1 ($C_{aro}H$), 126.3 ($C_{aro}H$), 126.6 ($C_{aro}H$), 127.5 ($C_{aro}H$), 128.7 ($C_{aro}H$), 132.0 (C_{aro}), 138.1 (C_{aro}), 142.7 (C_{aro}), 167.7 (C=O), 174.8 (C=O) ppm; LC-MS (ESI-QTOF) *m/z* $[M+H]^+$, found 338.1863. $C_{20}H_{23}N_3O_2$ requires 338.1869; FTIR (ATR) ν 3332, 3283, 3059, 3027, 2969, 1656, 1633, 1597, 1429, 1343 cm^{-1}.

(*S*)-*N*-(2-(Butylcarbamoyl)phenyl)pyrrolidine-2-carboxamide (3c)

White solid, yield 83 %, mp 124.4–124.9 °C, $[\alpha]^{20}_D$ = −3.6 (c = 1.65, $CHCl_3$); ^1H NMR ($CDCl_3$, 500 MHz) δ 0.95 (t, *J* = 7.0 Hz, 3H, CH_3), 1.37–1.44 (m, 2H, CH_2), 1.56–1.62 (m, 2H, CH_2), 1.68–1.78 (m, 2H, pro-γ), 1.98–2.04 (m, 1H, pro-β), 2.14–2.20 (m, 1H, pro-β), 2.22 (brs, 1H, NH), 3.02–3.11 (m, 2H, pro-δ), 3.35–3.42 (m, 1H, NCH_2), 3.44–3.51 (m, 1H, NCH_2), 3.84–3.87 (m, 1H, pro-α), 6.38 (brs, 1H, NH), 7.02–7.05 (m, 1H, ArH), 7.40–7.43 (m, 2H, ArH), 8.53 (d, *J* = 8.5 Hz, 1H, ArH), 11.74 (brs, 1H, NH) ppm; ^{13}C NMR ($CDCl_3$, 125 MHz) δ 13.8 (CH_3), 20.1 (CH_2), 26.1 (CH_2), 31.1 (pro-γ), 31.6 (pro-β), 39.7 ($NHCH_2$), 47.3 (pro-δ), 61.6 (pro-α), 121.5 ($C_{aro}H$), 122.9 ($C_{aro}H$), 123.1 ($C_{aro}H$), 126.6 ($C_{aro}H$), 131.8 (C_{aro}), 138.1 (C_{aro}), 168.5 (C=O),174.9 (C=O) ppm; LC-MS (ESI-QTOF) *m/z* $[M+H]^+$, found 290.1868. $C_{16}H_{23}N_3O_2$ requires 290.1869; FTIR (ATR) ν 3353, 3162, 3086, 3063, 2960, 2930, 2872, 1665, 1632, 1595, 1577, 1441, 1321 cm^{-1}.

(*S*)-*N*-(2-(Cyclohexylcarbamoyl)phenyl)pyrrolidine-2-carboxamide (3d)

White solid, yield 83 %, mp 189.6–190.3 °C; $[\alpha]^{20}_D$ = −10.0 (c = 0.82, $CHCl_3$); ^{1}H NMR ($CDCl_3$, 500 MHz) δ 1.18–1.28 (m, 3H, CH_2), 1.38–1.45 (m, 2H, CH_2), 1.65–1.67 (m, 1H, CH_2), 1.71–1.78 (m, 4H, 2 × CH_2), 2.00–2.05 (m, 3H, 2 × pro-γ ve pro-β), 2.08 (brs, 1H, NH), 2.14–2.22 (m, 1H, pro-β), 3.01–3.12 (m, 2H, pro-δ), 3.85–3.88 (m, 1H, NCH), 3.93–3.99 (m, 1H, pro-α), 6.05 (brs, 1H, NH), 7.03–7.06 (m, 1H, ArH), 7.41 (d, *J* = 8.2 Hz, 2H, ArH), 8.54 (d, *J* = 8.1 Hz, 1H, ArH), 11.71 (brs, 1H, NH) ppm; ^{13}C NMR ($CDCl_3$, 125 MHz) δ 24.8 (2 × CH_2), 25.5 (CH_2), 26.2 (CH_2), 31.1 (pro-γ), 33.0 (CH_2), 33.1 (pro-β), 47.4 (NCH), 48.5 (pro-δ), 61.6 (pro-α), 121.5 ($C_{aro}H$), 122.9 ($C_{aro}H$), 123.4 ($C_{aro}H$), 126.6 ($C_{aro}H$), 131.8 (C_{aro}), 138.1 (C_{aro}), 167.7 (C=O), 174.9 (C=O) ppm; LC-MS (ESI-QTOF) *m/z* $[M+H]^+$, found 316.2020. $C_{18}H_{25}N_3O_2$ requires 316.2025; FTIR (ATR) ν 3462, 3355, 3279, 3056, 2930, 2849, 1616, 1588, 1538, 1463, 1447, 1371, 1187 cm^{-1}.

(*S*)-*tert*-Butyl 2-((*S*)-1-(methoxycarbonyl)-2-phenylethylcarbamoyl)pyrrolidine-1-carboxylate (4a)

Yellow oil, yield 73 %, $[\alpha]^{20}_D$ = −38.7 (c = 1.24, $CHCl_3$);[45] ^{1}H NMR ($CDCl_3$, 500 MHz) δ 1.42 (bs, 9H, $C(CH_3)_3$), 1.77–1.86 (m, 2H, pro-γ), 1.88–2.06 (m, 2H, pro-β), 2.90–3.03 (m, 1H, $PhCH_2$), 3.19 (dd, *J* = 14.0, 5.5 Hz, 1H, $PhCH_2$), 3.29–3.39 (m, 2H, pro-δ), 3.72 (s, 3H, OCH_3), 4.19–4.29 (m, 1H, pro-α), 4.85 (bs, 1H, Phe-CH), 7.09 (bd, *J* = 7.0 Hz, 2H, ArH), 7.22–7.25 (m, 3H, ArH) ppm; ^{13}C NMR (CD_3OD, 125 MHz) δ 24.3 (pro-γ), 28.5 (3 × CH_3), 32.2 (pro-β), 38.1 ($PhCH_2$), 47.8 (pro-δ), 52.7 (Phe-CH), 55.1 (OCH_3), 61.6 (pro-α), 81.5 ($OC(CH_3)_3$), 127.9 ($C_{aro}H$), 129.5 ($C_{aro}H$), 130.1 ($C_{aro}H$), 138.3 (C_{aro}), 173.3 (C=O), 175.1 (C=O), 175.8 (C=O) ppm; FTIR (ATR) ν 3277, 3079, 3028, 2976, 2877, 1738, 1689, 1660, 1552, 1445, 1389, 1365, 1210 cm^{-1}.

(*S*)-*tert*-Butyl 2-(((*S*)-3-hydroxy-1-methoxy-1-oxopropane-2-yl)carbamoyl)-pyrrolidine-1-carboxylate (4c)

Colorless oil, yield 94 %, $[\alpha]^{20}_D$ = +88.0 (c = 1.00, CH_3OH);[46] ^{1}H NMR (CD_3OD, 500 MHz) δ 1.45 and 1.48 (s, 9H, 3 × CH_3, rotamers), 1.88–1.92 (m, 1H, pro-γ), 1.94–1.98 (m, 1H, pro-γ), 2.00–2.05 (m, 1H, pro-β), 2.12–2.29 (m, 1H, pro-β), 3.33 (brs, 1H, OH), 3.40–3.45 (m, 1H, pro-δ), 3.51–3.55 (m, 1H, pro-δ), 3.74 (s, 3H, OCH_3), 3.79–3.85 (m, 1H, CH_2OH), 3.91–3.96 (m, 1H, CH_2OH), 4.27–4.30 (m, 1H, pro-α), 4.53–4.55 (m, 1H, C<u>H</u>CH_2OH) ppm; FTIR (ATR) ν 3293, 3082, 2975, 2881, 1743, 1662, 1533, 1470, 1454, 1205, 1160 cm^{-1}.

(*S*)-2-((*S*)-*tert*-Butyl 2-carbamoylpyrrolidine-1-carboxyloyl)-3-phenyl-propanoic acid (5a)

White solid, yield 96 %, mp 143–144 °C (mp 145–147 °C)[45,47]; $[\alpha]^{20}_D$ = −43.1 (c= 1.3, $CHCl_3$). ^{1}H NMR ($CDCl_3$, 500 MHz) δ 1.38 (s, 9H, $C(CH_3)_3$), 1.74–1.86 (m, 3H, pro-γ and pro-β), 2.06–2.09 (m, 1H, pro-β), 3.05–3.07 (m, 1H, CH_2Ph), 3.27–3.37 (m, 3H, CH_2Ph and pro-δ), 4.25–4.29 (m, 1H, pro-**α), 4.87 (bs, 1H,** Phe-CH), 7.14–7.16 (m, 2H, NH and ArH), 7.20–7.27 (m, 4H, ArH) ppm; FTIR (ATR) ν 3425, 3314, 3060, 3028, 2977, 2930, 2881, 1735, 1660, 1651, 1526, 1392, 1367, 1243, 1160 cm^{-1}.

(*S*)-2-((*S*)-1-(*tert*-Butoxycarbonyl)pyrrolidine-2-carboxamido)-3-hydoxypropanoic Acid (5c)

White solid, yield 67 %, mp 139.4–140.1 °C; $[\alpha]^{20}_D$ = −106.0 (c = 1.00, CH_3OH); ^{1}H NMR ($CDCl_3$, 500 MHz) δ 1.30 (s, 9H, 3xCH_3), 1.66–1.75 (m, 2H, pro-γ), 1.90 (brs, 2H, pro-β), 3.24–3.37 (m, 2H, pro-δ), 3.71 (brs, 1H, CH_2OH), 3.88 (brs, 1H, CH_2OH), 4.17–4.23 (m, 2H, pro-α and <u>CH</u>CH_2OH), 7.12 (brs, 1H, OH), 7.53 and 7.69 (brs, 1H, NH, rotamers) ppm; ^{13}C NMR ($CDCl_3$, 125 MHz) δ 24.3 (pro-γ), 28.4 (3 × CH_3), 30.8 (pro-β), 47.3 (pro-δ), 56.4 (pro-α), 60.2 (<u>C</u>HCH_2OH), 62.3 (CH_2OH), 80.4 ($C(CH_3)_3$), 155.2 (C=O), 173.0 (C=O), 177.8 (C=O) ppm; LC-MS (ESI-QTOF) *m/z* $[M+Na]^+$, found 325.1368. $C_{13}H_{22}N_2O_6$ requires 325.1376; FTIR (ATR) ν 3487, 3275, 3079, 2974, 2932, 1733, 1654, 1540, 1479, 1457, 1281, 1163 cm^{-1}.

(*S*)-*tert*-Butyl 2-(((*S*)-1-(((*S*)-3-hydroxy-1-methoxy-1-oxopropane-2-yl-amino)-1-oxo-3-phenylpropane-2-yl) carbamoyl)pyrrolidine-1-carboxylate (6a)

Colorless oil, yield 68 %, $[\alpha]^{20}_D$ = +26.0 (c = 1.00, CH_3OH);[48] ^{1}H NMR (CD_3OD, 500 MHz) δ 1.29 and 1.46 (s, 9H, 3 × CH_3, rotamers), 1.73–1.80 (m, 3H, 2 × pro-**γ and pro-β), 2.06**–2.16 (m, 1H, pro-β), 2.91–3.04 (m, 1H, $PhCH_2$), 3.19–3.21 (m, 1H, $PhCH_2$), 3.34–3.38 (m, 1H, pro-δ), 3.41 (brs, 1H, pro-δ), 3.73 (s, 3H, OCH_3), 3.77–3.81 (m, 1H, CH_2OH), 3.88–3.89 (m, 1H, CH_2OH), 4.16 (brs, 1H, pro-α), 4.52 (brs, 1H, Phe-CH), 4.73 (brs, 1H, C<u>H</u>CH_2OH), 7.19–7.22 (m, 1H, ArH), 7.26–7.29 (m, 4H, ArH) ppm; LC-MS (ESI-QTOF) *m/z* $[M+H]^+$, found 464.2397. $C_{23}H_{33}N_3O_7$ requires 464.2392; FTIR (ATR) ν 3294, 3065, 3004, 2971, 2953, 2882, 1741, 1650, 1523, 1454, 1523, 1392, 1215, 1160 cm^{-1}.

(*S*)-*tert*-Butyl 2-(((*S*)-1-(2-(butylcarbamoyl)phenylamino)-1-oxo-3-phenylpropane-2-yl)-carbamoylpyrrolidine-1-carboxylate (6b)

White solid, yield 52 %, mp 166.2–166.7 °C; $[\alpha]^{20}_D$ = +32.0 (c = 1.00, CH_3OH); ^{1}H NMR ($CDCl_3$, 500 MHz) δ 0.89 (t, *J* = 6.9 Hz, 3H, CH_3), 1.30–1.37 (m, 12H, 3 × CH_3 ve 3xbutyl-CH_2), 1.48–1.54 (m, 2H, 1 × butyl-CH_2 ve 1 × pro-β), 1.67–1.77 (m, 3H, pro-γ ve pro-β), 3.01 (brs, 1H, $PhCH_2$), 3.19–3.32 (m, 5H, $PhCH_2$, 2 × pro-δ, 2 × $NHCH_2$), 4.15 and 4.42 (brs, 1H, pro-α, rotamers), 4.76–4.80 (m, 1H, Phe-CH), 6.13 (brs, 1H, NH), 6.98–7.01 (m, 1H, ArH), 7.08–7.17 (m, 5H, ArH), 7.33–7.38 (m, 2H, ArH), 8.45 (d, *J*=8.4 Hz, 1H, ArH), 11.36 (brs, 1H, NH) ppm; ^{13}C NMR ($CDCl_3$, 125 MHz) δ 12.7 (CH_3), 19.1 (CH_2), 23.5 (CH_2), 27.3 (3xCH_3), 30.4 (pro-γ), 37.2 (pro-β), 38.7 (Phe-CH_2), 45.9 ($NHCH_2$), 54.1 (pro-δ), 58.7

(Phe-CH), 60.0 (pro-α), 79.3 ($C(CH_3)_3$), 120.4 ($C_{aro}H$), 122.0 ($C_{aro}H$), 125.4 ($C_{aro}H$), 125.5 ($C_{aro}H$), 125.7 ($C_{aro}H$), 127.3 ($C_{aro}H$), 128.3 ($C_{aro}H$), 131.2 (C_{aro}), 135.6 (C_{aro}), 137.7 (C_{aro}), 154.8 (C=O), 167.5 (C=O), 168.7 (C=O), 171.1 (C=O) ppm; LC-MS (ESI-QTOF) *m/z* $[M+H]^+$, found 537.3071. $C_{30}H_{40}N_4O_5$ requires 537.3071; FTIR (ATR) ν 3314, 3059, 2928, 2850, 1682, 1625, 1536, 1443, 1393, 1240, 1163 cm^{-1}.

(*S*)-*tert*-Butyl 2-(((*S*)-3-hydroxy-1-(((*S*)-1-methoxy-1-oxo-3-phenylpropane-2-yl)-amino-1-oxopropane-2-yl) carbamoyl)pyrrolidine-1-carboxylate (6c)

Colorless oil, yield 62 %, $[\alpha]^{20}_D$ = −28.0 (c = 1.00, CH_3OH); ^1H NMR ($CDCl_3$, 500 MHz) δ 1.37 (s, 9H, 3xCH_3), 1.76–1.83 (m, 2H, pro-γ), 2.02 (brs, 2H, pro-β), 2.95–3.00 (m, 1H, $PhCH_2$), 3.06–3.10 (m, 1H, $PhCH_2$), 3.32 (brs, 1H, OH), 3.36–3.43 (m, 2H, pro-δ), 3.61 and 3.68 (s, 3H, OCH_3, rotamers), 3.83–3.86 (m, 2H, CH_2OH), 4.11–4.18 (m, 1H, pro-α), 4.37–4.40 (m, 1H, Phe-CH), 4.69–4.73 (m, 1H, C<u>H</u>CH_2OH), 7.06–7.08 (m, 2H, ArH), 7.12–7.15 (m, 1H, ArH), 7.18–7.22 (m, 2H, ArH), 7.28 (brd, *J* = 6.0 Hz, 1H, NH) ppm; ^{13}C NMR ($CDCl_3$, 125 MHz) δ 23.5 (pro-γ), 27.3 (3 × CH_3), 30.0 (pro-β), 36.6 ($PhCH_2$), 46.2 (pro-δ), 51.5 (OCH_3), 52.6 (pro-α), 53.6 (<u>C</u>HCH_2OH), 59.3 (Phe-CH), 61.6 (CH_2OH), 79.6 ($C(CH_3)_3$), 126.0 ($C_{aro}H$), 127.5 ($C_{aro}H$), 128.1($C_{aro}H$), 135.0 (C_{aro}), 154.5 (C=O), 169.8 (C=O), 170.8 (C=O),171.9 (C=O) ppm; LC-MS (ESI-QTOF) *m/z* $[M+H]^+$, found 464.2392. $C_{23}H_{33}N_3O_7$ requires 464.2397; FTIR (ATR) ν 3303, 3079, 2954, 2930, 1737, 1661, 1655, 1535, 1437, 1206, 1161 cm^{-1}.

(*S*)-Methyl 3-hydroxy-2-((*S*)-3-phenyl-2-((*S*)-pyrrolidine-2-carboxamido)propanamidopropanoate (7a)

White solid, yield 85 %, mp 52 °C; $[\alpha]^{20}_D$ = +120.0 (c = 1.00, CH_3OH); ^1H NMR ($CDCl_3$, 500 MHz) δ 1.42–1.48 (m, 1H, pro-**γ), 1.57**–1.64 (m, 2H, pro-γ and pro-β), 1.97–2.04 (m, 1H, pro-β), 2.73–2.77 (m, 1H, $PhCH_2$), 2.90–2.95 (m, 1H, $PhCH_2$), 2.96–3.01 (m, 1H, pro-δ), 3.22 (dd, *J*=5.5, 14.0 Hz, 1H, pro-δ), 3.58 (brs, 2H, pro-α and OH), 3.73 (s, 3H, OCH_3), 3.83–3.93 (m, 2H, <u>CH</u>$_2$OH), 4.58–4.61 (m, 1H, Phe-CH), 4.70 (brs, 1H, C<u>H</u>CH_2OH), 7.18–7.25 (m, 5H, ArH), 7.61 (d, *J* = 7.5 Hz, 1H, NH), 8.30 (brs, 1H, NH) ppm; ^{13}C NMR ($CDCl_3$, 125 MHz) δ 25.8 (pro-γ), 30.5 (pro-β), 37.9 ($PhCH_2$), 47.0 (pro-δ), 52.6 (OCH_3), 54.1 (pro-α), 54.9 (<u>C</u>HCH_2OH), 60.1 (Phe-CH), 62.4 (CH_2OH), 126.9 ($C_{aro}H$), 128.4 (C_{aro} H), 129.3 (C_{aro} H), 136.5 (C_{aro}), 170.8 (C=O), 171.3 (C=O), 175.8 (C=O) ppm; LC-MS (ESI-QTOF) *m/z* $[M+H]^+$, found 364.1869. $C_{18}H_{25}N_3O_5$ requires 364.1872; FTIR (ATR) ν 3272, 3100, 2963, 1660, 1559, 1442, 1299, 1189, 1132 cm^{-1}.

(*S*)-*N*-((*S*)-1-(2-(Butylcarbamoyl)phenylamino-1-oxo-3-phenylpropane-2-yl)pyrrolidine-2-carboxamide (7b)

White solid, yield 72 %, mp 117–118 °C; $[\alpha]^{20}_D$ = −96.0 (c = 1.00, $CHCl_3$); ^1H NMR ($CDCl_3$, 500 MHz) δ 0.95 (t, *J* = 7.5 Hz, 3H, CH_3), 1.35–1.42 (m, 2H, butyl-CH_2), 1.44–1.50 (m, 1H, pro-γ), 1.53–1.59 (m, 2H, butyl-CH_2), 1.61–1.67 (m, 2H, pro-γ ve pro-β), 2.02–2.06 (m, 1H, pro-β), 2.80–2.84 (m, 1H, $PhCH_2$), 2.90–2.95 (m, 1H, $PhCH_2$), 3.07–3.11 (m, 1H, pro-δ), 3.28–3.37 (m, 3H, 2 × butyl-CH_2, pro-δ), 3.79–3.82 (m, 1H, pro-α), 4.83–4.87 (m, 1H, Phe-CH), 6.33 (brt, 1H, NH), 7.04–7.07 (m, 1H, ArH), 7.18–7.21 (m, 3H, ArH), 7.25–7.28 (m, 3H, ArH), 7.41–7.44 (m, 2H, ArH), 8.24 (d, *J* = 9.0 Hz, 1H, NH), 8.60 (d, *J* = 8.5 Hz, 1H, NH), 11.52 (brs, 1H, NH) ppm; ^{13}C NMR ($CDCl_3$, 125 MHz) δ 13.7 (CH_3), 20.2 (CH_2), 25.7 (CH_2), 30.2 (pro-γ), 31.4 (pro-β), 37.8 (Phe-CH_2), 39.6 ($NHCH_2$), 46.8 (pro-δ), 54.4 (Phe-CH), 60.4 (pro-α), 121.0 ($C_{aro}H$), 121.2 ($C_{aro}H$), 123.0 ($C_{aro}H$), 126.4 ($C_{aro}H$), 126.8 ($C_{aro}H$), 128.4 ($C_{aro}H$), 129.3 ($C_{aro}H$), 132.4 (C_{aro}), 136.9 (C_{aro}), 139.8 (C_{aro}), 168.7 (C=O), 170.1 (C=O), 175.6 (C=O) ppm; LC-MS (ESI-QTOF) *m/z* $[M+H]^+$, found 437.2638. $C_{25}H_{32}N_4O_3$ requires 437.2553; FTIR (ATR) ν 3335, 3244, 3061, 3025, 2955, 2930, 1688, 1661, 1624, 1588, 1490, 1435, 1282, 1185 cm^{-1}.

(*S*)-Metyl 2-((*S*)-3-hydroxy-2-((*S*)-3-pyrrolidine-2-carboxamido)propanamido)-3-phenylpropanoate (7c)

Colorless oil, yield 90 %, $[\alpha]^{20}_D$ = +6.0 (c = 1.00, CH_3OH); ^1H NMR (CD_3OD, 500 MHz) δ 1.86–1.95 (m, 3H, 2 × pro-γ and pro-β), 2.24–2.31 (m, 1H, pro-β), 3.01–3.05 (m, 1H, $PhCH_2$), 3.12–3.20 (m, 3H, $PhCH_2$ and 2 × pro-δ), 3.66 (m, 2H, CH_2OH), 3.70 (s, 3H, OCH_3), 4.01–4.04 (m, 1H, pro-α), 4.47–4.49 (m, 1H, Phe-CH), 4.71–4.74 (m, 1H, C<u>H</u>CH_2OH), 7.20–7.31 (m, 5H, ArH) ppm; ^{13}C NMR (CD_3OD, 125 MHz) δ 26.1 (pro-γ), 31.5 (pro-β), 38.4 ($PhCH_2$), 47.7 (pro-δ), 52.7 (OCH_3), 55.2 (pro-α), 56.4 (<u>C</u>HCH_2OH), 61.4 (Phe-CH), 63.1 (CH_2OH), 128.0 ($C_{aro}H$), 129.5 ($C_{aro}H$), 130.3 ($C_{aro}H$), 137.8 (C_{aro}), 171.8 (C=O), 173.2 (C=O), 174.2 (C=O) ppm; LC-MS (ESI-QTOF) *m/z* $[M+H]^+$, found 364.1868. $C_{18}H_{25}N_3O_5$ requires 364.1872; FTIR (ATR) ν 3340, 2958, 2848, 1666, 1554, 1450, 1191, 1136 cm^{-1}.

General procedure for aldol reaction catalyzed by organocatalyst 7c

The catalyst **7c** (0.10 mmol) and benzoic acid (0.10 mmol) were stirred in water at 0 °C for 10 min. Then, aldehyde (1.00 mmol) and ketone (10.00 mmol) were added, and the reaction mixture was stirred at 0 °C until the reaction completed. After the evaporation of water, the crude products were purified by column chromatography, eluted by EtOAc/hexane mixture. The enantioselectivity was determined by chiral HPLC with a Chiralpak AD and AD-H columns (UV detection set at 254 nm, *i*-PrOH/hexane as eluent).

Acknowledgement

We thank Yildiz Technical University Scientific Research Foundation (2015-01-02-YL09) for financial support.

5. References

1. M. M. Heravi, V. Zadsirjan, M. Dehghani, N. Hosseintash, *Tetrahedron Asymm*. **2017**, *28*, 587–707. **DOI:**10.1016/j.tetasy.2017.04.006
2. G. Guillena, C. Najera, D. J. Ramon, *Tetrahedron Asymm*. **2007**, *18*, 2249–2293. **DOI:**10.1016/j.tetasy.2007.09.025
3. H. Akutsu, K. Nakashima, H. Yanai, A. Kotani, S.-i. Hirashima, T. Yamamoto, R. Takahashi, A. Yoshida, Y. Koseki, H. Hakamata, T. Matsumoto, T. Miura, *Synlett* **2017**, *28*, 1363–1367. **DOI:**10.1055/s-0036-1558971
4. D. Bhattacharjee, D. Sutradhar, A. K. Chandra, B. Myrboh, *Tetrahedron* **2017**, *73*, 3497–3504. **DOI:**10.1016/j.tet.2017.05.025
5. A. Yazdani-Elah-Abadi, S. A. Pour, M. Kangani, R. Mohebat, R. *Monatsh. Chem*. **2017**, *148*, 2135–2142. **DOI:**10.1007/s00706-017-2008-7
6. H. Hegde, N. S. Shetty, *Chem. Het. Comp*. **2017**, *53* (*8*), 883–886. **DOI:**10.1007/s10593-017-2152-3
7. S. Nagaraju, O. Perumal, P. K. Divakar, B. Paplal, D. Kashinath, *New J. Chem*. **2017**, *41*, 8993–9001. **DOI:**10.1039/C7NJ01021D
8. M. T. Robak, M. A. Herbage, J. A. Elman, *Tetrahedron* **2011**, *67*, 4412–4416. **DOI:**10.1016/j.tet.2011.03.030
9. P. Milbeo, K. Maurent, L. Moulat, A. Lebrun, C. Didierjean, E. Aubert, J. Martinez, M. Calmes, *Tetrahedron* **2016**, *72*, 1706–1713. **DOI:**10.1016/j.tet.2016.02.027
10. E. Machuca, E. Juaristi, *Tetrahedron Lett.* **2015**, *56*, 1144–1148. **DOI:**10.1016/j.tetlet.2015.01.079
11. Z. Y. Li, Y. Chen, C. Q. Zheng, Y. Yin, L. Wang, X. Q. Sun, *Tetrahedron* **2017**, *73*, 78–85. **DOI:**10.1016/j.tet.2016.11.052
12. O. Illa, O. Porcar-Tost, C. Robledillo, C. Elvira, P. Nolis, O. Reiser, V. Branchadell, R. M. Ortuno, *J. Org. Chem*. **2018**, *83*, 350–363. **DOI:**10.1021/acs.joc.7b02745
13. Q. Li, Y. Li, J. Wang, Y. Lin, Z. Wei, H. Duan, Q. Yang, F. Bai, Y. Li, *New J. Chem*. **2018**, *42*, 827–831. **DOI:**10.1039/C7NJ03912C
14. A. O. Zuniga, M. Milan, E. Juaristi, *Org. Lett*. **2017**, *19*, 1108–1111. **DOI:**10.1021/acs.orglett.7b00129
15. T. P. Kumar, R. C. Shekhar, K. S. Sunder, R. Vadaparthi, *Tetrahedron Asymm*. **2015**, *26*, 543–547. **DOI:**10.1016/j.tetasy.2015.03.009
16. E. Machuca, G. Granados, B. Hinajosa, E. Juaristi, *Tetrahedron Lett*. **2015**, *56*, 6047–6051. **DOI:**10.1016/j.tetlet.2015.09.062
17. L. L. Lou, J. Zhang, H. Du, B. Zhao, S. Li, W. Yu, K. Yu, S. Liu, *Catal. Today.* **2016**, *264*, 109–114. **DOI:**10.1016/j.cattod.2015.10.004
18. T. P. Kumar, N. Manjula, K. Katragunta, *Tetrahedron Asymm*. **2015**, *26*, 1281–1284. **DOI:**10.1016/j.tetasy.2015.09.018
19. G. Guo, Y. Wu, X. Zhao, J. Wang, L. Zhang, Y. Cui, *Tetrahedron Asymm*. **2016**, *27*, 740–746. **DOI:**10.1016/j.tetasy.2016.06.014
20. Y. Zhou, G. Yang, C. Lu, J. Nie, Z. Chen, J. Ren, *Catal.Commun*. **2016**, *75*, 23–27. **DOI:**10.1016/j.catcom.2015.11.017
21. W. Zhao, C. Qu, L. Yang, Y. Cui, *Chinese J. Catal*., **2015**, *36*, 367–371. **DOI:**10.1016/S1872-2067(14)60248-5
22. G. D. Yadav, S. Singh, *Tetrahedron Asymm*. **2016**, *27*, 123–129. **DOI:**10.1016/j.tetasy.2015.12.005
23. E.-J. Xu, Y. Song, Z.-L. Wei, R. Wang, H.-F. Duan, Y.-J. Lin, Q-B. Yang, Y.-X. Li, *Can. J. Chem*. **2019**, *97*, 352–359. **DOI:**10.1139/cjc-2018-0352
24. N. Mase, Y. Nakai, N. Ohara, H. Yoda, K. Takabe, F. Tanaka, C. F. Barbas III, *J. Am. Chem. Soc*. **2006**, *128*, 734–735. **DOI:**10.1021/ja0573312
25. M. Lei, L. Shi, G. Li, S. Chen, W. Fang, Z. Ge, T. Cheng, R. Li, *Tetrahedron* **2007**, *63*, 7892–7898. **DOI:**10.1016/j.tet.2007.05.077
26. A. Ahmetlli, N. Spiliopoulou, A. Magi-Oikonomopoulou, D.-T. Gerokonstantis, P. Moutevelis-Minakakis, C. G. Kokotos, *Tetrahedron* **2018**, *74*, 5987–5995. **DOI:**10.1016/j.tet.2018.08.038
27. Y.-H. Chen, P.-H. Sung, K. Sung, *Amino Acids* **2010**, *38*, 839–845. **DOI:**10.1007/s00726-009-0290-3
28. Z. Tang, Z.-H. Yang, L.-F. Cun, L.-Z. Gong, A.-Q. Mi, Y.-Z. Jiang, *Org. Lett*. **2004**, *6*, 2285–2287. **DOI:**10.1021/ol049141m
29. P. Krattiger, R. Kovasy, J. D. Revell, S. Ivan, H. Wennemers, *Org. Lett*. **2005**, *7*, 1101–1103. **DOI:**10.1021/ol0500259
30. J. D. Revell, H. Wennemers, *Adv. Synth. Catal*. **2008**, *350*, 1046–1052. **DOI:**10.1002/adsc.200800053
31. M. Orlandi, M. Benaglia, L. Raimondi, G. Celentano, G. *Eur. J. Org. Chem*. **2013**, 2346–2354. **DOI:**10.1002/ejoc.201201643
32. I. Vlasserou, M. Sfetsa, D. T. Gerokonstantis, C. G. Kokotos, P. Moutevelis-Minakakis, *Tetrahedron* **2018**, *74*, 2338–2349. **DOI:**10.1016/j.tet.2018.03.054
33. T. Yorulmaz, F. Aydogan, C. Yolacan, *Synth. Commun*. **2017**, *47*, 78–85. **DOI:**10.1080/00397911.2016.1252988
34. C. Yolacan, M. E. Mavis, F. Aydogan, *Tetrahedron* **2014**, *70*, 3707–3713. **DOI:**10.1016/j.tet.2014.04.016
35. A. Ozkan, M. E. Mavis, F. Aydogan, C. Yolacan, *J. Chem. Soc. Pak*. **2014**, *36*, 326–331.
36. M. Cicek, F. Aydogan, C. Yolacan, *Lett. Org. Chem*. **2017**, *14*, 778–786. **DOI:**10.2174/1570178614666170724125842
37. J. Priego, P. Flores, C. Ortiz-Nava, J. Escalate, *Tetrahedron Asymm*. **2004**, 15, 3545–3549. **DOI:**10.1016/j.tetasy.2004.08.032
38. M. M. Zhang, L. Lu, X. S. Wang, *J. Het. Chem*. **2014**, *51*, 1363–1368. **DOI:**10.1002/jhet.1826
39. J. Zhao, L. He, J. Jiang, Z. Tang, L.–F. Cun, L.–Z. Gong, *Tetrahedron Lett*. **2008**, *49*, 3372–3375. **DOI:**10.1016/j.tetlet.2008.03.131
40. S.-D. Fu, X.-K. Fu, S.-P. Zhang, X.-C. Zou, X.-J. Wu, *Tetrahedron Asymmetry*. **2009**, *20*, 2390–2396. **DOI:**10.1016/j.tetasy.2009.09.019
41. Q. Zhao, Y.-H. Lam, M. Kheirabadi, C. Xu, K. N. Houk, C. E. Schafmeister, *J. Org. Chem*. **2012**, *77*, 4784–4792. **DOI:**10.1021/jo300569c
42. V. Gauchot, A. R. Schmitzer, *J. Org. Chem.* **2012**, *77*, 4917–4923. **DOI:**10.1021/jo300737u

43. M. Lei, L. Shi, G. Li, S. Chen, W. Fang, Z. Ge, T. Cheng, R. Li, *Tetrahedron*. **2007**, *63*, 7892–7898. **DOI:**10.1016/j.tet.2007.05.077
44. C. A. Thomas, E. R. Talaty, J. G. Bann, *Chem. Commun*. **2009**, 3366–3368. **DOI:**10.1039/b821952d
45. S. Chaudhary, H. Kumar, H. Verma, A. Rajpoot, *Int. J. Pharm Tech Res*. **2012**, *4*, 194–200.
46. Z. Chen, J. Deng, T. Ye, *Arkivoc* **2003**, *7*, 268–285. **DOI:**10.3998/ark.5550190.0004.723
47. S. Cheng, X. Zhang, W. Wang, M. Zhao, M. Zheng, H. W. Chang, J. Wu, S. Peng, *Eur. J. Med. Chem*. **2009**, *44*, 4904–4919. **DOI:**10.1016/j.ejmech.2009.08.002
48. B. McKeever, G. Pattenden, *Tetrahedron* **2003**, *59*, 2713–2727. **DOI:**10.1016/S0040-4020(03)00294-1

Povzetek

Prispevek poroča o sintezi novih di- in triamidnih organokatalizatorjih, pridobljenih iz (L)-prolina, in njihovi uspešni uporabi v neposredni asimetrični aldolni kondenzaciji alifatskih ketonov in aromatskih aldehidov v vodi pri 0 °C v prisotnosti benzojske kisline kot ko-katalizatorja. (S)-metil-2-((S)-3-hidroksi-2-((S)-3-pirolidin-2-karboksamido)propanamido)-3-fenilpropanoat (7c) je kot organokatalizator pri teh reakcijskih pogojih pokazal najboljše rezultate z dobro diastereoselektivnostjo (do 99 %), enantioselektivnostjo (do 98 %) in izkoristkom reakcij (do 91 %).

Except when otherwise noted, articles in this journal are published under the terms and conditions of the Creative Commons Attribution 4.0 International License

DOI: 10.17344/acsi.2019.5007 *Acta Chim. Slov.* **2020,** *67,* 1024–1034
creative commons

Scientific paper

Synthesis and Antimicrobial Evaluation of Some New Pyrazolo[1,5-*a*]pyrimidine and Pyrazolo[1,5-*c*]triazine Derivatives Containing Sulfathiazole Moiety

Elsherbiny Hamdy El-Sayed,[1,*] Ahmed Ali Fadda[2] and Ahmed Mohamed El-Saadaney[1]

[1] *Department of Chemistry, Faculty of Science, Port Said University, 42526 Port Said, Egypt,*

[2] *Department of Chemistry, Faculty of Science, Mansoura University, Mansoura, Egypt,*

** Corresponding author: E-mail: Saeed201691@yahoo.com*
Tel.: +201024689767

Received: 01-31-2019

Abstract

A number of important fused heterocyclic systems have been prepared by the reaction of 4-((3,5-diamino-1*H*-pyrazol-4-yl)-diazenyl)-*N*-(thiazol-2-yl)-benzenesulfonamide with some bifunctional nucleophiles such as ethyl acetoacetate, acetylacetone or arylidenemalononononitrile derivatives to obtain pyrazolo[1,5-*a*]pyrimidine derivatives. The structures of the newly synthesized compounds were determined based on their IR, ^{1}H and ^{13}C NMR and mass spectroscopic data. Most of the compounds produced showed good antibacterial and antifungal activity.

Keywords: Sulfathiazole; benzenesulfonamide; pyrazole; antimicrobial evaluation.

1. Introduction

It is known that sulfathiazole derivatives have a decisive new and differentiating application in various areas of chemistry.[1–3] The pyrazole skeleton is a common core in many pharmaceutically active compounds and is important for a wide range of pharmacological activities including anti-inflammatory,[4,5] antiviral,[6] antimicrobial,[7] antifungal,[8,9] hypoglycemic,[10,11] antihyperlipidemic,[12] cyclooxygenase-2 inhibitors,[13] CDK2/cyclinA inhibitors,[14,15] and anti-angiogenic activity.[16] Furthermore, carbonyl cyanide-phenylhydrazone is an efficient decoupler of oxidative phosphorylation sites in a mitochondrial organism.[17] In this study, arylhydrazonomalononitrile was prepared and used as a reactive intermediate in the synthesis of various heterocyclic compounds with expected critical biological activity. Therefore, we report here on the synthesis of some new sulfathiazole derivatives to investigate their antimicrobial activity.

2. Experimental

All melting points were determined with the electrical melting point device from Gallenkamp and are uncorrected. Precoated Merck Silica gel plates 60F-254 were used for thin layer chromatography (TLC) and the spots were detected under UV light (254 nm). The infrared spectra (IR) were recorded with a Mattson 5000 FTIR spectrophotometer (KBr plate). The NMR spectra were recorded on Varian Gemini spectrometer at 400 MHz (^{1}H NMR) and 100 MHz (^{13}C NMR). Deuterated DMSO-d_6 was used as solvent and tetramethylsilane (TMS) as internal standard. The chemical shifts were measured in δ ppm relative to the TMS. Mass spectra were determined with a GC-MS QP-100 EX Shimadzu instrument, and elemental analysis was performed with a Perkin-Elmer 2400 elemental analyzer.

Synthesis of N-(4-(N-(thiazol-2-yl)sulfamoyl)phenyl)carbonohydrazonoyl dicyanide (2)

To a solution of malononitrile (0.66 g, 10 mmol) in ethanol (30 ml) 0,5 g anhydrous sodium acetate was added. The solution was then treated with a solution of diazonium salt of p-aminosulfathiazole (prepared from (2.55 g, 10 mmol p-aminosulfathiazole and the corresponding quantities of hydrochloric acid and sodium nitrite). The reaction mixture was stirred for 1 hour and the resulting

solid was filtered off, washed with water and recrystallized from ethanol to compound **2**. Golden yellow crystals; yield: 90%; mp 215–220 °C ; IR (KBr): ν 3234, 3188 (2NH), 2225 and 2216 (2CN), 1654 (C=N) 1565 (N=N) cm^{-1}; ^1H NMR (400 MHz, DMSO-d_6): δ 6.81(d, 1H, H-5, thiazole ring, *J*=4.2), 7.21(d, 1H, H-4, thiazole ring, *J*=4.2), 7.75 (d, 2H, Ar-H, *J*=8.5), 8.00 (d, 2H, Ar-H, *J*=8.5), 11.61 (s, 1H, NH), 12.30 (s, 1H , $NHSO_2$) ppm; ^{13}C NMR (100 MHz, DMSO-d_6): δ 85.6, 112.3, 114.5, 116.8, 129.7, 132.0, 139.6, 147.9, 171.5 ppm; MS: *m/z* (%) 332 (M^+, 31.8), 257 (49), 71 (44), 55 (72), 43 (100). Anal. Calcd. for $C_{12}H_8N_6O_2S_2$ (332.36): C, 43.37; H, 2.52; N, 25.29 %. Found: C, 43.51; H, 2.63; N, 25.39 %.

Synthesis of 4-((3,5-diamino-1H-pyrazol-4-yl)diazenyl)-N-(thiazol-2-yl)benzenesulfonamide (3)

A mixture of **2** (3.32 g, 10 mmol) and hydrazine hydrate (0.5 ml, 10 mmol) was added to ethanol (10 ml) under reflux for 3 hours and then cooled to room temperature. The precipitate formed was collected by filtration, dried and recrystallized from a mixture of DMF/EtOH (1:1) to obtain compound **3**. Yellow needles crystals; yield: 78%; mp 235–240 °C; IR (KBr): ν 3430, 3373, 3337, 3289, 3219 ($2NH_2$ and 2NH) cm^{-1}; ^1H NMR (400 MHz, DMSO-d_6): δ 6.27 (s, 4H, $2NH_2$), 6.81 (d, 1H, H-5, thiazole ring, *J*=4.2), 7.21 (d, 1H, H-4, thiazole ring, *J*=4.2), 7.73 (d, 2H, Ar-H, *J*=8.5), 7.79 (d, 2H, Ar-H, *J*=8.5), 12.64 (s, 1H, $NHSO_2$), 12.66 (s, 1H, NH) ppm; ^{13}C NMR (100 MHz, DMSO-d_6): δ 74.5, 112.4, 127.9, 129.7, 132.0, 139.6, 137.9, 151.5, 171.9 ppm; MS: *m/z* (%) 364 (M^+, 0.9), 275 (49) 147 (10), 97(34), 57 (81); Anal. Calcd for $C_{12}H_{12}N_8O_2S_2$ (364.40): C, 66.49; H, 4.82; N, 24.67%. Found: C, 66.43; H, 4.90; N, 24.70%.

General procedure for the reaction of 3,5-aminopyrazole 3 with ethylacetoacetate and 1,3 dicarbonyl compound (acetyl aceton) toward formation of compounds 5 and 6

To a solution of compound **3** (0.3 g, 1 mmol) in glacial acetic acid (25 ml) the corresponding 1,3-dicarbonyl compound such as ethyl acetoacetate and acetylacetone (1 mmol) was added. The reaction mixture was refluxed for 3 hours under reflux in a sand bath and then poured onto crushed ice. Shaped precipitate was collected by filtration, washed with ethanol, dried and recrystallised from a mixture of DMF/EtOH (1:1) to compounds **5** and **6** respectively.

4-((2-Amino-7-methyl-5-oxo-4,5-dihydropyrazolo[1,5-a]pyrimidin-3-yl)diazenyl)-N-(thiazol-2-yl)benzenesulfonamide (5)

Orange crystals; yield: 75%; mp 230–235 °C; IR (KBr): ν 3444–3380 (NH_2 and NH), 1661 (CO) cm^{-1}; ^1H NMR(400 MHz, DMSO-d_6): δ 2.01(s, 3H, CH_3), 6.27(s, 2H, NH_2), 6.81 (d, 1H, H-5, thiazole ring, *J*=4.2), 7.21 (d, 1H, H-4, thiazole ring, *J*=4.2), 7.26 (s, 1H, pyrimidine ring), 7.73 (d, 2H, Ar-H, *J*=8.5), 7.79 (d, 2H, Ar-H, *J*=8.5), 11.46 (s, 1H, NHCO), 12.64 (s, 1H, $NHSO_2$) ppm; ^{13}C NMR (100 MHz, DMSO-d_6): δ 22.2, 76.9, 104.3, 112.2, 127.4, 129.2, 131.9, 137.1, 139.8, 146.8, 147.9, 161.3, 171.8 ppm; MS: *m/z* (%) 430 (M^+, 1.0), 139 (28), 110 (19), 82 (29), 63 (40), 43 (100); Anal.Calcd for $C_{16}H_{14}N_8O_3S_2$ (430.46): C, 44.64; H, 3.28; N, 26.03%; Found: C, 44.73; H, 3.32; N, 26.08%.

4-((2-Amino-5,7-dimethylpyrazolo[1,5-a]pyrimidin-3-yl)diazenyl)-N-(thiazol-2-yl) benzenesulfonamide (6)

Brown powder; yield: 80%; mp 225–230 °C ; IR (KBr): ν 3437–3394 (NH_2 and NH), 1560 (N=N) cm^{-1}; ^1H NMR (400 MHz, DMSO-d_6): δ 2.08 (s, 3H, CH_3), 2.24 (s, 3H, CH_3), 5.74 (s, 2H, NH_2), 6.81 (d, 1H, H-5, thiazole ring, *J*=4.2), 7.08 (s, 1H, pyrimidine ring), 7.21 (d, 1H, H-4, thiazole ring, *J*=4.2), 7.73 (d, 2H, Ar-H, *J*=8.5), 7.79 (d, 2H, Ar-H, *J*=8.5), 12.67 (s, 1H, $NHSO_2$) ppm; ^{13}C NMR (100 MHz, DMSO-d_6): δ 17.7, 24.5, 87.8, 108.9, 112.3, 127.5, 129.4, 131.6, 137.7 139.8, 145.8, 152.8, 164.9, 171.9 ppm; MS: *m/z* (%) 428 (M^+, 7.0), 395 (28), 369 (17), 313 (22), 201 (50), 183 (38), 130 (68), 92 (100). Anal. Calcd for $C_{17}H_{16}N_8O_2S_2$ (428.49): C, 47.65; H, 3.76; N, 26.15%; Found: C, 47.74, H, 3.79, N, 26.20%.

General procedure for the reaction of 3,5-amino pyrazole (3) with 2-(4-chloro and 4-nitro benzylidene)malononitrile:

To a solution of compound **3** (0.3 g, 1 mmol) in ethanol (25 ml) the corresponding arylidene was added, namely 2-(4-chlorobenzylidene)malononitrile (0.189 mg, 1 mmol) and 2-(4-nitrobenzylidene)malononitrile (0.2 g, 1 mmol) containing a catalytic amount of pipridine. The reaction mixture was refluxed for 3 hours to obtain compounds **7** and **8**, respectively.

4-((2,5-Diamino-7-(4-chlorophenyl)-6-cyanopyrazolo[1,5-a]pyrimidin-3-yl)diazenyl)-N-(thiazol-2-yl)benzenesulfonamide (7)

Brown powder; yield: 81%; mp 240–245 °C ; IR (KBr): ν 3435–3300, 2191 (for $2NH_2$, NH and CN functional groups) cm^{-1}; ^1H NMR (400 MHz, DMSO-d_6): δ 6.28 (s, 2H, NH_2), 6.81 (d, 1H, H-5, thiazole ring, *J*=4.2), 7.21 (d, 1H, H-4, thiazole ring, *J*=4.2), 7.54 (s, 2H, NH_2), 7.56 (d, 2H, Ar-H), 7.73 (d, 2H, Ar-H, *J*=8.5), 7.79 (d, 2H, Ar-H, *J*=8.5), 7.98 (d, 2H, Ar-H), 12.64 (s, 1H, $NHSO_2$) ppm; MS: *m/z* (%) 551 (M^+, 10), 553 (M^++2, 1), 386 (28), 280 (35), 242 (28), 185 (75), 139 (57), 105 (71), 69 (61), 42 (52); Anal. Calcd for $C_{22}H_{15}ClN_{10}O_2S_2$ (551.00): C, 47.96; H, 2.74; N, 25.42%; Found: C, 47.86, H, 2.68, N, 25.34%.

4-((2,5-Diamino-6-cyano-7-(4-nitrophenyl)pyrazolo[1,5-a]pyrimidin-3-yl)diazenyl)-N-(thiazol-2-yl)benzenesulfonamide (8)

Dark brown powder; yield: 82%; mp 265–270 °C ; IR (KBr) ν 3426–3399, 2212, 1530 ($2NH_2$, NH, CN and NO_2) cm^{-1}; ^1H NMR (400 MHz, DMSO-d_6): δ 6.28 (s, 2H, NH_2),

6.81 (d, 1H, H-5, thiazole ring, *J*=4.2), 7.21 (d, 1H, H-4, thiazole ring, *J*=4.2), 7.53 (s, 2H, NH_2), 7.73 (d, 2H, Ar-H, *J*=8.5), 7.79 (d, 2H, Ar-H, *J*=8.5), 7.98 (d, 2H, Ar-H), 8.29 (d, 2H, Ar-H), 12.64 (s, 1H, $NHSO_2$) ppm; ^{13}C NMR (100 MHz, DMSO-d_6): δ 87.4, 88.3, 112.8, 116.2, 124.5, 126.3, 127.4, 129.2, 131.5, 137.3, 139.2, 140.9, 147.1, 147.8, 152.7, 165.6, 169.9, 171.8 ppm; MS: *m/z* (%) 561 (M^++1, 10), 331 (83), 267 (100), 185 (54), 157 (25), 116 (31), 48 (28); Anal. Calcd for $C_{22}H_{15}N_{11}O_4S_2$ (561.56): C, 47.06; H, 2.69; N, 27.44%; Found: C, 47.13, H, 2.71, N, 27.40%.

Synthesis of 4-((3-amino-5-(3-phenylthioureido)-1H-pyrazol-4-yl)diazenyl)-N-(thiazol-2-yl) benzenesulfonamide (9)

Compound **3** (0.3 g, 1 mmol) was added to a solution of phenyl isothiocyanate (1 mmol) in pyridine (10 ml) and the reaction mixture was refluxed for 3 hours. The mixture was then poured into crushed ice, a few drops of HCl were added and the resulting solid was filtered and recrystallized from ethanol to obtain compound **9**. Brown powder; yield: 76%; mp 245–250 °C ; IR (KBr) ν 3444, 3424 (NH_2 and 4NH), 1644–1561 (N=N); ^{1}H NMR (400 MHz, DMSO-d_6): δ 6.27 (s, 2H, NH_2), 6.81 (d, 1H, H-5, thiazole ring, *J*=4.2), 7.21 (d, 1H, H-4, thiazole ring, *J*=4.2), 7.31–7.79 (m, 5H,Ar-H), 7.73 (d, 2H, Ar-H, *J*=8.5), 7.79 (d, 2H, Ar-H, *J*=8.5), 10.7 (s, 1H, NHC=S), 11.20 (s, 1H, NHC=S), 12.42 (s, 1H, NH), 12.64 (s, 1H,$NHSO_2$) ppm; ^{13}C NMR (100 MHz, DMSO-d_6): δ 74.5, 112.2, 126.7, 127.4, 128.5, 129.1, 129.8, 131.9, 137.1, 138.6, 139.8, 151.4, 171.8, 179.9 ppm; MS: *m/z* (%) 500 (M^+, 30), 394 (7), 298 (5), 284 (19), 259 (23), 214 (10), 193 (11), 109 (63), 85 (100), 68 (68), 42 (95); Anal. Calcd for $C_{19}H_{17}N_9O_2S_3$ (499.59): C, 45.68; H, 3.43; N, 25.23%; Found: C, 45.77, H, 3.49, N, 25.25%.

General procedure for synthesis of compounds 11–14

Diazonium salt of **10** (10 mmol) was added dropwise in an ice-cold solution of malononitrile, 2-cyanoacetohydrazide, *N*-phenylacetamide and 3,5-dimethylphenol (10 mmol) in pyridine and stirred for 1 hour. The reaction mixture was then cooled and the resulting solid was collected by filtration and recrystallized from ethanol.

.4-((4,7-Diamino-3-cyanopyrazolo[5,1-c][1,2,4]triazin-8-yl)diazenyl)-N-(thiazol-2-yl) benzenesulfonamide (11)

Orange crystals; yield: 83%; mp 250–255 °C ; IR (KBr) ν 3447–3300 ($2NH_2$ and NH), 2227 (CN), 1644–1600 (N=N) cm^{-1}; ^{1}H NMR (400 MHz, DMSO-d_6): δ 6.27 (s, 4H, $2NH_2$), 6.81 (d, 1H, H-5, thiazole ring, *J*=4.2), 7.21 (d, 1H, H-4, thiazole ring, *J*=4.2), 7.73 (d, 2H, Ar-H, *J*=8.5), 7.79 (d, 2H, Ar-H, *J*=8.5), 12.64 (s, 1H, $NHSO_2$) ppm; ^{13}C NMR (100 MHz, DMSO-d_6): δ 87.8, 112.2, 113.4, 127.4, 129.2, 131.2, 137.2, 139.8, 147.2, 149.4, 150.2, 152.8, 171.8 ppm; MS: *m/z* (%) 441 (M^+, 1), 396 (29), 357 (19), 147(17), 125 (23), 97(34), 57 (100), 69 (67), 43 (76); Anal. Calcd for $C_{15}H_{11}N_{11}O_2S_2$ (441.45): C, 40.81; H, 2.51; N, 34.90%; Found: C, 40.89, H, 2.57, N, 34.95%.

4-(3-Amino-5-((5-amino-3-oxo-3H-pyrazol-4-yl)diazenyl)-1H-pyrazol-4-yl)diazenyl)-N-(thiazol-2-yl)benzenesulfonamide (12)

Orange powder; yield: 85%; mp 250–255 °C ; IR (KBr): ν 3417–3311 ($2NH_2$ and 2NH), 1678 (CO), 1565 (N=N) cm^{-1}; ^{1}H NMR (400 MHz, DMSO-d_6): δ 6.28 (s, 2H, NH_2), 6.56 (s, 2H, NH_2), 6.81 (d, 1H, H-5, thiazole ring, *J*=4.2), 7.21 (d, 1H, H-4, thiazole ring, *J*=4.2), 7.73 (d, 2H, Ar-H, *J*=8.5), 7.79 (d, 2H, Ar-H, *J*=8.5), 12.64 (s, 1H, $NHSO_2$), 13.26 (s, 1H NH pyrazole ring) ppm; ^{13}C NMR (100 MHz, DMSO-d_6): δ 87.8, 112.2, 118.4, 127.4, 129.2, 131.2, 137.2, 139.8, 145.6, 152.7, 160.3, 167.3, 171.8 ppm; MS: *m/z* (%) 472 (M^+, 0.8), 397 (4), 285 (9), 97 (29), 63 (100), 57 (77), 43 (90); Anal. Calcd for $C_{15}H_{12}N_{12}O_3S_2$ (472.46): C, 38.13; H, 2.56; N, 35.58%; Found: C, 38.20, H, 2.64, N, 35.63%.

2-((3-Amino-4-((4-(N-(thiazol-2-yl)sulfamoyl)phenyl) diazenyl)-1H-pyrazol-5-yl)diazenyl)-2-cyano-N-phenylacetamide (13)

Red powder; yield: 83%; mp 255–260 °C ; IR (KBr): ν 3444–3300 (NH_2 and 3NH), 2220 (CN), 1678 (CO), 1565 (N=N) cm^{-1}; ^{1}H NMR (400 MHz, DMSO-d_6): δ 3.97 (s, 1H, CHCN), 6.27 (s, 2H, NH_2), 6.81 (d, 1H, H-5, thiazole ring, *J*=4.2), 7.17–7.53 (m, 5H, Ar-H), 7.21 (d, 1H, H-4, thiazole ring, *J*=4.2), 7.73 (d, 2H, Ar-H, *J*=8.5), 7.79 (d, 2H, Ar-H, *J*=8.5), 10.02 (s,1H, NHCO), 12.64 (s,1H, $NHSO_2$), 13.27 (s, 1H NH pyrazole ring) ppm; ^{13}C NMR (100 MHz, DMSO-d_6): δ 54.5, 87.4, 112.3, 114.9, 121.7, 127.4, 128.9, 129.4, 130.6, 131.9, 137.5, 138.6, 139.8, 145.7, 152.8, 168.4, 171.9 ppm; MS: *m/z* (%) 535 (M^+, 0.8), 241 (6), 215 (7), 160 (40), 94 (24), 45 (100); Anal. Calcd for $C_{21}H_{17}N_{11}O_3S_2$ (535.56): C, 47.10; H, 3.20; N, 28.77%; Found: C, 47.19, H, 3.22, N, 28.83%.

4-(3-Amino-5-((4-hydroxy-2,6-dimethylphenyl)diazenyl)-1H-pyrazol-4-yl)diazenyl)-N-(thiazol-2-yl)benzenesulfonamide (14)

Red powder; yield: 78%; mp 245–250 °C ; IR (KBr): ν 3445, 3330 (NH_2 and 2NH), 3300 (OH), 1550–1600 (N=N) cm^{-1}; ^{1}H NMR (400 MHz, DMSO-d_6): δ 2.36 (s, 6H, $2CH_3$), 6.27 (s, 2H, NH_2), 6.60 (d, 2H, phenol ring), 6.81 (d, 1H, H-5, thiazole ring, *J*=4.2), 7.21 (d, 1H, H-4, thiazole ring, *J*=4.2), 7.73 (d, 2H, Ar-H, *J*=8.5), 7.79 (d, 2H, Ar-H, *J*=8.5), 9.19 (s, H, OH), 12.64 (s, 1H, $NHSO_2$), 13.27(s, 1H, NH pyrazole ring) ppm; ^{13}C NMR (100 MHz, DMSO-d_6): δ 18.6, 87.8, 111.8, 112.2, 119.8, 127.4, 129.2, 131.9, 137.1, 138.4, 139.8, 145.7, 152.8, 156.4, 171.8 ppm; MS: *m/z* (%) 497 (M^+, 0.8), 394 (7), 284 (19), 259 (23), 151 (14), 109 (63), 91 (33), 85 (100), 42 (95); Anal. Calcd for $C_{20}H_{19}N_9O_3S_2$ (497.55): C, 48.28; H, 3.85; N, 25.34%; Found: C, 48.32, H, 3.80, N, 25.33%.

N-Methyl-N-(4-(N-(thiazol-2-yl)sulfamoyl)phenyl)carbonohydrazonoyl dicyanide (15)

K_2CO_3 (0,137 g, 1 mmol) was added to a solution of compound **2** (0,3 g, 1 mmol) in ethanol (25 ml) and stirred

for 1 hour. CH_3I (0.14 ml, 1 mmol) was then added and the solution was stirred for 12 hours. The reaction mixture was poured into crushed ice and a few drops of HCl were added. The resulting solid was filtered off and recrystallized from ethanol to compound **15**. Yellow powder; yield: 76%; mp 240–245 °C ; IR (KBr): ν 3300 (NH), 2232 (2CN), 1565–1600 (N=N), 1601 (C=N) cm^{-1}; ^1H NMR (400 MHz, DMSO-d_6): δ 3.35 (s, 3H, CH_3), 6.81 (d, 1H, H-5, thiazole ring, *J*=4.2), 7.21 (d, 1H, H-4, thiazole ring, *J*=4.2), 7.73 (d, 2H, Ar-H, *J*=8.5), 7.79 (d, 2H, Ar-H, *J*=8.5), 12.45 (s, 1H, $NHSO_2$) ppm; ^{13}C NMR (100 MHz, DMSO-d_6): δ 34.4, 84.6, 112.5, 127.6, 128.8, 130.1, 137.2, 147.2, 171.8 ppm; MS: *m/z* (%) 346 (M^+, 3.3), 332 (14), 283 (11), 267 (8), 200 (10), 191 (18), 156 (42), 93 (100), 80 (34); Anal. Calcd for $C_{13}H_{10}N_6O_2S_2$ (346.38): C, 45.08; H, 2.91; N, 24.26%; Found: C, 45.09, H, 2.95, N, 24.31%.

2-Amino-2-hydrazineylidene-N-methyl-N-(4-(N-(thiazol-2-yl)sulfamoyl)phenyl) acetohydrazonoyl cyanide (16)

Hydrazine hydrate (0,05 ml, 1 mmol) was added to a solution of compound **15** (0.3 g, 1 mmol) in ethanol (25 ml) and the reaction mixture was refluxed for 4 hours. After cooling, the reaction mixture was poured into ice water, the precipitate was collected, filtered, dried and recrystallized from EtOH/DMF to obtain compound **16**. Orange powder; yield: 77%; mp 255–260 °C ; IR (KBr): ν 3443, 3410 ($2NH_2$), 3333 (NH), 2215 (CN) cm^{-1}; ^1H NMR (400 mHz, DMSO-d_6): δ 3.34 (s, 3H, CH_3), 5.80 (s, 2H, NH_2), 6.54 (s, 2H, NH_2), 6.81 (d, 1H, H-5, thiazole ring, *J*=4.2), 7.21 (d, 1H, H-4, thiazole ring, *J*=4.2), 7.73 (d, 2H, Ar-H, *J*=8.5), 7.79 (d, 2H, Ar-H, *J*=8.5), 12.46 (s, 1H, $NHSO_2$) ppm; ^{13}C NMR (100 MHz, DMSO-d_6): δ 36.8, 108.6, 112.2, 114.8, 115.2, 129.3, 130.2, 137.3, 147.4, 152.9, 171.8; MS: *m/z* (%) 378.14 (M^+, 8), 336 (31), 314 (32), 275 (31), 257 (80), 152 (59), 110 (53), 83 (100); Anal. Calcd. for $C_{13}H_{14}N_8O_2S_2$ (378.43): C, 41.26; H, 3.73; N, 29.61%; Found: C, 41.28; H, 3.77; N, 29.64%.

General procedure for the synthesis of 17 and 18

Thiourea (0.076 g, 1 mmol) and hydroxylamine hydrochloride (0.07 g, 1 mmol) containing a catalytic amount of pypridine (5 drops) were added to a solution of compound **2** (0.3 g, 1 mmol) in ethanol (25 ml) and returned under reflux for 4 hours. The reaction mixture was poured into ice water and the prepicitate collected, filtered, dried and recrystallized from EtOH with a few drops of DMF, to obtain **17** and **18** respectively.

4-(2-(4,6-Diamino-2-thioxopyrimidin-5(2H)-ylidene) hydrazineyl)-N-(thiazol-2-yl) benzenesulfonamide (17)

Brown powder; yield: 68%; mp 255–260 °C ; IR (KBr): ν 3434–3400, 1325 ($2NH_2$, 2NH and C=S) cm^{-1}; ^1H NMR (400 MHz, DMSO-d_6): δ 6.58 (s, 2H, NH_2), 6.61 (s, 2H, NH_2), 6.81 (d, 1H, H-5, thiazole ring, *J*=4.2), 7.21 (d, 1H, H-4, thiazole ring, *J*=4.2), 7.73 (d, 2H, Ar-H, *J*=8.5), 7.79 (d, 2H, Ar-H, *J*=8.5), 12.45 (s, 1H, $NHSO_2$), 12.86 (s, 1H, NH) ppm; ^{13}C NMR (100 MHz, DMSO-d_6): δ 112.2, 116.8, 129.1, 130.6, 137.2, 138.3, 147.4, 162.8, 171.8, 230.0 ppm; MS: *m/z* (%) 408 (M^+, 1), 397 (11), 353 (17), 285 (19), 258 (27), 257 (62), 168 (20), 55 (92), 43 (100); Anal. Calcd. for $C_{13}H_{12}N_8O_2S_3$ (408.47): C, 38.23; H, 2.96; N, 27.43%; Found: C, 38.28; H, 2.93; N, 27.42%.

4-(2-(3-Amino-5-iminoisoxazol-4(5H)-ylidene)hydrazineyl)-N-(thiazol-2-yl) benzenesulfonamide (18)

Deep orange powder; yield: 73%; mp 245–250 °C ; IR (KBr): ν 3444–3300, 1633 (NH_2, 3NH and N=N) cm^{-1}; ^1H NMR (400 MHz, DMSO-d_6): δ 6.62 (s, 2H, NH_2), 6.81 (d, 1H, H-5, thiazole ring, *J*=4.2), 7.21 (d, 1H, H-4, thiazole ring, *J*=4.2), 7.73 (d, 2H, Ar-H, *J*=8.5), 7.79 (d, 2H, Ar-H, *J*=8.5), 9.68 (s, 1H, NH isoxazole), 12.44 (s, 1H, $NHSO_2$), 12.87 (s, 1H, NH) ppm; ^{13}C NMR (100 MHz, DMSO-d_6): δ 112.3, 116.8, 129.8, 130.2, 136.9 137.2, 147.4, 151.8, 158.9, 171.9 ppm; MS: *m/z* (%) 365, (M^+, 8), 244 (9), 239 (16), 229 (15), 207 (21), 119 (40), 97 (91), 66 (100); Anal. Calcd. for $C_{12}H_{11}N_7O_3S_2$ (365.39): C, 39.45; H, 3.03; N, 26.83%; Found: C, 39.47; H, 3.10; N, 26.86%.

Antimicrobial studies

Whatman filter paper disks were prepared with standard size (5.0 mm diameter) and stored in 1.0 Oz screw-capped wide holders for sterilization. These bottles were stored in a hot air oven at 150 °C. The disks of sterilized standard filter paper impregnated with a solution of the test compound in DMSO (1 mg/mL) were then placed on a supplementary agar plate, which was seeded with the appropriate test organism in triplicates. Standard concentrations of 106 CFU/mL (Colony Forming U/mL) and 104 CFU/mL were used individually for the antibacterial and antifungal test. Pyrex glass petri dishes (9 cm diameter) were used and two disks of filter paper were inoculated in each plate. The test organisms used were *B. subtilis* and *S. aureus* as Gram-positive bacteria and *E. coli* and *P. aeruginosa* as Gram-negative bacteria. They were also tested for their in vitro antifungal potential against fungal strains of *F. oxysporum* and *C. albicans*. Chloramphenicol, cephalothin and cycloheximide were used individually as standard antibacterial and antifungal agents. DMSO alone was used as a control at the same concentrations mentioned above and showed no visible change in bacterial growth. The plates were incubated at 37 °C for 24 hours for bacteria and 48 hours for fungi. Compounds that exhibited significant growth inhibition zones (14 mm) using the double serial dilution technique were additionally examined for their minimum inhibitory concentrations (MICs).

Measurement of the minimum inhibition concentration (MIC)

The micro-dilution sensitivity tests in Müller-Hinton Broth (oxoid) and Sabouraud Liquid Medium (oxoid)

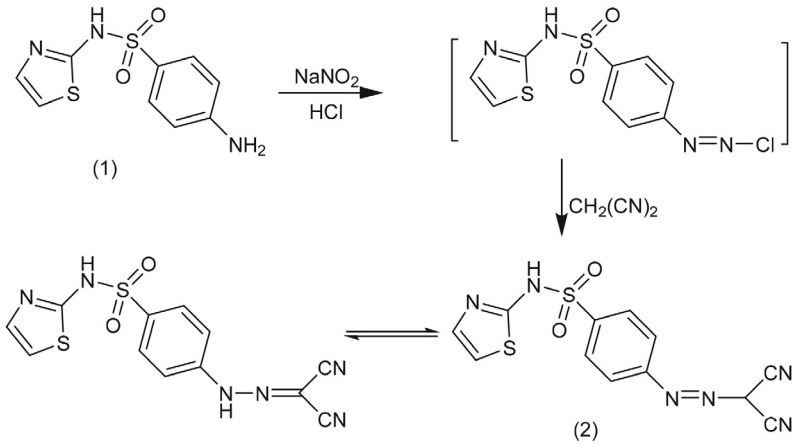
were used to determine antibacterial and antifungal activity. Stock solutions of the tested compounds, chloramphenicol, cephalothin and cycloheximide were prepared in DMSO at the concentration of 1000 mg/mL. Each stock solution was diluted with standard method broth to make serial twofold dilutions in the range 500–3.125 mg/mL. 10 mL of the broth containing about 106 CFU/mL of test bacteria were added to each well of the 96-well microtiter plate. The sealed microtiter plates were incubated for 24 hours at 37 °C for antibacterial activity and for 48 hours at 37 °C for antifungal activity in a humid chamber. At the end of the incubation period, the values of the minimum inhibitory concentrations (MIC) were recorded as the lowest concentrations of the substance that showed no visible turbidity. Control experiments with DMSO and uninoculated media were performed in parallel with the test compounds under the same conditions. The substance showed no visible turbidity.

3. Results and Discussion

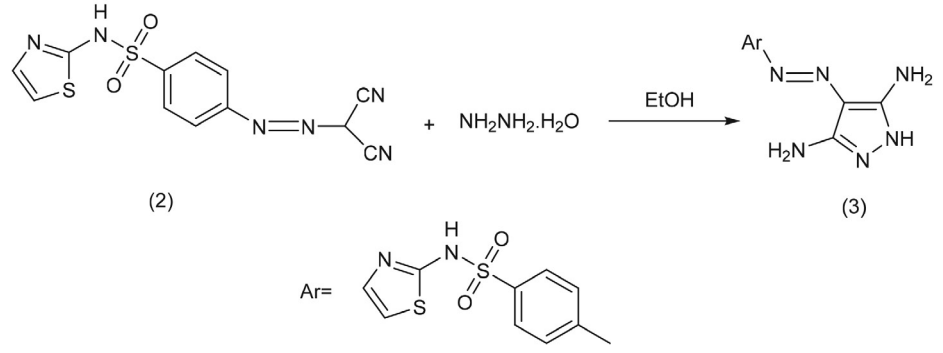
The synthetic strategies for obtaining the target compounds are shown in the Schemes 1–6. The main intermediate *N*-(4-(*N*-(thiazol-2-yl)sulfamoyl)phenyl)carbonohydrazonoyldicyanide (**2**) was prepared by diazotization of sulfathiazole, followed by coupling of the resulting diazonium salt with malononitrile.

The structure of compound **2** has been confirmed by its elemental and spectroscopic analysis. The IR spectrum of **2** showed absorption bands at 3234, 3188, 2225, 2216, 1654 and 1565 cm^{-1}, corresponding to two NH, two CN, C=N and N=N groups respectively. The mass spectrum of compound **2** showed a molecular ion peak at m/z 332 [M^+], which is consistent with the proposed structure. Recently, we have synthesized new heterocyclic compounds by studying the behavior of malononitrile derivatives towards different reagents.[18–22]

In continuation of this work we investigated the behavior of compound **2** towards hydrazine hydrate. The treatment of compound **2** with hydrazine hydrate in boiling ethanol yielded 4-((3,5-diamino-1*H*-pyrazol-4-yl)diazenyl)-*N*-(thiazol-2-ylbenzenesulfonamide (**3**). The structure of pyrazole derivative **3** was confirmed by its spectroscopic data and elemental analysis. The mass spectrum of compound 3 together with the elemental analysis confirmed the structure **3**. In addition, the IR spectrum of compound **3** showed the absence of an absorption peak for nitrile groups and the appearance of absorption bands at 3430, 3373, 3337, 3289 and 3219 cm^{-1} corresponding to two NH_2 and two NH groups, respectively, confirming the formation of pyrazole derivative **3** (Scheme 2).



Scheme 1. Synthetic pathway to sulfathiazole derivatives.

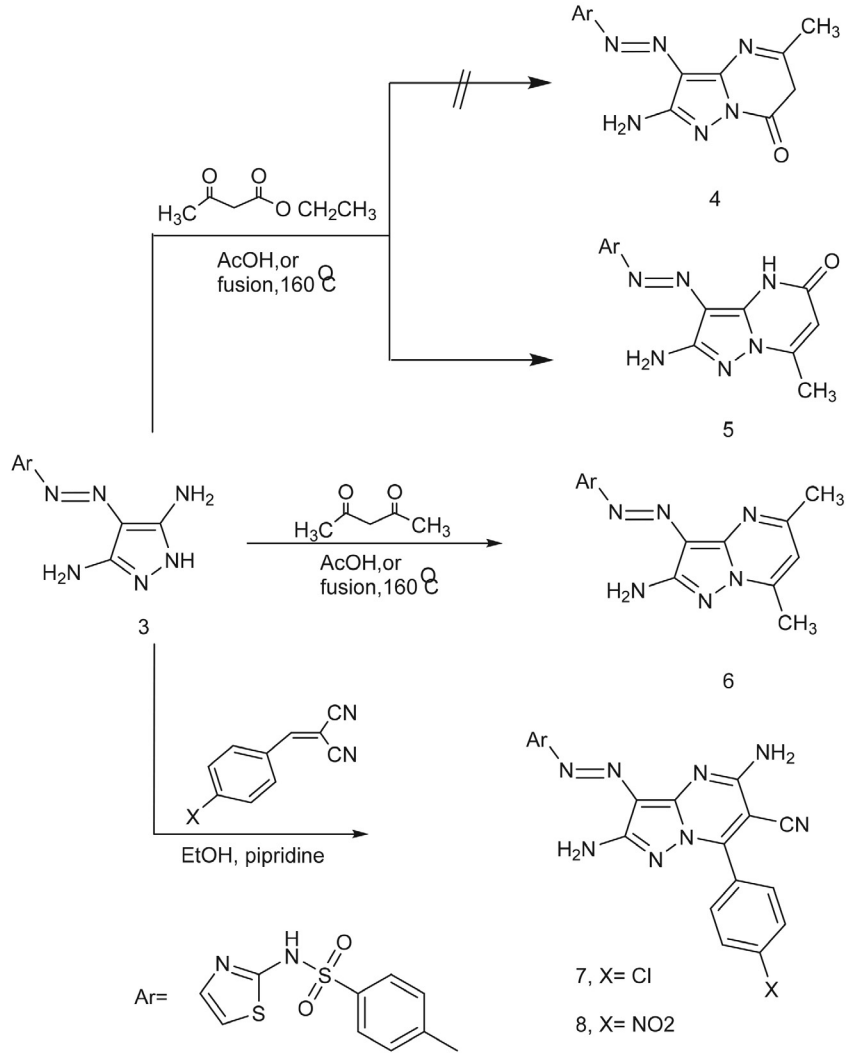


Scheme 2. Synthetic pathway to the aminopyrazole derivative **3**.

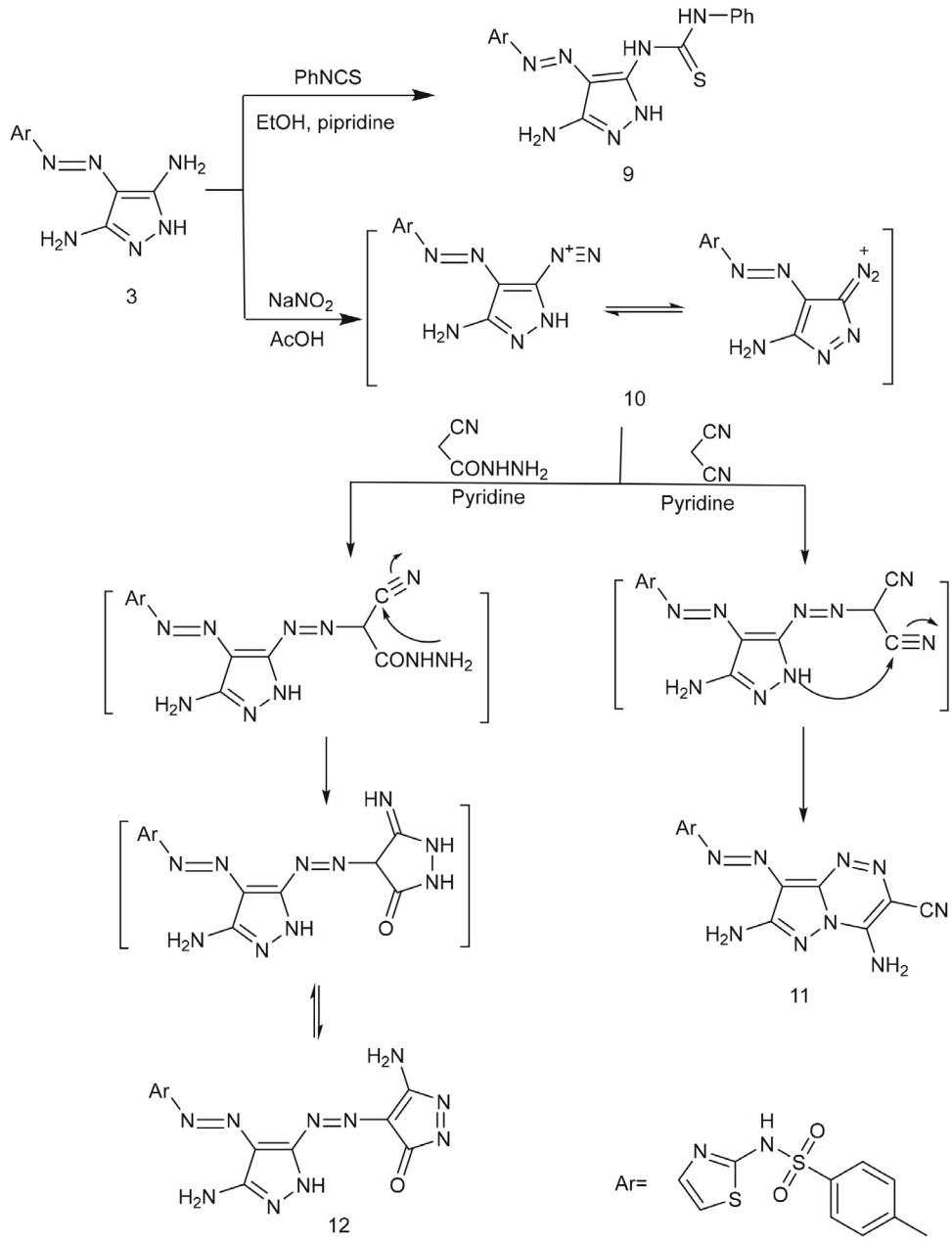
It has been found that pyrazolopyrimidines[23,24] and pyrazolotriazines[25] have major biological and medical activities as adenine analogs, antagonists and antitumor agents.[26–29] Therefore, we intend to prepare analogues of these compounds from 5-aminopyrazole derivatives (**3**) in high yield.

The treatment of 5-aminopyrazole derivative **3** with ethyl acetoacetate yielded a single product for which structures **4** or **5** seemed plausible (Scheme 3).[30,31] The ^{1}H NMR spectrum of the reaction product did not contain a singlet signal for CH_2 protons and instead two singlet signals were exposed at δ_H 7.26 and 11.46 ppm for the pyrimidine ring CH and NH protons, confirming structure **5** rather than structure **4**.[32] Structure **4** was also excluded on a chemical basis. Namely, that the reaction product did not condense with an aromatic aldehyde or couple with benzene diazonium salt, which happened promptly with active methylene azinones.[33]

In addition, compound **3** reacted with acetylacetone to form 4-((2-amino-5,7-dimethylpyrazolo[1,5-*a*]pyrimidin-3-yl)diazenyl)-*N*-(thiazol-2-yl)benzenesulfonamide (**6**, Scheme 3). Compound **6** was confirmed by elemental analysis and spectroscopic analysis. The IR spectrum of **6** showed absorption bands at ν_{max} 3437, 3394, and 1560 cm^{-1} due to the NH_2 and N=N functions, respectively. In addition, its ^{1}H NMR spectrum showed four singlet signals at δ_H 2.08, 2.24, 5.74, and 7.08 ppm assigned to two methyl, NH_2, and CH pyrimidine protons, respectively. In addition, its mass spectrum showed the molecular ion peak at m/z 428 [M^+], corresponding to its correct molecular formula [$C_{17}H_{16}N_8O_2S_2$]. The reaction of the 5-aminopyrazole derivative **3** with arylidene malononitrile derivatives offered the pyrazolopyrimidines **7** and **8** (Scheme 3). Their structure was determined on the basis of their elemental and spectroscopic investigations. The mass spectra of compounds **7** and **8** showed molecular ion peaks that confirmed their expected structures. The IR spectra of both compounds showed stretching frequencies for NH_2, NH and CN groups, which confirmed their proposed structures.



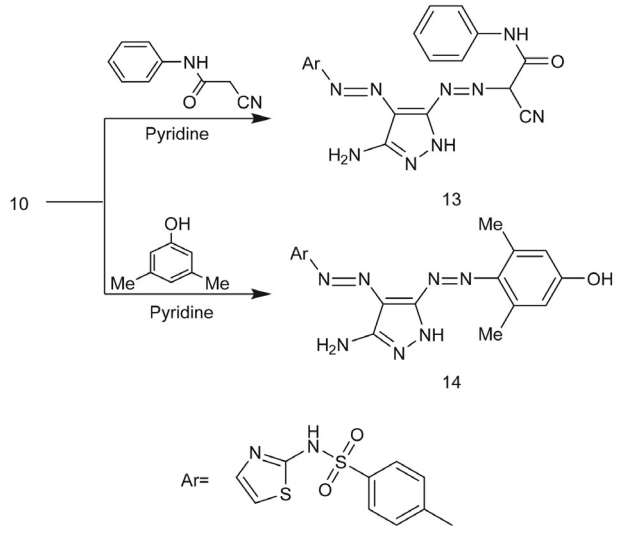
Scheme 3. Synthetic pathway to pyrazolo[1,5-*a*]pyrimidine derivatives.



Scheme 4. Synthetic pathway to pyrazolo[1,5-*c*]triazine and pyrazole derivatives.

The reaction of **3** with phenyl isothiocyanate yielded the pyrazolo-5-phenylthioureido derivative **9**, which was confirmed by analytical and spectroscopic data (Scheme 4). The coupling of diazonium salt **10** with malononitrile yields the pyrazolo[1,5-*c*]triazine **11**, while the coupling of **10** with 2-cyanoacetohydrazide yields pyrazolone derivatives **12**. The structures of **11** and **12** were confirmed based on their spectroscopic data. The IR spectrum of compound **11** showed stretching frequencies at 3447–3300 cm^{-1} due to NH_2 and NH groups and a sharp peak at 2227 cm^{-1} due to the CN group. Additionally, its mass spectrum showed a molecular ion peak at m/z 441, confirming the correct molecular formula. The IR spectrum of compound **12** showed bands at 3417–3311, 1678 and 1565 cm^{-1} corresponding to two NH_2, NH, CO and N=N groups, respectively. In addition, its mass spectrum showed a molecular ion peak at m/z 472, which is due to its molecular formula. Diazonium salt **10** was additionally reacted with 2-cyano-*N*-phenylacetamide and 3,5-dimethylphenol to obtain compounds **13** and **14**, respectively. The structure of compounds **13** and **14** was confirmed on the basis of elemental analysis and spectroscopic data, as already shown in the experimental part.

The significant biological and medical activity of the arylhydrazone of α-cyanoketone as an antituberculosis agent[34] and oxidative phosphorylation inhibitor[35] have



Scheme 5. Synthetic pathway to pyrazolo-4,5diazenyl derivatives.

stimulated research on this class of compounds. As part of our program, we report here on the synthesis of α cyanarylhydrazones **16** by treating hydrazine hydrate with *N*-methyl-*N*-(4-(*N*-(thiazol-2-yl)sulfamoyl)phenyl)carbonohydrazonoyldicyanide (**15**) (Scheme 6). The identity of compounds **15** and **16** was confirmed by their spectroscopic analysis.

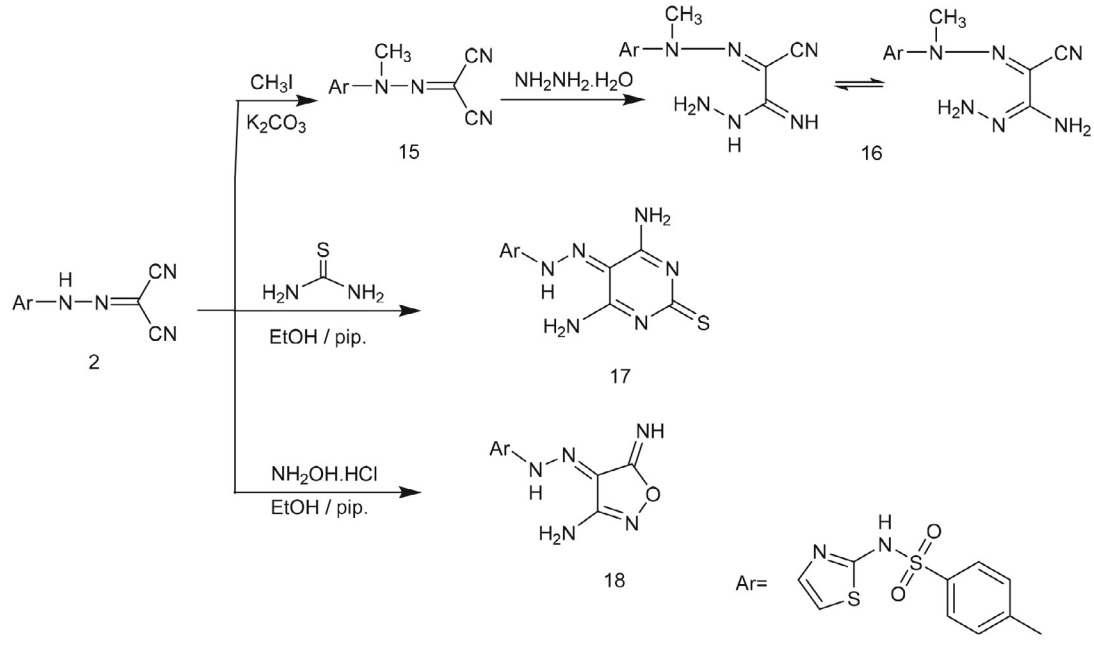
On the other hand, the reaction of compound **2** with different nucleophiles, for example thiourea and hydroxylamine hydrochloride, enabled 4-(2-(4,6-diamino-2-thioxopyrimidin-5(2*H*)-ylidene)hydrazinyl)-*N*-(thiazol-2-yl) benzenesulfonamide (**17**) and 4-(2-(2-(3-amino-5-iminoisoxazol-4(5*H*)-ylidene)hydrazinyl)-*N*-(thiazol-2-yl)benzenesulfonamide (**18**), respectively. The IR spectrum of **17** showed the presence of two NH_2 and two NH absorption bands at 3434–3400 cm^{-1}, the C=S group at 1325 cm^{-1} and the absence of CN groups. The mass spectra of compounds **17** and **18** showed a molecular ion peak that confirmed proposed structures.

4. Antimicrobial Evaluation

The synthesized compounds were evaluated against *Bacillus subtilis* and *Staphylococcus Aureus* as Gram-positive bacteria and against *Escherichia coli* and *Pseudomonas Aeruginosa* as Gram-negative bacteria. They were also tested for their in vitro antifungal potential against strains of *Fusarium oxysporum* and *Candida albicans*. The agar diffusion method with chloramphenicol, cephalothin and cycloheximide as reference drugs was used to determine the antibacterial and antifungal activity.

The results were recorded for each compound tested as the normal diameter of the bacterial or fungal growth inhibition zones (IZ) around the disks in mm. The MIC measurement was determined for compounds that had significant growth inhibition zones (>14 mm) using a twofold serial dilution method.[36,37] The values for MIC and inhibition zone diameters are shown in Table 1. Most of the compounds tested showed variable inhibitory activity for the growth of the Gram-positive and Gram-negative strains of bacteria tested and against the antifungal strain. In general, most of the compounds tested showed better activity against the Gram-positive than against the Gram-negative strains.

Regarding the structure-activity relationship of sulfathiazole derivatives against Gram-positive bacteria, the re-



Scheme 6. Synthetic pathway to pyrimidine and isoxazole derivatives.

Table 1. Minimum inhibiton concentration (MIC, μg/mL) and inhibition zone (mm) of the synthesized compounds.

Compound No.	MIC in μg/mL, and inhibition zone (mm)				
	Bacteria				Fungi
	Gram-positive bacteria		Gram-negative bacteria		
	B. subtilis	*S. aureus*	*E. coli*	*P. aeruginosa*	*C. albicans*
2	3.125 (40)	6.25 (37)	100 (15)	50 (19)	3.125 (36)
3	25 (27)	50 (15)	100 (15)	100 (16)	6.25 (28)
5	3.125 (45)	6.25 (38)	25 (25)	12.5 (33)	3.125 (40)
6	12.5 (33)	50 (14)	50 (20)	50 (19)	50 (20)
7	12.5 (32)	50 (20)	100 (15)	100 (15)	100 (16)
8	3.125 (44)	6.25 (37)	100 (14)	50 (20)	25 (19)
9	12.5 (32)	50 (20)	100 (15)	100 (15)	6.25 (30)
11	3.125 (41)	6.25 (37)	100 (15)	100 (16)	6.25 (25)
12	6.25 (38)	6.25 (30)	100 (14)	100 (15)	6.25 (26)
13	12.5 (32)	6.25 (38)	100 (15)	50 (19)	6.25 (30)
14	6.25 (37)	6.25 (37)	100 (15)	100 (15)	12.5 (32)
15	6.25 (38)	6.25 (37)	100 (15)	50 (19)	50 (20)
16	6.25 (38)	6.25 (37)	100 (15)	50 (19)	100 (16)
17	3.125 (40)	6.25 (37)	100 (15)	50 (19)	50 (20)
18	3.125 (41)	6.25 (38)	100 (15)	50 (19)	100 (16)
Chloramphenicol	3.125 (44)	3.125 (44)	6.25 (37)	6.25 (38)	NT
Cephalothin	6.25 (36)	6.25 (37)	6.25 (38)	6.25 (37)	NT
Cycloheximide	NT	NT	NT	NT	3.125 (42)

MIC values with SEM = 0.02 (the lowest concentration that inhibited bacterial growth). NT: Not tested.

sults showed that compounds **2**, **5**, **8**, **11**, **17** and **18** showed a broad antibacterial profile against the organisms tested and were equivalent to chloramphenicol in inhibiting the growth of *B. subtilis* (MIC, 3.125 μg/mL), while the activity was 50% lower than chloramphenicol against *S. aureus*. On the other hand, compounds **3**, **6**, **7**, **9**, **12**, **13**, **14**, **15** and **16** showed moderate growth-inhibiting activity against Gram-positive bacteria, as shown by their MIC values (6.25–50 μg/mL). Of these compounds, **12**, **14**, **15** and **16** showed good growth-inhibiting activity against *B. subtilis* (MIC, 6.25 μg/mL), while compounds **6**, **7**, **9** and **13** showed relatively good growth-inhibiting profiles against *B. subtilis* (MIC, 12.5 μg/mL), accounting for about 25% of the activity of chloramphenicol and 50% of cephalothin against the similar organism. The antibacterial activity of compound **6** showed a weak growth-inhibiting effect against the tested Gram-negative bacteria (MIC, 50nμg/mL). As for the activity of sulfathiazole derivative **2** against antifungal strains, the results showed their moderate to good antifungal activity.

Of the compounds studied, compounds **2** and **5** were equivalent to cycloheximide in inhibiting the growth of *C. albicans* (MIC 3.125 μg/mL). In contrast, compounds **3**, **9**, **11**, **12** and **13** showed 50% lower activity than cycloheximide in inhibiting the growth of *C. albicans* (MIC 6.25 μg/mL), while the activity of compound **14** was 25% lower than that of cycloheximide against *C. albicans* (MIC 12.5 μg/mL). In general, the tested compounds were more active against Gram-positive bacteria than Gram-negative bacteria, and it could be argued that the antimicrobial activity of the compounds is related to the cell wall structure of the bacteria. Indeed, the cell wall is essential for the survival of bacteria and some antibiotics are able to kill bacteria by inhibiting a step in the synthesis of peptidoglycan. Gram-positive bacteria have a thick cell wall that contains many layers of peptidoglycan and teichoic acids, but in contrast, Gram-negative bacteria have a relatively thin cell wall that consists of a few layers of peptidoglycan and is surrounded by a second lipid membrane that contains lipopolysaccharides and lipoproteins. These differences in cell wall structure can lead to differences in antibacterial susceptibility, and some antibiotics can only kill Gram-positive bacteria and are inactive against Gram-negative pathogens.[38]

By comparing the antimicrobial activity of the compounds reported in this study with their structures, the following structure-activity relationships (SAR) were postulated:

– The presence of a basic sulfathiazole skeleton is necessary for the broad spectrum of antimicrobial activity.

– The introduction of electron-withdrawing groups, such as CN or NO_2, increases the antimicrobial activity.

– Compounds **2**, **8**, **11**, **17** and **18** showed the highest antimicrobial activity, while the other compounds showed weak to moderate antimicrobial activity.

5. Conclusion

The present study reports on the efficacy of pyrazolo[1,5-*a*]pyrimidine and pyrazolo[1,5-*c*]triazine derivatives containing a sulfathiazole unit. The simple synthesis strategy and the very good yields of the compounds produced are the main advantages of the protocol presented.

The newly synthesized compounds showed moderate to good antibacterial and antifungal activities.

Acknowledgements

The authors are grateful to Pharmacology Department, Faculty of Pharmacy, Mansoura University, for the screening of the biological activity. The authors declare that there is no conflict of interest.

6. References

1. J. R. Anacona, J. L. Rodriguez, J. Camus, *Spectrochim Acta Part A,* **2014**, *129*, 96–102. **DOI:**10.1016/j.saa.2014.03.019
2. S. Ostovar, D. Rodriguez-Padron, F. Saberi, A. M. Balu, R. Luque, *Catalysts*, **2018**, *9*, 348. **DOI:**10.3390/catal9040348
3. H. Nikoofard, M. Sargolzaei, F. Faridbod, *Acta Chim. Slov.* **2017**, *64*, 842–848. **DOI:**10.17344/acsi.2017.3357
4. J. Elguero, P. Goya, N. Jagerovic, A. M .S. Silva, *in* Targets in Heterocyclic Systems: Chemistry and Properties, O.A. Attanasi, D. Spinelli (Eds.), sixth ed., Societ a Chimica Italiana, Roma, 2006, pp. 52–98.
5. G. Szabo, J. Fischer, A. Kis-Varga, K. Gyires, *J. Med. Chem.* **2008**, *51*, 142–147. **DOI:**10.1021/jm070821f
6. M. F. El-Shehry, E. M. El Telbani, M. I. Hegab, *Acta Chim. Slov.*, **2018**, *65*, 401–406. **DOI:**10.17344/acsi.2017.4144
7. H. Beyzaei, Z. Motraghi, R. Aryan, M. M. Zahedi, A. Samzadeh-Kermani, *Acta Chim. Slov.,* **2017**, *64*, 911–918. **DOI:**10.17344/acsi.2017.3609
8. A. Tanitame, Y. Oyamada, K. Ofuji, H. Terauchi, M. Kawasaki, M. Wachi, J. Yamagishi, *Bioorg. Med. Chem. Lett.* **2005**, *15*, 4299–4303. **DOI:**10.1016/j.bmcl.2005.06.103
9. A. Tanitame, Y. Oyamada, K. Ofuji, M. Fujimoto, K. Suzuki, T. Ueda, H. Terauchi, M. Kawasaki, K. Nagai, M. Wachi, J. Yamagishi, *Bioorg. Med. Chem*. **2004**, *12*, 5515–5524. **DOI:**10.1016/j.bmc.2004.08.010
10. N. Cho, M. Kamaura, T. Yogo, H. Imoto, PCT Int. Appl. (2009). WO 2009139340.
11. K. Dugi, M. Mark, F. Himmelsbach, PCT Int. Appl. (2009). WO 2009022009.
12. Y. Momose, T. Maekawa, H. Odaka, H. Kimura, PCT Int. Appl. (2001). WO 2001038325.
13. S. M. Rida, M. N. S. Saudi, A. M. Youssef, M. A. Halim, *Lett. Org. Chem.* **2009**, *6*, 282–288. **DOI:**10.2174/157017809788489909
14. M. G. Brasca, C. Albanese, R. Amici, D. Ballinari, L. Corti, V. Croci, D. Fancelli, F. Fiorentini, M. Nesi, P. Orsini, F. Orzi, W. Pastori, E. Perrone, E. Pesenti, P. Pevarello, F. Riccardi-Sirtori, F. Roletto, P. Roussel, M. Varasi, A. Vulpetti, C. Mercurio, *Chem. Med. Chem.* **2007**, *2*, 841–852. **DOI:**10.1002/cmdc.200600302
15. P. Pevarello, D. Fancelli, A. Vulpetti, R. Amici, M. Villa, V. Pittal_a, P. Vianello, A. Cameron, M. Ciomei, C. Mercurio, J. R. Bischoff, F. Roletto, M. Varasi, M. G. Brasca, *Bioorg. Med. Chem. Lett.* **2006**, *16*, 1084–1090. **DOI:**10.1016/j.bmcl.2005.10.071
16. A. H. Abadi, A. A. H. Eissa, G. S. Hassan, *Chem. Pharm. Bull.* **2003**, *51*, 838–844. **DOI:**10.1248/cpb.51.838
17. S. A. Margolis, G. Lenaz, H. Baum, *Arch. Biochem. Biophys*. **1967,** *118*, 224–230. **DOI:**10.1016/0003-9861(67)90301-3
18. H. M. Refat, A. A. Fadda, *Eur. J. Med. Chem*. **2013**, *70*, 419–426. **DOI:**10.1016/j.ejmech.2013.09.003
19. A. A. Fadda, K. S. Mohamed, H. M. Refat, E. E. El-Bialy, *Heterocycles*, **2015**, *91*, 134–148. **DOI:**10.3987/COM-14-13129
20. H. E. Elsherbiny, A. A. Fadda*, J. Heterocycl. Chem.* **2018**, *55*, 2251–2260. **DOI:**10.1002/jhet.3276
21. H. E. Elsherbiny, A. A. Fadda*, Acta Chim. Slov*. **2018**, *65*, 853–864. **DOI:**10.17344/acsi.2018.4506
22. S. M. Khaled, H. E. Elsherbiny, *Heterocycles*, **2018**, *96*, 1897–1909. **DOI:**10.3987/COM-18-13969
23. G. B. Elion, S. Callahan, H. Nathan, S. Bieber, R. W. Rundles, G. H. Hitchings, *Biochem. Pharmacol.* **1963**, *12*, 85–93. **DOI:**10.1016/0006-2952(63)90012-1
24. N. Polish, M. Nesterkina, N. Marintsova, A. Karkhut, I. Kravchenko, V. Novikov, A. Khairulin, *Acta Chim. Slov.* **2020**, 67, 934–939. **DOI:**10.17344/acsi.2020.5938
25. T. Novinson, R. Hanson, M. K. Dimmitt, L. N. Simon, R. K. Robins, D. E. O'Brien, *J. Med. Chem.* **1974**, *17*, 645–648. **DOI:**10.1021/jm00252a016
26. I. Ito, Japan Patent, 7030101. 1970 [Chem. Abstr. 1971, 74, 22827].
27. S. A. El-Hadidya, S. Abu-Melhab, *Acta Chim. Slov.* **2020**, 67, 167–178. **DOI:**10.17344/acsi.2019.5308
28. M. Abdel-Motaal, A. L. Alanzy, M. Asem, *Acta Chim. Slov.* **2020**, 67, 560–569. **DOI:**10.17344/acsi.2019.5571
29. R. R. Varma, J. G. Pandya, F. U. Vaidya, C. Pathak, B. S. Bhatt, M. N. Patel, *Acta Chim. Slov.* **2020**, 67, 957–969. **DOI:**10.17344/acsi.2020.6017
30. M. H. Elnagdi, E. M. Kandeel, K. U. Sadek, *Z. Naturforsch B Chem. Sci*. **1979,** *34*, 275– 279. **DOI:**10.1515/znb-1979-0227
31. M. H. Elnagdi, E. M. Kandeel, M. R. H. Elmoghayar, *Z. Naturforsch B Chem. Sci.* **1977**, *32*, 307–310. **DOI:**10.1515/znb-1977-0315
32. M. H. Elnagdi, E. M. Kandeel, E. M. Zayed, Z. E. Kandil, *J. Heterocycl. Chem*. **1977**, *14*, 155–158. **DOI:**10.1002/jhet.5570140132
33. A. A. Fadda, E. M. Afsah, S. Bondock, M. M. Hammouda, *Tetrahedron*, **2012**, *68*, 2081–2091. **DOI:**10.1016/j.tet.2011.12.016
34. T. Zsolnai, *Biochem. Pharmacol.* **1965**, *14*, 1325–1362. **DOI:**10.1016/0006-2952(65)90119-X
35. J. F. Ferris, *in* Biological junction and formation of cyano group in "The Chemistry of Cyano Group", Z. Rappaport (ed.), Interscience, New York; 1970, Chapt. 12, p 735.
36. A. U. Rahman, M. I. Choudhary, W. J. Thomsen, Bioassay Techniques for drug development, Harwood Academic Publishers, the Netherlands; 2001, p 16.
37. A. A. Fadda, E. M. Afsah, R. S. Awad, *Eur. J. Med. Chem.* **2013**, *60*, 421–430. **DOI:**10.1016/j.ejmech.2012.11.017
38. H. Abuo-Melha, A. A. Fadda, *J. Spectrochim. Acta Part A*. **2012**, *89*, 123–128. **DOI:**10.1016/j.saa.2011.12.054

Povzetek

Avtorji poročajo o pripravi večjega števila derivatov pirazolo[1,5-*a*]pirimidina z reakcijo 4-((3,5-diamino-1*H*-pirazol-4-il)-diazenil)-*N*-(tiazol-2-il))-benzensulfonamida z nekaterimi bifunkcionalnimi nukleofili, kot so etil acetoacetat, acetilaceton ali derivati arilidenmalononononitrila. Strukture novo sintetiziranih spojin so določili na podlagi njihovih IR, ^{1}H in ^{13}C NMR ter masnih spektroskopskih podatkov. Večina pripravljenih spojin je pokazala dobro protibakterijsko in protiglivično delovanje.

Except when otherwise noted, articles in this journal are published under the terms and conditions of the Creative Commons Attribution 4.0 International License

Scientific paper

Synthesis, Molecular Docking and Biological Properties of Novel Thiazolo[4,5-b]pyridine Derivatives

Taras I. Chaban,[1,*] Yulia E. Matiichuk,[1] Olga Ya. Shyyka,[2] Ihor G. Chaban,[3] Volodymyr V. Ogurtsov,[1] Ihor A. Nektegayev[4] and Vasyl S. Matiychuk[2]

[1] *Department of General, Bioinorganic, Physical and Colloidal Chemistry, Danylo Halytsky Lviv National Medical University, 69 Pekarska, Lviv, 79010, Ukraine*

[2] *Department of Organic Chemistry, Ivan Franko National University of Lviv, 6 Kyryla i Mefodia, Lviv, 79005, Ukraine*

[3] *Department of Pharmaceutical Chemistry FPGE, Danylo Halytsky Lviv National Medical University, 69 Pekarska, Lviv, 79010, Ukraine*

[4] *Department of Pharmacology, Danylo Halytsky Lviv National Medical University, 69 Pekarska, Lviv, 79010, Ukraine*

* *Corresponding author: E-mail: chabantaras@ukr.net (Taras I. Chaban)*
Tel. +38 098 942-79-56; Fax. +38 0322 75-77-34

Received: 07-24-2019

Abstract

The synthesis, anti-inflammatory and antioxidant properties of novel 5-hydroxy-7-methyl-3*H*-thiazolo[4,5-*b*]pyridin-2-one derivatives were discussed. Fused thiazolo[4,5-*b*]pyridin-2-ones were synthesized and modified at the N^3, C^5 and C^6 positions of the main core in order to obtain the compounds with a satisfactory pharmacological profile. The synthesized compounds were preselected via molecular docking for further testing of their anti-inflammatory activity *in vitro*. Evaluation of novel compounds over the carageenin induced rat paw edema revealed strong anti-inflammatory action of some compounds including (thiazolo[4,5-*b*]pyridin-3(2*H*)-yl) propanenitrile (**5**) and thiazolo[4,5-*b*]pyridin-3(2*H*)-yl) propanoic acid (**6**) even exceeding the standard – Ibuprofen. The antioxidant activity of the synthesized compounds was measured *in vitro* by the method of scavenging effect on 2,2-diphenyl-1-picrylhydrazyl (DPPH) radicals.

Keywords: Organic synthesis; thiazolo[4,5-*b*]pyridin-2-ones; anti-inflammatory activity; antioxidant activity; molecular docking

1. Introduction

Inflammation is an essential response of living organisms to the common ailments starting from traumatic disorder or fever associated with infection to major life-threatening diseases like myocardial infarction or brain haemorrhage or infarct.[1] Literature data survey has revealed that numerous nonsteroidal anti-inflammatory drugs (NSAIDs), which belong to different chemical classes, have been developed to treat inflammatory disorders. During the past few years, the long-term use of NSAIDs has been severely hampered by the emerging of several serious effects such as gastrointestinal ulcers, hepatotoxicity, renal dysfunction, and cardiotoxicity.[2] Unfortunately all of the proposed medications provoke serious side effects.[3]

In general, NSAIDs exert their pharmacological action by inhibiting the synthesis of prostaglandins (PGs) by non-selectively *cyclooxygenases 1* and *2* (COX-1 and COX-2), either selective COX-2 blocking. Inhibition of COX-1 is also responsible, in part, for gastrointestinal side effects, which are the most frequent side effects of NSAIDs.[4] These conditions generate one of the biggest challenges of modern medicinal chemistry for the development of alternative anti-inflammatory drugs with minimal adverse effects.[5–7]

No less challenging is the search for new antioxidants. Different environmental stress factors like pollution, drought, temperature, excessive light intensities, and nutritional limitation can increase the production of reactive oxygen species (ROS).[8–9] Oxidative stress is a major contributing factor for developing degenerative diseases

like atherosclerosis, ischemic heart disease, ageing, diabetes mellitus, cancer and others.[10] Antioxidants can interfere with the oxidation process by reacting with free radicals, and also by acting as reactive species scavenger.[11] Therefore, various natural well and synthetic antioxidants are used to scavenge free radicals. In this regard, it is important to synthesize new classes of compounds with antioxidant properties.

Fused bicyclic systems with thiazolidine core occupy a prominent place in medicinal chemistry due to their broad spectrum of pharmacological activities.[12–14] Previously, we have developed convenient and efficient method to form combinatorial libraries of fused azoles such as [1,2,4]triazolo[3,4-*b*][1,3,4]thiadiazole,[15–16] pyrazolo [3,4-*d*]pyridazines,[17] [1,2,4]triazolo[3,4-*b*][1,3,4]thiadiazines,[18] isoindolo[1,2-*a*]isoquinoline,[19] thiopyrano[2,3-*d*] [1,3]thiazoles,[20] thieno[3,2-*c*]pyridinone,[21] triazolo[4,5-*d*] pyridazine,[22] and thiazolo[4,5-*b*]pyridines.[23] In summing up the published scientific data fused thiazolopyridines are characterized by herbicidal,[24] antioxidant,[25–28] antimicrobial,[29] antifungal,[30] and anti-mitotic[31] activities. They also show potent inhibitory activities for Aβ42 fibrillization for Alzheimer's disease treatment.[32] It was established that thiazolopyridine derivatives exhibit anti-tuberculosis,[33] anti-inflammatory[34–36] and significant anticancer[37] activity, and also act as agonists of H3-histamine receptors.[38]

For the time being, exploration of different chemical modifications avenues of thiazolopyridines to obtain novel active compounds, and thus, the development of a new class of anti-inflammatory drugs with optimal pharmacokinetic properties should be continued.

The present work is devoted to the synthesis of a series of novel 3*H*-thiazolo[4,5-b]pyridine-2-ones by the structural modification of the core heterocycle in its N^3, C^5 and C^6 positions for further pharmacological *in vivo* anti-inflammatory activity assay based on the results obtained via computer simulation – molecular docking and *in vitro* antioxidant screenings.

2. Experimental Section

2. 1. Materials

All chemicals were of analytical grade and commercially available. All reagents and solvents were used without further purification and drying.

2. 2. Chemistry

All melting points were determined in an open capillary and are uncorrected. ^{1}H and ^{13}C NMR spectra were recorded on a Varian Mercury 400 (400 MHz for ^{1}H) instrument with TMS or deuterated solvent as an internal reference. Mass spectra were run using Agilent 1100 series LC/MSD, Agilent Technologies Inc. with an API–ES/APCI ionization mode. Satisfactory elemental analyses were obtained for new compounds (C ± 0.17, H ± 0.21, N ± 0.19).

General procedure for the synthesis 6-arylazo-5-hydroxy-7-methyl-3H-thiazolo[4,5-b]pyridin-2-ones (2, 3).

Sodium (0.2 mol) was dissolved in anhydrous methanol (100 mL). To the obtained solution 4-iminothiazolidin-2-one (50 mmol) and α-arylazo-derivative of ethyl acetoacetate (50 mmol) were added at 20 °C. The mixture was left for 7 days with the intermittent stirring. Afterwards, it was acidified with acetic acid to pH 5 and five-fold diluted with water. The precipitate was filtered off, washed with water, and dried at 100–110 °C. The obtained compounds were recrystallized from acetic acid.

4-((5-Hydroxy-7-methyl-2-oxo-2,3-dihydrothiazolo [4,5-b]pyridin-6-yl)diazenyl) benzene-sulfonic acid (2):

Red solid; yield: 88 %; mp > 280 °C; ^{1}H NMR (400 MHz, $CDCl_3$) δ 2.37 (s, 3H, CH_3), 7.59 (d, *J* = 8.1 Hz, 2H, C_6H_4), 7.69 (d, *J* = 7.9 Hz, 2H, C_6H_4), 13.30 (s, 1H, OH), 14.55 (s, 1H, NH); ^{13}C NMR (101 MHz, $CDCl_3$) δ 16.88, 116.35, 122.65, 125.27, 127.08, 140.78, 141.58, 145.48, 159.99, 166.28, 177.45; ESI-MS: m/z 366 $[M+H]^+$; anal. calcd. for $C_{13}H_{10}N_4O_5S_2$: C 42.62, H 2.75, N 15.29; found: C 43.01, H 2.68, N 15.35.

5-Hydroxy-7-methyl-6-(naphthalen-2-yldiazenyl)thiazolo[4,5-b]pyridin-2(3H)-one (3):

Red solid; yield: 84 %; mp 265 °C; ^{1}H NMR (400 MHz, $CDCl_3$) δ 2.45 (s, 3H, CH_3), 7.67 (d, *J* = 6.8 Hz, 2H, naphthalen), 7.74–7.77 (m, 1H, naphthalen), 7.88–7.90 (m, 1H, naphthalen), 7.98–8.07 (m, 3H, naphthalen), 13.46 (s, 1H, OH), 15.74 (s, 1H, NH);); ^{13}C NMR (101 MHz, $CDCl_3$) δ 16.90, 114.83, 115.86, 121.34, 125.49, 125.96, 127.17, 127.80, 127.84, 129.90, 131.46, 132.12, 133.26, 135.20, 136.17, 139.48, 140.50, 160.54; ESI-MS: m/z 336 $[M+H]^+$; anal. calcd. for $C_{17}H_{12}N_4O_2S$: C 60.70, H 3.60, N 16.66; found: C 60.44, H 3.63, N 16.58.

5-Hydroxy-7-methyl-3-phenylthiazolo[4,5-b]pyridin-2 (3H)-one (4):

Sodium (109 mmol) was dissolved in anhydrous methanol (150 mL). To the obtained solution 3-phenyl-4-iminothiazolidin-2-one (50 mmol) and ethyl acetoacetate (8,5 mL) were added at 20 °C. The mixture was left for 5 days with the intermittent stirring. Afterwards it was acidified with acetic acid to pH ~5, five-fold diluted with water; the precipitate was filtered off, washed with water, and dried. Yellow solid; yield: 65 %; mp 244 °C; ^{1}H NMR (400 MHz, $CDCl_3$) δ 2.51 (s, 3H, CH_3), 6.96 (t, *J* = 7.3 Hz, 1H, Py), 7.28 (t, *J* = 7.4 Hz, *J* = 7.7 Hz, 2H, C_6H_5), 7.45 (d, *J* = 8.1 Hz, 3H, C_6H_5), 8.67 (s, 1H, OH); ^{13}C NMR (101 MHz, $CDCl_3$) δ 17.51, 108.34, 114.33, 125.73, 127.90, 128.24, 140.18, 142.06, 145.08, 160.61, 168.96; ESI-MS: m/z 258 $[M+H]^+$; anal. calcd. for $C_{13}H_{10}N_2O_2S$: C 60.45, H 3.90, N 10.85; found: C 60.06, H 3.84, N 10.73.

3-(5-Hydroxy-7-methyl-2-oxothiazolo[4,5-b]pyridin-3 (2H)-yl) propanenitrile (5):

A mixture of pyridine (50 mL) and water (10 ml) with acrylonitrile (3 mL) was added to the 5-hydroxy- 7-methylthiazolo[4,5-*b*]pyridin-2(3*H*)-one (**1**, 10 mmol). The reaction mixture was refluxed for 5 h. On cooling, the precipitation was achieved with petroleum ether-water mixture (3:1). The precipitate was recrystallized from ethanol, filtered off, and dried. This compound was isolated as a white crystalline solid, well soluble in ethanol, chloroform, dioxane, DMF, acetic acid. White solid; yield: 74 %; mp 105 °C; ^{1}H NMR (400 MHz, $CDCl_3$) δ 2.27 (s, 3H, CH_3), 3.04 (t, *J* = 6.5 Hz, 2H, CH_2), 4.15 (t, *J* = 6.5 Hz, 2H, CH_2), 6.41 (s,1H, Py), 11.09 (s, 1H, OH); ^{13}C NMR (101 MHz, $CDCl_3$) δ 15.77, 19.15, 37.48, 105.11, 105.80, 118.12, 144.70, 146.16, 162.53, 167.96; ESI-MS: m/z 236 $[M+H]^+$; anal. calcd. for $C_{10}H_9N_3O_2S$: C 51.05, H 3.86, N 17.86; found: C 50.97, H 3.89, N 17.77.

3-(5-Hydroxy-7-methyl-2-oxothiazolo[4,5-b]pyridin-3 (2H)-yl) propanoic acid (6):

The mixture of the propanenitrile (**5**, 10 mmol), acetic acid (30 mL), and hydrochloric acid (15 mL) were placed into the round-bottomed flask. The reaction mixture was refluxed 3h and the product was precipitated with water. The mixture was left for 24 h at ambient temperature. The precipitate was filtered off and treated with toluene. The precipitate was recrystallized from ethanol, filtered off, and dried. This compound was isolated as a white crystalline powdered solid, well soluble in ethanol, chloroform, dioxane, DMF, acetic acid. White solid; yield: 66 %; mp 111 °C; ^{1}H NMR (400 MHz, $CDCl_3$) δ 2.25 (s, 3H, CH_3), 2.68 (t, *J* = 7.5 Hz, 2H, CH_2), 4.10 (t, *J* = 7.6 Hz, 2H, CH_2), 6.38 (s,1H, Py), 11.05 (s, 1H, OH), 12.07 (s, 1H, COOH); ^{13}C NMR (101 MHz, $CDCl_3$) δ 19.17, 31.76, 37.90, 104.77, 105.97, 144.45, 146.62, 162.50, 167.85, 171.90; ESI-MS: m/z 254 $[M+H]^+$; anal. calcd. for $C_{10}H_{10}N_2O_4S$: C 47.24, H 3.96, N 11.02; found: C 47.88, H 3.98, N 11.21.

General procedure for the synthesis of 3-(5-hydroxy-7-methyl-2-oxothiazolo[4,5-b]pyridin-3(2H)-yl)-N-aryl-l propanamides (7, 8).

The mixture of the propanoic acid (**6**, 10 mmol), thionyl chloride (57 mmol) and dioxane (30 mL) were placed into the round-bottomed flask. The reaction mixture was refluxed for 30 min and the product was precipitated with n-hexane, the precipitate was filtered off. The resulting acyl chlorides were used for further transformations without further purification. Obtained 3-(5-hydroxy-7-methyl-2-oxothiazolo[4,5-*b*]pyridin-3(*2H*)-yl)propanoyl chloride (10 mmol) was dissolved in anhydrous dioxane (10 mL), and appropriate aromatic amine (10 mmol) and triethylamine (10 mmol) were added to the solution. The reaction mixture was refluxed for 15 min. On cooling, the mixture was diluted with water and precipitated crystalline solid filtered off, washed with methanol and dried. The obtained compounds were recrystallized from acetic acid.

3-(5-Hydroxy-7-methyl-2-oxothiazolo[4,5-b]pyridin-3 (2H)-yl)-N-phenyl propanamide (7):

White solid; yield: 48 %; mp 214 °C; ^{1}H NMR (400 MHz, $CDCl_3$) δ 2.28 (s, 3H, CH_3), 2.71 (t, 2H, *J* = 7.1 Hz, CH_2), 4.13 (t, 2H, *J* = 7.2 Hz, CH_2), 6.42 (s, 1H, Py), 7.21–7.26 (m, 2H, C_6H_5), 7.40–7.48 (m, 3H, C_6H_5), 9.96 (s, 1H, NH), 11.09 (s, 1H, OH); ^{13}C NMR (101 MHz, $CDCl_3$) δ 19.21, 31.55, 37.54, 105.06, 105.89, 125.18, 128.32, 128.86, 140.85, 144.41, 146.32, 162.47, 167.79, 170.11; ESI-MS: m/z 329 $[M+H]^+$; anal. calcd. for $C_{16}H_{15}N_3O_3S$: C 58.35, H 4.59, N 12.76; found: C 58.43, H 4.67, N 12.88.

3-(5-Hydroxy-7-methyl-2-oxothiazolo[4,5-b]pyridin-3 (2H)-yl)-N-(4-nitrophenyl) propan-amide (8):

Yellow solid; yield: 53 %; mp 202 °C; ^{1}H NMR (400 MHz, $CDCl_3$) δ 2.36 (s, 3H, CH_3), 2.85 (t, 2H, *J* = 7.2 Hz, CH_2), 4.24 (t, 2H, *J* = 7.2 Hz, CH_2), 6.54 (s, 1H, Py), 7.35–7.41 (m, 2H, C_6H_4), 7.56–7.62 (m, 2H, C_6H_4), 10.18 (s, 1H, NH), 11.14 (s, 1H, OH); ^{13}C NMR (101 MHz, $CDCl_3$) δ 19.23, 31.65, 37.60, 104.89, 105.78, 122.25, 125.63, 126.97, 140.59, 144.24, 146.51, 162.51, 167.70, 170.24; ESI-MS: m/z 375 $[M+H]^+$; anal. calcd. for$C_{16}H_{14}N_4O_5S$: C 51.33, H 3.77, N 14.97; found: C 51.11, H 3.81, N 14.86.

7-Methyl-2-oxo-2,3-dihydrothiazolo[4,5-b]pyridin-5-yl 2-chloroacetate (9):

5-Hydroxy-7-methyl-thiazolo[4,5-*b*]pyridin-2(*3H*)-one (**1**, 5 mmol), an appropriate aliphatic chloroacetyl chloride (5 mmol), and triethylamine (5 mmol) were added to dioxane (20 mL). The reaction mixture was refluxed 15 min. On cooling, the formed crystalline precipitate was filtered off, washed with methanol and dried. The obtained compound was recrystallized from methanol. White solid; yield: 67 %; mp 191 °C; ^{1}H NMR (400 MHz, $CDCl_3$) δ 2.37 (s, 3H, CH_3), 4.72–4.74 (m, 2H, CH_2), 6.92 (s, 1H, Py), 12.71 (s, 1H, NH); ^{13}C NMR (101 MHz, $CDCl_3$) δ 19.43, 41.07, 110.76, 116.52, 145.16, 148.09, 154.79, 166.09, 168.31; ESI-MS: m/z 259 $[M+H]^+$; anal. calcd. for $C_9H_7ClN_2O_3S$: C 41.79, H 2.73, N 10.83; found: C 41.53, H 2.76, N 10.95.

General procedure for the synthesis of 7-methyl-2-oxo-2,3-dihydrothiazolo[4,5-b]pyridin-5-yl 4-carboxylates (10–14).

To a solution of pyridine (20 mL) an appropriate aromatic acyl chloride (5 mmol) and 5-hydroxy-7-methyl-thiazolo[4,5-*b*]pyridin-2(*3H*)-one (**1**, 5 mmol) were added. The reaction mixture was refluxed 30 min. On cooling, formed crystalline precipitate was filtered off, washed with acetic acid and dried. The obtained compounds were recrystallized from acetic acid.

7-Methyl-2-oxo-2,3-dihydrothiazolo[4,5-b]pyridin-5-yl 4-chlorobenzoate (10):

White solid; yield: 65 %; mp 214 °C; ^{1}H NMR (400 MHz, $CDCl_3$) δ 2.39 (s, 3H, CH_3), 7.06 (s, 1H, Py), 7.70 (d, *J* = 8.5 Hz, 2H, C_6H_4), 8.13 (d, *J* = 8.5 Hz, 2H, C_6H_4), 12.74

(s, 1H, NH); ^{13}C NMR (101 MHz, $CDCl_3$) δ 19.45, 111.25, 116.31, 127.14, 129.32, 131.67, 139.41, 145.08, 148.15, 155.32, 163.52, 168.35; ESI-MS: m/z 320 $[M+H]^+$; anal. calcd. for $C_{14}H_9ClN_2O_3S$: C 52.42, H 2.83, N 8.73; found: C 52.68, H 2.85, N 8.79.

7-Methyl-2-oxo-2,3-dihydrothiazolo[4,5-b]pyridin-5-yl 4-(benzyloxy) benzoate (11):

White solid; yield: 71 %; mp 197 °C; ^{1}H NMR (400 MHz, $CDCl_3$) δ 2.37 (s, 3H, CH_3), 7.01 (s, 1H, Py), 7.21 (d, J = 8.4 Hz, 2H, C_6H_4), 7.41 (d, J = 7.2 Hz, 2H, C_6H_5), 7.49 (d, J = 6.9 Hz, 3H, C_6H_5), 8.08 (d, J = 8.3 Hz, 2H, C_6H_4), 12.75 (s, 1H, NH); ^{13}C NMR (101 MHz, $CDCl_3$) δ 19.37, 69.64, 111.39, 114.56, 115.17, 120.45, 127.82, 128.45, 131.31, 132.08, 136.21, 144.95, 148.08, 155.65, 163.06, 163.91, 168.47; ESI-MS: m/z 393 $[M+H]^+$; anal. calcd. for $C_{21}H_{16}N_2O_4S$: C 64.27, H 4.11, N 7.14; found: C 64.05, H 4.14, N 7.24.

7-Methyl-2-oxo-2,3-dihydrothiazolo[4,5-b]pyridin-5-yl-(E)-3-(4-methoxyphenyl) acrylate (12):

White solid; yield: 65 %; mp 169 °C; ^{1}H NMR (400 MHz, $CDCl_3$) δ 2.39 (s, 3H, CH_3), 3.79 (s, 3H, CH_3-C_6H_4), 6.37 (d, 1H, J = 16.0 Hz, CH), 7.07 (s, 1H, Py), 6.97 (d, J = 8.7 Hz, 2H, C_6H_4), 7.55 (d, 1H, 16.0 Hz, CH), 7.63 (d, J = 8.7 Hz, 2H, C_6H_4), 12.17 (s, 1H, NH); ^{13}C NMR (101 MHz, $CDCl_3$) δ 19.64, 55.12, 105.11, 106.80, 114.29, 116.45, 126.77, 129.87, 143.69, 145.55, 146.82, 158.53, 160.88, 167.79, 169.55; ESI-MS: m/z 343 $[M+H]^+$; anal. calcd. for $C_{17}H_{14}N_2O_4S$: C 59.64, H 4.12, N 8.18; found: C 59.64, H 4.03, N 8.28.

7-Methyl-2-oxo-2,3-dihydrothiazolo[4,5-b]pyridin-5-yl 1-(3,4-dimethylphenyl)-5-methyl-1H-1,2,3-triazole-4-carboxylate (13):

White solid; yield: 77 %; mp 187 °C; ^{1}H NMR (400 MHz, $CDCl_3$) δ 1.99 (s, 3H, CH_3-triazole), 2.38 (s, 3H, CH_3), 2.40 (s, 3H, CH_3-C_6H_3), 2.41 (s, 3H, CH_3-C_6H_3), 7.08 (s, 1H, Py), 7.28 (d, J = 8.0 Hz, 1H, C_6H_3), 7.36–7.38 (m, 2H, C_6H_3), 12.78 (s, 1H, NH); ^{13}C NMR (101 MHz, $CDCl_3$) δ 9.34, 16.61, 19.46, 20.74, 111.26, 116.31, 127.08, 127.68, 131.33, 131.82, 134.14, 134.67, 140.78, 141.62, 145.08, 148.21, 154.98, 159.20, 168.37; ESI-MS: m/z 398 $[M+H]^+$; anal. calcd. for $C_{19}H_{17}N_5O_3S$: C 57.71, H 4.33, N 17.71; found: C 57.59, H 4.28, N 17.82.

7-Methyl-2-oxo-2,3-dihydrothiazolo[4,5-b]pyridin-5-yl 1-(2-chlorophenyl)-5-methyl-1H-1,2,3-triazole-4-carboxylate (14):

White solid; yield: 64 %; mp 178 °C; ^{1}H NMR (400 MHz, $CDCl_3$) δ 2.01 (s, 3H, CH_3-triazole), 2.37 (s, 3H, CH_3), 7.01 (s, 1H, Py), 6.94-6.98 (m, 1H, C_6H_4), 7.40-7.45 (m, 1H, C_6H_4), 7.53-7.58 (m, 2H, C_6H_4), 12.78 (s, 1H, NH); ^{13}C NMR (101 MHz, $CDCl_3$) δ 19.39, 20.70, 104.18, 111.03, 116.02, 144.05, 144.69, 144.71, 147.50. 148.31, 148.33, 148.38, 155.32, 162.36, 168.44, 168.88 168.11; ESI-MS: m/z 403 $[M+H]^+$; anal. calcd. for $C_{17}H_{12}ClN_5O_3S$: C 50.81, H 3.01, N 17.43; found: C 51.07, H 3.06, N 17.51.

2. 3. Molecular Docking

Molecular docking was conducted with OpenEye Scientific Software program package as a computer method approach to the search of molecules with affinity to certain biotargets. Used software includes Fred Receptor, Vida, Flipper, Babel 3, Omega 2 and Fred 2 programs.

2. 4. Anti-inflammatory Activity Evaluation Assays

Anti-inflammatory activity[39] was evaluated using carrageenan induced rat paw edema method in rats. Outbred (male/female) white rats weighing 180–220g were used for the edema test. The experiments were carried out in accordance with the requirements of the European convention for the protection of vertebrate animals used for experimental and other scientific purposes. The experimental protocol was approved by the Danylo Halytsky Lviv National Medical University ethics committee, constituted by the Ministry of Health of Ukraine.

Animals were divided into 15 groups comprising five rats per group. One group was kept as the control and remaining 14 groups (test groups) were used to determine the anti-inflammatory activity elicited by the 13 drug candidates, respectively. Rats were kept in the animal house under standard conditions of light and temperature on the general diet prior to the experiment. The standard drug, Ibuprofen (50 mg/kg body weight) and the test compounds (50 mg/kg body weight) were dissolved in DMSO and administered through intraperitoneal route. DMSO was injected to the control group. At 30 minutes later, 0.1 ml of 2 % carrageenan solution in saline was injected in the sub-plantar region of the right hind paw of each rat. After 4 h of the carrageenan injection, the volume of paw edema (in ml) was measured using water plethysmometer and decrease in paw edema was compared between the control group and the test groups. The inflammatory reaction inhibition was expressed as a percent of paw volume reduction and it was calculated using the following formula:

$$\% \text{ Inhibition} = \frac{V_{\text{control}} - V}{V_{\text{control}}} \cdot 100\,\% \qquad (1)$$

where V_{control} is the increase in paw volume in control group animals, and V is the increase in paw volume in animals injected with the test substances.

2. 5. Antioxidant Activity Evaluation Assays

The antioxidant activity was determined on the basis of free radical scavenging activity of stable 2,2-diphe-

nyl-1-picrylhydrazyl (DPPH). The effect of the studied compounds on DPPH radicals was estimated according to the method of Blois[40–41] with minor modifications. The solution of DPPH in ethanol with the concentration of 150 μmoles/L (4 mL) was mixed with the compound or control solution in ethanol its concentration been 250 μmoles/L (0.2 mL). The reaction mixture was vortex mixed thoroughly and incubated at room temperature in the dark for 60 min. Simultaneously, a control was prepared as ascorbic acid solution in ethanol (0.2 mL) mixed with of DPPH solution in ethanol (4 mL) without sample fraction. Reduction in the absorbance of the mixture was measured at 517 nm using ethanol as blank. Ascorbic acid was used as a standard. Also, the absorbance of DPPH solution was measured. Percentage of free-radical-scavenging activity was expressed as percent inhibition and it was calculated using the following formula:

$$\%\ \text{Inhibition} = \frac{\grave{A}_{DPPH} - A_c}{A_{DPPH}} \cdot 100\ \% \ ; \qquad (2)$$

where A_{DPPH} is the absorbance of DPPH free radicals solution, and A_c is the absorbance of a sample. Each experiment was performed in triplicate and average values were recorded. Results are expressed as the means ± S.D.

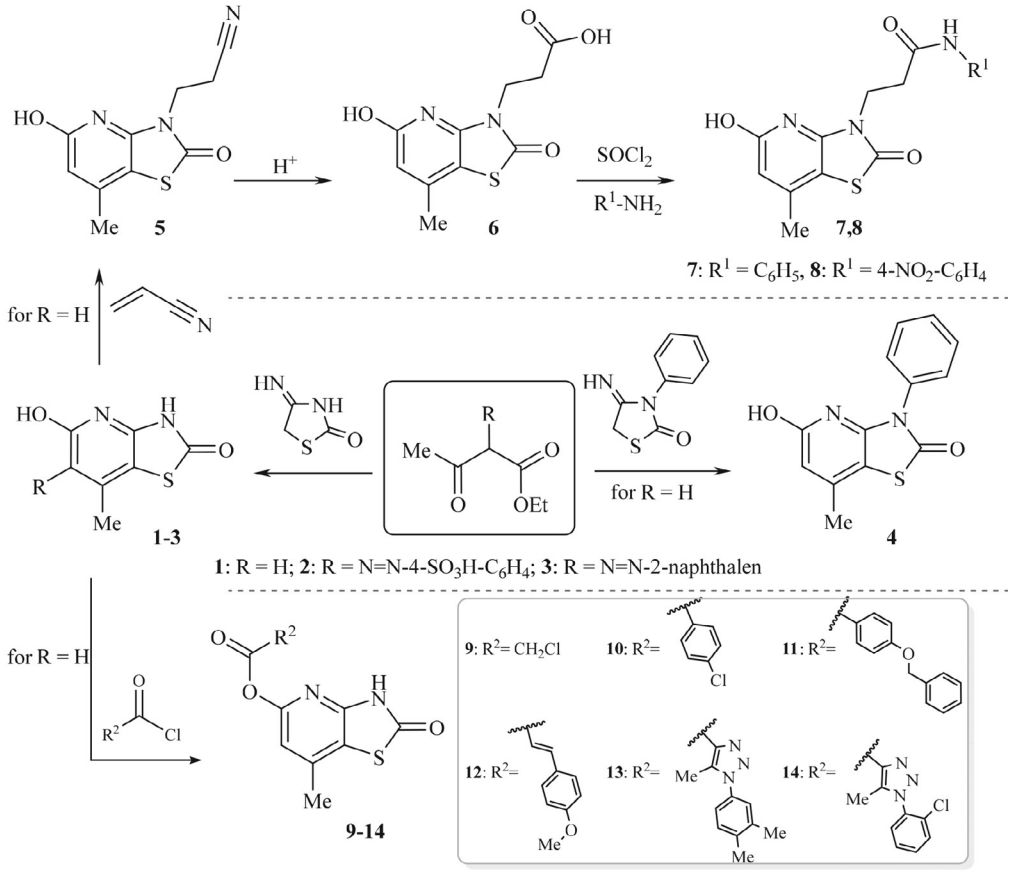
3. Results and Discussion

3. 1. Chemistry

Continuing systematic study of fused bicyclic systems as potential drug candidates we represented synthesis, anti-inflammatory and antioxidant activity evaluation of some thiazolo[4,5-*b*]pyridin-2-ones. The efficient synthetic approach for 3*H*-thiazolo[4,5-*b*]pyridin-2-one[23,36] system construction had been developed earlier and is based on [3 + 3] cyclocondensation of 4-iminothiazolidone-2 due its N,C-binucleophilic properties with dielectrophilic reagents like ethyl acetoacetate forming the above-mentioned fused heterocycle (**1**).[33]

We studied the behavior of 4-iminothiazolidin-2-one with α-arylazo- derivatives of ethyl acetoacetate in [3+3] cyclocondensation reaction. Under the chosen conditions the corresponding 6-arylazo-5-hydroxy-7-methyl-3*H*-thiazolo[4,5-*b*]pyridin-2-ones (**2, 3**) were obtained in good yields (Scheme).

We looked at a possibility to use the reported method for preparation of 3-phenyl-5-hydroxy-7-methyl-3*H*-thiazolo[4,5-*b*]pyridin-2-one (**4**) from above mentioned ethyl acetoacetate and 3-phenyl-4-iminothiazolidone-2-one. It was found that compound **4** was easily accessed with a high yield at the same conditions (Scheme).



Scheme 1. Synthesis of novel thiazolo[4,5-*b*]pyridine derivatives.

The further strategy included the core heterocycle structural modification at its N^3 position. Core thiazolo[4,5-*b*]pyridine scaffold had been extensively studied as electrophilic reagent due the presence of NH-group hydrogen atom. Therefore, the functionalization of thiazolo[4,5-*b*]pyridine could be easily performed via the addition reaction to the acrylonitrile. We have found out that the high yield of the product **5** could be achieved while treatment of the equimolar amounts of the thiazolo[4,5-*b*]pyridine (**1**) with acrylonitrile in pyridine – water medium (5:1). 3-(5-Hydroxy-7-methyl-2-oxothiazolo[4,5-*b*]pyridin-3(2*H*)-yl) propanenitrile (**5**) prepared in this way was subjected to hydrolysis leading to 3-(5-hydroxy-7-methyl-2-oxothiazolo[4,5-*b*]pyridin-3(*2H*)-yl) propanoic acid (**6**) formation (Scheme).

Besides, propanamides are highly reactive substances, hence suitable for creating and broadening the collection of building blocks useful for combinatorial chemistry including the design of biologically active compounds. The carboxyl group present in N^3 position of thiazolo[4,5-*b*]pyridinyl-propanoic acid (**6**) provides an entry to 3-(5-hydroxy-7-methyl-2-oxothiazolo[4,5-*b*]pyridin-3(2*H*)-yl)-N-aryl propanamides (**7, 8**). Dioxane was established to be the most suitable medium for the reaction of compound **6** with thionyl chloride. Prepared in this way, 3-(5-hydroxy-7-methyl-2-oxothiazolo[4,5-*b*]pyridin-3(*2H*)-yl) propanoyl chloride was reacted with corresponding aromatic amines. Refluxing the reaction mixture for 30 min in dioxane medium was defined as optimal condition for propanamides (**7, 8**) formation in good yields (Scheme).

Furthermore, compound **1**, due to the presence of hydroxyl- moiety in position 5 of thiazolo[4,5-*b*]pyridine core, represents a convenient reagent for thiazolo[4,5-*b*] pyridin-5-yl 4-carboxylates (**9–14**) generation via acylation reaction by chloroacetyl chloride or appropriate aromatic acyl chlorides (Scheme). Powders of these products are well soluble in DMF, DMSO and acetic acid, and sparingly soluble in water and in other organic solvents.

Structures of the obtained compounds were confirmed by ^1H and ^{13}C NMR spectroscopy, mass spectroscopy and elemental analysis. All these new compounds possess spectroscopic data in accordance with the proposed structures.

3. 2. Molecular Docking

Previously we have shown a good correlation between results obtained in computer simulation using OpenEye Software with that obtained in the corresponding *in vitro* assays.[42,43]

Crystallographic models of COX-1 and COX-2 (4O1Z and 5IKR correspondingly) were obtained from Protein Data Bank (www.rcsb.org). As research objects thiazolo[4,5-*b*]pyridine derivatives, common NSAIDs (aspirin, mefenamic acid, diclofenac, ibuprofen, indomethacin, ketoprofen, ketorolac, others) and well-known selective COX-2 inhibitors, such as parecoxib, lumiracoxib, etoricoxib and others, were chosen. To estimate *in silico* COX-2-compound and COX-1-compound binding seven scoring function values (Chemgauss 2, Chemscore, PLP, Screenscore, Shapegauss, Zapbind and Consensus) were calculated. Cumulative (Consensus) scoring function ranking allowed us to select compounds, which could prospectively be selective COX-2 inhibitors. Fred receptor program allows to extract the active sites (biotarget) of COX-2 and COX-1 from crystallographic models for molecular docking.

Molecular docking studies included generation of R-, S- and cys-trans isomers of ligands using program Flipper with further 3D optimization of isomers using program Hyper Chem 7.5 (www.hyper.com) (molecular mechanics method MM+ and semi-empirical quantum-mechanical method PM3). Conformers were generated via Omega 2. Further program Fred 2 choose minimum energy conformation for each molecule and 3D molecular docking was performed.

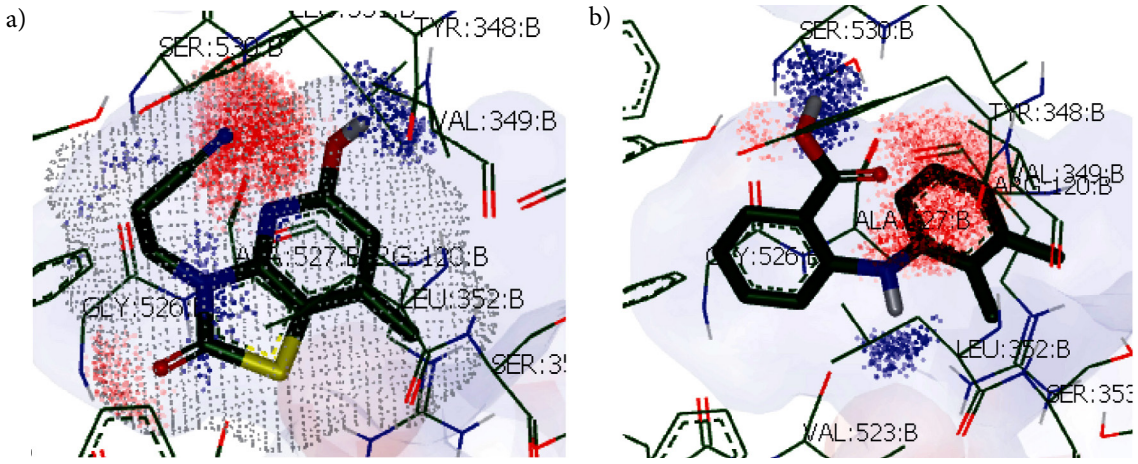


Figure 1. Compound **5** docked in the active site of COX-2 **(a)** in comparison with inhibitor mefenamic acid docked in the active site of COX-2. **(b)**.

Values of the seven scoring functions (Chemgauss 2, Chemscore, PLP, Screenscore, Shapegauss, Zapbind and Consensus) were obtained as a result. Ranking property (compound ranking) of the consensus scoring function, which includes values of all scoring functions, allowed to analyze the results easily.

Ranking and analysis of the molecular docking results were obtained using the selected compounds and crystallographic model of COX-2 with cumulative scoring function (consensus). Consensus results allowed us to select compounds, which could prospectively be selective COX-2 inhibitors at the level of mefenamic acid and Ibuprofen for future (in-depth) pharmacological studies for further evaluation of *in vitro* anti-inflammatory activity. The interactions between COX-2 active site and the most active compound **5** in comparison with selective inhibitor mefenamic acid is shown in Figure. Moreover, it should be noted that results predicted via docking correlate quite well with that obtained in the *in vitro* assay. The selected "lead" compound **5** based on the *in vitro* screening results was also predicted to be the most active in the docking studies.

On the contrast, generated conformations of thiazolo[4,5-*b*]pyridine derivatives did not possess the necessary parameters for successful binding to the target COX-1 active site and were found to be bad substrates of cyclooxygenase-1 during docking experiment.

3. 3. Anti-inflammatory Activity in Vivo Evaluation

Carrageenan-induced paw edema is the most widely used animal model of acute inflammation. *In vivo* studies of novel thiazolo[4,5-*b*]pyridine-2-one derivatives were carried out for anti-inflammatory activity employing the carrageenan-induced rat paw edema method. The NSAID drug Ibuprofen in its effective therapeutic dose was tested in parallel as an activity reference. Results of paw edema decreasing were expressed as the mean ± standard deviation and compared statistically with the control group using Student's t-test. A level of $p<0.05$ was adopted as the test of significance (Table 1). The percentage protection against inflammation was calculated as % inhibition by comparison between DMSO injected control group and drugs-tested groups.

Evaluation of anti-inflammatory activity indicated that 8 compounds (**2, 3, 7, 8, 10, 11, 12** and **13**) showed no significant decrease in edema; the inhibition rate for them was observed at the level of 22.6–30.1 % as compared to control group. The compounds **4, 9** and **14** possessed the anti-inflammatory activity in the range of 35.6–42.1 % which is comparable to the effect of Ibuprofen. The anti-inflammatory evaluation test for compounds **5** and **6** gave the result at the level of 45.3–48.8 % inhibition indicating that the compounds **5** and **6** were more potent than Ibuprofen.

The results of the pharmacological tests were analyzed concerning the structure of the compounds. Among the two arylazo substituted derivatives **2**-**3** none of them was defined as active indicating the nature and position of the substituted arylazo groups did not noticably influence on their anti-inflammatory activity. It was found out that for N^3-substituted 5-hydroxy-7-methyl-3*H*-thiazolo [4,5-b]pyridin-2-one derivative (**4**), obtained via [3+3]cyclocondensation 3-phenyl-4-iminothiazolidone-2-one with ethyl acetoacetate, the presence of phenyl goup in the N^3 position contributed to the inflammation inhibition efficiency. The presence of cyano and carboxy groups substituents (**5**, **6**) in the core scaffold N^3 position lead to the high anti-inflammatory activity even exceeding the Ibuprofen

Table 1. Anti-inflammatory effect of thiazolo[4,5-*b*]pyridine-2-ones on carrageenan-induced rat paw edema (ml) *in vivo* evaluation and % of protection from inflammation

compound ID	paw edema volume (mL) ± SEM*	inhibition, %	activity relative to Ibuprofen, %
control	2.20 ± 0.050	–	–
2	1.62 ± 0.035	26.3	*65.4*
3	1.60 ± 0.035	27.5	*68.4*
4	1.27 ± 0.020	42.1	*104.7*
5	1.13 ± 0.020	48.8	*121.4*
6	1.20 ± 0.020	45.3	*112.7*
7	1.65 ± 0.040	25.2	*62.7*
8	1.68 ± 0.040	23.7	*59.0*
9	1.42 ± 0.030	35.6	*88.6*
10	1.54 ± 0.030	30.1	*74.9*
11	1.64 ± 0.040	25.5	*63.4*
12	1.70 ± 0.040	22.6	*56.2*
13	1.62 ± 0.035	26.3	*65.4*
14	1.41 ± 0.030	36.1	*89.8*
Ibuprofen	1.32 ± 0.035	40.2	*100*

effect. Notably, among the six C^5-substituted 5-hydroxy-7-methyl-3*H*-thiazolo[4,5-*b*]pyridin-2-one derivatives, prepared by the acylation reaction, only two compounds: chloro-acetic acid (**9**) and 1-(2-chloro-phenyl)-5-methyl-1*H*-[1,2,3]triazole-4-carboxylic acid (**14**) possessed inflammation inhibition. The rest of substituents in the C^5 position did not notably affect on the anti-inflammatory activity of thiazolo[4,5-*b*]pyridin-2-ones.

3. 4. In Vitro Antioxidant Assay

The antioxidant activity was determined on the basis of free radical scavenging activity of 2,2-diphenyl-1-picrylhydrazyl (DPPH) free radical. The DPPH method is described as a simple, rapid and convenient method for screening of many samples for radical scavenging activity. These advantages make the DPPH method interesting for testing newly synthesized compounds to scavenge radicals and to find out antioxidant drug candidates.

DPPH radical had found many applications due to its high stability in a methanolic solution and intense purple color. In its oxidized form, the DPPH radical has an absorbance maximum at a wavelength of 540 nm. The absorbance decreases when the radical is reduced by antioxidants. Its reduction affords 2,2-diphenyl-1-picrylhydrazine (DPPH-H), or the corresponding anion($DPPH^-$) in basic medium. The DPPH radical acts as a scavenger for other odd-electron species which afford *para*-substitution products at phenyl rings. In the present paper, we demonstrate modified spectrophotometric method making use of the DPPH radical and its specific absorbance properties. The free-radical-scavenging activity of each compound was assayed using a stable DPPH and was quantified by decolorization the solution being mixed with DHHP at a wavelength of 540 nm. The absorbance of DPPH solution in ethanol (150 mmoles/l) was measured as 0.77. The absorbances and free-radical-scavenging activities % inhibitions of standard (ascorbic acid) and each compound are listed in Table 2.

Table 2. Values of Absorbance and % of inhibition of thiazolo[4,5-*b*] pyridine-2-ones.

compound / standard	Absorbance of a sample, A_s	inhibition, %
ascorbic acid	0.220 ± 0.010	71.5
2	0.718 ± 0.025	6.7
3	0.700 ± 0.025	9.1
4	0.671 ± 0.020	12.8
5	0.742 ± 0.025	3.7
6	0.759 ± 0.030	1.5
7	0.525 ± 0.015	31.8
8	0.549 ± 0.015	28.7
9	0.559 ± 0.020	27.4
10	0.546 ± 0.015	29.1
11	0.745 ± 0.030	3.3
12	0.523 ± 0.015	32.0
13	0.702 ± 0.025	8.8
14	0.571 ± 0.020	25.8

The antioxidant activity evaluation results showed that, in general, most of the tested compounds possess insignificant free radical scavenging effect being in the range of 1.5%–32.0%.

4. Conclusions

In summary, we presented an efficient synthetic approaches to a number of thiazolo[4,5-*b*]pyridin-2-one derivatives for their anti-inflammatory and antioxidant activity evaluation. We have shown that the proposed synthetic protocols provided the possibility to design 5-hydroxy-7-methyl-3*H*-thiazolo[4,5-*b*]pyridin-2-ones diversity with a considerable chemical novelty involving [3+3]cyclocondensation, cyanoethylation, hydrolysis, and acylation reactions. The obtained results of the performed biological activity evaluation suggested the core fused heterocycle as a promising scaffold in anti-inflammatory drug development. On the contrary, the free radical scavenging effect was found to be insignificant. Further optimization of the structure to improve biological activity is currently in progress.

5. References

1. P. Pirlamarla, R. M. Bond, *Trends Cardiovasc. Med.* **2016**, *26*, 675–680. **DOI:**10.1016/j.tcm.2016.04.011
2. M. J. Killeen, M. Linder, P. Pontoniere, R. Crea, *Drug Discovery Today* **2014**, *19*, 373–378. **DOI:**10.1016/j.drudis.2013.11.002
3. S. Bacchi, P. Palumbo, A. Sponta, M. Coppolino, *Anti-Inflamm. Anti-Allergy Agents Med. Chem.* **2012**, *11*, 52–64. **DOI:**10.2174/187152312803476255
4. A. M. Qandil, *Int. J. Mol. Sci.* **2012**, *13*, 17244–17274. **DOI:**10.3390/ijms131217244
5. O. Kolomoets, O. Voskoboynik, O. Antypenko, G. Berest, I. Nosulenko, V. Palchikov, O. Karpenko, S. Kovalenko, *Acta Chim. Slov*. **2017**, *64*, 902–910. **DOI:**10.17344/acsi.2017.3575
6. T. Chaban, V. Matiychuk, V. Ogurtsov, I. Chaban, S. Harkov, I. Nektegaev, *Pharmacia* **2019,** *65*, 51–62.
7. R. Paprocka, M. Wiese, A. Eljaszewicz, A. Helmin-Basa, A. Gzella, B. Modzelewska-Banachiewicz, J. Michalkiewicz, *Bioorg. Med. Chem. Lett.* **2015,** *25*, 2664–2667. **DOI:**10.1016/j.bmcl.2015.04.079
8. N. Smirnoff, *New Phytol.* **1993**, *125*, 27–58. **DOI:**10.1111/j.1469-8137.1993.tb03863.x
9. A. A. Arora, R. K. Sairam, G. C. Srivastava, *Curr. Sci.* **2002**, *82*, 1227–1238. **DOI:**10.4236/as.2015.68082
10. R. A. Jacob, B. J. Burri, *Am. J. Clin. Nutr.* **1996**, *63*, 985–990. **DOI:**10.1093/ajcn/63.6.985
11. H. Sies, W. Stahl, *Am. J. Clin. Nutr.* **1995**, *62*, 1315–1321. **DOI:**10.1093/ajcn/62.6.1315S

12. Z. Chaban, S. Harkov, T. Chaban, O. Klenina, V. Ogurtsov, I. Chaban, *Pharmacia* **2017**, *64,* 52–66.
13. N. G. Smirnova, I. V. Zavarzin, M. M. Krayushkin, *Chem. Heterocycl. Compd.* **2006**, *42*, 144–165. **DOI:**10.1007/s10593-006-0064-8
14. T. Chaban, O. Klenina, I. Chaban, V. Ogurtsov, S. Harkov, M. Lelyukh, *Pharmacia* **2018**, *65,* 54–70.
15. Yu. I. Gorak, N. D. Obushak, V. S. Matiichuk, R. Z. Lytvyn, *Russ. J. Org. Chem*. **2009**, *45*, 541–550. **DOI:**10.1134/S1070428009040125
16. N. T. Pokhodylo, R. D. Savka, V. S. Matiichuk, N. D. Obushak, *Russ. J. Org. Chem*. **2009**, *79*, 309–314. **DOI:**10.1134/S1070363209020248
17. V. S. Matiichuk, M. A. Potopnyk, N. D. Obushak, *Russ. J. Org. Chem*. ***2008***, *44*, 1352–1361. **DOI:**10.1134/S1070428008090182
18. N. D. Obushak, Yu. I. Gorak, V. S. Matiichuk, R. Z. Lytvyn, *Russ. J. Org. Chem.* **2008**, *44*, 1689–1694. **DOI:**10.1134/S1070428008110213
19. V. S. Sokolova, E. A. Khrustalev, V. N. Varlamov, M. D.Obushak, V. S.Matiychuk, E. A. Sokolova, V. N. Khrustalev, *Tetrahedron Lett*. **2010**, *51*, 6822–6824. **DOI:**10.1016/j.tetlet.2010.10.046
20. N. Zelisko, D. Atamanyuk, Y. Ostapiuk, A. Bryhas, V. Matiychuk, A. Gzella, R. Lesyk, *Tetrahedron*. **2015**, *71*, 9501–9508. **DOI:**10.1016/j.tet.2015.10.019
21. N. T. Pokhodylo, O. Ya. Shyyka, N. D. Obushak, *Chem. Heterocycl. Compd.* **2015**, *50,* 1748–1755. **DOI:**10.1007/s10593-015-1647-z
22. N. T. Pokhodylo, O. Ya. Shyyka, N. D. Obushak, *Chem. Heterocycl. Compd.* **2018**, *54,* 773–779. **DOI:**10.1007/s10593-018-2348-1
23. T. I. Chaban, B. S. Zimenkovskii, J. D. Komaritsa, I. G. Chaban, *Russ. J. Org. Chem.* **2012**, *48*, 268–272. **DOI:**10.1134/S1070428012020170
24. S. G. Hegde, M. D. Mahoney, *J. Agric. Food Chem.* **1993**, *41*, 2131–2134. **DOI:**10.1021/jf00035a058
25. O. Klenina, I. Drapak, T. Chaban, V. Ogurtsov, I. Chaban, I. Golos, *Chem. Chem. Technol.* **2013**, *7*, 397–404.
26. T. I. Chaban, V. V. Ogurtsov, I. G. Chaban, O. V. Klenina, J. D. Komarytsia, *Phosphorus, Sulfur Silicon Relat. Elem.* **2013**, 188, 1611–1620. **DOI:**10.1080/10426507.2013.777723
27. O. V. Klenina, T. I. Chaban, B. Zimenkovsky, S. Harkov, V. V. Ogurtsov, I. Chaban, I. Myrko, *Pharmacia* **2017**, *64*, 49–71.
28. T. Chaban, V. Ogurtsov, A. Mahlovanyy, N. Sukhodolska, I. Chaban, S. Harkov, V. Matiychuk, *Pharmacia* **2019**, *66,* 171–180. **DOI:**10.3897/pharmacia.66.e36764
29. H. H. Saeyd, E. M. Morsy, E. R. Kotb, *Sci. Commun*. **2010**, *40*, 2712–2722. **DOI:**10.1080/00397910903318674
30. S. Marzoog, Al-Thebeiti, *Il Farmaco* **2000**, *55*, 109–118. **DOI:**10.1016/S0014-827X(99)00130-5
31. V. Victor, B. Semenov, V. A. Lichitsky, N. A. Komogortsev, A. M. Dudinov, M. M. Krayushkin, *Eur. J. Med. Chem.* **2017**, *125*, 573–585. **DOI:**10.1016/j.ejmech.2016.09.075
32. Y. R. Lee, S. S. Yoo, *Bull. Korean Chem. Soc.* **2008**, *1*, 234–236.
33. T. Chaban, O. Klenina, I. Drapak, V. Ogurtsov, I. Chaban,V. Novikov, *Chem. Chem. Technol.* **2014**, *89*, 287–292.
34. T. Chaban, O. Klenina, B. Zimenkovsky, I. Chaban,V. Ogurtsov, L.Shelepeten. *Der Pharma Chem.* **2016**, *8*, 534–542.
35. T. Chaban, O. Klenina, S. Harkov, V. Ogurtsov, I. Chaban, I. Nektegaev, *Pharmacia.* **2017**, *64*, 16–30.
36. T. I. Chaban, V. V. Ogurtsov, V. S. Matiychuk, I. G. Chaban, I. L. Demchuk, I. A. Nektegayev, *Acta Chim. Slov.* **2019**, *66*, 103–111. **DOI:**10.17344/acsi.2018.4570
37. T. I. Chaban, R. R. Panchuk, O. V. Klenina, N. R. Skorokhyd, V. V. Ogurtsov, I. G. Chaban, *Biopolymers &Cell.* **2012**, *25*, 389–396. **DOI:**10.7124/bc.000075
38. A. U. Rao, A. Palani, X. Chen, Y. Huang, R. G. Aslanian, R. E. West, Jr. Shirley, M. Williams, R-L. Wu, J. Hwa, C. Sondey, J. Lachowicz, *Bioorg. Med. Chem. Lett*. **2009**, *19*, 6176–6180. **DOI:**10.1021/ml200250t
39. A. D. Pillai, P. D. Rathod, P. X. Franklin, H. Padh, K. K. Vasu, V. Sudarsanam, *Biochem. Biophys. Res. Commun.* **2004**, *317*, 1067–1074. **DOI:**10.1016/j.bbrc.2004.03.148
40. M. S. Blois, *Nature.* **1958**, *181*, 1199–1200. **DOI:**10.1038/1811199a0
41. P. Molyneux, *J. Sci. Technol.* **2004**, *26*, 211–219. **DOI:**10.1136/inpract.26.4.226
42. O. Shyyka, N. Pokhodylo, N. Finiuk, V. Matiychuk, R. Stoika, M. Obushak, *Sci. Pharm*. **2018**, *86*, E28. **DOI:**10.3390/scipharm86030028
43. N. T. Pokhodylo, O. Ya. Shyyka, V. S. Matiychuk, *Med. Chem. Res*. **2014**, *23,* 2426–2438. **DOI:**10.1007/s00044-013-0841-8

Povzetek

V prispevku je predstavljena sinteza ter protivnetne in antioksidativne lastnosti novih derivatov 5-hidroksi-7-metil-3*H*-tiazolo[4,5-*b*]piridin-2-ona. Kondenzirani tiazolo[4,5-*b*]piridin-2-oni so bili sintetizirani in modificirani na položajih N^3, C^5 in C^6 glavnega obroča in s tem dobili spojine z zadovoljivim farmakološkim profilom. Sintetizirane spojine so bile predhodno izbrane s pomočjo molekulskega modeliranja za nadaljnje testiranje njihove protivnetne aktivnosti *in vitro*. Vrednotenje novih spojin pri edemu podganjih tačk, ki ga povzroča karagenin, je pokazalo močno protivnetno delovanje nekaterih spojin, vključno s (tiazolo [4,5-*b*] piridin-3(2*H*)-il) propanenitrilom (**5**) in tiazolo[4,5-*b*]piridin-3(2*H*)-il) propanojsko kislino (**6**), ki celo presegata standard – Ibuprofen. Antioksidativno aktivnost sintetiziranih spojin so izmerili *in vitro* z metodo lovljenja na 2,2-difenil-1-pikrilhidrazil (DPPH) radikalih.

Except when otherwise noted, articles in this journal are published under the terms and conditions of the Creative Commons Attribution 4.0 International License

DOI: 10.17344/acsi.2019.5492 *Acta Chim. Slov.* **2020,** *67,* 1044–1052
creative commons

Scientific paper

Highly Active and Reusable Cu/C Catalyst for Synthesis of 5-Substituted 1*H*-Tetrazoles Starting from Aromatic Aldehydes

Reza Khalifeh,*,[1] Najme Rastegar[1] and Dariush Khalili[2]

[1] *Department of Chemistry, Shiraz University of Technology, Shiraz 71555-313, Iran*

[2] *Department of Chemistry, College of Science, Shiraz University, Shiraz, Iran*

* *Corresponding author: E-mail: khalifeh@sutech.ac.ir*
+987117354520; Fax:+987117354520. ORCID: 0000-0003-3060-5556

Received: 08-14-2019

Abstract

A new, efficient and convenient method for the synthesis of 5-substituted 1*H*-tetrazole derivatives with a wide range of substituents in good to excellent yields has been developed. The synthesis was performed by the one-pot three-component [3+2]cycloaddition reaction between aldehyde, hydroxylamine and sodium azide in the presence of Cu/C. The reaction probably proceeds by the in situ formation of nitriles followed by successive [3+2]cycloaddition with sodium azide. A variety of aldehydes were used to obtain the corresponding tetrazoles. The catalyst was recovered by simple filtration and reused at least five times without significant loss of catalytic activity. The use of this method offers additional advantages for the synthesis of 5-substituted 1*H*-tetrazole derivatives, including the easy availability of starting materials, mild conditions, experimental simplicity and good yields.

Keywords: Heterogeneous catalyst, Cu/C nanoparticle, Tetrazoles, One-pot three component reaction, [3+2] Cycloaddition reaction

1. Introduction

Tetrazoles are a representative class of heterocyclic polyaza compounds, which are extensively investigated due to their broad range of applications. Tetrazoles exhibit potential biological activities such as antibiotic,[1] anti-allergic,[2] antagonist,[3] antihypertensive,[4] and antiviral activities.[5] These compounds have also been used as an important part of the number of modern drugs.[6] More recently, tetrazoles have been used to bind arylthiotetrazolylacetanilides with HIV-1 reverse transcriptase.[7] In medical chemistry, tetrazoles are considered lipophilic spacers and metabolically stable surrogates for carboxylic acid.[8] In addition, tetrazoles have been used in organometallic chemistry as effective stabilizers of metal peptide structures, as peptide chelating agents[9,10] and as ligands with different coordination modes in coordination chemistry.[11,12] Tetrazoles have also been used as plant growth regulators, herbicides and fungicides.[13] In addition, tetrazole compounds are used in photography,[14] in specialty explosives[15] and in organocatalysis.[16]

Due to their potential advantages and their wide range of applications, various and new synthesis methods for tetrazoles have been intensively developed.[17,18] The [3+2]-cycloaddition of nitriles with sodium azide is known as one of the most conventional methods for the synthesis of 5-substituted 1*H*-tetrazoles. This reaction was carried out by using catalysts such as copper triflates,[19] $CdCl_2$,[20] $Fe(OAc)_2$,[21] zinc(II) salts,[22] $AlCl_3$,[23] BF_3-OEt_2,[24] $FeCl_3$-SiO_2,[25] TBAF,[26] 4-(*N*,*N*-dimethylamino)pyridinium acetate,[27] $Cu(OAc)_2$,[28] $AgNO_3$,[29] CoY zeolites,[30] ZnS,[31] Cu_2O,[32] amberlyst 15,[33] $CuFe_2O_4$ nanoparticles,[34] cuttlebone,[35] Cu(II) immobilized on Fe_3O_4@SiO_2@L-Arginine[36] and Ag/sodium borosilicate nanocomposite.[37]

In general, toxic and expensive substituted phenylnitriles are used as precursors for the synthesis of tetrazoles. Therefore, the use of more available starting material instead of nitriles and the use of comparatively cheaper and easily accessible catalysts are the two motives that led us to do this work.

Previously, we have reported on copper nanoparticles on charcoal (Cu/C) as an excellent heterogeneous cat-

alyst for the synthesis of triazole,[38] propargylamine,[39] benzimidazole,[40] 2-amino-3-cyanopyridine,[41] indazole[42] and imidazole derivatives.[43]

In continuation of our studies on the synthesis of heterocycles and the use of heterogeneous catalysts in organic reactions,[44–56] we describe here a new strategy for the preparation of tetrazole derivatives. The strategy is based on a one-pot three-component [3+2]cycloaddition reaction between aldehydes, hydroxylamine hydrochloride and sodium azide using Cu/C as heterogeneous catalyst. The core of our new strategy for the synthesis of tetrazoles is the use of aldehydes instead of nitriles in a tandem process.

2. Experimental Section

2. 1. Instrumentation, Analysis and Raw Materials

The NMR spectra were recorded on a Bruker Advance DPX-250 (^{1}H NMR at 250 MHz and ^{13}C NMR at 62.5 MHz) in pure deuterated solvents with tetramethylsilane (TMS) as internal standard. Mass spectra were determined with a Shimadzu GCMS-QP 1000 EX instrument at 70 or 20 eV. Melting points were determined in open capillary tubes in a Buchi-535 melting point device. FT-IR spectroscopy (Shimadzu FT -IR 8300 spectrophotometer) was used to characterize the heterogeneous catalyst. Reaction monitoring was performed by TLC on silica gel PolyGram SILG/UV254 plates. Chemical materials were obtained from Fluka, Aldrich and Merck Companies.

2. 2. General Procedure

A mixture of aldehyde (1 mmol), hydroxylamine hydrochloride (1 mmol), sodium azide (1 mmol) and catalytic amounts of Cu/C (5 mol%) in DMF (2 ml) was stirred at 120 °C for a reasonable time (Table 2). After completion of the reaction, as indicated by thin layer chromatography (TLC) with n-hexane/ethyl acetate (EtOAc) (1:2), the entire reaction mixture was passed directly through a celite and rinsed with EtOAc (3 × 15 mL). Then the reaction mixture was washed with distilled water (3 × 20 mL), extracted with EtOAc and the combined organic layers dried over anhydrous Na_2SO_4. It was then concentrated under vacuum and purified by recrystallisation in n-hexane/ethyl acetate (1:1) to obtain tetrazoles of high purity.

5-Phenyl-1*H*-tetrazole (1)

White solid; m.p. 216–217 °C (Lit. 214–216 °C);[57] IR (KBr): υ 3078, 3056, 3000, 2400, 1610, 1478, 1466, 1150, 688 cm^{-1}; ^{1}H NMR (250 MHz, DMSO-d_6): δ 7.57–7.63 (m, 3H), 8.01–8.04 (m, 2H); ^{13}C NMR (62.5 MHz, DMSO-d_6): δ 124.1, 126.9, 129.3, 131.1, 155.3; Anal. calcd. for $C_7H_6N_4$ (146.149): C, 57.53; H, 4.14; found: C, 57.39; H, 4.21.

5-(4-nitrophenyl)-1*H*-tetrazole (2)

Yellow solide; m.p. 217–218 °C (Lit. 218–220 °C);[58] IR (KBr): υ 3443, 2908, 1606, 2850, 1550, 1440, 1495, 1385, 712 cm^{-1}; ^{1}H NMR (250 MHz, DMSO-d_6): δ 8.14 (d, 1H, J = 7.0 Hz), 8.29 (dd, 2H, J_1 = 8.8, J_2 = 1.8 Hz), 8.43 (d, 1H, J = 8.9 Hz); ^{13}C NMR (62.5 MHz, DMSO-d_6): δ 123.7, 124.6, 128.2, 130.6, 148.7; Anal. calcd. for $C_7H_5N_5O_2$ (191.146): C, 43.98; H, 2.64; found: C, 44.09; H, 2.75.

Methyl 4-(1*H*-tetrazole-5-yl)benzoate (3)

White solid; m.p. 224–225 °C (Lit. 225 °C);[59] IR (KBr): υ 3450, 3101, 2649, 2554, 1750, 1431, 1505, 1550, 1610, 1163, 743 cm^{-1}; ^{1}H NMR (250 MHz, $CDCl_3$): δ 3.01 (s, 3H), 7.78 (d, 2H, J = 8.2 Hz), 8.21 (d, 2H, J = 8.1 Hz); ^{13}C NMR (62.5MHz, DMSO-d_6): δ 36.9, 117.9, 120.7, 130.5, 132.2, 163.4, 168.2; Anal. calcd. for $C_9H_8N_4O_2$ (204.185): C, 52.94; H, 3.95; found: C, 53.06; H, 4.07.

5-(4-Chloro-phenyl)-1*H*-tetrazole (4)

White solid; m.p. 261–263 °C (Lit. 261–263 °C);[60] IR (KBr): υ 3096, 3071, 1611, 1488, 1436, 1156, 820 cm^{-1}; ^{1}H NMR (250 MHz, DMSO-d_6): δ 7.68 (d, 2H, J = 8.5 Hz), 8.03 (d, 2H, J = 8.5 Hz); ^{13}C NMR (62.5 MHz, DMSO-d_6): δ 123.1, 128.6, 129.5, 135.8, 155.2; Anal. calcd. for $C_7H_5ClN_4$ (180.594): C, 46.55; H, 2.79; found: C, 46.63; H, 2.87.

5-(4-Methylphenyl)-1*H*-tetrazole (5)

White solid; m.p. 250–251 °C (Lit. 249–251°C);[61] IR (KBr): υ 3433, 3010, 2852, 1616, 1504, 1438, 1373, 1054, 824 cm^{-1}; ^{1}H NMR (250 MHz, DMSO-d_6): δ 2.35 (s, 3H), 7.37 (d, 2H, J = 7.6 Hz), 7.90 (d, 2H, J = 7.5 Hz); ^{13}C NMR (62.5 MHz, DMSO-d_6): δ 20.9, 121.2, 126.8, 129.8, 141.1, 154.9; Anal. calcd. for $C_8H_8N_4$ (160.176): C, 59.99; H, 5.03; found: C, 60.08; H, 4.91.

5-(3,5-dimethoxyphenyl)- 1*H*-tetrazole (6)

Brown solid; m.p. 204–205 °C (Lit. 204–205 °C);[35] IR (KBr): υ 3430, 3012, 2870, 2730, 1590, 1400, 911, 1250, 1035, 766 cm^{-1}; ^{1}H NMR (250 MHz, DMSO-d_6): δ 3.80 (s, 3H), 3.82 (s, 3H), 7.15 (d, 1H, J=8.7 Hz), 7.58–7.63 (m, 2H); ^{13}C NMR (62.5MHz, DMSO-d_6): δ 55.5, 109.9, 111.9, 116.1, 120.0, 149.0, 151.0, 154.8; Anal. calcd. for $C_9H_{10}N_4O_2$ (206.201): C, 52.42; H, 4.89; found: C, 52.29; H, 4.96.

***N,N*-dimethyl-4-(1*H*-tetrazole-5-yl)aniline (7)**

White solid; m.p. 240–241 °C (Lit. 218–220 °C);[62] IR (KBr): υ 3461, 3274, 2926, 2877, 2713, 1600, 1430, 1530, 1377, 814, 751 cm^{-1}; ^{1}H NMR (250 MHz, DMSO-d_6): δ 2.96 (s, 6H), 6.81 (d, 2H, J = 8.5 Hz), 7.82 (d, 2H, J = 8.6 Hz); ^{13}C NMR (62.5 MHz, DMSO-d_6): δ 39.6, 110.4, 111.8, 127.9, 151.8, 154.9; Anal. calcd. for $C_9H_{11}N_5$ (189.217): C, 57.13; H, 5.86; found: C, 57.24; H, 5.97.

4-(1*H*-tetrazole-5-yl)benzene-1,3-diol (8)

White solid; m.p. 247–248 °C; IR (KBr): υ 3386, 3232, 2853, 2770, 2693, 1600, 1586, 1430, 1134, 974, 814,

748 cm^{-1}; ^{1}H NMR (250 MHz, DMSO-d_6): δ 6.41 (dd, 1H, J_1 = 8.5, J_2 = 2.3 Hz), 6.47 (d, 1H, J = 2.2 Hz), 7.79 (d, 1H, J = 8.6 Hz), 10.01 (s, 2H); ^{13}C NMR (62.5 MHz, DMSO-d_6): δ 101.7, 102.4, 107.9, 130.0, 151.7, 156.8, 161.2; Anal. calcd. for $C_7H_6N_4O_2$ (178.148): C, 47.19; H, 3.39; found: C, 47.08; H, 3.26.

5-(2-Chloro-phenyl)-1*H*-tetrazole (9)

White solid; m.p. 178–180 °C (Lit. 175–177 °C);[57] IR (KBr): υ 3200, 3100, 2400, 1603, 1564, 1472, 1080, 784 cm^{-1}; ^{1}H NMR (250 MHz, DMSO-d_6): δ 7.37–7.45 (m, 1H), 7.50–7.53 (m, 2H), 7.74–7.78 (m, 1H); ^{13}C NMR (62.5 MHz, DMSO-d_6): δ 124.4, 127.7, 130.4, 131.7, 131.9, 132.4, 153.6; Anal. calcd. for $C_7H_5ClN_4$ (180.594): C, 46.55; H, 2.79; found: C, 46.43; H, 2.68.

5-(2,4-dichlorophenyl)-1*H*-tetrazole (10)

White solid; m.p. 165–166 °C (Lit. 169–170 °C);[63] IR (KBr): υ 3455, 3200, 1481, 1590, 1030, 756, 566, 538 cm^{-1}; ^{1}H NMR (250 MHz, DMSO-d_6): δ 7.62 (dd, 1H, J_1 = 8.4, J_2 = 2.0 Hz), 7.82–7.86 (m, 2H). ^{13}C NMR (62.5 MHz, DMSO-d_6): δ 116.8, 118.2, 124.9, 135.4, 138.5, 158.9; Anal. calcd. for $C_7H_4Cl_2N_4$ (215.039): C, 39.10; H, 1.87; found: C, 38.98; H, 1.75.

5-(furane-2-yl)-1*H*-tetrazole (11)

White solid; m.p. 203–204 °C (Lit. 203–204 °C);[64] ^{1}H NMR (250 MHZ, DMSO-d_6): δ 6.75 (s, 1H), 7.26 (s, 1H), 8.00 (s, 1H). ^{13}C NMR (62.5 MHz, DMSO-d_6): δ 118.7, 126.4, 136.3, 141.2, 154.5, 141.2; Anal. calcd. for $C_7H_4Cl_2N_4$ (136.111): C, 44.12; H, 2.96; found: C, 44.25; H, 3.09.

5-(1-methyl-1*H*-pyrrol-2-yl)-1*H*-tetrazole (12)

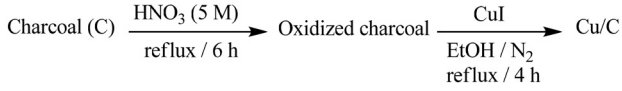
White solid; m.p.: 240–241 °C; IR (KBr): υ 3450, 3185, 3115, 2895, 1600, 1512, 1421, 702, 802 cm^{-1}; ^{1}H NMR (250 MHZ, DMSO-d_6): δ 2.48 (s, 3H), 7.64 (dd, 1H, J_1 = 5.0, J_2 = 1.2 Hz), 7.80 (dd, 1H, J_1 = 5.0, J_2 = 2.9 Hz), 7.77 (dd, 1H, J_1 = 2.9, J_2 = 1.1 Hz); ^{13}C NMR (62.5MHz, DMSO-d_6): δ 46.1, 125.9, 127.4, 128.7; Anal. calcd. for $C_6H_7N_5$ (149.153): C, 48.32; H, 4.73; found: C, 48.25; H, 4.62.

5-(thiophen-3-yl)-1*H*-tetrazole (13)

White solid; m.p. 244–245 °C (Lit. 244–245 °C);[65] IR (KBr): υ 3286, 1600, 1512, 1460, 1100, 999, 750 cm^{-1}; ^{1}H NMR (250 MHZ, DMSO-d_6): δ 8.07 (d, 1H, J = 6.2 Hz), 8.21–8.27 (m, 2H). ^{13}C NMR (62.5MHz, DMSO-d_6): δ 125.8, 126.9, 128.5, 129.2, 154.3; Anal. calcd. for $C_5H_4N_4S$ (152.177): C, 39.46; H, 2.65; found: C, 39.57; H, 2.78.

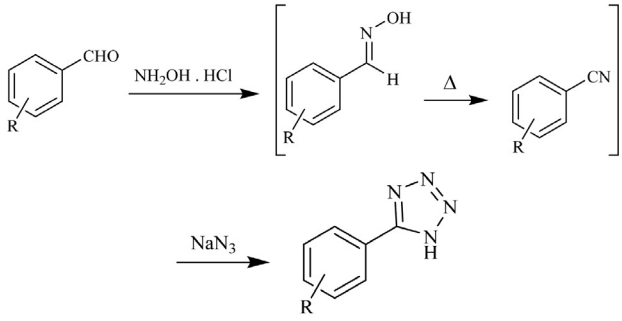
3. Results and Discussion

The copper nanoparticle on charcoal (Cu/C) as catalyst was synthesized according to our previously published methods (Scheme 1).[38]



Scheme 1. Preparation of copper nanoparticle on charcoal (Cu/C)

The potential of Cu/C as a catalyst in tetrazole synthesis via a one-pot three-component [3+2] cycloaddition reaction between aldehyde, hydroxylamine hydrochloride and sodium azide was investigated. This methodology is based on the initial formation of an oxime derivative resulting from the reaction of an aldehyde with hydroxylamine hydrochloride in the presence of Cu/C. Subsequently, the oxime derivative is dehydrated, resulting in structurally different nitriles. Finally, the [3+2]cycloaddition of nitrile with sodium azide yields the required tetrazole derivatives (Scheme 2).



Scheme 2. Proposed reaction pathway for the synthesis of tetrazoles from aldehydes.

To search for optimal reaction conditions, a three-component reaction model between hydroxylamine hydrochloride, benzaldehyde and NaN_3 using Cu/C as catalyst was investigated. Different reaction parameters like solvent, temperature, different catalysts and the amount of catalyst were investigated. The corresponding results were summarized in Table 1.

First, different solvents for the preparation of 5-substituted 1*H*-tetrazole were screened. No product was formed during the reaction in H_2O, CH_3CN and ethanol (Table 1, entries 1–3). In another attempt to synthesize the tetrazole ring, benzaldehyde, hydroxylamine and NaN_3 were used in PEG 200 at 120 °C, which provided the desired tetrazole in very low yield (Table 1, entry 4). When the model reaction was carried out in DMSO at 120 °C, the desired product was obtained in moderate yield as indicated in Table 1, entry 5. The solvent has a noticeable effect in this reaction, in which dimethylformamide (DMF) was the best solvent to achieve the highest yields of the desired tetrazole (Table 1, entry 6).

Next, we investigated the influence of temperature on the model reaction. A temperature increase from 120 to 140 °C had no significant effect on the yield and the reac-

Table 1. Optimization for the synthesis of tetrazole from aldehyde.[a]

Entry	Solvent	Catalyst (mol%)	Temperature (°C)	Time (h)	Yield (%)[b]
1	H_2O	Cu/C (5)	Reflux	9	–
2	MeCN	Cu/C (5)	Reflux	9	–
3	EtOH	Cu/C (5)	Reflux	9	–
4	PEG 200	Cu/C (5)	120	9	12
5	DMSO	Cu/C (5)	120	9	48
6	DMF	Cu/C (5)	120	9	87
7	DMF	Cu/C (5)	140	9	89
8	DMF	Cu/C (5)	100	9	48
9	DMF	Cu/C (5)	r.t	9	–
10	DMF	Cu/C (2)	120	9	68
11	DMF	Cu/C (10)	120	9	90
12	DMF	–	120	9	–
13	DMF	Charcoal	120	9	17
14	DMF	$Cu(OAC)_2$ (5)	120	9	48
15	DMF	CuI (5)	120	9	53
16	DMF	$CuSO_4$	120	9	41

[a] Reaction conditions: benzaldehyde (1 mmol), hydroxylamine hydrochloride (1 mmol), sodium azide (1 mmol) and Cu/C (5 mol%) in solvent (2 mL). [b] Isolated yields.

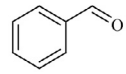
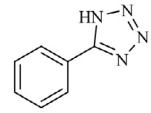
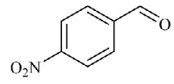
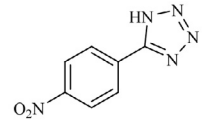
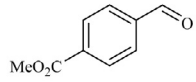
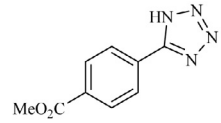
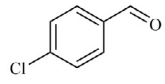
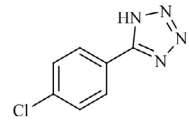
tion time (Table 1, entry 7). By lowering the temperature to 100 °C only a yield of 48% of the target product was obtained (Table 1, entry 8). Furthermore, no reaction took place at room temperature in the presence of the catalyst (Table 1, entry 9).

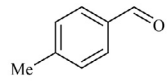
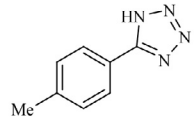
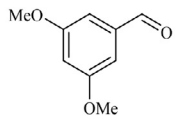
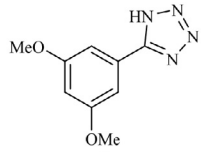
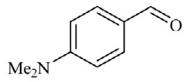
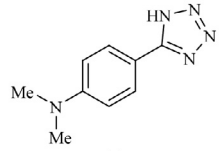
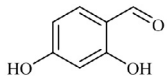
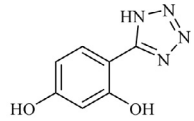
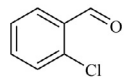
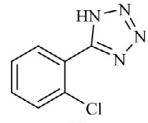
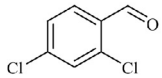
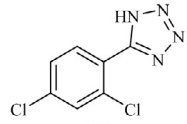
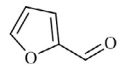
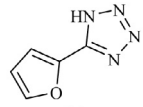
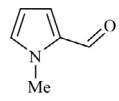
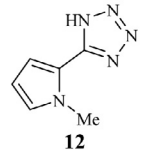
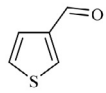
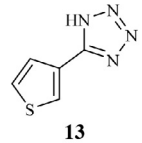
Then the different amounts of catalyst were tested to find the optimum state. The yield was reduced to 68% by reducing the amount of catalyst to 2 mol% (Table 1, entry 10). A further increase in the catalyst quantity did not significantly increase the product yield (Table 1, entry 11). A mixture of aldehyde, hydroxylamine hydrochloride and sodium azide in the absence of Cu/C catalyst was heated to 120 °C for 9 h, but the starting materials were recovered (Table 1, entry 12). To study the catalytic activity of copper, activated carbon was used as a catalyst to reach the target product. The low yield was achieved with activated carbon (Table 1, entry 13). As can be seen from Table 1, the presence of Cu was essential for substrate conversion, and in the absence of Cu, activated carbon did not catalyze the model reaction (entry 13).

To identify the role of Cu/C in this reaction, the catalytic activities of different copper sources were investigated under the same optimal experimental conditions. All alternative copper species produced the desired product in lower yields than Cu/C (Table 2, entries 14–16). Furthermore, separation and reuse of the catalyst was problematic due to its complete dissolution in DMF. The application of this protocol, which is based on the in-situ generation of nitriles, allowed us to efficiently produce tetrazole derivatives.

To determine the generality of this conversion, the reaction of different aldehydes with a multitude of substituents on the aromatic part in the presence of nanocopper on charcoal was investigated. It was found that the reaction is quite general and that it tolerates a large number of

Table 2. Sequential one-pot synthesis of 5-substituted 1*H*-tetrazoles from aldehydes via in-situ generation of nitriles followed by [2+3] cycloaddition with sodium azide using nano-Cu/C as a catalyst.[a]

Entry	Aldehyde	Product	Time (h)	Yield (%)[b]
1		 **1**	9	87
2		 **2**	9	89
3		 **3**	15	88
4		 **4**	9	84

Entry	Aldehyde	Product	Time (h)	Yield (%)[b]
5		 **5**	9	82
6		 **6**	9	79
7		 **7**	9	78
8		 **8**	15	80
9		 **9**	15	76
10		 **10**	15	74
11		 **11**	9	83
12		 **12**	9	85
13		 **13**	9	81

[a] Reaction conditions: aldehyde (1 mmol), hydroxylamine hydrochloride (1 mmol), sodium azide (1 mmol) and Cu/C (5 mol%) in DMF (2 mL) at 120 °C. [b] Isolated yields.

substituted benzaldehydes (Table 2). All reactions took place in less than 15 h, and tetrazole derivatives were isolated in good or even high yields (74–89%) without the need to isolate the aryl nitriles as an intermediate. In general, electronic and steric modifications did not have a remarkable effect on the reactivity of the aldehyde.

The influence of the withdrawing groups on the aromatic ring of benzaldehyde was also investigated. The reactions with nitro and ester groups were carried out in the isolated yields of 88–89% and the carbonyl functionality remained unaffected (Table 2, entries 2–3).

The [3+2] cycloaddition process was also extended to nitriles with electron donating groups such as methyl, methoxy and *N,N*-dimethyl. Using the optimal reaction conditions, the corresponding 5-substituted 1*H*-tetrazoles **5–7** were prepared in 9 h and isolated in good yield (Table 1, entries 5–7).

Benzaldehydes with electron donating groups at the ortho positions of the aromatic rings yielded the corresponding tetrazoles in good yield. However, sterically hindered ortho-substituted benzaldehydes required a longer reaction time (Table 2, entries 8–10).

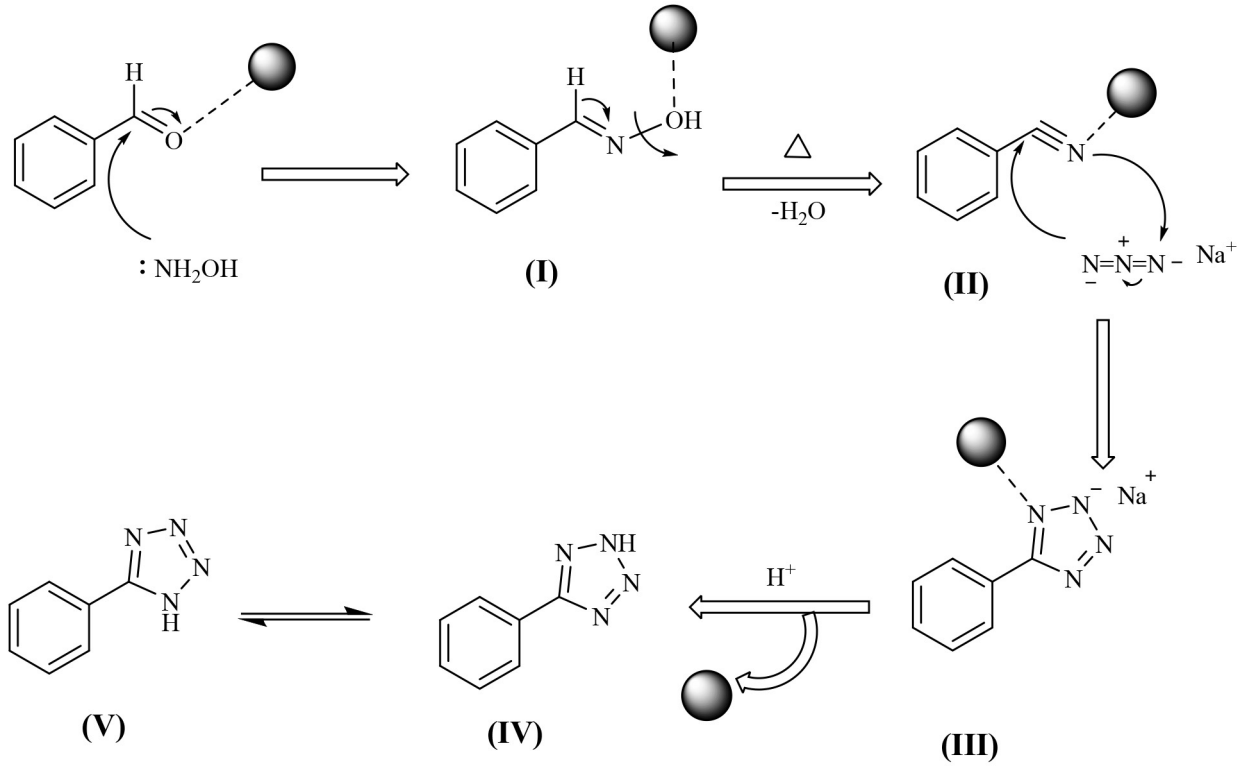
The above results showed that this reaction can be applied to benzaldehyde for a wide range of functional groups. The reaction proceeded well, regardless of the position and electronic nature of the substituents on the aromatic ring. Next, the reactivity of acid-sensitive heterocyclic aldehydes was investigated. The reaction of furfural, *N*-methylpyrrole-2-carbaldehyde and thiophene-3-carbaldehyde resulted in the desired tetrazoles 11–13 in good yields (Table 2, entries 11–13).

To check the reusability of the catalyst, the reaction was carried out with benzaldehyde, hydroxylamine hydrochloride and sodium azide under the optimized reaction conditions. After completion of the reaction, the catalyst was separated from the reaction mixture by simple filtration, washed with ethyl acetate and dried for reuse under air atmosphere. As shown in Figure 1, five recoveries of catalyst were found without significant loss of catalytic activity.



Figure 1. Recovery and reuse of Cu/C nanoparticles for the synthesis of 5-phenyl-1*H*-tetrazole from benzaldehyde via benzonitrile.

The plausible mechanism for the synthesis of 5-substituted 1*H*-tetrazoles from aldehydes was shown in Scheme 3 using Cu/C as catalyst. First, oxime is formed on the aldehyde according to the activation of the carbonyl group of the aldehyde and the nucleophilic attack of the



Scheme 3: Plausible mechanism for the synthesis of 5-substituted 1*H*-tetrazoles from aldehydes catalyzed by Cu/C.

Table 3: Comparison between the efficiency of Cu/C as catalyst and some other catalysts for the synthesis of 5-substituted 1*H*-tetrazole derivatives.

Entry	Reaction Condition	Time (h)	Yield (%)	Ref.
1	$Ni(OH)_2$ Nanoparticles, H_2O, Reflux	10	98	66
2	$Cu(OAc)_2$, DMF, 120 °C	12	96	67
3	Cu-MCM-41, DMF, 140 °C	12	90	68
4	$(NH_4)_2Ce(SO_4)_4.2H_2O$, DMF, 140 °C	5	72	69
5	$Bi(OTf)_3$, DMF, 120 °C	24	87	70
6	Cu/C, DMF, 120 °C	9	87	This work

nitrogen atom of the hydroxylamine. In the next step, the nitrile product is formed by splitting off water. Then the nitrile group is activated by Cu/C, which accelerates the cyclization step. The cycloaddition between the nitrile group and the azide ion takes place immediately to form the intermediate product III. After removal of the catalyst by simple filtration and acidic processing, IV and V tautomers are obtained. The more stable tautomer V (5-substituted-1*H*-tetrazole) is accepted as the significant product.

The efficiency of Cu/C as a catalyst for the synthesis of 5-substituted 1*H*-tetrazoles starting from aldehydes was compared with that of other catalysts reported in the literature. The results were summarized in Table 3. It is clear that Cu/C is the most effective catalyst for the synthesis of 5-substituted 1*H*-tetrazole derivatives.

4. Conclusion

In summary, we have developed an efficient direct route for the synthesis of tetrazole derivatives from aromatic aldehydes, hydroxylamine hydrochloride and sodium azide. The reaction was carried out by copper-catalyzed [3+2]cycloaddition to produce 5-substituted 1*H*-tetrazole in a sequential one-pot three-component reaction without isolation of the nitrile intermediate. The main advantage of this method is the replacement of toxic nitrile precursors by aldehydes. This method demonstrates the potential of the nanocatalyst Cu/C as a very user-friendly, cost-effective and efficient catalyst for the production of 5-substituted 1*H*-tetrazoles. The catalyst can be easily recovered and reused.

Acknowledgement

We are grateful for the support of the Shiraz University of Technology for this work.

5. References

1. J. H. Toney, P. M. Fitzgerald, N. Grover-Sharma, S. H. Olson, W. J. May, J. G. Sundelof, D. E. Vanderwall, K. A. Cleary, S. K. Grant, J. K. Wu, *Chem. Biol.* **1998**, *5*, 185–196. **DOI:**10.1016/S1074-5521(98)90632-9
2. A. Nohara, H. Kuriki, T. Saijo, H. Sugihara, M. Kanno, Y. Sanno, *J. Med. Chem.* **1977**, *20*, 141–145. **DOI:**10.1021/jm00211a030
3. J. L. Castro, R. G. Ball, H. B. Broughton, M. G. Russell, D. Rathbone, A. P. Watt, R. Baker, K. L. Chapman, A. E. Fletcher, S. Patel, A. J. Smith, G. R. Marshall, W. Ryecroft, V. G. Matassa, *J. Med. Chem.* **1996**, *39*, 842–849. **DOI:**10.1021/jm9506736
4. M. J. Choi, G. H. Kwon, N. S. Han, B. W. Yoo, J. H. Kim, S. H. Paik, Y. H. Chi, K.-T. Lee, J. Y. Lee, *Bioorg. Med. Chem. Lett.* **2013**, *23*, 4540–4546. **DOI:**10.1016/j.bmcl.2013.06.041
5. K.-S. Yeung, Z. Qiu, Z. Yang, L. Zadjura, C. J. D'Arienzo, M. R. Browning, S. Hansel, X. S. Huang, B. J. Eggers, K. Riccardi, P.-F. Lin, N. A. Meanwell, J. F. Kadow, *Bioorg. Med. Chem. Lett.* **2013**, *23*, 209–212. **DOI:**10.1016/j.bmcl.2012.10.125
6. O. Mesenzani, A. Massarotti, M. Giustiniano, T. Pirali, V. Bevilacqua, A. Caldarelli, P. Canonico, G. Sorba, E. Novellino, A. A. Genazzani, G. C. Tron, *Bioorg. Med. Chem. Lett.* **2011**, *21*, 764–768. **DOI:**10.1016/j.bmcl.2010.11.113
7. A. Gagnon, S. Landry, R. Coulombe, A. Jakalian, I. Guse, B. Thavonekham, P. R. Bonneau, C. Yoakim, B. Simoneau, *Bioorg. Med. Chem. Lett.* **2009**, *19*, 1199–1205. **DOI:**10.1016/j.bmcl.2008.12.074
8. R. J. Herr, *Biorg. Med. Chem.* **2002**, *10*, 3379–3393. **DOI:**10.1016/S0968-0896(02)00239-0
9. E. Łodyga-Chruścińska, D. Sanna, G. Micera, L. Chruściński, J. Olejnik, R. J. Nachman, J. Zabrocki, *Acta Biochim. Pol.* **2006**, *53*, 65–72. **DOI:**10.18388/abp.2006_3362
10. E. Łodyga-Chruścińska, S. Ołdziej, G. Micera, D. Sanna, L. Chruściński, J. Olczak, J. Zabrocki, *J. Inorg. Biochem.* **2004**, *98*, 447–458. **DOI:**10.1016/j.jinorgbio.2003.11.011
11. P. N. Gaponik, S. V. Voitekhovich, O. A. Ivashkevich, *Russ. Chem. Rev.* **2006**, *75*, 507–539. **DOI:**10.1070/RC2006v075n06ABEH003601
12. H. Zhao, Z.-R. Qu, H.-Y. Ye, R.-G. Xiong, *Chem. Soc. Rev.* **2008**, *37*, 84–100. **DOI:**10.1039/B616738C
13. G. Sandmann, C. Schneider, P. Böger, *Bioscience* **1996**, *51*, 534–538. **DOI:**10.1515/znc-1996-7-812
14. G. I. Koldobskii, V. A. Ostrovskii, *Russ. Chem. Rev.* **1994**, *63*, 797–814. **DOI:**10.1070/RC1994v063n10ABEH000119
15. R. P. Singh, R. D. Verma, D. T. Meshri, J. M. Shreeve, *Angew. Chem. Int. Ed.* **2006**, *45*, 3584–3601. **DOI:**10.1002/anie.200504236
16. A. J. Cobb, D. M. Shaw, D. A. Longbottom, J. B. Gold, S. V. Ley, *Org. Biomol. Chem.* **2005**, *3*, 84–96. **DOI:**10.1039/b414742a

17. C. G. Neochoritis, T. Zhao, A. Dömling, *Chem. Rev.* **2019**, *119*, 1970–2042. **DOI:**10.1021/acs.chemrev.8b00564
18. G. M. Ojeda-Carralero, J. Coro, A. Valdés-Palacios, *Chem. Heterocycl. Compd.* **2020**, *56*, 408–421. **DOI:**10.1007/s10593-020-02676-7
19. L. Bosch, J. Vilarrasa, *Angew. Chem. Int. Ed.* **2007**, *46*, 3926–3930. **DOI:**10.1002/anie.200605095
20. G. Venkateshwarlu, A. Premalatha, K. Rajanna, P. Saiprakash, *Synth. Commun.* **2009**, *39*, 4479-4485. **DOI:**10.1080/00397910902917682
21. J. Bonnamour, C. Bolm, *Chem. Eur. J.* **2009**, *15*, 4543–4545. **DOI:**10.1002/chem.200900169
22. Z. P. Demko, K. B. Sharpless, *J. Org. Chem.* **2001**, *66*, 7945–7950. **DOI:**10.1021/jo010635w
23. D. P. Matthews, J. E. Green, A. J. Shuker, *J. Comb. Chem.* **2000**, *2*, 19–23. **DOI:**10.1021/cc990035z
24. A. Kumar, R. Narayanan, H. Shechter, *J. Org. Chem.* **1996**, *61*, 4462–4465. **DOI:**10.1021/jo952269k
25. M. Nasrollahzadeh, Y. Bayat, D. Habibi, S. Moshaee, *Tetrahedron Lett.* **2009**, *50*, 4435–4438. **DOI:**10.1016/j.tetlet.2009.05.048
26. D. Amantini, R. Beleggia, F. Fringuelli, F. Pizzo, L. Vaccaro, *J. Org. Chem.* **2004**, *69*, 2896–2898. **DOI:**10.1021/jo034752y
27. N. Nowrouzi, S. Farahi, M. Irajzadeh, *Tetrahedron Lett.* **2015**, *56*, 739–742. **DOI:**10.1016/j.tetlet.2014.12.106
28. U. B. Patil, K. R. Kumthekar, J. M. Nagarkar, *Tetrahedron Lett.* **2012**, *53*, 3706–3709. **DOI:**10.1016/j.tetlet.2012.04.093
29. P. Mani, A. K. Singh, S. K. Awasthi, *Tetrahedron Lett.* **2014**, *55*, 1879–1882. **DOI:**10.1016/j.tetlet.2014.01.117
30. V. Rama, K. Kanagaraj, K. Pitchumani, *J. Org. Chem.* **2011**, *76*, 9090–9095. **DOI:**10.1021/jo201261w
31. L. Lang, B. Li, W. Liu, L. Jiang, Z. Xu, G. Yin, *Chem. Commun.* **2010**, *46*, 448–450. **DOI:**10.1039/B912284B
32. T. Jin, F. Kitahara, S. Kamijo, Y. Yamamoto, *Tetrahedron Lett.* **2008**, *49*, 2824–2827. **DOI:**10.1016/j.tetlet.2008.02.115
33. R. Shelkar, A. Singh, J. Nagarkar, *Tetrahedron Lett.* **2013**, *54*, 106–109. **DOI:**10.1016/j.tetlet.2012.10.116
34. B. Sreedhar, A. S. Kumar, D. Yada, *Tetrahedron Lett.* **2011**, *52*, 3565–3569. **DOI:**10.1016/j.tetlet.2011.04.094
35. S. S. Ghodsinia, B. Akhlaghinia, *RSC Adv.* **2015**, *5*, 49849–49860. **DOI:**10.1039/C5RA08147E
36. A. Ghorbani-Choghamarani, L. Shiri, G. Azadi, *RSC Adv.* **2016**, *6*, 32653–32660. **DOI:**10.1039/C6RA03023H
37. M. Nasrollahzadeh, M. Sajjadi, M. R. Tahsili, M. Shokouhimehr, R. S. Varma, *ACS Omega* **2019**, *4*, 8985–9000. **DOI:**10.1021/acsomega.9b00800
38. H. Sharghi, R. Khalifeh, M. M. Doroodmand, *Adv. Synth. Catal.* **2009**, *351*, 207–218. **DOI:**10.1002/adsc.200900353
39. H. Sharghi, R. Khalifeh, F. Moeini, M. Beyzavi, A. S. Beni, M. Doroodmand, *J. Iran. Chem. Soc.* **2011**, *8*, S89–S103. **DOI:**10.1007/BF03254285
40. H. Sharghi, R. Khalifeh, S. G. Mansouri, M. Aberi, M. M. Eskandari, *Catal. Lett.* **2011**, *141*, 1845–1850. **DOI:**10.1007/s10562-011-0671-6
41. R. Khalifeh, M. Ghamari, *J. Braz. Chem. Soc.* **2016**, *27*, 759–768. **DOI:**10.5935/0103-5053.20150327
42. R. Khalifeh, F. Karimzadeh, *Can. J. Chem.* **2019**, *97*, 303–309. **DOI:**10.1139/cjc-2018-0428
43. R. Khalifeh, A. Niknam, *Org. Prep. Proced. Int.* **2020**, *52*, 91–98. **DOI:**10.1080/00304948.2020.1716433
44. R. Khalifeh, R. Shahimoridi, M. Rajabzadeh, *Catal. Lett.* **2019**, *149*, 2864–2872. **DOI:**10.1007/s10562-019-02818-3
45. A. Ebadi, M. Rajabzadeh, R. Khalifeh, *ChemistrySelect* **2019**, *4*, 7211–7218. **DOI:**10.1002/slct.201901237
46. M. Rajabzadeh, R. Khalifeh, H. Eshghi, M. Sorouri, *Catal. Lett.* **2019**, *149*, 1125–1134. **DOI:**10.1007/s10562-019-02666-1
47. F. Rezaei, M. A. Amrollahi, R. Khalifeh, *Inorg. Chim. Acta* **2019**, *489*, 8–18. **DOI:**10.1016/j.mtchem.2020.100353
48. M. Rajabzadeh, R. Khalifeh, H. Eshghi, M. Bakavoli, *J. Catal.* **2018**, *360*, 261–269. **DOI:**10.1016/j.jcat.2018.01.028
49. M. Rajabzadeh, H. Eshghi, R. Khalifeh, M. Bakavoli, *Appl. Organomet. Chem.* **2018**, *32*, e4052. **DOI:**10.1002/aoc.4052
50. R. Khalifeh, F. Shahriarpour, H. Sharghi, M. Aberi, *J. Iran. Chem. Soc.* **2018**, *15*, 813–821. **DOI:**10.1007/s13738-017-1280-0
51. M. Rajabzadeh, H. Eshghi, R. Khalifeh, M. Bakavoli, *Appl. Organomet. Chem.* **2017**, *31*, e3647. **DOI:**10.1002/aoc.3647
52. K. P. Boroujeni, Z. Heidari, R. Khalifeh, *Acta Chim. Slov.* **2016**, *63*, 602–608. **DOI:**10.17344/acsi.2016.2291
53. M. Rajabzadeh, H. Eshghi, R. Khalifeh, M. Bakavoli, *RSC Adv.* **2016**, *6*, 19331–19340. **DOI:**10.1039/C5RA26020E
54. H. Sharghi, R. Khalifeh, Z. Rashidi, *Mol. Divers.* **2013**, *17*, 721–730. **DOI:**10.1007/s11030-013-9468-4
55. R. Khalifeh, H. Sharghi, Z. Rashidi, *Heteroat. Chem.* **2013**, *24*, 372–383. **DOI:**10.1002/hc.21103
56. H. Sharghi, M. Jokar, M. M. Doroodmand, R. Khalifeh, *Adv. Synth. Catal.* **2010**, *352*, 3031–3044. **DOI:**10.1002/adsc.201000319
57. P. Akbarzadeh, N. Koukabi, E. Kolvari, *Mol. Divers.* **2020**, *24*, 319–334. **DOI:**10.1007/s11030-019-09951-6
58. J.-M. Chrétien, G. Kerric, F. Zammattio, N. Galland, M. Paris, J.-P. Quintard, E. Le Grognec, *Adv. Synth. Catal.* **2019**, *361*, 747–757. **DOI:**10.1002/adsc.201801117
59. R. R. Chakraborty, P. Ghosh, *Tetrahedron Lett.* **2018**, *59*, 3616–3619. **DOI:**10.1016/j.tetlet.2018.08.050
60. S. M. Galani, A. B. Panda, *Chem. -Asian J.* **2019**, *14*, 612–620. **DOI:**10.1002/asia.201801745
61. F. Carpentier, F.-X. Felpin, F. Zammattio, E. Le Grognec, *Org. Process Res. Dev.* **2020**, *24*, 752–761. **DOI:**10.1021/acs.oprd.9b00526
62. C. P. Tüllmann, S. Steiner, P. Knochel, *Synthesis* **2020**, *52*, 2357–2363. **DOI:**10.1055/s-0039-1691734

DOI: 10.1055/s-0039-1691734

63. I. Fatima, H. Zafar, K. M. Khan, S. M. Saad, S. Javaid, S. Perveen, M. I. Choudhary, *Bioorg. Chem.* **2018**, *79*, 201–211. **DOI:**10.1016/j.bioorg.2018.04.021
64. X. Xiong, C. Yi, X. Liao, S. Lai, *Tetrahedron Lett.* **2019**, *60*, 402–406. **DOI:**10.1016/j.bioorg.2018.04.021
65. J. Dudley, L. Feinn, H. DeFrancesco, E. Lindsay, A. Coca, E. L. Roberts, *Med. Chem.* **2018**, *14*, 550–555. **DOI:**10.2174/1573406413666171120162420

66. M. Halder, M. M. Islam, P. Singh, A. Singha Roy, S. M. Islam, K. Sen, *ACS Omega* **2018**, *3*, 8169–8180. **DOI:**10.1021/acsomega.8b01081
67. M. M. Heravi, A. Fazeli, H. A. Oskooie, Y. S. Beheshtiha, H. Valizadeh, *Synlett* **2012**, *23*, 2927–2930. **DOI:**10.1055/s-0032-1317671
68. M. Abdollahi-Alibeik, A. Moaddeli, *New J. Chem.* **2015**, *39*, 2116–2122. **DOI:**10.1039/C4NJ01042F
69. B. Mitra, S. Mukherjee, G. C. Pariyar, P. Ghosh, *Tetrahedron Lett.* **2018**, *59*, 1385–1389. **DOI:**10.1016/j.tetlet.2018.02.067
70. M. Sridhar, K. K. R. Mallu, R. Jillella, K. R. Godala, C. R. Beeram, N. Chinthala, *Synthesis* **2013**, *45*, 507–510. **DOI:**10.1055/s-0032-1318108

Povzetek

Razvita je nova, učinkovita in priročna metoda za sintezo 5-substituiranih derivatov 1*H*-tetrazola s široko paleto substituentov in z dobrimi izkoristki. Sinteza je bila izvedena z enostopenjsko trikomponentno reakcijo [3+2] cikloadicije med aldehidom, hidroksilaminom in natrijevim azidom v prisotnosti Cu/C kot katalizatorja. Reakcija verjetno poteka z *in-situ* tvorbo nitrila, čemur sledi nadaljnja [3+2] cikloadicija z natrijevim azidom. Za pridobitev ustreznih tetrazolov so uporabili različne aldehide. Katalizator so rekuperirali s preprosto filtracijo in ponovno uporabili v najmanj petih poskusih, brez večje izgube katalitične aktivnosti. Uporaba te metode ponuja nove možnosti za sintezo 5-substituiranih derivatov 1*H*-tetrazola, vključno z lahko dostopnimi vhodnimi snovmi, blagimi reakcijskimi pogoji, enostavno izvedbo reakcije in dobrimi izkoristki.

Except when otherwise noted, articles in this journal are published under the terms and conditions of the Creative Commons Attribution 4.0 International License

Scientific paper

Differential Pulse Anodic Voltammetric Determination of Chlorzoxazone in Pharmaceutical Formulation using Carbon Paste Electrode

Sayed I. M. Zayed[1,*] and Yousry M. Issa[2]

[1] *Faculty of Technology and Education, Beni-Suef University, Beni-Suef, Egypt*

[2] *Chemistry Departement, Faculty of Science, Cairo University, Giza, Egypt*

** Corresponding author: E-mail: simzayed2011@hotmail.com*
Tel. :00201009381364; Fax: 0020822241932

Received: 01-27-2020

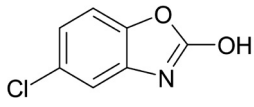
Abstract

The electrochemical behavior of chlorzoxazone at the carbon paste electrode was investigated in 0.04 mol/L Britton-Robinson buffer pH 6.50 using cyclic and differential pulse voltammetric techniques. Cyclic voltammetric studies indicated that the oxidation of the drug was irreversible and controlled mainly by diffusion. Experimental and instrumental parameters were optimized (50 mV/s scan rate, 50 mV pulse amplitude, and 0.04 mol/L Britton-Robinson (BR) buffer pH 6.50 as a supporting electrolyte) and a sensitive differential pulse anodic voltammetric method has been developed for the determination of the drug over the concentration range 0.17–1.68 μg/mL chlorzoxazone, with detection and quantitation limits of 0.05 and 0.16 μg/mL, respectively. The proposed voltammetric method was successfully applied to the determination of the drug in its pharmaceutical formulation (Myoflex tablets), and in spiked human urine samples.

Keywords: Chlorzoxazone; carbon paste electrodes; differential pulse anodic voltammetry Pharmaceutical dosage form; human urine samples.

1. Introduction

Chlorzoxazone, 5-chloro-2-hydroxy benzoxazole [95-25-0] (Scheme 1), is a centrally acting skeletal muscle relaxant with sedative properties. It is claimed to inhibit muscle spasm by exerting an effect primarily at the level of the spinal cord and subcortical area of the brain. It is used as an adjunct in the symptomatic treatment of painful muscle spasm.[1,2]



Scheme 1. Structural formula of chlorzoxazone

Various analytical methods have been reported in the literature for the determination of chlorzoxazone. These include high performance liquid chromatography,[3–13] thin layer chromatography,[14–17] liquid chromatography-tandem mass spectrometry,[18] packed column supercritical fluid chromatography,[19–20] gas chromatography,[21–23] spectrophotometry,[24–35] fluorimetry,[36] and capillary zone electrophoresis.[37] Two papers have been described in literature concerning the voltammetric determination of chlorzoxazone based on the oxidation of the drug at the glassy carbon electrode and gold electrode.[38,39] The carbon paste electrodes have been extensively used in electroanalytical methods due to their excellent properties, like, wide potential range, low background current, easy surface renewal, easy preparation, and low cost. There is no published work concerning the anodic voltammetric determination of chlorzoxazone using the carbon paste electrode and thus in continuation of our previous work,[40–43] in this work, the electrochemical behavior of chlorzoxazone at carbon paste electrode was investigated, and a differential pulse anodic voltammetric method was developed for the determination of this drug.

2. Experimental

2. 1. Reagents and Materials

All chemicals were of analytical grade. Double distilled water was used throughout all experiments. Pure grade chlorzoxazone and the pharmaceutical preparation Myoflex tablets (250 mg chlorzoxazone and 450 mg paracetamol per tablet) were kindly supplied by the Nile Co., for Pharmaceuticals and Chemical Industries, Cairo, Egypt. Graphite powder (1–2 mm) was from Aldrich, and paraffin oil from B.D.H. As a supporting electrolyte, a series of 0.04 mol/L Britton-Robinson (BR) buffer pH 2.0–11.5 (a mixture of acetic, orthophosphoric, and boric acids), adjusted to the required pH with 0.2 mol/L sodium hydroxide was prepared.

2. 2. Apparatus

All voltammetric measurements were performed using Metrohm 797 VA Computrace (Herisau, Switzerland) equipped with a Metrohm VA 694 stand. Three electrodes assembly cell (consisted of carbon paste electrode (CPE) as the working electrode, an Ag/AgCl in 3 mol/L KCl as a reference electrode, and platinum wire as an auxiliary electrode) was used. The pH measurements were carried out with Hanna pH 211 microprocessor pH-meter.

2. 3. Preparation of Carbon Paste Electrode

The carbon paste was prepared by thoroughly mixing 5 g of graphite powder with 1.8 mL of paraffin oil in a mortar with a pestle. The carbon paste was packed into the hole of the electrode body and smoothed on a clean paper until it had a shiny appearance. The electrode body was constructed by pressing a small rode of stainless steel (diameter 2 mm) inside a micropipette tip (1 mL volume capacity) leaving a depression at the surface tip approximately 1 mm for housing the carbon paste, and thin wire was inserted through the opposite end to establish electrical contact.[44] The carbon paste electrode was immersed in the supporting electrolyte placed in the cell and several sweeps were applied to obtain a low background current.

The area of the prepared carbon paste electrode was calculated by plotting the relation between the anodic current and square root of the scan rate for 10^{-3} M solution of potassium ferricyanide as a probe using cyclic voltammetry. For a reversible process, The Randles-Sevcik equation was used[45]

$$I_{pa} = \left(2.69 \times 10^{5}\right) n^{\frac{3}{2}} A D_o^{\frac{1}{2}} C_o \nu^{\frac{1}{2}} \quad (1)$$

Where I_{pa} is the anodic current, n is the number of transferred electrons, A is the surface area of the electrode, D_o is the diffusion coefficient, ν is scan rate, and C_o is the concentration of potassium ferricyanide.

For 10^{-3} mol/L solution of potassium ferricyanide in 0.1 mol/L KCl electrolyte, n = 1 and $D_o = 7.6 \times 10^{-6}$ cm^2/s, then from the slope of the relation between anodic current and the square root of scan rate, the surface area of the electrode was calculated and found to be 0.036 cm^2.

2. 4. Procedure

A 10 mL of 0.04 mol/L Britton-Robinson buffer pH 6.5 was introduced into the voltammetric cell and a known amount of the drug solution was pipetted into the cell and differential pulse technique was applied by scanning from 0 to 1.4 V with a scan rate 50 mV/s and pulse amplitude 50 mV.

2. 5. Determination of Chlorzoxazone in Myoflex Tablets (250 mg Chlorzoxazone and 450 mg Paracetamol per Tablet)

Ten tablets were accurately weighed and finely powdered. An adequate amount of the powder corresponding to prepare 1×10^{-3} mol/L chlorzoxazone was weighed and transferred to a beaker. The tablets powder was dissolved in methanol and filtered to 100 mL calibrated flask using a Whatman 41 filter paper. The residue was washed several times with methanol and the washings were collected in the measuring flask and completed to the mark. Then the analysis was done as described in the general procedure.

2. 6. Determination of Chlorzoxazone in Spiked Human Urine Samples

0.0170 g of chlorzoxazone was dissolved in methanol and introduced into 100 mL volumetric flask, 5 mL of urine from a healthy person was added, and the mixture was completed to the mark by methanol to prepare 10^{-3} mol/L chlorzoxazone in the spiked human urine sample. 10 mL of 0.04 mol/L BR buffer pH 6.5 was introduced into the voltammetric cell, different amounts of the above spiked human urine sample were added and the procedure was repeated as described before. The amount of chlorzoxazone was determined using the standard addition method.

3. Results and Discussion

3. 1. Cyclic Voltammetric Studies

The repetitive cyclic voltammograms for 3.85×10^{-5} mol/L solution of chlorzoxazone in 0.04 mol/L BR buffer pH 6.5 and the scan rate of 50 mV/s using carbon paste electrode were illustrated (Figure 1). A well defined anodic peak at 1.01 V was observed which may be due to the oxidation of the hydroxyl group in the chlorzoxazone molecule. No peak was observed in the reverse cathodic scan, indicating that the process is irreversible. A decrease in the oxidation peak current during the successive cyclic vol-

tammograms was observed. This decrease in current may be attributed to the fouling of the electrode surface due to the adsorption of the oxidation products on the surface of the electrode. The effect of the scan rate on the peak current and peak potential was tested from 10 to 100 mV/s (Figure 2). The relation between oxidation current and scan rate and oxidation current and the square root of the scan rate was studied. Linear relationship was found between oxidation current and the square root of the scan rate, which could be represented by the equation, $I_p = 8.22\, v^{\frac{1}{2}} + 33.35$, $r^2 = 0.9949$. which indicates that the oxidation process is controlled by diffusion.[46,47] This is confirmed by plotting the logarithm of the peak of oxidation current vs. the logarithm of the scan rate, which gave a straight line relation with a slope of 0.38, which is close to the theoretically expected 0.5 value for a diffusion-controlled process. The relation is represented by the equation $I_p = 0.38 \log v + 1.31$, $r^2 = 0.9921$. Also the peak potential shifts to more positive values on increasing the scan rate confirm the irreversibility of the oxidation process.

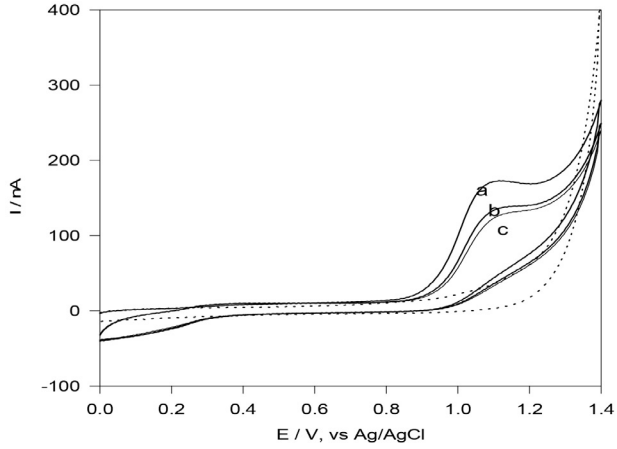


Figure 1. Successive cyclic voltammograms for 3.85×10^{-5} mol/L solution of chlorzoxazone in 0.04 mol/L Britton-Robinson buffer pH 6.5 and scan rate of 50 mV/s on carbon paste electrode. Voltammograms: a, first cycle; b, second cycle; c, third cycle, and the dotted voltammogram represents the blank.

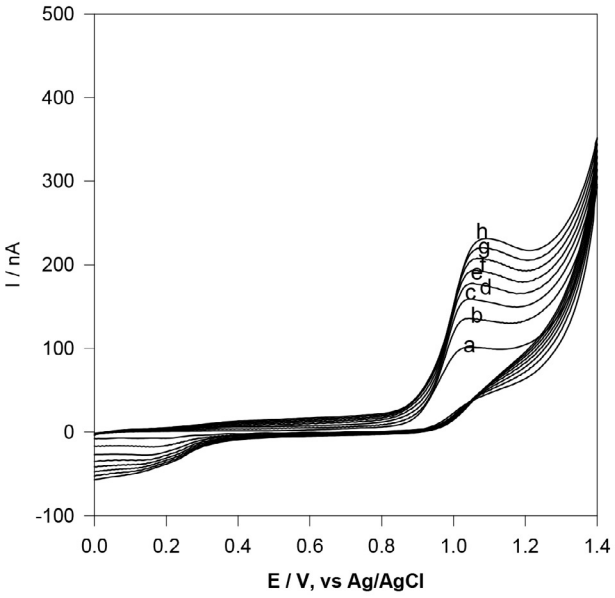


Figure 2. Cyclic voltammograms for 3.85×10^{-5} mol/L solution of chlorzoxazone in 0.04 mol/L Britton-Robinson buffer pH 6.5, on carbon paste electrode with different scan rates; a, 10; b, 20; c, 30; d, 40; e, 50; f, 60; g, 70; and h, 80 mV/s.

In addition, the oxidation peak potential and logarithm of the scan rate showed a straight line relation with slope equal to 0.0647 as represented by the following equation:

$$E_p = 0.9033 + 0.0647 \log\upsilon \quad (r = 0.9947) \qquad (2)$$

For an irreversible process according to Laviron[48]

$$E_p = E^0 + \left(\frac{2.303RT}{\alpha nF}\right)\log\left(\frac{RT^0k^0}{\alpha nF}\right) + \left(\frac{2.303RT}{\alpha nF}\right)\log\nu \qquad (3)$$

Where α is the transfer coefficient, k^0 is the standard heterogeneous rate constant of the reaction, n is the number of transferred electrons, ν is the scan rate and E^0 is the formal redox potential. So the value αn can be calculated from the slope of the straight line relation between E_p and log ν by substituting the values of R, T, and F. The calculated value of αn was found to be 0.914.

The transfer coefficient α for an irreversible process can be calculated from the relation[38]

$$\alpha = \frac{47.7}{E_p - E_{P/2}} \qquad (4)$$

Where $E_{P/2}$ is the potential at which the current equals half of the peak current. The value of α was found to be 0.723 and the calculated value of n = 1.26.

3. 2. Differential Pulse Voltammetric Studies

The electrochemical behavior of chlorzoxazone (3.98×10^{-6} mol/L) in different media such as 0.1 mol/L phosphate, 0.1 mol/L BR, and 0.1 mol/L citrate buffers was tested by differential pulse voltammetry. The oxidation peak is higher in the case of BR buffer than in the case of phosphate buffer, but in the case of citrate buffer, the oxidation peak disappeared (Figure 3A). And hence, BR was selected as the best medium. The effect of pH on the anodic peak current and oxidation potential was tested in the pH range 2.0–11.0 (Figure 3B). The oxidation peak current increased with an increase in the pH until it attained its maximum at pH 6.50. The study of the effect of the supporting electrolyte (BR buffer) concentrations (0.02, 0.04, and 0.1 mol/L) indicated that the highest peak current was obtained at 0.04 and 0.1 mol/L BR buffer (Figure 3A). So 0.04 mol/L BR buffer pH 6.50 was selected as the medium for the de-

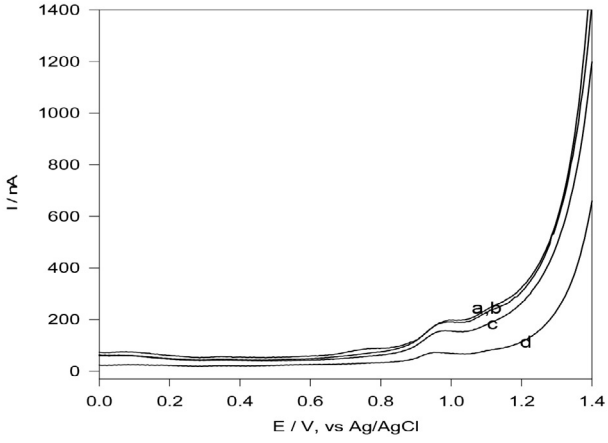


Figure 3A. Differential pulse voltammograms for 3.98×10^{-6} mol/L chlorzoxazone in different media: a, 0.04 mol/L; b, 0.1 mol/L, c, 0.02 mol/L BR buffer pH 6.5, and d, 0.1 mol/L phosphate buffer pH 6.5.

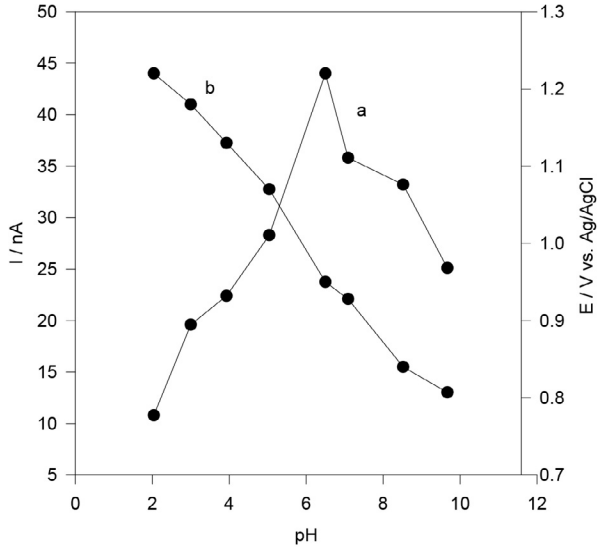


Figure 3B. Effect of pH on the differential pulse anodic peak current (a), and peak potential (b) of 3.98×10^{-6} mol/L chlorzoxazone in 0.04 mol/L BR buffer, pulse amplitude 50 mV, and scan rate 50 mV/s.

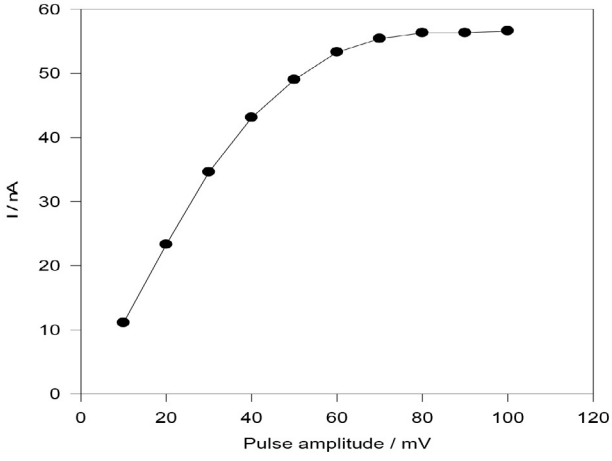


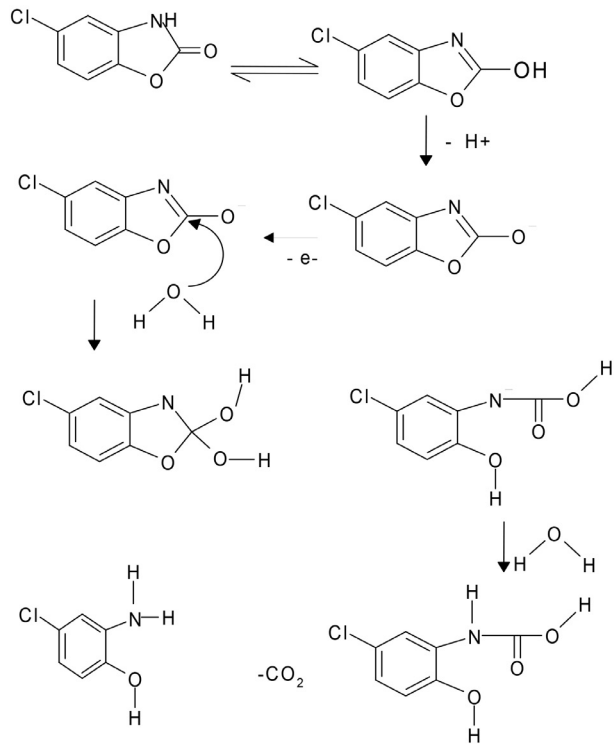
Figure 4. Effect of pulse amplitude on the oxidation current for 3.98×10^{-6} mol/L chlorzoxazone in 0.04 mol/L BR buffer pH 6.5 and scan rate of 50 mV/s.

termination of chlorzoxazone. The oxidation potential shifted negatively with increasing the pH, suggesting that the protons are involved in the electrode reaction process.

The effect of oxidation current of 3.98×10^{-6} mol/L chlorzoxazone with the change in pulse amplitude was tested in the range 10–100 mV pulse amplitude (Figure 4). The oxidation current increases from 10 to 50 mV, then remains nearly constant, so 50 mV pulse amplitude was used for this work.

Proposed Mechanism

The proposed mechanism for the oxidation of chlorzoxazone (Scheme 2) is one electron, one proton process as reported by Abbar and Nandibewoor[38,39]



Scheme 2. Mechanism of electrooxidation of chlorzoxazone at carbon paste electrode

3. 3. Analytical Performance of the Proposed Method

On the basis of electrochemical oxidation of chlorzoxazone at the carbon paste electrode under the optimum conditions, differential pulse anodic voltammetric method was proposed for the determination of the drug over the working linear range 0.17–1.68 μg/mL. Figure 5 represents the differential pulse anodic voltammograms recorded using the standard addition method. The linear regression parameters are listed in Table 1. The limit of detection (LOD = $3(SD_a)/b$) and limit of quantitation (LOQ = $10(SD_a)/b$) were calculated,[49] where SD_a is the standard deviation of the intercept and b is the slope of the calibra-

Table 1. The analytical parameters for the proposed differential pulse anodic voltammetric method for the determination of chlorzoxazone using carbon paste electrode.

Parameter	
Regression equation	I (nA) = 59.72 × *C*(μg/mL) + 6.41
Linear range, μg/mL	0.17–1.68
Slope	59.72
Intercept	6.41
Correlation coefficient (r)	0.9991
LOD, μg/mL	0.05
LOQ, μg/mL	0.16
Recovery, %	97.18–99.77
Intra day precision, SD, nA	0.29
Inter day precision, SD, nA	0.73

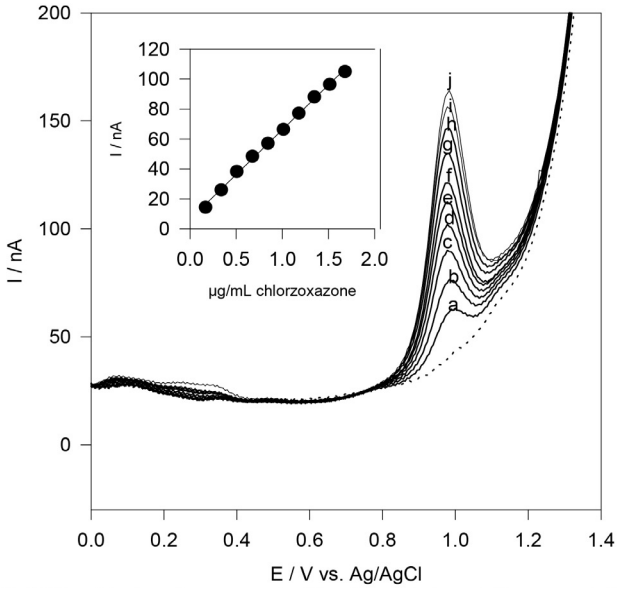


Figure 5. Differential pulse voltammograms for different concentrations of chlorzoxazone in 0.04 mol/L Britton–Robinson buffer pH 6.5, scan rate of 50 mV s^{-1} and pulse amplitude 50 mV: a, 0.169; b, 0.339; c, 0.507; d, 0.676; e, 0.844; f, 1.012; g, 1.179; h, 1.346; i, 1.513 and j, 1.679 μg/ml chlorzoxazone. The dotted line represents the blank solution. Insert: the corresponding calibration plot

tion graph. The linear range and limit of detection of the proposed method were also compared with the previously reported methods (Table 2). It is observed that the detection limit was better than in the reported HPLC method,[3] and the lower linear range was lower than in the published HPLC methods,[3,4,7,10] spectrophotometric methods,[24,32,33] capillary zone electrophoresis,[37] and the voltammetric method using the gold electrode.[39]

Validation of the proposed procedure

The validation of the proposed method was tested via linear range, the limit of detection (LOD), the limit of quantitation (LOQ), repeatability, precision, accuracy, selectivity, and robustness. The linear dependence of the oxidation current versus drug concentration was represented by the following straight line relation

$$I(\text{nA}) = 59.72 \times C(\mu\text{g/mL}) + 6.41,\ (r = 0.9991,\ n = 10),\ \text{in the linear range } 0.17\text{–}1.68\ \mu\text{g/mL}. \quad (5)$$

The sensitivity of the proposed method was tested in terms of limit of detection (LOD) and limit of quantitation (LOQ) values. The values of LOD and LOQ were found to be 0.05 and 0.16 μg/mL, and these values indicate that the proposed method could be considered sensitive.

The repeatability of the proposed method was tested on the same day (intra-day) and in three different days (day-to-day) precision from seven repeated measurements of 0.17 μg/mL chlorzoxazone. The intra-day and inter-day precision expressed as standard deviations were found to be 0.29 and 0.73, respectively. The accuracy of the proposed method was determined by calculating the recoveries of 9.99×10^{-7} and 2×10^{-6} mol/L chlorzoxazone using the standard addition method. The estimated mean recoveries based on four replicate measurements were 97.18% ± 2.03% and 99.77% ± 2.28%, respectively, which indicates the high accuracy of the proposed procedure.

The selectivity of the method under the optimum conditions for the assay of 9.99×10^{-7} mol/L of the drug

Table 2. Comparison of linear range and limit of detection for the determination of chlorzoxazone with previously published methods

Method	Linear range, μg/mL	Detection limit, μg/mL	References
HPLC	125–375	0.5	3
	0.5–100		4
	5–50	0.02	7
	2.5–250		10
Spectrophotometry	6–20		24
	5–25		32
	25–125		33
Capillary zone electrophoresis	100–600		37
Voltammetry/ GC electrode	0.14–1.70	0.01	38
Voltammetry/Gold electrode	0.85–16.96	0.01	39
Voltammetry/CP electrode	0.17–1.68	0.05	Present work

was examined in presence of common excipients usually present in pharmaceutical formulations. No interference (<3.0% change in oxidation current) was observed in the presence of 100-fold excess of lactose, talc, starch, magnesium stearate, or titanium dioxide, and inorganic cations e.g. Na^+, K^+, Mg^{2+}, Zn^{2+}. Cu^{2+}, and Mn^{2+}. Species such as ascorbic acid, dopamine hydrochloride, and uric acid which can coexist with chlorzoxazone in urine samples, were also tested.

No interference was found in the presence of 2.5-fold excess of dopamine hydrochloride, 7-fold of uric acid, and 9-fold of ascorbic acid. The robustness[49] of the proposed method was examined by evaluating the effect of small changes in some of the most important procedure parameters, including the pH of the Britton–Robinson (BR) buffer (6.3–6.7) and the pulse amplitude (47–53 mV). None of the changes significantly affected the drug recovery (Table 3); consequently, the optimized procedure was reliable for the assay of chlorzoxazone and it could be considered robust.

Table 3. Robustness results of the proposed method.

Variable		Recovery, %	SD, %
pH	6.3	97.84	0.60
	6.5	97.18	2.03
	6.7	95.68	2.49
Pluse amplitude			
	47	96.83	0.80
	50	97.18	2.03
	53	99.94	2.15

(Average of four determinations)

3. 4. Determination of Chlorzoxazone in Myoflex Tablets

The proposed differential pulse anodic voltammetric method was successfully applied for the assay of chlorzoxazone in Myoflex tablets (250 mg chlorzoxazone + 450 mg paracetamol per tablet). The percentage mean recovery for four replicate determinations and the relative standard deviation values are listed in Table 4. The anodic differential pulse voltammograms recorded using the standard addition technique for determination of chlorzoxazone in its tablets are depicted in Figure 6 (in the Supplementary Material). The data indicate that there is no interference from the other drug paracetamol present in the tablet or from the excipients which are used in tablets formulation, and the results were in good agreement with the values obtained using the HPLC reference method.[8] Statistical comparison of the accuracy and precision of the proposed method with the reference method (Table 4) was performed using Student's *t*- and the F-ratio tests at a 95% confidence level.[50] The *t*- and F-values did not exceed the theoretical values; there is no significant difference in accuracy or precision between the proposed and the reference HPLC method.

Table 4. Statistical comparison between the results of Myoflex tablets using the proposed DP voltammetric method and the reference method.

Parameters	Proposed DP voltammetric method	Reference method[8]
Mean recovery, %	98.59	97.44
SD	1.30	0.55
RSD, %	1.32	0.56
F-ratio (9.28)	5.59	
t-test (2.45)	1.95	

(Average of four determinations for the proposed and reference methods)

3. 5. Determination of Chlorzoxazone in Spiked Human Urine Samples

Chlorzoxazone was also successfully determined in spiked human urine samples at four levels of concentrations 9.99×10^{-7}, 2.00×10^{-6}, 2.49×10^{-6}, and 3.49×10^{-6} mol/L (0.17, 0.34, 0.42, and 0.59 μg/mL) chlorzoxazone by using the proposed method. The limits of detection (LOD) and quantitation (LOQ) of chlorzoxazone spiked in human urine calculated by using the proposed method were found to be 3.40×10^{-7} and 1.13×10^{-6} mol/L (0.06 and 0.19 μg/mL), respectively. The precision of the analysis was calculated from eight replicate measurements. The mean recovery for the four concentration levels was 99.30, 98.50, 95.73, and 103.60% with the relative standard deviation of 0.72, 0.75, 3.68, and 0.75, respectively (Table 5). Representative voltammograms are shown in Figure 7 (in the Supplementary Material).

Table 5. Determination of chlorzoxazone in spiked urine samples using the proposed method.

Taken (mol/L)	Found (mol/L)	Recovery, %	RSD, %
9.99×10^{-7}	9.92×10^{-7}	99.30	0.72
2.00×10^{-6}	1.97×10^{-6}	98.50	0.75
2.49×10^{-6}	2.38×10^{-6}	95.73	3.68
3.49×10^{-6}	3.61×10^{-6}	103.60	0.75

(Average of eight determinations)

4. Conclusions

The present work describes an effective procedure for the determination of chlorzoxazone. The proposed method has advantages, such as being simple, sensitive, rapid, inexpensive, low detection limit, and ease of preparation and renewable for carbon paste electrode. The developed procedure can be considered as an alternative for HPLC techniques in quality control laboratories.

5. References

1. S. C. Sweetman, "*Martindale", The complete Drug Reference*, 36th ed., Pharmaceutical Press, London, (2009).

2. J. T. Stewart, Analytical Profiles of Drug Substance, Vol. 16 (1987).
3. S. S. Zarapkar, N. P. Bhandari, U. P. Halkar, *Indian Drugs*, **2000**, *37*, 469–473.
4. K. Rajnarayana, S. R. Mada, J. Vidyasagar, P. Kishore, D. R. Krishna, *Die Pharmazie*, **2002**, *57*, 811.
5. E. Dinc, A. Ozdemir, H. Aksoy, D. Baleanu, *J. Liq. Chromatog. & Related Technol.* **2006**, *29*, 1803–1822. **DOI:**10.1080/10826070600717023
6. M. S. Ali, S. Rafiuddin, M. Ghori, A. R.Kahtri, *J. AOAC International*, **2007**, *90*, 82–93. **DOI:**10.1093/jaoac/90.1.82
7. R. Joshi, R. Sharma, *Anal. Lett.* **2008**, *41*, 3297–3308. **DOI:**10.1080/00032710802515086
8. K. A. Shaikh, A. B. Devkhile, *J. Chromatog. Sci*., **2008**, *46*, 649–652. **DOI:**10.1093/chromsci/46.7.649
9. M. Peng, Y. J. Yang, D. M. Song, *Yaowu Fenxi Zazhi*, **2010**, *30*, 737.
10. E. F. Elkady, M. A. Fouad, *J. Liq. Chromatog. & Related Technol.* **2012**, *35*, 882. **DOI:**10.1080/10826076.2011.613142
11. M. E. El-Kommos, N. A. Mohamed, A. F. A. Hakiem, *J. Liq. Chromatog. & Related Technol.* **2012**, *35*, 2188. **DOI:**10.1080/10826076.2011.629390
12. J. K. Mbinze, P. Lebrun, B. Debrus, A. Dispas, N. Kalenda, J. M. T. Mbay, T. Schofield, B. Boulanger, E. Rozet, P. Hubert, R. D. Marini, *J. Chromatog. A*., **2012**, *1263*, 113. **DOI:**10.1016/j.chroma.2012.09.038
13. C. Aybaba, I. M. Palabiyik, M. G. Caglayan, F. Onur, *J. AOAC International,* **2013**, *96,* 723. **DOI:**10.5740/jaoacint.11-092
14. R. A. Sodhi, J. L. Chawla, R. T. Sane, *Indian Drugs*, **1996**, *33*, 280.
15. L. I. Bebawy, N. M. El-Kousy, *J. Pharm. Biomed. Anal*., **1999**, *20*, 663–670. **DOI:**10.1016/S0731-7085(99)00039-4
16. R. T. Sane, M. Gadgil, *J. Planar Chromatography, Modern TLC*, **2002**, *15*, 76. **DOI:**10.1556/JPC.15.2002.1.16
17. E. A. Abdelaleem, N. S. Abdelwahab, *J. Chromatog. Sci*., **2013**, *51*, 187–191. **DOI:**10.1093/chromsci/bms125
18. D. Mohamed, M. A. Hegazy, M. S. Elshahed, S. S. Toubar, M. I. Helmy, *Biomed. Chromatogr*., **2018**, *32*, 4232. **DOI:**10.1002/bmc.4232
19. V.R. Bari, U. J. Dhorda, M. Sundaresan, *Talanta*, **1997**, *45*, 297–302. **DOI:**10.1016/S0039-9140(97)00153-7
20. P. P. Desai, N. R. Patel, O.D. Sherikar, P. J. Mehta, *J. Chromatogr. Sci*., **2012**, *50*, 769–774.
21. A. B. Avadhanulu, A. R. R. Pantulu, Y. Anjaneyulu, *Indian Drugs*, **1994**, *31*, 201.
22. J. L. Chawla, R. A. Sodhi, R. T. Sane, *Indian Drugs*, **1996**, *33*, 171.
23. C. B. Eap, C. Schnyder, L. Savary, *J. Chromatog. B: Biomed. Appl.* **1998**, *705*, 139–144. **DOI:**10.1016/S0378-4347(97)00501-X
24. P. K. Chatterjee, C. L. Jain, P. D. Sethi, *J. Pharm. Biomed. Anal*., **1989**, *7*, 693–698. **DOI:**10.1016/0731-7085(89)80113-X
25. C. Yucesoy, *FABAD Farm. Bilimler Derg*., **1990**, *15*, 175.
26. C. Yucesoy, *Turk Eczacilari Birligi Dergisi Pharmacia*, **1990**, *30*, 13.
27. M. K. S. El-Din, M. A. Abuirjeie, M. H. Abdel-Hay, *Anal. Lett*., **1991**, *24*, 2187. **DOI:**10.1080/00032719108053044
28. M. S. Bhatia, S. R. Dhaneshwar, *Indian Drugs*, **1995**, *32*, 446.
29. M. S. Bhatia, S. G. Kaskhedikar, S. C. Chaturvedi, *Indian Drugs*, **1997**, *34*, 149.
30. S. R. Sankar, M. Vasudevan, B. Duraiswamy, B. Suresh, B. Abraham, *Indian Drugs*, **1997**, *34*, 450.
31. L. Y. Ding, C. Q. Yang, W. H. Zhan, H. Y. Wu, K. M. Zheng, *Spectroscopy and Spectral Analysis*, **2000**, *20*, 423.
32. C. S. P. Sastry, R. Chintalapati, B. S. Sastry, C. S. R. Lakshmi, *Anal. Letters*, **2000**, *33*, 2501. **DOI:**10.1080/00032710008543205
33. D. Mrinalini, A. Madgulkar, D. Juvale, B. Awate, A. Zambre, *Indian Drugs*, **2001**, *38*, 576.
34. X. R. Huang, Y. M. Cai, Y. Tai, D. Cao, *Spectroscopy and Spectral Analysis*, **2005**, *25*, 620.
35. R. Chen, *Yaowu Fenxi Zazhi*, **2010**, *30*, 1770.
36. J. T. Stewart, C. W. Chan, *J. Pharm. Sci*., **1979**, *68*, 910. **DOI:**10.1002/jps.2600680735
37. H. F. Chen, P. Lu, *Yaowu fenxi Zazhi*, **2003**, *23*, 26
38. J. C. Abbar, S. T. Nandibewoor, *Ind. Eng. Chem. Res*., **2012**, *51*, 111. **DOI:**10.1021/ie2021812
39. J. C. Abbar, S. T. Nandibewoor, *Crit. Rev. Anal Chem*., **2012**, *42*, 272. **DOI:**10.1080/10408347.2012.680336
40. S. I. M. Zayed, *Anal. Sci*., **2011**, *27*, 535–539. **DOI:**10.1051/medsci/2011275020
41. S. I. M. Zayed, R. A. H. Oraby, A. E. A. El-Thobety, M. M. Abdel-Moaty, *Port. Electrochimica Acta*, 2017, *35*, 305–312. **DOI:**10.4152/pea.201705305
42. S. I. M. Zayed, A. A. H. Al-Talhi, A. E. Al-Thagafi, *J. Chil. Chem. Soc*., **2018**, *63*, 4064–4067. **DOI:**10.4067/s0717-97072018000304064
43. S. I. M. Zayed, H. A. M. Arida, *Int. J. Electrochem. Sci*., **2015**, *10*, 3250–3259.
44. A. Elyacoubi, S. I. M. Zayed, B. Blankert, J.-M. Kauffmann, *Electroanalysis*, **2006**, *18*, 345–350. **DOI:**10.1002/elan.200503418
45. V. P. Pattar, S. T. Nandibewoor, *Sensors and Actuators A*, **2016**, *250*, 40–47. **DOI:**10.1016/j.sna.2016.09.011
46. P. Monk, "*Fundamentals of Electroanalytical Chemistry*,"**2001**, Wiley, 162.
47. E. R. Sartori, R. A. Medeiros, R. C. Rocha-Filho, O. Fatibello-Filho, *Talanta*, **2010**, *81*, 1418–1424. **DOI:**10.1016/j.talanta.2010.02.046
48. J. I. Gowda, G. S. Hurakadli, S. T. Nandibewoor, *Anal. Chem. Lett.*, **2017**, *7*, 389–401. **DOI:**10.1080/22297928.2017.1354720
49. M. Swartz and I. S. Krull, "*Analytical Method Development and Validation*", **1997**, Marcel Dekker, Inc., 61.
50. J. C. Miller and J. N. Miller, "*Statistics for AnalyticalChemistry*", 3rd ed., **1993**, Ellis Horwood, Chichester, 53.

Povzetek

Raziskali smo elektrokemijsko obnašanje klorzoksazona na elektrodi iz ogljikove paste v 0,04 mol/L Britton-Robinsonovem pufru s pH 6,50 ob uporabi cikličnih in diferencialno-pulznih voltametrijskih tehnik. Študije s ciklično voltametrijo so pokazale, da je oksidacija učinkovine ireverzibilna in pretežno difuzijsko kontrolirana. Optimizirali smo eksperimentalne in instrumentalne parametre (hitrost preleta 50 mV/s, amplituda pulza 50 mV in 0,04 mol/L Britton-Robinsonov (BR) pufer pri pH 6,50 kot pomožni elektrolit) ter razvili občutljivo metodo na osnovi diferencialne pulzne anodne voltametrije za določanje učinkovine v koncentracijskem območju 0,17–1,68 μg/mL klorzoksazona, z mejo zaznave 0,05 μg/mL in mejo kvantifikacije 0,16 μg/mL. Predlagano voltametrijsko metodo smo uspešno uporabili za določitev učinkovine v njeni farmacevtski formulaciji (tablete Myoflex) in v vzorcih človeškega urina z dodatkom učinkovine.

Except when otherwise noted, articles in this journal are published under the terms and conditions of the Creative Commons Attribution 4.0 International License

Scientific paper

Synthesis and Biological Evaluation of Novel Pyrane Glycosides

Avula Srinivas,[1,*] Malladi Sunitha[2] and Sriramoju Shamili[1]

[1] *Department of Chemistry, Vaagdevi Degree & PG College Kishanpura, Warangal, Telangana, India 506001*

[2] *Jayamukhi Institute of Technological Sciences, Narsampet, Warangal, Telangana*

[*] *Corresponding author: E-mail: avula.sathwikreddy@gmail.com*

Received: 11-30-2019

Abstract

A series of novel (5*R*)-5-((2*S*,3*S*)-3-((1-(4-chlorophenyl)-1*H*-1,2,3-triazol-4-yl)methoxy)-3,6-dihydro-2*H*-pyran-2-yl)-3-(4-fluorophenyl)-2,6-diphenyl-3,3a,5,6-tetrahydro-2*H*-pyrazolo[3,4-*d*]thiazoles **11a–g** and (5*R*)-5-((2*S*,3*S*)-3-((1-(4-chlorophenyl)-1*H*-1,2,3-triazol-4-yl)methoxy)-3,6-dihydro-2*H*-pyran-2-yl)-3-(4-fluorophenyl)-6-phenyl-3,3a,5,6-tetrahydroisoxazolo[3,4-*d*]thiazoles **12a–g** were synthesized by the reaction of chalcone derivatives of (*R*,*Z*)-2-((2*S*,3*S*)-3-((1-(4-chlorophenyl)-1*H*-1,2,3-triazol-4-yl)methoxy)-3,6-dihydro-2*H*-pyran-2-yl)-5-(4-fluorobenzylidene)-3-phenylthiazolidin-4-ones **10a–g** with phenylhydrazine and hydroxylamine hydrochloride. The chemical structures of newly synthesized compounds were elucidated by IR, NMR, MS and elemental analysis. The compounds **11a–g** and **12a–g** were evaluated for their antibacterial activity and antifungal activity.

Keywords: Glycosides; click reaction; cyclisation; thiazolopyrazoles; thiazoloisoxazoles; antimicrobial activity

1. Introduction

Carbohydrates, are the most ample class of bio-molecules, a vital source of energy and structural components having an important role in biological processes. Carbohydrates, besides being the most abundant class of bio-molecules, a vital source of energy and structural components, have an important role in biological processes, organic synthesis and chemical industries.[1] They have been mostly used in chemical industries and their large scale applications include their use as feedstocks in different chemical industries, like pharmaceutical, food, cosmetic and detergent industries.[2] In the formation of glycoconjugates (glycolipids, glycoproteins and polysaccharides) and in many biological processes they play decisive role in cell physiology such as intercellular recognition, bacterial and viral infection, cancer metastasis, apoptosis and neuronal proliferation, etc.[3]

Their fascinating properties, such as hydrophilicity, lowered toxicity and emphasized bioactivities, in addition of carbohydrates affiliation to many systems make them often very effective.[4] Organic chemists have linked carbohydrates to various biologically potent compounds to enhance their biological applications, such as steroids, aminoacids and other therapeutic agents.[5] One of the chemical reactions which is involved in making such links is carbohydrate affiliation with a potential compound through a triazole ring.[6] To obtain cyclised products with biological potential a process according to an efficient method is used, being an alkyne-azide cyclization reaction and the introduction of a triazole ring.[7] The strategy of linking a carbohydrate moiety with another species *via* a triazole ring is gaining importance in organic synthesis, natural products chemistry and biochemistry.[8] The combination of biocompatibility and presence of stereogenic centres stemming from the carbohydrate, together with the polar nature and possible hydrogen bonding ability of a triazole ring, makes gluco-based triazoles very fancinating for organic synthetic chemists.

The derivatives of thiazolidinone are known to possess significant pharmacological[9] and biological activities,[10] like sedative,[11] anti inflammatory,[12] anti tubercular,[13] anticancer,[14] anti tumor,[15] anti-HIV,[16] anti bacterial,[17] anti fungal,[18] analgesic, hypotermic,[19] anesthetic,[20] nematicidal,[21] and CNS stimulant.[22] Furthermore, thiazolidinones have been used for the treatment of cardiac diseases,[23] diabetic complications, like contract nephropathy, neuropathy,[24] and as a selective anti platelet activating fac-

tor.[25] Moreover, isoxazole derivatives are an important class of bio active molecules, which exhibit significant activities, such as anti fungal.[26] The cardinal derivatives include such having antidepressant activity, hampering proteinekinase,[27] possessing antiviral,[28] antihelmintic,[29] anti inflammatory,[30] anticonvulsant,[31] insecticidal,[32] antitubercular,[33] immunomodulatory,[34] and hypolipermic activities. Additionally, derivatives of pyrazole are considered as feasible antimicrobial agents.[35]

We have developed a series of novel triazole-linked pyrene glycosides; additionally we screened them for their antimicrobial activity, connected with the affluent introduction of pyrazoles, thiazolidinones, and triazoles as shown by parts of our previous work on biologically active heterocyclics.[36–43] We have also developed a series of novel triazole-linked pyrene glycosides and evaluated their antimicrobial activity.

2. Results and Discussion

For the synthesis, the title compound was prepared according to the procedure outlined in the Scheme 1, where the key intermediate **8** is required. From 3,4,6-tri-*O*-acetyl-D-glucal (**1**) by treating with triethylsilane and boron trifluoride diethyl etherate, diacetyl-D-glucal (**2**) was prepared, giving with NaOMe in methanol at 0 °C after 1 h compound **3** (77%), which has on subsequent treatment with TBDMSCl in dichloromethane in the presence of NEt_3 after 12 h afforded TBS ether **4** (80%), which on treatment with propargyl bromide in toluene in the presence of tetrabutylammonium hydrogensulphate produced diether **5**. After deprotection of TBS ether **5**, the propargyl ether **6** was converted into triazole **7** (82%) by using 1,3-dipolar cycloaddition with *para*-chlorophenyl azide carried out at ambient temperature in the presence of $CuSO_4$ and sodium ascorbate in a mixture of 1:1 CH_2Cl_2–H_2O. The synthesis of triazole-linked thiazolidinone glycosides was carried out by the condensation reaction of **8**, obtained by the oxidation of **7** with IBX in acetonitrile. Compound **8** was in the next step reacted with R-substituted primary aromatic amine and thioglycolic acid in the presence of $ZnCl_2$ under microwave irradiation (Scheme 1) furnishing set of compound **9a**–**g**. These compounds were isolated by conventional work-up, when the reaction was completed in only 5–10 minutes, the **9a**–**g** were obtained in satisfactory yields. Then the compounds **9a**–**g** were reacted with *para*-fluorobenzaldehyde in the presence of anhydrous NaOAc in glacial AcOH at reflux temperature gaving chalcone derivatives of triazole-linked thiazolidinone glycosides **10a**–**g**. Further, these compounds upon cyclocondensation with arylhydrazines in the presence of anhydrous NaOAc in glacial AcOH at reflux temperature gave **11a**–**g** in good yields. Compound **10a**–**g** on cyclocondensation with hydroxylamine hydrochloride in the presence of anhydrous NaOAc in glacial AcOH at reflux temperature gave compounds **12a**–**g**. By IR, NMR, and MS the structures of the synthesized compounds were confirmed and then evaluated for their antimicrobial activity.

3. Antimicrobial Activity

By the filter paper disc method, the antimicrobial activity of the synthesized compounds**11a**–**g** and **12a**–**g** has been evaluated[44] against *Staphylococcus aureus* ATCC6538P, *Bacillus subtilis* ATCC6633, *Pseudomonas aeruginosa* ATCC9027, and *Echerichia coli* ATCC8739. Antifun-

Table 1. Antimicrobial and antifungal activity of 11a–g and 12a–g

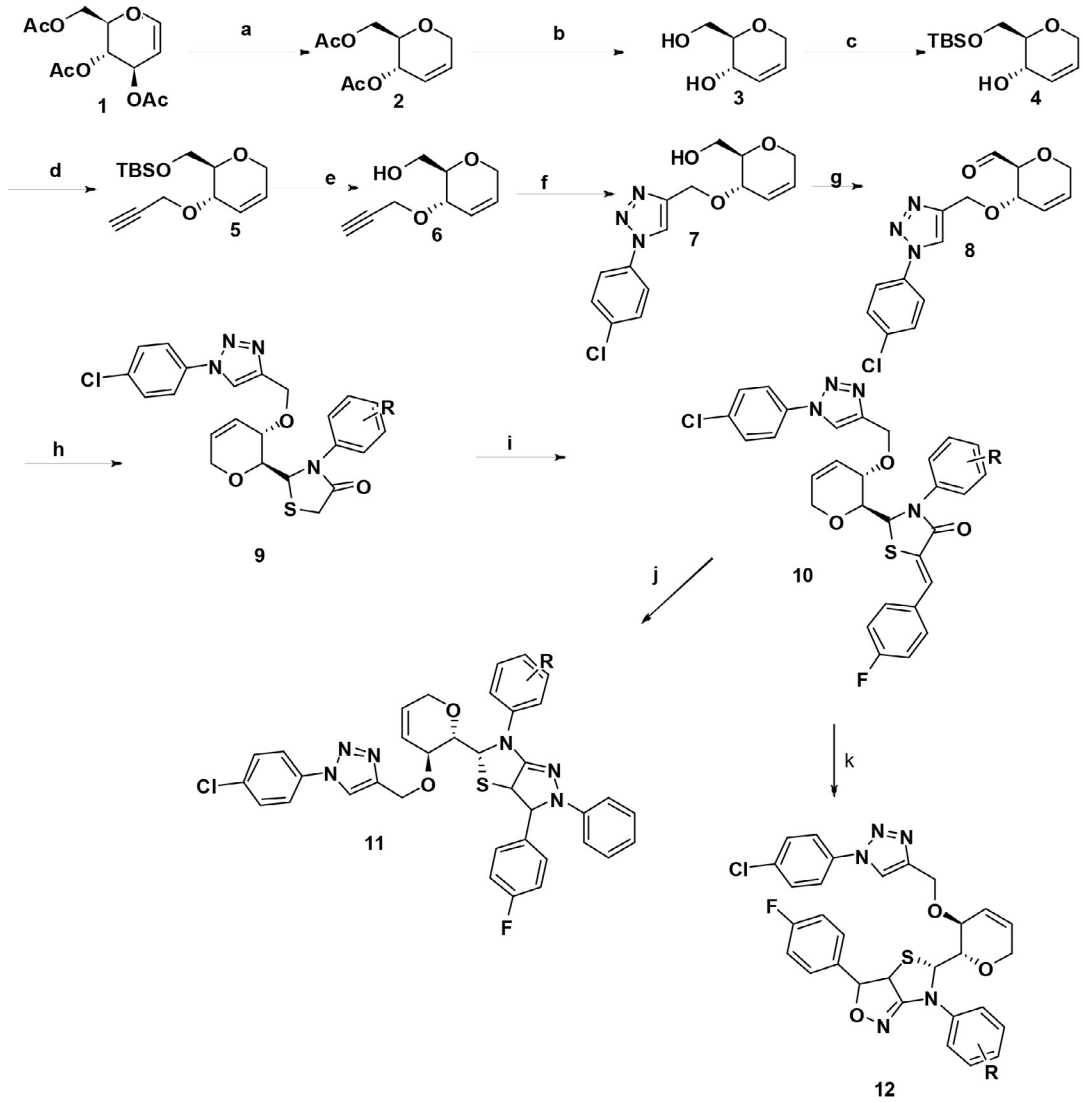
Compounds	Gram positive		Gram Negative		Fungi	
	Staphylococcus aureus	*Bacillus subtilis*	*Pseudomonas aeruginosa*	*Echerichia coli*	*Candida albicans*	*Aspergillus niger*
11a	17	16	18	20	15	13
11b	24	22	20	19	14	12
11c	15	16	15	14	15	14
11d	20	23	10	7	14	15
11e	15	16	11	9	21	15
11f	16	17	19	17	9	7
11g	22	24	15	14	22	16
12a	16	18	19	18	17	14
12b	20	23	19	18	15	13
12c	10	8	15	16	14	13
12d	20	22	6	10	14	12
12e	16	15	12	10	20	17
12f	17	16	19	18	7	8
12g	20	21	16	15	21	16
Ampicilin	22	26	20	19	_	_
Micostatin	_	_	_	_	22	16

gal activity of the synthesized compounds has been tested against *Candida albicans* ATCC2091, and *Aspergillus niger*, at a concentration of 500 μg/mL in DMF.

To culture the bacteria and fungi, nutrient agar and potato dextrose agars were used, respectively. The plates were cultured by the bacteria or fungi and incubated for 24 h at 37 °C for bacteria and for 72 h at 27 °C for fungi and then the inhibition zones of microbial growth surrounding the filter paper disc (5 mm) were measured in millimeters. Ampicillin and mycostatin, at a concentration 500 μg/mL, were used as standard against bacteria and fungi, respectively. All test results are shown in Table 1. From the data it is clear that compounds **11b**, **12b**, **11d**, **12d**, **11g**, and **12g** possess high activity, while compounds **11a**, **12a**, **11c**, **11e**, **12e**, **11f**, and **12f** possess moderate activity against Gram positive bacteria. The compounds **11a**, **12a**, **11b**, **12b**, **11f**, and **12f** showed high activity as Gram negative microorganisms are concerned, while compounds **11c**, **12c**, **11g** and **12g** display moderate activity. Compounds **11e**, **12e**, **11g**, and **12g** also exerted high activity, while compounds **11a**, **12a**, **11c**, **12c**, **11d**, **12d**, **11b**, and **12b** have moderate activity against fungi.

4. Experimental

All the used reagents were supplied as commercially available. According to the literature, when necessary, the solvents used (except analytical reagent and grade) were dried and purified. By thin-layer chromatography (TLC)



R = H, 4-Cl, 4-NO_2, 2-CH_3, 4-CH_3, 3-OH, 4-OH

Reagents and conditions: (a) BF_3, Et_2O, Et_3SiH, CH_2Cl_2; (b) MeOH, NaOMe; (c) TBDMSCl, Et_3N, CH_2Cl_2 ; (d) propargyl bromide, NaH, *n*-Bu_4N-HSO_4, 35% NaOH, toluene; (e) TBAF, THF; (f) 4-Cl-C_6H_4-N_3, $CuSO_4$, sodium ascorbate, CH_2Cl_2, H_2O (1:1); (g) IBX, CH_3CN; (h) R-C_6H_4-NH_2, AcOH, $SHCH_2COOH$, $ZnCl_2$, C_6H_6; (i) 4-F-C_6H_4-CHO, NaOAc, AcOH; (j) $PhNHNH_2$, NaOAc, AcOH; (k) NH_2OH, NaOAc, AcOH.

on pre-coated silica gel F254 plates from Merck the reaction progress and purity of the compounds was checked. They were is visualized either by exposure to UV light or dipping in 1% aqueous potassium permanganate solution. Silica gel chromatographic columns (60–120 mesh) were used for separations. Optical rotations were measured on an Perkin–Elmer 141 polarimeter by using a 2 mL cell with a path length of 1 dm with $CHCl_3$ or $CDCl_3$ as the solvent. By using Fisher–Johns apparatus all the melting points were measured and are corrected. IR spectra were recorded as KBr disks on a Perkin–Elmer FT IR spectrometer. Microwave reactions were carried out in mini lab microwave catalytic reactor (ZZKD, WBFY-201). On Varian Gemini spectrometer (300 MHz for ^{1}H and 75 MHz for ^{13}C) the ^{1}H NMR and ^{13}C NMR spectra were recorded; chemical shifts are reported as δ in ppm against TMS as the internal reference, coupling constants (*J*) are reported in Hz units. On a VG micro mass 7070H spectrometer mass spectra were recorded. Elemental analysis (C, H, N) were determined by a Perkin–Elmer 240 CHN elemental analyzer and were within ± 0.4% of theoretical values.

((2*R*,3*S*)-3-Acetoxy-3,6-dihydro-2*H*-pyran-2-yl)methyl Acetate (2)

Tri-*O*-acetyl-D-glucal (**1**) (6.0 g, 22.04 mmol) was dissolved in anhydrous dichloromethane (10 mL). The solution was cooled to about 0 °C, and triethylsilane (3.06 g, 26.44 mmol) was added and the mixture was stirred for five minutes. Then boron trifluoride diethyl etherate (690 μL of a 40 w% solution in diethyl ether, 11.02 mmol) was added drop wise and the reaction mixture was stirred for 90 min. The mixture was poured into a saturated solution of $NaHCO_3$. Then the organic layer was washed with water and dried over Na_2SO_4 and concentrated under reduced pressure.

Column chromatography on silica gel (PE/EtOAc, 3:1) yielded the title compound **2** (4.48 g, 20.84 mmol, 95%) as a colorless syrup. $[\alpha]^D_{20}$: +115.5 (*c* = 1.00, $CHCl_3$). ^{1}H NMR (300 MHz, $CDCl_3$) *δ* 5.87–5.84 (m, 2H, =CH), 4.95 (t, 1H, OCH), 4.03–3.99 (m, 1H, CH), 4.12–4.09 (m, 4H, OCH_2), 2.20 (s, 6H, CO CH_3); ^{13}C NMR (75 MHz, $CDCl_3$) *d* 170.2, 127.2, 125.8, 73.6, 65.1, 64.0, 62.5, 21.1; MS *m/z* (M^++H) 215. Anal. calcd. for $C_{10}H_{14}O_5$: C, 56.07; H, 6.59. Found: C, 55.82; H, 6.35.

(2*R*,3*S*)-2-((*tert*-Butyldimethylsilyloxy)methyl)-3,6-dihydro-2*H*-pyran-3-ol (4)

At room temperature diacetate **2** (4.20 g, 19.53 mmol) was treated by a catalytic amount of sodium methoxide in 100 mL of methanol. The free hydroxyl unsaturated glycoside **3** was obtained in quantitative yield and used without further purification after evaporation of the solvent. This diol **3** was treated with 5 equiv of TBDMSCl (6.28 g, 42.28 mmol), 4.6 equiv of NEt_3 (6.4 mL, 44.8 mmol), and 0.10 equiv of imidazole (60 mg, 0.86 mmol) in CH_2Cl_2 (60 mL) at room temperature for 24 h (until TLC analysis showed no more starting material). Thereafter, 25 mL of water were added and extraction with 3 × 30 mL of CH_2Cl_2 followed; the organic layer was dried, evaporation of solvent under reduced pressure furnished the residue that was purified by column chromatography using petroleum ether/ethyl acetate as the eluent yielding the title compound **4** (3.84 g, 73.70%) as a colourless syrup. ^{1}H NMR (300 MHz, $CDCl_3$) *δ* 6.0–5.82 (m, 2H, =CH), 5.42 (d, *J* = 6.5 Hz, 1H, CH), 4.50 (brs, 1H, OH), 4.20–4.12 (m, 1H, CH), 3.91–3.80 (m, 4H, CH_2), 0.98 (s, 9H, *t*-Bu), 0.24 (s, 6H, CH_3); ^{13}C NMR (75 MHz, $CDCl_3$) *d* 127.5, 125.6, 84.6, 81.5, 73.6, 62.7, 25.6, 18.1; MS *m/z* (M^++Na) 267. Anal. calcd. for $C_{12}H_{24}O_3Si$: C, 58.97; H, 9.90. Found: C, 58.62; H, 9.75.

***tert*-Butyldimethyl(((2*R*,3*S*)-3-(prop-2-ynyloxy)-3,6-dihydro-2*H*-pyran-2-yl)methoxy)silane (5)**

To a solution of alcohol **4** (3.50 g,13.10 mmol) in toluene (3.2 mL) was added 35% aqueous solution of NaOH (6.4 mL), propargyl bromide (80% solution in toluene, 363 μL, 2.4 mmol, 1.5 equiv), and *n*-Bu_4NHSO_4 (360 mg, 1.6 mmol, 1 equiv). After 6 h of vigorous stirring at rt, Et_2NH (6.4 mL) was added. The reaction mixture was stirred for 1 h, poured into ice water, cautiously neutralized by addition of a 3M solution of hydrochloric acid, and extracted with EtOAc. The combined organic extracts were washed with brine, dried over $MgSO_4$, filtered, and concentrated under reduced pressure. The crude material was purified by flash chromatography on silica gel (hexane/EtOAc 85:15) to afford propargyl ether **5** as a colorless oil (3.1 g, 83%). ^{1}H NMR (300 MHz, $CDCl_3$) *δ* 6.03–5.80 (m, 2H, =CH), 4.69 (t, *J* = 3.9 Hz, 1H, CH), 3.68 (dd, *J* = 8.9 Hz, 4.1 Hz, 1H, OCH), 3.99–3.89 (m, 6H, CH_2), 3.20 (s, 1H, CH), 0.96 (s, 9H, *t*-Bu), 0.23 (s, 6H, CH_3); ^{13}C NMR (75 MHz, $CDCl_3$) *δ* 127.2, 124.9, 78.0, 76.2, 74.2, 64.2, 63.2, 58.5, 25.3, 18.5; MS *m/z* (M^++H) 283. Anal. calcd. for $C_{15}H_{26}O_3Si$: C, 63.78; H, 9.28. Found: C, 63.62; H, 8.95.

((2*R*,3*S*)-3-(Prop-2-ynyloxy)-3,6-dihydro-2*H*-pyran-2-yl)methanol (6)

To a stirred solution of **5** (3 g, 10.600 mmol) in tetrahydrofuran, catalytic amount of TBAF was added and stirred the reaction mixture at room temperature for 15 min, extracted the product with ethyl acetate (50 mL). The combined organic extracts were washed with brine, dried over $MgSO_4$, filtered, and concentrated under reduced pressure. The crude material was purified by flash chromatography on silica gel (60–120 mesh, hexane/EtOAc 70:30) to afford alcohol **6** as a yellow oil (1.5 g, 83%). ^{1}H NMR (300 MHz, $CDCl_3$) *δ* 5.95–5.75 (m, 2H, =CH), 4.65 (d, *J* = 3.9 Hz, 1H, CH), 4.52 (brs, 1H, OH), 4.09–4.11 (m, 4H, OCH_2), 3.64 (dd, *J* = 4.1 Hz, 8.9 Hz, 1H, OCH), 3.76 (d, *J* = 6.8 Hz, 2H, OCH_2), 3.28 (s, 1H, CH); ^{13}C NMR (75 MHz, $CDCl_3$) *d* 127.2, 125.6, 78.3, 76.1, 74.1, 64.2, 61.4, 58.0; MS *m/z* (M^++H) 169. Anal. calcd. for $C_9H_{12}O_3$: C, 64.27; H, 7.10. Found: C, 64.02; H, 6.95.

((2*R*,3*S*)-3-((1-(4-Chlorophenyl)-1*H*-1,2,3-triazol-4-yl) methoxy)-3,6-dihydro-2*H*-pyran-2yl)methanol (7)

The a solution containing alkyne **6** (1.4 g, 8.28 mmol), *para*-chlorophenylazide (1.25 g, 8.11 mmol) in dichloromethane (10 mL) and water (10 mL) were added $CuSO_4 \cdot 5H_2O$ (0.110 g) and sodium ascorbate (0.114 g). The resulting suspension was stirred at room temperature for 6 h. Then, the mixture was diluted with 5 mL dichloromethane and 5 mL water. The organic phase was separated, dried with sodium sulphate and concentrated under reduced pressure. The crude product was purified by using column chromatography on silica gel (60–120 mesh, hexane/EtOAc 65:35) to afford **7** (2 g, 75%) as a white powder. M.p. 149–151.0 °C. ^{1}H NMR (300 MHz, $CDCl_3$) δ 8.05 (s, 1H, Ar-H), 7.56 (d, J = 9.2 Hz, 2H, Ar-H), 7.45 (d, J = 8.9 Hz, 2H, Ar-H), 5.85–5.79 (m, 2H, =CH), 4.59 (s, 2H, OCH_2), 4.50 (brs, 1H, OH), 3.88–3.99 (m, 4H, OCH_2), 3.8–3.75 (m, 2H, OCH); ^{13}C NMR (75 MHz, $CDCl_3$) *d* 140.9, 134.5, 134.1, 128.4, 127.5, 125.4, 122.1, 111.5, 78.6, 68.5, 65.7, 64.2, 62.4; MS *m/z* (M^++H) 322. Anal. calcd. for $C_{15}H_{16}ClN_3O_3$: C, 55.90; H, 5.01; N, 13.06. Found: C, 55.65; H, 4.95; N, 12.86.

(*R*)-2-((2*S*,3*S*)-3-((1-(4-Chlorophenyl)-1*H*-1,2,3-triazol -4-yl)methoxy)-3,6-dihydro-2*H*-pyran-2-yl)-3-phenylthiazolidin-4-ones 9a–g

At room temperature for about 30 min, to the solution of alcohol **7** (1.9 g, 5.90 mmol) in CH_2Cl_2 (10 mL), a catalytic amount of IBX was added at 0 °C and stirred. The reaction mixture was filtered and washed with CH_2Cl_2 (2 × 10 mL). It was dried (Na_2SO_4) and evaporated to give the aldehyde **8** (1.6 g) in quantitative yield as a yellow liquid, which was used for the next reaction.

To the corresponding aromatic aniline (0.712 mmol), the stirred mixture of **8** (0.712 mmol), anhydrous thioglycolic acid (0.070 g, 0.760 mmol) in dry toluene (10 mL), $ZnCl_2$ (0.100 g, 0.751 mmol) was added after 2 min and irradiated in microwave bath reactor at 280 W for 4–7 minutes at 110 °C. The filtrate was concentrated to dryness under reduced pressure and the residue was taken up in ethyl acetate after cooling. The ethyl acetate layer was washed with 5% sodium bicarbonate solution and finally it was dried. At reduced pressure, the organic layer was dried over Na_2SO_4 and evaporated to dryness. The crude product **9** was obtained and it was purified by column chromatography on silica gel (60–120 mesh) with hexane–ethyl acetate mixture as the eluent.

(*R*)-2-((2*S*,3*S*)-3-((1-(4-Chlorophenyl)-1*H*-1,2,3-triazol-4-yl)methoxy)-3,6-dihydro-2*H*-pyran-2-yl)-3-phenylthiazolidin-4-one (9a). M.p. 157–159 °C. Yield 75% (0.249 g). ^{1}H NMR (300 MHz, $CDCl_3$) δ 8.04 (s, 1H, Ar-H), 7.50 (d, J = 9.2 Hz, 2H, Ar-H), 7.40 (d, J = 8.9 Hz, 2H, Ar-H), 7.10–6.20 (m, 5H, Ar-H), 5.80–5.71 (m, 2H, =CH), 4.90 (d, J = 5.2 Hz, 1H, CH-S), 4.52 (s, 2H, OCH_2), 4.09–3.94 (m, 2 × CH), 3.79 (d, J = 6.6 Hz, 2H, OCH_2), 3.72 (s, 2H, CH_2); ^{13}C NMR (75 MHz, $CDCl_3$) *d* 170.4, 144.1, 141.8, 134.1, 128.2, 125.6, 122.4, 119.4, 85.6, 72.6, 66.4, 64.0, 51.4, 33.9; MS *m/z* (M^++H) 469. Anal. calcd. for $C_{23}H_{21}ClN_4O_3S$: C, 58.91; H, 4.51; N, 11.95. Found: C, 58. 68; H, 4.35; N, 11.66.

(*R*)-3-(4-Chlorophenyl)-2-((2*S*,3*S*)-3-((1-(4-chlorophenyl)-1*H*-1,2,3-triazol-4-yl)methoxy)-3,6-dihydro-2*H*-pyran-2-yl)thiazolidin-4-one (9b). M.p. 226–228 °C. Yield 69% (0.256 g). ^{1}H NMR (300 MHz, $CDCl_3$) δ 8.05 (s, 1H, Ar-H), 7.54 (d, J = 9.4Hz, 4H, Ar-H), 7.42 (d, J = 8.6Hz, 4H, Ar-H), 5.84–5.75 (m, 2H, =CH), 4.94 (d, J = 5.2 Hz, CH-S), 4.50 (s, 2H, OCH_2), 4.06–3.96 (m, 2H, 2 × CH), 3.80 (t, 2H, OCH_2), 3.72 (s, 2H, CH_2); ^{13}C NMR (75 MHz, $CDCl_3$) *d* 170.5, 144.2, 139.2, 134.2, 129.2, 125.5, 122.2, 119.4, 85.4, 72.8, 65.4, 63.4, 51.2, 34.1; MS *m/z* (M^++Na) 525. Anal. calcd. for $C_{23}H_{20}Cl_2N_4O_3S$: C, 54.88; H, 4.00; N, 11.13. Found: C, 54.58; H, 3.75; N, 10.86.

(*R*)-2-((2*S*,3*S*)-3-((1-(4-Chlorophenyl)-1*H*-1,2,3-triazol-4-yl)methoxy)-3,6-dihydro-2*H*-pyran-2-yl)-3-(4-nitrophenyl)thiazolidin-4-one (9c). M.p. 211–213 °C. Yield 71% (0.259 g). ^{1}H NMR (300 MHz, $CDCl_3$) δ 8.26 (d, J = 8.7 Hz, 2H, Ar-H), 8.03 (s, 1H, Ar-H), 7.61 (d, J = 9.4 Hz, 2H, Ar-H), 7.46 (d, J = 8.5 Hz, 2H, Ar-H), 6.84 (d, J = 9.8Hz, 2H, Ar-H), 5.86–5.79 (m, 2H, =CH), 4.96 (d, J = 5.2 Hz, CH-S), 4.55 (s, 2H, OCH_2), 4.05–3.95 (m, 2H, 2 × CH), 3.85 (d, J = 6.9Hz, 2H, OCH_2), 3.82 (s, 2H, CH_2); ^{13}C NMR (75 MHz, $CDCl_3$) *d* 171.5, 144.0, 141.8, 134.2, 128.5, 125.4, 119.5, 85.4, 72.4, 65.9, 63.6, 51.5, 34.6; MS *m/z* (M^++H) 514. Anal. calcd. for $C_{23}H_{20}ClN_5O_5S$: C, 53.75; H, 3.92; N, 13.63. Found: C, 53.58; H, 3.75; N, 13.39.

(*R*)-2-((2*S*,3*S*)-3-((1-(4-Chlorophenyl)-1*H*-1,2,3-triazol-4-yl)methoxy)-3,6-dihydro-2*H*-pyran-2-yl)-3-*o*-tolylthiazolidin-4-one (9d). M.p. 191–193 °C. Yield 65% (0.222 g). ^{1}H NMR (300 MHz, $CDCl_3$) δ 8.08 (s, 1H, Ar-H), 7.56 (d, J = 9.2 Hz, 2H, Ar-H), 7.49 (d, J = 8.7 Hz, 2H, Ar-H), 7.45–7.39 (m, 4H, Ar-H), 5.76 (m, 2H, =CH), 4.93 (d, J = 5.2 Hz, 1H, CHS), 4.60 (s, 2H, OCH_2), 4.05–3.96 (m, 2H, CH), 3.90 (t, 2H, OCH_2), 3.81 (s, 2H, CH_2), 2.1 (s, 3H, CH_3); ^{13}C NMR (75 MHz, $CDCl_3$) *d* 170.5, 144.2, 138.2, 134.2, 130.7, 128.6, 125.6, 122.0, 119.5, 116.5, 85.4, 72.6, 65.8, 63.4, 52.0, 32.3, 17.5; MS *m/z* (M^++H) 483. Anal. calcd. for $C_{24}H_{23}ClN_4O_3S$: C, 59.68; H, 4.80; N, 11.60. Found: C, 59.48; H, 4.55; N, 11.49.

(*R*)-2-((2*S*,3*S*)-3-((1-(4-Chlorophenyl)-1*H*-1,2,3-triazol-4-yl)methoxy)-3,6-dihydro-2*H*-pyran-2-yl)-3-*p*-tolylthiazolidin-4-one (9e). M.p. 195–198 °C. Yield 79% (0.270 g). ^{1}H NMR (300 MHz, $CDCl_3$) δ 8.05 (s, 1H, Ar-H), 7.51 (d, J = 9.2 Hz, 2H, Ar-H), 7.45 (d, J = 8.7 Hz, 2H, Ar-H), 7.25 (d, J = 8.2 Hz, 2H, Ar-H), 6.84 (d, J = 9.4 Hz, 2H, Ar-H), 5.72–5.68 (m, 2H, =CH), 4.95 (s, 1H, CHS), 4.59 (s, 2H, OCH_2), 4.04–3.99 (m, 2H, CH), 3.98 (t, 2H, OCH_2), 3.90 (s, 2H, CH_2), 2.32 (s, 3H, CH_3); ^{13}C NMR (75

MHz, $CDCl_3$) *d* 170.5, 144.2, 138.6, 136.2, 14.1, 133.2, 129.4, 127.5, 122.5, 119.5, 85.4, 72.0, 66.4, 63.5, 51.5, 34.0, 21.4; MS *m/z* (M^++H) 483. Anal. calcd. for $C_{24}H_{23}ClN_4O_3S$: C, 59.68; H, 4.80; N, 11.60. Found: C, 59.58; H, 4.65; N, 11.43.

(*R*)-2-((2*S*,3*S*)-3-((1-(4-Chlorophenyl)-1*H*-1,2,3-triazol-4-yl)methoxy)-3,6-dihydro-2*H*-pyran-2-yl)-3-(3-hydroxyphenyl)thiazolidin-4-one (9f). M.p. 218–219 °C. Yield 85% (0.360 g). ^{1}H NMR (300 MHz, $CDCl_3$) δ 9.40 (brs, 1H, Ph-OH), 8.08 (s, 1H, Ar-H), 7.58 (d, *J* = 9.3 Hz, 2H, Ar-H), 7.49 (d, *J* = 8.6 Hz, 2H, Ar-H), 6.83–6.76 (m, 4H, Ar-H), 5.72–5.68 (m, 2H, =CH), 4.94 (d, *J* = 5.2 Hz, 1H, CHS), 4.64 (s, 2H, OCH_2), 4.12 (t, 2H, OCH_2), 4.01–3.94 (m, 2H, CH), 3.92 (s, 2H, CH_2); ^{13}C NMR (75 MHz, $CDCl_3$) *d* 170.5, 158.2, 143.8, 134.5, 130.4, 128.6, 125.6, 122.4, 119.5, 114.8, 106.5, 85.4, 72.5, 66.4, 63.4, 51.5, 34.1; MS *m/z* (M^++Na) 507. Anal. calcd. for $C_{23}H_{21}ClN_4O_4S$: C, 59.96; H, 4.36; N, 11.55. Found: C, 59.28; H, 4.65; N, 11.43.

(*R*)-2-((2*S*,3*S*)-3-((1-(4-Chlorophenyl)-1*H*-1,2,3-triazol-4-yl)methoxy)-3,6-dihydro-2*H*-pyran-2-yl)-3-(4-hydroxyphenyl)thiazolidin-4-one (9g). M.p. 273–275 °C. Yield 82% (0.282 g). ^{1}H NMR (300 MHz, $CDCl_3$) δ 9.42 (brs, 1H, Ph-OH), 8.05 (s, 1H, Ar-H), 7.56 (d, *J* = 9.2 Hz, 2H, Ar-H), 7.46 (d, *J* = 8.4Hz, 2H, Ar-H), 7.32 (d, *J* = 8.6Hz, 2H, Ar-H), 7.02 (d, *J* = 8.8 Hz, 2H, Ar-H), 5.89–5.80 (m, 2H, =CH), 4.96 (d, *J* = 5.4 Hz, 1H, CHS), 4.66 (s, 2H, OCH_2), 4.09 (d, *J* = 2H, OCH_2), 4.04–3.98 (m, 2H, CH), 3.94 (s, 2H, CH_2); ^{13}C NMR (75 MHz, $CDCl_3$) *d* 170.9, 154.1, 144.4, 134.9, 134.8, 128.8, 127.2, 125.6, 123.2, 119.4, 116.4, 85.4, 72.6, 66.5, 64.0, 51.6, 34.5; MS *m/z* (M^++H) 485. Anal. calcd. for $C_{23}H_{21}ClN_4O_4S$: C, 59.96; H, 4.36; N, 11.55. Found: C, 59.38; H, 4.75; N, 11.33.

General Procedure for the Synthesis of 10a–g

In anhydrous glacial acetic acid (20 mL), a mixture of compound **9a** (0.235 g, 0.501 mmol), *para*- fluorobenzaldehyde (0.065 g, 0.524 mmol) and sodium acetate (0.01 mol) was refluxed for about 3 h. The reaction mixture was concentrated and then poured into ice cold water, the solid thus separated, then it was filtered, and washed with water and crystallized from glacial acetic acid, to afford pure **10a** as a yellow solid.

(*R,Z*)-2-((2*S*,3*S*)-3-((1-(4-Chlorophenyl)-1*H*-1,2,3-triazol-4-yl)methoxy)-3,6-dihydro-2*H*-pyran-2-yl)-5-(4-fluorobenzylidene)-3-phenylthiazolidin-4-one (10a). M.p. 235–237 °C. Yield 85% (0.244 g). ^{1}H NMR (300 MHz, $CDCl_3$) δ 8.07 (s, 1H, Ar-H), 7.80 (s, 1H, CH=C), 7.72 (d, *J* = 9.6 Hz, 2H, Ar-H), 7.40 (d, *J* = 9.2 Hz, 2H, Ar-H), 7.45 (d, *J* = 8.9 Hz, 2H, Ar-H), 7.19 (d, *J* = 8.2 Hz, 2H, Ar-H),7.02–6.80 (m, 5H, Ar-H), 5.80–5.74 (m, 2H, =CH), 4.90 (d, *J* = 5.2 Hz, 1H, CH-S), 4.52 (s, 2H, OCH_2), 4.09–3.94 (m, 2H, 2 × CH), 3.79 (d, *J* = 6.6 Hz, 2H, OCH_2); ^{13}C NMR (75 MHz, $CDCl_3$) *d* 170.4, 162.1, 144.1, 141.8, 139.8, 134.1, 130.4, 128.2, 125.6, 124.6, 122.4, 119.4, 115.5, 85.6, 72.6, 66.4, 64.0, 51.5; MS *m/z* (M^++H) 575. Anal. calcd. for $C_{30}H_{24}ClFN_4O_3S$: C, 62.66; H, 4.21; N,9.74. Found: C, 62.48; H, 4.15; N, 9.56.

Similarly all the compounds**(10b-e)** prepared according to above procedure

(*R,Z*)-3-(4-Chlorophenyl)-2-((2*S*,3*S*)-3-((1-(4-chlorophenyl)-1*H*-1,2,3-triazol-4-yl)methoxy)-3,6-dihydro-2*H*-pyran-2-yl)-5-(4-fluorobenzylidene)thiazolidin-4-one (10b). M.p. 216–218 °C. Yield 72% (0.207 g). ^{1}H NMR (300 MHz, $CDCl_3$) δ 8.09 (s, 1H, Ar-H), 7.75 (s, 1H, CH=C), 7.62 (d, *J* = 9.5 Hz, 2H, Ar-H), 7.52 (d, *J* = 9.4 Hz, 4H, Ar-H), 7.40 (d, *J* = 8.6 Hz, 4H, Ar-H), 7.19 (d, *J* = 8.1 Hz, 2H, Ar-H), 5.84–5.75 (m, 2H, =CH), 4.94 (d, *J* = 5.2 Hz, 1H, CHS), 4.52 (s, 2H, OCH_2), 4.06–3.94 (m, 2H, 2 × CH), 3.80 (t, 2H, OCH_2); ^{13}C NMR (75 MHz, $CDCl_3$) *d* 170.5, 162.1, 144.2, 139.2, 134.2, 130.4, 129.2, 125.5, 124.1, 122.2, 119.4, 85.4, 72.8, 65.4, 63.4, 51.2; MS *m/z* (M^++Na) 632. Anal. calcd. for $C_{30}H_{23}Cl_2FN_4O_3S$: C, 59.12; H, 3.80; N,9.19. Found: C, 59.01; H, 3.45; N, 8.96.

(*R,Z*)-2-((2*S*,3*S*)-3-((1-(4-Chlorophenyl)-1*H*-1,2,3-triazol-4-yl)methoxy)-3,6-dihydro-2*H*-pyran-2-yl)-5-(4-fluorobenzylidene)-3-(4-nitrophenyl)thiazolidin-4-one (10c). M.p. 221–223 °C. Yield 75% (0.216 g). ^{1}H NMR (300 MHz, $CDCl_3$) δ 8.29 (d, *J* = 8.7 Hz, 2H, Ar-H), 8.09 (s, 1H, Ar-H), 7.69 (d, *J* = 9.1 Hz, 2H, Ar-H), 7.65 (s, 1H, CH=C), 7.61 (d, *J* = 9.4 Hz, 2H, Ar-H), 7.46 (d, *J* = 8.5 Hz, 2H, Ar-H), 7.18 (d, *J* = 8.3 Hz, 2H, Ar-H), 6.84 (d, *J* = 9.8 Hz, 2H, Ar-H), 5.86–5.79 (m, 2H, =CH), 4.96 (d, *J* = 5.2 Hz, CH-S), 4.55 (s, 2H, OCH_2), 4.05–3.95 (m, 2H, 2 × CH), 3.85 (d, *J* = 6.9 Hz, 2H, OCH_2); ^{13}C NMR (75 MHz, $CDCl_3$) *d* 171.5, 162.1, 144.0, 141.8, 134.2, 130.4, 128.5, 125.4, 119.5, 115.4, 85.4, 72.4, 65.9, 63.6, 51.5; MS *m/z* (M^++H) 620. Anal. calcd. for $C_{30}H_{23}ClFN_5O_5S$: C, 58.11; H, 3.74; N, 11.29. Found: C, 57.98; H, 3.55; N, 11.09.

(*R,Z*)-2-((2*S*,3*S*)-3-((1-(4-Chlorophenyl)-1*H*-1,2,3-triazol-4-yl)methoxy)-3,6-dihydro-2*H*-pyran-2-yl)-5-(4-fluorobenzylidene)-3-*o*-tolylthiazolidin-4-one (10d). M.p. 201–203 °C. Yield 85% (0.217 g). ^{1}H NMR (300 MHz, $CDCl_3$) δ 8.08 (s, 1H, Ar-H), 7.69 (d, *J* = 8.5 Hz, 2H, Ar-H), 7.62 (s, 1H, CH=C), 7.56 (d, *J* = 9.2 Hz, 2H, Ar-H), 7.49 (d, *J* = 8.7 Hz, 2H, Ar-H), 7.45–7.39 (m, 4H, Ar-H), 7.10 (d, *J* = 9.1 Hz, 2H, Ar-H), 5.76 (m, 2H, =CH), 4.93 (d, *J* = 5.2 Hz, 1H, CHS), 4.60 (s, 2H, OCH_2), 4.05–3.96 (m, 2H, CH), 3.90 (t, 2H, OCH_2), 2.1 (s, 3H, CH_3); ^{13}C NMR (75 MHz, $CDCl_3$) *d* 170.8, 162.9, 144.6, 137.2, 133.2, 130.6, 130.4, 128.2, 125.9, 122.7, 119.2, 116.2, 115.4, 84.4, 72.1, 65.3, 63.1, 52.5, 32.0, 17.5; MS *m/z* (M^++H) 589. Anal. calcd. for $C_{31}H_{26}ClFN_4O_3S$: C, 63.21; H, 4.45; N, 9.51. Found: C, 62.75; H, 4.25; N, 9.29.

(*R,Z*)-2-((2*S*,3*S*)-3-((1-(4-Chlorophenyl)-1*H*-1,2,3-triazol-4-yl)methoxy)-3,6-dihydro-2*H*-pyran-2-yl)-5-(4-fluorobenzylidene)-3-*p*-tolylthiazolidin-4-one(10e).

M.p. 205–215 °C. Yield 66% (0.209 g). ^{1}H NMR (300 MHz, $CDCl_3$) δ 8.02 (s, 1H, Ar-H), 7.69 (s, 1H, CH =C),7.65 (d, J = 9.1 Hz, 2H, Ar-H), 7.54 (d, J = 9.2 Hz, 2H, Ar-H), 7.42 (d, J = 8.7 Hz, 2H, Ar-H), 7.35 (d, J = 8.2 Hz, 2H, Ar-H), 7.18 (d, J = 8.8 Hz, 2H, ArH), 6.80 (d, J = 9.4 Hz, 2H, ArH), 5.70–5.69 (m, 2H, =CH), 4.94 (s, 1H, CHS), 4.55 (s, 2H, OCH_2), 4.04–3.98 (m, 2H, CH), 3.96 (t, 2H, OCH_2), 2.32 (s, 3H, CH_3); ^{13}C NMR (75 MHz, $CDCl_3$) *d* 170.1, 162.5, 144.1, 139.5, 137.6, 135.2, 133.2, 130.4, 129.1, 127.5, 124.1, 122.5, 119.5, 115.3, 85.1, 72.5, 66.1, 63.2, 51.2, 21.6; MS *m/z* (M^++H) 589. Anal. calcd. for $C_{31}H_{26}ClFN_4O_3S$: C, 63.21; H, 4.45; N, 9.51. Found: C, 62.98, H, 4.25; N, 9.33.

(*R*,*Z*)-2-((2*S*,3*S*)-3-((1-(4-Chlorophenyl)-1*H*-1,2,3-triazol-4-yl)methoxy)-3,6-dihydro-2*H*-pyran-2-yl)-5-(4-fluorobenzylidene)-3-(3-hydroxyphenyl)thiazolidin-4-one (10f). M.p. 218–219 °C. Yield 82% (0.219 g). ^{1}H NMR (300 MHz, $CDCl_3$) δ 9.42 (brs, 1H, PhOH), 8.08 (s, 1H, ArH), 7.71 (d, J = 9.7 Hz, 2H, ArH), 7.65 (s, 1H, CH=C), 7.59 (d, J = 9.3 Hz, 2H, Ar-H), 7.44 (d, J = 8.6 Hz, 2H, Ar-H), 7.15 (d, J = 8.4Hz, 2H, ArH), 6.80–6.78 (m, 4H, Ar-H), 5.70–5.68 (m, 2H, =CH), 4.92 (d, J = 5.2 Hz, 1H, CHS), 4.64 (s, 2H, OCH_2), 4.10 (t, 2H, OCH_2), 4.01–3.98 (m, 2H, CH); ^{13}C NMR (75 MHz, $CDCl_3$) *d* 170.5, 162.1, 158.2, 143.8, 139.8, 134.5, 130.8, 128.6, 125.6, 124.1, 122.4, 119.5, 115.7, 114.8, 106.5, 85.4, 72.5, 66.4, 63.4, 51.5; MS *m/z* (M^++H) 591. Anal. calcd. for $C_{30}H_{24}ClFN_4O_4S$: C, 60.96; H, 4.09; N, 9.48. Found: C, 60.58; H, 3.85; N,9.13.

(*R*,*Z*)-2-((2*S*,3*S*)-3-((1-(4-Chlorophenyl)-1*H*-1,2,3-triazol-4-yl)methoxy)-3,6-dihydro-2*H*-pyran-2-yl)-5-(4-fluorobenzylidene)-3-(4-hydroxyphenyl)thiazolidin-4-one (10g). M.p. 283–285 °C. Yield 62% (0.203 g). ^{1}H NMR (300 MHz, $CDCl_3$) δ 9.42 (brs, 1H, Ph-OH), 8.05 (s, 1H, Ar-H), 7.85 (d, J = 9.3 Hz, 2H, Ar-H), 7.65 (s, 1H, CH=C), 7.56 (d, J = 9.2 Hz, 2H, Ar-H), 7.46 (d, J = 8.4 Hz, 2H, Ar-H), 7.32 (d, J = 8.6 Hz, 2H, Ar-H), 7.19 (d, J = 8.3 Hz, 2H, ArH), 7.02 (d, J = 8.8 Hz, 2H, ArH), 5.89-5.80 (m, 2H, =CH), 4.96 (d, J = 5.4 Hz, 1H, CHS), 4.66 (s, 2H, OCH_2), 4.09 (d, J = 2H, OCH_2), 4.04–3.98 (m, 2H, CH); ^{13}C NMR (75 MHz, $CDCl_3$) *d* 170.9, 162.5, 154.1, 144.4, 139.8, 134.9, 134.8, 130.4, 128.8, 127.2, 125.6, 123.2, 119.4, 116.4, 115.9, 85.4, 72.6, 66.5, 64.0, 51.6; MS *m/z* (M^++H) 591. Anal. calcd. for $C_{30}H_{24}ClFN_4O_4S$: C, 60.96; H, 4.09; N, 9.48. Found: C, 60.58; H, 3.95; N,9.23.

General Procedure for the Synthesis of 11a–g

To the anhydrous sodium acetate (0.191 mmol) a mixture of compound **10a** (0.191 mmol), phenyl hydrazine (0.191 mmol), in glacial acetic acid (10 mL), was refluxed for about 7 h. Then the reaction mixture was concentrated and cooled at room temperature, the solid was separated and filtered off, then it was washed thoroughly with water, the crude product was obtained and it was purified by column chromatography on silica gel with hexane–ethyl acetate as the eluent to afford pure compounds **11**.

(5*R*)-5-((2*S*,3*S*)-3-((1-(4-Chlorophenyl)-1*H*-1,2,3-triazol-4-yl)methoxy)-3,6-dihydro-2*H*-pyran-2-yl)-3-(4-fluorophenyl)-2,6-diphenyl-3,3a,5,6-tetrahydro-2*H*-pyrazolo[3,4-*d*]thiazole (11a). M.p. 245–247 °C. Yield 85% (0.107 g). IR (KBr) ν 3090, 3010, 1620, 1604, 1480, 1369, 1240, 1132, 764 cm^{-1}; ^{1}H NMR (300 MHz, $CDCl_3$) δ 8.08 (s, 1H, Ar-H), 7.74 (d, J = 9.6 Hz, 2H, Ar-H), 7.46 (d, J = 9.2 Hz, 2H, Ar-H), 7.45 (d, J = 8.9Hz, 2H, Ar-H), 7.18 (d, J = 8.2 Hz, 2H, Ar-H), 7.05–6.99 (m, 5H, Ar-H), 6.83–7.10 (m, 5H, Ar-H), 5.80–5.79 (m, 2H, =CH), 5.62 (d, J = 2.2 Hz, 1H, S-CH), 5.25 (d, J = 2.2 Hz, 1H, CH-N), 4.95 (d, J = 5.2 Hz, 1H, CH-S), 4.50 (s, 2H, OCH_2), 4.09–3.97 (m, 2H, 2 × CH), 3.79 (d, J = 6.6 Hz, 2H, OCH_2); ^{13}C NMR (75 MHz, $CDCl_3$) *d* 170.8, 162.5, 144.4, 143.4, 141.2, 134.5, 130.1, 129.8, 128.7, 125.6, 122.4, 120.8, 119.4, 115.5, 116.5, 85.6, 72.6, 66.4, 64.0, 51.0; MS *m/z* (M^++H) 665. Anal. calcd. for $C_{36}H_{30}ClFN_6O_2S$: C, 65.0; H, 4.45; N, 12.63. Found: C, 64.58; H, 4.15; N, 12.46.

Similarly, all the compounds **11b–g** were prepared according to the above procedure.

(5*R*)-6-(4-Chlorophenyl)-5-((2*S*,3*S*)-3-((1-(4-chlorophenyl)-1*H*-1,2,3-triazol-4-yl)methoxy)-3,6-dihydro-2*H*-pyran-2-yl)-3-(4-fluorophenyl)-2-phenyl-3,3a,5,6-tetrahydro-2*H*-pyrazolo[3,4-*d*]thiazole (11b). M.p. 216–218 °C. Yield 65% (0.071 g). IR (KBr) ν 3080, 3014, 1632, 1609, 1462, 1359, 1250, 1228, 1140, 742 cm^{-1}; ^{1}H NMR (300 MHz, $CDCl_3$) *d* 8.04 (s, 1H, Ar-H), 7.60 (d, J = 9.5 Hz, 2H, Ar-H), 7.55 (d, J = 9.4 Hz, 4H, Ar-H), 7.42 (d, J = 8.6 Hz, 4H, Ar-H), 7.16 (d, J = 8.1 Hz, 2H, Ar-H), 6.90–7.02 (m, 5H, Ar-H), 5.82–5.78 (m, 2H, =CH), 5.62 (d, J = 2.2 Hz, 1H, S-CH), 5.25 (d, J = 2.2 Hz, 1H, CH-N), 4.94 (d, J = 5.2 Hz, 1H, CHS), 4.52 (s, 2H, OCH_2), 4.06–3.94 (m, 2H, 2 × CH), 3.80 (t, 2H, OCH_2); ^{13}C NMR (75 MHz, $CDCl_3$) *d* 170.5, 162.1, 144.2, 143.8, 134.2, 130.4, 129.2, 125.5, 122.2, 120.8, 119.4, 116.8, 85.1, 72.5, 65.3, 63.2, 51.0; MS *m/z* (M^++H) 699. Anal. calcd. for $C_{36}H_{29}Cl_2FN_6O_2S$: C, 61.80; H, 4.18; N, 12.01. Found: C, 61.61; H, 3.95; N, 11.86.

(5*R*)-5-((2*S*,3*S*)-3-((1-(4-Chlorophenyl)-1*H*-1,2,3-triazol-4-yl)methoxy)-3,6-dihydro-2*H*-pyran-2-yl)-3-(4-fluorophenyl)-6-(4-nitrophenyl)-2-phenyl-3,3a,5,6-tetrahydro-2*H*-pyrazolo[3,4-*d*]thiazole (11c). M.p. 231–233 °C. Yield 85% (0.096 g). IR (KBr) ν 3098, 3019, 1611, 1601, 1540, 1472, 1359, 1262, 1121, 694 cm^{-1}; ^{1}H NMR (300 MHz, $CDCl_3$) δ 8.20 (d, J = 8.7 Hz, 2H, Ar-H), 8.05 (s, 1H, Ar-H), 7.68 (d, J = 9.1 Hz, 2H, Ar-H), 7.61 (d, J = 9.4 Hz, 2H, Ar-H), 7.42 (d, J = 8.5 Hz, 2H, Ar-H), 7.28 (d, J = 8.3 Hz, 2H, Ar-H), 7.10–6.88 (m, 5H, Ar-H), 6.74 (d, J = 9.8 Hz, 2H, Ar-H), 5.86–5.79 (m, 2H, =CH), 5.58 (d, J = 2.2 Hz, 1H, S-CH), 5.21 (d, J = 2.2 Hz, 1H, CH-N), 4.96 (d, J = 5.2Hz, CH-S), 4.55 (s, 2H, OCH_2), 4.05–3.95 (m, 2H, 2 × CH), 3.85 (d, J = 6.9 Hz, 2H, OCH_2); ^{13}C NMR (75 MHz, $CDCl_3$) *d* 171.5, 162.1, 144.0, 144.9, 134.2, 130.4, 129.5, 128.5, 125.4, 120.8, 119.5, 116.4, 115.4, 85.4, 72.4, 65.9, 63.6,

51.5; MS *m/z* (M^++H) 710. Anal. calcd. for $C_{36}H_{29}ClFN_7O_4S$: C, 60.88; H, 4.12; N, 13.81. Found: C, 60.58; H, 4.01; N, 13.59.

(5*R*)-5-((2*S*,3*S*)-3-((1-(4-Chlorophenyl)-1*H*-1,2,3-triazol-4-yl)methoxy)-3,6-dihydro-2*H*-pyran-2-yl)-3-(4-fluorophenyl)-2-phenyl-6-*o*-tolyl-3,3a,5,6-tetrahydro-2*H*-pyrazolo[3,4-*d*]thiazole (11d). M.p. 211–213 °C. Yield 89% (0.105 g). IR (KBr) ν 3084, 3013, 2928, 1621, 1609, 1462, 1374, 1239, 1129, 712 cm^{-1}; ^1H NMR (300 MHz, $CDCl_3$) *δ* 8.06 (s, 1H, Ar-H), 7.65 (d, *J* = 8.5 Hz, 2H, Ar-H), 7.52 (d, *J* = 9.2 Hz, 2H, Ar-H), 7.47 (d, *J* = 8.7 Hz, 2H, Ar-H), 7.42–7.40 (m, 4H, Ar-H), 7.12 (d, *J* = 9.1 Hz, 2H, Ar-H), 6.89–6.80 (m, 5H, ArH), 5.73 (m, 2H, =CH), 5.62 (d, *J* = 2.2 Hz, 1H, S-CH), 5.25 (d, *J* = 2.2 Hz, 1H, CH-N), 4.91 (d, *J* = 5.2 Hz, 1H, CHS), 4.50 (s, 2H, OCH_2), 4.02–3.99 (m, 2H, CH), 3.92 (t, 2H, OCH_2), 2.14 (s, 3H, CH_3); ^{13}C NMR (75 MHz, $CDCl_3$) *d* 170.8, 162.9, 144.6, 137.2, 133.2, 130.6, 130.4, 128.2, 125.9, 122.7, 119.2, 116.2, 115.4, 84.4, 72.1, 65.3, 63.1, 52.5, 32.0, 17.5; MS *m/z* (M^++Na) 701. Anal. calcd. for $C_{37}H_{32}ClFN_6O_2S$: C, 65.43; H, 4.75; N, 12.37. Found: C, 65.15; H, 4.45; N, 12.09.

(5*R*)-5-((2*S*,3*S*)-3-((1-(4-Chlorophenyl)-1*H*-1,2,3-triazol-4-yl)methoxy)-3,6-dihydro-2*H*-pyran-2-yl)-3-(4-fluorophenyl)-2-phenyl-6-*p*-tolyl-3,3a,5,6-tetrahydro-2*H*-pyrazolo[3,4-*d*]thiazole(11e). M.p. 205–215 °C. Yield 67% (0.078 g). IR (KBr) ν 3099, 3018, 2875, 1635, 1614, 1459, 1371, 1229, 1130, 745 cm^{-1}; ^1H NMR (300 MHz, $CDCl_3$) *δ* 8.04 (s, 1H, Ar-H), 7.62 (d, *J* = 9.1Hz, 2H, Ar-H), 7.53 (d, *J* = 9.2 Hz, 2H, Ar-H), 7.40 (d, *J* = 8.7 Hz, 2H, Ar-H), 7.32 (d, *J* = 8.2 Hz, 2H, Ar-H), 7.15 (d, *J* = 8.8 Hz, 2H, Ar-H), 6.92–6.87 (m, 5H, ArH), 6.84 (d, *J* = 9.4 Hz, 2H, Ar-H), 5.70–5.69 (m, 2H, =CH), 5.62 (d, *J* = 2.2 Hz, 1H, S-CH), 5.25 (d, *J* = 2.2 Hz, 1H, CH-N), 4.94 (s, 1H, CHS), 4.55 (s, 2H, OCH_2), 4.04–3.98 (m, 2H, CH), 3.96 (t, 2H, OCH_2), 2.32 (s, 3H, CH_3); ^{13}C NMR (75 MHz, $CDCl_3$) *d* 170.1, 162.5, 143.8, 137.6, 135.2, 133.2, 130.4, 129.1, 127.9, 122.8, 120.2, 119.0, 116.6, 115.3, 85.4, 72.8, 66.5, 63.4, 51.5, 21.8; MS *m/z* (M^++H) 679. Anal. calcd. for $C_{37}H_{32}ClFN_6O_2S$: C, 65.43; H, 4.75; N, 12.37. Found: C, 65.28; H, 4.45; N, 12.03.

3-((5*R*)-5-((2*S*,3*S*)-3-((1-(4-Chlorophenyl)-1*H*-1,2,3-triazol-4-yl)methoxy)-3,6-dihydro-2*H*-pyran-2-yl)-3-(4-fluorophenyl)-2-phenyl-3,3a-dihydro-2*H*-pyrazolo[3,4-*d*]thiazol-6(5*H*)-yl)phenol (11f).

M.p. 218–219 °C. Yield 85% (0.097 g). IR (KBr) ν 3546, 3100, 1640, 1609, 1471, 1359, 1252, 1110, 779 cm^{-1}; ^1H NMR (300 MHz, $CDCl_3$) *δ* 9.40 (brs, 1H, Ph-OH), 8.05 (s, 1H, Ar-H), 7.61 (d, *J* = 9.7 Hz, 2H, Ar-H), 7.56 (d, *J* = 9.3 Hz, 2H, Ar-H), 7.42 (d, *J* = 8.6 Hz, 2H, Ar-H), 7.14 (d, *J* = 8.4 Hz, 2H, Ar-H) 6.98–6.91 (m, 5H, ArH), 6.80–6.78 (m, 4H, Ar-H), 5.70–5.67 (m, 2H, =CH), 5.65 (d, *J* = 2.2 Hz, 1H, S-CH), 5.28 (d, *J* = 2.2 Hz, 1H, CH-N), 4.92 (d, *J* = 5.2 Hz, 1H, CHS), 4.66 (s, 2H, OCH_2), 4.13 (t, 2H, OCH_2), 4.02–3.99 (m, 2H, CH); ^{13}C NMR (75 MHz, $CDCl_3$) *d* 170.5, 162.1, 158.2, 143.8, 134.5, 130.8, 129.5, 128.6, 125.6, 122.4, 120.7, 119.5, 116.8, 115.7, 114.8, 106.5, 85.4, 72.5, 66.4, 63.4, 51.5; MS *m/z* (M^++H) 681. Anal. calcd. for $C_{36}H_{30}ClFN_6O_3S$: C, 63.48; H, 4.44; N, 12.34. Found: C, 63.18; H, 4.15; N, 12.13.

4-((5*R*)-5-((2*S*,3S)-3-((1-(4-Chlorophenyl)-1*H*-1,2,3-triazol-4-yl)methoxy)-3,6-dihydro-2*H*-pyran-2-yl)-3-(4-fluorophenyl)-2-phenyl-3,3a-dihydro-2*H*-pyrazolo[3,4-*d*]thiazol-6(5*H*)-yl)phenol (11g).

M.p. 283–285 °C. Yield 65% (0.074 g). IR (KBr) ν 3369, 3092, 1635, 1616, 1602, 1492, 1372, 1274, 1120, 723 cm^{-1}; ^1H NMR (300 MHz, $CDCl_3$) *δ* 9.40 (brs, 1H, Ph-OH), 8.08 (s, 1H, Ar-H), 7.85 (d, *J* = 9.3 Hz, 2H, Ar-H), 7.52 (d, *J* = 9.2Hz, 2H, Ar-H), 7.48 (d, *J* = 8.4 Hz, 2H, Ar-H), 7.32 (d, *J* = 8.6 Hz, 2H, Ar-H), 7.19 (d, *J* = 8.3 Hz, 2H, ArH), 7.02 (d, *J* = 8.8 Hz, 2H, Ar-H), 6.85–6.80 (m, 5H, ArH), 5.89–5.85 (m, 2H, =CH), 4.86 (d, *J* = 5.4Hz, 1H, CHS), 4.56 (s, 2H, OCH_2), 4.08 (d, *J* = 2H, OCH_2), 4.05–3.99 (m, 2H, CH); ^{13}C NMR (75 MHz, $CDCl_3$) *d* 170.5, 162.3, 154.1, 144.4, 143.8, 134.9, 134.8, 130.4, 128.8, 127.2, 125.6, 123.2, 120.8, 119.4, 116.4, 115.9, 85.4, 72.6, 66.5, 64.0, 51.6; MS *m/z* (M^++H) 681. Anal. calcd. for $C_{36}H_{30}ClFN_6O_3S$: C, 63.48; H, 4.44; N, 12.34. Found: C, 63.18; H, 4.15; N, 12.03.

General Procedure for Synthesis of Compounds 12a–g

In anhydrous glacial acetic acid (10 mL), a mixture of compound **10a** (0.191 mol), hydroxylamine hydrochloride (0.4 mol) and sodium acetate (0.191 mol) was refluxed for about 8 h. The reaction mixture was concentrated and then poured into ice cold water, the solid thus separated, was filtered, and washed with ice water, and crystallized from ethanol to afford pure **12a** (87% yield) as a brown solid.

(5*R*)-5-((2*S*,3*S*)-3-((1-(4-Chlorophenyl)-1*H*-1,2,3-triazol-4-yl)methoxy)-3,6-dihydro-2*H*-pyran-2-yl)-3-(4-fluorophenyl)-6-phenyl-3,3a,5,6-tetrahydroisoxazolo[3,4-*d*]thiazole (12a). M.p. 255–257 °C. Yield 71% (0.070 g). IR (KBr) ν 3086, 3002, 1616, 1464, 1360, 1309, 1220, 1129, 759 cm^{-1}; ^1H NMR (300 MHz, $CDCl_3$) *δ* 8.09 (s, 1H, Ar-H), 7.70 (d, *J* = 9.6 Hz, 2H, Ar-H), 7.45 (s, 1H, CH-N), 7.42 (d, *J* = 9.2 Hz, 2H, Ar-H), 7.40 (d, *J* = 8.9 Hz, 2H, Ar-H), 7.32–7.20 (m, 5H, Ar–H), 7.16 (d, *J* = 8.2 Hz, 2H, Ar-H), 5.83–5.77 (m, 2H, =CH), 5.70 (d, *J* = 2.2 Hz, 1H, CH-O), 4.69 (d, *J* = 2.2 Hz, 1H, CH-S), 4.55 (s, 2H, OCH_2), 4.08–3.96 (m, 2H, 2 × CH), 3.89 (d, *J* = 6.6 Hz, 2H, OCH_2); ^{13}C NMR (75 MHz, $CDCl_3$) *d* 160.4, 144.1, 135.8, 130.4, 127.2, 122.4, 120.0, 119.4, 115.8, 81.0, 72.6, 66.6, 64.0, 61.0, 40.1; MS *m/z* (M^++H) 590. Anal. calcd. for $C_{30}H_{25}ClFN_5O_3S$: C, 61.06; H, 4.27; N, 11.87. Found: C, 60.88; H, 4.05; N, 11.56.

Similarly all the compounds **12b**–**g** prepared according to the above procedure.

(5*R*)-6-(4-Chlorophenyl)-5-((2*S*,3*S*)-3-((1-(4-chlorophenyl)-1*H*-1,2,3-triazol-4-yl)methoxy)-3,6-dihydro-2*H*-pyran-2-yl)-3-(4-fluorophenyl)-3,3a,5,6-tetrahydrothiazolo[4,5-*c*]isoxazoles (12b). M.p. 242–244 °C. Yield 85% (0.100 g). IR (KBr) ν 3076, 3011, 1620, 1459, 1342, 1320, 1264, 1219, 1151, 764 cm^{-1}; ^1H NMR (300 MHz, $CDCl_3$) δ 8.03 (s, 1H, Ar-H), 7.67 (d, J = 9.5 Hz, 2H, Ar-H), 7.50 (d, J = 9.4 Hz, 4H, Ar-H), 7.44 (s, 1H, CH-N), 7.40 (d, J = 8.6 Hz, 4H, Ar-H), 7.29 (d, J = 8.1 Hz, 2H, Ar-H), 5.82–5.78 (m, 2H, =CH), 5.70 (d, J = 2.2 Hz, 1H, CH-O), 4.69 (d, J = 2.2 Hz, 1H, CH-S), 4.50 (s, 2H, OCH_2), 4.08–3.96 (m, 2H, 2 × CH), 3.84 (t, 2H, OCH_2); ^{13}C NMR (75 MHz, $CDCl_3$) d 164.5, 162.1, 144.4, 136.2, 129.6, 127.2, 126.0, 124.7, 122.0, 119.1, 117.5, 115.7, 85.4, 73.1, 66.0, 63.8, 61.0, 40.2; MS m/z (M^++H) 624. Anal. calcd. for $C_{30}H_{24}Cl_2FN_5O_3S$: C, 57.70; H, 3.87; N, 11.21. Found: C, 57.51; H, 3.49; N, 11.46.

(5*R*)-5-((2*S*,3*S*)-3-((1-(4-Chlorophenyl)-1*H*-1,2,3-triazol-4-yl)methoxy)-3,6-dihydro-2*H*-pyran-2-yl)-3-(4-fluorophenyl)-6-(4-nitrophenyl)-3,3a,5,6-tetrahydrothiazolo[4,5-*c*]isoxazoles (12c). M.p. 251–254 °C. Yield 75% (0.095 g). IR (KBr) ν 3089, 3010, 1619, 1608, 1537, 1442, 1349, 1336, 1221, 1131, 754 cm^{-1}; ^1H NMR (300 MHz, $CDCl_3$) δ 8.23 (d, J = 8.7 Hz, 2H, Ar-H), 8.06 (s, 1H, Ar-H), 7.55 (d, J = 9.1 Hz, 2H, Ar-H), 7.44 (s, 1H, CH-N), 7.40 (d, J = 9.4 Hz, 2H, Ar-H), 7.36 (d, J = 8.5 Hz, 2H, Ar-H), 7.15 (d, J = 8.3 Hz, 2H, Ar-H), 6.86 (d, J = 9.8 Hz, 2H, Ar-H), 5.84–5.80 (m, 2H, =CH), 5.72 (d, J = 2.2 Hz, 1H, CH-O), 4.70 (d, J = 2.2 Hz, 1H, CH-S), 4.53 (s, 2H, OCH_2), 4.07–3.98 (m, 2H, 2 × CH), 3.83 (d, J = 6.9 Hz, 2H, OCH_2); ^{13}C NMR (75 MHz, $CDCl_3$) d 164.0, 161.8, 150.5, 144.4, 134.9, 128.5, 127.3, 126.9, 124.7, 122.0, 119.5, 115.4, 84.4, 73.4, 65.9, 63.6, 61.0, 40.5; MS m/z (M^++Na) 657. Anal. calcd. for $C_{30}H_{24}ClFN_6O_5S$: C, 56.74; H, 3.81; N, 13.23. Found: C, 56.58; H, 3.55; N, 13.09.

(5*R*)-5-((2*S*,3*S*)-3-((1-(4-Chlorophenyl)-1*H*-1,2,3-triazol-4-yl)methoxy)-3,6-dihydro-2*H*-pyran-2-yl)-3-(4-fluorophenyl)-6-*o*-tolyl-3,3a,5,6-tetrahydrothiazolo[4,5-*c*]isoxazoles (12d). M.p. 221–223 °C. Yield 81% (0.082 g). IR (KBr) ν 3091, 3008, 2918, 1630, 1426, 1396, 1347, 1232, 1146, 785 cm^{-1}; ^1H NMR (300 MHz, $CDCl_3$) δ 8.02 (s, 1H, Ar-H), 7.59 (d, J = 8.5 Hz, 2H, Ar-H), 7.54 (d, J = 9.2 Hz, 2H, ArH), 7.50 (d, J = 8.7 Hz, 2H, ArH), 7.45 (s, 1H, CHN), 7.40–7.35 (m, 4H, ArH), 7.10 (d, J = 9.1 Hz, 2H, ArH), 5.76 (m, 2H, =CH), 5.72 (d, J = 2.2 Hz, 1H, CH-O), 5.68 (d, J = 2.2Hz, 1H, S-CH), 4.93 (d, J = 5.2 Hz, 1H, CHS), 4.64 (s, 2H, OCH_2), 4.05–3.98 (m, 2H, CH), 3.92 (t, 2H, OCH_2), 2.2 (s, 3H, CH_3); ^{13}C NMR (75 MHz, $CDCl_3$) d 164.8, 162.9, 144.6, 141.3, 136.2, 134.2, 131.6, 128.2, 126.9, 122.2, 119.2, 116.2, 115.8, 108.8, 84.4, 81.3, 73.1, 66.3, 63.8, 61.3, 46.1, 17.9; MS m/z (M^++H) 604. Anal. calcd. for $C_{31}H_{27}ClFN_5O_3S$: C, 61.63; H, 4.50; N, 11.59. Found: C, 61.35; H, 11.55; N, 11.29.

(5*R*)-5-((2*S*,3*S*)-3-((1-(4-Chlorophenyl)-1*H*-1,2,3-triazol-4-yl)methoxy)-3,6-dihydro-2*H*-pyran-2-yl)-3-(4-fluorophenyl)-6-*p*-tolyl-3,3a,5,6-tetrahydrothiazolo[4,5-*c*]isoxazoles (12e). M.p. 221–223 °C. Yield 65% (0.066 g). IR(KBr) ν 3069, 3032, 2850, 1653, 1462, 1362, 1242, 1156, 794 cm^{-1}; ^1H NMR (300 MHz, $CDCl_3$) δ 8.09 (s, 1H, Ar-H), 7.62 (d, J = 9.1 Hz, 2H, Ar-H), 7.58 (d, J = 9.2 Hz, 2H, Ar-H), 7.40 (d, J = 8.7 Hz, 2H, Ar-H), 7.42 (s, 1H, CH-N), 7.33 (d, J = 8.2 Hz, 2H, Ar-H), 7.18 (d, J = 8.8 Hz, 2H, Ar-H), 6.80 (d, J = 9.4 Hz, 2H, Ar-H), 5.70 (d, J = 2.2 Hz, 1H, CH-O), 5.62 (d, J = 2.2 Hz, 1H, S-CH), 5.60–5.56 (m, 2H, =CH), 4.55 (s, 2H, OCH_2), 4.04–3.98 (m, 2H, CH), 3.96 (t, 2H, OCH_2), 2.32 (s, 3H, CH_3); ^{13}C NMR (75 MHz, $CDCl_3$) d 164.9, 162.5, 144.4, 141.3, 136.2, 134.2, 129.8, 128.8, 127.5, 125.9, 122.5, 119.5, 115.3, 84.5, 73.5, 71.8, 66.5, 63.9, 61.2, 40.1, 21.3; MS m/z (M^++H) 604. Anal. calcd. for $C_{31}H_{27}ClFN_5O_3S$: C, 61.63; H, 4.50; N, 11.59. Found: C, 61.48; H, 4.35; N, 11.43.

3-((5*R*)-5-((2*S*,3*S*)-3-((1-(4-Chlorophenyl)-1*H*-1,2,3-triazol-4-yl)methoxy)-3,6-dihydro-2*H*-pyran-2-yl)-3-(4-fluorophenyl)-3,3a-dihydrothiazolo[4,5-*c*]isoxazol-6(5*H*)-yl)phenol (12f). M.p. 228–231 °C. Yield 83% (0.084 g). IR(KBr) ν 3426, 3109, 1662, 1495, 1395, 1272, 1156, 712 cm^{-1}; ^1H NMR (300 MHz, $CDCl_3$) δ 9.46 (brs, 1H, Ph-OH), 8.12 (s, 1H, Ar-H), 7.61 (d, J = 9.7 Hz, 2H, Ar-H), 7.59 (d, J = 9.3 Hz, 2H, Ar-H), 7.44 (d, J = 8.6 Hz, 2H, Ar-H), 7.42 (s, 1H, CH-N), 7.18 (d, J = 8.4 Hz, 2H, Ar-H), 6.80–6.78 (m, 4H, Ar-H), 5.70 (d, J = 2.2 Hz, 1H, CH-O), 5.67–5.64 (m, 2H, =CH), 5.62 (d, J = 2.2 Hz, 1H, S-CH), 4.92 (d, J = 5.2 Hz, 1H, CHS), 4.62 (s, 2H, OCH_2), 4.09 (t, 2H, OCH_2), 4.01–3.99 (m, 2H, CH); ^{13}C NMR (75 MHz, $CDCl_3$) d 164.5, 162.1, 159.2, 144.8, 136.8, 130.9, 128.6, 126.9, 125.6, 124.1, 122.4, 119.1, 115.7, 112.8, 106.5, 98.2, 85.4, 84.6, 73.1, 72.5, 66.4, 63.9, 61.0, 40.5; MS m/z (M^++H) 606. Anal. calcd. for $C_{30}H_{25}ClFN_5O_4S$: C, 59.45; H, 4.16; N, 11.56. Found: C, 59.28; H, 3.95; N, 11.33.

4-((5*R*)-5-((2*S*,3*S*)-3-((1-(4-Chlorophenyl)-1*H*-1,2,3-triazol-4-yl)methoxy)-3,6-dihydro-2*H*-pyran-2-yl)-3-(4-fluorophenyl)-3,3a-dihydrothiazolo[4,5-*c*]isoxazol-6(5*H*)-yl)phenol (12g). M.p. 283–285 °C. Yield 88% (0.093 g). IR(KBr) ν 3639, 3072, 1654, 1618, 1482, 1379, 1294, 1150, 796 cm^{-1}; ^1H NMR (300 MHz, $CDCl_3$) δ 9.49 (brs, 1H, Ph-OH), 8.05 (s, 1H, Ar-H), 7.82 (d, J = 9.3 Hz, 2H, Ar-H), 7.56 (d, J = 9.2 Hz, 2H, Ar-H), 7.48 (d, J = 8.4 Hz, 2H, Ar-H), 7.30 (d, J = 8.6 Hz, 2H, Ar-H), 7.16 (d, J = 8.3 Hz, 2H, ArH), 7.05 (d, J = 8.8 Hz, 2H, ArH), 5.90–5.86 (m, 2H, =CH), 4.98 (d, J = 5.4 Hz, 1H, CHS), 4.63 (s, 2H, OCH_2), 4.12 (d, J = 2H, OCH_2), 4.02–3.96 (m, 2H, CH); ^{13}C NMR (75 MHz, $CDCl_3$) d 164.7, 161.8, 146.4, 144.4, 139.8, 137.0, 134.9, 134.3, 128.8, 126.9, 125.6, 122.0, 119.1, 116.7, 81.4, 73.6, 66.5, 64.0, 61.0, 40.9; MS m/z (M^++Na) 628. Anal. calcd. for $C_{30}H_{25}ClFN_5O_4S$: C, 59.45; H, 4.16; N, 11.56. Found: C, 59.18; H, 3.95; N, 11.63.

5. Conclusions

A series of novel pyranose glycosides **11a–g** and **12a–g** was prepared and evaluated for their antimicrobial activity; we found out that compounds **11b**, **12b**, **11d**, **12d**, **11g**, and **12g** possess high activity, while compounds **11a**, **12a**, **11c**, **11e**, **12e**, **11f**, and **12f** possess moderate activity against Gram positive strains. As far as Gram negative microorganisms are concerned, compounds **11a**, **12a**, **11f**, **12f**, **11b**, and **12b** showed high activity while compounds **11c**, **12c**, **11g**, and **12g** display moderate activity. Compounds **11e**, **12e**, **11g**, and **12g** also exerted high activity while compounds **11a**, **12a**, **11c**, **12c**, **11d**, **12d**, **11b**, and **12b** have moderate activity against fungi.

Acknowledgements

The authors are thankful to CSIR- New Delhi for the financial support (Project funding 02/247/15/EMR-II), Director, CSIR- IICT, Hyderabad, India, for NMR and MS spectral analysis.

6. References

1. A. Farran, C. Cai, M. Sandoval, *Chem. Rev*. **2015**, *115*, 6811–6853. **DOI:**10.1021/cr500719h
2. N. Galonde, K. Nott, A. Debuigne, *J. Chem. Tech. Biotechnol.* **2012**, *87*, 451–471. **DOI:**10.1002/jctb.3745
3. M. E. Caines, H. Zhu, M. Vuckovic, *J. Bio. Chem.* **2008**, *283*, 31279–31283. **DOI:**10.1074/jbc.C800150200
4. C. R. Bertozzi, L. L. Kiessling, *Chem. Glyc. Bio. Sci*. **2001**, *291*, 2357–2364. **DOI:**10.1126/science.1059820
5. V. K. Tiwari, R. C. Mishra, A. Sharma, R. P. Tripathi, *Mini Rev. Med. Chem.* **2012**, *12*, 1497–1519. **DOI:**10.2174/138955712803832654
6. R. Huisgen, G. Szeimies, L. Moebius, *Chem. Ber*. **1967**, *100*, 2494–2507. **DOI:**10.1002/cber.19671000806
7. R. Huisgen, *Angew. Chem. Int. Ed. Engl*. **1963**, *2*, 565–598. **DOI:**10.1002/anie.196305651
8. F. G. Heras, R. Alonso, G. Alonso, *J. Med. Chem.* **1979**, *22*, 496–501. **DOI:**10.1021/jm00191a007
9. (a) R. B. Patel, P. S. Desai, K. R. Desai, K. H. Chikalia, *Indian J. Chem., Sect. B* **2006**, *45B*, 773–778;
   (b) A. Bishnoi, S. Krishna, C. K. M. Tripathi, *Indian J. Chem. Sect. B* **2006**, *45B*, 2136–2139.
10. C. V. Dave, M. C. Shukla, *Indian J. Chem., Sect. B* **2000**, *39B*, 210–214.
11. W. J. Doran, H. A. Shoukla, *J. Org. Chem.* **1939**, *93*, 626–633.
12. J. S. Biradar, S. Y. Manjunath, *Indian J. Chem., Sect. B* **2004**, *43B*, 389–392.
13. N. P. Buu-Hoi, N. D. Young, F. Binon, *J. Chem. Soc*. **1948**, *70*, 3436–3439. **DOI:**10.1021/ja01190a064
14. B. R. Shah, N. C. Desai, P. B. Trivedi, *Indian J. Heterocycl. Chem., Sect. B* **1993**, *2*, 249–252.
15. L. L. Chijavasakaya, I. Gopnovich, R. S. Chelchenko, *Chem. Abstr*. **1969**, *70*, 10641y.
16. A. Chimmiri, S. Grasso, A. M. Monforte, P. Monoforte, M. Zappala, *II Farmaco* **1991**, *46*, 817–823.
17. V. M. Barot, *Asian J. Chem*. **1996**, *100*, 8802–8806. **DOI:**10.1021/jp952984y
18. M. H. Khan, Nizamuddin, *J. Food Agric. Chem.* **1995**, *43*, 2719–2729.
19. V. K. Ahulwalia, C. Gupta, *Heterocycles*, **1991**, *32*, 907–914.
20. H. D. Trautmen, L. M. Longe, *J. Am. Chem. Soc*. **1948**, *70*, 3434–3436. **DOI:**10.1021/ja01190a063
21. M. R. Manrao, J. Monika, V. K. Kaul, *Pl. Dis. Res*, **1997**, *12*, 94–96.
22. G. French, *Chem. Abstr.* **1996**, *65*, 4439.
23. T. Kato, T. Ozaki, N. Ohi, *Tetraherdon Asymetry* **1999**, *10*, 3963–3968. **DOI:**10.1016/S0957-4166(99)00441-3
24. R. B. Desyk, B. S. Zimenskovsky, *Curr. Org. Chem.* **1992**, *35*, 2712–2719.
25. Y. Tanabe, H. Yamamoto, M. Murakami, I. K. Yanag, Y. Kubota, Y. Sanimistu, G. Suzukamo, *J. Chem. Soc., Perkin Trans. 1* **1975**, *7*, 935–938.
26. J. T. Desai, C. K. Desai, K. R. Desai, *J. Iran. Chem. Soc*. **2008**, *5*, 67–73. **DOI:**10.1007/BF03245817
27. Y. C Sung, H. A. Jin, D. H. Jae, K. K. Seung, Y. B. Ji, S. H. Sang, Y. S. Eun, S. K. Sang, R. K. Kwang, G. C. Hyae, K. C. Joong, *Bull. Kor. Chem. Soc*. **2003**, *24*, 1455–1464.
28. Y. S. Lee, S. M. Park, B. H. Kim, *Bioorg. Med. Chem. Lett.* **2009**, *19*, 1126–1128.
29. J. Hansen, S. A. Stronge, *J. Heterocycl. Chem*. **1977**, *14*, 1289–1290.
30. T. K. Adhikari, A. Vasudeva, M. Girisha, *Indian J. Chem., Sect. B* **2009**, *48B*, 430–437.
31. S. Balalie, A. Sharifi, A. Ahangarian, *Indian J. Heterocycl. Chem.* **2000**, *10*, 149–150.
32. H. Kai, T. Ichiba, M. Tomida, H. Nakai, K. Morita, *J. Pest. Sci*. **2000**, *25*, 267–269. **DOI:**10.1584/jpestics.25.267
33. V. V. Kachadia, M. R. Patel, S. H. Joshi, *J. Sci. I. R. Iran* **2004**, *15(1)*, 47–51.
34. M. Mączyński, M. Zimecki, E. Drozd-Szczygieł, S. Ryng, *Cell. Mol. Biol. Lett*, **2005**, *10*, 613–618.
35. N. R. Nagar, V. H. Shan, *Indian J. Heterocycl. Chem.* **2003**, *13*, 173–175.
36. A. Srinivas, M. Sunitha, P. Karthik, G. Nikitha, K. Raju, B. Ravinder, S. Anusha, T. Rajasri, D. Swapna, D. Swaroopa, K. Srinivas, K. Vasumathi Reddy, *J. Heterocycl. Chem*, **2017**, *54*, 3250–3257. **DOI:**10.1002/jhet.2943
37. A. Srinivas, *Acta Chim. Slov.* **2016**, 63,173–179.
38. A. Srinivas, M. Sunitha, *Indian J. Chem., Sect. B* **2016**, *55B*, 102–109.
39. A. Srinivas, M. Sunitha, *Indian J. Chem., Sect. B* **2016**, *55B*, 231–239.
40. C. S. Reddy, A. Srinivas, M. Sunitha, A. Nagaraj, *J. Heterocycl. Chem*, **2010**, *47*, 1303–1309. **DOI:**10.1002/jhet.474
41. A. Srinivas, C. S. Reddy, A. Nagaraj, *Chem. Pharm. Bull.* **2009**, *57*, 685–693.

42. C. S. Reddy, A. Srinivas, A. Nagaraj, *J. Heterocycl. Chem.* **2009**, *46*, 497–502. **DOI:**10.1002/jhet.100
43. C. S. Reddy, A. Srinivas, A. Nagaraj, *J. Heterocycl. Chem* **2008**, *45*, 1121–1125. **DOI:**10.1002/jhet.5570450428
44. Y. L. Nene, P. N. Thapliyal, *Fungicides in Plant Disease Control*, IBH, New Delhi, India, 1982.

Povzetek

Z reakcijo med halkonskimi derivati (*R*,*Z*)-2-((2*S*,3*S*)-3-((1-(4-klorofenil)-1*H*-1,2,3-triazol-4-il)metoksi)-3,6-dihidro-2*H*-piran-2-il)-5-(4-fluorobenziliden)-3-feniltiazolidin-4-onov **10a**–**g** s fenilhidrazinom ali hidroksilamin hidrokloridom smo pripravili serijo novih (5*R*)-5-((2*S*,3*S*)-3-((1-(4-klorofenil)-1*H*-1,2,3-triazol-4-il)metoksi)-3,6-dihidro-2*H*-piran-2-il)-3-(4-fluorofenil)-2,6-difenil-3,3a,5,6-tetrahidro-2*H*-pirazolo[3,4-*d*]tiazolov **11a**–**g** in (5*R*)-5-((2*S*,3*S*)-3-((1-(4-klorofenil)-1*H*-1,2,3-triazol-4-il)metoksi)-3,6-dihidro-2*H*-piran-2-il)-3-(4-fluorofenil)-6-fenil-3,3a,5,6-tetrahidroizoksazolo[3,4-*d*]tiazolov **12a**–**g**. Kemijske strukture novih pripravljenih spojin smo določili z IR, NMR, MS in elementno analizo. Za spojine **11a**–**g** in **12a**–**g** smo določili tudi učinkovitost delovanja proti bakterijam in glivam.

Except when otherwise noted, articles in this journal are published under the terms and conditions of the Creative Commons Attribution 4.0 International License

DOI: 10.17344/acsi.2020.5832 *Acta Chim. Slov.* **2020,** *67,* 1072–1081
creative commons

Scientific paper

Removal of Trihalomethanes from Water using Modified Montmorillonite

Majid Hamouni Haghighat[1] and Ali Mohammad-Khah[1,2,*]

[1] *Department of Chemistry, Faculty of Science, University of Guilan, Rasht, Iran, P.O. Box 41635-19141*

[2] *Department of Water and Environmental Engineering, Caspian Sea Basin Research Center, University of Guilan, Rasht, Iran, P.O. Box 41635-1914*

** Corresponding author: E-mail: mohammadkhah@guilan.ac.ir*
Tel: +98-13-33343630-5(Ext.218), Fax: +98-13-33367262

Received: 01-12-2020

Abstract

Trihalomethanes (THMs) are formed during the water chlorination process through the reaction between chlorine and the organic materials. In this research, montmorillonite (MMT) and its modified form were used to remove the THMs from the water. The optimum conditions for the best adsorption capacity were evaluated using the Taguchi design of experiments. The result of comparing MMT with its modified sulfonated form (SMMT) indicated that SMMT is a more effective adsorbent than MMT. The evaluations showed that the optimum conditions for the THMs removal occur at 20 °C, 10 mg of adsorbent, 1 mg/L of THMs concentration, and 120 min for the adsorption time. The maximum adsorption capacity of $CHCl_3$, $CHBrCl_2$, $CHBr_2Cl$, and $CHBr_3$ was achieved: 0.49, 0.45, 0.43, and 0.38 mg/g at C_0 = 0.10 mg/L; 1.71, 1.62, 1.56, and 1.45 mg/g at C_0 = 0.50 mg/L; and 4.43, 4.35, 4.23, and 3.67 mg/g for C_0 = 5.00 mg/L, respectively. The THMs adsorption was compared between SMMT, powdered activated carbon (PAC), and granular activated carbon (GAC) and the results showed that SMMT is as effective as PAC and better than GAC and its production cost is lower than for the activated carbon.

Keywords: Acivated carbon; adsorption; clay; isotherm; langmuir; modification; montmorillonite; taguchi; trihalomethanes

1.Introduction

Trihalomethanes (THMs) are a group of chemicals which are the product of substituting the halogen atoms (F, Cl, Br, I) with three hydrogen atoms of methane. Studies have confirmed that in certain conditions, the water chlorination process creates the four well-known components including the chloroform (trichloromethane; $CHCl_3$), bromodichloromethane ($CHBrCl_2$), dibromochloromethane ($CHBr_2Cl$), and bromoform (tribromomethane; $CHBr_3$).[1]

The humic substances are the organic materials, which are widely spread in the aquatic environment. They are the major components of the natural organic matter and one of the important precursors of the THMs, most of which cannot be removed by the usual treatment processes. Because these materials produce the mutagenic and carcinogenic organic halogenated compounds during the chlorination of water, the THMs' removal from the drinking water is a critical undertaking.[2]

Researches have shown that the chloroform influences the respiratory system and it can trigger some respiratory allergies. Considering the other known side-effects of THMs such as liver and kidney damages, their effect on the reproduction, and their damaging effects on the nervous system and blood circulation,[3] there is no doubt about the health risk of THMs. THMs were categorized as class A carcinogen by the United States Environmental Protection Agency (USEPA) and the World Health Organization (WHO) in 1975. Both organizations emphasized on the necessity of removing these compounds from the drinking water. The USEPA guideline for the total THMs is 80 μg/L, while the guideline of WHO is 560 μg/L.[3,4,5]

Since 1980 ample research has been conducted on the removal of THMs and its precursors, and the THMs removal through the adsorption has been changed to an interesting subject. The powdered activated carbon (PAC) and the granular activated carbon (GAC) are widely employed as the industrial adsorbents of the THMs.[6,7,8] Ad-

sorbents such as activated carbon fibre,[9] modified synthetic carbon,[10] carbon nanotubes,[11] and nano-TiO_2[12] have also been studied.

The removal of the hazardous material by clays has been considered during the last 20 years, due to their low cost and high efficacy. Like the clay, the montmorillonite (MMT) could be an appropriate adsorbent for removing cations, heavy metals, and organic matter because of its special adsorption properties, the modification abilities, the low price, and availability. MMT is a set of dense layers with few nanometres close to each other and also the sodium or calcium cations as the interlayer ions. The structure of each layer of MMT consists of two types of octagonal and tetrahedral structural sheets. Each layer consists of an octahedral sheet located between two tetrahedral sheets. Water molecules, calcium, or sodium ions are between the two layers.[13] The modification of MMT changes its efficiency, and the acid modification is one of the improved methods to increase its adsorption capacity and catalytic properties. MMT is cheap, its modification process with acid has low cost and the price of the sulfonated montmorillonite (SMMT) is lower than the activated carbon. Ravichandran and Sivasankar used hydrochloride acid-activated MMT as a catalyst for the isopropylation of benzene.[14] The modification of montmorillonite clay with the 2-mercaptobenzimidazole and the investigation of their antimicrobial properties,[15] the sorption of naphthalene onto the modified MMT,[16] and the sorption of heavy metals from the automobile effluent[17] are examples of the acid-modified MMT applications.

Also, MMT and its modified forms were used to adsorb the sulfamethoxazole and tetracycline,[18] chromium(IV) retention,[19] cationic dyes,[20] tetracycline antibiotics,[21] acid Red 17,[22] calcium ion and bisphenol A,[23] bisphenol A,[24] rhodamine and hexavalent chromium,[25] thiabendazole,[26] and soil humic acid.[27]

In this study, the effects of MMT and its modified forms with the chlorosulfonic acid (SMMT) were evaluated for the adsorption of the THMs. Finally, the important factors such as the temperature, contact time, adsorbent amount, and the initial THMs concentrations were optimized by the Taguchi design of experiments.[28] Furthermore, the adsorption of THMs on the MMT and SMMT were compared for the powdered and granular activated carbon. The adsorption mechanism and the adsorption isotherms were also studied.

2. Experimental

2. 1. Preparation of SMMT and THMs Solutions

Chlorosulfonic acid (Merck KGaA, Darmstadt, Germany) was used for the sulfonation of MMT (calcium form) with the dimensions of 1–2 nm (Sigma-Aldrich, St. Louis, Missouri, United States) through the modification of the method developed by Shirini, Mamaghani and Atghia.[29] 100 mL beaker was filled with 1 g MMT, and 0.3 g chlorosulfonic acid was added slowly over a period of 30 min and the mixture was agitated by a glass rod. The beaker was put in an ice bath during the sulfonating period. After the sulfonating step, the product was dried for 3 h at 90 °C and then it was kept in a desiccator for the subsequent uses.

Based on the theory, there are 2.14 mmol sulfonic groups per 1 g SMMT. To determine the SMMT acidity, 50 ml of NaOH (0.1 M) was added to a 250 ml flask and the reaction product of 1 g MMT and 0.3 g sulfonic acid was added to the solution. The flask was placed on a shaker at 150 RPM for 2 h, and the solution was titrated with 0.1 M hydrochloric acid. Assuming that all the chlorosulfonic acid reacts with the MMT and the acidity belongs to the sulfonic groups, there is 2.00 mmol of sulfonic groups per gram of SMMT.

Scanning electron microscopy (SEM) (S-4160, Hitachi, Japan) was performed to determine the surface characterisation of MMT and SMMT. A very thin coating of gold was placed on the samples by sputtering at an accelerating voltage of 15 kV. The Fourier Transform Infrared (FTIR) spectra in the ATR mode were recorded using Magna-IR 560, Nicolet Ltd., England, in the range of 2000 to 650 cm^{-1} with 8 scans and a resolution of 2 cm.

X-ray diffraction (XRD) analysis was performed using XRD (INEL, Equinox 3000, France) diffractometer with Cu-Kα radiation.

The required solutions with different concentrations were prepared by diluting 2000 μg/mL standard solution of the THMs (Supelco Inc. Bellefonte, PA, USA). The concentrations of $CHCl_3$, $CHBrCl_2$, $CHBr_2Cl$, and $CHBr_3$ were equal and the deionized water with a conductivity of less than 0.5 μΩ/cm was used for the dilution.

2. 2. Design of the Experiments to Determine the Optimum Conditions using the Taguchi Design

The Taguchi design is a designed experiment that lets one choose a product or process that functions more consistently in the operating environment. The Taguchi design recognizes that all factors that cause variability could not be controlled. These uncontrollable factors are called the noise factors. The Taguchi design tries to identify the controllable factors (control factors) that minimize the effect of the noise factors. During the experimentation, one manipulates the noise factors to force the variability to occur and then identify the optimal control factor settings that make the process or product robust, or resistant to variation from the noise factors. A process that has been designed with this goal would produce more consistent output and would deliver more consistent performance regardless of the environment in which it is used.[30] Using the Minitab software (Minitab Inc., PA, USA) and the design of

experiments based on the Taguchi design, a number of tests for the four control factors, i.e., the adsorption temperature, the contact time, the adsorbent amount, and the initial concentration of THMs were run at three levels: adsorption temperature (10, 20, and 30 °C), contact time (10, 60, and 120 min), amount of adsorbent (10, 25, and 50 mg), and the total concentration of THMs (0.1, 0.5, and 1 mg/L). The effect of pH was not considered and all samples were prepared at neutral pH, because the water pH in water treatment plants is 6.5 to 7.5 and the pH of the water after chlorination was also in the same range.[31] Nine tests were performed according to the specified factors and levels. Each test was repeated three times, and the average of the results was used for the next calculations. The water temperature levels were set based on the average water temperature of the treatment plants at different seasons of the year in the northern part of Iran. The THMs levels were determined based on the USEPA and WHO guidelines.

2. 3. Batch Adsorption Tests

Considering the design of the experiments with the Taguchi design, the test conditions were determined in accordance with Table 1.

Table 1. Batch adsorption test conditions based on the Taguchi design of the experiment

Run	Adsorbent (mg)	Temperature (°C)	Total THMs concentration (mg/L)	Time (min)
1	10	10	0.1	10
2	10	20	0.5	60
3	10	30	1	120
4	25	10	0.5	120
5	25	20	1	10
6	25	30	0.1	60
7	50	10	1	60
8	50	20	0.1	120
9	50	30	0.5	10

The adsorbent was poured into 200 mL Erlenmeyer flask and the THMs solution was added. The flask opening was covered with parafilm and it was placed in a refrigerator shaker incubator (NB-205VL, N-BIOTEK, Korea) at 120 RPM. After the adsorption period, the concentrations of the THMs were determined by gas chromatography (Younglin, Korea) equipped with the Pulsed Discharge Electron Capture Detector (PDECD). Helium as the carrier gas with the flow of 6 mL/min, dopant gases (a mixture of 3% xenon in helium) with the flow rate of 3 mL/min, and a one-meter column of the same type as the main column (as pre-column to protect the main column) were used. Two microliters of the aqueous samples were injected using a split method with a ratio of one to five. The injector and the detector temperatures were set at 180 °C and 200 °C, respectively. Furthermore, the oven temperature was set at 90 °C for 3 min and then increased at 10 °C/min to 120 °C. Consequently, it remained at this temperature for 3 min.[32] In all cases, the THMs control solution without adsorbent was used to eliminate the effect of the factors other than the adsorption.[33] GAC (Merck, Darmstadt, Germany, with granular size about 1.5 mm, Merck No. 102514), PAC (Merck, Darmstadt, Germany, with particle size under 100 μm, Merck No. 122186), MMT and SMMT were used as the adsorbents.

2. 4. Adsorption Isotherms

Two well-known equations, i.e., the Langmuir and Freundlich equations describe the adsorption isotherms and they could be applied to the solid/liquid system. These two isotherms were used to study the THMs adsorption onto the SMMT. The Langmuir model is based on the monolayer adsorption and it follows the equation (1):

$$\frac{1}{q_e} = \frac{1}{a} + \frac{1}{abC_e} \quad (1)$$

Freundlich isotherm is based on the multilayer adsorption and it follows the equation (2):

$$\log q_e = \log k_f + \frac{1}{n}\log C_e \quad (2)$$

In the equation (1), C_e is the concentration of the adsorbate at the equilibrium time, q_e is the equilibrium adsorption capacity of the adsorbent, and a and b are the Langmuir constants. Moreover, in the equation (2), k_f and n are the Freundlich constants. To study the THMs adsorption isotherms, the THMs solutions with 8 different concentrations (0.10, 0.25, 0.50, 0.75, 1.0, 2.0, 5.0, and 10.0 mg/L) were prepared and eight 200 mL Erlenmeyer flasks were filled with 50 mL of each concentration of the THMs solution. The adsorption of THMs was measured after keeping for 150 min in the optimum conditions (10 mg adsorbent, 20 °C, and neutral pH) and the data were used to study the THMs' adsorption isotherms.

3. Results and Discussion

3. 1. Adsorption Properties of MMT and SMMT

Given the fact that the modification is a means to increase the adsorption properties of the MMT, the sulfonic groups were added to the structure of the MMT by the chlorosulfonic acid. Figures 1 and 2 show the SEM images of MMT and SMMT, respectively. The comparison of the figures indicates that the MMT surface changed after the sulfonation. This change in the surface can be due to the sulfonation of the surface and the reduction of interlayer water.

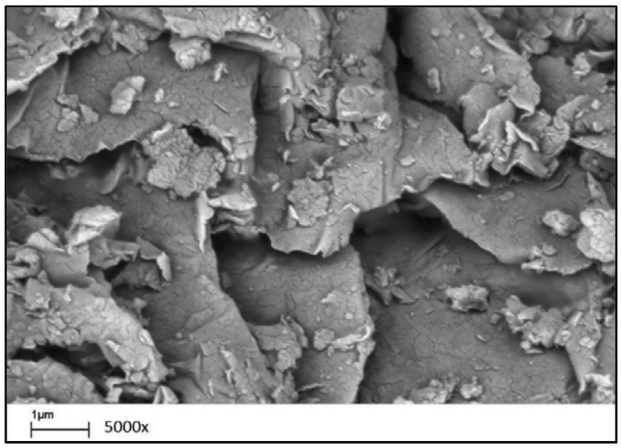


Figure 1. SEM image of MMT

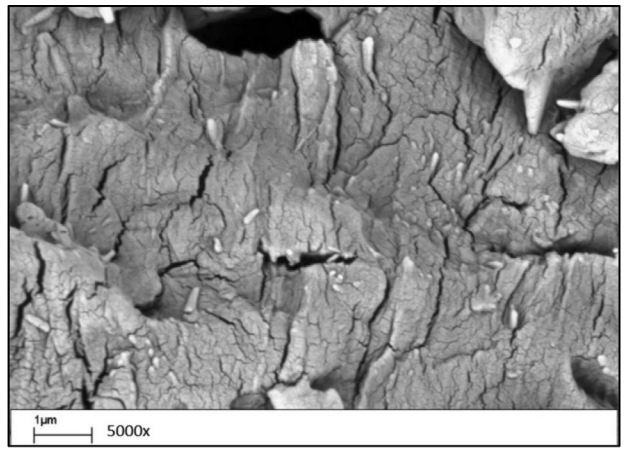


Figure 2. SEM image of SMMT

Figure 3 shows the FT-IR spectra of MMT and SMMT. In the spectrum (a), the peak at 1047 cm^{-1} is related to the stretching vibration of Si-O bond. The peak observed at 1640 cm^{-1} and the broad peak at 3420 cm^{-1} is the representation of crystalline water in MMT lattice. The peak at 3632 cm^{-1} could be attributed to the OH units in MMT. In the spectrum (b), the symmetric stretching vibration of S=O bond appears at 1045 cm^{-1}. The peak at 1058 cm^{-1} is related to the overlap of the asymmetric stretching vibration of S=O and stretching vibration of Si-O bonds. The peaks at 674 and 878 cm^{-1} are related to the stretching vibration of S-O bond. After the sulfonating, the interlayer water decreased and the peak at 1640 cm^{-1} disappeared (spectrum b) and the peak at 3314 cm^{-1} is related to the OH stretching vibration of SO_2-OH (sulfonic groups). As a result, the sulfonation of the MMT is confirmed.

Figure 4 shows the XRD images of MMT and SMMT. Based on the XRD image results, the crystalline structure appears to have changed after the sulfonating.

To confirm the effect of the sulfonation on the adsorption, the batch adsorption tests on the MMT and the SMMT were conducted under the same conditions with the Taguchi design (Table 1) and the total THMs adsorption percentage for MMT and SMMT were calculated. The results are demonstrated in Table 2.

To study the significance of the differences between each pair of the data that are mutually linked, the Wilcoxon signed-rank test was run.[34] The differences between them were significant ($p \leq 0.05$).

Since in the seven out of the nine tests, the total amount of the THMs adsorption on SMMT were more than on the other adsorbent, the sulfonation led to positive

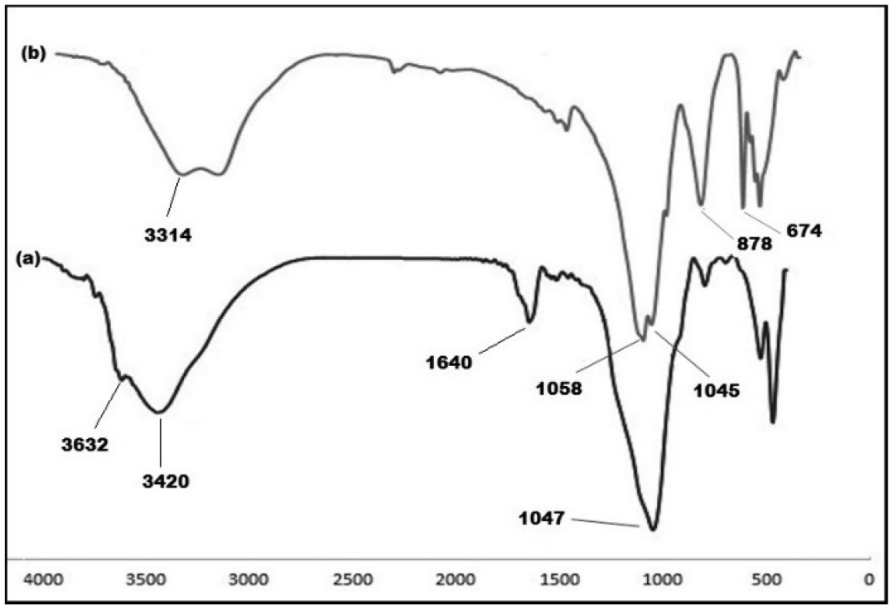


Figure 3. The FT-IR spectrum of MMT and SMMT

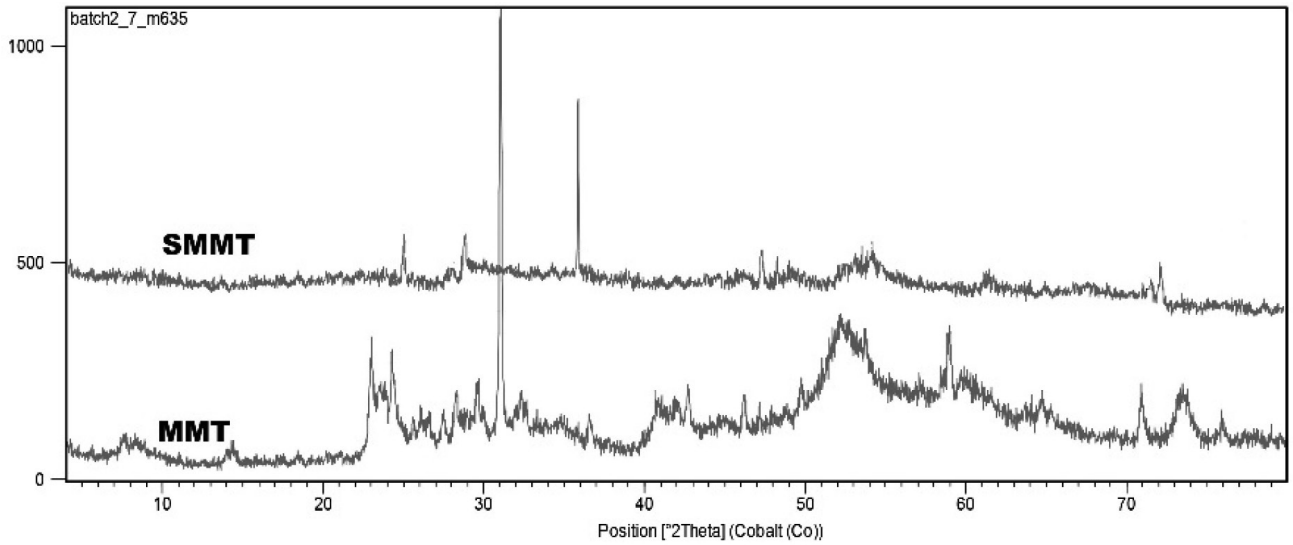


Figure 4. The XRD images of MMT and SMMT

Table 2. Batch adsorption test results based on the Taguchi design with the two adsorbents: MMT and SMMT

Run No.	Total adsorption % for MMT	Total adsorption % for SMMT
1	20.3 ± 0.6	25.3 ± 0.9
2	53.5 ± 2.5	74.0 ± 1.6
3	75.0 ± 2.4	64.1 ± 1.8
4	58.1 ± 0.8	64.2 ± 1.5
5	28.2 ± 1.3	56.2 ± 2.7
6	73.0 ± 1.5	69.8 ± 2.8
7	62.0 ± 2.5	80.6 ± 2.1
8	69.2 ± 2.9	84.3 ± 3.1
9	39.6 ± 0.8	41.7 ± 1.4

effects and it increased the adsorption and effectiveness of MMT. For further confirmation, the batch adsorption tests at the same conditions were conducted for the control factors (adsorbent: 10 mg per 50 mL solution, THMs concentration 1 mg/L, temperature 20 °C, and contact time 120 min) and for the two adsorbents, and each test was repeated 5 times. Also, the adsorption amount of THMs on the PAC and GAC (the two common adsorbents for the THMs removal) was determined and compared with MMT and SMMT. The results are shown in Table 3.

The result of the ANOVA (Analysis of Variance) test showed that there was a significant difference between the means of the two sets of data at $p \leq 0.05$ level of significance. As it was demonstrated in all of the 5 tests by SMMT, the total percentage of the THMs removal are more than at the other adsorbents, so the sulfonation increases the adsorption efficiency. Also, on average, 87% of the total THMs were removed by the sulfonated form (SMMT).

The average adsorption percentage for the PAC and GAC were 86.3% and 79.6%, respectively. There was a significant difference between the means of the PAC and GAC adsorption data at $p \leq 0.05$ and PAC was a more effective adsorbent than GAC. However, there was no significant difference between the means for SMMT and PAC. Therefore, based on experimental conditions, SMMT is as effective as PAC and it is better than GAC for the THMs removal.

Table 3. Results of the THMs batch adsorption percentage at the same conditions for MMT, SMMT, PAC, and GAC

	THMs adsorption% on MMT	THMs adsorption% on SMMT	THMs adsorption% on PAC	THMs adsorption% on GAC
Run 1	62.7	85.0	82.3	78.0
Run 2	61.0	86.5	85.7	80.2
Run 3	63.2	88.1	89.4	79.1
Run 4	60.5	85.7	88.9	78.7
Run 5	65.0	89.8	85.3	76.1
Mean	62.5	87.0	86.3	78.4
Standard deviation	1.8	1.9	2.9	1.5

3. 2. The Effect of the Contact Time, Adsorption Temperature, Initial Concentration of THMs, and the Amount of the Adsorbent on the Adsorption of THMs

Because of the better performance of the SMMT against MMT, SMMT was used in the further experiments. After the batch adsorption tests, which were run at the same conditions explained in Table 1, the adsorption capacity was calculated using the following equation (3):

$$q = \frac{(C_o - C_t)}{M} V \quad (3)$$

In this equation, q is the adsorption capacity, C_0 is the initial THMs concentration, C_t is the THMs concentration after the adsorption, M is the adsorbent amount and V is the THMs solution volume. All data were entered into the Minitab software, and the optimum conditions were calculated using the "Larger is Better" option by analysing the Taguchi design. The results are shown in Figure 5.

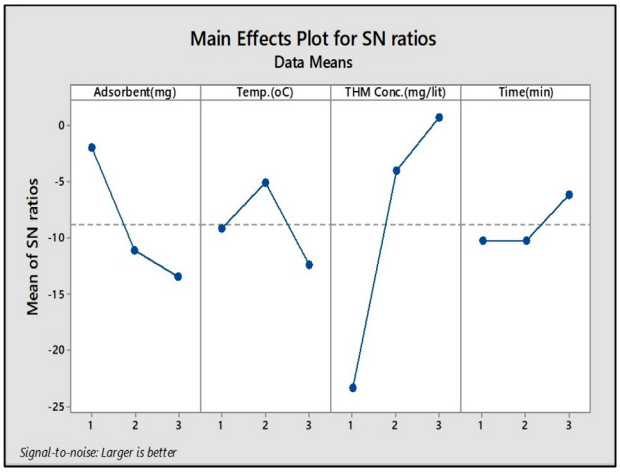


Figure 5. The results of the Taguchi design – adsorbent: 1= 10, 2 = 25, 3 = 50 mg; temperature: 1= 10, 2= 20, 3= 30 °C; the total concentration of THMs 1= 0.1, 2= 0.5 and 3 = 1 mg/L; and adsorption time: 1=10, 2= 60, 3=120 min. In each case the highest point indicates the optimum condition.

The optimum temperature to remove the THMs was 20 °C and the minimum adsorption capacity was acquired at 30 °C. Since an increase in the temperature over 20 °C leads to the decrease in the adsorption, it can be a sign of the physical adsorption on the surface of the adsorbent.

The analysis showed that the optimum adsorption capacity was obtained using 10 mg SMMT that indicated the good performance of the adsorbent. Furthermore, as expected, the analysis showed that the optimum contact time was 120 min. The Minitab calculation showed that the means of the signal to noise ratio (S/N) in the optimum condition was 14.2. The higher values of the S/N identified the best control factor setting and the minimum uncontrollable factor.[35] Moreover, the effect of the THMs contact time was determined via the three solutions with the initial and equal THMs concentrations of 0.1, 0.5, and a high concentration of 5.0 mg/L (C_0) and 10 mg adsorbent at 20 °C (the optimum conditions resulted from the Taguchi design for the adsorbent amount and temperature). The results are shown in Figures 6A, 6B and 6C.

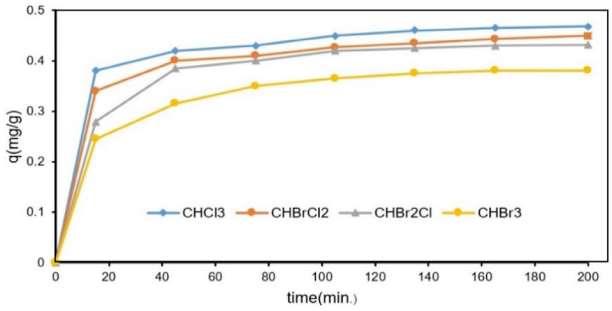


Figure 6A. Adsorption capacity of THMs over the time at the initial concentration of 0.1 mg/L and 10 mg adsorbent at 20 °C

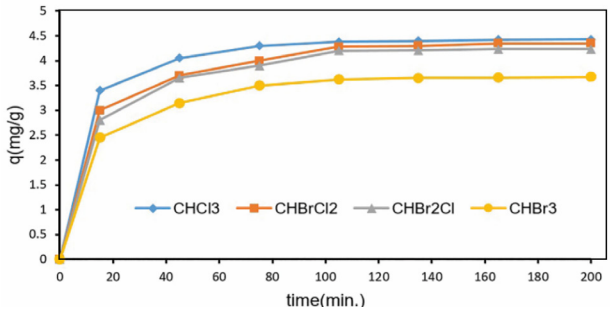


Figure 6B. Adsorption capacity of THMs over the time at the initial concentration of 0.5 mg/L and 10 mg adsorbent at 20 °C

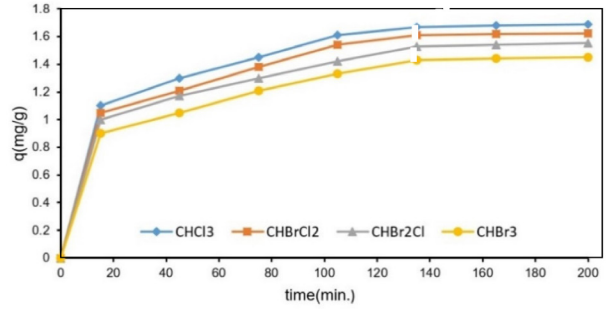


Figure 6C. Adsorption capacity of THMs over the time in the initial concentration of 5.0 mg/L and 10 mg adsorbent at 20 °C

The maximum adsorption capacities of SMMT (mg/g) for $CHCl_3$, $CHBrCl_2$, $CHBr_2Cl$, and $CHBr_3$ at the different initial concentrations of THMs (C_0) are shown in Table 4. The equilibrium time was 165 min for C_0 = 0.1 mg/L, 155 min for C_0 = 0.5 mg/L, and 120 min for C_0 = 5 mg/L. Since the increase of THMs concentration could in-

Table 4. The maximum adsorption capacity of SMMT (mg/g) for $CHCl_3$, $CHBrCl_2$, $CHBr_2Cl$, and $CHBr_3$ at different initial concentrations of THMs (C_0).

C_0 (mg/L)	$CHCl_3$	$CHBrCl_2$	$CHBr_2Cl$	$CHBr_3$
0.1	0.468	0.450	0.431	0.381
0.5	1.711	1.623	1.555	1.449
5	4.431	4.354	4.230	3.676

crease the diffusion flux through the THMs solution to the adsorbent surface, the adsorption occurs more quickly. The adsorption of $CHCl_3$ and $CHBr_3$ on SMMT resulted in the highest and the lowest capacity. This indicates that smaller molecules are adsorbed better than others. Over 70% of the THMs were adsorbed in 50 min, which shows the good adsorption efficiency of the adsorbent.

3. 3. Adsorption Mechanism

According to the Brunauer–Emmett–Teller (BET) analysis of MMT and SMMT, the specific surface area of MMT and SMMT were obtained as 180.2 and 138.7 m^2/g, respectively. The specific surface area decreased after the sulfonating of MMT because the sulfonation has changed the surface. The SO_3 groups cover the surface and the steric hindrance of the SO_3 group could reduce the N_2 adsorption on the surface of MMT. The larger group can further decrease the surface area.[36,37]

Several mechanisms could be proposed for adsorbing the organic matter on MMT as follows:

1– Physical adsorption–adsorption due to van der Waals' forces (the summation of the dipole-dipole interactions, the dipole-induced dipole interactions, and the induced dipole-induced dipole interactions).

2– Chemical adsorption

3– Hydrogen bonding

4– Coordination complexes [38]

Given the nature of the THMs, the weak polarity of these molecules and the presence of the OH groups at the surface of MMT, it seems that the physical adsorption on the surface is done because of the van der Waals' forces. By the reaction of the surface of MMT with chlorosulfonic acid, the SO_3 functional groups are replaced with the OH groups, van der Waals' interactions are enhanced and the adsorption is increased. Chloroform is more polar than the other THMs and this molecule has the highest adsorption. This can be a confirmation of the proposed adsorption mechanism. Since an increase in the temperature over 20 °C leads to a decrease in the adsorption, it could be a sign of the physical adsorption mechanism on the surface of the adsorbent.

3. 4. THMs Adsorption Isotherms

To determine the compatibility of the Langmuir or Freundlich isotherm with the THMs adsorption, the correlation coefficients of both lines were calculated according to the equations (1) and (2). The results are shown in Table 5.

The results showed that the correlation coefficients of the adsorption of the THMs on SMMT matched the Langmuir isotherm. All the correlation coefficients for the Langmuir isotherm were greater than 0.986. In the Freundlich isotherm, the poorest match was observed with a correlation coefficient of 0.9711 for $CHCl_3$. In the other THMs, the coefficients gradually became lower. Regarding the better match with the Langmuir isotherm, it could be stated that the maximum adsorption takes place on the surface of SMMT. The adsorption of THMs increases because the modification by chlorosulfonic acid affects the surface layers of MMT and enhances the van der Waals' forces. Considering the Freundlich isotherm, the correlation coefficients decreased from $CHCl_3$ to $CHBr_3$. The $CHCl_3$ molecule is the smallest THM, so it diffuses better among the layers. For the molecules larger than the $CHCl_3$, the multi-layer adsorption has decreased and in the case of the $CHBr_3$ it is minimized. The Langmuir isotherm charts are shown in Figure 7.

4. Conclusions

The World Health Organization and the United States Environmental Protection Agency have emphasized the necessity of the trihalomethanes' removal from the drinking water, so removing them and their precursors from the water sources is essential. Montmorillonite is a low-cost adsorbent, and it can remove a large quantity of the organic and inorganic contaminants from the water. Its performance could be improved by the sulfonic acid mod-

Table 5. Constants and correlation coefficients of the Langmuir and Freundlich isotherms

THMs	Langmuir isotherm			Freundlich isotherm		
	Correlation coefficient (R2)	a (mg/g)	b (L/mg)	Correlation coefficient (R2)	kf (mg/g)	n (L/mg)
$CHCl_3$	0. 9993	0.2698	8.85×10^{-3}	0.9711	4.41×10^{-3}	1.09
$CHBrCl_2$	0.9865	0.2621	7.51×10^{-3}	0.9654	3.84×10^{-4}	1.38
$CHBr_2Cl$	0.9895	0.2519	6.07×10^{-3}	0.9593	3.73×10^{-4}	2.41
$CHBr_3$	0.9947	0.2023	5.50×10^{-3}	0.8546	3.47×10^{-4}	5.23

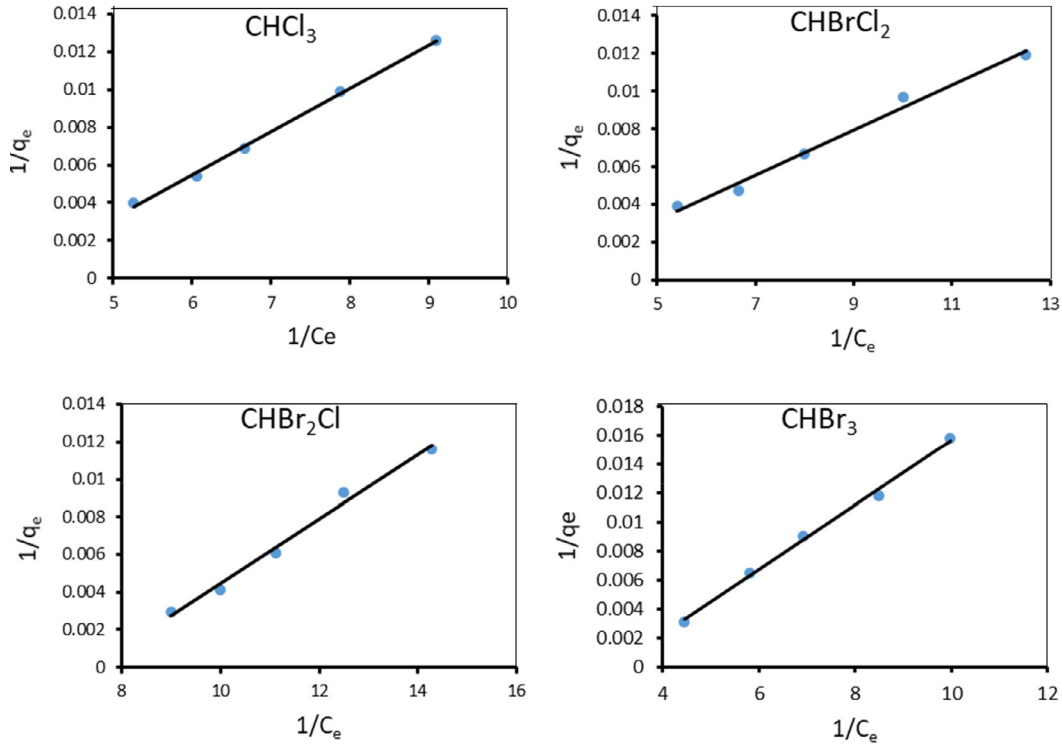


Figure 7. The Langmuir isotherm charts for THMs

ification. The results of this study showed that the sulfonated montmorillonite is as effective as powdered activated carbon and it is better than granular activated carbon for removing the trihalomethanes. Also its production cost is lower than for activated carbon. It has high adsorption capacity and short adsorption equilibrium time. Consequently, it is reasonable to use it as an ideal adsorbent to remove the trihalomethanes. Moreover, it could be used to improve the filtration system for the water treatment plants that use chlorine without any changes in the treatment system. The reaction of the chlorine with the organic materials in the swimming pools could lead to a high probability of the trihalomethanes formation. Using the sulfonated montmorillonite in the treatment process of the swimming pools could reduce or eliminate the trihalomethanes and the organic materials. The results showed that the adsorption of the trihalomethanes on the sulfonated montmorillonite matches the Langmuir isotherm.

Conflicts of interest

There are no conflicts of interest to declare.

5. Acknowledgments

The authors appreciate the office of the postgraduate studies of the University of Guilan for the financial support and also the Guilan Science and Technology Park for the laboratory support. Furthermore, they appreciate Dr. Hassan Zavvar Mousavi and Dr. Nematollah Omidikia for their valuable recommendations. Last but not least, they would like to thank Miss Mojgan Solouki, Mrs. Nour Rizk and Mr. Afshin Firoozmanesh for editing their manuscript.

6. References

1. J. J. Rook, *Water Treat. Exam.***1977,** *23*, 234–243. **DOI:**10.1049/ep.1977.0128
2. K. Roberts, Trihalomethane Formation and Control. *Proceeding of Safe Drinking Water Seminar*, Gander, Newfoundland, Canada, **2011.**
3. World Health Organization (WHO), Guidelines for Drinking Water Quality, https://www.who.int/water_sanitation_health/publications/drinking-water-quality-guidelines-4-including-1st-addendum/en/ (accessed: December 22, 2019).
4. United State Environmental Protection Agency (USEPA), National Primary Drinking Water Regulations, https://www.epa.gov/ground-water-and-drinking-water/national-primary-drinking-water-regulations (accessed: December 22, 2019).
5. Center for Disease Control and Prevention (CDC), Disinfection By-Products and the Safe Water System, http://www.cdc.gov/safewater/publications_pages/thm.pdf (accessed: December 22, 2019).
6. B. Lykins, R. Clark, J. Adams, *Granular activated carbon*

for controlling THMs (Trihalomethanes) (journal version). U.S. Environmental Protection Agency, Washington, D.C., EPA/600/J-88/051 (NTIS PB89104640).
7. R. J. Potwora, http://www.drinknwaterplus.com/documents/Trihalomethane%20removal.pdf (accessed: December 22, 2019).
8. I. N. Najm, V. L. Snoeyink, B. W. Lykins, J. Q. Adams, *Am. Water Works Assoc.* **1991**, *83*, 65–76. **DOI:**10.1002/j.1551-8833.1991.tb07087.x
9. A. Sakoda, M. Suzuki, R. Hirai, K. Kawazoe, *Water Res.* **1991**, *25*, 219–225. **DOI:**10.1016/0043-1354(91)90032-L
10. A. W. Morawski, M. Inagaki, *Desalination* **1997**, *114*, 23–27. **DOI:**10.1016/S0011-9164(97)00150-1
11. C. Lu, Y. L. Chung, K. F. Chang, *Water Res.* **2005**, *39*,1183–1089. **DOI:**10.1016/j.watres.2004.12.033
12. P. Gharbani, S.M. Tabatabaei, S. Dastmalchi, S. Ataie, A. Mosenharzandi, A. Mehrizad, *Int J Nano Dimens.* **2010**, *1*, 287–296. **DOI:**10.7508/ijnd.2010.04.007
13. R. Zhu, Q. Chen, Q Zhou, Y Xi, J Zhu, H He, *Appl. Clay Sci.* **2016**, *123*, 239–258. **DOI:**10.1016/j.clay.2015.12.024
14. J. Ravichandran, B. Sivasankar, *Clays Clay Miner.* **1997**, *45*, 854–858. **DOI:**10.1346/CCMN.1997.0450609
15. M. Edraki, D. Zaarei, *Int. J. Min. Met. Mater.* **2019**, *26*, 86–97. **DOI:**10.1007/s12613-019-1712-1
16 C. N. Owabor, U. M. Ono, A. Isuekevbo, *Adv. Chem. Eng. Sci.* **2012**, *2*, 330–335. **DOI:**10.4236/aces.2012.23038
17. K. G. Akpomie, F. A. Dawodu, *Beni-Suef Univ J. Basic Appl. Sci.* **2016**, *5*, 1–12. **DOI:**10.1016/j.bjbas.2016.01.003
18. M. Wua, S. Zhao, M. Tang, R. Jing, Y. Shao, X. Liu, Y. Dong, M. Li, Q. Liao, G. Lv, Q. Zhang, *Colloids Surf. A.* **2019**, *575*, 264–270. **DOI:**10.1016/j.colsurfa.2019.05.025
19. C. Morantes, F. Yarza, M. Montes, R. Mercader, G. Curutchet, R. S. Torres, *Water Air Soil Pollut.* **2020** *231*, 29–36. **DOI:**10.1007/s11270-020-4403-7
20. A. Afroozan, A. Mohammad-khah, F. Shirini, *J. Appl. Res. Water Wastewater* **2015**, *2*, 150–155. **DOI:**10.1016/j.clay.2015.08.001
21. H. Wu, H. Xie, G. He, Y. Guan, Y. Zhang, *Appl. Clay Sci.* **2016**, *119*, 161–169. **DOI:**10.1016/j.clay.2015.08.001
22. O. Acisli, A. Khataee, S. Karaca, M. Sheydaei, *Ultrason. Sonochrom.* **2016**, *31*, 116–121. **DOI:**10.1016/j.ultsonch.2015.12.012
23. C. Liu, P. Wu, Y. Zhu, L. Tran, *Chemosphere* **2016**, *144*, 1026–1032. **DOI:**10.1016/j.chemosphere.2015.09.063
24. Q. Yang, M. Gao, Z. Luo, S. Yang, *Chem. Eng. J.* **2016**, *285*, 27–38. **DOI:**10.1016/j.cej.2015.09.114
25. L. Ma, Y. Xi, H. He, G. A. Ayoko, R. Zhu, J. Zhu, *Appl. Clay Sci.* **2016**, *120*, 9–15. **DOI:**10.1016/j.clay.2015.11.010
26. M. Gamba, M. Olivelli, J. M. Lázaro-Martínez, G. Gaddi, G. Curutchet, R. M. T. Sánchez, *Chem. Eng. J.* **2017**, *320*, 11–21. **DOI:**10.1016/j.cej.2017.03.034
27. H. Chen, L. K. Koopal, J. Xiong, M. Avena, W. Tan, *J. Colloid Interface Sci.* **2017**, *504*, 457–467. **DOI:**10.1016/j.jcis.2017.05.078
28. K. R. Ranjit: Design of Experiments Using the Taguchi Approach: 16 Steps to Product and Process Improvement, John Wiley & Sons, USA, **2001.**
29. F. Shirini, M. Mamghani, S.V. Atghia, *j.Nanostructure in Chem.* **2012,** *3*, 2–5. **DOI:**10.1186/2193-8865-3-2
30. Minitab support webpage, https://support.minitab.com/en-us/minitab/18/help-and-how-to/modeling-statistics/doe/supporting-topics/taguchi-designs/taguchi-designs/ (accessed: July 09, 2020).
31. Chlorine disinfection of produce washwater, Michigan state university, https://msu.edu/~brook/publications/aeis/aeis653.htm (accessed: July 09, 2020)
32. M.H. Haghighat, A. Mohammad-Khah, *Asian J. Green Chem.* **2020**, *4*, 297–305 **DOI**: 10.33945/SAMI/AJGC.2020.3.6
33. S.M. Yakout, *Adsorption Sci. Tech.* **2010**, 28, 601–610 **DOI:**10.1260/0263-6174.28.7.601
34. S.W. Scheff: Fundamental Statistical Principles for the Neurobiologist, Elsevier Science, **2016.**
35. Minitab support webpage, http://support.minitab.com/en-us/minitab/17/topic-library/modeling-statistics/doe/taguchi-designs/what-is-the-signal-to-noise-ratio (accessed: December 22, 2019).
36. K. Song, G. Sandí, *Clays Clay Miner.* **2001**, *49*, 119–125. **DOI:**10.1346/CCMN.2001.0490202
37. D. Hillel: Environmental Soil Physics. Academic Press, New York, **1998.**
38. G. W. Bailey, J. L. White, T. Rothberg, *Soil Sci. Soc. Am. J. Abst.*, **1968**, *32*, 222–234. **DOI:**10.2136/sssaj1968.03615995003200020021x

Povzetek

Trihalometani (THM) nastanejo med procesom kloriranja vode v reakciji med klorom in organsko snovjo. V tej raziskavi smo uporabili montmorilonit (MMT) in njegovo modificirano obliko za odstranjevanje THM iz vode. Optimalne pogoje za najboljšo adsorpcijsko kapaciteto smo opredelili s pomočjo Taguchijevega eksperimentalnega načrta. Rezultati primerjave MMT z njegovo modificirano sulfonirano obliko (SMMT) so pokazali, da je SMMT bolj učinkovit adsorbent kot MMT. Preverjanje pogojev je pokazalo, da so optimalni pogoji za odstranjevanje THM pri 20 °C, 10 mg adsorbenta, koncentraciji THM 1 mg/L in adsorpcijskem času 120 min. Dosežena maksimalna adsorpcijska kapaciteta za $CHCl_3$, $CHBrCl_2$, $CHBr_2Cl$ in $CHBr_3$ je bila: 0,49, 0,45, 0,43 in 0,38 mg/g pri C_0=0,10 mg/L; 1,71, 1,62, 1,56 in 1,45 mg/g pri C_0=0,50 mg/L; ter 4,43, 4,35, 4,23 in 3,67 mg/g pri C_0=5,00 mg/L. Adsorpcijo THM smo primerjali med SMMT, uprašenim aktivnim ogljem (PAC) in granularnim aktivnim ogljem (GAC). Rezultati so pokazali, da je SMMT enako učinkovit kot PAC in boljši kot GAC, stroški njegove proizvodnje pa so nižji kot za aktivno oglje.

Except when otherwise noted, articles in this journal are published under the terms and conditions of the Creative Commons Attribution 4.0 International License

DOI: 10.17344/acsi.2020.5857 *Acta Chim. Slov.* **2020,** *67,* 1082–1091
creative commons

Scientific paper

Visible Light-Driven Photocatalytic Activity of Magnetic Recoverable Ternary $ZnFe_2O_4$/rGO/g-C_3N_4 Nanocomposites

Martin Tsvetkov,[1,*] Elzhana Encheva,[1] Albin Pintar,[2] and Maria Milanova[1]

[1] *Department of Inorganic Chemistry, Faculty of Chemistry and Pharmacy, St. Kl. Ohridski University of Sofia, J. Bourchier 1, 1164 Sofia, Bulgaria*

[2] *Laboratory for Environmental Sciences and Engineering, National Institute of Chemistry, Hajdrihova 19, 1001 Ljubljana, Slovenia*

* *Corresponding author: E-mail: mptsvetkov@gmail.com*

Received: 01-25-2020

Abstract

$ZnFe_2O_4$/rGO/g-C_3N_4 ternary nanocomposite photocatalysts with different $ZnFe_2O_4$/g-C_3N_4 weight ratio (0.5, 0.75, 1) were prepared by a stepwise solvothermal method using ethylene glycol as the solvent. Physicochemical methods such as X-ray diffraction, UV-Vis diffuse reflectance spectroscopy and photoluminescence spectroscopy were applied in order to characterize the composites. The formation of a meso-/macroporous structure with specific surface area between 67 and 77 $m^2\ g^{-1}$ was confirmed by N_2 adsorption/desorption. The bandgap of the composites was found to be lower (2.30 eV) than that of g-C_3N_4 (2.7 eV). In contrast to pure g-C_3N_4, the composites showed no fluorescence, i.e. no recombination of e^-/h^+ took place. All samples, including pure g-C_3N_4 and $ZnFe_2O_4$, were tested for adsorption and photocatalytic degradation of aqueous malachite green model solutions (10^{-5} M) under visible light irradiation ($\lambda > 400$ nm). The results show that the prepared nanocomposites have higher absorption and photocatalytic activity than the pristine g-C_3N_4 and $ZnFe_2O_4$ and can be successfully used for water purification from organic azo-dyes.

Keywords: Graphitic carbon nitride; reduced graphene oxide; zinc ferrite; photocatalysis; malachite green decomposition.

1. Introduction

Synthetic organic dyes are severe water pollutants causing environmental problems. They are typically aromatic compounds with structural variations, many of them resistant to degradation.[1] Among them, malachite green is an organic water pollutant known to be harmful for living creatures because of its potential carcinogenicity, mutagenicity and teratogenicity in mammals.[2] Depending on the polluted water composition, different methods have been applied in order to solve water contamination problems, including biological reactions,[3] sedimentation,[4–6] coagulation,[7,8] adsorption,[5] reverse osmosis,[9,10] membrane filtration,[11] ion exchange,[12] etc. Photocatalytic processes have also been applied, and much effort has been spent on the development of different semiconductors as photocatalysts among which TiO_2 and its modifications is well known.[13-18]

The aim of the research presented here is to develop new photocatalysts and to overcome the main limitation of TiO_2, i.e. its wide band gap (3.2 eV) that makes it active under UV light irradiation only (about 5% of sunlight). Recently the graphite analogue, graphitic carbon nitride, g-C_3N_4, raised interest due to its unique electronic structure. It is a non-metallic polymer with n-type semiconducting behavior and unique electrical, optical, structural and physicochemical properties. Like graphite, g-C_3N_4 has a two-dimensional planar π conjugation structure, able to enhance the electron transfer processes due to its excellent electronic conductivity.[19] With its medium-sized band gap and its thermal and chemical stability in ambient environment, it has become one of the most promising photocatalytic materials.[19] The interest in its application as a photocatalyst increased after its photocatalytic properties were discovered by Wang et al..[20] However, g-C_3N_4 also has some disadvantages such as a small specific surface area, a small number of active centers, quick recombination of the photo-induced e^-/h^+, low mobility of photoinduced e^-/h^+[21] and an wide band gap (2.7 eV).[22] These shortcomings can be avoided by adding a co-catalyst to g-C_3N_4 to pre-

pare nanocomposites. In recent years, particular interest has appeared in composites of g-C_3N_4 and reduced graphite oxide, rGO, due to the large specific surface area of rGO and its ability to efficiently separate photo-induced charges.[23] The above effect can also be achieved by combining g-C_3N_4 with multi-wall carbon nanotubes.[24] However, these nanocomposites can only solve two of the above disadvantages of g-C_3N_4 as a photocatalyst. The wide band gap of 2.7 eV limits the application of visible light. In order to use g-C_3N_4 as a photocatalyst with visible light, it may be combined with other semiconductor materials with a narrower forbidden zone. Due to its narrow band gap of 1.9 eV, $ZnFe_2O_4$ as a co-catalyst can absorb a wider range of visible light wavelengths. It may also show improved separation of photogenerated electron-hole pairs. Its magnetic properties facilitate the removal of the composites from the reaction mixture, so they can be reused.[25] In the literature available, there are publications presenting studies on triple nanocomposites such as $CoMoS_2$/rGO/C_3N_4 with visible light photocatalytic activity for hydrogen evolution,[26] C_3N_4/rGO/TiO_2[27,28] for decomposition of methyl orange, rhodamine B, and phenol under visible light, and C_3N_4/rGO/WO_3 for degradation of methylene blue.[29] Both the studies mentioned and our experience with $ZnFe_2O_4$ as photocatalyst suggested that $ZnFe_2O_4$/rGO/g-C_3N_4 would be a promising composition to study, as it potentially could overcome g-C_3N_4 shortcomings as photocatalyst as well as take advantage of rGO for the separation of photo-induced charges. The photocatalytic properties of the nanocomposites $ZnFe_2O_4$/rGO/g-C_3N_4 were tested for removal of malachite green as representative pollutant under visible light irradiation, showing better activity than the individual semiconductors. The work presented here on the preparation and the properties of $ZnFe_2O_4$/rGO/g-C_3N_4 can contribute both to the knowledge of inorganic synthesis of such composites and to the improved photocatalytic removal of organic dyes from water.

2. Experimental

2. 1. Materials

Chemicals such as urea (puriss. p.a., Fluka, Switzerland), graphite, $Zn(NO_3)_2 \cdot 6H_2O$, $Fe(NO_3)_3 \cdot 9H_2O$, and $CH_3COONa \cdot H_2O$ (all p.a., Sigma-Aldrich, USA) were used in this study.

2. 2. Synthesis of the Samples

2. 2. 1. Synthesis of Graphitic Carbon Nitride, g-C_3N_4

Thermal polycondensation of urea in a closed crucible at 550 °C for 5 h was applied. The powder was dispersed in water and homogenized by stirring for 1 h, followed by filtering, washing and drying at 50 °C overnight. The successful synthesis was confirmed by XRD and TEM analyses.

2. 2. 2. Synthesis of Reduced Graphene Oxide, rGO

Graphene oxide was prepared by using the modified Hummer's method starting from graphite flakes.[30] In a typical procedure, 0.5 g of graphite was dispersed in 50 mL mixture of conc. H_2SO_4 and conc. H_3PO_4 (volume ratio 9:1) and then ultrasonicated for 1 hour. After that, 6 g of $KMnO_4$ was added and magnetically stirred for 5 h followed by 12 h stirring at 50 °C. The so prepared mixture was cooled to room temperature and transferred in a beaker containing 100 g of ice. After stirring and melting of the ice, 20 mL of 30% H_2O_2 solution was added dropwise in order to remove the unreacted $KMnO_4$. The suspension immediately changed its color from purple to yellow, indicating the formation of graphene oxide. The solid phase was separated by filtration and then dispersed in 100 mL of 5% HCl solution in order to remove all the metal cations and then separated again by centrifugation and washing with water untill a pH = 7. The GO obtained was reduced further to rGO by hydrothermal treatment in a PTFE-lined autoclave at 180 °C for 12 h using hydrazine as a reducing agent.

2. 2. 3. Synthesis of the Composites $ZnFe_2O_4$/rGO/g-C_3N_4

A solvothermal method was used to prepare the composites. The metal salts $Zn(NO_3)_2 \cdot 6H_2O$ and $Fe(NO_3)_3 \cdot 9H_2O$ were dissolved in 50 mL of ethylene glycol, EG, with ratio $n(Zn^{2+}):n(Fe^{3+}) = 1:2$. The rGO was added and dispersed by 30 min magnetic stirring and 2 h of sonication. After g-C_3N_4 was added, the suspension was stirred for 30 min by magnetic stirring, followed by 30 min sonication in an ultrasonic bath. After adding 3 g of $CH_3COONa \cdot 2H_2O$ and stirring for 30 min, the metal ions were precipitated. The mixture was transferred to a 75 mL PTFE autoclave and kept at 180 °C for 24 h. By varying the $ZnFe_2O_4$/g-C_3N_4 mass ratio (0.5, 0.75, 1), three $ZnFe_2O_4$/rGO/g-C_3N_4 composites containing 5 wt% rGO were prepared. They are mentioned further in the text as CN50 ($ZnFe_2O_4$: g-C_3N_4 = 0.5), CN75 ($ZnFe_2O_4$: g-C_3N_4 = 0.75), and CN100 ($ZnFe_2O_4$: g-C_3N_4 = 1).

2. 3. Methods for Characterization of the Samples

X-Ray Diffraction to determine the crystal structure of the materials was performed using a PANalytical Empyrean X-ray diffractometer in the 2θ range of 15–80° using CuKα radiation (λ = 0.15405 nm) for the nanocomposites and in 2θ range of 10–80° for the individual components, steps of 0.01° and 20 seconds exposure time at each step. The average crystallite size was calculated using the well-known Scherrer's equation.[31] The microstructural information of the $ZnFe_2O_4$ was extracted by

full profile Rietveld method using the FullProf Suite software.[32] *UV-Vis absorption spectroscopy* was applied using an Evolution 300 UV-Vis spectrometer (Thermo Scientific) for measuring the absorption of the samples in the range of 200-900 nm. *Bandgap energies* were calculated from the UV-Vis absorption spectra in the range from 200 to 400 nm according to Tauc's equation $\alpha h\nu = A(h\nu - E_g)^{n/2}$, where A is a constant independent of $h\nu$, E_g is the semiconductor bandgap and n depends on the type of transition.[33] *Textural characteristics* such as specific surface area, total pore volume, and pore size distribution were determined at –196 °C using a TriStar II 3020 apparatus (Micromeritics). The total pore volume was estimated at a relative pressure P/P_0 0.989. *Transmission electron microscopy* (TEM): a JEOL JEM 2100 microscope was used at 200 kV and up to 100k magnification for characterization of the morphology of the samples. *Particle size distribution analysis* was performed by using ImageJ software.[34]

2. 4. Photocatalytic Tests

The photocatalytic tests were performed using a slurry of 0.5 g catalyst L^{-1} and a 10^{-5} M aqueous solution of Malachite Green oxalate (MG), (Chroma GmbH) as a model pollutant. The equipment and the procedure applied were similar with those used in our previous studies.[14–18,35,36] For illumination 15W white LED (manufactured by V-TAC), 418–700 nm, situated at 10 cm distance above the slurry was used.

3. Results and Discussion

3. 1. Characterization of the Samples

3. 1. 1. Characterization of the Phase Composition by X-ray Diffraction

The phase composition, cell parameters and crystallite size of the samples were determined using the X-ray diffrac-

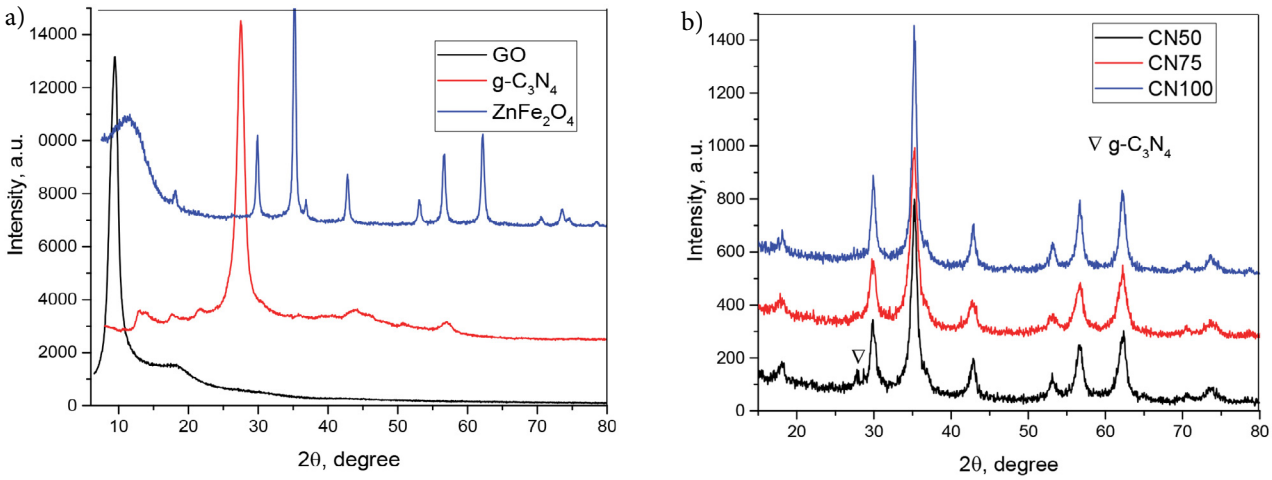


Figure 1. XRD patterns, from bottom to top (a) of the initial samples r-GO, g-C_3N_4, $ZnFe_2O_4$ and (b) of the nanocomposites CN50, CN75, CN100

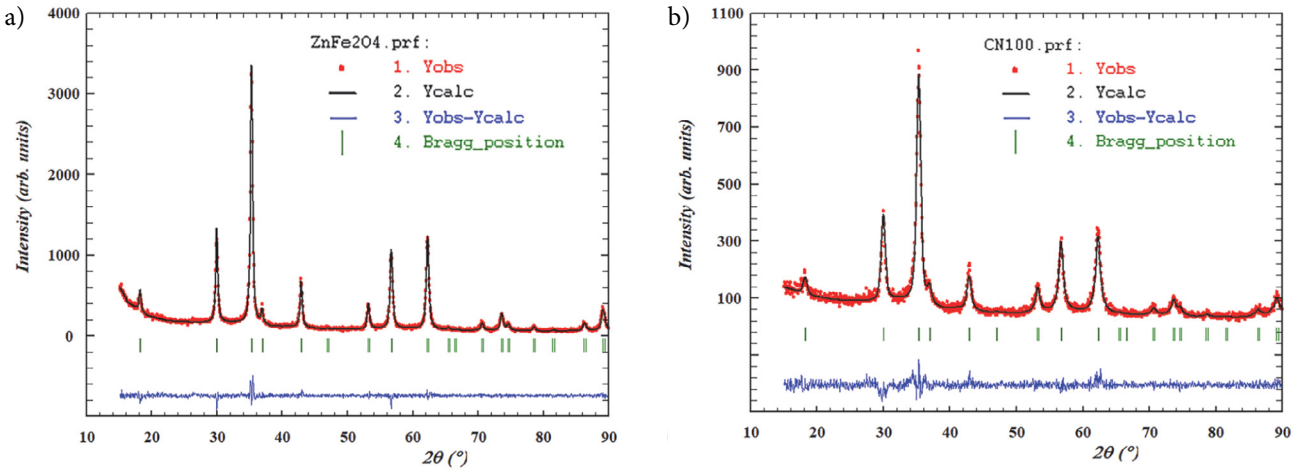


Figure 2. Experimentally observed (dots), Rietveld calculated (continuous line) and difference (continuous bottom line) profiles, obtained after Rietveld analysis of the XRD data (a) $ZnFe_2O_4$ and (b) the composite CN100. Peak positions are shown at the base line as small markers.

tion analysis. The composition of the initial substances r-GO, g-C_3N_4 and $ZnFe_2O_4$ were confirmed (Fig. 1, a). The strong diffraction peak observed at 27° 2theta in the pure g-C_3N_4 can be assigned to the (002) diffraction plane of layered g-C_3N_4 (JCPDS 87-1526) (Fig. 1, a). It corresponds to the characteristic interlayer stacking of aromatic segments.[37] The nanocomposites mainly show the presence of $ZnFe_2O_4$ (Fig. 1, b). The presence of g-C_3N_4 in the composites is detected below 30° 2theta shown by an inversed "Δ" (Fig. 1, b).

Rietveld analysis of the XRD data of $ZnFe_2O_4$ and the composite CN100 was performed (Fig. 2, a, b). The information obtained by the Rietveld refinement was the crystallite size and microstrains as both are related (to extend) to the catalytic properties of the materials.[38,39]

This is also proven by the BET measurements as it can be seen later in the text (Part 3.1.3). On the other side, the microstrains are related to the density of the defects in the crystal structure. The defects, known as active centres in catalysis, are places (especially on the surface) with lower potential energy where the reaction between solid/liquid (or solid/vapor) occurs. Although this is not always true in context of photocatalysis as defects can also act as recombination centres for photogenerated e^-/h^+ pairs leading to lower activity.

The lattice parameters, crystallite size, and the microstrain of the composites and the pure $ZnFe_2O_4$ are shown in Table 1. It can be seen that the increasing content of $ZnFe_2O_4$ in the composites is causing changes in all the parameters mentioned. All the values are getting closer to those of the pure $ZnFe_2O_4$. The microstrain is decreasing in the line 0.0177 (CN50), 0.0147(CN75), 0.0116 (CN100), and 0.0053 for the pure $ZnFe_2O_4$, respectively. The structure of the composites is more defective at lower zinc ferrite content. The latter can be observed in the reduction of the unit cell volume as a result of the microstrains.

3. 1. 2. Characterization of the Sample Morphology by TE

The morphology and the structure of as-synthesized samples observed by TEM are shown in Figure 3. The layered structure of the individual g-C_3N_4 can be seen in Fig. 3, a. The $ZnFe_2O_4$ particles are flower-shaped on the surface of g-C_3N_4 (Fig. 3, b). The electron diffraction of the samples g-C_3N_4 and $ZnFe_2O_4$ is shown in Fig. 3, c, d, respectively. It is used as supplementary analysis to the XRD and approves the successful preparation of $ZnFe_2O_4$ and g-C_3N_4.

With increasing $ZnFe_2O_4$ content in the composites, polydispersed agglomerates are formed. The particle size distribution for CN50 is between 5–10 nm (Fig. 3, e), in accordance with the XRD data.

3. 1. 3. Textural Characterization

Nitrogen adsorption – desorption isotherms measured at −196 °C on powdered samples (Fig. 4, a) showed that the samples are of type IV, which is the typical characteristic of mesoporous materials according to the IUPAC classification.[40] The isotherm of $ZnFe_2O_4$ with H1 loop is typical for well-defined cylindrical pores or agglomerates of approximately uniform spheres (Fig. 4, a). The H3 loop for the g-C_3N_4 and the composites are distinctive for non-rigid aggregates of plate-like particles with slit-shaped pores. The hysteresis loops observed are characteristic of mesoporous solids and their shape exhibits a change in the pore structure. Macropores may be present as well, based on the shape of the hysteresis loops near $P/P_0 = 1$.[41] The average pore size is rather close for the samples g-C_3N_4, CN50 and CN75 (Table 2), while that of $ZnFe_2O_4$ is larger and that of CN100 smaller. The composites show a maximum in the pore size distribution at about 25–50 nm,

Table 1. Lattice parameters, crystallite size and microstrain; CN50 ($ZnFe_2O_4$: g-C_3N_4 = 0.5), CN75 ($ZnFe_2O_4$: g-C_3N_4 = 0.75), and CN100 ($ZnFe_2O_4$: g-C_3N_4 = 1).

Sample	Unit cell, Å	Crystallite size, nm	Microstrain, %	R_{wp}, %	χ^2
CN50	8.4312 ± 0.0007	8 ± 0.2	1.77	9.1	1.74
CN75	8.4321 ± 0.0005	9 ± 0.4	1.47	8.4	1.71
CN100	8.4325 ± 0.0003	11 ± 0.4	1.16	7.9	1.68
$ZnFe_2O_4$	8.4342 ± 0.0002	23 ± 0.3	0.53	7.2	1.53

Table 2. Textural characteristics of the samples studied.

Sample	Specific surface area, S_{BET}, $m^2\ g^{-1}$	Total pore volume, V_{total}, $cm^3\ g^{-1}$	Average pore size, $D_{average}$, nm
g-C_3N_4	88	0.47	22
$ZnFe_2O_4$	34	0.27	32
CN50	72	0.44	25
CN75	77	0.44	23
CN100	67	0.23	14

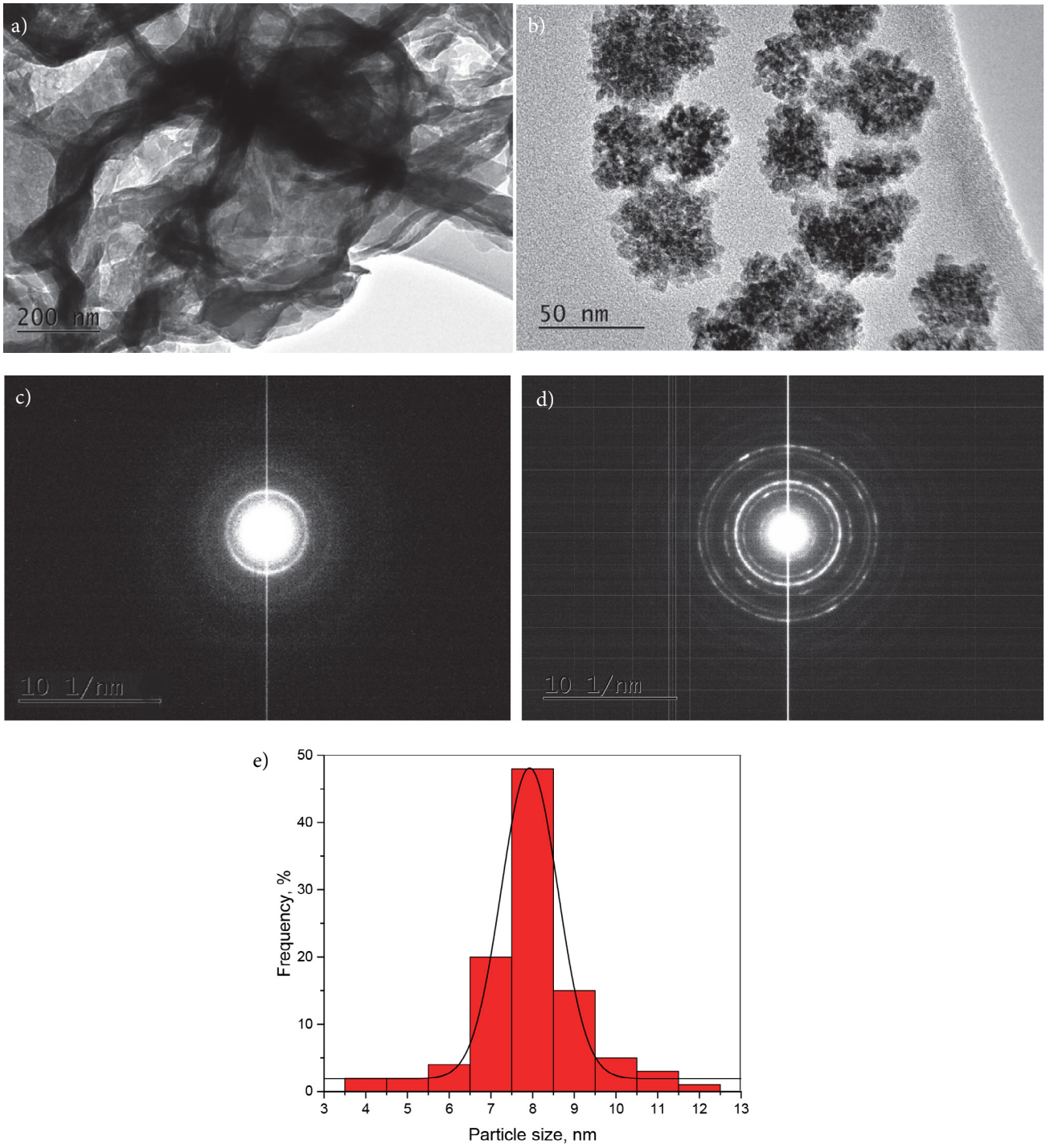


Figure 3. TEM micrographs of (a) g-C_3N_4 and (b) CN50 presented along with the electron diffraction (c) and (d), respectively. The particles size distribution for CN50 is shown in (e).

while CN100 shows a broad polydispersed pore size distribution (Fig. 4, b).

The pure g-C_3N_4 sample has the largest specific surface area, 88 $m^2 g^{-1}$, while pure $ZnFe_2O_4$ with 34 $m^2 g^{-1}$ has the lowest one among the samples tested (Table 2). In spite of the statement that g-C_3N_4 exhibits low S_{BET},[42] 88 $m^2 g^{-1}$ is a reasonably good value, comparing for example with 9.6 $m^2 g^{-1}$ reported in ref.[42] for g-C_3N_4 obtained by the same hydrothermal method for 48 h/180 °C (12 h/180 °C in present work). Apparently, the duration of the hydrothermal treatment is influencing the agglomeration of the sample. The addition of rGO and $ZnFe_2O_4$ caused a reduction of the specific surface area leading to composites with 77, 72, and 67 $m^2 g^{-1}$ surface area, which could be due to

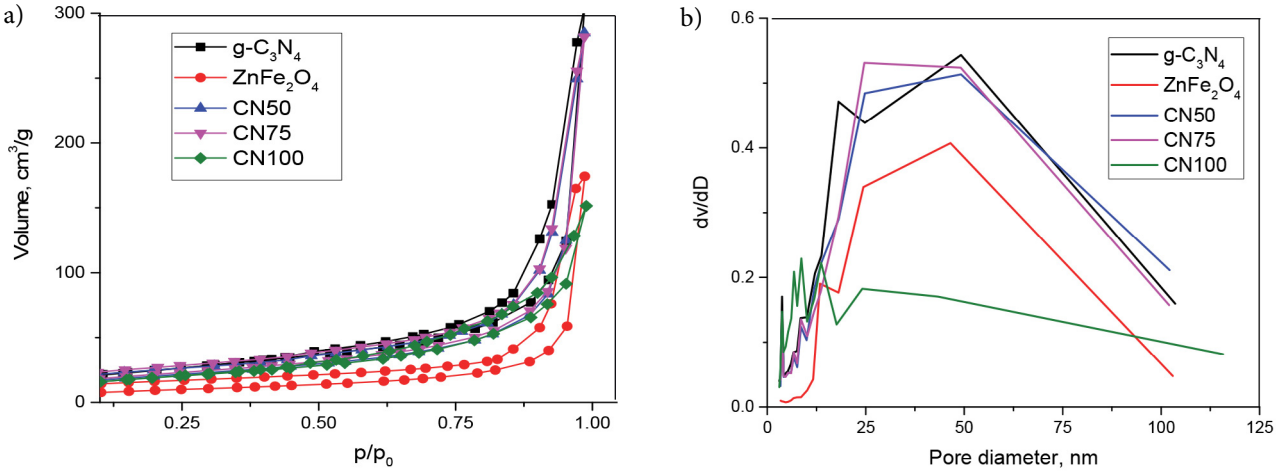


Figure 4. Adsorption-desorption isotherms of the pure g-C_3N_4 and $ZnFe_2O_4$, and the composites CN50, CN75, CN100 (a) and BJH pore diameter distribution, determined from the desorption branch of the isotherm (b); V- pore volume, D – pore diameter.

their deposition on the pores of carbon nitride. Quite likely the presence of g-C_3N_4 inhibits the agglomeration of $ZnFe_2O_4$ particles and makes them uniformly dispersed.

3. 2. Optical and Photocatalytic Properties

3. 2. 1. Optical Properties

The UV/Vis spectra of g-C_3N_4, $ZnFe_2O_4$ and the composites are presented in Fig. 5, a, clearly showing enhanced light absorption of the composites, probably due to interfacial interaction between g-C_3N_4 and $ZnFe_2O_4$.[43] It can be expected that the enhanced light absorption could lead to higher photocatalytic activity by generating more photoinduced charge carriers under visible light. Based on these UV/Vis spectra, the band gap energy was calculated for all the samples (Fig. 5, b). The values for the similar band gaps of the composites with energy of 2.30–2.31 eV (538–536 nm), between the values of g-C_3N_4, 2.7 eV (458

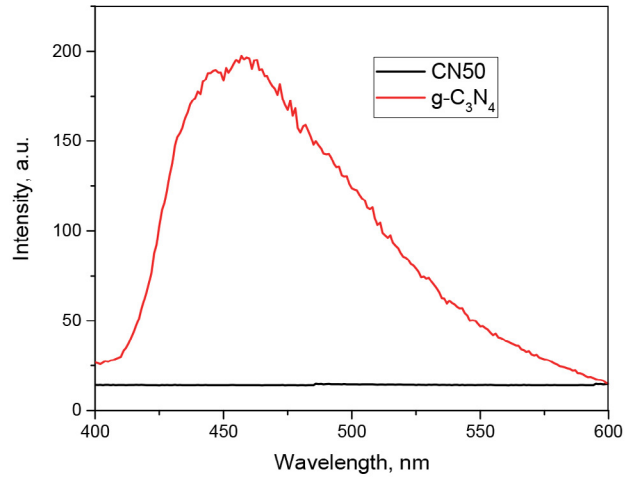


Figure 6. Typical photoluminescence of g-C_3N_4, compared with the absence for CN50.

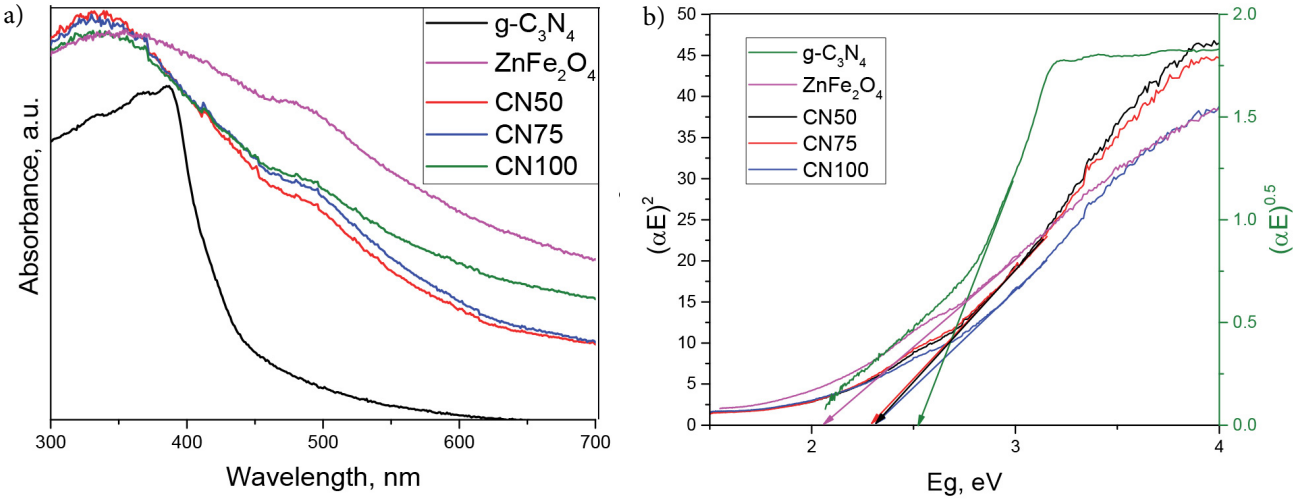


Figure 5. (a) UV/Vis spectra and (b) the energy of the forbidden zone, E_g, for all the samples studied

nm) and $ZnFe_2O_4$, 2.06 eV (600 nm), confirm their prospective for photocatalytic activity higher than that of g-C_3N_4.

Such a prospective is also indicated by the absence of fluorescence in the composites, which provides evidence for efficient inhibition of radiative recombination of photogenerated e^-/h^+ (Fig. 6). The strong fluorescence of the pure g-C_3N_4 related to strong e^-/h^+ recombination (Fig. 6), may explain the low photocatalytic activity of the pristine sample.

3. 2. 2. Degradation of Malachite Green Under Visible Light Irradiation

The photocatalytic performance of the samples for degradation of malachite green under visible light illumination is shown in Fig. 7. In the given range of reaction conditions, adsorption of malachite green on the catalyst surface cannot be neglected (Table 3). However, this was well considered in the subsequent interpretation of collected experimental data. The relevant data for the rate constants are summarized in Table 3.

The rate constant obtained for the photolysis was 0.6 × 10^{-3} min^{-1}. The pure samples g-C_3N_4 and $ZnFe_2O_4$ showed low values for their rate constants: 2.9 and 4.6 × 10^{-3} min^{-1}, respectively. The rate constants of the composites were higher, and showed increasing values with increasing $ZnFe_2O_4$/g-C_3N_4 ratio (0.5, 0.75, 1), i.e. 4.0 × 10^{-3}, 5.1 × 10^{-3} and 7.7 × 10^{-3} min^{-1}, respectively. Apparently, $ZnFe_2O_4$ and g-C_3N_4 show a synergetic effect, which is best demonstrated for the composite CN100. The highest degradation of malachite green achieved was 63 % for 150 min illumination with visible light. In Table 3, the data for the ratio k/S_{BET} (min^{-1} g m^{-2}) are presented, showing the best activity for $ZnFe_2O_4$, followed closely by the composite CN100.

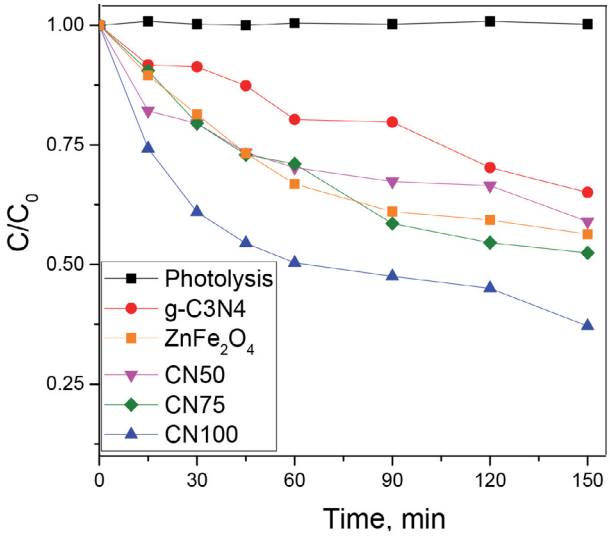


Figure 7. Photocatalytic performance of as-prepared samples for degradation of malachite green under visible-light illumination.

The observed photocatalytic activity may be correlated to the physical properties of the catalysts, such as: *(i)* Surface area: the largest S_{BET} surface area of g-C_3N_4 among the samples tested could provide more active sites to adsorb and convert MG molecules in comparison with the $ZnFe_2O_4$ and the composites. However, this is not observed; g-C_3N_4 may be less active than expected because of its strong e^-/h^+ recombination shown by the fluorescence (Fig. 6). Among the composites, CN100 has less than average S_{BET} but showed the best photocatalytic activity. *(ii)* Large pore volume: it would favor the diffusion of MG molecules within the pores towards the active sites on the surface of the photocatalysts. However, g-C_3N_4 with the largest pore volume shows the lowest activity. *(iii)* Pore size distribution: The composite CN100 has a very broad pore size distribution showing best activity i.e. positively influencing the activity (Fig. 4, b). *(iv)* Bandgap energy: among all samples tested, the composites have the lowest and equal value for E_g but show different activity. Thus the band gap energy alone cannot explain all differences; the activity is determined by a combination of factors. From this it can be concluded that the most active composite CN100 has an optimum combination of band gap value, $ZnFe_2O_4$/g-C_3N_4 ratio and absence of e^-/h^+ recombination. The rGO, being present in equal amounts for all the composites, has the function of solid-state electron mediator,[28, 29] adsorbent, photosensitizer and electron acceptor.[28]

For the discussion of the mechanism of the photocatalytic reaction, the values of the band edges i.e. the potentials of the current band (CB) and the valence band (VB) of the semiconductors $ZnFe_2O_4$ and g-C_3N_4 should be considered. Some of the literature data are summarized

Table 3. Rate constants and extent of malachite green removal based on adsorption on the catalyst surface and degradation.

Sample	Rate constant, × 10^{-3} min^{-1}	Rate constant to S_{BET}, × 10^{-4}, min^{-1} g m^{-2}	Adsorption, %	Degradation after 150 min, %
g-C_3N_4	2.9	0.395	47	35
$ZnFe_2O_4$	4.6	1.353	63	44
CN50	4.0	0.556	76	41
CN75	5.1	0.66	78	48
CN100	7.7	1.149	86	63

Table 4. Potentials of current band (CB) and valence band (VB) of $ZnFe_2O_4$ and g-C_3N_4.

№	$ZnFe_2O_4$			g-C_3N_4			Ref.
	CB, eV	VB, eV	E_g, eV	CB, eV	VB, eV	E_g, eV	
1	0.29	2.35	2.06	–1.08	1.54	2.62	Present work
2	0.41	2.38	1.97	–	–	–	45
3	–0.06	1.8	1.76	–1.03	1.64	2.67	42
4	–1.54	0.38	1.92	–1.26	1.34	2.60	40
5	–	–	–	–	1.54	–	43

and presented in Table 4 along with data from our study. It can be seen that in the literature for g-C_3N_4 similar values were reported, i.e. CB -1.03 and VB 1.64 eV[44] as well as –1.26 and 1.34 eV[42]. This is in good agreement with the value for the VB of g-C_3N_4 (1.54 eV) determined by X-ray photoelectron spectroscopy.[45] The literature data for $ZnFe_2O_4$ are less consistent: values observed include –0.06 and 1.8 eV[44] as well as -1.54 eV and 0.38 eV.[42] Taking into account the literature data for the current and valence band it should be mentioned that the CB and VB values for $ZnFe_2O_4$ are lying over those for g-C_3N_4 according to ref.[44] but under values of g-C_3N_4 according to ref.[42] i.e. inconsistency in the data is observed. This can lead to a different way of the interpretation of energy transfer during the photocatalytic process, particularly the migration of electrons and holes between the current band and the valence band of the semiconductors $ZnFe_2O_4$ and g-C_3N_4.

For the samples synthesized $ZnFe_2O_4$ and g-C_3N_4 the band edge positions were evaluated applying the simple equations $E_{VB} = X–E_0+0.5E_g$ and $E_{CB} = E_{VB}–E_g$. The symbols used E_{CB}, E_{VB}, and X are showing the potentials of the conduction band, of the valence band and the electronegativity of the semiconductors $ZnFe_2O_4$ or g-C_3N_4 defined as the geometric average of the absolute electronegativity of the constituent atoms.[46] According the literature data the energy of the free electrons on the hydrogen scale E_0 is about 4.5 eV.[46] For the semiconductors $ZnFe_2O_4$ and g-C_3N_4 the X values were calculated to be 5.82 and 4.73 eV, respectively. Following this, the bottom of current band and the top of valence band were calculated to be –1.08 eV and 1.54 eV for g-C_3N_4, and 0.29 eV and 2.35 eV for $ZnFe_2O_4$, respectively (Table 4). The data for $ZnFe_2O_4$ are in good agreement with data in ref.[47] in spite of the different synthetic method used, influencing the value.

Based on these results, a mechanism for photodegradation of MG over $ZnFe_2O_4$/r-GO/g-C_3N_4 composites can be proposed (Fig. 8). When $ZnFe_2O_4$/r-GO/g-C_3N_4 composites are exposed to visible light, both $ZnFe_2O_4$ and g-C_3N_4 are excited. The photogenerated holes and electrons are in the valence band and conduction band, respectively. g-C_3N_4 can effectively absorb visible light to form photoexcited charge carriers.

Because the current band of g-C_3N_4 is more negative than that of $ZnFe_2O_4$, the electrons migrate into the current band of $ZnFe_2O_4$; holes in the valence band of $ZnFe_2O_4$ simultaneously migrate to the VB of g-C_3N_4. By this the photogenerated electrons are accumulated on $ZnFe_2O_4$ and holes accumulated on g-C_3N_4. This in turn with water-dissolved oxygen and adsorbed water molecules causes the formation of radicals. These are well known as oxidizing species and as a result MG degradation takes place. The rGO is improving the photocatalytic properties of the composites obtained by efficient separation of photo-induced charges.[23]

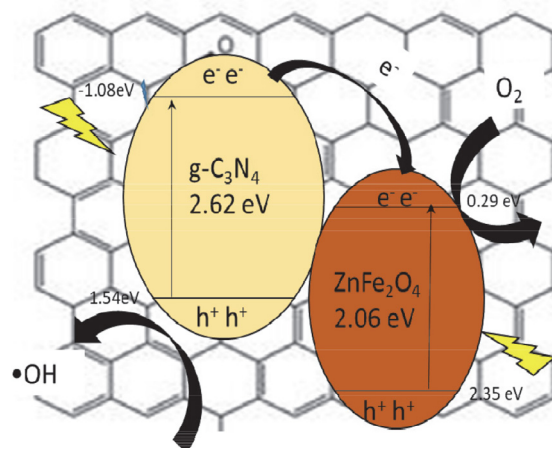


Figure 8. Illustration of the mechanism of the photocatalytic activity of as prepared $ZnFe_2O_4$/GO/g-C_3N_4 samples.

4. Conclusions

Nanocomposites of the type $ZnFe_2O_4$/r-GO/g-C_3N_4, based on coupling of two semiconductors, were successfully prepared by applying solvothermal synthesis, where ethylene glycol was used as a solvent. All of the composites, including the stand alone components, were tested and showed activity for photocatalytic degradation of malachite green in aqueous solution under visible light irradiation. The composites show better activity than the pristine g-C_3N_4 and $ZnFe_2O_4$, with the CN100 sample in which g-C_3N_4 and $ZnFe_2O_4$ were present in equal amount showing the highest activity. The improved photocatalytic activity was due to the synergy and the charge transfer between g-C_3N_4 and $ZnFe_2O_4$ as well as the efficient separa-

tion of photo-induced charges by rGO. More research has to be done to find the optimum $ZnFe_2O_4$/g-C_3N_4 ratio. The examined composites show potential for degradation of water-dissolved organic pollutants.

Acknowledgements.

M.T. acknowledges the financial support from the program "Young scientists and Postdoctoral candidates" of the Bulgarian Ministry of Education and Science, MCD № 577/2018. The textural measurements were done in Prof. Albin Pintar's Laboratory, National Institute for Chemistry, Slovenia.

5. References

1. J. Longbo, Y. Xingzhong, P. Yang, L. Jie, Z. Guangming, W. Zhibin, W. Hou, *Appl. Catal. B-Environ.* **2017,** *217*, 388–406.
2. E. Sudova, J. Machova, Z. Svobodova, T. Vesely, *Veterinarni Med.* **2007**, *52*, 527–539. **DOI:**10.17221/2027-VETMED
3. N. J. Karrer, G. Ryhiner, E. Heinzle, *Water Res.* **1997**, *31*, 1013–1020. **DOI:**10.1016/S0043-1354(96)00356-9
4. L. Ying-yu, L. Lin, L. Xiao-yan, *J. Clean. Prod*. **2020**, *244*, 118705. **DOI:**10.1016/j.jclepro.2019.118705
5. L. Boutilier, R. Jamieson, R. Gordon, C. Lake, W. Harte, *Water Res.* **2009**, *43*, 4370–4380. **DOI:**10.1016/j.watres.2009.06.039
6. S. Bhattacharjee, S. Datta, C. Bhattacharjee, *Desalination* **2007**, *212*, 92–102. **DOI:**10.1016/j.desal.2006.08.014
7. X. Zi-Peng, S. De-Zhi, *J. Hazard. Mater.* **2009**, *168*, 1264–1268. **DOI:**10.1016/j.jhazmat.2009.03.008
8. S. Zodi, O. Potier, F. Lapicque, J.-P. Leclerc, *Desalination* **2010**, *261*, 186–190. **DOI:**10.1016/j.desal.2010.04.024
9. S. S. Mansouri, I. A. Udugama, A. Mitic, A. Rubin, L. Rudolfsson, K. V. Gernaey, *Comput. Aided Chem. Eng.* **2017**, *40*, 391–396. **DOI:**10.1016/B978-0-444-63965-3.50067-2
10. A. F. S. Foureaux, E. O. Reis, Y. Lebron, V. Moreira, L. V. Santos, M. S. Amaral, L. C. Lange, *Sep. Purif. Technol.* **2019**, *212*, 171–179. **DOI:**10.1016/j.seppur.2018.11.018
11. W. Pronk, A. Ding, E. Morgenroth, N. Derlon, P. Desmond, M. Burkhardt, B. Wu, A. G. Fane, *Water Res.* **2019**, *149*, 553–565. **DOI:**10.1016/j.watres.2018.11.062
12. R. Bochenek, R. Sitarz, D. Antos, *Chem. Eng. Sci.* **2011**, *66*, 6209–6219. **DOI:**10.1016/j.ces.2011.08.046
13. C. Guillard, H. Lachheb, A. Houas, M. Ksibi, E. Elaloui, J. M. Hermann. J. *Photochem. Photobiol. A Chem.* **2003**, *158*, 27–36. **DOI:**10.1016/S1010-6030(03)00016-9
14. R. Kralchevska, M. Milanova, M. Tsvetkov, D. Dimitrov, D. Todorovsky, *J. Mater. Sci.* **2012**, *47*, 4936–4945. **DOI:**10.1007/s10853-012-6368-4
15. R. Kralchevska, M. Milanova, D. Hristov, A. Pintar, D. Todorovsky, *Mater. Res. Bull.* **2012**, *47,* 2165–2177. **DOI:**10.1016/j.materresbull.2012.06.009
16. R. Kralchevska, M. Milanova, P. Kovacheva, J. Kolev, G. Avdeev, D. Todorovsky, *Cent. Eur. J. Chem.* **2011**, *9*, 1027–1038. **DOI:**10.2478/s11532-011-0089-4
17. M. Uzunova-Bujnova, R. Kralchevska, M. Milanova, R. Todorovska, D. Hristov, D. Todorovsky, *Catal. Today* **2010**, *151*, 14–20. **DOI:**10.1016/j.cattod.2010.02.058
18. M. Uzunova-Bujnova, R. Todorovska, M. Milanova, R. Kralchevska, D. Todorovsky, *Appl. Surf. Sci.* **2009**, *256*, 830–837. **DOI:**10.1016/j.apsusc.2009.08.069
19. G. Dong, Y. Zhang, Q. Pan, J. Qiu, *J. Photochem. Photobiol. C Photochem. Reviews* **2014**, *20*, 33–50.
20. X. Wang, K. Maeda, A.Thomas, K. Takanabe, G. Xin, J. M. Carlsson, K. Domen, M. Antonietti, *Nat. Mater.* **2009,** *8*, 76–80. **DOI:**10.1038/nmat2317
21. J. Wen, J. Xie, X. Chen, X. Li, *Appl. Surf. Sci.* **2017**, *391*, 72–123. **DOI:**10.1016/j.apsusc.2016.07.030
22. L. Shi, F. Wang, J. Zhang, J. Sun, *Ceram. Int.* **2016**, *42*, 18116–18123. **DOI:**10.1016/j.ceramint.2016.08.124
23. V. S. Amrutha, K. S. Anantharaju, D. S. Prasanna, *Arabian J. Chem.* **2017**, *10* **DOI:**10.1016/j.arabjc.2017.11.016
24. K. Woan, G. Pyrgiotakis, W. Sigmund, *Adv. Mater.* **2009**, *21*, 2233–2239. **DOI:**10.1002/adma.200802738
25. Q. Ming, S. Qin, W. Guanglei, Zh. Bohan, W. Zhengdong, W. Hongjing, *Mater. Sci. Eng. B* **2017**, *224*, 125–138. **DOI:**10.1016/j.mseb.2017.07.016
26. X. Xuejun, S. Zhichun, L. Liping, W. Zehao, C. Ze, R. Rui, H. Yonghong, W. Duan, *Appl. Surf. Sci.* **2018**, *435*, 1296–1306.
27. M. Huang, J. Yu, Q. Hu, W. Su, M. Fan, B. Li, L. Dong, *Appl. Surf. Sci.* **2016**, *389*, 1084–1093. **DOI:**10.1016/j.apsusc.2016.07.180
28. F. Wu, X. Li, W. Liu, S. Zhang, *Appl. Surf. Sci.* **2017**, *405*, 60–70. **DOI:**10.1016/j.apsusc.2017.01.285
29. G. Zhao, X. Huang, F. Fin, G. Zhang, J. T. S. Irvine, *Catal. Sci. Technol.* **2015**, *6*, 3416–3422. **DOI:**10.1039/C5CY00379B
30. W. S. Hummers, R. E. Offeman, *J. Am. Chem. Soc.* **1958**, *806*, 1339–1339. **DOI:**10.1021/ja01539a017
31. M. Tsvetkov, M. Milanova, L. C. J. Pereira, J. C. Waerenborgh, Z. Cherkezova-Zheleva, J. Zaharieva, I. Mitov, *Chem. Papers,* **2016,** *70,* 1600–1610.
32. J. Rodriguez-Carvajal, *Newsletter*, **2001**, *26*, 12–19.
33. J. Tauc, R. Grigorovici, A. Vancu, *Phys. Status Solidi* **1966**, *15*, 627–637. **DOI:**10.1002/pssb.19660150224
34. C. A. Schneider, W. S. Rasband, K. W. Eliceiri, *Nature methods*, **2012**, *9*, 671–675, PMID 22930834. **DOI:**10.1038/nmeth.2089
35. M. Tzvetkov, M. Milanova, Z. Cherkezova-Zheleva, I. Spassova, E. Valcheva, J. Zaharieva, I. Mitov, *Acta Chim. Slov.* **2017**, *64*, 299–311. **DOI:**10.17344/acsi.2016.3049
36. K. Zaharieva, V. Rives, M. Tsvetkov, Z. Cherkezova-Zheleva, B. Kunev, R. Trujillano, I. Mitov, M. Milanova, *Mater. Chem. Phys.* **2015**, *160*, 271–278. **DOI:**10.1016/j.matchemphys.2015.04.036
37. G. Tzvetkov, M. Tsvetkov, T. Spassov, *Superlattice Microst.* **2018**, *119*, 122–133. **DOI:**10.1016/j.spmi.2018.04.048
38. I. N. Leontyev, A. B. Kuriganova, M. Allix, A. Rakhmatullin, P. E. Timoshenko, O. A. Maslova, A. S. Mikheykin, N. V. Smirnova, *Phys. Status Solidi B* **2018**, 1800240. **DOI:**10.1002/pssb.201800240

39. W. L. Smith, *J. Appl. Crystalography* **1972**, *5*, 127–130. **DOI:**10.1107/S0021889872008921
40. K. S. W. Sing, D. H. Everett, R. A. W. Haul, L. Moscou, R. A. Pierotti, J. Rouquerol, T. Siemieniewska, *Pure Appl. Chem.* **1985**, *57*, 603–604.
41. J. G. Yu, Q. J. Xiang, M. H. Zhou, *Appl. Catal. B-Environ.* **2009**, *90*, 595–602. **DOI:**10.1016/j.apcatb.2009.04.021
42. L. Chen, W. Ma, J. Dai, J. Zhao, C. Li, Y. Yan, *J. Photochem. Photobiol. A* **2016**, *328*, 24–32. **DOI:**10.1016/j.jphotochem.2016.04.026
43. S. Borthakur, L. Saikia, *J. Environ. Chem. Eng.* **2019**, *7*, 103035. **DOI:**10.1016/j.jece.2019.103035
44. S. Patnaik, K. K. Das, A. Mohanty, K. Parida, *Catal. Today*, **2018**, *315*, 52–66. **DOI:**10.1016/j.cattod.2018.04.008
45. W. Hu, J. Yu, X. Jiang, X. Liu, R. Jin, Y. Lu, L. Zhao, Y. Wu, Y. He, *Colloids Surf. A Physicochem. Eng. Asp.* **2017**, *514*, 98–106. **DOI:**10.1016/j.colsurfa.2016.11.058
46. R. Beranek, *Adv. Phys. Chem*. **2011**, *2011*, ID 786759, 20 pages, **DOI:**10.1155/2011/786759
47. L. Jing, Y. Xu, C. Qin, J. Liu, S. Huang, M. He, H. Xu, H. Li, *Mater. Res. Bull.* **2017,** *95*, 607–615. **DOI:**10.1016/j.materresbull.2017.06.003

Povzetek

Nanokompozitni fotokatalizatorji $ZnFe_2O_4$/rGO/g-C_3N_4 z različnimi masnimi razmerji $ZnFe_2O_4$/g-C_3N_4 (0,5; 0,75; 1) so bili pripravljeni z večstopnejsko solvotermalno metodo ter uporabo etilen glikola kot topila. Za karakterizacijo kompozitov so bile uporabljene različne metode, kot so rentgenska difrakcija, UV-Vis spektroskopija in fotoluminiscenčna spektroskopija. Nastanek mezo-/makroporozne strukture s specifično površino med 67 in 77 $m^2\ g^{-1}$ je bil potrjen z adsorpcijo/desorpcijo N_2. Ugotovljeno je bilo, da je v primerjavi z g-C_3N_4 (2,7 eV) širina prepovedanega pasu kompozitov manjša (2,30 eV). V nasprotju s g-C_3N_4, kompoziti niso izkazovali fluorescence, torej ni prišlo do rekombinacije e^-/h^+. Vsi vzorci, vključno s g-C_3N_4 in $ZnFe_2O_4$, so bili testirani za adsorpcijo in fotokatalitično razgradnjo vodnih raztopin zelenega malahita (10^{-5} M) pri obvsevanju z vidno svetlobo ($\lambda > 400$ nm). Rezultati kažejo, da imajo pripravljeni nanokompoziti večjo absorpcijo in fotokatalitično aktivnost kot nemodificirana g-C_3N_4 in $ZnFe_2O_4$ in so zato potencialni kandidati za razgradnjo organskih azobarvil v vodi.

Except when otherwise noted, articles in this journal are published under the terms and conditions of the Creative Commons Attribution 4.0 International License

DOI: 10.17344/acsi.2020.5881 *Acta Chim. Slov.* **2020,** *67,* 1092–1099
creative commons

Scientific paper

Determination of Morin and Quercetin in Fruit Juice Samples using Air-Assisted Liquid-Liquid Microextraction Based on Solidification of Floating Organic Droplet and HPLC-UV

Armin Fallah and Mohammad Reza Hadjmohammadi*

Department of Analytical Chemistry, Faculty of Chemistry, University of Mazandaran, NirooHavayii boulevard, 47416-95447 Babolsar, Iran

** Corresponding author: E-mail: hadjmr@umz.ac.ir*
Tel.: +98 1135342350; fax: +98 1135342350

Received: 02-05-2020

Abstract

In this study, a rapid and efficient method has been used for the extraction and determination of morin and quercetin in fruit juice samples based on air-assisted liquid-liquid microextraction based on solidification of floating organic droplet and HPLC-UV. The effects of 7 important parameters on the extraction recovery were examined and were optimized by Plackett-Burman design and Central Composite design. According to the Plackett-Burman design results, ionic strength of the sample solutions, the aspiration/dispersion cycles, and the rate and time of centrifuge did not show significant effects on the extraction of morin and quercetin. The optimized conditions of extraction were as follows; the volume of the extraction solvent of 83.6 μL, pH of 4.34 for the sample, and 1-undecanol as extraction solvent. Under these conditions, the linear calibration curve was in the ranges of 1–1000 ng/mL and 0.5–1000 ng/mL for morin and quercetin, respectively, with the determination coefficient values above 0.99. The limit of detection of morin and quercetin was 0.3 and 0.2 ng/mL, respectively. The extraction recoveries for 10 ng/mL of morin and quercetin were 98.9% and 96.5%, respectively; while, relative standard deviations (n = 3) were lower than 3.2%.

Keywords: Morin; quercetin; fruit juices, air-assisted liquid–liquid microextraction based on solidification of floating organic droplet; HPLC

1. Introduction

Flavonoids are an important group of natural polyphenolic compounds, which are the essential plant metabolites with antioxidant activity.[1] Morin (MR) and quercetin (QR) are isomeric antioxidant flavonols widely distributed in fruits and vegetables.[2] Studies have shown that MR has numerous pharmacological activities such as coronary artery disease prevention, inhibition of proliferation of tumors, antioxidant, anticancer, anti-inflammatory, as well as free radicals scavenging activity.[3] It has been published that QR has several biological properties in the inhibition of human diseases, such as cancer, ulcer, diabetes, cataract, and allergies.[4]

Based on these activities, many investigations have been undertaken to determine QR and MR in recent decades. Several techniques including high-performance liquid chromatography (HPLC),[5-7] thin-layer chromatography (TLC),[8] gas chromatography (GC),[9] micellar electrokinetic chromatography (MEKC),[10] capillary electrophoresis (CE),[11] and electrochemical methods[12] have been employed for the determination of MR and/or QR in various samples.

Due to the low concentration of the target compounds in the samples and the complexity of the real sample, the sample preparation step plays a crucial role in the analysis of QR and MR. Thus, the extraction methods including solid-phase extraction (SPE),[13-14] dispersive micro-solid-phase extraction,[15] liquid-liquid extraction (LLE),[16] molecularly imprinted polymer (MIP),[17] and inverted dispersive liquid-liquid microextraction (IDLLME)[18] have been utilized for the preconcentration of MR or/and QR.

Conventional sample preparation techniques for the preconcentration of flavonoids are based on SPE and

LLE.[16] These techniques are inadequate for the analysis of the fruit juice samples due to the high consumption of dangerous and expensive organic solvents and time-consuming processes. Thus, various microextraction techniques were masterminded to overcome SPE and LLE disadvantages.

In 2006, Rezaee et al. developed a method based on the LPME method called dispersive liquid-liquid microextraction (DLLME). It was widely used because of its advantages like simplicity, high enrichment factor, and low costs. In DLLME, a three-phase solvent system including the extraction solvent, the aqueous solution sample, and the organic disperser solvent is used.[19] Despite the previously mentioned advantages, DLLME is not considered a biocompatible method because it uses a disperser solvent and toxic organic extractants such as dichloromethane, carbon tetrachloride, and chloroform. The DLLME-SFO method was introduced in 2007.[20] In this method, solvents with the melting points near the room temperature and less toxicity were used. However, using the organic disperser solvent in this method can increase the consumption of the dangerous solvent. To solve this problem, these methods were replaced by methods such as VALLME[21] and USAEME[22] that do not have the disperser solvent. These methods use vortex or ultrasonic waves to help the distribution of the organic phase in the aqueous solution. The AALLME method is another transformation that has been done on the DLLME method.

In 2012, AALLME method was introduced by Farajzadeh et al. to improve the performance of the extraction techniques.[23] This method does not use the disperser solvent. After the injection of the extraction solvent, the mixture is sucked into one glass syringe and then injected in the sample tube repeatedly. Equilibrium is achieved quickly due to this process and the analyte to carry from the aqueous phase to the organic phase which is one of its main advantages. In this method, the production of a high number of tiny droplets of organic solvent in water leads to the increase in mass transfer; as a result, the extraction efficiency increases. Comparing AALLME with other DLLME methods indicates that this is more easy, efficient, and simple.[24] This method has been recently used for the preconcentration of aromatic amines in the aqueous sample,[25] tricyclic antidepressant drugs,[26] azathioprine,[27] bisphenols, parabens, benzophenones, triclosan, and triclocarban in human urine,[28] benzophenone,[29] and toxic heavy metals in food sample.[30]

The purpose of our study was to investigate the applicability of AALLME-SFO technique as a simple and fast method for the extraction of MR and QR from fruit juice samples and their analyses by RP-HPLC-UV. The disperser solvent was not used in this method. Also, the harmful effects of the toxic organic solvents on the operator and environment are decreased by replacing the heavy-density chlorine solvents with lighter and less toxic solvents. In addition, using the aeration method to increase the dispersion of the extraction solvent in the aqueous sample reduced the cost and the probability of the sample destruction. Also, it makes the process simpler compared to the ultrasonic or vortex. The fast injection of air into the sample solution has decreased the equilibration time. The main advantages of the proposed method are the simultaneous extraction of flavonoids in a short time along with high recovery, low detection limit, and low-cost. According to our knowledge, no usage of AALLME-SFO in the extraction of MR and QR from fruit juice samples has yet been reported. The effective factors were optimized in two stages by PBD and response surface methodology using the CCD. Also, this method was applied to several real samples.

2. Experimental

2. 1. Chemicals and Materials

Quercetin (≥98%), 1-dodecanol and 2-dodecanol were obtained from Sigma–Aldrich (Steinheim, Germany). Standard of morin (≥98%), methanol (HPLC-grade), 1-undecanol, *n*-hexadecane, phosphoric acid, tetrahydrofuran (THF), and sodium chloride (98%) were purchased from Merck (Darmstadt, Germany). DDW was utilized for the preparation of the mobile phase, which was filtered through a 0.45 m filter (Millipore membranes, Bedford MA, USA). The stock solution (100 mg/L) was prepared in methanol and stored at 4 °C. The working solutions were prepared daily by diluting the standard solution with DDW.

2. 2. Instrumentation and Conditions

Separation and detection were carried out by a Waters HPLC system equipped with a 1525 pump and a model 2487 UV detector set at 275 nm (Milford, MA, USA), 7725i manual injector (Cotati, CA, USA) fitted with a 20 µL loop. The isocratic elution was done at a flow rate of 1.0 mL/min on a C18 (250 mm × 4.6 mm, 10 µm) column from Dr. Maisch GmbH (Beim Brueckle, Germany). The mobile phase consisted of methanol, 0.4% phosphoric acid, and THF (40:59.7:0.3, *v/v/v*). For the adjustment of sample solution pH, a 3030 Jenway pH meter was used. A Hettich centrifuge model Universal 320 (Kirchlengern, Germany) was utilized to accelerate the phase separation.

2. 3. Extraction Procedure

Initially, 9 mL of the aqueous solution sample (containing 0.5 mg/L of each analyte) was added to a centrifuge tube. Then 100 µL of 1-undecanol was injected into the aqueous sample by applying a syringe. The process of sucking out the mixture and rapidly injecting it was done several times. A cloudy solution was formed, and the compounds were extracted. The cloudy solution was then centrifuged at 5000 rpm for 5 min to separate the phases. Then the sample vial was placed in a beaker containing ice for 5 min and 1-undecanol was solidified accordingly. The

solid solvent was transferred into a conical vial by spatula, where it rapidly melted.[31] Finally, 20 µL of the sample was injected into the HPLC-UV system.

2. 4. Real Samples Preparation

Fresh apple, orange, red grape, peach, and commercial apple juice were purchased at a local supermarket. Apple, orange, red grape, and peach samples were placed in a commercial juice extractor. The resulted fruit juice samples and commercial apple juice were centrifuged for 15 min at 5000 rpm, and the supernatants were filtered. Finally, the pH of samples was adjusted to 4.3 using HCl 1 mmol/L and the extraction process was undertaken according to section 2.3.

2. 5. Optimization Strategy

In order to obtain the most desirable extraction conditions, various experimental parameters were investigated which according to past studies can potentially affect the extraction performance, such as type and volume of the extraction solvent, pH of the solution, amount of salt, number of extractions, and rate and time of the centrifuging process. These parameters were evaluated to select and determine the significant parameters to obtain the highest total peak areas. In the first step, PBD was used for screening the parameters and selecting the effective experimental factors. Then, RSM based on CCD was applied to determine the optimized point. The statistical analysis and experimental design were done by Minitab software. Also, it is essential to say that all the experiments were done three times.

3. Results and Discussion

The extraction recovery (ER) was applied to evaluate the extraction performance. The ER is calculated via the following equation:

$$ER\% = \left(\frac{V_o}{V_{aq}}\right) EF \times 100 \quad (1)$$

Where V_{aq} and V_o are the volumes of the aqueous and organic phases, respectively. EF is calculated according to the ratio of the final concentrations of analyte in the floating phase (C_o) to its initial concentration in an aqueous sample (C_{aq}).

$$EF = \frac{C_o}{C_{aq}} \quad (2)$$

3. 1. Selection of Extraction Solvent

The selection of an appropriate extraction solvent is crucial in the optimization of the AALLME-SFO process because of the effects of its physical and chemical properties. In this study, the extraction solvent must have special features, such as lower density than water, low water solubility in order to be stable at the extraction period and to extract analytes well. Therefore, several extraction solvents, including 1-dodecanol, *n*-hexadecane, 1-undecanol, and 2-dodecanol were investigated. According to the results for three repeats, which are shown in Fig. 1, 1-undecanol showed the highest peak area for MR and QR compared to other solvents. This may be because of the good dispersion of this solvent in the aqueous sample and/or its hydrophobicity similar to the analytes. Hence, 1-undecanol was chosen as the extraction solvent for subsequent experiments.

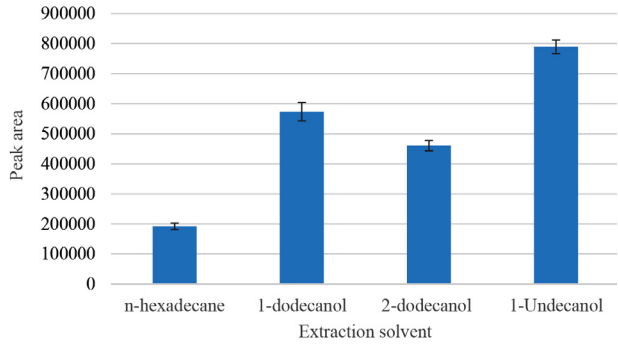


Figure 1. Selection of the extraction solvent used in the microextraction of morin and quercetin (n = 3).

3. 2. Screening of Significant Variables

The PBD was used to screen the effective factors among the previously mentioned six experimental factors. PBD is based on the first-order polynomial model and does not define the exact value. It is an advantageous method for the quick search of the effective variables and calculation of their main effects in fewer experiments.[32] Each of these factors was investigated at two levels. The experimental design included 12 experiments that were done. The sum of the peak areas was applied as the corresponding response to investigate the extraction in various conditions. The levels of factors were chosen according to the previous trials and 12 experiments were randomly done to avoid the uncontrollable errors. The main effects were determined by the analysis of variance (ANOVA) and the effective factors on the extraction were identified by the Pareto chart with the confidence level of 95% (Fig. 2). The bars beyond the line are related to the significant effects. Based on these results, pH was identified as the most effective factor with a negative effect. The volume of the extraction solvent was considered as the second most effective factor after pH. Therefore, these two factors were chosen for CCD in the next step. The level of the other factors was selected according to the previous experiment. Thus, in the following experiments, the number of ex-

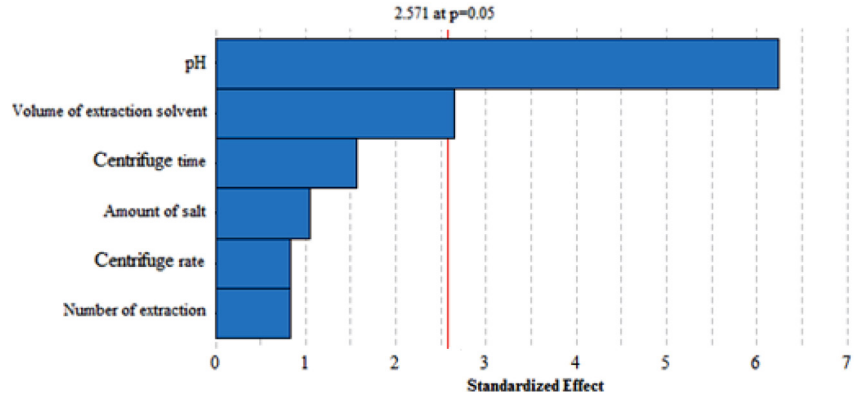


Figure 2. Pareto chart of the main effects obtained from the Plackett–Burman design.

tractions, the amount of salt, the rate and time of centrifuge were set at 15 cycles, 0 mg/mL, 5000 rpm, and 8 min, respectively.

3. 3. Optimization of Extraction Conditions

To achieve the proper response surface for the extraction of MR and QR with the AALLME-SFO method, CCD was used. To determine the optimal point in this method, it is necessary to examine the effect of each factor on the five levels coded as α, -α (axial points), 1,-1 (factorial points), and 0 (central point). The significant factors and their levels are shown in Table S1. The following equation calculates the number of experiments (N) in CCD:

$$N = 2^K + 2K + Cp \quad (3)$$

In this equation, K and Cp are the number of the factors and repetitions of the experiments in the central point, respectively. Table S2 shows the design matrix. Also, the trials were carried out randomly to decrease the effects of uncontrolled variables. The results of the CCD method were evaluated by ANOVA at 95% confidence level (Table 1). The *p*-value for the LOF of the model was 0.291, thus, LOF was not significantly related to the pure error. Thus, the best second-order equation that matched the data was achieved as follows:

$$Peak\ area = 832762 - 65731X_1 - 19826X_2 - \\ - 80181X_1^2 - 44538X_1 \\ * X_2 \quad (4)$$

The coefficient of determination (R^2) value for this model was 92.6%, which showed that this model could explain 92.6% of the variability of the responses. The response surface of the experiments according to the above model is shown in Fig. 3. The response surfaces showed that by increasing the amount of pH, the response increases accordingly. Also, by increasing the volume of 1-undecanol, the response will fluctuate (first increases and then decreases).

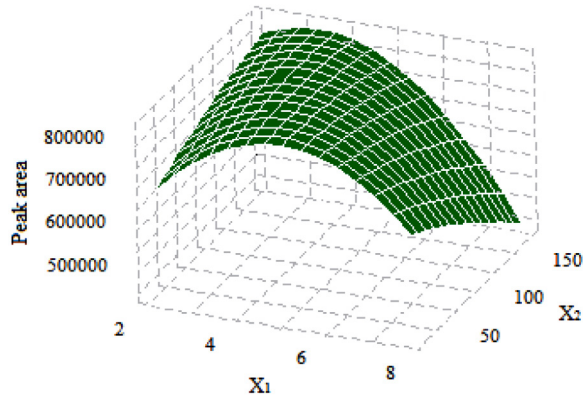


Figure 3. The response surface plots for the peak area as a function of the pH of the sample solution and volume of extraction solvent.

Table 1. Analysis of Variance (ANOVA) of CCD

Source	DF	Adj SS	Adj MS	F-Value	P-Value
X_1	1	34564032309	34564032309	168.38	0.000
X_2	1	3144553668	3144553668	15.32	0.006
X_1^2	1	44331878523	44331878523	217.87	0.000
X_2^2	1	437028613	437028613	2.13	0.188
$X_1 X_2$	1	7934444700	7934444700	38.65	0.000
Residual Error	7	1436943011	205277573		
Lack-of-Fit	3	819802309	273267436	1.77	0.291
Pure Error	4	617140703	154285176		
Total	12	91848880824			

Therefore, the optimal values for pH and the volume of 1-undecanol were obtained as 4.34 and 83.6 μL, respectively. To evaluate the predicted optimum conditions, the experiment was replicated three times and the average of ERs was satisfactorily consistent with the predicted results.

3. 4. Method Validation

The analytical performance of this method including RSD, LOD, LOQ, the recovery of extraction (ER), the linear range (LR), and the enrichment factor (EF) was studied by plotting the calibration curves for the MR and QR samples, and the further calculations were done about them. The linear range was investigated for each sample solution, and it was in the range of 1-1000 ng/mL for MR and 0.5–1000 ng/mL for QR with R^2>0.99 for both compounds, respectively. The LODs of MR and QR at the signal-to-noise ratio of 3 (S/N=3) were calculated as 0.3 and 0.2 ng/mL, respectively. The LOQ was calculated based on the signal-to-noise ratio of 10 (S/N=10). The RSDs (n = 3) were calculated as lower than 3.2% for 10 ng/mL of MR and QR. Their values are suitable and confirm the application of this technique. The analytical performance results are shown in Table 2.

3. 5. Analysis of the Real Samples

To investigate the applicability of the proposed method for determining flavonoids in real samples, apple,

Table 2. Analytical performance of AALLME-SFO for the determination of morin and quercetin

Sample	LOD (ng/mL)	LOQ (ng/mL)	LR (ng/mL)	R^2	RSD (%) Intra-day (n = 3)	RSD (%) Intra-day (n = 3)	EF	ER%
morin	0.3	0.9	1–1000	0.996	2.6	3.2	106.5	98.9
quercetin	0.2	0.6	0.5–1000	0.999	1.7	2.2	104	96.6

Table 3. The application of presented method for the determination of morin and querectin in fruit juices samples

Sample	Analyte	C_{added} (ng/mL)	C_{found} (ng/mL)	RSD% (n = 3)	RR %
Apple juice	morin	–	7.3	–	–
		10	17.1	2.4	97.5
		30	36.0	3.0	95.7
	querectin	–	9.7	–	–
		10	18.6	2.8	89
		30	37.5	2.1	92.7
Red grape juice	morin	–	6.7	-	-
		10	16.3	3.1	96.2
		30	34.7	2.7	93.3
	querectin	–	12.7	–	–
		10	22.5	3.3	98
		30	41.8	2.9	97
Commercial apple juice	morin	–	N.D	–	–
		10	9.9	3.6	99.5
		30	27.3	3.4	91
	querectin	–	N.D	–	–
		10	8.8	3.1	87.8
		30	27.6	3.7	92.1
Orange juice	morin	–	14.5	–	–
		10	24.0	3.5	95
		30	42.8	3.4	94.2
	querectin	–	8.6	–	–
		10	18.3	3.7	96.8
		30	38.3	2.8	99
Peach juice	morin	–	N.D	–	–
		10	9.6	2.6	96.4
		30	28.7	3.2	95.7
	querectin	–	1.8	–	–
		10	12.0	3.6	102
		30	29.8	3.3	93.2

commercial apple, red grape, peach, orange, and commercial apple juice samples were studied under the optimized conditions. The determination of morin and quercetin was carried out by the standard addition method. The samples were spiked with standards at three levels, extracted, and eventually analyzed by HPLC (Table. 3). The relative recovery (RR) of MR and QR was calculated as follows:

$$RR = \frac{C_{found} - C_{real}}{C_{added}} \times 100 \quad (5)$$

where C_{found} and C_{real} are the concentration of analyte after adding a known amount of the standard to the real sample, and the initial concentration of the analyte in the real sample, respectively. C_{added} also represents the spiked standard concentration in the real sample. The analytical results are shown in Table 3. Regarding the complexity of the matrices studied, the extraction recoveries for MR and QR were compatible with those values of the standard that was added to the samples; while, the RSDs (n = 3) were lower than 3.7%. Fig. 4 shows the obtained chromatograms for each sample.

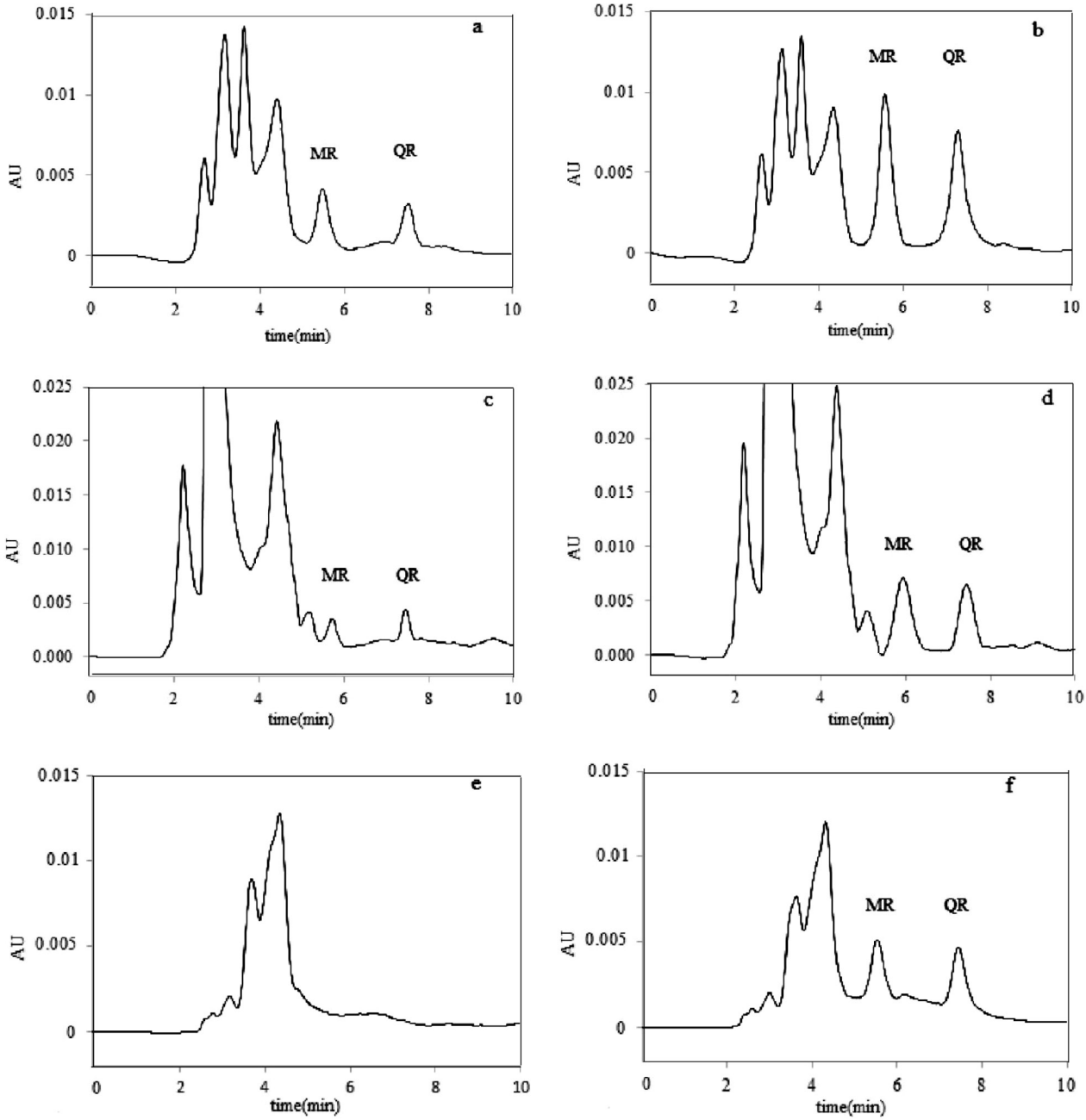


Figure 4. Typical chromatograms of (a) orange sample; (b) spiked orange sample; (c) apple sample; (d) spiked apple sample; (e) commercial apple sample ; (f) spiked commercial apple sample. HPLC conditions and experimental details were described in the text. Samples were spiked with 10 ng/mL of MR and QR. MR = morin and QR = quercetin.

Table 4. Comparison between the presented method and other reported methods for the determination of morin and quercetin

Method	Sample	Analyte	LOD	LR	RSD%	RE%	Time of extraction	Ref.
Dispersive micro-SPE-HPLC	Onion, apple and green tea	morin	0.91	3-500	3.8	97.7	medium	[15]
HF-LPME-HPLC	*E. platylob DC. and M. piperita*	morin quercetin	1.5 4	5–500 10–500	3.2 4.6	80 45	medium	[33]
DSDME-GC-MS	Fruit juices and functional foods	quercetin	0.06 1	0.5–500	6	99	high	[34]
IDLLME-HPLC-UV	Plasma, urine and honey	quercetin	0.26	0.5–500	<5	97	low	[18]
UA-D-μ-SPE-UV–Vis	*Nasturtium officinale extract and fruit juice*	quercetin	4.35	20–4000	<6	90.3-97.28	medium	[35]
SBME-DES-HPLC-UV	Apple, orange, pineapple, onion	morin quercetin	0.2 2.6	1–500 10–500	2.3 3.6	90.3 94.4	medium	[36]
SPE-HPLC-UV	plasma urine	quercetin quercetin	0.35 0.35	4–700 20–1000	7 35	- -	high	[37]
AALLME-SFO-HPLC-UV	Fruit juices	morin quercetin	0.28 0.19	1–1000 0.5–1000	3.2 2.2	98.9 96.6	low	Present study Present study

According to Table 4, a comparison between the AALLME-SFO-HPLC-UV method and the other reported techniques for the extraction and determination of MR and QR indicates that the present method reveals low LOD, desirable linear range, and high extraction recovery. Furthermore, AALLME-SFO is a simple, inexpensive, and fast method for the preconcentration and extraction of QR and MR from fruit juice samples.

3. 6. Conclusion

Affecting parameters on AALLME-SFO-HPLC-UV were optimized through CCD and the results showed that this method is applicable for the extraction, preconcentration, and determination of morin and quercetin in fruit juice samples. This technique is less harmful and, therefore, is more environmentally friendly than the conventional DLLME methods due to the use of low-density extraction solvent and non-consumption of the organic disperser solvent. Moreover, the possibility of a fast injection of air into the sample solution increases the surface contact between the extraction solvent and analytes. Fast equilibration of the extraction is another advantage of this method. The experimental results showed high recoveries, low detection limits, wide linearity range, simplicity of the extraction, and inexpensive and rapid extraction which make it useful to determine morin and quercetin in fruit juice samples.

Abbreviations:

AALLME-SFO, air-assisted liquid-liquid microextraction based on solidification of floating organic droplet; ANOVA, analysis of variance; CCD, Central Composite design; DDW, double distilled/deionized water; DLLME-SFO, dispersive liquid-liquid microextraction based on solidification of floating organic droplet; EF, enrichment factor; ER, extraction recovery; IDLLME, inverted dispersive liquid–liquid microextraction; LOD, limit of detection; LOF, lack of fit; LOQ, limit of quantification; LR, linear range; LLE, liquid-liquid extraction; LPME, liquid-phase microextraction; MIP, molecularly imprinted polymer; PBD, Plackett-Burman design; RE, recovery of extraction; RPM, rounds per minute; RR, relative recovery; RSD, relative standard deviation; RSM, response surface methodology; SPE, solid-phase extraction; TBP, tributyl phosphate; THF, tetrahydrofuran; USAEME, ultrasound-assisted emulsification-microextraction; VALLM, vortex-assisted liquid–liquid microextraction.

4. References

1. R. Cermak, S. Wolffram, *Curr. Drug Metab.* **2006**, *7*(7), 729–744. **DOI:**10.2174/138920006778520570
2. L. Jiang, G. Fang, Y. Zhang, G. Cao, S. Wang, *J. Agric. Food Chem*. **2008**, *56*(24), 11571–11577. **DOI:**10.1021/jf802567r
3. S. Subash, P. Subramanian, *Mol. Cell. Biochem*. **2009**, 327, 153. **DOI:**10.1007/s11010-009-0053-1
4. M. Lesjak, I. Beara, N. Simin, D. Pintać, T. Majkić, K. Bekvalac, D. Orčić, N. Mimica-Dukić, *J. Funct. Food* **2018**, *40*, 68–75. **DOI:**10.1016/j.jff.2017.10.047
5. F. Fang, J.-M. Li, Q.-H. Pan, W.-D. Huang, *Food Chem.* **2007**, *101*, 428–433. **DOI:**10.1016/j.foodchem.2005.12.036

6. T. H. Sani, M. R. Hadjmohammadi, M. H. Fatemi, *J. Sep. Sci.* **2020**, **DOI:**10.1002/jssc.201900527
7. M. R. Hadjmohammadi, S. S. S. Nazari, *J. Sep. Sci.* **2013**, *36*, 3667–3672. **DOI:**10.1002/jssc.201300920
8. M. A. Maobe, L. Gitu, E. Gatebe, H. Rotich, P. O. Box, *Acad. J. Cancer Res.* **2012**, *5*(2), 31–39. **DOI**:10.5829/idosi.ajcr.2012.5.2.66210
9. Y. Nolvachai, C. Kulsing, R. I. Boysen, M. T. Hearn, P. J. Marriott, *J. Sep. Sci.* **2014**, *37*, 1018–1025. **DOI:**10.1002/jssc.201301009
10. J. M. Herrero-Martínez, F. Z. Oumada, M. Rosés, E. Bosch, C. Ràfols, *J. Sep. Sci.* **2007**, *30*, 2493–2500. **DOI:**10.1002/jssc.200700124
11. D. Goltz, S. Ahmadi, J. Crawford, D. Craig, *J. Liq. Chromatogr. Relat. Technol*. **2016,** *39*(16), 768–774. **DOI:**10.1080/10826076.2016.1247714
12. M. L. Yola, V. K. Gupta, T. Eren, A. E. Şen, N. Atar, *Electrochim. Acta* **2014**, *120*, 204–211. **DOI:**10.1016/j.electacta.2013.12.086
13. A. Michalkiewicz, M. Biesaga, K. Pyrzynska, *J. Chromatogr. A* **2008**, *1187*, 18–24. **DOI:**10.1016/j.chroma.2008.02.001
14. M. R. Hadjmohammadi, S. Nazari, K. Kamel, *Chromatographia* **2009**, *69*, 1291–1297. **DOI:**10.1365/s10337-009-1073-4
15. S. M. Majidi, M. R. Hadjmohammadi, *J. Sep. Sci.* **2019**. **DOI**:10.1002/jssc. 201900234
16. S. Kongkiatpaiboon, P. Tungsukruthai, K. Sriyakool, K. Pansuksan, A. Tunsirikongkon, H. Pandith, *J. chromatogr. Sci.* **2017**, *55*, 346–350. **DOI:**10.1093/chromsci/bmw191
17. J. Xie, L. Zhu, H. Luo, L. Zhou, C. Li, X. Xu, *J. Chromatogr. A* **2001**, *934*, 1–11. **DOI:**10.1016/S0021-9673(01)01294-8
18. E. Ranjbari, P. Biparva, M. R. Hadjmohammadi, *Talanta* **2012**, *89*, 117–123. **DOI:**10.1016/j.talanta.2011.11.079
19. M. Rezaee, Y. Assadi, M.-R. M. Hosseini, E. Aghaee, F. Ahmadi, S. Berijani, *J. Chromatogr. A* **2006**, *1116*, 1–9 **DOI:**10.1016/j.chroma.2006.03.007
20. M. R. K. Zanjani, Y. Yamini, S. Shariati, J. Å. Jönsson, *Anal. Chim. Acta* **2007**, *585*, 286-293. **DOI:**10.1016/j.aca.2006.12.049
21. E. Yiantzi, E. Psillakis, K. Tyrovola, N. Kalogerakis, *Talanta* **2010**, *80*, 2057–2062. **DOI:**10.1016/j.talanta.2009.11.005
22. J. Regueiro, M. Llompart, C. Garcia-Jares, J. C. Garcia-Monteagudo, R. Cela, *J. Chromatogr. A* **2008**, *1190*, 27–38. **DOI:**10.1016/j.chroma.2008.02.091
23. M. A. Farajzadeh, M. R. A. Mogaddam, *Anal. Chim. acta* **2012**, *728*, 31–38. **DOI:**10.1016/j.aca.2012.03.031
24. M. A. Farajzadeh, A. Mohebbi, A. Pazhohan, M. Nemati, M. R. A. Mogaddam, *TrAC Trends in Anal. Chem.* **2020**, *122*, 115734. **DOI:**10.1016/j.trac.2019.115734
25. M. Torbati, A. Mohebbi, M. A. Farajzadeh, M. R. A. Mogaddam, *Anal. Chim. acta* **2018**, *1032*, 48–55. **DOI:**10.1016/j.aca.2018.06.025
26. A. Mohebbi, S. Yaripour, M. A. Farajzadeh, M. R. A. Mogaddam, *J. Chromatogr. A* **2018**, *1571*, 84–93. **DOI:**10.1016/j.chroma.2018.08.022
27. A. Fallah, M. R. Hadjmohammadi, *J. Iran. Chem. Soc.* 2020, 1–8. **DOI:**10.1007/s13738-020-01895-1
28. B. Alves Rocha, A. R. M. de Oliveira, F. Barbosa, *Talanta* **2018**, *183*, 94–101. **DOI:**10.1016/j.talanta.2018.02.052
29. D. Ge, Y. Zhang, Y. Dai, S. Yang, *J. Sep. Sci.* **2018**, *41*, 1635–1643. **DOI:**10.1002/jssc.201701282
30. M. Shirani, S. Habibollahi, A. Akbari, *Food chem.* **2019**, *281*, 304–311. **DOI:**10.1016/j.foodchem.2018.12.110
31. X. You, Z. Xing, F. Liu, X. Zhang, *Anal. Chim. acta*, **2015**, *875*, 54–60. **DOI:**10.1016/j.aca.2015.03.033
32. R. L. Plackett, J. P. Burman, *Biometrika* **1946**, *33*, 305–325. **DOI:**10.2307/2332195
33. M. Hadjmohammadi, H. Karimiyan, V. Sharifi, *Food chem.* **2013**, *141*, 731–735. **DOI:**10.1016/j.foodchem.2013.02.083
34. P. Viñas, N. Martínez-Castillo, N. Campillo, M. Hernández-Córdoba, *J. Chromatogr. A* **2011**, *1218*, 639–646. **DOI:**10.1016/j.chroma.2010.12.026
35. A. Asfaram, M. Ghaedi, H. Javadian, A. Goudarzi, *Ultrason. Sonochem.* **2018**, *47*, 1–9. **DOI:**10.1016/j.ultsonch.2018.04.008
36. N. N. Nia, M. R. Hadjmohammadi, *Anal. Methods* **2019**, *11*(40), 5134–5141. **DOI:**10.1039/C9AY01704F
37. K. Ishii, T. Furuta, Y. Kasuya, J. *Chromatogr. B* **2003**, *794*, 49–56. **DOI:**10.1016/S1570-0232(03)00398-2

Povzetek

V tej študiji smo uporabili hitro in učinkovito metodo za ekstrakcijo in določitev morina in kvercetina v vzorcih sadnih sokov. Metoda je osnovana na mikroekstrakciji tekoče-tekoče s pomočjo zraka in strjevanja plavajoče kapljice topila, ter HPLC-UV. Učinek 7 pomembnih parametrov na izkoristek ekstrakcije smo preiskovali in optimizirali s Plackett-Burmanovim načrtom in centralnim kompozitnim načrtom. Glede na rezultate pri Plackett-Burmanovem načrtu ionska moč vzorca, aspiracijsko-disperzijski cikli, hitrost in čas centrifugiranja nimajo znatnega vpliva na ekstrakcijo morina in kvercetina. Optimizirani pogoji ekstrakcije so bili: volumen ekstrakcijskega topila 83,6 µL, pH vzorca 4,34 ter 1-undekanol kot ekstrakcijsko topilo. Pod temi pogoji je bila kalibracijska krivulja linearna v območju 1–1000 ng/mL za morin in 0,5–1000 ng/mL za kvercetin, koeficienti determinacije pa so bili nad 0,99. Meja zaznave je bila 0,3 ng/mL za morin in 0,2 ng/mL za kvercetin. Izkoristek ekstrakcije za 10 ng/mL morina in kvercetina je bil 98,9 % oziroma 96,5 %, medtem ko je bil relativni standardni odklon (n = 3) nižji od 3,2 %.

Except when otherwise noted, articles in this journal are published under the terms and conditions of the Creative Commons Attribution 4.0 International License

DOI: 10.17344/acsi.2020.5892 *Acta Chim. Slov.* **2020,** *67,* 1100–1110
creative commons

Scientific paper

Development and Validation of RP–HPLC Method for Estimation of Curcumin from Nanocochleates and Its Application in *in–vivo* Pharmacokinetic Study

Sameer Nadaf[1] and Suresh Killedar[1]

[1]*Sant Gajanan Maharaj College of Pharmacy, Mahagaon-416503, Maharashtra, India.*

* *Corresponding author: E-mail: sam.nadaf@rediffmail.com*

Received: 02-07-2020

Abstract

A reliable RP-HPLC analytical method with UV detection at 421 nm was developed and validated for the quantitative determination of curcumin from rat plasma after oral administration of curcumin loaded nanocochleates (CU-NC) to rats. The chromatographic separation was performed on HIQ SIL, C18 (250 mm × 4.6 mm) column using methanol and water (80:20 *v/v*) as mobile phase, at 1.0 mL/min flow rate. Validation parameters included linearity, accuracy, precision, and limit of quantitation and detection. Good linearity was obtained over the range of 2.5–100 μg/mL (R^2 = 0.9979) of curcumin. The developed HPLC method was precise, with <2% relative standard deviation. Accuracy, stability, and robustness studies were also found to be acceptable. Bland-Altman plot showed an acceptable repeatability coefficient. The method was under statistical control, revealed by a control chart. After CU–NC administration, pharmacokinetic parameters i.e. C_{max}, $AUC_{0-\infty}$, and $AUMC_{0-\infty}$, were observed to be 97.69 ± 10.84 μg/mL, 1402.77 ± 9.67 (μg/mL) · h, and 35140.16 ± 14.67 (μg/mL) · h^2, respectively. This simple and precise method can be effectively implemented for routine analysis.

Keywords: Capability analysis; HPLC-UV method; control chart; curcumin; nanocochleates; rat plasma; bioavailability; biodistribution.

1. Introduction

Curcumin, a phytochemical isolated from *Curcuma longa* rhizomes, is widely recognized for its several health benefits including antitumor activity against different tumor cells.[1-5] Curcumin is regarded as safe and can be administered at high dosage. Despite its effectiveness and curative potential, the use of curcumin as an anticancer agent is restricted due to poor aqueous solubility, poor tissue absorption, rapid systemic clearance, faster metabolism, rapid degradation at neutral-alkaline pH, and impaired tumor targeting.[6–8] To override these drawbacks, different nanoparticulate drug delivery systems such as liposomes, solid lipid nanoparticles, nanostructured lipid carriers, polymeric nanoparticles, micelles, and nanoemulsions, have been investigated.[9] On the same ground, we prepared the curcumin loaded nanocochleates (CU–NC) using solvent evaporation technique to avoid the problems associated with curcumin absorption. Such a formulation has not been reported earlier. Nanocochleates (NC) are stable rod–shaped phospholipid–cation precipitates and rolled cylindrical structures that can offer attractive characteristics, for example, improved efficacy, biocompatibility, and reduced side effects.[7]

Notably, during the fabrication of diverse nanoparticulate systems, the encapsulation methods determine the percentage of encapsulants. In the case of the solvent evaporation technique, the amount of entrapped material is also subjective to partitioning between aqueous and organic phases.[10] Exact quantification of curcumin is imperative because of the loss or degradation during the formulation of curcumin nanocochleates. Therefore, extensively characterized, reliable, and validated analytical methods are needed for quantitative estimation of curcumin in biological samples and pharmaceutical formulations, as it could influence the estimation and interpretation of pharmacokinetic data.[1,10–12]

A literature survey revealed several spectrophotometric methods,[13–15] HPLC methods,[1,16–20] high-performance thin-layer chromatography (HPTLC) methods,[21–22] and liquid chromatography-mass spectroscopy (LC-MS) methods[23–24] for the quantitative determination of cur-

cumin in biological samples. Nevertheless, HPLC methods with UV detection (HPLC–UV) have been used more frequently compared to other techniques, due to their high sensitivity and precision in the detection of curcumin in biological samples. Few studies on curcumin estimation from pharmaceutical formulations, such as *in–situ* gelling liquid crystals,[1] eudragit E 100 nanoparticles,[6] poly-(lactic-co-glycolic acid), as well as poly-(lactic-co-glycolic acid)-polyethyleneglycol nanoparticles,[25] ethosomes, and transferosomes[8] have been reported.

Albeit effectual in determining the curcumin in nanoformulations, hitherto, there is no report on an analytical method for effective quantification of curcumin in the nanocochleates. Further, there are no established HPLC methods involving the validation of the proposed method using statistical techniques like Bland-Altman plot, capability analysis, and control charts.

Bland–Altman plot is a difference plot and more often used in analyzing the agreement between two diverse techniques. It is also helpful to determine the repeatability of a single method on a series of samples. Capability analysis corroborates whether a proposed method is statistically able to meet a set of predetermined specifications or not. Whereas control charts (process–behavior charts) are useful to monitor process changes over time.

In this study, an attempt was made to develop and apply a validated simple and rapid reverse-phase high performance liquid chromatographic (RP–HPLC) method for curcumin estimation in rat plasma after CU–NC administration. Data obtained were processed using novel statistical techniques like Bland-Altman plot, capability analysis, and control chart.

2. Material and Methods

2. 1. Chemicals and Reagents

Sami Labs Limited, Bangalore, India, provided the curcumin as a gift sample. Methanol used was of HPLC grade and purchased from Merck Chemicals, India. Analytical grade ethanol and Tween 80 were procured from Merck Chemicals, India. Phosphatidylcholine (Phospholipon 90G) was a gift by Lipoid GmbH Ludwigshafen, Germany. Cholesterol was purchased from Research-Lab Fine Chem Industries Ltd, Mumbai, India. All other chemicals and reagents used were of analytical grade.

2. 2. HPLC Method Development

2. 2. 1. Instrumentation

Analysis of curcumin was performed using RP–HPLC (Model LC-4000 Jasco, Japan) equipped with a pump (Jasco, PU–4180) and a 20 µL sample injector. The flow rate and run time were 1.0 mL/min and 10 min, respectively. Chromatographic separation was achieved on HIQ SIL, C18 T–5 column (250 mm × 4.6 mm; 5 µm) using UV-Vis (Jasco, UV–4075) detector operated at C1 channel at an analytical wavelength of 421 nm. Instrument operation was controlled using 'Chromonav version 2.2' software.

2. 2. 2. Selection of Mobile Phase

In the extensive preliminary experiments aimed for chromatographic estimation of curcumin in rat plasma, two combinations, namely acetone: water and methanol: water were tested at different ratios (45:55 *v/v* to 95:05 *v/v*) and different pH values. The composition was selected based on the number of theoretical plates and peak separation achieved. The mobile phase was degassed every time and filtered through a 0.45 µm membrane filter before use.

2. 2. 3. Stock and Working Solutions of Curcumin in Plasma

Stock solution (100 mg/mL) of curcumin was prepared in triplicate by dissolving 100 mg of curcumin in 100 mL of methanol and used to spike whole rat plasma. The plasma calibration standards were prepared by spiking 900 µL of blank plasma with the appropriate quantity of standard solution to get final concentrations of 2.5, 5, 10, 25, 50, 75, and 100 µg/mL. Stock solution and working standards were appropriately stored in a tightly-stoppered container at 2–8 °C until HPLC analysis.

2. 2. 4. Preparation of Calibration Curve

All the calibration standards were injected into the HPLC system in triplicate and analyzed at 421 nm. Peak area vs. drug concentration was plotted to obtain a calibration curve.

2. 2. 5. Drug Extraction from Plasma

200 µL of methanol was added to the plasma sample (0.2 mL) to facilitate the protein precipitation. The mixture was then vortexed for 1 min and subjected to centrifugation at 4000 rpm for 10 min to separate the precipitate from the organic phase. A clear supernatant aliquot (20 µL) was loaded in the system.

2. 3. Analytical Method Validation

2. 3. 1. Selection of Wavelength

A working solution of 10 µg/mL concentration was scanned in the visible range (400–800 nm) to obtain the wavelength corresponding to maximum absorption.

2. 3. 2. System Suitability

Six replicates of standard solution (10 µg/mL) were analyzed using proposed method considering the tailing factor (<1.5), relative standard deviation (% RSD) of peak

area, retention time, and theoretical plate count (>3000) as accepted parameters.[6]

2. 3. 3. Specificity and Selectivity

Method selectivity was established by analyzing curcumin and methanol extracted blank rat plasma samples (n=6), to monitor endogenous interference of plasma components during estimation of the curcumin.[1,26]

2. 3. 4. Linearity

To determine linearity, curcumin working standards prepared in the concentration range of 2.5–100 μg/mL were injected in triplicate to the HPLC system. Linearity was evaluated by the least-squares regression, Shapiro-Wilk test, and one-way analysis of variance (ANOVA) ($\alpha = 0.05$).

2. 3. 5. Accuracy

The accuracy of the method was determined by performing recovery experiments. To the previously analyzed standard curcumin solution, a known quantity of solution was spiked at different levels in triplicate and reanalyzed by the proposed method. The recovery was determined using the following equation 1 [15,27]

$$\% \text{ Recovery} = \frac{(\text{Detected amount} - \text{Standard amount})}{\text{Spiked amount}} \times 100 \quad (1)$$

2. 3. 6. Precision

To determine repeatability (intraday precision) and inter-day (intermediate) precision, working standard solutions (5, 10, and 25 μg/mL) were injected in triplicate to the HPLC system. To determine intraday precision, working standards were analyzed at seven-time intervals on the same day, whereas inter-day precision was determined by analyzing samples on the three consecutive days using the proposed method. The obtained data were expressed as % RSD and processed statistically by two-tailed student's *t*-test ($p<0.05$).[1,15,26]

2. 3. 7. Sensitivity

LOD and LOQ were determined from the calibration curve to estimate the sensitivity of the proposed method using the following equations 2 an 3

$$\text{LOD} = \frac{3\sigma}{b} \quad (2)$$

$$\text{LOQ} = \frac{10\sigma}{b} \quad (3)$$

where 'σ' is the standard deviation of the y-intercept of the regression line, and 'b' is the slope of the calibration curve.[15,20,27]

2. 3. 8. Robustness

Optimized parameters were customized and a standard solution of curcumin was injected in triplicate to determine the robustness of the proposed method. The ratio of methanol in the mobile phase, flow rate, and wavelength was varied by ± 0.2%, ± 0.1 mL/min, and ± 2 nm, respectively.[28,29] The % assay, retention time, and theoretical plate count were determined.

2. 3. 9. Ruggedness

To determine the ruggedness, the same standard solutions were injected by different analysts under analogous operating conditions.[29]

2. 3. 10. Stability

Stability assessment of the working solutions provides the effect of each storage period on the curcumin concentration. Obtained outcomes were compared with the initial concentration (zero cycle).[26]

Short-term and long-term stability

Short-term stability and long-term stability of working standards prepared at three different quality control levels (5, 10, and 25 μg/mL) were determined by storing the samples at room temperature for 24 h and –20 °C for 30 days, respectively. After a specified time, samples were analyzed and compared with the freshly prepared samples.

Freeze-thaw stability

Working solutions (n = 3) prepared at three different levels were initially frozen for 24 h and then thawed at room temperature for 2 h. This cycle was repeated for three times and meanwhile, the solutions were analyzed and compared with the freshly processed samples.[26,30]

2. 4. Statistical Analysis of the Proposed Method

2.4.1. Normality of the Data and Outlier Detection

To examine the normality of data, a normal quantile-quantile plot (Q–Q plot) was constructed. Data were processed by the Shapiro-Wilk test and the Shapiro-Francia test for normal distribution. Data distribution, variability, and outliers were detected using Grubbs–double-sided test.[15]

2. 4. 2. Coefficient of Repeatability by Bland-Altman Plot

Repeatability coefficient (CR, Eq. 4) or precision of a method was determined using the Bland–Altman plot.[31,32]

$$CR = 1.96 \times \frac{\sqrt{\sum (D_2 - D_1)^2}}{n} \quad (4)$$

where D_2 and D_1 are two measurements.

2. 4. 3. Control Charts

Control charts were computed to ensure the capability of the projected method to produce precise results.

2. 4. 4. Zone Test

The zone test verifies whether the process is influenced by variables or not. Control chart was divided equally into Zone A, B, and C.[15]

2. 4. 5. Capability Analysis of the Proposed Method

Briefly, the working solution of known concentration (10 μg/mL) was prepared and analyzed using HPLC. Lower specification limit (LSL), nominal value, and upper specification limit (USL) were set at 9.85, 10.00, and 10.15, respectively.[33]

Process capability (C_p) was calculated using the following equation 5

$$C_{p=\frac{USL-LSL}{6\sigma_{within}}} \quad (5)$$

Process capability index (Cpk) was calculated using the following equation 6

$$C_{pk} = \text{minimum of}\left(\frac{\text{mean}-\text{LSL}}{3\sigma}, \frac{\text{USL}-\text{Mean}}{3\sigma}\right) \quad (6)$$

C_p and C_{pk} were determined using SPC for Excel and should always be <1.

2. 5. Preparation and Characterization of Nanocochleates Containing Curcumin

2. 5. 1. Formulation of Curcumin Encapsulated Nanoliposomes (CU-NL)

As stated in our previous report,[7] nanoliposomes were prepared using an ethanol injection method and Box–Behnken design (data not shown). A total of 17 batches (100 mL) of CU–NL were prepared by varying the phospholipid concentration (600–750 mg), cholesterol concentration (150–200 mg), and stirring speed (1000–1800 rpm). Briefly, a specified quantity of cholesterol, phospholipid, and curcumin (100 mg), was mixed with ethanol (20 mL) and heated to form a clear solution. The solution was injected into a cold aqueous phase (100 mL) and stirred for 30 min at specified rotations with high–speed homogenizer (Remi, India) to achieve the even-sized liposomal dispersion. After complete evaporation of ethanol, the dispersion was volume adjusted (100 mL) and subjected to membrane filtration (0.45 μm).[7]

2. 5. 2. Formulation of CU-NC

To the previously formed optimized liposomal dispersion, 0.1 M calcium chloride (50 μL) was dropwise added under the vortex to form the cigar-shaped nanocochleates.

2. 6. Characterization of CU–NL and CU–NC

2. 6. 1. Particle Size

The particle size of CU–NL and CU–NC was determined using dynamic light scattering (DLS) technique (Nano-S90 ZetaSizer, Malvern Instruments, Worcestershire, UK). Samples were adequately diluted with water and analysis was performed in triplicate at a scattering angle of 90° at 25 °C.

2. 6. 2. Entrapment Efficiency (% EE)

1 mL of CU–NL and CU–NC were separately transferred to a centrifuge tube and centrifuged at 4000 rpm for 30 min at 4 °C in a cooling centrifuge (Remi, India). The supernatant was separated and settled vesicles were disrupted using ethanol to release the entrapped curcumin. Suitable diluted samples were analyzed at 421 nm and %EE was calculated using the following equation 7

$$\%EE = \frac{W_E}{W_T} \times 100 \quad (7)$$

where W_T is the total amount of drug added and W_E is the amount of entrapped drug.

2. 6. 3. Zeta Potential

Zeta potential of CU–NL and CU–NC were determined using Zetasizer 3000 HSA (Malvern Instruments, Malvern, UK).[7]

2. 7. Application to Pharmacokinetics and Biodistribution Study

2. 7. 1. Animals

Different pharmacokinetic parameters were estimated using healthy Wistar albino rats (200–250 g). Animals were kept in the cages and had free access to food and wa-

ter. The day before the experimentation, rats fasted overnight with the provision of water only.

2. 7. 2. Procedure

The protocol of the experiment was permitted by the Animal Ethical Committee of Bharati Vidyapeeth College of Pharmacy, Kolhapur, India (Approval No. BVCPK/CPCSEA/IAEC/ 01/15/2017-2020). Briefly, eight animals were assigned randomly into three groups (I, II, and III). Group-I consisting of two animals has received a single oral dose (50 mg/kg) of curcumin suspension (curcumin dispersed in 1% carboxymethylcellulose), while CU–NL and CU–NC at a dose of 50 mg/kg (corresponding to curcumin) were administered to group II and III (three animals in each group), respectively. Rats were anesthetized using chloroform and blood (0.5 mL) was withdrawn at 1, 3, 6, 12, and 24 h using retro-orbital puncture technique. Obtained blood samples were centrifuged at 4000 rpm for 10 min at 4 °C (Remi, Mumbai, India) to separate the plasma from the whole blood. Plasma samples were stored at –20 °C until HPLC analysis using a validated method.

2. 7. 3. Pharmacokinetic Parameters Estimation

The non-compartmental approach was implemented to determine the pharmacokinetic parameters. Peak plasma concentration (C_{max}) and time to acquire peak concentration (T_{max}) were estimated directly from the individual plasma concentration-time profile. The first-order elimination rate constant (K_e) was determined by the linear regression of the terminal data points. The terminal elimination half-life ($t_{1/2}$), the area under the plasma concentration-time curve ($AUC_{0-\infty}$), area under the first moment time curve ($AUMC_{0-\infty}$), mean residence time ($MRT_{0-\infty}$), clearance (Cl), and apparent volume of distribution (V_D) was also calculated. The relative bioavailability (F_{rel}) was calculated as $F_{rel} = (AUC_{CU-NC}/AUC_{curcumin}) \times 100$. Statistical significance between various pharmacokinetic parameters established for the different groups was considered significant at $p<0.05$.

2. 7. 4. Biodistribution Study

Following the bioavailability study, one rat from each group was sacrificed by cervical dislocation. Different organs like spleen, heart, liver, lung, kidney, and brain were excised, rinsed in ice-cold saline, and blotted to remove excess fluid. Tissues were weighed and subsequently homogenized with a double weight of normal saline. The mixture of homogenate (200 µL) was transferred to 200 µL of methanol, vortexed for 4 min, and followed by centrifugation at 4000 rpm for 10 min. 20 µL supernatant was separated and analyzed using the proposed HPLC method.

Fig. 2. Calibration curve of curcumin in rat plasma

3. Results and Discussion

3. 1. Optimization of Chromatographic Conditions

The different chromatographic conditions, such as mobile phase composition, flow rate, and the wavelength of analysis, were optimized after several trials. To get the sharp and separated peaks from plasma components, different solvents, viz. acetonitrile, methanol, and water were screened in varying compositions. Acetonitrile–water composition showed better sensitivity but variation in the composition resulted in altered retention time and a lower number of theoretical plate count. Conversely, methanol-water composition showed well-separated peaks of the drug from plasma and exhibited good resolution with reduced tailing, as well as improved theoretical plate count. Hence the mobile phase composition was changed from acetonitrile:water to methanol:water.

Flow rates ranging from 0.9 to 1.1 mL/min were tried to evaluate the resolution of plasma and curcumin peak. Low flow rate showed the merging of the peaks whereas broadening was achieved at a higher flow rate. Henceforth, 1 mL/min was selected as the optimum flow rate based on higher resolution and theoretical plates. Finally, the pH of mobile phase consisting of methanol and water (80:20 v/v) was adjusted to 4.5 with acetic acid. Curcumin showed maximum absorbance at 421 nm hence it was selected as detection wavelength. Notably, gradient elution mode showed an inferior separation than the isocratic mode.

3. 2. Extraction Method Optimization

Different solvents (methanol, diethyl ether, and acetonitrile) were assessed to acquire better extraction efficiency of curcumin from aliquots of rat plasma. As an optimized solvent, screening trials of methanol performed in the range of 100 to 500 µL revealed that the best recovery of curcumin was observed at 200 µL. Methanol showed good extraction efficiency (98.23 ± 2.06%) compared to acetonitrile (68.27 ± 3.97%) and diethyl ether (54.36 ± 2.81%), so it was used for subsequent analysis.

3. 3. Method Validation

3. 3. 1. System-suitability and Specificity

System suitability testing parameters are the acceptance criteria that must be fulfilled before sample analysis as they corroborate the validity of the developed method.[34] Six replicates of standard curcumin solution (10 µg/mL) were analyzed and evaluated for different principle peak parameters viz. peak area, tailing factor (T), theoretical plate number (N), and retention time (t_R). Detailed results are shown in Table 1. The chromatogram (Fig. 1) shows good peak resolution, indicating the high specificity and selectivity of this method. Being insoluble, no in-

Table 1. System suitability of the developed method

Sample No.	Peak area	Plate counts	Retention time (min)	Tailing factor
1	349796	3058	5.33	1.49
2	350473	3140	5.36	1.43
3	368647	3230	5.47	1.49
4	353307	3097	5.46	1.46
5	359219	3180	5.22	1.42
6	358462	3167	5.32	1.46
Mean	356650.7	3145.33	5.36	1.46
S.D.	7072.76	61.37	0.09	0.03
R.S.D. (%)	1.98	1.95	1.75	2.01

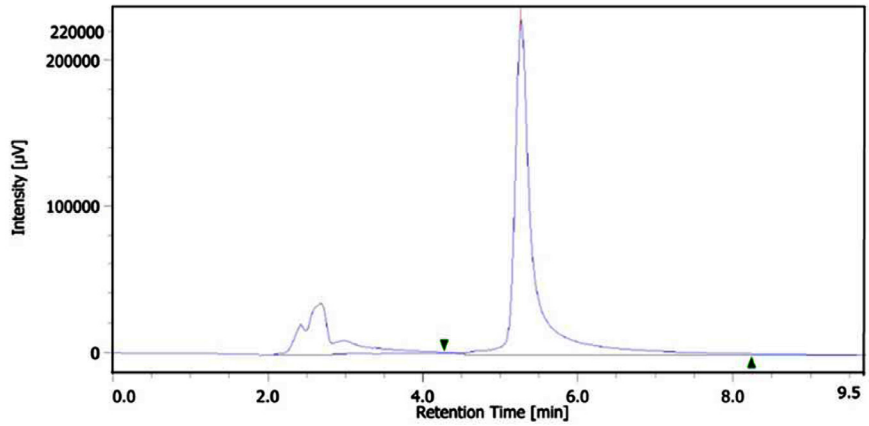
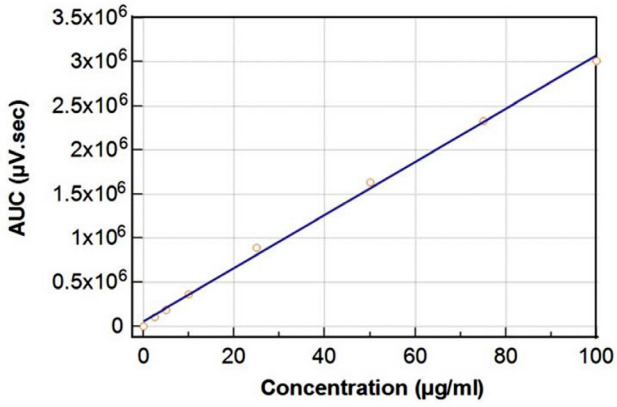


Fig. 1. HPLC chromatogram of curcumin in rat plasma

terference was detected due to excipients and additives. The proposed method meets the acceptance limits of the system suitability.

3. 3. 2. Linearity

The standard plot of working solutions of curcumin followed the Beer–Lambert law over the concentration range of 2.5–100 µg/mL (Fig. 2). Linear regression equation was found to be $y = 30206 \cdot x + 54551$ ($R^2 = 0.9979$).



Assay validity was confirmed using ANOVA ($p<0.05$). Shapiro-Wilk test (W = 0.92) and the D'Agostino-Pearson test (P = 0.45) accepted the linearity of the data. The results of the regression analysis are shown in Table 2.

3. 3. 3. Accuracy

An accuracy study indicated the reliability of the method in the routine analytical application. The % recovery was ranged from 98.60 to 99.64% with %RSD ranging from 1.53 to 1.81 ensuring that the fluctuation in drug concentration can be detected with high accuracy (Table 3).

3. 3. 4. Precision

As shown in Table 3, intra-day and inter-day precision were ranged from 98.60 to 99.64% and 96.40 to 99.16%, respectively. Lower %RSD ensured high precision. Two-tailed student's *t*-test showed no significant difference.

3. 3. 5. Sensitivity

LOD and LOQ are the lowest concentration that can be detected and quantified respectively using the proposed method. LOD and LOQ were found to be 0.09 µg/mL and 0.34 µg/mL, respectively.

Table 2. Regression analysis of the data

Dependent variable –Y			AUC (μV.sec)		
Independent variable – X			Concentration (μg/mL)		
Least squares regression					
Sample size			8		
Coefficient of determination (R^2)			0.9979		
Residual standard deviation			5.61×10^4		
Regression Equation					
$y = 5.46 \times 10^4 + 3.02 \times 10^4 \cdot x$					
Parameter	**Coefficient**	**Std. Error**	**95% CI**	**t**	**P**
Intercept	5.46×10^4	2.73×10^4	-1.23×10^4 to 1.21×10^5	2.00	0.09
Slope	3.02×10^4	563	2.88×10^4 to 3.16×10^4	53.69	<0.0001
Analysis of variance					
Source		DF	Sum of Squares		Mean Square
Regression		1	9.07×10^{12}		9.07×10^{12}
Residual		6	1.89×10^{10}		3.14×10^9
	F-ratio		2883		
	Significance level		P < 0.0001		
Residuals					
Shapiro-Wilk test for Normal distribution			W = 0.92		
			accept Normality (P = 0.45)		

Table 3. Precision and accuracy for estimation of curcumin in mobile phase using HPLC

Theoretical concentration	**Intra- and inter-day precision**					
	Experimental concentration		**Precision (%)[a]**		**Recovery (%)[b]**	
(μg/mL)	**Intra-day**	**Inter-day**	**Intra-day**	**Inter-day**	**Intra-day[c]**	**Inter-day**
5	4.94 ± 0.09	4.82 ± 0.12	1.81	2.59	99.60	96.40
10	9.86 ± 0.15	9.76 ± 0.30	1.56	3.04	98.60	97.60
25	24.9 ± 0.38	24.79 ± 0.50	1.53	1.90	99.64	99.16

[a] Expressed as relative standard deviation, RSD [b] Expressed as (mean observed concentration/actual concentration) × 100 [c] Expressed as accuracy (%)

3. 3. 6. Ruggedness and Robustness

Robustness was determined after deliberate modifications in the optimized chromatographic conditions. One way ANOVA showed no significant difference between retention times, theoretical plates, and percent recovery. %RSD less than 2 assured the reliability, robustness, and

Table 4. Robustness and ruggedness evaluation of the developed method for curcumin

Parameters	**Changes incorporated**	**Retention time**		**Theoretical plate**		**% assay**	
		Mean ± SD (min)	**RSD (%)**	**Mean ± SD**	**RSD (%)**	**Mean ± SD (%)**	**RSD (%)**
Mobile phase composition	80:20	5.36 ± 0.09	1.75	3145 ± 61	1.95	98.60 ± 1.63	1.65
(Methanol:	82:18	5.44 ± 0.06	1.18	3895 ± 77	1.97	93.64 ± 1.33	1.42
water)	78:22	5.32 ± 0.10	1.82	3079 ± 49	1.60	91.38 ± 2.35	2.57
Flow rate	1	5.36 ± 0.09	1.75	3145 ± 61	1.95	98.60 ± 1.63	1.65
(mL/min)	0.9	5.56 ± 0.11	1.92	3544 ± 55	1.54	94.67 ± 1.55	1.64
	1.1	5.29 ± 0.09	1.75	3792 ± 76	2.00	89.34 ± 1.37	1.53
Detection	421	5.36 ± 0.09	1.75	3145 ± 61	1.95	98.60 ± 1.63	1.65
wavelength (nm)	423	5.34 ± 0.09	1.60	3687 ± 56	1.53	93.65 ± 1.39	1.49
	419	5.35 ± 0.07	1.21	4300 ± 85	1.99	92.350 ± 1.58	1.71

Table 5. Stability of curcumin in rat plasma at different conditions (n = 3)

Concentration (μg/mL)	Short-term stability		Long-term stability		Freeze-thaw stability	
	Mean ± SD	RSD (%)	Mean ± SD	RSD (%)	Mean ± SD	RSD (%)
5	4.92 ± 0.010	1.95	4.88 ± 0.09	1.93	4.69 ± 0.11	2.43
10	9.8 ± 0.17	1.68	9.57 ± 0.27	2.77	9.76 ± 0.18	1.89
25	24.71 ± 0.44	1.78	24.51 ± 0.15	0.60	24.76 ± 0.26	1.05

validity of the method. Analysis of the same sample by the different analysts also showed more than 98% of the recovery. Detailed results are shown in Table 4.

3. 3. 7. Stability

Short term, long term, and freeze-thaw stability for curcumin were evaluated at three different concentration levels (5, 10, and 25 μg/mL). At room temperature, curcumin showed stability for 24 h. The working solutions showed stability in plasma for 15 days and RSD of peak area and retention time was 1.84 and 1.92, respectively (Table 5). Chromatographic analysis of curcumin working solutions after freeze-thaw cycles indicated no significant degradation and signs of instability.

3. 4. Statistical Analysis of Proposed Method

3. 4. 1. Normality of the Data and Outlier Detection

The normal Q–Q plot (Fig. 3) constituted a spike of identical values. The coefficient of skewness and coefficient of kurtosis was found to be 1.04 (P = 0.07) and –1.46 (P = 0.19). Kolmogorov-Smirnov test (D = 0.14) accepted the data normality. Grubbs–double-sided test (α = 0.05) and Tukey's test confirmed the nonexistence of outliers.

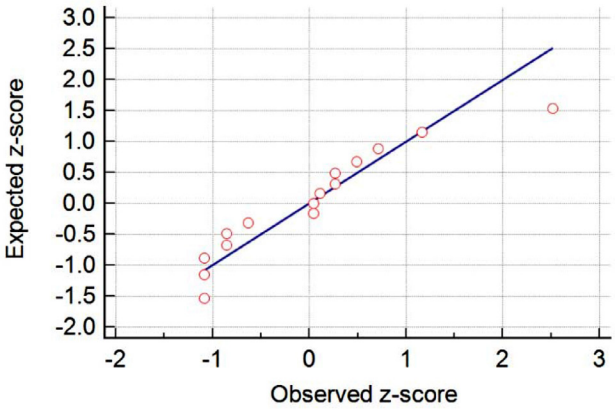


Fig. 3. Quantile-Quantile plot depicting goodness of fit

3. 4. 2. Coefficient of Repeatability by Bland-Altman Plot

Acceptable repeatability (67.440) was observed. Remarkably, 95% confidence intervals of the limit of agreements (LOA) were within the maximum allowed difference between runs, indicative of the closeness of the results (Fig. 4).[15]

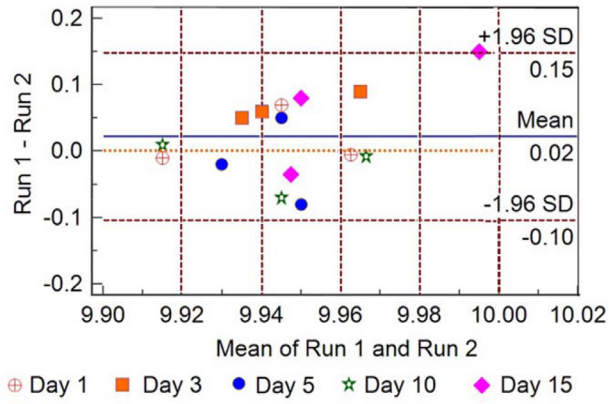


Fig. 4. The Bland-Altman plot for repetitive measurements for the same method

3. 4. 3. Control Charts and Zone Test

Control charts identify the causes of systematic errors and can control the variations in the analytical method.[35] The absence of analytical points beyond the control limits ensured the nonexistence of special cause variation in the method and no deviation from the predetermined limits. As revealed from Fig. 5, no two measurement value out of three successive results fell in 3 standard deviations (zone A) or beyond, no four out of five succeeding measurement values fell in warning limits (zone B), i.e. 2 standard deviations or beyond, and no seven consecutive re-

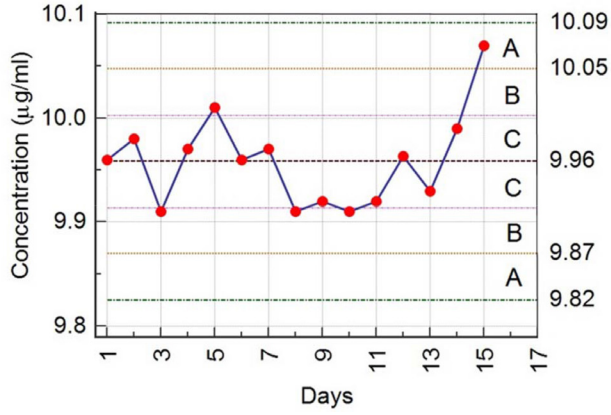


Fig. 5. Control chart showing the accuracy of the method

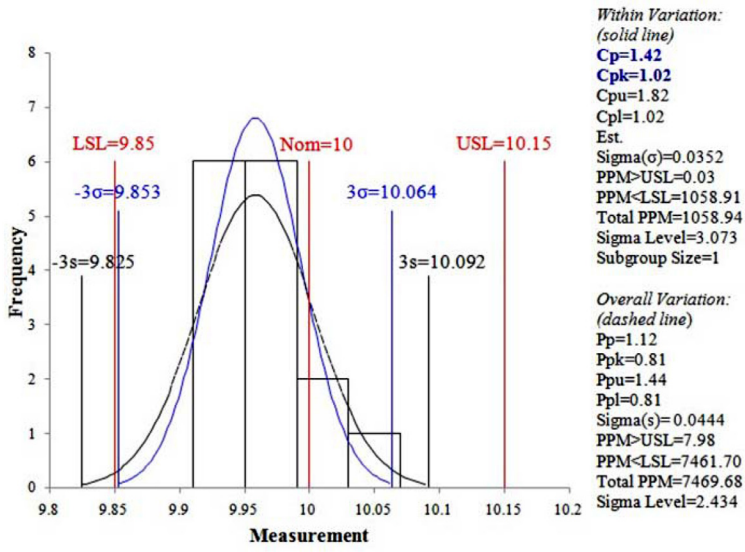


Fig. 6. Capability analysis of the proposed method

sults fell in 1 standard deviation, i.e. zone C or beyond. No point exceeded the warning limits. Hence, analytical method can be classified as in–control.

3. 4. 4. Capability Analysis of the Proposed Method

As depicted in Fig. 6, process performance (P_p) considers the overall variation, and C_p uses the within variation. Notably, 6σ was less broad than the specification width and the values of C_p (1.42) and C_{pk} (1.02) were <1. The developed method can meet the predetermined values consistently with minimum deviation.[15]

3. 5. Characterization of CU–NL and CU–NC

Particle size, zeta potential, and entrapment efficiency of optimized CU–NL and CU–NC are reported in Table 6.

Table 6. Characterization of CU–NL and CU–NC

Parameters	CU–NL	CU–NC
Particle Size (nm)	235.64 ± 11.46	261.27 ± 8.42
EE (%)	71.55 ± 4.42	79.67 ± 5.67
Zeta Potential (mV)	–14.51 ± 2.29	–9.88 ± 0.70

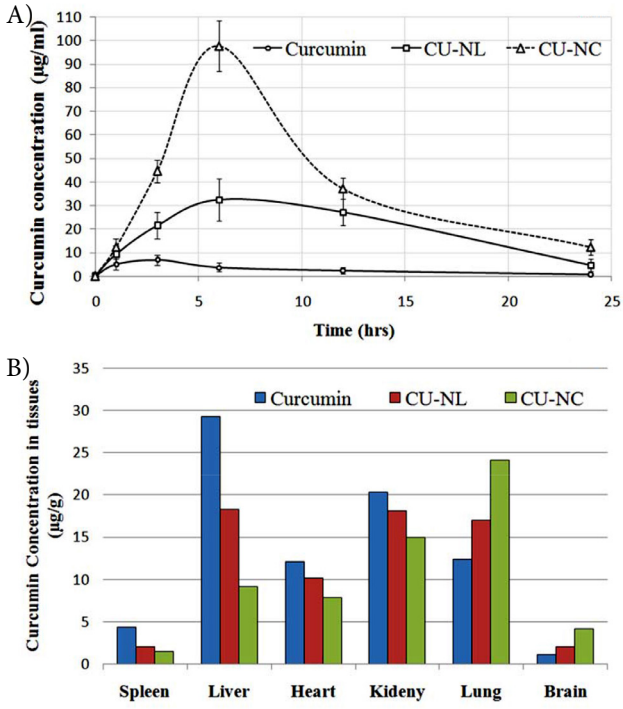


Fig. 7. (A) Mean plasma concentration-time profiles and (B) tissue distribution of curcumin after oral administration of curcumin dispersion, CU-NL and CU-NC in Wistar albino rats

3. 6. Application of Method

3. 6. 1. Pharmacokinetics Study

The plasma concentration of curcumin in rat plasma samples were estimated for 24 h after oral administration of CU–NL, CU–NC, and curcumin dispersion (Fig. 7A).

Based on a comparative analysis of all the pharmacokinetic parameters enlisted in Table 7, it is quite clear that nanocochleates significantly improved the plasma concentrations of curcumin compared to nanoliposomes and free curcumin. Throughout the study period, the curcumin plasma concentrations in CU–NC administered rats were significantly higher ($P< 0.05$) than CU–NL and curcumin-treated rats. CU–NC demonstrated the 14.1-, 22.1-, 3-, and 2.5-fold enhancement in C_{max}, $AUC_{0-\infty}$, $T_{1/2}$, and MRT, respectively, than free curcumin. Noteworthy, CU–NC showed 3-, 2.3-, 1.4-, and 1.6-fold enhancement in C_{max}, $AUC_{0-\infty}$, $T_{1/2}$, and MRT, respectively, compared to

Table 7. Estimated pharmacokinetic parameters of curcumin, CU-NL, and CU-NC after oral administration in plasma samples of Wistar albino rats

Parameters	Curcumin	CU-NL	CU-NC
Dose (mg/kg)	50	50	50
C_{max} (μg/mL)	6.92 ± 2.15	32.57 ± 8.97	97.69 ± 10.84
T_{max} (h)	3	6	6
$AUC_{(0-t)}$ [(μg/mL) · h]	56.49 ± 3.57	499.43 ± 8.98	996.41 ± 10.38
$AUC_{(0-\infty)}$ [(μg/mL) · h]	63.33 ± 5.38	598.17 ± 5.61	1402.77 ± 9.67
$AUMC_{(0-t)}$ [(μg/mL) · h^2]	378.06 ± 5.37	4673.76 ± 6.37	12032.50 ± 12.87
$AUMC_{(0-\infty)}$ [(μg/mL) · h^2]	612.42 ± 4.68	9121.91 ± 12.38	35140.16 ± 14.67
$t_{1/2}$ (h)	7.11 ± 0.81	14.59 ± 0.67	20.72 ± 0.97
K_e (h^{-1})	0.10 ± 0.005	0.05 ± 0.002	0.03 ± 0.008
MRT (h)	9.67 ± 1.24	15.25 ± 2.37	25.05 ± 2.19
CL (L/h · kg)	0.79 ± 0.08	0.08 ± 0.015	0.04 ± 0.012
V_D (L/kg)	8.07 ± 1.30	1.76 ± 0.27	1.17 ± 0.24
F_{rel} (%)	–	944.53	2215.02

CU–NL. A significant difference was also observed in the T_{max} of CU–NC and free curcumin administered rats.

Conclusively, CU–NC exhibited the 22- and 2.3-fold improvements in oral bioavailability of curcumin compared to curcumin dispersion and CU–NL. This improvement is attributed to the improved absorption, improved MRT, enhanced contact time with wall of intestine, reduced metabolism, lesser macrophage uptake, and prolonged release of curcumin from intact and stable structure of nanocochleates.

3. 6. 2. Biodistribution Study

Compared to free curcumin, CU–NC showed 2.9-, 1.5-, 3.1-, and 1.35-fold reduced distribution to spleen, heart, liver, and kidney, whereas 1.9- and 3.4-fold higher distribution was observed to brain and lungs, respectively. Compared to CU–NL, CU–NC showed 1.3-, 1.2-, 1.9-, and 1.2-fold reduction in distribution to spleen, heart, liver, and kidney, respectively. This may be attributed to a lower volume of distribution of CU–NC, as revealed in bioavailability study. Lower distribution of curcumin from CU–NC to spleen and liver suggests that the CU–NC diminishes the elimination of curcumin through reticuloendothelial system (RES). Compared to CU–NL, CU–NC showed 1.4- and 2.0-fold higher distribution to brain and lungs, respectively (Fig. 7B). These results confirm the potential of CU–NC to preferentially target the curcumin to brain and lungs. Hence, the obtained results undoubtedly corroborate the efficacy of the developed method with the purpose of implementation to the therapeutic drug monitoring and pharmacokinetic analysis.

4. Conclusion

An accurate, simple, rapid, robust, and reliable HPLC method was developed and optimized for the quantitative determination of curcumin in rat plasma. Different pharmacokinetic parameters were also estimated after the oral administration of CU–NC and CU–NL. A developed method precisely determined the minute quantity of curcumin. Hence, the method can be used routinely to analyze the curcumin from the different pharmaceutical formulations and can be explored for clinical applications and further studies.

Acknowledgments and Funding

This research received no specific grant from any funding agency in the public, commercial, or not-for-profit sectors.

Disclosure statement

Authors have no conflicts of interest to disclose.

5. References

1. B. Fonseca-Santos, M. P. D. Gremiao, M. Chorilli, *Arabian J. Chem.* **2017**, *10*, 1029–1037. **DOI:**10.1016/j.arabjc.2016.01.014
2. L. Hui-Tien, H. Yuan-Soon, Food Sci. *Human Wellness* **2018**, *7*, 134–137. **DOI:**10.1016/j.fshw.2018.06.001
3. B. C. Jordan, C. D. Mock, R. Thilagavathi, C. Selvam, *Life sci.* **2016**, *152*, 135–144. **DOI:**10.1016/j.lfs.2016.03.036
4. Z. C. Gersey, G. A. Rodriguez, E. Barbarite, A. Sanchez, W. M. Walters, K. C. Ohaeto, R. M. Graham, BMC Cancer **2017**, *17*, 99. **DOI:**10.1186/s12885-017-3058-2
5. T. Zhang, Y. Chen, Y. Ge, Y. Hu, M. Li, Y. Jin, *Acta Pharmaceutica Sinica B.* **2018**, *8,* 440–448. **DOI:**10.1016/j.apsb.2018.03.004
6. C. Moorthi, C. S. Kumar, S. Mohan, K. Krishnan, K. Kathiresan, *J. pharm. res.* **2013**, *7*, 224–229. **DOI:**10.1016/j.jopr.2013.03.006

7. S. J. Nadaf, S. G. Killedar, *J. Drug Del. Sci. Techn.* **2018**, *47*, 337–350. **DOI:**10.1016/j.jddst.2018.06.026
8. M. R. Peram, S. S. Jalalpure, S. A. Joshi, M. B. Palkar, P. V. Diwan, *J. Liq. Chromatogr. R. T.* **2017**, 40, 487–498. **DOI:**10.1080/10826076.2017.1329742
9. C. Mohanty, M. Das, S. K. Sahoo, *Expert Opin. Drug Deliv.* **2012**, 9, 1347–1364. **DOI:**10.1517/17425247.2012.724676
10. R. A. Silva-Buzanello, A. C. Ferro, E. Bona, L. Cardozo-Filho, P. H. Araujo, F. V. Leimann, O. H. Gonçalves, *Food Chem.* **2015**, *172*, 99–104. **DOI:**10.1016/j.foodchem.2014.09.016
11. M.vA. Korany, R. S. Haggag, M. A. A. Ragab, O. A. Elmallah, *Arabian J. Chem.* **2017**, *10*, S1711-S1725. **DOI:**10.1016/j.arabjc.2013.06.021
12. V. P. Shah, K. K. Midha, S. Dighe, I. J. McGilveray, J. P. Skelly, A. Yacobi, et al.,. *Eur. J. Drug Metab. Pharmacokinet.* **1992**, *16(4)*, 249-255.
13. P. V. Kadam, C. L. Bhingare, R. Y. Nikam, S. A. Pawar, *Pharm. Methods* **2013**, *4*, 43–45. **DOI:**10.1016/j.phme.2013.08.002
14. K. Ahmed, Y. Li, D. J. McClements, H. Xiao, *Food Chem.* **2012**, *132*, 799-807. **DOI:**10.1016/j.foodchem.2011.11.039
15. S. J. Nadaf S. G. Killedar, *Pharm. Methods* **2018**, *9*, 56-63. **DOI:**10.5530/phm.2018.2.11
16. H. K. Syed, K. B. Liew, G. O. Loh, K. K. Peh, *Food Chem.* **2015**, *170*, 321-326. **DOI:**10.1016/j.foodchem.2014.08.066
17. J. Mahale, L. M. Howells, R. Singh, R. G. Britton, H. Cai, K. Brown, *Biomed. Chromat.* **2018,** e4280. **DOI:**10.1002/bmc.4280
18. Y. Long, W. Zhang, F. Wang, Z. Chen, *J. Pharma. Anal.* **2014**, *4*, 325-330. **DOI:**10.1016/j.jpha.2013.10.002
19. H. S. Koop, R. A. de Freitas, L. M. de Souza, G. R. Martinez, J. L. M. Silveira, *Chromatogr.* **2013**, *76*, 1041–1048. **DOI:**10.1007/s10337-013-2402-1
20. Guidance for Industry, Bioanalytical Method Validation, U.S. Department of Health and Human Services, Food and Drug Administration Centre for Drug Evaluation and Research (CDER), Centre for Veterinary Medicine (CVM), May, 2001.
21. S. Kharat, A. Namdeo, P. Mehta, *J. Taibah Univ Sci.* **2017**, 11, 775–781. **DOI:**10.1016/j.jtusci.2016.10.004
22. V. A. Pkekre, S. G. Walode, *Int. J. Pharm. Sci. Res.* **2012**, 3, 3796–3800.
23. S. R. Kunati, S. Yang, B. M. William, Y. Xu, *J. Pharm. Biomed. Anal.* **2018**, 156, 189–198. **DOI:**10.1016/j.jpba.2018.04.034
24. Y. Cao, R. X. Xu, Z. Liu, J. *Chromatogr. B Analyt. Technol. Biomed. Life Sci.* **2014**, 949-950, 70–78. **DOI:**10.1016/j.jchromb.2013.12.039
25. T. C. F. do Nascimento, D. M. Casa, L. F. Dalmolin, A. C. de Mattos, N. M. Khalil, R. M. Mainardes, *Curr. Pharm. Anal.* **2012**, 8, 324. **DOI:**10.2174/157341212803341654
26. B. Kurangi, S. Jalalpure, S. Jagwani, J. *Chromatogr. B.* **2019**, *1122–1123,* 39–48. **DOI:**10.1016/j.jchromb.2019.05.017
27. S. Kongkiatpaiboon, N. Duangdee, S. Chewchinda, O. Poachanukoon, K. Amnuaypattanapon, *J. King Saud Univ. Sci.* **2019**, *31*, 48–51. **DOI:**10.1016/j.jksus.2017.05.016
28. S. S. Perumal, S. P. Ekambaram, S. Raja, *J. food drug anal.* **2014**, *22*, 520–526. **DOI:**10.1016/j.jfda.2014.05.003
29. S. Deya, S. S. Patro, N. S. Babu, P. N. Murthy, S. K. Panda, *J. Pharm. Anal.* **2017**, *7*, 134–140. **DOI:**10.1016/j.jpha.2013.12.002
30. L. Xie, X. N. Li, D. X. Jiang, D. Zhang, *J. Pharm. Anal.* **2011**, *1*, 297–301. **DOI:**10.1016/j.jpha.2011.09.004
31. J. Bland, D. Altman, *The Lancet.* **1986**, *327*, 307–310. **DOI:**10.1016/S0140-6736(86)90837-8
32. J. Bland, D. Altman, *Stat. Methods in Medical Res.* **1999**, *8*, 135–160. **DOI:**10.1191/096228099673819272
33. S. Koppel, S. Chang, *Procedia Manufacturing.* **2016**, *5,* 122–131. **DOI:**10.1016/j.promfg.2016.08.012
34. F. S. Bandarkar, P. R. Vavia, *Trop. J. Pharm. Res.* **2009**, *8*, 257–264. **DOI:**10.4314/tjpr.v8i3.44543
35. P. Masson, *J. Chromatogr. A.* **2007**, *1158*, 168–173. **DOI:**10.1016/j.chroma.2007.03.003

Povzetek

Razvili in validirali smo zanesljivo RP-HPLC analizno metodo z UV detekcijo pri 421 nm za kvantitativno določanje kurkumina v podganji plazmi po oralni administraciji s kurkuminom napolnjenih nanoškoljkic (nanokohleati, CU-NC) podganam. Kromatografska ločba je potekala na koloni HIQ SIL, C18 (250 mm × 4,6 mm) z metanolom in vodo (80:20 *v/v*) kot mobilno fazo pri pretoku 1,0 mL/min. Preverjali smo naslednje validacijske parametre: linearnost, točnost, natančnost, mejo določanja in mejo zaznave. Linearnost je bila potrjena v območju 2,5–100 μg/mL kurkumina (R^2 = 0,9979). Razvita HPLC metoda je bila natančna z <2% relativnega standardnega odmika. Tudi parametri točnosti, stabilnosti in robustnosti so bili sprejemljivi. Bland-Altman graf je pokazal sprejemljiv koeficient ponovljivosti. Metoda je bila statistično kontrolirana, kar je bilo razvidno iz kontrolne karte. Po administraciji CU–NC podganam smo določili naslednje farmakokinetične parametre: C_{max} 97,69 ± 10,84 μg/mL, $AUC_{0-\infty}$ 1402,77 ± 9,67 (μg/mL) · h in $AUMC_{0-\infty}$ 35140,16 ± 14,67 (μg/mL) · h^2. To preprosto in natančno metodo lahko učinkovito uporabimo za rutinske analize.

Except when otherwise noted, articles in this journal are published under the terms and conditions of the Creative Commons Attribution 4.0 International License

Scientific paper

Crystal Structure and Photophysical Properties of a Novel Dy-Hg Isonicotinic Acid Compound with One-Dimensional Chain-Like Cations

Wen-Tong Chen*

[1] *Institute of Applied Chemistry, School of Chemistry and Chemical Engineering, Ji'an Key Laboratory of Photoelectric Crystal Materials and Device, Humic Acid Utilization Engineering Research Center of Jiangxi Province, Jiangxi Province Key Laboratory of Coordination Chemistry, Jinggangshan University, 343009, Ji'an, Jiangxi, China*

[2] *Department of Ecological and Resources Engineering, Fujian Key Laboratory of Eco-Industrial Green Technology, Wuyi University, Wuyishan, Fujian 354300, China*

[3] *State Key Laboratory of Structural Chemistry, Fujian Institute of Research on the Structure of Matter, Chinese Academy of Sciences, Fuzhou, Fujian 350002, China*

** Corresponding author: E-mail: wtchen_2000@aliyun.com*
Tel & Fax: Tel.: +86(796)8100490; fax +86(796)8100490

Received: 02-17-2020

Abstract

A novel Dy-Hg compound $[Dy(HIA)_3(H_2O)_2]_{2n} \cdot 2n HgCl_4 \cdot n HgCl_5 \cdot n H_3O \cdot 3n H_2O$ (**1**; HIA = isonicotinic acid) was prepared through a hydrothermal reaction and characterized by X-ray diffraction. The compound crystallizes in the space group of *C*2/*c* of the monoclinic system. The crystal structure of compound **1** has one-dimensional (1-*D*) chain-like cations. A photoluminescence experiment with a solid-state sample revealed that this compound exhibits a yellow emission band at 575 nm and, this emission band shall come from the 4*f* electron $^4F_{9/2} \rightarrow {}^6H_{13/2}$ characteristic transfer of Dy^{3+} ions. The compound features CIE chromaticity coordinates of 0.5168 and 0.4824 in the yellow region. A UV-visible diffuse reflectance spectrum with a solid-state sample unveiled that this compound possesses a wide optical band gap of 3.39 eV.

Keywords: Chromaticity coordinate; mercury; dysprosium; photoluminescence; lanthanide

1. Introduction

It is well-known that most of lanthanide(III) ions (not including La^{3+} and Lu^{3+} ions) can usually show fine photoluminescence performances and, in recent years, new lanthanide materials with interesting photoluminescence properties have drawn more and more attention from the researchers in chemical, physical, material and other domains.[1–5] As of today, a large number of researchers have been devoting themselves to the preparation, structures, physical and chemical characterization of new lanthanide materials, in order to explore their various potential applications in luminescent probes, cell imaging, catalysts, magnetic materials, electrochemical displays, sensors, light-emitting diodes, and so forth.[6–12] Relative to the large number of investigations on the photoluminescence behavior of new lanthanide materials, only very few investigations on the semiconductor properties of lanthanide materials have been explored so far and, therefore, more studies are still necessary.[13]

Many transition metal-containing compounds generally possess attractive properties that enable them to display potential applications in the areas of chemistry, materials, physics, biology and other fields. As a result, new transition metal-containing materials with novel properties also have attracted more and more interest since many years ago.[14–27] In recent years, a large amount of effort has been carried out to explore new transition metal-containing materials.[28–40] As a member of transition metal-containing compounds, group 12 (IIB) metal-containing compounds are also attractive.[41–45] Moreover, isonicotinic acid is an attractive and important organic molecule, because it can be applied as a useful synthetic ligand. This is due to the fact that it features two carboxyl oxygen chelating atoms at

one end and one nitrogen atom at the other end. It is known that oxygen atoms are favorable to coordinate to lanthanide metals, while nitrogen atoms are favorable to coordinate to transition metals. So, it is believed that the isonicotinic acid is able to simultaneously bind to lanthanide and transition metals and form an extended motif. Over these years, the investigations on new materials with novel photoluminescence and semiconductor behavior, especially lanthanide-mercury-containing compounds, have become one of my research topics. In present paper, a novel Dy-Hg material $[Dy(HIA)_3(H_2O)_2]_{2n}{\cdot}2n HgCl_4{\cdot}n HgCl_5{\cdot}n H_3O{\cdot}3n H_2O$ (**1**; HIA = isonicotinic acid) is reported with its hydrothermal synthesis, X-ray structure, photophysical behaviors as well as thermogravimetry. This compound is characterized by one-dimensional (1-*D*) chain-like cations.

2. Experimental Section

2. 1. Materials and Characterization

In this study all of the chemicals applied for the preparation of **1** were AR grade purity and commercially available. Elemental microanalyses of carbon, hydrogen and nitrogen were carried out on an Elementar Vario EL elemental analyzer. The FT-IR data set was measured on a PE Spectrum-One FT-IR spectrophotometer with a KBr pellet. The photoluminescence spectrum was carried out with a solid-state sample of **1** on a F97XP spectrometer. The UV-visible diffuse reflectance spectrum was carried out with a solid-state sample of **1** on a TU1901 spectrometer. A thermogravimetry (TG) diagram was measured on a NETZSCH TG 209F3 TG analyzer under nitrogen atmosphere.

2. 2. Synthesis of $[Dy(HIA)_3(H_2O)_2]_{2n}\cdot 2nHgCl_4\cdot nHgCl_5\cdot nH_3O\cdot 3nH_2O$ (*1*)

A mixture of 3.5 mmol $HgCl_2$ (952 mg), 3 mmol isonicotinic acid (369 mg), 1 mmol $DyCl_3{\cdot}6H_2O$ (377 mg) and 10 mL distilled water was added into a 25 mL Teflon-lined stainless steel vessel and the vessel was heated at 433 K for two weeks under autogenous pressure, then powered off. Colorless block crystals can be found when the vessel temperature was cooled down. The yield was 33% calculated on $HgCl_2$. Anal. Calcd. For $C_{36}H_{47}Cl_{13}Dy_2Hg_3N_6O_{20}$: C, 19.04; H, 2.09; N, 3.70. Found: C, 19.11; H, 2.12; N, 3.75. FTIR peaks (cm^{-1}): 3450(vs), 3143(w), 3072(m), 2889(w), 1691(m), 1592(vs), 1410(vs), 1233(m), 1077(w), 1050(w), 999(w), 848(m), 759(s), 681(s), 540(m) and 410(m).

2. 3. Crystal Structure Determination and Refinement

A carefully selected single crystal with dimensions 0.10 mm × 0.07 mm × 0.04 mm was adhered on the top of a glass fiber, then mounted to a SuperNova CCD diffractometer with the X-ray source being of a graphite monochromatic Mo-*Kα* radiation (λ = 0.71073 Å). The X-ray intensity data set was measured with an ω scan mode. The CrystalClear software was used for data reduction and absorption correction. The single crystal molecular structure of the title compound was solved by means of the direct methods and the structure was finally refined on F^2 with full-matrix least-squares and the Siemens SHELXTL^{TM} V5 program. All of the non-hydrogen atoms were set on their difference Fourier peaks and anisotropically refined. Hydrogen atoms were theoretically generated, except for several on water molecules were generated on difference Fourier peaks. Hydrogen atoms at O1W and O4W were not found. Some bad equivalents were cut off in order to obtain more reasonable structure. 14 distance or angle restraints were used, in order to get more accurate results. Important crystal data and refinement details are depicted in Table 1 and some important bond lengths and angles are shown in Table 2.

Table 1. Crystal data of **1**.

Formula	$C_{36}H_{47}Cl_{13}Dy_2Hg_3N_6O_{20}$
M_r	2271.42
color	colorless
Crystal system	monoclinic
Space group	*C*2/*c*
a (Å)	24.2350(4)
b (Å)	20.8170(4)
c (Å)	15.3597(2)
β (°)	127.925(2)
V (Å^3)	6112.51(17)
Z	4
Reflections collected	16912
Independent, observed reflections (R_{int})	5296, 4646 (0.0196)
$d_{calcd.}$ (g/cm^3)	2.468
μ (mm^{-1})	10.564
F(000)	4232
T (K)	293(2)
R^1, wR^2	0.0330, 0.0848
S	1.053
Largest and Mean Δ/σ	0.001, 0
$\Delta\rho$ (max, min) (e/Å^3)	3.145, –1.346

Table 2. Some bond lengths (Å) and angles (°)

Hg1–Cl1	2.474(5)	Cl4–Hg2–Cl7	105.78(7)
Hg1–Cl2	2.463(4)	O4#2–Dy1–O1	145.78(17)
Hg1–Cl3	2.262(4)	O4#2–Dy1–O2#3	78.05(16)
Hg1–Cl3#1	2.633(3)	O1–Dy1–O2#3	76.60(16)
Hg1–Hg1#1	1.2373(14)	O4#2–Dy1–O3	103.56(15)
Hg2–Cl4	2.477(2)	O1–Dy1–O3	81.75(16)
Hg2–Cl5	2.4502(19)	O2#3–Dy1–O3	139.23(16)

Hg2–Cl6	2.4628(19)	O4#2–Dy1–O6#3	138.03(16)
Hg2–Cl7	2.5641(17)	O1–Dy1–O6#3	76.09(16)
Dy1–O1	2.382(4)	O2#3–Dy1–O6#3	126.09(16)
Dy1–O4#2	2.378(4)	O3–Dy1–O6#3	80.04(16)
Dy1–O3	2.404(4)	O4#2–Dy1–O5	80.99(16)
Dy1–O2#3	2.384(4)	O1–Dy1–O5	113.47(16)
Dy1–O5	2.421(4)	O2#3–Dy1–O5	74.59(16)
Dy1–O6#3	2.411(4)	O3–Dy1–O5	146.17(17)
Dy1–O1W	2.529(4)	O6#3–Dy1–O5	75.16(16)
Dy1–O2W	2.489(5)	O4#2–Dy1–O2W	71.39(15)
		O1–Dy1–O2W	140.56(16)
Cl3–Hg1–Cl2	108.81(13)	O2#3–Dy1–O2W	140.46(16)
Cl3–Hg1–Cl1	122.95(9)	O3–Dy1–O2W	73.66(16)
Cl2–Hg1–Cl1	91.49(10)	O6#3–Dy1–O2W	69.72(15)
Cl3–Hg1–Cl3#1	111.45(15)	O5–Dy1–O2W	76.34(16)
Cl2–Hg1–Cl3#1	111.13(13)	O4#2–Dy1–O1W	77.38(15)
Cl1–Hg1–Cl3#1	109.15(8)	O1–Dy1–O1W	72.50(15)
Cl5–Hg2–Cl6	117.08(7)	O2#3–Dy1–O1W	69.72(14)
Cl5–Hg2–Cl4	113.82(7)	O3–Dy1–O1W	70.99(15)
Cl6–Hg2–Cl4	109.83(7)	O6#3–Dy1–O1W	139.63(15)
Cl5–Hg2–Cl7	104.21(6)	O5–Dy1–O1W	141.24(15)
Cl6–Hg2–Cl7	104.91(6)	O2W–Dy1–O1W	124.81(15)

Symmetry codes: #1 $-x + 1, y, -z + 5/2$; #2 $-x + ½, -y + ½, -z + 1$; #3 $-x + 1, y, -z + 3/2$

Table 3. Hydrogen bonding interactions

D–H···A	D–H, Å	H···A, Å	D···A, Å	D–H···A, °
N1–H1B···Cl7#1	0.86	2.36	3.151(10)	154
N2–H2B···Cl4#2	0.86	2.58	3.298(8)	141
N3–H3A···O4W#3	0.86	2.00	2.827(14)	162
O3W–H3WA ···Cl4#3	0.85(11)	2.41(13)	3.211(11)	157(15)
O3W–H3WB···Cl5	0.86(11)	2.39(14)	3.215(10)	161(17)
O2W–H2WB···Cl6	0.85(7)	2.37(7)	3.199(5)	166(8)
C7–H7A···Cl2#5	0.93	2.57	3.395(11)	148

Symmetry codes: #1: $½ + x, -½ + y, z$; #2: $x, 1 - y, -½ + z$; #3 $x, 1 - y, ½ + z$; #4 $½ - x, ½ - y, 1 - z$; #5 $-½ + x, ½ - y, -3/2 + z$.

3. Results and Discussion

The FT-IR spectrum exhibits that the bands of compound **1** are mainly in the frequency range of 410–1691 cm^{-1}. A very strong band at 3450 cm^{-1} can be ascribed to the ν_{O-H} stretching vibration mode of the coordinating water. The middle intense peak at 3072 cm^{-1} should be ascribed to the ν_{C-H} stretching vibration mode of the pyridyl ring of the isonicotinic acid ligand. The very strong bands at 1592 and 1410 cm^{-1} can be ascribed to the ν_{C-O} stretching vibration mode of the coordinating carboxylic moieties and, this means that all carboxylic moieties are coordinated to the metal. The strong peak at 759 cm^{-1} should be ascribed to the ν_{C-H} bending vibration mode of the pyridyl rings.

As analyzed by X-ray single crystal diffraction, compound **1** crystallizes in the monoclinic system *C*2/*c* space group. As depicted in Fig. 1, the asymmetric molecular structure includes crystallographically independent Hg1 (in the *C*2 axis with 0.5 occupancies), Hg2, Dy1, Cl1 (in the *C*2 axis with 0.5 occupancies), Cl2 to Cl7, three isonicotinic acid ligands, two coordinating water and two lattice water molecules. So, most of the atoms reside at a general position, but Hg1 (in 0.5 occupancies) as well as Cl1 (in 0.5 occupancies) locate at a special position.

The ion Hg1 is bound by five chloride ions and forms a distorted $HgCl_5$ triangular bipyramidal coordination geometry with the bond angle Cl–Hg1–Cl in the range of 91.49(10)–122.95(9)° and the bond distance Hg1–Cl in the span of 2.262(4)–2.633(3) Å. The ion Hg2 is bound by four chloride ions and forms a distorted $HgCl_4$ tetrahedron with the bond angle Cl–Hg2–Cl in the range of 104.21(6)–117.08(7)° and the bond distance Hg2–Cl in the span of 2.4502(19)–2.5641(17) Å. The bond distances of Hg–Cl are comparable with that previously reported in the references.[46,47] The dysprosium ion Dy1 is surrounded by eight oxygen atoms of which two are water oxygen atoms and six are isonicotinic acid oxygen atoms. The bond distances of Dy–O are in the span of 2.378(4)–2.529(4) Å with a mean value of 2.424(5) Å that is also in the normal region.[48] The bond angles of O–Dy–O are in the range of 69.72(14)–146.17(17)°. The neighbouring DyO_8 polyhedra connect to each other through two or four isonicotinic acid moieties to give a one-dimensional (1-D) Dy-$(HIA)_2$-Dy-$(HIA)_4$-Dy-$(HIA)_2$-Dy-$(HIA)_4$-Dy- chain running along the *a*-axis, as shown in Fig. 2. In the title compound, there are many hydrogen bonding interactions, i.e. N–H···Cl, N–H···O, O–H···O, O–H···Cl and C–H···Cl (see Table 3, please). These hydrogen bonding interactions link the $[Dy(HIA)_3(H_2O)_2]_{2n}^{6+}$ chains, $HgCl_4^{2-}$ ions, $HgCl_5^{3-}$ ions, and lattice water molecules together to complete a three-dimensional (3-D) supramolecular network, as shown in Fig. 3.

Up to date, some similar compounds have been reported by our group.[49–53] These compounds are prepared under similar conditions. They have different lanthanides

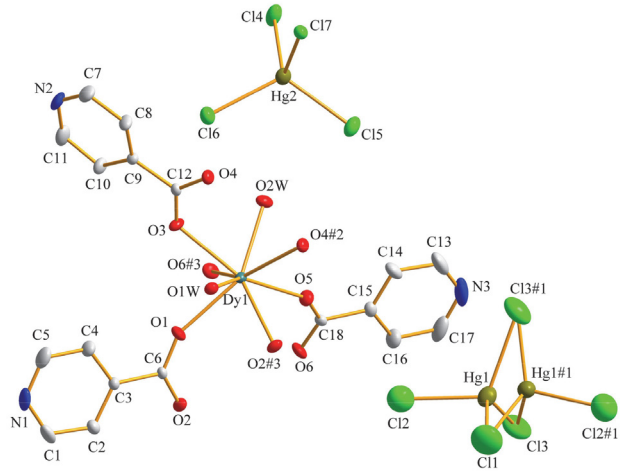


Figure 1. An ORTEP figure of compound **1** at 30% thermal ellipsoids. The lattice water molecules and H atoms have been omitted for clarity.

with nicotinic acid or isonicotinic acid as ligands. All of these compounds show one-dimensional (1-D) chain-like cations.

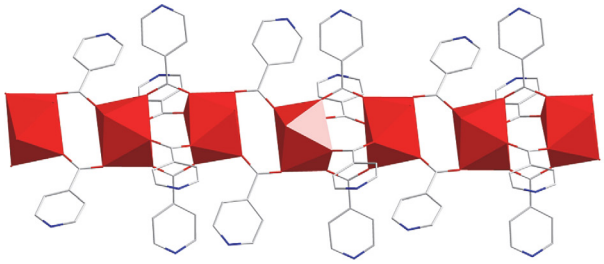


Figure 2. A 1-D chain running along the *a*-axis with the polyhedra representing the DyO_8 moieties

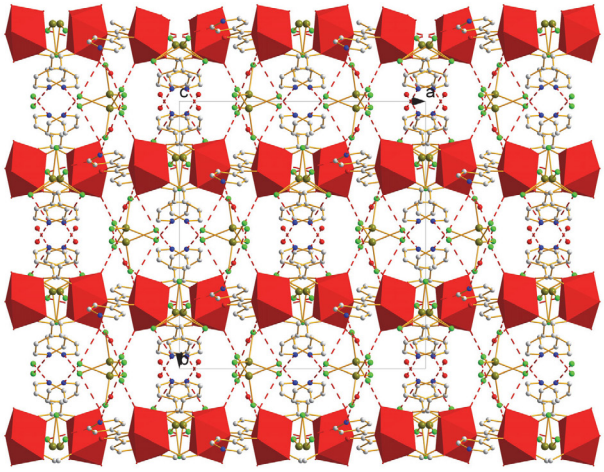


Figure 3. A packing view of **1** with the polyhedra representing the DyO_8 moieties. The dashed lines are hydrogen bonding interactions (see Table 3, please).

It is known that mercury compounds and dysprosium compounds can generally show photoluminescence performances. As a result, the photoluminescence behavior of the title compound was measured with solid state samples under room temperature. As given in Fig. 4, the photoluminescence adsorption of the title compound locates in the span of 530–560 nm and the maximum peak resides at 547 nm. When the title compound was excited by the 547 nm wavelength, it exhibits one photoluminescence emission peak that locates at 575 nm (in yellow region). This emission band shall be attributed to the 4*f* electrons $^4F_{9/2} \rightarrow {}^6H_{13/2}$ characteristic transfer of the Dy^{3+} ions.[64] With regard to compound **1**, it features CIE chromaticity coordinates of 0.5168 and 0.4824 in the yellow region, as shown in Fig. 5. As a result, compound **1** may be a potential yellow photoluminescence emitting material. Some similar compounds[49–53] reported by our group show different luminescence properties, because they have different lanthanide ions, such as gadolinium, neodymium, erbium, lanthanum and praseodymium.

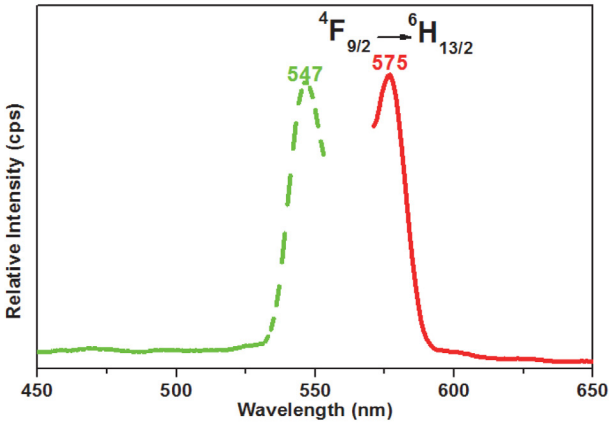


Figure 4. The solid state photoluminescence spectra of **1** measured at room temperature. Green dashed lines represent excitation and red solid lines represent emission.

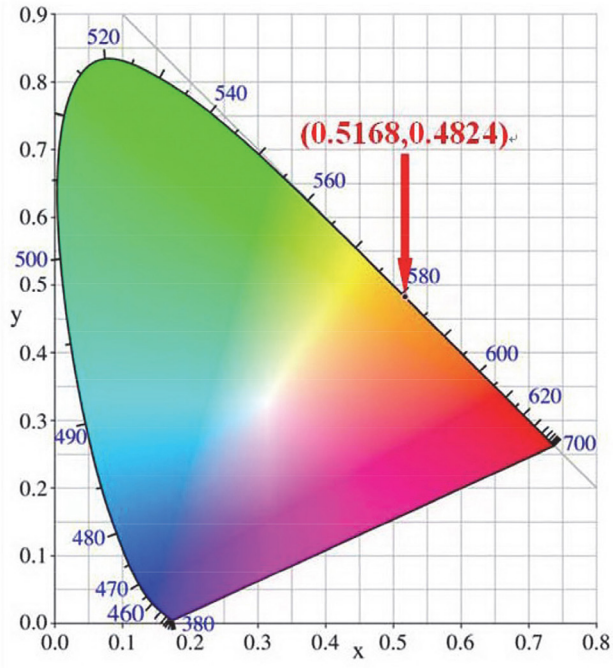


Figure 5. A CIE figure of compound **1**.

In general, dysprosium compounds and mercury compounds can exhibit semiconductive behaviors. The title compound consists of both dysprosium and mercury elements; therefore, it can probably show semiconductive properties. For the sake of further studying the photophysical behaviors of compound **1**, its solid state UV-visible diffuse reflectance spectrum was measured at room temperature with powder samples. Its solid state UV-visible diffuse reflectance spectrum data set was converted with the Kubelka-Munk formula $\alpha/S = (1 - R)^2/2R$ that is commonly used for related researches. With regard to the Kubelka-Munk formula, the α, S and R indicate the absorption coefficient, scattering coefficient and the reflec-

tion rate, respectively. By means of the linear epitaxy of the maximum absorption edge on the *α/S* versus energy diagram of compound **1**, the semiconductor band gap value can be ascertained. As a result, with the use of this method, the semiconductor band gap value of compound **1** can be found to be 3.39 eV that is shown in Fig. 6. On the *α/S* versus energy curve, several small bands between 2.5 eV and 3.3 eV can be found and they shall be attributed to the Dy(III) ions. Based on this band gap value of 3.39 eV, it is believed that compound **1** may be a wide optical band gap semiconductor material. The maximum absorption edge of the curve is steep, which means that it should undergo a direct transition in the title compound.[55]

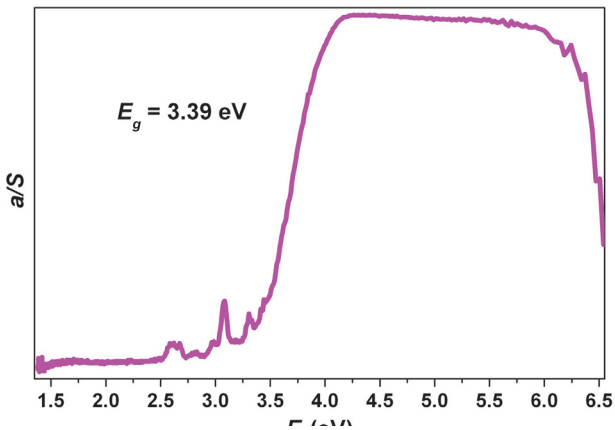


Figure 6. A solid-state diffuse reflectance spectrum of **1**.

The thermogravimetry (TG) diagram of compound **1** was measured under nitrogen atmosphere. Complex **1** shows a four-step decomposition process with the mass loss being of 3.19%, 32.87%, 31.88% and 13.15%, respectively, as depicted in Fig. 7. The total mass loss of compound **1** is 81.09%. At the first stage (until 90.1 °C), the mass loss is 3.19% of the total mass loss; this is due to the leave of all lattice water molecules (calculated 3.21%). From 90.1 °C to 262.9 °C is the second stage and, at this stage, the mass loss is 32.87% that can be assigned to the leave of all coordination water molecules and $HgCl_4$ moieties (calculated 33.32%). At the third stage (from 262.9 °C to 421.6 °C), the mass loss is 31.88% which is probably because of the loss of all isonicotinic acid ligands (calculated 32.49%). The last step is from 421.6 °C to 600 °C and, at this stage, the weight loss is 13.15% that is because of the loss of some $HgCl_5$ moieties (calculated 16.64%).

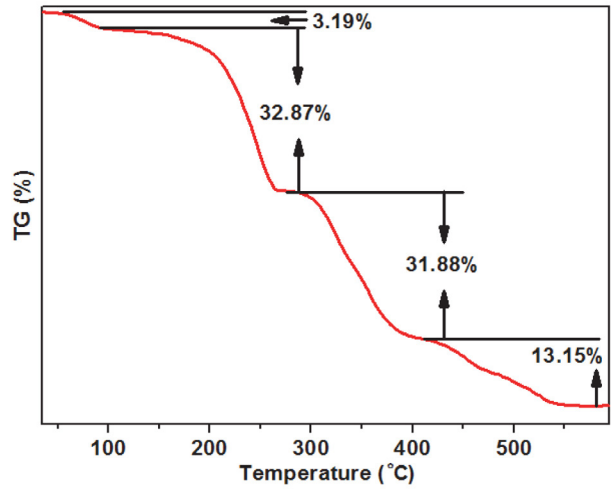


Figure 7. A TG diagram of **1**.

4. Conclusions

A novel Dy-Hg compound was hydrothermally prepared and the crystal structure was characterized. The crystal structure has one-dimensional chain-like cations. This compound exhibits a yellow photoluminescence emission peak and this emission peak shall come from the 4*f* electrons $^4F_{9/2} \rightarrow {}^6H_{13/2}$ characteristic transfer of Dy^{3+} ions. The compound is characteristic of a CIE chromaticity coordinate of (0.5168, 0.4824) in the yellow region. A UV-visible diffuse reflectance spectrum measured with a solid-state sample unveiled that the compound possesses a wide optical band gap of 3.39 eV. Therefore, the compound may be a candidate of yellow photoluminescence emission materials and wide optical band gap semiconductor materials.

Acknowledgments

The present work is supported by the open foundation of the State Key Laboratory of Structural Chemistry, Fujian Institute of Research on the Structure of Matter, Chinese Academy of Sciences (20180008).

5. Supplementary Material

Crystallographic data for the structural analysis has been deposited with the Cambridge Crystallographic Data Centre, CCDC No. 1983374. Copies of this information may be obtained free of charge from the Director, CCDC, 12 Union Road, Cambridge, CBZ 1EZ, UK (Fax: +44-1223-336033; email: deposit@ccdc.cam.ac.uk or www: http://www.ccdc. cam.ac.uk).

6. References

1. G. X. Wen, M. L. Han, X. Q. Wu, Y. P. Wu, W. W. Dong, J. Zhao, D. S. Li, L. F. Ma, *Dalton Trans.* **2016**, *45*, 15492–15499. **DOI:**10.1039/C6DT03057B
2. A. E. Sedykh, D. G. Kurth, K. Mueller-Buschbaum, *Eur. J. Inorg. Chem.* **2019**, *42*, 4564–4571. **DOI:**10.1002/ejic.201900872

3. S.-J. Liu, C. Cao, C.-C. Xie, T.-F. Zheng, X.-L. Tong, J.-S. Liao, J.-L. Chen, H.-R. Wen, Z. Chang, X.-H. Bu, *Dalton Trans.* **2016**, *45*, 9209–9215. **DOI:**10.1039/C6DT01349J
4. K. Burek, J. Dengler, F. Emmerling, I. Feldmann, M. U. Kumke, J. Stroh, *ChemistryOpen* **2019**, *8*, 1441–1452. **DOI:**10.1002/open.201900249
5. Z. Zhou, J. P. Gu, X. G. Qiao, H. X. Wu, H. R. Fu, L. Wang, H. Y. Li, L. F. Ma, *Sensor. Actuat. B-Chem*. **2019**, *282*, 437–442. **DOI:**10.1016/j.snb.2018.11.103
6. X. H. Xiong, Y. Tao, Z. W. Yu, L. X. Yang, L. J. Sun, Y. L. Fan, F. Luo, *Chem. Engin. J*. **DOI:**10.1016/j.cej.2019.123240.
7. F. Oukhatar, S. V. Eliseeva, C. S. Bonnet, M. Placidi, N. K. Logothetis, S. Petoud, G. Angelovski, E. Toth, *Inorg. Chem.* **2019**, *58*, 13619–13630. **DOI:**10.1021/acs.inorgchem.9b00887
8. S.-J. Liu, C. Cao, S.-L. Yao, T.-F. Zheng, Z.-X. Wang, C. Liu, J.-S. Liao, J.-L. Chen, Y.-W. Li, H.-R. Wen, *Dalton Trans*. **2017**, *46*, 64–70. **DOI:**10.1039/C6DT03589B
9. X. Yao, G. H. An, Y. X. Li, P. F. Yan, W. Z. Li, G. M. Li, *J. Solid State Chem*. **2019**, *274*, 295–302. **DOI:**10.1016/j.jssc.2019.03.044
10. J.-H. Wei, J.-W. Yi, M.-L. Han, B. Li, S. Liu, Y.-P. Wu, L.-F. Ma, D.-S. Li, *Chem.- Asian J*. **2019**, *14*, 3694–3701. **DOI:**10.1002/asia.201900706
11. W.-S. Lin, W.-T. Chen, H.-M. Kuang, H. Luo, *Acta Chim. Slov.* **2018**, *65*, 1008–1013. **DOI:**10.17344/acsi.2017.4833
12. H. Khajuria, M. Kumar, L. Tashi, R. Singh, H. N. Sheikh, *Acta Chim. Slov.* **2020**, *67*, 119–129. **DOI:**10.17344/acsi.2019.5274
13. Y. Hasegawa, T. Kawai, *CSJ Curr. Rev*. **2012**, *9*, 139–144.
14. H. Q. Wu, C. S. Yan, F. Luo, R. Krishna, *Inorg. Chem*. **2018**, *57*, 3679–3682. **DOI:**10.1021/acs.inorgchem.8b00341
15. S. A. Yaseen, A. S. Alameen, F. A. Saif, S. B. Undre, P. W. Khirade, P. B. Undre, *Integr. Ferroelectr.* **2020**, *205*, 131–145. **DOI:**10.1080/10584587.2019.1675009
16. Y. Zhao, Z. M. Zhai, X. Y. Liu, X. G. Yang, L. F. Ma, L. Y. Wang, *J. Solid State Chem.* **2019**, *278*, 120913. **DOI:**10.1016/j.jssc.2019.120913
17. K. Nishio, N. Nakamura, K. Horiba, M. Kitamura, H. Kumigashira, R. Shimizu, T. Hitosugi, *Appl. Phys. Lett.* **2020**, *116*, 053901/1–053901/5. **DOI:**10.1063/1.5133879
18. J. Q. Li, L. L. Gong, X. F. Feng, L. Zhang, H. Q. Wu, C. S. Yan, Y. Y. Xiong, H. Y. Gao, F. Luo, *Chem. Eng. J*. **2017**, *316*, 154–159. **DOI:**10.1016/j.cej.2017.01.046
19. X. X. Wu, H. R. Fu, M. L. Han, Z. Zhou, L. F. Ma, *Cryst. Growth Des.* **2017**, *17*, 6041–6048. **DOI:**10.1021/acs.cgd.7b01155
20. C. B. Fan, L. L. Gong, L. Huang, F. Luo, R. Krishna, X. F. Yi, A. M. Zheng, L. Zhang, S. Z. Pu, X. F. Feng, M. B. Luo, G. C. Guo, *Angew. Chem. Int. Ed.* **2017**, *56*, 7900–7906. **DOI:**10.1002/anie.201702484
21. Z. T. Omar, S. Jadhav, M. Rai, *Integr. Ferroelectr*. **2020**, *205*, 88–94. **DOI:**10.1080/10584587.2019.1675003
22. Y. P. Wu, J. W. Tian, S. Liu, B. Li, J. Zhao, L. F. Ma, D. S. Li, Y. Q. Lan, X. Bu, *Angew. Chem. Int. Ed.* **2019**, *58*, 12185–12189. **DOI:**10.1002/anie.201907136
23. L. L. Gong, X. F. Feng, F. Luo, X. F. Yi, A. M. Zheng, *Green Chem.* **2016**, *18*, 2047–2055. **DOI:**10.1039/C5GC02182K
24. Z. Li, A. Yang, X. Ma, Z. Liu, *J. Chem. Res.* **2020**, *44*, 97–103. **DOI:**10.1177/1747519819880693
25. Y. J. Cheng, R. Wang, S. Wang, X. J. Xi, L. F. Ma, S. Q. Zang, *Chem. Commun.* **2018**, *54*, 13563–13566. **DOI:**10.1039/C8CC07784C
26. W. H. Yin, Y. Y. Xiong, H. Q. Wu, Y. Tao, L. X. Yang, J. Q. Li, X. L. Tong, F. Luo, *Inorg. Chem*. **2018**, *57*, 8722–8725. **DOI:**10.1021/acs.inorgchem.8b01457
27. X.-N. Fang, J. Li, X.-G. Yi, Q. Luo, J.-Y. Chen, Y.-X. Li, *Acta Chim. Slov.* **2019**, *66*, 414–420. **DOI:**10.17344/acsi.2018.4885
28. Z. M. Zhai, X. G. Yang, Z. T. Yang, X. M. Lu, L. F. Ma, *CrystEngComm* **2019**, 21, 5862–5866. **DOI:**10.1039/C9CE00944B
29. P. Heiss, J. Hornung, X. Zhou, C. Jandl, A. Poethig, C. Gemel, R. A. Fischer, *Inorg. Chem.* **2020**, *59*, 514–522. **DOI:**10.1021/acs.inorgchem.9b02798
30. H. Wang, W. Meng, J. Wu, J. Ding, H. Hou, Y. Fan, *Coor. Chem. Rev*. **2016**, *307*, 130–146. **DOI:**10.1016/j.ccr.2015.05.009
31. H. R. Fu, Y. Zhao, Z. Zhou, X. G. Yang, L. F. Ma, *Dalton Trans.* **2018**, *47*, 3725–3732. **DOI:**10.1039/C8DT00206A
32. X. G. Yang, Z. M. Zhai, X. M. Lu, Y. Zhao, X. H. Chang, L. F. Ma, *Dalton Trans*. **2019**, *48*, 10785–10789. **DOI:**10.1039/C9DT02178G
33. M. B. Luo, Y. Y. Xiong, H. Q. Wu, X. F. Feng, J. Q. Li, F. Luo, *Angew. Chem. Int. Ed.* **2017**, *56*, 16376–16379. **DOI:**10.1002/anie.201709197
34. B. Samannan, J. Selvam, J. Thavasikani, *Asian J. Chem*. **2020**, *32*, 297–302. **DOI:**10.14233/ajchem.2020.22321
35. Y. Zhao, D. S. Deng, L. F. Ma, B. M. Ji, L. Y. Wang, *Chem. Commun*. **2013**, *49*, 10299–10301. **DOI:**10.1039/c3cc45310c
36. W. R. Osterloh, G. Galindo, M. J. Yates, E. Van Caemelbecke, K. M. Kadish, *Inorg. Chem*. **2020**, *59*, 584-594. **DOI:**10.1021/acs.inorgchem.9b02838
37. X. G. Yang, L. F. Ma, D. P. Yan, *Chem. Sci.* **2019**, *10*, 4567–4572. **DOI:**10.1039/C9SC00162J
38. H. R. Fu, N. Wang, J. H. Qin, M. L. Han, L. F. Ma, F. Wang, *Chem. Commun.* **2018**, *54*, 11645–11648. **DOI:**10.1039/C8CC05990J
39. K. Anuja, K. H. Reddy, K. Srinivasulu, D. Dhanalakshmi, *Asian J. Chem.* **2020**, *32*, 322–328. **DOI:**10.14233/ajchem.2020.22389
40. Y. Zhao, L. Wang, N. N. Fan, M. L. Han, G. P. Yang, L. F. Ma, *Cryst. Growth Des.* **2018**, *18*, 7114–7121. **DOI:**10.1021/acs.cgd.8b01290
41. Y. Zhao, X. G. Yang, X. M. Lu, C. D. Yang, N. N. Fan, Z. T. Yang, L. Y. Wang, L. F. Ma, *Inorg. Chem.* **2019**, *58*, 6215–6221. **DOI:**10.1021/acs.inorgchem.9b00450
42. N. Ahmad, S. Sultana, S. M. Faisal, A. Ahmed, S. Sabir, M. Z. Khan, *RSC Adv.* **2019**, *9*, 41135–41150. **DOI:**10.1039/C9RA06493A
43. Z. Zhou, M. L. Han, H. R. Fu, L. F. Ma, F. Luo, D. S. Li, *Dalton Trans.* **2018**, *47*, 5359–5365. **DOI:**10.1039/C8DT00594J
44. D. Bouokkeze, J. Massoudi, W. Hzez, M. Smari, A. Bougoffa, K. Khirouni, E. Dhahri, L. Bessais, *RSC Adv.* **2019**, *9*, 40940–40955. **DOI:**10.1039/C9RA07569K

45. J. H. Qin, Y. D. Huang, Y. Zhao, X. G. Yang, F.-F. Li, C. Wang, L. F. Ma, *Inorg. Chem*. **2019**, *58*, 15013–15016. **DOI:**10.1021/acs.inorgchem.9b02203
46. D. F. Back, G. N. M. De Oliveira, R. A. Burrow, E. E. Castellano, U. Abram, E. S. Lang, *Inorg. Chem*. **2007**, *46*, 2356–2358. **DOI:**10.1021/ic070006q
47. J. Prakasha Reddy, V. R. Pedireddi, *Eur. J. Inorg. Chem*. 2007, *8*, 1150–1158. **DOI:**10.1002/ejic.200600867
48. M. G. B. Drew, M. R. StJ. Foreman, M. J. Hudson, K. F. Kennedy, *Inorg. Chim. Acta* **2004**, *357*, 4102–4112. **DOI:**10.1016/j.ica.2004.06.032
49. W.-T. Chen, Y.-P. Xu, Q.-Y. Luo, X.-N. Fang, H.-L. Chen, *Z. Anorg. Allg. Chem.* **2008**, *634*, 529–533.
50. W.-T. Chen, J.-S. Huang, X.-N. Fang, Y.-P. Xu, Q.-Y. Luo, *Chinese. J. Struct. Chem*. **2008**, *27*, 1270–1274.
51. W.-T. Chen, J.-S. Huang, D.-S. Liu, J.-H. Liu, S.-M. Ying, *Chinese. J. Struct. Chem*. **2008**, *27*, 1299–1304.
52. W.-T. Chen. *Russ. J. Inorg. Chem.* **2009**, *54*, 1230–1235.
53. W.-T. Chen. *J. Mol. Struct.* **2011**, *992*, 102–105.
54. M. A. Katkova, V. A. Ilichev, A. N. Konev, I. I. Pestova, G. K. Fukin, M. N. Bochkarev, *Org. Electron*. **2009**, *10*, 623–630. **DOI:**10.1016/j.orgel.2009.02.020
55. F. Q. Huang, K. Mitchell, J. A. Ibers, *Inorg. Chem.* **2001**, *40*, 5123–5126. **DOI:**10.1021/ic0104353

Povzetek

S hidrotermalno sintezo smo pripravili nov Dy-Hg kompleks $[Dy(HIA)_3(H_2O)_2]_{2n} \cdot 2n HgCl_4 \cdot n HgCl_5 \cdot n H_3O \cdot 3n H_2O$ (**1**; HIA = izonikotinska kislina) in ga strukturno okarakterizirali z rentgensko monokristalno analizo. Spojina kristalizira v monoklinski prostorski skupini *C*2/*c*. Kristalna struktura spojine **1** ima eno-dimenzionalno (1-*D*) verigo kationa. Fotoluminiscentni eksperiment v trdnem stanju razkriva, da ima spojina rumen emisijski pas pri 575 nm ter da ta emisijski pas nastane na podlagi karakterističnega $^4F_{9/2} \rightarrow {}^6H_{13/2}$ prehoda 4*f* elektronov na Dy^{3+} ionih. Spojina ima CIE kromatične koordinate 0.5168 in 0.4824 v rumenem področju. UV-vidna difuzna refleksija v trdnem razkrije, da ima spojina širok optični pas 3.39 eV.

Except when otherwise noted, articles in this journal are published under the terms and conditions of the Creative Commons Attribution 4.0 International License

DOI: 10.17344/acsi.2020.5939 *Acta Chim. Slov.* **2020,** *67,* 1118–1123
creative commons

Scientific paper

Dispersive Liquid-Liquid Semi-Microextraction of Cu(II) with 6,7-dihydroxy-2,4-diphenylbenzopyrylium Chloride for its Spectrophotometric Determination

Alexander Chebotarev, Anastasiia Klochkova, Vitaliy Dubovyi and Denys Snigur*

Odessa I.I. Mechnikov National University, Department of Analytical and Toxicological Chemistry, Dvoryanskaya str., 2, Odessa 65082, Ukraine

** Corresponding author: E-mail: 270892denis@gmail.com*

Received: 04-09-2020

Abstract

A novel dispersive liquid-liquid semi-microextraction (DLLsME) procedure for copper(II) preconcentration is proposed. The system containing copper(II) and 6,7-dihydroxy-2,4-diphenylbenzopyrylium chloride (DHDPhB), after addition a mixture of chloroform and methanol becomes cloudy and the formation of the organic phase was observed immediately. The optimal conditions of DLLsME were found to be: pH 5, absorption band maximum was 570 nm, 1 cm^3 of 1×10^{-3} mol/dm^3 of DHDPhB, and mixed extractant containing 1 cm^3 of chloroform and 1 cm^3 of methanol. Under optimal conditions, the calibration plot was linear in the range of copper(II) concentration 4.32–65 $\mu g/dm^3$ and the limit of detection was 1.29 $\mu g/dm^3$. The rocks and tap water samples were successfully analyzed according to the suggested procedure with RSD no more than 4.9%.

Keywords: Dispersive liquid-liquid semi-microextraction; spectrophotometry; copper(II); rocks analysis; water analysis.

1. Introduction

Copper is an essential element that plays a significant role in various biological processes that are necessary to sustain life. Wherein, excessive intake of copper(II) compounds in the human body can lead to irritation of the nose and throat, nausea, vomiting, and diarrhea.[1] Copper is usually in trace level in environmental samples and food products. Moreover, well-known analytical methods for the copper(II) determination, such as flame atomic absorption spectroscopy, atomic absorption spectroscopy with a graphite furnace, ion chromatography and UV/Vis spectrophotometry, are often coupled with analyte preconcentration stage.

Many various techniques for copper(II) preconcentration have been proposed. For example, cloud point extraction,[2–4] solid-phase extraction,[5–7] liquid extraction[8–10] etc., while most often copper(II) is pre-bound into ion pairs or complexes (chelates in particular) using reagents such as sodium diethyldithiocarbamate,[11–13] 1-(2-pyridylazo)-2-naphthol,[4,14] and dimethyl-1,10-phenanthroline (neocuproine).[15,16] It is important to note that interest in the development and modernization of various cloud point extraction and liquid extraction techniques does not disappear even today.[17–21]

Liquid-liquid extraction has well-known advantages, namely, such as the possibility of increasing the concentration of the analyte, simplicity, high speed, low cost, and efficiency. Such modifications of liquid-liquid extraction as vortex-assisted LLE and dispersive LLE have been actively developed recently. The last one is based on the transfer of the analyte from the aqueous phase to another immiscible liquid phase, which is an extractant. A certain amount of a mixture of extraction and dispersive solvents is rapidly introduced into the aqueous phase of the sample containing the analyte, forming a cloudy solution. The cloudy state is caused by the formation of small droplets of water-immiscible extracting solvent that is dispersed in the sample solution. However, this is not often effective enough and is also being modified. For example, it was proposed to additionally irradiate the solution with ultrasound,[22] introduce an auxiliary solvent,[23] or use the vortex technique.[24]

Since preconcentration of copper(II) initially implies its conversion into some intensely colored hydrophobic

complexes, UV/Vis spectrophotometry seems to be the most attractive detection method. At the same time, the wide availability of equipment, speed, accuracy, ease of operation, and low operating costs make UV/Vis spectrophotometry still attractive to use.

In this work, dispersive liquid-liquid semi-microextraction coupled with UV/Vis spectrophotometry (DLLsME-UV/Vis) was used for the preconcentration and quantification of Cu(II). On the one hand, the use of semi-microtechniques notably reduces the environmental load and does not require special equipment like microextraction and is not fraught with errors related to dosing microliter volumes. On the other hand, the proposed DLLsME-UV/Vis procedure for copper(II) determination does not need extra time-consuming steps like, for example, heating and cooling of solution,[3] so the method is quite rapid. The 6,7-dihydroxy-2,4-diphenylbenzopyrylium chloride (DHDPhB) was chosen as the chelating ligand whose synthesis, physio-chemical, spectroscopic, and complexing properties were described in detail in our previous works.[25,26]

2. Experimental

2. 1. Chemicals

The Cu(II) 1×10^{-2} mol/dm^3 stock solution was prepared by dissolving $CuCl_2 \cdot 2H_2O$ in distilled water and standardized by iodometric titration.

The DHDPhB was synthesized (Fig. 1) by condensation of 1,2,4-triacetoxybenzene (TOR, Ukraine) with 1,3-diphenyl-1,3-propanedione (Acros, Belgium) in glacial acetic acid, while sparging dry hydrogen chloride, and recrystallized from ethanol.[25]

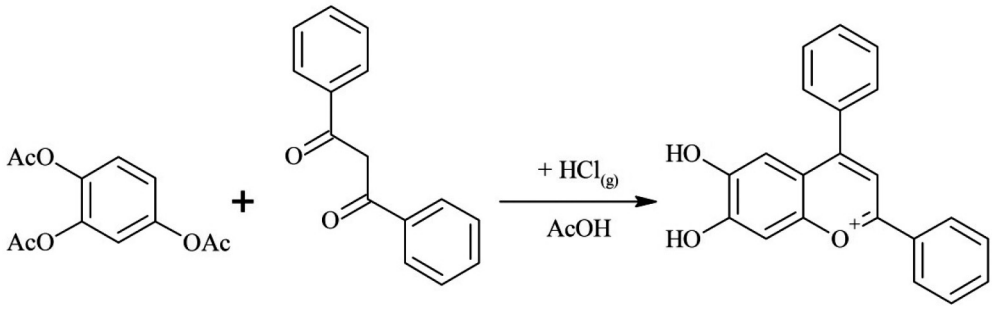


Fig. 1. Synthesis of DHDPhB reagent.

The chemical structure of DHDPhB was confirmed by ^{1}H and ^{13}C NMR:

^{1}H NMR (500 MHz, DMSO-d_6) δ (ppm): 8.327 (s, J = 7.14 Hz, 1H, Ar), 8.18–8.16 (m, 3H), 7.988 (d, J = 8.23 Hz, 1H, Ar), 7.37–7.64 (m, 4H, Ar), 7.58–7.55 (m, 4H, Ar), 7.34 (s, 1H, Hetaryl).

^{13}C NMR (500 MHz, DMSO-d_6) δ (ppm): 185.24 (C=O); 136–127 (Ar, Hetaryl), 102.74 (C-OH), 93.17 (C-OH).

A 1×10^{-3} mol/dm^3 DHDPhB solution was prepared by dissolving its suitable weight in ethanol. The pH of the mixture was adjusted by the acetate buffer solution (concentrations of acetic acid and sodium acetate were 0.1 mol/dm^3 and 0.0468 mol/dm^3, respectively). Some organic solvents, such as methanol, acetonitrile, acetone, ethanol, chloroform, benzene, butyl acetate, isoamyl alcohol, and their mixtures were used for dispersive extraction. All organic solvents and chemicals used in the present study were analytically pure grade.

2. 2. Instrumentations

An SF-56 spectrophotometer (OKB "Spectr", Russia), equipped with 10 mm semi-micro quartz cells, was used for absorbance measurements. The pH measurements were carried out on an I-160 potentiometer (ZIP, Belarus) equipped with a combined glass electrode. A centrifuge model MPW-340 with conical 50 cm^3 tubes was used for phase separation acceleration.

2. 3. General Procedure

Appropriate amounts (0.1–3.0 cm^3) of 1×10^{-5} mol/dm^3 Cu(II) solution, 1.0 cm^3 of 1×10^{-3} mol/dm^3 ethanolic solution of DHDPhB, 8 cm^3 of acetate buffer with pH 5 were placed into 50 cm^3 centrifuge test tubes and diluted up to 30 cm^3 with distilled water. Then a mixture of 1 cm^3 of chloroform and 1 cm^3 of methanol was injected using a syringe for dispersive extraction and the solution immediately became cloudy. The tubes were centrifuged for 5 min at 3,000 rpm to accelerate phase separation. The heavier organic phase, which contained the extracted complex, was at the bottom, and the upper aqueous layer was carefully removed from the test tube.

2. 4. Sampling and Sample Pretreatment

The certified reference materials (CRM) of geological samples, such as carbonate-silicate loose sediments SGHM-1 (CRM №3483-86) and rock ST-1a Trap (CRM №519-74) were used to test the proposed method. A 0.1-0.3 g of CRM sample was transferred to a platinum crucible and 2 g of potassium persulfate was added and melted at 600 °C in a muffle for 25–30 min. After that, the melt

was cooled and dissolved in water and diluted to 100 cm^3. The obtained solutions were used for analysis by the proposed method.

Tap water samples were collected in our laboratory and directly analyzed according to the proposed procedure without any special treatment.

3. Results and Discussion

3. 1. Effect of Variables

Several factors were studied such as pH, type and volume of extracting solvent, type and volume of dispersive solvent, the concentration of DHDPhB, interfering ions that affect the efficiency of copper(II) determination after its DLLsME preconcentration.

3. 1. 1. Effect of pH

To study the effect of pH on the procedure, many solutions were prepared, which required pH level that was reached by the addition of standard acetate buffer with a pH of 3–8, and then 1 cm^3 of chloroform was added for extraction.

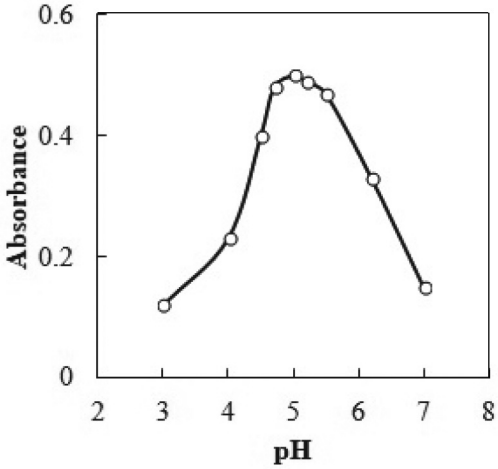


Fig. 2. Effect of pH on the extraction: 3.33×10^{-5} mol/dm^3 of DHDPhB, 5×10^{-7} mol/dm^3 of Cu(II), $V_{Chloroform}$ = 1 cm^3, λ = 570 nm.

As seen in Fig. 2, the optical absorbance increases to pH 5 and then decreases. Probably, in a strongly acidic medium the reagent is in a protonated form, which prevents the effective binding of copper(II). In a strongly alkaline medium, destructive hydrolysis of the DHDPhB takes place; therefore, the influence of the acidity of the medium was studied in the pH range 3-7. Henceforward, whole analysis is carried out at a pH of 5.

3. 1. 2. Effect of Type and Volume of Extracting Solvent

The solvent which is used for extraction has some mandatory requirements: insolubility or poor solubility in water, a large difference in density with water, an affinity for the extracted substance. According to these requirements, organic solvents such as benzene, chloroform, isoamyl alcohol, and butyl acetate were tested. It was shown that chloroform removes a complex of copper(II) with DHDPhB from an aqueous solution best of all.

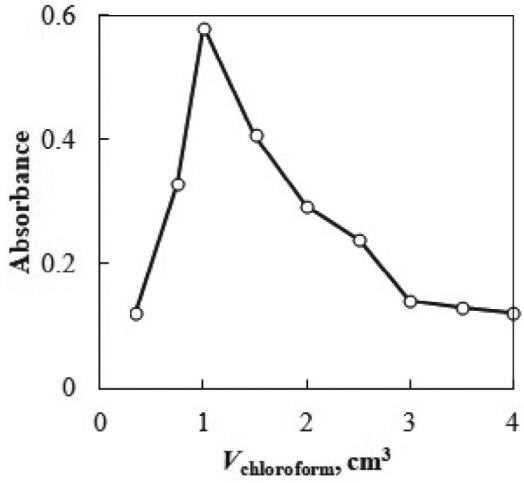


Fig. 3. Effect of volume of extracting solvent (chloroform) on extraction: 3.33×10^{-5} mol/dm^3 of DHDPhB, 6.67×10^{-7} mol/dm^3 of Cu(II), λ = 570 nm.

The effect of the volume of extractant on the recovery of the copper(II) complex with DHDPhB was studied (Fig. 3). As seen, 1 cm^3 of chloroform is sufficient to extract the complex.

3. 1. 3. Effect of Type and Volume of Dispersive Solvent

Dispersive solvents are often used to increase the rate and efficiency of LLE. Such a solvent must dissolve both in the selected organic solvent and in water. Among the solvents considered, such as acetonitrile, acetone, ethanol, and methanol, methanol proved to be the most effective (Fig. 4a).

To determine the optimal volume of methanol for extraction, 1 cm^3 of chloroform and 0.25–3.5 cm^3 of methanol were added to several solutions. As shown in Fig. 4b, as the amount of dispersing solvent increases, the degree of complex recovery also increases. Thus, the ratio of the extracting and dispersive solvents in the mixture was 1:1, since a further increase in the volume of the dispersing solvent does not lead to an increase in optical absorbance. It is interesting to note that the complex has a high affinity for chloroform, and the use of the vortex technique does not significantly affect the extraction efficiency.

3. 1. 4. Effect of the Concentration of DHDPhB

The effect of the concentration of the chelating ligand on the efficiency of copper(II) extraction was studied.

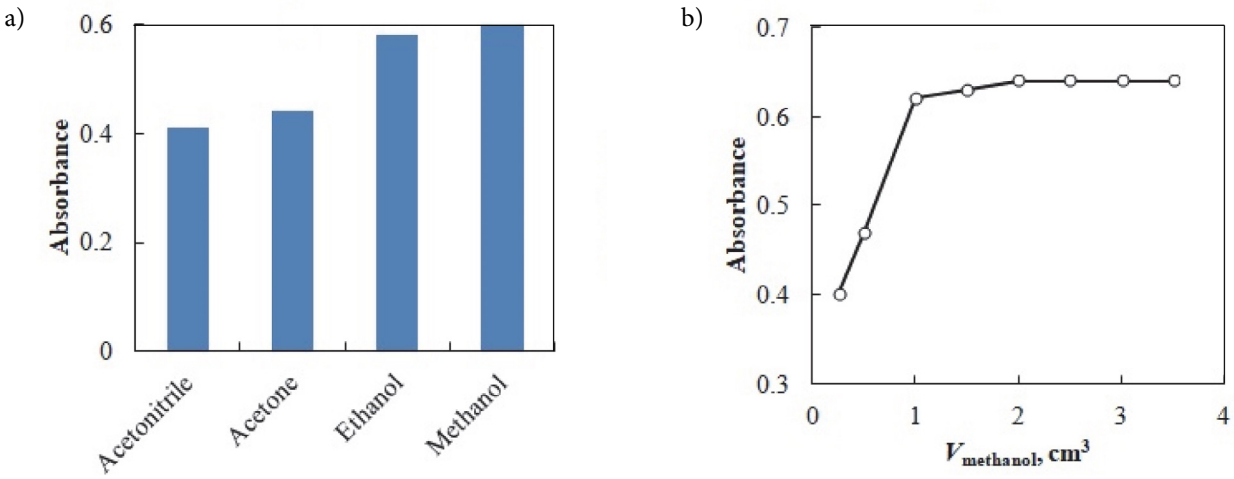


Fig. 4. Effect of type (a) and volume (b) of dispersive solvent on extraction: 3.33×10^{-5} mol/dm³ of DHDPhB, 6.67×10^{7} mol/dm³ of Cu(II), $V_{Chloroform}$ = 1 cm³, λ = 570 nm.

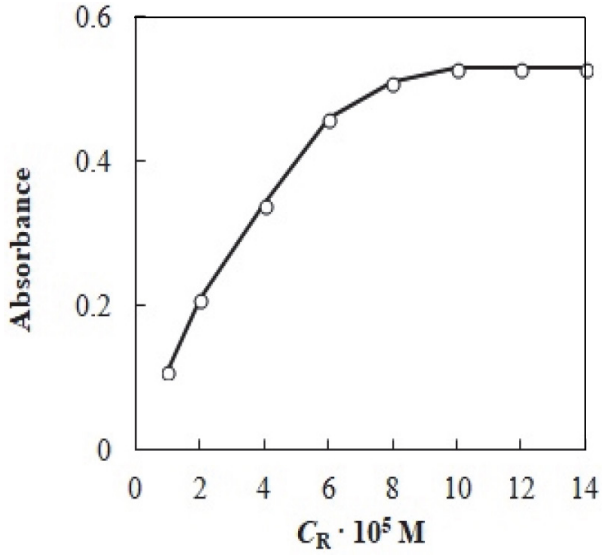


Fig. 5. The effect of the concentration of DHDPhB on the extraction of 5×10^{-7} mol/dm³ of Cu(II), $V_{Chloroform}$ = 1 cm³, $V_{Methanol}$ = 1 cm³, λ = 570 nm.

As seen in Fig. 5, it is necessary to introduce a 200-fold excess of the reagent to maximize the binding of copper(II) to the complex and its extraction.

3. 2. Analytical Figures of Merit and Interferences Study

Analytical figures of merit for the developed DLLsME – UV/Vis procedure obtained under optimal conditions are shown in Table 1. The precision and accuracy of the proposed technique were checked by performing 5 measurements at a concentration level of Cu(II) 30 μg/dm³ over two consecutive days.

Table 1. Analytical figures of merit for Cu(II) determination by the developed DLLsME – UV/Vis spectrophotometry method

Regression equation	$A = 0.0154\,C + 0.1273$
R^2	0.999
Linear range, μg/dm³	4.32–65
LOD, μg/dm³	1.29
LOQ, μg/dm³	4.32
RSD (n = 5, P = 0,95, $C_{Cu(II)}$ = 30 μg/dm³)	4.8%
Recovery	97–104%
Preconcentration factor	39

To investigate an interfering effect, the following ions were studied (Table 2):

Table 2. Study of interfering ions.

Interfering ions	**Tolerable concentration (analyte:interfering ion)[a]**
Fe^{2+}, Fe^{3+}	1:1
Al^{3+}	1:5
I^-	1:25
Zn^{2+}, Ni^{2+}, Co^{2+}, Cd^{2+}, Mn^{2+}, HPO_4^{2-}, CO_3^{2-}, SO_4^{2-}	1:100
Na^+	1:250
K^+, Br^-, Cl^-	1:500
Ca^{2+}, Mg^{2+}, NO_3^-	1:5000

[a] At this ratio no interfering effect was observed.

As seen, Fe^{2+} and Fe^{3+} ions interfere most of all and 2.5% solution of NaF was used to mask them. Besides, Al^{3+} ions can be masked by 0.1 mol/dm³ solution of malonic acid. A 1–3 cm³ of masking reagents solutions were used, because their required amount depends on the analyzed sample weight.

3. 3. Analysis of CRMs and Comparison with Literature Studies

The DLLsME–UV/Vis procedure was successfully applied to the preconcentration and determination of Cu(II) in CRM rocks samples and tap water sample (Table 3). As can be seen from Table 3, a good agreement was found between the proposed method data and certified values. Thus, the developed technique is suitable for the determination of copper in rocks and tap water samples.

4. Conclusions

A cheap, simple, sensitive and environmentally friendly dispersive liquid-liquid semi-microextraction method for preconcentration and quantification of Cu(II) which is based on the complex formation with 6,7-dihydroxy-2,4-diphenylbenzopyrilium chloride was described. In optimal conditions, the calibration graph was linear in the range of Cu(II) concentrations 4.32–65 $\mu g/dm^3$. The proposed DLLsME–UV/Vis method has been successfully applied to the quantification of Cu(II) traces in rocks and tap water samples.

Table 3. Application of suggested procedure to the preconcentration and spectrophotometric determination of Cu(II) in CRM and tap water samples (n = 5; P = 0.95)

CRMs	Certified values, μg/g	Spiked, μg/L	Found*	Recovery, %	RSD, %	**Student's *t*-test
SGHM-1	220 ± 20	–	215.7 ± 13	98.1	4.9	0.91
№3483-86		50	263.3 ± 15	97.0	4.5	–
ST-1a Trap	48 ± 5	–	46.4 ± 3	96.7	4.7	1.64
№519-74		50	97.2 ± 6	98.3	4.6	–
Tap water	–	–	19.9 ± 1	–	4.4	–
		10	30.1	99.0	4.8	–

* Concentration is given in μg/g for rocks samples and in $\mu g/dm^3$ for tap water sample.
** The experimental *t*-values were calculated according to equation $\mu = x_{average} \pm tS/n^{½}$; The critical *t*-value for five replicate measurements at a confidence level of 0.95 was 2.78.

Table 4. Comparison between the analytical performances of the described method for Cu(II) quantification with some other studies previously reported in the literature

Method	**Reagent**	**SV[a] cm^3**	**LOD $\mu g/dm^3$**	**PF[b]**	**Detection**	**Ref.**
CPE[c]	–	10	1.5	14	FAAS[f]	27
CPE	Monocarboxylic acid	100	10	10	FAAS	28
HLLME[d]	8-Hydroxy quinoline	5	1.74	25	FAAS	29
DLLME[e]	Salophen	10	1.9	70.9	HPLC-UV[g]	30
CPE	Isoleucine	25	5	22	UV/Vis[h]	31
CPE	DHMPhB[i]	15	6	–	UV/Vis	2
DLLsME	DHDPhB	30	1.29	39	UV/Vis	This study

[a]Sample volume, [b]Preconcentration factor, [c]Cloud point extraction, [d]Homogeneous liquid–liquid microextraction, [e]Dispersive liquid-liquid microextraction, [f]Flame atomic absorption spectroscopy, [g]High-performance liquid chromatography-ultraviolet detection, [h]Ultraviolet-visible spectrophotometry, [i]6,7-dihydroxy-4-methyl-2-phenylbenzopyrilium perchlorate

A comparison of the suggested DLLsME – UV/Vis technique for preconcentration and quantification of Cu(II) with some studies described in the literature are summarized in Table 4. The suggested method has a wider or comparable linear range and a better limit of detection. Also, the developed DLLsME procedure does not require special equipment, large sample amounts and also does not require significant quantities of toxic organic solvents. Moreover, suggested DLLsME– UV/Vis method is cheap, sensitive and easy to perform.

5. References

1. WHO, Copper in drinking-water: Background document for development of WHO guidelines for drinking-water quality. Geneva: World Health Organization (WHO/SDE/WSH/03.04/88), **2004**.
2. D. Snigur, A. Chebotarev, V. Dubovyi, et al., *J. Serb. Chem. Soc.*, **2020**, *85*, 89–96. **DOI:**10.2298/JSC190212087S
3. H. Reffas, T. Benabdallah, M. H. Youcef et al., *J. Surfact. Deterg.*, **2014**, *17*, 27–35. **DOI:**10.1007/s11743-013-1501-1
4. A. Pérez-Gramatges, A. Chatt, *J. Radioanal. Nucl. Chem.*,

2012, *294*, 163–170. **DOI:**10.1007/s10967-012-1708-z
5. J. Shah, M. R. Jan, Anjum, *J. Anal. Chem.*, **2018**, *73*, 1146–1153. **DOI:**10.1134/S1061934818120055
6. S. Bahar, F. Karami, *J. Iran. Chem. Soc.*, **2015**, *12*, 2213–2220. **DOI:**10.1007/s13738-015-0699-4
7. A. Samadi, M. Amjadi, *Microchim Acta*, **2015**, *182*, 257–264. **DOI:**10.1007/s00604-014-1327-1
8. A. R. Garifzyanov, E. O. Chibirev, M. R. Cherkasov et al., *Russ. J. Gen. Chem.*, **2016**, *86*, 2723–2724. **DOI:**10.1134/S107036321612029X
9. S. M. Sorouraddin, M. A. Farajzadeh, M. Ghorbani, *J. Iran. Chem. Soc.*, **2018**, *15*, 201–209. **DOI:**10.1007/s13738-017-1224-8
10. F. Tokay, S. Bağdat, *J. Am. Oil. Chem. Soc.*, **2015,** *92*, 317–322. **DOI:**10.1007/s11746-015-2603-x
11. L. Wang, J. B. Zhou, X. Wang et al., *Anal. Bioanal. Chem.*, **2016**, *408*, 4445–4453. **DOI:**10.1007/s00216-016-9542-8
12. S. Touati, A. H. Meniai, *Theor. Found, Chem. Eng.*, **2012**, *46*, 719–726. **DOI:**10.1134/S0040579512060231
13. M. Arvand, E. Bozorgzadeh, M. A. Zanjanchi et al., *J. Anal. Chem.*, **2014,** *69*, 243–247. **DOI:**10.1134/S1061934814030022
14. Z. Erbas, R. Maulana, E. Yilmaz, S. Ozdemir, E. Kilinc, M. Soylak, *Int. J. Environ. Anal. Chem.*, **2019**, 1–12. **DOI:**10.1080/03067319.2019.1646737
15. S. Shariati, M. Golshekan, *J. Anal. Chem.*, **2014**, *69*, 248–254. **DOI:**10.1134/S1061934814030125
16. S. Shariati, M. Golshekan, *Acta Chim Slov.*, **2011**, *58*, 311–317.
17. Z. Su, Y. Zhang, B. Liu et al., *JOM*, **2017**, *69*, 2364–2372. **DOI:**10.1007/s11837-017-2509-1
18. S. M. Pourmortazavi, Z. Saghafi, A. Ehsani et al., *J. Food Sci. Technol.*, **2018,** *55*, 2813–2823. **DOI:**10.1007/s13197-018-3205-z
19. K. Rovina, L. A. Acung, S. Siddiquee et al., *Food Anal. Methods*, **2017**, *10,* 773–787. **DOI:**10.1007/s12161-016-0645-9
20. M. Hemmati, M. Rajabi, A. Asghari, *Microchim Acta*, **2018,** *185,* 160. **DOI:**10.1007/s00604-018-2670-4
21. D. Snigur, A. Chebotarev, K. Bulat, V. Duboviy, *Anal. Biochem.*, **2020**, *597*, 113671. **DOI:**10.1016/j.ab.2020.113671
22. B. Daneshvand, F. J. Raofie, *Iran. Chem. Soc.*, **2015,** *12,* 1287–1292. **DOI:**10.1007/s13738-015-0593-0
23. S. Zaruba, A. B. Vishnikin, V. Andruch, *Talanta*, **2016**, *149*, 110–116. **DOI:**10.1016/j.talanta.2015.11.049
24. A. Bazmandegan-Shamili, A. M. Haji Shabani, S. Dadfarnia, et al., *J. Iran. Chem. Soc.*, **2017,** *14,* 843-851. **DOI:**10.1007/s13738-016-1037-1
25. D. Snigur, A. Chebotarev, K. Bevziuk, Moscow university chemistry bulletin, **2017**, *72*, 187–191. **DOI:**10.3103/S0027131417040095
26. A. Chebotarev, V. Dubovyi, A. Demchuk, A. Klochkova, D. Snigur, *Ukrainian Chemistry Journal*, **2018**, *84*, 104–109 (in Russian).
27. V. A. Lemos, M. S. Santos, M. J. Silvados Santos, *Microchim. Acta.*, **2007**, *157*, 215–222. **DOI:**10.1007/s00604-006-0652-4
28. S. A. Kulichenko, V. O. Doroschuk, S. O. Lelyushok, *Talanta*, **2003**, *59*, 767–773. **DOI:**10.1016/S0039-9140(02)00617-3
29. M. A. Farajzadeh, M. Bahram, S. Zorita, B. G. Mehr, *Journal of Hazardous Materials*, **2009**, *161,* 1535–1543. **DOI:**10.1016/j.jhazmat.2008.05.041
30. A. Asghari, M. Ghazaghi, M. Rajabi, M. Behzad, M. Ghaedi, *J. Serb. Chem. Soc.*, **2014**, *79*, 63–76. **DOI:**10.2298/JSC062212081A
31. P. Liang, J. Yang, *Journal of Food Composition and Analysis*, **2010**, *23*, 95–99. **DOI:**10.1016/j.jfca.2009.01.015

Povzetek

Predlagamo postopek nove disperzivne semi-mikroekstrakcije tekoče-tekoče (DLLsME) za predkoncentracijo bakra(II). Sistem, ki je vseboval baker(II) in 6,7-dihidroksi-2,4-difenilbenzopirilijev klorid (DHDPhB), je po dodatku zmesi kloroforma in metanola postal moten in takoj je bilo opaziti tvorbo organske faze. Optimalni pogoji DLLsME so bili: pH 5, absorpcijski maksimum 570 nm, 1 cm^3 raztopine 1×10^{-3} mol/dm^3 DHDPhB in ekstrakcijska zmes, ki je vsebovala 1 cm^3 kloroforma in 1 cm^3 metanola. Pri optimalnih pogojih je bila kalibracijska krivulja linearna v območju koncentracij bakra(II) 4,32–65 μg/dm^3, meja zaznave pa je bila 1,29 μg/dm^3. S predlaganim postopkom smo uspešno analizirali vzorce kamnin in vodovodne vode, pri tem je bil RSD pod 4,9 %.

Except when otherwise noted, articles in this journal are published under the terms and conditions of the Creative Commons Attribution 4.0 International License

DOI: 10.17344/acsi.2020.5963 *Acta Chim. Slov.* **2020,** *67,* 1124–1138
creative commons

Scientific paper

GO/PAMAM as a High Capacity Adsorbent for Removal of Alizarin Red S: Selective Separation of Dyes

Mohammad Rafi,[1] Babak Samiey[1,*] and Chil-Hung Cheng[2]

[1] *Department of Chemistry, Faculty of Science, Lorestan University, Khoramabad 68137–17133, Lorestan, Iran*

[2] *Department of Chemical Engineering, Ryerson University, M5B 2K3, Toronto, Ontario, Canada*

* *Corresponding author: E-mail: babsamiey@yahoo.com , samiey.b@lu.ac.ir*

Received: 03-16-2020

Abstract

Adsorption of Alizarin Red S (ARS) on graphene oxide/poly(amidoamine) (GO/PAMAM) was studied at different ARS initial concentrations, temperatures, pHs, shaking rates and contact times. Adsorption sites of GO/PAMAM were phenolic –*OH* (*Ph*) group of GO and amine groups ($-NH_2$, $-NH^+_3$ and $-NHR^+_2$) of PAMAM dendrimer moieties of GO/PAMAM. At pH = 2 and 318 K, maximum adsorption capacity ($q_{e,max}$) of the adsorbent was 1275.2 mg g^{-1} which is one of the highest capacity in the literature. Thus, GO/PAMAM in this work acted as a superadsorbent for ARS. At the incipient of adsorption, ARS^- molecules were adsorbed on *Ph* sites that was reaction-controlled step, (E_a = 114.5 kJ mol^{-1}). Adsorption of ARS^-on the remaining sites was diffusion–controlled. In alkaline media, two other types of ARS molecules were identified during that were adsorbed on *Ph* and $-NH^+_3$ sites. Further increasing the pH of the solution, decreased the number these two sites and yielded a reduced adsorption capacity ($q_{e,max}$). Methylene blue (MB), thionine (Th), pyronin Y (PY), acridine orange (AO), methyl blue (MEB) and janus green (JG) dyes were selectively separated from their mixtures with ARS molecules using GO/PAMAM at pH of 2. The used adsorbent was recycled efficiently by using ethylenediamine very fast.

Keywords Alizarin Red S; GO/PAMAM; Adsorption; ARIAN model; KASRA model; ISO equation

1. Introduction

Wastewater generated by different industries contains pollutant compounds that are hazardous to the health of human beings and animals. Dye compounds included in these pollutants of wastewater are produced by industries like food, paper, rubber, textile, printing, tanning, dyestuff and pigment industries. During the last decades extensive progress has been made for treatment of industrial wastewaters. A number of techniques used for this purpose are filtration,[1] chemical oxidation,[2] ion exchange,[3] biological degradation,[4] reverse osmosis,[5] coagulation,[6] and adsorption.[7] Adsorption is a facile, cost effective and widely-applied method to remove dye compounds from wastewater systems and in many cases can be recycled easily.

Alizarin Red S (ARS), sodium 3,4-dihydroxy-9,10-dioxo-9,10-dihydroanthracene-2-sulfonate, is also known as Mordant Red 3 or Alizarin Carmine which is an anthraquinone and anionic dye. ARS is applied as an acid-base indicator,[8] a red textile dye,[9] for staining in histology[10] and as a chromogenic agent for selective spectroscopic determination of some compounds.[11]

For removing ARS from wastewaters, various kinds of adsorbents were used, such as activated carbon/γ-Fe_2O_3 nano-composite,[12] modified nano-sized silica,[13] magnetic chitosan,[14] *lantana camara*,[15] coconut shell activated carbon,[16] activated clay modified by iron oxide,[17] Fe_3O_4/CeO_2 nanocomposite,[18] calcined [Mg/Al, Zn/Al and MgZn/Al]-LDH,[19] nanocrystalline $Cu_{0.5}Zn_{0.5}Ce_3O_5$,[20] activated carbon engrafted with Ag nanoparticles,[21] nano-Fe_3O_4 and corn cover composite[22] and chitosan/ZnO nanorod composite.[23] The $q_{e,max}$ value values of these adsorbents are tabulated in Table 1.

In this study, graphene oxide/poly(amidoamine) (GO/PAMAM) was synthesized by grafting poly(amidoamine) (PAMAM) dendrimer to graphene oxide.[24–26]

The as-synthesized GO/PAMAM and ARS–adsorbed GO/PAMAM were characterized by different techniques like BET (Brunauer-Emmett-Teller), SEM (Scanning Electron Microscope), EDS (Energy Dispersive X-Ray Spectroscopy), XRD (X-Ray Diffraction) and FTIR

Table 1. Maximum adsorption capacity ($q_{e,max}$) of ARS on a series of adsorbents.

Adsorbent	T (K)	$q_{e,max}$ (mg g^{-1})	Ref.
Activated carbon/γ-Fe2O3	298	108.7	12
Modified nano-sized silica	293	200.0	13
Magnetic chitosan	303	40.1	14
Activated clay modified by iron oxide	298	32.7	17
Fe_3O_4/CeO_2 nanocomposite	303	90.5	18
Activated carbon engrafted with Ag nanoparticles	298	232.6	21
Nano-Fe_3O_4 and corn cover composite	298	10.4	22
GO/PAMAM	328	1275.2	This work

(Fourier Transform Infrared Spectroscopy) techniques. The adsorption process of ARS on GO/PAMAM surface was carried out under different experimental conditions including ARS concentration, ionic strength, pH, temperature, shaking rate and contact time. Due to high adsorption capacity of GO/PAMAM for ARS, GO/PAMAM was considered as a superadsorbent for ARS dye, Table 1.

Kinetics and thermodynamics of adsorption of ARS on GO/PAMAM surface were investigated using the ARIAN and KASRA models respectively that elucidated the process mechanism. Also, high capacity adsorption of GO/PAMAM in acidic pHs for ARS was used for selective separation of a number of dyes from their mixtures with ARS.

2 Experimental

2. 1. Chemicals

Alizarin Red S, alizarin, methylene blue, acridine orange, thionine, pyronin Y, methyl blue, janus green B, sodium hydroxide, sodium chloride, sodium nitrate, potassium permanganate, concentrated sulfuric acid (98%), hydrochloric acid (37%), hydrogen peroxide (30%), methanol (≥99.9%), ethanol (≥99.9%), ethylenediamine (≥99%), diethylenetriamine (≥98%), methyl acrylate (≥99%), *N,N*-dimethylformamide (DMF) (≥99.8%), tetrahydrofuran (THF) (≥99%), acetone (99.8 %), benzene (>99%), dimethylsulfoxide (DMSO) (≥99.9%) and diethyl ether (≥99.7%) were purchased from Merck. Graphite powder (<20 μm) (≥99.9%) was purchased from Sigma-Aldrich. All chemicals were used without further purification.

2. 2. Synthesis of GO/PAMAM

Generation 2 PAMAM (G2 PAMAM) dendrimer (the first generation in this kind of nomenclature is called G–0.5), graphene oxide (GO) and GO/PAMAM were synthesized based on the published procedure.[26]

2. 3. Characterization of GO/PAMAM

The nitrogen-based BET specific surface area of GO/PAMAM was determined by a Pore Size Micrometrics-tristar 3020 instrument, Figure S1. The obtained BET isotherm for GO/PAMAM was type IV and its BET surface area, maximum pore volume (slit pore geometry), adsorption average pore diameter (by BET) and pore volume were 9.59 $m^2 g^{-1}$, 0.0044 $cm^3 g^{-1}$, 18.9 nm and 0.045 $cm^3 g^{-1}$, respectively. It is noticeable that BET surface and pore volume of GO/PAMAM in this work are several times higher than those of reported.[26] Also, its hysteresis loop was H3 which in this case aggregates of platelike GO/PAMAM nanoparticles form slit-like pores.[27]

Scanning electron micrographs (SEM) of GO/PAMAM and ARS-adsorbed GO/PAMAM samples at pHs of 0, 2 and 13 were taken using a MIRA3 TESCAN equipment at 15 keV. The SEM photos of pristine GO/PAMAM and its samples obtained under different conditions exhibited similar surface morphology which were aggregations of PAMAM-covered particles with a porous morphology, Figures 1(a)–1(h). The average size of GO/PAMAM particles estimated by SEM technique was about 30 nm, Figure S2.

EDS spectrum of the as-synthesized GO/PAMAM was acquired by a MIRA3 TESCAN equipment. According to the results of EDS, the atomic percentages of elements on its surface were similar to the published results[26] which confirmed the formation of GO/PAMAM, Figure S3. The XRD pattern of as-synthesized GO/PAMAM was recorded by a Rigaku D-max C III, X-ray diffractometer using Ni-filtered Cu-Kα radiation (λ = 1.5406 Å). The smooth intensity with broad peaks at around 2θ of 26.7° showed that the main structure of GO/PAMAM was amorphous, Figure 2(a). The XRD spectrum of GO/PAMAM was similar to that in the literature.[26]

Also, the FTIR spectrum of GO/PAMAM was taken by a Nicolet IR 100 (Thermo Scientific) FTIR spectrophotometer using KBr pellet technique, Figure 3(a). The peak at 1185 cm^{-1} was assigned to the stretching vibration of C–OH (phenolic) groups of GO/PAMAM.[26,28,29] The spectrum was very similar to that of the previous report for GO/PAMAM.[26] The absence of the peak at 1680–1760 cm^{-1} confirmed the lack of carboxylic acid group in GO/PAMAM. Diminishing the C=O band of GO at 1731cm^{-1} and the appearance bands at 1637 cm^{-1} (C=O amide I stretching vibration mode),[24,29,30] in the IR spectrum of as-synthesized GO/PAMAM confirmed that the GO/PAMAM was synthesized.

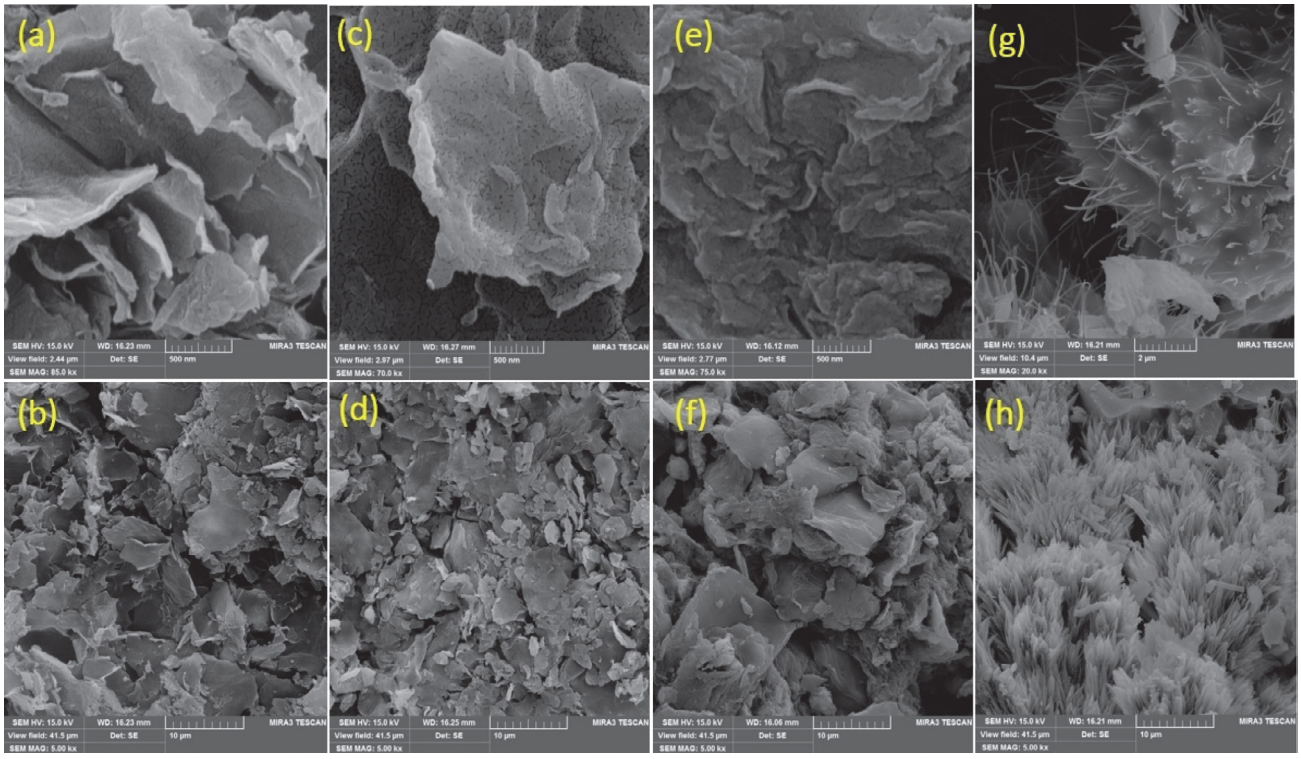


Figure 1. SEM images of (a,b) pristine GO/PAMAM, (c,d) GO/PAMAM modified at pH = 0 and ARS-adsorbed GO/PAMAM samples at (e,f) pH = 2 and (g,h) pH = 13.

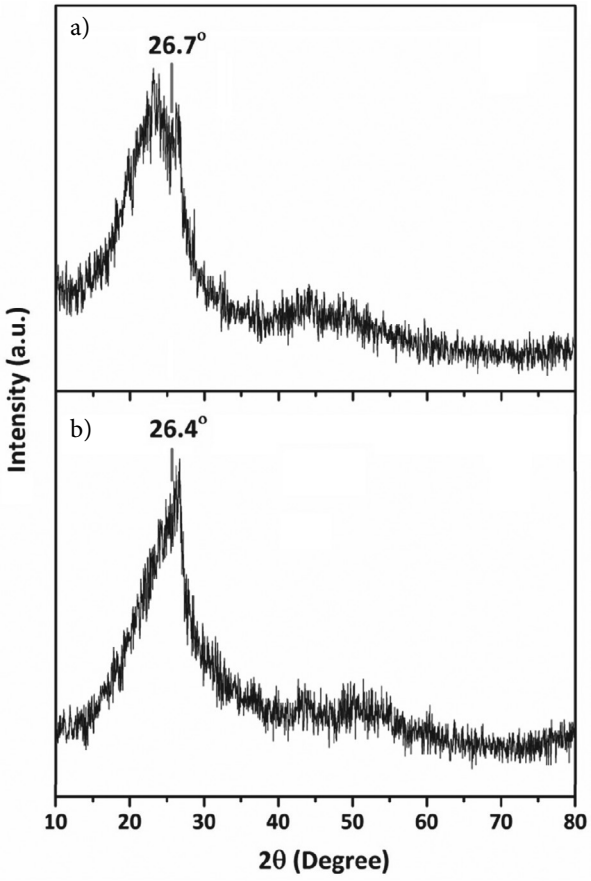


Figure 2. XRD spectra of (a) pristine GO/PAMAM, (b) GO/PAMAM modified at pH = 0.

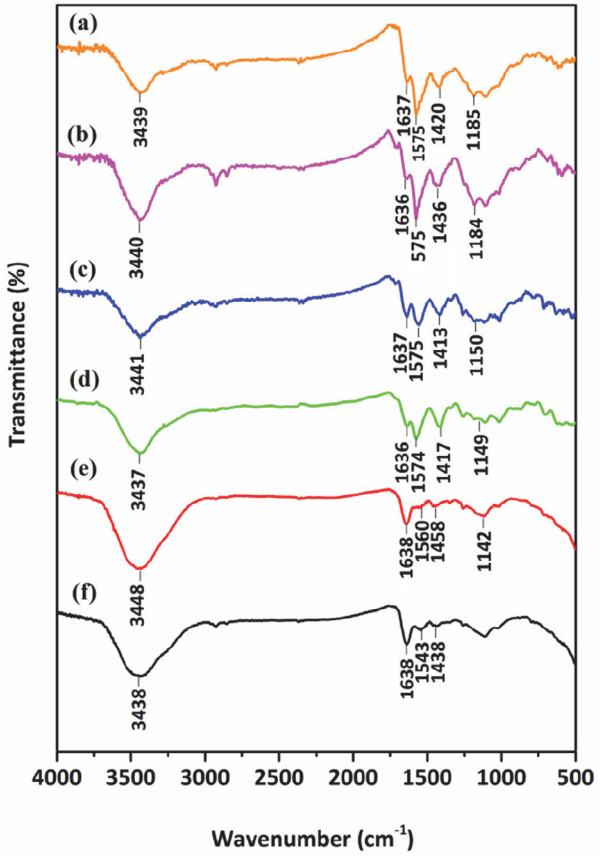


Figure 3. IR spectra of (a) pristine GO/PAMAM, (b) GO/PAMAM modified at pH = 0 and ARS–adsorbed GO/PAMAM at (c) pH = 0, (d) pH = 2, (e) pH = 5 and (f) pH = 10.

Chemical analysis of pristine GO/PAMAM by a ECS 4010 CHNS–O elemental analyzer showed that this compound contains 17.22% nitrogen, 64.02% carbon and 4.39% hydrogen by mass, Figure S4.

2. 4. Adsorption Experiments, Equations and Models

Adsorption capacity relation, adsorption experiment details, kinetic and thermodynamic equations and models used for analysis of adsorption experiments and all symbols and abbreviations were explained in detail in Supplementary Materials, Figures S5 and S6.[26,32–38]

3 Results and Discussion

3. 1. Thermodynamics of Adsorption of ARS on GO/PAMAM

The ARS molecule has two pK_a values, pK_{a1} = 5.5 and pK_{a2} = 11.5.[39,40] This compound, under experimental conditions, at pH ≤ 3 and pHs of 11 and 13 was in the forms of ARS^- (yellow), ARS^{2-} (red) and ARS^{3-} (violet) molecules respectively, Figures 6(a) and 6(b). The chemical structure used for ARS^- was confirmed before.[41] Thus, there were one or two ARS forms in solutions within the applied pH range in this work. These ARS forms are potential species in the solution, interacting with GO/PAMAM surface.

As published,[29,42] protonated primary amine (–NH^+_3), phenolic –OH and protonated tertiary amine (–NHR^+_2) groups of GO/PAMAM started to be deprotonated at pHs higher than 9.54 and 8.24 and 4, respectively. Thus, in acidic solutions these three functional groups and in alkaline media protonated and deprotonated primary amine groups of GO/PAMAM were its probable candidate groups for the adsorption of ARS molecules. Role of the –CO–NH– (amide) groups of the GO/PAMAM in the adsorption process was studied using FTIR spectra.

The peak of stretching vibration of phenolic C–OH group at 1185.5 cm^{-1} in the IR spectrum of GO/PAMAM, Figure 3(a), shifted to 1149.1 cm^{-1} in ARS-adsorbed GO/PAMAM at pH = 0, Figure 3(c), 1149.4 cm^{-1} in ARS-adsorbed GO/PAMAM at pH = 2, Figure 3(d) and 1141.6 cm^{-1} in ARS-adsorbed GO/PAMAM at pH = 5, Figure 3(e). This red-shifting validated interaction of this group with sulfonate group of ARS^- molecules. Also, the peak of amide group in GO/PAMAM at 1637 cm^{-1}, Figure 3(a), was observed at 1637, 1637 and 1638 cm^{-1} in spectra of ARS-adsorbed GO/PAMAM at pHs of 0, 2 and 5, Figures 3(c)–3(e), respectively and did not have wavelength shift. Therefore, from FTIR spectra, it was concluded that in acidic solutions –NH^+_3 and phenolic –*OH* groups of GO/PAMAM interacted with sulfonate group of ARS^- molecules. In this work, the functional groups of GO/PAMAM that interacted with ARS molecules are called its adsorption sites.

At first, the adsorption of ARS molecules in alkaline media was studied. From its pK_{a1} and pK_{a2} value, ARS deprotonated into ARS^{2-} molecules at pH = 10 and ARS^{3-} molecules at pHs of 13 and 14, respectively. Adsorption isotherms at pHs of 10, 13 and 14 consisted of two curves, Figures 7(a) and 7(b). At pH = 10, ARS^{2-} molecules and at pH = 13, ARS^{3-} molecules interacted first with –NH^+_3 (in the first curve) and subsequently with –NH_2 (in the second curve) sites of GO/PAMAM surface, respectively.

The observed decrease in q_{sssB} value in isotherm at pH = 10 compared to isotherm at pH = 13 was resulted from a decrease in the number of –NH^+_3 groups of adsorbent surface. An increase in the negative charge of ARS molecule, as solution Ph was increased from 10 to 13, resulted in an increase in the electrostatic repulsion between adsorption sites and ARS molecules which in turn resulted in a decrease in *K* values of regions I, IIA and IIB from pH

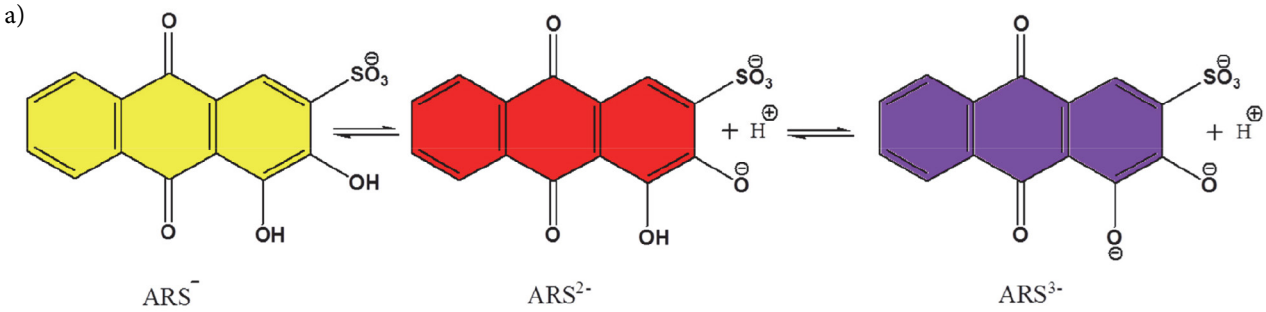


Figure 6. (a) Equilibrium relations among different types of ARS molecules at various pHs and (b) various forms of ARS molecules at (1) pH = 3, (2) pH = 5, (3) pH = 11 and pH = 13.

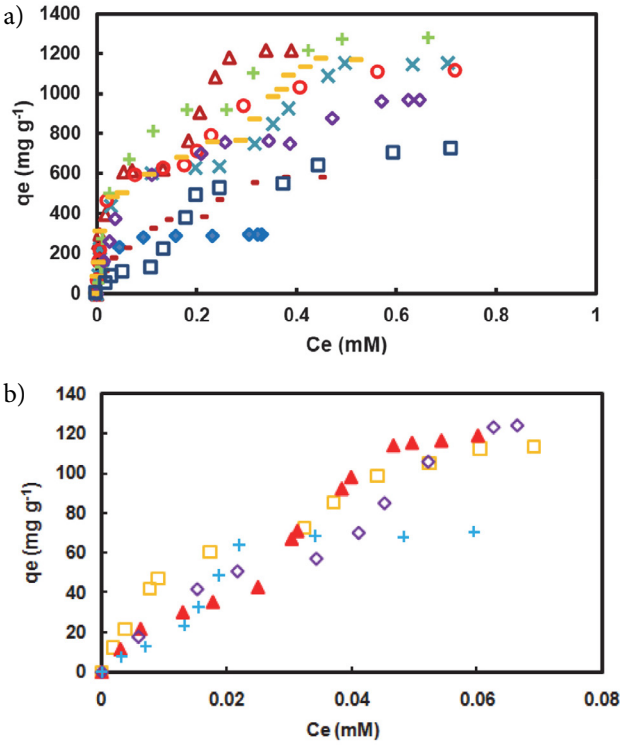


Figure 7. Adsorption isotherms of ARS on GO/PAMAM at 100 rpm and (a) at ♦ pH = 0, – pH = 0.3, Δ pH = 1, – pH = 3 and □ pH = 5 at 318 K and pH = 2 at × 308, ○ 318 and + 328 K and (b) at □ pH = 10, ▲ pH = 13 and + pH = 14 at 318 K.

= 10 to pH = 13, Table 2.

At pH = 14, ARS^{3-} molecules interacted with $-NH_2$ sites. As seen from Table 2, adsorption binding constants of ARS^{3-} molecules with $-NH_2$ site at pH = 14 (region IIA) and $-NH_2$ site at pH = 13 (region IIB) and the adsorption binding constant of ARS^{2-} molecules with $-NH_2$ site at pH = 10 (region IIB) were comparable.

In alkaline solutions, due to the low adsorption of ARS molecules on the surface, no CRAC was observed in adsorption isotherms, Table 3.

Then, the adsorption of ARS molecules on the surface of GO/PAMAM was studied in a water solution. The pH of these series of ARS solutions was about 5. Both ARS^- and ARS^{2-} species appeared in the aqueous solution, in which ARS^- was the predominate species. Under the pH environment, *Ph* and $-NH^+_3$ sites were present on the surface of adsorbent. Given that the polarity of O–H bond is stronger than that of N–H bond, in region I and IIA (the first curve), ARS^- molecules interact with *Ph* sites first and then with $-NH^+_3$ sites, respectively.

Before adding adsorbent to the solutions, the color of solutions was brown (a mixture of ARS^- and ARS^{2-} molecules). At the end of region IIB (the second curve) and $CRAC_{C2-C3}$ (the CRAC between regions IIB and IIC), the color of the solutions in region IIC (the third curve) became red that confirmed ARS^- molecules adsorbed on the surface of GO/PAMAM in regions I, IIA and IIB. With an increase in the initial concentration of solution the color became paler, Figures 8(a) and 8(b). By considering the changes in the color of ARS solutions, it was speculated that in regions I, IIA and IIB, ARS^- molecules (in brown color) adsorbed on *Ph* and then on $-NH^+_3$ sites respectively. This adsorption step is followed by ARS^{2-} molecules (in red color) adsorbed on the remaining $-NH^+_3$ sites in region IIC. As seen from experimental data in Table 2, the

Table 2. Adsorption equilibrium constants obtained from the Henry and Temkin equations based on the ARIAN model and experimental ssc_A, q_{sssA}, ssc_B, q_{sssB}, c_{max} and $q_{e,max}$ values for adsorption of ARS on GO/PAMAM in water, alkaline and acidic solutions in regions I, IIA, IIB and IIC at 100 rpm and 308–328 K.

Solvent	T	Henry (region I)			Temkin (region IIB)			Temkin (region IIC)					
	(K)	K	ssc_B	q_{sscB}	c_2	ssc_C	q_{sscC}	c_2	c_{max}	$q_{e,max}$			
		ARS^- on *Ph* site			ARS^- on $-NH^+_3$ site			ARS^- on $-NHR^+_2$ site					
pH = 0	318	3.32×10^7	2.25×10^{-3}	72.7	1.55×10^6	0.16	291.1	–	–	–	–	–	–
pH = 0.3	318	8.41×10^6	1.29×10^{-2}	107.9	1.96×10^5	0.21	380.4	1.58×10^4	0.37	575.6	–	–	–
pH = 1	318	7.19×10^7	3.56×10^{-3}	252.6	2.26×10^5	0.18	759.6	1.08×10^4	0.27	1182.6	–	–	–
pH = 2	308	4.95×10^7	4.45×10^{-3}	222.7	1.73×10^6	0.25	636.7	7.39×10^3	0.38	929.4	–	–	–
	318	3.22×10^7	4.81×10^{-3}	154.7	6.19×10^5	0.18	633.2	1.60×10^4	0.41	1027.6	–	–	–
	328	1.09×10^7	7.03×10^{-3}	133.7	2.85×10^5	0.18	919.3	2.36×10^4	0.49	1275.2	–	–	–
pH = 3	318	3.09×10^7	4.96×10^{-3}	154.2	8.43×10^5	0.23	754.2	9.26×10^3	0.39	1091.5	–	–	–

Adsorption in		Henry (region I)[A]			Temkin (region IIA)[A]			Temkin (region IIB)[B]			Temkin (region IIC)[C]		
		K	ssc_A	q_{sscA}	c_2	ssc_B	q_{sscB}	c_2	ssc_C	q_{sscC}	c_2	c_{max}	$q_{e,max}$
pH = 5*	318	2.47×10^6	3.15×10^{-2}	79.1	2.39×10^5	0.16	291.1	1.15×10^4	0.38	544.3	1.49×10^4	0.45	637.0
pH = 10*[D]	318	5.70×10^6	3.74×10^{-3}	21.4	7.29×10^5	0.03	72.6	9.98×10^4	6.5×10^{-2}	112.5	–	–	–
pH = 13*[D]	318	3.50×10^6	6.19×10^{-3}	21.7	6.66×10^5	0.02	42.8	5.86×10^4	4.7×10^{-2}	114.0	–	–	–
pH = 14*[E]	318	1.71×10^6	1.32×10^{-2}	23.3	9.94×10^4	0.03	63.7	–	–	–	–	–	–

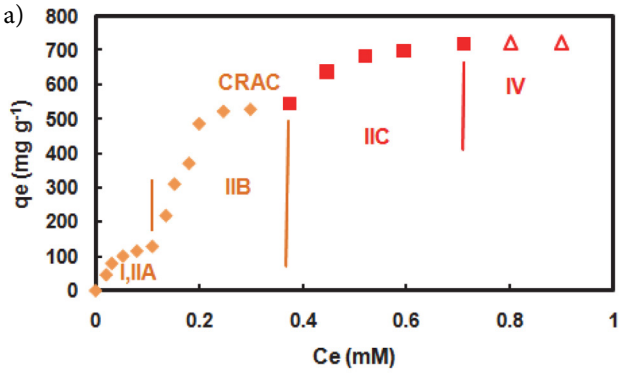
Units of K and c_2 are in mg g^{-1} M^{-1} and M^{-1}. Units of ssc_A, ssc_B, ssc_C and c_{max} are in mg. Units of q_{sscA}, q_{sscB}, q_{sscC} and $q_{e,max}$ are in mg g^{-1}. *Adsorption sites and ARS types at these pHs are discussed in text. [A]Regions I and IIA are in the first curve (Ph site). [B]Region IIB is in the second curve ($-NH^+_3$ site). [C]Region IIC is in the third curve ($-NHR^+_2$ site). [D]At pHs of 10 and 13, $q_{sscC} = q_{e,max}$ and $ssc_c = c_{max}$. [E]At pH = 14, $q_{sscB} = q_{e,max}$ and $ssc_B = c_{max}$.

Table 3. CRACs for the adsorption of ARS on GO/PAMAM in water, alkaline and acidic solutions at 100 rpm and 308–328 K.

Solvent	*T* (K)	ssc_B (mM)	$CRAC_{C1-C2}$ (mM)	– –	ssc_C (mM)	c_{max} (mM)	$q_{e,max}$ (mg g^{-1})
pH = 0	318	2.25×10^{-3}	–	–	0.16	0.16	291.1
pH = 0.3	318	1.29×10^{-2}	0.14–0.21	–	0.21	0.37	575.6
pH = 1	318	3.56×10^{-3}	0.07–0.18	–	0.18	0.27	1182.6
pH = 2	308	4.45×10^{-3}	0.20–0.25	–	0.25	0.38	929.4
	318	4.81×10^{-3}	0.14–0.18	–	0.18	0.41	1027.6
	328	7.03×10^{-3}	0.18–0.26	–	0.18	0.49	1275.2
pH = 3	318	4.96×10^{-3}	0.23–0.29	–	0.23	0.39	1091.5
Solvent	***T***	ssc_A	ssc_B	$CRAC_{C2-C3}$	ssc_C	c_{max}	$q_{e,max}$
pH = 5	318	3.15×10^{-2}	0.11	0.25–0.38	0.38	0.45	637.0
Solvent	***T***	ssc_A	$CRAC_{C1-C2}$	ssc_B	ssc_C	c_{max}	$q_{e,max}$
pH = 10	318	3.74×10^{-3}	–	3.2×10^{-2}	–	6.5×10^{-2}	112.5
pH = 13	318	6.19×10^{-3}	–	2.5×10^{-2}	–	4.7×10^{-2}	114.0
pH = 14	318	1.32×10^{-2}	–	–	–	3.4×10^{-2}	63.7

ssc_A, ssc_B, $ssc_C$are the starting concentrations of regions IIA, IIB and IIC respectively and their units are in mM. $CRAC_{C1-C2}$ and $CRAC_{C2-C3}$ are the concentration range of leveling off the adsorption isotherm between the first and second and the second and third curves, respectively and their unit is in mM.

maximum adsorption capacity of regions I and IIA is q_{sscB} = 291,1 mg g^{-1}, which was much bigger than those of reported for ARS[43] and orange IV[44] which interacted with



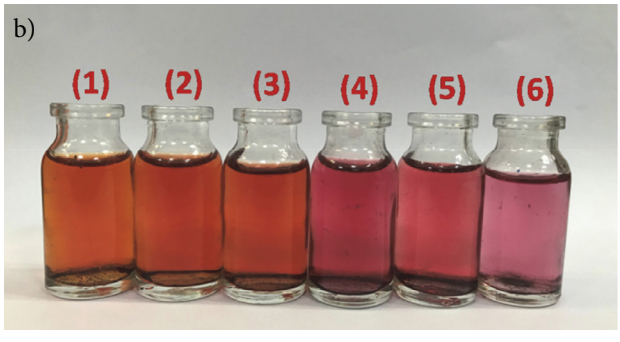


Figure 8. (a) Adsorption isotherm of ARS on GO/PAMAM at pH = 5 which showed adsorption of ARS^- molecules on *Ph* (region I) and $-NH^+_3$ (region IIA) sites and ARS^{2-} molecules on $-NH^+_3$ (region IIB) sites, respectively. (b) Solutions in bottles 1-3 belonged to regions I, IIA and the second CRAC. Solutions in bottles 4-6 belonged to region IIB and initial ARS concentrations increased from bottles 1 to 6.

GO. However, our q_{sscB} was smaller than that of the second and third curves, $q_{max,e} - q_{sscB}$ = 345,9 mg g^{-1}, Table 2. Then, it was concluded that in region IIC, ARS^{2-} molecules interacted with some remaining $-NH^+_3$ sites.

As seen from Table 2, at pH = 5 and 318 K, ARS^- in region IIB and then ARS^{2-} in region IIC interacted with $-NH^+_3$ sites. The *K* value of the former interaction was higher than the latter one. Given the negative charge of $ARS^{2-}$was higher than that of ARS^-, the *K* values observed in region IIC were less than those in region II, Figures 8 and 9. The observation of K values was attributed from two aspects: (1) the steric hindrance caused by the adsorbed ARS molecules; (2) increasing repulsion interaction between ARS molecules and negatively charged adsorbent surface.

Alizarin (AZ) was used to determine the functional group responsible for interacting ARS with GO/PAMAM in alkaline media. AZ molecule shares the same structure as ARS except for the missing sulfonate group, Figure 10. The pK_a of AZ is 6.77 and both hydroxyl groups of AZ are ionized under an alkaline environment.[45] Experiments showed that AZ adsorption capacity of GO/PAMAM at pH = 12 was 21.6 mg g^{-1} that was much less than the ARS adsorption capacity of 113.4 mg g^{-1} under similar conditions. This test verified that the sulfonate group of ARS^{2-} and ARS^{3-} molecules but not their $-O^-$ groups interacted with GO/PAMAM in alkaline media.

Finally, the adsorption of ARS on GO/PAMAM was studied in acidic solutions, pH ≤ 3. Visible spectroscopy technique showed that only ARS^- molecules appeared in this range of pHs. As reported before,[42] with the decrease in pH (pH < 4) all the tertiary amines were protonated. Due to the repulsion between primary and tertiary amines of PAMAM dendrimer, its structure was opened, yielding

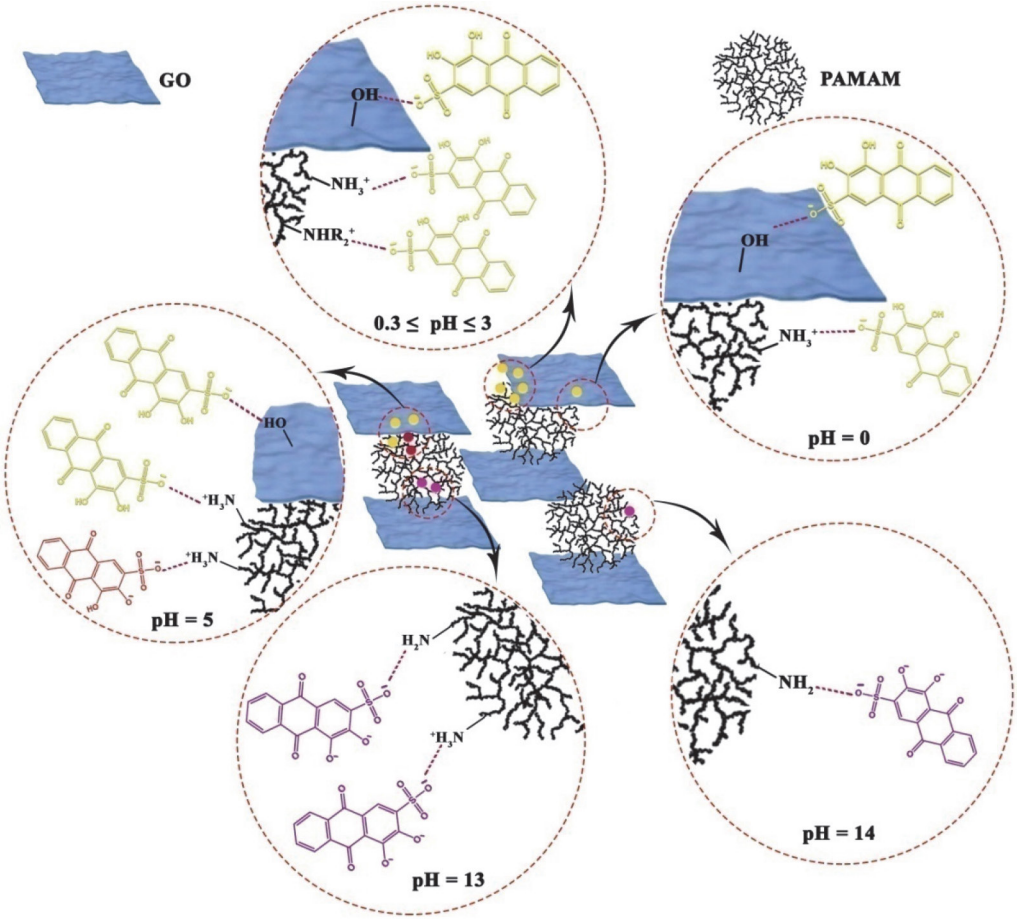


Figure 9. Adsorption sites of GO/PAMAM for different types of ARS molecules at different pHs.

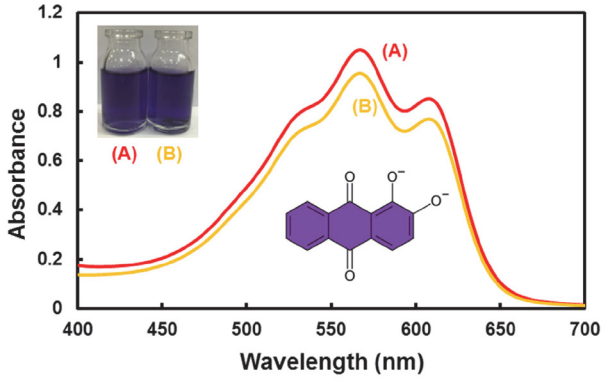


Figure 10. Absorption spectra of (A) 0.1 mM AZ and (B) 0.1 mM AZ in the presence of 0.001 g GO/PAMAM. The molecular structure of AZ at pH = 12 is shown in this figure.

an ideal interaction between the *Ph* groups of GO moiety of adsorbent and *ARS*$^-$ molecules. Thus, the adsorption of ARS on the pristine GO/PAMAM obeyed only from the Henry equation (region I) without forming region IIA. Under these conditions more primary and tertiary amine groups exposed to *ARS*$^-$ molecules. Due to binding three alkyl groups to N atom of tertiary amines, the polarity of N–H bond of protonated tertiary amines form is less than that for N–H bond of protonated primary amines $-NH^+_3$ and O–H bond of *Ph* groups.

As shown in Tables 2, S1–S3 and Figure 7, the adsorption of *ARS*$^-$ molecules at pH≤ 3 occurred in three regions (I, IIB and IIC). However, the adsorption of *ARS*$^-$ molecules at pH = 0 happened in two regions (I and IIB) and their related adsorption isotherms were formed from two curves.

Thus, *ARS*$^-$ molecules adsorbed on *Ph*, $-NH^+_3$ and $-NHR^+_2$ sites in region I and sections IIB and IIC, respectively. As shown in Tables 2, 3, S1–S3 and Figures 7(a) and 7(b), the maximum experimental adsorption capacity ($q_{e,max}$) of the adsorption of *ARS*$^-$ molecules on GO/PAMAM at pHs of 1, 2 and 3 were comparable. This implied that an increase in ionic strength of solutions at pHs from 3 to 1 did not affect the $q_{e,max}$ of process. The adsorption binding constants (K) in regions I and IIB at 318 K increased from pHs 1 to 3. However, K values in region IIC (on the $-NH^+_3$ sites) were approximately constant. Each of the adsorption isotherms at pHs of 1, 2 and 3 consisted of two curves and a CRAC appeared between them, Table 3. The presence of

CRACs was due to the high adsorption capacity of adsorbent for ARS^- molecules in the concentration range of the first curve which resulted in steric hindrance of adsorbed ARS^- molecules on the adsorbent surface and electrostatic repulsion between adsorbent surface and ARS^- molecules.

At pH = 2, thermodynamic parameters of interaction of ARS^- molecules with *Ph*, $-NH^+_3$ and $-NHR^+_2$ sites in regions I, IIB and IIC respectively, were calculated using the adsorption binding constants obtained from the Henry, Temkin and Temkin isotherms respectively, Table 2. ΔH and ΔS values were 63.2 kJ mol^{-1} and –57.1 J mol^{-1} K^{-1} in region I, 75.8 kJ mol^{-1} and –127.2 J mol^{-1} K^{-1} in region IIB and 48.9 kJ mol^{-1} and 237.8 J mol^{-1} K^{-1} in region IIC, respectively.

Afterwards, the Thermodynamic parameters of the adsorption were analyzed. Adsorption in the liquid phase, occurred through two kinds of interactions. One of them is the interaction of adsorbate molecules with surface of adsorbent and the other is due to replacing water molecules attached to the surface by adsorbate molecules.

The former interaction, by immobilization of adsorbate molecules, lowers the entropy of adsorption system. The latter one increases the disorder and thus the entropy of adsorption system which is result of the mobility of detached water molecules. At pH = 2, the negative ΔS values observed in adsorption of ARS^- molecules on the surface of GO/PAMAM in region I and sections IIB, showed electrostatic (ion-ion or ion-dipole) interaction occurred between ARS^- molecules with *Ph* and $-NH^+_3$ adsorption sites of GO/PAMAM. The negative ΔH values of these interactions indicated that the adsorption process in these two regions were exothermic.

On the other hand, the large positive ΔS value in region IIC showed after initial electrostatic interaction between ARS^- molecules and $-NHR^+_2$ adsorption sites of GO/PAMAM surface, a hydrophobic interaction happened between ARS^- molecules and hydrocarbon chains of $-NHR^+_2$ adsorption site that detached a large number of water molecules solvating ARS^- molecules and GO/PAMAM surface. The positive sign of ΔH value of this interaction was due to: (1) required energy to separate more number of water molecules from the GO/PAMAM surface and ARS^- molecules and (2) subsequent hydrophobic interactions between ARS^- molecules and GO/PAMAM surface.[46,47]

It was observed that adsorption capacities of these two curves of isotherms (specially the second curve) decreased from pH = 1 to pH = 0. Adsorption capacities of the second curve decreased about 50% from pH = 1 to pH = 0.3 and further disappeared at pH = 0 which showed gradual decrease in the availability of the second adsorption site with an increase of HCl concentration.

This observation was further investigated using the following tests. The comparison of EDS spectra of ARS–adsorbed GO/PAMAM modified by 1 M HCl for 10 hours and pristine GO/PAMAM showed that atomic percentages of nitrogen were comparable, which were 24.75% and 23.13% in the former and latter samples, respectively (without considering atomic percentage of its chlorine), Figures S3(a) and S3(b).

According to the measurements of nitrogen physisorption BET technique for pristine GO/PAMAM, ARS-adsorbed GO/PAMAM at pH = 2 and ARS-adsorbed GO/PAMAM at pH = 0, BET surface area, maximum pore volume for slit pore geometry, adsorption average pore diameter (by BET) and pore volume were 9.59 m^2 g^{-1}, 0.0044 cm^3 g^{-1}, 18.9 nm and 0.045 cm^3 g^{-1} for the first sample, 1.92 m^2 g^{-1}, 0.001 cm^3 g^{-1}, 14.2 nm and 0.0069 cm^3 g^{-1} for the second sample and 1.35 m^2 g^{-1}, 0.0006 cm^3 g^{-1}, 10.7 nm and 0.0036 cm^3 g^{-1} for the third sample respectively, Figures S1(a)-S1(c). The t-plot micropore area for ARS-adsorbed GO/PAMAM at pH = 0 was 0.0075 m^2 g^{-1} and ARS-adsorbed GO/PAMAM at pH = 2 and pristine adsorbent were lack of micropores. These results showed that as GO/PAMAM at pH = 0 adsorbed less ARS molecules than GO/PAMAM at pH = 2, the BET surface area and slit pore volume of adsorbent at pH = 0 were less than those values at pH = 2 and part of adsorbent pores at pH = 0 changed to micropores.

The comparison of IR spectra of ARS-adsorbed GO/PAMAM modified by 1 M HCl for 10 hours and pristine GO/PAMAM showed that those IR spectra were very similar, Figures 3(a) and 3(b). Also, the shift of broad peak around 2θ of 26.7° in the XRD spectrum of GO/PAMAM to 26.4° in the XRD spectrum of GO/PAMAM modified at pH = 0 showed a change in the structure of the latter one, Figures 2(a) and 2(b).

This evidence confirmed that the decrease in the adsorption capacities of the first and second curves of adsorption isotherms at pHs of 0.3 and 0 was due to masking the adsorption sites of GO/PAMAM. Indeed, a decrease in pH to less than 1 and an increase in ionic strength of solutions resulted in a shrinkage in PAMAM structure[42] and possible interactions were between $-NH^+_3$ and polyamide groups of PAMAM dendrimer and between functional groups of PAMAM with a number of functional groups on the GO planes of adsorbent like its C = C bonds and compressed its structure. This resulted in a decrease in the number of free *Ph* and $-NH^+_3$ groups and entrapment of $-NHR^+_2$ groups in internal structure of PAMAM and thus, resulted in a decrease in the availability of *Ph*, $-NH^+_3$ and $-NHR^+_2$ adsorption sites of GO/PAMAM for ARS^- molecules.

Finally, relative adsorption capacities of isotherms for regions I $\left(\frac{q_{sscA}}{q_{e,\max}}\right)$, IIA $\left(\frac{q_{sscB}-q_{sscA}}{q_{e,\max}}\right)$, IIB $\left(\frac{q_{sscC}-q_{sscB}}{q_{e,\max}}\right)$ and IIC $\left(\frac{q_{e,\max}-q_{sscC}}{q_{e,\max}}\right)$ were given in Table S4. For example, because at pH = 5 the concentration of ARS^{2-} molecules was less than ARS^- molecules, the adsorbent's relative adsorption capacity for ARS^{2-} (region IIC) was 0.15 of $q_{e,\max}$ value.

3. 2. Kinetics of Adsorption of ARS on GO/PAMAM

The adsorption mechanism of ARS on GO/PAMAM was studied by the KASRA model, and intraparticle diffusion and ISO equations using different ARS initial concentrations, temperatures, pHs and shaking rates. At 318 K, using 0.25 mM ARS at pH = 0 and using 0.07 mM ARS at pH = 2, only one adsorption curve was observed in their kinetic diagrams without the presence of TRAK, implying that the adsorption of ARS^- molecules occurred on the *Ph* sites of adsorbent, Figures 11(a) and 11(b) and Table 4.

gions (curves) were observed in all kinetic diagrams: ARS^- molecules interacted with *Ph* sites in the first curve, followed by interaction with $-NH^+_3$ and $-NHR^+_2$ sites in the second one. It was observed that at pH = 2, ISO rate constants for the adsorption on the *Ph* sites (in the first region) increased with an increase of the shaking rate. Also, an increase in pH from 2 to 3 increased the ISO rate constants for the adsorption on *Ph*, $-NH^+_3$ and $-NHR^+_2$ sites.

At pH = 2, adsorption acceleration, initial velocity and k_{dif} for adsorption on *Ph*, $-NH^+_3$ and $-NHR^+_2$ sites increased with temperature, shaking rate and ARS initial concentration. The k_{I1} values at 0.7 mM and 100 rpm, that

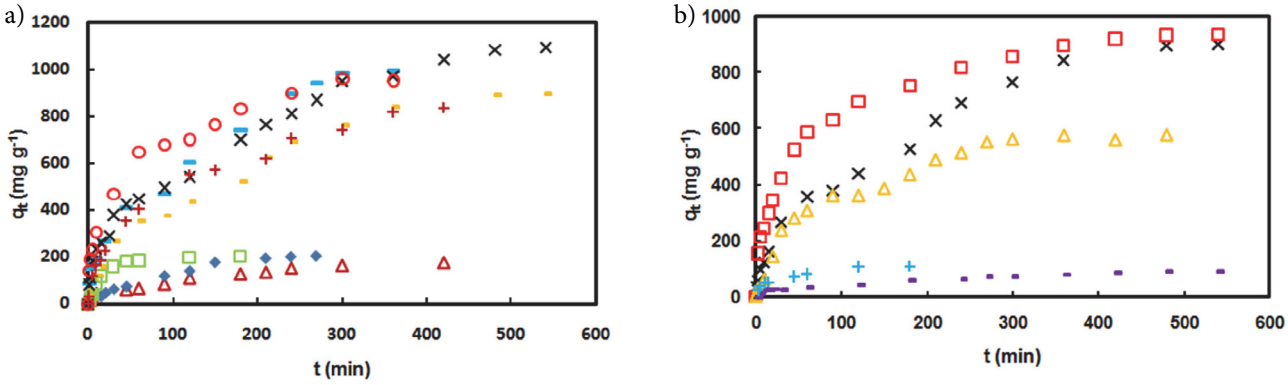


Figure 11. Kinetic curves of adsorption of ARS on GO/PAMAM (a) at ♦ pH = 0 and 0.25 mM ARS and □ pH = 2 and 0.07 mM ARS at 318 K and 100 rpm; at pH = 2, 0.7 mM ARS and – 308, × 318 and ○ 328 K at 100 rpm; at Δ pH = 2, 0.07 mM ARS, 318 K and 100 rpm; at pH = 2, 0.7 mM ARS and 318 K at - 40 and + 70 rpm, respectively and (b) at × pH = 2, 0.7 mM ARS, 318 K and 40 rpm; at □ pH = 3 and 0.7 mM ARS, Δ pH = 5 and 1 mM ARS, - pH = 10 and 0.07 mM ARS and + pH = 13 and 0.07 mM ARS at 318 K and 100 rpm.

Table 4. TRAKs for adsorption of ARS on GO/PAMAM in water, alkaline and acidic solutions at 100 rpm and 308–328 K.

Solvent	T (K)	$[ARS]_0$ (mM)	rpm	$TRAK_{C1-C2}$ (min)	$q_{TRAKC1-C2}$ (mg g^{-1})	t_e (min)	q_e (mg g^{-1})
pH = 0	318	0.25	100	–	–	270	206.3
pH = 2	318	0.07	100	–	–	180	202.3
(0.1 M NaCl)	318	0.07	100	–	–	420	174.0
	308	0.70	100	–	–	360	991.9
	318	0.70	100	–	–	420	965.9
	328	0.70	100	–	–	300	960.1
	318	0.70	70	–	–	360	815.4
	318	0.70	40	–	–	480	893.4
pH = 3	318	0.70	100	–	–	480	931.5
pH = 5	318	1.00	100	90–120	362.2–362.5	360	577.8
pH = 10	318	0.07	100	10–30	25.7–27.1	480	90.4
pH = 13	318	0.07	100	10–15	51.6–53.7	120	109.0

$TRAK_{C1-C2}$ is the TRAK between the first and second kinetic curves. t_e is the time of starting plateau.

As seen from Tables 5 and 6 and S5–S7, adsorption acceleration, initial velocity, k_{dif}, k_{I1} and k_{I2a} decreased as pH decreased from 2 to 0. This was resulted from the compression of the adsorbent structure at pH = 0, that blocked interior adsorption sites. Using 0.7 mm ARS at pHs of 2 and 3 at different shaking rates and temperatures two re-

implied the interaction of *Ph* sites with ARS^- molecules increased with temperature. The activation energy of the adsorption in region I was 114.5 kJ mol^{-1}. Therefore the adsorption of ARS on *Ph* sites was reaction-controlled. The adsorption in region I in region I only spanned about 6–8% of the whole adsorption duration but was accounted

Table 5. Coefficients of the intraparticle diffusion equation for kinetics of ARS adsorption on GO/PAMAM at different temperatures and in various shaking rates and ARS initial concentrations.

Solvent	T (K)	$[ARS]_0$ (mM)	rpm	KASRA region 1 (1st curve) k_{dif}	a_1	(t_2, q_2)	KASRA region 2 (1st curve) k_{dif}	a_2	TRAK	KASRA region 2 (2nd curve) (t_3, q_3)	k_{dif}	a_3	TRAK
Corresponding to thermodynamic				**ARIAN region I**			**ARIAN section IIB**			**ARIAN section IIC**			
At $pH \leq 3$ adsorption of ARS^- on				***Ph* site**			**$-NH^+_3$ site**			**$-NHR^+_2$ site**			
pH = 0	318	0.25	100	11.2	−0.048	(45,73.7)	14.1	-4.0×10^{-3}	–	–	–	–	–
pH = 2	318	0.07	100	**32.6**	**−0.23**	**(45,181.8)**	**3.2**	$\mathbf{-2.0 \times 10^{-3}}$	**Adsorption only on *Ph* site**		–		–
(0.1 M NaCl)	318	0.07	100	**19.2**	**−0.47**	**(10,44.8)**	**8.2**	$\mathbf{-1.6 \times 10^{-3}}$	**Adsorption only on *Ph* site**		–		–
	308	0.70	100	97.1	−10.40	(5,169.9)	44.3	−0.11	–	(90,469.2)	56.2	−0.012	–
	318	0.70	100	82.5	−14.28	(5,184.2)	50.7	−0.13	–	(60,449.2)	45.4	−0.006	–
	328	0.70	100	105.7	−16.94	(5,232.6)	65.0	−0.14	–	(90,681.0)	37.9	−0.004	–
	318	0.70	70	66.3	−4.00	(9,120.6)	52.5	−0.08	–	(60,402.8)	35.3	−0.002	–
	318	0.70	40	43.8	−2.40	(10,120.1)	38.4	−0.11	–	(90,376.7)	44.9	−0.004	–
pH = 3	318	0.70	100	119.4	−8.45	(5,213.8)	71.6	−0.11	–	(60,585.1)	24.9	−0.002	–
pH = 5*	318	1.00	100	24.9	−1.19	(10,61.8)	75.0	−0.106	–	(30,237.0)	70.1	−0.006	90–120

Solvent	T (K)	$[ARS]_0$ (mM)	rpm	KASRA region 1 (1st curve) k_{dif}	a_1	(t_2, q_2)	a_2	a_3	TRAK	KASRA region 2 (2nd curve) (t_3, q_3)	k_{dif}	a_3	TRAK
Corresponding to thermodynamic				**ARIAN region I and section IIA**						**ARIAN section IIB**			
pH = 10*	318	0.07	100	7.7	−0.65	–	–	–	10–30	(30,27.1)	4.0	-4.0×10^{-4}	–
pH = 13*	318	0.07	100	19.8	−0.95	–	–	–	10–15	(15,53.7)	7.8	-4.0×10^{-3}	–

Unit of k_{dif} is in mg g^{-1} $min^{-0.5}$. Units of a_1, a_2 and a_2 are in mg g^{-1} min^{-2}. Units of t_1, t_2 and t_3 are in min and those of q_1, q_2 and q_3 are in mg g^{-1} and $t_1 = q_1 = 0$. Boundary points coordinates of diffusion regions, (t_n, q_n), are similar to those of the KASRA model, (t_{0n}, q_{0n}) in Table S5. *At pH = 5, data from left to right belong to the first and second kinetic curves and the third kinetic curve (corresponding to the ARIAN section IIC) starts after second TRAK (90–120 min) and for that k_{dif} and $a_4$are 36.3 mg g^{-1} $min^{-0.5}$ and −0.006 mg g^{-1} min^{-2}, respectively. Adsorption sites and ARS types involved at pHs = 5, 10 and 13 are discussed in text.

Table 6. Coefficients of region 1 and region 2 (parts 2*a* and 2*b*) of the ISO equation for kinetics of ARS adsorption on different sites of GO/PAMAM at 308–328 K.

Solvent	T (K)	$[ARS]_0$ (mM)	rpm	KASRA regions 1 and 2 (1st curve) k_{I1}	k_{I2a}	k_{I2b}	$([ARS]_E, t_E, q_E)$	k_{I2a}	k_{I2b}	KASRA region 2 (2nd curve) $([ARS]_e, t_e, q_e)$
Corresponding to thermodynamic							**ARIAN region I and section IIA**			
At $pH \leq 3$ adsorption of ARS^- on				***Ph* site**		**$-NH^+_3$ site**			**$-NHR^+_2$ site**	
pH = 0	318	0.25	100	2.83×10^4	8.43×10^3	2.32×10^4	–	–	–	(0.196,270,206.3)
pH = 2	318	0.07	100	$\mathbf{3.91 \times 10^5}$	$\mathbf{1.87 \times 10^5}$	–	**Adsorption only on *Ph* site**		–	$(2.27 \times 10^{-2}$, 180,202.2)
(0.1 M NaCl)	318	0.70	100	$\mathbf{6.46 \times 10^4}$	$\mathbf{1.44 \times 10^4}$	$\mathbf{9.33 \times 10^4}$	**Adsorption only on *Ph* site**		–	$(2.42 \times 10^{-2}$, 420,174)
	308	0.70	100	1.69×10^4	1.83×10^4	3.89×10^4	(0.59,90,469.2)	1.40×10^4	5.39×10^4	(0.49,360,991.9)
	318	0.70	100	8.57×10^4	1.70×10^4	7.11×10^4	(0.556,60,449.2)	1.39×10^4	7.86×10^4	(0.418,420,965.9)
	328	0.70	100	2.57×10^5	2.88×10^4	7.84×10^4	(0.521,90,681.0)	9.81×10^3	2.21×10^4	(0.391,300,960.1)
	318	0.70	70	6.55×10^4	1.66×10^4	2.99×10^4	(0.606,60,402.8)	6.12×10^3	1.22×10^4	(0.533,360,815.4)
	318	0.70	40	3.15×10^4	3.19×10^4	–	(0.59,90,376.7)	8.76×10^3	6.57×10^4	(0.204,480,893.4)
pH = 3	318	0.70	100	1.27×10^5	6.23×10^3	1.35×10^4	(0.563,60,585.1)	7.73×10^3	1.15×10^4	(0.482,480,931.5)
pH = 5*	318	1.00	100	1.78×10^4	1.75×10^4	1.11×10^4	(0.85,90,362.2)	7.81×10^3	1.77×10^4	(0.814,360,577.8)
pH = 10**	318	0.07	100	1.98×10^5	–	–	$(6.32 \times 10^{-2}$, 10,25.7)	3.70×10^3	9.25×10^3	$(4.89 \times 10^{-2}$, 480,90.4)
pH = 13***	318	0.07	100	2.35×10^5	–	–	$(5.79 \times 10^{-2}$, 10,51.6)	3.59×10^4	1.14×10^5	$(5.21 \times 10^{-2}$, 180,110.0)

$[ARS]_E$, t_E and q_E are ARS concentration, time and adsorption capacity at the end of adsorption on a type of adsorption site, respectively (corresponding to $[ARS]_e$, t_e and q_e in the last curve). $[ARS]_e$, t_e and q_e are ARS concentration, time and adsorption capacity at the beginning of the plateau. Units of k_{I1}, k_{I2a} and k_{I2b} are in min^{-1}. $[ARS]_E$ and $[ARS]_e$ are in mM. *At pH = 5, data from left to right belong to the adsorption of ARS^- on *Ph* sites (1st kinetic curve), ARS^- on$-NH^+_3$ sites (2nd kinetic curve) and ARS^{2-} on $-NH^+_3$ sites (3rd kinetic curve), respectively. **At pH = 10, data from left to right belong to the adsorption of ARS^{2-} on $-NH^+_3$ (1st kinetic curve) and $-NH_2$ sites (2nd kinetic curve), respectively. ***At pH = 13, data from left to right belong to the adsorption of ARS^{3-} on $-NH^+_3$ (1st kinetic curve) and $-NH_2$ sites (2nd kinetic curve), respectively.

for about 34–41% of the adsorption capacity of GO/PAMAM. The adsorption on Ph sites was much faster than those on the $-NH^+_3$ and $-NHR^+_2$ sites. On the other hand, under similar conditions, other rate constants obtained from the ISO equation changed randomly with temperature and thus the adsorption on the $-NH^+_3$ and $-NHR^+_2$ sites was diffusion-controlled.

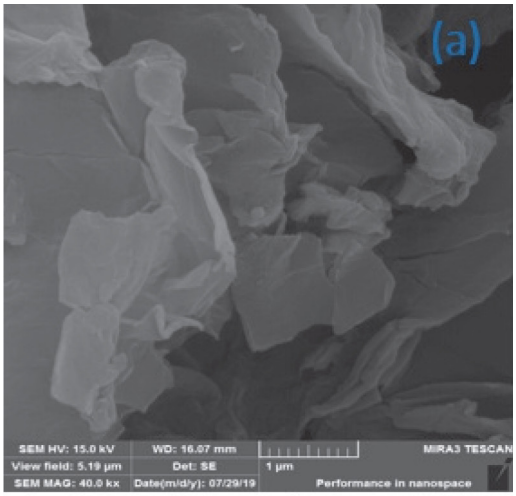
At pH = 2 and 0.07 mM ARS in 0.1 M NaCl, adsorption acceleration, initial velocity and k_{I1} increased slightly compared to those values in a solution without NaCl. This was due to more availability of ARS^- molecules to internal structure of PAMAM dendrimer with the ionic strength of solution. The slight increase in k_{I1} value with an increase in the ionic strength of solution confirmed that the adsorption interaction in region I occurs between ARS^- molecules and uncharged *Ph* groups of adsorbent.

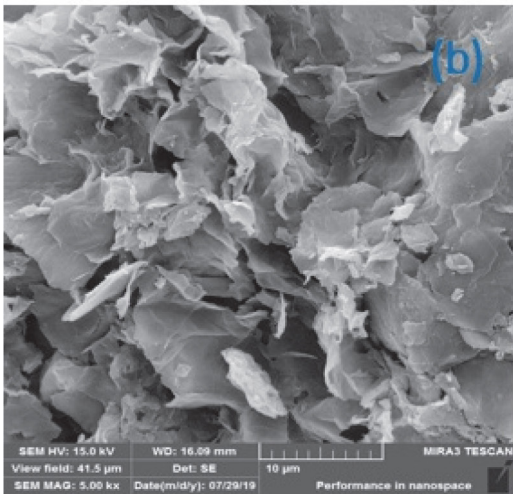
At pH = 5, 318 K and 1 mM ARS, adsorption acceleration, initial velocity, k_{dif} and k_{I1} of the adsorption on *Ph* and $-NH^+_3$ sites (first curve) were less than those at pH = 2, 318 K and 0.7 mM ARS. Because, at pH < 4, all the primary and tertiary amines were protonated and the repulsion interaction between these amine groups of PAMAM dendrimer, its structure swelled[42] to expose more adsorbent inner surface compared to that at pH = 5, Tables 5 and 6.

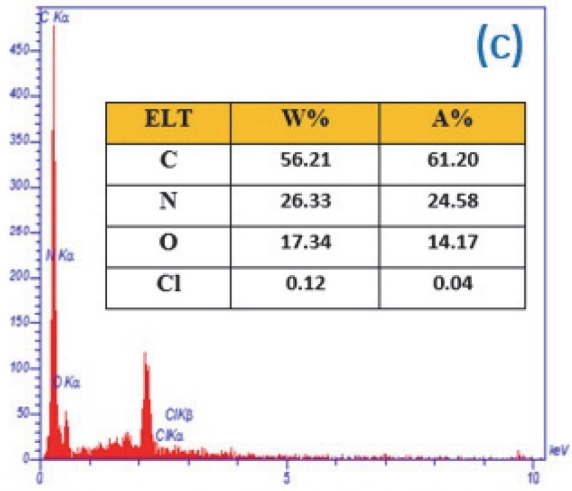
At 318 K and 0.07 mM ARS, ARS^{2-} molecules at pH = 10 and ARS^{3-} molecules at pH = 13 were adsorbed on $-NH^+_3$ sites (first curve) and $-NH_2$ sites (second curve) respectively. As the pH increased from 5 to 13, the electron charge density on the adsorbent surface became higher, that increased the electrostatic repulsion between ARS molecules and adsorbent surface. The repulsive interaction yielded the appearance of TRAK in the kinetic diagrams Table 4.

3. 3 Recycling ARS-adsorbed GO/PAMAM

For recycling ARS-adsorbed GO/PAMAM, several solvents were tested, such as, diethyl ether, methanol, ethanol, benzene, DMF, THF, DMSO, diethylenetriamine and alkaline and acidic aqueous solutions, none of them could extract ARS from the used adsorbent. However, we found







ELT	W%	A%
C	56.21	61.20
N	26.33	24.58
O	17.34	14.17
Cl	0.12	0.04

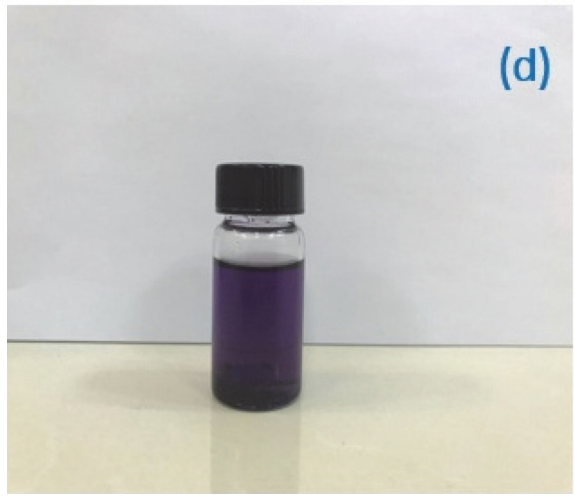


Figure 12. (a,b) SEM and (c) EDS images of the recycled GO/PAMAM and (d) extraction of ARS from the ARS-adsorbed GO/PAMAM by ethylenediamine.

ethylenediamine extracted ARS from the ARS-adsorbed GO/PAMAM very fast and effectively. In a series of experiments, 0.006 g samples of pristine GO/PAMAM were added to 30 ml of 10^{-3} M ARS solution at pH = 3 at ambient temperature. The ARS-adsorbed adsorbents were separated from supernatant after 10 h followed by washing and drying. Then, about 45 ml of ethylenediamine was added to the about 0.0025 g of the used adsorbent in three steps (15 ml/step). The adsorption capacity of pristine GO/PAMAM was fully regenerated. The EDS spectrum of the recycled adsorbent showed no trace of sulfur atom. The SEM images of the recycled adsorbent showed that its morphology was similar to that of the pristine GO/PAMAM, Figures 12(a)–12(d). Finally, ARS was separated from the ethylenediamine solution (in purple) by the distillation process.

3. 4. Selective separation of some cationic dyes from ARS using GO/PAMAM

The selective adsorption of ARS from these dyes can be used for making photochemical and electrochemical sensors.[48–50] For studying selective separation capability of dyes from ARS by GO/PAMAM, methylene blue (MB), acridine orange (AO), pyronin Y (PY), thionine (Th) and janus green B (JG) cationic and methyl blue (MEB) anionic dyes were mixed with ARS at pH = 2, Figures 13 and S5. Maximum wavelengths of ARS, MB, AO, PY, Th, JG and MEB were at 422, 664, 491, 546, 599, 820 and 599 nm, respectively.

At this pH, GO/PAMAM had its maximum adsorption capacity for ARS. Using the adopted initial ARS concentration, ARS was fully removed from the solution. Comparison of the UV-Vis spectra of pure dyes solutions with those of ARS-dye mixtures (in the absence of adsorbent) showed that the strength of dye-ARS interaction followed the trend: JG (by formation of deposit) > MB, AO, PY >Th > MEB, peaks B and D of Figures 14(b) –14(g). The final concentrations of Th, MB, AO and PY in their mixtures with ARS were 95%, 56%, 45% and 56% of their initial concentrations, respectively. As shown in peaks B and D of Figure 14(f), MEB and ARS anionic dyes do not interact together.

As shown in absorption peaks of B and C of Figures 14(b)–14(g), the final concentrations of Th, MB, AO, PY, JG and MEB after adsorption on the surface of GO/PAMAM were 67%, 84%, 83%, 93%, 70% and 22% of their initial concentrations, respectively.

But, as seen in peaks of B, E of Figures 14(b)–14(g), due to interaction of Th, MB, AO, PY and JG with adsorbed ARS on the surface of GO/PAMAM and adsorption of MEB on the surface of GO/PAMAM in the mixture of these dyes with ARS in the presence of GO/PAMAM, their final

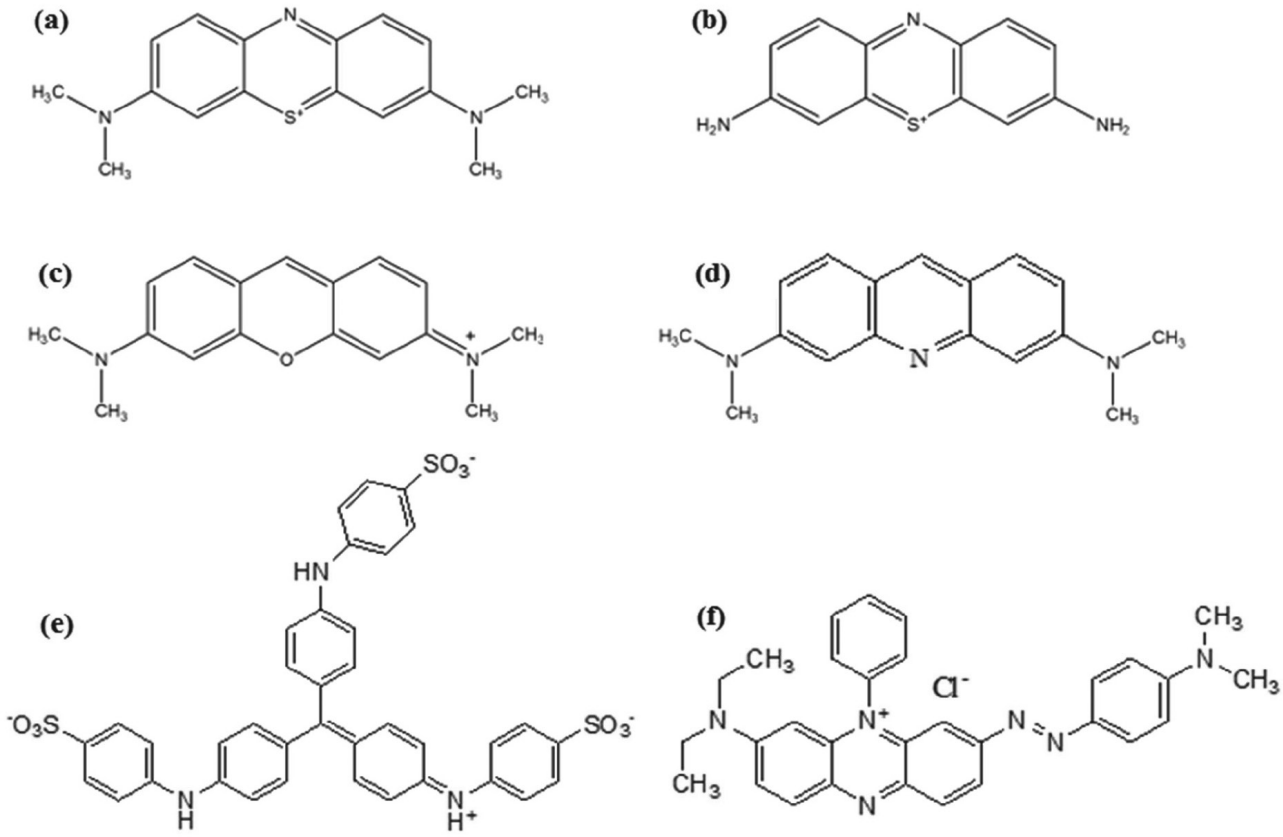


Figure 13. Molecular structure of (a) MB, (b) Th, (c) PY, (d) AO, (e) MEB and (f) JG.

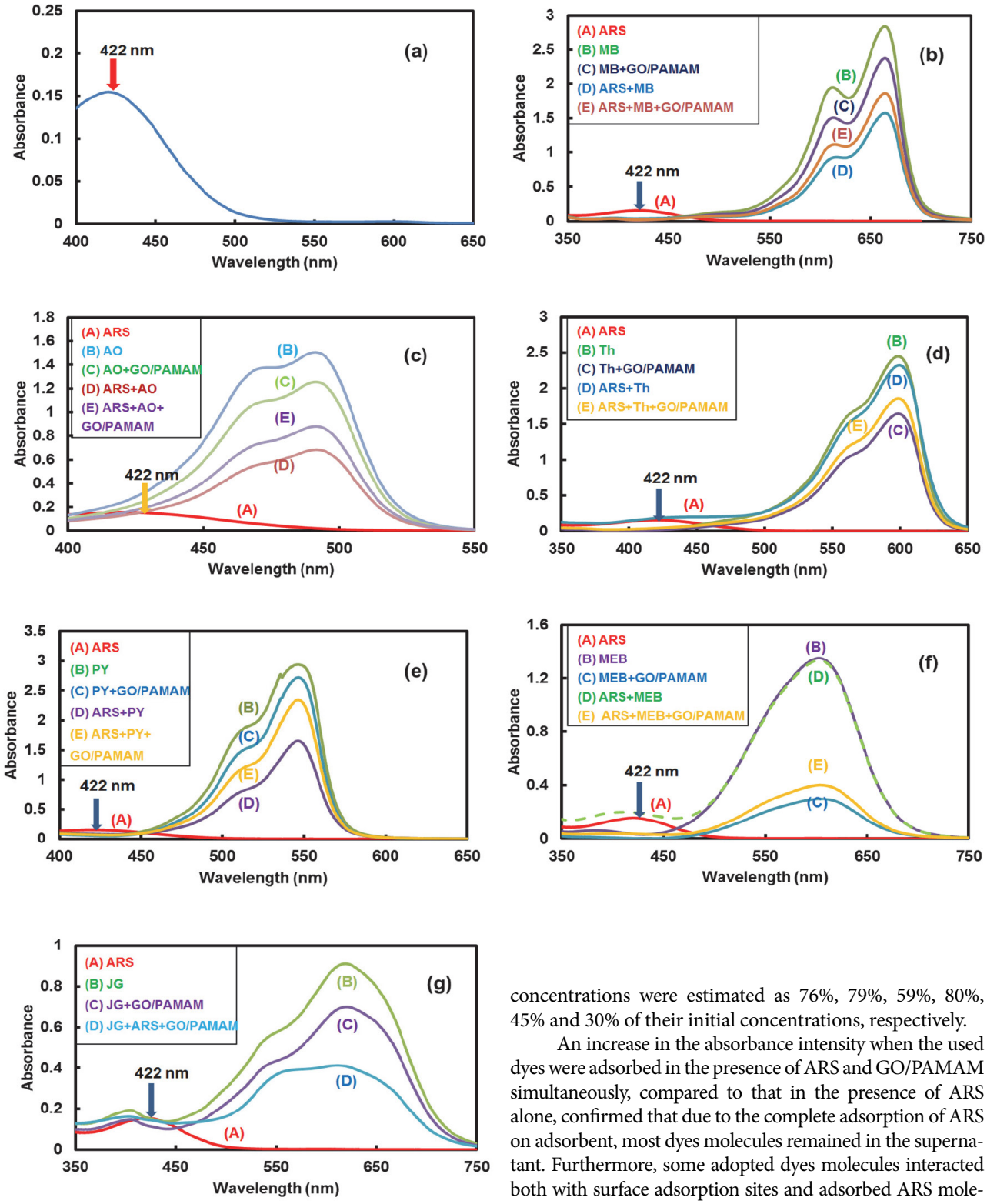


Figure 14. (a) Absorption peak of ARS at pH = 2. In all solutions, concentration of ARS was 5×10^{-2} mM and those of MB in (b), AO in (c), Th in (d), PY in (e) and MEB in (f) were 5×10^{-2} mM and concentration of JG in (g) was 2.5×10^{-2} mM. Tests were carried out at pH = 2 and room temperature. In curves (C) and (E) of all figures the weight of used GO/PAMAM was 0.001 g.

concentrations were estimated as 76%, 79%, 59%, 80%, 45% and 30% of their initial concentrations, respectively.

An increase in the absorbance intensity when the used dyes were adsorbed in the presence of ARS and GO/PAMAM simultaneously, compared to that in the presence of ARS alone, confirmed that due to the complete adsorption of ARS on adsorbent, most dyes molecules remained in the supernatant. Furthermore, some adopted dyes molecules interacted both with surface adsorption sites and adsorbed ARS molecules, peaks of B, C of Figures 14(b)–14(g). It was observed that in the used initial concentrations of ARS and JG, the ARS–JG deposit formed in their mixture was completely dissolved in the presence of GO/PAMAM and the solution turned blue from colorless which was due to complete adsorption of ARS, Figure S5 and peak D of Figure 14(g).

4 Conclusions

The adsorption of ARS on the surface of GO/PAMAM was studied under different temperatures, pHs, ARS initial concentrations, contact times and shaking rates. Adsorption isotherms were analyzed by the ARIAN model and its kinetic curves were investigated by the KASRA model and ISO and intraparticle diffusion equations. Analysis of adsorption isotherms and kinetic curves showed that phenolic *–OH* groups of GO moiety *(Ph)* and $–NH_2$, $–NHR^+_2$ and $–NH^+_3$ groups of PAMAM dendrimer moiety of GO/PAMAM were adsorption sites of the adsorbent. Depending on the solution pH, due to deprotonation, ARS formed three different species as ARS^-, ARS^{2-} and ARS^{3-}. At acidic pHs, ARS^- molecules interacted with *Ph*, $–NH^+_3$ and $–NHR^+_2$ in sequence. The adsorption on the *Ph* and $–NH^+_3$ sites were exothermic and the adsorption on the $–NHR^+_2$ sites was endothermic, respectively.

At pHs of 1, 2 and 3, $q_{e,max}$ of the adsorbent for ARS^- attained to maximum value and were similar together. At pH = 2 and 328 K, $q_{e,max}$ of GO/PAMAM (as a superadsorbent) for the adsorption of ARS^- was 1275.6 mg g^{-1}. This was attributed to the open GO/PAMAM structure after the protonation of all primary and tertiary amine groups of PAMAM dendrimer. Due to the repulsion interaction between these groups, GO/PAMAM structure became very open and resulted in an increase in adsorption capacity of GO/PAMA for ARS. At pH = 2, binding constant values of ARS^- molecules to *Ph* sites were higher than those of $–NH^+_3$ and $–NHR^+_2$ sites of adsorbent. The interaction of ARS^- molecules with *Ph* sites was faster than that of $–NH^+_3$ and $–NHR^+_2$ sites. The adsorption of ARS^- on *Ph* sites was reaction-controlled. The activation energy obtained from its ISO rate constant was 114.5 kJ mol^{-1}. However, the adsorption of ARS^- on the $–NH^+_3$ and $–NHR^+_2$ sites was diffusion-controlled.

The decrease in the pH of solutions from 1 to 0 resulted in a decrease in $q_{e,max}$, which could be owe to fewer available *Ph*, $–NH^+_3$ and $–NHR^+_2$ groups of GO/PAMAM for ARS molecules that was caused by a shrinkage in GO/PAMAM structure and masking some of functional groups of GO/PAMAM. Also, this resulted in a decrease in ISO rate constants with a decrease in pH from 2 to 0. At pH = 5, ARS^- interacted first with *Ph* sites and then with $–NH^+_3$ sites. In continuation, ARS^{2-} interacted with $–NH^+_3$ adsorption sites.

At pHs of 11 and 13, ARS^{3-} molecules at first interacted with $–NH^+_3$ and then $–NH_2$ adsorption sites. At pH of 14, ARS^{3-} molecules interacted with $–NH_2$ adsorption sites only. Different types of ARS molecules in acidic and alkaline media interacted with GO/PAMAM adsorption sites through their sulfonate head.

By using GO/PAMAM, several dyes including MB, AO, Th, PY, MEB and JG were separated from their mixtures with ARS at pH of 2. Our extensive study illustrated that used adsorbent was regenerated completely and efficiently using ethylenediamine at ambient temperature.

Furthermore, GO/PAMAM can be used to selectively remove ARS from dye mixtures at pH of 2. The finding could be beneficial to fabricate photochemical and electrochemical sensors.

5. References

1. M. F. Hamoda, I. Al-Ghusain, N. Z. Al-Mutairi, *Desalination*, **2004**, *164*, 203–211. **DOI:**10.1016/S0011-9164(04)00189-4
2. O. Tunay, E. Erdeml, N. Işık Kabdaşlı, T. Olmez, *Environ. Technol.*, **2008**, *29*, 1045–1051. **DOI:**10.1080/09593330802175823
3. G. Al-Enezi, M. Hamoda, N. Fawzi, *J. Environ. Sci. Health A*, **2004**, *39*, 455–464. **DOI:**10.1081/ESE-120027536
4. R. Hesnawi, K. Dahmani, A. Al–Swayah, S. Mohamed, S. A. Mohammed, *Procedia Eng.*, **2014**, *70*, 810–814. **DOI:**10.1016/j.proeng.2014.02.088
5. S. Palit, *IJCA*, **2012**, *3*, 302–305.
6. E. Nutiu, *Proc. Technol.*, **2015**, *19*, 479–482. **DOI:**10.1016/j.protcy.2015.02.068
7. F. Gorzin, M. M. Bahri Rasht Abadi, *Adsorpt. Sci. Technol.*, **2017**, *36*, 149–169. **DOI:**10.1177/0263617416686976
8. T. Erban, J. Hubert, *J. Insect Sci.*, **2010**, *10*, 1–12. **DOI:**10.1673/031.010.4201
9. J. Šíma, P. Hasal, *Chem. Eng. Trans.*, **2013**, *32*, 79–84.
10. J. H. Miller, J. L. Kotenko, *Stain Technol.*, **1987**, *62*, 237–245. **DOI:**10.3109/10520298709108001
11. M. S. Raghu, K. Basavaiah, K. N. Prashanth, K. B. Vinay, *ISRN Spectroscopy*, **2012**, Article ID 648510. **DOI:**10.5402/2012/648510
12. M. Fayazi, M. Ghanei-Motlagh, M. A. Taher, *Mater. Sci. Semicond. Process.*, **2015**, *40*, 35–43. **DOI:**10.1016/j.mssp.2015.06.044
13. D. Li, Q. Liu, S. Ma, Z. Chang, L. Zhang, *Adsorpt. Sci. Technol.*, **2011**, *29*, 289–300. **DOI:**10.1260/0263-6174.29.3.289
14. L. Fan, Y. Zhang, X. Li, C. Luo, F. Lu, H. Qiu, *Colloids Surf. B: Biointerfaces*, **2012**, *91*, 250–257. **DOI:**10.1016/j.colsurfb.2011.11.014
15. R. K. Gautam, P. K. Gautam, M.C. Chattopadhyaya, S. Banerjee, J. D. Pandey, *Proc. Natl. Acad. Sci., India, Sect. A Phys. Sci.*, **2014**, *84*, 495–504. **DOI:**10.1007/s40010-014-0154-4
16. P. B. Wagh, V. S. Shrivastava, *J. Sci. Res. Rep.*, **2014**, *3*, 2197–2215. **DOI:**10.9734/JSRR/2014/8005
17. F. Fu, G. Ziwei, L. Gao, D. Li, *Ind. Eng. Chem. Res.*, **2011**, *50*, 9712–9717. **DOI:**10.1021/ie200524b
18. S. Gao, W. Zhang, *Adsorpt. Sci. Technol.*, **2019**, *37*, 185–204. **DOI:**10.1177/0263617418819164
19. M. Aissat, S. Hamouda, N. Benhadria, R. Chellali, N. Bettahar, *AIP conference proceedings 1968*, **2018**, ID.020005.
20. H. V. Jadhava, S. M. Khetre, S. R. Bamane, *Der Chemica Sinica*, **2011**, *2*, 68–75.
21. M. Jamshidi, M. Ghaedi, K. Dashtian, S. Hajati, A. Bazrafshan, *RSC Adv.*, **2015**, *5*, 59522–59532. **DOI:**10.1039/C5RA10981G

22. J. Zolgharnein, Z. Choghaei, M. Bagtash, S. Feshki, M. Rastgordani, P. Zolghadrian, *Desalin. Water Treat.*, **2016**, *57*, 27672–27685.
23. O. Ali, S. Mohamed, *Turk. J. Chem.*, **2017**, *41*, 967–986. **DOI:**10.3906/kim-1703-72
24. F. Zhang, B. Wang, S. He, R. Man, *J. Chem. Eng. Data*, **2014**, *59*, 1719–1726. **DOI:**10.1021/je500219e
25. Q. C. Compton, D. A. Dikin, K. W. Putz, L. C. Brinson, S. T. Nguyen, *Adv. Mater.*, **2010**, *22*, 892–896. **DOI:**10.1002/adma.200902069
26. M. Rafi, B. Samiey, C-H Cheng, *Materials*, **2018**, *11*, 496. **DOI:**10.3390/ma11040496
27. K. S. W. Sing, D. H. Everett, R. A. W. Haul, L. Moscou, R. A. Pierotti, J. Rouquerol, T. Siemieniewska, *Pure Appl. Chem.*, **1985**, *57*, 603–619.
28. R. M. Silverstein, G. C. Bassler, T. C. Morrill: Spectrometric Identification of Organic Compounds. Fourth Edition, John Wiley and Sons, New York, 1981.
29. Y. Piao, T. Wu, B. Chen, *Ind. Eng. Chem. Res.*, **2016**, *55*, 6113–6121. **DOI:**10.1021/acs.iecr.6b00947
30. C. Wang, Y. Duan, N. S. Zacharia, B. D. Vogt, *Soft Matter***, 2017, *13*,** 1161–1170. **DOI:**10.1039/C6SM02439D
31. H. Gunzlr, H. U. Gremlich: IR Spectroscopy: An Introduction, Weinheim, Wiley-VCH, 2002.
32. B. Samiey, S. Golestan, *Cent. Eur. J. Chem.*, **2010**, *8*, 361–369. **DOI:**10.2478/s11532-009-0135-7
33. B. Samiey, S. Abdollahi Jonaghani, *J. Pollut. Eff. Cont.*, **2015.** **DOI:**10.4172/2375-4397.1000139
34. I. Langmuir, *J. Am. Chem. Soc.*, **1918**, *40*, 1361–1403. **DOI:**10.1021/ja02242a004
35. M. Boudart, G. Djega-Mariadassou: Kinetics of Heterogeneous Catalytic Reactions. Princeton University Press, New Jersy, 1984. **DOI:**10.1515/9781400853335
36. T. Sekine, T., Nakatani, K., *Langmuir*, **2002**, *18*, 694–697. **DOI:**10.1021/la0110500
37. B. Samiey, A. Dadkhah Tehrani, *JCCS*, **2015**, *62*, 149–162. **DOI:**10.1002/jccs.201400093
38. N. Safar Beyranvand, B. Samiey, A. Dadkhah Tehrani, *Acta Chim. Slov.*, **2019**, *66*, 443–454. **DOI:**10.17344/acsi.2018.4920
39. J. Ghasemi, S. Lotfi, M. Safaeian, A. Niazi, M. M. Ardakani, M. Noroozi, *J. Chem. Eng. Data.*, **2006**, *51*, 1530–1535. **DOI:**10.1021/je050535d
40. J. Ghasemi, A. Niazi, G. Westman, M. Kubista, *Talanta*, **2004**, *62*, 835–841. **DOI:**10.1016/j.talanta.2003.10.003
41. A. Córdoba, I. Magario, M. L. Ferreira, *J. Mol. Catal. A-Chem.*, **2012**, *355*, 44–60. **DOI:**10.1016/j.molcata.2011.12.011
42. P. K. Maiti, T. Çağin, S-T Lin, W. A. Goddard, *Macromolecules*, **2005**, *38*, 979–991. **DOI:**10.1021/ma049168l
43. P. Nuengmatcha, R. Mahachai, S. Chanthai, *Orient. J. Chem.*, **2016**, *32*, 1399–1410. **DOI:**10.13005/ojc/320314
44. Y. Guo, J. Deng, J. Zhu, C. Zhou, X. Zhou, R. Bai, *RSC Advances*, **2016**, *6*, 39762–39773. **DOI:**10.1039/C6RA03423C
45. R. W. Sabins: Handbook of Biological Dyes and Stains: Synthesis and Industrial Applications, John Wiley & Sons, Inc., New Jersey, 2010.
46. M. I. Chaudhari, S. A. Holleran, H. S. Ashbaugh, L. R. Pratt, *PNAS*, **2013**, *110*, 20557–20562. **DOI:**10.1073/pnas.1312458110
47. S. Lüdemann, R. Abseher, H. Schreiber, O. Steinhauser, *J. Am. Chem. Soc.*, **1997**, *119*, 4206–4213. **DOI:**10.1021/ja953439d
48. D. W. Kimmel, G. LeBlanc**,** M. E. Meschievitz**,** D. E. Cliffel, *Anal. Chem.*, **2012**, *842*, 685–707. **DOI:**10.1021/ac202878q
49. F. Li, J. Peng, Q. Zheng, X. Guo, H. Tang, S. Yao, *Anal. Chem.*, **2015**, *879*, 4806–4813.
50. Z. Wang, N. Zhong, M. Chen, H. Chang, D. Zhong, Y. Wu, H. Liu, X. Xin, M. Zhao, B. Tang, T. Song, S. Shi, *Applied Optics*, **2019**, *58*, 2091–2099. **DOI:**10.1364/AO.58.002091

Povzetek

Preučevana je adsorpcija alizarin rdeče S (ARS) na grafen oksid/poli(amidoamin) (GO/PAMAM) glede na različne začetne koncentracije ARS, temperaturo, pH vrednosti, hitrost mešanja in kontaktni čas. Adsorpcijska mesta GO/PAMAM so bile fenolne skupine –*OH* (*Ph*) GO in aminske skupine ($-NH_2$, $-NH^+_3$ in $-NHR^+_2$) PAMAM dendrimernih enot GO/PAMAM. Pri pH vrednosti 2 in temperaturi 318K je bila dosežena maksimalna kapaciteta ($q_{e,max}$) adsorbenta, ki je znašala 1275.2 mg g^{-1} in predstavlja eno najvišjih kapacitet opisanih v literaturi. Zato lahko smatramo, da deluje GO/PAMAM kot superadsorbent za ARS. V začetni fazi je adsorpcija kontrolirana z reakcijo (E_a = 114.5 kJ mol^{-1}) in se ARS^- molekule adsorbirajo na *Ph* mesta. Kasnejša adsorpcija na preostala adsorpcijska mesta pa je difuzijsko omejena. V bazičnem okolju smo identificirali dve drugi obliki ARS molekul, ki so se adsorbirale na *Ph* in $-NH^+_3$mesta. Nadaljnje povečevanje bazičnosti raztopine se je odrazilo v nižanju števila adsorpcijskih mest in posledično nižanju adsorpcijske kapacitete ($q_{e,max}$). Poleg tega smo pri pH vrednosti 2 lahko s pomočjo GO/PAMAM ločili ARS molekule od molekul metilensko modrega, (MB), tionina (Th), pironina Y (PY), akridin oranžnega (AO), metil modrega (MEB) in janus zelenega (JG).



Except when otherwise noted, articles in this journal are published under the terms and conditions of the Creative Commons Attribution 4.0 International License

Scientific paper

Design, Synthesis and Biological Screening of Novel 1,5-Diphenyl-3-(4-(trifluoromethyl)phenyl)-2-pyrazoline Derivatives

Fatih Tok[1] and Bedia Koçyiğit-Kaymakçıoğlu[1,*]

[1] *Department of Pharmaceutical Chemistry, Faculty of Pharmacy, Marmara University, Istanbul-34668, Turkey*

** Corresponding author: E-mail: bkaymakcioglu@marmara.edu.tr*
Tel: +90-216-4142963/1023

Received: 04-01-2020

Abstract

1-Phenyl-5-substituted-3-(4-(trifluoromethyl)phenyl)-4,5-dihydro-1*H*-pyrazole derivatives were synthesized from chalcone derivatives. The structures of compounds were characterized by IR, ^{1}H NMR spectroscopic methods and elemental analysis. All compounds were evaluated for their *in vitro* antioxidant activity using DPPH and ABTS methods, anti-inflammatory activity using lipoxygenase inhibitory method and antidiabetic activity using the α-glucosidase inhibitory method. Especially, pyrazoline derivatives exhibited stronger anti-inflammatory activity than the reference drug indomethacin (IC_{50}: 50.45 μM) and their IC_{50} values were in the range of 0.68 and 4.45 μM. In addition, the ADME properties of all chalcone and pyrazoline derivatives were calculated by Lipinski's and Veber's rules.

Keywords: 2-Pyrazoline; lipoxygenase enzyme; α-glucosidase; ABTS and DPPH

1. Introduction

Pyrazoline scaffolds bearing five-membered heterocyclic ring systems are used frequently in organic synthesis and medicinal chemistry because of their broad spectrum of activities.[1] Pyrazoline rings have important pharmacological and biological properties such as antioxidant, anti-inflammatory, analgesic, antimicrobial, antimalarial, antihypertensive, anticonvulsant, antidepressant, anticancer.[2–6] We studied the synthesis and antiproliferative activity of some pyrazoline compounds in our previous study.[7] Pyrazolines exhibited these different activities by interacting with some receptors or enzymes. For example, ElBordiny *et al.* demonstrated in their study that pyrazolines are superior lipoxygenase enzyme inhibitors compared to the reference drug.[8] Furthermore, Chaudhry *et al.* and Sathish *et al.* reported pyrazoline derivatives as alpha-glucosidase inhibitors.[9,10] Additionally, many studies proved different activities of pyrazoline derivatives as receptor tyrosine kinase, topoisomerase 1, carbonic anhydrase and cholinesterase inhibitors. It was found that nitrogen atoms of the pyrazoline ring and at least one substitution with aryl moiety are essential for anti-inflammatory activity (Gawad *et al.*, 2012).[11–15]

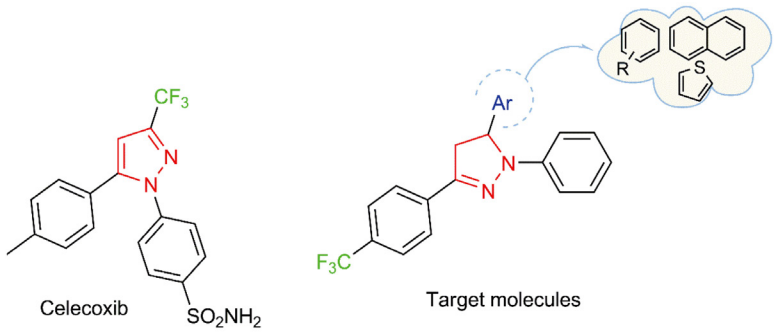


Figure 1. Chemical structure of designed compounds and celecoxib

Several drug molecules carrying pyrazole core with different activities are currently available in the market, for example, antipyrine (analgesic), celecoxib (anti-inflammatory), pyrazofurin (antibiotic).[16]

It is known that fluorine substitution increases biological activity and metabolic-chemical stability (compared to C–H bond) in drug research. Furthermore, fluorine alters physicochemical properties and enhances binding affinity to target protein easily.[17–18] We designed new molecules which are carrying pyrazoline core and trifluoromethyl substitution on the aromatic ring (Figure 1).

In this study, we synthesized chalcone derivatives from 4'-(trifluoromethyl)acetophenone in the first step. Then we synthesized new 2-pyrazoline derivatives from chalcones. We aimed to show different biological activities of pyrazoline derivatives. Therefore all synthesized compounds were screened for their antioxidant activity using DPPH and ABTS method, anti-inflammatory activity using lipoxygenase inhibitory method, and antidiabetic activity using α-glucosidase inhibitory methods.

2. Experimental

2. 1. Synthesis

Chemicals and solvents were obtained from Sigma Aldrich (St. Louis, MO, USA) or Merck (Darmstadt, Germany). The progress of the reaction was monitored *via* thin layer chromatography (TLC), performed on commercially available silica gel (Kieselgel 60, F254) coated aluminum sheets (Merck) by using developing systems: petroleum ether/acetone (60:40 v/v) as a solvent system. The visualization on TLC was done under ultraviolet (UV) light (λ = 254 nm). Melting points were determined by Schmelzpunktbestimmer SMP II apparatus. Infrared spectra were recorded on a Shimadzu FTIR 8400S Spectrometer and data was expressed in wavenumber ν (cm^{-1}). Proton nuclear magnetic resonance (NMR) (400 MHz) spectra were recorded with a Bruker ACP 200 spectrometer (Bruker Corp., Billerica, MA, USA). Deuterated dimethylsulfoxide (DMSO-d_6) was used as the solvent and tetramethylsilane (TMS) as the internal standard. The chemical shift values (δ) were expressed in ppm. Elemental analyses (C, H and N) was performed on a CHNS-Thermo Scientific Flash 2000 (Waltham, MA, USA).

2. 1. 1. General Procedure for the Synthesis of Chalcone

1 mmol of 4'-(trifluoromethyl)acetophenone and equimolar quantities of substituted aromatic aldehydes were dissolved in methanol, then NaOH (50% water solution) was added to the reaction mixture. It was stirred at room temperature for 16 h and then poured into ice-cold water. The precipitated product was washed with water, filtered and recrystallized from methanol.[19]

2. 1. 2. General Procedure for the Synthesis of Pyrazoline

10 mmol of chalcone derivatives, 10 mmol of phenylhydrazine hydrochloride and 10 mL of glacial acetic acid were put in a reaction flask. The content was refluxed and stirred for 12 h. Then, it was neutralized with dilute ammonia solution. The precipitate was washed with water, filtered and recrystallized from ethanol.[20]

3-(2,6-Dimethylphenyl)-1-(4-(trifluoromethyl)phenyl) prop-2-en-1-one (1a)

White powder, yield 77%, mp 74.3–74.5 °C. IR (KBr) ν 3064, 2978, 2912, 1696, 1606, 1591, 1573, 1510, 1408, 1315, 1213, 1161, 1064, 835 cm^{-1}. ^{1}H NMR (400 MHz, DMSO-d_6) δ 2.38 (s, 6H, $2CH_3$), 7.12–7.87 (m, 5H, Ar-H and CH=CH), 7.92 (d, J = 8.4 Hz, 2H, Ar-H) 8.27 (d, J = 8.4 Hz, 2H, Ar-H). Anal. Calcd for $C_{18}H_{15}F_3O$: C, 71.04; H, 4.97. Found: C, 70.82; H, 4.86%.

3-(2,6-Dichlorophenyl)-1-(4-(trifluoromethyl)phenyl) prop-2-en-1-one (1b)

Yellow powder, yield 65%, mp 62.3–62.7 °C. IR (KBr) ν 3072, 1696, 1606, 1573, 1508, 1467, 1408, 1305, 1213, 1161, 1064, 835 cm^{-1}. ^{1}H NMR (400 MHz, DMSO-d_6) δ 7.41–8.24 (m, 9H, Ar-H and CH=CH). Anal. Calcd for $C_{16}H_9Cl_2F_3O$: C, 55.68; H, 2.63. Found: C, 55.48; H, 2.78.

3-*o*-Tolyl-1-(4-(trifluoromethyl)phenyl)prop-2-en-1-one (1c)

Yellow powder, yield 75%, mp 89.0–89.8 °C. IR (KBr) ν 3053, 2978, 2897, 1683, 1595, 1510, 1462, 1410, 1317, 1211, 1161, 1064, 833 cm^{-1}. ^{1}H NMR (400 MHz, DMSO-d_6) δ 2.42 (s, 3H, CH), 7.26–8.32 (m, 10H, Ar-H and CH=CH). Anal. Calcd for $C_{17}H_{13}F_3O$: C, 70.34; H, 4.51. Found: C, 70.56; H, 4.55.

3-(4-Isopropylphenyl)-1-(4-(trifluoromethyl)phenyl) prop-2-en-1-one (1d)

White powder, yield 81%, mp 84.7–85.3 °C. IR (KBr) ν 3053, 2960, 2928, 1660, 1600, 1579, 1510, 1408, 1319, 1215, 1165, 1066, 821 cm^{-1}. ^{1}H NMR (600 MHz, DMSO-d_6) δ 1.23 (d, J = 7.2 Hz, 6H, CH_3), 2.94 (m, 1H, CH), 7.35–8.33 (m, 10H, Ar-H and CH=CH). Anal. Calcd for $C_{19}H_{17}F_3O$: C, 71.69; H, 5.38. Found: C, 71.44; H, 5.46.

3-Phenyl-1-(4-(trifluoromethyl)phenyl)prop-2-en-1-one (1e)

White powder, yield 75%, mp 113.7–114.3 °C. IR (KBr) ν 3063, 1664, 1600, 1573, 1510, 1410, 1317, 1217, 1159, 1064, 839 cm^{-1}. ^{1}H NMR (600 MHz, DMSO-d_6) δ 7.44–8.35 (m, 11H, Ar-H and CH=CH). Anal. Calcd for

$C_{16}H_{11}F_3O$: C, 69.56; H, 4.01. Found: C, 69.78; H, 4.07 (CAS Number: 62056-10-4).[21]

3-(4-Chlorophenyl)-1-(4-(trifluoromethyl)phenyl) prop-2-en-1-one (1f)

White powder, yield 69%, mp 125.2–125.7 °C (CAS Number: 57076-98-9).[22]

3-*p*-Tolyl-1-(4-(trifluoromethyl)phenyl)prop-2-en-1-one (1g)

White powder, yield 72%, mp 147.8–148.4 °C (CAS Number: 1551606-21-3).[23]

3-*m*-Tolyl-1-(4-(trifluoromethyl)phenyl)prop-2-en-1-one (1h)

White powder, yield 82%, mp 92.0–92.5 °C. IR (KBr) ν 3061, 2978, 2922, 1662, 1600, 1573, 1510, 1450, 1410, 1317, 1217, 1159, 1064, 837 cm^{-1}. ^1H NMR (400 MHz, DMSO-d_6) δ 2.34 (s, 3H, CH), 7.26–8.31 (m, 10H, Ar-H and CH=CH). Anal. Calcd for $C_{17}H_{13}F_3O$: C, 70.34; H, 4.51. Found: C, 70.47; H, 4.44.

3-(Thiophen-2-yl)-1-(4-(trifluoromethyl)phenyl)prop-2-en-1-one (1i)

White powder, yield 65%, mp 135.4–135.9 °C (CAS Number: 1372376-05-0).[24]

3-(4-(Dimethylamino)phenyl)-1-(4-(trifluoromethyl) phenyl)prop-2-en-1-one (1j)

White powder, yield 75%, mp 140.5–141.2 °C (CAS Number: 1940174-93-5).[25]

3-(Naphthalen-1-yl)-1-(4-(trifluoromethyl)phenyl) prop-2-en-1-one (1k)

Yellow powder, yield 74%, mp 92.0–92.5 °C. IR (KBr) ν 3078, 2980, 1660, 1593, 1573, 1435, 1408, 1319, 1215, 1163, 1064, 839 cm^{-1}. ^1H NMR (400 MHz, DMSO-d_6) δ 7.59–8.64 (m, 13H, Ar-H and CH=CH). Anal. Calcd for $C_{20}H_{13}F_3O$: C, 73.61; H, 4.12. Found: C, 73.87; H, 4.22.

5-(2,6-Dimethylphenyl)-1-phenyl-3-(4-(trifluoromethyl)phenyl)-4,5-dihydro-1*H*-pyrazole (2a)

Yellow powder, yield 75%, mp 133.3–133.8 °C. IR (KBr) ν 3068, 2974, 2912, 1616, 1593, 1510, 1408, 1319, 1215, 1163, 1064, 839 cm^{-1}. ^1H NMR (300 MHz, DMSO-d_6) δ 2.04 and 2.55 (2s, 6H, $2CH_3$), 3.16 (dd, *Jax* = 6.33 Hz, *Jab* = 17.88 Hz, 1H, Ha), 4.02 (dd, *Jbx* = 13.75 Hz, *Jab* = 17.88 Hz, 1H, Hb), 5.75 (dd, *Jax* = 6.33 Hz, *Jbx* = 13.76 Hz, 1H, Hx), 6.72–7.17 (m, 8H, Ar-H), 7.77 (d, *J* = 8.1 Hz, 2H, Ar-H), 7.92 (d, *J* = 8.1 Hz, 2H, Ar-H). Anal. Calcd for $C_{24}H_{21}F_3N_2$: C, 73.08; H, 5.37; N, 7.10. Found: C, 73.55; H, 5.27; N, 7.35.

5-(2,6-Dichlorophenyl)-1-phenyl-3-(4-(trifluoromethyl)phenyl)-4,5-dihydro-1*H*-pyrazole (2b)

Yellow powder, yield 65%, mp 142.2–142.9 °C. IR (KBr) ν 3055, 1618, 1587, 1521, 1498, 1321, 1247, 1118, 1064, 839 cm^{-1}. ^1H NMR (400 MHz, DMSO-d_6) δ 3.24 (dd, *Jax* = 6.12 Hz, *Jab* = 17.44 Hz, 1H, Ha), 3.96 (dd, *Jbx* = 13.96 Hz, *Jab* = 17.44 Hz, 1H, Hb), 6.14 (dd, *Jax* = 6.12 Hz, *Jbx* = 13.96 Hz, 1H, Hx), 6.72–7.92 (m, 12H, Ar-H). Anal. Calcd for $C_{22}H_{15}Cl_2F_3N_2$: C, 60.71; H, 3.47; N, 6.44. Found: C, 60.22; H, 3.37; N, 6.66.

1-Phenyl-5-*o*-tolyl-3-(4-(trifluoromethyl)phenyl)-4,5-dihydro-1*H*-pyrazole (2c)

Yellow powder, yield 77%, mp 119.6–120.1 °C. IR (KBr) ν 3059, 2980, 2916, 1616, 1587, 1521, 1495, 1319, 1217, 1163, 1064, 839 cm^{-1}. ^1H NMR (400 MHz, DMSO-d_6) δ 2.43 (s, 3H, CH_3), 3.04 (dd, *Jax* = 6.55 Hz, *Jab* = 17.52 Hz, 1H, Ha), 3.99 (dd, *Jbx* = 13.60 Hz, *Jab* = 17.52 Hz, 1H, Hb), 5.64 (dd, *Jax* = 6.56 Hz, *Jbx* = 13.60 Hz, 1H, Hx), 6.72–7.25 (m, 9H, Ar-H), 7.74 (d, *J* = 8.4 Hz, 2H, Ar-H), 7.91 (d, *J* = 8.4 Hz, 2H, Ar-H). Anal. Calcd for $C_{23}H_{19}F_3N_2$: C, 72.62; H, 5.03; N, 7.36. Found: C, 72.32; H, 5.17; N, 7.47.

5-(4-Isopropylphenyl)-1-phenyl-3-(4-(trifluoromethyl) phenyl)-4,5-dihydro-1*H*-pyrazole (2d)

Orange powder, yield 81%, mp 89.1–89.4 °C. IR (KBr) ν 3051, 2960, 2899, 1618, 1595, 1556, 1498, 1319, 1249, 1163, 1064, 839 cm^{-1}. ^1H NMR (400 MHz, DMSO-d_6) δ 0.97 and 1.55 (2d, 6H, $2CH_3$), 2.79 (m, 1H, CH), 3.14 (dd, *Jax* = 6.24 Hz, *Jab* = 17.28 Hz, 1H, Ha), 3.95 (dd, *Jbx* = 13.45 Hz, *Jab* = 17.27 Hz, 1H, Hb), 5.56 (dd, *Jax* = 6.24 Hz, *Jbx* = 13.44 Hz, 1H, Hx), 6.72–7.52 (m, 9H, Ar-H), 7.73 (d, *J* = 8.1 Hz, 2H, Ar-H), 7.93 (d, *J* = 8.1 Hz, 2H, Ar-H). Anal. Calcd for $C_{25}H_{23}F_3N_2$: C, 73.51; H, 5.68; N, 6.86. Found: C, 73.77; H, 5.49; N, 6.75.

1,5-Diphenyl-3-(4-(trifluoromethyl)phenyl)-4,5-dihydro-1*H*- pyrazole (2e)

Yellow powder, yield 73%, mp 108.2–108.4 °C. IR (KBr) ν 3064, 1618, 1595, 1554, 1496, 1321, 1249, 1163, 1064, 837 cm^{-1}. ^1H NMR (600 MHz, DMSO-d_6) δ 3.17 (dd, *Jax* = 6.66 Hz, *Jab* = 17.46 Hz, 1H, Ha), 3.96 (dd, *Jbx* = 12.49 Hz, *Jab* = 17.44 Hz, 1H, Hb), 5.58 (dd, *Jax* = 6.66 Hz, *Jbx* = 12.49 Hz, 1H, Hx), 6.74–7.51 (m, 10H, Ar-H), 7.78 (d, *J* = 8.4 Hz, 2H, Ar-H), 7.94 (d, *J* = 8.4 Hz, 2H, Ar-H). Anal. Calcd for $C_{22}H_{17}F_3N_2$: C, 72.12; H, 4.68; N, 7.65. Found: C, 72.31; H, 4.63; N, 7.77.

5-(4-Chlorophenyl)-1-phenyl-3-(4-(trifluoromethyl) phenyl)-4,5-dihydro-1*H*-pyrazole (2f)

Orange powder, yield 66%, mp 79.1–79.3 °C. IR (KBr) ν 3055, 1618, 1597, 1554, 1496, 1319, 1249, 1163, 1064, 839 cm^{-1}. ^1H NMR (400 MHz, DMSO-d_6) δ 3.16 (dd, *Jax* = 6.24 Hz, *Jab* = 17.28 Hz, 1H, Ha), 3.96 (dd, *Jbx* = 12.40 Hz, *Jab* = 17.28 Hz, 1H, Hb), 5.60 (dd, *Jax* = 6.23 Hz, *Jbx* = 12.41 Hz, 1H, Hx), 6.74–7.51 (m, 9H, Ar-H), 7.75 (d, *J* = 8.4 Hz, 2H, Ar-H), 7.91 (d, *J* = 8.4 Hz, 2H, Ar-H). Anal. Calcd for $C_{22}H_{16}ClF_3N_2$: C, 65.92; H, 4.02; N, 6.99. Found: C, 65.75; H, 3.88; N, 6.72.

1-Phenyl-5-*p*-tolyl-3-(4-(trifluoromethyl)phenyl)- 4,5-dihydro-1*H*-pyrazole (2g)

Yellow powder, yield 80%, mp 123.4–123.7 °C. IR (KBr) ν 3007, 2924, 2852, 1614, 1597, 1552, 1498, 1321, 1244, 1168, 1064, 835 cm^{-1}. ^1H NMR (300 MHz, DMSO-d_6) δ 2.25 (s, 3H, CH_3), 3.16 (dd, *Jax* = 6.30 Hz, *Jab* = 17.91 Hz, 1H, Ha), 3.93 (dd, *Jbx* = 12.42 Hz, *Jab* = 17.91 Hz, 1H, Hb), 5.56 (dd, *Jax* = 6.31 Hz, *Jbx* = 12.40 Hz, 1H, Hx), 6.72–7.19 (m, 9H, Ar-H), 7.77 (d, *J* = 8.1 Hz, 2H, Ar-H), 7.94 (d, *J* = 8.1 Hz, 2H, Ar-H). Anal. Calcd for $C_{23}H_{19}F_3N_2$: C, 72.62; H, 5.03; N, 7.36. Found: C, 72.35; H, 5.20; N, 7.57.

1-Phenyl-5-*m*-tolyl-3-(4-(trifluoromethyl)phenyl)- 4,5-dihydro-1*H*-pyrazole (2h)

Yellow powder, yield 75%, mp 145.9–146.3 °C. IR (KBr) ν 3028, 2926, 1614, 1585, 1552, 1498, 1321, 1244, 1155, 1064, 835 cm^{-1}. ^1H NMR (400 MHz, DMSO-d_6) δ 2.24 (s, 3H, CH_3), 3.14 (dd, *Jax* = 6.61 Hz, *Jab* = 17.57 Hz, 1H, Ha), 3.95 (dd, *Jbx* = 12.24 Hz, *Jab* = 17.56 Hz, 1H, Hb), 5.50 (dd, *Jax* = 6.60 Hz, *Jbx* = 12.24 Hz, 1H, Hx), 6.71–7.22 (m, 9H, Ar-H), 7.75 (d, *J* = 8.4 Hz, 2H, Ar-H), 7.91 (d, *J* = 8.4 Hz, 2H, Ar-H). Anal. Calcd for $C_{23}H_{19}F_3N_2$: C, 72.62; H, 5.03; N, 7.36. Found: C, 72.47; H, 4.89; N, 7.56.

1-Phenyl-5-(thiophen-2-yl)-3-(4-(trifluoromethyl)phenyl)-4,5-dihydro-1*H*-pyrazole (2i)

Orange powder, yield 65%, mp 127.0–127.5 °C. IR (KBr) ν 3097, 1618, 1591, 1529, 1479, 1315, 1220, 1166, 1064, 825 cm^{-1}. ^1H NMR (300 MHz, DMSO-d_6) δ 3.25 (dd, *Jax* = 6.56 Hz, *Jab* = 17.61 Hz, 1H, Ha), 3.93 (dd, *Jbx* = 12.33 Hz, *Jab* = 17.61 Hz, 1H, Hb), 5.96 (dd, *Jax* = 6.57 Hz, *Jbx* = 12.33 Hz, 1H, Hx), 6.77–7.38 (m, 8H, Ar-H), 7.76 (d, *J* = 8.1 Hz, 2H, Ar-H), 7.96 (d, *J* = 8.1 Hz, 2H, Ar-H). Anal. Calcd for $C_{20}H_{15}F_3N_2S$: C, 64.50; H, 4.06; N, 7.52. Found: C, 64.14; H, 4.13; N, 7.47.

***N,N*-Dimethyl-4-(1-phenyl-3-(4-(trifluoromethyl)phenyl)-4,5-dihydro-1*H*-pyrazol-5-yl)aniline (2j)**

Yellow powder, yield 77%, mp 128.8–129.4 °C. IR (KBr) ν 3070, 2955, 2845, 1614, 1587, 1519, 1492, 1320, 1240, 1163, 1055, 806 cm^{-1}. ^1H NMR (400 MHz, DMSO-d_6) δ 2.81 (s, 6H, $2CH_3$), 3.10 (dd, *Jax* = 6.35 Hz, *Jab* = 17.46 Hz, 1H, Ha), 3.86 (dd, *Jbx* = 12.33 Hz, *Jab* = 17.47 Hz, 1H, Hb), 5.44 (dd, *Jax* = 6.32 Hz, *Jbx* = 12.31 Hz, 1H, Hx), 6.63–7.17 (m, 9H, Ar-H), 7.72 (d, *J* = 8.4 Hz, 2H, Ar-H), 7.91 (d, *J* = 8.4 Hz, 2H, Ar-H). Anal. Calcd for $C_{24}H_{22}F_3N_3$: C, 70.40; H, 5.42; N, 10.26. Found: C, 70.56; H, 5.35; N, 10.43.

5-(Naphthalen-1-yl)-1-phenyl-3-(4-(trifluoromethyl) phenyl)-4,5-dihydro-1*H*-pyrazole (2k)

Orange powder, yield 79%, mp 94.4–94.6 °C. IR (KBr) ν 3059, 1635, 1591, 1533, 1483, 1321, 1259, 1168, 1064, 835 cm^{-1}. ^1H NMR (400 MHz, DMSO-d_6) δ 3.12 (dd, *Jax* = 6.56 Hz, *Jab* = 17.40 Hz, 1H, Ha), 4.01 (dd, *Jbx* = 12.81 Hz, *Jab* = 17.39 Hz, 1H, Hb), 6.26 (dd, *Jax* = 6.56 Hz, *Jbx* = 12.80 Hz, 1H, Hx), 6.71–8.00 (m, 16H, Ar-H). Anal. Calcd for $C_{26}H_{19}F_3N_2$: C, 74.99; H, 4.60; N, 6.73. Found: C, 75.43; H, 4.49; N, 6.56.

2. 2. Biological Studies

2. 2. 1. Antioxidant Activity

2. 2. 1. 1. DPPH Radical Scavenging Activity

Free radical scavenging capacity of chalcone and pyrazoline derivatives was carried out according to the methods described previously.[26,27] Briefly, 1 mg of the compound was dissolved in DMSO and four different concentrations (0.250–0.048 µg/mL, approximately) were prepared. 190 µL methanol solution of DPPH (0.1 mM) was added on this mixture in a well of 96-well plate. The mixture was allowed to stand in the dark at room temperature for 30 min. Absorbance readings were carried out at 517 nm. The DPPH stock solution without compounds was taken as the negative control. The percentage of inhibition was calculated according to the following:

$$\text{DPPH scavenging effect (\%)} = \frac{A_{\text{control}} - A_{\text{compound}}}{A_{\text{control}}} \cdot 100 \quad (1)$$

A_{control}: Absorbance of the control (containing all reagents except the synthesized compounds).

A_{compound}: Absorbance of the synthesized compounds.

Tests were repeated in quadruplicate. Ascorbic acid was used as the positive control.

2. 2. 1. 2. ABTS Radical Scavenging Activity

ABTS radical cations were prepared by dissolving 7 mM ABTS and 4.9 mM potassium persulfate, allowing them to react for 16 h at room temperature in the dark. Then, the ABTS radical solution was diluted with 96% ethanol to an absorbance recorded at 734 nm. Four different concentrations of the analyzed compounds were prepared according to the above method, DPPH radical scavenging activity.[27] Absorbance readings were recorded at 734 nm. The percentage of inhibition was calculated according to the following:

$$\text{ABTS scavenging effect (\%)} = \frac{A_{\text{control}} - A_{\text{compound}}}{A_{\text{control}}} \cdot 100 \quad (2)$$

Tests were repeated in quadruplicate. Trolox was used as the positive control.

2. 2. 2. Anti-Inflammatory Activity

The anti-lipoxygenase activity was evaluated as described by Phosrithong and Nuchtavorn with slight modifications described by Yıldırım *et al.*[28,29] Four different concentrations of chalcone and pyrazoline derivatives

were added to 250 µL of 0.1 M borate buffer pH 9.0, followed by the addition of 250 µL of type V soybean lipoxygenase solution in a buffer (20.000 U/mL). The mixture was incubated at 25 °C for 5 min and 1000 µL of 0.6 mM linoleic acid solution was added, mixed well and the change in absorbance at 234 nm was measured for 6 min. The percentage of inhibition was calculated from the following equation:

$$\% \text{ inhibition} = \frac{A_{\text{control}} - A_{\text{compound}}}{A_{\text{control}}} \cdot 100 \qquad (3)$$

Tests were repeated in quadruplicate. Indomethacin was used as the positive control. The IC_{50} values were determined as the concentration of the synthesized compounds required to inhibit lipoxygenase enzyme activity by 50%.

2. 2. 3. Antidiabetic Activity

2. 2. 3. 1. α-Glucosidase Inhibitory Assay

The α-glucosidase inhibitor activity was evaluated as described by Ramakrishna *et al.* with slight modifications described by Sen *et al.*[30,31] 40 µL of 0.1 M sodium phosphate buffer (pH 6.8) was mixed with 10 µL of the synthesized compound at 37 °C. The mixtures were incubated at 25 °C for 10 minutes with 100 µL of α-glucosidase which was obtained from *Saccharomyces cerevisiae.* Then, 50 µL of 5 mM *p*-nitrophenyl-α-D-glucopyranoside (pNPG) which was prepared in the buffer, was added to the mixture. The resulting solution was incubated at 25 °C for 5 minutes again, and absorbance was recorded before and after incubation at 405 nm.

The percentage of inhibition was calculated from the following equation:

$$\% \text{ inhibition} = \frac{A_{\text{control}} - A_{\text{compound}}}{A_{\text{control}}} \cdot 100 \qquad (4)$$

Tests were repeated in quadruplicate. Acarbose was used as the positive control. The IC_{50} values were determined as the concentration of the synthesized compounds required to inhibit α-glucosidase enzyme activity by 50%.

2. 2. 4. Statistical Analysis

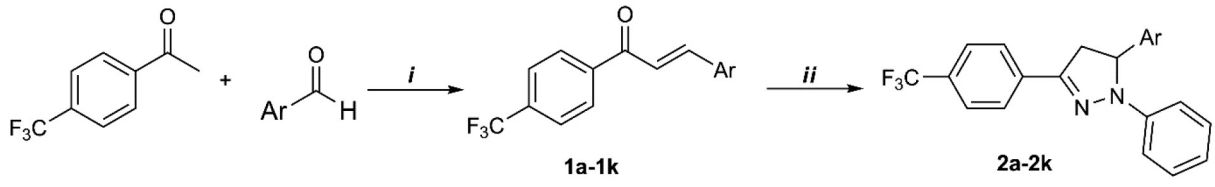
The data were given as means ± standard deviations and analyzed by one-way analysis of variance (ANOVA) followed by the Tukey's multiple comparison tests using GraphPad Prism 5. Differences between means at $p < 0.05$ level were considered significant.

3. Results and Discussion

3. 1. Chemistry

Pyrazoline derivatives were synthesized as depicted in Figure 2. Firstly, chalcone derivatives were obtained from 4'-(trifluoromethyl)acetophenone according to Claisen–Schmidt condensation reaction. Then, 2-pyrazoline derivatives were obtained from synthesized chalcones by refluxing in the presence of acidic medium (Figure 2). The structures of the compounds were confirmed by IR, ^{1}H NMR spectroscopic methods and elemental analysis. Physicochemical and spectroscopic characterization of the chalcone derivatives **1e**,**f**,**g**,**i**,**j** have been previously described.[21–25]

IR spectra of pyrazoline derivatives afforded aromatic C–H (3097–3007 cm^{-1}) stretching, pyrazoline C=N stretching (1635–1614 cm^{-1}) and C–F stretching (1168–1118 cm^{-1}) bands. When ^{1}H NMR spectra of pyrazoline derivatives were examined, three different characteristic signals belonging to the methylene group at position 4 (Ha and Hb) and the methine group at position 5 (Hx) of the pyrazoline ring were determined. These signals appeared as doublet of doublets due to ABX spin system in the structures (Figure 3). The Ha, Hb and Hx protons resonated at 3.04–3.25 ppm (J_{ab} = 17.28–17.91 Hz), 3.86–4.02 ppm (J_{ax} = 6.12–6.66 Hz) and 5.44–6.26 ppm (J_{bx} = 12.24–13.96 Hz), respectively. Aromatic CH protons were seen at 6.63–8.00 as multiplet. Especially *ortho* protons belonging to ar-



1a and **2a**: Ar=2,6-dimethylphenyl,
1b and **2b**: Ar=2,6-dichlorophenyl,
1c and **2c**: Ar=2-methylphenyl,
1d and **2d**: Ar=4-isopropylphenyl,
1e and **2e**: Ar=phenyl,
1f and **2f**: Ar=4-chloro,
1g and **2g**: Ar=4-methylphenyl,
1h and **2h**: Ar=3-methylphenyl,
1i and **2i**: Ar=thiophen-2-yl,
1j and **2j**: Ar=4-dimethylaminophenyl,
1k and **2k**: Ar=naphthalen-1-yl

Figure 2. The synthetic pathway for compounds **1a-1k** and **2a-2k**. Reagents and conditions: (***i***) methanol, NaOH, 10 h; (***ii***) phenylhydrazine hydrochloride, acetic acid, reflux, 12 h.

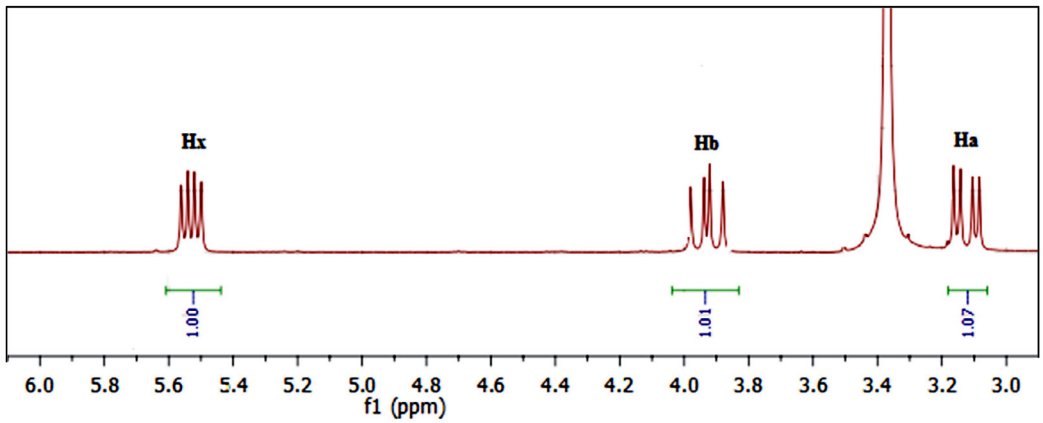


Figure 3. Esxample ^{1}H NMR spectrum of pyrazoline protons (Ha, Hb and Hx).

omatic ring (bearing trifluoromethyl substituent) were observed as doublet (J = 8.1–8.4 Hz) at 7.72–7.96 ppm.

3. 2. Biological Evaluation

All chalcone and pyrazoline derivatives were screened for *in vitro* antioxidant activity with DPPH and ABTS assays, anti-inflammatory activity with lipoxygenase (LOX) inhibition assay and antidiabetic activity with α-glucosidase inhibition assay. All IC_{50} values of compounds against reference standards were given as Table 1. Results demonstrated that all pyrazoline derivatives had a very strong anti-inflammatory activity with IC_{50} values between 0.68 ± 0.07 and 4.45 ± 0.25 μM when compared to

Table 1. Antioxidant, anti-inflammatory and antidiabetic activities of synthesized compounds*

Compound	IC_{50} (μM) Antioxidant activity DPPH activity	ABTS activity	Anti-inflammatory activity Anti-lipoxgenase activity	Antidiabetic activity α-glucosidase inhibitory activity
1a	>1000	>1000	128.40 ± 3.92^{f}	381.20 ± 9.29^{c,d}
1b	>1000	852.80 ± 51.42^{c}	48.47 ± 2.29^{c}	460.50 ± 3.89^{d,e}
1c	211.60 ± 3.48^{b}	869.00 ± 64.4^{c}	121.50 ± 4.77^{f}	746.10 ± 20.95^{h,i,j}
1d	389.50 ± 2.22^{c,d,e,f}	807.00 ± 16.88^{c}	79.35 ± 0.93^{d}	338.60 ± 29.32^{c}
1e	282.10 ± 15.92^{b,c}	>1000	304.60 ± 1.61^{h}	>1000
1f	>1000	>1000	50.97 ± 2.75^{c}	377.40 ± 4.35^{c,d}
1g	286.10 ± 19.48^{b,c}	635.80 ± 11.45^{b,c}	105.90 ± 0.02^{e}	>1000
1h	321.30 ± 9.96^{b,c}	>1000	38.42 ± 3.02^{b}	>1000
1i	>1000	907.40 ± 26.80^{c}	85.13 ± 1.56^{d}	>1000
1j	494.00 ± 10.41^{e,f,g,h,i}	204.40 ± 4.29^{a,b}	193.60 ± 0.33^{g}	>1000
1k	>1000	>1000	83.07 ± 2.31^{d}	823.8 ± 0.43^{j}
2a	534.40 ± 5.02^{h,i,j}	136.30 ± 3.97^{a}	0.68 ± 0.07^{a}	81.09 ± 0.70^{a,b}
2b	586.10 ± 44.19^{i,j}	117.40 ± 0.18^{a}	0.76 ± 0.09^{a}	463.40 ± 6.50^{d,e}
2c	505.80 ± 23.04^{f,g,h,i}	127.00 ± 0.90^{a}	1.56 ± 0.08^{a}	613.80 ± 14.13^{f,g}
2d	342.90 ± 3.29^{b,c,d}	108.00 ± 2.92^{a}	2.15 ± 0.13^{a}	596.90 ± 18.00^{f,g}
2e	645.00 ± 22.0^{j}	130.10 ± 2.00^{a}	1.73 ± 0.04^{a}	519.50 ± 18.72^{e,f}
2f	524.20 ± 20.82^{g,h,i,j}	92.62 ± 5.45^{a}	3.11 ± 0.05^{a}	451.30 ± 13.76^{c,d,e}
2g	898.90 ± 5.76^{k}	112.20 ± 2.12^{a}	4.45 ± 0.25^{a}	637.90 ± 1.67^{f,g}
2h	>1000	150.90 ± 0.57^{a}	2.14 ± 0.11^{a}	657.30 ± 14.68^{g,h}
2i	855.60 ± 19.93^{k}	136.40 ± 0.15^{a}	4.41 ± 0.02^{a}	812.70 ± 5.13^{i,j}
2j	>1000	57.13 ± 0.03^{a}	1.19 ± 0.05^{a}	201.10 ± 5.22^{b}
2k	464.80 ± 11.38^{d,e,f,g}	94.24 ± 0.86^{a}	1.22 ± 0.07^{a}	417.60 ± 10.53^{c,d,e}
Ascorbic acid	14.56 ± 0.60^{a}			
Trolox		12.67 ± 0.28^{a}		
Indomethacin			50.45 ± 0.20^{c}	
Acarbose				62.04 ± 3.32^{a}

* Each value in the table is represented as mean ± SD (n = 4). Different letter superscripts in the same column indicate significant differences (p < 0.05).

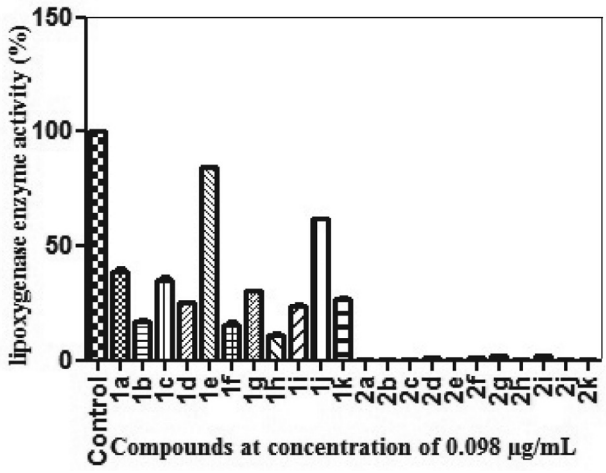


Figure 4. Anti-lipoxygenase activity of chalcone and pyrazoline derivatives.

reference standard indomethacin (IC_{50} = 50.45 ± 0.20 µM). Additionally, compound **2a** inhibited 5-lipoxygenase activity by 99.73% at a concentration of 0.098 µg/mL. Chalcone derivatives **1a**–**k** at a concentration of 0.098 µg/mL inhibited lipoxygenase enzyme activity with the inhibition rate of 88.85–15.83% compared to the control (Figure 4).

Synthesized compounds exhibited low antioxidant activity. Only compound **2j** showed the best antioxidant activity according to ABTS assay with IC_{50} value of 57.13 ± 0.03 µM compared to the reference standard trolox (12.67 ± 0.28 µM).

Antidiabetic activity of all compounds was evaluated by the α-glucosidase inhibition assay. These results showed that compound **2a** showed maximum α-glucosidase inhibitory activity with the IC_{50} value of 81.09 ± 0.70 µM (IC_{50} for acarbose 62.04 ± 3.32 µM).

3. 3. ADME Calculations

The prediction of ADME properties of the compounds is a very important development of new drug candidates. Therefore the druglike molecule was carried out by using the Lipinski rule of five and Veber rule.[32–34] Calculations were performed using molinspiration online server. The screening results were presented in Table 2.

The molecular weights varied from 276.25 to 435.27 for the synthesized compounds which are lower than the maximum molecular weight of 500. All the compounds are having logP in the range of 3.48–6.22. The number of hydrogen bond acceptors of all compounds is 4 which is less than the maximum value of ten. On the other hand, all the compounds have zero hydrogen bond donors which must be less than the maximum value of five. Furthermore, the number of rotatable bonds is in the range of 4–5 which is lower than the maximum value of 10. Similarly the polar

Table 2. Predicted ADME, Lipinski and Veber parameters of the synthesized compounds.

Compound	Lipinski rule of five				Veber rule	
	MW	Log P	*n*-ON	*n*-OHNH	*n*-ROTB	TPSA
1a	304.31	4.78	4	0	4	17.07
1b	345.14	5.32	4	0	4	17.07
1c	290.28	4.55	4	0	4	17.07
1d	318.33	5.01	4	0	5	17.07
1e	276.25	4.32	4	0	4	17.07
1f	310.70	4.82	4	0	4	17.07
1g	290.28	4.55	4	0	4	17.07
1h	290.28	4.55	4	0	4	17.07
1i	282.28	3.48	4	0	4	45.31
1j	319.32	4.12	4	0	5	20.31
1k	326.31	5.04	4	0	4	17.07
2a	394.43	5.69	4	0	4	15.60
2b	435.27	6.22	4	0	4	15.60
2c	380.41	5.48	4	0	4	15.60
2d	408.46	5.89	4	0	5	15.60
2e	366.38	5.27	4	0	4	15.60
2f	400.82	5.75	4	0	4	15.60
2g	380.41	5.48	4	0	4	15.60
2h	380.41	5.48	4	0	4	15.60
2i	372.41	4.88	4	0	4	43.84
2j	409.45	5.07	4	0	5	18.84
2k	416.44	5.91	4	0	4	15.60

TPSA: Topological polar surface area, *n*-ON: number of hydrogen bond acceptors, *n*-OHNH: number of hydrogen bond donors, *n*-ROTB: number of rotatable bonds. Calculations were performed using Molinspiration online property calculation toolkit (http://www.molinspiration.com).

surface area of all synthesized compounds is indicated to be in the range of 15.60–45.31 Å^2 which is less than the maximum value of 140 Å^2. These values demonstrate that none of the synthesized compounds are violating the Lipinski and Veber rules.

4. Conclusion

New pyrazoline derivatives were synthesized from chalcone derivatives and the designed molecules were investigated for their drug-likeness properties which were defined as Lipinski and Veber rules. All compounds were tested for their antioxidant (DPPH and ABTS), anti-lipoxygenase and α-glucosidase inhibitory activities. These results showed that pyrazoline derivatives exhibited better activity than chalcone derivatives. Especially pyrazoline derivatives **2a–k** showed very strong anti-lipoxygenase activity each with greater activity than reference drug indomethacin. Also, compounds **2j** and **2a** demonstrated good antioxidant and α-glucosidase inhibitory activity, respectively. These findings revealed that the pyrazoline core could lead to considerably active molecules.

Conflict of Interest

Authors declare no conflict of interest.

5. References

1. M. Asad, M. N. Arshad, S. A. Khan, M. Oves, M. Khalid, A. M. Asiri, A. A. C. Braga, *J. Mol. Struct*. **2020**, 1201, 1–14. **DOI:**10.1016/j.molstruc.2019.127186
2. M. R. Bhosle, A. R. Deshmukh, S. Pal, A. K. Srivastava, R. A. Mane, *Bioorg. Med. Chem. Lett*. **2015**, 25, 2442–2446. **DOI:**10.1016/j.bmcl.2015.03.068
3. C. Kharbanda, M. S. Alam, H. Hamid, K. Javed, S. Shafi, Y. Ali, P. Alam, M. A. Q. Pasha, A. Dhulap, S. Bano, S. Nazreen, S. Haider, *Bioorg. Med. Chem. Lett*. **2014**, *24*, 5298–5303. **DOI:**10.1016/j.bmcl.2014.09.044
4. D. S. Raghuvanshi, N. Verma, S. V. Singh, S. Khare, A. Pal, A. S. Negi, *Bioorg. Chem*. **2019**, *88*, 1–11. **DOI:**10.1016/j.bioorg.2019.102933
5. G. Turan-Zitouni, P. Chevallet, F. S. Kılıç, K. Erol, *Eur. J. Med. Chem*. **2000**, *35*, 635–641. **DOI:**10.1016/S0223-5234(00)00152-5
6. C. Kharbanda, M. S. Alam, H. Hamid, K. Javed, S. Bano, A. Dhulap, Y. Ali, S. Nazreen, S. Haider, *Bioorgan. Med. Chem*. **2014**, *22*, 5804–5812. **DOI:**10.1016/j.bmc.2014.09.028
7. F. Tok, B. İ. Abas, Ö. Çevik, B. Koçyiğit-Kaymakçıoğlu, *Bioorg. Chem*. **2020**, *102*, 104063. **DOI:**10.1016/j.bioorg.2020.104063
8. H. S. ElBordiny, M. M. El-Miligy, S. E. Kassab, H. Daabees, W. A. M. Ali, S. A. M. El-Hawash, *Eur. J. Med. Chem*. **2018**, *145*, 594–605. **DOI:**10.1016/j.ejmech.2018.01.026
9. F. Chaudhry, S. Naureen, R. Huma, A. Shaukat, M. Al-Rashida, N. Asif, M. Ashraf, M. A. Munawar, M. A. Khan, *Bioorg. Chem*. **2017**, *71*, 102–109. **DOI:**10.1016/j.bioorg.2017.01.017
10. M. Sathish, G. Meenakshi, S. Xavier, S. Sebastian, S. Periandy, N. Ahmad, J. Jamalis, M. Rosli, H. Fun, *J. Mol. Struct*. **2018**, *1164*, 420–437. **DOI:**10.1016/j.molstruc.2018.03.004
11. B. Sever, M. D. Altıntop, M. O. Radwan, A. Ozdemir, M. Otsuka, M. Fujita, H. I. Ciftci, *Eur. J. Med. Chem*. **2019**, *182*, 1–17. **DOI:**10.1016/j.ejmech.2019.111648
12. B. Shu, Q. Yu, D. Hu, T. Che, S. Zhang, D. Li, *Bioorg. Med. Chem. Lett*. **2020**, *30*, 1–4. **DOI:**10.1016/j.bmcl.2019.126925
13. D. Moi, A. Nocentini, A. Deplano, G. Balboni, C. T. Supuran, V. Onnis, *Eur. J. Med. Chem*. **2019**, *182*, 1–11. **DOI:**10.1016/j.ejmech.2019.111638
14. A. Mumtaz, A. Majeed, S. Zaib, S. Rahman, S. Hameed, A. Saeed, H. Rafique, E. Mughal, A. Maalik, I. Hussain, J. Iqbal, *Bioorg. Chem*. **2019**, *90*, 1–9. **DOI:**10.1016/j.bioorg.2019.103036
15. N. M. A. Gawad, G. S. Hassan, H. H. Georgey, *Med. Chem. Res*. **2012**, *21*, 983–994. **DOI:**10.1007/s00044-011-9606-4
16. S. Viveka, P. Shama, G. K. Nagaraja, S. Ballav, S. Kerkar, *Eur. J. Med. Chem*. **2015**, *101*, 442–451. **DOI:**10.1016/j.ejmech.2015.07.002
17. P. Shah, A. D. Westwell, *J. Enzym Inhib. Med. Chem*. **2007**, *22*, 527–540. **DOI:**10.1080/14756360701425014
18. K. Haranahalli, T. Honda, I. Ojima, *J. Fluorine Chem*. **2017**, *217*, 29–40. **DOI:**10.1016/j.jfluchem.2018.11.002
19. N. Beyhan, B. Kocyigit-Kaymakcioglu, S. Gümrü, F. Arıcıoğlu, *Arab. J. Chem*. **2017**, *10*, 2073–2081. **DOI:**10.1016/j.arabjc.2013.07.037
20. A. Ahmad, A. Husain, S. A. Khan, M. Mujeeb, A. Bhandari, *J. Saudi Chem. Soc*. **2016**, *20*, 577–584. **DOI:**10.1016/j.jscs.2014.12.004
21. X. Huang, J. Li, X. Li, J. Wang, Y. Peng, G. Song, *RSC. Adv*. **2019**, *9*, 26419–26424. **DOI:**10.1039/C9RA05708K
22. T. T. Nguyen, G. D. Kortman, K. L. Hull, *Organometallics,* **2016**, *35*, 1713–1725. **DOI:**10.1021/acs.organomet.6b00111
23. D. Liu, J. Yu, J. Cheng, *Tetrahedron*, **2014**, *70*, 1149–1153. **DOI:**10.1016/j.tet.2013.12.077
24. W. Katsuaki, G. Takuya, O. Yuichi, S. Katsuhiko, A. Takahisa, A. Wolfram, H. Achim, L. Peter, Preparation of nematicidal pyrazoles, US Patent Number 6310049, date of patent October 30, **2001**.
25. R. Shalaby, J. P. Petzer, A. Petzer, U. M. Ashraf, E Atari, F. Alasmari, S. Kumarasamy, Y. Sari, A. Khalil, *J. Enzym Inhib. Med. Ch*. **2019**, *34*, 863–876. **DOI:**10.1080/14756366.2019.1593158
26. Y. Zou, S. K. C. Chang, Y. Gu, S. Y. Qian, *J. Agric. Food Chem*. **2011**, *59*, 2268–2276. **DOI:**10.1021/jf104640k
27. A. Şen, *Marmara Pharm. J*. **2018**, *22*, 328–333. **DOI:**10.12991/mpj.2018.71
28. A. Yıldırım, A. Şen, A. Doğan, L. Bitiş, *Int. J. Sec. Metabolite*, **2019**, *6*, 211–222.
29. N. Phosrithong, N. Nuchtavorn, *Eur. J. Integr. Med*. **2016**, *8*, 281–285. **DOI:**10.1016/j.eujim.2015.10.002

30. R. Ramakrsihna, D. Sarkar, P. Schwarz, K. Shetty, *Ind. Crops Prod*. **2017**, *107*, 509–517. **DOI:**10.1016/j.indcrop.2017.03.033
31. A. Sen, M. Kurkcuoglu, I. Senkardes, L. Bitis, K. H. C. Baser, *J. Essent. Oil Bear. Pl.* **2019**, *22*, 1048–1057. **DOI:**10.1080/0972060X.2019.1662333
32. R. Matsa, P. Makam, M. Kaushik, S.L. Hoti, T. Kannan, *Eur. J. Pharm. Sci*. **2019**, *137*, 1–12. **DOI:**10.1016/j.ejps.2019.104986
33. C. A. Lipinski, *Drug Discov. Today Technol.* **2004**, *1*, 337–341. **DOI:**10.1016/j.ddtec.2004.11.007
34. D. F. Veber, S. R. Johnson, H. Y. Cheng, B. R. Smith, K. W. Ward, K. D. Kopple, *J. Med. Chem*. **2002**, *45*, 2615–2623. **DOI:**10.1021/jm020017n

Povzetek

Iz halkonskih derivatov smo sintetizirali serijo 1-fenil-5-substituiranih-3-(4-(trifluorometil)fenil)-4,5-dihidro-1*H*-pirazolov. Strukture spojin smo določili s pomočjo IR ter ^{1}H NMR spektroskopskih metod in z elementno analizo. Za vse spojine smo določili *in vitro* antioksidativno aktivnost s pomočjo DPPH in ABTS metod, antiinflamatorno aktivnost s pomočjo metode inhibicije lipooksigenaze ter antidiabetično aktivnost s pomočjo metode inhibicije α-glukozidaze. Še zlasti pirazolinski derivati so izkazali visoke antiinflamatorne aktivnosti, celo večje kot referenčna učinkovina indometacin (IC_{50}: 50.45 μM) z IC_{50} vrednostmi v območju od 0.68 do 4.45 μM. V nadaljevanju smo določili še ADME lastnosti vseh halkonskih in pirazolinskih derivatov skladno s pravili Lipinskega in Vebra.

Except when otherwise noted, articles in this journal are published under the terms and conditions of the Creative Commons Attribution 4.0 International License

DOI: 10.17344/acsi.2020.6045 *Acta Chim. Slov.* **2020,** *67,* 1148–1154
creative commons

Scientific paper

Cu(I) Arylsulfonate π-Complexes with 3-Allyl-2-thiohydantoin: The Role of the Weak Interactions in Structural Organization

Andrii Fedorchuk,[1] Evgeny Goreshnik,[2,*] Yurii Slyvka[3] and Marian Mys'kiv[3]

[1] Institute of Nuclear Physics, Polish *Academy of Sciences, Radzikowskiego 152, PL-31342 Krakow, Poland*

[2] *Department of Inorganic Chemistry and Technology, Jožef Stefan Institute, Jamova 39, SI-1000 Ljubljana, Slovenia*

[3] *Department of Inorganic Chemistry, Ivan Franko National University of Lviv, Kyryla i Mefodiya 6, 79005 Lviv, Ukraine*

* *Corresponding author: E-mail: evgeny.goreshnik@ijs.si Phone: +386 1 477 36 45*

Received: 04-12-2020

Abstract

The present work is directed toward preparation and structural characterization of two novel Cu(I) arylsulfonate π-complexes with 3-allyl-2-thiohydantoin, namely $[Cu_2(Hath)_4](C_6H_5SO_3)_2$ (**1**) and $[Cu_2(Hath)_4](p\text{-}CH_3C_6H_4SO_3)_2 \cdot 2H_2O$ (**2**) (*Hath* = 3-allyl-2-thiohydantoin), obtained by the means of alternating current electrochemical synthesis and studied with X-ray diffraction method. In both structures, the inner coordination sphere is represented by the cationic dimer $[Cu_2(Hath)_4]^{2+}$ with one crystallographically independent copper(I) atom which has a trigonal pyramidal coordination environment formed by three *Hath* thiogroup S atoms and double C=C bond of its allyl group. $[Cu_2(Hath)_4]^{2+}$ fragments in both coordination compounds are very similar, despite some divergences such as a big difference in Cu–S distance to the apical S atom (3.0374(8) Å in **1** and 2.7205(9) Å in **2**). This difference was explained by the impact of the system of weak interactions, which are quite different.

Keywords: Copper(I) arylsulfonate; π-complex; thiohydantoin; weak interaction; crystal structure.

1. Introduction

In the last years both 2-thiohydantoin (2-thioxoimidazolidin-4-ones) and hydantoin core fragments were studied as useful scaffolds in medicinal chemistry due to their synthetic feasibility and versatility of substituents. [1–5] Moreover, their derivatives are already used in commercially available drugs such as Phenytoin, Dantrolene and Allantoin. The presence of several active chemical groups, as well as simple synthetic route advantages, could make them interesting not only as biologically active compounds but also as compounds of great interest in the chemistry of coordination compounds too. Although, due to the presence of capable for complex compound formation functional groups, 2-thiohydantoin based compounds were found to have an application in the analytical chemistry as reagents for the determination of several *d*-metals (including Cu and Ag).[6, 7] Despite the small number of such representatives (according to the Cambridge Crystallographic Database only 12 copper coordination compounds with 2-thiohydantoin still known),[8] it was already investigated that they could have a potential interest as optical materials due to their fluorescence sensing properties and luminescence towards Cu^+ and Cu^{2+} as well as the possibility of successful usage in crystal engineering of organometallics.[9,10] Moreover, previously, we have shown, that Cu(I) π-complexes with allyl derivatives of heterocycles can possess noticeable non-linear optical properties.[11–15]

This work is the continuation of our previous studies, in which we have studied the coordination behavior of

3-allyl-2-thiohydantoin (*Hath*) regarding Ag(I), where obtained coordination compounds have already shown interesting structural peculiarities, confirming the status of 2-thiohydantoin-based molecules as the potential ligands in the structural engineering.[16,17]

2. Experimental

2. 1. General Consideration

Unless otherwise mentioned, all chemicals were obtained from a commercial source (Sigma Aldrich) and used without further purification. The NMR experiments: ^{1}H NMR (500 MHz), ^{13}C{^{1}H} NMR (125 MHz) spectra for *Hath* were recorded on a Bruker Avance 500 MHz NMR spectrometer. The chemical shifts are reported in ppm relative to the residual peak of the deuterated CD_3OD for the ^{1}H and ^{13}C{^{1}H} NMR spectra. Carbon, hydrogen, nitrogen and sulfur contents for *Hath*, **1** and **2** compounds were determined using a CHNS elemental analyzer vario EL cube (Elementar) operating in the CHNS mode. The infrared (IR) spectrum for *Hath* was recorded on the Bruker IFS-88 spectrometer as nujol mulls. Diffraction data for **1** and **2** were collected on a Gemini+ diffractometer with Mo K_a radiation (λ = 0.71073 Å) and Atlas CCD detector.

2. 2. Preparation of 3-allyl-2-thioxoimidazolidin-4-one (Hath)

Ligand *Hath* was synthesized from allylisothiocyanate and glycine at the presence of triethylamine and pyridine, in accordance with the reported method. [16] Yield 57%. M.p. 91–92 °C. Anal. calcd. for $C_6H_8N_2OS$: C, 46.13; H, 5.16; N, 17.93; S, 20.53; found: C, 45.93; H, 5.44; N, 17.92; S, 20.65.

^{1}H NMR (500 MHz, CD_3OD) *δ*, 5.84 p.p.m. (ddt, *J* = 17.1, 10.4, 5.6 1H, =CH), 5.18 p.p.m. (ddd, *J* = 17.1, 2.9, 1.5 Hz, 1H, CH_2=), 5.14 p.p.m. (ddd, *J* = 10.5, 2.5, 1.0 Hz, 1H, -CH_2=), 4.38 p.p.m. (dt, *J* = 5.6 Hz, 1.5 2H, CH_2), 4.14 (s, 2H, CH_2).

^{13}C{^{1}H} NMR (125 MHz, CD_3OD) *δ*, p.p.m. 185.74 p.p.m. (-C=S), 174.17 p.p.m. (-C=O), 132.62 p.p.m. (=CH), 117.94 p.p.m. (CH_2=), 49.48 p.p.m. (CH_2), 43.80 p.p.m. (CH_2).

IR (nujol, cm^{-1}): 3488 (w), 3225 (s), 3091 (w), 3011 (vw), 1864 (vw), 1751 (vs), 1650 (m), 1524 (vs), 1431 (vs), 1367 (w), 1344 (vs), 1306 (s), 1289 (w), 1260 (s), 1176 (vs), 1106 (m), 1048 (m), 1029 (m), 994 (m), 977 (w), 930 (s), 893 (m), 755 (vw), 719 (w), 700 (vs), 610 (m), 581 (m), 563 (m), 541 (m), 515 (m), 474 (m), 440 (vw).

2. 3. Preparation of Complexes

2. 3. 1. Preparation of $[Cu_2(Hath)_4](C_6H_5SO_3)_2$ (1)

To the solution of $Cu(C_6H_5SO_3)_2{\cdot}6H_2O$ (0.157 g, 0.4 mmol) in 4.5 ml of *n*-propanol 0.156 g (1 mmol) of 3-allyl-2-thiohydanthoine (*Hath*) was added and obtained mixture was stirred. The resulting orange-brown solution was placed into a 5 mL test tube and then copper-wire electrodes in cork were inserted. The inner mixture in the obtained cell was subjected to alternating-current electrochemical recovery (0.6 V, 50 Hz) for 5 days.[18] Crystals **1**, suitable for X-ray diffraction studies, were formed on copper wires while maintaining this reactor for 2 weeks at –3 °C. Yield 35%. M.p. 128 °C. Anal. calcd. for $C_{18}H_{21}CuN_4O_5S_3$: C, 40.55; H, 3.97; N, 10.51; S, 18.04; found: C, 40.08; H, 3.72; N, 10.67; S, 17.86.

2. 3. 2. Preparation of $[Cu_2(Hath)_4](p\text{-}CH_3C_6H_4SO_3)_2 \cdot 2H_2O$ (2)

To 5 ml of a solution of 0.198 g (0.4 mmol) of $Cu(p\text{-}CH_3C_6H_4SO_3)_2 \cdot 6H_2O$ in *n*-propanol was added 0.156 g (1 mmol) of 3-allyl-2-thiohydanthine (*Hath*) and stirred. The resulting orange-brown solution was placed into a 5 mL test tube and then copper-wire electrodes in cork were inserted. The inner mixture in the obtained cell was subjected to alternating-current electrochemical recovery (0.6 V, 50 Hz) during 2 days. Crystals **2**, suitable for X-ray diffraction studies, were formed on copper wires. Yield 43%. M.p. 113 °C. Anal. calcd. for $C_{19}H_{25}CuN_4O_6S_3$: C, 40.38; H, 4.46; N, 9.91; S, 17.02; found: C, 40.17; H, 4.34; N, 9.86; S, 17.21.

2. 4. X–Ray Crystal Structure Determination

The collected data for **1** & **2** were processed with CrysAlis Pro program.[19] The structures were solved by dual-space algorithm using SHELXT and refined by least squares method on F^2 by SHELXL-2014 with the following graphical user interfaces of OLEX^2.[20–22] Atomic displacements for non-hydrogen atoms were refined using an anisotropic model. Hydrogen atoms were placed in ideal positions and refined as riding atoms with relative isotropic displacement parameters. The figures were prepared using DIAMOND 3.1 software. Crystal parameters, data collection and the refinement parameters are summarized in Table 1.

3. Results and Discussion

π-Complex $[Cu_2(Hath)_4](C_6H_5SO_3)_2$ (**1**) forms triclinic crystals in the centrosymmetric space group $P\bar{1}$. This compound is composed of the centrosymmetric cationic $[Cu_2(Hath)_4]^{2+}$ dimers (Fig. 1) with one crystallographically independent Cu atom and outer coordination sphere represented by benzenesulfonate anions. Cu(I) atom in **1** has a trigonal pyramidal coordination environment (geometric index τ_4 = 0.80).[23] Sulfur atom and C5A=C6A olefine group from one *Hath* moiety and S centre from another ligand unit form basal plane of the metal ion coordination

Table 1. Selected crystal data and structure refinement parameters of **1** and **2**.

	$[Cu_2(Hath)_4](C_6H_5SO_3)_2$ (**1**)	$[Cu_2(Hath)_4](CH_3C_6H_4SO_3)_2 \times 2H_2O$ (**2**)
Formula weight (g·mol^{-1})	533.11	565.15
Crystal system and space group	Triclinic, $P\bar{1}$.	Triclinic, $P\bar{1}$.
a(Å)	9.1664(6)	9.4494(3)
b(Å)	10.7387(6)	10.3035(4)
c(Å)	12.4008(6)	14.4419(6)
α(°)	93.096(4)	94.228(3)
β(°)	95.581(5)	94.821(3)
γ(°)	114.254(6)	116.983(4)
V(Å^3)	1101.71(12)	1238.64(9)
Z	2	2
D (g/cm^3)	1.607	1.515
μ (mm^{-1})	1.31	1.18
F(000)	548	584
Crystal size (mm)	0.53 × 0.42 × 0.34	0.60 × 0.36 × 0.25
Crystal colour	colourless	colourless
Temperature of the data collections (K)	150(2)	150(2)
θ range for data collection (°)	3.7 – 28.9	3.5–28.8
Index ranges	$-12 \le h \le 9$ $-14 \le k \le 13$ $-16 \le l \le 16$	$-11 \le h \le 11$ $-13 \le k \le 13$ $-19 \le l \le 18$
Measured reflections	7786	8562
Independent reflections	4534	5143
Reflections with $I > 2\sigma(I)$	3954	4274
Refined parameters	288	302
R_{int}	0.022	0.024
$R[F^2 > 2\sigma(F^2)]$	0.038	0.047
$wR(F^2)$	0.091	0.132
$\Delta\rho_{max}/\Delta\rho_{min}$(e/Å^3)	1.11, −0.65	1.04, −0.78

Table 2. Selected bond lengths (Å) and angle values (°) in **1** and **2**.

	1	**2**
Bond	***d*, Å**	
Cu1–S1	2.2573(8)	2.2785(8)
Cu1–S2	2.2556(7)	2.2644(9)
Cu1–S1^X	3.0374(8)	2.7205(9)
Cu1–m^*	1.978(3)	1.994(3)
C5A–C6A	1.361(4)	1.363(5)
Angles	***ω*, °**	
S2–Cu1–S1	112.97(3)	112.06(3)
S1–Cu1–S1^{X**}	97.04(3)	97.21(3)
m–Cu1–S1	117.03(8)	116.37(3)
m–Cu1–S2	129.53(8)	128.32(3)

$^*m$ – middle point of C5A–C6A bond; $^{**}S1^X$ – $S1^i$ atom for **1** and $S1^{ii}$ atom for **2** Symmetry codes: (*i*) 1–*x*, 2–*y*, 1–*z*; (*ii*) 2–*x*, 1–*y*, 1–*z*.

sphere, and sulfur atom from one more *Hath* molecule is located at the apical position. The distance to the apical sulfur atom Cu1–S1^i is equal to 3.0374(8) Å and is significantly greater than Cu–S distances to the equatorial S1 and S2 atoms (Table 2).

In the mentioned cationic fragment $[Cu_2(Hath)_4]^{2+}$ there are two crystallographically independent molecules of organic ligand *Hath*. One of them is coordinated to the Cu atom by the thiogroup S1 atom and double C=C bond of the allyl group. Thus, the first ligand molecule possesses a bidentate chelate function, forming a seven-membered $\{C_4NSCu\}$ cycle. The aforementioned S1 atom of the first ligand is also coordinated to the Cu1^i atom, and, due to the cetrosymmetricity of the structure, a flat four-membered $\{Cu_2S_2\}$ cycle with a S1–Cu1–S1^i angle of 97.04(3)° is formed. Second ligand molecule is coordinated to the Cu1 atom only through its S2 atom, complementing copper's coordination number to four. Accordingly – allyl group of the second ligand molecule doesn't participate in the metal bonding and is freely located in the crystal structure with anticlinal conformation (119.8(3)°) relative to the C4B–C5B bond.

The structure of the complex $[Cu_2(Hath)_4](p\text{-}CH_3C_6H_4SO_3)_2 \cdot 2H_2O$ (**2**) is quite similar to the structure **1**. It has similar cationic $[Cu_2(Hath)_4]^{2+}$ fragments, but the outer coordination sphere is filled with *p*-toluenesulfonate anions and water molecules (Fig. 3). Regarding the cationic fragment, the main differences are in the noticeable shortening of the Cu–S distance to the apical atom

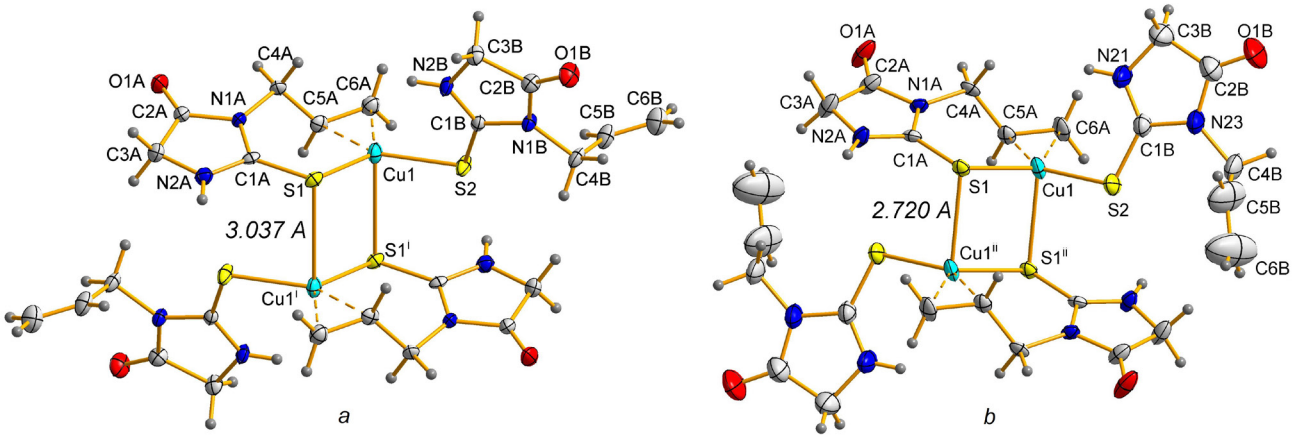


Figure. 1. Cationic fragment $[Cu_2(hath)_4]^{2+}$ in the structures **1** (*a*) and **2** (*b*). Symmetry codes: (*i*) 1–*x*, 2–*y*, 1–*z*; (*ii*) 2–*x*, 1–*y*, 1–*z*.

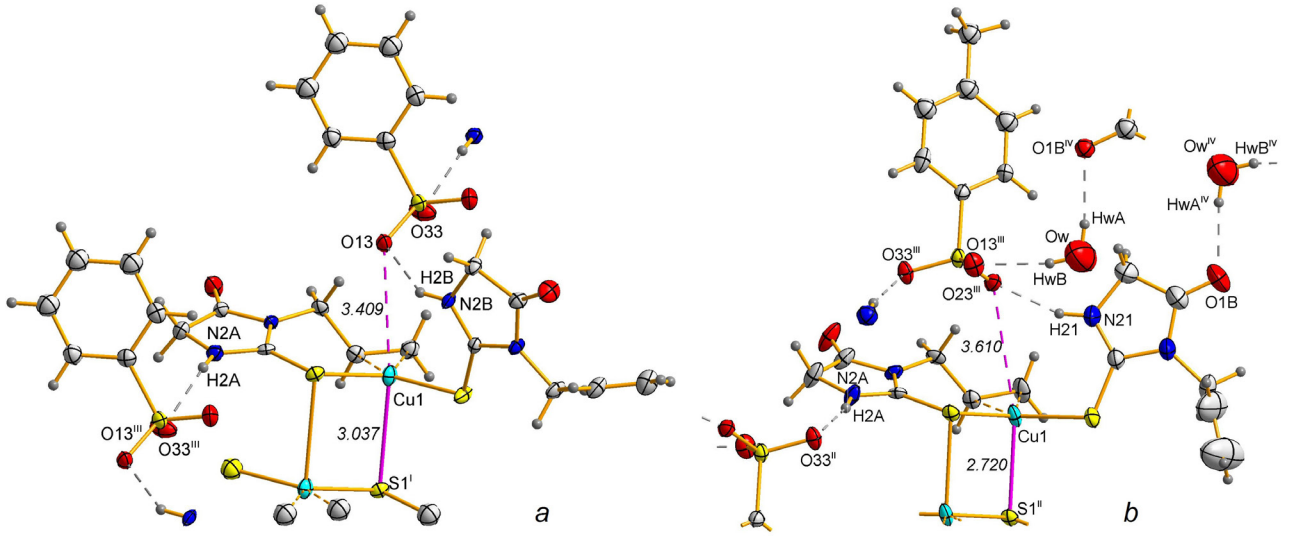


Figure. 2. Systems of weak bonding in the structure **1** (*a*) and **2** (*b*). Symmetry codes: (*i*) 1–*x*, 2–*y*, 1–*z*; (*ii*) 2–*x*, 1–*y*, 1–*z*; (*iii*) *x*–1, *y*, *z*; (*iv*) 1– *x*, –*y*, –*z*.

(2.7205(9) Å in **2** compared to 3.0374(8) Å in **1**) (Table 2) and a slightly different conformation of the uncoordinated ligand molecule, in particular, the torsion angle N23–C4B–C5B–C6B is equal to 142.6(7)° (in contrast to 119.8(3)° in **1**). These differences can be explained, taking into account some features of the differences in the outer coordination sphere (Fig 2).

Benzenesulfonate anions are located in the outer coordination sphere and take part in the formation of weak bonding in the structure **1**. Two out of three oxygen atoms of the same anion (O13 and O33) participate in N–H···O bonding (Table 3, Fig. 2) with N–H groups of different cationic fragments, connecting them into infinite H-bonded chain (Fig 3). Also, one of the oxygen atoms of $C_6H_5SO_3^-$ anion (O13) forms a weak Cu–O contact with a bond length of 3.409(5) Å. Nevertheless, this distance is noticeably longer than the sum of van der Waals radii of Cu and O by Bondi (2.92 Å),[24,25] it is still less than the corresponding value according to both Batsanov and Alvarez studies – namely 3.55 Å and 3.88 Å respectively.[26,27]

The system of hydrogen bonding in **2** is much more complicated than in **1** due to the presence of the water

Table 3. Geometry of selected hydrogen bonds in **1**.

Atoms involved	Distances, Å			Angle, deg
D–H···A	D···H	D···H	D···H	D–H···A
N2A–H2A···O33^{iii}	0.86	1.99	2.743(3)	146
N2B–H2B···O13	0.86	2.01	2.774(3)	148

Symmetry code: (*iii*) *x*–1, *y*, *z*.

Table 4. Geometry of selected hydrogen bonds in **2**.

Atoms involved D–H···A	Distances, Å D···H	H···A	D···A	Angle, deg D–H···A
N21–H21···O23^{iii}	0.88	1.93	2.761(4)	156
N2A–H2A···O33^{ii}	0.88	1.91	2.764(3)	164
O*w*–H*wA*···O1*B*^{iv}	0.85	2.00	2.841(6)	173
O*w*–H*wB*···O13^{iii}	0.85	2.08	2.914(5)	168

Symmetry codes: (*ii*) 2–*x*, 1–*y*, 1–*z*; (*iii*) *x*–1, *y*, *z*; (*iv*) 1–*x*, –*y*, –*z*.

molecule (Table 4, Fig 3). As one of the results of its presentence in **2** all three anion's O atoms participate in a formation of hydrogen bonding – two of them (O23 and O33) form N–H···O bonding, like in **1**, and the third one (O13) is connected with water molecule H*w*B atom. Second water hydrogen H*w*A atom is involved in O*w*–H*wA*···O1*B*^{iv} H-bonding with carbonyl C=O *Hath* group. As a result of all bonding, 2*D* H-bonded net is formed (Fig 3). Also, like in **1**, there is a weak Cu–O bonding but in structure **2**, the corresponding distance is noticeably greater and is equal to 3.610(3) Å, which is still less than the sum of van der Waals radii by Alvarez (3.88 Å).

As it was shown before, Cu1–S1^X distance to the apical S1^X atom (X = *i* in **1** and *ii* in **2**) is noticeably different in these two structures. Moreover, since all other distances and angles within the coordination environment of Cu atom are almost the same (Table 2) as well as a composition of the cationic fragment, it can be concluded that the cause of these differences should be found in the outer coordination sphere. As a possible reason, we would like to introduce the confrontation of Cu–S bonding and Cu–O weak interaction. One can notice that in **1** structure Cu–S interaction is weaker (3.0374(8) Å) in comparison with **2** (2.7205(9) Å) and vise versa – Cu–O interaction in **1** is

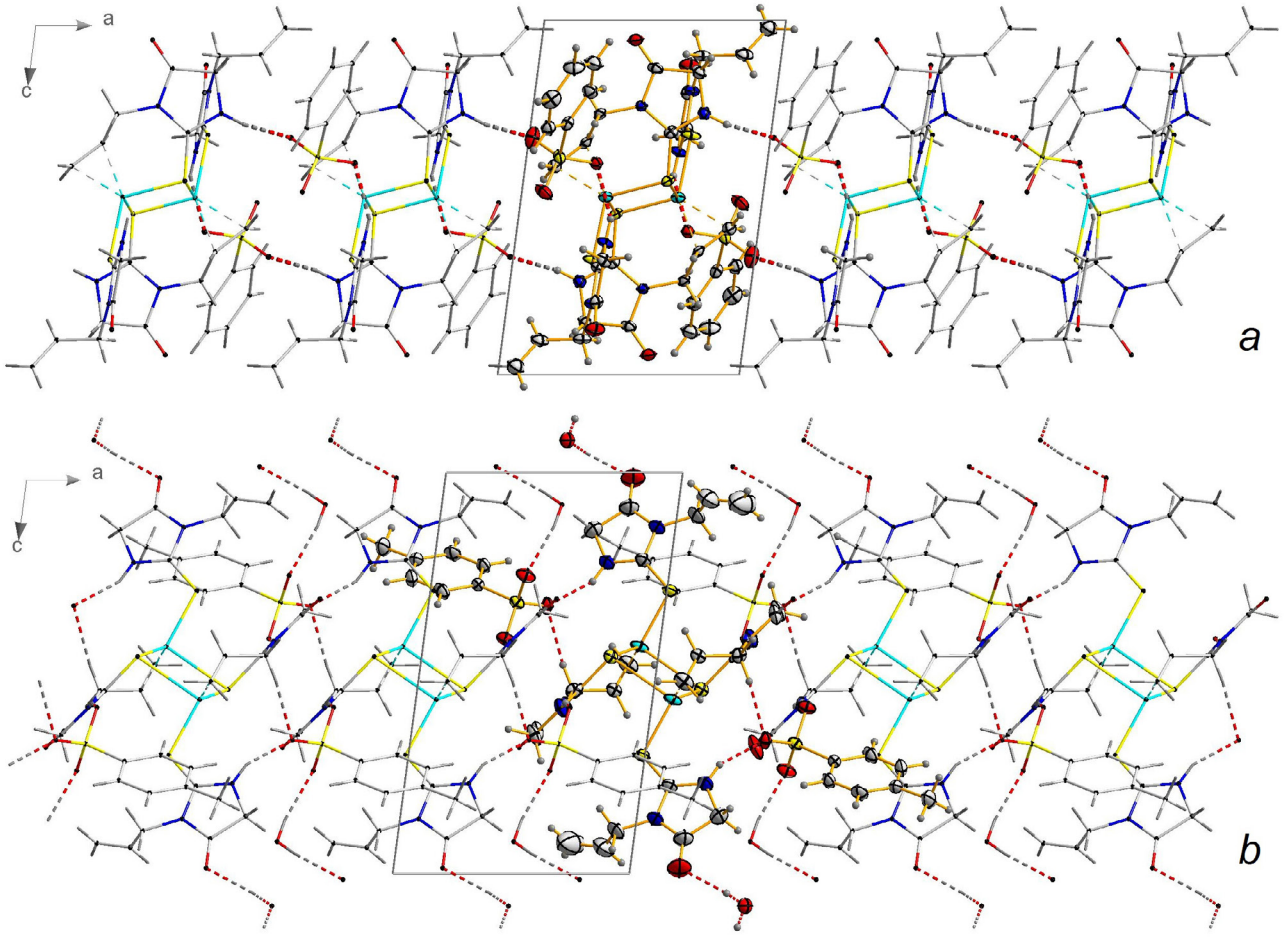


Figure. 3. 1*D* H-bonded chain in **1** (*a*) and 2*D* H-bonded net in **2** (*b*).

stronger (3.409(3) Å) than in 2 (3.610(3) Å) (Fig 2). In our previous works we have shown an impact of a weak interactions, including hydrogen bonding, on the structural organization in π-complex compounds.[28–30] The weakening of the Cu–O interaction in **2** (and the strengthening of Cu–S as a result) can be explained by the fact, that the anion in **2** is involved in a larger number of the H-bonding, due to the presence of the water molecule, all of which competes with the Cu–O interaction. Finally, since the water was presented in both reaction mixtures, but co-crystallized only in **2**, its presence in its crystal structure should be explained by the different character of benzene- and *p*-toluenesulfonate anions.

In our previous works we have synthesized a series of Ag(I) arylsulfonates coordination compounds with *Hath* possessing a completely different geometry and more complicated geometry, namely $[Ag_2(Hath)_4(C_6H_5SO_3)_2] \cdot 0.5C_3H_7OH$, $[Ag_2(Hath)_4(CH_3C_6H_4SO_3)_2]$ and $[Ag_2(Hath)(ath)(CH_3C_6H_4SO_3)]$.[16,17] In the first two coordination compounds, a complex coordination chain is formed, within which there are three crystallographically independent Ag(I) atoms with different coordination environments (tetragonal pyramidal, seesaw and distorted octahedral), four crystallographically independent molecules of *Hath* ligand and two anions of benzene- or toluenesulfonate. The *Hath* molecule is coordinated exclusively through the S atom of the thiogroup, which is bonded to several metal centers simultaneously. In complex $[Ag_2(Hath)(ath)(CH_3C_6H_4SO_3)]$, part of the molecules of 3-allyl-2-thiohydantoin is in the deprotonated form (*ath*). In all these three compounds double bonds of allyl groups have stayed unbounded. The lack of coordination of the 2-thiohydantoin ligand C=C by the double bond of the allyl group in the case of Ag(I) complexes in contrast to Cu(I) ones, can be explained by the greater philicity of the Ag(I) atom to the exocyclic Sulfur atom, which in case of Ag(I) complexes tend to be bonded with a maximal amount of Ag(I) atoms.

4. Conclusions

Two novel copper(I) π-complexes $[Cu_2(Hath)_4](C_6H_5SO_3)_2$ (**1**) and $[Cu_2(Hath)_4] \cdot 2CH_3C_6H_4SO_3 \cdot 2H_2O$ (**2**) (*Hath* = 3-allyl-2-thiohydantoine) were synthesized and characterized by the X-ray diffraction method. Both structures contain centrosymmetric cationic dimer $[Cu_2(Hath)_4]^{2+}$ in which Cu(I) atom has a trigonal pyramidal coordination environment. In contrast to $Ag(C_6H_5SO_3)$ & $Ag(CH_3C_6H_4SO_3)$ complexes, in which Ag(I) prefers to be bound with ligand by S-atom only, copper(I) coordination environment in **1** & **2** includes both ligand`s exocyclic sulfur atom and allylic C=C bond. Nevertheless, both $[Cu_2(Hath)_4]^{2+}$ are very similar, there are some differences, including the difference in the $Cu1–S1^X$ distance (3.0374(8) Å in **1** and 2.7205(9) Å in **2**). As a possible explanation, the confrontation of Cu–S and Cu–O weak interaction was proposed. Due to this model this difference is explained by the fact, that the anion in **2** is involved in a larger number of the H-bonding, due to the presence of the water molecule in it, and acts on Cu(I) atom weaker than in **1**.

Supplementary material

CCDC numbers 1997084 (**1**) and 1997085 (**2**) contains the supplementary crystallographic data for this paper. Copies of the data can be obtained free of charge on applications to the Director, CCDC, 12 Union Road, Cambridge CB2 1EZ, UK (Fax: int. code +(1223)336–033; e-mail for inquiry: fileserv@ccdc.cam.ac.uk).

5. References

1. Seo Hyun Choa, Seok-Ho Kim, Dongyun Shin, *Eur. J. Med. Chem.* **2019**, *164*, 517–545.
2. S. Suzen, E. Buyukbingol, *Il Farmaco.* **2000**, 55, 246–248. **DOI:**10.1016/S0014-827X(00)00028-8
3. M. E. Jung, S. Ouk, D. Yoo, C. L. Sawyers, C. Chen, C. Tran, J. Wongvipat, *J. Med. Chem.* **2010**, *53*, 2779–2796. **DOI:**10.1021/jm901488g
4. Y. S. Bae, S. Choi, J. J. Park, J. H. Joo, M. Cui, H. Cho, W. J. Lee, S. H. Lee, *Bioorg. Med. Chem.* **2016**, *24*, 4144–4151. **DOI:**10.1016/j.bmc.2016.06.056
5. R. Raj, V. Mehra, J. Gut, P. J. Rosenthal, K. J. Wicht, T. J. Egan, M. Hopper, L. A. Wrischnik, K. M. Land, V. Kumar, *Eur. J. Med. Chem.* **2014**, *84*, 425–432. **DOI:**10.1016/j.ejmech.2014.07.048
6. M. T. M. González, J. L. G. Ariza, F. Pino, R. G. Villanova, *Talanta* **1978**, *25*, 331–337. **DOI:**10.1016/0039-9140(78)80137-4
7. M. T. M. González, J. L. G. Ariza, *Talanta* **1980**, *27*, 613–614. **DOI:**10.1016/0039-9140(80)80192-5
8. C. R. Groom, I. J. Bruno, M. P. Lightfoot, S. C. Ward, *Acta Cryst. B* **2016**, *72*, 171–179. **DOI:**10.1107/S2052520616003954
9. Weifeng Zeng, Xiaodong Yang, Xiuli Chen, Yichen Yan, Xinwei Lu, Jinqing Qu, Ruiyuan Liu, *Eur. Polym. J.* **2014**, *61*, 309–315. **DOI:**10.1016/j.eurpolymj.2014.10.015
10. P. Aslanidis, S. Kyritsis, M. Lalia-Kantouri, B. Wicher, M. Gdaniec, *Polyhedron* **2012**, *48*, 140–145 **DOI:**10.1016/j.poly.2012.08.065
11. Yu.I. Slyvka, A. A. Fedorchuk, N. T. Pokhodylo, T. Lis, I. V. Kityk, M. G. Mys'kiv, *Polyhedron* **2018**, *147*, 86–93. **DOI:**10.1016/j.poly.2018.03.015
12. A. A. Fedorchuk, Yu. I. Slyvka, E. A. Goreshnik, I. V. Kityk, P. Czaja, M. G. Mys'kiv, *J. Mol. Struct*. **2018**, *1171*, 644–649. **DOI:**10.1016/j.molstruc.2018.06.017
13. Yu. Slyvka, A.A. Fedorchuk, E. Goreshnik, G. Lakshminarayana, I.V. Kityk, P. Czaja, M. Mys'kiv, *Chem. Phys. Lett*. **2018**, *694*, 112–119. **DOI:**10.1016/j.cplett.2018.01.041
14. Yu. Slyvka, E. Goreshnik, G. Veryasov, D. Morozov, A. A. Fe-

dorchuk, N. Pokhodylo, I. Kityk, M. Mys'kiv, *J. Coord. Chem.* **2019**, *72*, 1049–1063. **DOI:**10.1080/00958972.2019.1580699
15. A. A. Fedorchuk, Yu. Slyvka, V. Kinzhybalo, I. Kityk, J. Jędryka, K. Ozga, M. Mys`kiv, *J. Coord. Chem.* **2019**, *72*, 3222–3236. **DOI:**10.1080/00958972.2019.1687891
16. A. A. Fedorchuk, Yu. I. Slyvka, V. Kinzhybalo, T. Lis, M. G. Mys'kiv, *Inorg. Chim. Acta* **2019**, *481*, 79–86. **DOI:**10.1016/j.ica.2018.09.029
17. A. A. Fedorchuk, Yu. I. Slyvka, M. G. Mys'kiv, *Voprosy khimii i khimicheskoi tekhnologii* **2019**, *4*, 172–178.
18. B. M. Mykhalichko, M. G. Mys'kiv. Ukraine Patent UA 25450A, Bull. № 6, **1998**.
19. Agilent Technologies, CrysAlis PRO, Agilent Technologies, Yarnton, England, **2011**.
20. G. M. Sheldrick, *Acta Cryst. Sect. A.* **2015**, *A71*, 3–8. **DOI:**10.1107/S2053229614024218
21. G. M. Sheldrick, *Acta Cryst. Sect. C.* **2015**, *C71*, 3–8. **DOI:**10.1107/S2053229614024218
22. O. V. Dolomanov, L. J. Bourhis, R. J. Gildea, J. A. K. Howard, H. Puschmann, *J. Appl. Cryst.* **2009**, *42*, 339–341. **DOI:**10.1107/S0021889808042726
23. L.Yang, D. R. Powell, R. P. Houser, Dalton Trans. **2007**, 9, 955–964. **DOI:**10.1039/B617136B
24. Bondi, *J. Phys. Chem.* **1964**, *68*, 441–451. **DOI:**10.1021/j100785a001
25. Bondi, *J. Phys. Chem.* **1966**, *70*, 3006–3007. **DOI:**10.1021/j100881a503
26. S. S. Batsanov, *Inorg. Mater.* **2001**, *37*, 871–885. **DOI:**10.1023/A:1011625728803
27. S. A. Alvarez, *Dalton Trans.* **2013**, *42*, 8617–8636. **DOI:**10.1039/c3dt50599e
28. Yu. Slyvka, E. Goreshnik, N. Pokhodylo, O. Pavlyuk, M. Mys'kiv, *Acta. Chim. Slov.* **2016**, *63*, 399–405.
29. B. Ardan, V. Kinzhybalo, Yu. Slyvka, O. Shyyka, M. Luk'yanov, T. Lis, M. Mys'kiv, Acta. Cryst. *Sect. C.* **2017**, *C73*, 36–46. **DOI:**10.1107/S2053229616018751
30. E. A. Goreshnik, G. Veryasov, Yu. I. Slyvka, B. R. Ardan, M. G. Mys'kiv, *J. Organomet. Chem.* **2016**, *810*, 1–11. **DOI:**10.1016/j.jorganchem.2016.03.001

Povzetek

V tem delu je predstavljena sinteza in strukturna karakterizacija dveh novih Cu(I) arilsulfonatnih π-kompleksov z 3-alil-2-tiohidantoinom, in sicer $[Cu_2(Hath)_4](C_6H_5SO_3)_2$ (**1**) in $[Cu_2(Hath)_4](p\text{-}CH_3C_6H_4SO_3)_2{\cdot}2H_2O$ (**2**) (*Hath* = 3-alil-2-tiohidantoin). Spojini smo pridobili z elektrokemijsko sintezo s spremenljivim tokom in preučevali z rentgensko difrakcijo. V obeh spojinah je notranja koordinacijska sfera sestavljena iz kationskega dimera $[Cu_2(Hath)_4]^{2+}$ z enim kristalografsko neodvisnim Cu(I) atomom ki ima trigonalno piramidalno okolje ki ga tvorijo trije S atomi iz *Hath* tioskupin in dvojna C=C vez iz alilne skupine. Fragmenti $[Cu_2(Hath)_4]^{2+}$ so zelo podobni v obeh koordinacijskih spojinah kljub nekaterim odstopanjem, npr. Veliki razliko v razdalji Cu-S do apikalnega S atoma (3.0374(8) Å v **1** in 2.7205(9) Å v **2**). To razliko lahko razložimo z vplivom sistema šibkih interakcij, ki so bistveno različne.

Except when otherwise noted, articles in this journal are published under the terms and conditions of the Creative Commons Attribution 4.0 International License

Scientific paper

Synthesis, Characterization, Crystal Structures, and Urease Inhibition of Copper(II) and Zinc(II) Complexes Derived from Benzohydrazones

Fu-Ming Wang,[1,*] Li-Jie Li,[2] Guo-Wei Zang,[2] Tong-Tong Deng[2] and Zhong-Lu You[3]

[1] *Key Laboratory of Coordination Chemistry and Functional Materials in Universities of Shandong, Department of Chemistry, Dezhou University, Dezhou 253023, P. R. China*

[2] *School of Chemistry and Chemical Engineering, Beijing Institute of Technology, Beijing 100081, P. R. China*

[3] *Department of Chemistry and Chemical Engineering, Liaoning Normal University, Dalian 116029, P. R. China*

* *Corresponding author: E-mail: wfm99999@126.com*

Received: 04-24-2020

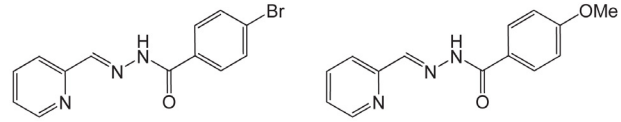
Abstract

A new copper(II) complex $[Cu(L^1)(NCS)(CH_3OH)]$ (**1**) and a new zinc(II) complex $[ZnCl_2(HL^2)] \cdot CH_3OH$ (**2**), derived from 4-bromo-*N*'-(pyridin-2-ylmethylene)benzohydrazide (HL^1) and 4-methoxy-*N*'-(pyridin-2-ylmethylene)benzohydrazide (HL^2), were prepared and characterized by elemental analysis, IR and UV-Vis spectroscopy and single crystal X-ray diffraction. The hydrazone HL^1 coordinates to the Cu atom in enolate form, while the hydrazone HL^2 coordinates to the Zn atom in carbonyl form. Single crystal structural analyses indicate that the hydrazones coordinate to the metal atoms through the pyridine N, imino N, and enolate/carbonyl O atoms. The Cu atom in complex **1** is in square pyramidal coordination, and the Zn atom in complex **2** is in trigonal-bipyramidal coordination. The inhibitory effects of the complexes on *Jack bean* urease were studied, which show that the copper complex has strong activity on urease.

Keywords: Hydrazone; copper complex; zinc complex; crystal structure; urease inhibition

1. Introduction

Urease (EC 3.5.1.5; urea amidohydrolase) is a binuclear nickel-dependent hydrolase enzyme, which can be synthesized by numerous organisms, including plants, bacteria, algae, fungi, and invertebrates, and occurs widely in animal and soil.[1] Urease enzyme catalyzes the decomposition of urea into ammonia and carbon dioxide in high efficiency,[2] with the rate of catalyzed reaction 10^{14} times higher than the non-catalyzed reaction.[3] The enzyme possesses harmful effects on both human health and fertile soil.[4] In recent years, Schiff base complexes are reported to have interesting urease inhibitory activities,[5] especially the copper complexes with Schiff bases or hydrazones are promising types of lead structures as urease inhibitors.[6] As a continuation of the work on the exploration of new urease inhibitors, a new copper(II) complex $[Cu(L^1)(NCS)(CH_3OH)]$ (**1**) and a new zinc(II) complex $[ZnCl_2(HL^2)] \cdot CH_3OH$ (**2**), derived from 4-bromo-*N*'-(pyridin-2-ylmethylene)benzohydrazide (HL^1) and 4-methoxy-*N*'-(pyridin-2-ylmethylene)benzohydrazide (HL^2; Scheme 1), were prepared and studied on their urease inhibition activity.



Scheme 1. HL^1 and HL^2

2. Experimental

2. 1. Materials and Measurements

All reagents and solvents were of commercially available reagent grade quality and were used without further purification. HL^1 was synthesized according to the literature method.[7] *Jack bean* urease was purchased from Sig-

ma-Aldrich. Elemental analyses were performed on a Perkin-Elmer 240C elemental analyzer. IR spectra were recorded on a Jasco FT/IR-4000 spectrometer as KBr pellets in the 4000–400 cm^{-1} region. UV-Vis spectra were recorded on a Perkin-Elmer Lambda 900 spectrometer. ^1H NMR and ^{13}C NMR spectra were recorded on a 500 MHz Bruker Advance instrument. The urease inhibitory activity was measured on a Bio-Tek Synergy HT microplate reader. Single crystal structures were determined by Bruker Smart 1000 CCD area diffraction.

2. 2. Synthesis of HL^2

2-Pyridinecarboxaldehyde (0.01 mol, 1.07 g) and 4-methoxybenzohydrazide (0.01 mol, 1.66 g) were dissolved in methanol (100 mL). The mixture was stirred at reflux for 1 h and the solvent removed by distillation at reduced pressure. The solid product was re-crystallized from methanol to give colorless crystals. Yield: 1.72 g (68%). Characteristic IR data (KBr, cm^{-1}): 3227 (NH), 1645 (C=O), 1607 (C=N). UV–Vis data (methanol, λ/nm): 305, 370. Anal. Calcd for $C_{14}H_{13}N_3O_2$: C, 65.87; H, 5.13; N, 16.46. Found: C, 65.71; H, 5.25; N, 16.32%. ^1H NMR (DMSO-d_6, 500 MHz) δ (ppm): 11.96 (s, 1H, N*H*), 8.62 (d, 1H, Py*H*), 8.47 (s, 1H, C*H*=N), 7.99-7.89 (m, 4H, Py*H* + Ar*H*), 7.42 (q, 1H, Py*H*), 7.10 (d, 2H, Ar*H*), 3.84 (s, 3H, CH_3). ^{13}C NMR (DMSO-d_6, 126 MHz) δ (ppm): 162.70, 162.11, 153.37, 149.43, 147.36, 136.76, 129.62, 125.16, 124.19, 119.74, 113.71, 55.40.

2. 3. Synthesis of the Complex 1

HL^1 (1.0 mmol, 0.30 g) was dissolved in methanol (20 mL), to which $Cu(ClO_4)_2 \cdot 6H_2O$ (1.0 mmol, 0.37 g) and ammonium thiocyanate (1.0 mmol, 0.076 g) dissolved in methanol (20 mL) were added dropwise. The mixture was stirred for 10 min at room temperature and filtered. The filtrate was kept in air for a few days, to form crystals suitable for single crystal X-ray diffraction. The crystals were isolated by filtration. Yield: 0.18 g (39%). Characteristic IR data (KBr, cm^{-1}): 3450 (OH), 2043 (NCS), 1602 (CH=N), 1447, 1372, 1161, 1070, 952, 860, 535. UV–Vis data (methanol, λ/nm): 270, 370. Anal. Calcd for $C_{15}H_{13}BrCuN_4O_2S$: C, 39.44; H, 2.87; N, 12.26. Found: C, 39.27; H, 2.98; N, 12.41%.

2. 4. Synthesis of the Complex 2

HL^2 (1.0 mmol, 0.26 g) was dissolved in methanol (20 mL), to which $ZnCl_2$ (1.0 mmol, 0.14 g) dissolved in methanol (20 mL) was added dropwise. The mixture was stirred for 10 min at room temperature and filtered. The filtrate was kept in air for a few days, to form crystals suitable for single crystal X-ray diffraction. The crystals were isolated by filtration. Yield: 0.26 g (61%). Characteristic IR data (KBr, cm^{-1}): 3463 (OH), 1672 (C=O), 1604 (CH=N), 1455, 1369, 1276, 1158, 1078, 947, 860, 544, 520. UV–Vis data (methanol, λ/nm): 305, 380. Anal. Calcd for $C_{15}H_{17}Cl_2N_3O_3Zn$: C, 42.53; H, 4.05; N, 9.92. Found: C, 42.71; H, 4.13; N, 9.80%.

Table 1. Crystallographic and experimental data for the compounds

Compound	HL^2	1	2
Formula	$C_{14}H_{15}N_3O_3$	$C_{15}H_{13}BrCuN_4O_2S$	$C_{15}H_{17}Cl_2N_3O_3Zn$
M_r	273.3	456.8	423.6
Crystal system	Triclinic	Monoclinic	Triclinic
Space group	$P\bar{1}$	$P2_1/n$	$P\bar{1}$
a (Å)	6.6036(12)	7.3009(5)	7.8943(4)
b (Å)	14.6112(11)	17.3938(13)	8.3352(5)
c (Å)	15.2091(13)	13.7578(10)	14.7609(9)
α (°)	71.232(2)	90	104.246(1)
β (°)	84.436(2)	96.629(1)	100.125(1)
γ (°)	84.520(2)	90	99.016(1)
V (Å^3)	1379.7(3)	1735.4(2)	906.16(9)
Z	4	4	2
D_c (g cm^{-3})	1.316	1.748	1.552
μ (Mo-Ka) (mm^{-1})	0.095	3.696	1.668
F(000)	576	908	432
Reflections collected	8135	8964	4869
Unique reflections	5104	3218	3345
Observed reflections ($I \geq 2\sigma(I)$)	3655	2514	2995
Parameters	381	221	231
Restraints	6	1	2
Goodness-of-fit on F^2	1.041	1.039	1.060
R_1, wR_2 [$I \geq 2\sigma(I)$]	0.0535, 0.1425	0.0381, 0.0891	0.0256, 0.0658
R_1, wR_2 (all data)	0.0775, 0.1609	0.0545, 0.0959	0.0301, 0.0681
Large diff. peak and hole (eÅ^{-3})	0.223, –0.249	0.977, –0.471	0.274, –0.234

2. 5. X-Ray Crystallography

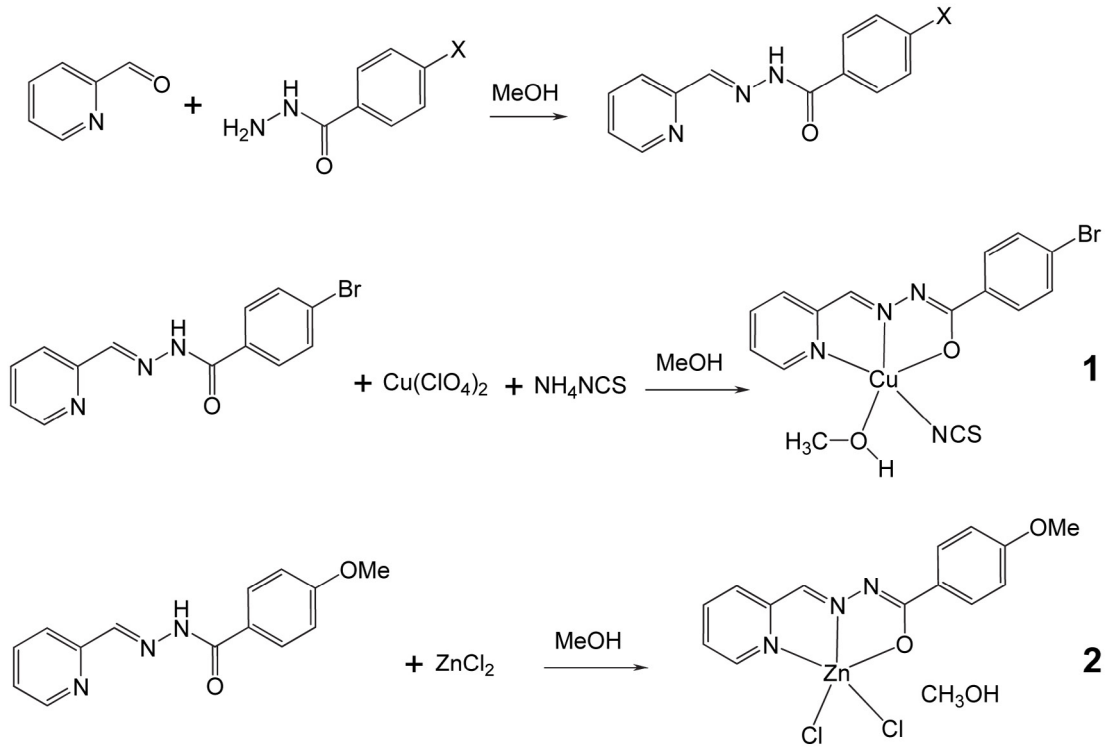
Diffraction intensities for HL^2 and the complexes were collected at 298(2) K using a Bruker Smart 1000 CCD area diffractometer with MoKα radiation (λ = 0.71073 Å). The collected data were reduced with SAINT,[8] and multi-scan absorption correction was performed using SADABS.[9] Structures of HL^2 and the complexes were solved by direct methods and refined against F^2 by full-matrix least-squares method using SHELXTL.[10] All of the non-hydrogen atoms were refined anisotropically. The amino and methanol H atoms in the compounds were located from difference Fourier maps and refined isotropically, with N–H and O–H distances restrained to 0.90(1) and 0.85(1) Å, respectively. The remaining hydrogen atoms were placed in calculated positions and constrained to ride on their parent atoms. Crystallographic data for HL^2 and the complexes are summarized in Table 1. Selected bond lengths and angles are given in Table 2.

2. 6. Urease Inhibitory Activity Assay

The measurement of urease inhibitory activity was carried out according to the literature method.[11] The assay mixture containing 75 μL of *Jack bean* urease and 75 μL of tested compounds with various concentrations (dissolved in DMSO) was pre-incubated for 15 min on a 96-well assay plate. Acetohydroxamic acid was used as a reference. Then 75 μL of phosphate buffer at pH 6.8 containing phenol red (0.18 mmol L^{-1}) and urea (400 mmol L^{-1}) were added and incubated at room temperature. The reaction time required

Table 2. Selected bond lengths/Å and angles/° for the compounds

HL^2			
C6–N2	1.272(3)	N2–N3	1.375(2)
N3–C7	1.356(3)	C7–O1	1.229(3)
C20–N5	1.273(3)	N5–N6	1.369(2)
N6–C21	1.360(3)	C21–O3	1.229(2)
C6–N2–N3	116.4(2)	N2–N3–C7	118.6(2)
C20–N5–N6	116.9(2)	N5–N6–C21	118.1(2)
1			
Cu1–N1	2.007(3)	Cu1–N2	1.928(3)
Cu1–O1	1.965(3)	Cu1–O2	2.284(4)
Cu1–N4	1.927(4)		
C6–N2	1.280(4)	N2–N3	1.375(4)
N3–C7	1.333(4)	C7–O1	1.277(5)
N4–Cu1–N2	159.33(18)	N4–Cu1–O1	99.50(14)
N2–Cu1–O1	79.18(12)	N4–Cu1–N1	97.74(15)
N2–Cu1–N1	80.75(12)	O1–Cu1–N1	159.48(13)
N4–Cu1–O2	111.53(19)	N2–Cu1–O2	89.14(13)
O1–Cu1–O2	90.15(14)	N1–Cu1–O2	93.81(15)
C6–N2–N3	124.4(3)	N2–N3–C7	107.2(3)
2			
Zn1–N1	2.1462(16)	Zn1–N2	2.1149(16)
Zn1–Cl1	2.2233(6)	Zn1–Cl2	2.2348(6)
Zn1–O1	2.2979(14)		
N2–Zn1–N1	74.91(6)	N2–Zn1–Cl1	115.82(5)
N1–Zn1–Cl1	101.84(5)	N2–Zn1–Cl2	124.21(5)
N1–Zn1–Cl2	103.10(5)	Cl1–Zn1–Cl2	118.93(3)
N2–Zn1–O1	70.54(5)	N1–Zn1–O1	145.28(6)
Cl1–Zn1–O1	96.04(5)	Cl2–Zn1–O1	93.65(4)



Scheme 2. The synthetic procedure of the hydrazones and the complexes. X = Br for HL^1, OMe for HL^2.

for enough ammonium carbonate to form to raise the pH phosphate buffer from 6.8 to 7.7 was measured by micro-plate reader (560 nm) with end-point being determined by the color change of phenol-red indicator.

3. Results and Discussion

3. 1. Chemistry

The synthetic procedure of the hydrazones and the complexes is shown in Scheme 2. The hydrazone HL^2 was prepared by the condensation reaction of equimolar quantities of 2-pyridinecarboxaldehyde and 4-methoxybenzohydrazide. The copper complex was prepared by reaction of equimolar quantities of HL^1, copper perchlorate, and ammonium thiocyanate in methanol. The zinc complex was prepared by reaction of equimolar quantities of HL^2 and zinc chloride in methanol. Single crystals of HL^2 and the complexes were obtained by slow evaporation of the methanolic solution of the compounds.

3. 2. Structure Description of HL^2

The molecular structure of HL^2 is shown in Figure 1. The compound contains two hydrazone molecules and two water molecules of crystallization. The hydrazone molecules adopt *E* configuration with respect to the methylidene unit. The distances of the methylidene bonds confirm them as typical double bonds. The shorter distances of the C–N bonds and the longer distances of the C=O bonds for the –C(O)–NH– units than usual, suggests the presence of conjugation effects in the hydrazone molecules. The remaining bond lengths in the compounds are within normal values.[12] The dihedral angles between the pyridine and benzene rings are 61.0(3)° for one molecule and 18.4(3)° for the other one. The hydrazone molecules are linked by water molecules through hydrogen bonds of O–H···O and O–H···N (Table 3, and Figure 2).

3. 3. Structure Description of the Copper Complex

Molecular structure of the copper complex is shown in Figure 3. The Cu atom is in square pyramidal geometry, with the pyridine N, imino N, and enolate O atoms of the hydrazone ligand, and the thiocyanato N atom located at the basal plane, and with the methanol O atom located at the apical position. The Cu atom deviates from the least-squares plane defined by the four basal donor atoms by 0.242(1) Å. The coordinate bond lengths in the complex

Table 3. Hydrogen bond distances (Å) and bond angles (°) for the compounds

D–H···*A*	*d*(*D*–H)	*d*(H···*A*)	*d*(D···*A*)	Angle (*D*–H···*A*)
HL^2				
O5–H5B···N1	0.85(1)	2.18(2)	2.982(3)	157(2)
O5–H5A···O3	0.85(1)	1.99(1)	2.808(2)	162(3)
O6–H6B···O1^{i}	0.85(1)	1.99(1)	2.830(3)	165(3)
O6–H6A···N4^{i}	0.85(1)	2.19(2)	2.981(3)	155(3)
N3–H3···O6	0.86	2.04	2.863(3)	161(3)
N6–H6C···O5^{ii}	0.86	2.07	2.898(2)	162(3)
1				
O2–H2···N3^{iii}	0.85(1)	1.99(2)	2.840(4)	171(4)
2				
O3–H3B···O1^{i}	0.82	2.26	2.997(2)	149(3)
N3–H3···O3	0.89(1)	1.93(1)	2.785(2)	161(3)

Symmetry codes: (i) –1 + *x*, *y*, *z*; (ii) 1 + *x*, *y*, *z*; (iii) –*x*, –*y* + 2, –*z* + 2.

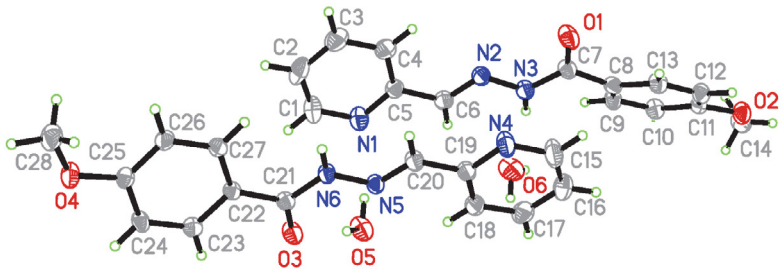


Figure 1. Molecular structure of HL^2, showing the atom-numbering scheme. Displacement ellipsoids for non-hydrogen atoms are drawn at 30% probability level.

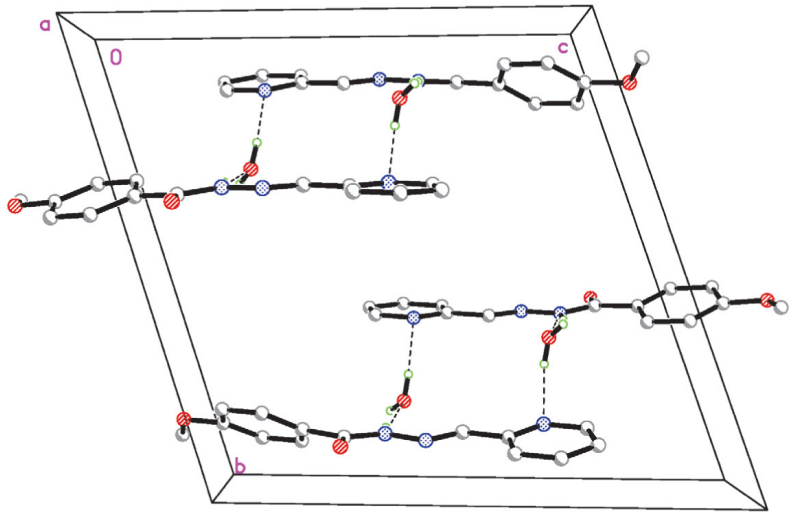


Figure 2. Molecular packing structure of HL, viewed along the *a* axis. Hydrogen bonds are shown as dashed lines.

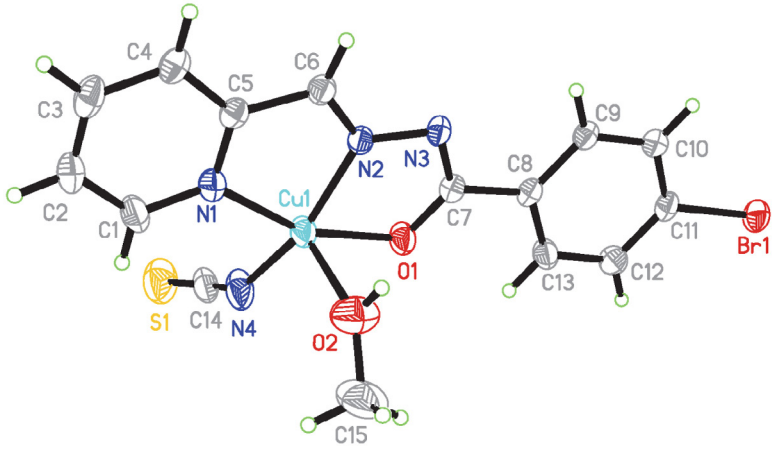


Figure 3. Molecular structure of **1**, showing the atom-numbering scheme. Displacement ellipsoids for non-hydrogen atoms are drawn at 30% probability level.

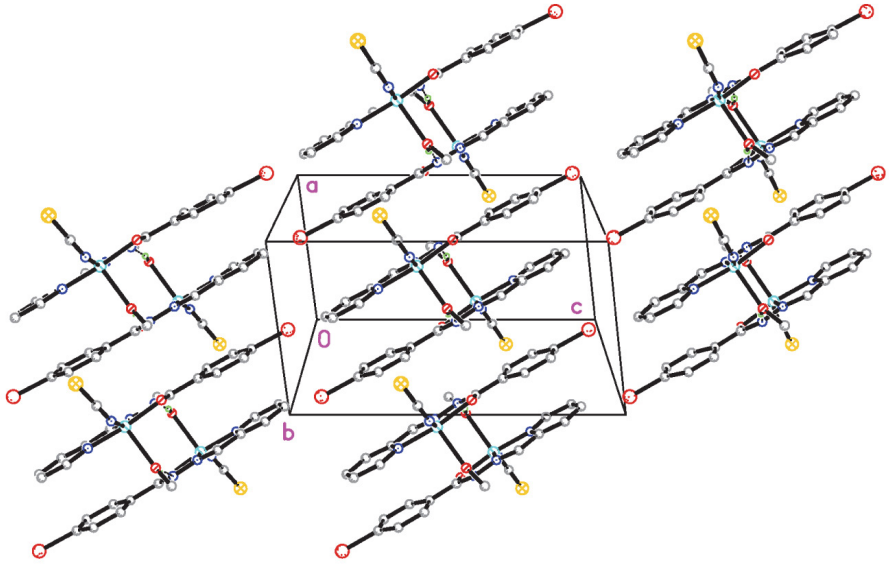


Figure 4. Molecular packing structure of **1**, viewed along the *b* axis. Hydrogen bonds are shown as dashed lines.

are comparable to those observed in copper(II) complexes with hydrazone ligands.[6a,13]

In the crystal structure of the complex, two complex molecules are linked through intermolecular hydrogen bonds of O–H···N (Table 3), to form a dimer (Figure 4).

3. 4. Structure Description of the Zinc Complex

Molecular structure of the zinc complex is shown in Figure 5. The Zn atom is in trigonal bipyramidal geometry, with the imino atom of the hydrazone ligand, and two chloride atoms located at the basal plane, and with the pyridine N and carbonyl O atoms located at the axial positions. The Zn atom deviates from the least-squares plane defined by the three basal donor atoms by 0.129(1) Å. The coordinate bond lengths in the complex are comparable to those observed in zinc(II) complexes with hydrazone ligands.[14]

In the crystal structure of the complex, the complex molecules are linked through intermolecular hydrogen bonds of O–H···O (Table 3), to form chains along the *b* axis (Figure 6).

3. 5. Biological Study

The percent inhibition of the compounds at concentration of 100 μmol L^{-1} on *Jack bean* urease is summarized in Table 4. The hydrazones and the zinc complex have weak activity. However, the copper complex showed strong

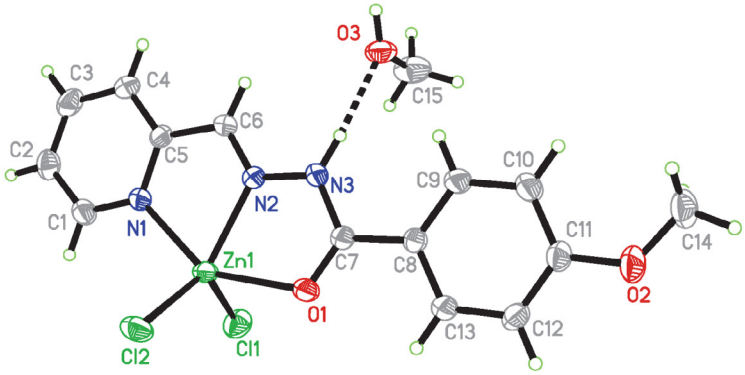


Figure 5. Molecular structure of **2**, showing the atom-numbering scheme. Displacement ellipsoids for non-hydrogen atoms are drawn at 30% probability level.

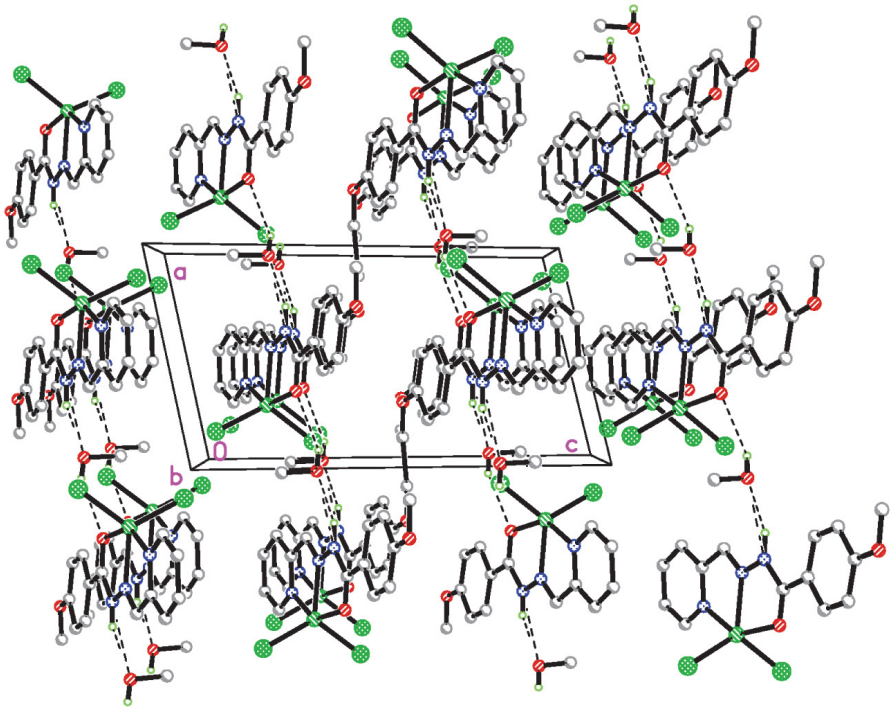


Figure 6. Molecular packing structure of **2**, viewed along the *b* axis. Hydrogen bonds are shown as dashed lines.

Table 4. Inhibition of urease by the tested materials

Tested materials	Percentage Inhibition rate[#]	IC_{50} (μmol L^{-1})
HL^1	32.7 ± 2.1	> 100
HL^2	25.3 ± 1.7	> 100
1	97.3 ± 3.2	1.4 ± 0.8
2	45.0 ± 2.6	> 100
Copper perchlorate	87.5 ± 2.6	8.8 ± 1.4
Zinc chloride	–	> 100
Acetohydroxamic acid	84.3 ± 3.9	37.2 ± 4.0

[#] The concentration of the tested material is 100 μmol L^{-1}.

urease inhibitory activity, with IC_{50} value of 1.4 ± 0.8 μmol L^{-1}. As a comparison, acetohydroxamic acid (AHA) was used as a reference drug with the percent inhibition of 84.3 ± 3.9, and with IC_{50} value of 37.2 ± 4.0 μmol L^{-1}. Copper perchlorate can inhibit urease activity, with IC_{50} value of 8.8 ± 1.4 μmol L^{-1}. Thus, the present copper complex is a good model for urease inhibition.

4. Conclusion

In summary, a new hydrazone compound 4-methoxy-*N*'-(pyridin-2-ylmethylene)benzohydrazide was prepared and structurally characterized. With the hydrazones, a new copper(II) complex and a new zinc(II) complex were obtained. The complexes were characterized by physico-chemical method, and their structures were confirmed by single crystal X-ray determination. The copper complex has strong urease inhibitory activity, which deserves further study to explore novel and efficient urease inhibitors.

Supplementary Data

CCDC 1998916 (HL^2), 1547384 (**1**) and 1813293 (**2**) contain the supplementary crystallographic data for this paper. These data can be obtained free of charge *via* http://www.ccdc.cam.ac.uk/conts/retrieving.html, or from the Cambridge Crystallographic Data Centre, 12 Union Road, Cambridge CB2 1EZ, UK; fax: (+44) 1223-336-033; or e-mail: deposit@ccdc.cam.ac.uk. The IR and UV-Vis spectra are given in the supplementary information.

5. References

1. (a) T. Myrach, A. T. Zhu, C. P. Witte, *J. Biol. Chem.* **2017**, *292*, 14556–14565; **DOI:**10.1074/jbc.M117.780403
   (b) T. Arshad, K. M. Khan, N. Rasool, U. Salar, S. Hussain, H. Asghar, M. Ashraf, A. Wadood, M. Riaz, S. Perveen, *Bioorg. Chem.* **2017**, *72*, 21–31; **DOI:**10.1016/j.bioorg.2017.03.007
   (c) S. Yalcin, A. Basman, *Food Chem.* **2015**, *169*, 203–210. **DOI:**10.1016/j.foodchem.2014.07.114
2. A. B. Mira, H. Cantarella, G. J. M. Souza-Netto, L. A. Moreira, M. Y. Kamogawa, R. Otto, *Agr. Ecosyst. Environ.* **2017**, *248*, 105–112. **DOI:**10.1016/j.agee.2017.07.032
3. R. J. Dempsey, N. A. Slaton, R. J. Norman, T. L. Roberts, *Agron. J.* **2017**, *109*, 363–377. **DOI:**10.2134/agronj2016.06.0374
4. (a) M. Taha, N. H. Ismail, S. Imran, A. Wadood, F. Rahim, M. Riaz, *J. Bioorg. Med. Chem.* **2015**, *23*, 7211–7218; **DOI:**10.1016/j.bmc.2015.10.017
   (b) Z. Amtul, R. A. Siddiqui, M. I. Choudhary, *Curr. Med. Chem.* **2002**, *9*, 1323–1348; **DOI:**10.2174/0929867023369853
   (c) M. A. S. Aslam, S. U. Mahmood, M. Shahid, A. Saeed, J. Iqbal, *Eur. J. Med. Chem.* **2011**, *46*, 5473–5479; **DOI:**10.1016/j.ejmech.2011.09.009
   (d) A. Saeed, S. Zaib, A. Pervez, A. Mumtaz, M. Shahid, J. Iqbal, *Med. Chem. Res.* **2013**, *22*, 3653–3662; **DOI:**10.1007/s00044-012-0376-4
   (e) A. Saeed, M. S. Khan, H. Rafique, *Bioorg. Chem.* **2014**, *52*, 1–7. **DOI:**10.1016/j.bioorg.2013.10.001
5. (a) C. L. Jing, C. F. Wang, K. Yan, K. D. Zhao, G. H. Sheng, D. Qu, F. Niu, H. L. Zhu, Z. L. You, *Bioorg. Med. Chem.* **2016**, *24*, 270–276; **DOI:**10.1016/j.bmc.2015.12.013
   (b) Y. Y. Zhu, C. F. Wang, K. Yan, K. D. Zhao, G. H. Sheng, Q. Q. G. Hu, L. Y. Zhang, Z. L. You, *J. Coord. Chem.* **2016**, *69*, 2493–2499; **DOI:**10.1080/00958972.2016.1186801
   (c) Z. L. You, M. Y. Liu, C. F. Wang, G. H. Sheng, X. L. Zhao, D. Qu, F. Niu, *RSC Advances* **2016**, *6*, 16679–16690; **DOI:**10.1039/C6RA00500D
   (d) D. Qu, F. Niu, X. L. Zhao, K. X. Yan, Y. T. Ye, J. Wang, M. Zhang, Z. L. You, *Bioorg. Med. Chem.* **2015**, *23*, 1944–1949; **DOI:**10.1016/j.bmc.2015.03.036
   (e) X. F. Chen, C. F. Wang, S. Kong, C. Li, X. Zhou, C. Y. Zhang, G. H. Sheng, H. L. Zhu, *J. Struct. Chem.* **2017**, *58*, 797–803. **DOI:**10.1134/S0022476617040229
6. (a) Z. You, H. Yu, B. Zheng, C. Zhang, C. Lv, K. Li, L. Pan, *Inorg. Chim. Acta* **2018**, *469*, 44–50; **DOI:**10.1016/j.ica.2017.09.011
   (b) S. H. Guo, T. R. Wang, J. J. Xin, Q. Q. G. Hu, S. F. Ren, G. H. Sheng, L. Pan, C. L. Zhang, K. Li, Z. L. You, *J. Coord. Chem.* **2017**, *70*, 3449–3458; **DOI:**10.1080/00958972.2017.1390569
   (c) J. Wang, D. Qu, J. X. Lei, Z. L. You, *J. Coord. Chem.* **2017**, *70*, 544–555; **DOI:**10.1080/00958972.2016.1262538
   (d) L. Pan, C. F. Wang, K. Yan, K. D. Zhao, G. H. Sheng, H. L. Zhu, X. L. Zhao, D. Qu, F. Niu, Z. L. You, *J. Inorg. Biochem.* **2016**, *159*, 22–28. **DOI:**10.1016/j.jinorgbio.2016.02.017
7. Y. Tan, *Acta Chim. Slov.* **2019**, *66*, 1002–1009. **DOI:**10.17344/acsi.2019.5297
8. Bruker, SMART (Version 5.628) and SAINT (Version 6.02); Bruker AXS: Madison, Wisconsin, USA (1998).
9. G. M. Sheldrick, SADABS Program for Empirical Absorption Correction of Area Detector; University of Göttingen: Germany (1996).
10. G. M. Sheldrick, *Acta Crystallogr.* **2008**, *A64*, 112–122. **DOI:**10.1107/S0108767307043930
11. W.-J. Mao, P.-C. Lv, L. Shi, H.-Q. Li, H.-L. Zhu, *Bioorg. Med. Chem.* **2009**, *17*, 7531–7536. **DOI:**10.1016/j.bmc.2009.09.018

12. (a) F. Zhi, N. Shao, Q. Wang, Y. Zhang, R. Wang, Y. Yang, *J. Struct. Chem.* **2013**, *54*, 148–154;
DOI:10.1134/S0022476613010216
(b) X. L. Wang, Z. L. You, C. Wang, *J. Chem. Crystallogr.* **2011**, *41*, 621–624;
(c) J. Xu, T. Zhou, Z. Q. Xu, X. N. Gu, W. N. Wu, H. Chen, Y. Wang, L. Jia, T. F. Zhu, R. H. Chen, *J. Mol. Struct.* **2017**, *1128*, 448–454. **DOI:**10.1016/j.molstruc.2016.09.016
13. (a) K. Hu, G. M. Zhou, Z. Zhang, F. Y. Li, J. G. Li, F. P. Liang, *RSC Advances* **2016**, *6*, 36077–36084;
DOI:10.1039/C6RA03478K
(b) Z. You, H. Yu, Z. Li, W. Zhai, Y. Jiang, A. Li, S. Guo, K. Li, C. Lv, C. Zhang, *Inorg. Chim. Acta* **2018**, *480*, 120–126.
DOI:10.1016/j.ica.2018.05.020
14. H. Yu, S. Guo, J.-Y. Cheng, G. Jiang, Z. Li, W. Zhai, A. Li, Y. Jiang, Z. You, *J. Coord. Chem.* **2018**, *71*, 4164–4179.
DOI:10.1080/00958972.2018.1533959

Povzetek

Sintetizirali smo nov bakrov(II) kompleks [Cu(L^1)(NCS)(CH_3OH)] (**1**) in nove cinkov(II) kompleks [ZnCl_2(HL^2)]·CH_3OH (**2**) z vezavo 4-bromo-*N*'-(piridin-2-ilmetilen)benzohidrazida (HL^1) in 4-metoksi-*N*'-(piridin-2-ilmetilen)benzohidrazida (HL^2) ter ju okarakterizirali z elementno analizo, IR in UV-Vis spektroskopijo ter monokristalno rentgensko difrakcijo. Hidrazon HL^1 se koordinira na Cu atom v enolatni obliki, medtem ko se hidrazon HL^2 koordinira na Zn atom v karbonilni obliki. Rentgenska monokristalna analiza razkrije, da se hidrazona koordinirata na kovisnki atom preko piridinskega N atoma, imino N atoma in enolatnega/karbonilnega O atoma. Cu atom v kompleksu **1** je koordiniran kvadratno piramidalno, medtem ko je Zn atom v kompleksu **2** koordiniran trigonalno bipiramidalno. Proučili smo inhibitorni vpliv kompleksov na ureazo stročnice *Canavalia ensiformis*, ki kaže, da ima bakrov kompleks večjo aktivnost na ureazo.

Except when otherwise noted, articles in this journal are published under the terms and conditions of the Creative Commons Attribution 4.0 International License

Scientific paper

Determination of Camelina Oil Sterol Composition and Its Application for Authenticity Studies

Zala Kolenc,[1] Tanja Potočnik,[2] Urban Bren[1] and Iztok Jože Košir[2,*]

[1] *Faculty of Chemistry and Chemical Technology, University of Maribor, Smetanova ulica 17, SI-2000, Maribor, Slovenia*

[2] *Slovenian Institute of Hop Research and Brewing, Cesta Žalskega tabora 2, SI-3310 Žalec, Slovenia*

* *Corresponding author: E-mail: address: iztok.kosir@ihps.si. Tel.: 00386 03 71 21 608*

Received: 07-10-2020

Abstract

Camelina oil has a high sterol concentration and is rather expensive compared to other vegetable oils. Because of its higher price, it is often adulterated by the addition of other, cheaper oils. This study was performed to validate a method for sterol determination in camelina oil, enabling the detection of camelina oil adulteration. Sterol levels in camelina oil samples were determined by gas chromatography after saponification and solid phase extraction. The method was validated, and the results proved that the chosen method is specific and selective, repeatable and accurate. The quantitatively assessed average contents of sterols in camelina oil samples of Slovenian origin were 21.4 mg 100 g^{-1} for brassicasterol, 153.6 mg 100 g^{-1} for campesterol, 3.9 mg 100 g^{-1} for stigmasterol, and 447.0 mg 100 g^{-1} for β-sitosterol. Results of camelina oil authenticity studies regarding botanical origin, performed by Principal Component Analysis (PCA) and Regularized Discriminant Analysis (RDA) enabled us to differentiate 100 % camelina oils from camelina oils adulterated with 10%–40% added sunflower, rapeseed or soya oil.

Keywords: *Camelina sativa*; sterols, authenticity; botanical origin; chemometrics

1. Introduction

In Slovenia, the production of camelina (*Camelina sativa* (L.) *Crantz*) is maintained as an alternative oilseed crop with nutritionally important value in seed or oil form. Botanically, camelina belongs to the *Brassicaceae* family; it is also known as false flax, gold of pleasure, or leindotter.[1–4] Recently, camelina oil has been recognized as a potential functional food because of its positive properties and its chemical composition.[1–3] Camelina oil is also used for biofuel and in the cosmetics industry.[5] It is an economically beneficial crop plant as it is drought tolerant, with low need for pesticide and fertilizer inputs.[3] Dried camelina seeds contain 30%–40% oil, depending on the season of harvesting.[5] Camelina oil is produced by crushing and warm-pressing the seeds, although it is very susceptible to oxidation that can lead to oil quality loss.[3–5]

The nutritional value of a functional food depends on its chemical composition. Camelina oil is comprised of 50% polyunsaturated fatty acids, 40% α-linolenic acid, and about 15% linoleic acid.[1,3,4] Unlike other common cooking oils (such as soya, sunflower, or olive oil), camelina oil is the only oil containing oleic acid (15%–20%), gondoic acid (10%–15%) and erucic acid (3%).[1,4,5] From the nutritional point of view, a diet with camelina oil could improve n6/n3 balance.[1] Furthermore, camelina oil has self-protective antioxidative efficiency because of its high tocoferol content, 700 mg kg^{-1} on average (α-tocoferol, β-tocoferol, δ-tocoferol).[4,6] High glucosinolate content in camelina oil indicates it has more positive effects due to oxidative stability.[6] Toward the oil oxidation high phenolic compounds content as chlorogenic acid in the range of 128 mg kg^{-1} could have big impact on oil quality.[5]

Phytosterols (plant sterols) are considered to be nutritionally important dietary lipids as unsaponifiable components of oils. Recently, phytosterols have been incorporated into functional foods.[7] It has been suggested that phytosterols, in cooperation with other secondary plant metabolites, could act as cancer preventive substances.[8] Chemical structure and biochemical functions of phytosterols are similar to that of cholesterol, however there are differences in synthesis, intestinal absorption and metabolic rate. Consequently, phytosterols compete with cholesterol for absorption, causing the inhibition of cholester-

ol absorption, and the reduction of total plasma cholesterol and low-density lipid (LDL) cholesterol.[9–11] The exact mechanisms involved in the inhibition of cholesterol absorption are poorly understood, although there are various theories.[12] 30%–50% of cholesterol is absorbed into blood, while the phytosterols are absorbed in less than 15%.[13] Recent literature indicates that phytosterols are absorbed under the same conditions as cholesterol and other lipids.[7] It has been shown that a 2 g daily intake of stanols and sterols reduces LDL by 10%, while higher intakes of stanols and sterols does not result in bigger reduction of LDL.[13] More recently, a 10% reduction of total cholesterol concentration was observed in plant sterol therapy. In addition, there was no observed difference between low-fat diets and phytosterol consumption, resulting in a lowering of cholesterol levels.[10] Sitosterol, campesterol and stigmasterols are the most abundant phytosterols among more than 40 identified phytosterols in plant oils.[13]

Choosing the appropriate method for sterol concentration determination in vegetable oils is not an easy task, particularly where the mixture of the non-saponifiable components in food lipids results in a complex matrix. The analytical technique for sterol determination includes extraction, isolation, separation, purification, detection, and quantification steps. The combination of Solid Phase Extraction (SPE) with the use of a Gas Chromatography–Single Flame Ionization Detector (GC-FID) is considered as the most used and appropriate method for determination of sterol concentration.[2,9,12,14–21]

The aim of this study is to validate the method of sterol determination in camelina oil. Additionally, the weather effect on sterol concentration was checked. Due to its high quality, camelina oil is a target of fraudulent adulteration with cheaper products of lower quality. Therefore, in this study the validated method was used for authenticity studies in order to exclude oils adulterated with soya, sunflower, rapeseed, or other oils that belong to the same or different botanical families (*Asteroidae, Fabacae*, etc.) from 100 % camelina oils. Apparently, these oils are widely used for this purpose, especially soya and sunflower oil.[14,17] Rapeseed oil was used since it is quite common, relatively cheap, and falls into the same family as camelina (*Brassicacae*),[5,14] unlike of sunflower (*Asteroidae*) and soya (*Fabacae*). Some reports are available where camelina oil is considered to be unique according to the chemical composition in comparison to sunflower, rapeseed and soya oil.[1,5] To investigate the fraudulent adulteration of camelina oil, 10%–40% by weight of soya, sunflower or rapeseed oil was added. Obtained results of sterol concentration in analysis were then used as input parameters for PCA and RDA to determine if they could be used for the differentiation of pure camelina oil from other oils. PCA and RDA are multivariate statistical methods that are widely used in authenticity studies of agricultural and food products where botanical and geographical origins are investigated.[5,22]

2. Experimental

2. 1. Vegetable Oils

Twenty-one authentic camelina seed samples, representing *Camelina sativa* landrace grown by local farmers in the Koroška region, Slovenia, were obtained from suppliers and farmers in three consecutive years (2007, 2008, 2009) as described by Hrastar et al..[5] Samples were accompanied by the details of year of harvest. Seeds were cold pressed with a manual oil expeller (Piteba, The Netherlands) at room temperature. Pure sunflower, rapeseed, and soya oil was purchased at a local oil producer and used for preparing the adulterated samples. Samples were frozen at 20 °C until use.

2. 2. Chemicals

The reagents ethanol (99.8%), betulin (97.5%), chloroform (99.0%–99.4%), methanol (99.9%), stigmasterol (95%), campesterol (65%), brassicasterol (98%), and β-sitosterol (90%) were bought from Sigma-Aldrich. Potassium hydroxide was purchased from Riedel-de Haën. Bulk standards of individual sterols were prepared in a methanol/chloroform solution (5% v/v). Working reference standards were prepared in the following concentrations: campesterol (1 mg mL^{-1}), β-sitosterol (5 mg mL^{-1}), stigmasterol (10 mg mL^{-1}) and brassicasterol (5 mg mL^{-1}). All used chemicals were of p.a.

2. 3. Sample Preparation

Sample preparation is one of the most critical steps in the analysis. Saponification was first employed, followed by solid phase extraction.[18,19] For sterol determination, gas chromatography was used. Our protocol was developed based on the protocol described by Toivo et al. with minor modifications.[18]

We used 0.74 g of oil sample and 10 ml 0.5 M KOH in ethanol was added. After mixing, the samples were heated to 77 °C for 20 minutes and then cooled. Adding 10 ml of betulin (internal standard in concentration of 0.22 mg mL^{-1}) in chloroform was performed, and the solution was mixed well for 5 minutes. After the sludge settled, the liquid in upper portion of the container was used for further extraction. The phytosterols were then extracted by SPE, using C18-E cartridges (conditioned strata with silicon-based sorbent type), purchased from Phenomenex. The tubes volume was 6 mL and the sorbent mass 500 mg. For conditioning the cartridges were washed out with methanol (5 mL) and then with chloroform (5 mL). Then, in saponificated sample 1 mL of internal standard was added and transferred into the tube. Sterols were eluted with 15 mL methanol in chloroform (5 % v/v). The extract was evaporated to dryness with vacuum evaporation at 35 °C and the sterol fraction was re-dissolved in 1 mL of the same solvent (methanol in chloroform (5 % v/v) after it.

2. 4. Gas Chromatography

Gas chromatography was performed with Agilent model Hewlett-Packed 6890 gas chromatograph (Hoofdoorp, The Netherlands) equipped with a flame ionization detector. An HP-5 GC column (J&W Scientific, 30 m × 0.25 mm i.d. with film thickness 0.25 μm, 5% diphenil/95% dimethylpolysiloxan) was used. A constant flow of helium at 1 ml min^{-1} was used as a carrier gas in splitless mode. Injector temperature was 32 °C and the temperature of the detector was set to 300 °C. The temperature program was increased from 220 to 350 °C at a rate of 3 °C/min, and then kept at 350 °C an additional 6 minutes. The sample injection volume was 2 μL. Brassicasterol, stigmasterol, β-sitosterol, and campesterol were identified by comparing the retention times of the pure standards. For identification of brassicasterol, stigmasterol, β-sitosterol, and campesterol, the retention times were compared to external standards. Additionaly standards were added into the sample to check the matching of the increasing of individual peaks in chromatograms. The quantification was performed by using internal standard betulin.

2. 5. Method Validation

Specificity and selectivity was checked by comparison of retention times for brassicasterol, campesterol, stigmasterol and β-sitosterol. Repeatability and reproducibility was done on two consecutive days with six measurements of the same camelina oil sample. Recovery was performed with the addition of 16.7 mg of brassicasterol, 3.6 mg of stigmasterol, 81.2 mg of stigmasterol, and 16.6 mg of β-sitosterol sepaterely for each of them and the standards were added before the extraction of sample. The linearity of the method for standards was made with the calculation of correlation coefficient over the working range of 0.058 to 0.220 g L^{-1} for betulin, 0.00154 to 0.15 g L^{-1} for brassicasterol, 0.00544 to 0.6 g L^{-1} for campesterol, 0.00307 to 0.3 g L^{-1} for stigmasterol, and 0.0082 to 0.8 g L^{-1} for β-sitosterol.

2. 6. Weather Conditions' Impact to Sterol Composition in Camelina Oil

The sterol composition of samples from three different years was compared, considering the climate conditions of average temperature, amount of precipitation, and relative humidity during the growing season of March 1 through August 31. Climate data was obtained from the Slovenian Environmental Agency's weather forecast station Šmartno pri Slovenj Gradcu.

2. 7. Detection of Camelina Oil Adulteration

For adulteration analyses, the mixtures of camelina oil with sunflower, rapeseed, and soya oils at levels of 10, 20, 30, and 40% were prepared. Statistical analysis was performed using the SCANWIN software (Minitab Inc., USA). The applied chemometric methods were principal component analysis and regularized discriminate analysis.

3. Results and Discussion

3. 1. Method Validation

At first, camelina oil samples collected from Slovenian producers were used for the method validation in the laboratory. Chromatographic peaks were identified on the basis of retention time in comparison with the standards brassicasterol, campesterol, stigmasterol, and β-sitosterol, and the internal standard betulin. Retention times were from 7.20 to 8.05 minutes for sterols and 10.63 minutes for the internal standard betulin. A random sample was used to determine the specificity and selectivity of the method, as shown in Figure 1 and Table 1. The described sample preparation enabled the complete separation of the sterols of interest from the camelina oil. The results show that the method is specific and selective since there were no overlapping peaks.

Table 1. Retention times for sterols and internal standard (betulin).

Sterol name	t_r (min)	Linear Retention Indices	Identifier
brassicasterol	7.218	2640 iu	1
campesterol	7.419	2632 iu	2
stigmasterol	7.806	2739 iu	3
β-sitosterol	8.053	2731 iu	4
internal standard (betulin)	10.631	3090 iu	5

The validation shows the method is repeatable, reproducible, linear, and with good recovery of samples from 85.08 to 98.11%, together with acceptably low standard deviation (Table 2). Repeatability of the method was tested with 12 individual determinations at the concentrations comparable with those determined in real samples. Relative standard deviations for all four sterols were between 4.9 and 7.8% (Table 2). Accuracy was tested with relatively low concentrations with the standard addition of a particular sterol into the real sample. Recoveries for all four sterols were higher than 85% (Table 2). Linearity of the method was tested at 6 different concentrations covering the range where all analysed samples were found to be. The correlation coefficient were all higher than 0.99. For the purpose of method validation limits of detection and quantifications were not determined since all analysed sterols were present in the samples at much higher concentrations within the linear concentration range and the results for repeatability and accuracy showed satisfactory results.

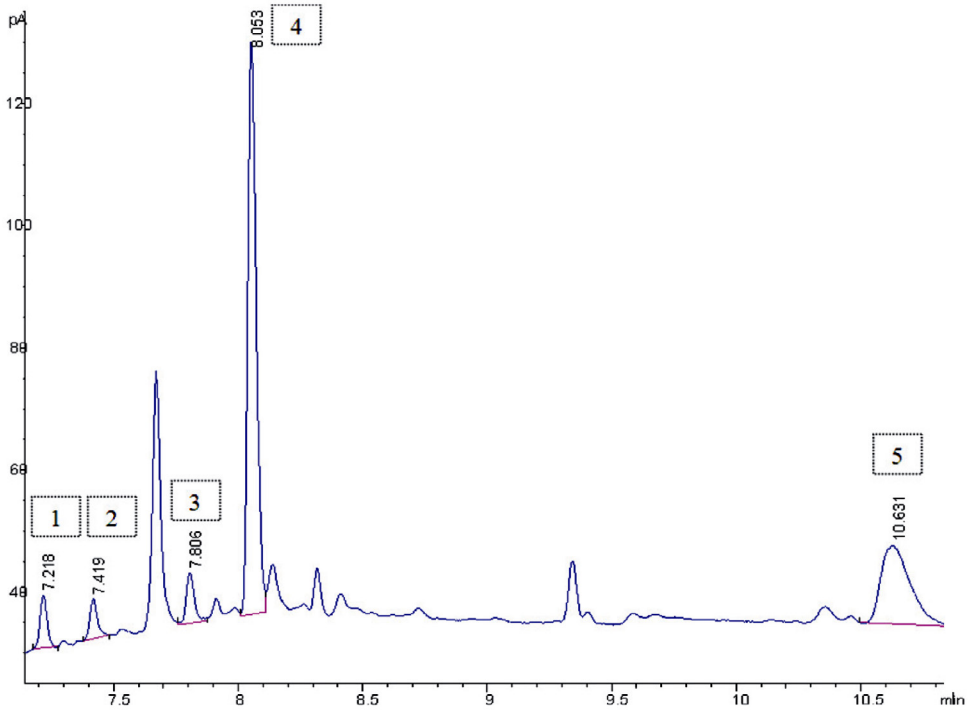


Figure 1. Gas chromatogram of camelina oil sample. Identifiers are the same as in Table 1.

Table 2. Results of the method validation parameters.

Sterol name	Linearity-range* (mg L^{-1})	Linearity – equation	Correlation coeficient – R^2	SD** (mg 100 g^{-1})	RSD (%)	Recovery*** (%)
brassicasterol	1.54 –150	y=1827x + 6.345	0.994	± 0.9	± 4.9	85.72
campesterol	5.44 –600	y=2588x – 19.05	0.997	± 11.2	± 6.6	89.95
stigmasterol	3.07 –300	y=2381x – 3.831	0.991	± 0.4	± 7.8	85.08
β-sitosterol	8.20 –800	y=2181x – 32.73	0.996	± 36.5	± 6.9	98.11

*linearity at 6 points **standard deviation at 12 repetitions for brassicasterol at concentration in oil 18.5 mg 100 g^{-1}, campesterol at concentration 177.5 mg 100g^{-1}, stigmasterol 5.1 mg 100 g^{-1}, **β-sitosterol** 521.1 mg 100 g^{-1}. ***recovery for brassicasterol at concetration 5.55 mg L^{-1}, campesterol at concentration 3.34 mg L^{-1}, stigmasterol at concentration 8.12 mg L^{-1}, **β-sitosterol at** concentration 16.67 mg L^{-1}.

3. 2. Sterol Content in Camelina Oil

Sterols were found in 21 samples of authentic camelina oil. The results for each year of production are presented in Table 3.

The average concentration of brassicasterol in all camelina oil samples, regardless of the year of production, was 21.4 mg 100 g^{-1}, which is comparable with other research results,[11] who found the same sterol in camelina oil in the concentration 27 mg 100 g^{-1}. For campesterol, we determined the concentration averaged 153.6 mg 100 g^{-1}, while in other research[11] it was determined their concentration as 117 mg 100 g^{-1}. In addition, the stigmasterol concentration of 3.9 mg 100 g^{-1} was comparable to other,[11] who found a concentration of 5.6 mg 100 g^{-1}. The β-sitosterol concentration was 447.0 mg 100 g^{-1} in our camelina samples, while Schwartz et al. found lower[11] but comparable values (300 mg 100 g^{-1}).

3. 3. Sterol Content in Three Different Years of Harvest

Detailed camelina oil samples of different harvest years were used to determine the correlation, and the effects of growth conditions, on sterol content as it was described for fatty acids and tocopherols.[1] The results of the sterol content analyses in camelina oil from the harvest years 2007, 2008, and 2009 revealed small differences. There were no statistically significant differences in sterol composition in the different harvest years. This was confirmed using calculated t-values between different years (data not shown here). The basic data for sterol composition in three consecutive years is presented in Table 3.

In Table 4, the weather conditions during the growing seasons (usually March 1 through August 31[2,5]) are described. There were no significant differences between

Table 3. Camelina oil samples detailed with year of oil production and sterol composition. Mean, Standard Deviation, Relative Standard Deviation, Minimum and Maximum of Camelina oil samples with regard to the year are given.

	Brassicasterol	Campesterol	Stigmasterol	β-sitosterol
Camelina oil samples (year 2007)				
Mean (N = 8) (mg 100 g^{-1})	23.2	162.6	3.8	492.1
± SD	5.1	21.5	1.8	65.1
± RSD (%)	22.1	13.2	48.5	13.2
min	18.7	134.8	1.7	391.0
max	34.5	199.4	6.9	549.7
Camelina oil samples (year 2008)				
Mean (N = 6) (mg 100 g^{-1})	20.6	153.8	4.3	432.5
± SD	4.3	20.5	1.5	59.0
± RSD (%)	21.1	13.4	35.0	13.6
min	15.9	135.8	2.1	405.0
max	27.7	187.7	6.6	552.8
Camelina oil samples (year 2009)				
Mean (N = 7) (mg 100 g^{-1})	20.1	143.1	3.6	407.8
± SD	3.6	18.9	1.8	54.3
± RSD (%)	18.0	13.2	49.1	13.3
min	16.1	121.8	1.4	324.1
max	26.6	176.4	5.6	472.5
Mean of all camelina oil samples (N=21) (mg 100 g^{-1})	**21.4**	**153.6**	**3.9**	**447.0**

Table 4. Weather conditions from March to August reported by the Slovenian Environmental Agency.

Year	Average temperature (°C)	Average relative humidity (%)	Total amount of precipitation (mm)
2007	14.7 ± 5.5	73.2 ± 4.4	798.4
2008	13.9 ± 6.2	74.8 ± 3.8	746.9
2009	14.5 ± 5.7	73.0 ± 2.4	706.5

the three years. There is no connection between weather conditions and sterol content.

3. 4. Sterol Content in Other Oils

Sunflower, rapeseed, and soya oils were also analyzed, and the sterol content of these oils is presented in Table 5.

For sunflower oil, there were concentrations detected at 35.9 mg 100 g^{-1}, 91.1 mg 100 g^{-1}, 91.5 mg 100 g^{-1}, and 345.5 mg 100 g^{-1}, respectively for brassicasterol, campesterol, stigmasterol and β-sitosterol. In another study were found lower concentrations of brassicasterol, campesterol and stigmasterol.[11] While the obtained β-sitosterol concentration was comparable with our results. For rapeseed oil, our results for sterol concentrations were comparable to similar research.[11,21] One study found brassicasterol content in rapeseed oil as 71–78 mg 100 g^{-1}, 271–315 mg 100 g^{-1} for campesterol, 3–5 mg 100 g^{-1} for stigmasterol, and 376–430 mg 100 g^{-1} for sitosterol.[11] Also, it was found that sterol composition of rapeseed oil was comparable to our results: brassicasterol 69.6 mg 100 g^{-1}, campesterol 232.5 mg 100 g^{-1}, stigmasterol 2.4 mg 100 g^{-1}, and β-sitosterol 324.7 mg 100 g^{-1}.[23] In soya oil, only two sterols were found: stigmasterol in average concentration of 114.7 mg 100 g^{-1}, and 314.7 mg 100 g^{-1} for β-sitosterol (Table 5, Figure 2).

3. 5. Authenticity Studies of Camelina Oil

For the authenticity studies, the sunflower, rapeseed and soya oils were used to adulterate camelina oil in ranges of 10, 20, 30, and 40%. The results of sterol determination are shown in Table 6.

Table 5. Sterol content in sunflower, rapeseed and soya oils used for adulteration.

	Sterol concentration (mg 100 g^{-1})			
Oil/sterol name	**Brassicasterol**	**Campesterol**	**Stigmasterol**	**β-sitosterol**
Sunflower	35.9 ± 3.2	91.1 ± 50.2	91.5 ± 13.0	345.5 ±142.5
Rapeseed	10.4 ± 5.1	472.4 ± 25.6	5.5 ± 5.7	565.9 ± 84.1
Soya	0.0	0.0	114.7 ±16.7	314.7 ± 8.0

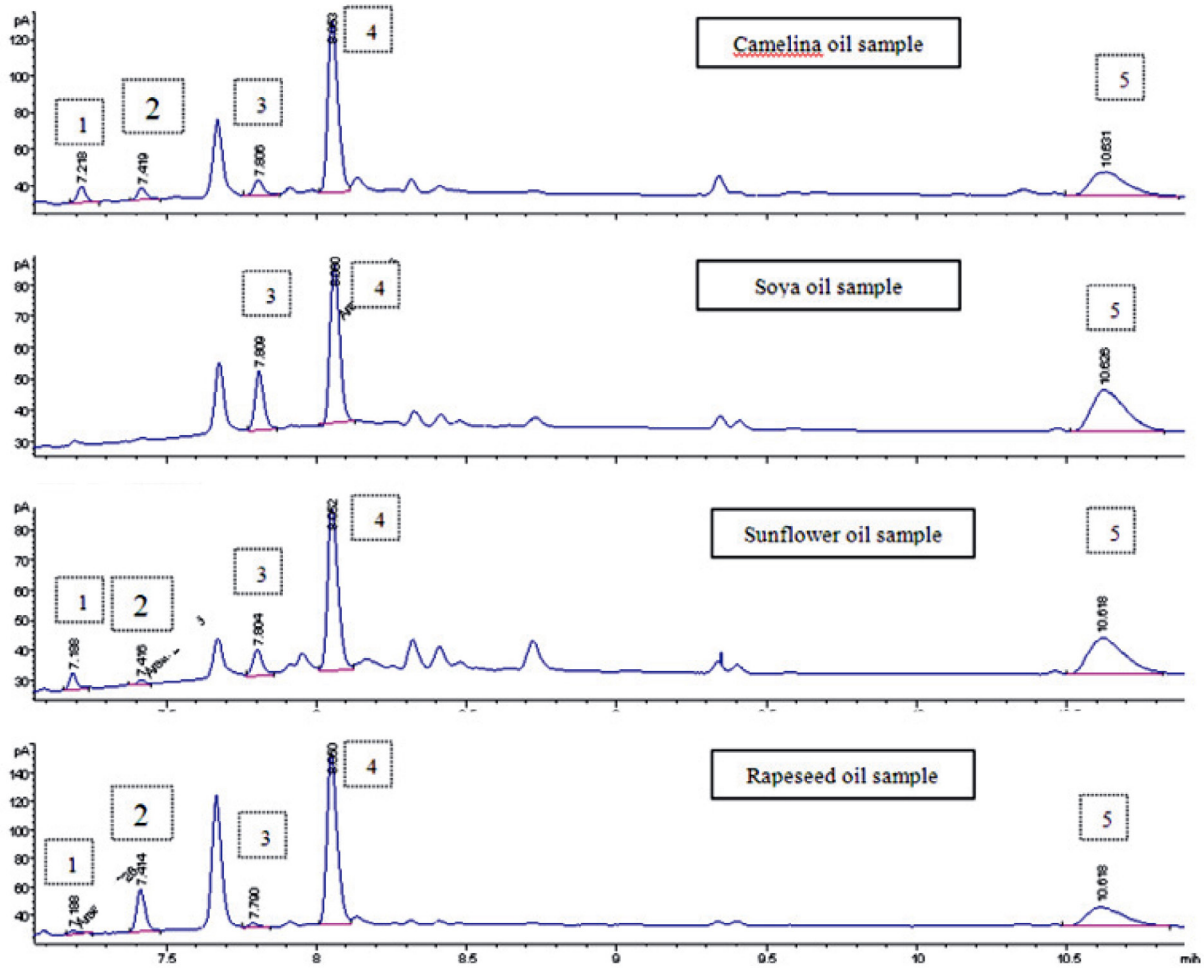


Figure 2. Comparison of camelina, soya, sunflower and rapeseed oil sample gas chromatogram: identifiers are the same as in Table 1.

Table 6. Sterol content of adulterated camelina oil (mg 100 g^{-1}) with sunflower, rapeseed or soya oil.

Oil mixture name	% of oil adulteration	Brassicasterol	Campesterol	Stigmasterol	β -sitosterol
Camelina+Sunflower	10 %	55.7	206.3	7.4	463.1
	20 %	41.0	182.8	9.8	437.6
	30 %	35.2	197.1	14.3	495.7
	40 %	43.9	172.3	17.6	460.4
Camelina+Rapeseed	10 %	48.2	275.7	9.8	585.7
	20 %	41.7	286.3	4.0	550.8
	30 %	40.2	314.8	6.9	568.8
	40 %	34.5	371.1	5.9	640.0
Camelina+Soya	10 %	50.7	277.3	23.1	648.2
	20 %	45.8	265.7	28.6	616.2
	30 %	41.1	251.7	45.7	569.9
	40 %	34.4	211.6	49.3	452.4

PCA (Figure 3) was applied to the data matrix formed by sterol composition in pure camelina oils, and in samples mixed with sunflower, rapeseed and soya oils. On the score plot of the first two principle components, which account for 60.6% and 22.7% of variance respectively, good visual discrimination was obtained. The first two PC account 83.3% of total variance, while PC3 and PC4 contain 12.4 and 4.3% of variance. Results clearly indicate that the PCA analysis separated pure camelina oil samples from the adulterated ones. Moreover, three different groups of adulterat-

ed oils were found, according to the oil used for adulteration. Comparison of the distribution taking into account also PC3 and PC4 has not resulted in a satisfactory discrimination of groups what is expectable since they are carrying low variance information of 12.4 and 4.3% only.

Table 7. Loadings values of the variables associated with principal components calculated using sterol composition data

Sterol name	PC1	PC2	PC3	PC4
brassicasterol	–0.520	–0.107	0.831	–0.167
campesterol	–0.563	0.315	–0.162	0.747
stigmasterol	–0.338	–0.885	–0.316	0.050
β-sitosterol	–0.546	0.326	–0.428	–0.642

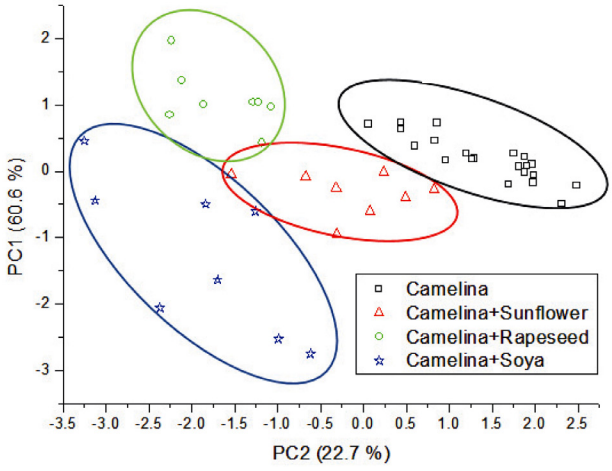


Figure 3. Projection of 21 objects of camelina oil and 4 for mixtures of camelina with sunflower oil, 4 for mixtures of camelina with rapeseed oil and 4 for mixtures of camelina with soya oil, onto the plot defined by the first and second principal components. The PCA model was calculated based on sterol composition.

The loading values of the variables associated to the first two principal components are reported in Table 7 and shown in Figure 4. In the Table 7 and Figure 4 the contribution of the variables to the more significant principal components is shown. According to these values, pure camelina oils are described as samples with the lowest campesterol, mixtures with soya oil contain highest amount of stigmasterol, while mixtures with rapeseed oil are the most abounded by campesterol.

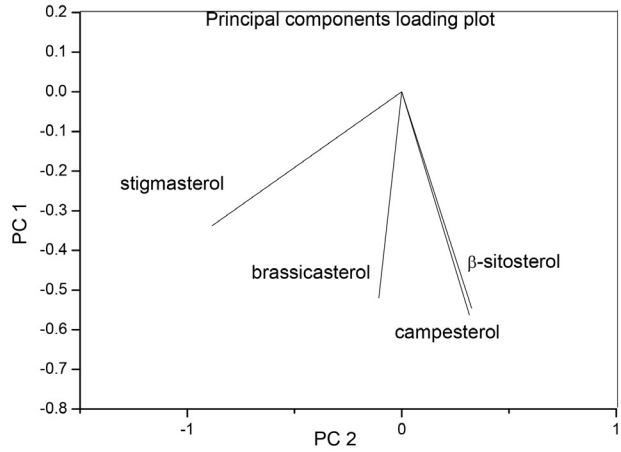


Figure 4. Principal components loading plot for PC1 and PC2 for the PCA model calculated based on sterol composition of 21 objects of camelina oil and 4 for mixtures of camelina with sunflower oil, 4 for mixtures of camelina with rapeseed oil and 4 for mixtures of camelina with soya oil.

After PCA (an example of an unsupervised chemometric method), RDA (an example of a supervised method), was used to calculate the model for discrimination of samples and to validate the constructed model. Analysis with RDA (Figure 5) resulted in the formation of

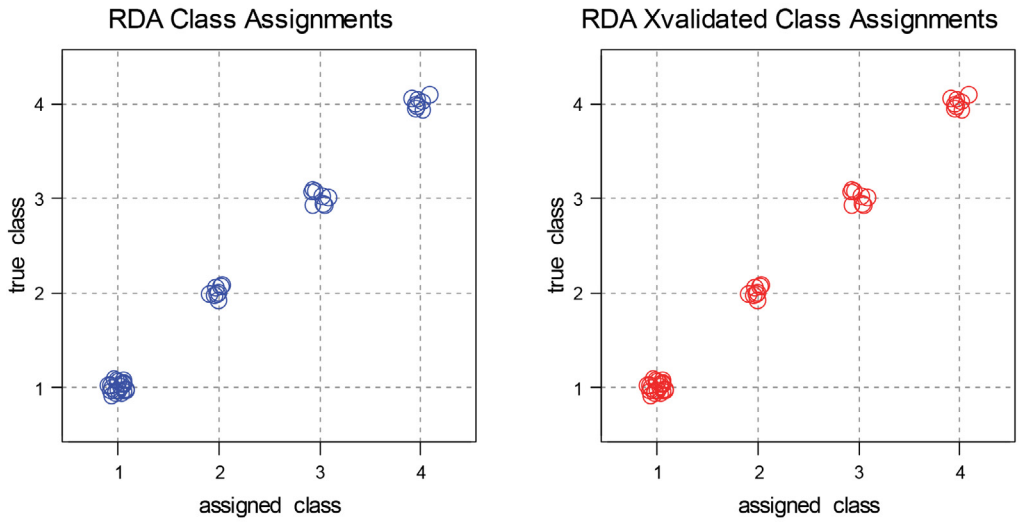


Figure 5. Classification of pure camelina oil and mixture clusters on the basis of the calculated RDA model and the results of validation model, using the cross-validation test. RDA model was calculated based on sterol composition. The RDA model was obtained based on sterol composition.

four classes: pure camelina oil, camelina oil adulterated with sunflower oil, camelina oil adulterated with rapeseed oil, and camelina oil adulterated with soya oil. All applied samples were identified correctly according to their botanical origin, independent of the amount of oils added.

4. Conclusions

In conclusion, the present work proves that the method used is appropriate for sterol determination in camelina oil. This study confirms the unique sterol composition of camelina oil as a prerequisite for authenticity studies, based on sterol determination using gas chromatography. Results of camelina oil authentication verify the use of authenticity studies based on sterol composition. For further research, it is recommended that sterol determination be combined with other minor components for adulteration investigations. This method would enhance the ability to prevent fraudulent adulteration.

Acknowledgements

This work was financially supported by the Slovenian Ministry of Education, Science and Sports through programme grants F4F, Ab Free and C3330-19-952022 and Slovenian Research Agency through research programme P1-0242.

5. References

1. J. Zubr, B. Matthäus, *Ind. Crop. Prod*. **2002**, *15*, 155–162. **DOI:**10.1016/S0926-6690(01)00106-6
2. J. Zubr, *Ind. Crop. Prod*. **1997**, *6*, 113–119. **DOI:**10.1016/S0926-6690(96)00203-8
3. L. Fan, N. A. M Eskin, *Recent Res. Devel. Lipids.* **2013**, *9*, 125–137.
4. H. Abramovič, V. Abram, *Food Technol. Biotechnol*. **2005**, *43*, 63–70.
5. R. Hrastar, M. G. Petrišič, N. Ogrinc, I. J. Košir, *J. Agric. Food Chem.* **2009**, *57*, 579–585. **DOI:**10.1021/jf8028144
6. M. A. Berhow, U. Polat, J. A. Glinski, M. Glensk, S. F. Vaughn, T. Isbell, I. Ayala-Diaz, L. Marek, C. Gardner, *Ind. Crop. Prod.* **2013**, *43*, 119–125. **DOI:**10.1016/j.indcrop.2012.07.018
7. G. García-Llatas, M. T. Rodríguez-Estrada, *Chem. Phys. Lipids.* **2011**, *164*, 607–624. **DOI:**10.1016/j.chemphyslip.2011.06.005
8. B. Cañabate-Díaz, S. Carretero, A. Fernández-Gutiérrez, A. Belmonte Vega, A. Garrido Frenich, J. L. Martínez Vidal, J. Duran Martos, *Food Chem*. **2007**, *102*, 593–598.
9. J. Toivo, K. Phillips, A. M. Lampi, V. Piironen, *J. Food Comp. Anal*. **2001**, *14*, 631–643. **DOI:**10.1006/jfca.2001.1019
10. M. H. Moghadasian, J. J. Frohlich, *Am. J. Med.* **1999**, *107*, 588–594. **DOI:**10.1016/S0002-9343(99)00285-5
11. H. Schwartz, V. Ollilainen, V. Piironen, A. M. Lampi, *J. Food Comp. Anal*. **2008**, *21*, 152–161. **DOI:**10.1016/j.jfca.2007.07.012
12. M. J. Lagarda, G. García-Llatas, R. Farré, *J. Pharmaceut. Biomed.* **2006**, *41*, 1486–1496. **DOI:**10.1016/j.jpba.2006.02.052
13. M. B. Katan, S. M. Grundy, P. Jones, M. Law, T. Miettinen, R. Paoletti, *Mayo Clin Proc*. **2003**, *78*, 965–978. **DOI:**10.4065/78.8.965
14. R. Aparicio, R. Aparicio-Ruíz, *J. Chromatogr. A*. **2000,** *881*, 93–104. **DOI:**10.1016/S0021-9673(00)00355-1
15. E. O. Aluyor, C. E. Ozigagu, O. I. Oboh, P. Aluyor, *Sci. Res. Essays.* **2009**, *4*, 191–197.
16. S. L. Abidi, *J. Chromatogr. A*. **2001**, *935*, 173–201. **DOI:**10.1016/S0021-9673(01)00946-3
17. K. M. Al-Ismail, A. K. Alsaed, R. Ahmad, M. Al-Dabbas, *Food Chem.* **2010**, *121*, 1255–1259. **DOI:**10.1016/j.foodchem.2010.01.016
18. J. Toivo, V. Piironen, P. Kalo, P. Varo, *Chromatographia*. **1998**, *48*, 745–750. **DOI:**10.1007/BF02467642
19. J. Toivo, A. M. Lampi, S. Aalto, V. Piironen, *Food Chem*. **2000**, *68*, 239–245. **DOI:**10.1016/S0308-8146(99)00201-0
20. C. Ö. Yücel, H. Ertaş, F. N. Ertas. *Turkish Journal of Agriculture – Food Science and Technology.* **2017**, *5*(11), 1274. **DOI:**10.24925/turjaf.v5i11.1274-1278.1267
21. A. Gorassini, G. Verardo, R. Bortolomeazzi, *Food Chem. 2019, 283*, 177–182. **DOI:**10.1016/j.foodchem.2018.12.120
22. I. J. Košir, M. Kocjančič, N. Ogrinc, J. Kidrič, *Anal. Chim. Acta*. **2001**, *429*, 195–206. **DOI:**10.1016/S0003-2670(00)01301-5
23. A. Szterk, M. Roszko, E. Sosińska, D. Derewiaka, P.P. Lewicki, *J. Am Oil Chem Soc.* **2010**, *87*, 637–645. **DOI:**10.1007/s11746-009-1539-4

Povzetek

Ričkovo olje ima visoko vsebnost sterolov in je v primerjavi z drugimi rastlinskimi olji precej drago. Zaradi višje cene so zelo pogoste potvorbe ričkovega olja z dodatkom drugih, cenejših olj. Zgoraj opisana študija je bila izvedena za potrditev metode za določanje sterolov v ričkovem olju, ki omogoča odkrivanje potvorb ričkovega olja. Koncentracije sterolov v vzorcih ričkovega olja so bile določene s plinsko kromatografijo, pred tem pa smo opravili saponifikacijo in ekstrakcijo na trdni fazi. Metoda je bila validirana, rezultati pa so dokazali, da je izbrana metoda specifična in selektivna, ponovljiva in natančna. Kvantitativno določena povprečna vsebnost sterolov v vzorcih ričkovega olja slovenskega izvora je bila 21,4 mg 100 g^{-1} za brasikasterol, 153,6 mg 100 g^{-1} za kampesterol, 3,9 mg 100 g^{-1} za stigmasterol in 447,0 mg 100 g^{-1} za β-sitosterol. Potvorbe ričkovega olja glede na botanični izvor olja, smo opravili z analizo glavnih komponent (angl. Principal Component Analysis, PCA) in z regulatorno analizo diskriminacije (angl. Regularized Discriminant Analysis, RDA). Rezultati študije so pokazali, da lahko ločimo 100 % ričkovo olja od ričkovega olja, ki je potvorjeno z 10 % – 40 % dodanega sončničnega, repičnega ali sojinega olja .

Except when otherwise noted, articles in this journal are published under the terms and conditions of the Creative Commons Attribution 4.0 International License

DOI: 10.17344/acsi.2020.6065 *Acta Chim. Slov.* **2020,** *67,* 1172–1179
creative commons

Scientific paper

Epoxy Functionalized Carboxymethyl Dextran Magnetic Nanoparticles for Immobilization of Alcohol Dehydrogenase

Katja Vasić,[1] Željko Knez,[1,2] Sanjay Kumar,[3] Jitendra K. Pandey[4] and Maja Leitgeb[1,2*]

[1] *University of Maribor, Faculty of Chemistry and Chemical Engineering, Smetanova 17, SI-2000 Maribor, Slovenia, phone: +386 2 2294 462, e-mail: maja.leitgeb@um.si*

[2] *University of Maribor, Faculty of Medicine, Taborska ulica 8, SI-2000 Maribor, Slovenia*

[3] *University of Petroleum and Energy Studies, Department of Chemistry, Dehradun, Uttarakhand, India*

[4] *University of Petroleum and Energy Studies, Research and Developments, Dehradun, Uttarakhand, India*

** Corresponding author: E-mail: maja.leitgeb@um.si*

Received: 04-25-2020

Abstract

Microbial inhibition of carboxymethyl dextran (CMD) magnetic nanoparticles (MNPs) was investigated on two different bacterial cultures, *Escherichia coli* and *Staphylococcus aureus*, where inhibition properties of CMD-MNPs were confirmed, while uncoated MNPs exhibited no inhibition properties. To such CMD-MNPs, enzyme alcohol dehydrogenase (ADH) from *Saccharomyces cerevisiae* was immobilized. Later on, CMD-MNPs were functionalized, using an epoxide cross-linker epiclorohydrin (EClH) for another option of ADH immobilization. Residual activities of immobilized ADH onto epoxy functionalized and non-functionalized CMD-MNPs were determined. Effect of cross-linker concentration, temperature of immobilization and enzyme concentration on residual activities of immobilized ADH were determined, as well. With optimal process conditions (4% (v/v) EClH, 4 °C and 0.02 mg/mL of ADH), residual activity of immobilized ADH was 90%. Such immobilized ADH was characterized using FT-IR, SEM and DLS analysis.

Keywords: Alcohol dehydrogenase, carboxymethyl dextran, epoxy functionalization, epichlorohydrin, enzyme activity

1. Introduction

As versatile and efficient enzyme, alcohol dehydrogenases (ADH) has always had an important role in modern green chemistry, especially since it can perform selective oxidations and reductions.[1,2] ADHs have many applications in production of various intermediates in chemical industries, such as production of chiral compounds, regeneration of different cofactors and in biosensors.[3-6] However, poor stability presents a limitation in the industrial use of ADH and many strategies have been developed to improve and increase its stability. These methods include protein engineering, chemical modification and most commonly used immobilization.[7–11]

Iron oxide nanoparticles are often used as nanocarriers for enzyme immobilization and present a promising tool in various medical fields, which has numerous clinical applications, such as targeted drug delivery, cell labelling, tissue repairment and various applications in biosensors.[12–16] Magnetic nanoparticles (MNPs) have unique properties, such as superparamagnetism, large surface area and low toxicity.[17–19] However, they are inclined to aggregate, because of their strong magnetic dipole.[20,21] To avoid such aggregation, modification of nanoparticles is in place. In our study, we used organic polymer carboxymethyl dextran (CMD) to provide better biocompatibility and biodegradability with low toxicity of synthesized MNPs.[22–25]

Modified MNPs are usually further functionalized using different functionalization groups. Epoxy functional group is a very active group, which can react with proteins, enzymes and nucleic acids, resulting in beneficial immobilization of biomolecules. Epoxy groups are also very stable

at neutral pH values, therefore different commercial supports can be prepared at a far position, where the enzyme has to be immobilized, which means epoxy-activated supports are very suitable biological systems to develop easy enzyme immobilization protocols.[26,27] EClH is an epoxide with bifunctional alkylating activity and is routinely used in the production of numerous synthetic materials, including epoxy, phenoxy and polyamide resins, cross-linked starch, surfactants and many pharmaceutical products.[28] There are studies describing epoxy-functionalized nanoparticles, modified with silica, as a carrier for immobilization of ADH from horse liver to be a suitable support for immobilization of ADH,[29,30] and studies reporting of immobilization of lipase and laccase covalently immobilized on magnetic microspheres, silica nanoparticles or chitosan magnetic beads via active epoxy groups.[31–33] All reported studies show the importance and significance of epoxy-functionalized nanoparticles, suitable for enzyme immobilization.

As there are many research studies investigating immobilization of ADH onto different magnetic supports, there are none that report about immobilization of ADH onto functionalized CMD-MNPs, using epichlorohydrin as an epoxide cross-linker. In our study, effect of process parameters was investigated, such as cross-linker concentration, temperature of immobilization and enzyme concentration to obtain the highest residual activity of immobilized ADH. Additionally, characterization of such immobilized ADH was performed using FT-IR, SEM and DLS analysis.

2. Materials and Methods

2. 1. Materials

CMD sodium salt, sodium phosphate, sodium pyrophosphate, EClH (1-Chloro-2,3-epoxypropane), ethanol, β-nicotinamide adenine dinucleotide (β-NAD) and ADH from *S. cerevisiae* were purchased from Sigma-Aldrich. Iron (III) chloride hexahydrate ($FeCl_3 \cdot 6H_2O$), iron (II) chloride tetrahydrate ($FeCl_2 \cdot 4H_2O$), Coomassie brilliant blue, Peptone from meat, Meat extract, agar, Yeast extract and Tryptic soy broth were obtained from Merck. Ammonium hydroxide was purchased from Chem-Lab, Belgium. All reagents in this work were of analytical purity and used without further purification. In all experiments, deionized water was used.

2. 2. Methods

2. 2. 1. Synthesis and Toxicity of CMD-MNPs

CMD-MNPs were prepared by protocol developed in our previous research, published by Vasić et al.[34] Further we wanted to investigate the toxicity of the prepared CMD-MNPs. This was tested on two different bacterial cultures, Gram negative *E. coli* and Gram positive *S. aureus*. Growth media for both bacterial cultures was prepared according to **Table 1**, later on sterilized and prepared as growth medium in a petri dish. *E. coli* and *S. aureus* with concentration of 10^5 CFU/mL were smeared on a petri dish, to which 10–30 mg of CMD-MNPs was added. Petri dishes with culture *E. coli* and *S. aureus*, together with CMD-MNPs, were incubated at 37 °C for 24 hours.

Table 1. Growth media for *E. coli* and *S. aureus*

E. coli		***S. aureus***	
Peptone from meat	5 g	Tryptic Soy Broth	30 g
Meat extract	3 g	Yeast extract	3 g
Agar	15 g	Agar	15 g
Distilled H2O	1 L	Distilled H_2O	1 L

2. 2. 2. Immobilization of ADH Onto CMD-MNPs

To CMD-MNPs, ADH and sodium acetate buffer (10 mM) were added with a volumetric ratio 1:9. Final ADH concentration in the reaction mixture was 0.02 mg/mL. Immobilization was carried out for 2 hours at 4 °C and 22 °C, with 500 rpm.

2. 2. 3. Epoxy Functionalization of CMD-MNPs

CMD-MNPs were functionalized with 4 % (v/v) EClH (0.5 M) in 10 mM sodium acetate buffer, pH 7.5. Functionalization was carried out with continuous mixing for 1 hour at 300 rpm and 22 °C. After functionalization, the supernatant was removed and epoxy functionalized CMD-MNPs were obtained.

2. 2. 4. Immobilization of ADH Onto Epoxy Functionalized CMD-MNPs

To epoxy functionalized CMD-MNPs, ADH and sodium acetate buffer (10 mM) were added with a volumetric ratio 1:9. Final ADH concentration in the reaction mixture was 0.02 mg/mL. Immobilization was carried out for 2 hours at 4 °C and 22 °C, with 500 rpm.

2. 2. 5. Assay for ADH Activity

The activity of soluble and immobilized ADH was determined spectrophotometrically using ethanol as a substrate. The standard reaction mixture in a total volume of 3 mL contained 22 mM sodium pyrophosphate, 3.2% (v/v) ethanol, 7.5 mM β-NAD, 0.3 mM sodium phosphate and 0.003 (w/v) % BSA. The reaction was initiated by the addition of ethanol and β-NAD to soluble or immobilized ADH, and subsequently the increase in absorbance at 340 nm due to formation of β-NADH was measured.

The activity of soluble and immobilized ADH was calculated using the following equation:

$$\frac{Units}{mL} enzyme = \\ = \frac{((\Delta A_{340\,nm} / \text{min}) \text{ of SAMPLE} - (\Delta A_{340\,nm} / min) of\ BLANK) * 3 * df}{6.22 * 0.1} \quad (1)$$

where:

3 – total volume (mL) of assay
df – dilution factor
6.22 – millimolar extinction coefficient of β-NADH at 340 nm
0.1 – volume (mL) of enzyme used

Enzymatic activity of ADH was measured in triplicates by enzymatic assay for ADH by Sigma-Aldrich protocol,[35] and the residual activity was calculated from the following equation:

$$Residual\ activity\ (\%) = \frac{\text{activity of immobilized ADH}}{\text{activity of soluble ADH}} * 100 \quad (2)$$

2. 2. 6. Protein amount determination and immobilization efficiency calculation

The protein amount of non-immobilized and immobilized ADH was determined by measuring the protein concentration by Bradford method using Bovine serum albumin (BSA) as a standard.[36] The amount of ADH immobilized on the surface of CMD-MNPs was determined on the basis of the protein amount in supernatant fraction (c_s) and later calculated by subtracting the measured amount (c_s) from the amount of non-immobilized ADH (c_e).

Immobilization efficiency was calculated using the following equation:

$$Immobilization\ efficiency\ (\%) = \frac{c_e - c_s}{c_e} * 100 \quad (3)$$

where:

c_s – protein concentration in supernatant fraction of immobilized ADH
c_e – protein concentration of non-immobilized ADH

All measurements for activity and protein amount determination were performed in triplicates and exhibited a standard deviation of less than 2%.

2. 3. Characterization

2. 3. 1. FT-IR

FT-IR spectra were recorded to study chemical bonds formed between ADH immobilized CMD-MNPs. FT-IR analysis of the samples was performed by pressing the samples to form a tablet using KBr as the matrix. The spectra were detected over a range of 4000–500 cm^{-1} and recorded by a FT-IR spectrophotometer (Perkin Elmer 1600 Fourier transform infrared spectroscopy spectrophotometer).

2. 3. 2. SEM

The morphology and size of CMD-MNPs and ADH-CMD-MNPs was investigated by SEM analysis using a scanning electron microscope (FE, SEM SIRION, 400 NC, FEI). The samples were measured on a gold (Au) substrate.

2. 3. 3. DLS

The particle size distribution, hydrodynamic size and ζ-potentials of the samples were measured using DLS (Zetasizer Nano ZS). Each diameter value was the average of three consecutive measurements. Higher values indicate a very broad size distribution, whereas lower values correspond to more or less monodisperse particle size distributions. Measurements were carried out under equilibrium conditions. Measured samples were dispersed in water with neutral pH at room temperature. Concentration of all CMD-MNPs and ADH-CMD-MNPs were 2 mg/mL.

3. Results and Discussion

3. 1. Toxicity of CMD-MNPs

Inhibition properties of synthesized CMD-MNPs on the growth of bacterial cultures *E. coli* and *S. aureus* were investigated, compared to uncoated magnetic nanoparticles. Qualitative assessment of inhibition properties was determined after incubation for 24 hours at 37 °C. If the

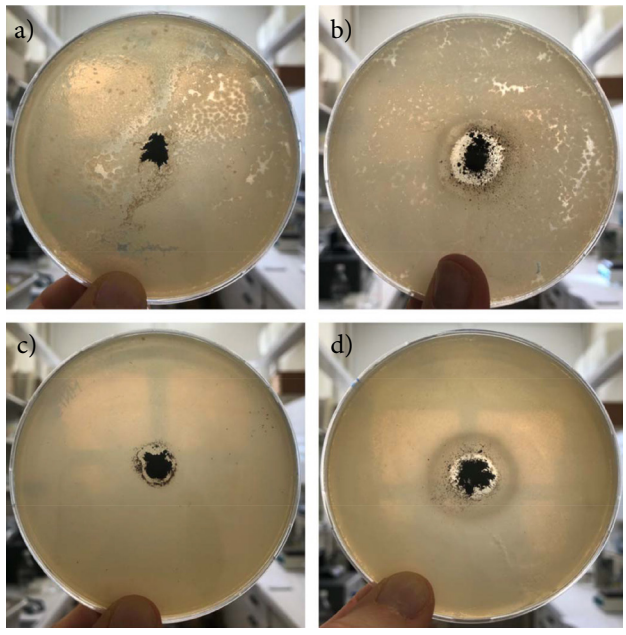


Figure 1. Uncoated MNPs on bacterial culture *E. coli* after incubation at 37 °C for 24 hours (a), CMD-MNPs on bacterial culture *E. coli* after incubation at 37 °C for 24 hours, where inhibition zone can be seen (b), uncoated MNPs on bacterial culture *S. aureus* after incubation at 37 °C for 24 hours (c) and CMD-MNPs on bacterial culture *S. aureus* after incubation at 37 °C for 24 hours, where inhibition zone can be seen (d).

inhibition zone was present, additional quantitative assessment was performed. **Figure 1** shows that inhibition occurs when CMD-MNPs were incubated with both bacterial cultures, while uncoated MNPs exhibited no inhibition properties. Additional quantitative assessment revealed that the average inhibition zone was 19.7 mm when incubated with *E. coli* and 19 mm, when incubated with *S. aureus*. CMD-MNPs exhibit antibacterial properties, since they are modified with organic polymer CMD. The modification of MNPs with organic polymers makes MNPs biocompatible, biodegradable and mostly non-toxic, which is a favourable advantage with using suitable support for immobilization of enzymes.[17,18,37]

3. 2. ADH Immobilization

ADH was immobilized onto CMD-MNPs, which were not epoxy functionalized and onto epoxy functionallized CMD-MNPs at two different immobilization temperatures, 4 °C and 22 °C. As seen from **Figure 2a**, residual activities increased drastically, when ADH was immobilized onto epoxy functionalized CMD-MNPs. Residual activity at 22 °C increased from 15% to 39%, while at 4 °C it increased even more, from 26% to 87%. Results suggest that epoxy functionalized CMD-MNPs ensure more successful immobilization of ADH onto the surface of the carrier, since the functionalization of CMD-MNPs provides additional epoxy functional groups, to which the amino groups of the enzyme can bind.

Further, we the influence of cross-linker concentration on the residual ADH activity was studied. The concentration of EClH was optimized by performing immobilization of ADH onto CMD-MNPs with different volumetric ratios of 0.5 M EClH as a cross-linking reagent. Enzyme residual activity was determined with the help of enzymatic assay for ADH determination, using ethanol as a substrate and immobilization efficiency was determined with the help of estimating the protein concentration with Bradford method in supernatants after immobilization and 2 times washing of the immobilized ADH-CMD-MNPs. As shown in **Figure 2b**, when applying 2% (v/v) of EClH, the residual activity was very low, only 19%, which could suggest that low cross-linker concentration gives poor mechanism strength, easily leading to leaching of the enzyme from carrier support. By doubling the concentration of cross-linker EClH to 4% (v/v), the residual activity started to increase and was found to be optimal volumetric concentration, since it retained 88% of the original enzyme activity. With increasing cross-linker concentration, the amount of free active groups on the surface of the carrier resulted in higher ADH loading, causing higher residual activity of immobilized ADH. Also, immobilization efficiency was very high, resulting in 100%. In this case, immobilization efficiency goes hand-in-hand with the residual activity of ADH. With doubling the concentration of cross-linker EClH again, to 8% (v/v), residual activity and enzyme immobilization efficiency started to decrease. The significant residual activity decrease to 21% at 8% (v/v) of EClH suggests that the limit of cross-linking was reached. Too high concentration of cross-linker can result in enzyme deactivation on one hand and on the other hand the loss of activity happens because access concen-

Table 1. Residual activities and immobilization efficiency of ADH immobilized onto epoxy functionalized CMD-MNPs, while investigating time of immobilization.

Time of immobilization [h]	Residual activity [%]	Immobilization efficiency [%]
2	87	100
12	37	96

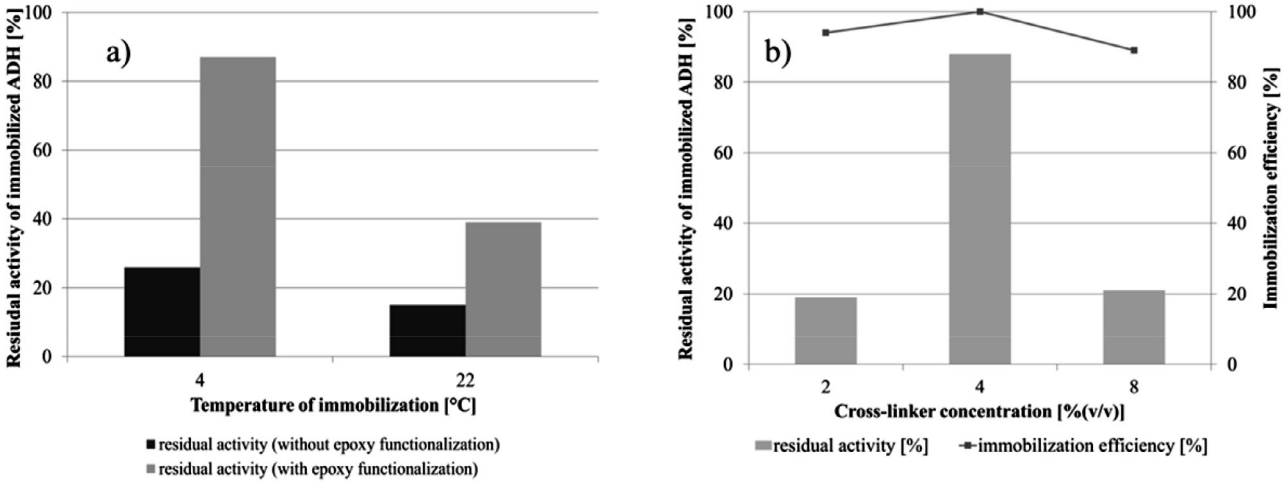


Figure 2. Residual activities of ADH immobilized onto CMD-MNPs, while investigating temperature of immobilization with and without epoxy functionalization (a) and cross-linker concentration (b).

trations of cross-linker result in blocking of enzyme active groups.[38] Immobilization efficiency was 89% for 8% (v/v) and 94% for 2% (v/v) of used EClH.

The influence of immobilization time is presented in **Table 1**. At first, immobilization time was investigated at 2 hours, and later on prolonged to 12 hours. When performing immobilization for 2 hours, residual activity of immobilized ADH-CMD-MNPs of 87% with 100% immobilization efficiency was achieved. When the immobilization time was prolonged to 12 hours, the residual activity of immobilized ADH-CMD-MNPs decreased drastically, to 37% with 96% immobilization efficiency. The results indicate that the immobilization time has an important effect on residual activity of immobilized ADH-CMD-MNPs and that the optimal immobilization lasts for 2 hours, which is sufficient time to bind enzyme ADH effectively to CMD-MNPS surface with its highest possible activity.

Table 2. Residual activities and immobilization efficiency of ADH immobilized onto epoxy functionalized CMD-MNPs, while investigating enzyme concentration.

Enzyme concentration [mg/mL]	Residual activity [%]	Immobilization efficiency [%]
0.02	87	100
0.04	42	31

An increase in ADH concentration is suggested to yield in a more active product. However, with increase of enzyme concentration to 0.04 mg/mL the residual activity of immobilized ADH-CMD-MNPs decreased. When the ADH concentration was increased from 0.02 mg/mL to 0.04 mg/mL the residual activity decreased to 42% and immobilization efficiency decreased slightly more, to 31%. Results can be observed in **Table 2**. The decrease in residual activity with increasing enzyme concentration can be attributed to the oversaturation of the enzyme over the support surface. As enzyme has an active site, it is available for substrate binding to form a product. When enzyme molecules crowd on the support surface, due to high enzyme concentration, enzyme molecules tend to overlap each other. That overlapping leads to inaccessibility of enzyme molecules' active sites, therefore can not be bind with the substrate. As a consequence of this inaccessibility, the product can not be formed, which is expressed as reduced enzyme activity or denaturation of immobilized enzyme.[39–42]

3. 3. Characterization

3. 3. 1. FTIR, SEM, DLS

Present peaks from FT-IR spectra of CMD-MNPs, ADH-CMD-MNPs and free ADH are presented in **Table 3**. ADH enzyme complex in ADH-CMD-MNPs shows characteristic absorption peaks at 1330 cm^{-1}, 1640 cm^{-1} and 1450 cm^{-1} which can also be observed in the free ADH spectra, exhibiting characteristic frequencies of ADH complex at 1640 cm^{-1} and 1390 cm^{-1}. The symmetric ring stretching frequency of the epoxy ring around 813, 921, and 1269 cm^{-1} were presented, indicating the existence of epoxy group on epoxy functionalized CMD-MNPs. The absorption peaks at 569 cm^{-1} and 682 cm^{-1} belong to the stretching vibration modes of Fe–O bond of synthesized MNPs. Characteristic adsorption peaks are shown at 1010 cm^{-1}, which corresponds to CMD νC–O vibrations, while the broad absorption peak at 3408 cm^{-1} corresponds to the characteristic νO–H stretching and δO–H deformation modes of CMD hydroxyl groups, also CMD carboxyl groups are represented in absorption peak at 1642 cm^{-1}. FT-IR spectra is available in Supplementary Material 1.

The morphology of epoxy functionalized CMD-MNPs with immobilized ADH was investigated by SEM. **Figure 3** shows SEM images of CMD-MNPs and epoxy functionalized ADH-CMD-MNPs. It is evident that CMD-MNPs and ADH-CMD-MNPs are spherical in shape and monodispersed. However, before immobilization of ADH, CMD-MNPs had more uniform size, which was in average 28 nm, as can be observed in our previous

Table 3. Peaks from FT-IR spectra, present in soluble ADH, CMD-MNPs and ADH-CMD-MNPs.

Wavenumber [cm^{-1}]	Functional group	Soluble ADH	CMD-MNPs	ADH-CMD-MNPs
569	Fe-O		x	x
682	Fe-O		x	x
813	epoxy		x	x
921	epoxy		x	x
1010	νC–O		x	x
1269	epoxy		x	x
1330	ADH complex	x		x
1390	ADH complex	x		x
1450	ADH complex	x		x
1640	ADH complex	x		x
3408	νO–H, δO–H		x	x

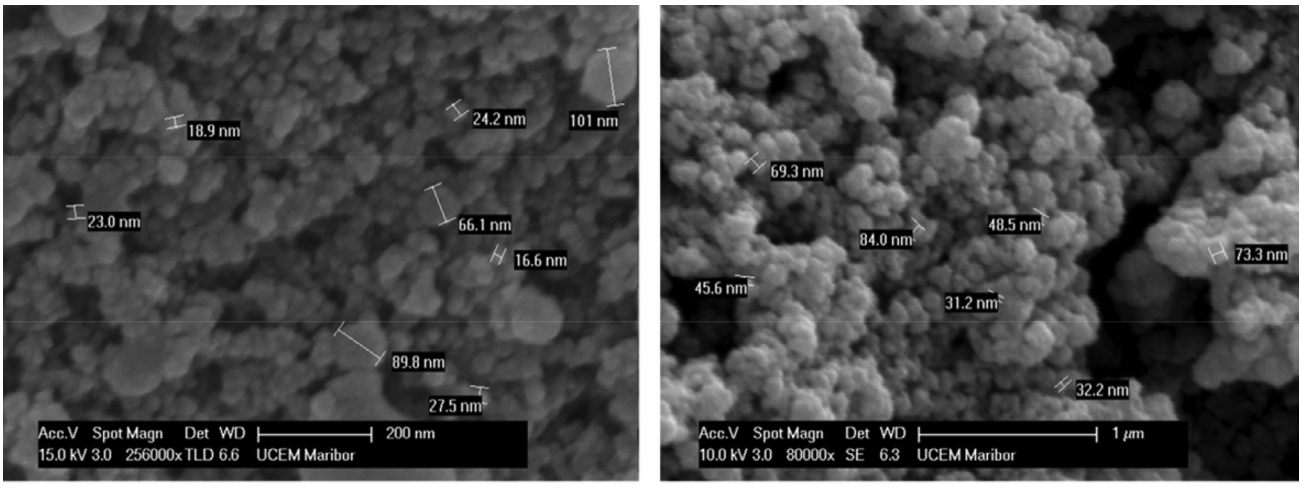


Figure 3. SEM images of CMD-MNPs (left) and ADH-CMD-MNPs (right).

research.[34] After immobilization CMD-MNPs are covered with a layer of enzyme due to epoxy functionalization, which allows ADH to covalently bind to CMD-MNPs. The sizes are slightly uneven and increased in diameter, ranging from 57 nm to 84 nm. Therefore, SEM images give additional evidence that ADH has been successfully bound to the surface of CMD-MNPs by covalent attachment resulting in the nano-sized product.

Zeta potential of CMD-MNPs and ADH-CMD-MNPs was measured to indicate the stability of colloidal dispersion. Both prepared CMD-MNPs and immobilized ADH-CMD-MNPs exhibit negative zeta potentials, –31.9 mV and –26.8 mV, respectively, which indicate negatively charged hydroxyl and carboxyl groups of CMD present on the surface of nanoparticles. Zeta potentials indicate that CMD-MNPs and ADH-CMD-MNPs show good dispersion in the aqueous phase. The size distribution of nanoparticles is expressed in polydispersity index (PdI). The PdI of ADH-CMD-MNPs is slightly higher, which is due to the layer of ADH, immobilized on the surface of CMD-MNPs, which can also be observed from SEM images. Because ADH-CMD-MNPs are slightly uniform in size, the PdI index increases, as well. PdI values are presented in **Table 4**.

Table 4. Zeta-potential and PdI obtained by DLS analysis of CMD-MNPs and ADH-CMD-MNPs. Sample

Sample	Zeta-potential (mV)	PdI
CMD-MNPs	–31.9	0.31
ADH-CMD-MNPs	–26.8	0.53

4. Conclusions

To conclude, CMD-MNPs were successfully functionalized with cross-linking of epoxide EClH for covalent attachment of ADH. Cross-linker concentration, temperature of immobilization and enzyme concentration were successfully optimized, resulting in 90% of residual activity of immobilized ADH. Characterization of immobilized ADH onto functionalized CMD-MNPs revealed successful covalent attachment and confirmed immobilization of ADH. The resulting CMD-MNPs with immobilized ADH were spherical in shape and measured from 57 nm to 84 nm in diameter. The results indicated that epoxy functionalized CMD-MNPs are favourable for ADH immobilization.

Acknowledgment

The authors acknowledge the financial support from the Slovenian Research Agency, research core funding Nr. P2-0046 – "Separation Processes and Product Design" and research core funding Nr. J2-1725 – "Smart materials for bioapplications", "and grant INT/Slovenia/P-16/2014".

6. References

1. de Smidt, O.; du Preez, J. C.; Albertyn, J. *FEMS Yeast Res* **2008**, *8*, 967–978. **DOI:**10.1111/j.1567-1364.2008.00387.x
2. Raj, S. B.; Ramaswamy, S.; Plapp, B. V. *Biochemistry* **2014**, *53*, 5791–5803. **DOI:**10.1021/bi5006442
3. Hummel, W.; Kula, M.-R. *European Journal of Biochemistry* **1989**, *184*, 1–13. **DOI:**10.1111/j.1432-1033.1989.tb14983.x
4. Alpat, S.; Telefoncu, A. *Sensors (Basel)* **2010**, *10*, 748–764. **DOI:**10.3390/s100100748
5. Patel, R. N. *Coordination Chemistry Reviews* **2008**, *252*, 659–701. **DOI:**10.1016/j.ccr.2007.10.031
6. Demirkòran, N.; Ekinci, E. *Acta Chim Slov* **2012**, *59*, 302–306.
7. Bernal, C.; Rodríguez, K.; Martínez, R. *Biotechnology Advances* **2018**, *36*, 1470–1480. **DOI:**10.1016/j.biotechadv.2018.06.002
8. Cowan, D. A.; Fernandez-Lafuente, R. *Enzyme and Microbial Technology* **2011**, *49*, 326–346. **DOI:**10.1016/j.enzmictec.2011.06.023

9. Ahmad, R.; Sardar, M. *Biochemistry & Analytical Biochemistry* **2015**, *0*, 1–8. **DOI:**10.4172/2161-1009.1000178
10. Stojkovič, G.; Znidaršič-Plazl, P. *Acta Chim Slov* **2010**, *57*, 144–149.
11. Primožič, M.; Podrepšek, G.H.; Pavlovič, I.; Škerget, M.; Knez, Ž.; Leitgeb, M. *Acta Chimica Slovenica* **2019**, *66*, 732–739. **DOI:**10.17344/acsi.2019.5013
12. Hola, K.; Markova, Z.; Zoppellaro, G.; Tucek, J.; Zboril, R. *Biotechnology Advances* **2015**, *33*, 1162–1176. **DOI:**10.1016/j.biotechadv.2015.02.003
13. Tarvirdipour, S.; Vasheghani-Farahani, E.; Soleimani, M.; Bardania, H. *International Journal of Pharmaceutics* **2016**, *501*, 331–341. **DOI:**10.1016/j.ijpharm.2016.02.012
14. Agiotis, L.; Theodorakos, I.; Samothrakitis, S.; Papazoglou, S.; Zergioti, I.; Raptis, Y.S. *Journal of Magnetism and Magnetic Materials* **2016**, *401*, 956–964. **DOI:**10.1016/j.jmmm.2015.10.111
15. Masood, F. *Materials Science and Engineering: C* **2016**, *60*, 569–578. **DOI:**10.1016/j.msec.2015.11.067
16. Kravanja, G.; Primožič, M.; Knez, Ž.; Leitgeb, M. *Molecules* **2019**, *24*, 1–23. **DOI:**10.3390/molecules24101960
17. Leitgeb, M.; Heržič, K.; Podrepšek, G.H.; Hojski, A.; Crnjac, A.; Knez, Z. Toxicity of magnetic chitosan micro and nanoparticles as carriers for biologically active substances. *Acta Chim Slov* **2014**, *61*, 145–152.
18. Liu, G.; Gao, J.; Ai, H.; Chen, X. *Small* **2013**, *9*, 1533–1545. **DOI:**10.1002/smll.201201531
19. Markides, H.; Rotherham, M.; El Haj, A.J. *Journal of Nanomaterials* **2012**, *2012*, 1–11. **DOI:**10.1155/2012/614094
20. Hauser, A.K.; Mathias, R.; Anderson, K.W.; Zach Hilt, J. *Materials Chemistry and Physics* **2015**, *160*, 177–186. **DOI:**10.1016/j.matchemphys.2015.04.022
21. Wei, Y.; Han, B.; Hu, X.; Lin, Y.; Wang, X.; Deng, X. *Procedia Engineering* **2012**, *27*, 632–637. **DOI:**10.1016/j.proeng.2011.12.498
22. Agiotis, L.; Theodorakos, I.; Samothrakitis, S.; Papazoglou, S.; Zergioti, I.; Raptis, Y.S. *Journal of Magnetism and Magnetic Materials* **2016**, *401*, 956–964. **DOI:**10.1016/j.colsurfb.2012.10.030
23. Asmathunisha, N.; Kathiresan, K. *Colloids and Surfaces B: Biointerfaces* **2013**, *103*, 283–287. **DOI:**10.1016/j.nano.2016.01.005
24. Alcantara, D.; Lopez, S.; García-Martin, M.L.; Pozo, D. *Nanomedicine: Nanotechnology, Biology and Medicine* **2016**, *12*, 1253–1262. **DOI:**10.1016/j.taap.2010.08.029
25. Loh, J.W.; Yeoh, G.; Saunders, M.; Lim, L.-Y. *Toxicology and Applied Pharmacology* **2010**, *249*, 148–157. **DOI:**10.1021/bm0257661
26. Mateo, C.; Torres, R.; Fernández-Lorente, G.; Ortiz, C.; Fuentes, M.; Hidalgo, A.; López-Gallego, F.; Abian, O.; Palomo, J. M.; Betancor, L.; et al. *Biomacromolecules* **2003**, *4*, 772–777. **DOI:**10.2478/boca-2014-0001
27. Spinelli, D.; Coppi, S.; Basosi, R.; Pogni, R. *Biocatalysis* **2014**, *1*, 1–12. **DOI:**10.2478/boca-2014-0001.
28. National Toxicology Program Epichlorohydrin. *Rep Carcinog* **2011**, *12*, 180–183. **DOI:**10.1016/j.bbapap.2012.03.010
29. Petkova, G.A.; Záruba, K.; Král, V. *Biochimica et Biophysica Acta (BBA) - Proteins and Proteomics* **2012**, *1824*, 792–801. **DOI:**10.1016/j.ijbiomac.2016.03.031
30. Jiang, X.-P.; Lu, T.-T.; Liu, C.-H.; Ling, X.-M.; Zhuang, M.-Y.; Zhang, J.-X.; Zhang, Y.-W. *Int. J. Biol. Macromol.* **2016**, *88*, 9–17. **DOI:**10.1016/j.jmmm.2008.08.047
31. Lei, L.; Bai, Y.; Li, Y.; Yi, L.; Yang, Y.; Xia, C. *Journal of Magnetism and Magnetic Materials* **2009**, *321*, 252–258. **DOI:**10.1016/j.bej.2015.04.020
32. Babaki, M.; Yousefi, M.; Habibi, Z.; Brask, J.; Mohammadi, M. *Biochemical Engineering Journal* **2015**, *101*, 23–31. **DOI:**10.1007/s00449-009-0345-6
33. Bayramoglu, G.; Yilmaz, M.; Yakup Arica, M. *Bioprocess Biosyst Eng* **2010**, *33*, 439–448. **DOI:**10.1016/j.molcatb.2015.06.004
34. Vasić, K.; Knez, Ž.; Konstantinova, E.A.; Kokorin, A.I.; Gyergyek, S.; Leitgeb, M. *Reactive and Functional Polymers* **2020**, *148*, 1–13. **DOI:**10.1016/j.jbiotec.2006.01.028
35. Kägi, J.H.; Vallee, B.L. *J. Biol. Chem.* **1960**, *235*, 3188–3192. **DOI:**10.1016/j.jmmm.2010.08.008
36. Bradford, M.M. A rapid and sensitive method for the quantitation of microgram quantities of protein utilizing the principle of protein-dye binding. *Analytical Biochemistry* **1976**, *72*, 248–254. **DOI:**10.1016/j.ijbiomac.2014.10.045
37. Bystrzejewska-Piotrowska, G.; Golimowski, J.; Urban, P.L. *Waste Management* **2009**, *29*, 2587–2595. **DOI:**10.1016/j.btre.2018.e00260
38. Chen, H.; Zhang, Q.; Dang, Y.; Guowei, S. *Advanc Journal of Food Science and Technology* **2013**, *5*, 932–935. **DOI:**10.1016/j.ijbiomac.2008.01.005
39. Jiang, D.-S.; Long, S.-Y.; Huang, J.; Xiao, H.-Y.; Zhou, J.-Y. *Biochemical Engineering Journal* **2005**, *25*, 15–23. **DOI:**10.1016/j.procbio.2012.01.012
40. Prousoontorn, M.H.; Pantatan, S. *J Incl Phenom Macrocycl Chem* **2007**, *57*, 39–46. **DOI:**10.1016/j.reactfunctpolym.2020.104481
41. Talbert, J.N.; Goddard, J.M. *Colloids and Surfaces B: Biointerfaces* **2012**, *93*, 8–19. **DOI:**10.1016/j.colsurfb.2012.01.003.
42. Jamil, N.; Che Man, R.; Suhaimi, S.; Md Shaarani, S.; Iffah Mohd Arshad, Z.; Kholijah Abdul Mudalip, S.; Zubaidah Sulaiman, S. *Materials Today: Proceedings* **2018**, *5*, 22036–22042. **DOI:**10.1016/0003-2697(76)90527-3

Povzetek

Mikrobno inhibicijo magnetnih nanodelcev (MNP) prekritih z karboksimetil dekstranom (CMD) smo preučili na dveh bakterijskih kulturah, *Escherichia coli* in *Staphylococcus aureus.* Dokazali smo inhibicijske lastnosti CMD-MNP-jev, medtem ko neprekriti MNP-ji niso imeli te lastnosti. Na CMD-MNP smo imobilizirali alkohol dehidrogenazo (ADH) iz *Saccharomyces cerevisiae.* Poleg tega smo CMD-MNP-je funkcionalizirali z zamreževalcem epiklorhidrinom (EClH) kot alternativa za ADH imobilizacijo. Primerjali smo aktivnost ADH imobilizirane na epoksi funkcionalizirane CMD-MNP-je in nefunkcionalizirane. Pod optimalnimi pogoji priprave (4% (v/v) EClH, 4 °C in 0.02 mg/mL ADH) je imobilizirana ADH ohranila 90% aktivnosti. Tako imobilizirano ADH smo okarakterizirali z FT-IR, SEM in DLS.

Except when otherwise noted, articles in this journal are published under the terms and conditions of the Creative Commons Attribution 4.0 International License

DOI: 10.17344/acsi.2020.6067 *Acta Chim. Slov.* **2020,** *67,* 1180–1195
creative commons

Scientific paper

Elaboration of Lamellar and Nanostructured Materials Based on Manganese: Efficient Adsorbents for Removing Heavy Metals

Amina Amarray,[1*] Sanae El Ghachtouli,[1*] Mohammed Ait Himi,[1] Mohamed Aqil,[2] Khaoula Khaless,[3] Younes Brahmi,[2] Mouad Dahbi[2] and Mohammed Azzi[1]

[1] *Laboratoire Interface Matériaux – Environnement, Faculté des Sciences Ain-Chock, Université Hassan II de Casablanca, B.P 5366 Maarif, Casablanca, Maroc.*

[2] *Materials Science and Nano-engineering Department, Mohammed VI Polytechnic University (UM6P), Ben Guerir, Morocco.*

[3] *Department of Chemical and Biochemical Sciences, Green Process Engineering CBS. Mohammed VI Polytechnic University, Ben Guerir, Morocco.*

** Corresponding author: E-mail: s.elghachtouli@gmail.com.*

Received: 04-25-2020

Abstract

The lamellar and nanostructured manganese oxide materials were chemically synthesized by soft and non-toxic methods. The materials showed a monophasic character, symptomatic morphologies, as well as the predominance of a mesoporous structure. The removal of heavy metals Cd(II) and Pb(II) by the synthesized materials Na-MnO_2, Urchin-MnO_2 and Cocoon-MnO_2 according to the mineral structure and nature of the sites were also studied. Kinetically, the lamellar manganese oxide material Na-MnO_2 was the most efficient of the three materials which had more vacancies in the MnO_6 layers as well as in the space between the layers. The nanomaterials Urchin-MnO_2 and Cocoon-MnO_2 could exchange with the metal cations in their tunnels and cavities, respectively. The maximum adsorbed quantities followed the order (Pb(II): Na-MnO_2 (297 mg/g)>Urchin-MnO_2 (264 mg/g)>Cocoon-MnO_2 (209 mg/g), Cd(II): Na-MnO_2 (199 mg/g)>Urchin-MnO_2 (191 mg/g)>Cocoon-MnO_2 (172 mg/g)). Na-MnO_2 material exhibited the best stability among the different structures, Na-MnO_2 presented a very low amount of the manganese released. The results obtained showed the potential of lamellar manganese oxides (Na-MnO_2) and nanostructures (Urchin-MnO_2 and Cocoon-MnO_2) as selective, economical, and stable materials for the removal of toxic metals in an aqueous medium.

Keywords: Cadmium; lead; Wastewater; manganese oxide; kinetic; mesoporous structure

1. Introduction

The depletion of drinking water resources had been a global problem in recent years, due to water pollution by heavy metals mainly from intensive human activities. These pollutants were not biodegradable and toxic.[1] Moreover, all along the food chain, some of them were concentrated in living organisms, which posed major risks to the environment and human health.[2–4] This contamination was certainly the most serious case among the problems posed by environmental pollution.[5–7] Metal ions were more precisely cadmium and lead were generally released without appropriate treatment during industrial processes,[8,9] such as in metal factories, paint industries, battery production as well in the combustion of motor gasoline (lead), etc... Lead and cadmium were persistent metals in the subsoil. Consequently, lead contamination of soil and groundwater was a serious problem.[10] Exposure to Pb(II) and as it was known worldwide could damage the nervous system and be carcinogenic to humans.[11–14] It could also damage the kidneys, cellular processes, and the reproductive system.[15] Toxic symptoms could occur in several ways, such as anemia, insomnia, headaches, muscle weakness, hallucinations, and kidney

damage.[16] The United States Environmental Protection Agency had classified cadmium as a probable human carcinogen.[17] Chronic exposure to cadmium posed serious risks, including kidney dysfunction and high levels of exposure leading to death.[18] Environmental requirements were becoming increasingly stringent in the paint industry, as for all industrial activities.

Intensive research and development efforts were being used worldwide to develop effective processes to reduce or eliminate toxic metal ions in aqueous solutions using precipitation of several metals such as lead,[19] cadmium[20] and magnesium.[21] Still, they provided that this process was carried out at a pH between 8 and 11.[18,22] Others have used polyamide membranes to remove Cd(II)[23] and Cu(II)[24] cations by reverse osmosis. Other processes had adopted elaborate materials such as zeolite,[25,26] which had been used as an adsorbent to remove some heavy metals, but with adequate pretreatment systems for suspended solids removal before applying ion exchange. However, the application of these methods was limited due to their high energy costs, their complex operation and equipment, their secondary pollution, and the problem of regeneration. The adsorption technique had proven to be the most efficient process due to its simplicity, ease of implementation, and high efficiency over a wide range of concentrations.[27] Additionally, it was a cost-effective method for treating large quantities of wastewater containing low levels of pollutants.[28] Unlike many techniques based on oxidation/reduction reactions or photocatalytic reactions, adsorption remained a method that does not lead to the formation of products/by-products that may be more or less toxic, or that subsequently caused secondary contamination. For this purpose, several types of adsorbents had been used, either synthetic[29,30] or natural such as calcium hydroxyapatite (CaHAP)[31] and barium hydroxyapatite (BaHAP),[32] perlite which has been used to remove cadmium and nickel ions in the aqueous medium.[33] Peat,[34] carbon nanotubes,[35] alumina,[36] mesoporous silica,[37] and clays[38,39] had also been applied to remove or reduce some heavy metals at different concentrations. However, these adsorbents had several disadvantages. They were characterized by their low adsorption capacity, reactivity and long equilibrium time to remove heavy metals.[40–42]

The manganese oxides materials existed widely in a large variety of forms in the upper crust. They were very important minerals because of their abundance and high reactivity. They were the strongest oxides in soils and were characterized by high sorption power.[43] They had a high capacity to remove several organic pollutants from soils and sediments.[44]

In general, manganese oxides materials were characterized by a low point of zero charge (PZC),[45] a relatively large surface area, and strong acid sites, which gave them a high adsorption capacity and excellent oxidation and catalysis activity.[46] Moreover, the layered manganese oxide structure (lamellar structure) was used as an effective adsorbent to remove several heavy metals.[47] These materials had a variable number of octahedral cationic vacancies within the MnO_6 layers, which were important and significant adsorption sites for metal cation.[48] The MnO_6 layers in this type of structure were assembled in the form of sandwiches separated from each other to form spaces of 7 Å (birnessite) or 10 Å (buserite), this generated a large part of the sorption sites.[49] Tunnel structures were generally made up of single, double or triple chains that were connected by their vertices to form tunnels of square or rectangular cross-section with inserted cations (H^+ or K^+).[50]

The use of this type of material to remove metal cations was favorable and generally carried out by ion charge equilibrium exchange with cations inserted in tunnels that were characterized by a space of 4.6 Å.[51] The removal of several metals, including arsenic (III) and (V) from aqueous medium, had been studied using materials based on manganese with a compact structure (hausmannite).[52] Various studies had been carried out to remove several metals such as copper,[53] nickel,[54,55] lead,[56,57] cadmium[27] and zinc[58] ions using iron and modified manganese oxides as adsorbents. A research study reported that despite the high reactivity of iron oxides, the manganese oxides had shown an efficiency 40 times higher than iron oxides in the case of Pb(II) ions.[59] Indeed several studies have shown that the use of manganese oxides for the coating of some materials such as biochar (BC),[60] wool,[61] and zeolite,[62] allowed to increase their specific surface as well as the volume of the pores and consequently to favor the adsorption phenomenon. This showed the very important role of manganese oxides for the removal of metal ions from aqueous medium.

In this work, we investigated the possibility of removing Pb(II) and Cd(II) ions from the aqueous medium by three manganese oxide materials (marked as Na-MnO_2, Urchin-MnO_2, and Cocoon-MnO_2) with different lamellar structures and nanostructures. The composition, morphology, and distribution of the sites of each material were determined by different spectroscopic techniques. To better understand the removal process of Pb(II) and Cd(II) by manganese oxides materials, the effect of pH, kinetics and adsorption studies were examined. To study the stability of the materials, the total amount of manganese released during removal processes will be elucidated. These materials will be characterized by X-ray diffraction after interaction. To verify the reusability of the materials for the removal of Pb(II) and Cd(II), five successive cycles were performed, as well as examining their stability.

To better understand the removal process of Pb(II) and Cd(II) by manganese oxides materials the performing kinetic and adsorption studies were examined. Finally, these materials will be characterized after the interaction by X-ray diffraction. To study the stability of the materials,

the total amount of manganese released, and the amount of heavy metal removed will be elucidated.

2. Experimental Section

2. 1. Chemical Compounds

All chemicals used in this study were purchased from Sigma Aldrich (St. Louis, MO, USA) and were used without further purification. Solutions were prepared with demineralized water from the Adrona crystal water system (quality ≤ 0.05 μS/cm).

2. 2. Synthesis of Na-MnO_2

Manganese oxide Na-MnO_2 was obtained by precipitation at room temperature. During stirring, 10 mL of hydrogen peroxide mixed with 2.16 g of sodium hydroxide dissolved in 90 mL of water was added dropwise to the manganese sulfate solution ($MnSO_4$. H_2O) (2.535 g, 50 mL). The mixture remained agitated overnight at room temperature. The deep brown precipitate obtained after filtration was washed with water and ethanol. The product was recovered by filtration and dried at 50 °C.[63]

2. 3. Synthesis of Urchin-MnO_2 Nanostructure

Urchin manganese oxide MnO_2 nanostructure was synthesized by the reflux method under acidic conditions.[64] 2 g of manganese sulfate ($MnSO_4$. H_2O) was dissolved in 100 mL of distilled water. In a water bath and under vigorous stirring, 1 mL of sulfuric acid was added by dripping. After stirring, 66 mL of potassium permanganate (0.1 M) was added to the mixture. Stirring was maintained at 80 °C for 24 hours. The resulting black colored product was isolated and washed several times with water and absolute ethanol. Finally, the product obtained was dried at 60 °C.

2. 4. Synthesis of Cocoon-MnO_2 Nanostructures

Synthesis of manganese oxide type cocoon was based on the reduction of Mn(VII) and Mn(II) under ambient temperature conditions. [64] 100 mL of potassium permanganate $KMnO_4$ solution (0.1 M) was added dropwise under vigorous agitation to 150 mL of manganese sulfate solution (0.1 M). The resulting mixture was agitated for 6 hours. The resulting black colored product was isolated, washed several times with water and absolute ethanol, and dried at 60 °C.

2. 5. Chemical Analysis

The chemical composition of the three materials was determined by dissolving 0.1 g of sample with 1 g of hydroxylamine hydrochloride in 250 mL of the distilled water.[65] The resulting Mn, K, and Na content in the solution was determined by atomic absorption spectrometry device (Shimadzu AA-7000) (Shimadzu Corporation, Japon).

Manganese average oxidation state (AOS) was determined by potentiometric determination using sodium pyrophosphate. This method avoids errors related to mass and reagent concentration measurements, and the only parameters to be determined were equivalent volumes.[66] All chemical analysis was repeated three times, and the average was determined.

2. 6. Characterization

X-ray diffraction patterns were recorded on a Bruker D8 (Bruker, France S.A.S). Advance diffractometer equipped with a graphite monochromator, a Lynx-Eye detector, and parallel beam optics using Cu Kα radiation (λ = 1.5418 Å). Phase identification and material structures were determined by the High Score software (XRD data processing software).

The morphology of the particles of the various synthesized samples was studied by scanning electron microscopy (JEOL Ltd Gemini 15-25, Japon).

The specific surface area analysis was performed using the Brunauer-Emmett-Teller (BET) method and the pore size distribution was determined using the Barrett–Joyner–Halenda (BJH) method from N_2 adsorption and desorption isotherms using Micromeritics Gemini VII system (Micromeritics Instruments Corporation, USA). 0.1 g of the sample was degassed before measurement at 110 °C for 3 hours under vacuum equilibrium.

2. 7. Batch Experiment of Cd(II) and Pb(II) Removal

The Cd(II) and Pb(II) ions removal experiments were performed by placing 100 mg of the synthesized material in a 50 mL of an aqueous solution containing 30 ppm of the Cd(II) or Pb(II) respectively as $Cd(NO_3)_2$ or $Pb(NO_3)_2$. The content was agitated (500 rpm) during the interaction. The metal cation removal experiments were performed under ambient conditions at different values of pH. The solution pH was adjusted using NaOH (0.1 M) or H_2SO_4 (0.1 M). The solution was filtered through a 0.45 μm membrane, and the residual concentration of the metal cation Cd(II) and Pb(II) concentration in the solution was analyzed using atomic absorption spectrophotometer (AAS). This allowed us to evaluate the removal efficiency of heavy metal (R%) using Eq. (1) and the adsorbed amount q(t) in mg/g using Eq. (2). Measurements under the same conditions were proceeded three times.

$$R(\%) = \left(1 - \frac{C_r}{C_0}\right) x100 \quad (1)$$

$$q(t) = \frac{(C_0 - C_r)xV}{m} \quad (2)$$

Where: m: mass of manganese oxide material (100 mg).

V: Volume of the solution used (50 mL).

C_0 and C_r were the initial and residual concentrations of metal ions (cadmium or lead).

3. Results and Discussion

3. 1. XRD of MnO_2 Lamellar and Nanostructures

The diffractograms (Figure 1) of the synthesized manganese oxides, namely: Na-MnO_2, Cocoon-MnO_2, and Urchin-MnO_2, showed that materials were different and therefore, they don't had the same crystalline structure.

The diffractogram of the Cocoon-MnO_2 material (Figure 1) had a very low-intensity signal. This could be explained by the low crystallinity of the material. The poor crystallinity of the material was due to its synthesis at room temperature. The increase in the synthesis temperature made it possible to improve the material crystallinity but also to generate different morphologies.[64,67] Nevertheless, the diffractogram revealed the presence of two diffraction peaks at 2θ = 37° (311) and 65° (440), which had been indexed for the MnO_2 type structure. It was deduced that the sample was in a weakly crystalline state with α-MnO_2 crystallographic forms.[68] This material was characterized by a crystalline structure as $K_2Mn_4O_9$ (Table 1).

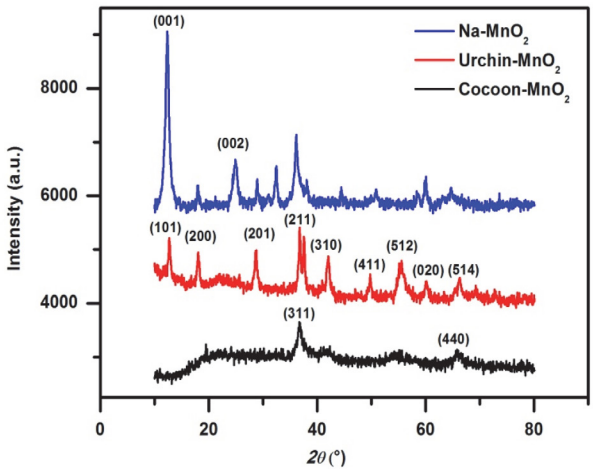


Figure 1. X-ray diffractograms of the synthesized manganese oxides materials.

For the Urchin-MnO_2 material, the diffractogram showed several well-defined and symmetrical peaks indicating that the material was well crystallized. The peaks observed, at 2θ =12.8° (101), 17.8° (200), 28.6° (201), 37.4° (211), 41.6° (310), 49.5° (411), 59.9° (512), 65° (020) and 69.7° (514), could easily be indexed with cryptomelane (KMn_8O_{16}) with a space group (I2/m(12) (JCPDS sheet No 44-1386).[64] This material had a tunnel structure whose cation K^+ was present in these cavities.[69]

The last diffractogram of Na-MnO_2 material, as shown in (Figure 1) had well-defined with symmetrical diffraction peaks (001) and (002) (JCPDS card #01-073-9669).[70] They indicated that material was single-phase mineral and well crystallized. This phase corresponds to the family of birnessite type sodium manganese, which has a layered structure with crystal water and Na^+ between the MnO_6 octahedral sheets.[71] This oxide had a basal spacing of 0.714 nm along the c-axis with a single crystal water sheet between the MnO_6 octahedral sheets. The diffraction peaks could be easily indexed as a monoclinic structure (space group: C2/m).[72] From the diffractograms, we noticed that the various synthesized oxides had slightly wide peaks. These materials had slightly different surface areas. The chemical formula, structures, the Mn (AOS) of each material were illustrated in Table 1. The spacing between layers for Na-MnO_2 and the size of the tunnels for Urchin-MnO_2 was calculated from the 2θ values of the peaks using a value of 1.541Å (copper anticathode wavelength).

Table 1. Crystalline parameters and composition of manganese oxide materials (Na-MnO_2, Cocoon-MnO_2, and Urchin-MnO_2).

Material	Chemical formula*	d (Å)	Mesh parameters (Å)*	Structure*	Composition in element (ppm)**	(AOS) of Mn
Na-MnO_2	$Na_{0.55}Mn_2O_4.(H_2O)_{1.5}$ (Birnessite)	7.14	a = 5.1750 b = 2.8490 c = 7.3380	Monoclinic	[Mn] = 388.87 [Na] = 75	3.580
Cocoon-MnO_2	$K_2Mn_4O_9$	–	a =b = 11.2950 c = 21.870	Hexagonal	[Mn] = 704. 16 [K] = 34.79	3.650
Urchin- MnO_2	KMn_8O_{16} (Cryptomelane)	4.85	a = b = 9.840 c = 2.850	Tetragonal	[Mn] = 637.86 [K] = 33.765	3.730

** determined by HighScore software. ** determined by atomic absorption spectroscopy (AAS).*

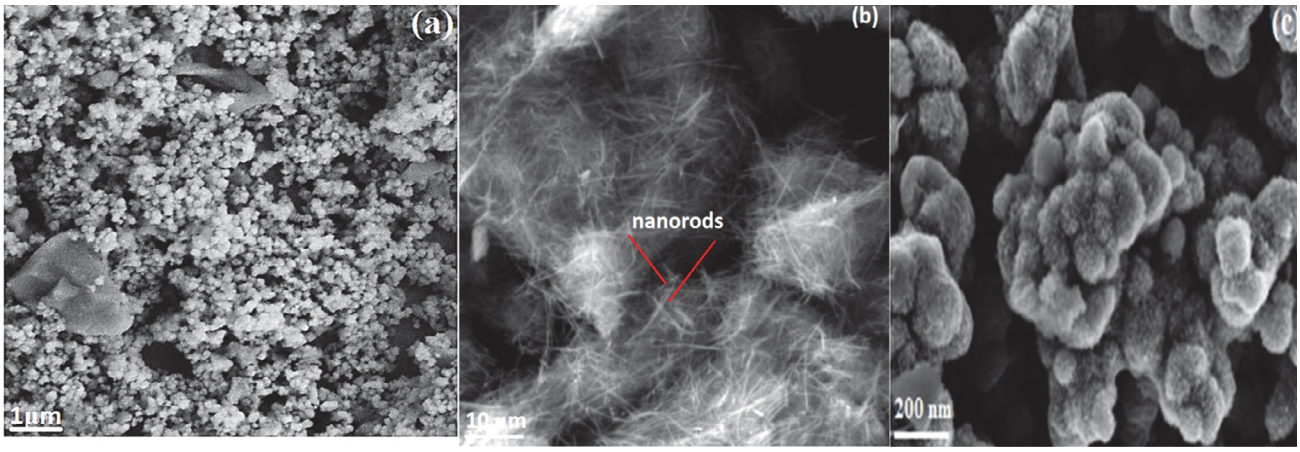


Figure 2. SEM images of (a) Na-MnO_2, (b) Urchin-MnO_2, and (c) Cocoon-MnO_2.

3. 2. SEM of MnO_2 Lamellar and Nanostructures

Scanning electron microscopy (SEM) was used to study the detailed surface morphology of the different synthesized materials. As seen in (Figure 2), the morphology of the materials was different.

The different SEM images showed that the surface morphology of these different materials was highly dependent on the preparation technique. Figure 2 showed that the Na-MnO_2 material (Figure 2 a) was composed of thin sheets which were agglomerated together to form particles several micrometers in size. The nanostructured material (Urchin-MnO_2) obtained at 80 °C (Figure 2 b) had an urchin morphology and composed of a large number of nanorods with different sizes intertwining each other while the material obtained at room temperature (Figure 2 c) had a cocoon-shaped morphology composed of microspheres.[64]

3. 3. Isotherm BET

All the characteristics of each material, including pore volume, pore size and specific surface area were determined using conventional nitrogen isothermal analysis. From Eq. (S1) we could determine the specific surface area of each material. The evolution of with of was linear (Figure 3).

Figure 3 showed the BET isothermal models for the three materials. The results of this study showed a high correlation between relative pressures $\frac{P}{P_0}$ and $\frac{1}{Q[(\frac{P_0}{P})-1]}$ that allowed us to determine the specific surface area of each material. According to Table 2, the three materials were characterized by a large specific surface area ranging from 30 to 44 m^2/g. These results showed that a large specific BET surface area provided an effective adsorbent. The BET surface of the Na-MnO_2 material was the lowest of the three materials, this weakness may be attributed to sodium insertion into the material.

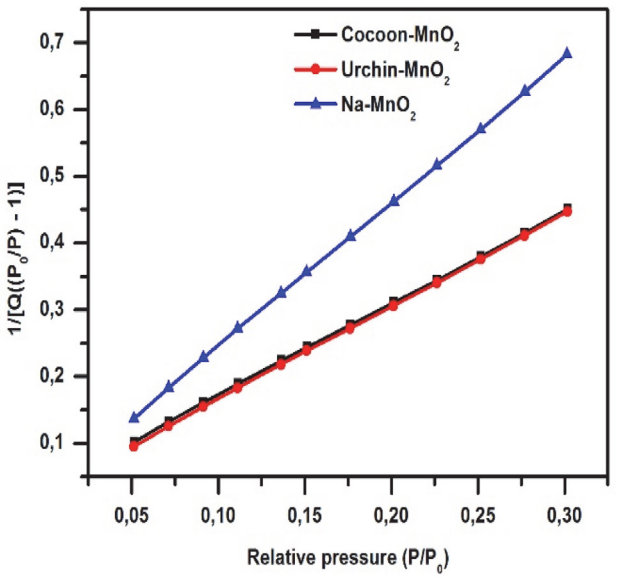


Figure 3. BET isotherm of materials Na-MnO_2, Cocoon-MnO_2, and Urchin-MnO_2.

Table 2. Isotherm parameters for BET models.

	Constant C	S_{BET} (m^2/g)	Q_m	R^2
Na-MnO_2	75.1	30.5 ± 1.7	0.457	0.9999
Urchin-MnO_2	52.9	44.3 ± 3.0	0.705	0.9998
Cocoon-MnO_2	41.1	43.9 ± 3.3	0.709	0.9998

Adsorption/desorption studies of N_2 were performed to characterize the pore size distribution of the three materials, the resulting isotherms and Barrett-Joyner-Halenda (BJH) pore size distribution diagrams were presented in Figure S1. According to the International Union of Pure and Applied Chemistry Classification (IUPAC),[73] the curve corresponding to the Na-MnO_2 material had a type V shape with a type H3 hysteresis loop

attributed to mesoporous solids. In contrast, the two materials Urchin-MnO_2 and Cocoon-MnO_2, their curves had a type II shape that corresponded to non-porous rather than macroporous solids.

The pore size classification suggested by the IUPAC[74] was adopted. Analysis of the BJH pore distribution of the Na-MnO_2 material showed that mesopores (d > 50 Å) had about 52% of the total porous surface area. These results showed the predominance of mesopores in the Na-MnO_2 material. This parameter would be a factor and an essential element for the removal of metal ions. The two materials Urchin-MnO_2 and Cocoon-MnO_2, mesoporous, had 52% to 54% of the total area (Table S1). The average pore diameters for the two materials (Urchin-MnO_2 and Cocoon-MnO_2) were slightly small compared to Na-MnO_2 (Table S1). It was also noted from Figure S1 that the pore volume was distributed according to all pore sizes studied. All these parameters allowed having the materials with a high affinity of adsorption of heavy metals. During this study, we also surveyed the average diameters of the adsorption and desorption pores of the BJH model, as well as the cumulative volume of adsorption/desorption, the results obtained were illustrated in Table S1.

4. Pb(II) and Cd(II) Removal by Manganese Oxides Materials

4. 1. Effect of Contact Time on the Removal Efficiency of Heavy Metals

The equilibrium study between the adsorbate (liquid phase) and the adsorbent (solid) was achieved with a speed that depended not only on the rate at which the components diffused into the adsorbent and in the fluid, but also on the adsorbent-adsorbate interaction. The time-dependent study of the adsorption of a compound on an adsorbent allowed us to examine the influence of contact time on its retention. The effect of contact time for the interaction studies between Pb(II), Cd(II), and the synthesized materials in an aqueous medium under ambient temperature conditions were given in Figure 4.

Figure 4 demonstrated that the prepared materials had a very high removal efficiency. The removal of lead ion could rapidly achieve the equilibrium within 15 min allowed to have a removal efficiency of 97.44, 93.15, and 98.77% for Na-MnO_2, Urchin-MnO_2, and Cocoon-MnO_2, respectively. In the case of Cd(II) ions, the materials also showed high reactivity to this metal cation during contact. The highest yield was up to 99% for Na-MnO_2 material during 30 minutes of interaction, while in the case of Urchin-MnO_2 and Cocoon-MnO_2, the yields were 55.33% and 80.26% respectively.

Several parameters could be discussed to explain the behavior of Pb(II) and Cd(II) ions during interaction with synthesized materials such as the specific surface area, the acid-base properties of the materials, and certainly their composition and Mn (AOS). In this work, we determined the Mn (AOS) for each material using a specific dosage. The results showed that the materials had an oxidation degree average about 3.5. Therefore, the manganese oxide material was a mixture of Mn(III) and Mn(IV) with Mn(IV) dominated (Table 1). Studies had been done to examine the effect of oxidation degree on the removal efficiency of heavy metals.[49] The results showed that adsorption capacity increased with increasing oxidation degree. This significant correlation may indicate that samples with a high degree of oxidation contained more octahedral cationic vacancy sites, which were primarily responsible for heavy metals sorption. According to the BET isotherm

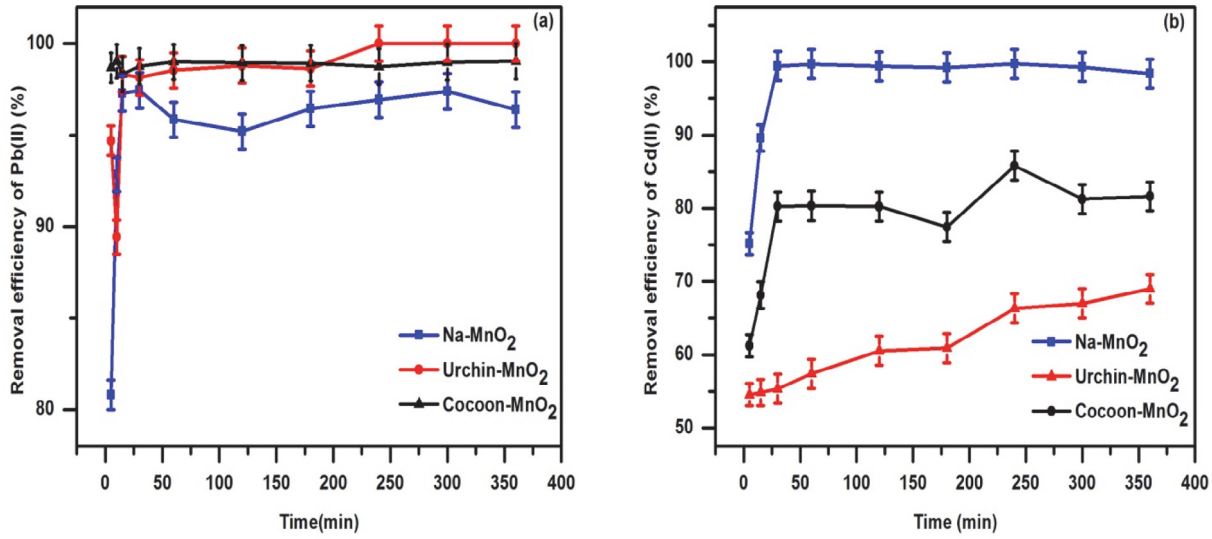


Figure 4. Effect of contact time on (a) Pb(II) and (b) Cd(II) removal by Na-MnO_2, Urchin-MnO_2 and Cocoon-MnO_2 ($[Pb(II)]_{initial}$=$[Cd(II)]_{initial}$ =30ppm).

performed for the three synthesized materials, we had found that these oxides had high specific surfaces (Table 2). This parameter was an essential factor in the properties of an adsorbent. The pore diameter could make possible to enhance metal ions elimination. Also, as noticed previously that the Na-MnO_2 material was characterized by the largest pore diameter (d = 66.63 Å) compared to the two types of manganese oxides (Table S1). Higher yields recorded for the two metal ions were also enhanced at high pH, which was attributed to the formation of MOH^+ (M = metal cation) species with the increase in pH. Therefore, the formation of MOH^+ species conducted to higher adsorption. S. Wan et al. have shown that manganese oxides can trapped metal ions, specifically Pb(II) and Cd(II) ions, by electrostatic forces and formation of inner-sphere complexes,[75] rendered it an efficient material for the removal of metal ions in the aqueous medium.

The comparative study on the performance obtained during the interaction of oxides with Pb(II) and Cd(II) (Figure S2) showed that the Na-MnO_2 material had a significant affinity for (Cd(II) and Pb(II)) removal in an aqueous medium. On the other hand, the Urchin-MnO_2 and Cocoon-MnO_2 materials had more affinity for Pb(II) than Cd(II). Several parameters can explain the difference between the yields recorded for Cd(II) and Pb(II). When the lamellar materials (Na-MnO_2) interacted with the Pb(II) and Cd(II) ions, the Pb(II) ions occupied the interlayer MnO_6 and surface sites,[76] while the Cd(II) mainly occupied the sites above and below the octahedrons of MnO_6.[65,77] The removal efficiency for each metal ion depended strongly on its hydrolysis constant. Indeed, this elimination capacity increased with the hydrolysis constants[78] of Pb(II) and Cd(II), which were respectively $10^{-7.7}$ and $10^{-10.1}$. The cationic exchange was better at low pK value.[79] The pH of the medium studied (pH = 6.5) was less than the pK of Pb(II) and Cd(II) (7.7 and 10.1), indicating that the hydroxylation cations were formed by hydrolysis induced by the surfaces of the manganese oxide.[80] The metal valency, as well as it's a hydrated radius ($r_{hydrated}$ = r ion + $2r_{H2O}$ with r_{H2O} = 0.138 nm) was also an important parameter in adsorption phenomenon.[59] Indeed, the higher the valency of the cation, the higher the affinity of the material towards this cation. For equal valence, the cations with a high volume that will be fixed first (Pb(II) (1.19 Å) > Cd(II) (0.95 Å).

4. 2. Effect of pH on the Removal Efficiency of Heavy Metals

To investigate the effect of pH on the removal efficiency of metal ions by different materials, the adsorption of Pb(II) or Cd(II) ions was studied in the pH range of 2.0 to 9.0. The evolution of removal efficiencies of Pb(II) and Cd(II) pH solution after 30 min interaction were shown in Figure 5.

For the different materials, the removal percentages of the two metal ions were favored by the increase in pH from 2.0 to 9.0. This behavior may be explained by the increase in the number of negatively charged sites on the surface of the materials, which promoted the diffusion process of the metal ions and thus facilitated their removal by the different types of manganese oxide material. At lower pH values (pH = 2), the lamellar material maintained its adsorptive power with yields of 83% and 71% in the case of Pb(II) and Cd(II) respectively. The slight decrease in removal efficiencies of Pb(II) and Cd(II) ions by the different materials may be due to the effect of competition between H^+ ions and metal ions.[81] The highest removal > 94% in the case of Pb(II) was recorded at pH = 6.5. In the case of Cd(II) and above this pH, the highest efficiencies were achieved with the lamellar material Na-MnO_2 with a value

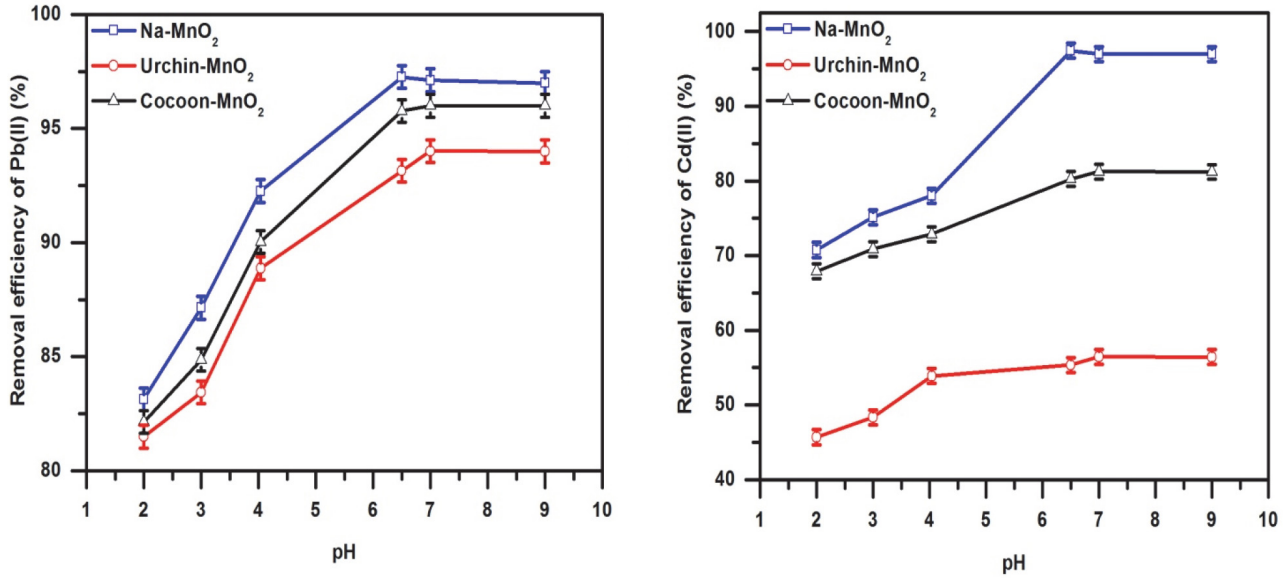


Figure 5. Effect of pH on the removal efficiency of metal ions by manganese oxide materials.

of 97%. In comparison, the two nanostructured materials recorded efficiencies of 56% and 81% for Urchin-MnO_2 and Cocoon-MnO_2, respectively. At values of pH ≥ 6.5, the removal efficiencies of metal ions were increased and remained almost stable up to pH = 9, which reflected the effect that under alkaline conditions, the concentration of H^+ protons was changed and the material, therefore, maintained its performance and removal capacity. In addition to these pH values, the two phenomena of adsorption and precipitation could be the predominant mechanisms for removing the two metal ions.[81] In effect, the further treatment during this study was carried out at a free pH (6.5).

4. 3. Study of Manganese Oxides Stability During Interaction with Metal Cations

During metal ion removal processes, manganese oxides could release manganese ions. To evaluate the manganese oxides stability, it was necessary to determine the Mn released by the different materials at different pH solutions. Figure 6 showed the percentages of manganese released in the case of interaction between the different materials and two metal ions Pb(II) and Cd(II).

From Figure 6, we noticed that during the removal of the two metal ions, the percentages of Mn released decreased with the pH increased from 2.0 to 9.0. At acidic pH values (2.0–4.0), the materials released more manganese. This release was probably due to the dissolution of manganese ions during the removal of metal ions. In pH ≥ 6.5, the manganese released by materials during interaction with Pb(II) and Cd(II) was low or even negligible. These results showed very high stability of the materials in neutral and alkaline pH. The greatest stability was recorded for the Na-MnO_2 lamellar material. For example, at pH = 6.5, in the case of Na-MnO_2 lamellar material, the percentages of manganese released were very weak (0.013% (0.123 mmol/Kg) and 0.31% (2.822 mmol/Kg) during Pb(II) and Cd(II) adsorption respectively). The Urchin-MnO_2 material released a very small amount of 0.93% (4.034 mmol/Kg) of the total manganese during Pb(II) removal, whereas in the case of cadmium, a release rate of 6.08% (26.422 mmol/Kg) was recorded. The highest amount of released manganese was obtained in the case of the Cocoon-MnO_2 material (6.3% (66.787 mmol/Kg) during the removal of Pb(II) and 7.09% (75.22 mmol/Kg) during the removal of Cd(II)). The results obtained showed that for the two nanostructures Urchin-MnO_2 and Cocoon-MnO_2 that the maximum amount of total manganese released decreased with increasing Mn AOS[47] (Mn AOS: Urchin-MnO_2 (3.730)>Cocoon-MnO_2 (3.650).

This study indicated that manganese oxide materials presented high stability. The high stability of these materials was strongly due to the stabilizing power and binding strength of the Na^+ and K^+ cations present in the structure of the three materials.[82] The best stability among the different structures was recorded in the case of the lamellar structure (Na-MnO_2), which presented a very low amount of the manganese release. This result confirmed that the use of Na-MnO_2 material with a lamellar structure compared to nanostructures responded to several requirements such as fast elimination kinetics and high reactivity to both heavy metals and also the factors of stability. This parameter is an essential factor in the use of materials in the form of the adsorbent. Na-MnO_2 material can be used in more advanced applications and more precisely in the industrial sector for the treatment of contaminated waste by heavy metals.

4. 4. Adsorption Kinetics

The sorption kinetics of Pb(II) and Cd(II) on manganese oxide materials was evaluated, and the results were shown in Figure 7. The adsorption equilibrium was achieved within 30 min. The kinetics data were fitted according to pseudo-first order (Eq. (4)) and pseudo-second

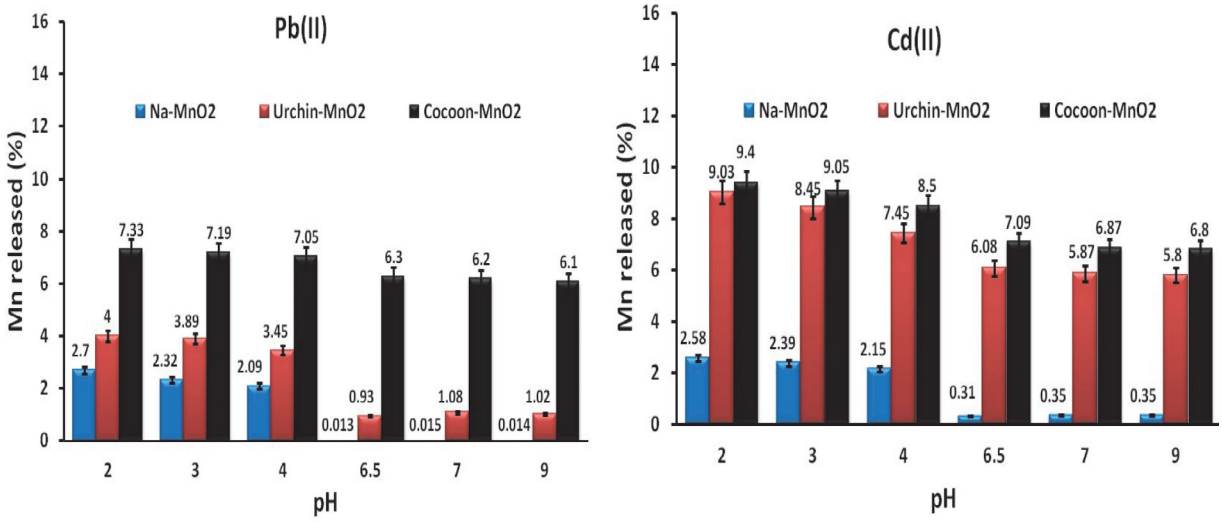


Figure 6. Percentages of manganese released by manganese oxides during interaction with Pb(II) and Cd(II) at different pH solution.

order (Eq. (5)) equations. The adsorbed quantities q_{exp}, the order of the constants K and regression coefficients R^2 were shown in Table S2.

$$\ln(q_e - q_t) = -Kt + \ln(q_e) \quad (4)$$

$$\frac{t}{q_t} = \frac{1}{(k \times q_e^2)} + \left(\frac{1}{q_e}\right) t \quad (5)$$

With:

q_e(mg/g) and q_t(mg/g) were the adsorbed quantities of Pb(II) or Cd(II) at equilibrium and time t (min).

K : rate constant of the pseudo-first order model (min^{-1}).

k : rate constant of the pseudo-second order model ($mg.g^{-1}.min^{-1}$).

Figure 7 and Table S2 showed that the second-order R^2 values are very high and were all higher than those obtained with the pseudo-first order model. The quantities fixed at equilibrium q_e were closed to the values obtained experimentally for the two metals. The adsorption process of Pb(II) and Cd(II) followed the pseudo-second order model. This model suggested the existence of chemisorption with the formation of a monomolecular layer.[83] In fact, the pseudo-second order constant (K) gave an idea of the affinity of the material towards metal ions.[77] Based on the results shown in Table S2, we could deduce that the three materials used have a higher affinity for Pb(II) than for Cd(II).

4. 5. Influence of the Initial Concentration of Metal Ions on the Removal Efficiency of Manganese Oxides

The influence of the initial concentration of metal ions on manganese oxide removal efficiencies was carried

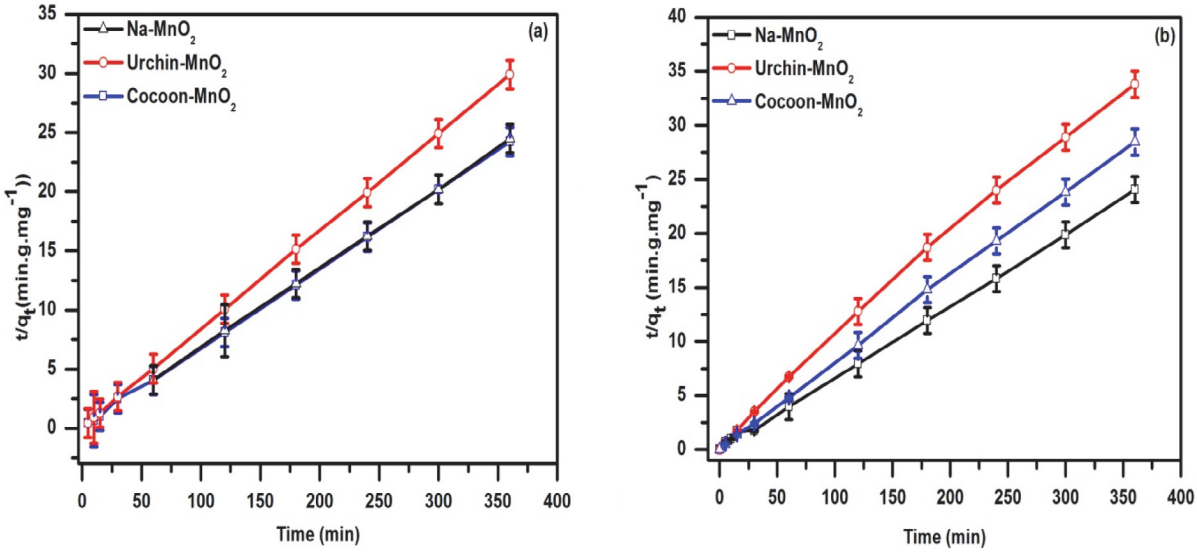


Figure 7. Adsorption kinetic diagram of (a) Pb(II) and (b) Cd(II) on Na-MnO_2, Urchin-MnO_2 and Cocoon-MnO_2.

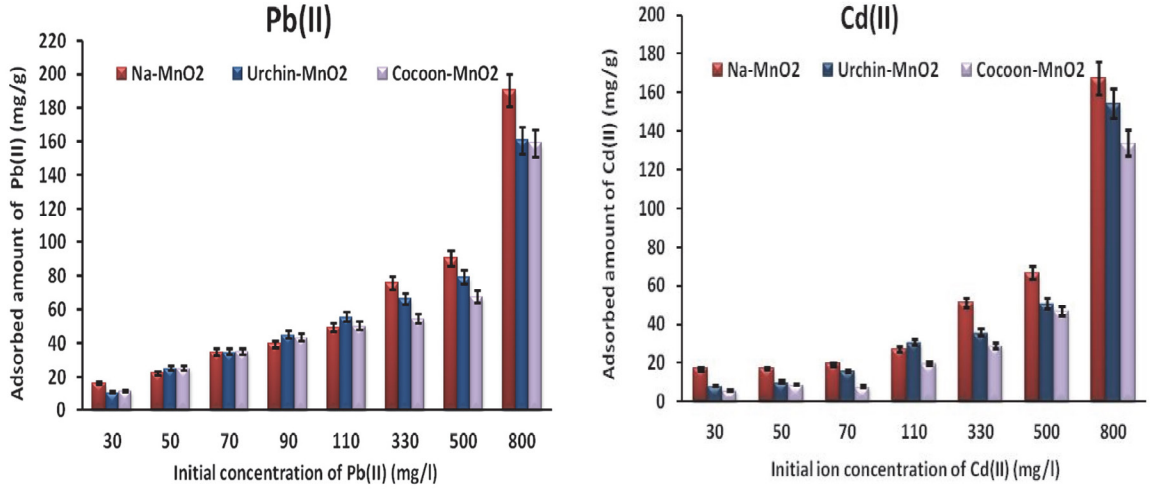


Figure 8. Influence of the initial concentration of metal ions on the removal efficiencies of Pb(II) and Cd(II) by manganese oxides.

out with different metal ion concentrations ranging from 30 to 800 ppm for 30 minutes of interaction. The results obtained were shown in Figure 8.

The examination of Figure 8 showed an increase in the removal efficiency of metal cations with increasing concentration. High removal capacities were recorded for Pb(II) for all three materials due to their high affinity toward this metal. For an initial concentration of 800 ppm of Pb(II), Urchin-MnO_2 and Cocoon-MnO_2 materials were able to absorb 160 mg/g, while Na-MnO_2 adsorbed a larger amount of 190 mg/g. For the same initial concentration of Cd(II), the three materials removed an quantity ranging from 140 to 160 mg/g with the highest amount recorded for Na-MnO_2.

4. 6. Isotherm Models

In this study, the adsorption equilibrium was modeled using three mathematical laws Langmuir, Freundlich, and Temkin, which represented the equilibrium relationship between the amount of metal cation in the liquid phase (C_e) and that adsorbed on the material (q_e).

Adsorption studies were conducted for 30 minutes at different initial concentrations of Pb(II) and Cd(II) metal ions and 100 mg of the material. The isotherms were given in Figure S3. The following equations represented the models of each isotherm applied in this study:

$$\text{Langmuir isotherm: } \frac{C_e}{q_e} = \left(\frac{1}{b \times q_m}\right) + C_e\left(\frac{1}{q_m}\right) \quad (6)$$

$$\text{Freundlich isotherm: } \log q_e = \log K_F + \frac{1}{n}(\log C_e) \quad (7)$$

$$\text{Temkin isotherm: } q_e = \left(\frac{RT}{b_T}\right)\ln K_T + \left(\frac{RT}{b_T}\right)\ln C_e \quad (8)$$

For the Langmuir isotherm, another parameter could also be expressed as a constant representing the separation factor defined by Eq. (9).

$$R_L = \frac{1}{1 + b \times C_0} \quad (9)$$

A separation factor R_L>1 indicated that the adsorption was unfavorable, if R_L = 1 the adsorption was described as linear, the adsorption was considered to be favorable when 0<R_L<1 and a zero separation factor (R_L = 0) indicated that the adsorption was irreversible.[84]

With:

C_e: the equilibrium concentration of substrates in the solution (mg/L).

q_e: the adsorption capacity at equilibrium (mg/g).

q_m: the maximum amount of adsorption (mg/g).

b: the adsorption equilibrium constant (L/mg).

K_F: a constant representing the adsorption capacity.

n: the constant showing the adsorption intensity.

R= 8.314 J mol $^{-1}$ K^{-1}.

T: absolute temperature in (K), K_T: Temkin constant in (L mg $^{-1}$).

C_0: the initial concentration of the adsorbate (mg L^{-1}).

Figure S3 showed the most appropriate isotherms for the three materials Na-MnO_2, Urchin-MnO_2, and Cocoon-MnO_2. In table S3 all parameters of the isotherms for the two metals were given. After studying the isothermal adsorption of Pb(II) and Cd(II) ions by manganese oxides,

Table 3. Comparison of Pb(II) and Cd(II) adsorption capacities of Na-MnO_2, Urchin-MnO_2, Cocoon-MnO_2 and other reported adsorbents.

Sorbent	Adsorption capacity (mg/g)	Conditions	References
	Pb(II)		
K-Birnessite	164.30	pH = 5, T° = 25 °C	85
Al_2O_3-supported iron oxide	28.98	pH = 5, T° = 27 °C	86
Fe_3O_4 nanoparticles	83		87
TiO_2 nanoparticles	159	pH = 7, T°= 25 °C	
Cocoon-MnO_2	209		
Urchin-MnO_2	264	pH = 6.5, T°= 25 °C	*This study*
Na-MnO_2	297		
	Cd(II)		
Birnessite	34	pH = 7, T° = 25 ° C	88
Synthetic zeolites	50.8	pH = 6, T° = 25 °C	89
Activated carbon cloth	146	pH = 6, T° = 25 °C	90
Cocoon-MnO_2	172		
Urchin-MnO_2	191	pH = 6.5, T° = 25 °C	*This study*
Na-MnO_2	199		

it could be seen that the best description of the adsorption phenomenon was obtained with the Langmuir model with a high correlation coefficient R^2 (Table S3). This applied model allowed us to determine the maximum adsorption quantity q_m (mg/g) for all materials interacting with the two metal cations (Table S3). For Pb(II), the maximum quantities adsorbed were 297 mg/g (Na-MnO_2), 264 mg/g (Urchin-MnO_2), and 209 mg/g for the material Cocoon-MnO_2. For Cd(II), the adsorbed quantities were 199 mg/g (Na-MnO_2), 191 mg/g (Urchin-MnO_2), and 172 mg/g (Cocoon-MnO_2). In addition, the developed lamellar materials and nanostructures had shown a high adsorption capacity compared to other types of adsorbents (Table 3).

The description of the adsorption of Pb(II) and Cd(II) by the Langmuir model that the adsorption of these ions by the materials was done by the formation of a monolayer on the external surface of the adsorbent. Thus, this concordance could be explained by the homogeneity of the adsorption sites on the surface of these materials. Indeed, during the interaction, there would be a direct contact of metal ions on the surface of the materials up to the coverage of the monolayer. Based on the calculated R_L values, all values were between 0 and 1, indicating favorable adsorption.

In the structure of synthesized manganese oxides of the birnessite type ($A_xMnO_2{,}zH_2O$) (with A = Na^+ (case: Na-MnO_2)), either Na^+ and H^+ [91] or Mn^{2+}, two proton or $(Mn(III)OH)^{2+}$ were located on each side of a vacant cationic site to obtain local charge balance of material.[47] The analysis of sodium (Na^+) in solution during the removal of Cd(II) and Pb(II) confirmed this hypothesis. The result indicated that Na-MnO_2 material released a quantity of Na^+ ions during removal processes (Figure S4).

As shown in X-ray diffractogram, the two materials Urchin-MnO_2 (KMn_8O_{16}) and Cocoon-MnO_2 ($K_2Mn_4O_9$) had two different structures, with K^+ ions inserted into their cavities. The removal of Cd(II) and Pb(II) occurred by exchanging K^+ from the tunnel site and also on the external surface of the materials.[92] The exchange between the metal ions and the K^+ caused it to be released into the solution during the metal removal process (Figure S5).

5. Analysis of the Adsorption Mechanism

5. 1. X-ray Diffraction

The characterization by X-ray diffraction of the materials after interaction with metallic cations was important to determine the totality of structures formed. The diffractograms before and after interaction with Pb(II) and Cd(II) were illustrated in Figure 9.

After the interaction of the manganese oxide materials with Pb(II) and Cd(II), the diffractograms of each material were not similar. The peaks obtained from each material were analyzed to determine the phases formed. The crystallographic parameters of each phase were represented in Table 4.

In the case of Na-MnO_2, after interaction with Pb(II) and Cd(II), a slight decrease in the intensity of some peaks occurred. The identification of the phases formed made it possible to determine the MnO_2 manganese oxide phase and the appearance of new PbO phases observed at 2θ = 30.66° (110), 64.40° (002) and for the $Cd(OH)_2$ phase was indexed in two peaks located at 2θ = 50° (231), 53.64° (002) indicating that the Pb(II) and Cd(II) ions had been inserted into the material. The iden-

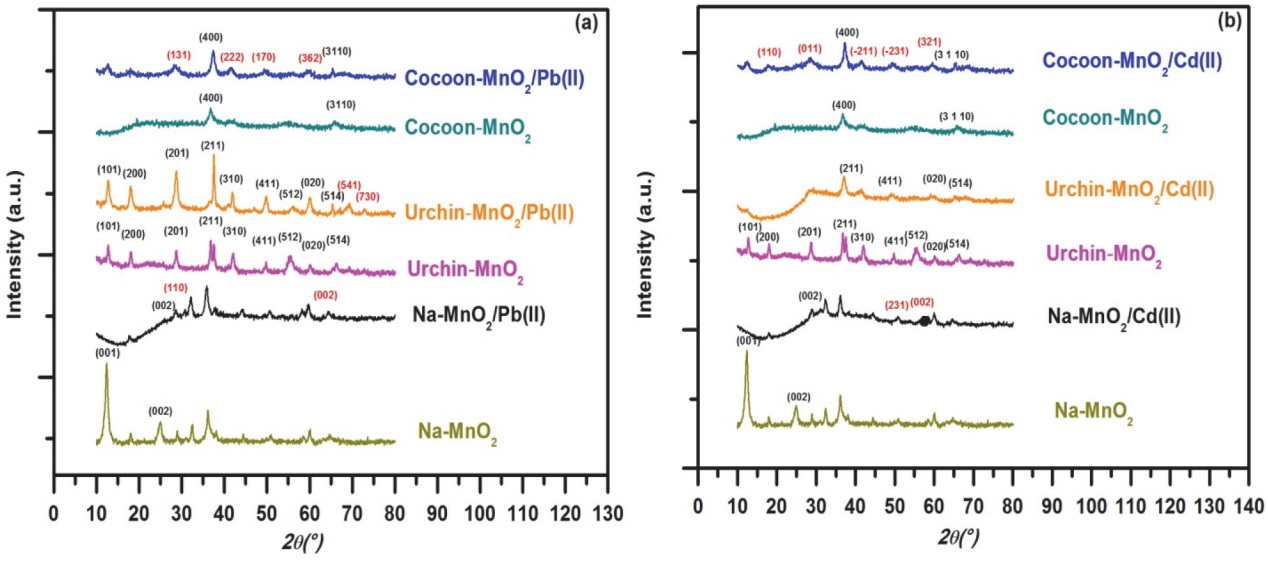


Figure 9. X-ray diffractograms of manganese oxides before and after interaction with (a) Pb(II) and (b) Cd(II).

Table 4. Crystallographic parameters of the structures formed after interaction of Pb(II) and Cd(II) ions with the materials.

	Phases formed	Mesh parameter (Å)	Crystal system
Na-MnO_2 (Before interaction)	$Na_{0.55}Mn_2O_4.(H_2O)_{1.5}$ (Birnessite)	a = 5.1750 b = 2.8490 c = 7.3380	Monoclinic
Na-MnO_2 (After interaction: Pb(II))	PbO	a = 3.9744 b = 3.9744 c = 5.0220	Tetragonal
	$Na_{0.55}Mn_2O_4.(H_2O)_{1.5}$ (Birnessite)	a = 5.1750 b = 2.8490 c = 7.3380	Monoclinic
Na-MnO_2 (After interaction: Cd(II))	$Cd(OH)_2$	a = 5.6700 b = 10.2500 c = 3.4100	Monoclinic
	$Na_{0.55}Mn_2O_4.(H_2O)_{1.5}$ (Birnessite)	a = 5.1750 b = 2.8490 c = 7.3380	Monoclinic
Urchin-MnO_2 (Before interaction)	KMn_8O_{16} (Cryptomelane)	a = b = 9.840 c = 2.850	Tetragonal
Urchin-MnO_2 (After interaction: Pb(II))	$Pb_2Mn_8O_{16}$	a = b = 9.8900 c = 2.8620	Tetragonal
	KMn_8O_{16} (Cryptomelane)	a = b = 9.840 c = 2.850	Tetragonal
Urchin-MnO_2 (After interaction: Cd(II))	$Cd(OH)_2$	a = 5.6700 b = 10.2500 c = 3.4100	Monoclinic
	KMn_8O_{16} (Cryptomelane)	a = b = 9.840 c = 2.850	Tetragonal
Cocoon-MnO_2 (Before interaction)	$K_2Mn_4O_9$	a = b= 11.2950 c = 21.870	Hexagonal
Urchin-MnO_2 (After interaction: Cd(II))	Pb_2MnO_4	a = b = 12.7700 c = 5.1300	Tetragonal
	$K_2Mn_4O_9$	a = b = 11.2950 c= 21.870	Hexagonal
Cocoon-MnO_2 (After interaction: Cd(II))	$Cd(OH)_2$	a = 5.6700 b = 10.2500 c = 3.4100	Monoclinic
	$K_2Mn_4O_9$	a = b = 11.2950 c = 21.870	Hexagonal

tification of the phases formed for the nanostructured material Urchin-MnO_2 after interaction with Pb(II) ions (Figure 9 a) and Cd(II) ions (Figure 9 b), showed the existence of the characteristic phase (KMn_8O_{16}) of Urchin-MnO_2 with the occurrence of $Pb_2Mn_8O_{16}$ and $Cd(OH)_2$ (Table 4). For Cocoon-MnO_2, the characteristic phase of this material still existed with the formation of the Pb_2MnO_4 phase (Table 4) in the case of interaction with Pb(II) ions (Figure 9 a) and $Cd(OH)_2$ in the case of Cd(II) (Figure 9 b). All diffractograms of the materials after interaction showed that the intensity of some peaks decreased while others disappeared. This deformation was due to the insertion of metal cations in the vacant octahedral sites and in the interlayer space between the MnO_6 layers (case of Na-MnO_2) or in the cavities (case of Urchin-MnO_2 and Cocoon-MnO_2) which created a disorder in the materials.[27] Based on the results obtained, it could be said that the removal of metal ions after interac-

tion with the materials was achieved either by insertion as MO oxide (PbO) or by adsorption as $M(OH)_2$ hydroxide ($Cd(OH)_2$) or by the formation of new phases such as Pb_2MnO_4 and $Pb_2Mn_8O_{16}$. As shown, subsequent studies reported that the analysis of materials after interaction with Cd(II) ions by X-ray photoelectron spectroscopy (XPS) showed that Cd(II) was adsorbed on MnO_2 as CdO and $Cd(OH)_2$. [27]

6. Stability and Reusability of the Na-MnO_2

In this study, the lamellar material Na-MnO_2 showed the highest removal efficiency of metal ions at different pH values, a high removal capacity as well as a very high stability compared to nanostructured materials. In this context, the reusability of this material for the removal of Pb(II) and Cd(II) ions was studied. Five successive adsorption cycles were investigated. After each cycle, the nanomaterial Na-MnO_2 was recovered by filtration, washed with water and dried, it was used in the subsequent cycle. As shown in Figure 10, the nanomaterial Na-MnO_2 could remove 97.26% Pb(II) and 97.44% Cd(II) in the initial cycle. A gradual decrease in removal efficiencies from 97.26 % to 78.05% and 97.44% to 69% were observed after five reuses for Pb(II) and Cd(II) respectively. It was clear that the reusable capability of the nanomaterial Na-MnO_2 decreased slightly with an increase in the number of cycles. But in general, Na-MnO_2 was maintained at a relatively high removal efficiency.

The slight decrease in heavy metal removal efficiency could be due to the dissolution or release of a low concentration of manganese ions and the change in morphology of the material by reducing its available active sites. Simultaneously, AAS was employed to measure Mn concentration in the solution after each cycle (Figure 10, black line). Therefore, after 5 cycles of use the percentage of Mn released from the material was less than 0.1% and 0.48% in the case of Pb(II) and Cd(II) respectively, indicating good stability of Na-MnO_2.

7. Conclusions

XRD and SEM analysis showed that the prepared manganese oxides: Na-MnO_2, Urchin-MnO_2, and Cocoon-MnO_2 were composed of a monophase characteristic of each structure elaborated, these oxides had particular morphologies. Studies of adsorption/desorption of N_2 of the materials showed that their structures were composed of a mixture of pores with a predominance of mesopores of more than 53% of the total porous surface. This study showed that structure and morphology had a direct effect on the elimination of metal cations Pb(II) and Cd(II). All materials (lamellar: Na-MnO_2 and nanostructures: Urchin-MnO_2 and Cocoon-MnO_2) showed a high reactivity towards both metals with a high yield of more than 90% for a very short duration (less than 15 minutes) at free pH (6.5). These materials also demonstrated high stability during the removal process. In the case of the Na-MnO_2 lamellar material, the removal efficiency of metal cations was very high above 99%, and the release rates of manganese were lower than 0.4%. The reusability of the lamellar material Na-MnO_2 showed that it could be used more than 5 cycles without loss of performance and stability. The lamellar material Na-MnO_2 was very efficient, had a high removal capacity was very stable and suitable for several uses for the removal of metal ions.

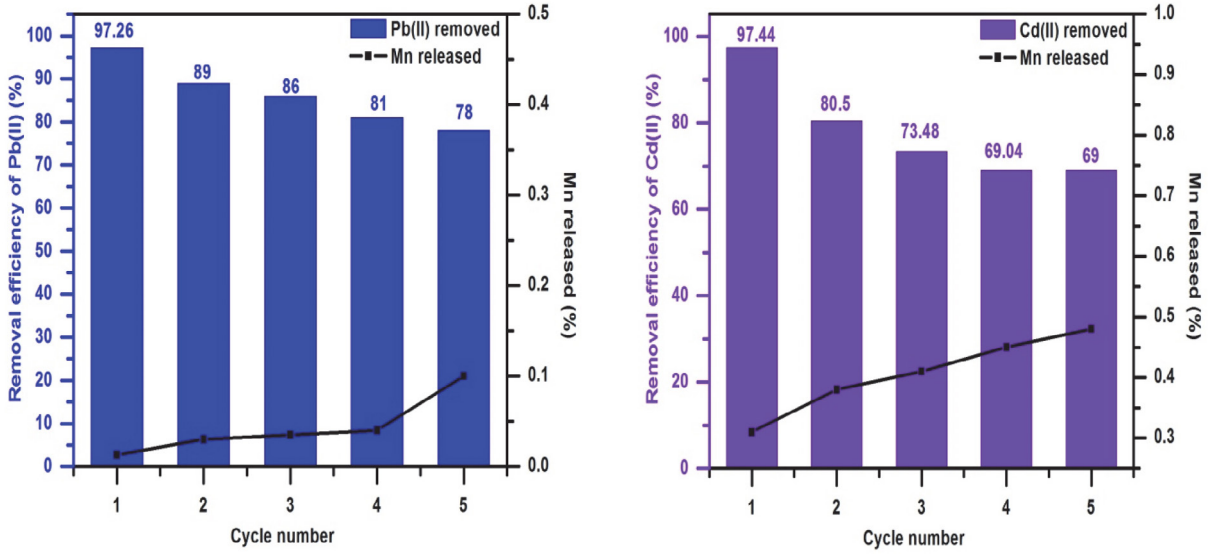


Figure 10. Stability and reusability of Na-MnO_2 to remove Pb(II) and Cd(II) (Conditions: initial concentration of metal ions= 30 ppm, t = 30 min for each cycle).

Supporting Information

The equation (S1), pore size distributions of three MnO_2 (lamellar and nanostructures), comparative study of Cd(II) and Pb(II) removal efficiencies. Langmuir isotherm plot for Pb(II) and Cd(II) adsorption, Amount of Na^+ released during the removal of Pb(II), and Cd(II) ions by Na-MnO_2. Amount of K^+ released during the removal of Pb(II) and Cd(II) ions by Urchin-MnO_2 and Cocoon-MnO_2. Porous structure parameters of each material, Adsorption coefficients of Pb(II) and Cd(II) of the pseudo-first-order and pseudo-second-order models. Isotherm parameters for Langmuir, Freundlich, and Temkin models.

Acknowledgments

The authors warmly thank the OCP (Office Chérifien des Phosphates), R&D Foundation (Research and Development) for the financial support of this project National Centre for Scientific and Technical Research (CNRST), Ministry of Higher Education Scientific Research.

Conflicts of Interest

The authors declare no conflict of interest.

8. References

1. A. S. Ertürk, M. U. Gürbüz, M. Tülü, A.E. Bozdoğan, *J. Acta Chim. Slov.* **2018**, *65*, 65–74. **DOI:**10.17344/acsi.2017.3485
2. S. Sharma, A. K. Nagpal, I. Kaur, *J. Chemosphere*. **2019**, *227*, 179–190. **DOI:**10.1016/j.chemosphere.2019.04.009
3. A. Karimi, A. Naghizadeh, H. Biglari, R. Peirovi, A. Ghasemi, A. Zarei, *J. Environ. Sci. Pollut. Res.* **2020**, *27*, 10317–10327. **DOI:**10.1007/s11356-020-07642-6
4. D. Humelnicu, L.V. Soroaga, C. Arsene, I. Humelnicu, R.I. Olariu, *J. Acta Chim. Slov*. **2019**, *66*, 326–336. **DOI:**10.17344/acsi.2018.4821
5. S. Z. Ahmad Nurain, W. N. Wan Salleh, A. Fauzi Ismail, N. Yusof, M. Z. M. Yusop, F. Aziz, *J. Chemosphere*. **2020**, *248*, 1–16. **DOI:**10.1016/j.chemosphere.2020.126008
6. F. Alshahri, *J. Environ. Sci. Pollut. Res.* **2016**, *24*, 1821–1831. **DOI:**10.1007/s11356-016-7961-x
7. S.M. Mousavi, S.A. Hashemi, H. Esmaeili, A.M. Amani, F. Mojoudi, *J. Acta Chim. Slov*. **2018**, *65*, 750–756. **DOI:**10.17344/acsi.2018.4536
8. X. Xu, Y. Yang, G. Wang, S. Zhang, Z. Cheng, T. Li, Z. Yang, J. Xian, Y. Yang, W. Zhou, *J. Chemosphere*. **2020**, *246*, 125816. **DOI:**10.1016/j.chemosphere.2020.125816
9. J. Xue, Y. Zhi, L. Y. Wu, J. Shi, L. Zeng, L. Wu, *J. Env. Sci Pollut Res*. **2014**, *21*, 7698–7707. **DOI:**10.1007/s11356-014-2726-x
10. C. Lee, T. Kim, S. Komarneni, S. Han,Y. Cho, *J. Appl. Clay Sci.* **2013**, *83–84*, 263–269. **DOI:**10.1016/j.clay.2013.08.035
11. G. Zheng, L. Tian, Y. Liang, K. Broberg, L. Lei, W. Guo, J. Nilsson, I. A. Bergdahl, S. Skerfving , T. Jin, *J. Neurotoxicology*. **2011**, *32*, 374–382. **DOI:**10.1016/j.neuro.2011.03.006
12. P. Aendo, S. Thongyuan, T. Songserm, P. Tulayakul, *J. Sci. Total Environ.* **2019**, *689*, 215–222. **DOI:**10.1016/j.scitotenv.2019.06.414
13. T. Shah, F. Munsif, D. Roberto, L. Nie, *J. Chemosphere*. **2019**, *246*, 125766. **DOI:**10.1016/j.chemosphere.2019.125766
14. B. Nunes, R. C. Capela, T. Sérgio, C. Caldeira, F. Gonçalves, A. T. Correia, *J. Env. Sci Pollut Res*. **2014**, *21*, 5689–5700. **DOI:**10.1007/s11356-013-2485-0
15. C. M. Liu, J.-Q. Ma, Y.-Z. Sun, *J. Environ. Toxicol. Pharmacol.* **2010**, *30*, 264–271. **DOI:**10.1016/j.etap.2010.07.002
16. N. D. Bustamante, W. L. Macias-konstantopoulos, *J. Emerg. Med.* **2016**, *51*, 45–49. **DOI:**10.1016/j.jemermed.2016.02.025
17. P. Chen, X. Duan, M. Li, C. Huang, J. Li, R. Chu, H. Ying, H. Song, X. Jia, Q. Ba, H. Wang, *J. Toxicol. Appl. Pharmacol.* **2016**, *310*, 150–158. **DOI:**10.1016/j.taap.2016.09.006
18. F. Fu, Q. Wang, *J. Environ. Manage.* **2011**, *92*, 407–418. **DOI:**10.1016/j.jenvman.2010.11.011
19. P. Zhang, S. Ouyang, P. Li, Z. Sun, N. Ding, Y. Huang, *J. Clean. Prod.* **2019**, *246*, 118728. **DOI:**10.1016/j.jclepro.2019.118728
20. S. Hu, F. Lian, J. Wang, *J. Sci. Total Environ.* **2019**, *666*, 956–963. **DOI:**10.1016/j.scitotenv.2019.02.285
21. P. Caecilia, S. Ketut, N. Yustina, H. Prasetyo, *J. Matec Web Conf.* **2016**, *58*, 10–13. **DOI:** 10.1051/matec conf/20165801022
22. F. Scholz, H. Kahlert, *J. ChemTexts*, **2015**, *7*, 1–9. **DOI:**10.1007/s40828-015-0006-0
23. J. Kheriji, D. Tabassi, B. Hamrouni, *J. Water Sci. Technol.* **2015**, *7*, 1206–1216. **DOI:**10.2166/wst.2015.326
24. A. El-Gendi, S. Ali, H. Abdalla, M. Saied, *J. Memb.Wat. Tre.* **2016**, *7*, 55–70. **DOI:**10.12989/mwt.2016.7.1.055
25. S. M. Shaheen, A. S. Derbalah and F. S. Moghanm, *J. Environ. Sci. Dev.* **2012**, *3*, 362–367. **DOI:**10.7763/IJESD.2012.V3.248
26. M. Araissi, I. Ayed, E. Elaloui, Y. Moussaoui, *J. Water Sci. Technol.* **2016**, *73*, 1628–1636. **DOI:**10.2166/wst.2015.640
27. L. Peng, Q. Zeng, B. Tie, M. Lei, J. Yang, S. Luo, Z. Song, *J. Colloid interface Sci.* **2015**, *456*, 108–115. **DOI:**10.1016/j.jcis.2015.06.017
28. Y. Cho, S. Jang, Y. Kim, S. Komarneni, S. Kim, *J. Porous Mater*. **2011**, *18*, 125–131. **DOI:**10.1007/s10934-010-9430-0
29. N. N. Nassar, *J. Hazard. Mater.* **2010**, *184*, 538–546. **DOI:**10.1016/j.jhazmat.2010.08.069
30. H. N. Trana, D. T. Nguyenb, G. T. Le, F. Tomul, E. C. Lima, S. H. Woo, A. K. Sarmah, H. Q. Nguyen, P. T. Nguyen, D. D. Nguyen, T. V. N. S. Vigneswaran, N. V. Dai-Viet, H.-P. Chaol, *J. Hazard. Mater.* **2019**, *373*, 258–270. **DOI:**10.1016/j.jhazmat.2019.03.018
31. A. Avram, T. Frentiu, O. Horovitz, A. Mocanu, F. Goga, M. Tomoaia-cotisel, *J. Stud. Ubb Chem.* **2017**, *4*, 93–104. **DOI:** 10.24193/subbchem.2017.4.08
32. A. A. Hanna, M. A. Sherief, R. M. Aboelenin, S. M. Mousa, *Can. J. Pure Appl. Sci.* **2010**, *4*, 1087–1093. J. Pure Appl. Sci. 2010, 4, 1087-1093.
33. M. Torab-Mostaedi, H. Ghassabzadeh, M. Ghannadi-Maragheh, S. J. Ahmadi, H. Taheri, *Brazilian J. Chem. Eng.* **2010**, *27*, 299–308. **DOI:**10.1590/S0104-66322010000200008
34. N. Mohamad, I. Abustan, M. Mohamad, K. Samuding, *J. Ma-*

ter. Today Proc. **2018**, *5*, 21832–21840. **DOI:**10.1016/j.matpr.2018.07.039
35. S. Deng, X. Liu, J. Liao, H. Lin, F. Liu, *J. Chem. Eng.* **2019**, *375*, 122086. **DOI:**10.1016/j.cej.2019.122086
36. M. Hojamberdiev, S. S. Daminova, Z. C. Kadirova, K. T. Sharipov, F. Mtalo, M. Hasegawa, *J. Environ. Chem. Eng.* **2018**, *6*, 4623–4633. **DOI:**10.1016/j.jece.2018.06.070
37. H. Vojoudi, A. Badiei, S. Bahar, G. M. Ziarani, F. Faridbod, M. R. Ganjali, *J. Magn. Magn. Mater.* **2017**, *441*, 193–203. **DOI:**10.1016/j.jmmm.2017.05.065
38. S. Mnasri-ghnimi, N. Frini-srasra, *J. Appl. Clay Sci.* **2019**, *179*, 1–17. **DOI:**10.1016/j.clay.2019.105151
39. A. Djukic, U. Jovanovic, T. Tuvic, V. Andric, J. Novakovic Grbovic, N. Ivanovic, L. Matovic, *J. Ceram. Int.* **2013**, *39*, 7173–7178. **DOI:**10.1016/j.ceramint.2013.02.061
40. N. M. Mubarak, J. N. Sahu, E. C. Abdullah and N. S. Jayakumar, *J. Sep. Purif. Rev.* **2014**, *43*, 37–41. **DOI:** 10.1080/15422119.2013.821996
41. J. H. Potgieter, S. S. Potgieter-Vermaak and P. D. Kalibantonga, *J. Miner. Eng.* **2006**, *19*, 463–470. **DOI:**10.1016/j.mineng.2005.07.004
42. A. Afkhami, M. Saber-tehrani and H. Bagheri, *J. Hazard. Mater.* **2010**, *181*, 836–844. **DOI:**10.1016/j.jhazmat.2010.05.089
43. D. Sofronov, A. Krasnopyorova, N. Efimova, A. Oreshina, E. Bryleva, G. Yuhno, S. Lavrynenko, M. Rucki, *J. Process Saf. Environ. Prot.* **2019**, *125*, 157–163. **DOI:**10.1016/j.psep.2019.03.013
44. S. Hoseini, N. Rahemi, S. Allahyari, M. Tasbihi, *J. Clean. Prod.* **2019**, *232*, 1134–1147. **DOI:**10.1016/j.jclepro.2019.05.227
45. A. M. Muliwa, M. S. Onyango, A. Maity, A. Ochieng, *Int. J. Environ. Sci. Technol.* **2018**, *16*, 2895–2904. **DOI:**10.1007/s13762-018-1817-5
46. L. Liu, Q. Peng, G. Qiu, J. Zhu, W. Tan, C. Liu, L. Zheng, Z. Dang, *J. Environ. Pollut.* **2019**, *244*, 783–791. **DOI:**10.1016/j.envpol.2018.10.062
47. W. Zhao, X. Feng, W. Tan, F. Liu, S. Ding, *J. Environ. Sci.* **2009**, *21*, 520–526. **DOI:**10.1016/S1001-0742(08)62302-5
48. P. Yang, E. Post, Q. Wang, W. Xu, R. Geiss, P. R. Mccurdy, M. Zhu, *J. Environ. Sci. Technol.* **2019**, *53*, 7453–7462. **DOI:**10.1021/acs.est.9b01242
49. Y. Wang, X. Feng, M. Villalobos, W. Tan, F. Liu, *J. Chem. Geol.* **2012**, *292–293*, 25–34. **DOI:**10.1016/j.chemgeo.2011.11.001
50. H. Antoni, D. M. Morales, J. Bitzer, Q. Fu, Y. Chen, J. Masa, W. Kleist, W. Schuhmann, M. Muhler, *J. Catalysis*. **2019**, *374*, 335–344. **DOI:**10.1016/j.jcat.2019.05.010
51. H. M. Abuzeid, S. A. Elsherif, N. A. Abdelghany, A. M. Hashem, *J. Energy Storage*. **2019**, *21*, 156–162. **DOI:**10.1016/j.est.2018.11.021
52. S. Garcia, S. Sardar, S. Maldonado, V. Garcia, C. Tamez, J. G. Parsons, *J. Microchemical*. **2014**, *117*, 52–60. **DOI:**10.1016/j.microc.2014.06.008
53. M. H. Salmani, M. Vakili, M. H. Ehrampoush, *J. Toxicol. Environ. Health Sci.* **2013**, *5*, 150–155. **DOI:**10.5897/JTEHS2013.0275
54. N. N. Nassar, *Can. J. Chem. Eng.* **2012**, *90*, 1231–1238. **DOI:**10.1002/cjce.20613
55. D. C. Ong, S. M. B. Pingul-ong, C. Kan, M. Daniel, G. De Luna, *J. Clean. Prod.* **2018**, *190*, 443–451. **DOI:**10.1016/j.jclepro.2018.04.175
56. S. Rahimi, R. M. Moattari, L. Rajabi, A. Ashraf, M. Keyhani, *J. Ind. Eng. Chem.* **2015**, *23*, 33–43. **DOI:**10.1016/j.jiec.2014.07.039
57. G. Tan, Y. Liu, D. Xiao, *Carbohydr. Polym.* **2019**, *219*, 306–315. **DOI:**10.1016/j.carbpol.2019.04.058
58. Q. Su, B. Pan, S. Wan, W. Zhang, L. Lv, *J. Colloid Interface Sci.* **2010**, *349*, 607–612. **DOI:**10.1016/j.jcis.2010.05.052
59. R. M. Mckenzie, *Aust. J. Soil Res.* **1980**, *18*, 61–73. **DOI:**10.1071/SR9800061
60. H. Zhang, F. Xu, J. Xue, S. Chen and J. Wang, *J. Sci. Rep.* **2020**, *10*, 6067–6079. **DOI:**10.1038/s41598-020-63000-z
61. E. S. A. Nouh, *J. Environ. Anal. Chem.* **2020**, *00*, 1–14. **DOI:** 10.1080/03067319.2020.1751834
62. E. S. A. Nouh, M. Amin, M. Gouda and A. Abd-elmagid, *J. Biochem. Pharmacol.* **2015**, *3*, 523–528. **DOI:**10.1016/j.jece.2015.01.013
63. Q. Nan, C. Hong, Y. Zhaoming, S. Sen, W. Yuan, *J. Electrochim. Acta*. **2018**, *272*, 154–160. **DOI:** 10.1016/j.electacta.2018.04.012
64. X. Yu, J. He, D. Wang, Y. Hu, H. Tian, Z. He, *J. Phys. Chem. C.* **2012**, *116*, 851–860. **DOI:**10.1021/jp208947e
65. Q. Peng, L. Liu, Y. Luo, Y. Zhang, W. Tan, F. Liu, S. L. Suib, G. Qiu, *J. Appl. Matererials Interfaces*. **2016**, *50*, 34405–34413. **DOI:**10.1021/acsami.6b12224
66. H. Boumaiza, A. Renard, M. R. Robinson, L. Vidal, C. Ruby, L. Bergaoui, R. Coustel, *J. Solid State Chem.* **2019**, *272*, 234–243. **DOI:**10.1016/j.jssc.2019.02.017
67. C. M. Julien and A. Mauger, *J. Nanomaterials*. **2017**, *7*, 396–437. **DOI:**10.3390/nano7110396
68. H. Lin, D. Chen, H. Liu, X. Zou, T. Chen, *J. Aerosol Air Qual. Res.* **2017**, *17*, 1011–1020. **DOI:**10.4209/aaqr.2017.01.0013
69. A. S. Poyraz, J. Huang, C. J. Pelliccione, X. Tong, S. Cheng, L. Wu, Y. Zhu, A. C. Marschilok, K. J. Takeuchi, E. S. Takeuchi, *J. Mater. Chem. A*. **2017**, *5*, 16914–16928. **DOI:**10.1039/C7TA03476H
70. Y. R. Li, A. C. Marschilok, E. S. Takeuchi, K. J. Takeuchi, *J. Electrochem. Soc.* **2016**, *163*, A281–A285. **DOI:**10.1149/2.0501602jes
71. H. Gao, I. D. Seymour, S. Xin, L. Xue, G. Henkelman, J. B. Goodenough, *J. Am. Chem. Soc.* **2018**, *140*, 18192–18199. **DOI:**10.1021/jacs.8b11388
72. G. Zoua, B. Gea, H. Zhanga, Q. Zhangb, C. Fernandezc, W. Lid, J. Huanga, Q. Peng, *J. Mater. Chem. A*. **2019**, *6*, 3091–3101. **DOI:** 10.1039/C9TA00744J
73. C. Yuan, B. Gao, L. Su, X. Zhang, *J. Colloid Interface Sci.* **2008**, *322*, 545–550. **DOI:**10.1016/j.jcis.2008.02.055
74. T. Mathialagan, T. Viraraghavan, *J. Hazard. Mater.* **2006**, *B134*, 257–267. **DOI:** 10.1016/j.jhazmat.2005.11.052
75. S. Wan, J. Wu, S. Zhou, R. Wang, B. Gao and F. He, *J. Sci. Total Environ.* **2018**, *616*, 1298–1306. **DOI:**10.1016/j.scitotenv.2017.10.188
76. K. D. Kwon, K. Refson, G. Sposito, *J. Geochim. Cosmochim. Acta*. **2010**, *23*, 6731–6740. **DOI:** 10.1016/j.gca.2010.09.002

77. L. Della Puppa, F. Bordas, M. Komárek, J. Bollinger, E. Joussein, *J. Colloid Interface Sci.* **2013**, *399*, 99–106. **DOI:**10.1016/j.jcis.2013.02.029
78. X. H. Feng, L. M. Zhai, W. F. Tan, F. Liu, J. Z. He, *J. Environ. Pollut.* **2007**, *147*, 366–373. **DOI:**10.1016/j.envpol.2006.05.028
79. K. Parida, P. K. Satapathy, N. DAS, *J. Colloid Interface Sci.* **1996**, *181*, 456–462. **DOI:**10.1006/jcis.1996.0402
80. L. Liu, G. Qiu, S. L. Suib, F. Liu, L. Zhen, W. Tan, L. Qin, *J. Chem. Eng.* **2017**, *328*, 464–473. **DOI:**10.1016/j.cej.2017.07.066
81. R. Han, W. Zou, Z. Zhang, J. Shi and J. Yang, *J. Hazard. Mater.* **2006**, *137*, 384–395. **DOI:**10.1016/j.jhazmat.2006.02.021
82. Q. Kang, L. Vernisse, R. C. Remsing, A. C. Thenuwara, S. L. Shumlas, I. G. McKendry, M. L. Klein, E. Borguet, M. J. Zdilla, D. R. Strongin, *J. Am. Chem. Soc.* **2017**, *139*, 1863–1870. **DOI:**10.1021/jacs.6b09184
83. D. Robati, *J. Nanostructure Chem.* **2013**, *3*, 55–60. **DOI:**10.1186/2193-8865-3-55
84. D. Sidiras, F. Batzias, E. Schroeder, R. Ranjan, M. Tsapatsis, *J. Chem. Eng.* **2011**, *171*, 883–896. **DOI:**10.1016/j.cej.2011.04.029
85. E. Eren, H. Gumus and A. Sarihan, *J. Desalination*. **2011**, *279*, 75–85. **DOI:**10.1016/j.desal.2011.05.058
86. Y. Huang, C. Hsueh, C. Huang, L. Su and C. Chen, *J. Sep. Purif. Technol.* **2007**, *55*, 23–29. **DOI:**10.1016/j.seppur.2006.10.023
87. S. Recillas, A. García, E. González, E. Casals, V. Puntes, A. Sánchez and X. Font, *J. Desalination*. **2011**, *277*, 213–220. **DOI:**10.1016/j.desal.2011.04.036
88. C. Andrea, C. Rosas, M. Franzreb, F. Valenzuela and W. H. Höll, *J. React. Funct. Polym.* **2010**, *70*, 516–520. **DOI:**10.1016/j.reactfunctpolym.2010.03.011
89. E.Alvarez-Ayuso, A. Garcia-Sàncheza and X. Querol, *J. Water Res.* **2003**, *37*, 4855–4862. **DOI:**10.1016/j.watres.2003.08.009
90. J. R. Rangel-Mendez and M. Streat, *J. Water Res. 36*. **2002**, *36*, 1244–1252. **DOI:**10.1016/S0043-1354(01)00343-8
91. M. J. Young, A. M. Holder, S. M. George, C. B. Musgrave, *J. Chem. Mater.* **2015**, *27*, 1172–1180. **DOI:**10.1021/cm503544e
92. H. Li, F. Liu, M. Zhu, X. Feng, J. Zhang, H. Yin, *J. Environ. Sci.* **2015**, *34*, 77–85. **DOI:**10.1016/j.jes.2015.02.006

Povzetek

Z netoksičnimi metodami smo sintetizirali lamelarne in nanostrukturirane manganove okside. Materiali so bili enofazni z značilnimi morfologijami in pretežno mezoporozno strukturo. Preučevali smo možnosti odstranjevanja težkih kovin Cd(II) in Pb(II) s sintetiziranimi materiali Na-MnO_2, u-MnO_2 (v obliki morskih ježkov) in c-MnO_2 (v obliki zapredkov). Z vidika kinetike je bil najučinkovitejši od treh preizkušenih materialov lamelarni Na-MnO_2 ki ima več praznin v plasteh MnO_6 kot tudi med posameznimi plastmi. Nanomateriala u-MnO_2 in c-MnO_2 sta izmenjevala katione v tunelih in vdolbinah. Maksimalne adsorbirane količine so si sledile za Pb(II): Na-MnO_2 (297 mg/g) > u-MnO_2 (264 mg/g) > c-MnO_2 (209 mg/g) in za Cd(II): Na-MnO_2 (199 mg/g) > u-MnO_2 (191 mg/g) > c-MnO_2 (172 mg/g). Na-MnO_2 je izkazoval najboljšo stabilnost med strukturami in sproščal le male količine mangana. Rezultati kažejo potencial lamelarnih (Na.MnO_2) in nanostrukturiranih (U-MnO_2 in C-MnO_2) manganovih oksidov kot selektivnih, ekonomičnih in stabilnih materialov za odstranjevanje toksičnih kovin v vodnem mediju.

Except when otherwise noted, articles in this journal are published under the terms and conditions of the Creative Commons Attribution 4.0 International License

DOI: 10.17344/acsi.2020.6095 *Acta Chim. Slov.* **2020,** *67,* 1196–1201
creative commons

Scientific paper

Study of Selected Morphologic, Structural and Optical Effects of Silver Coated CBD-CdS Thin Films

Angel Roberto Torres-Duarte,[1] Horacio Antolín Pineda-Leon,[1,2] Aned de Leon,[3,*] Ramón Ochoa-Landín[4] and Santos Jesús Castillo[1]

[1] *Departamento de Investigación en Física, Universidad de Sonora, Apdo. Postal 5-088, CP. 83000, Hermosillo, Sonora, México*

[2] *Departamento de Matemáticas, Universidad de Sonora, CP. 83000, Hermosillo, Sonora, México*

[3] *Departamento de Ciencias Químico Biológicas, Universidad de Sonora, C.P. 83000, Hermosillo, Sonora, México.*

[4] *Departamento de Física, Universidad de Sonora, CP. 83000, Hermosillo, Sonora, México*

* *Corresponding author: E-mail: aned.deleon@unison.mx*

Received: 05-08-2020

Abstract

This work focused on comparing cadmium sulphide (CdS) thin films with and without CdS silver aggregates (CdS:Ag) deposited on the surface. We report absorption and transmission responses. Using the Tauc method, we obtained direct band gap energies with values of 2.50 (CdS) and 2.49 eV (CdS:Ag). We performed a scanning electron microscope characterization at different magnifications were cluster formations with granular shapes were observed. The highest magnification of 50,000× showed silver clusters as shiny granulates, which were confirmed by microprobe elemental mapping at a magnification of 18,000×. Energy Dispersive Spectroscopy revealed that the light composition of the silver clusters was the unique difference from the CdS thin film. X-Ray Diffraction results only detected the hexagonal CdS pattern, but not that of silver. The crystallite size was of around 13 nm. A Surface-Enhanced Ramman Scattering effect was observed upon the silver coating of the CdS thin film at 293.3 cm^{-1}.

Keywords: CdS thin films; Ag coated film; CBD; characterization

1. Introduction

Cadmium sulphide has been applied in some optoelectronical devices, window layers,[1] and on thin film solar cells due to their suitable band gaps, absorption coefficient and high optical transparency in the visible light range spectrum, in addition to being low-cost.[2,3] However, upon direct contact, CdS is a hazardous material for living beings.[4] It has been reported that silver (Ag) has no negative effect on humans.[5] This work focuses on applying a silver coating on a CdS thin film and characterizing: a) the pure CdS and b) the silver coated CdS thin films. At this point, we examined if the properties were modified upon the presence of silver and how. The coating we examined in this case was formed of discrete clusters.

The synthesis methods of CdS are pulsed laser deposition (PLD),[6] molecular beam epitaxy (MBE),[7] thermal evaporation, sputtering, chemical vapor deposition (CVD),[8] chemical bath deposition (CBD),[9] among others. In this work we chose CBD since it is the most simple, fast and cheap technique that yields thin films with similar properties than those obtained with more complicated and expensive methodologies.[10]

In 2000, SJ Castillo et al. diffused metallic indium on a CdS thin film.[11] In 2010, A. de Leon et al. theoretically studied the interactions between CdS and glycine.[12] In 2011, A. Apolinar-Iribe et al. synthesized hexagonal CdS thin films with acetylacetone as complexing agent through CBD.[13] In 2017, M. Ruiz-Preciado et al. developed criteria to adjust the growth of both, CdS and CdTe Thin Films elaborated by the PLD technique.[14] In 2011, S. Rengaraj et al. developed a solution phase synthesis method for cubic CdS hollow microspheres of around 2.5 μm in diameter,

with photocatalytic activity.[15] In 2019, Chao Xu et al. predicted the formation of clusters of combined elements including cadmium, silver, sulfur and oxygen with promising semiconducting and photocatalytic activity.[16] T. Zhai et al. have synthesized CdS micro/nanowires, nanorods, nanotubes and other nanostructures for applications in electronic and optoelectronic devices.[17]

J. Kaur et al. synthesized CdSe thin films doped with Ag and analyzed some morphological, optical and structural properties.[18] Furthermore, CdS thin films were prepared via thermal evaporation and then immersed on a silver nitrate ($AgNO_3$).[19]

2. Experimental

In this section, we explain the CdS thin film and the silver coated CdS thin film recipes. The cadmium source for the CdS thin film, was 10 mL of a 0.1M solution of cadmium nitrate, $Cd(NO_3)_2$. To this solution we added 20 mL of a 0.5 M solution of the complexing agent, sodium citrate, $Na_3C_6H5O_7$. To control the pH of the reaction, we used 10 mL of a 0.3 M solution of potassium hydroxide (KOH). Afterwards, we poured 10 mL of a 0.5M solution of thiourea, $CS(NH_2)_2$, as the sulfur source. Next, we included 5 mL of a pH 11 buffer, NH_4OH/NH_4Cl. Finally, we added deionized water to an afforated volume of 95 mL. Furthermore, we vertically immersed 4 Corning brand soda lime glass substrates in the reactor at 70 °C for 30 min. After this, we obtained 4 CdS thin films deposited on the glass substrate. Two of these samples were used for characterization. The other two were reimmersed on a colloidal silver suspension at 24 °C for 20 min. The colloidal silver suspension was prepared with 2.5 mL of Microdyn brand commercial colloidal silver (0.082% volume of colloidal silver). Two silver coated CdS thin films were obtained.

The CdS and silver coated CdS thin films were characterized through different devices. Transmission and adsorption characterizations were performed with a UV-Vis Nanodrop 2000 ThermoScientific brand spectrophotometer. SEM and EDS characterizations were carried out with JEOL JSM-7800F equipment. The XRD characterization was realized with a RIGAKU Dmax2100 equipment. The Raman characterization was done with Dilor Labram II equipment at an excitation line of 632.8 nm.

3. Results and Discussion

As it can be seen on Fig. 1, the CdS thin film has a low absorption between 553 and 1100 nm. While it has an absorption edge at wavelengths lower than 496 nm. On the other hand, the transmission graph for this thin film shows a transmission higher than 70% for wavelengths higher than 553 nm. The CdS:Ag thin film has a low absorption between 615 and 1100 nm. It has an absorption edge at wavelengths lower than 498 nm. On the other hand, the transmission graph for this thin film shows a transmission higher than 70% for wavelengths higher than 615 nm. The transmission curves between CdS and CdS:Ag thin films differ from 492 to 894 nm, where the CdS layer coated with silver decreases its transmission mildly. It should be noted that CdS thin films are yellowish, while the resulting CdS thin films coated with silver change to an amber-like color.

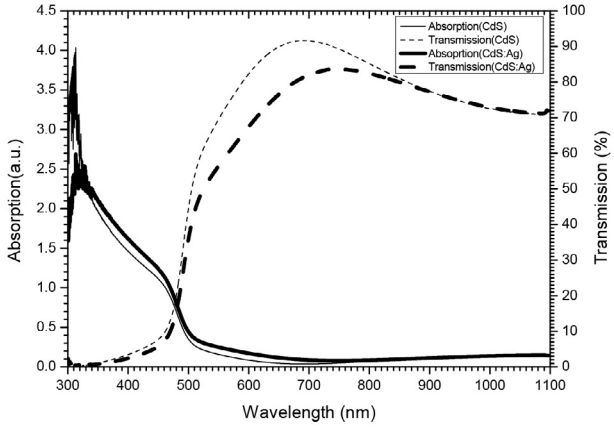


Figure 1. Absorption and transmission responses for CdS and silver coated CdS thin films.

We processed the optical absorption data generated on Fig. 1 in order to obtain Fig. 2 where we evaluated the direct band gaps through the Tauc method.[20] We performed linear regressions (see supplementary material) to both curves on Fig. 2 to obtain the band gap and the error propagation. The direct band gaps were of 2.49 ± 0.007 eV and 2.50 ± 0.009 eV. This reduction can be interpreted as a very localized doping on the surface. These energy band gap values correspond to 496 and 498 nm for the CdS and silver coated CdS thin film, respectively. On the study performed by Shah et al.,[19] the CdS thin film reached a maxi-

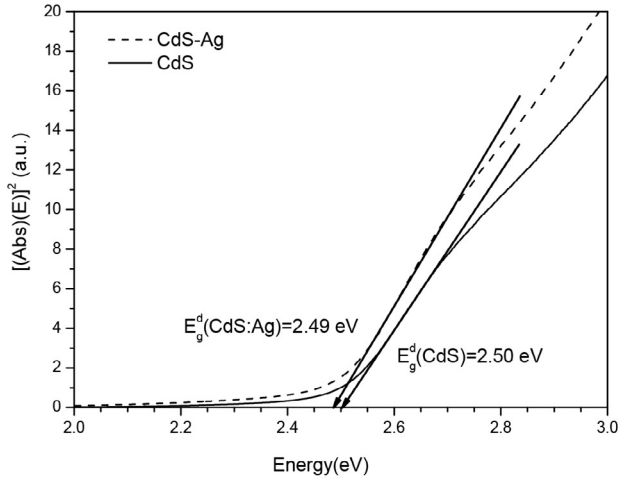


Figure 2. Direct band gaps obtained via the Tauc method.

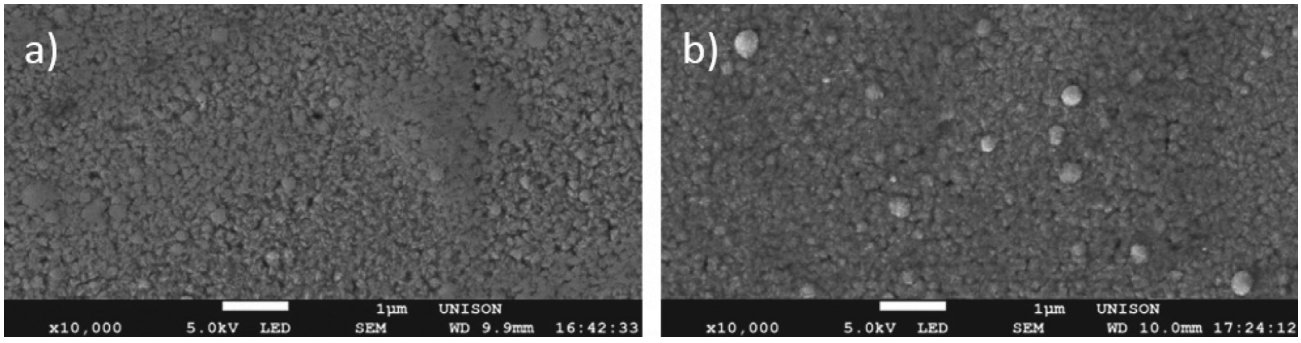


Figure 3. SEM 1μm images at a magnification of 10,000× of a) CdS thin film, b) silver coated thin film.

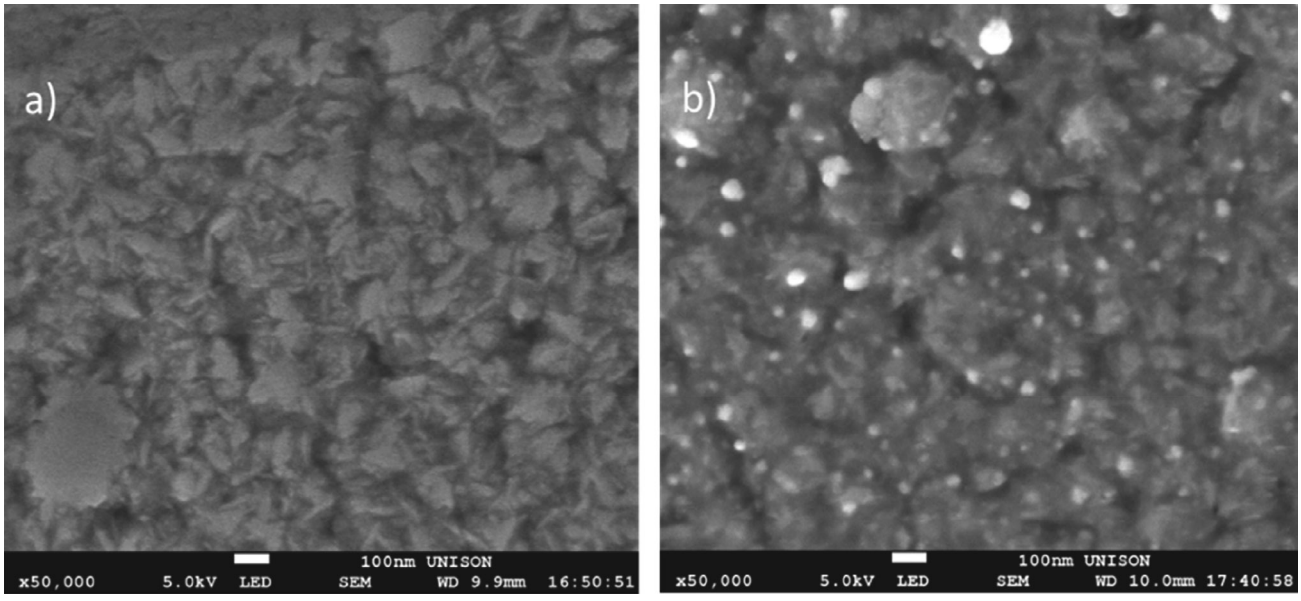


Figure 4. SEM 100 nm images at a magnification of 50,000x of a) CdS thin film, b) silver coated thin film.

mum transmission value of 80%. Our results show that beyond 589 nm the transmission values were higher than 80% and up to 92% on the visible region.

The morphologic studies performed by the SEM technique show differences on the surfaces of the films. Figure 3 depicts a scale of 1 μm at a magnification of 10,000×. Part a) corresponds to the CdS thin film where a flat background is observed with some imperfections. Part b) corresponds to the silver coated CdS thin film. Additional isolated spheres appeared, which we expect to be

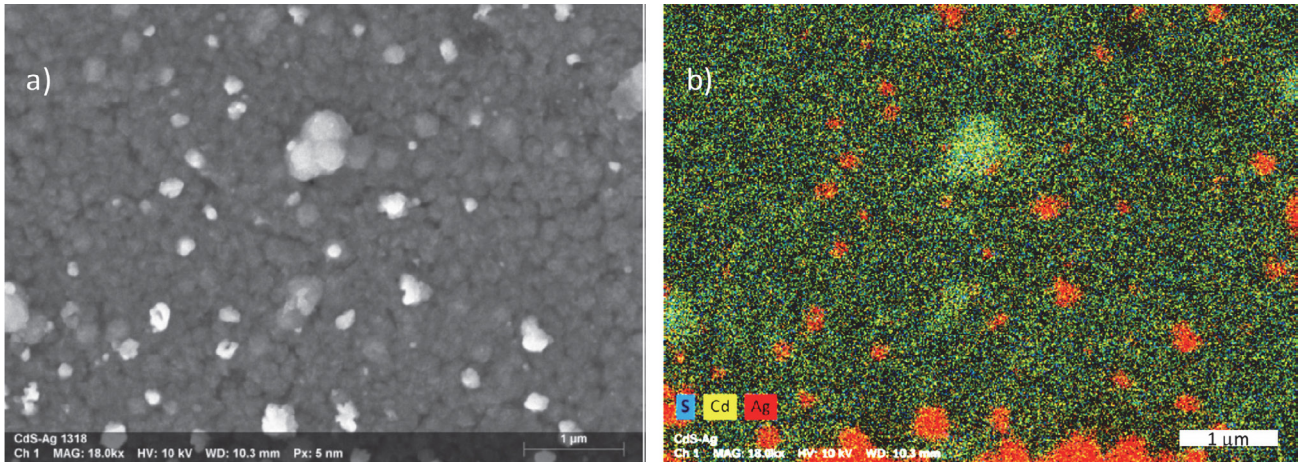


Figure 5. Silver coated thin film images: a) SEM 1μm at a magnification of 18,000×, b) EDS coupled to SEM surface mapping.

silver since the CdS thin films were immersed in a colloidal silver suspension.

Figure 4 displays the films of Figure 3 at a scale of 100 nm and a magnification of 50,000×. Part a) corresponds to the CdS thin film with flat background and granular formations (CdS clusters). Part b) corresponds to the silver coated CdS thin film. We presume that the small, shiny grains formed were Ag aggregates.

An elemental mapping was carried out on the bilayer of the silver coated CdS thin film with the distributions of the elements sulphur, cadmium and silver. Part a) corresponds to a morphologic image on a gray scale formed by secondary electrons. Part b) is formed by a EDS energy detector coupled to the SEM generating a surface mapping of the indicated element distribution. As it can be seen, the bright spots have a high composition of silver as indicated on part b) of Figure 7. Related theoretical research can be found with this configuration of materials on the scientific literature by Chao Xu et al.[16] The research made by Shah et al. obtained noticeably different morphology and did not present the formation of silver aggregates.[19]

EDS measurements were performed to both films. The distribution of elements was portrayed on Figure 6, where the curves of both films are superposed. The CdS thin film curve has well-defined signals for oxygen, sodium, silicon, sulphur, cadmium and other elements. Cadmium and Sulphur signals are due to the film, yet the rest of them are originated from the substrate.

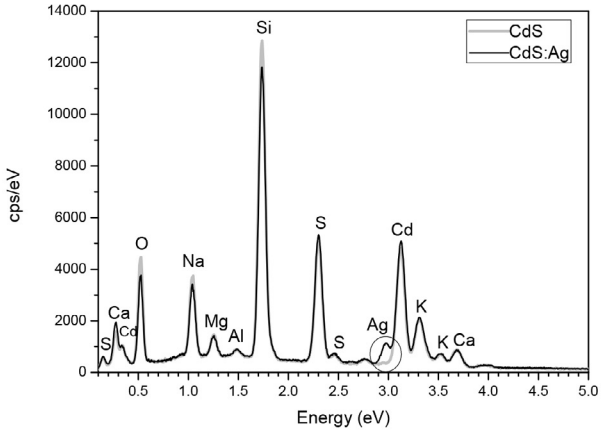


Figure 6. EDS measurements of CdS (gray solid line) and silver coated CdS (black solid line) thin films.

In the case of the silver coated CdS thin film, signals corresponding to the elements aforementioned were present. In addition, a signal corresponding to the energy of silver at 2.98 KeV arose. This characterization enhances the slight difference between both systems of thin films. This justifies a surface difference in chemical composition.

Table I lists EDS measurements (mass %) and the calculated atomic percentages of the elements labeled on Figure 6. The study focused on the next elements: carbon, oxygen, sodium, silicon, sulphur, cadmium and silver. Sulphur and cadmium percentages almost remained constant on both films. However, in the thin film immersed in a colloidal silver suspension, an atomic percentage of silver of 1.90 % emerged. In comparison to the work of Shah et al. a similar trend in composition for the EDS was observed.[19]

Table I. EDS measurements: mass and atomic percentages.

	CdS		CdS:Ag	
Element	**Mass (%)**	**Atoms (%)**	**Mass (%)**	**Atoms (%)**
C	3.93	11.25	4.50	13.44
O	12.8	27.53	10.44	23.39
Na	4.07	6.09	4.09	6.37
Si	21.68	26.56	20.72	26.45
S	9.89	10.61	9.79	10.94
Cd	42.76	13.09	40.39	12.88
Ag	–	–	5.71	1.90
Others	4.87	4.87	4.36	4.63

The next characterization is XRD. Figure 7 compiles the XRD patterns for CdS and CdS:Ag. The identified planes indicated on the figure are: (002), (101), (103) and (112). These correspond to hexagonal CdS (PDF# 41-1049). As it can be appreciated, the pattern for the silver coated CdS film is mildly more defined. This enhancement could be due to the silver clusters deposited on CdS. From the CdS pattern we calculated the crystallite size () by using the Debye-Scherrer equation.

$$c_s = \frac{0.9\lambda}{\beta cos\theta} \tag{1}$$

Where is the used X-ray wavelength = 1.5418 Å; is the full width at half maximum (FWHM) of the main peak, 0.0108 rad and is half of angular value at the peak location in the diffraction pattern, .

$$c_s = \frac{0.9(1.5418\text{Å})}{0.0108(cos13.36°)} = 132.057\text{Å} = 13.2057\text{ nm} \tag{1}$$

This crystallite size was obtained utilizing the XRD for the CdS thin film.

Finally, Figure 8 presents the comparison of the Raman dispersion spectra. The black curve shows sequential disperson bands of low amplitude, without well defined peaks. On the other hand, when the CdS layer was coated with silver, the Raman dispersion spectrum was modified significantly at 293.3 cm^{-1} (first order longitudinal optic mode 1LO), where the peak is significantly higher than that of the CdS thin film, represented by the gray curve. This behavior has been reported on the literature.[15] The fundamental modification consists on an extreme magnification on the 1LO dispersion due to the SERS (sur-

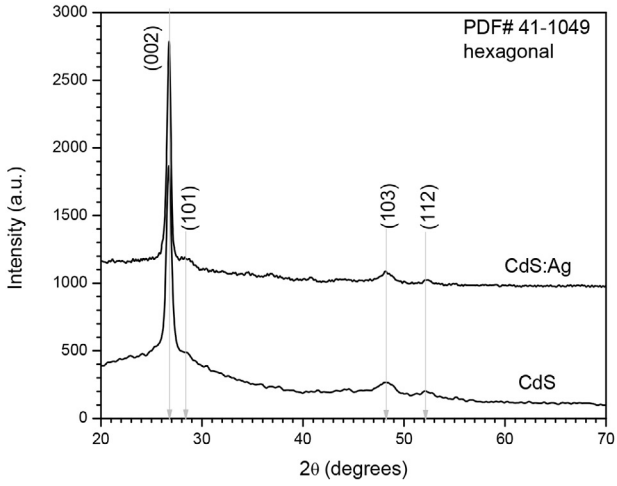


Figure 7. XRD patterns for CdS (lower) and silver coated CdS (upper) thin films.

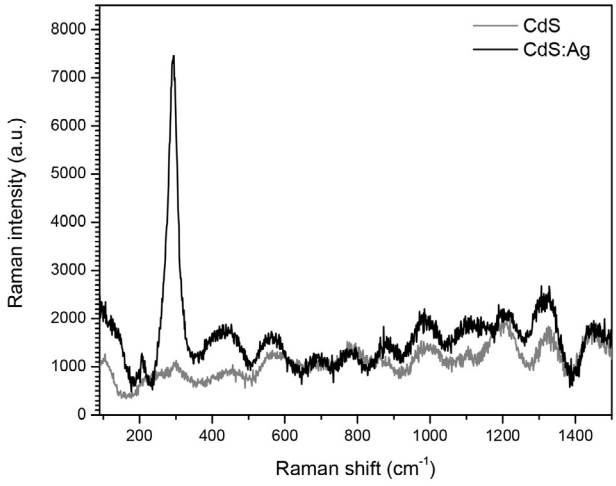


Figure 8. Raman dispersion spectra of CdS (gray solid line) and silver coated CdS (black solid line) thin films.

face-enhanced Raman scattering) effect. Similar results were obtained in the literature.[19]

4. Conclusions

On the comparative study of CdS and silver coated CdS thin films slight differences on their properties were observed. The most important differences were the formation of silver discrete aggregates and the SERS effect on the Raman characterization. In addition, the absorption and transmission properties varied slightly from 492 to 894 nm, causing the band gap to decrease in only 0.01 eV. XRD studies did not detect the presence of silver.

5. References

1. M. Isshiki, J. Wang, II-IV Semiconductors for Optoelectronics: CdS, CdSe, CdTe. In: S. Kasap, P. Capper (Ed.) Springer, Cham. **2017**, 853–865. **DOI:**10.1007/978-3-319-48933-9_33
2. J. M. Kephart, R. M. Geisthardt, W. S. Sampath, *Prog. Photovolt*. **2015**, 23, 1484–1492. **DOI:**10.1002/pip.2578
3. M. F. Rahman, J. Hossain, A. Kuddus, S. Tabassum, M. H. K. Rubel, H. Shirai, A. B. M. Ismail, Appl. Physics A. **2020**, 126, 145:1–11. **DOI:**10.1007/s00339-020-3331-0
4. A. Pramanik, A. K. Datta, S. Gupta, B. Ghosh, D. Das, D. V. Kumbhakar, *Int. J. Res. Pharm. Sci*. **2017**, *8*, 741–753.
5. S. Sarkar, A. D. Jana, S.K. Samanta, G. Mostafa, *Polyhedron* **2007**, *26*, 4419–4426. **DOI:**10.1016/j.poly.2007.05.056
6. H. Pengchen, L. Bing, F. Lianghuan, W. Judy, J. Haibo, Y. Huimin, X. Xinju, *Surf. & Coat. Technol.* **2012**, *213*, 84–89.
7. W. P. Mc Cray, *Nature Nanotech* **2007**, *2*, 259–261. **DOI:**10.1038/nnano.2007.121
8. M. A. Buckingham, A. L. Catherall, M. S. Hill, A. L. Johnson, J. D. Parish, *Cryst. Growth Des.* **2017,** *17*, 907–912. **DOI:**10.1021/acs.cgd.6b01795
9. K. Mokurala, L. L. Baranowski, F. W. de Souza-Lucas, S. Siol, F. A. Maikel, M. van Hest, S. Mallick, P. Bhargava, A. Zakutayev, *ACS Combinatorial Sci.* **2016**, *18*, 583–589. **DOI:**10.1021/acscombsci.6b00074
10. M. F. Rahman, J. Hossain, A. Kuddus, M. M. A. Moon, A. B. M. Ismail, *SN App. Sci.*, 2, 590:1–12.
11. S. J. Castillo, A. Mendoza-Galvan, R. Ramirez-Bon, F. J. Espinoza-Beltrán, M. Sotelo-Lerma, J. González-Hernández, G. Martínez, *Thin Solid Films*, **2000**, *373*, 10–14. **DOI:**10.1016/S0040-6090(00)01080-4
12. A. de Leon, M. C. Acosta-Enriquez, S. J. Castillo, D. Berman-Mendoza, A. F. Jalbout, *J. Molec. Struct.: THEOCHEM*, **2010**, *951*, 34–36. **DOI:**10.1016/j.theochem.2010.04.003
13. A. Apolinar-Iribe, M. C. Acosta-Enriquez, M. A. Quevedo-Lopez, R. Ramirez-Bon, S. J. Castillo, *Chalc. Lett*. **2011** *8*, 77–82.
14. M. Ruiz-Preciado, M. A. Quevedo-Lopez, A. G. Rojas-Hernandez, A. de Leon, A. Apolinar-Iribe, R. Ochoa-Landin, G. Valencia-Palomo, S. J. Castillo, *Digest J. Nanomater. and Biostruct.* **2017**, *12*, 1057–1067.
15. S. Rengaraj, S. H. Jee, S. Venkataraj, Y. Kim, S. Vijayalakshmi, E. Repo, A. Koistinen, M. Sillanpää, *J. Nanosci. Nanotechnol.* **2011**, *11*, 2090–2099. **DOI:**10.1166/jnn.2011.3760
16. X. Chao, S. Ming-Ming, S. Hua-Tian, M. Strømme, Z. Qian-Feng, *Dalton Trans*. **2019**, *48*, 5505–5510. **DOI:**10.1039/C9DT00480G
17. T. Zhai, X. Fang, L. Li, Y. Bando, D. Golberg, *Nanoscale* **2010**, *2*, 168–187. **DOI:**10.1039/b9nr00415g
18. J. Kaur, R. Kaur, S. K. Tripathi, *Acta Metallurgica Sinica (Eng. Lett.)* **2019**, *32*, 541–549. **DOI:**10.1007/s40195-018-0824-3
19. N. A. Shah, A. Nazir, W. Mahmood, W. A. A. Syed, S. Butt, Z. Ali, A. Maqsood, *J. Alloys and Compounds* **2012**, *512*, 27–32. **DOI:**10.1016/j.jallcom.2011.08.081
20. J. Tauc, *Mater. Research Bull.* **1968**, *3*, 37–46. **DOI:**10.1016/0025-5408(68)90023-8

Povzetek

V delu je opisana priprava tankih filmov kadmijeveda sulfida (CdS) z metodo sinteze plasti iz raztopin in nalaganjem prevleke iz delcev srebra (CdS:Ag). Merili smo absorpcijske in transmisijske odzive. Izračunane širine prepovedanega pasu so 2.50 (CdS) in 2.49 eV (CdS:Ag). Z metodo vrstične elektronske mikroskopije smo opazovali tvorbo skupkov granularne oblike. Pri največji povečavi 50000x smo opazili granulate srebrovih skupkov in jih karakterizirali z elementnim mapiranjem pri povečavi 18000x. Energijsko disperzijska spektroskopija (EDX) je pokazala razliko med srebrovimi skupki in tankim filmom CdS. Rentgenska difrakcija je pokazala samo vrhove CdS, ne pa tudi srebra. Velikost kristalitov je približno 13 nm. Ramansko sipanje na srebrovi prevleki CdS filmov smo opazili pri 293.3 cm^{-1}.

Except when otherwise noted, articles in this journal are published under the terms and conditions of the Creative Commons Attribution 4.0 International License

DOI: 10.17344/acsi.2020.6108 *Acta Chim. Slov.* **2020,** *67,* 1202–1215
creative commons

Scientific paper

Assessment of Interaction of Human OCT 1-3 Proteins and Metformin Using Silico Analyses

Faruk Berat Akçeşme,[1,*] Nail Beşli,[2] Jorge Peña-García[3] and Horacio Pérez-Sánchez[3]

[1] *Department of Biostatistics and Medical Informatics, Faculty of Medicine, University of Health Sciences, Istanbul, Turkey*

[2] *Department of Medical Biology, Faculty of Medicine, University of Health Sciences, Istanbul, Turkey.*

[3] *Bioinformatics and High Performance Computing Research Group (BIO-HPC), Computer Engineering Department, Universidad Católica de Murcia (UCAM), Guadalupe, 30107, Spain.*

** Corresponding author: E-mail: farukberat.akcesme@sbu.edu.tr*
Tel: +090-537- 502 2634

Received: 05-13-2020

Abstract

Metformin, a drug frequently used by diabetic patients as the first-line treatment worldwide, is positively charged and is transported into the cell through human organic cation transporter (hOCT 1-3) proteins. We aimed to mimic the cellular uptake of metformin by hOCT1-3 with various bioinformatics methods and tools. 3D structure of OCT1-3 proteins was predicted by considering the structures and function of these proteins. We predicted functional regions (active and ligand binding sites) of OCT1-3 and performed comparative bioinformatics analysis. The predicted structure of hOCT1-3 was then analyzed in the Blind Docking server and the results were confirmed with predicted binding site residues and conserved domain regions. We simulated the OCT1-3 and metformin docking and also validated the docking procedure with other substrates of HOCT1-3 proteins. We selected the best poses of metformin docking simulations as per binding energy (–5.27 to –4.60 kcal/mol). Lastly, we validated the static description of protein-ligand (OCT-Metformin) interactions by performing molecular dynamics simulation. Eventually, we obtained stable simulation of OCT-metformin interaction.

Keywords: Organic cation transporters; metformin; protein structure prediction; model Validation; docking

1. Introduction

Membrane proteins are associated with the prominent functions in the cell, approximately responsible for 30% genes in the human genome[1] and currently possessing 50% of pharmaceutical drug discovery.[2] Membrane proteins perform a broad variety of particular roles during cellular events.[3] Due to its structural and physicochemical properties, the plasma membrane has a selective permeability for organic and inorganic substances including cation and anion compounds. Hence, it assists to sustain the unique content both inside and outside of the cell.

One of the protein families that provide translocation of cationic organic and inorganic compounds that localized in the cell membrane is SLC (Solute carrier) family from the MFS superfamily. The SLC family is a 22-membered cell membrane transporter. A subfamily of the SLC family is SLC22A1,2 and 3 (cd17379: MFS_SLC22A1_2_3).[4] Besides many essential cation molecules for the cell, the SLC transporters are the target of drugs with high pharmacological value. The human body constitutes more than 400 important SLC transporters for a broad range of tasks including drug metabolism as absorption, distribution, and excretion. Hence, there is a growing interest in the effects of the drug on the development and progression of interactions with these transporters.[5]

Metformin, categorized as an anti-diabetic medication, is uptaken by the cell via SLC transporter proteins encoded by SLC22A1-3 (also named OCT1-3) genes.[6] OCT1-3 membrane proteins are expressed at different levels in several tissues, to name a few, the renal expression level of OCT-2 is high, whereas OCT-3 is most commonly expressed in skeletal muscle,[7] and OCT-1 is expressed primarily in hepatocytes.[8] Metformin is hydrophilic (logD –6.13 pH 6.0) and its pKa (physiological pH) is 12.4.[9] Functional elimination of OCT-1 in pri-

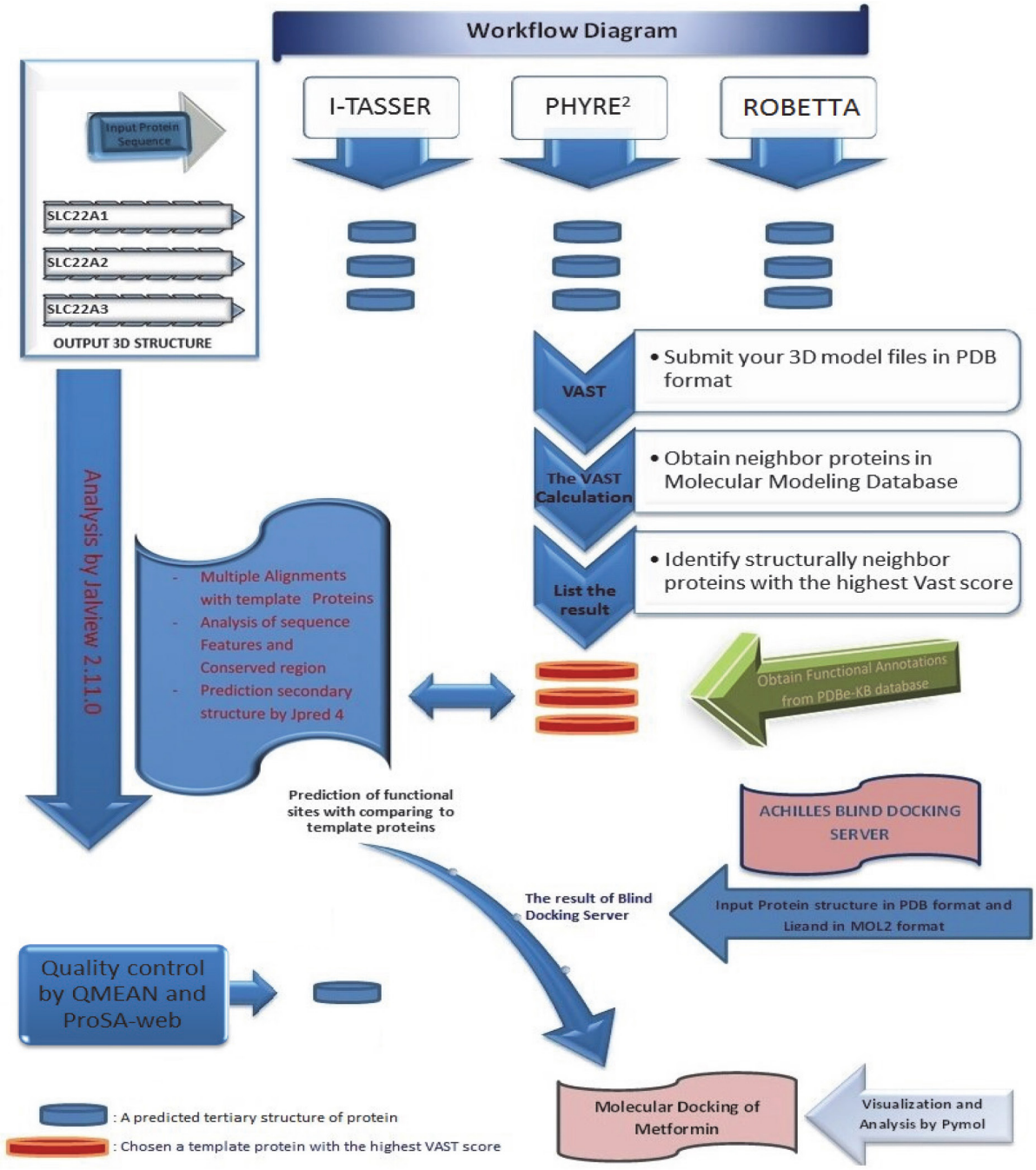


Figure 1. The identification of the molecular modeling of OCT1-3 and metformin. There are four main steps in the workflow. The first step is the prediction of the 3D structure of OCT1-3 proteins and quality control of the model protein structures. The second one is the identification of the template proteins with the VAST. The third one is the analysis of the sequence data by Jalview 2.11.0 while the fourth is the molecular docking by Achilles Blind Docking Server.

mary mouse hepatocyte culture and OCT-1 has been demonstrated to play an important role in metformin response in vivo mouse model.[10] Following the entry into the cell via HOCT1-3, metformin exhibits its anti-diabetic properties in several ways. It is broadly believed that the blood-glucose-lowering impact of metformin is mediated chiefly through the repression of hepatic glucose production by decreasing gluconeogenesis and blocking glucagon-mediated signaling in the liver.[11,12] Furthermore, some mechanisms have been suggested that metformin can activate AMPK (AMP-activated protein kinase) by the upstream liver kinase B1,[11] enhanced AMP/ATP rate hereby the restraint of mitochondrial respiratory chain complex I.[13] Metformin improves the activity of the insulin receptor and IRS-2 (insulin receptor substrate 2) and boosts glucose uptake through enhanced translocation of

glucose transporters, such as GLUT-1, to the plasma membrane.[14]

In the current study, we aimed to predict the three-dimensional structure of human OCT1-3 using various computational approaches through consideration of the current authenticated/trusted bioinformatics tools. The molecular docking was also performed under the inspiration of the in vitro and in vivo foundings. We also performed Molecular dynamics (MD) simulation of metformin and hOCT1-3 dockings at the atomic level for validation. The computational approaches to OCT1-3 proteins, the particular structure prediction of the proteins and the simulations using MD, have been broadly implemented for investigating their dynamic actions.

Given the pharmacological importance of SLC22A1,2 and 3 proteins in humans, determination of the structure of these proteins, the estimation of their active sites, and the definition of how the transport mechanism works have aroused great interest. In the present study, we have reported and defined the ligand-dependent interactions of hOCT1-3 with metformin and the other ligands utilizing computational approaches and explored the found interactions through comparative analysis, homology modeling, and molecular dynamic studies. This study is the first attempt to demonstrate OCT1-3 interaction with metformin. This interaction has characterized by docking analysis and the results were validated with MD simulations. This is an important study that uses the predicted structure of OCT proteins to stimulate the interaction which stays highly stable throughout the MD analysis.

2. Materials and Methods

2. 1. Computational Structural Modeling of OCT1-3

2. 1. 1. Prediction of Secondary and Tertiary Structure of OCT1-3 Proteins

We retrieved OCT1, 2, and 3 (Accession no: AAI26365.1, NP_003049.2, and NP_068812.1, respectively) from GenBank in FASTA format, predicted the secondary structure of the proteins using JPred4,1[5] which is the latest version of the JPred online prediction server supplying by the JNet algorithm.

Each of OCT1-3 protein structures was predicted on PHYRE[2],[16] Robetta[17,18] and I-TASSER[19,21] (protein structure prediction servers). In these prediction tools, homology modeling (or comparative modeling) was used to compare experimentally determined proteins as templates. To control the quality of the model proteins, we performed the local structural quality of transmembrane protein models analysis using (QMEANBrane)[22] and ProSAweb.[23]

We compared each of the obtained models to all PDB proteins in MMDB (Molecular Modeling Database) to find 3D similar structures in VAST (Vector Alignment Search Tool).[24] The VAST analysis was contributed to the following proteins with the highest scores, PDB Id: 4zw9_A, 4zwc_A, and 5c65_A. Each of the OCT1-3 protein structures obtained from the Robetta server was then selected as a model since its neighboring proteins have the highest VAST scores and %Ids, compared to the other prediction tools (See Fig1).

The Computed Atlas of Surface Topography of proteins (CASTp)[25] 3.0 was utilized to predict the surface of the binding pocket of the model proteins for the interaction with their substrates.

2. 1. 2. Sequence Analysis

We performed a pairwise in BLASTP[26] and multiple sequence alignment in Clustal OMEGA[27] for each of the OCT1, 2, and 3 proteins with the selected template proteins (4zw9, 4zwc, and 5c65) obtained from the VAST. Parameters for the alignment with the Clustal OMEGA were set as –GAPEXT :0.1, ENDGAPS: 0.5, GAPDİST: 1, GAPOPEN:10, and MATRIX: BLOSUM62. We analyzed and interpreted the results in the Jalview 2.11.[28]

To analyze the feature of the sequences, functional annotations of template proteins were retrieved from the PDBe-KB database[29], followed by the comparison of these proteins with the model proteins to identify the conserved regions- the sequence features. In this way, we assigned the predicted functional sites, predicted PTM sites, and predicted ligand binding sites, and ligand binding sites, and interaction interfaces for our model proteins.

2. 1. 3. Visualization

The visualization of the primary and secondary structures of the proteins was performed using the Jalview 2.11. The PyMOL[30] software was utilized to represent and analyze the atomic structure of proteins.

2. 1. 4. Molecular Docking Simulations

One of the most essential steps in this study is the molecular simulation as given in the workflow in Fig1. For the preparation of the docking process, hOct1-3 proteins were downloaded from the Robetta server in PDB format. All ligands (Metformin, Phenformin, and Norepinephrine) of hOct1-3 were retrieved within the SDF format from PubChem.[31] We removed the water, added the polar hydrogen to the model proteins. Then, we charged the model proteins and the ligands by the computation of Gasteiger before converting to pdbqt format using the AutoDock Vina.[32] Prior to the docking process, the 3D model protein structure was subjected to the energy minimization method in chimera 1.14[33] with the default parameters: the steepest descent:100 with 0.02 step sizes, without fixing any atoms, followed by 10 steps of conjugate gradient steps with 0.02 step size (Å) minimization.

The docking study was carried out under the ACHILLES BLIND DOCKING SERVER3[4] protocol (https://biohpc.ucam.edu/achilles/). The figures were prepared using the PyMOL.

2. 1. 5. Molecular Dynamics (MD) Simulations

To evaluate the structural constancy and validate the static description of the protein-ligand (hOCT-metformin) interactions, we ran an MD simulation using the Desmond Software.[35] The dynamic nature of protein-ligand interactions has been studied and atomic-level interactions were investigated.

3. Results and Discussion

3. 1. Alignments

We aligned a range of 146–445 aa of OCT-1 with 85–397 aa of 4ZW9 and 4ZWC as explained previously. The OCT-1 sequence has shown a 22.77% sequence identity with 4zw9 and 4zwc. We aligned a range of 146–540 aa of OCT-1 with of 63–477 aa of 5c65 by 22.51% of identity.

In the case of OCT-2, we aligned a range of 24–546 aa of OCT-2 with of 93–510 aa of 4ZW9 and 4ZWC, and 71–438 aa of 5c65 by the same percentage of identity (26.57%).

Table 1. The list of the results of the sequence features analyzing multiple alignments. The residues of OCT 1-3 proteins that interact with metformin, phenformin, and norepinephrine and functional annotations of template proteins from PDBe-KB.

		Exported Functional Annotations of the templates proteins from PDBe-KB
		OCT-1
Metformin	GLU^{137} PRO^{481} ARG^{488}	Conserved Domain 4zw9; Predicted Ligand binding sites, 5c65; Ligand binding sites
Phenformin	GLN^{152} ASN^{156} LYS^{214} TRP^{354} ASP^{357} GLN^{362} ILE^{446}	4zw9; Predicted Ligand binding and functional sites, Ligand binding sites 4zw9; Ligand binding sites, Conserved Domain 4zw9; Predicted Ligand binding and functional sites 4zw9; Predicted Ligand binding sites, Conserved Domain 4zw9; Predicted Ligand binding and functional sites, Ligand binding sites 4zw9; Predicted Ligand binding and functional sites, Conserved Domain
		OCT-2
Metformin	ASN^{157} CYS^{474} ASP^{475}	4zw9; Predicted Ligand binding sites, Ligand binding sites, Conserved Domain 4zw9; Predicted Ligand binding sites, 4zwc; Predicted PTM sites, 5c65; Ligand binding sites, Conserved Domain 4zw9; Predicted Ligand binding sites
Phenformin	TYR^{37} ASN^{157} LYS^{215} TYR^{245} TYR^{362} CYS^{474} ASP^{475}	 4zw9; Predicted Ligand binding sites, Ligand binding sites, Conserved Domain 4zw9; Predicted Ligand binding and functional sites 4zw9; Predicted Ligand binding and functional sites, Ligand binding sites 4zw9; Predicted Ligand binding sites, Ligand binding sites, Predicted functional sites, 5c65; Predicted PTM sites, Conserved Domain 4zw9; Predicted Ligand binding sites, 4zwc; Predicted PTM sites, 5c65; Ligand binding sites, Conserved Domain 4zw9; Predicted Ligand binding sites
		OCT-3
Metformin	VAL^{37} ASN^{162} ARG^{212} GLN^{366}	 4zw9; Predicted Ligand binding sites, Ligand binding sites, Conserved Domain 4zw9; Predicted Ligand binding sites, Ligand binding sites, Conserved Domain 4zw9; Predicted Ligand binding sites, Ligand binding sites, Conserved Domain
Norepinephrine	PHE^{36} VAL^{39} GLN^{158} ASN^{162} ARG^{212}	 4zw9; Predicted Ligand binding and functional sites, Ligand binding sites 4zw9; Predicted Ligand binding sites, Ligand binding sites, Conserved Domain 4zw9; Predicted Ligand binding sites, Ligand binding sites, Conserved Domain

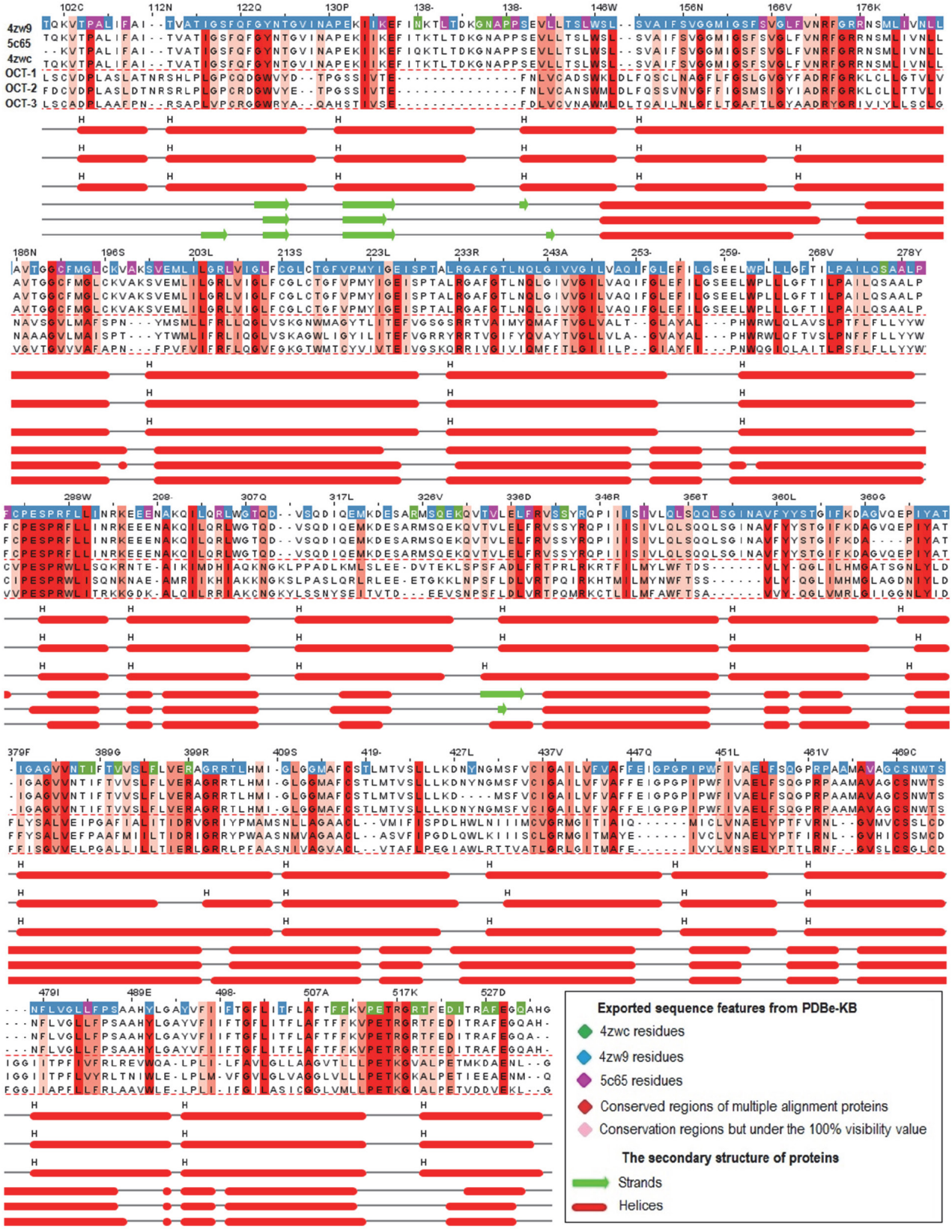


Figure 2. The representation of primary and secondary structure of 4zw9, 5c65, and 4zwc, and OCT1-3 proteins. The visualization of sequence features and the Conserved Domain of the protein residues are colored through an analysis performed by the Jalview 2.11.0. The probability of conserved regions decreases through the dark red to the pink. After the multiple alignments, the OCT-1 protein was set as the reference for the sequence numbering. As a result of multiple sequencing, the overlapping regions of the proteins were solely exhibited.

In OCT-3, we aligned a range 60–353 aa of OCT-3 with of 86–513 aa of 4zw9 and 4zwc by 24.53% of identity, whereas we aligned a range of 84–353 aa of OCT-3 with of 64–473 aa of 5c65 by 24.53% of identity.

3. 2. Analysis of Conserved Domain and Sequence Features of OCT1-3

After subjecting OCT1-3 and template proteins sequences to multiple alignments, we detected the conserved

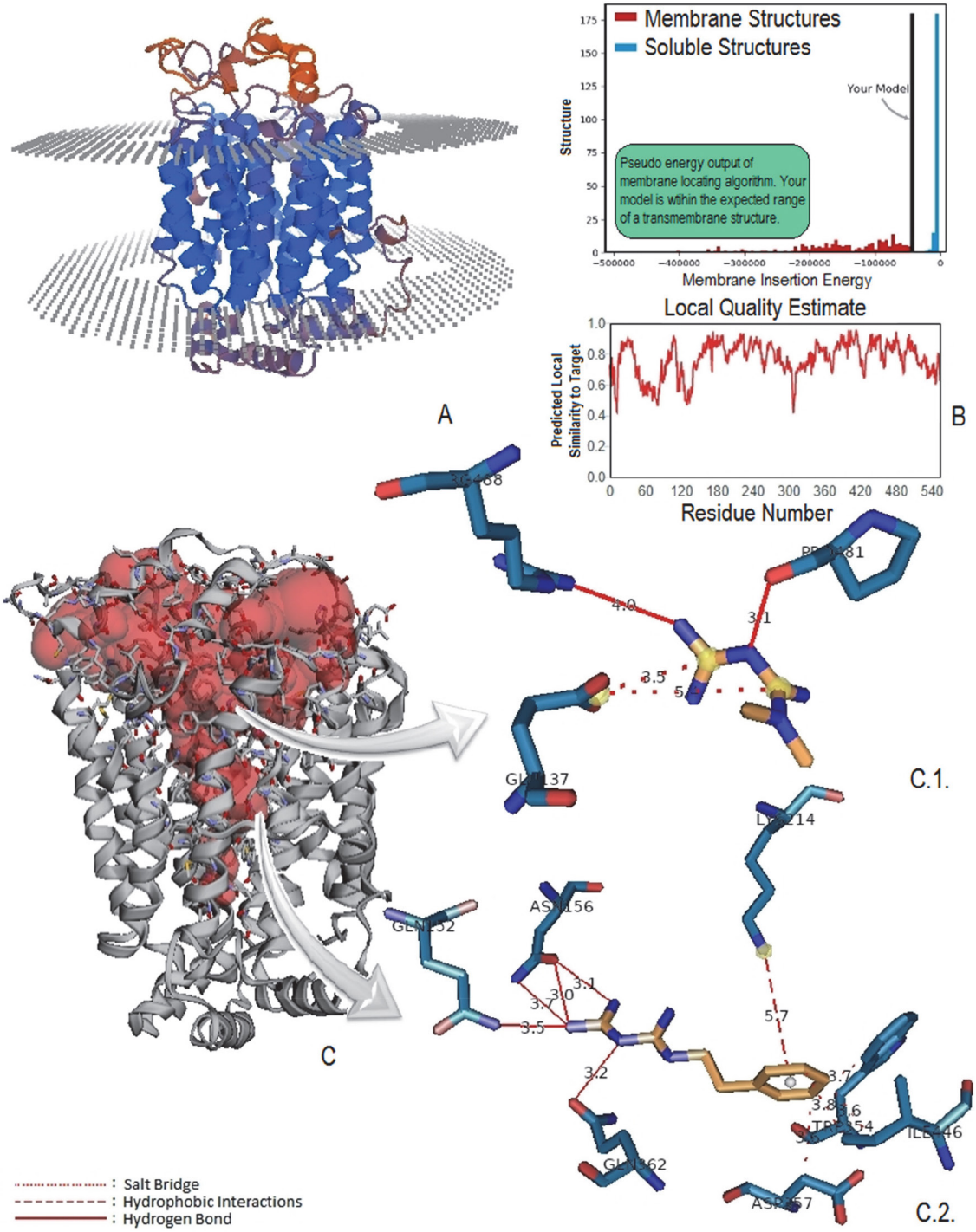


Figure 3. The representation of the molecular modeling of OCT-1 and metformin, and phenformin. A. OCT-1 transmembrane protein embedded in the plasma membrane model was predicted by QMEANBrane. B. Structure validation of modeled OCT-1 concerning membrane insertion energy and the local quality estimate of the residues of the model OCT-1. C. The surface of the binding pocket of the model OCT-1 as computed using CASTp 3.0. Molecular simulation of the best pose of the interaction of OCT1 and metformin(C1), phenformin(C2) with the highest docking scores.

Table 2. The list of the best binding energy poses of metformin, phenformin, and norepinephrine, and hOCT1-3 proteins through the Autodock Vina

Cluster Populations The highest binding energy (kcal/mol)		
	Metformin	Phenformin
OCT-1	–4.60	–7.00
OCT-2	–5.20	–8.60
	Metformin	Norepinephrine
OCT-3	–5.27	–5.93

regions through the comparative analysis in the Jalview 2.11.0 (See Fig2). We summarized the results of the comparative analysis as a list in Table1.

The cellular and biological functions of a protein are highly related to its 3D structure. The pharmacodynamics of a drug on the cell decreases or has no effect if the functional parts of these proteins are mutated in the genome. On the other hand, defining protein-ligand binding sites and explaining functional parts of the protein are critical approaches for drug discovery.[36] Regarding the pharmaco-

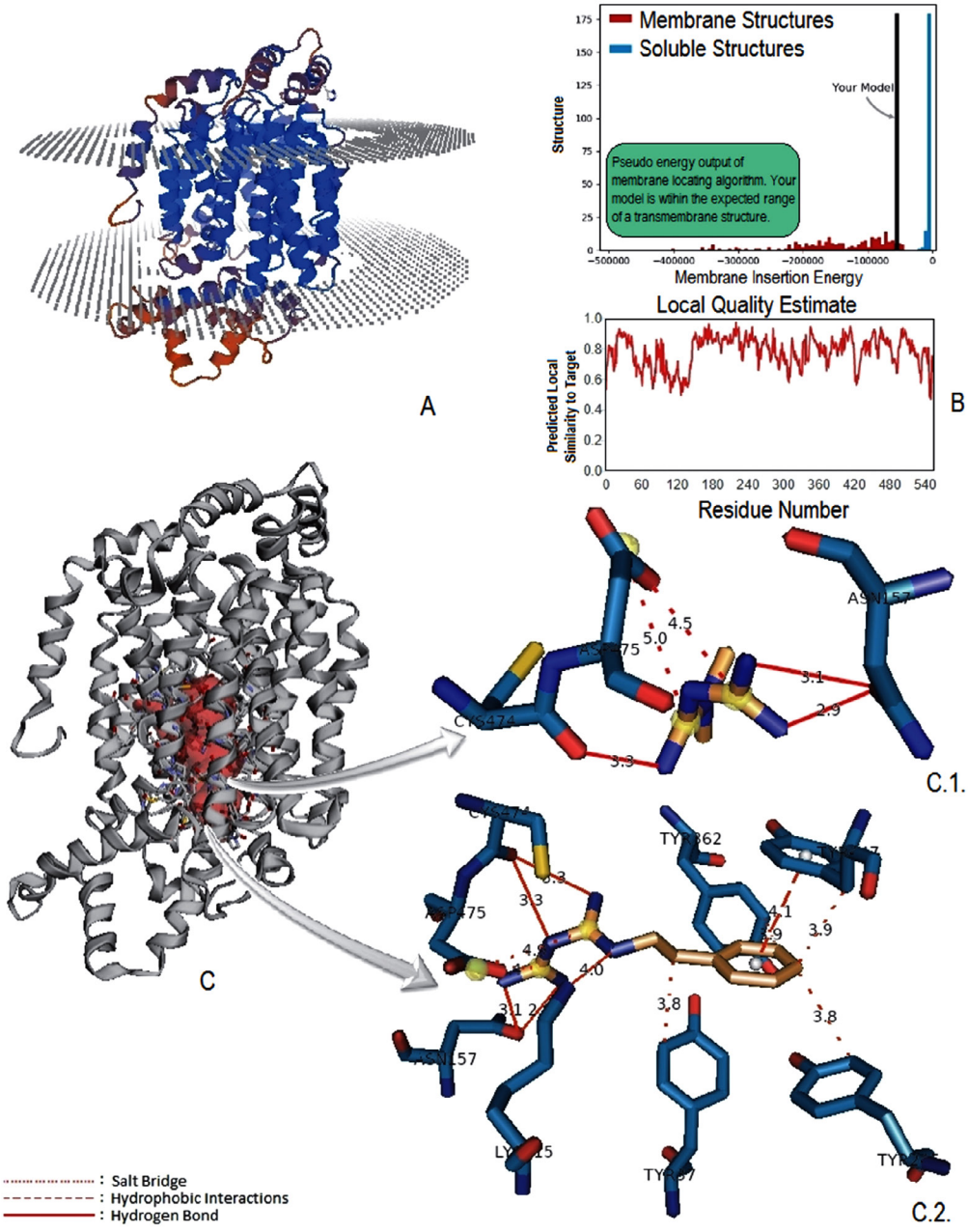


Figure 4. Representation of molecular modeling of OCT-2 and metformin, and phenformin. A. OCT-2 transmembrane protein embedded in the plasma membrane model was predicted by QMEANBrane. B. Structure validation of modeled OCT-1 concerning membrane insertion energy and the local quality estimate of the residues of the model OCT-2. C. The surface of the binding pocket of the model OCT-2 as computed using CASTp 3.0. Molecular simulation of the best pose of the interaction of OCT-2 and metformin(C1), phenformin(C2) with the highest docking scores.

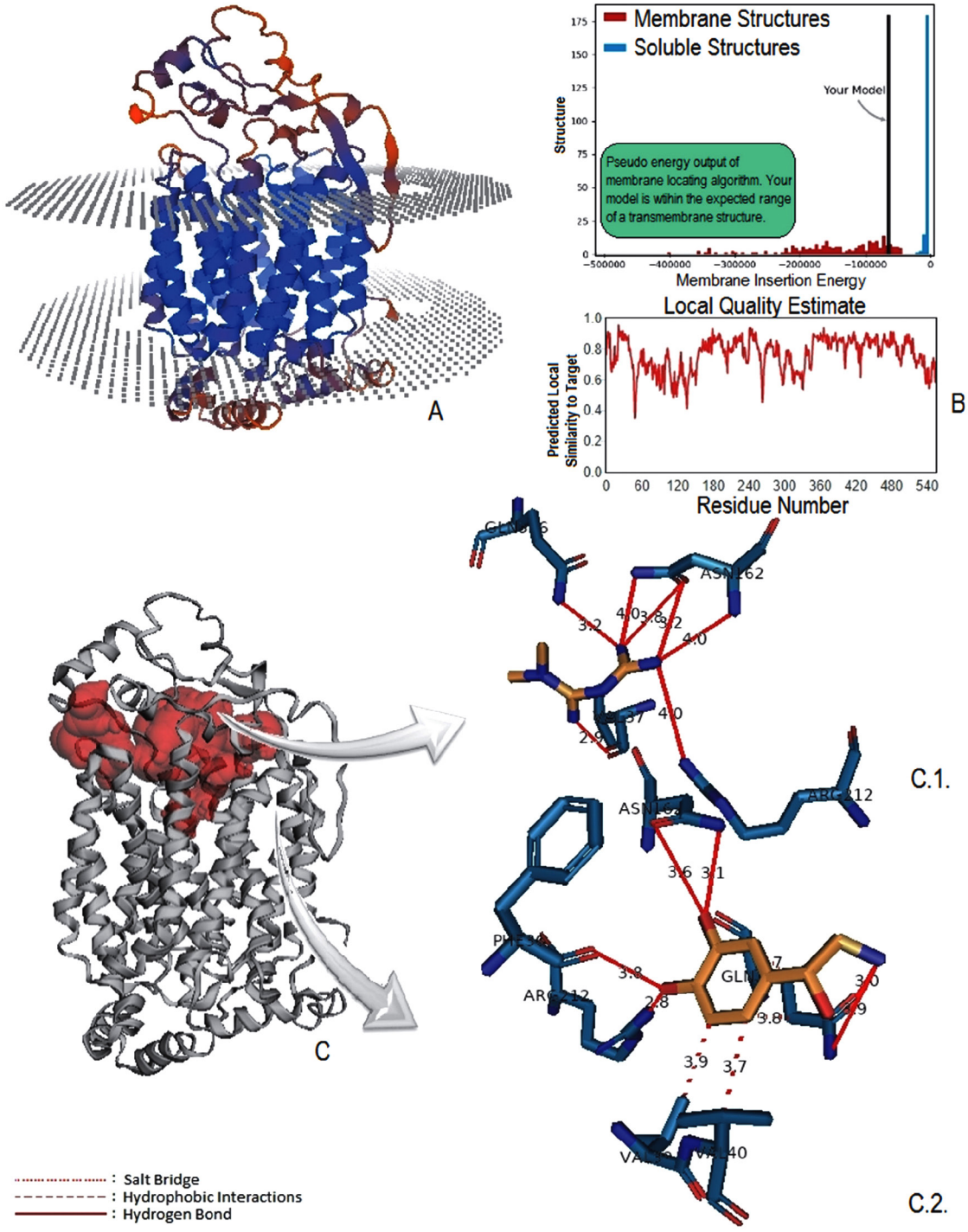


Figure 5. Representation of the molecular modeling of OCT-3 and metformin, and norepinephrine. A. OCT-3 transmembrane protein embedded in the plasma membrane model was predicted by QMEANBrane. B. Structure validation of modeled OCT-1 concerning membrane insertion energy and the local quality estimate of the residues of the model OCT-3. C. The surface of the binding pocket of the model OCT-3 is computed using CASTp 3.0. Molecular simulation of the best pose of the interaction of OCT-3 and metformin(C1), norepinephrine (C2) with the highest docking scores.

dynamics of metformin, the 3D prediction of OCT1-3 proteins and the determination of ligand binding sites in the functional sites are critical to investigate their effects on the cell.

Recent studies and meta-analyses have shown that patients with T2DM have a lower incidence of tumor development than healthy controls and cancer patient that use metformin has a lower risk of mortality.[37] Metformin

takes more attention after the discovery of its role in cancer prevention and treatment has been revealed. Improving or managing cellular uptake of therapeutic entities is mostly related to the understanding of the molecular mechanism of the interaction with the components of the cell membrane and therapeutic entities. This paper aimed to predict the 3D structure of OCT1-3 protein and identify its role in the uptake of metformin into the cells that have been studied by in vitro and in vivo studies previously.[38,39]

Sequence and structure analysis of proteins of unknown function with those of proteins of known function enable us to discover and deduce the function of the unknown proteins. Characterization of protein function by in vivo and in vitro studies is both time and labor-consuming. Furthermore, some proteins, especially membrane proteins are exceedingly difficult to be crystallized by experimental tools. In the modern genomic and proteomic era, a protein is mostly identified before its function is determined, therefore the role of in silico studies in structural analyses of proteins becomes more important in recent years.

The structure of OCT1-3 proteins has not been uncovered yet by any experimental tools although some of the protein`s structures have already known in the same protein family. This paper is important for being the first attempt to study and predict the 3D structure of OCTs to reveal the information about how these proteins facilitate the uptake of metformin into the cells. Even though our analysis indicates no significant similarity between OCTs and the proteins of the database at a sequence level, the predicted OCTs are similar with its conservative regions to some carrier proteins that share a similar function.

It is known that 30 percent of all sequences are membrane proteins. Unlike globular proteins, a 3D model for membrane proteins can hardly be computed. Another important aspect of this paper is presenting a new pipeline to stimulate the docking of protein molecules in the absence of a similar sequence in the database. The recent algorithms in 3D structure prediction of proteins enable us to predict the structure of proteins in high accuracy even in the absence of sequence similarity. In silico analyses helped us to stimulate this biological process and propose the uptake of metformin by OCTs as it is shown in Fig 3–5.

Dakal et al. modeled the 3D structures of hOCTs by only one tool- I-TASSER in 2017.[40] In Fig 1, four key steps of this pipeline have been shown as the workflow. One of the very critical points, the prediction of the 3D structure of the protein, was performed by three different tools; Iterative Threading ASSEmbly Refinement, Phyre2 that uses protein homology, and Robetta. The output model proteins were then exposed to all proteins in the PDB by the calculation in the VAST. This approach is reflected in our results through an elevation in the accuracy in the protein structure prediction. We were eager to increase the accuracy of the prediction through the validation of these structures using the experimentally determined proteins as templates. After obtaining the structure of the OCTs, the orientation of these molecules in the plasma membrane was predicted using the QMEANBrane scoring function.

Transmembrane proteins play vital roles in a diverse range of essentially biological processes. Knowing about the protein position within the lipid bilayer is important and requires a computational approach, since identifying the correct orientation is possible by defining the relationship between sequence, structure, and the lipid environment. One of the commonly used tools to localize the structure of proteins within the lipid player by knowledge-based statistical potential, QMEANBrane was used and the predicted position as exhibited in Fig 3–5. As a result, all model proteins are within the expected range of transmembrane structures.

Models obtained from the other tools were determined to be inapplicable for the docking process. The Robetta is continuously evaluated with CAMEO (Continuous Automated Model EvaluatiOn), which constantly assesses the accuracy and reliability of the prediction. Among other prediction tools, CAMEO, Robetta, and QMEANBrane are the first-line with time-based statistical confidence and they show reliable performance. We also used the ProSAweb to verify the quality of the model protein structures. The Z-score designates the entire model-quality for OCT1-3, (Z-score:–8.59, –7.04, and –5.95, respectively) as shown in Figure 6.

To analyze sequence features, functional annotations of template proteins were retrieved from the PDBe-KB database. The recently released database, PDBe-KB, give us a great opportunity to analyze and visualize sequence features of the similar proteins that are used as the template to assign a novel function to our sequence of interest. Even though the sequence similarity is low, as shown in the results, there are significantly conserved regions. In this way, we assigned the predicted functional sites, predicted PTM sites, and predicted ligand binding sites, and ligand binding sites, and interaction interfaces to OCTs.

Representation of molecular modeling of OCTs and metformin was performed using the Blind Docking server. The server mainly utilizes a customized version of Autodock Vina[32] for the blind docking calculations. We obtained binding energy plots, and, in this way, the most energetically favorable dockings have been selected as the first best pose according to binding energy frequencies (See supplementary Fig1). Taking into account the model protein uncertainty as well as the small size of the metformin molecule, it is not surprising that many different ligands pose with similar scores. To cope with this, we used the CASTp bioinformatics tool and compared the predicted active sites of model proteins with the first best poses as the docking results. Interestingly, both output results from two servers were similar. Besides, for the results to be more meaningful, the pharmacologically important phenformin from metformin analogs was validated by the docking study of OCT-1 and OCT-2, whereas OCT-3 by

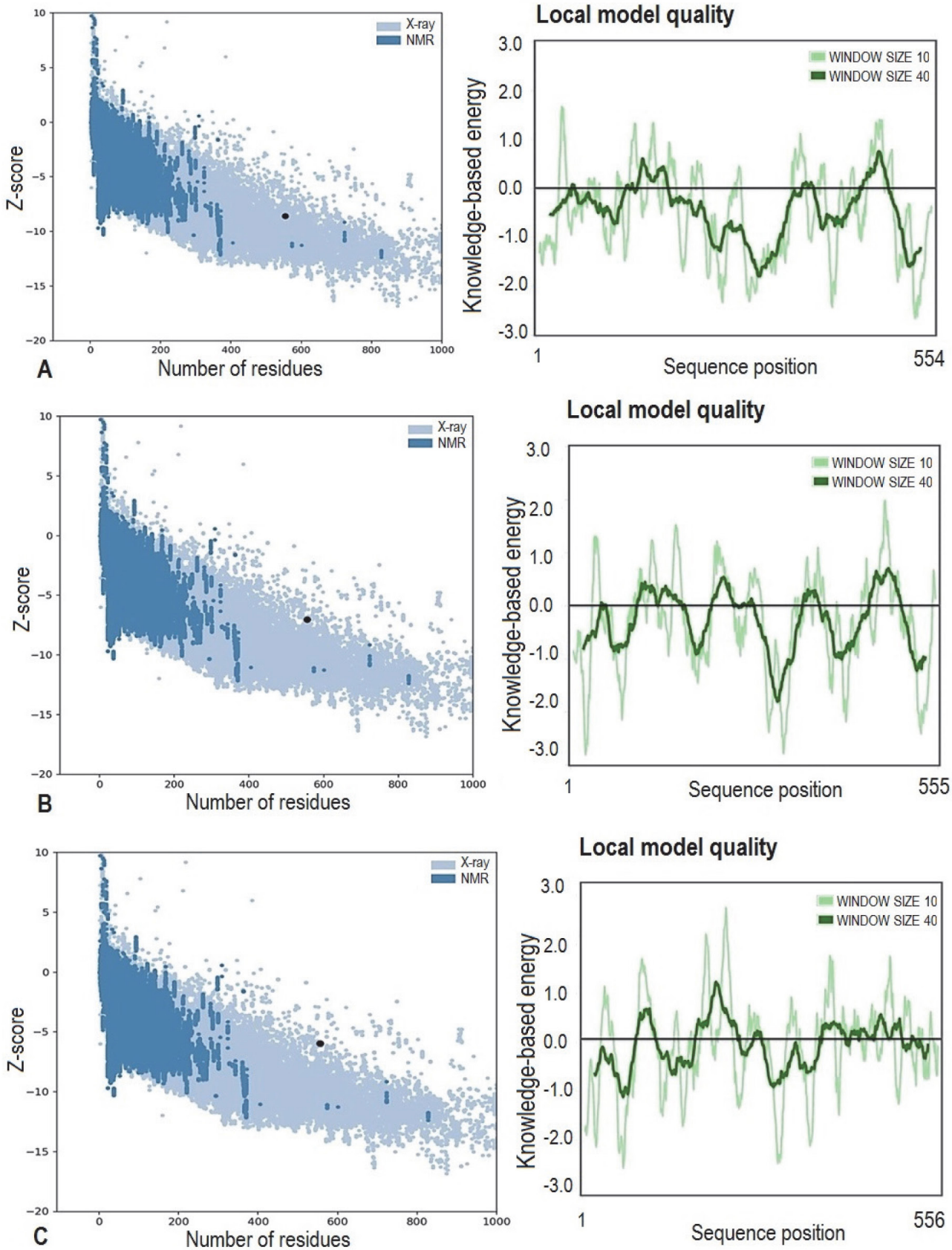


Figure 6. ProSA-web service analysis of human OCT1-3 proteins. The black points represent that model hOCT1-3 proteins are in the range of Z-score values of the experimental structures according to several residues. The other graph shows the local quality concerning many sequence positions (A; OCT-1, B; OCT-2, C; OCT-3). respectively (Z-score:–8.59, –7.04, –5.95).

the norepinephrine compound. We also combined these outputs with outcomes from exported functional annotations of the template proteins from PDBe-KB. We visualized the interaction of metformin, phenformin, and norepinephrine, and OCTs in PyMOL to better examine the poses and extract our images.

As listed in Table 1, OCT-1 forms hydrogen bonds with docked ligand molecules with the residue number of PRO481, ARG488, and GLN152, and ASN156, and GLN362. The other four residues in the predicted site (LYS214, TRP354, and ASP357, and ILE446) interacted by hydrophobic and salt-bridge bonds. Chen et al.[41] have reported that OCT-1 interacts with its ligands by hydrogen binding and non-covalent interaction through the ASP357, TRP354, and ASN156, and ILE446 residues among their predicted residues. OCT-2 interacted with both metformin and phenformin through ASN157, CYS474, and ASP475 residues with noncovalent interactions such as hydrogen bond, salt bridge, and hydrophobic interaction (See Figure 4). OCT-3 protein contacts with norepinephrine and metformin in the same residue (ASN162 and ARG212) by hydrogen bonds. Given the extensive hydrogen bonding motif of metformin, water may be involved. This may significantly impact and alter the results and

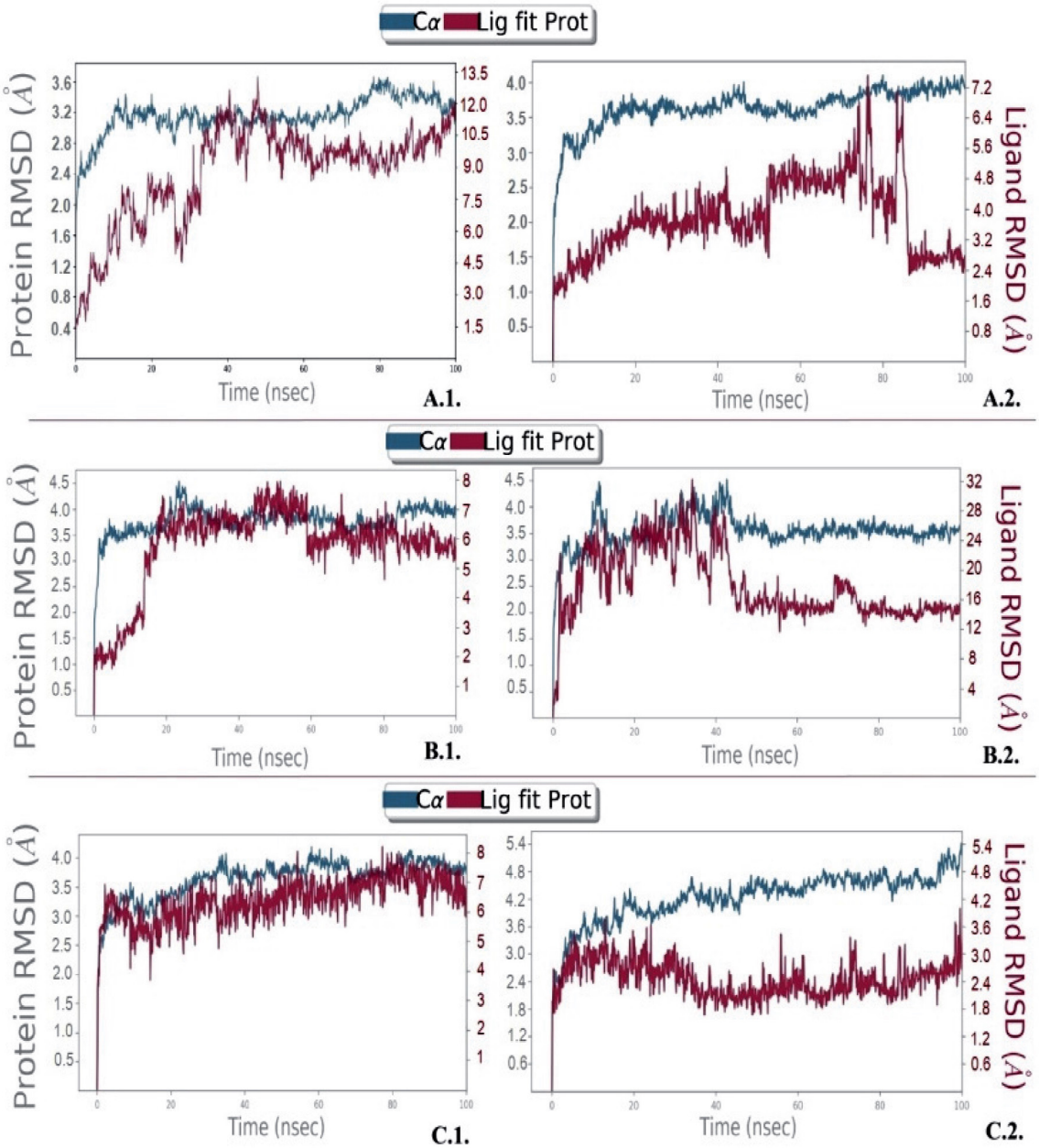


Figure 7: Desmond MD calculated Protein and Ligand RMSD: A.1.: OCT-1 and Metformin, A.2.: OCT-1 and Phenformin, B.1.: OCT-2 and Metformin, B.2.: OCT-2 and Phenformin, C.1.: OCT-3 and Metformin and C.2: OCT-3 and Norepinephrine

conclusions. Thus, we have considered performing the classic MD simulation for the docked complexes.

One of the residues that OCT-1 interacts with phenformin is GLN152 but OCT-3 interacts with norepinephrine through GLN158 as the same residue. The difference in the number of the residue is due to the setting of the sequenced reference. Our results suggest that human OCT proteins are predominantly expressed in different tissues of the human body and the active binding sites of these proteins also vary.

Although the methodology, including template definition, comparative protein modeling, and structure analysis, and molecular docking, seems pretty standard and employed in hundreds of research projects as in our workflow, there is a validation such as the quality control of the model proteins using Web services at almost every stage to increase reliability in achieving and evaluating meaningful results. Thus, the described pipeline is highly useful due to its ability to integrate the ligand-binding site and interaction interface information that is obtained from the PDBe-KB database to the information that is derived from similarity analysis and prediction tools. This pipeline is also promising to assign a function to predict the 3D structure even in the absence of any sequence similarity.

3. 3. MD Simulations

Root mean square deviation (RMD) of protein and ligand was calculated during the MDS concerning their initial structure. RMSD of the OCTs shows its stable conformation throughout the simulation which indicates the stability of the interaction with metformin and phenformin. Besides OCT3 was stable with norepinephrine throughout the simulation.

Each OCT proteins attained equilibrium in a few nsec and remain stable throughout the simulation time up to 100 nces. Initially, the RMSD plot for metformin attained equilibrium in a few nsec as well and remain stable throughout to stimulation. Some deviations observed but no bigger changes of the order of 1–3 Å are seen in our analysis. Similar RMSD scores were recorded with the phenformin interactions as well.

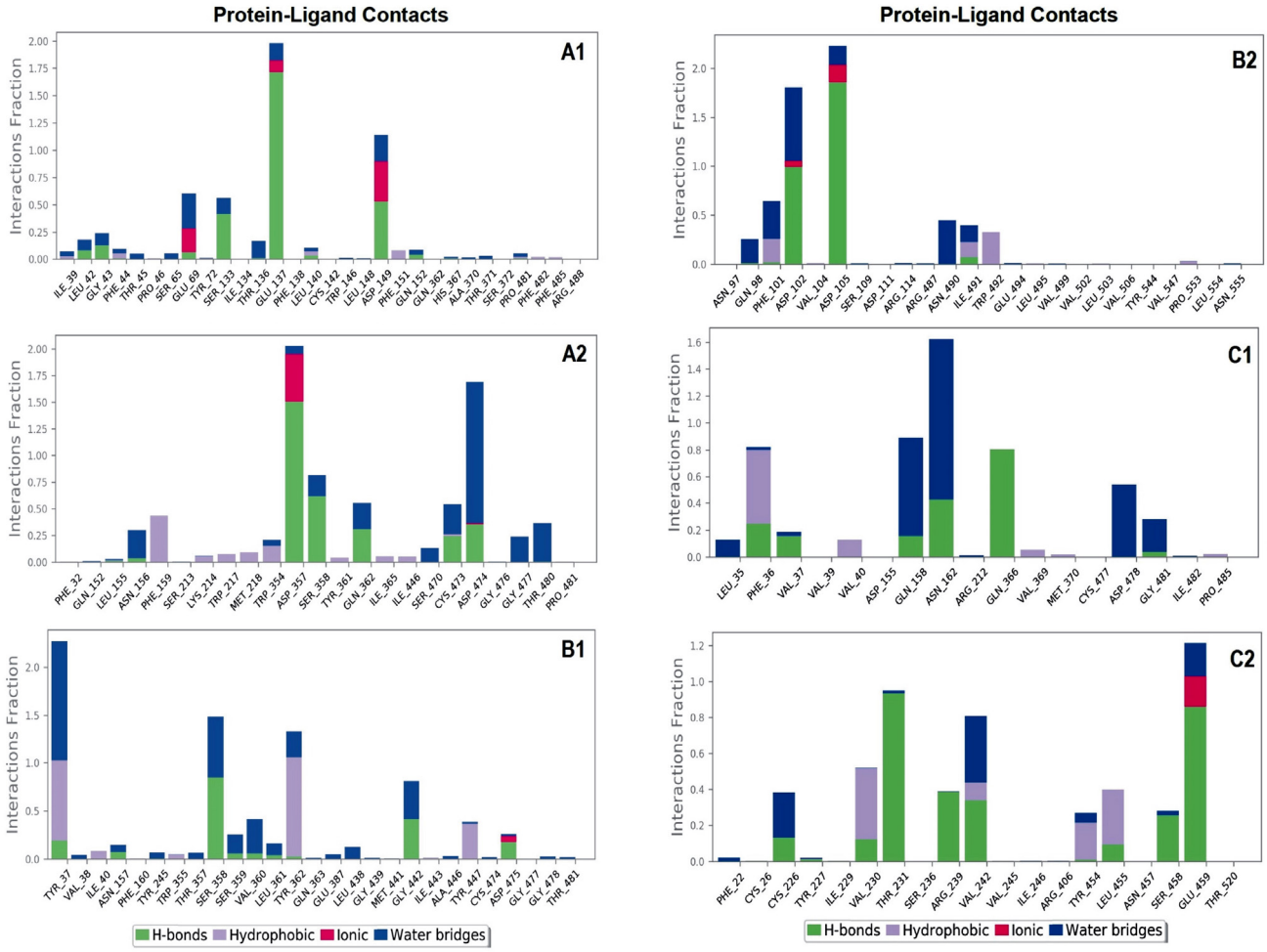


Figure 8: Protein-ligand contact interaction profile analyzed for the A1. OCT-1 and metformin, A2. OCT-1 and phenformin, B1. OCT-2 and metformin, B2. OCT-2 and phenformin, C1. OCT-3 and metformin, and C2. OCT-3 and norepinephrine

OCT1-3 interactions with the ligands were monitored throughout the simulation. The interactions are rich with H bonds these play significant roles in ligand binding.

Even though the involvement of human OCT in the uptake/transport of metformin is already mentioned in the literature, this study is demonstrating the hOCTs-metformin interaction at the atomic level for the first time and describing how and where the binding occurs. Mimicking this binding with the absence of the structural information of the protein was possible with the unique approach that was described in the pipeline in Figure 1.

4. Conclusion

The three-dimensional structure of a protein is a direct association with its comprehensive cellular and biological function. To investigate the tertiary atomic structure of OCT1-3 proteins and their localization in the cell membrane, it is significant to evaluate the pharmacodynamics of metformin, frequently preferred in Type 2 Diabetes Mellitus medication, through the determination of the residues which interact with metformin in the case of cell translocation of these proteins. One of the important limitations of mimicking protein-ligand interactions is the absence of the protein 3D structure. The presented new pipeline is promising especially for the interaction simulation studies that are conducted with proteins with unknown structures. To determine the therapeutic effect of Metformin or other life-saving drugs into the cells, further studies are needed to examine genetic variants of human OCTs in specific patient populations. Analyzing insertions, deletions, and other genetic variants effects on hOCTs in structure level are important to explore the role of these proteins in metformin pharmacokinetics and response. Our study could be a front preparation and inspiration for future positively charged drug discoveries and development by examining the atomic level of OCT proteins.

Conflict Of Interest

The authors declare that they do not have any conflict of interest.

Acknowledgements

We are thankful to Mungo Carstairs and his coworkers from the Barton group for their support in our study in the Jalview 2.11. This work has been funded by grants from the Spanish Ministry of Economy and Competitiveness (CTQ2017-87974), and by Fundacioń Seńeca de la Regioń de Murcia under Project 20988/PI/18. This research was partially supported by the supercomputing infrastructure of Poznan Supercomputing Center, the e-infrastructure program of the Research Council of Norway via the supercomputer center of UiT–the Arctic University of Norway, and by the supercomputing infrastructure of the NLHPC (ECM-02), Powered@NLHPC. This research project has been co-financed by the European Union (European Regional Development Fund– ERDF)

5. Reference

1. T. M. Bakheet, A. J. Doig, *Bioinformatics.* **2009**, *25*, 451–457. **DOI:**10.1093/bioinformatics/btp002
2. L. Fagerberg, K. Jonasson, G. Von Heijne, M. Uhlén, L. Berglund, *Proteomics.* **2010**, *10*, 1141–1149. **DOI:**10.1002/pmic.200900258
3. S. Tan, T. T. Hwee, M. C. M. Chung, *Proteomics.* **2008**, *8*, 3924–3932. **DOI:**10.1002/pmic.200800597
4. A. Marchler-Bauer, Y. Bo, L. Han, J. He, C. J. Lanczycki, S. Lu, F. Chitsaz, M. K. Derbyshire, R. C. Geer, N. R. Gonzales, et al., *Nucleic Acids Res.* **2016**, *45*, D200-D203. **DOI:**10.1093/nar/gkw1129
5. C. Colas, P. M. U. Ung, A. Schlessinger, *Medchemcomm.* **2016**, *7*, 1069–1081. **DOI:**10.1039/C6MD00005C
6. I. Pernicova, M. Korbonits, *Nat. Rev. Endocrinol.* **2014**, *10*, 143. **DOI:**10.1038/nrendo.2013.256
7. L. Chen, B. Pawlikowski, A. Schlessinger, S. S. More, D. Stryke, S. J. Johns, M. A. Portman, E. Chen, T. E. Ferrin, A. Sali, et al., *Pharmacogenet. Genomics.* **2010**, *20*), 687. **DOI:**10.1097/FPC.0b013e32833fe789
8. A. T. Nies, H. Koepsell, K. Damme, M. Schwab, *Handb. Exp. Pharmacol.* **2011**, 105–167. **DOI:**10.1007/978-3-642-14541-4_3
9. R. Saitoh, K. Sugano, N. Takata, T. Tachibana, A. Higashida, Y. Nabuchi, Y. Aso, *Pharm. Res.* **2004**, *21*, 749–755. **DOI:**10.1023/B:PHAM.0000026423.48583.e2
10. D.-S. Wang, J. W. Jonker, Y. Kato, H. Kusuhara, A. H. Schinkel, Y. Sugiyama, *J. Pharmacol. Exp. Ther.* **2002**, *302*, 510–515. **DOI:**10.1124/jpet.102.034140
11. R. J. Shaw, K. A. Lamia, D. Vasquez, S.-H. Koo, N. Bardeesy, R. A. DePinho, M. Montminy, L. C. Cantley, *Science (80-.).* **2005**, *310*, 1642–1646. **DOI:**10.1126/science.1120781
12. H. D. Mclntyre, C. A. Paterson, A. Ma, P. J. Ravenscroft, D. M. Bird, D. P. Cameron, *Aust. N. Z. J. Med.* **1991**, *21*, 714–719. **DOI:**10.1111/j.1445-5994.1991.tb01375.x
13. M. R. Owen, E. Doran, A. P. Halestrap, *Biochem. J.* **2000**, *348*, 607–614. **DOI:**10.1042/bj3480607
14. J. E. Gunton, P. J. D. Delhanty, S.-I. Takahashi, R. C. Baxter, *J. Clin. Endocrinol. Metab.* **2003**, *88*, 1323–1332. **DOI:**10.1210/jc.2002-021394
15. A. Drozdetskiy, C. Cole, J. Procter, G. J. Barton, *Nucleic Acids Res.* **2015**, *43*, W389–W394. **DOI:**10.1093/nar/gkv332
16. L. A. Kelley, S. Mezulis, C. M. Yates, M. N. Wass, M. J. E. Sternberg, *Nat. Protoc.* **2015**, *10*, 845. **DOI:**10.1038/nprot.2015.053
17. Y. Song, F. DiMaio, R. Y.-R. Wang, D. Kim, C. Miles, T. J. Brunette, J. Thompson, D. Baker, *Structure* **2013**, *21*, 1735–1742. **DOI:**10.1016/j.str.2013.08.005

18. S. Raman, R. Vernon, J. Thompson, M. Tyka, R. Sadreyev, J. Pei, D. Kim, E. Kellogg, F. DiMaio, O. Lange, et al., *Proteins Struct. Funct. Bioinforma.* **2009**, *77*, 89–99. **DOI:**10.1002/prot.22540
19. A. Roy, A. Kucukural, Y. Zhang, *Nat. Protoc.* **2010**, *5*, 725. **DOI:**10.1038/nprot.2010.5
20. J. Yang, R. Yan, A. Roy, D. Xu, J. Poisson, Y. Zhang, *Nat. Methods* **2015**, *12*, 7. **DOI:**10.1038/nmeth.3213
21. J. Yang, Y. Zhang, *Nucleic Acids Res.* **2015**, *43*, W174-W181. **DOI:**10.1093/nar/gkv342
22. G. Studer, M. Biasini, T. Schwede, *Bioinformatics* **2014**, *30*, i505-i511. **DOI:**10.1093/bioinformatics/btu457
23. M. Wiederstein, M. J. Sippl, *Nucleic Acids Res.* **2007**, *35*, W407-W410. **DOI:**10.1093/nar/gkm290
24. J.-F. Gibrat, T. Madej, S. H. Bryant, *Curr. Opin. Struct. Biol.* **1996**, *6*, 377–385. **DOI:**10.1016/S0959-440X(96)80058-3
25. W. Tian, C. Chen, X. Lei, J. Zhao, J. Liang, *Nucleic Acids Res.* **2018**, *46*, W363–W367. **DOI:**10.1093/nar/gky473
26. S. F. Altschul, W. Gish, W. Miller, E. W. Myers, D. J. Lipman, *J. Mol. Biol.* **1990**, *215*, 403–410. **DOI:**10.1016/S0022-2836(05)80360-2
27. H. McWilliam, W. Li, M. Uludag, S. Squizzato, Y. M. Park, N. Buso, A. P. Cowley, R. Lopez, *Nucleic Acids Res.* **2013**, *41*, W597-W600. **DOI:**10.1093/nar/gkt376
28. A. M. Waterhouse, J. B. Procter, D. M. A. Martin, M. Clamp, G. J. Barton, *Bioinformatics* **2009**, *25*, 1189–1191. **DOI:**10.1093/bioinformatics/btp033
29. Pdb.-K. consortium, *Nucleic Acids Res.* **2019**. **DOI:**10.1093/nar/gkz853.
30. Schrödinger, LLC, *The {PyMOL} Molecular Graphics System, Version~1.8*, **2015**.
31. S. Kim, P. A. Thiessen, E. E. Bolton, J. Chen, G. Fu, A. Gindulyte, L. Han, J. He, S. He, B. A. Shoemaker, et al., *Nucleic Acids Res.* **2016**, *44*, D1202–D1213. **DOI:**10.1093/nar/gkv951
32. O. Trott, A. J. Olson, *J. Comput. Chem.* **2010**, *31*, 455–461.
33. E. F. Pettersen, T. D. Goddard, C. C. Huang, G. S. Couch, D. M. Greenblatt, E. C. Meng, T. E. Ferrin, *J. Comput. Chem.* **2004**, *25*, 1605–1612. **DOI:**10.1002/jcc.20084
34. I. Sánchez-Linares, H. Pérez-Sánchez, J. M. Cecilia, J. M. García, *BMC Bioinformatics* **2012**, *13*, S13. **DOI:**10.1186/1471-2105-13-S14-S13
35. S. Release, others, *Maest. Interoperability Tools, Schrödinger, New York, NY* **2017**.
36. Q. Wu, Z. Peng, Y. Zhang, J. Yang, *Nucleic Acids Res.* **2018**, *46*, W438-W442. **DOI:**10.1093/nar/gky439
37. F. Zi, H. Zi, Y. Li, J. He, Q. Shi, Z. Cai, *Oncol. Lett.* **2018**, *15*, 683–690.
38. A. T. Nies, U. Hofmann, C. Resch, E. Schaeffeler, M. Rius, M. Schwab, *PLoS One* **2011**, *6*, e22163. **DOI:**10.1371/journal.pone.0022163
39. M. Foretz, B. Guigas, L. Bertrand, M. Pollak, B. Viollet, *Cell Metab.* **2014**, *20*, 953–966. **DOI:**10.1016/j.cmet.2014.09.018
40. T. C. Dakal, R. Kumar, D. Ramotar, *Comput. Biol. Chem.* **2017**, *68*, 153–163. **DOI:**10.1016/j.compbiolchem.2017.03.007
41. E. C. Chen, N. Khuri, X. Liang, A. Stecula, H.-C. Chien, S. W. Yee, Y. Huang, A. Sali, K. M. Giacomini, *J. Med. Chem.* **2017**, *60*, 2685–2696. **DOI:**10.1021/acs.jmedchem.6b01317

Povzetek

Metformin, zdravilo, ki ga bolniki s sladkorno boleznijo pogosto uporabljajo kot prvi izbor zdravljenja po vsem svetu, je pozitivno nabit in se v celice vnaša s pomočjo človeških transportnih proteinov za organske katione (hOCT 1-3). Z različnimi metodami in bioinformatičnimi orodji smo želeli posnemati celični privzem metformina s hOCT1-3. 3D struktura proteinov OCT1-3 je bila napovedana z upoštevanjem struktur in funkcij teh proteinov. Predvideli smo funkcionalne regije (aktivna in ligand-vezavna mesta) OCT1-3 in izvedli primerjalno bioinformatično analizo. Napovedana struktura hOCT1-3 je bila nato analizirana na strežniku Blind Docking in rezultati potrjeni s predvidenimi preostanki vezavnih mest in ohranjenimi regijami domen. Simulirali smo sidranje OCT1-3 in metformina ter potrdili postopek sidranja z drugimi substrati proteinov HOCT1-3. Izbrali smo najboljše konformacije simuliranja sidranja metformina glede na energijo vezave (-5,27 do -4,60 kcal/mol). Nazadnje smo statični opis interakcij protein-ligand (OCT-Metformin) potrdili s simulacijo molekularne dinamike. Pri tem smo dosegli stabilno stimulacijo interakcije OCT-metformin.

Except when otherwise noted, articles in this journal are published under the terms and conditions of the Creative Commons Attribution 4.0 International License

DOI: 10.17344/acsi.2020.6111 *Acta Chim. Slov.* **2020,** *67,* 1216–1226
creative commons

Scientific paper

Ruthenium Oxide Hexacyanoferrate as an Effective Electrode Modifier for Amperometric Detection of Iodate and Hydrogen Peroxide

Totka Dodevska,* Ivan Shterev, Yanna Lazarova and Dobrin Hadzhiev

Department of Organic Chemistry and Inorganic Chemistry, University of Food Technologies, 26, Maritsa Boulevard, Plovdiv 4002, Bulgaria

** Corresponding author: E-mail: dodevska@mail.bg*
Tel.: +359 32 603 679; Fax: +359 32 644 102

Received: 07-10-2020

Abstract

Ruthenium oxide hexacyanoferrate (RuOHCF) film was electrochemically deposited onto a glassy carbon (GC) surface using consecutive cyclic voltammetry as a facile and green synthetic strategy. The electrochemical behaviour and electrocatalytic properties of the modified electrode RuOHCF/GC were evaluated with regards to electroreduction of hydrogen peroxide and iodate in a strong acidic medium (pHs 1.0–2.0) by using different electrochemical techniques, including cyclic voltammetry and amperometry at a constant potential. Electrochemical studies indicated that RuOHCF/GC possess a high catalytic activity in both studied reactions, fast response and good reproducibility of the current signal. The RuOHCF/GC exhibits enhanced electrocatalytic behaviour compared with other modified electrodes reported before. The simple and reproducible procedure for electrode fabrication, the wide linear range, anti-interference performance and long-time stability of the RuOHCF/GC make it a promising sensing material for practical quantitative determination of hydrogen peroxide and iodate. Remarkably, the reported modified electrode provided superior sensitive (1050 μA mM^{-1} cm^{-2}) and highly selective amperometric detection of iodate.

Keywords: Ruthenium oxide hexacyanoferrate; sensor; iodate; hydrogen peroxide

1. Introduction

Recently, as an important class of inorganic poly-nuclear compounds Prussian blue (ferric hexacyanoferrate, PB) and its analogues transition metal hexacyanoferrates (MHCF) have received considerable attention in material science and solid-state electrochemistry due to their unique characteristics – easy and cheap synthesis, ability to mediate/catalyze electrochemical reactions and faster kinetics.[1] MHCF have been investigated for various applications, including electrochemical sensors/biosensors, solid-state batteries, catalysts and charge storage.[2]

MHCF are known as useful electrocatalysts in selected processes – electrode materials modified with MHCF enhance slow electron transfer reactions of target analytes, thus being useful as electrochemical sensors. These well-organized inorganic polymers are intensively suited for electrochemical application due to their simple preparative procedure, good stability and the ease by which interfacial properties can be controlled.[3] Therefore, synthesis and deposition of MHCF and their use as electrode modifiers are of great interest.

Various metals have been used to prepare MHCF-modified electrodes by chemical[4] or electrochemical[2,5–11] methods. Data show that most of the modified electrodes were prepared via electrochemical deposition techniques owing to its low cost, low time consuming and well-defined structure forming ability by controlling the time, cycle number and nature of the electrolyte. Direct electrodeposition process using cyclic voltammetry (CV) is an efficient, "green", facile approach to assemble MHCF films on electrode surface. The use of CV as a modification technique makes it possible to convert relatively inexpensive substrate electrodes into electrocatalytically active and highly specific reusable electrochemical sensors.

The MHCF electrocatalytic effects were confirmed for H_2O_2,[1,4,10] NO[11] and some easily oxidizable species as ascorbic acid,[2,8] dopamine,[2,6] glucose,[9] sulfite.[5,7] The preparation of hexacyanoferrate films with ruthenium also has been reported. Generally, the formed films on the elec-

trode surface exhibit high electrocatalytic activity in the cathodic reduction of H_2O_2[12] and anodic oxidation of ethyl alcohol,[13,14] isopropyl alcohol,[13] L-cysteine,[13] epinephrine,[15] ranitidine,[16] hydrazine,[17] deoxyguanosine,[18] ascorbic acid,[13,15] uric acid,[15] sulfite.[19] New type mixed-valent ruthenium oxide/hexacyanoruthenate film modified electrodes were applied successfully for electrocatalytic oxidation of NADH, dopamine, SO_3^{2-}, $S_2O_3^{2-}$ and hydrazine.[20]

To the best of our knowledge, no reports are available on the application of ruthenium oxide hexacyanoferrate as a catalyst in electroreduction of iodate. Potassium iodate has been used for iodination of commercial table salt. The use of iodized salt in household and in food manufacture is established as a safe and cost-effective measure to ensure sufficient iodine intake by all individuals. This is the most effective and sustainable strategy for mass prevention of iodine deficiency disorders (IDD) – a major worldwide public health problem affecting all groups of people of which pregnant women, lactating women and infants are the most vulnerable categories.[21] Iodine is critical to brain and nervous system maturation during fetal/early postnatal life. Iodine deficiency and hypothyroidism during pregnancy result in impaired somatic growth, neurocognition and low child intelligence quotient. On the other hand, an iodine-induced hyperthyroidism and thyrotoxicosis may result from acute or chronic excess iodine exposure, including the consumption of excessively iodized salt. Therefore, to ensure that the correct amounts of iodate are added in table salt, the sensitive and rapid quantitative determination is of great importance to preventing thyroid diseases. [22,23] Several analytical techniques, such as spectrophotometry,[24] flame atomic absorption spectrometry (FAAS),[25] chemiluminescence[26] and gas chromatography-mass spectrometry[27] have been used for iodate sensing. However, most of these methods are not suitable for routine analysis as they required expensive equipment and some of them are based on indirect reactions where species with appropriate characteristics have to be produced for quantitative detection of the target analyte. Compared with these techniques, electrochemical sensors provide a simple, selective and inexpensive approach to monitor iodate content. Moreover, electrochemical sensing devices are portable, particularly well-suited for the sample-limited cases (capable of working in microliter to nanoliter volumes) without sacrificing sensitivity and can provide fast/automated analysis.

In the field of electroanalytical chemistry a significant challenge is development of sensors for accurate and fast quantitative detection of hydrogen peroxide (H_2O_2) – an analyte of great interest in clinical, pharmaceutical, industrial and environmental analysis. Recently, there are a numerous studies on the development of effective electrocatalysts for reduction of H_2O_2 in neutral or weakly acidic medium because the low-potential detection of H_2O_2 is one of the most successful strategy for oxidase-based biosensors providing both sensitivity and extremely high selectivity in the presence of easily oxidizable compounds.[28–34] H_2O_2 is also an industrially relevant analyte – it is used in aseptic processing of food, beverages and pharmaceuticals; for industrial wastewater disinfection and decontamination; as an oxidizing and bleaching agent in the paper and textile industries. The acidic bleaching process is useful for textiles which are not stable in alkaline medium and is very selective for the coloured impurities, which means that even at high concentrations of bleaching agent, damage or degradation of the textile structure is not observed.[35] H_2O_2 is also believed to play a main role in the chemical degradation of polymer membranes in proton-exchange membrane fuel cells (PEMFCs), affecting the long-term performance and durability of PEMFCs. Under PEMFC operating conditions, H_2O_2 is produced to some extent and degrades the proton-exchange membrane, deteriorating the proton conductivity of the membrane.[36] Hence, the direct H_2O_2 determination in an acidic medium is actually significant and appropriate. However, only a few studies have addressed hydrogen peroxide electroreduction in strongly acidic environment.[10,37–43]

In order to extend the application of MHCF in the field of the electrochemical sensors, we have electrochemically deposited RuOHCF onto glassy carbon (GC) and further used RuOHCF/GC as a working electrode for reduction of iodate and hydrogen peroxide that has a potential in electrochemical sensor applications. This work demonstrates that the modified electrode RuOHCF/GC remains functional and provides stable and reproducible measurements of H_2O_2 and iodate in a strong acidic medium (pHs 1.0–2.0). The investigation of RuOHCF film stability and electrocatalytic effect on iodate reduction demonstrated that GC modified with RuOHFC works as an efficient catalyst with higher sensitivity and wider linear range compared to other sensors.

2. Experimental

2. 1. Materials, Apparatus and Measurements

$RuCl_3 \times nH_2O$, $K_3[Fe(CN)_6]$, HCl, KCl, H_3PO_4, H_2O_2 and KIO_3 were purchased from Fluka; $Na_2HPO_4 \times 12H_2O$ and $NaH_2PO_4 \times 2H_2O$ were purchased from Sigma-Aldrich. All chemicals used were of analytical grade and double distilled water was used to prepare aqueous solutions. 0.1 M phosphate buffer solutions (PBS) with pH values 1.0, 2.0 and 3.0 were made of monobasic and dibasic sodium phosphates using a pH meter MS2006 (Microsyst, Bulgaria).

The electrochemical measurements were performed on electrochemical workstation EmStat2 (PalmSens BV, The Nederland), equipped with 'PSTrace 2.5.2' licensed software. Three-electrode system was employed to study the electrochemical performance of the modified electrode; Pt wire was used as a counter electrode and an Ag/AgCl (3 M KCl) as a reference electrode. The modified electrode was

investigated using cyclic voltammetry and amperometry at a constant potential. Cyclic voltammograms were recorded at scan rates from 50 to 500 mV s^{-1}; peak intensities of CVs were reported with baseline correction. Amperometric (*I-t*) curves were monitored at a constant applied potential under hydrodynamic condition – magnetic stirrer was used to achieve effective mass transport across the working electrode. To remove oxygen, the background solution was purged with pure argon for about 20 min before performing electrochemical experiments and a continuous flow of argon was maintained during measurements.

2. 2. Electrochemical Deposition of RuOHCF on a Glassy Carbon Electrode

Glassy carbon (GC) electrode (d = 3 mm) was mechanically polished with 0.05 μm alumina slurry, cleaned by ultrasonication in double distilled water for 5 min and allowed to dry at a room temperature. The preparation of the modified electrode RuOHCF/GC was done by electrochemical deposition of ruthenium hexacyanoferrate (RuOHCF) film on the glassy carbon surface by cyclic voltammetry from –0.5 to 1.3 V (vs. Ag/AgCl, 3 M KCl) in aqueous solution containing 0.05 M HCl + 0.5 M KCl + 1% $RuCl_3$ + 5 mM $K_3[Fe(CN)_6]$ applying 50 cycles at a scan rate of 100 mV s^{-1}. The modified electrode RuOHCF/GC was stored dry at a room temperature and no pre-treatment procedures were performed prior to the measurements.

3. Results and Discussion

3. 1. Electrochemical Behaviour of RuOHCF/GC Modified Electrode

CV is a powerful technique widely applied both in the preparation and characterization of various nano- and microstructured materials.[44–46] The electrochemical behaviour of the modified electrode RuOHCF/GC was evaluated in strongly acidic aqueous solution by recording cyclic voltammograms in electrolyte 0.05 M HCl + 0.5 M KCl (pH 1.7). Fig. 1A presents CVs of the bare GC and RuOHCF/GC registered in the potential range from –0.5 V to 1.3 V. Compared with the bare GC electrode (red curve), the background voltammetric response of the modified electrode (black curve) is much higher indicating that the effective surface area is significantly enhanced. The voltammogram proves that the redox activity of RuOHCF film is based on the electron transfer processes involving Ru(II)/Ru(III)/Ru(IV) and Fe(II)/Fe(III) species and oxygen uptake. Four well-defined pairs of symmetrical anodic and cathodic peaks are registered. The redox couples I, III and IV with formal potentials $E_p^0 = (E_p^a + E_p^c)/2$ occurring at about 0.008, 0.85 and 1.03 V are attrib-

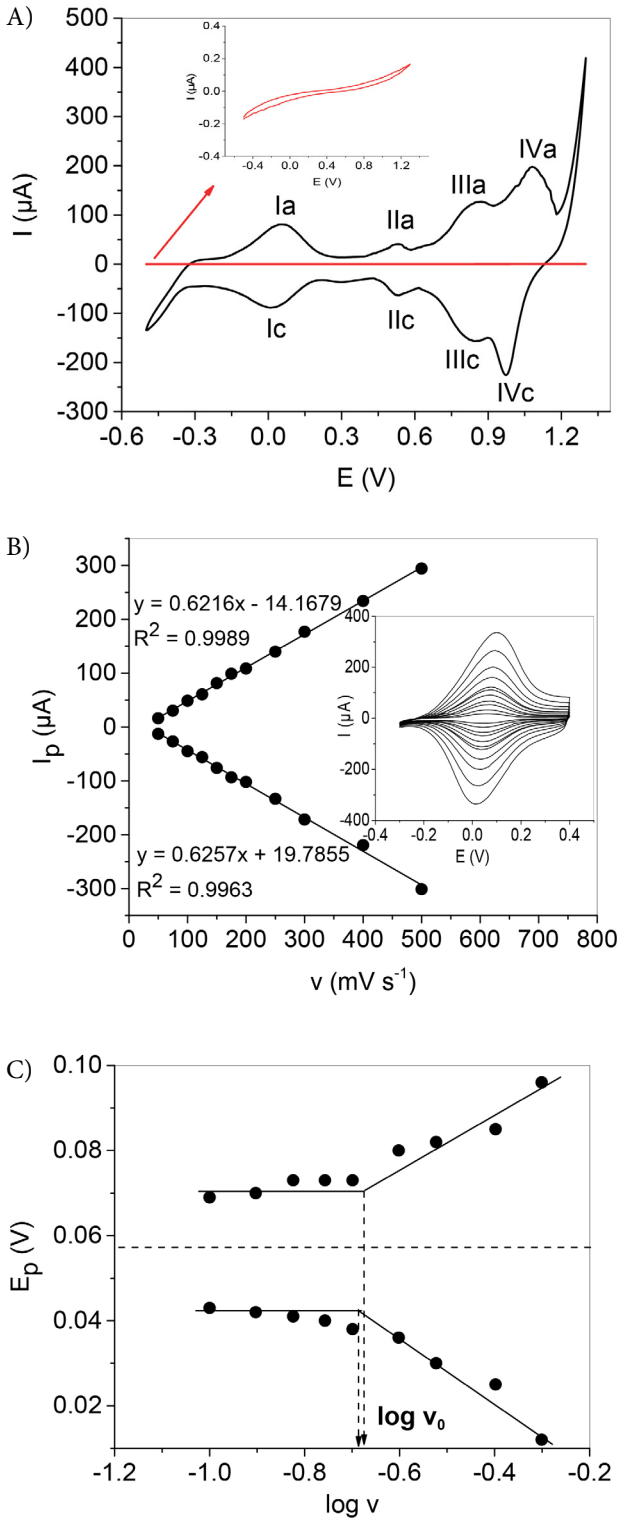


Fig. 1. A) CVs of unmodified GC electrode (red curve) and modified electrode RuOHCF/GC (black curve) recorded in electrolyte 0.05 M HCl + 0.5 M KCl (pH 1.7) at a scan rate of 100 mV s^{-1}; *Inset*: enlarged plot showing the CV of bare GC. **B)** Plot of anodic and cathodic peak currents *vs.* scan rate for the first redox couple; *Inset*: CVs of RuOHCF/GC at different scan rates (from inner to outer: 50, 75, 100, 125, 150, 175, 200, 250, 300, 400, 500 mV s^{-1}). **C)** Dependence of E_p on log(v).

utable to the [Ru(II)-O/Fe(II)-CN]/[Ru(III)-O/Fe(II)-CN], [Ru(III)-O/Fe(II)-CN]/[Ru(III)-O/Fe(III)-CN] and [Ru(III)-O/Fe(III)-CN]/[Ru(IV)-O/Fe(III)-CN] reactions. The redox coupe II (with formal potential at about 0.54 V) exhibiting a small peak currents is due to the redox reaction of the electroactive iron sites [Ru(III)-NC-Fe(II)]/[Ru(III)-NC-Fe(III)]. This result confirms formation of mixed RuOHCF and RuHCF film on the GC electrode surface.[13] It can be concluded that the used electrolyte, as well as the methodology for electrode modification described here, are reliable.

Chen et al.[13] studied the pH effect of the supporting electrolyte on the voltammetric profile of RuOHCF films and demonstrated that the formal potentials of all four redox couples showed a positive shift due to the increase of acidity in the pH range 0.5–3.0. At higher pHs a film loss has been reported,[47] hence all the electrochemical measurements in this work were performed in supporting electrolytes with pH values in the range 1.0–3.0.

Fig. 1B shows the different scan rates results of RuOHCF/GC in the potential range between –0.3 and 0.4 V (redox couple I). As illustrated, the anodic and cathodic peak currents increased linearly according to the scan rate as expected for the thin layer electrochemistry process. The corresponding linear regression equations were: I_p^a (μA) = 0.6216ν (mV s^{-1}) – 14.1679 (R^2 = 0.9989) and I_p^c (μA) = 0.6257ν (mV s^{-1}) + 19.7855 (R^2 = 0.9963); the ratio of the anodic to the cathodic peak current (I_p^a/I_p^c) was equal to unity. The peak-to-peak potential separation ($\Delta E_p = E_p^a - E_p^c$) is small and about 30 mV for sweep rates below 200 mV s^{-1}, suggesting facile charge transfer kinetics over this range of sweep rate. The behaviour illustrated in Fig. 1B is consistent with a diffusionless, reversible electron transfer process at low scan rates.

The apparent electron transfer rate constant k^0 were calculated from Tafel diagrams, using the theoretical value 0.5 for the charge transfer coefficient (α). Fig. 1C illustrates the graphical calculation of the critical scan rate ν_0. Mean values of k^0 = 9.6 ± 0.1 s^{-1} were evaluated from the experimental data applying the equation $k^0 = 2.303\alpha nF\nu_0/RT$.

3. 2. Electrocatalytic Reduction of H_2O_2 at RuOHCF/GC

In the following section it has been experimentally proven that in such extreme acidic conditions the here presented RuOHCF/GC effectively reduces H_2O_2 and the electrode response is linear in a wide linear range of H_2O_2 concentrations. Voltammograms recorded in supporting electrolyte 0.05 M HCl + 0.5 M KCl before and after the addition of hydrogen peroxide are shown in Fig. 2A. A current signal due to the [Ru(II)-O/Fe(II)-CN]/[Ru(III)-O/Fe(II)-CN] redox process is registered – significant increase in the cathodic current and a decrease in the anodic current were observed when H_2O_2 is added. The obtained result indicates that the Ru(II/III) couple is responsible for the electrocatalytic reduction of H_2O_2.

Electroreduction of H_2O_2 at the surface of the modified electrode was studied by means of hydrodynamic amperometry – one of the most widely employed electrochemical technique for sensors. The amperometric measurements were carried out in deaerated constantly stirred background electrolyte 0.05 M HCl + 0.5 M KCl. The electrode working potential was held at 0.0 V, and was selected from the CV (Fig. 2A). Fig. 2B displays the authentic record of amperometric response of RuOHCF/GC when different concentrations of H_2O_2 were injected consecutively at regular intervals of time. It can be seen that a stable and well-defined amperometric response was observed. Upon addition of H_2O_2 the modified electrode shows increasing staircase current response corresponding to the electrochemical reduction of the analyte. RuOHCF/GC responds rapidly to the changes in H_2O_2 concentration producing a

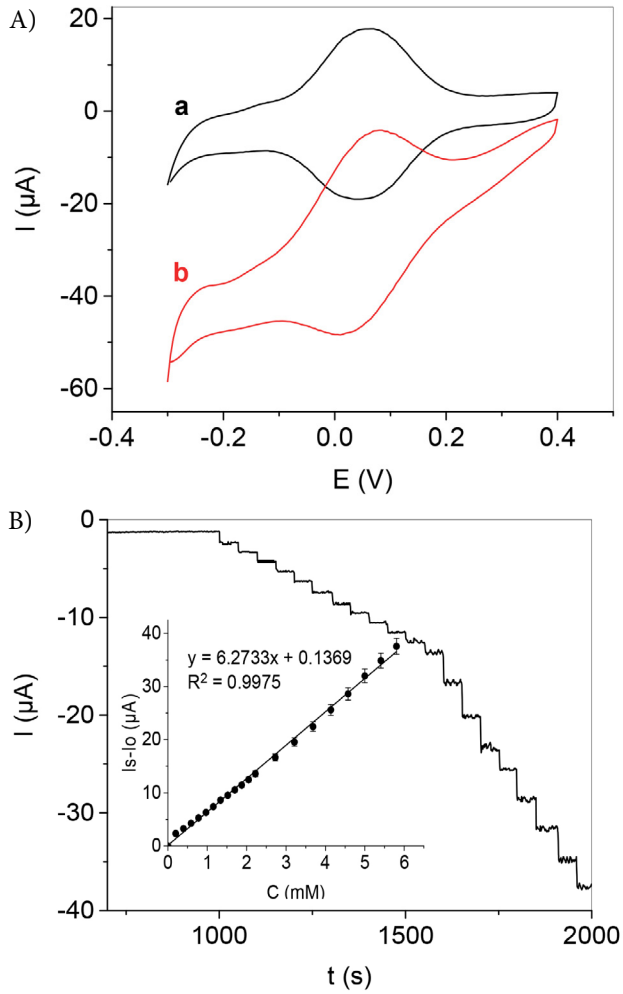


Fig. 2. A) CVs of RuOHCF/GC at scan rate of 50 mV s^{-1} in absence (curve a, black) and in presence of 3.0 mM H_2O_2 (curve b, red). **B)** Authentic record of the amperometric response for successive additions of H_2O_2 at an applied potential of 0.0 V; *Inset:* the corresponding calibration plot. Supporting electrolyte 0.05 M HCl + 0.5 M KCl.

Table 1. Comparison of the operational characteristics of amperometric sensors for H_2O_2 detection in strongly acidic medium with the achieved in the present work.

Modifier/Electrode	Method E, (V)	Electrolyte	Sensitivity	Linear range, (M)	Detection limit, (M)
SnHCF/CCE[10]	CA −0.1[b]	ABS/KNO_3 (pH 4.0)	0.588[d]	4.0×10^{-6}–5.0×10^{-5}	1.47×10^{-6}
PMo_{12}-doped gel film/Pt[37]	CA 0.0[b]	0.5 M H_2SO_4	3.6[e]	2.0×10^{-5}–3.0×10^{-2}	7.0×10^{-6}
PLL-GA-SiMo/GC[38]	CA −0.05[a]	0.1 M H_2SO_4	0.6[e]	5.0×10^{-5}–5.0×10^{-4}	–
APS-$PFeW_{11}$/CPE[39]	FIA 0.0[a]	0.5 M H_2SO_4	0.183[c]	1.0×10^{-5}–2.0×10^{-4}	7.4×10^{-6}
Vanadium-17-molybdophosphate/ graphite/methylsilicate composite[40]	CA 0.205[a]	0.5 M H_2SO_4	324.0[f]	1.0×10^{-3}–7.5×10^{-2}	4.0×10^{-4}
PLL-GA-PW/GC[41]	CA −0.3[a]	0.1 M H_2SO_4	1.69[e]	2.5×10^{-6}–6.8×10^{-3}	–
P_2Mo_{18}/OMC/GC[42]	CA 0.0[a]	1.0 M H_2SO_4	–	1.6×10^{-4}–4.4×10^{-2}	5.3×10^{-5}
PB/FTO[43]	CA −0.1[a]	HCl/KCl (pH 2.0)	0.05[h]	9.0×10^{-5}–3.5×10^{-4}	3.6×10^{-5}
RuOHCF/GC[This work]	CA 0.0[a]	HCl/KCl (pH 1.7)	88.7[g]	8.0×10^{-5}–6.0×10^{-3}	5.0×10^{-5}

[a] Reference electrode: Ag/AgCl, 3 M KCl (0.200 V *vs.* SHE); [b] Reference electrode: saturated calomel electrode (SCE) (0.242 V *vs.* SHE); [c] in: nA μM^{-1}; [d] in: $\mu A\ \mu M^{-1}$; [e] in: $\mu A\ mM^{-1}$; [f] in: nA mM^{-1}; [g] in: $\mu A\ mM^{-1}\ cm^{-2}$; [h] in: $\mu A\ \mu M^{-1}\ cm^{-2}$; CCE – carbon ceramic electrode; CPE – carbon paste electrode; CA – chronoamperometry; FIA – flow injection analysis; PMo_{12} – 12-molybdophosphoric acid; PLL-GA-SiMo – silicomolybdate-doped-glutaraldehyde-crosslinked poly-l-lysine film; APS-$PFeW_{11}$ – $[PFeW_{11}O_{39}]^{4-}$ polyoxoanion supported on modified amorphous silica gel; PLL-GA-PW – phosphotungstate-doped-glutaraldehyde-cross-linked poly-l-lysine film; P_2Mo_{18} – polyoxometalate $H_6P_2Mo_{18}O_{62}{\cdot}xH_2O$; OMC – ordered mesoporous carbon; PB – Prussian blue; FTO – F-doped tin oxide; ABS – acetate buffer solution.

stable current signal in less than 8 s. The observed features confirm the catalytic ability of RuOHCF film and indicate a fast electron-transfer process at the modified electrode surface. The background subtracted steady-state current response of RuOHCF/GC was proportional to the H_2O_2 concentration up to 6.0 mM; the regression equation was I (μA) = 6.2733C (mM) + 0.1369 with a correlation coefficient of 0.9975, indicating that the regression line is very well fitted with the experimental data. Therefore, the calibration equation can be used for the determination of unknown samples. The electrode shows electrochemical sensitivity of 88.7 $\mu A\ mM^{-1}\ cm^{-2}$ (normalization is based on the electrode geometric surface area) calculated on the basis of 20 points. The detection limit was estimated to be 0.05 mM H_2O_2 (based on signal-to-noise ratio S/N=3).

To assess the reproducibility of the measurements, the response (reduction current) for 1.0 mM H_2O_2 was recorded five times using the same electrode. The results confirmed that the electrode signal of RuOHCF/GC had good reproducibility with a relative standard deviation (RSD) less than 5.0 %.

A limited number of H_2O_2 sensors operating in strongly acidic medium have been reported in literature. To the best of our efforts, eight various H_2O_2 amperometric sensors are summarized in Table 1 with respect to the opetaring conditions (electrolyte and applied potential), sensitivity, linear range and detection limit.[10,37–43] It is apparent that the operational characteristics for H_2O_2 quantitative determination at RuOHCF/GC are comparable and even better than those obtained by using other modified electrodes. Despite the detection limit of RuOHCF/GC is not so low when compared to other electrodes, the proposed sensor exhibited a wider linear concentration range. Moreover, it should be pointed that lower values of detection limit and higher sensitivity could be achieved increasing the amount of electrodeposited material onto to the surface of glassy carbon electrode. We are convinced that these operational characteristics of the proposed electrode could be improved by optimizing the scan rate and the number of cycles applied for modification of the glassy carbon carrier. In this regard, the aim of our future research is to determine how the parameters of electrodeposition process affect the catalytic activity of RuOHCF/GC in the target reaction (H_2O_2 electroreduction).

3. 3. Electrocatalytic Reduction of Iodate at RuOHCF/GC

Voltammetric characteristics of the RuOHCF film are pH-dependent. Therefore, all the electrochemical measurements were carry out in buffer solution (pH 1.0) in order to maintain a constant pH of the supporting electrolyte. Under the same experimental conditions Salimi et al.[48] have studied the activity of glassy carbon

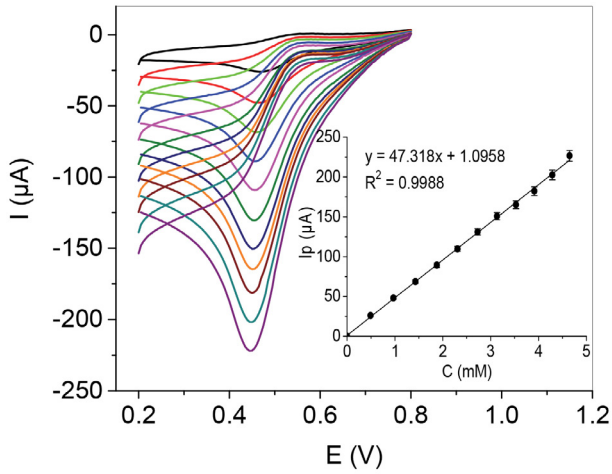


Fig. 3. Voltammetric response of RuOHCF/GC in PBS (pH 1.0) containing different concentration of iodate; scan rate of 100 mV s^{-1}; *Inset*: plot of catalytic peak current *vs.* iodate concentration.

on the reduction of IO_3^- and have shown that unmodified GC electrode responds sluggish to iodate at potentials more negative than –0.5 V (vs. Ag/AgCl). In order to investigate the electrocatalytic activity of RuOHCF/GC for reduction of iodate, CV responces of the modified electrode were obtained in PBS (pH 1.0) in absence and presence of IO_3^- (Fig. 3). After addition of iodate into the supporting buffer solution the voltammetric behavior of RuOHCF/GC was changed dramatically – a remarkable cathodic peak at about 0.45 V was observed, indicating that the RuOHCF film can electrocatalyze reduction of iodate. The voltammetric responces of the modified electrode were recorded for different concentrations of KIO_3. From the inset, it can be seen that with the increase of the iodate concentration, the corresponding catalytic currents enhanced linearly, suggesting that RuOHCF/GC would have potential applications in the quantitative detection of IO_3^- . The sensitivity of the proposed electrode was calculated to be 669.3 μA mM^{-1} cm^{-2} up to 4.8 mM iodate.

Electroreduction of iodate at the surface of RuOHCF/GC was studied also by means of hydrodynamic amperometry. For sensing purposes chronoamperometry under stirred conditions is preferred over CV technique because it provides a higher sensitivity, best selectivity and a lower detection limit. The amperometric response of RuOHCF/GC to iodate was investigated in deaerated constantly stirred buffer solution (pH 1.0). A potential of 0.45 V was kept as an applied potential considering the reduction peak from the CV record (Fig. 3). Fig. 4A shows typical current-time curve for successive additions of iodate. The current immediately changed after the addition of iodate and reached steady-state value within 5 s (Fig. 4A, inset a). Inset b of Fig. 4A shows the fast response of the catalyst as well as the stability of the signal in presence of 0.1 mM iodate during a prolonged 8 min experiment. The response remained stable throughout the experiment, indicating no

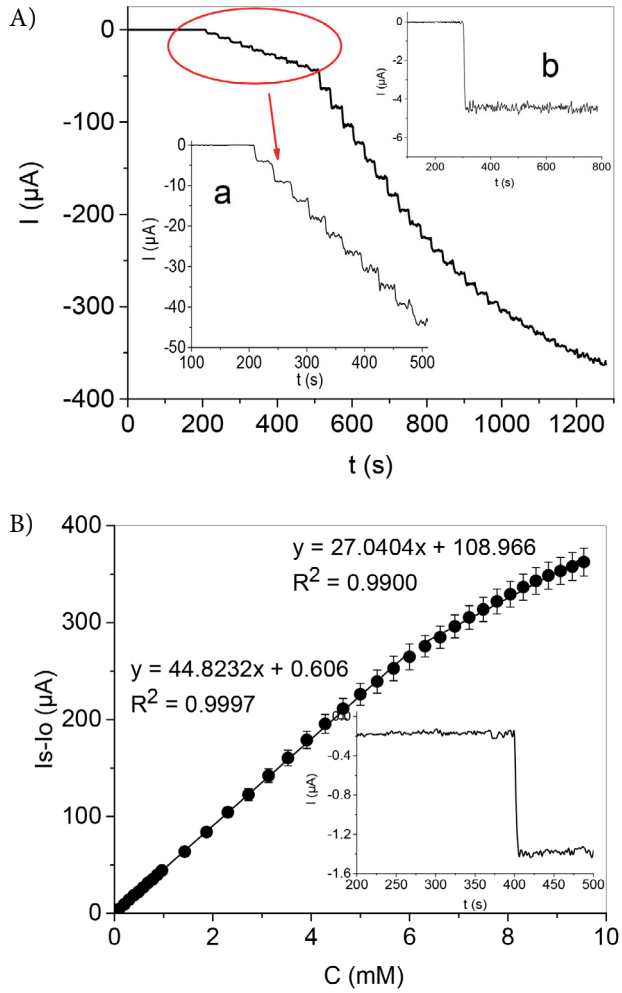


Fig. 4. A) Authentic record of the amperometric response of RuOHCF/GC in PBS (pH 1.0) for successive additions of iodate at potential of 0.45 V; *Insets: a)* The enlarged initial section of the amperometric curve (10 injections of 0.1 mM KIO_3 were added); *b)* Recorded amperogram of 0.1 mM iodate (added in 300 s) during long period time 8 min. **B)** Calibration plot of chronoamperometric currents *vs.* iodate concentration in two concentration ranges: from 0.1 to 6.0 mM (23 points) and from 6.0 to 9.5 mM (14 points); *Inset:* Amperometric response for 20 μM iodate.

inhibiting effect of KIO_3 and/or its reduction products on the RuOHCF/GC surface.

Fig. 4B presents calibration plot of the background subtracted currents *vs.* iodate concentration in the range 0.1 – 9.5 mM. The plot shows two segmented linear calibration ranges – the first one is up to 6.0 mM iodate with a linear regression equation I (μA) = 44.8232C (mM) + 0.606 and a correlation coefficient of 0.9997. The high active surface area has given superior performance – the electrode shows electrochemical sensitivity of 634.0 μA mM^{-1} cm^{-2} calculated on the basis of 23 points. In the concentration range from 6.0 to 9.5 mM iodate the linear regression equation is I (μA) = 27.0404C (mM) + 108.966; the sensitivity and the correlation coefficient are 392.5 μA mM^{-1} cm^{-2} and 0.990, respectively. The detection limit

was estimated to be 1.0 μM (Fig. 4B, inset), based on the criterion of S/N = 3.

In order to evaluate the reproducibility of the electrochemical performance of the modified electrode RuOHCF/GC, amperometric measurements at a constant potential of 0.45 V were repeatedly performed five times in a solution containing 0.1 mM KIO_3. The proposed electrode showed a good repeatable and reproducible response for iodate. The current values for 0.1 mM iodate were detected with RSD of 3.4 % (n = 5).

Additional experiments with glassy carbon electrodes modified with RuOHCF by applying 15 and 75 cycles, respectively, were performed. Amperometric responses of the so-modified catalysts were registered in the presence of 0.1 mM KIO_3 at an applied potential of 0.45 V. It was established that the electrode modified by 15 cycles has a lower current response accompanied with a high noise and it is not applicable for analytical measurement of iodate. As expected, increasing the amount of electrodeposited RuOHCF onto the GC surface, the current signal has been improved – results obtained with the electrode modified with a thicker RuOHCF layer (75 cycles) were better in terms of higher signal and lower noise levels, i. e. lower limit of detection values could be achieved increasing the amount of electrodeposited material onto the GC electrode. Comparison of the catalytic current of electrode modified by 50 cycles with that of electrode modified by 75 cycles clearly indicates that the catalytic ability of both electrodes toward reduction of iodate is an identical. These results suggest that the electrodeposition procedure with 50 cycles of CV is favourable for a good catalytic activity, stable response and long durability. Therefore, all the electrochemical data presented below were obtained using an electrode modified with RuOHCF by applying 50 cycles.

In amperometric *I-t* detection the potential applied to the working electrode directly affects the sensitivity, detection limit and selectivity of the electrochemical sensor. With regard to the latter, we have investigated the effect of the applied potential on the current response of RuOHCF/GC towards reduction of IO_3^-. A series of chronoamperometric measurements of different concentrations of KIO_3 were done at potentials around 0.0 V (vs. Ag/AgCl, 3 M KCl). At such a low potentials the current response of other electroactive species is eliminated (or minimized), which is crucial for the selectivity of the sensor system.

Fig. 5 displays the calibration graph based on the results obtained at a constant potential of 0.0 V. It is apparent that the modified electrode shows staircase current response corresponding to the electrochemical reduction of the analyte, which evidences a stable and efficient catalytic property of RuOHCF film at low potentials (Fig. 5, inset a). Experimental data show that this decrease in the applied potential affects the process of iodate electroreduction on the modified electrode. Comparing the results obtained at potentials of 0.45 V and 0.0 V, higher currents (Fig. 5, insets) and hence better electrode sensitivity were observed at the lower potential. However, the linear dynamic range is shortened significantly – the authentic record of the amperometric response at 0.0 V clearly shows that the signal noise increases rapidly with each subsequent injection of IO_3^- stock solution. The limit of detection was calculated to be 1.0 μM iodate.

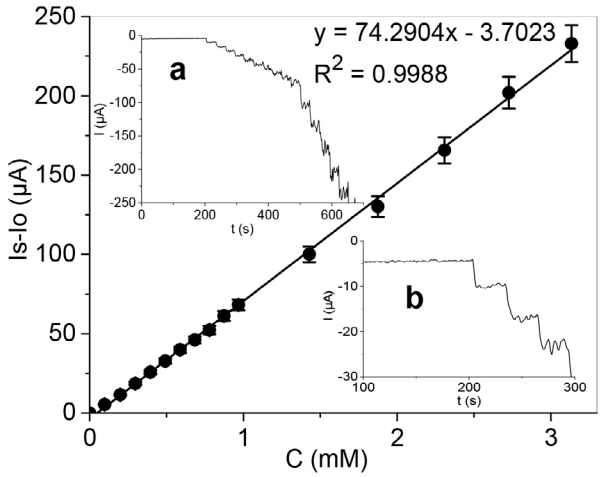


Fig. 5. Calibration plot of chronoamperometric currents *vs.* iodate concentration at an applied potential of 0.0 V; *Insets: a)* Authentic record of the amperometric response of RuOHCF/GC in PBS (pH 1.0) for successive additions of iodate; *b)* The enlarged initial section of the amperometric curve (3 injections of 0.1 mM KIO_3 were added).

Table 2. Analytical parameters of RuOHCF/GC for iodate detection in PBS (pH 1.0); temperature 25 °C.

E, (V)	Regression equation	Electrode sensitivity, (μA mM^{-1} cm^{-2})	Linearity, (M)	Detection limit, (M)
–0.1	y = 73.0277x – 3.1551 (R^2 = 0.9989)	1033.0	8.0×10^{-6}–2.7×10^{-3}	5.0×10^{-6}
0.0	y = 74.2904x – 3.7023 (R^2 = 0.9988)	1050.8	5.0×10^{-6}–3.2×10^{-3}	1.0×10^{-6}
0.1	y = 69.4068x – 1.1804 (R^2 = 0.9997)	981.7	5.0×10^{-6}–2.7×10^{-3}	1.0×10^{-6}
0.45	y = 44.8232x + 0.606 (R^2 = 0.9997)	634.0	8.0×10^{-6}–6.0×10^{-3}	1.0×10^{-6}

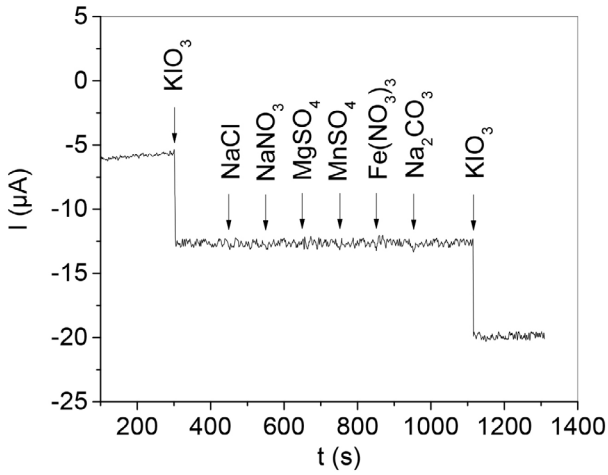


Fig. 6. Amperometric *I-t* curve of modified electrode RuOHCF/GC for the determination of 0.1 mM KIO_3 in the presence of 3.3 mM of different interfering species added one by one with an interval of 100 s to PBS (pH 1.0) at an applied potential of –0.1 V.

To estimate the sensing properties of modified electrode, the analytical parameters in terms of sensitivity, linear range and detection limit at four applied potentials were defined and compared (Table 2). From the data presented it is evident that as the polarization potential become more negative than 0.45 V, the sensitivity increases. The comparison made shows that at potentials of –0.1, 0.0 and 0.1 V the electrode sensitivity values are very close and the range of the strict linear concentration dependence of the current signal is almost unaffected by the applied potential.

In order to examine the pH effect on the catalytic reduction behaviour, the current response at an applied potential of –0.1 V of RuOHCF/GC in 0.1 mM KIO_3 at different pH values (1.0, 2.0 and 3.0) was studied. It was found that the catalytic currents began to decrease with the increasing of the pH. The modified electrode shows excellent electrocatalytic activity at pH 1.0; 20 % decrease in current was observed at pH 2.0; at pH 3.0 the results were not repeatable. The observed features prove that the pH value has an effect on the electrode behaviour and this is related to the proton taking part in the electrochemical reaction.

To investigate the selectivity and anti-interference ability of RuOHCF/GC, a number of interfering species which possibly coexist with iodate in samples were added to the PBS (pH 1.0) containing 0.1 mM KIO_3 at an applied potential of –0.1 V. As can be seen from Fig. 6, various ions such as Na^+, Fe^{3+}, Mg^{2+}, Mn^{2+}, Cl^-, SO_4^{2-}, NO_3^- and CO_3^{2-} (30-fold concentration relative to iodate) did not produce apparent current response, while a significant and stable signal was observed after addition of KIO_3. Therefore, the RuOHCF/GC can be used as a selective and highly sensitive sensor for iodate detection even in the presence of high concentrations of different electroactive ions.

The reproducibility and reliability of the fabrication procedure also were studied – four RuOHCF/GC electrodes were prepared independently under the same conditions and immediately after the surface modification were tested by amperometry at –0.1 V. The RSD of the modified electrodes responces toward 0.1 mM iodate was 6.3 %, indicating good reproducibility between different RuOHCF/GC electrodes and confirming that the fabrication method is reliable.

It is known that the long-term stability as well as the chemical stability in contact with the supporting electrolyte of the modified electrode are crucial in terms of prac-

Table 3. Analytical parameters reported for different modified electrodes towards iodate detection.

Modifier/Electrode	E, (V)	pH	Sensitivity	Linear range, (M)	Detection limit, (M)
AgNPs/PGS/GC[49]	–1.25[b]	6.7	250[i]	1.0×10^{-4}–8.0×10^{-4}	5.0×10^{-5}
OMC/AgNPs/GC[50]	–0.65 [b]	3.0	1.92[h]	1.5×10^{-5}–4.43×10^{-3}	3.01×10^{-6}
FAD-SiO_2/ZrO_2/C[51]	–0.41[b]	4.0	–	4.9×10^{-5}–2.4×10^{-3}	1.46×10^{-6}
WO_3/PANI/C cloth [52]	–0.25[b]	–	0.541[d]	1.0×10^{-5}–5.0×10^{-4}	2.7×10^{-6}
IrO_x/GC[23]	–0.2[a]	1.0	739.7[g]	1.0×10^{-6}–4.6×10^{-3}	5.0×10^{-7}
MWCNT@RB/GE [53]	–0.1[a]	2.0	0.77[e]	2.5×10^{-5}–7.5×10^{-4}	2.7×10^{-6}
MWCNTs/[C_8Py][PF_6]-PMo_{12}/GC[54]	0.0[a]	2.59	14.81[e]	2.0×10^{-5}–2.0×10^{-3}	1.5×10^{-5}
RuOHCF/GC[This work]	0.0[a]	1.0	1050.8[g]	5.0×10^{-6}–3.2×10^{-3}	1.0×10^{-6}
RuONPs/GC[55]	0.078[b]	3.0	0.01[d]	1.5×10^{-6}–5.2×10^{-4}	9.0×10^{-7}
AuNPs/PEI/CNTs–COOH/ORC/Au[56]	0.15 [a]	2.0	–	1.0×10^{-6}–2.0×10^{-3}	1.7×10^{-7}
V-Schiff base complex/MWCNT/GC[57]	0.3[a]	2.0	23.4[c]	5.0×10^{-7}–5.0×10^{-4}	3.5×10^{-7}
RuOHCF/GC[This work]	0.45[a]	1.0	634.0[g] 392.5[g]	8.0×10^{-6}–6.0×10^{-3} 6.0×10^{-3}–9.5×10^{-3}	1.0×10^{-6}
IrO_x/GC[48]	0.7[a]	1.0	140.9[c]	1.0×10^{-7}–3.5×10^{-5}	5.0×10^{-9}

NPs – nanoparticles; PGS – pure graphite sheets; OMC – ordered mesoporous carbon; FAD – flavin adenine dinucleotide; PANI – polyaniline; MWCNT – multiwall carbon nanotubes; RB – riboflavin; ([C_8Py][PF_6]) – n-octylpyridinum hexafluorophosphate; (PMo_{12}) – phosphomolybdic acid; PEI – polyethyleneimine; (CNTs–COOH) – carbon nanotubes functionalized with a carboxylic acid group; ORC – organoruthenium(II) complexes. [i] in: A M^{-1} m^{-2}. Other abbreviations are the same as Table 1.

Table 4. Iodate content in iodized table salt samples determined by different methods.

Table salt sample	Proposed amperometric method, (mg kg^{-1})	Reference titration method, (mg kg^{-1})	RE*, (%)
Salt sample 1	32.5	33.6	–3.3
Salt sample 2	46.2	48.8	–5.3

*Relative error RE = [100 × (electrochemical method – reference method)]/ reference method

tical applications. The storage stability of the here presented electrode was tested – the current response toward 0.1 mM iodate at an applied potential of –0.1 V was measured every day. Results revealed the good stability of the electrodeposited RuOHCF film – the modified electrode retained about 90% of its initial catalytic activity after 10 days storage. Similar data on stability of electrodes modified with MHCF films have been reported by other authors.[5,8,10]

The performance of the as-prepared catalyst was compared with other sensors, as it shown in Table 3.[23,48–57] The sensor systems were arranged in order of increasing the working potential. Clearly, the detection limit of some sensors is better than our results. However, the sensitivity and linear range for RuOHCF/GC are superior to many sensor systems, such as AgNPs/PGS/GC[49], FAD-SiO_2/ZrO_2/C[51], WO_3/PANI/C[52], MWCNT@RB/GE[53], MWCNTs/[C_8Py][PF_6]-PMo_{12}/GC[54], RuONPs/GC[55]. Hence, it is conclusive that the reported RuOHCF/GC exhibited substantial electrocatalytic behaviour toward the electrochemical sensing of iodate.

3. 4. Real Sample Analysis

To evaluate the feasibility of the modified electrode RuOHCF/GC for quantitative analysis of iodate in real samples, RuOHCF/GC was applied to detect iodate content in two different samples of commercial iodized table salt. Following the previously described methodology[23] amperometric measurements were carried out at a constant potential of –0.1 V applying the standard addition method. The iodate content was also determined using classical procedure (titration with thiosulfate) to test the accuracy. The results obtained by RuOHCF-based electrochemical sensor and by titration were in good agreement and the relative error was below 6 % indicating that the proposed amperometric method is reliable (Table 4).

All the results mentioned above suggest that the RuOHCF/GC would represent promising material for future applications in amperometric sensor for fast and precise sensing of iodate in commercial salt.

4. Conclusion

In this work we have demonstrated the electrochemical behaviour of modified electrode RuOHCF/GC in a strong acidic medium (pHs 1.0–2.0) and its electrocatalytic activity towards the reduction of H_2O_2 and iodate. RuOHCF/GC was used for sensitive detection of H_2O_2 and IO_3^- using hydrodynamic amperometry technique. The modified electrode showed wide concentration range and good reproducibility for H_2O_2 determination at an applied potential of 0.0 V (vs. Ag/AgCl, 3 M KCl), and provided a platform for the development of a robust electroanalytical system. The results presented in this work associated with the extremely high sensitivity, anti-interference ability, good accuracy and the response stability of RuOHCF/GC in electroreduction of IO_3^- predict a favorable application of the sensor for iodate quantitative analysis.

5. References

1. A. Karyakin, *Electroanalysis* **2001**, *13*, 813–819. **DOI:**10.1002/1521-4109(200106)13:10<813::AID-ELAN813> 3.0.CO;2-Z
2. Q. Wang, Q. Tang, *Microchim. Acta* **2015**, *182*, 671–677. **DOI:**10.1007/s00604-014-1371-x
3. R. Ojani, J.-B. Raoof, B. Norouzi, *Electroanalysis* 2008, *20*, 1996–2002. **DOI:**10.1002/elan.200804278
4. H. Pang, Y. Zhang, T. Cheng, W.-Y. Lai, W. Huang, *Nanoscale* **2015**, *7*, 16012–16019. **DOI:**10.1039/C5NR04322K
5. K. Pandi, M. Sivakumar, S.-M. Chen, M. Sakthivel, G. Raghavi, T.-W. Chen, Y.-C. Liu, R. Madhu, *J. Electrochem. Soc.* **2018**, *165*, B469–B474. **DOI:**10.1149/2.1171810jes
6. T. Selvaraju, R. Ramaraj, *J. Chem. Sci.* **2014**, *126*, 11–16. **DOI:**10.1007/s12039-013-0547-y
7. B. Devadas, M. Sivakumar, S. M. Chen, S. Cheemalapati, *Electrochim. Acta* **2015**, *176*, 350–358. **DOI:**10.1016/j.electacta.2015.07.022
8. T.-H. Tsai, T.-W. Chen, S.-M. Chen, *Electroanalysis* **2010**, *22*, 1655–1662. **DOI:**10.1002/elan.200900610
9. Z. Xue, N. He, H. Rao, C. Hu, X. Wang, H. Wang, X. Liu, X. Lu, *Appl. Surf. Sci.* **2017**, *396*, 515–522. **DOI:**10.1016/j.apsusc.2016.10.185
10. H. Razmi, A. Taghvimi, *Int. J. Electrochem. Sci.* **2010**, *5*, 751–760. http://www.electrochemsci.org/papers/vol5/5060751.pdf
11. L. Berisha, A. Maloku, E. Andoni, T. Arbneshi, *Am. J. Anal. Chem.* **2014**, *5*, 308–315. **DOI:**10.4236/ajac.2014.55038
12. T. Paixão, M. Bertotti, *Electroanalysis* **2008**, 20, 1671–1677.

DOI:10.1002/elan.200804231
13. S.-M. Chen, M.-F. Lu, K.-C. Lin, *J. Electroanal. Chem.* **2005**, *579*, 163–174. **DOI:**10.1016/j.jelechem.2005.02.006
14. W. Costa, W. Cardoso, E. Marques, C. Bezerra, A. Ferreira, C. Song, J. Zhang, A. Marques, *J. Braz. Chem. Soc*. **2013**, *24*, 651–656. **DOI:**10.1016/j.tetasy.2013.04.014
15. J. B. Raoof, R. Ojani, M. Baghayeri, *Anal. Methods* **2011**, *3*, 2367–2373. **DOI:**10.1039/c1ay05305a
16. W. de Araújo, T. Paixão, *Electroanalysis* **2011**, 23, 2549–2554. **DOI:**10.1002/elan.201100102
17. W. Costa, A. Marques, E. Marques, C. Bezerra, E. Sousa, W. Cardoso, C. Song, J. Zhang, *J. Appl. Electrochem.* **2010**, *40*, 375–382. **DOI:**10.1007/s10800-009-0006-0
18. T. Paixão, M. Bertotti, *Electrochim. Acta* **2007**, *52*, 2181–2188. **DOI:**10.1016/j.electacta.2006.08.035
19. R. Montes, E. Richter, R. Munoz. *Electrochem. Commun.* **2012**, 21, 26–29. **DOI:**10.1016/j.elecom.2012.05.005
20. S.-M. Chen, S.-H. Hsueh, *J. Electroanal. Chem.* **2004**, *566*, 291–303. **DOI:**10.1016/j.jelechem.2003.11.040
21. G. Medeiros-Neto, I. Rubio, *Endocrinology: Adult and Pediatric (Seventh Edition)* **2016**, 1584–1600.e3. **DOI:**10.1016/B978-0-323-18907-1.00091-3
22. R. Katagiri, X. Yuan, S. Kobayashi, S. Sasaki, *PLoS ONE* **2017**, *12(3)*, e0173722. **DOI:**10.1371/journal.pone.0173722
23. Y. Lazarova, I. Shterev, T. Dodevska, *Monatsh. Chem.* **2018**, *149*, 1955–1962. **DOI:**10.1007/s00706-018-2275-y
24. M. Araya, S. García, S. Pizarro, *Anal. Methods* **2020**, *12*, 205–211. **DOI:**10.1039/C9AY02249J
25. Ö. Yalçinkaya, A. Türker, *Acta Chim. Slov*. **2010**, *57*, 491–497. http://acta-arhiv.chem-soc.si/57/57-2-491.pdf
26. O. Zui, A. Terletskaya, *Fresenius J. Anal. Chem.* **1995**, *351*, 212–215. **DOI:**10.1007/BF00321640
27. J. Dorman, S. Steinberg, *Environ. Monit. Assess.* **2010**, *161*, 229–236. **DOI:**10.1007/s10661-008-0740-5
28. V. Januzaj, V. Mula, G. Turdean, L. Muresan, *Acta Chim. Slov.* **2015**, *62*, 28–34. **DOI:**10.17344/acsi.2014.672
29. T. Dodevska, Y. Lazarova, I. Shterev, *Acta Chim. Slov.* **2019**, *66*, 762–776. **DOI:**10.17344/acsi.2019.5261
30. T. Dodevska, E. Horozova, N. Dimcheva, *Anal. Bioanal. Chem.* **2006**, *386*, 1413–1418. **DOI:**10.1007/s00216-006-0682-0
31. E. Horozova, T. Dodevska, N. Dimcheva, *J. Chem. Technol. Metall.* **2008**, *43*, 59–64. http://dl.uctm.edu/journal/node/j2008-1/8_Horozova_Dodevska-59-64.pdf
32. E. Horozova, T. Dodevska, N. Dimcheva, *Bioelectrochemistry* **2009**, *74*, 260–264. **DOI:**10.1016/j.bioelechem.2008.09.003
33. T. Dodevska, E. Horozova, N. Dimcheva, *Cent. Eur. J. Chem.* **2010**, *8*, 19–27. **DOI:**10.1016/j.bioelechem.2008.09.003
34. E. Horozova, T. Dodevska, N. Dimcheva, R. Mussarlieva, *Int. J. Electrochem.* **2011**, Article ID 697698, 8 pages. **DOI:**10.4061/2011/697698
35. C. Pastore, P. Kiekens, Surface Characteristics of Fibers and Textiles, *Volume 94 of Surfactant Science,* CRC Press, **2000**, **ISBN**:1482289784, 9781482289787
36. T. Tsuneda, R. Singh, A. Iiyama, K. Miyatake, *ACS Omega* **2017**, *2*, 4053–4064. **DOI:**10.1021/acsomega.7b00594
37. W. Song, Y. Liu, N. Lu, H. Xu, C. Sun, *Electrochim. Acta* **2000**, *45*, 1639–1644. **DOI:**10.1016/S0013-4686(99)00326-6
38. Y.-C. Wu, R. Thangamuthu, S.-M. Chen, *Electroanalysis* **2009**, *21*, 210–214. **DOI:**10.1002/elan.200804423
39. H. Hamidi, E. Shams, B. Yadollahi, F. Esfahani, *Electrochim. Acta* **2009**, *54*, 3495–3500. **DOI:**10.1016/j.electacta.2008.12.063
40. P. Wang, X. Wang, G. Zhu, *Chem. Lett.* **2000**, *29*, 820–821. **DOI:**10.1246/cl.2000.820
41. R. Thangamuthu, Y.-C. Pan, S.-M. Chen, *Sens. Actuators B* **2011**, *151*, 377–383. **DOI:**10.1016/j.snb.2010.08.028
42. M. Zhou, L. Guo, F. Lin, H. Liu, *Anal. Chim. Acta* **2007**, *587*, 124–131. **DOI:**10.1016/j.aca.2007.01.017
43. B. Pires, F. Galdino, J. Bonacin, *Inorg. Chem. Acta* **2017**, *466*, 166–173. **DOI:**10.1016/j.ica.2017.06.003
44. T. Dodevska, I. Shterev, Y. Lazarova, *Acta Chim. Slov.* **2018**, *65*, 970–979. **DOI:**10.17344/acsi.2018.4672
45. Y. Lazarova, T. Dodevska, *Food Science and Applied Biotechnology* **2018**, *1*, 63–69. **DOI:**10.30721/fsab2018.v1.i1.4
46. T. Dodevska, E. Horozova, N. Dimcheva, *Mater. Sci. Eng. B* **2013**, *178*, 1497–1502. **DOI:**10.1016/j.mseb.2013.08.012
47. L. Shaidarova, S. Ziganshina, L. Tikhonova, G. Budnikov, *J. Anal. Chem.* **2003**, *58*, 1144–1150. **DOI:**10.1023/B:JANC.0000008953.67244.c2
48. A. Salimi, R. Hallaj, B. Kavosi, B. Hagighi, *Anal. Chim. Acta* **2010**, *661*, 28–34. **DOI:**10.1016/j.aca.2009.12.005
49. L. Guadagnini, D. Tonelli, *Sens. Actuat. B* **2013**, *188*, 806–814. **DOI:**10.1016/j.snb.2013.07.077
50. H. Heidari, B. Habibi, F. B. Vaigan, *Anal. Methods* **2016**, *8*, 4406–4412. **DOI:**10.1039/C6AY01087C
51. E. Marafon, L. Kubota, Y. Gushikem, *J. Solid State Electrochem.* **2009**, *13*, 377–383. **DOI:**10.1007/s10008-008-0564-9
52. B.-X. Zou, X.-X. Liu, D. Diamond, K.-T. Lau, *Electrochim. Acta* **2010**, *55*, 3915–3920. **DOI:**10.1016/j.electacta.2010.02.034
53. S. Nellaiappan, A. Kumar, *Electrochim. Acta* **2013**, *109*, 59–66. **DOI:**10.1016/j.electacta.2013.07.076
54. B. Haghighi, H. Hamidi, L. Gorton, *Electrochim. Acta* **2010**, *55*, 4750–4757. **DOI:**10.1016/j.electacta.2010.03.041
55. F. Chatraei, H. Zare, *Mat. Sci. Eng. C* **2013**, *33*, 721–726. **DOI:**10.1016/j.msec.2012.10.024
56. A. Azadbakht, A. Abbasi, Z. Derikvand, S. Amraei, *Mater. Sci. Eng. C* **2015**, *48*, 270–278. **DOI:**10.1016/j.msec.2014.12.034
57. A. Salimi, H. Mamkhezri, S. Mohebbi, *Electrochem. Commun.* **2006**, *8*, 688–696. **DOI:**10.1016/j.elecom.2006.02.019

Povzetek

Film rutenijev oksid heksacianoferat (RuOHCF) je bil elektrokemično deponiran na stekleno ogljikovo površino (GC) z uporabo zaporedne ciklične voltametrije kot posredne in zelene sintetične strategije. Elektrokemijsko obnašanje in elektrokatalizne lastnosti modificirane elektrode RuOHCF / GC so bile ovrednotene na podlagi elektroredukcije vodikovega peroksida in jodata v močnem kislems mediju (pH 1,0–2,0) z uporabo različnih elektrokemijskih tehnik, vključno s ciklično voltametrijo in amperometrijo s konstantnim potencialom. Elektrokemijske študije so pokazale, da ima RuOHCF / GC visoko katalitično aktivnost pri obeh študiranih reakcijah, hiter odziv in dobro obnovljivost signala za tok. RuOHCF / GC ima izboljšano elektrokatatalitsko vedenje v primerjavi z drugimi modificiranimi elektrodami iz literature. Enostaven in ponovljiv postopek za izdelavo elektrod, široko linearno območje, minimalne interference in dolgotrajna stabilnost RuOHCF / GC naredijo ta senzoričen material obetaven za praktično kvantitativno določanje vodikovega peroksida in jodata. Izjemno je, da je poročana modificirana elektroda zagotavljala nadčutljive občutljivosti (1050 μA mM^{-1} cm^{-2}) in zelo selektivno amperometrično detekcijo jodata.

Except when otherwise noted, articles in this journal are published under the terms and conditions of the Creative Commons Attribution 4.0 International License

Scientific paper

Influence of TiO_2 on Mucosal Permeation of Aceclofenac: Analysis of Crystal Strain and Dislocation Density

Souvik Nandi, Satyaki Aparajit Mishra, Rudra Narayan Sahoo, Rakesh Swain and Subrata Mallick*

School of Pharmaceutical Sciences, Siksha 'O' Anusandhan (Deemed to be University), Bhubaneswar, Odisha, India, 751003

** Corresponding author: E-mail: profsmallick@gmail.com; subratamallick@soa.ac.in*
Fax: +91-674-2350642, Tel: +91-674-2350635

Received: 05-22-2020

Abstract

Titanium dioxide can adhere with human epithelial cells and have good tolerability. Present work has been undertaken to explore the influence of TiO_2 on mucosal permeation of aceclofenac. Mucosal permeation of aeclofenac solution containing TiO_2 has been carried out. In fourier transform infrared spectrosopy (FTIR), the intensity of the peaks has decreased along with the increase of TiO_2 content in the formulation indicating a possible binding between drug and TiO_2. Melting enthalpy has been decreased with the increased content of TiO_2 in the solid. The status of crystal strain and dislocation density of TiO_2 and aceclofenac in the solid state formulation has also been evaluated from Xray Diffraction data using Debye-Scherrer's equation. Mucosal permeation of aceclofenac has shown sustained effect for more than 20 h in presence of titanium dioxide. Titanium dioxide could be used in designing formulation for sustaining mucosal aceclofenac delivery after performing risk assessment study.

Keywords: Aceclofenac; titanium dioxide; mucosal permeation; crystal strain; dislocation density; in vitro diffusion.

1. Introduction

Titanium Dioxide (TiO_2) is a biocompatible and stable material,[1] and has a wide range of application in various kinds of cosmetics. TiO_2 is accepted as food additive and also approved by Food and Drug Administration to be used in toothpaste, oral formulations etc.[2] Chen et al, 2011 described that TiO_2 is responsible for increasing intracellular Ca^{2+} concentration leading to elevated secretion of mucin.[3] TiO_2 coating is very much useful to adhere on epithelial tissues.[4] Masa and his colleagues, 2018 reported that TiO_2 has a property to attach with human epithelial cells along with a good tolerability.[5] TiO_2 nanoparticles interact instantly with the buccal mucosa upon contact and show a long residence time in the oral cavity.[6]

Aceclofenac is a widely used Biopharmaceutics Classification System (BCS) class II non-steroidal anti-inflammatory drug (NSAID).[7–9] It suffers from shorter elimination half-life and low oral bioavailability because of low aqueous solubility.[10–12] The toxic effects of this NSAID include gastric abnormalities like abdominal pain, gastric bleeding, dyspepsia etc. It is known that if the first pass metabolism is bypassed avoiding oral administration, improved bioavailability could be observed.[13] Aceclofenac eye drop has shown a marked reduction in ocular inflammation in post-operative cases of cataract operation.[14] Topical administration has been done frequently (2 hourly) for improved permeation through ocular mucosa. In vitro prolonged release has been studied for transmucosal delivery of aceclofenac using mucoadhesive dillenia fruit gum.[15] Katara et al., prepared a nano particle formulation of aceclofenac and claimed that the drug efficacy in local action can be improved if residence time of the formulation is amplified.[16]

In this present study the influence of TiO_2 has been explored on the mucosal permeation of aceclofenac in liquid formulation after topical administration. Any sort of sustained permeation of drug due to long residence time of TiO_2 upon interacting with the mucosal tissue has been examined. Solid state crystal strain and dislocation density have also been analysed.

2. Experimental

2. 1. Materials

Aceclofenac was received from Mannequin Pharmaceuticals Pvt. Ltd., (Bhubaneswar, India) as a gift sample. Titanium Dioxide was procured from Merck Specialities Pvt. Ltd, (Mumbai India).

2. 2. Preparation of Aceclofenac TiO_2 Kneaded Mixture

Aceclofenac was dissolved in a minimal amount of acetone and a kneaded mixture was prepared with titanium dioxide at different ratios (Table 1). [17,18] The mass was dried at 50 °C until constant weight and preserved in a desiccator.

2. 3. FTIR Study

KBR pellet method was used to carry out the FTIR study of pure drug and formulated powders.[19] A mean of 80 times was taken to obtain the average FTIR spectrum from 400 to 4000 cm^{-1} (Model: JASCO FTIR 4100 type A).

2. 4. DSC Study

Differential scanning calorimetry (DSC) cell was calibrated with Indium (melting point: 156.5 C, ΔH_{fus} = 28.54 J/g).[20] The thermogram was recorded under nitrogen atmosphere (50 ml/min) while taking a sample weighing between 4–6 mg in an aluminium crucible. The rate of heating was 10 °C/min and the upper limit was set as 200 °C. [21,22]

2. 5. XRD Study

X-ray diffraction pattern of pure aceclofenac and kneaded mixtures were subjected for XRD study. The scan was carried out at a speed of 1°/ min from 5–70° in Rigaku Ultima IV. CU was used as a source for Xray.

2. 6. *In vitro* Drug Release Study

In vitro drug diffusion study was done in both side open glass tube using dialysis membrane (HIMEDIA Dialysis Membrane-150) (surface area of diffusion = 1.54 cm^2). Acurately weighed amount of the powder samples were taken inside the diffusion tube with 2 ml of fresh liquid medium. The dialysis tube was placed in vessel containing 200 ml phosphate buffer (pH 7.4 at 34 ± 0.5 °C) under a paddle speed of 50 rpm.[23,24] Aliquot of 10 ml was drawn at particular time intervals and replaced with same volume of fresh medium. The absorbance was checked in a UV-Visible spectrophotometer (JASCO V-630 UV-Visible spectrophotometer) at 274 nm.

2. 7. *Ex vivo* Permeation Study

The similar diffusion system was used to study drug permeation through the corneal mucosa. Whole fresh eye ball of goat was brought from the local butcher shop. The cornea was carefully separated out along with 2 to 4 mm of surrounding sclera tissue and washed thoroughly. The cornea was tied tightly with thread along the circumference of vertical cylindrical diffusion tube to prevent any kind of leakage. Powder samples were taken inside the tube with 2 ml of fresh liquid medium and the tube was placed in vessel containing 200 ml phosphate buffer (pH 7.4 at 34 ± 0.5 °C) under a paddle speed of 50 rpm. The tubes were attached with paddle using adhesive tapes and paddles were put down as the as the cornea just touches the dissolution medium. Samples (10 ml) were withdrawn at 0.5, 1, 2, 3, 4, 5, 6, 7, 11, 20 h and replenished with 10 ml of fresh medium. The samples were filtered through 0.45 µm syringe driven filter and analysed by UV-Visible spectrophotometer. The studies of all formulations were performed in triplicate.[25]

3. Results and Discussion

3. 1. FTIR

As depicted in Figure 1, an intense peak was observed at 3317 cm^{-1} may be due to the amine group.[26] Peaks at 1715 and 1771 cm^{-1} may be formed due to stretch-

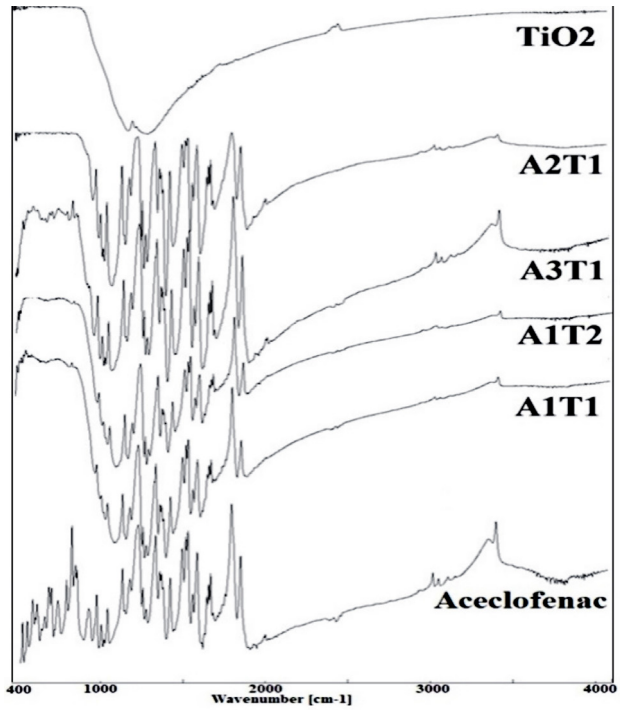


Figure 1. FTIR spectra of pure aceclofenac, TiO_2 and solid formulations.

ing of two carbonyl (C=O) groups in the drug structure.[27,28] The peak at 2969 cm^{-1} may be because of symmetric stretching of CH2 in both pure drug and formulations.[29] In the formulations, the intensity of the peaks has decreased along with the increase of TiO_2 indicating a possible binding between drug and TiO_2. The decrease of the peak intensity at 3317 with the increase of TiO_2 may be considered as the possible binding site with the oxygen present in titanium dioxide with the amine group of aceclofenac.

3. 2. DSC

The pure drug has shown a sharp melting point at 152.97 °C (Figure 2). The formulations have showed a ± 2 °C shifting of melting point along with lower peak intensity comparing to the pure drug. The pure drug has the highest enthalpy of melting (–155.76 jg^{-1}), where the enthalpy has reduced along with the decreased content of aceclofenac and increased content of TiO2 (Table 1). Probably the bond formation between TiO2 and aceclofenac is the cause of the decreased enthalpy of the formulations.

Table 1. Thermal behaviour of TiO_2 kneaded aceclofenac formulation

Formulation Code (Drug:TiO2)	Onset of Melting (°C)	Endset of Melting (°C)	Melting Point (°C)	Enthalpy (jg^{-1})
Aceclofenac	152.01	156.77	152.97	–155.76
A1T1 (1:1)	149.50	156.44	153.73	–62.11
A1T2 (1:2)	147.15	155.02	151.57	–32.23
A2T1 (2:1)	149.07	157.31	153.83	–66.67
A3T1 (3:1)	150.81	155.83	153.16	–153.09

3. 3. XRD Study

X ray diffraction data is portrayed in Figure 3. The TiO_2 as well as the formulations has shown a particular kind of diffraction pattern at 38.5° and 55° 2θ. The diffraction position and pattern proved that the TiO_2 anatase crystals has not changed in the formulations.[30] The most intense peaks then subjected to further calculation and an average value was taken as a representation for the whole formulation. The particle size was determined from the Debye-Scherrer's equation.[31]

$$D = \frac{K\lambda}{\beta Cos\theta} \quad (1)$$

Where, D is the crystal size (nm), K is a constant with a value of 0.9, λ is the wavelength of the Xray (0.1541 nm) and β is the value of FWHM (full width at half maxima) in radian. The X-ray diffraction pattern of TiO2 is evident to be at anatase phase[30,31] and the typical anatase TiO2 crystals have the octahedral structure.[32] Typically the K value can be considered as 0.9 and Anku et al., (2016) also estimated particle size of TiO2 anatase using Scherrer's Formula considering the shape factor 'K' as 0.9.[33]

Other characteristic properties of the formulations like, strain and dislocation density are tabulated in Table 2. Dislocation density can be described as the length of dislocation lines per unit volume of the crystals where dislocation is a linear defect found in crystals[34]. The untreated and treated pure TiO_2 has shown dislocation density of 0.80 and 0.71 respectively whereas the formulation with highest content of aceclofenac has shown almost 1.4 times higher dislocation lines per unit area. The similarity has also followed in the case of pure TiO_2 crystal strain (0.73) and the formulation, A3T1 has

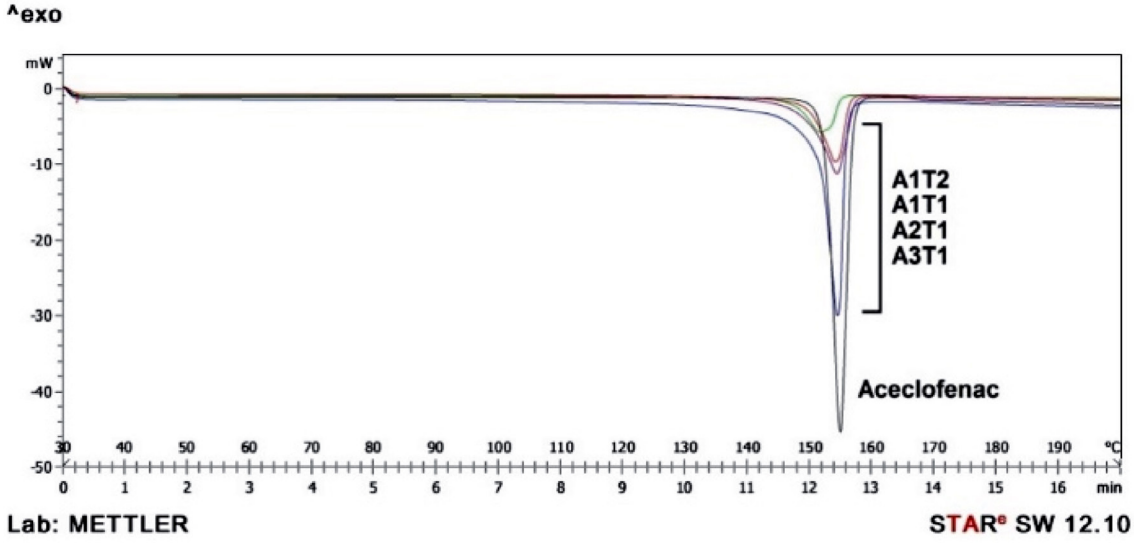


Figure 2. DSC Thermogram of aceclofenac and the formulations.

Table 2. Solid state particle properties of aceclofenac-titanium dioxide kneaded products

Formulation Code	TiO_2			Aceclofenac		
	Particle Size (nm)	Strain	Dislocation Density*10^{-3}	Particle Size (nm)	Strain	Dislocation Density *10^{-3}
Aceclofenac	–	–	–	98.08 ± 16.5	0.114 ± 0.014	0.44 ± 0.10
T1 (untreated TiO_2)	70.89 ± 3.64	0.073 ± 0.016	0.80 ± 0.088	–	–	–
T2 (Acetone treated TiO_2)	74.87 ± 1.60	0.068 ± 0.012	0.71 ± 0.030	–	–	–
A1T1	68.65 ± 0.84	0.075 ± 0.013	0.84 ± 0.021	73.47 ± 19.46	0.157 ± 0.037	0.90 ± 0.50
A1T2	64.44 ± 1.34	0.079 ± 0.015	0.96 ± 0.040	59.67 ± 11.56	0.132 ± 0.054	1.22 ± 0.40
A2T1	65.88 ± 3.15	0.077 ± 0.010	0.92 ± 0.092	71.09 ± 14.81	0.158 ± 0.054	0.98 ± 0.40
A3T1	63.01 ± 1.25	0.081 ± 0.013	1.00 ± 0.041	70.88 ± 14.58	0.149 ± 0.036	0.87 ± 0.30

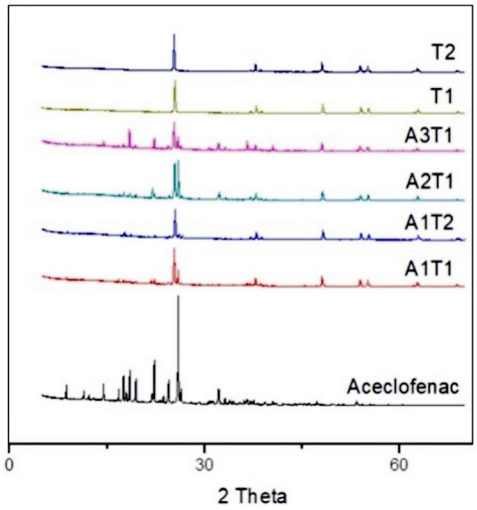


Figure 3. Powder Xray diffraction overlay of pure drug, formulation, untreated and treated titanium dioxide (T1 and T2 respectively).

shown the highest strain. The above mentioned changes may have occurred due to the binding of aceclofenac with titanium dioxide.[19] A similar phenomenon was noticeable in the case of aceclofenac where the dislocation density of A1T2 was higher than any other formulations or the pure drug itself. Particle size was found to be lowest in the case of the A1T2 formulation than the pure drug (98.08 nm).

3. 4. *In vitro* Diffusion Study

The observation was replicated in triplicate and the mean value is used to prepare the time vs cumulative percent release in Figure 4. The highest release was found in the case of A2T1 (89.88%) at 2 hours followed by A1T1 (89.13%). The formulation containing highest amount of TiO2 (A1T2) has shown lowest amount of drug release 82.55% in contrast to others at 120 mins.

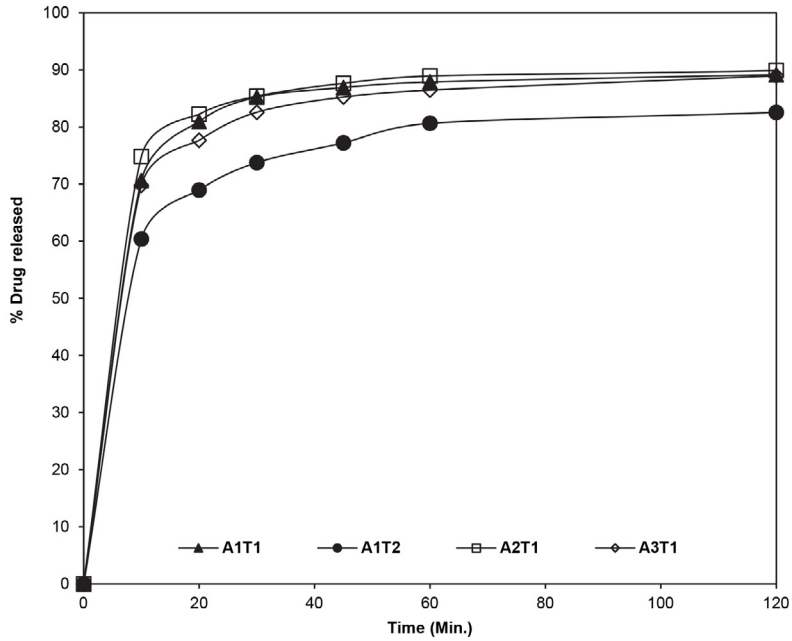


Figure 4. *In vitro* drug diffusion profile of the formulation

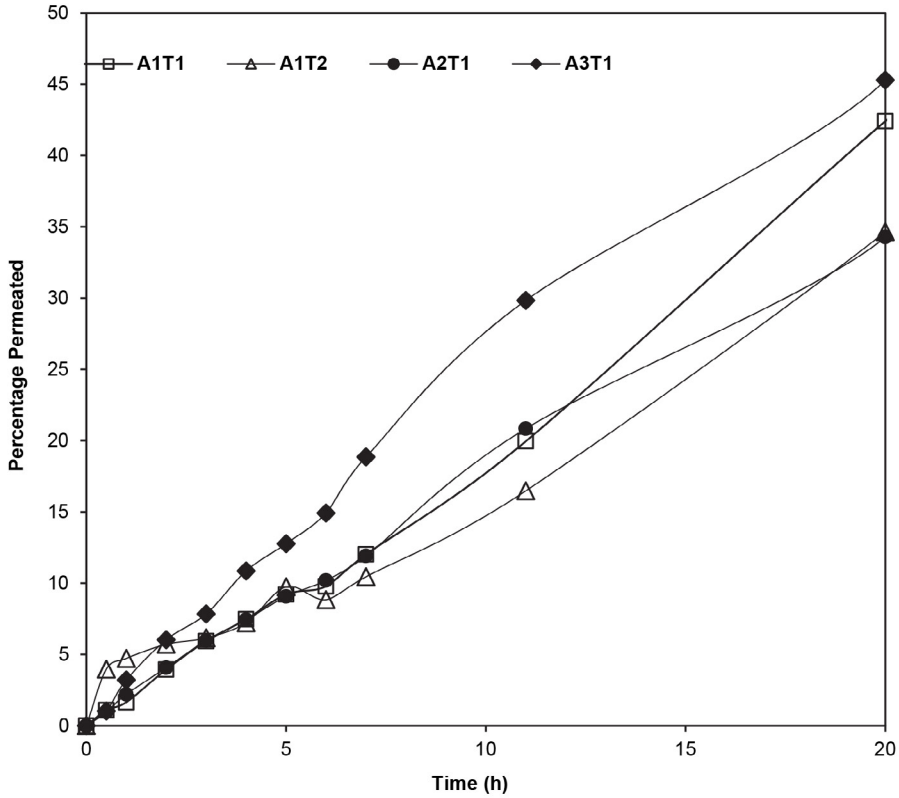


Figure 5. *Ex vivo* permeation study of the formulations through goat corneal mucosa

3. 5. *Ex vivo* Permeation Study

The data was presented as a plot of time vs percentage permeated in Figure 5. The highest release was found in the case of A3T1 (45.29 %) at 20 hours followed by A1T1 (42.40 %). In all of the formulations the permeation was continued up to 20 hours while maintaining an increasing order. Aceclofenac 0.1 % solution exhibited goat corneal permeation of almost 50–90 % within 2 h only in the pH range of 7–7.4.[14]

4. Conclusion

Influence of titanium dioxide on mucosal permeation of aceclofenac has been carried out in aqueous state. FTIR results revealed the decreased intensity of some characteristic peaks of aceclofenac in the formulation with the decreased content of aceclofenac and increased content of TiO_2 indicating possible binding between drug and TiO_2. Thermal analysis has also exhibited decreased melting enthalpy with the decrease of aceclofenac and increase of TiO_2 content in the solid. The change in crystal strain and dislocation density of TiO_2 and aceclofenac in the solid formulation has been noticed. Sustained mucosal permeation of aceclofenac has been observed for more than 20 h in presence of titanium dioxide. Titanium dioxide could be used in designing formulation for sustaining and controlling mucosal delivery of aceclofenac after assessing risk factor associated with TiO_2.

Acknowledgement

The authors are grateful to Dr. Monojranjan Nayak, President, Siksha 'O'Anusandhan University for financial support and laboratory facility. We are also grateful to receive Aceclofenac as gift sample from Mannequin Pharmaceuticals Pvt. Ltd., Bhubaneswar, Odisha.

Conflict of Interest

The authors declare no conflict of interests.

5. References

1. H. M. A. Shawish, H. Tamous, S. Saadeh, A. Tbaza, *Acta Chim. Slov*. **2018**, *65*, 811–822. **DOI:**10.17344/acsi.2018.4383
2. M. Skocaj, M. Filipic, J. Petkovic, S. Novak, *Radiol. Oncol.* **2011**, *45*, 227–247. **DOI:**10.2478/v10019-011-0037-0
3. E. Y. Chen, M. Garnica, Y. C. Wang, C. S. Chen, W. C. Chin, *PloS one*. **2011**, *6*, e16198. **DOI:**10.1371/journal.pone.0016198
4. S. Riivari, K. Shahramian, I. Kangasniemi, J. Willberg, T. O. Närhi, *Int. J. Oral Maxillofac. Implants*. **2019**, *34*, 313–319. **DOI:**10.11607/jomi.6862

5. R. Masa, Á. Deák, G. Braunitzer, Z. Tóth, J. Kopniczky, I. Pelsőczi-Kovács, K. Ungvári, I. Dékány, K. Turzó, *J. Nanosci. Nanotechnol*. **2018**, *18*, 3916–3924. **DOI:**10.1166/jnn.2018.15261
6. B. J. Teubl, G. Leitinger, M. Schneider, C. M. Lehr, E. Fröhlich, A. Zimmer, E. Roblegg, *Nanotoxicology*, **2015**, *9*, 253–261. **DOI:**10.3109/17435390.2014.921343
7. T. Soni, C. Nagda, T. Gandhi, N. P.Chotai, *Dissolut. Technol.* **2008**, *15*, 31–35. **DOI:**10.14227/DT150208P31
8. M. Grau, J. Guasch, J. L. Montero, A. Felipe, E. Carrasco, S. Juliá, *Arzneim-Forsch Drug Res*, **1991**, *41*, 1265–1276.
9. N. Sethuraman, S. Shanmuganathan, K. Sandhya, B. Anbarasan, *Indian J. Pharm. Educ.* **2018**, *52*, 581–586. **DOI:**10.5530/ijper.52.4.67
10. R. Raj, P. Mongia, A. Ram, N. K. Jain, *Artif Cells Nanomed. Biotechnol*. **2016**, *44*, 1434–1439.
11. https://pubchem.ncbi.nlm.nih.gov/compound/Aceclofenac#section=Melting-Point
12. B. Tubić, A. Uzunović, S. Pilipović, Ž. Gagić, *Acta Chim. Slov*. **2016**, *63*, 193–9. **DOI:**10.17344/acsi.2015.2168
13. S. Korani, M. Korani, S. Bahrami, T. P. Johnston, A. E. Butler, M. Banach, A. Sahebkar, *Drug Discov. Today*. **2019**, *24*, 567–574. **DOI:**10.1016/j.drudis.2018.09.023
14. V. Dave, S. Paliwal, *Saudi Pharm. J*. **2014**, *22*, 240–245. **DOI:**10.1016/j.jsps.2013.03.001
15. M. S. Hasnain, P. Rishishwar, S. Ali, A. K. Nayak, *SN App. Sci.* **2020**, *2*, 1–8. **DOI:**10.1007/s42452-019-1756-x
16. R. Katara, D. K. Majumdar, *Colloid Surface B*. **2013**, *103*, 455–462. **DOI:**10.1016/j.colsurfb.2012.10.056
17. A. Modi, P. Tayade, *AAPS PharmSciTech*. **2006**, *7*, E87. **DOI:**10.1208/pt070368
18. S. Nandi, S. A. Mishra, R. N. Sahoo, R. Swain, S. Mallick, *Indian J. Pharm. Educ.* **2020**, *54*, 68–72. **DOI:**10.5530/ijper.54.1.8
19. M. Starsinic, R. L. Taylor, P. L. Walker Jr, P. C.Painter, *Carbon*. **1982**, *21*, 69–74. **DOI:**10.1016/0008-6223(83)90158-6
20. G. Vanden, V. B. F.Mathot, *Thermochim. Acta*. **2006**, *446*, 41–54. **DOI:**10.1016/j.tca.2006.02.022
21. R. N. Sahoo, A. Nanda, A. Pramanik, S. Nandi, R. Swain, S. K. Pradhan, S. Mallick, *Acta Chim. Slov.* **2019**, *66*, 923–933. **DOI:**10.17344/acsi.2019.5139
22. M. Acharya, S. Mishra, R. N. Sahoo, S. Mallick, *Acta Chim. Slov.* **2017**, *64*, 45–54. **DOI:**10.17344/acsi.2016.2772
23. S. A. Agnihotri, T. M. Aminabhavi, *J. Control. Release.* **2004**, *96*, 245–259. **DOI:**10.1016/j.jconrel.2004.01.025
24. M. S. Bhandari, S. M. Wairkar, U. S. Patil, N. R. Jadhav, *Acta Chim. Slov*, **2018**, *65*, 492–501. **DOI:**10.17344/acsi.2017.3822
25. M. S. Kaynak, M. Celebier, S. Sahin, S. Altinöz, *Rev. Chim. (Bucharest).* **2013**, *64*, 27–30.
26. R. Mohapatra, S. Senapati, C. Sahoo, S. Mallick, *Farmacia*. **2016**, *64*, 72–81.
27. C. Y. Won, C. C. Chu, J. D. Lee, *Polymer*, **1998**, *39*, 6677–6681. **DOI:**10.1016/S0032-3861(98)00032-9
28. W. J. Ray, J. E. Katon, B. Phillips, *J. Mol. Struct.* **1981**, *74*, 75–84. **DOI:**10.1016/0022-2860(81)80009-9
29. P. S. Thomas, J. Guerbois, G. F. Russell, B. J.Briscoe, *J. Therm. Anal. Cal.* **2001**, *64*, 501–508. **DOI:**10.1023/A:1011578514047
30. A. Di Paola, M. Bellardita, B. Megna, F. Parrino, L. Palmisano, *Catal. Today.* **2015**, *252*, 195–200. **DOI:**10.1016/j.cattod.2014.09.012
31. W. Anku, S. O. Oppong, S. K. Shukla, P. P. Govender, *Acta Chim. Slov.* **2016**, *63*, 380–391. **DOI:**10.17344/acsi.2016.2385
32. S. Yang, N. Huang, Y. M. Jin, H. Q. Zhang, Y. H. Su, H. G. Yang, *Cryst. Eng. Comm.*, **2015**;*17*, 6617–6631. **DOI:**10.1039/C5CE00804B
33. A. Bishnoi, S. Kumar, N. Joshi, in: Microscopy Methods in Nanomaterials Characterization, Elsevier, **2017**, pp. 313–337. **DOI:**10.1016/B978-0-323-46141-2.00009-
34. I. Boukhoubza, M. Khenfouch, M. Achehboune, B. M. Mothudi, I. Zorkani, A. Jorio, in: *J. Phy.: Conference Series*, IOP Publishing, **2019**, *1292*, 012011. **DOI:**10.1088/1742-6596/1292/1/012011

Povzetek

Titanov dioksid se lahko adherira na človeške epitelijske celice in se dobro prenaša. Opisano delo je proučevalo vpliv TiO_2 na prepustnost sluznice za aceklofenak. Izvedena je bila študija prepustnosti sluznice za raztopino aceklofenaka, ki je vsebovala TiO_2. Pri infrardeči spektroskopiji s Fourierjevo transformacijo (FTIR) se je intenzivnost vrhov zmanjšala hkrati s povečanjem vsebnosti TiO_2 v formulaciji, kar kaže na morebitno vezavo med učinkovino in TiO_2. Entalpija taljenja se je zmanjšala s povečanjem vsebnosti TiO_2 v trdni snovi. Stanje kristalne oblike in dislokacijska gostota TiO_2 in aceklofenaka v trdni formulaciji sta bila ocenjena iz podatkov rentgenske difrakcije z uporabo Debye-Scherrerjeve enačbe. Prepustnost sluznice za aceklofenak je v prisotnosti titanovega dioksida pokazala podaljšano delovanje za več kot 20 ur. Titanov dioksid bi se po izvedbi študije ocene tveganja lahko uporabil pri oblikovanju formulacije za zadrževanje acekolofenaka na sluznici.

Except when otherwise noted, articles in this journal are published under the terms and conditions of the Creative Commons Attribution 4.0 International License

Scientific paper

Synthesis, Crystal Structures, Characterization and Catalytic Property of Manganese(II) Complexes Derived from Hydrazone Ligands

Yao Tan

School of Environmental and Chemical Engineering, Chongqing Three Gorges University, Chongqing 404000, P.R. China

** Corresponding author: E-mail: 18696838310@163.com*

Received: 05-23-2020

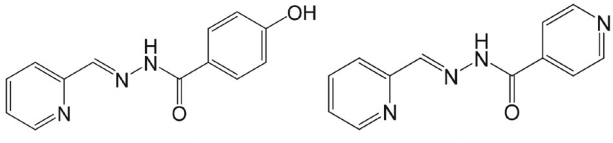
Abstract

A new bromido-coordinated mononuclear manganese(II) complex $[MnL^1Br_2(OH_2)]$ (**1**), and a new nitrato-coordinated mononuclear manganese(II) complex $[Mn(L^2)_2(ONO_2)(OH_2)]NO_3$ (**2**), with the hydrazone ligands 4-hydroxy-*N*'-(pyridin-2-ylmethylene)benzohydrazide (HL^1) and *N*'-(pyridin-2-ylmethylene)isonicotinohydrazide (HL^2), have been synthesized and structurally characterized by physico-chemical methods and single crystal X-ray determination. Single crystal structural analysis shows that the Mn atom in complex **1** is in octahedral coordination, and that in complex **2** is in pentagonal bipyramidal coordination. The catalytic property for epoxidation of styrene by the complexes was evaluated.

Keywords: Manganese complex; hydrazone ligand; crystal structure; catalytic property

1. Introduction

Hydrazone compounds are a series of important ligands in coordination chemistry.[1] The hydrazone ligands are capable of binding various transition and rare earth metal atoms to form complexes with versatile structures and properties.[2] To date, most hydrazone complexes have been reported to have remarkable catalytic properties, such as asymmetric epoxidation, oxidation of sulfides, and various type of polymerization.[3] Among the complexes, those with Mn centers are of particular interest for their catalytic properties.[4] In this paper, a new bromido-coordinated mononuclear manganese(II) complex $[MnL^1Br_2(OH_2)]$ (**1**), and a new nitrato-coordinated mononuclear manganese(II) complex $[Mn(L^2)_2(ONO_2)(OH_2)] \cdot NO_3$ (**2**), with the hydrazone ligands 4-hydroxy-*N*'-(pyridin-2-ylmethylene)benzohydrazide (HL^1) and *N*'-(pyridin-2-ylmethylene)isonicotinohydrazide (HL^2) (Scheme 1), are presented.



HL^1 HL^2

Scheme 1. The preparation of the hydrazone ligands HL^1 and HL^2.

2. Experimental

2. 1. Materials

Manganese bromide, manganese nitrate, 2-pyridinecarboxaldehyde, 4-hydroxybenzohydrazide, and 4-pyridylcarbonylhydrazine were purchased from Aldrich. All other reagents with AR grade were used as received without further purification.

2. 2. Physical Measurements

Infrared spectra (4000–400 cm^{-1}) were recorded as KBr discs with a FTS-40 BioRad FT-IR spectrophotometer. Microanalyses (C, H, N) of the complex were carried out on a Carlo-Erba 1106 elemental analyzer. Solution electrical conductivity was measured at 298 K using a DDS-11 conductivity meter. GC analyses were performed on a Shimadzu GC-2010 gas chromatograph.

2. 3. X-Ray Crystallography

Crystallographic data of the complexes were collected on a Bruker SMART 1000 CCD area diffractometer with graphite monochromated Mo-Kα radiation (λ = 0.71073 Å) at 298(2) K. Absorption corrections were applied by using the multi-scan program.[5] The structures of the complexes were solved by direct methods and successive Fourier dif-

ference syntheses, and anisotropic thermal parameters for all nonhydrogen atoms were refined by full-matrix least-squares procedure against F^2.[5] All non-hydrogen atoms were refined anisotropically. The water and amino H atoms were located from electronic density maps and refined isotropically with O–H, N–H and H···H distances restrained to 0.85(1), 0.90(1) and 1.37(2) Å, respectively. The crystallographic data and experimental details for the structural analysis are summarized in Table 1.

Table 1. Crystallographic data for the single crystal of the complexes.

Compound	1	2
Empirical formula	$C_{13}H_{13}Br_2MnN_3O_3$	$C_{24}H_{22}MnN_{10}O_9$
Formula weight	474.02	649.46
Temperature (K)	298(2)	298(2)
Crystal system	Monoclinic	Triclinic
Space group	$P2_1/n$	P-1
a (Å)	8.1584(7)	9.1540(13)
b (Å)	16.6952(14)	10.3954(15)
c (Å)	12.0488(10)	14.4801(17)
α (°)	90	83.219(2)
β (°)	96.255(2)	86.581(2)
γ (°)	90	89.383(2)
V (Å^3)	1631.4(2)	1365.8(3)
Z	4	2
F(000)	924	666
Data/restraints/ parameters	4008/4/209	5088/5/409
Goodness-of-fit on F^2	1.062	1.049
R_1, wR_2 [$I > 2\sigma(I)$]	0.0380, 0.0977	0.0475, 0.1375
R_1, wR_2 (all data)	0.0609, 0.1070	0.0747, 0.1639

2. 4. Synthesis of $[MnL^1Br_2(OH_2)]$ (1)

2-Pyridinecarboxaldehyde (1.0 mmol, 0.11 g) was reacted with 4-hydroxybenzohydrazide (1.0 mmol, 0.15 g) in methanol (20 mL) for 30 min at room temperature with stirring. Then, manganese bromide tetrahydrate (1.0 mmol, 0.29 g) was added, and the mixture was stirred at room temperature for another 30 min. The deep brown solution was evaporated to remove three quarters of the solvents under reduced pressure, yielding brown solid product of the complex. Yield: 63%. Well-shaped single crystals suitable for X-ray diffraction were obtained by recrystallization of the solid from methanol. Anal. calcd. for $C_{13}H_{13}Br_2MnN_3O_3$ (%): C, 32.94; H, 2.76; N, 8.86. Found (%): C, 32.76; H, 2.83; N, 8.77. IR data (KBr, cm^{-1}): 3465, 1645, 1446, 1366, 1161, 1069, 952, 860, 537. UV-Vis data in methanol [λ_{max} (nm)]: 292, 375.

2. 5. Synthesis of $[Mn(L^2)_2(ONO_2)(OH_2)]NO_3$ (2)

2-Pyridinecarboxaldehyde (1.0 mmol, 0.11 g) was reacted with 4-pyridylcarbonylhydrazine (1.0 mmol, 0.14 g) in methanol (20 mL) for 30 min at room temperature with stirring. Then, manganese nitrate tetrahydrate (1.0 mmol, 0.25 g) was added, and the mixture was stirred at room temperature for another 30 min. The deep brown solution was evaporated to remove three quarters of the solvents under reduced pressure, yielding brown solid product of the complex. Yield: 36%. Well-shaped single crystals suitable for X-ray diffraction were obtained by recrystallization of the solid from methanol. Anal. calcd. for $C_{24}H_{22}MnN_{10}O_9$ (%): C, 44.39; H, 3.41; N, 21.57. Found (%): C, 44.53; H, 3.50; N, 21.49. IR data (KBr, cm^{-1}): 3440, 1645, 1551, 1468, 1445, 1433, 1412, 1384, 1358, 1312, 1218, 1153, 1107, 1160, 1036, 1004, 920, 850, 782, 749, 690, 589, 520. UV-Vis data in methanol [λ_{max} (nm)]: 297, 370.

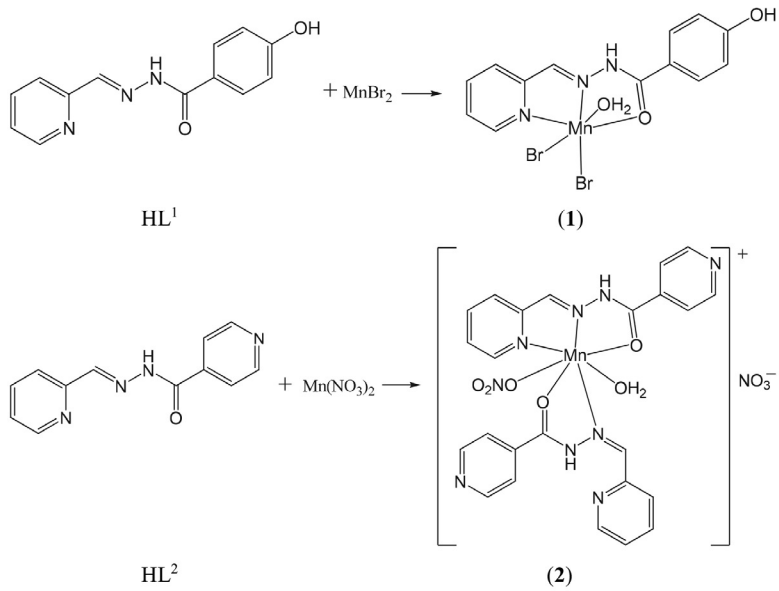
2. 6. Styrene Epoxidation

The epoxidation reaction catalyzed by the complexes was carried out at room temperature in MeCN under nitrogen atmosphere. The reaction mixture contains styrene (2.00 mmol), chlorobenzene (internal standard; 2.00 mmol), the complex (catalyst; 0.10 mmol) and iodosylbenzene or sodium hypochlorite (oxidant; 2.00 mmol), and MeCN (5.00 mL). When sodium hypochlorite was used as the oxidant, the solution was buffered to pH = 11.2. GC was used to determine the composition of reaction medium with styrene and styrene epoxide quantified by the internal standard method (chlorobenzene). For each catalyst, the reaction time for the maximum epoxide yield was determined by withdrawing periodically 0.1 mL aliquots from the mixture and this time was used to monitor the efficiency of the catalyst on performing at least two independent experiments. Blank experiments with each oxidant and using the same experimental conditions without catalyst were carried out.

3. Results and Discussion

3. 1. Synthesis

The hydrazones were facile prepared by reaction of 2-pyridinecarboxaldehyde with 4-hydroxybenzohydrazide and 4-pyridylcarbonylhydrazine, respectively, in MeOH. The complexes **1** and **2** were synthesized from the hydrazones with manganese bromide tetrahydrate (for **1**) and manganese nitrate tetrahydrate (for **2**) in MeOH (Scheme 2). Notably, even though the synthetic procedures are different, the structure of the bromido-coordinated complex **1** is similar to the chlorido-coordinated manganese(II) complex.[6] In the synthesis of the chlorido-coordinated manganese(II) complex, triethylamine was added to remove the hydrogen of the amino group. To the best of our knowledge, it is no need to introduce triethylamine in the preparation of Schiff base complexes. The molar conductivities (Λ_M = 35 Ω^{-1} cm^2 mol^{-1} for **1** and 138 Ω^{-1} cm^2 mol^{-1} for **2**) are consistent with the values expected for non-electrolyte and 1:1 electrolyte.[7]



Scheme 2. The preparation of the complexes.

3. 2. Description of the Structure of Complex 1

Single-crystal X-ray analysis reveals that compound **1** is a bromido-coordinated mononuclear manganese(II) complex. The ORTEP plot of the complex is shown in Figure 1. The manganese atom is in a distorted octahedral geometry, which is coordinated by the N_2O donor atoms of the hydrazone ligand and one Br atom in the equatorial plane, and one Br atom and one water O atom in the axial positions. The distortion of the octahedral coordination of the structure can be observed from the bond angles (Table 2) related to the Mn atom. The *cis*- and *trans*- angles related to the Mn atom are in the range of 69.48(9)–118.88(7)° and 140.29(10)–173.42(7)°, respectively. The bond lengths of Mn–O and Mn–N (Table 2) are close to those in other Mn complexes with Schiff base ligands.[8] As expected, the bond lengths in the axial positions are elongated due to a Jahn-Teller distortion effect. The hydrazone ligand coordinates to the Mn atom through neutral state. The molecules are linked through N–H···Br, O–H···Br and O–H···O hydrogen bonds (Table 3), to generate chains along the *c* axis (Figure 2).

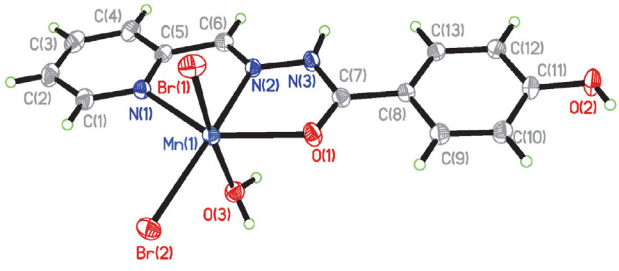


Figure 1. ORTEP diagram of complex **1** (30% thermal ellipsoid).

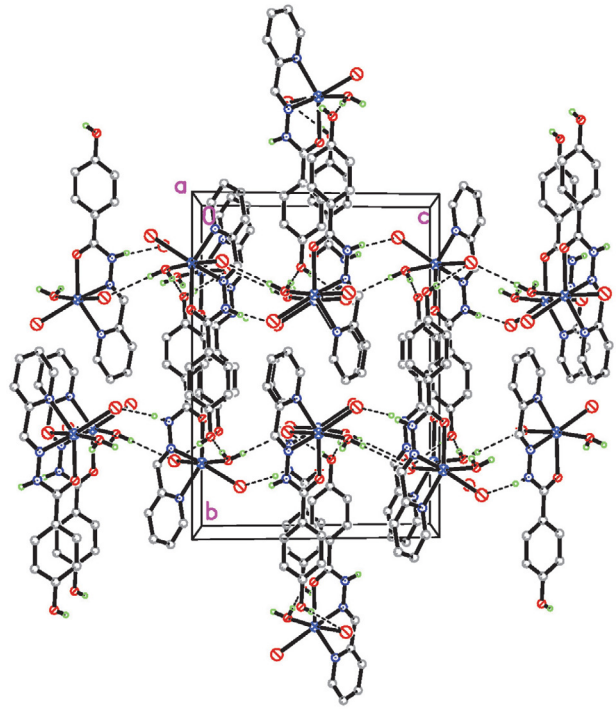


Figure 2. Molecular packing structure of complex **1** linked by hydrogen bonds.

3. 3. Description of the Structure of Complex 2

Single-crystal X-ray analysis reveals that compound **2** is a nitrato-coordinated mononuclear manganese(II) complex. The compound contains a $[Mn(L^2)_2(ONO_2)(OH_2)]$ cation and a nitrate anion. The ORTEP plot of the complex is shown in Figure 3. The manganese atom is in a

distorted pentaganol-bipyramidal geometry, which is coordinated by the N_2O donor atoms of one hydrazone ligand and the NO donor atoms of the other hydrazone ligand in the equatorial plane, and one nitrate O atom and one water O atom in the axial positions. The distortion of the pentagonal bipyramidal coordination of the structure can be observed from the bond angles (Table 2) related to the Mn atom. The equatorial angles related to the Mn atom are in the range of 65.99(8)–80.66(9)° and 132.55(9)–149.33(9)°. The bond lengths of Mn–O and Mn–N (Table 2) are close to those in other Mn complexes with Schiff base ligands.[7] The hydrazone ligands coordinate to the Mn atom through neutral state. The complex cations and the nitrate anions are linked through N-H···N, O-H···N, O-H···O and N-H···O hydrogen bonds (Table 3), to generate a network (Figure 4).

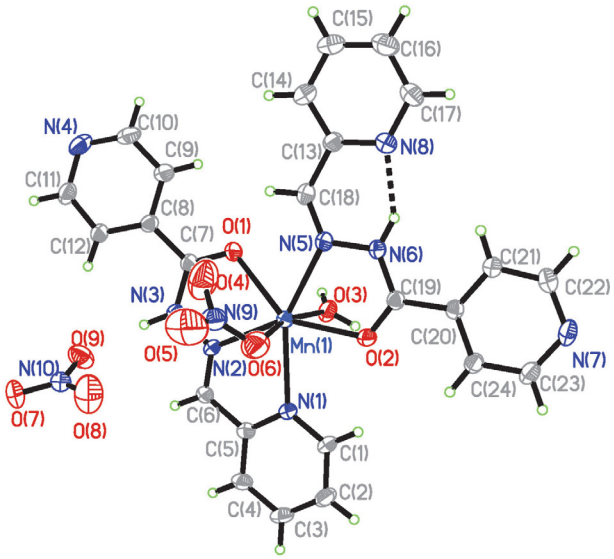


Figure 3. ORTEP diagram of complex **2** (30% thermal ellipsoid).

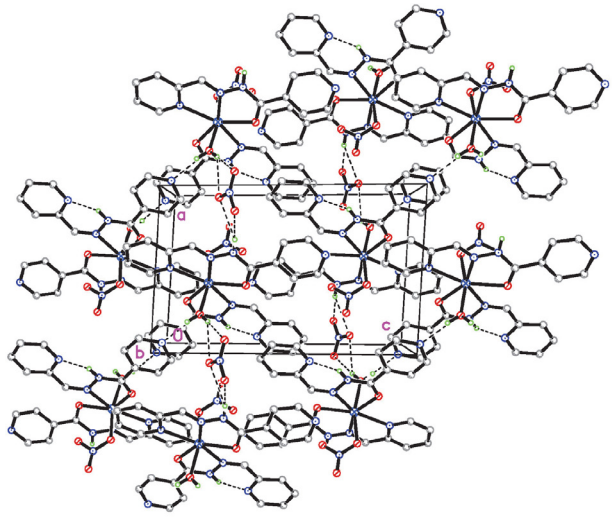


Figure 4. Molecular packing structure of complex **2** linked by hydrogen bonds.

Table 2. Selected bond distances (Å) and bond angles (°) for the complexes.

1			
Bond distance			
Mn1–N1	2.287(3)	Mn1–N2	2.229(3)
Mn1–O1	2.272(2)	Mn1–O3	2.265(3)
Mn1–Br2	2.5517(7)	Mn1–Br1	2.6499(7)
Bond angle			
N2–Mn1–O3	82.62(10)	N2–Mn1–O1	69.48(9)
O3–Mn1–O1	83.37(10)	N2–Mn1–N1	70.81(10)
O3–Mn1–N1	91.24(10)	O1–Mn1–N1	140.29(10)
N2–Mn1–Br2	163.56(7)	O3–Mn1–Br2	84.37(7)
O1–Mn1–Br2	118.88(7)	N1–Mn1–Br2	99.53(7)
N2–Mn1–Br1	98.38(7)	O3–Mn1–Br1	173.42(7)
O1–Mn1–Br1	90.87(7)	N1–Mn1–Br1	95.24(7)
Br2–Mn1–Br1	95.69(2)		
2			
Bond distance			
Mn1–N1	2.387(3)	Mn1–N2	2.288(3)
Mn1–N5	2.363(3)	Mn1–O1	2.412(2)
Mn1–O2	2.263(2)	Mn1–O3	2.163(3)
Mn1–O6	2.226(3)		
Bond angle			
O3–Mn1–O6	164.30(11)	O3–Mn1–O2	83.24(9)
O6–Mn1–O2	83.05(11)	O3–Mn1–N2	94.49(10)
O6–Mn1–N2	93.40(12)	O3–Mn1–N5	91.89(11)
O6–Mn1–N5	90.26(12)	O3–Mn1–N1	87.25(10)
O6–Mn1–N1	83.02(11)	O3–Mn1–O1	83.05(9)
O6–Mn1–O1	112.58(11)	O2–Mn1–N2	149.33(9)
O2–Mn1–N5	68.81(8)	N2–Mn1–N5	141.84(9)
O2–Mn1–N1	80.66(9)	N2–Mn1–N1	68.67(9)
N5–Mn1–N1	149.33(9)	O2–Mn1–O1	143.07(8)
N2–Mn1–O1	65.99(8)	N5–Mn1–O1	77.56(9)
N1–Mn1–O1	132.55(9)		

Table 3. Hydrogen bond distances (Å) and bond angles (°) for the complexes.

D–H···*A*	*d*(*D*–H)	*d*(H···*A*)	*d*(*D*···*A*)	Angle (*D*–H···*A*)
1				
N3–H3B···Br2	0.90(1)	2.445(14)	3.329(3)	169(5)
O3–H3A···Br1$^{\#1}$	0.85(1)	2.518(14)	3.354(3)	169(4)
O3–H3B···O2$^{\#2}$	0.85(1)	1.973(13)	2.820(4)	173(5)
O2–H2···Br1$^{\#3}$	0.82	2.46	3.268(3)	167(5)
2				
O3–H3A···N7$^{\#4}$	0.84(1)	1.971(14)	2.801(4)	169(5)
O3–H3B···O7$^{\#5}$	0.84(1)	2.290(13)	3.123(5)	171(4)
O3–H3B···O8$^{\#6}$	0.84(1)	2.33(3)	2.934(5)	129(3)
N6–H6···N8	0.90(1)	1.84(3)	2.627(4)	144(4)
N3–H3···O9	0.90(1)	2.035(13)	2.929(4)	172(4)
N3–H3···O8	0.90(1)	2.52(4)	3.163(5)	129(4)
N3–H3···N10	0.90(1)	2.63(2)	3.480(4)	157(4)

Symmetry codes: #1: –½ + *x*, ½ – *y*, –½ + *z*; #2: 1 – *x*, 1 – *y*, 2 – *z*; #3: 2 – *x*, 1 – *y*, –*z*; #4: 2 – *x*, 1 – *y*, 2 – *z*; #5: 1 + *x*, *y*, *z*.

3. 4. Spectral Characterization

The weak and broad absorptions in the region 3430–3470 cm^{-1} are attributed to the O–H bonds of the phenol groups and water ligands. The intense bands at 1645 cm^{-1} are assigned to the vibration of the C=N groups.[9] Nitrato complexes show IR bands in the range 1410–1448 (ν_5), 1290–1317 (ν_1), and 1073–1077 cm^{-1} (ν_2) due to NO stretches.[10] The value of $\Delta(\nu_5 - \nu_1)$, i.e., 102–131 cm^{-1}, suggests monodentate coordination. The spectrum of complex **2** has ν_5 at 1312 cm^{-1} and ν_1 at 1433 cm^{-1}, and has the $\Delta(\nu_5 - \nu_1)$ value of 121 cm^{-1}. IR spectrum of complex **2** also shows a band at 1384 cm^{-1} due to ionic nitrate.[11]

In the UV-Vis spectra of the complexes, the bands at 370–375 nm are attributed to the azomethine chromophore π–π* transition. The bands at higher energy (290–300 nm) are associated with the benzene π–π* transition.[12]

3. 5. Catalytic Epoxidation Results

Epoxidation of styrene was carried out at room temperature with complexes **1** and **2** as the catalysts and PhIO and NaOCl as oxidants. The brown color of the solutions containing the catalysts and the substrate was intensified after the addition of oxidant indicating the formation of oxo-metallic intermediates of the catalysts. After completion of the oxidation reaction, the solution regains its initial color. The percentage of conversion of styrene, selectivity for styrene oxide, yield of styrene oxide and reaction time to obtain maximum yield using both the oxidants are given in Table 4. The data reveals that the complexes as catalysts convert styrene most efficiently in the presence of both oxidants. Nevertheless, the catalysts are selective towards the formation of styrene epoxides despite of the formation of by-products which have been identified by GC-MS as benzaldehyde, phenylacetaldehyde, styrene epoxides derivative, alcohols *etc.* From the data it is also clear that the complexes exhibit excellent efficiency for styrene epoxide yield. When the reactions are carried out with PhIO and NaOCl, most of the oxidation was occurred in the first one hour. When the reaction time was prolonged to two hours for complex **1** and three hours for complex **2**, the styrene conversions were about 89 and 77% for complex **1**, and 78 and 70% for complex **2**, respectively. It is evident that between PhIO and NaOCl, the former acts as a better oxidant with respect to both styrene conversion and styrene epoxide selectivity. The epoxide yields for the complexes **1** and **2** using PhIO and NaOCl as oxidants are 77 and 65%, and 73 and 57%, respectively. It is also obvious that complex **1** has better catalytic property than complex **2**. Nitrogeneous ligands are reported to lengthen and weaken the M–O bond in the oxidized form of the catalyst by donating electron density into the M–O antibonding orbital, which can account for the improved reactivity.[13]

Kochi *et al.* reported epoxide yields of 50–75% for the epoxidation of various types of olefins, including substituted styrenes, stilbenes, and cyclic and acyclic alkenes, within 15 min at room temperature in acetonitrile using PhIO as the oxidant and several Mn(III)–salen complexes as catalysts.[14] Hosseini-Monfared *et al.* reported the cyclohexene epoxide yield ranging from 43-68% in presence of PhIO as oxidant.[6] Lei and Yang reported the styrene oxide yields of 75 and 60%, respectively, with the oxidant PhIO and NaOCl.[15] Thus, manganese complexes with Schiff base and hydrazone ligands are a kind of excellent catalysts for the oxidation reactions.

4. Conclusion

A new bromido-coordinated mononuclear manganese(II) complex and a new nitrato-coordinated mononuclear manganese(II) complex derived from hydrazone ligands were prepared and characterized. Single crystal X-ray analysis indicates that the Mn atom in complex **1** is in octahedral coordination, and that in complex **2** is in pentagonal bipyramidal coordination. The complexes have effective catalytic property for the epoxidation of styrene.

Supplementary Data

Supplementary data are available from the Cambridge Crystallographic Data Center (CCDC 1857989 for **1** and 1857990 for **2**), 12 Union Road, Cambridge CB2 1EZ, UK (fax: +44-1223-336-033; e-mail: deposit@ccdc.cam.ac.uk; or *via* www.ccdc.cam.ac.uk/conts/retrieving.html) on request, quoting the deposition numbers: CCDC 1403969.

Acknowledgements

This project was supported by the Scientific and Technological Research Program of Chongqing Municipal Education Commission (Grant No. KJQN201801222), the Chunhui Project from Education Ministry of China (Grant No. Z2015140), and the Science and Technology Research

Table 4. Catalytic epoxidation results.

Time (hour)	Oxidant	Conversion (%)		Epoxide yield (%)		Selectivity (%)	
		1	**2**	**1**	**2**	**1**	**2**
2	PhIO	89	78	77	73	92	83
3	NaOCl	77	70	65	57	89	81

Program of Chongqing Education Commission (No. KJQN202001243).

5. References

1. (a) S. Dasgupta, S. Karim, S. Banerjee, M. Saha, K. D. Saha, *Dalton Trans.* **2020**, *49*, 1232–1240; **DOI:**10.1039/C9DT04636D
(b) N. Biswas, S. Bera, N. Sepay, T. K. Mukhopadhyay, K. Acharya, S. Ghosh, S. Acharyya, A. K. Biswas, M. G. B. Drew, *New J. Chem.* **2019**, *43*, 16714–16729; **DOI:**10.1039/C9NJ04171K
(c) A. A. Khandar, Z. M. Azar, M. Eskandani, C. B. Hubschle, S. Van Smaalen, B. Shaabani, Y. Omidi, *Polyhedron* **2019**, *171*, 237–248; **DOI:**10.1016/j.poly.2019.06.026
(d) D. Kuriakose, M. R. P. Kurup, *Polyhedron* **2019**, *170*, 749-761; **DOI:**10.1016/j.poly.2019.06.041
(e) M. Mehmood, Imtiaz-ud-Din, M. N. Tahir, B. Ihsan-Ul Haq, S. S. Zahra, *Inorg. Chim. Acta* **2019**, *486*, 387–394. **DOI:**10.1016/j.ica.2018.10.009
2. (a) X.-W. Zhu, *Acta Chim. Slov.* **2018**, *65*, 939–945; **DOI:**10.17344/acsi.2018.4607
(b) M. Liang, N. Sun, D.-H. Zou, *Acta Chim. Slov.* **2018**, *65*, 964–969; **DOI:**10.17344/acsi.2018.4625
(c) Z. You, H. Yu, Z. Li, W. Zhai, Y. Jiang, A. Li, S. Guo, K. Li, C. Lv, C. Zhang, *Inorg. Chim. Acta* **2018**, *480*, 120–126; **DOI:**10.1016/j.ica.2018.05.020
(d) Z. You, H. Yu, B. Zheng, C. Zhang, C. Lv, K. Li, L. Pan, *Inorg. Chim. Acta* **2018**, *469*, 44–50; **DOI:**10.1016/j.ica.2017.09.011
(e) D. Sadhukhan, M. Maiti, E. Zangrando, S. Pathan, S. Mitra, A. Patel, *Polyhedron* **2014**, *69*, 1–9; **DOI:**10.1016/j.poly.2013.11.007
(f) Y. Tan, *Acta Chim. Slov.* **2019**, *66*, 1002–1009. **DOI:**10.17344/acsi.2019.5297
3. (a) B. Shaabani, A. A. Khandar, H. Mobaiyen, N. Ramazani, S. S. Balula, L. Cunha-Silva, *Polyhedron* **2014**, *80*, 166–172; **DOI:**10.1016/j.poly.2014.03.033
(b) E. M. M. Ramadan, I. M. El-Mehasseb, *Transition Met. Chem.* **1998**, *23*, 183–189; **DOI:**10.1023/A:1006959513023
(c) M. Bagherzadeh, M. Amini, H. Parastar, M. Jalali-Heravi, A. Ellern, L. K. Woo, *Inorg. Chem. Commun.* **2012**, *20*, 86–89; **DOI:**10.1016/j.inoche.2012.02.023
(d) Z. Ma, M. Sutradhar, A. V. Gurbanov, A. M. Maharramov, R. A. Aliyeva, F. S. Aliyeva, F. N. Bahmanova, V. I. Mardanova, F. M. Chyragov, *Polyhedron* **2015**, *101*, 14–22; **DOI:**10.1016/j.poly.2015.07.054
(e) S. Yousef Ebrahimipour, M. Abaszadeh, J. Castro, M. Seifi, *Polyhedron* **2014**, *79*, 138–150. **DOI:**10.1016/j.poly.2014.04.069
4. (a) O. Pouralimardan, A. C. Chamayou, C. Janiak, H. Hosseini-Monfared, *Inorg. Chim. Acta*, **2007**, *360*, 1599–1608; **DOI:**10.1016/j.ica.2006.08.056
(b) R. Bikas, M. Ghorbanloo, R. Sasani, I. Pantenburg, G. Meyer, *J. Coord. Chem.*, **2017**, *70*, 819–830; **DOI:**10.1080/00958972.2017.1281918
(c) M. S. Shongwe, K. S. Al-Barhi, M. Mikuriya, H. Adams, M. J. Morris, *Chem. Eur. J.* **2014**, *20*, 9693–9701. **DOI:**10.1002/chem.201402634
5. G. M. Sheldrick, *Acta Crystallogr.* **2015**, *C71*, 3–8.
6. O. Pouralimardan, A.-C. Chamayou, C. Janiak, H. Hosseini-Monfared, *Inorg. Chim. Acta* **2007**, *360*, 1599–1608. **DOI:**10.1016/j.ica.2006.08.056
7. W. J. Geary, *Coord. Chem. Rev.* **1971**, *7*, 81–122. **DOI:**10.1016/S0010-8545(00)80009-0
8. (a) C. Bourchameni, C. Beghidja, A. Beghidja, P. Rabu, R. Welter, *Polyhedron* **2011**, *30*, 1774–1778; **DOI:**10.1016/j.poly.2011.04.007
(b) B. F. Ali, Z. Judeh, K. Ayub, *Polyhedron* **2015**, *101*, 118–125. **DOI:**10.1016/j.poly.2015.07.036
9. N. Zhang, C.-Y. Huang, D.-H. Shi, Z.-L. You, *Inorg. Chem. Commun.* **2011**, *14*, 1636–1639. **DOI:**10.1016/j.inoche.2011.06.027
10. S. Chandra, A. K. Sharma, *J. Coord. Chem.* **2009**, *62*, 3688–3700. **DOI:**10.1080/00958970903121305
11. S. Chandra, A. K. Sharma, *Spectrochim. Acta A* **2009**, *72*, 851–857. **DOI:**10.1016/j.saa.2008.12.022
12. Y.-M. Zhou, X.-R. Ye, F.-B. Xin, X.-Q. Xin, *Transition Met. Chem.* **1999**, *24*, 118–120. **DOI:**10.1023/A:1006989707001
13. (a) A. Gold, K. Jayaraj, P. Doppelt, R. Weiss, G. Chottard, E. Bill, X. Ding, A. X. Trautwein, *J. Am. Chem. Soc.* **1988**, *110*, 5756–5761; **DOI:**10.1021/ja00225a028
(b) M. J. Gunter, P. Turner, *J. Mol. Catal. A* **1991**, *66*, 121–127. **DOI:**10.1016/0304-5102(91)85027-Y
14. K. Srinivas, P. Michand, J. K. Kochi, *J. Am. Chem. Soc.* **1986**, *108*, 2309–2320. **DOI:**10.1021/ja00269a029
15. Y. Lei, Q. W. Yang, *Inorg. Nano-Met. Chem.* **2017**, *47*, 446–449. **DOI:**10.1080/15533174.2016.1186070

Povzetek

Sintetizirali smo nov enojedrni manganov(II) bromido kompleks $[MnL^1Br_2(OH_2)]$ (**1**), in nov enojedrni manganov(II) nitrato kompleks $[Mn(L^2)_2(ONO_2)(OH_2)]NO_3$ (**2**) z hidrazonskim ligandom 4-hidroksi-*N*'-(piridin-2-ilmetilen)benzohidrazidom (HL^1) in *N*'-(piridin-2-ilmetilen)izonikotinohidrazidom (HL^2) ter ju okarakterizirali s fiziko-kemijskimi metodami in rentgensko monokristalno difrakcijo. Strukturna analiza razkriva, da ima Mn atom v kompleksu **1** oktaedrično koordinacijo, v kompleksu **2** pa pentagonalno bipiramidalno koordinacijo. Določili smo katalitične lastnosti obeh kompleksov za epoksidacijo stirena.

Except when otherwise noted, articles in this journal are published under the terms and conditions of the Creative Commons Attribution 4.0 International License

Scientific paper

Ammoniacal Carbonate Leaching: Effect of Dissolved Sulfur in the Distillation Operation

Armando Rojas Vargas,[1,2,*] María Elena Trujillo Nieves[3] and Yudith González Diaz[4,*]

[1] *Empresa de Servicios Técnicos de Computación, Comunicaciones y Electrónica "Rafael Fausto Orejón Forment", Holguín, Cuba.*

[2] *Universidad de Holguín "Oscar Lucero Moya", Holguín, Cuba.*

[3] *Centro de Investigaciones del Níquel "Alberto Fernández Monte de Oca", Holguín, Cuba.*

[4] *Universidad de Oriente, Faculty of Chemical Engineering, Santiago de Cuba, Cuba*

** Corresponding author: E-mail: arojas@eros.moa.minem.cu)*
Tel: +53-24-51-6695

Received: 07-03-2020

Abstract

The distillation process in the Ammoniacal Carbonate Leaching technology was studied at bench-scale and on industrial scale. The dissolved sulfur effect in the *Product-liquor* that feeds to the columns, on the *Basic Nickel Carbonate* (BNC) properties and the operation expenses was determined. When increasing the sulfur in the *liquor*, we augment the selectivity towards the sulfate formation in the BNC molecule; therefore the energy consumption to the BNC thermal decomposition in the calcination process increases. Also, the nickel dissolved in the columns effluent increases due to complex reaction with $[SO_4^{2-}]$ and $[S_2O_3^{2-}]$ ions, thus the expenses for consumption precipitation reagent increase too. Feeding carbonated *liquor* in the range $1.60 \leq NH_3/CO_2 < 1.80$ and CO_2-rich solution increases the CO_2 in the BNC with decreasing in sulfate; then, the mean diameter particle increases, the filtration resistance and the cake moisture diminish, which augments the productivity and reduces the energy consumption in the process of filtration and calcination. Keeping a pH between 8.4 and 8.7 in the columns outlet the greatest economic benefit is obtained of 0,125 ($\$ \cdot h^{-1}$) per ($m^3 \cdot h^{-1}$) of *Product-liquor*.

Keywords: Basic Nickel Carbonate; steam-stripped columns; sulfur, leaching

1. Introduction

The ammoniacal carbonate leaching technology for the selective extraction of nickel and cobalt from lateritic ores began operations in the mid 1940´s in Cuba, in the Nicaro nickel plant. The process was originally described by M. H. Caron in 1924 and combines both hydro- and pyrometallurgy processes, it consists of the following main stages (see Fig. 1):

The lateritic ore is crushed and dried to reduce moisture from approximately 35% to 5% with combustion gases in a rotary dryer. The dried laterites are ground to size of 83% or more of the –0.074 mm class, before being reduction-roasting, into Herreshoff multiple-hearth furnaces. The additive fuel oil is fed in the mineral weighing system to enable high temperature inside the furnace through its partial combustion and provide the reducing agent for the reduction process, Eqs. (1), (2).

$$2(Ni,Co)O_{(s)} + (CO + II_2)_{(g)} \rightarrow 2Ni_{(s)} + 2Co_{(s)} + CO_{2(g)} + II_2O_{(g)} \quad (1)$$

$$2Fe_2O_{3(s)} + 3(CO + H_2)_{(g)} \rightarrow 4Fe_{(s)} + 3CO_{2(g)} + 3H_2O_{(g)} \quad (2)$$

The reduced ore cooled under neutral atmosphere below 250 °C is subsequently mixed with ammonia carbonate solution, and the resulting slurry is leached in aerated tanks, flow model perfect mixed. In this process, the nickel is selectively leached from the roast product, as described the following simplified reaction, Eq. (3): [1]

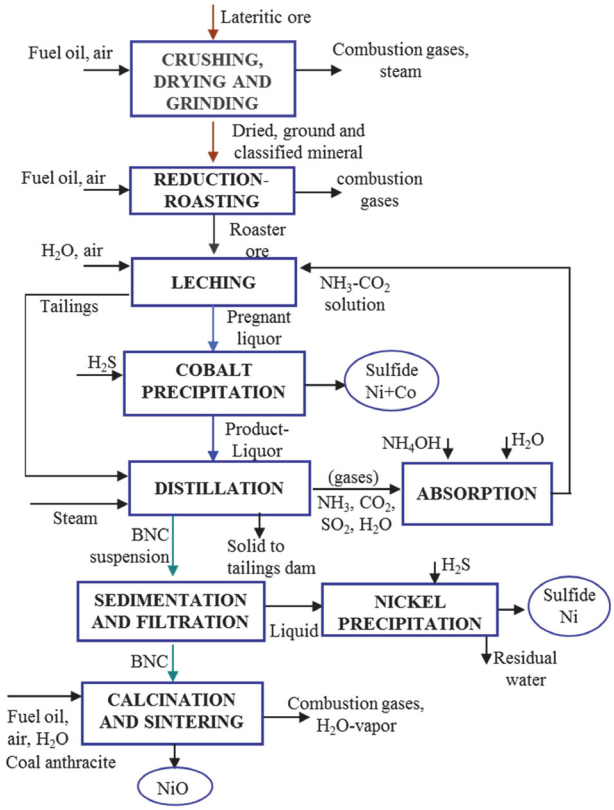


Figure 1. Process flowsheet of the nickel and cobalt producer plant in Nicaro

$$Ni_{(s)} + \tfrac{1}{2}O_{2(g)} + 4NH_{3(ac)} + (NH_4)_2CO_{3(ac)} \rightarrow \rightarrow Ni(NH_3)_6^{2+} + CO_3^{2-} + H_2O \quad (3)$$

Iron, cobalt and sulfur also are dissolved in leaching process. The Fe metal complex is unstable and precipitates as iron hydroxide. The sulfur remainder in the roast product, coming from the fuel oil, is oxidized to thiosulfate [$S_2O_3^{2-}$], polythionates ($S_nO_m^{2-}$, 2 < n < 6), sulfite [SO_3^{2-}], sulfate [SO_4^{2-}] y sulphamate [$SO_3NH_2^-$], Eq. (4).

$$S^{2-} \rightarrow S^0 \rightarrow S_2O_3^{2-} \leftrightarrow S_4O_6^{2-} \rightarrow \rightarrow S_3O_6^{2-} \rightarrow SO_3^{2-} \rightarrow SO_4^{2-} + SO_3NH^- \quad (4)$$

The pregnant liquor is then separated from the undissolved solid in settler tank and later Cobalt is removed from the liquor by chemistry precipitation in a tubular reactor. Then, the *Product-liquor* is fed in the steam-stripped columns, descends by gravity and it is brought into direct contact and counter flow with the superheated steam in multiple bubble cap trays. The volatiles compounds NH_3, CO_2 and SO_2 evaporate, ascend and are separated by the top of the column; in turn, the *Basic Nickel Carbonate* (BNC) precipitates and it is obtained by the bottom in a suspension of concentration between 2,5% and 4,0% by weight, temperature of 80 °C to 90 °C and dissolved chemical species in the proportions 1.5 < NH_3/CO_2 < 2.0; 1.8 < Ni/S < 3.2; 10.4 < CO_2/S < 13.8 and pH of 7.4 to 9.0, Eqs. (5), (6).[2]

$$5Ni(NH_3)_6^{2+} + 5CO_3^{2-} + 7H_2O \rightarrow \rightarrow 2NiCO_3 \cdot 3Ni(OH)_2 \cdot 4H_2O_{(s)} + 3CO_{2(g)} + 30NH_{3(g)} \quad (5)$$

$$6Ni(NH_3)_6^{2+} + 5CO_3^{2-} + SO_4^{2-} + 3H_2O \rightarrow \rightarrow 2NiCO_3 \cdot 3Ni(OH)_2 \cdot NiSO_{4(s)} + 3CO_{2(g)} + 36NH_{3(g)} \quad (6)$$

The BNC is separated from the liquid in a settler tank and afterward, by filtering process. Nickel dissolved remainder in the liquid is precipitated in a tubular reactor by chemistry reaction with H_2S, but NH_3 constitutes a loss affecting the operating expenses.

The BNC is subsequently processed in a rotary kiln operated under slightly reducing atmosphere conditions, and it is calcined at maximum temperatures between 1000 and 1200 °C, Eq. (7).

$$2Ni(OH)_2 \cdot 3NiCO_3 \cdot NiSO_4 \rightarrow \rightarrow 6NiO_{(s)} + 3CO_{2(g)} + SO_{2(g)} + 2H_2O_{(g)} + \tfrac{1}{2}O_{2(g)} \quad (7)$$

Calcination process consists in four stages of BNC decomposition to NiO. The first stage is the removal of physically entrained water, which represents between the 45% and 55% of heat supplied to the kiln,[3,4] on the other hand, the last stage belong to sulfate decomposition and require activation energy higher than the rest of the stages, of 324.4 (+/–23.8) kJ · mol^{-1},[5] researchers suggested that high reduction temperature of 900 °C substantially diminishes the sulfur content,[6] so the BNC must have the minimum humidity before being fed to the process and the lower sulfur concentration to reduce the energy consumption. Besides, during BNC decomposition, the surface segregation of sulfur, among other phenomena that occur simultaneously such as recrystallization and agglomeration, contribute to the change the chemical-physical properties of the particles, affecting the NiO final microstructure.[7]

Finally, the mixture of NiO and anthracite coal is fed to the sintering process and a product with 93% Ni, 0.060% S and size 40% (+2 mm) is obtained.

This work focuses on the process of *Product-liquor* distillation and obtaining the *Basic Nickel Carbonate*. Several studies have been carried out with the purpose of reducing the concentration of nickel and ammonia in the liquid effluents of the distillation columns, also to improve the chemical-physical properties of BNC, as well as to diminish the operating expenses.

A complementary operating norm was proposed to control the thermal profile of the columns, which consists of measuring the pH of the BNC suspension at the bottom outlet of the columns and adopting the necessary corrective actions. The study was carried out on a bench-scale and industrial-scale, at the nickel producing plants in Nicaro and Punta-Gorda, Cuba. The recommended pH range

was between 8.3 and 8.7, it was obtained by optimizing the convenience function at a minimum expense due to ammonia losses and consumption of dissolved nickel precipitation reagent. If pH > 8.7, the *Product-liquor* distillation is characterized by low thermal profile, the concentration of dissolved NH_3 and Ni is high, therefore the operation expenses increases in relation to the recommended range (sub-distillation conditions). If pH < 8.3, so the thermal profile is high, the nickel is leached from BNC increasing the Ni cation in solution, thus the operation expenses increases although the NH_3 concentration continuous lowering (over-distillation conditions). The convenience function was based on the second-order polynomial function between Ni vs. pH, and the potential function between NH_3 vs. pH.[2,8,9]

Based on the principles of simultaneous equilibrium and mass balance, a series of thermodynamic equations of Ni(II)-NH_3-CO_3-H_2O systems at 25 °C were deduced and thermodynamic diagrams of log[Ni] versus pH at different solution compositions were drawn, to explain the mechanism of precipitation particles with different microscopic shapes. When de pH is above 7.0, the precipitation proceeds slowly and leads to the formation of dense spherical particles. Between pH 6 to 8, the nickel concentration in the solution goes down with pH to a minimum point, then goes up to a maximum point following a parabolic function, when concentration of $[CO_3^{2-}]$ increases, more nickel ions precipitate as the solid particle which leads to decrease of nickel in the solution. $[Ni^{2+}]$ cation gradually increase with increasing $[NH_3]$ by the formation of nickel ammine-complexes, $Ni(NH_3)_n^{2+}$, (n = 1–6). The higher the concentration of ammonia is, the higher $[Ni^{2+}]$ in the solution are.[10] For the system Ni(II)-NH_3-CO_2-SO_2-H_2O these diagrams were drawn simulating the concentration of the ionic species at the bottom outlet of the columns, $[Ni^{2+}]$ cation increase with increasing $[SO_4^{2-}]$ and $[S_2O_3^{2-}]$ ions concentration because of complex reactions. As the sulfur concentration increases, the minimum point of nickel concentration shift towards a more alkaline pH.[2] Ni's dependence on pH in both studies was similar to the results obtained experimentally in the distillation columns for 6.0 ≤ pH ≤ 8.0.

From experimental measurements in the distillation process at the nickel producing plants in Nicaro and Punta-Gorda, a statistical model was obtained by Multiple Linear Regression, for the nickel dissolved estimate, in function of the concentration of [S], $[NH_3]$ and $[CO_2]$ in the *Product-liquor* that feeds the distillation columns and the pH in the BNC suspension. The evaluation of the model indicated that when operating with a high Ni/S ratio (Ni/S ≥ 1.8) and a correct carbonation ($1.60 \leq NH_3/CO_2 \leq 1.75$), in the suspension of BNC at the column outlet, a lower concentration of dissolved nickel is obtained and therefore the consumption of reagents for the chemical precipitation diminish resulting in lower expenses.[2] This was explained because it increases the selectivity towards the carbonate formation in the BNC molecule, while decreases the sulfate formation; however, no experimental results have been presented that show these changes in the chemical composition of BNC.

The effect of carbon dioxide dissolved in the *Product-liqueur* over the BNC characteristic was represented in pseudo-equilibrium diagram, log[NH_3] versus log[CO_3^{2-}], for the Ni-NH_3-CO_3^{2-}-H_2O system at 100 °C, Eh 0.5V, Ni 0.001M, pH 6.75. This diagram indicated that the CO_2 concentration should be controlled in the *liquor*, to avoid the nickel hydroxide precipitation. The formation of hydroxylated products is undesirable, since their drying and dissolution properties are lower than that of *Basic Nickel Carbonate*.[11] For the Ni(II)-NH_3-SO_4-H_2O systems, the speciation of nickel in ammonia solution has been examined by distribution-pH diagrams, 1M $(NH_4)_2SO_4$ solution, 0.01M Ni^{2+}. In the region between pH 1.5 and pH 8 the predominant nickel species is a soluble, negatively charged sulfate complex $[Ni(SO_4)_2^{2-}]$, in the region from pH 8 to pH 12, there is a series of nickel ammine-complexes with successively increasing number of incorporated ammonia ligands, $Ni(NH_3)_n^{2+}$, (n = 1–6). In 0.05M Ni^{2+} solution, nickel hydroxyl-sulfate precipitates in the region around pH 8,[12] which suggests that at pH<8.3 (according to the operating norm by pH), the nickel leaching from BNC may be particularly associated with the presence of sulfate in the BNC molecule, what is accentuated to conditions of low carbonation of the *Product-liqueur*. It should be highlighted that in more diluted aqueous solution of nickel(II) sulfate, 10^{-3}M, the ions $[Ni_2(SO_4)(H_2O)_n]^{2+}$ and $[Ni_m(SO_4)_{m-1}(H_2O)_n]^{2+}$ (m≈6, n≈12) have been identified, also, at $5 \cdot 10^{-4}$M, triple ion $[Ni(SO_4)_2]^{2-}$, nickel cluster $[Ni_2(SO_4)_3]^{2-}$, $[Ni_5(SO_4)_6]^{2-}$ and higher-mass ions $[Ni_3(SO_4)_2(H_2O)_n]^{2+}$ ($0 \leq n \leq 2$).[13]

Few investigations on *Basic Nickel Carbonate* have considered the presence of sulfur in the molecule. Structures such as: $2NiCO_3 \cdot 3Ni(OH)_2 \cdot 4H_2O$, $NiCO_3 \cdot 2Ni(OH)_2 \cdot 4H_2O$ and $NiCO_3 \cdot Ni(OH)_2 \cdot 2H_2O$ are reported, the particles are spherical and ellipsoidal in shape, ranging from 0.4 to 23 μm in diameter. The BNC dried at 105 °C contained approximately 52% wt Ni, 12.9% wt CO_2 and 0.001% wt S.[7] On the other hand, considering sulfur, the general structure $(NiCO_3)_x \cdot (Ni(OH)_2)_y \cdot (NiSO_4)_z \cdot nH_2O$ is presented.[5] The BNC dried at 60 °C contained 45.6–50.0% wt Ni, 1.9–4.9% wt CO_2, 1.8–3,1% wt S, real density 2.8–3.2 $mg \cdot L^{-1}$ and 12–22 μm in mean diameter of microparticles.[3,14]

Colloidal processing supplies great possibilities to obtain smart materials by means of manipulation of molecular structures and control of inter-particle forces.[15] A colloid is a chemical system, in which one substance is microscopically dispersed evenly throughout another medium substance of a continuous phase. The behavior of colloidal particles in aqueous medium is a consequence of interaction between particles surface and liquid medium. Colloidal particle size distribution, between 10^{-3} μm and 1

μm, shape, surface area, density, as well as chemical composition is related to the stabilization of the colloidal system. The properties of starting material have substantial influence on rheological properties; filtration, drying, sintering process; and in the final microstructure.[7,14]

The particle behaviour in suspension and its stability can be understood using electric double layer model (EDL) or DLVO theory (Derjaguin, Landau, Verwey and, Overbeek), as well as the concepts surface potential, isoelectric point and zeta potential.[15,16] Stability refers to the condition in which the colloidal particles do not aggregate at a significant rate. Aqueous suspension stabilization can be controlled by the mechanisms electrostatic, steric, electrosteric and nanoparticle haloing stabilization, by the following methods: adjusting either ionic strength or pH of the electrolyte solution; adding a component like a surfactant or polymer that adsorbs on the colloidal particles and changes their surface properties; a polyelectrolyte that impart electrostatic and steric stabilization to a given colloidal dispersion; or highly charged nanoparticles by forming a nonadsorbing nanoparticle layer around neutral colloidal particle, which presents as an effective surface charge and produces an electrostatic repulsion that mitigates the inherent van der Waals attraction between them.[17,18] A method for purifying *Basic Nickel Carbonate* of Na^+, Cl^- ions and other impurities on its surface was clarified by the electric double layer model and it was proposed a washing-drying-rewashing-drying process,[19] but other studies have not been performed about colloidal processing or sulfur removal of Ni(II)-NH_3-CO_2-SO_2-H_2O system.

The purpose of this work was to determine the dissolved-sulfur concentration effect in the *Product-liquor,* on the BNC properties, the expenses in the distillation process and determine the pH range for the greatest economic benefit.

2. Materials and Methods

The evaluation was carried out on a bench-scale and industrial-scale.

A steam-stripped mini-column was used with 200 mm diameter, 1320 mm height, 2 separating trays at the top, 8 bubble cap trays, 1 cup/trays of 106 mm diameter and 1 sampler/ trays, which allowed performing the concentration profile of dissolved chemical species in six inner positions along the column, (Fig. 1).

On the other hand, the industrial-scale steam-stripped columns, at the Nicaro nickel plant, have 3.4 m in diameter, 18.0 m height, 18 bubble cap trays, 24 cups/trays, operating pressure at the bottom of 127.5 MPa and samplers in the fifth tray.[20]

The samples were taken in the *Product-liquor*, in the BNC suspension at the columns outlet, and in the corresponding samplers along the columns. Also, a CO_2-reach

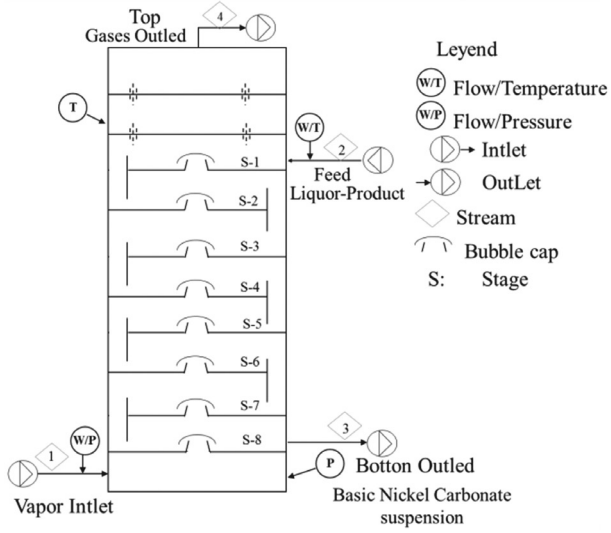


Figure 2. Steam-stripped mini-column

solution was used, which is produced in the gases absorption systems of the industrial process, with NH_3 130–140 g · L^{-1} and CO_2 90–100 g · L^{-1}.

The BNC suspension samples were processed as follows: the aliquot needed to determine the suspension pH and the dissolved compounds concentration (g · L^{-1}) [NH_3], [CO_2], [Ni], [S], [SO_4^{2-}], [$S_2O_3^{2-}$] was taken; the rest was filtered in a Büchner funnel connected to a side-arm flask and a vacuum pump, the BNC was dried at 60 °C and it was characterized according the concentration (%) of [Ni], [Co], [MgO], [CO_2], [S]. The real and apparent BNC density was determined.

The chemical analyzes were performed applying volumetric, gravimetric, potentiometric and Atomic Absorption Spectrophotometry (AAS) methods. All the pH measurements were made at 25 °C, using a pH meter PHILIPS PW-9420115-230 V, 50–60 Hz, precision 0,001pH/ °C; and for determining the size distribution, the Laser-Particle-Sizer Analysette 22.

Experimental runs were performed in three stages:

Stage 01. Bench-scale. A full-factorial design, two-level, 2^k experimental runs, *k*-factors with one center point, was carried out at the mini-column, with the aim of determining the effect of the independent variables and their domain, on the concentration of dissolved nickel and the BNC properties, also, the interaction Ni(II) and NH_3 versus pH. The independent variables (factors) were: temperature at the top: 80, 85 and 90 °C, and *liquor* flow: 12, 16 and 20 L · h^{-1}, 15 experiments in total, each lasting 10 hours. Once the operation stabilized, the samples were taken in 100 mL plastic bottles. The *Liquor Product* chemical composition remained fixed, it had a Ni/S ratio 2.66; Ni/[SO_4^{2-}] 5.08, Ni/[$S_2O_3^{2-}$] 3.11 and NH_3/CO_2 1.73.

Stage 02. Bench-scale. In the mini-column, 6 experiments in total were carried out with and without feeding CO_2-rich solution by a side trays of the column, at a flow of 2 L · h^{-1}, with the purpose of conducting an exploratory

study and determining the effect on the concentration of nickel dissolved and the BNC properties. The temperature at the top was 90 °C and the *Product-liquor* flow of 20 L · h^{-1}, at the minimum nickel concentration in solution obtained in step 01. The *Product-liquor* chemical composition had a Ni/S ratio 3.32, Ni/[SO_4^{2-}] 6.82, Ni/[$S_2O_3^{2-}$] 4.25 and NH_3/CO_2 1.78. The specific cake resistance and the medium resistance of filtration was determined, to a temperature of 80 °C, 16% in weight of solids and constant pressure drop of 37581.75 N/m^2, applying the Kraft paper as membrane.[14]

Stage 03. Industrial-scale. The experimental runs were carried out at Nicaro nickel plant, in order to validate the results previously obtained in the mini-column, at different ionic composition of the *Product-liquor*. The variables *Liquor* flow (Qa) 56.4 $m^3 \cdot h^{-1}$ (±4.5), temperature at the column top (Tp) 83.0 °C (± 1.4), and quotient between *Liquor* flow and steam flow (Qa/Wv) 5.7 $m^3 \cdot kg^{-1}$ (± 1.2) were fixed. The sampling was carried out in several periods or campaigns to guarantee the representativeness in the ionic composition of the *Liquors* processed in the columns, every 4 hours in 100 mL plastic bottles. The *Product-liquor* chemical composition was: 1.0 ≤ Ni/S ≤ 2.8, 1.8 ≤ Ni/[SO_4^{2-}] ≤ 4.0, 1.2 ≤ Ni/[$S_2O_3^{2-}$] ≤ 3.0, 1.60 ≤ NH_3/CO_2 ≤ 1.94.

The operating variables: flow, temperature and pressure were monitored in real-time using Supervisory Control and Data Acquisition EROS (SCADA EROS) and the values were taken from the data historian.

The chemical analysis database was organized into dataset (j = 1 to 10) according to the Ni/S and NH_3/CO_2 ratio in the *Product-liquor*, maintaining a standard deviation approximately equal to 0.5 g · L^{-1}. Only in this way was it possible to obtain the interactions of [Ni] and [NH_3] versus pH, due to the concentration variation and diversity of chemical species in solution.[2,9]

The relative frequency distribution (f_j) in which each dataset (j) appears was calculated from the number of samples that compose it, thus, f_j represents the fraction of data values that fall in a dataset. In addition, frequency histograms ware constructed in each dataset, for the pH values in the BNC suspension in the columns outlet stream, interval class width 0.1 (classes: pH < 7.7; 7.7 ≤ pH < 7.8; ...; 8.8 ≤ pH < 8.9; pH > 8.9), the number of class intervals (i) of greatest interest was i =13 (7.7 ≤ pH ≤ 8.9) and the relative frequency distribution for pH (f_i).

Then, for each dataset, the nickel concentration was fitted to polynomial function, and the ammonia to potential function. The best fitting was appreciated by the high coefficient of determination (R^2), Eqs. (8), (9). [2,8,9]

$$[Ni] = c_1 + c_2 \cdot pH + c_3 \cdot pH^2 \quad (8)$$

$$[NH_3] = c_4 \cdot pH^{c_5} \quad (9)$$

To perform the economic valuation, Eq. (10) to (13) were applied.

$$Q_l = Q_a \cdot \left(1 + \frac{15}{100}\right) \cdot \left(1 - \frac{\rho_p - \rho_l}{\rho_s - \rho_l}\right) \quad (10)$$

$$G_i = Q_l \cdot \left\{[NH_3]_i \cdot P_1 + [Ni]_i \cdot d \cdot P_2\right\} \quad (11)$$

$$G = \sum_{j=1}^{10} f_j \cdot G_j = \sum_{j=1}^{10} f_j \cdot \sum_{i=1}^{13} f_i \cdot G_i \quad (12)$$

$$A = \sum_{j=1}^{10} f_j \cdot \left(G_j - \overline{G}_i\right) \quad (13)$$

The liquor flow in the columns effluent, Q_l ($m^3 \cdot h^{-1}$), was determined in function of the density, ρ (kg/m^3), corresponding to the solid (s), the liquid (l) and the suspension (p), taking a flow of *Product-liquor* (Qa) of 1 m^3/h (base) and a 15% of volume increase due to steam condensation, according to design data of the industrial installation, Eq. (10).

The operation expenses, G_i ($ · h^{-1}) per ($m^3 \cdot h^{-1}$), for each class interval (i) of pH considered in the frequency histograms were calculated. The prognostic models of [NH_3] and [Ni] concentration (g · L^{-1}) as a pH function were used, in the interval 7.7 ≤ pH_i ≤ 8.9 (pH_1 = 7.7; pH_2 = 7,8, …, pH_{13} = 8,9). The ammonia price (P_1) of 0,350 $·$kg^{-1}$ and of nickel precipitation reagent (P_2) 0,740 $ · kg^{-1} was considered, as well as the reagent consumption dose (d) 1.33 kg · kg^{-1} of precipitated nickel, Eq. (11).

The operation global expense, G ($ · h^{-1}) per ($m^3 \cdot h^{-1}$) was calculated taking into consideration relative frequency distribution (f_j) and (f_i), Eq. (12).

The economic benefit, A ($ · h^{-1}) per ($m^3 \cdot h^{-1}$), expresses numerically the amount of money that can be saved as the result of operating the distillation columns maintaining in the BNC suspension, in the outlet stream, certain pH range, that minimizes the expenses due to losses of dissolved ammonia and the consumption of reagent to precipitate the remainder nickel.

To determine the economic benefit, certain pH range was set, and the average expense ($\overline{G}_i$) was calculated. The interval width of pH was 0.4 (classes: 7.7 ≤ pHi ≤ 8.0; 7.8 ≤ pHi ≤ 8.1; …; 8.6 ≤ pHi ≤ 8.9) and the number of class intervals equal to 13. Then, the economic benefit (A) for any range of pH was determined as the difference between the operating expenses in a dataset (G_j) with the average expenses ($\overline{G}_i$) of the fixed pH range, considering relative frequency distribution (f_j) to make the summation. From this calculation, the pH range to operate at the greatest economic benefit was determined, Eq. (13).

3. Results and Discussion

3. 1. pH Interaction with Dissolved Nickel and Ammonia

The nickel and ammonia profile (g · L^{-1}) as a pH function at 25 °C in the in the steam-stripped mini-column are shown in Figure 3.

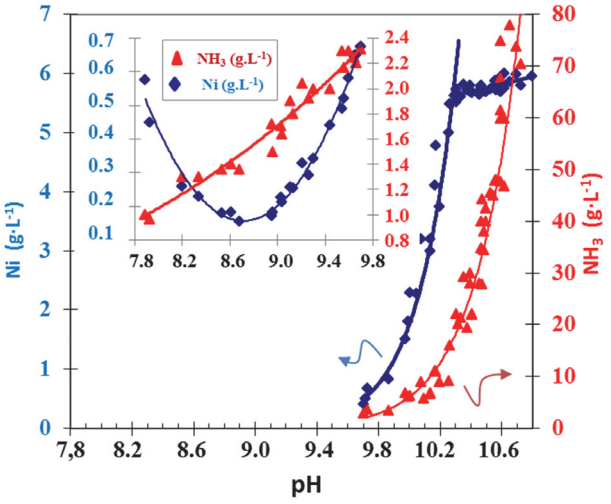


Figure 3. Profile of nickel and ammonia dissolved versus pH at 25 °C in the mini-column (Stage 01). Ni/S = 2.66, Ni/$[SO_4^{2-}]$ = 5.08, Ni/$[S_2O_3^{2-}]$ = 3.11, NH_3/CO_2 = 1.73

The relationship between nickel and ammonia with pH, in the trays along the mini-column, for the different levels of the factors temperature at the top and *liquor* flow was obtained. The alkalinity of the suspension decreased in the range of 9.7 ≤ pH ≤ 10.7 with the fall of ammonia concentration from 80 g · L^{-1} up to 3 g · L^{-1}, following a potential function, Eq. (14).

$$[NH_3] = 2.1941 \cdot 10^{-36} \cdot pH^{36.55} \qquad R^2 = 0.9643 \tag{14}$$

With regard to nickel cation, a slight descent of the concentration was appreciated due to the BNC precipitation, until reaching pH 10,3 and $[NH_3]$ 20 g · L^{-1}; starting from this point, Ni(II) cation precipitated according to a potential function, Eq. (15).

$$[Ni] = 3.32 \cdot 10^{-42} \cdot pH^{41.73} \qquad R^2 = 0.9696 \tag{15}$$

In this Figure 3, a view of the interaction between nickel and ammonia versus pH to pH<9.7 is included, corresponding to low concentrations in the inferior trays of the mini-column. Nickel in solution decreased with pH to a minimum point, and then increased to a maximum point in the BNC suspension, following parabolic function (over-distillation), Eq. (16).

$$[Ni] = 0.5384 \cdot pH^2 - 9.3621 \cdot pH + 40.93 \qquad R^2 = 0.9696 \tag{16}$$

On the other hand, form pH 9.7 to pH 7.8, the ammonia concentration diminished reaching concentrations as low as 1.0 g · L^{-1} following a potential function; but this could result in a leaching of nickel from the BNC molecule and an increase in the Ni cation in solution, Eq. (17).

$$[NH_3] = 2.05 \cdot 10^{-4} \cdot pH^{4.1082} \qquad R^2 = 0.9610 \tag{17}$$

The interactions (Ni vs. pH, NH_3 vs. pH) were valid although CO_2-rich solution was fed to the mini-column, as it is shown in the Figure 4. At pH equal to 10.33, the precipitation of the BNC began, with a linear decrease of nickel concentration and slope m_1 = 2.8 (with CO_2-rich solution) and m_2 = 2.3 (without dissolution) until reaching pH 10.1 and $[NH_3]$ 15.8 g · L^{-1}. From that pH, $[Ni^{2+}]$ cation precipitated intensely according to a potential function and exponents k_1 = 39.3 and k_2 = 36.7 with fit quality, R^2, 95% and 97% respectively.

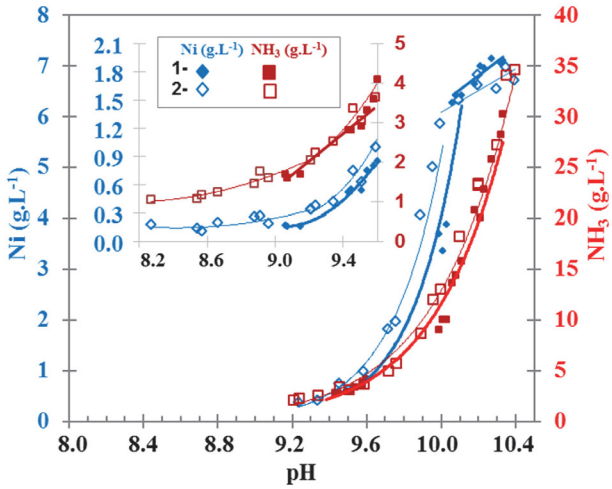


Figure 4. Profile of nickel and ammonia dissolved versus pH at 25 °C in the mini-column (Stage 02). *Product-liquor* distillation with$^{(1-)}$ and without$^{(2-)}$ CO_2-reach solution. Ni/S 3.32, Ni/$[SO_4^{2-}]$ 6.82, Ni/$[S_2O_3^{2-}]$ 4.25, NH_3/CO_2 1.78

From figure 4, at pH<9.6, corresponding to the lower trays, the concentration of both compounds decreased. For the same pH value, the dissolved nickel had a tendency to be slightly lower with the feeding of CO_2-rich solution, than when this solution was not supplied (k_1>k_2); and the ammonia concentration was similar in both experiments, keeping 90 °C in the top of the mini-column.

On the other hand, on an industrial-scale, according to the Ni/S and NH_3/CO_2 ratio in the *Product-liquor*, ten dataset were conformed, and similar interactions were obtained like these previously exposed. From Figure 5, for a *liquor* characterized by Ni/S 1.2, Ni/$[SO_4^{2-}]$ 2.5, Ni/$[S_2O_3^{2-}]$ 1.7 and NH_3/CO_2 1.63, at pH<9.08 while the $[NH_3]$ concentration decreased following a potential function (R^2 = 96.8%), the $[Ni^{2+}]$ dissolved had a second-order polynomial tendency (R^2 = 94.08%) and at pH < 8.5, the nickel concentration in the BNC suspension began to increase, due to the $[Ni^{2+}]$ leaching of the BNC molecule (over-distillation).

These experimental results showed the possibility of controlling the distillation operation, setting a pH range in

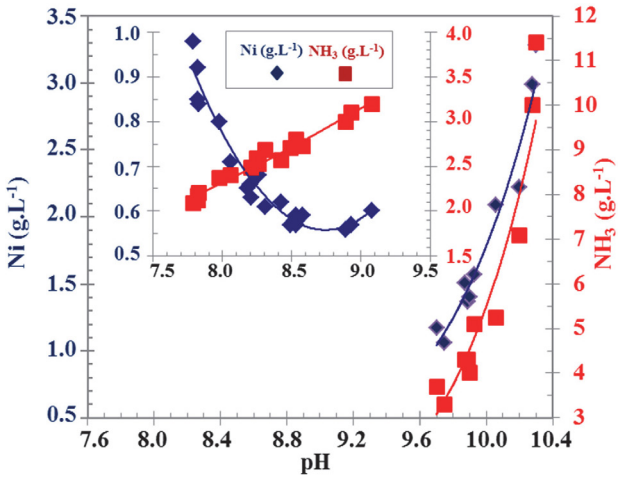


Figure 5. Profile of nickel and ammonia dissolved versus pH at 25 °C in the column-industrial (Stage 03). Ni/S 1.2, Ni/[SO_4^{2-}] 2.5, Ni/[$S_2O_3^{2-}$] 1.7, NH_3/CO_2 1.63.

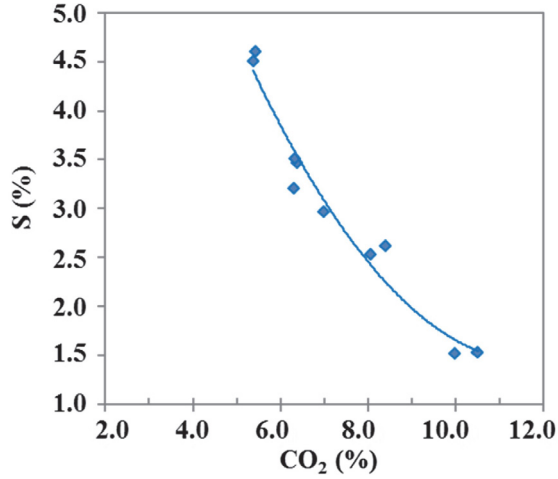


Figure 6. Interaction between sulfur and carbon dioxide in the *Basic Nickel Carbonate*, distillation mini-column (Stage 01).

the BNC suspension, in the outflow of the columns, at the minimum expenses due to ammonia losses and reagent consumption for the chemical precipitation of the dissolved nickel. Other similar experimental results have already been reported.[2,8,9]

3. 2. Effect of Sulfur on the BNC Chemical Composition

The chemical-physical characterization of *Basic Nickel Carbonate* was performed, with regard to the nickel (Ni), cobalt (Co), magnesium expressed as magnesium oxide (MgO), carbon dioxide (CO_2), sulfur (S) concentration and the real and apparent density, the average values are shown in table 1. The mean diameter ranged from 19 to 32 mm.

In the mini-column, when the [CO_2] in the BNC increased, a tendency to decrease the [S] was obtained, with a second-order polynomial function and coefficient of determination, R^2, 92.1%, (Fig. 6). From the experimental design, the biggest concentration of CO_2 in the BNC molecule was obtained at lowest thermal profile in the mini-column (low temperature and high flow), but the nickel dissolved at the mini-column effluent was high because of pH value 9.75 (+/–0.07), at sub-distillation conditions (see Fig. 3).

When CO_2-rich solution was fed in the steam-stripped mini-column, the CO_2 in the BNC molecule increased (table 1, Stage 02) as well as the mean diameter of particle from 24 to 32 mm. The specific resistance presented by the filter cake diminished from 20 to $5 \cdot 10^6$ m·kg^{-1} and the membrane resistance was constant equal to $1.5 \cdot 10^9$ kg^{-1}; the moisture content in filter cakes decreased form 70% to 63%, which benefits the subsequent process of filtration and calcination as for the productivity and energy consumption.

On the other hand, for the industrial process, the ionic composition of the *Product-liquor* was variable. In the period characterized by a carbonation in the range $1.60 \leq NH_3/CO_2 < 1.80$, when the [$CO_2$] in the BNC increased, the sulfur (S), although first it had a tendency to increase between 0.2% and 0.5%, later it decreased as a second-order polynomial function, a similar result to those obtained in the mini-column, Fig. 7.

From Figure 7, it can be seen the strong dependence of the sulfur (%) in the BNC with regard to the sulfur dissolved (g · L^{-1}) in the *Product-liquor*: to lower [S] dissolved and higher Ni/S ratio, the sulfur concentration in the BNC was lower. However, for an [NH_3/CO_2] ratio greater than 1.80 in the *Liquor*, the [S] increased with a directly proportional relationship with the [CO_2] in the BNC. Then, a correct carbonation of the *Liquor,* as well as feeding CO_2-rich

Table 1. Characterization of *Basic Nickel Carbonate*

Experimental stage	Concentration (%)					Density (kg/m^3)	
	Ni	Co	MgO	CO_2	S	real	apparent
01	47.1	0.38	0.20	7.38	3.04	2.98	0.40
02[1-]	47.8	0.43	0.09	9.68	2.39	2.85	0.46
02[2-]	47.4	0.40	0.07	7.45	4.12	2.86	0.39
03	48.5	0.35	0.28	3.34	5.96	2.89	0.59

[1-]Distillation of *Product-liquor* with CO_2-rich solution [2-]Distillation without this dissolution

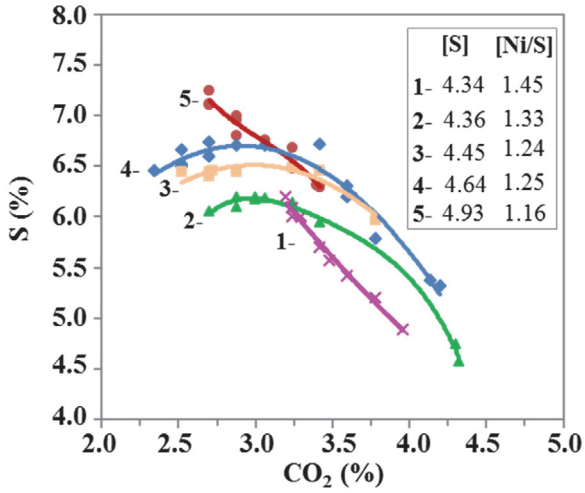


Figure 7. Interaction between sulfur and carbon dioxide in the *Basic Nickel Carbonate*, industrial process (Stage 03). The [S] concentration ($g{\cdot}L^{-1}$) and the [Ni/S] ratio in the *Product-liquor* can be appreciated. $1.60 \leq NH_3/CO_2 < 1.80$.

solution by a side tray of the steam-stripped column, increases the selectivity towards the carbonate formation in the BNC molecule with sulfate decreasing, which is favorable for the calcination process reducing the energy consumption.

Regarding the effect of the pH of the BNC suspension, the sulfur concentration decreased in the BNC molecule with the increase in the alkalinity of the suspension ($7.7 \leq pH \leq 9.1$), which suggests that the thermodynamic equilibrium of the system tend to increase the relative stability (predominance) of $NiCO_3$ while deceases for $NiSO_4$, although both species coexistent in the solid phase (Fig. 8 and Fig. 9). Figures 5 to 9 also suggest that under over-distillation conditions, nickel leached appreciably with a strong dependence on sulfur concentration.

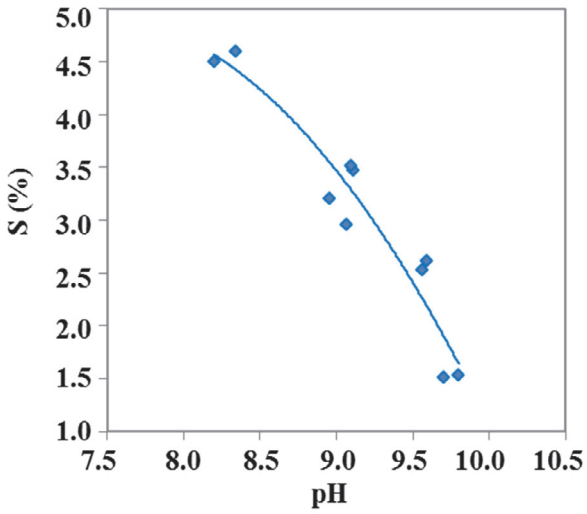


Figure 8. Interaction between sulfur contained in the BNC and pH suspension, mini-column (Stage 01).

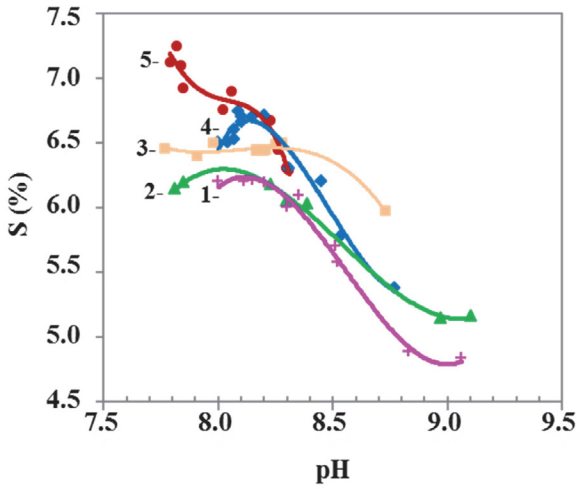


Figure 9. Interaction between sulfur contained in the BNC and pH suspension, industrial process (Stage 03). $1.60 \leq NH_3/CO_2 < 1.80$.

3. 3. Sulfur Effect on the Operating Expenses

Operating expenses, (*G*), were calculated for 10 dataset, and these were plotted as a pH function in the BNC suspension at the bottom outlet of the columns. The average values of sulfur concentration ($g \cdot L^{-1}$), ratio Ni/S, Ni/$[S_2O_3^{2-}]$ and Ni/$[SO_4^{2-}]$ in the *Product-liquor*, were included in the graph, for the dataset that overlapped in the expense curve, in the interval $8.2 \leq pH \leq 8.7$, (Fig. 10).

As shown in Figure 10, for the periods of operation characterized by carbonation according to $1.60 \leq NH_3/CO_2 < 1.80$ in the *Product-liquor*, between pH 8.3 and pH 8.7, there were a directly proportional relationship between the expenses and dissolved-sulfur concentration, and inversely proportional to the Ni/$[S_xO_y^{z-}]$ ratio; there-

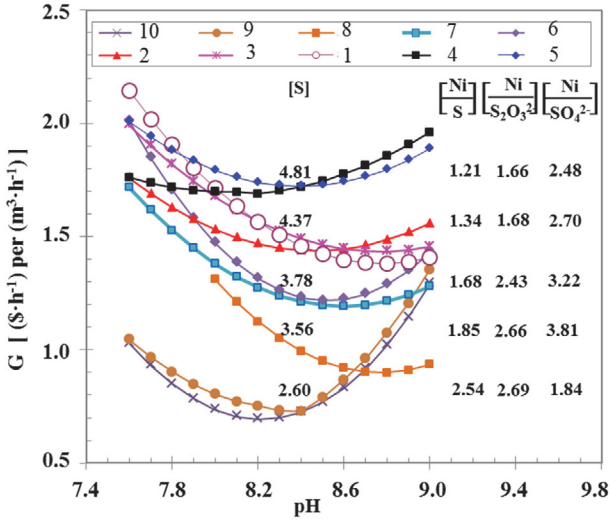


Figure 10. Operating expenses in pH function ($1.60 \leq NH_3/CO_2 < 1.80$). The [S] average concentration ($g{\cdot}L^{-1}$), [Ni/S], [Ni/$S_2O_3^{2-}$], [Ni/SO_4^{2-}] ratio in the *Product-liquor* can be appreciated (Stage 03).

fore, at a low sulfur concentration and a high Ni/[$S_xO_y^{z-}$] ratio, the expenses for ammonia losses and the consumption of nickel precipitation reagent decrease. This tendency was similar for carbonation corresponding to 1.80 ≤ NH_3/CO_2 ≤ 2.0. The nickel cation concentration tends to increase, coordinated with [$S_xO_y^{z-}$] ligand, thus the operating expenses augments.

The economic benefit (*A*) was calculated for several pH ranges. The greatest economic benefit of 0.125 ($\$ \cdot h^{-1}$) per ($m^3 \cdot h^{-1}$) of *Product-liquor* was obtained in the range 8.4 ≤ pH ≤ 8.7 (Fig. 11, curve A). The losses are represented to *A* ≤ 0, consequently, the operation for pH doesn't produce an economic benefit due to the high operation expenses, so, should be avoided operating in pH ranges less than 8.0 in the BNC suspension. The curve B was estimated by increasing the price of ammonia and the precipitation reagent by 70%; and the curve C, modifying only the ammonia price by that same percent.

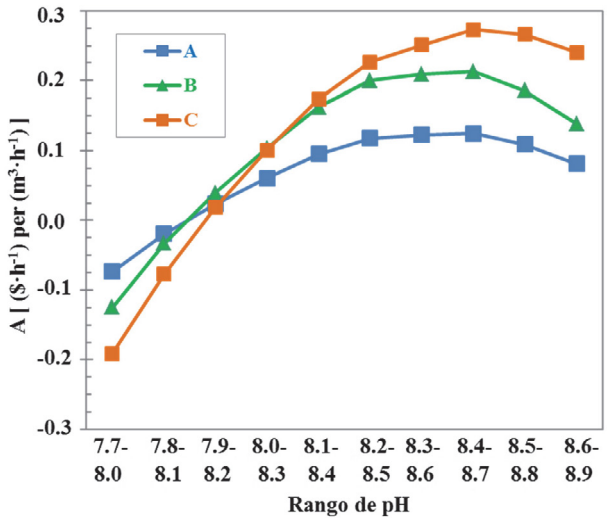


Figure 11. Interaction of suspension pH with the economic benefit (A, $\$ \cdot h^{-1}$ per $m^3 \cdot h^{-1}$), regarding ammonia losses and nickel precipitation reagent consumption.

3. 4. Nickel Leaching of BNC Molecule by Effect of Dissolved Sulfur

The nickel leaching of the *Basic Nickel Carbonate* in the distillation process, occur due to the interactions between the variables ionic species concentration in the liquid medium (system Ni(II)-NH_3-CO_2-SO_2-H_2O) and the chemistry composition of the BNC molecule, which, in turn, depends on the chemical composition of the *Product-liquor* that is fed to the process, the thermal profile in the columns and pH in the BNC suspension.

The sulfur ions [$S_xO_y^{z-}$] will be present in the solution; these are formed by oxidation of the sulfur that is incorporated to the process with the petroleum. On the other hand, the equilibrium NH_4^+/NH_3 and HCO_3^-/CO_3^{2-} depend on the suspension pH. The following reactions are proposed: Eqs. (18)– (22): [2,21]

$$NiSO_4 + NH_4OH + nNH_3 \rightarrow \rightarrow Ni(NH_3)_{n+1}SO_4 + H_2O \quad (1 \le n \le 5) \tag{18}$$

$$NiCO_3 + (NH_4)_2SO_4 + (n+2)NH_3 + H_2O \rightarrow \rightarrow Ni(NH_3)_{4+n}SO_4 + CO_2 + 2H_2O \quad (0 \le n \le 2) \tag{19}$$

$$Ni(OH)_2 + (NH_4)_2SO_4 + nNH_3 \rightarrow \rightarrow Ni(NH_3)_{2+n}SO_4 + 4H_2O \quad (1 \le n \le 4) \tag{20}$$

$$Ni(OH)_2 + (NH_4)_2S_2O_3 + nNH_3 \rightarrow \rightarrow Ni(NH_3)_{2+n}S_2O_3 + 2H_2O \quad (1 \le n \le 4) \tag{21}$$

$$Ni^{2+} + NH_4OH + (n-1)NH_3 + CO_2 + (n-1)H_2O \rightarrow \rightarrow Ni(NH_3)_nCO_2 + nH_2O \quad (2 \le n \le 6) \tag{22}$$

When the sulfur concentration increases in the *Product-liquor*, the selectivity towards sulfate formation in the BNC molecule increases while the carbonate formation decreases (Fig. 6 and Fig. 7); this favors the nickel leaching of the BNC molecule (Fig. 8 and Fig. 9), increases the Ni cation in solution and the operational costs (Fig. 10).

The complex compounds concentration, simulating the species ionic in the steam-stripped columns discharge, were determined at [NH_3] 0.01M, [CO_3^{2-}] 0.1M, [SO_4^{2-}] 0.02M and [$S_2O_3^{2-}$] 0.01M. In the measure that diminishes the pH in the BNC suspension in the columns effluents, the nickel cation concentration tend to decreasing coordinated with [NH_3] ligand with high coordination number, but tend to increasing with [S_xO_y] ligands, propitiating the nickel leaching of the BNC molecule, (Fig. 12).

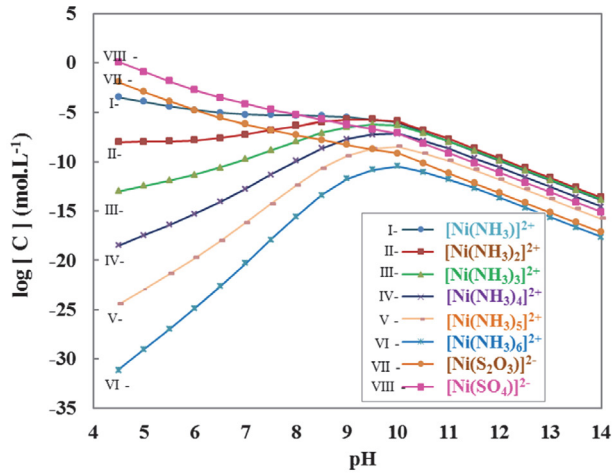


Figure 12. Log concentration of nickel complex compounds, [NH_3] 0.01M, [CO_3^{2-}] 0.1M, [SO_4^{2-}] 0.02M, [$S_2O_3^{2-}$] 0.01M

The predominance area diagram, (Fig. 13), represent thermodynamic stability area of solid and aqueous species, in function of pH and [CO_3^{2-}] anion concentration, under

approximately the same conditions when the deep precipitation of BNC begin: pH < 10.33, Ni(II) 0.14M, [NH_3] 1.2M, [SO_4^{2-}] 0.03M and $-0.7 \leq \log[CO_3^{2-}] \leq -0.16$. Based on this diagram, at higher carbonation of the *Product-liquor*, the thermodynamic stability area of $NiCO_3$ increases, while it decreases for the $Ni(OH)_2$; furthermore, it is important to control the pH, in order to reduce the tendency to $NiSO_4$ conversion, (Fig. 8 and Fig. 9). The experimental results have shown that when a *Product-liquor* is fed with low sulfur concentration, the highest Ni/S and Ni/[$S_xO_y^z$] ratio, $NH_3/CO_2 < 1.8$, as well as CO_2-rich solution by a side trays of the columns, it is also favorable to reducing the dissolved nickel, improve the BNC composition and its chemical-physical properties, (Fig. 4).

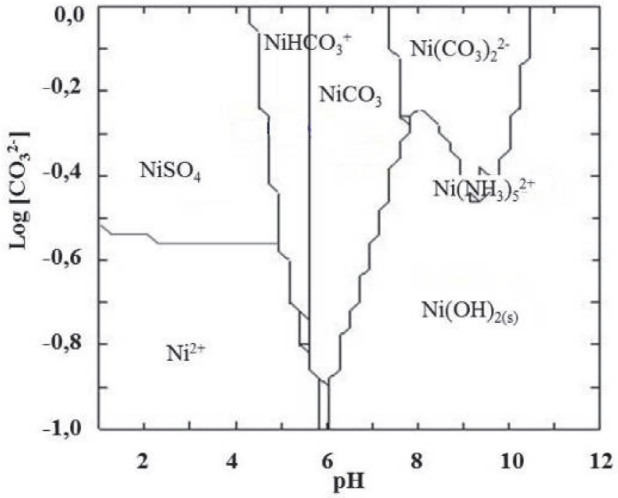


Figure 14. Predominance area diagram, Ni(II) 0.14M, [NH_3] 1.2M, [SO_4^{2-}] 0.03M.

Using the complementary norm for the operation control by pH ($8.4 \leq pH \leq 8.7$), it is possible to adjust the thermal profile in the steam-stripped columns to reduce the nickel leaching from the BNC molecule and the [Ni^{2+}] cation in solution, which allow to reduce expenses due to ammonia losses and in the nickel chemical precipitation process; in addition, the chemical-physical properties of BNC are improved, favoring the subsequent filtration and calcination processes. It is proposed to measure the pH at 25 °C in the BNC suspension at the columns outlet. If $pH \leq 8.4$ (over-distillation), the temperature at the top of the column should be lowered by reducing the steam flow until reaching a pH in the recommended range; but if $pH \geq 8.7$ (sub-distillation), the temperature should be raised by increasing the steam flow.

4. Conclusions

The distillation process in the Ammoniacal Carbonate Leaching technology was studied at bench-scale and industrial, in order to determine the dissolved sulfur effect in the *Product-liquor* that feeds to the steam-stripped columns, over the *Basic Nickel Carbonate* (BNC) properties and the operation expenses.

The BNC general structure is $(NiCO_3)_x \cdot (Ni(OH)_2)_y \cdot (NiSO_4)_z \cdot nH_2O$. When increasing the sulfur concentration in the *liquor*, augment the selectivity towards the [SO_4^{2-}] formation with diminishing of [CO_3^{2-}] in the molecule; also, when decreases the alkalinity of the BNC suspension ($7.8 \leq pH \leq 10{,}0$) the thermodynamic stability area of $NiSO_4$ tend to increasing, which affects the operation expenses due to the sulfur requires high energy consumption for the thermal decomposition in the calcination process.

The concentration of species ionic in the system Ni(II)-NH_3-CO_2-SO_2-H_2O is dependent of pH, when decrease the alkalinity of the suspension the nickel is leached form the BNC, increases Ni(II) cation in solution because of complex reaction with [SO_4^{2-}] and [$S_2O_3^{2-}$] ions; therefore, it goes up consumption precipitation reagent and the operation expenses.

Feeding carbonated *Product-liquor* in the range $1.60 \leq NH_3/CO_2 < 1.80$ and CO_2-rich solution increase the CO_2 in the BNC with decreasing of sulfate; thus, the mean diameter particle increase, the filtration specific resistance and the cake moisture diminishes, which increase the productivity and decrease the energy consumption in the process of filtration and calcination; furthermore, keeping a pH between 8.4 and 8.7 in the columns outlet the greatest economic benefit is obtained of 0.125 ($\$ \cdot h^{-1}$) per ($m^3 \cdot h^{-1}$) of *Product-liquor*.

5. Acknowledgment

Thanks to Maela Margarita Mariño-Pérez, Professor Associate University of Holguín; Georgina Aguilera Saborí, Professor Associate, University of Moa; Nélida Powery Ebanks, NICAROTEC Co.; and colleagues of the Chemical Analysis Laboratory, CEDINIQ, Nicaro, Cuba, for their collaboration.

Conflict of Interest

The authors declare no conflict of interest

6. References

1. A. R. C. Chang, A. V. Vargas, *Tecnol. Quim.* **2009**, *29*, 98–107.
2. A. V. Rojas, M. E. H. Magaña, R. A. Ricardo, *Rev. Metal. (Madrid, Spain).* **2019**, *55*, 1–11. **DOI:**10.3989/revmetalm.149
3. A. R. C. Chang, R. H. Molina, E. R. Vega, M. R. Ortiz. *Minería y Geología*, **2003**, *19*, 59–64.
4. Y. D. Gainza, M.E. Magaña, A. V. Rojas, C. G. Sánchez. *Tecnol. Quim.* **2016**, *36*, 407–416. **DOI**: 10.1590/2224-6185.2016.3.8
5. M. M. R. Romero, J. C. Y. Llópiz. *Minería y Geología*, **1996**, *13*, 61–67.

6. M. A. Rhamdhani. Metall. Trans. B. **2008**, *39B*, 234–245. **DOI:**10.1007/s11663-008-9139-5
7. M. A. Rhamdhani. Metall. Trans. B. **2008**, *39B*, 218–233. **DOI:**10.1007/s11663-007-9124-4
8. M. E. H. Magaña, A. V. Rojas, *Tecnol. Quim.* **2013**, *33*, 200–205. **DOI**: 10.1590/2224–6185.2013.3.%25x
9. A. V. Rojas, M. E. N. Trujillo, *Tecnol. Quim.* **2012**, *32*, 177–185. **DOI:**10.5482/HAMO-12-05-0003
10. X. Y. Guo, K. Huang, D. M. Zhang, *Nonferr. Metal. Soc. China*. **2014**, *14*, 1006–1011. **DOI:** 1003-6326(2004)05-1006-07.
11. K. Osseo-Asare, S.W. Asihene, In: Proceedings of International Laterite Symposium, New Orleans, LA, **1979**, pp. 19–21.
12. D. Grujicic, B. Pesic, *Electrochim Acta*. **2006**, *51*, 2678–2690. **DOI:**10.1016/j.electacta.2005.08.017
13. O. Söhnel, J. Mullin, *Cryst. Res. Technol.* **1979**, *14*, 217–228. **DOI:**10.1002/crat.19790140215
14. J. R. O. Gutiérrez, A. V. Rojas, *Tecnol. Quim.* **2018**, *38*, 24–35. **DOI**: 10.1590/2224-6185.2018.1.%25x
15. S. C. Santos, O. Rodrigues, L. L. Campos. *Curr. Smart Mater.*, **2018**, *3*, 3–20. **DOI:**10.2174/2405465802666171012143956
16. L. Pilon, H. Wang, A. d'Entremont. *J. Electrochem. Soc.* **2015**, *162*, A5158–A5178. **DOI:**10.1149/2.0211505jes
17. V. Tohver, J. E. Smay, A. Braem, P. V. Braun, J. A. Lewis. *Proc. Natl. Acad. Sci. U.S.A.* **2001**, *98*, 8950–8954. **DOI:**10.1073/pnas.151063098
18. M. Moradi, Q. He, G. A. Willing. *Colloids Surf. A*. **2019**, *577*, 532–540. **DOI:**10.1016/j.colsurfa.2019.06.021
19. L. Fang, L. Na, Z. Zhao, P. Shaofang. *J. Wuhan Univ. Technol. Mater. Sci. Ed.* **2008**, *23*, 331–333. **DOI:**10.1007/s11595-007-3331-3
20. C. G. Anderson, in: C. G. Anderson, R. C. Dunne, J. L. Uhrie (Ed.): Minerals Processing and Extractive Metallurgy: 100 years of innovation, Englewood, Colorado: Society for Mining, Metallurgy & Exploration, **2014**, pp. 403–426.
21. N. E. Kotelnikova, A.M., Mikhailidi. *Cell. Chem. Technol.* **2012**, *46*, 27–33.

Povzetek

V laboratorijskem in industrijskem merilu smo preučevali proces destilacije v tehnologiji amoniakalnega karbonatnega izpiranja. Ugotavljali smo vpliv žvepla v raztopini, ki jo dovajamo na kolone, na lastnosti bazičnega nikljevega karbonata in obratovalne stroške. S povečanjem vsebnosti žvepla v raztopini smo izboljšali selektivnost pri tvorbi sulfata v molekuli BNC; povečala se je poraba energije pri termičnem razkroju BNC v procesu kalcinacije. Prav tako se je povečala količina niklja raztopljenega v raztopini na kolonah zaradi tvorbe kompleksov z ioni [SO_4^{2-}] in [$S_2O_3^{2-}$], kar je zvišalo stroške povezane z obarjalnim reagentom. Če na kolone dovajamo raztopino z dodatkom CO_2 v območju $1.60 \leq NH_3/CO_2 < 1.80$ povečamo vsebnost CO_2 v BNC ob sočasnem zmanjšanju vsebnosti sulfata, povečamo povprečni premer delcev, zmanjšamo upor pri filtraciji in tako izboljšamo produktivnost in zmanjšamo porabo energije pri filtraciji in kalcinaciji. Z vzdrževanjem pH med 8.4 in 8.7 v iztoku iz kolon dobimo največjo ekonomičnost procesa 0,125 ($\$ \cdot h^{-1}$) na ($m^3 \cdot h^{-1}$) produkta.

Except when otherwise noted, articles in this journal are published under the terms and conditions of the Creative Commons Attribution 4.0 International License

DOI: 10.17344/acsi.2020.6157 *Acta Chim. Slov.* **2020,** *67,* 1250–1261
creative commons

Scientific paper

Effects of Extraction Methods and Conditions on Bioactive Compounds Extracted from *Phaeodactylum tricornutum*

Saniye Akyıl,[1] Işıl İlter,[1] Mehmet Koç,[2,*] Zeliha Demirel,[3] Ayşegül Erdoğan,[4] Meltem Conk Dalay[3] and Figen Kaymak Ertekin[1]

[1] *Faculty of Engineering, Food Engineering Department, Ege University, Bornova, 35100, İzmir, Turkey,*

[2] *Faculty of Engineering, Food Engineering Department, Aydın Adnan Menderes University, 09010, Aydın, Turkey,*

[3] *Faculty of Engineering, Bio Engineering Department, Ege University, Bornova, 35100, İzmir, Turkey,*

[4] *Ege University Application and Research Center for Testing and Analysis (EGE MATAL), Bornova, 35100, İzmir, Turkey,*

** Corresponding author: E-mail: mehmetkoc@adu.edu.tr*
Tel.: 902562137503

Received: 05-30-2020

Abstract

The effect of homogenization, ultrasound and microwave extraction methods and conditions on fucoxanthin content, total phenolic content and antioxidant activity of extracts obtained from *Phaeodactylum tricornutum* were investigated in this study. The solvent/biomass ratio was the most effective parameter on fucoxanthin content, total phenolic content and antioxidant activity. The maximum fucoxanthin content (5.60 ± 0.06 mg/g) and antioxidant activity (763.00 ± 15.88 EC_{50} μg/mL extract) were obtained with the homogenization extraction method whose optimum conditions were 1.93% biomass/solvent ratio, ~5200 rpm homogenization rate and 14.2 min extraction time. Although the ultrasonic extraction method has reached the approximately same level of fucoxanthin content (5.24 ± 0.07 mg/g)), TPC (67.68 ± 1.58 mg gallic acid/L) and antioxidant activity (619.90 ± 17.16 EC_{50} μg/mL extract) at an amplitude of 55.72%, a higher biomass/solvent ratio (2.72%) and a longer extraction time (17.37 min) have been required. The lowest fucoxanthin content, total phenolic content and antioxidant activity were determined for the microwave extraction method.

Keywords: Fucoxanthin; microwave extraction; optimization; *Phaeodactylum tricornutum*; total phenolic compounds; ultrasonic extraction

1. Introduction

Fucoxanthin (orange-yellow pigment), a major marine xanthophyll present in the chloroplasts of micro and macroalgae, contains more than 10% of approximate sum of carotenoid production in fresh and marine water.[1,2] Fucoxanthin has uncommonly structure with an allenic bond, epoxy, hydroxyl, carbonyl and carboxyl parts and is metabolized into fucoxanthinol, amarouciaxanthin A, and halocynthiaxanthin after absorption detected in rats and mice plasma and the liver.[3,4] Recently, several studies were indicated that fucoxanthin and its bioactive compounds have useful pharmaceutical properties including anticancer, antihypertensive, anti-inflammatory, antidiabetic and anti-obesity activities.[5–7] Additively, it has indicated that the protective properties on liver, blood vessels of the brain, bones, skin, and eyes.[8]

Extraction of fucoxanthin is mostly obtained from the waste of brown seaweeds, abundantly harvested in Asia.[9,10] However, microalgae are also considered as potential source of fucoxanthin for industrial production. The concentration of fucoxanthin in diatom contains of 2.24–18.23 mg/g dry weight while in macroalgae includes about 0.1–1 mg/g amount of dry cell weight.[11–13] For this reason, large scale production from a diatom that produces fucoxanthin in high amounts has attracted more attention nowadays.

Phaeodactylum tricornutum, a single-cell microalgae belonging to the Bacillariophyta, is a diatom species living

in the marine environment.[14] It biosynthesizes proteins, fats, carbohydrates, minerals, pigments, hydrocarbons, polysaccharides, phenolic compounds, antibiotics and many other metabolites that is commonly utilized in feed source in aquaculture. It can be used as a source of. *P. tricornutum* is typically rich in eicosapentaenoic acid (EPA), long chain unsaturated fatty acids (PUFAs) and has a high content of the carotenoid fucoxanthin.[15,16] Fucoxanthin, antioxidant compounds, which is part of the photosynthetic apparatus of microalgae for participates in photo protection from excess light.[17] Moreover, McClure et al.[18] explained that the productivity of fucoxanthin from *P. tricornutum* determines enhancing using various culture conditions such as the light intensity, medium composition and CO_2 addition on production. The difficulty and low efficiency in chemical synthesis limits the industrial production of fucoxanthin. The diatoms have not only xanthophyll but also phenolic compounds and both of them are emphasized strongly possessing antioxidant activity.[19]

In general, various extraction methods of bioactive compounds has its own advantages and disadvantages therefore it is necessary to determine the most appropriate extraction method of the biomass being studied by considering factors such as the extraction time, cost, yield and purity. Many of the studies focused on extraction of fucoxanthin from *P. tricornutum*, little attention has been paid for its efficient extraction by altering some variables systematically using response surface methodology.

In this study, it was used to optimize following Central Composite Rotatable Design (CCRD) the extraction conditions of fucoxanthin and phenolic compounds from *P. tricornutum*. The aim of this study was to compare different extraction methods (homogenization solvent, ultrasound and microwave assisted extraction methods) for the recovery of fucoxanthin from frozen biomass of *P. tricornutum* and their conditions targeting maximum fucoxanthin content, acceptable amount of total phenolic compounds with antioxidant activity using response surface methodology.

2. Experimental

2. 1. Microorganism

Phaeodactylum tricornutum Bohlin EGEMACC 71 was supplied from the Ege University Microalgae Culture Collection (http://www.egemacc.com/) in Izmir, Turkey. In the microalgal biotechnology laboratory of Ege University, *P. tricornutum* was cultured using F/2 medium,[20] in laboratory photobioreactors at 55 µmol photons/m^2s light intensity, aerated with air bubbles at 2 L/min and incubated at 20 ± 2 °C. After exponential phase, *P. tricornutum* cells were harvested by centrifuge (PrO-Research, Centrium Scientific Limited, UK) on the fourteenth day and the biomass stored at –20°C under dark conditions for using.[21]

2. 2. Chemicals

Folin-Ciocalteu reagent (Merck, Darmstadt, Germany), sodium carbonate (Fisher Science, UK) and gallic acid (Merck, Darmstadt, Germany) were measured by total phenolic content. Trolox (Hoffman-La Roche) (6-hydroxy-2,5,7,8-tetramethychroman-2-carboxylic acid; Aldrich Chemical Co., Gillingham, Dorset, UK) was as applied as a standard antioxidant. Ethanol (Merck, Darmstadt, Germany), Ethanol (32205-2.5 L) was supplied from Sigma-Aldrich Chemical Co. (Steinheim, Germany) and used in the extraction protocol. HPLC-DAD standards, all-*trans* fucoxanthin (16337-1 mg) and all-*trans*-neoxanthin (54764-1 mg) were purchased from also Sigma-Aldrich Chemical Co. (Steinheim, Germany). Methanol and acetonitrile (LC-grade) were purchased from Merck (Darmstadt, Germany) for the HPLC-DAD analysis of extracts.

2. 3. Extraction Methods of *P. tricornutum*

Fucoxanthin and total phenolics were extracted from *P. tricornutum* frozen biomass in 80% ethanol/water (v/v). The freezing of biomass was collected in a freezer (Arçelik, Model 5223, Turkey) at –20 ± 2 °C for using when the drying process was performed in a drying oven (Vacucell 22, USA) at 50 ± 2 °C until it reached to approximately 6% moisture content. To detect the effect of freezing biomass form on fucoxanthin concentration the amount of dry matter content of the biomass in the extraction medium was kept constant.

Homogenization extraction (CE), Microwave extraction (ME) and Ultrasound extraction (UE) techniques were applied to use a mechanical homogenizer, a microwave extraction device (Milestone, Start E, Italy), and an ultrasound bath (Daihan Wisd WUC-D06H, Korea) respectively.[22] In CE and UE process, the temperature of the extraction medium was kept constant at 25 ± 2 °C with the circulator water bath whereas in the ME process, the temperature in the extraction chamber didn't exceed 40 ± 2 °C.

2. 4. Optimization of the Extraction Protocol

The effect of extraction process variables (time, biomass/solvent ratio, homogenization rate, amplitude, microwave power) on fucoxanthin content, total phenolic content and DPPH antioxidant activity of extracts was investigated following Central Composite Rotatable Design (CCRD) as given in Table 1

The optimum homogenization rate (rpm) for CE, amplitude for UE, microwave power for ME, time (min) and biomass/solvent ratio (%) was determined targeting the maximum concentration of fucoxanthin and acceptable amount of total phenolic content (TPC) and DPPH antioxidant activity considering desirability function approach. 80% ethanol (v/v) was used as an extraction medium for all the extraction methods.

Table 1. Extraction process variables and levels for the specific CCRD experimental design

Extraction Method	Independent Variables		Coded Values				
			–1.682	–1	0	1	1.682
Homogenization Extraction (CE)	Biomass/Solvent Ratio (%)	(A)	0.32	1	2	3	3.68
	Hom. Rate (rpm)	(B)	3636	5000	7000	9000	10363
	Time (min)	(C)	1.59	5	10	15	18.41
Ultrasonic Extraction (UE)	Biomass/Solvent Ratio (%)	(A)	0.32	1	2	3	3.68
	Amplitude (%)	(D)	19.77	30	45	60	70.23
	Time (min)	(C)	4.89	10	17.5	25	30.11
Microwave Extraction (ME)	Biomass/Solvent Ratio (%)	(A)	0.32	1	2	3	3.68
	Power (W)	(E)	65.91	100	150	200	234.09
	Time (s)	(C)	19.09	60	120	180	220.91

The process parameters specific to each extraction method, biomass/solvent ratio (%) and extraction time were optimized to provide Multiple regression analysis was carried out for fitting the Eq. (1, 2, and 3) to the experimental data and significant terms of the model were measured by ANOVA. The CCRD and the corresponding data analysis were implemented by using the Design-Expert 7.0.0 (Stat-Ease Inc., MN, USA).

$$FX = \beta_0 + \sum_{i=1}^{k} \beta_i x_i + \sum_{i=1}^{k} \beta_{ii} x_i^2 + \sum_{i=1}^{k-1} \sum_{j=i+1}^{k} \beta_{ij} x_{ji} \; (k = 1, 2, 3) \quad (1)$$

$$TPC = \beta_0 + \sum_{i=1}^{k} \beta_i x_i + \sum_{i=1}^{k} \beta_{ii} x_i^2 + \sum_{i=1}^{k-1} \sum_{j=i+1}^{k} \beta_{ij} x_{ji} \; (k = 1, 2, 3) \quad (2)$$

$$DPPH = \beta_0 + \sum_{i=1}^{k} \beta_i x_i + \sum_{i=1}^{k} \beta_{ii} x_i^2 + \sum_{i=1}^{k-1} \sum_{j=i+1}^{k} \beta_{ij} x_{ji} \; (k = 1, 2, 3) \quad (3)$$

2. 5. Analysis

2. 5. 1 Fucoxanthin Analysis

The extracts were centrifuged using a refrigerated centrifuge (Nuve NF400, Turkey) at 4000 rpm, 10 minutes at 20 °C and supernatant was passed through a filtration apparatus (PTFE filter with a diameter of 0.20 μm) to remove the cell residue. The amount of fucoxanthin in the extracts was determined by HPLC-DAD (Agilent 1260, USA) using YMC carotenoid C_{30} column (25 cm, 4.6 ID, 5 μm). For the separation of fucoxanthin, 70:30 methanol: acetonitrile (v/v) was used as the mobile phase at a flow rate of 1 mL/min. Under these conditions, standards fucoxanthin and neoxanthin gave an absorbance at 450 nm and 442 nm, respectively. Therefore, peak areas are considered at these wavelengths.

Retention times for fucoxanthin (FX) and neoxanthin (NX) were 7 and 9 minutes, respectively, as determined by HPLC-DAD. Calibration curve was constructed for fucoxanthin (0.5–5 mg/L) using internal standard as neoxanthin according to the procedure applied in previous studies.[23]

2. 5. 2. DPPH Antioxidant Activity

The antioxidant activity of the extracted samples was investigated by the DPPH (2,2-diphenyl-1-picrylhydrazyl radical scavenging capacity) method. The DPPH solution of measuring the ability to inhibit free radicals was used and the reaction time in methanol was determined according to the results measured at 515 nm by spectrophotometer (Varian Cary 50 Bio, UV / VIS Spectrophotometer). This method is based on the scavenging of DPPH radicals by antioxidants due to a redox reaction.[1]

2. 5. 3. Determination of Total Phenolic Content (TPC)

The total phenolic content of the fucoxanthin extracts was defined spectrophotometrically using the Folin-Ciocalteu method according to.[22]

3. Results and Discussion

In this study, three different extraction methods, namely ultrasound (UE) and microwave (ME) and ho-

Table 2. Fucoxanthin, total phenolic content and DPPH antioxidant activity of three extraction methods at 20 different experimental conditions.

Exp. No	A	X*	C	CE			UE			ME		
				FX (mg/g)	TPC (mg gallic acid/L)	EC_{50} (μg/mL extract)	FX (mg/g)	TPC (mg gallic acid/L)	EC_{50} (μg/mL extract)	FX (mg/g)	TPC (mg gallic acid/L)	EC_{50} (μg/mL extract)
1	−1	−1	−1	3.24 ± 0.32	29.52 ± 2.79	727.07 ± 27.89	2.48 ± 1.09	34.85 ± 1.28	521.90 ± 58.29	1.93 ± 1.60	19.02 ± 4.72	830.68 ± 51.84
2	1	−1	−1	4.33 ± 0.75	25.93 ± 0.99	953.57 ± 55.50	4.58 ± 1.60	48.71 ± 1.97	501.87 ± 73.89	4.18 ± 0.59	54.46 ± 3.45	463.85 ± 81.23
3	−1	1	−1	4.09 ± 1.33	47.11 ± 2.84	599.48 ± 64.30	3.12 ± 1.73	51.04 ± 3.70	773.15 ± 62.78	1.59 ± 0.96	20.09 ± 0.83	542.96 ± 40.17
4	1	1	−1	6.13 ± 0.53	46.57 ± 0.67	1228.3 ± 25.07	5.63 ± 0.88	58.77 ± 3.23	495.02 ± 92.39	4.50 ± 1.58	37.49 ± 3.56	370.90 ± 1.73
5	−1	−1	1	6.66 ± 1.21	36.46 ± 1.15	830.21 ± 19.26	1.99 ± 1.23	26.28 ± 1.80	1006.45 ± 80.27	2.30 ± 0.96	11.16 ± 1.44	680.81 ± 15.68
6	1	−1	1	5.83 ± 1.17	74.77 ± 0.59	485.75 ± 29.20	4.06 ± 0.001	31.48 ± 3.55	966.87 ± 98.23	4.55 ± 0.31	42.44 ± 2.52	439.40 ± 58.16
7	−1	1	1	4.81 ± 0.23	37.10 ± 2.59	912.90 ± 44.25	3.86 ± 1.55	41.89 ± 1.61	539.39 ± 59.66	1.83 ± 1.5	18.03 ± 3.11	410.16 ± 68.98
8	1	1	1	5.51 ± 0.26	66.89 ± 2.23	941.28 ± 23.15	5.39 ± 0.60	61.92 ± 1.82	553.96 ± 75.55	4.29 ± 0.88	60.06 ± 3.25	649.27 ± 78.39
9	−1.68	0	0	2.62 ± 0.37	18.20 ± 0.86	695.30 ± 7.06	0.2 ± 0.01	19.82 ± 2.20	838.83 ± 50.66	0	8.87 ± 1.69	661.99 ± 50.82
10	1.68	0	0	4.62 ± 0.24	46.90 ± 1.07	1083.24 ± 23.4	5.12 ± 0.72	63.78 ± 4.92	639.08 ± 51.45	4.07 ± 1.04	63.86 ± 1.29	684.87 ± 42.82
11	0	−1.68	0	6.78 ± 0.25	70.18 ± 0.54	642.10 ± 59.39	3.49 ± 2.16	31.40 ± 3.64	704.81 ± 90.00	3.72 ± 0.32	23.95 ± 1.95	500.45 ± 8.170
12	0	1.68	0	5.45 ± 1.04	49.05 ± 0.83	869.72 ± 66.84	5.63 ± 0.64	76.87 ± 4.82	557.77 ± 94.88	3.42 ± 2.04	22.86 ± 0.33	381.81 ± 53.15
13	0	0	−1.68	4.33 ± 0.92	48.96 ± 0.58	754.22 ± 39.78	3.25 ± 0.24	43.23 ± 2.58	684.75 ± 66.15	3.12 ± 2.53	35.87 ± 0.19	832.62 ± 60.99
14	0	0	1.68	6.73 ± 0.42	50.36 ± 3.28	806.73 ± 79.73	4.44 ± 1.58	45.24 ± 0.76	1083.85 ± 48.30	3.79 ± 0.26	29.63 ± 1.61	598.16 ± 86.91
15	0	0	0	5.33 ± 0.22	59.87 ± 0.71	858.94 ± 66.88	5.99 ± 2.79	40.78 ± 2.33	720.70 ± 83.91	3.34 ± 0.73	30.50 ± 1.47	590.89 ± 28.66
16	0	0	0	5.38 ± 0.07	51.99 ± 2.38	992.85 ± 19.02	5.22 ± 0.15	64.17 ± 3.27	666.52 ± 15.62	3.45 ± 0.26	28.87 ± 2.27	573.18 ± 48.61
17	0	0	0	5.47 ± 1.26	57.19 ± 1.20	1060.2 ± 50.52	5.78 ± 2.14	39.84 ± 2.56	793.31 ± 69.62	3.82 ± 1.77	38.63 ± 0.49	632.86 ± 75.81
18	0	0	0	5.90 ± 1.52	53.02 ± 2.82	996.47 ± 63.27	4.70 ± 0.05	41.17 ± 4.41	698.94 ± 67.90	3.07 ± 0.55	28.09 ± 1.20	569.05 ± 9.59
19	0	0	0	5.56 ± 0.77	51.47 ± 4.96	932.98 ± 33.18	4.92 ± 0.83	39.86 ± 0.58	759.33 ± 72.89	3.69 ± 1.67	38.33 ± 3.30	782.30 ± 25.80
20	0	0	0	5.51 ± 0.57	50.64 ± 0.43	933.07 ± 17.63	5.15 ± 0.06	62.44 ± 0.10	747.50 ± 49.44	3.94 ± 1.30	37.65 ± 1.97	643.94 ± 28.96

*X expresses the specific extraction parameters; homogenization rate (rpm) for CE, amplitude (%) for UE and power (W) for ME

Table 3. ANOVA results for each response variables of the optimization process in terms of fucoxanthin content (FX), total phenolic content (TPC) and DPPH antioxidant activity (EC_{50}) with three extraction methods

Source	df	CE						UE						ME					
		FX (mg/g)		TPC (mg gallic acid/L)		EC_{50} (µg/mL extract)		FX (mg/g)		TPC (mg gallic acid/L)		EC_{50} (µg/mL extract)		FX (mg/g)		TPC (mg gallic acid/L)		EC_{50} (µg/mL extract)	
		SS	*p-value*	SS	*p-value*	SS	*p-value*	SS	*p-value*	SS	*p-value*	SS	*p-value*	SS	*p-value*	SS	*p-value*	SS	*p-value*
Model	9	21.86	<0.000*	3187	0.006*	478000	0.007*	38.6	0.000*	3010	0.047*	478000	0.000*	23.89	<0.000*	3963	<0.000*	269000	0.034*
A	1	2.970	<0.000*	922.3	0.003*	81679	0.003*	19.9	<0.000*	1067	0.011*	36013	0.016*	18.79	<0.000*	3500	<0.000*	18505	0.177
X*	1	0.240	0.176	1.510	0.880	63696	0.881	5.290	0.001*	1621	0.003*	51750	0.006*	0.280	0.084	3.360	0.729	30083	0.094
C	1	6.020	<0.000*	343.2	0.043*	959	0.042*	0.160	0.467	59.1	0.477	162000	0.000*	0.490	<0.031*	7.110	0.616	13106	0.230
AX*	1	0.770	0.025*	3.730	0.316	51145	0.814	0.002	0.931	9.460	0.773	7572	0.215	0.310	0.072	6.660	0.627	57005	0.029*
AC	1	1.330	0.006*	652.0	0.009	134100	0.01*	0.130	0.514	1.650	0.904	6668	0.243	0.170	0.173	52.40	0.190	35991	0.070
X*C	1	2.900	0.000*	259	0.071	34659	0.072	0.290	0.339	49	0.516	146400	0.000*	0.250	0.100	203.8	0.020*	12792	0.255
A^2	1	6.470	<0.000*	893.4	0.004*	6927	0.004*	10.9	0.000*	104.1	0.350	2663	0.451	3.390	<0.000*	28.6	0.324	54.41	0.939
X^2	1	0.650	0.036*	41.5	0.438	68761	0.438	0.550	0.194	40.4	0.555	38457	0.013*	0.050	0.437	145.1	0.041*	92663	0.009*
C^2	1	0.0002	0.963	47.9	0.406	52551	0.406	2.890	0.010*	48.1	0.520	20585	0.054	0.004	0.814	0.240	0.925	4056	0.512
Residual	10	1.110		636.3		46104		2.840		1081		43230		0.770		265.0		87777	
Lack of Fit	5	0.910	0.063	569.0	0.018	22024	0.018	1.600	0.394	379.5	0.742	32981	0.113	0.240	0.797	138.6	0.461	55921	0.276
Pure Error	5	0.200		67.3		24080		1.240		701.9		10248		0.530		126.4		31845	
Cor Total	19	22.97		3824		524000		41.5		4092		520000		24.66		4228		356000	
R^2		0.952		0.834		0.912		0.931		0.736		0.917		0.969		0.937		0.755	
R^2_{adj}		0.908		0.684		0.833		0.870		0.498		0.842		0.941		0.881		0.534	
C.V. %		6.39		16.41		7.91		12.55		22.52		9.200		8.490		15.84		15.82	
PRESS		7.26		4446		204100		14.11		3979		278700		2.580		1397		486100	
Adeq Precision		16.44		10.11		11.95		13.21		6.739		11.83		21.93		16.01		8.310	

*X expresses the specific extraction parameters; homogenization rate (rpm) for CE, amplitude (%) for UE and power (W) for ME

mogenization extraction (CE) were used to determine the effect of process conditions on fucoxanthin content (FX), total phenolic content (TPC) and DPPH antioxidant activity. The extraction process conditions arranged to CCRD (Table 2) were evaluated for responses; FX, TPC and DPPH antioxidant activity of the extracts. The experimental data are described to be compatible with the quadratic models (Eqs. 1, 2 and 3) ($p < 0.05$). The significance level of the effect of model terms on the responses and the suitability of the obtained models are given in Table 3. In addition, the effects of the three extraction methods process conditions on the responses were explained in detail.

3. 1. Fucoxanthin Content (FX)

The extraction method and conditions were found to be significant for the effective extraction of fucoxanthin. As given in Table 3, the extraction process conditions were the important factors for the extraction of fucoxanthin. Increasing the ratio of biomass/solvent increases dissolution of the solvent into cells and provides more extracts. Xu et al.[25] explained that the excess solvent absorbed the cavitation energy in the extraction system and resulted in a lower extraction efficiency. The amount of fucoxanthin increased with increasing amount of biomass in all extraction methods (Fig. 1–3). Although the amount of fucoxanthin increased with the increase of biomass/solvent ratio in the homogenization extraction method (Fig. 1), the homogenization rate did not significantly affect the amount of fucoxanthin (Table 3). However, when the biomass/solvent ratio was maximum, the amount of fucoxanthin increased with the increase in the rate of homogenization in the short extraction process times. *P. tricornutum,* which has a silica structure needs to mechanical spalling. During CE period, this process breaks the outer silicon wall and accelerates the solvent uptake. That's why, the higher solvent uptake brought about the higher diffusivity through the cell walls. The high extraction efficiencies obtained by the CE method can be attributed to the fact that by breaking down the cell walls as a result of mechanical destroying, it can facilitate the washing of the cell contents.[26] In the case of prolongation of the extraction time, the increase in homogenization rate showed a negative effect on the amount of fucoxanthin. The fucoxanthin appeared to degrade gradually during the long extraction period.[11] This circumstance was also approved by the ANOVA results (Table 3). While the effect of homogenization rate on linear dimension was insignificant, the effect of homogenization rate and time interaction on fucoxanthin amount was statistically significant.

In the ultrasonic assisted extraction (UE) process, the amount of fucoxanthin increased with the increase of the biomass solvent ratio. Although the effect of the homogenization rate on the amount of fucoxanthin in the homogenization extraction process remained limited, the increase in the amplitude clearly resulted in an increase in the amount of fucoxanthin as seen in Fig. 2. The increase of amplitude increased the amount of fucoxanthin because the biomass and the solvent had a larger surface area in the UE due to effective cavitation and/or solvent penetration into the cell. The higher contact surface area between the solvent and the biomass also favored the extraction of phycocyanin.[24] The effect of extraction time in ultrasonic assisted extraction was not statistically found significant on fucoxanthin amount ($p > 0.05$) (Table 3). However, Fig. 2 showed that short and long ultrasound application decreased the amount of fucoxanthin. Kim et al.[11] reported that ethanol allowed to extract the highest fucoxanthin in the ultrasonic extraction process.

As in the other two extraction methods, the most effective independent variable on the amount of fucoxanthin in the microwave extraction method was the biomass solvent ratio. With the increase in the biomass solvent ratio, the amount of fucoxanthin obtained from *P. tricornutum* was increased by microwave extraction method. The effect of the extraction time and the microwave power on fucoxanthin extraction remained very limited in addition to the biomass/ solvent ratio. This was also confirmed by the change of fucoxanthin in Fig. 3 with respect to independent variables. However, the effect of the extraction time and microwave power on fucoxanthin should not be completely ignored. The shortening of the extraction time and the increase of microwave power resulted in an increase in the amount of fucoxanthin. Zhang et al.[14] reported that the longer extraction time in microwave extraction method resulted in the lower yield of fucoxanthin. They explained this reduction as follows; the constant high temperature caused fucoxanthin deterioration.

The maximum fucoxanthin (5.99 ± 2.79 mg/g) was extracted with UE method at 45% of amplitude for 17.5 min extraction time when the biomass/solvent ratio was 2%. However, the maximum fucoxanthin (4.55 ± 0.31 mg/g) was obtained when 3% biomass/solvent ratio, 100 W microwave power and 180 s of extraction time conditions were used in ME method (Table 2). Gilbert-Lopez et al.[17] carried out fucoxanthin extraction (4.59 mg/g) from *P. tricornutum* by microwave assisted extraction in ethanol at 30 °C for 2 min. The CE method was more suitable for the extraction of fucoxanthin at maximum concentration (6.78 ± 0.25 mg/g) (Exp. No: 11) for the biomass/solvent ratio of 2%, homogenization rate of 3636 rpm and extraction time of 17.5 min as compared to the other methods. Although UE and ME increased extraction yields in many marine materials, the maximum fucoxanthin extraction was achieved in CE method. Kawee et al.[27] explained the lower yield of fucoxanthin extraction by ultrasonic extraction by the rigid cell wall of *P. tricornutum*. Besides, Kim et al.[11] also reported that ultrasonic assisted extraction method does not change the fucoxantin yield when compared with other extraction methods. Compared to the other two extraction methods, the lower amount of fucoxanthin was reached in the microwave extraction. However, the microwave ex-

traction was superior to the other two methods in terms of extraction times. Pasquet et al.[26] tried to extract fucoxanthin from *Cylindrotheca closterium* compared different extraction methods. Microwave extraction of *C. closterium* allowed total extraction of fucoxanthin in 3–5 min that equivalent to the yield obtained after 60 min soaking at 20 °C or 56 °C.

3. 2. Total Phenolic Content (TPC)

Phenolic compounds act as important antioxidants due to their skill to give a hydrogen atom or an electron to form stable radical intermediates. Extraction of *P. tricornutum* has significant pharmaceutical activities. Moreover, it uses as a safe food and sustainable feed source used in aquaculture.[28] The total phenolic contents of extracts obtained with different extraction methods and conditions were determined and stated as gallic acid equivalent. The 3-D response surface graphs for TPC are shown in Fig. 1–3. TPC was considerably affected from the biomass/solvent ratio for all extraction methods. For each extraction procedure, TPC content increased as the biomass/solvent ratio increased.

As expected, the excessive amount of biomass resulted in higher TPC content in the extraction medium due to diffusion of phenolic compounds through the extraction medium. The results showed that the biomass/solvent ratio caused significant differences in TPC in all extraction methods. (Table 3). Furthermore, UE method provided higher TPC content (76.87 ± 4.82 mg gallic acid /L) (Table 2), due to tissue destruction as a function of time and intensity of ultrasound waves. Both et al.[29] and Deng et al.[30] explained the higher phenolic compounds releasing to extraction medium with the working principals of ultrasound extraction which caused acoustic cavitation, increasing temperature of extraction medium, lowering the particle size of biomass, cell wall fragmentation, rising the degree of solvent penetration into the cells. Several studies have reported that the TPC increased quickly with the increase of biomass ratio at room temperature, as well as by use of high temperature or in the existence of ultrasound.[24] According to Pearson correlation test, fucoxanthin content was highly correlated with TPC and correlation coefficients (r) were 0.645, 0.707 and 0.733 for CE, UE and ME, respectively. Foo et al.[31] also observed a stronger correlation between major component of carotenoid (fucoxanthin) and phenolics (gallic acids). The maximum TPC (76.87 ± 4.82 mg gallic acid/L) was found for the biomass/solvent ratio of 2%, amplitude of 70.22% and extraction time of 17.5 min with UE method whereas the minimum TPC (8.87 ± 1.69 mg gallic acid/L) was for biomass/solvent ratio of 0.32%, microwave power of 150 W and extraction time of 120 s with ME method. In addition, CE method gave the maximum TPC (74.77 ± 0.59 mg gallic acid/L) for biomass/solvent ratio of 3%, homogenization rate of 5000 rpm and extraction time of 25 min.

3. 3 DPPH Antioxidant Activity

The DPPH (2,2-diphenyl-1-picrylhydrazyl or 1,1-diphenyl-2-picrylhydrazyl) scavenging test utilizes a stable nitrogen centered free radical. DPPH are effectively scavenged by antioxidants through the donation of hydrogen to form the reduced DPPH–H.[32] This method has been commonly used to determine the antioxidant activity of brown seaweeds. Airanthi et al.[33] reported that the antioxidant effect of seaweed was mainly due to the antioxidant activity of phenolic compounds. Holdt et al.[34] also stated that many compounds possessing antioxidant activity that were isolated from brown algae were phenolic antioxidants. Moreover, brown algae have higher antioxidant activity than red or green algae.[35] Fucoxanthin, the most abundant marine-based carotenoid, has been considered as a potential antioxidant activity, in terms of its free scavenging activity.[36]

The 3-D response surface graph of the predicted model for DPPH is shown in Fig. 1–3. The effect of biomass/solvent ratio and extraction time was statistically found significant on antioxidant activity of extracts (Table 3). The maximum DPPH antioxidant activity (1228.3 ± 25.07 EC_{50} μg/mL extract) (Exp. No: 4) was for biomass/solvent ratio of 3%, homogenization rate of 9000 rpm and extraction time of 10 min with CE method (Table 2). Whereas the minimum DPPH antioxidant activity (370.9 ± 1.73 μg/mL extract) (Exp. No: 4) was obtained for the biomass/solvent ratio of 3%, microwave power of 200W and extraction time of 60 s with ME method (Table 2). ME method was not successful to extract fucoxanthin from biomass *P. tricornutum* with high antioxidant capacity. There are several studies about the investigation of antioxidant activity of fucoxanthin from different types of microalgae and macroalgae.[19,27,33,35,37] Airanthi et al.[33] have been reported to have observed the highest DPPH radical scavenging activity in methanol extract with 58.63 ± 5.24 μg α-tocopherol equivalent per milligram and 33.46 ± 4.69 μg α-tocopherol equivalent per milligram for *Eisenia bicyclis* (Arame) and *Kjellmaniella crassifolia* (Gagome) macroalgae respectively. Foo et al.[19] observed that *Chaetoceros calcitrans* extract with ethanol by homogenization extraction method (9500 rpm for 15 min) exhibited the DPPH scavenging activity of 0.844 mg/g (dried weight).

3. 4. Optimization

The process conditions of homogenization (CE), ultrasonic (UE) and microwave (ME) extraction methods in terms of ultrasound (amplitude) (%), microwave power (W), homogenization rate (rpm) biomass/solvent ratio (%) and extraction time were optimized targeting maximum fucoxanthin content and acceptable amounts of total phenolic content and DPPH antioxidant activity. Graphical illustrations of the optimization were seen in Figure 1–3.

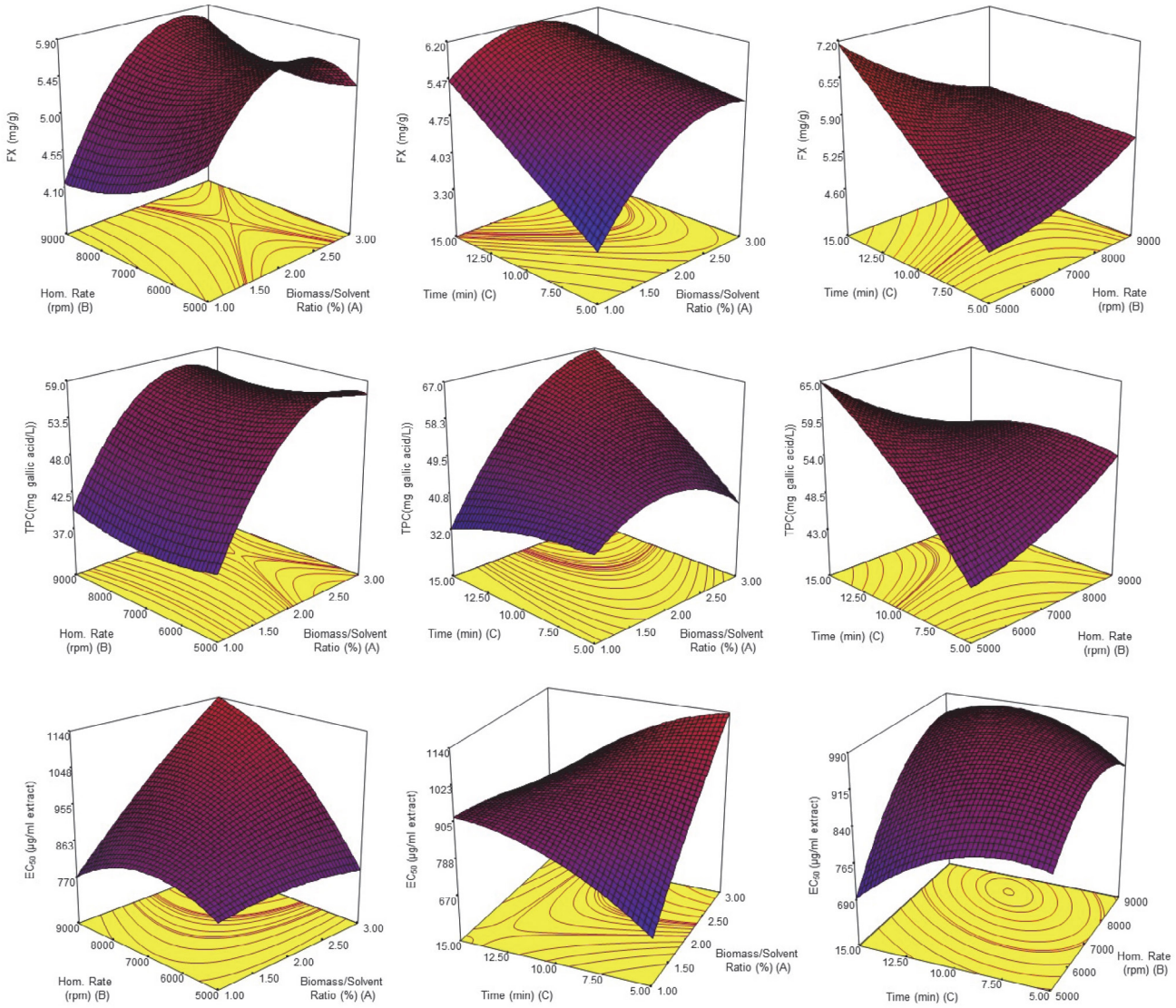


Figure 1. Calculated effects of homogenization extraction process variables on fucoxanthin content (mg/g), total phenolic content (mg gallic acid /L) and antioxidant activity (EC_{50} µg/mL extract).

The experimental data were well fitted to the second order polynomial models, as given in Table 3. The models of fucoxanthin content, TPC and DPPH antioxidant activity of extracts obtained from different extraction methods were statistically significant at level $p < 0.05$. In order to define optimum extraction process conditions, desirability function approach was applied. The desirability function approach is commonly used to optimize multiple response processes.

When the desirability function approach was used, the optimum CE process conditions were 1.93% for the biomass/solvent ratio, 5203.25 rpm for the homogenization rate and 14.20 min for the extraction time. The optimum process conditions for the extraction process carried out by the UE method were 2.72% for the biomass/solvent ratio, 55.72% for the amplitude, and 17.37 min for the extraction time. ME method for fucoxanthin extraction gave the optimum process conditions as follows: 3.0% biomass/solvent ratio, 100 W and 179.97 s extraction time. In order to validate these extraction conditions, five validation experiments were performed at these optimum extraction process conditions. The average value of FX was found to be significantly ($p < 0.05$) different from the predicted values, while TPC and DPPH antioxidant activity were not significantly ($p > 0.05$) different from the predicted values determined by Design Expert-version 7.0 software as given in Table 4.

A comparison was made to evaluate the results of each extraction method, given that the equipment and methods had their own characteristics and the experiments could not be performed under the same conditions. As given in Table 2, the highest amount of FX was obtained using homogenization and ultrasound extraction methods, while TPC was higher in homogenization method

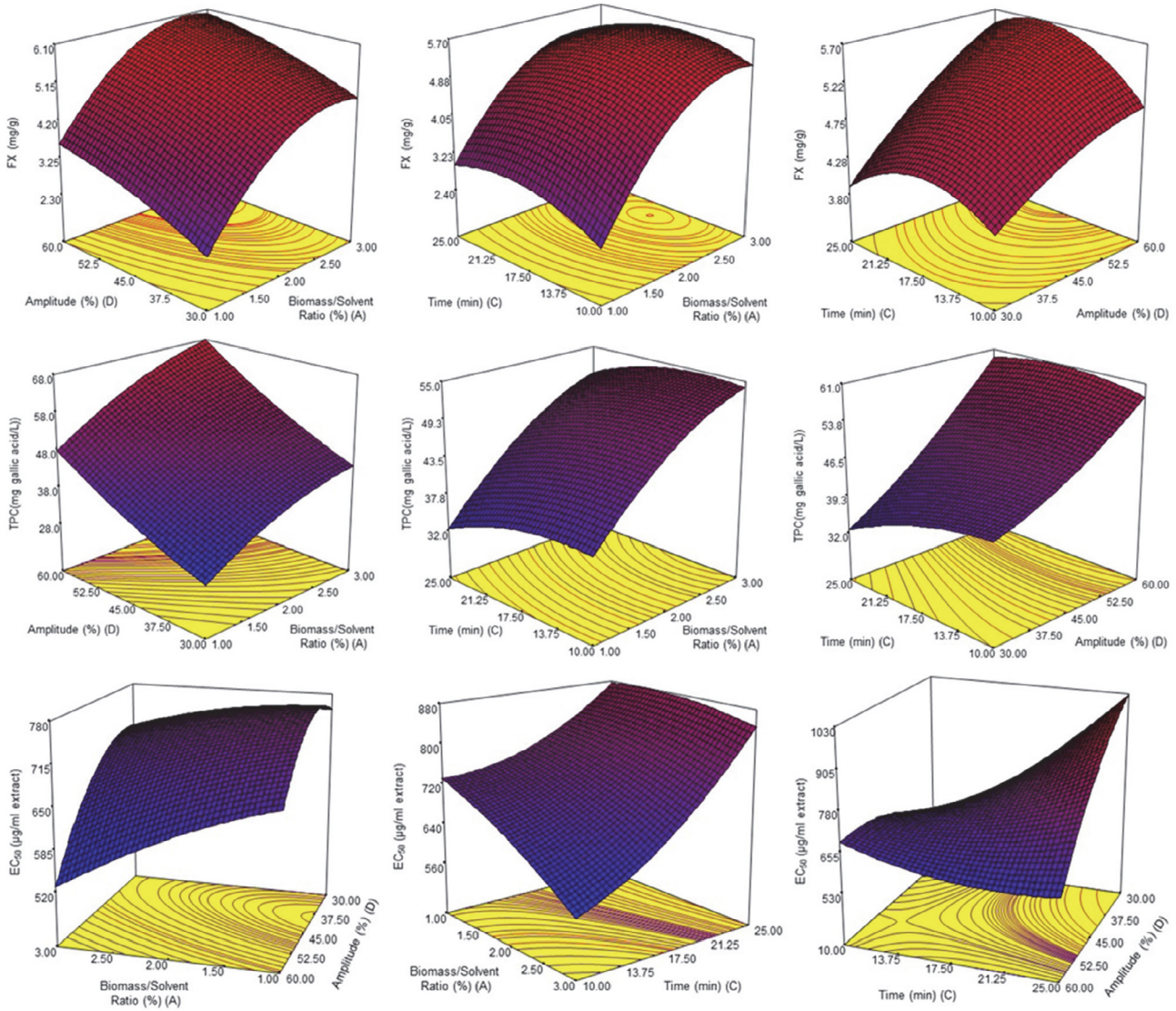


Figure 2. Calculated effects of ultrasound extraction process variables on fucoxanthin content (mg/g), total phenolic content (mg gallic acid /L) and antioxidant activity (EC_{50} µg/mL extract).

Table 4. Results of statistical analysis for verification of optimization

Extraction method	Responses	Predicted Value	Experimental Value[x]	SE[y]	Difference	% Error[z]	*p*-Value
CE	FX (mg/g)	6.83	5.60 ± 0.06	0.0299	1.237	22.05	0.000
	TPC (mg gallic acid /L)	61.84	63.66 ± 1.34	0.669	1.824	2.86	0.053
	DPPH (EC_{50} µg/mL extract)	767.91	763.00 ± 15.88	7.939	4.91	0.64	0.570
UE	FX (mg/g)	6.03	5.24 ± 0.07	0.035	0.79	15.07	0.000
	TPC (mg gallic acid /L)	62.27	67.68 ± 1.58	0.787	5.413	7.997	0.002
	DPPH (EC_{50} µg/mL extract)	615.82	619.90 ± 17.16	8.578	4.08	0.658	0.659
ME	FX (mg/g)	4.49	4.11 ± 0.04	0.019	0.38	9.24	0.000
	TPC (mg gallic acid /L)	40.68	40.87 ± 2.69	1.342	0.193	0.473	0.892
	DPPH (EC_{50} µg/mL extract)	497.44	484.53 ± 9.98	4.992	12.91	2.66	0.061

x Experimental values were expressed as mean ± standard deviation
y Mean standard error
z The % error=(|yexp−ypre|/yexp) × 100

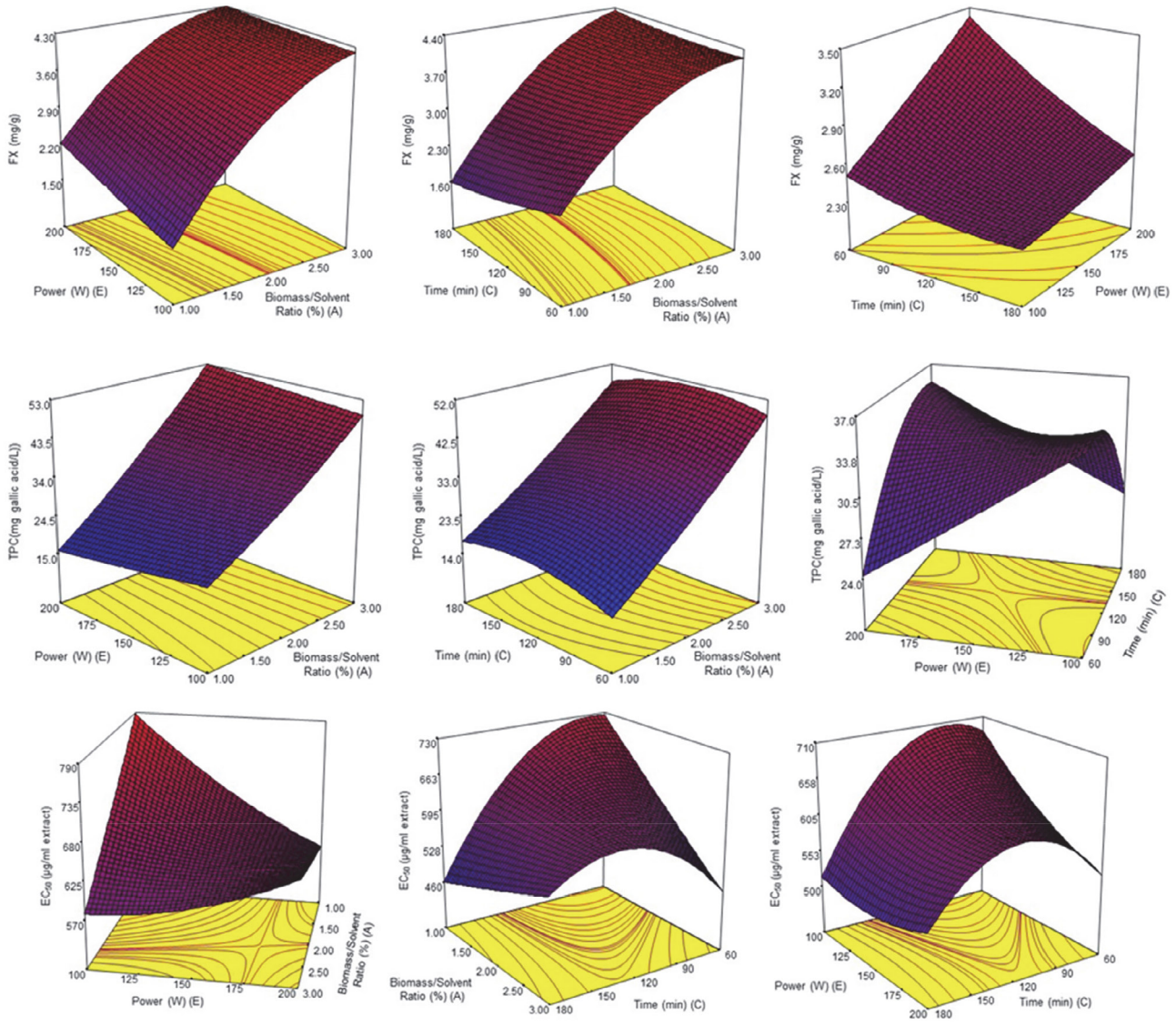


Figure 3. Calculated effects of microwave extraction process variables on fucoxanthin content (mg/g), total phenolic content (mg gallic acid /L) and antioxidant activity (EC_{50} µg/mL extract).

than those obtained from other methods. The amounts of FX obtained by homogenization (5.60 ± 0.06 mg/g) and ultrasound (5.24 ± 0.07 mg/g) extraction methods were close to each other. However, when the biomass/solvent ratio (homogenization extraction: 1.93%, ultrasonic extraction: 2.72%) was compared, homogenization extraction method was found to be more effective than ultrasonic extraction method considering using less biomass.

4. Conclusion

In this study, the effects of extraction method and conditions on fucoxanthin and total phenolic compounds extracted from *Phaeodactylum tricornutum* were evaluated. The optimum points to provide the maximum FX and the acceptable TPC and DPPH antioxidant activity for the process conditions (biomass/solvent ratio, extraction time, amplitude specific to ultrasonic extraction, microwave power specific to microwave extraction and homogenization rate specific to homogenization extraction) of the extraction methods were determined for ultrasonic, microwave and homogenization extraction methods. It was found that the most effective independent variable in obtaining fucoxanthin from *P. tricornutum* was the biomass/solvent ratio for three different extraction methods and the FX, TPC and DPPH antioxidant activity of the extracts increased with the increase in biomass ratio. However, the effect of the extraction time and the process parameters specific to the extraction method should not be ignored. The optimum conditions for all three extraction methods showed that the maximum fucoxanthin of the extracts was

obtained with homogenization and ultrasound extraction methods. However, when the biomass/solvent ratio was compared, homogenization extraction method was found to be more effective than ultrasonic extraction due to using less biomass. This study showed that the extraction process parameters should be evaluated as a whole. In choosing the appropriate extraction method, extraction costs, applicability and sustainability concepts should be considered.

Acknowledgments

This study was a part of Cost Action ES1408 and the authors would like to thank The Scientific and Technological Research Council of Turkey (TUBITAK-115O578) for financial support.

5. References

1. S. Xia, K. Wang, L. Wan, A. Li, Q. Hu, C. Zhang, *Mar. Drugs* **2013**, *11*, 2667–2681. **DOI:**10.3390/md11072667
2. J. Peng, J. P. Yuan, C. F. Wu, J. H. Wang, *Mar. Drugs* **2011**, *9*, 1806–1828. **DOI:**10.3390/md9101806
3. E. Kotake-Nara, A. Nagao, *Mar. Drugs* **2011**, *9*, 1024–1037. **DOI:**10.3390/md9061024
4. R. K. Sangeetha, N. Bhaskar, S. Divakar, V. Baskaran, *Mol. Cell. Biochem.* **2010**, *333*, 299–310. **DOI:**10.1007/s11010-009-0231-1
5. P. Sun, C. C. Wong, Y. Li, Y. He, X. Mao, T. Wu, Y. Ren, F. Chen, *Food Chem.* **2019**, *277*, 566–572. **DOI:**10.1016/j.foodchem.2018.10.133
6. M. Petrushkina, E. Gusev, B. Sorokin, N. Zotko, A. Mamaeva, A. Filimonova, M. Kulikovskiy, Y. Maltsev, I. Yampolsky, E. Guglya, V. Vinokurov, Z. Namsaraev, D. Kuzmin, *Algal Res.* **2017**, *24*, 387–393. **DOI:**10.1016/j.algal.2017.03.016
7. J. C. Kim, *Sep. Sci. Technol.* **2014**, *49*, 410–415. **DOI:**10.1080/01496395.2013.839703
8. A. Piovan, R. Seraglia, B. Bresin, R. Caniato, R. Filippini, *Molecules* **2013**, *18*, 6298–6310. **DOI:**10.3390/molecules18066298
9. A. Fung, N. Hamid, J. Lu, *Food Chem.* **2013**, *136*, 1055–1062. **DOI:**10.1016/j.foodchem.2012.09.024
10. H. Maeda, M. Hosokawa, T. Sashima, K. Funayama, K. Miyashita, *Biochem. Biophys. Res. Commun.* **2005**, *332*, 392–397. **DOI:**10.1016/j.bbrc.2005.05.002
11. S. M. Kim, Y. J. Jung, O. N. Kwon, K. H. Cha, B. H. Um, D. Chung, C. H. Pan, *Appl. Biochem. Biotechnol.* **2012**, *166*, 1843–1855. **DOI:**10.1007/s12010-012-9602-2
12. L. J. Wang, Y. Fan, R. Parsons, G. R. Hu, P. Y. Zhang, F. L. Li, *Mar. Drugs* **2018**, *16*, 33. **DOI:**10.3390/md16010033
13. A. Gómez-Loredo, J. González-Valdez, M. González-González, J. Benavides, M. Rito-Palomares, *J. Chem. Technol. Biotechnol.* **2018**, *93*, 2033–2039. **DOI:**10.1002/jctb.5494
14. W. Zhang, F. Wang, B. Gao, L. Huang, C. Zhang, *Algal Res.* **2018**, *32,* 193–200. **DOI:**10.1016/j.algal.2018.04.002
15. H. Wu, T. Li, G. Wang, S. Dai, H. He, W. Xiang, *Chinese J. Oceanol. Limnol.* **2016**, *34*, 391–398. **DOI:**10.1007/s00343-015-4325-1
16. A. R. Fajardo, L. E. Cerdán, A. R. Medina, F. G. A. Fernández, P. A. G. Moreno, E. M. Grima, *Eur. J. Lipid Sci. Technol.* **2007**, *109*, 120–126. **DOI:**10.1002/ejlt.200600216
17. B. Gilbert-López, A. Barranco, M. Herrero, A. Cifuentes, E. Ibáñez, *Food Res. Int.* **2017**, *99*, 1056–1065. **DOI:**10.1016/j.foodres.2016.04.022
18. D. D. McClure, A. Luiz, B. Gerber, G. W. Barton, J. M. Kavanagh, *Algal Res.* **2018**, *29*, 41–48. **DOI:**10.1016/j.algal.2017.11.015
19. S. C. Foo, F. M. Yusoff, M. Ismail, M. Basri, N. M. H. Khong, K. W. Chan, S. K. Yau, *Asian Pac. J. Trop. Biomed.* **2015**, *5*, 834–840. **DOI:**10.1016/j.apjtb.2015.06.003
20. R. R. L. Guillard, J. H. Ryther, *Can. J. Microbiol.* **1962**, *8*, 229–239. **DOI:**10.1139/m62-029
21. Z. Demirel, R. Tok, I. İlter, S. Akyıl, A. Erdoğan, M. Koç, F. Kaymak-Ertekin, M. Conk-Dalay, *Aquat. Res.* **2018**, *1*, 52–64. **DOI:**10.3153/AR18008
22. I. İlter, S. Akyıl, Z. Demirel, M. Koç, M. Conk-Dalay, F. Kaymak-Ertekin, *J. Food Compos. Anal.* **2018**, *70*, 78–88. **DOI:**10.1016/j.jfca.2018.04.007
23. A. Erdogan, Z. Demirel, M. Conk-Dalay, A. E. Eroglu, *Turkish J. Fish. Aquat. Sci.* **2016**, *16*, 491–498. **DOI:**10.4194/1303-2712-v16_3_01
24. G. Oboh, *LWT - Food Sci. Technol.* **2005**, *38,* 513–517. **DOI:**10.1016/j.lwt.2004.07.007
25. Y. Xu, F. Cai, Z. Yu, L. Zhang, X. Li, Y. Yang, G. Liu, *Food Chem.* **2016**, *194*, 650–658. **DOI:**10.1016/j.foodchem.2015.08.061
26. V. Pasquet, J. R. Chérouvrier, F. Farhat, V. Thiéry, J. M. Piot, J. B. Bérard, R. Kaas, B. Serive, T. Patrice, J. P. Cadoret, L. Picot, *Process Biochem.***2011**, *46*, 59–67. **DOI:**10.1016/j.procbio.2010.07.009
27. A. Kawee-ai, A. Kuntiya, S. M. Kim, *Nat. Prod. Commun.* **2013**, *8,* 1381–6. **DOI:**10.1177/1934578X1300801010
28. H. Maeda, S. Fukuda, H. Izumi, N. Saga, *Mar. Drugs* **2018**, *16*, 255. **DOI:**10.3390/md16080255
29. S. Both, F. Chemat, J. Strube, *Ultrason. Sonochem.* **2014**, *21*, 1030–1034. **DOI:**10.1016/j.ultsonch.2013.11.005
30. Y. Deng, Y. Zhao, O. Padilla-Zakour, G. Yang, *Ind. Crops Prod.* **2015**, *74*, 803–809. **DOI:**10.1016/j.indcrop.2015.06.014
31. S. C. Foo, F. M. Yusoff, M. Ismail, M. Basri, S. K. Yau, N. M. H. Khong, K. W. Chan, M. Ebrahimi, *J. Biotechnol.* **2017**, *241*, 175–183. **DOI:**10.1016/j.jbiotec.2016.11.026
32. W. Brand-Williams, M. E. Cuvelier, C. Berset, *LWT - Food Sci. Technol.* **1995**, *28*, 25–30. **DOI:**10.1016/S0023-6438(95)80008-5
33. M. K. W. A. Airanthi, M. Hosokawa, K. Miyashita, *J. Food Sci.* **2011**, *76*, 104–11. **DOI:**10.1111/j.1750-3841.2010.01915.x
34. S. L. Holdt, S. Kraan, *J. Appl. Phycol.* **2011**, *23*, 543–597. **DOI:**10.1007/s10811-010-9632-5
35. E. M. Balboa, E. Conde, A. Moure, E. Falqué, H. Domínguez, *Food Chem.* **2013**, *138*, 1764–1785. **DOI:**10.1016/j.foodchem.2012.11.026

36. N. M. Sachindra, E. Sato, H. Maeda, M. Hosokawa, Y. Niwano, M. Kohno, K. Miyashita, *J. Agric. Food Chem.* **2007**, *55,* 8516–8522. **DOI:**10.1021/jf071848a

37. S. C. Foo, F. M. Yusoff, M. Ismail, M. Basri, S. K. Yau, N. M. H. Khong, K. W. Chan and M. Ebrahimi, *J. Biotechnol*, **2017**, *241*, 175–183. **DOI:**10.1111/j.1750-3841.2010.01915.x

Povzetek

Preučili smo vpliv ekstrakcije s homogenizacijo, ultrazvokom in mikrovalovi, ter pogoje ekstrakcije, na vsebnost fukoksantina in celotnih fenolov ter antioksidativno aktivnost ekstraktov pridobljenih iz *Phaeodactylum tricornutum*. Za vse troje se je kot najpomembnejši dejavnik izkazalo razmerje med količino topila in biomase. Najvišjo vsebnost fukoksantina (5.60 ± 0.06 mg/g) in antioksidativne aktivnosti (763.00 ± 15.88 EC50 μg/mL ekstrakta) smo dosegli z ekstrakcijo s homogenizacijo pri razmerju biomasa/topilo 1.93 %, homogenizacijo pri ~5200 rpm in časom ekstrakcije 14.2 min. Čeprav smo pri ekstrakciji z mikrovalovi dosegli približno enako stopnjo vsebnosti fukoksantina (5.24 ± 0.07 mg/g), TPC (67.68 ± 1.58 mg galne kisline/L) in antioksidativne aktivnosti (619.90 ± 17.16 EC50 μg/mL ekstrakta) pri amplitudi 55.72 %, smo za to potrebovali višje razmerje biomasa/topilo (2.72 %) in daljši čas ekstrakcije (17.37 min). Najnižja vsebnost fukoksantina in TPC ter antioksidativna aktivnost pa so bili določeni pri ekstrakciji z mikrovalovi.

Except when otherwise noted, articles in this journal are published under the terms and conditions of the Creative Commons Attribution 4.0 International License

DOI: 10.17344/acsi.2020.6175 *Acta Chim. Slov.* **2020,** *67,* 1262–1272
creative commons

Scientific paper

Assessment of the Interaction of Aggregatin Protein with Amyloid-Beta (Aβ) at the Molecular Level via In Silico Analysis

Nail Besli[1] and Guven Yenmis[2,*]

[1] *Department of Medical Biology, Faculty of Medicine, University of Health Sciences, Istanbul, Turkey*

[2] *Department of Medical Biology, Faculty of Medicine, Biruni University, Istanbul, Turkey*

* *Corresponding author: E-mail: gyenmis@biruni.edu.tr ; guvenyenmis@yahoo.com*

Received: 06-08-2020

Abstract

Alzheimer's disease is a major neurodegenerative illness whose prevalence is increasing worldwide but the molecular mechanism remains unclear. There is some scientific evidence that the molecular complexity of Alzheimer's pathophysiology is associated with the formation of extracellular amyloid-beta plaques in the brain. A novel cross- phenotype association analysis of imaging genetics reported a brain atrophy susceptibility gene, namely FAM222A and the protein Aggregatin encoded by FAM222A interacts with amyloid-beta (Aβ)-peptide (1-42) through its N-terminal Aβ binding domain and facilitates Aβ aggregation. The function of Aggregatin protein is unknown, and its three-dimensional structure has not been analyzed experimentally yet. Our goal was to investigate the interaction of Aggregatin with Aβ in detail by in silico analysis, including the 3D structure prediction analysis of Aggregatin protein by homology modeling. Our analysis verified the interaction of the C-terminal domain of model protein with the N-terminal domain of Aβ. This is the first attempt to demonstrate the interaction of Aggregatin with the Aβ. These results confirmed in vitro and in vivo study reports claiming FAM222A helping to ease the aggregating of the Aβ-peptide.

Keywords: Alzheimer's disease; amyloid-Beta; aggregatin; protein-peptide docking; protein structure prediction

1. Introduction

Alzheimer's disease (AD) is observed as a widespread and incurable ailment worldwide because of the elevated average human lifespan in recent years. Although the risk factors described as an increased lifetime and aging; the classic Mendelian inheritance with autosomal dominant pattern and multi-factorial features have also suggested as possible risk factors. The elevation of AD patient number in the population has become a social and an economic problem as an AD patient becomes dependent on another person.[1,2] The global number of AD patients who have dementia was estimated to be 43·8 million worldwide[3] and over 5 million in the USA. Through the middle of the century, this number may dramatically increase in the USA to 13.8 million people with Alzheimer's dementia.[4]

The neuropathology indicator of AD, which in turn leads to dementia, is the presence of neurofibrillary tangles inside the cell, and the formation of amyloid-beta (Aβ) peptides out of the cell, resulting in cerebral atrophy.[5] One of these main pathologic characteristics of AD, Aβ aggregation results from the presence of oligomeric Aβ due to the processing of proteolytic lysis of the amyloid precursor protein (APP) in an inaccurate form and finally aggregation in Aβ fibrils and plaques as an intracellular lesion.[6] It is unclear what the exact function of APP is, however, its role in cell growth and biological activities including signal transduction and neuronal development has been shown in several studies.[7]

Understanding the crucial patterns of the origin of the Aβ pathology is based on figuring out the mechanisms that show how the monomers that build up the Aβ aggregates are formed and how oligomeric clusters form the lesions. Many erroneous peptides formed by proteolytic processing of APP might be the major basis on the neuronal dysfunction in AD. These peptides are mostly being encountered in the hippocampus region in the brain.[8] The cleavage of APP may be processed in two alternative pathways, non-amyloidogenic and amyloidogenic, respectively. In the non-amyloidogenic proteolytic pathway, for example, APP is normally processed through α-secretase and λ-secretase, producing soluble peptides, while it forms

indissoluble fragments as amyloid-beta peptides that aggregate in the amyloidogenic process.[6,9] Further investigations are required to clarify the mechanisms associated with AD in the case of aggregation of these peptides after proteolytic processing.

The amino acid(aa) sequence of Aβ42 from amyloid plaques was initially uncovered in the 1980s for the first time.[10] Aβ is commonly thought to be intrinsically unstructured and therefore cannot be crystallized by standard techniques. Hence, various studies were deduced on the structure optimization that can preserve Aβ peptides. The 3D structure of various Aβ peptides was identified by the experimental tools including nuclear magnetic resonance (NMR, PDB: 1AMC, 1AMB, 1BA4, 1IYT, 1QWP, 1Z0Q) and X-ray crystallography (PDB: 2Y29, 4M1C, 4MVI, 4MVK, 4MVL). Not interestingly, most of the information about the structure of Aβ was gained from NMR and molecular dynamics.[9] Attained models of Aβ peptide structure (1–28) by NMR represented a conversion-folding of α-helix into the β-sheet structure- taking place during the early stages of amyloid deposition in the AD.[10] Aβ peptide (1-28) is the main part of the amyloid plaques in AD and histidine-13 and lysine-16 of its chains are on the same face of the helix. Also, Aβ (1–40) peptide in the physiological condition is present in an α-helical structure whilst amyloid fibrils by these proteins shaped β-sheet structures. This structural modulation from α-helix to β-sheet is considered as the critical step in the formation of aggregation.[9]

Most of the studies carried out in vivo and in vitro so far have been focused on elucidating their molecular complexity concerning the accumulation of amyloid-beta and the hyperphosphorylated microtubule protein tau in the pathology of Alzheimer. In a very recent study, Yan and et al. have reported that a brain atrophy susceptibility gene-FAM222A (Family 222 member A) agglomerates in amyloid deposits, interacting by amyloid-β (Aβ) via its N-terminal Aβ binding domain. The expression of the protein synthesized termed as Aggregatin was typically detected in the brain and spinal cord of the central nervous system (CNS) using a specific antibody in vitro. The length of Aggregatin is 452 aa long and its function is still uncertain. In this survey, they showed how FAM222A accumulation interacts physically with amyloid-β via its N-terminal Aβ binding domain. This is one of the most critical studies performed on a patient with AD and in an AD mouse model that shed a light on the pathophysiology of AD.[5]

In the current study, we aimed to predict the three-dimensional structure of Aggregatin using various approaches considering the findings that show the interaction of the molecules of interest. The molecular docking was also performed based on the inspiration of this founding. We used homology modeling to obtain model proteins and then performed a protein-peptide docking study with several approaches. The prediction of protein structure by homology modeling has been performed broadly for folding proteins whereas it is limited in misfolded protein and aggregate applications. As summarized in Figure 1, we used all authenticated/trusted bioinformatics tools to predict the three-dimensional structure of Aggregatin protein. To increase the accuracy and docking performance of the model protein, we subjected the model proteins from each bioinformatics server to two different tools for the structural-quality analysis and preferred the higher quality one. Besides, we monitored the domain analysis on the primer structure of Aggregatin and predicted which part of its amino acids related to the localization in the plasma membrane. On the other hand, we investigated functionally similar genes with the FAM222A gene.

More mechanistic studies are necessary to get sufficient information about the 3D structure and the characterization of the FAM222A gene product association with Alzheimer's pathology. Considering the critical roles of Aggregatin, it is fundamental to pinpoint its physicochemical characteristics at the atomic structure level. Our computational approach based results will broaden the horizon of our knowledge on the pathogenesis of AD and support to clarify a candidate protein to play a possible critical role in amyloidosis.

2. Materials and Methods

2. 1. Prediction of the 3D Structure of Aggregatin by Homology Modeling

All the work-flow was summarized in Fig.1. The protein sequence encoded by Human FAM222A (Reference Sequence: NP_116218.2) and FAM222B (Family 222 member B) (UniProtKB/Swiss-Prot: Q8WU58.1) from NCBI in FASTA format were fetched from NCBI in FASTA format, PSIPRED[11] was used to predict the secondary structure of the Aggregatin. The amino acid sequence was subjected to I-TASSER[12], PHYRE2 [13], Robetta[14,15] common tools for based-homology modeling to have a tertiary structure of Aggregatin as a model,. The Qualitative Model Energy Analysis (QMEANDisCo)[16] and ProSAweb[17] tools were used for the quality control of model proteins.

2. 2. Sequence Analysis

PSI-BLAST (Position-Specific Iterated BLAST)[18] was performed for pairwise. All general and scoring parameters including MATRIX: BLOSUM62 and the threshold value (0.005) were left as the default settings. The primary structure of the sequence was predicted using DomPred[19] (Protein Domain Prediction) and the outputs were interpreted in Jalview 2.11.0.[20]

2. 3. Visualization of Molecular Docking

The primary structure of Aggregatin was visualized using Jalview 2.11 and the PyMOL[21] software was used to

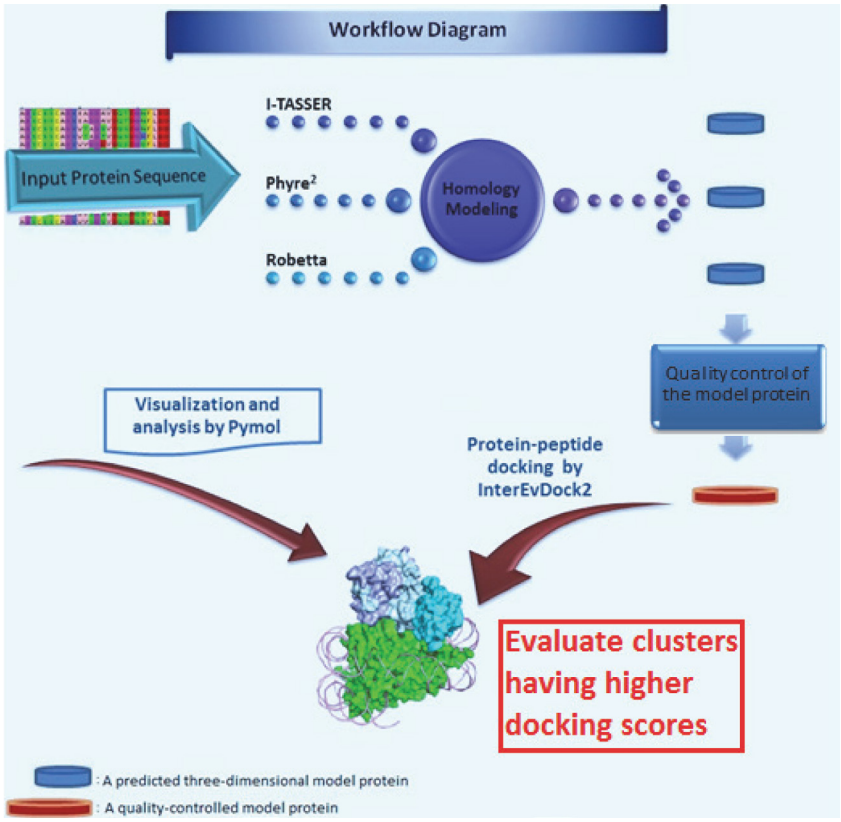


Figure 1. A pipeline of molecular docking of Aggregatin and Amyloid-beta(Aβ) peptide. There are four key steps in the pipeline. First, the prediction of the 3D structure of Aggregatin. Second, the model protein structure analysis for quality. Third, protein-peptide docking by the InterEvDock2 server. Forth, the final analysis by the PyMOL software.

represent the tertiary structure proteins-peptides and analyze the docking results at the atomic structure level. The NMR monomer structures of Amyloid Beta-Peptide (1–28 Aβ) (PDB ID:1AMB), and (1–42 Aβ) (PDB:1IYT) from PDB (Protein Data Bank) at http://www.rcsb.org/ were retrieved for the protein-peptide interaction study. Fig.3 was

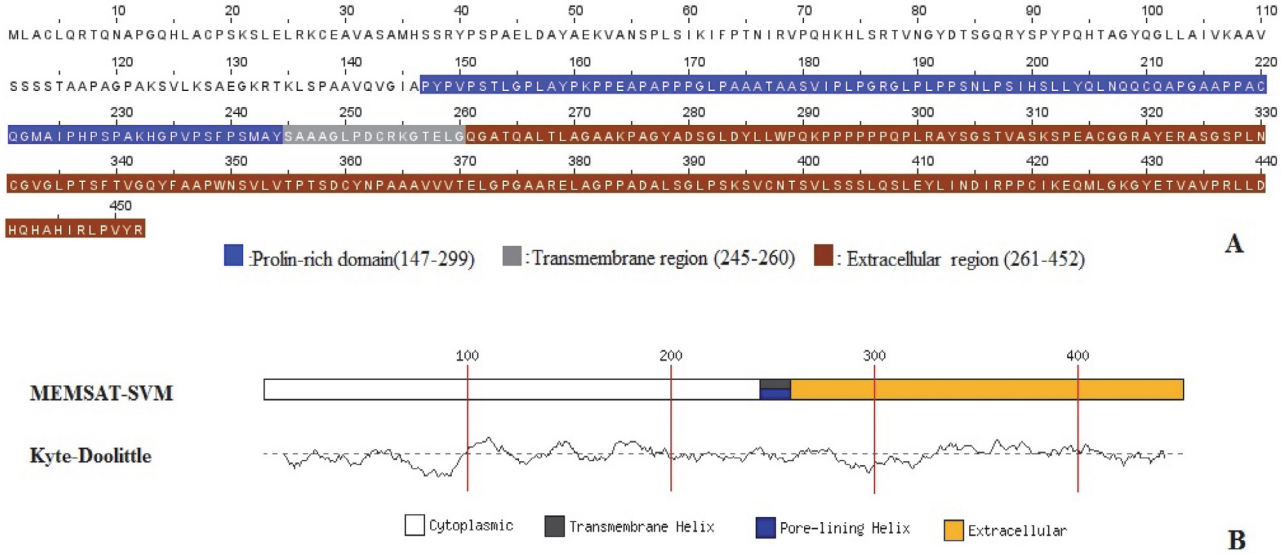


Figure 2. A.) The primary structure of FAM222A encoded Aggregatin protein. PSIPRED was used to predict the actual primary structure. The cytoplasmic part is colorless, the proline-rich region(147–299) gained from the UniProt tool is colored with navy blue. The transmembrane region (245–260 residues) is gray and the extracellular part region (261–452) is colored with brown. B.) MEMSAT-SVM shows the transmembrane helix topology and the Kyte-Doolittle scale presents the hydrophobic amino acids.

retrieved from the Protein Data Bank in Europe (PDBe) which is available at https://www.ebi.ac.uk/pdbe/ to visualize the N-terminal and C- terminal domain of Amyloid-beta peptide 42. All docking complexes were conducted by InterEvDock2[22–24] online server via using the FRODOCK2[25] and SOAP_PP.[26]

3. Results

3. 1. Domain Prediction Analysis

In the domain prediction analysis with DomPred, the parts to be localized in the transmembrane region in certain series domains were predicted as hydrophobic amino acids represented by the Kyte-Doolittle scale denotes. According to the primary structure of the Aggregatin, the range 147–299 aa is a proline-rich region and bound to the membrane in a helix form, and the remained part extends as the extracellular part. Besides, its N-terminal part is in the cytoplasm, whereas the C-terminal is outside the cell and the sequence of 244–259 aa -the pore-lining part- is in the membrane (See Fig.2).

We also performed the domain prediction of the sequence of FAM222B protein. We used the GeneMANIA[29] online server to search whether FAM222A is functionally related to any gene. We found that FAM222A has a shared domain with FAM222B. Thus, we also performed the domain prediction of the sequence of FAM222B protein, which -we think- would be a clue for in vitro studies (see Fig. 3). The FAM222A and FAM222B are localized in the nucleoplasm, share the same domain, and belong to the same protein family, and their alignments result per ident 49.04% in the blastp. Although the FAM222B has been confirmed in vitro to be localized merely in the nucleoplasm, it's transmembrane and extracellular part, the glycine-rich region, and the signal peptide part domains were predicted to be in the cell membrane (not shown).

3. 2. The PDB sequence viewer of Amyloid-Beta$_{42}$

To find out which residues is N- or C-terminal domain, thus the interaction between β-Amyloid$_{42}$ peptide and Aggregatin at the atomic side level, we attained the Aβ_{42} chart retrieved from PDBe.

According to this chart, the N-terminal domain of the Aβ_{42} sequence was the first 27 residues, owing to the combination of the data from several databases such as CATH[31] and SCOPE [32] (See Fig.4).

3. 3. The Selection of Model Aggregatin Protein

QMEAN tool was used to control the quality of the model protein before the docking process and determine the accuracy rate of the three bioinformatics tools selected for Aggregatin. As a result, the model protein from the Robetta was subjected to protein-peptide docking. Models retrieved from the other tools were determined to be inapplicable for the docking process.

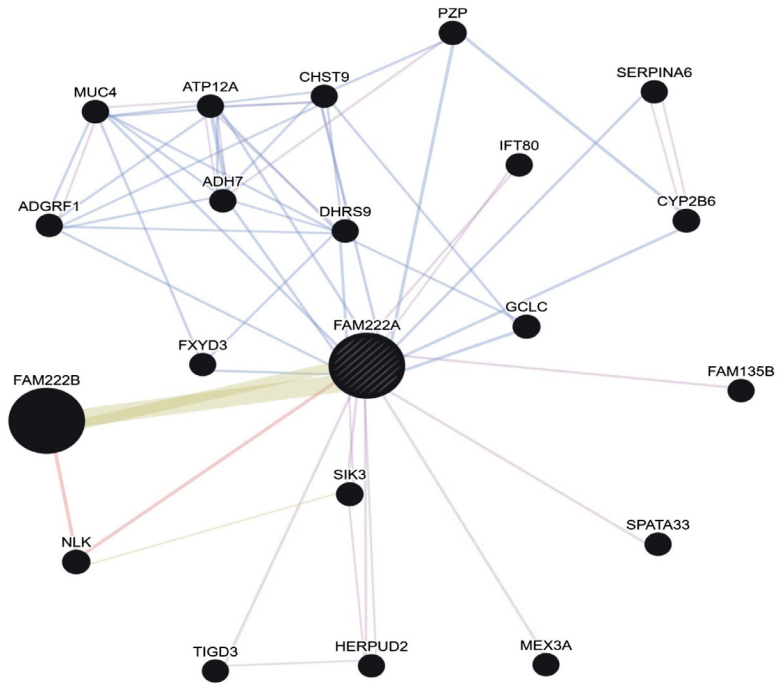


Figure 3. GeneMANIA found functionally similar genes using a wealth of genomics and proteomics data of FAM222A related genes. According to this network, between FAM222A and FAM222B have shared protein domains, and sequence similarities (0.59%) concerning INTERPRO and PFAM.

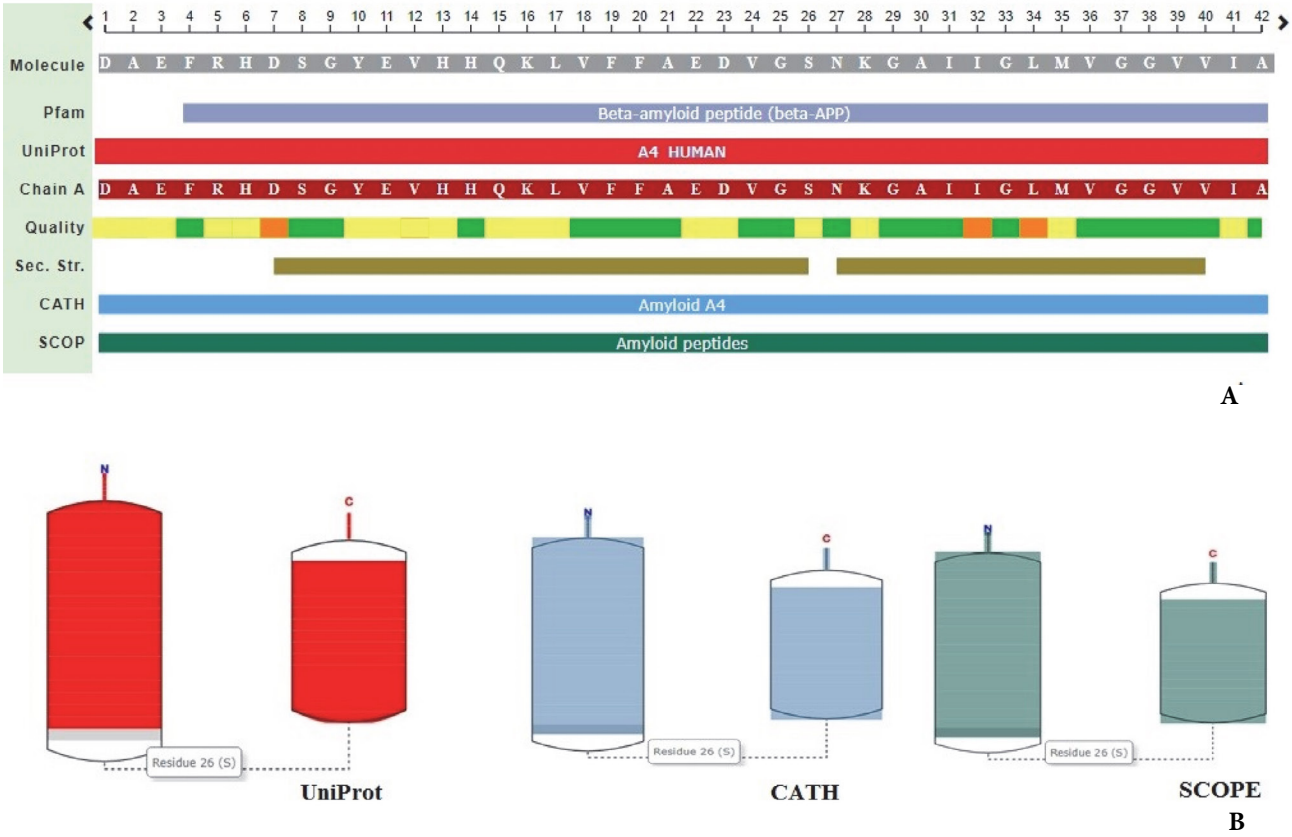


Figure 4. A.) The chart represents the sequence viewer of the N-terminal and C- terminal domains of 1–42 Aβ peptide (PDB:1IYT). On the quality band, the residue of validation in yellow color indicates side chain or ramachandran outliers, in orange color indicates together both side chair and ramachandran outliers, and in green color represents no validation reported issue (Protein Data Bank in Europe). B.) According to some databases such as UniProt (red), CATH (blue), and SCOPE (green), 1–26 residues of Aβ peptide represent the N-terminal domain, and 27–42 residues of Aβ peptide represent C- terminal domain.

3. 4. Alignment

Although the sequence per identity retrieved from the homology modeling by PSI-BLAST is 31–26% (see Table 1), there are sufficiently acceptable docking results as shown in Fig. 6-10. Besides, the sequence similarity under 30% does not mean that the model protein retrieved from the comparative analysis will have low reliability. Some primary sequences may have been conserved, and homology modeling can predict as accurately as experimental low-resolution models.[34]

Table 1. The list of PSI-BLAST results of the amino acid sequence of Aggregatin. The list of homolog proteins is arranged according to their percent identities with Aggregatin. According to the outcomes, the percent identity of the proteins ranges between 31-26%.

Description(Sequences with E-value WORSE than the threshold)	Max Score	Total Score	Query Cover	E value	Per. ident	Accession
Chain C, Apoptosis-stimulating of p53 protein 2 [Homo sapiens]	32.3	32.3	16%	0.95	26.67	6GHM_C
Chain B, APOPTOSIS STIMULATING OF P53 PROTEIN 2 [Homo sapiens]	32.3	32.3	16%	1.1	26.67	4A63_B
Chain B, 53BP2 [Homo sapiens]	32.3	32.3	16%	1.1	26.67	1YCS_B
Chain B, Light chain (kappa) of CBTAU-24.1 antibody [Homo sapiens]	31.2	31.2	15%	2.6	29.11	5ZIA_B
Chain L, fAb Light chain [Mus musculus]	30	30	14%	5.8	31.34	5OBF_L
Chain L, Fab Fragment, Light Chain [Mus musculus]	29.3	29.3	17%	9.4	27.72	1MHP_L
Chain E, VL of Fab 11G1 [Mus musculus]	28.5	28.5	15%	9.4	29.63	6AJ9_E

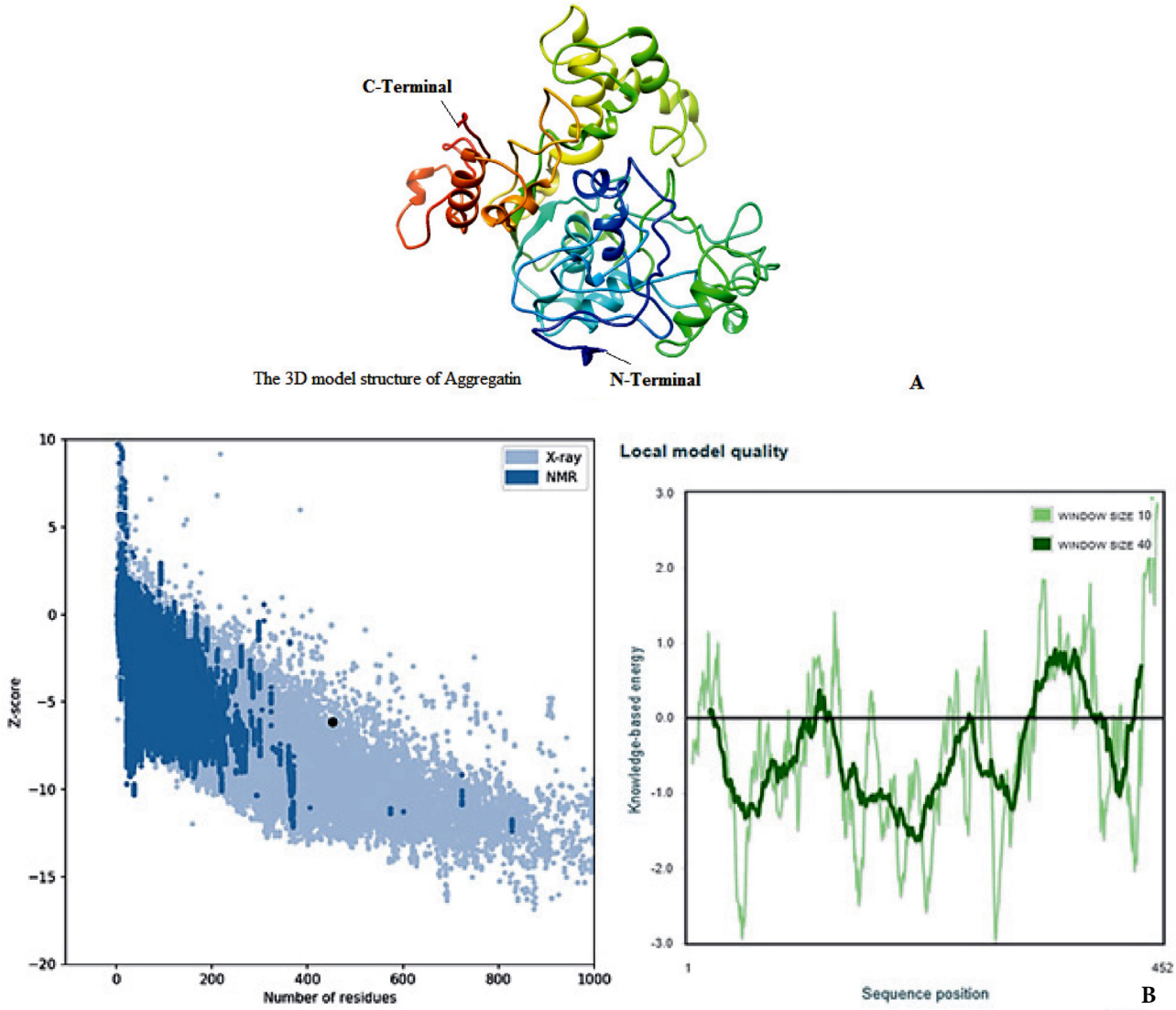


Figure 5. A.) The overall 3D structure of predicted Aggregatin. Robetta server predicted the 3D model structure of Aggregatin protein by the homology model. The model was subjected to a procedure of protein-peptide docking. The cartoon model representation and image were generated with Chimera 1.14.[33] Structures are symbolized as interactive colored ribbons to show strand and helix forms. B.) ProSA-web service analysis of Aggregatin. The black dot denotes that the input Aggregatin is between Z-score values of the experimental structures relative to the several amino acid residues and energy graph of the predicted Aggregatin. The Z-score or the overall model-quality was designated to be –6.15 in the X-ray region of the plot(Left). The other plot represents the local quality concerning the number of sequence positions (Right).

3. 5. Docking Outcomes of Aggregatin and Amyloid-Beta Peptides

The docking score and interaction outcomes are listed in Table 2–3. As shown in the representative models from 8 best clusters in Table 2, IES1_A and FRODOCK1_C by higher scores and SOAP_A by lower energy score are top consensus complexes. According to the docking online server, in IES6_ B docking complex, the residues of GLN442, HIS443 (Aggregatin chain) and HIS13, PHE20 (Aβ peptide) between the top 5 residues (on each chain) predicted to be involved in contacts based on the consensus of top 10 models from each method (see Figure 6.A, B, C). As an overall result of docking, Aggregatin protein contacted the residues in the C-terminal region from the N-terminal region of the amyloid-beta 42.

Representative models from 7 best clusters were shown in Table 3, FRODOCK2_A and IES2_B_1 docking complexes, and SOAP_A_2 are the top consensus complexes. According to the docking online server, IES6_ B docking complex interacts the residue ARG447, GLY429 (Aggregatin chain in C-terminal region) and HIS13, LYS16 (Aβ peptide in N-terminal region) between the top 5 residues (on each chain) predicted to be involved in contacts based on the consensus of top 10 models from each method (see Fig. 9B and Fig. 10 B2).

Table 2. Probable interface residues on each protein between the model of Aggregatin and $A\beta_{42}$ peptides. IES and FRODOCK2 score (higher is better), SOAP_PP score (lower is better).

Docking complexes	Residue number($A\beta_{42}$)	Aggregatin	Docking score
IES1_A	HIS6	TYR303	423.1
IES6_ B	HIS13, LEU17, PHE20	ASP359, HIS443 GLN442	372.17
IES9_C	TYR10, HIS13	ALA365, VAL333	360.15
SOAP_B	TYR10, VAL18	ARG447, HIS443	–16473.52
SOAP_A	HIS6, GLY9, GLY37	ARG447,HIS445,LEU353	–16148.85
FRODOCK2_A	GLY29, ILE32	GLN442	2267.23
FRODOCK4_B	ARG5, HIS13	PRO147, TYR321	2062.62
FRODOCK1_C	GLU11, LYS16, GLU22 ILE31, LEU34	TYR148, ARG319, SER312, SER241	2290.05

Table 3. The interface residues on each protein between the model of Aggregatin and $A\beta_{28}$ peptides. IES and FRODOCK2 score (higher is better), SOAP_PP score (lower is better).

Docking complexes	Residue number($A\beta_{28}$)	Aggregatin	Docking score
FRODOCK2_A	ARG5, TYR10	LYS135, GLY155	1727.14
FRODOCK4_B	HIS13, LYS16	ARG447, GLY429	1699.13
FRODOCK8_C	TYR10	HIS445	1646.18
SOAP_A_1	LYS16	ASP284,TYR285,CYS360	–15623.78
SOAP_A_2	GLN15	ASN195	–15795.12
IES2_B_1	TYR10, HIS6	LYS135, ARG133	236.81
IES3_B_2	HIS13, LYS16	ARG447, GLY429	226.48

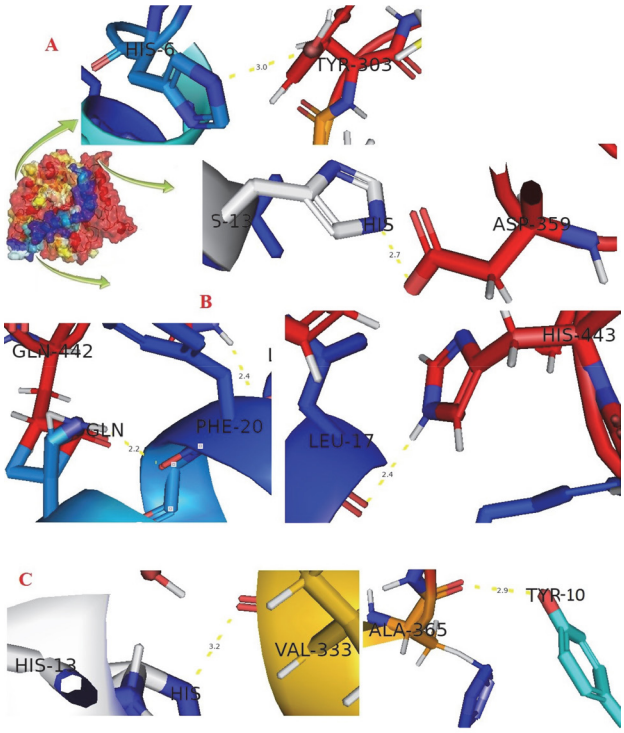


Figure 6. The InterEvDock2 model results of Aggregatin and Aβ42 peptides. The docking complex is represented in a surface representation, colored by (Aβ42 in blue color and Aggregatin in red) A.) Aggregatin(TYR303) interacts with the residue HIS6 of Aβ42 having the highest energy score. B.) Aggregatin(ASP359) interacts with HIS13, GLN442 with PHE20, and HIS443 with LEU17. C.) Aggregatin(VAL333) interacts with HIS13, and ALA365 with TYR10 in the N-terminal domain of Aβ1-42 peptide. The highest score belongs to the model in section A (see Table 2).

The results of both Aβ42 and Aβ28 docking with Aggregatin protein are ARG5 HIS6, HIS13, and TYR10 residues that commonly interact. Binding modes of Aggregatin with $A\beta_{42}$ and $A\beta_{28}$ by molecular docking simulation

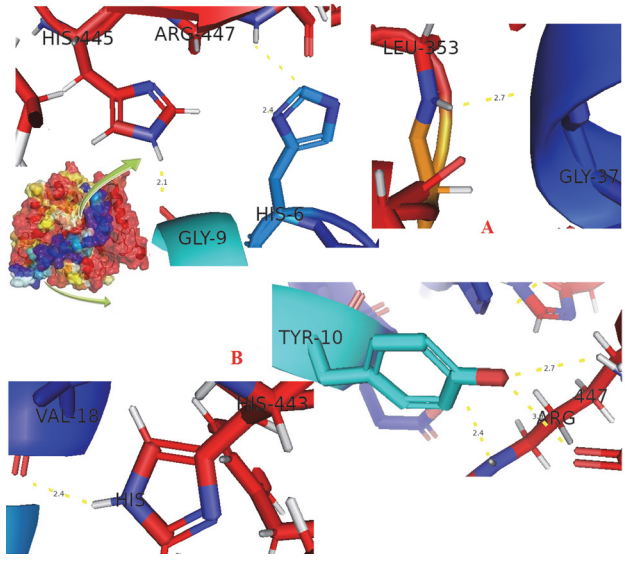


Figure 7. The SOAP_PP model results of Aggregatin and Aβ42 peptides. Binding modes of Aggregatin and $A\beta_{42}$ in surface representations are shown. A.) Aggregatin(HIS445) interacts with GLY9, ARG447 with HIS6, LEU353 with GLY37 of Aβ42 with a lower energy score. B.) Aggregatin(ARG447) interacts with TYR10 and HIS443 with VAL18 of $A\beta_{42}$. HIS6, GLY9 (of section A), and TYR10, and VAL18 (of section B) are in the N-terminal domain of the $A\beta_{1\text{-}42}$ peptide whereas GLY37 in section A is in the C-terminal domain of the $A\beta_{42}$.

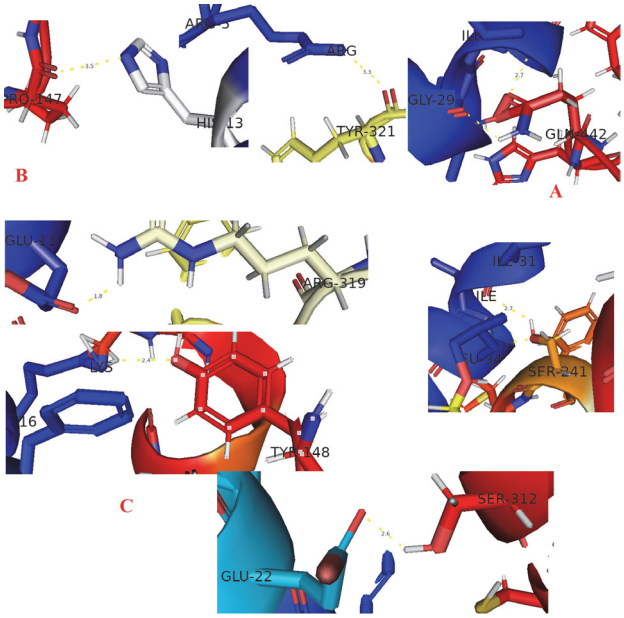


Figure 8. The FRODOCK2 model result of Aggregatin and Aβ42 peptides. Binding modes of Aggregatin and Aβ42 in surface representations are shown. A.) Aggregatin(GLN442) interacts with the residue GLN29 and ILE32 of Aβ. B.) Aggregatin(TRY321) interacts with ARG5, PRO147 with HIS13. C.) Aggregatin(TYR148) interacts with LYS16, ARG319 with GLU11, and SER312 with GLU22, and SER241 with ILE31/LEU34. In this binding mode of the simulation, GLU11, LYS16, and GLU22(of section A) and ARG5, and HIS13(of section B) are in the N-terminal domain of Aβ1-42 peptide whereas GLY29, ILE32, and ILE31, and LEU34 (of section C) are in the C-terminal domain of $A\beta_{42}$.

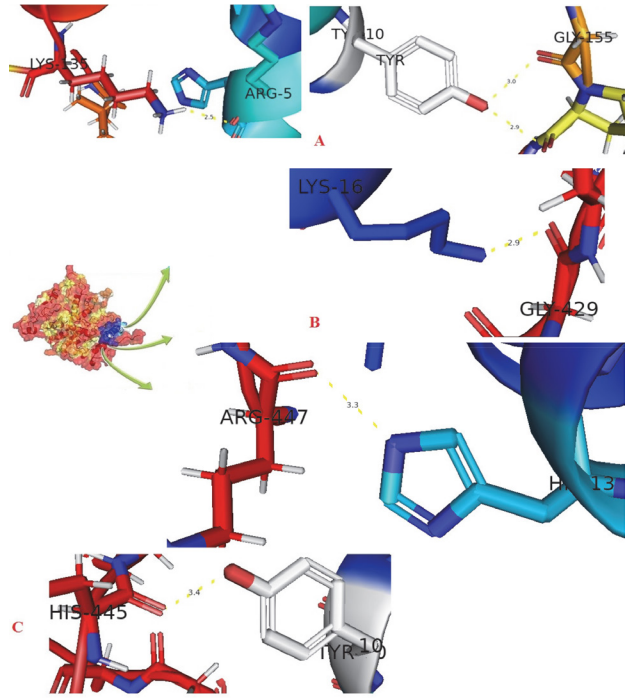


Figure 9. The FRODOCK2 model results of Aggregatin and $A\beta_{28}$ peptides. Binding modes of Aggregatin and Aβ42 in surface representations are shown. A.) Aggregatin(LYS135) interacts with the residue of ARG5, GLY155 with TYR10 of the $A\beta_{28}$. Aggregatin(LYS429) interacts with LYS16, ARG447 with HIS13 of the $A\beta_{28}$. C.) Aggregatin(HIS445) interacts with TYR10 of the $A\beta_{28}$. In this binding mode, TYR10, HIS13, and ARG5 residues are common to both $A\beta_{28}$ and $A\beta_{42}$ in docking results.

are shown in Figure 6-10. Binding mode is colored by red (Aggregatin) and blue (amyloid-beta). Figures are generated by PyMOL.

4. Discussion

This research seeks to address the association of Aggregatin protein, whose function and three-dimensional structure is not characterized yet, with Alzheimer's pathology using in silico analysis. The interaction of Aggregatin with Amyloid-beta and lesion-forming complex of both was elucidated since an extracellular aggregate formation observed in Alzheimer's pathology.[5] Even though Aggregatin is expressed in the nerve cells, it remains uncertain from which part of the cell and compartment it is released and how it forms a core with the extracellular amyloid-beta plaques. Yet, the in vitro studies carried out so far showed that Aggregatin is located in the nucleoplasm and plasma membrane of the cell parts as well as in the mitochondria and focal adhesion.[27]

Protein structures may comprise of multiple intense foldable parts named domains. These domains contain typical hydrophobic cores, can be folded free of each other, and frequently connected to establish distinct functions.[28] For this purpose, our first approach in this study was to predict the domain of the Aggregatin's aa sequence and find out if there is a potential significant aa sequence such as a signal peptide being used as the protein binding interfaces.

Domain prediction using the actual sequence may lead to crucial consequences linking theoretical knowledge to the experimental studies. During the structural research of the proteins by experimental studies such as NMR or X-ray crystallography, the achievement is limited to single-domain proteins rather than full multi-domain proteins.[30] Thus, for structural biologists, it would be meaningful to analyze the primary structure of proteins as it would be more logical to classify single-domain proteins in a distinct category than the multi-domain ones. In our results, Computational analysis of the membrane localization of Aggregatin protein validates in vitro studies (see Fig. 2).

Robetta is a protein structure prediction service continuously evaluated with CAMEO (Continuous Automated Model EvaluatiOn), which constantly assesses the accuracy and reliability of the prediction. Among other prediction tools of CAMEO, Robetta and QMEAN are the first-line by time-based statistical confidence and reliable performances. In addition to these tools, the ProSA-web

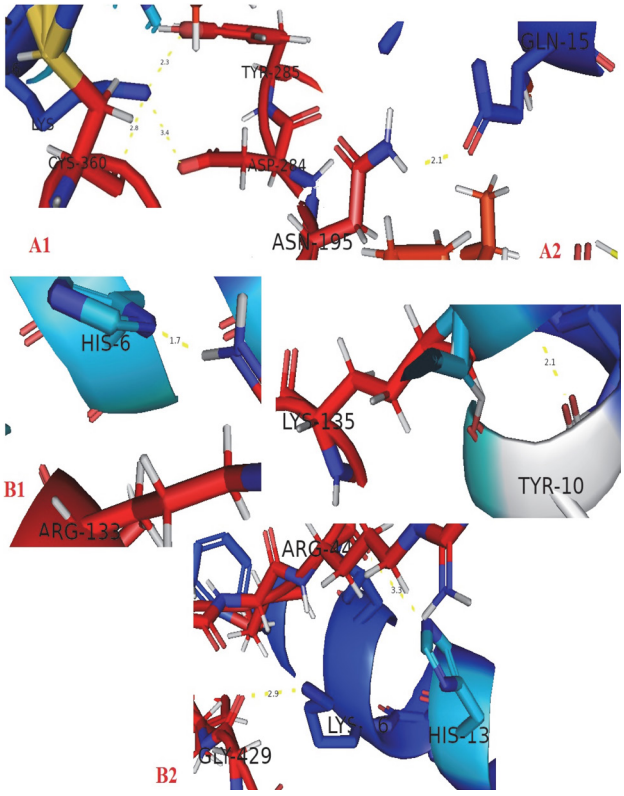


Figure 10. The SOAP and IES model results of Aggregatin and $A\beta_{28}$ peptides. A1.) Aggregatin (ASP284, TYR285, CYS360) interacts with the residue of LYS16 of $A\beta_{28}$. A2.) The interaction is between Aggregatin(ASN195) and GLN15 of $A\beta_{28}$. B1.) The docking is between the residue of Aggregatin(ARG133)-HIS6($A\beta_{28}$) and LYS135-TYR10. B2.) In the binding mode, Aggregatin(GLY447) interacts with the residue of HIS13 and GLY429 with LYS16 of $A\beta_{28}$. In this simulation, TYR10, HIS13, and LYS16, and HIS6 residues are common to both $A\beta_{28}$ and $A\beta_{42}$ in docking results.

was used to verify the quality of the model protein. The overall model quality or the Z-score was designated to be -6.15 as shown in Figure 5. The Z-score indicates total model quality and calculates the deviation of the total energy of the structure regarding the energy distribution that comes from random conformations (see Figure 5A, B). Consequently, the model Aggregatin is reliable to subject to molecular docking procedure.

The structural simulations of the protein-protein interactions are fundamental to explain how each cell machinery assembles at the molecular level. These simulations may be helpful to assess multiple sequence alignments and their structures, thus unmask the binding interfaces when neighboring proteins have possible homologous sequences. In the docking procedure of the current study, a free online tool, InterEvDock2 was used for protein-protein docking operation and a potential InterEvScore was produced to combine evolutionary information. The InterEvScore has determined the heteromeric protein interfaces and the integration of the evolutionary information retrieved from the multiple sequence alignments of each protein in the clusters with a residual-based multi-body statistical potential.

In this online server, docking searching is systematically applied using the FRODOCK2 and the results are re-calculated by InterEvScore[24] and SOAP_PP atom-based statistical potential to boost the confidence of the predictions.

As mentioned before, we predicted acceptable clusters using the InterEvDock2 server. This server predicts the top 10 consensus complexes for 239 out of 812 tested cases. The selected clusters for each of Aggregatin-$A\beta_{42}$ peptide and $A\beta_{28}$ peptide are represented in Tables 2 and 3. Besides, the InterEvDock2 server predicts the top 5 of residues interacting at the interface of a complex by a scoring system for the top 10 clusters of 30 models retrieved from InterEvDock2, FRODOCK2, and SOAP_PP.

In our study, we aimed to address the docking of Aggregatin with both $A\beta_{42}$ and $A\beta_{28}$ peptides since both peptides are involved in the amyloidosis process. $A\beta_{28}$ peptide is the major part of the amyloidosis process as it is deposited in AD in the early phase of amyloidosis. Here, we revealed that the side chains of HIS13 and LYS16 in the $A\beta_{28}$ are localized on the same face of the helix. Interestingly enough, the docking process with HIS13 and LYS16 residues of the $A\beta_{28}$ peptide is among the highest binding energy results as shown in Table 3. The interaction of $A\beta_{42}$ peptide with Aggregatin through LYS16 HIS13 residues retrieved from FRODOCK2 outcomes also possesses higher binding energy (See Table 2). Our expectation in the study was to find out whether our docking results were compatible with the in vitro analysis performed by Yan et al.[5] and if Aggregatin binds to amyloid-beta from the N-terminal region.

Taken together, we reached the adequately satisfactory docking results as represented in Figures 6–10. As shown in Figure 4, the N-terminal domain of $A\beta_{42}$ peptide is composed of the first 1–26 amino acids as we have demonstrated the 3D model structure of Aggregatin and its both N- and C-terminal ends. When comparing docking results with amyloid beta-42 and –28, the common residues that Aggregatin and amyloid peptides interact are ARG5, HIS6, and HIS13, and TYR10. These residues are in the N- terminal domain of Aβ42. The interaction of ARG5 and TYR10 in Aβ28 by Aggregatin and HIS6 and TYR10 in Aβ28 by Agregatin has higher binding energy score the other one (see Table 3). The binding mode of TYR303 in Aggregatin has the highest energy score with the residue HIS6 of Aβ42 (See Fig. 6A). Besides, the molecular simulation of Aggregatin(ARG447) with TYR10 and HIS443 with VAL18 of Aβ42 have better energy docking scores (See Fig. 7B). The critical point is which residue in the N-terminal domain of Aβ42 interacts with a higher binding energy in the calculation. Our calculation results show that the Amyloid Beta-42 generally interacts with its residues in the C-terminal region of Aggregation. As three scoring programs in the docking process have confirmed each other, we concluded that the models with the highest

binding energy are the complexes that interact with residues (1–26) in the N-terminal region of the Amyloid beta.

5. Conclusion

Alzheimer's disease has no known specific remedy yet, and the treatment is limited to slowing the progression of the disease while increasing the quality of life. Unfortunately, there is no predictable result for Alzheimer's patients since some experience cognitive problems slightly whereas the others may undergo a quicker onset of symptoms with faster disease progression. Here, the strategies on how to implement the therapies have gained importance with molecular and cellular approaches. We claim that two different lengths of the amyloid-beta peptide with known NMR structures are docked to the model Aggregatin, and have critical interactions between residues measured by the computational calculation but the fact that the two proteins interact, is not enough to link this process to the amyloid plaque formation. This interaction might only suggest a role of Aggregatin in the amyloid-beta pathway, but in vivo and in vitro experiments should be performed to explain its actual role in plaque formation in Alzheimer's pathology, if any. The domain analysis of Aggregatin supports its localization within the cell as confirmed in vitro. This study will help us to understand the possible conformational changes in the three-dimensional structure of Aggregatin, which might be screened by the experimental methods as mutations such as deletions and single nucleotide polymorphisms.

Declarations

Funding: Not Applicable
Conflict Of Interest: We have no conflict of interest to declare.
Available of Data: Analysis data is ready to be shared upon request
Code Availability: Not Applicable
Authors Contributions: Both authors hypothesized the subject. Besli performed the analysis. Both authors evaluated the results and wrote the manuscript.

6. Reference

1. K. Dassel, J. Butler, J. Telonidis, L. Edelman, *Educ. Gerontol.* **2020**, *46*, 150–157. **DOI:**10.1080/03601277.2020.1717079
2. R. E. Tanzi, *Cold Spring Harb. Perspect. Med.* **2012**, *2*, a006296. **DOI:**10.1101/cshperspect.a006296
3. E. Nichols, C. E. I. Szoeke, S. E. Vollset, N. Abbasi, F. Abd-Allah, J. Abdela, M. T. E. Aichour, R. O. Akinyemi, F. Alahdab, S. W. Asgedom, et al., *Lancet Neurol.* **2019**, *18*, 88–106.
4. A. Association, *Alzheimer's Dement.* **2019**, *15*, 321–387. **DOI:**10.1016/j.jalz.2019.01.010
5. T. Yan, J. Liang, J. Gao, L. Wang, H. Fujioka, X. Zhu, X. Wang, *Nat. Commun.* **2020**, *11*, 1–16. **DOI:**10.1038/s41467-019-13962-0
6. D. J. Selkoe, *Annu. Rev. Neurosci.* **1994**, *17*, 489–517. **DOI:**10.1146/annurev.ne.17.030194.002421
7. R. J. O'Brien, P. C. Wong, *Annu. Rev. Neurosci.* **2011**, *34*, 185–204. **DOI:**10.1146/annurev-neuro-061010-113613
8. A. Viswanathan, S. M. Greenberg, *Ann. Neurol.* **2011**, *70*, 871–880. **DOI:**10.1002/ana.22516
9. G. Chen, T. Xu, Y. Yan, Y. Zhou, Y. Jiang, K. Melcher, H. E. Xu, *Acta Pharmacol. Sin.* **2017**, *38*, 1205–1235. **DOI:**10.1038/aps.2017.28
10. G. G. Glenner, C. W. Wong, *Biochem. Biophys. Res. Commun.* **1984**, *120*, 885–890. **DOI:**10.1016/S0006-291X(84)80190-4
11. D. T. Jones, *J. Mol. Biol.* **1999**, *292*, 195–202. **DOI:**10.1006/jmbi.1999.3091
12. A. Roy, A. Kucukural, Y. Zhang, *Nat. Protoc.* **2010**, *5*, 725. **DOI:**10.1038/nprot.2010.5
13. L. A. Kelley, S. Mezulis, C. M. Yates, M. N. Wass, M. J. E. Sternberg, *Nat. Protoc.* **2015**, *10*, 845. **DOI:**10.1038/nprot.2010.5
14. Y. Song, F. DiMaio, R. Y.-R. Wang, D. Kim, C. Miles, T. J. Brunette, J. Thompson, D. Baker, *Structure* **2013**, *21*, 1735–1742. **DOI:**10.1016/j.str.2013.08.005
15. S. Raman, R. Vernon, J. Thompson, M. Tyka, R. Sadreyev, J. Pei, D. Kim, E. Kellogg, F. DiMaio, O. Lange, et al., *Proteins Struct. Funct. Bioinforma.* **2009**, *77*, 89–99. **DOI:**10.1002/prot.22540
16. A. Waterhouse, M. Bertoni, S. Bienert, G. Studer, G. Tauriello, R. Gumienny, F. T. Heer, T. A. P. de Beer, C. Rempfer, L. Bordoli, et al., *Nucleic Acids Res.* **2018**, *46*, W296–W303. **DOI:**10.1093/nar/gky427
17. M. Wiederstein, M. J. Sippl, *Nucleic Acids Res.* **2007**, *35*, W407–W410. **DOI:**10.1093/nar/gkm290
18. S. F. Altschul, T. L. Madden, A. A. Schäffer, J. Zhang, Z. Zhang, W. Miller, D. J. Lipman, *Nucleic Acids Res.* **1997**, *25*, 3389–3402. **DOI:**10.1093/nar/25.17.3389
19. D. T. Jones, D. Cozzetto, *Bioinformatics* **2015**, *31*, 857–863. **DOI:**10.1093/bioinformatics/btu744
20. A. M. Waterhouse, J. B. Procter, D. M. A. Martin, M. Clamp, G. J. Barton, *Bioinformatics* **2009**, *25*, 1189–1191. **DOI:**10.1093/bioinformatics/btp033
21. Schrödinger, LLC, *The {PyMOL} Molecular Graphics System, Version~1.8*, **2015**.
22. C. Quignot, J. Rey, J. Yu, P. Tufféry, R. Guerois, J. Andreani, *Nucleic Acids Res.* **2018**, *46*, W408–W416. **DOI:**10.1093/nar/gky377
23. J. Yu, M. Vavrusa, J. Andreani, J. Rey, P. Tufféry, R. Guerois, *Nucleic Acids Res.* **2016**, *44*, W542–W549. **DOI:**10.1093/nar/gkw340
24. J. Andreani, G. Faure, R. Guerois, *Bioinformatics* **2013**, *29*, 1742–1749. **DOI:**10.1093/bioinformatics/btt260
25. E. Ram\'\irez-Aportela, J. R. López-Blanco, P. Chacón, *Bioinformatics* **2016**, *32*, 2386–2388. **DOI:**10.1093/bioinformatics/btw141

26. G. Q. Dong, H. Fan, D. Schneidman-Duhovny, B. Webb, A. Sali, *Bioinformatics* **2013**, *29*, 3158–3166. **DOI:**10.1093/bioinformatics/btt560
27. M. Uhlén, L. Fagerberg, B. M. Hallström, C. Lindskog, P. Oksvold, A. Mardinoglu, Å. Sivertsson, C. Kampf, E. Sjöstedt, A. Asplund, et al., *Science (80-.).* **2015**, *347*, 1260419. **DOI:**10.1126/science.1260419
28. J. S. Richardson, in *Adv. Protein Chem.*, Elsevier, **1981**, pp. 167–339. **DOI:**10.1016/S0065-3233(08)60520-3
29. D. Warde-Farley, S. L. Donaldson, O. Comes, K. Zuberi, R. Badrawi, P. Chao, M. Franz, C. Grouios, F. Kazi, C. T. Lopes, et al., *Nucleic Acids Res*. **2010**, *38*, W214–W220. **DOI:**10.1093/nar/gkq537
30. K. Bryson, D. Cozzetto, D. T. Jones, *Curr. Protein Pept. Sci.* **2007**, *8*, 181–188. **DOI:**10.2174/138920307780363415
31. T. E. Lewis, I. Sillitoe, N. Dawson, S. D. Lam, T. Clarke, D. Lee, C. Orengo, J. Lees, *Nucleic Acids Res.* **2017**, *46*, D435–D439. **DOI:**10.1093/nar/gkx1069
32. N. K. Fox, S. E. Brenner, J.-M. Chandonia, *Nucleic Acids Res.* **2013**, *42*, D304–D309. **DOI:**10.1093/nar/gkt1240
33. E. F. Pettersen, T. D. Goddard, C. C. Huang, G. S. Couch, D. M. Greenblatt, E. C. Meng, T. E. Ferrin, *J. Comput. Chem.* **2004**, *25*, 1605–1612. **DOI:**10.1002/jcc.20084
34. D. Petrey, Z. Xiang, C. L. Tang, L. Xie, M. Gimpelev, T. Mitros, C. S. Soto, S. Goldsmith-Fischman, A. Kernytsky, A. Schlessinger, et al., *Proteins Struct. Funct. Bioinforma.* **2003**, *53*, 430–435. **DOI:**10.1002/prot.10550

Povzetek

Alzheimerjeva bolezen je glavna nevrodegenerativna bolezen, katere razširjenost se po vsem svetu povečuje, vendar njen molekularni mehanizem ostaja nejasen. Obstaja nekaj znanstvenih dokazov, da je molekularna kompleksnost patofiziologije Alzheimerjeve bolezni povezana s tvorbo zunajceličnih plakov amiloida-beta v možganih. Nova navzkrižna fenotipska asociacijska analiza s slikovno genetiko je opisala gen za dovzetnost za možgansko atrofijo FAM222A, in protein Aggregatin, ki ga kodira FAM222A, v interakciji s peptidom amiloid-beta (Aβ) (1–42) prek njegove N-končne Aβ-vezavne domene, kar olajša agregacijo Aβ. Funkcija proteina Aggregatina ni znana, njegova tridimenzionalna struktura pa še ni bila eksperimentalno določena. Naš cilj je bil podrobno proučiti medsebojno interakcijo Aggregatina in Aβ z in silico analizo, vključno s 3D-analizo napovedovanja strukture proteina Aggregatina s homolognim modeliranjem. Naša analiza je potrdila interakcijo C-terminalne domene modelnega proteina z N-terminalno domeno Aβ. To je prvi poskus dokazovanja interakcije Aggregatina z Aβ. Pridobljeni rezultati so potrdili in vitro in in vivo poročila raziskav, ki trdijo, da FAM222A pomaga olajšati agregacijo peptida Aβ.

Except when otherwise noted, articles in this journal are published under the terms and conditions of the Creative Commons Attribution 4.0 International License

Scientific paper

Rapid and Sensitive Analytical Method for the Determination of Insulin in Liposomes by Reversed-Phase HPLC

Eliete de Souza Von Zuben,[1,*] Josimar Oliveira Eloy,[2] Victor Hugo Sousa Araujo,[1] Maria Palmira Daflon Gremião[1] and Marlus Chorilli[1]

[1] *São Paulo State University (UNESP), School of Pharmaceutical Sciences, Department of Drugs and Medicines, Rodovia Araraquara-Jaú, km1, 14800-903, Araraquara, São Paulo, Brazil.*

[2] *Federal University of Ceará, School of Pharmacy, Dentistry and Nursing, Department of Pharmacy, Fortaleza – CE, Brazil*

** Corresponding author: E-mail: eliete.vz@gmail.com*
Tel.: +551633016960

Received: 08-20-2020

Abstract

Insulin is an important anabolic hormone that regulates the metabolism of carbohydrates, lipids and proteins. In this study, a reverse-phase liquid chromatography (RP-LC) method was successfully validated and tested for the encapsulation efficiency assay of insulin and in vitro release studies. HPLC analyses were carried out using a RP C18- Luna® Phenomenex (4.6 × 250 mm, 5 μm particle size) column maintained at room temperature, using a mobile phase constituted by a mixture of acetonitrile and 0.1% TFA aqueous solution (60:40, v/v), in an isocratic mode with a flow rate of 1.0 mL/min, with ultraviolet detection at 214 nm and 20 μL of injection volume. Method validation was performed according recognized guidelines for system suitability, specificity, linearity, precision, accuracy, LOD, LOQ and robustness. The method was shown to be linear in the range of 0.5–100 μg/mL ($r^2 = 0.9993$) selective, precise, robust, accurate with LOD and LOQ values were 0.097 μg/mL and 0.294 μg/mL, respectively. The developed method proved to be adequate to analyze the encapsulation efficiency and the profile of insulin release from liposomes.

Keywords: Insulin; liposome; liquid Chromatography; validation Method; in Vitro Release; encapsulation Efficiency.

1. Introduction

Insulin is a polypeptide with a molecular weight of 5.8 kDa, synthesized in the pancreas by β-cells of the islets of Langerhans, from a larger molecule called proinsulin. Proinsulin is enzymatically cleaved to generate insulin (which contains 51 amino acids arranged in two chains interconnected by disulfide bonds, α being 21 amino acids and β with 30 amino acids) and the C peptide. The insulin and peptide C are secreted in equimolar amounts when beta-pancreatic cells are stimulated, however, peptide C does not play any physiological function.[1]

Insulin is an important anabolic hormone that regulates the metabolism of carbohydrates, lipids and proteins. The uptake of glucose by organs such as liver, skeletal muscle and adipose tissue is performed by the action of insulin. In the absence of insulin, the uptake of glucose by said organs and tissues is affected leading to hyperglycemia. Other insulin functions are related to ion transport, cell proliferation and differentiation, and nitric oxide synthesis.[2]

Recent research has triggered the development of new insulin delivery systems that allow the use of alternative routes to parenteral (subcutaneous injection). The injection of insulin preparations sometimes results in subcutaneous adipose tissue hypertrophy, if it will be administrating repeatedly in the same place and the other side effect is the risk of hypoglycemia when treatment becomes continuous.[3]

Liposomes in 1995 were the first nanoscale release system to be used for clinical use. Since then, work based on this type of release systems has grown considerably and brought enormous development with significant clinical implications.[4] Several researchers used nanostructured systems such as liposomes for encapsulation and release of insulin.[5–7]

Over the recent years, some methods for the quantification of insulin in the formulation, bulk and nanostructured systems by HPLC have appeared in the literature.[8–12]

Thus, the purpose of the present paper was to develop and validate a simple, sensitive and fast reversed-phase HPLC method for the measurement of insulin in liposomes. This method was validated following the ICH and FDA guidelines together Brazilian National Health Surveillance Agency (ANVISA) resolution, assuring the therapeutic efficacy and contributing to the improvement of the quality control.[13–15]

2. Experimental

2. 1. Chemical and Reagents

The human insulin solution Novolin R® (100IU/mL, Lot GS63F52) was purchased from Novo Nordisk, Kalundborg, Denmark. Soybean phosphatidylcholine (Lipoid S100; PC > 96%) was obtained from Lipoid GmbH, Germany. Cholesterol (CH) was purchased from Sigma-Aldrich, USA (purity ≥99 %). Chloroform obtained from Merck, USA. Acetonitrile and methanol were acquired from J.T. Baker®, USA (HPLC grade) and trifluoroacetic acid (TFA) were purchased from Sigma-Aldrich, USA. Amicon®-100 kDa ultrafiltration filter was purchased from Millipore. Water was prepared by Milli-Q reverse osmosis (Millipore, USA). All other reagents were commercially available and of analytical grade. Phosphate buffered saline (PBS) is made of NaCl 137 mmol/L, KCl 2.6 mmol/L, $Na_2HPO_4 \cdot 12H2O$ 6.4 mmol/L and NaH_2PO_4 1.4 mmol/L, pH 7.4.

2. 2. Preparation of Reference Standard Solution

The stock solution of 700 μg/mL was prepared by direct dilution of 2 mL of human insulin Novolin R® (100 IU/mL) in a 10 mL volumetric flask. The volume was completed with phosphate buffer solution (PBS), pH 7.4. From the stock solution, calibration curves for seven human insulin standard solutions were prepared at concentrations of 0,5, 1, 5, 20, 40, 50 and 100 μg/mL in phosphate buffer solution (PBS) pH 7.4. All solutions were filtered through a 0.45 μm PVDF membrane filter (Millipore) prior to injection and assayed by HPLC.

2. 3. HPLC System and Chromatographic Conditions

The RP-LC method was performed on an Agilent Technologies LC system, model 1200 DAD/UV–visible detector and was carried out the adaptation (change in the proportion of the mobile phase) of the method described by Sarmento and collaborators. The detector was set to 214 nm and peak areas were integrated automatically using a computer system with ChemStation data acquiring software. RP C18- Luna® Phenomenex (4.6 × 250 mm, 5 μm particle size) column was employed for chromatographic separation with a mobile phase constituted by a mixture of acetonitrile and 0.1% TFA aqueous solution (60:40, v/v), in an isocratic mode with a flow rate of 1.0 mL/min. The HPLC system was performed at room temperature (25 ± 1 °C). The injection volume was 20 μL for both the reference substance solution and the sample solution. Prior to use, acetonitrile and 0.1% TFA aqueous solution prepared with deionized water (Milli-Q®), filtered with a 0.45 μm filter and degassed for 30 min. All samples were filtered through a 0.45 μm PVDF membrane filter from Millipore, USA.

2. 4. Validation of HPLC Method

Method validation was performed in agreement with ICH and FDA guidelines together Brazilian National Health Surveillance Agency (ANVISA) resolution for system suitability, specificity, linearity, precision, accuracy, limit of detection (LOD), limit of quantitation (LOQ) and robustness.[13–15]

2. 4. 1. System Suitability Test

In order to assure the performance and reproducibility of the chromatographic system before and during the analysis, six injections of insulin standard solution were carried out at a concentration of 50 μg/mL. The parameters measured were retention time, peak area, peak symmetry, tailing factor and number of theoretical plates.[14]

2. 4. 2. Selectivity

Chromatograms of mobile-phase components, samples of phosphate buffer solution (PBS), pH 7.4 and samples of blank liposomes prepared without adding insulin were obtained to evaluate the selectivity of the method. All samples were filtered through a 0.45 μm PVDF membrane filter (Millipore) and injected in triplicate.

2. 4. 3. Linearity

The linearity was evaluated by the construction of three analytical curves, determined by the analysis of seven levels of concentration in three different days. Standard solutions at the concentrations of 0.5, 1, 5, 20, 40, 50 and 100 μg/mL were prepared from the insulin stock solution (700 μg/mL) using phosphate buffer solution (PBS, pH 7.4) as the diluent. For each described concentration, three injections were carried out previously filtered through a 0.45 μm PVDF membrane filter (Millipore). Linearity was determined by the calculation of a linear regression using the least-squares method and the statistical analysis was performed by analysis of variance (ANOVA).

2. 4. 4. Precision

The precision of the analytical method was evaluated by determination of the repeatability and the intermediate precision. The repeatability (intra-day) was determined by injection of six independent preparations of insulin standard solutions at a concentration of 50 µg/mL, on the same day and under the same experimental conditions. The intermediate precision (inter-day) was tested using two different analysts on different days, with the same LC instrument, in the same laboratory. The % RSD of assays was calculated.

2. 4. 5. Accuracy

The accuracy was assessed by standard addition technique where liposomes were spiked with known quantities of insulin standard solution, at three different levels (lower, medium and upper concentration) corresponding to 5, 20 and 50 µg/mL. The samples were prepared in triplicate and the recovery percentage was determined as the percentage of the drug recovered from the sample and expressed as a relative percentage (%).

2. 4. 6. Limit of Detection (LOD) and Quantitation (LOQ)

The LOD and LOQ were calculated, using the mean values of three independent analytical curves, determined by a linear regression model, based on the standard deviation of the response and on the slope of the calibration curve, according to following equations 1 and 2 respectively:

$$LOD = 3.3\ (\sigma/S) \quad (1)$$

$$LOQ = 10\ (\sigma/S) \quad (2)$$

where "σ" represents the standard deviation of y-intercept of regression line and "S" denotes the slope of regression line.

2. 4. 7. Robustness

Robustness was assessed by varying four parameters independently. The flow rate of the mobile phase (0.9 mL/min and 1.1 mL/min), wavelength (213 nm and 215 nm), column temperature (24 °C and 26 °C) and the ratio of mobile phase constituted by a mixture of acetonitrile and 0.1% TFA aqueous solution (61:39 and 59:41). For this study, the analysis was performed using a concentration of 50 µg/mL and all samples were filtered through a 0.45 µm PVDF membrane filter (Millipore) and injected in triplicate.

2. 5. Application of the Method

2. 5. 1. Preparation of Blank Liposome and Insulin-loaded Liposome

Blank liposomes and insulin-loaded liposomes were prepared by the hydration of the thin lipid film as previously described by Bangham *et al.*[16] Briefly, a phospholipid mixture of 100mg, including soybean phosphatidylcholine (PC) and cholesterol (CH) was weighed (weight ratios of 5:3) into a round-bottom flask and dissolved in a chloroform / methanol mixture (1:2 v/v), evaporated using a rotary evaporator at 40 °C for 30 minutes. Then, to prepare blank liposomes, the lipid film formed was hydrated with 10 mL of phosphate buffer (PBS, pH 7.4) for 30 min at 40 °C / 100 rpm, obtaining the liposomal suspension. To prepare the liposome loaded with insulin, hydration was performed with 10 mL of phosphate buffer (PBS, pH 7.4), containing 4 mL of insulin solution, equivalent to 1400 µg / mL, obtaining the liposomal suspension.[17]

2. 5. 2. Insulin Encapsulation Efficiency (EE)

For the determination of the encapsulation efficiency of insulin, an indirect method was used by determining the free amount of insulin, non-encapsulated. Briefly, 1 mL of the encapsulated insulin from the liposome was separated from the free insulin by ultracentrifugation of liposomes using Amicon®-100 kDa ultrafiltration filter at 13.000 rpm for 12 min. After centrifugation, 250 µl of the filtrate was diluted to 2 mL with phosphate buffer (PBS, pH 7.4) and measured by an HPLC using the validated analytical method described previously. All experiments were performed in triplicate. The EE % of insulin was calculated according to equation 3 below.[18–19]

$$EE\%\ \text{of insulin} = \left(\frac{\text{Total amount of insulin (µg)} - \text{Free amount of insulin}}{\text{Total amount of insulin (µg)}} \right) x100 \quad (3)$$

2. 5. 3. In Vitro Release of Insulin Solution and Insulin from Liposomes

In vitro insulin release profile from solution and liposome was investigated using Franz diffusion cells (Hanson MicroettePlus® equipment, Chatsworth, CA, USA). The cells were filled with 7.0 mL of receptor solution composed by phosphate buffer solution (PBS, pH 7.4), stirred at 300 rpm and heated at 32 °C ± 0.5 °C to simulate nasal temperature.[20,21] Aliquots of samples (2,8 mL) were withdrawn automatically at predetermined intervals (0.08, 0.5, 1, 2, 4, 8, 12, 16 and 24 h) and sample volumes were replenished with fresh receptor solution.

The amount of insulin released from solution and the liposomes was quantified by the HPLC method as described in the section 2.3.

3. Results and Discussion

A reversed-phase HPLC method for the determination of insulin in liposomes has been developed. The analytical parameters of selectivity, linearity, precision, accuracy, LOD, LOQ, and robustness were evaluated to validate the method, according to recognized guidelines (FDA, ICH e Anvisa). During preliminary studies, some chromatographic conditions were tested.[5,9,12] It was decided to carry out the adaptation of a method previously reported.[9] However, the proportion of the mobile phase was modified using the isocratic mode as a choice and this modification provided a reduced run time, best chromatographic peak resolution and good symmetry. Moreover, no degradation peak was observed.

3. 1. Validation of HPLC Method

Validation of the method was performed according to ICH and FDA guidelines together Brazilian National Health Surveillance Agency (ANVISA) resolution.[13–15] Table 1 represents the HPLC conditions for the determination of insulin in liposome.

The system suitability is used to check if the chromatographic system is suitable for the intended analysis that will be executed.[22] Figure 1 shows two peaks (between 1.6 minutes and 3 minutes) from the mobile phase and the phosphate buffer (PBS, pH 7.4) and a representative peak of insulin (4.5 minutes). Besides, no peak of possible degradation products was observed in the chromatograms, as verified in the selectivity tests. The following results were obtained: tailing factor of 1.41, peak asymmetry of 0.64 and theoretical plates of 5089. All parameters found are in agreement with the FDA and ICH guidelines.13–14 The average retention time was 4.5 minutes and the % RSD of peak area was 0.22%.

Table 1. HPLC conditions for determination of insulin in liposomes.

System	Parameters
HPLC equipment	HPLC AGILENT, model 1200
Mobile phase	Acetonitrile : 0.1% TFA aqueous solution (60:40,v/v)
Column	RP C18- Luna® Phenomenex (4.6 × 250 mm, 5 µm particle size)
Wavelength	214 nm
Flow rate	1.0 mL/min
Volume of injection	20 µL
Temperature	25 ± 1 °C
Retention time	4.5 min

In this selectivity parameter mobile-phase components, samples of phosphate buffer solution (PBS), pH 7.4 and the samples of blank liposomes composed by soybean phosphatidylcholine and cholesterol prepared without adding insulin were previously diluted with acetonitrile, sonicated for 10 minutes, filtered (0.45 µm) and then analyzed by HPLC. All the samples were injected separately and the assay was performed in triplicate and the peaks obtained showed that there was no interference of the samples injected at the peak of insulin.

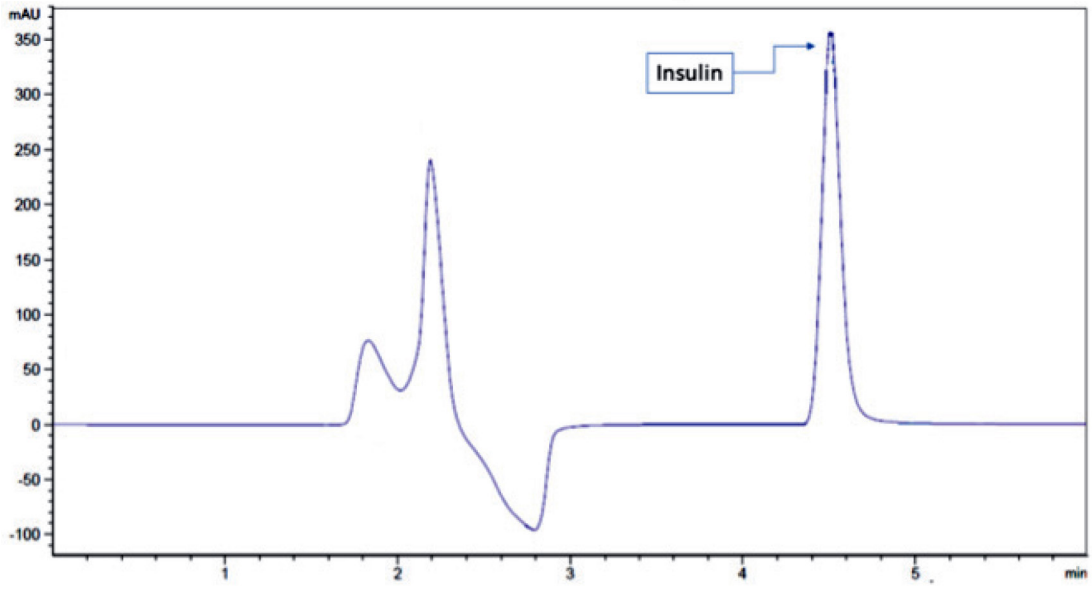


Figure 1. Representative chromatogram of insulin reference substance. Conditions: mixture of acetonitrile and 0.1% TFA aqueous solution (60:40,v/v) as mobile phase, flow rate at 1.0 mL/min, column temperature 25 ± 1 °C, RP C18- Luna® Phenomenex (4.6 × 250 mm, 5 µm particle size) column, UV detection wavelength at 214 with 20 µL of injection volume.

Table 2. Analysis of variance (ANOVA) for linearity

Source of variation	DF	SS	MS	F calculated	F critical
Between groups	6	71158775	11859796	2.80	2.96
Within groups	14	2222	159		
Total	20	71160997			

DF-degrees of freedom; SS-Sum of squares; MS-Mean square

The linearity of the method was assessed by plotting peak area against seven concentrations. For each concentration, three injections were performed and the average results of the chromatographic peak areas obtained were used for the study of linear regression using the least-squares method.[13–15] The analytical curve of insulin based on three calibration curves was shown to be linear over the proposed range (0.5–100 μg/mL) resulting in linear regression $y = 55.01775x + 36.56067$, with $r^2 = 0.9993$, as advised [23] and shown in Figure 2. The statistical analysis was evaluated by ANOVA (Table 2) and data no presented significant linearity deviation at a 5% level of variance, exhibiting F calculated (2.80) lower than the F critical (2.96) demonstrating that the method used is linear in the range of 0.5 to 100 μg/mL.[24]

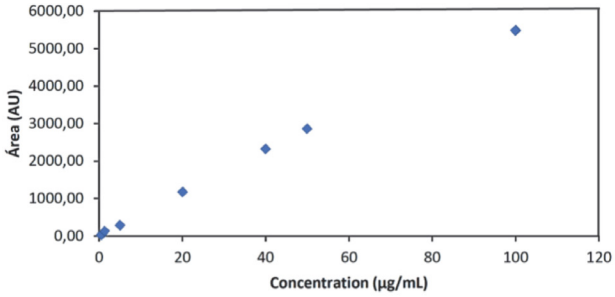


Figure 2. Calibration curve obtained with insulin standard solutions at seven concentration levels in the range of 0.5 to 100 μg/mL (n = 21).

The precision was evaluated by calculating of relative standard deviation (RSD) of the samples, submitted to the repeatability (intra-day) and intermediate precision (inter-day). According to Table 3, the precision values were less than 5% as recommended,[15] where 0.77% was found for repeatability and 1.18% was found for intermediate precision. These results indicate that the analytical method presented has good precision.

Table 3. Results of intra and inter-day precision for determination of insulin in standard solutions.

Level	Concentration μg/mL	RSD[a] (%)
Repeatability (intra-day)	50 μg/mL	0.77 (n = 6)
Intermediated precision (inter-day)	50 μg/mL	1.18 (n = 12)

[a]RSD: relative standard deviation.

The accuracy of the method was determined by recovery studies, where the method of standard addition was used at three different levels (5, 20 and 50 μg/mL). The results are shown in Table 4 and the average recoveries for insulin were 97.58% within the range of 80–120% with an RSD of 1.27%, evidencing the method is appropriate in quantify concentrations of insulin in liposome with accuracy.

The LOD and LOQ are used to measure the sensitivity of the method. DL represents the smallest amount of drug present in the sample that can be detected, but not necessarily quantified while QL represents the smallest amount of drug in the sample that can be measured with precision and accuracy by the method developed.[13–15] The calculated LOQ and LOQ values were 0.097 μg/mL and 0.294 μg/mL, respectively, demonstrating that the proposed method is adequate and safe for the quantification and detection of low insulin concentrations.

Robustness is a parameter typically performed in the development of the analytical method that indicates its ability to withstand small and deliberate variations in analytical conditions.[15] It was evaluated by small modifications in four pre-established parameters, such as flow rate of the mobile phase, ratio of mobile phase, column tem-

Table 4. Determination of the recovery of the analytical method for insulin in liposomes

Insulin standard solution added (μg/mL)		Insulin standard solution found [a] (μg/mL)	Recovery (%)	RSD [b] (%)	Average Recovery (%)
R1	5	4.88	93.88	2.26	97.58
R2	20	19.85	99.26	0.27	
R3	50	49.74	99.61	1.28	

[a] Mean of three replicates analysis. [b] RSD: relative standard deviation.

Table 5. Robustness of the analytical method for insulin quantification

Chromathografic conditions	Recovery(%)	RSD [a] (%)
Flow rate of the mobile phase		
0.9 mL/min	98.8	0.60
1.1 mL/min	104.4	0.18
Ratio of mobile phase		
61:39	99.3	0.05
59:41	98.0	0.20
Column temperature (°C)		
24°C	101.3	0.58
26°C	99.2	0.49
Wavelength (nm)		
213 nm	100.8	0.83
215 nm	100.3	0.34

[a] RSD: relative standard deviation.

perature and wavelength (nm), using a concentration of 50 μg/mL. According to Table 5, it was possible to verify that the method is robust since even with the variations made in the analytical conditions, the recovery results are within a previously specified range of 80–120% and RSD values showed less than 2%.

3. 2. Application of the Validated Method

Liposomes constituting important systems for the encapsulation, transport and sustained release of drugs, because their morphology is similar to that cellular membranes, besides protecting the drug against degradation.[25–27] The validated method was used for the determination of insulin in liposomes composed by soybean phosphatidylcholine and cholesterol prepared by the thin film-hydration technique, through the encapsulation efficiency assay and the *in vitro* release profile of insulin from the liposomes. The encapsulation efficiency of insulin from liposome was found to be 67.19% ± 2.4 (SD, n = 3), which shows a result superior to that found in similar papers.[6,7,28] However, as far as we know, no study reported in the literature has addressed the encapsulation efficiency of insulin from liposomes using Amicon ultrafiltration filter extraction with consequent HPLC quantification. A study by Wallace and colleagues showed that ultrafiltration has several advantages over ultracentrifugation, such as rapid separation with low centrifugal forces, suggesting less potential for particle deformation and therefore less impairment of particle integrity.[29] Figure 3 shows the release profiles of insulin in solution (PBS, pH 7.4) and insulin from the liposome. Both profiles have a biphasic release behavior, that is, it was observed an initial burst effect (fast release) in the first 2 hours, followed slower and sustained release delivery of insulin in the next hours. However, comparing the two release profiles it is noted that the release of insulin from the liposome was slower and sustained, suggest it is originated from the drug encapsulated in the aqueous liposome compartment and due to the process of diffusion of insulin through the bilayers. Pardakhty and collaborators obtained similar results in their studies as well as Zhang and collaborators.[30,31]

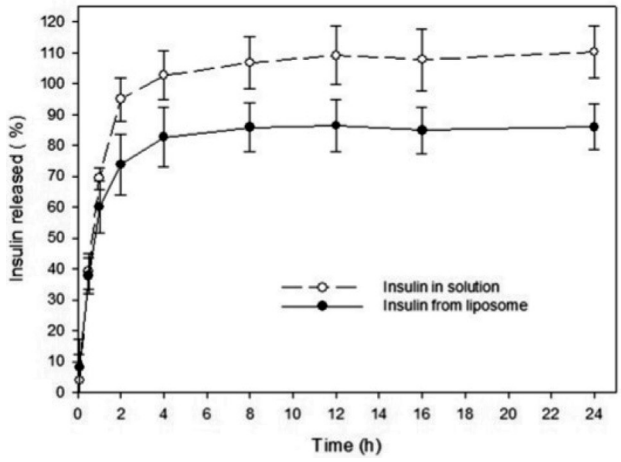


Figure 3. Release profiles of insulin in solution (open circles) and insulin from the liposome (solid circles). Each value express mean± standard deviation, n = 5.

4. Conclusion

The RP-HPLC method was developed and validated according to recognized guidelines (FDA, ICH and Anvisa) for the measurement of insulin in liposomes composed by soybean phosphatidylcholine and cholesterol and prepared using the hydration technique. The insulin encapsulation efficiency assay in liposomes and the in vitro release study using Franz diffusion cells were evaluated. The results indicated that the analytical method was linear, selective, precise, accurate and robust with low detection and quantification limits in a range from 0.5 to 100 μg/mL and are within the limits proposed by those guidelines. The method is simple, rapid and sensitive and may be used to determine insulin in liposomes in a short analysis time (about 4.5 minutes), which shows an advantage of the proposed method over those described in the literature. The suggested method can be used to analyze the encapsulation efficiency with adequate reliability. Regarding release profile of insulin from liposomes the data demonstrated a biphasic release behavior characterized by burst effect followed slower and sustained release.

Acknowledgements

The authors gratefully thank to FAPESP (São Paulo, Brazil), PADC-FCFar-UNESP (Araraquara, Brazil) and FUNDUNESP (São Paulo, Brazil) for financial support. This study was financed in part by the Coordenação de Aperfeiçoamento de Pessoal de Nível Superior – Brasil (CAPES) - Finance Code 001.

Conflict of Interest

There are no conflicts to declare.

5. References

1. L. L. Brunton and B. C. Knollmann, *As Bases Farmacológicas da Terapêutica de Goodman e Gilman*, 13th ed. AMGH Editora. **2018**.
2. S. Genuth, Type 1 diabetes mellitus. *ACP Medicine*. **2008**, 1–19.
3. B. G. Katzung and A. J. Trevor, *Farmacologia Básica e Clínica*, 13th ed. AMGH Editora. **2017**.
4. C. Zylberberg and S. Matosevic. *Drug Delivery*. **2016,** *23*, 3319–3329. **DOI:**10.1080/10717544.2016.1177136
5. W. Zheng-Hong, P. Qi-neng, W. Yi and L. Jia-ming, *Acta Pharmacol Sin*. **2004,** *25*, 966–972.
6. N. Zhang, Q. N. Ping, G. H. Huang and W. F. Xu, *Int. J. Pharm*. **2005**, *294*, 247–259. **DOI:**10.1016/j.ijpharm.2005.01.018
7. M. Niu, Y. Lu, L. Hovgaard and W. Wu, *Int. J. Nanomedicine*. **2011**, *6*, 1155–1166.
8. P. Moslemi, A. R. Najafabadi and H. Tajerzadeh, *Journal of Pharmaceutical and Biomedical Analysis*. **2003**, *33*, 45–51. **DOI:**10.1016/S0731-7085(03)00336-4
9. B. Sarmento, A. Ribeiro, F. Veiga and D. Ferreira, *Biomedical Chromatography*. **2006,** *20*, 898–903. **DOI:**10.1002/bmc.616
10. E. Déat-Lainé, V. Hoffart, J. M. Cardot, M. Subirade and E. Beyssac, *Journal of Pharmaceutics*. **2012**, *439*, 136–144. **DOI:**10.1016/j.ijpharm.2012.10.003
11. K. B. Chalasani, G. J. Russell-Jones, A. K. Jain, P. V. Diwan and S. K. Jain, *Journal of Controlled Release*. **2007**, *122*, 141–150. **DOI:**10.1016/j.jconrel.2007.05.019
12. E. Déat-Lainé., V. Hoffart, G. Garrait and E. Beyssac, *International Journal of Pharmaceutics.* **2013**, *453*, 336–342. **DOI:**10.1016/j.ijpharm.2013.06.016
13. ICH, *Q2 (R1); Validation of analytical procedures: text and methodology, International Conference on Harmonization*. Geneva. **2005**, pp.11–12.
14. FDA - Food and Drug Administration. *Validation of Chromatographic Methods. Washington: Center for Drug and Evaluation and Research* (CDER), Washington. **1994**.
15. Brazil, *Guide for validation of analytical and bioanalytical methods*. Resolution RDC 166 of Brazilian National Health Surveillance Agency (ANVISA), **2017**.
16. A. D. Bangham, M. M. Standish and J. C. Watkins, J. Mol. Biol. **1965**, *13*, 238–252. **DOI:**10.1016/S0022-2836(65)80093-6
17. K. M. Hosny, *AAPS PharmSciTech*. **2010**, *11*, 241–246. **DOI:**10.1208/s12249-009-9373-4
18. Z. Degim, N. Ünal, D. Eşsiz and U. Abbasoglu, *Life Sciences*. **2004**, *75*, 2819–2827. **DOI:**10.1016/j.lfs.2004.05.027
19. X. Xu, M. A. Khan and D. J. Burgess, *International Journal of Pharmaceutics*. **2012**, *423*, 410–418. **DOI:**10.1016/j.ijpharm.2011.12.019
20. J. Lindemann, R. Leiacker, G. Rettinger, and T. Keck, *Clinical Otolaryngology & Allied Sciences*. **2002***, 27*, 135–139. **DOI:**10.1046/j.1365-2273.2002.00544.x
21. T. Keck, R. Leiacker, H. Riechelmann and G. Rettinger, *The Laryngoscope*. **2000**, *110*, 651–654. **DOI:**10.1097/00005537-200004000-00021
22. FDA. Food and Drug Administration - *Analytical Procedures and Methods Validation for Drugs and Biologics*. Guidance for Industry. **2015**, pp. 1–15.
23. N. A. Épshtein, *Pharmaceutical Chemistry Journal*. **2004**, *38*, 212–228. **DOI:**10.1023/B:PHAC.0000038422.27193.6c
24. I. C. Pinto, C. Cerqueira-Coutinho, Z. M. F.D. Freitas, E. P, D. Santos, F. A. D. Carmo and E. R. Junior, *Brazilian Journal of Pharmaceutical Sciences*. **2017**, *53*, 1–8. **DOI:**10.1590/s2175-97902017000216033
25. N. C. Santos and M.A.R.B. Castanho, *Química Nova*. **2002**, *25*, 1181–1185. **DOI:**10.1590/S0100-40422002000700019
26. G. Bozzuto and A. Molinari, *International Journal of Nanomedicine*. **2015**, *10*, 975–999. **DOI:**10.2147/IJN.S68861
27. J. O. Eloy, M. C. D. Souza, R. Petrilli, J. P. A. Barcellos, R. J. Lee and, J. M. Marchetti, *Colloids and surfaces B: Biointerfaces*. **2014**, *123*, 345–363. **DOI:**10.1016/j.colsurfb.2014.09.029
28. S. J. Park, S. G. Choi, E. Dava and J. S. Park, *International Journal of Pharmaceutics.* **2011**, *415*, 267–272. **DOI:**10.1016/j.ijpharm.2011.05.061
29. S. J. Wallace, J. Li, R. L, Nation. & B. J. Boyd, *Drug Delivery and Translational Research*. **2012,** *2*, 284–292. **DOI:**10.1007/s13346-012-0064-4
30. A. Pardakhty, J. Varshosaz and A. Rouholamini, *International Journal of Pharmaceutics.* **2007**, *328*, 130–141. **DOI:**10.1016/j.ijpharm.2006.08.002
31. X. Zhang, X. Zheng, Z. Wu, X. Gao, S. Shu, Z. Wang and C. Li, *Carbohydrate Polymers*. **2011**, *84*, 1419–1425. **DOI:**10.1016/j.carbpol.2011.01.057

Povzetek

Inzulin je pomemben anabolični hormon, ki uravnava presnovo ogljikovih hidratov, lipidov in beljakovin. V tej raziskavi je bila metoda reverzno fazne tekočinske kromatografije (RP-LC) uspešno validirana in preizkušena na učinkovitost enkapsulacije inzulina in *in vitro* študij sproščanja. HPLC analize smo izvedli s kolono RP C18-Luna® Phenomenex (4,6 × 250 mm, velikost delcev 5 µm), pri sobni temperaturi, z uporabo mobilne faze sestavljene iz mešanice acetonitrila in 0,1 % vodne raztopine TFA (60:40 , v/v), v izokratskem načinu s pretokom 1,0 mL/min, z ultravijolično detekcijo pri 214 nm, volumen injicirane raztopine pa je znašal 20 µL. Validacija metode je bila izvedena v skladu s priznanimi smernicami glede ustreznosti sistema, specifičnosti, linearnosti, natančnosti, točnosti, meje detekcije (LOD), meje kvantizacije (LOQ) in robustnosti. Pokazalo se je, da je metoda linearna v območju od 0,5-100 µg/mL (r^2 = 0,9993) selektivna, natančna, robustna, točna z vrednostmi LOD in LOQ, 0,07 µg/mL oziroma 0,294 µg/mL. Razvita metoda se je izkazala za ustrezno za analizo učinkovitosti enkapsulacije in analizo profila sproščanja inzulina iz liposomov.

Except when otherwise noted, articles in this journal are published under the terms and conditions of the Creative Commons Attribution 4.0 International License

Scientific paper

Two Vanadium(V) Complexes Derived from Bromo and Chloro-Substituted Hydrazone Ligands: Syntheses, Crystal Structures and Antimicrobial Property

Zi-Qiang Sun,[1] Shun-Feng Yu,[1] Xin-Lan Xu,[1] Xiao-Yang Qiu[1,2,*] and Shu-Juan Liu[1,*]

[1] *College of Science & Technology, Ningbo University, Ningbo 315315, P.R. China*

[2] *State Key Laboratory of Structural Chemistry, Fujian Institute of Research on the Structure of Matter, Chinese Academy of Sciences, Fuzhou, Fujian 350002, P.R. China*

** Corresponding author: E-mail: lsj_578@163.com*

Received: 07-02-2020

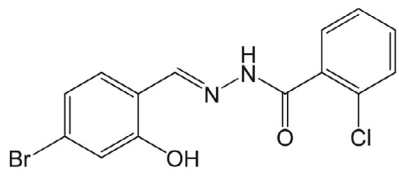
Abstract

Two vanadium(V) complexes derived from the bromo and chloro-substituted hydrazones *N*'-(4-bromo-2-hydroxybenzylidene)-2-chlorobenzohydrazide (H_2L^1) and *N*'-(3-bromo-5-chloro-2-hydroxybenzylidene)-3-methylbenzohydrazide (H_2L^2) with the formula [$VOL^1(OCH_3)(CH_3OH)$] (**1**) and [$VOL^2(OCH_3)(CH_3OH)$] (**2**) were newly synthesized and characterized by IR, UV-Vis and ^{1}H NMR spectroscopy. The structures of H_2L^1 and the complexes were further confirmed by single crystal X-ray diffraction. Both vanadium complexes are mononuclear, with the metal atoms coordinated by the hydrazone ligands, methanol ligands, and methanolate ligands, and the oxo groups, forming octahedral geometry. The hydrazones and the vanadium complexes were assayed for the antimicrobial activities on *Bacillus subtilis*, *Staphylococcus aureus*, *Escherichia coli*, and *Pseudomonas fluorescence*, and the fungi *Candida albicans* and *Aspergillus niger*. The existence of the bromo and chloro groups in the hydrazone ligands may improve the antimicrobial property.

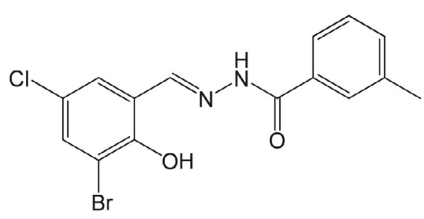
Keywords: Hydrazone; vanadium; crystal structure; antimicrobial property

1. Introduction

Hydrazone compounds and their metal complexes have received particular attention due to their interesting biological aspects like antibacterial,[1] antifungal,[2] and antitumor.[3] It has been proved that the compounds with electron-withdrawing substituent groups can enhance their antimicrobial ability.[4] Rai *et al.* reported some compounds with fluoro, chloro, bromo, and iodo-substituted groups, and their remarkable antimicrobial property.[5] Schiff base complexes of vanadium have potential antibacterial property.[6] Recently, our research group has reported some hydrazone vanadium complexes with bromo or chloro-substituent groups.[7] In pursuit of novel vanadium complex based antimicrobial agents, in this work, the bromo and chloro-substituent groups are incorporated together in the hydrazone compounds *N*'-(4-bromo-2-hydroxybenzylidene)-2-chlorobenzohydrazide (H_2L^1) and *N*'-(3-bromo-5-chloro-2-hydroxybenzylidene)-3-meth-



H_2L^1



H_2L^2

ylbenzohydrazide (H_2L^2), and then coordinate with vanadium, to form two new new vanadium(V) complexes, [$VOL^1(OCH_3)(CH_3OH)$] (**1**) and [$VOL^2(OCH_3)(CH_3OH)$] (**2**). The antimicrobial properties of the compounds are presented.

2. Experimental

2. 1. Materials and Methods

4-Bromosalicylaldehyde, 3-bromo-5-chlorosalicylaldehyde, 2-chlorobenzohydrazide, 3-methylbenzohydrazide and $VO(acac)_2$ with AR grade were obtained from Sigma-Aldrich. All other chemicals were commercial obtained from Xiya Chemical Co. Ltd. Elemental analyses of C, H and N were carried out in a Perkin-Elmer automated model 2400 Series II CHNS/O analyzer. The molar conductivity was determined using DDS-11A conductor device. FT-IR spectra were obtained on a Perkin-Elmer 377 FT-IR spectrometer with samples prepared as KBr pellets. UV-Vis spectra were obtained on a Lambda 35 spectrometer. ^{1}H NMR data were recorded on a Bruker 500 MHz spectrometer. X-ray diffraction was carried out on a Bruker APEX II CCD diffractometer. Thermal analyses were carried out in Schimatzu DT6-60H thermogravimetric analyzer.

2. 2. Synthesis osf H_2L^1

4-Bromosalicylaldehyde (0.010 mol, 2.0 g) and 2-chlorobenzohydrazide (0.010 mol, 1.7 g) were reacted in methanol (50 mL) at room temperature for 30 min. The solvent was removed by distillation, and the residue was recrystallized from methanol to give colorless crystalline product. Yield 92%. *Anal.* Calc. for $C_{14}H_{10}BrClN_2O_2$: C, 47.55; H, 2.85; N, 7.92. Found: C, 47.37; H, 2.93; N, 7.81%. IR data (cm^{-1}): 3433, 3208, 1643, 1614. UV-Vis data (MeOH, λ_{max}, nm): 223, 287, 312, 320, 405. ^{1}H NMR (500 MHz, d^6-DMSO): δ 12.32 (s, 1H, O*H*), 11.31 (s, 1H, N*H*), 8.66 (s, 1H, C*H*=N), 7.69 (d, 1H, Ar*H*), 7.61 (t, 1H, Ar*H*), 7.53-7.40 (m, 3*H*, ArH), 7.17 (s, 1H, Ar*H*), 7.12 (d, 1H, Ar*H*). ^{13}C NMR (126 MHz, d^6-DMSO): δ 164.18, 161.27, 145.22, 136.73, 134.12, 132.59, 132.26, 129.81, 128.33, 127.10, 123.35, 122.08, 116.34, 114.91.

Single crystals of the compound H_2L^1 were obtained by slow evaporation of the methanolic solution in air for a week.

2. 3. Synthesis of H_2L^2

3-Bromo-5-chlorosalicylaldehyde (0.010 mol, 2.3 g) and 3-methylbenzohydrazide (0.010 mol, 1.5 g) were reacted in methanol (50 mL) at room temperature for 30 min. The solvent was removed by distillation, and the residue was recrystallized from methanol to give colorless crystalline product. Yield 95%. *Anal.* Calc. for $C_{15}H_{12}BrClN_2O_2$: C, 49.01; H, 3.29; N, 7.62. Found: C, 48.83; H, 3.22; N, 7.45%. IR data (cm^{-1}): 3430, 3201, 1645, 1613. UV-Vis data (MeOH, λ_{max}, nm): 225, 290, 310, 323, 402. ^{1}H NMR (500 MHz, d^6-DMSO): δ 12.51 (s, 1H, O*H*), 11.27 (s, 1H, N*H*), 8.64 (s, 1H, C*H*=N), 7.82 (d, 1H, Ar*H*), 7.71 (s, 1H, Ar*H*), 7.55 (s, 1H, Ar*H*), 7.51-7.46 (m, 2*H*, ArH), 7.35 (t, 1H, Ar*H*), 2.38 (s, 3H, CH_3). ^{13}C NMR (126 MHz, d^6-DMSO): δ 164.03, 160.15, 145.31, 139.12, 137.06, 133.39, 132.22, 131.58, 129.74, 129.31, 128.45, 125.67, 121.17, 114.49, 21.08.

2. 4. Synthesis of Complex 1

H_2L^1 (0.10 mmol, 35 mg) and $VO(acac)_2$ (0.10 mmol, 26 mg) were reacted in methanol (10 mL) at reflux for 1 h and then cooled to room temperature. Block brown single crystals of the complex, suitable for X-ray diffraction, were grown from the solution upon slowly evaporation within a few days. The crystals were isolated by filtration. Yield 45%. Anal. calc. for $C_{16}H_{15}BrClN_2O_5V$: C, 39.90; H, 3.14; N, 5.82; found: C, 39.72; H, 3.26; N, 5.95%. IR data (cm^{-1}): 3451 (w), 1607 (s), 956 (m). UV-Vis data (MeOH, λ_{max}, nm): 275, 331. ^{1}H NMR (500 MHz, d^6-DMSO): δ 8.92 (s, 1H, C*H*=N), 7.82 (d, 1H, Ar*H*), 7.67 (d, 1H, Ar*H*), 7.58-7.45 (m, 3*H*, ArH), 7.19 (s, 1H, Ar*H*), 7.17 (d, 1H, Ar*H*), 5.28 (s, 3H, CH_3), 3.17 (s, 3H, CH_3). ^{13}C NMR (126 MHz, d^6-DMSO): δ 170.71, 163.20, 152.57, 134.30, 131.99, 131.78, 131.20, 130.75, 130.62, 127.77, 127.12, 122.56, 119.50, 119.38, 74.43, 48.58. Λ_M (10^{-3} M in methanol): 37 Ω^{-1} cm^2 mol^{-1}.

2. 5. Synthesis of Complex 2

H_2L^2 (0.10 mmol, 37 mg) and $VO(acac)_2$ (0.10 mmol, 26 mg) were reacted in methanol (10 mL) at reflux for 1 h and then cooled to room temperature. Block brown single crystals of the complex, suitable for X-ray diffraction, were grown from the solution upon slowly evaporation within a few days. The crystals were isolated by filtration. Yield 38%. Anal. calc. for $C_{17}H_{17}BrClN_2O_5V$: C, 41.20; H, 3.46; N, 5.65; found: C, 41.32; H, 3.53; N, 5.57%. IR data (cm^{-1}): 3445 (w), 1605 (s), 955 (m). UV-Vis data (MeOH, λ_{max}, nm): 273, 327. ^{1}H NMR (500 MHz, d^6-DMSO): δ 8.92 (s, 1H, C*H*=N), 7.92 (d, 1H, Ar*H*), 7.85-7.83 (m, 3H, Ar*H*), 7.40–7.27 (m, 2*H*, ArH), 5.39 (s, 3H, CH_3), 3.17 (s, 3H, CH_3), 2.39 (s, 3H, CH_3). ^{13}C NMR (126 MHz, d^6-DMSO): δ171.46, 157.45, 150.84, 137.91, 135.15, 132.40, 131.19, 130.34, 128.59, 128.55, 125.41, 122.74, 121.95, 111.95, 75.17, 48.57, 20.93. Λ_M (10^{-3} M in methanol): 33 Ω^{-1} cm^2 mol^{-1}.

2. 6. X-ray Crystallography

X-ray diffraction was carried out at a Bruker APEX II CCD area diffractometer equipped with MoKα radiation (λ = 0.71073 Å). The collected data were reduced with

Table 1. Crystallographic and refinement data for the complexes

Complex	H_2L^1	1	2
Formula	$C_{14}H_{10}BrClN_2O_2$	$C_{16}H_{15}BrClN_2O_5V$	$C_{17}H_{17}BrClN_2O_5V$
Formula weight	353.60	481.60	495.63
T (K)	298(2)	298(2)	298(2)
Crystal system	Monoclinic	Monoclinic	Monoclinic
Space group	$P2_1/n$	$P2_1/c$	$P2_1/c$
a (Å)	7.3644(12)	10.7402(12)	13.1333(10)
b (Å)	26.8935(13)	20.4546(15)	18.6524(12)
c (Å)	7.6148(12)	8.3295(7)	7.9156(7)
α (°)	90	90	90
β (°)	112.277(1)	94.601(1)	89.986(1)
γ (°)	90	90	90
V (Å^3)	1395.6(3)	1824.0(3)	1939.1(3)
Z	4	4	4
D_{calc} (g cm^{-3})	1.683	1.754	1.698
μ (Mo Kα) (mm^{-1})	3.138	2.911	2.741
F(000)	704	960	992
Measured reflections	8162	10588	13404
Unique reflections	2587	3378	2919
Observed reflections (I ³ 2σ(I))	1275	1693	2030
Parameters	187	238	250
Restraints	2	1	3
GOF	1.009	0.979	1.061
R_1, wR_2 [$I \geq 2\sigma(I)$][a]	0.0630, 0.1356	0.0655, 0.1226	0.0833, 0.1941
R_1, wR_2 (all data)[a]	0.1523, 0.1746	0.1556, 0.1542	0.1232, 0.2154

[a] $R_1 = \Sigma||F_o| - |F_c||/\Sigma|F_o|$, $wR_2 = \{\Sigma[w(F_o^2 - F_c^2)^2]/\Sigma[w(F_o^2)^2]\}^{1/2}$

Table 2. Selected bond distances (Å) and angles (°) for the complexes

	1	2
V1–O1	1.851(5)	1.887(5)
V1–O2	1.961(5)	1.977(6)
V1–O3	2.308(5)	2.329(6)
V1–O4	1.756(5)	1.756(5)
V1–O5	1.573(5)	1.582(7)
V1–N1	2.109(6)	2.138(6)
O5–V1–O4	101.6(2)	103.3(3)
O5–V1–O1	100.1(2)	98.1(3)
O4–V1–O1	104.7(2)	100.9(3)
O5–V1–O2	97.7(2)	98.5(3)
O4–V1–O2	92.6(2)	96.3(2)
O1–V1–O2	152.0(2)	152.5(2)
O5–V1–N1	95.0(2)	94.4(3)
O4–V1–N1	160.0(2)	160.9(3)
O1–V1–N1	82.9(2)	83.5(2)
O2–V1–N1	74.1(2)	73.6(2)
O5–V1–O3	175.6(2)	175.0(3)
O4–V1–O3	82.5(2)	81.3(2)
O1–V1–O3	80.2(2)	82.5(2)
O2–V1–O3	80.4(2)	79.1(2)
N1–V1–O3	80.6(2)	80.8(2)

SAINT,[8] and multi-scan absorption correction was performed using SADABS.[9] The structures of the complexes were solved by direct method, and refined against F^2 by full-matrix least-squares method using SHELXTL.[10] All of the non-hydrogen atoms were refined anisotropically. The hydrogen atoms bond to N and O atoms were located from electronic density maps with O-H and N-H groups refined fixing the bond lengths. The U_{iso}(H) were set to 1.5U_{eq}(O) and 1.2U_{eq}(N). The remaining hydrogen atoms were placed in calculated positions and constrained to ride on their parent atoms. The crystallographic data and refinement parameters for H_2L^1 and the complexes are listed in Table 1. Selected bond lengths and angles are listed in Table 2.

2. 7. Antimicrobial Assay

The antibacterial activities of the hydrazone compounds and the vanadium complexes were tested against *B. subtilis*, *S. aureus*, *E. coli*, and *P. fluorescence* using MH (Mueller–Hinton) medium. The antifungal activities of the compounds were tested against *C. albicans* and *A. niger* using RPMI-1640 medium. The MIC values of the tested compounds were determined by a colorimetric method using the dye MTT.[11] A stock solution of the compound (150 μg mL^{-1}) in DMSO was prepared and graded quantities (75, 37.5, 18.8, 9.4, 4.7, 2.3, 1.2, 0.59 μg mL^{-1}) were incorporated in specified quantity of the corresponding sterilized liquid medium. A specified quantity of the medium containing the compound was poured into micro-titration plates. Suspension of the microorganism was pre-

pared to contain approximately 1.0×10^5 cfu mL^{-1} and applied to microtitration plates with serially diluted compounds in DMSO to be tested and incubated at 37 °C for 24 h and 48 h for bacteria and fungi, respectively. Then the MIC values were visually determined on each of the microtitration plates, 50 μL of PBS (phosphate buffered saline 0.01 mol L^{-1}, pH = 7.4) containing 2 mg of MTT mL^{-1} was added to each well. Incubation was continued at room temperature for 4–5 h. The content of each well was removed and 100 μL of isopropanol containing 5% HCl (1 mol L^{-1}) was added to extract the dye. After 12 h of incubation at room temperature, the optical density was measured with a microplate reader at 550 nm.

3. Results and Discussion

3. 1. Synthesis and Characterization

The hydrazones H_2L^1 and H_2L^2 were readily prepared by the condensation reaction of a 1:1 molar ratio of 4-bromosalicylaldehyde with 2-chlorobenzohydrazide, and 3-bromo-5-chlorosalcylaldehyde with 3-methylbenzohydrazide, respectively in methanol. Single crystals of H_2L^1 were obtained by slow evaporation of its methanolic solution. However, it is difficult to obtain the single crystals of H_2L^2 even with the attempts of various solvents. The vanadium complexes were obtained by the reaction of the hydrazones with $VO(acac)_2$ in methanol, followed by recrystallization. Elemental analyses of the hydrazones and the vanadium complexes are in accordance with the molecular structures determined by the single crystal X-ray analysis.

3. 2. Spectroscopic Studies

In the spectra of the hydrazone compounds H_2L^1 and H_2L^2, and the vanadium complexes, the weak bands in the range 3400–3500 cm^{-1} are attributed to the vibration of the O–H bonds. The sharp bands of the hydrazone compounds H_2L^1 and H_2L^2 observed at 3200–3210 cm^{-1} are assigned to the vibration of the N–H bonds. The strong absorptions at 1643–1645 cm^{-1} of the hydrazone compounds are generated by the vibrations of the C=O bonds, whereas the bands at 1613–1614 cm^{-1} by the C=N bonds. The absence of the ν(C=O) and ν(N–H) bands, which present in the spectra of the hydrazones, implies the enolization of the amide functionality upon coordination to the V atoms. The strong absorption bands at 1605–1607 cm^{-1} can be assigned to the stretching vibrations of the C=N bonds. The typical bands at 955–956 cm^{-1} for the complexes could be clearly identified to the ν(V=O) for the complexes.[12]

In the UV-Vis spectra of the hydrazones and the vanadium complexes, the bands at 320-340 nm are assigned to the intra-ligand $\pi \rightarrow \pi^*$ absorptions. In the spectra of the vanadium complexes, the lowest energy transition bands observed at 400 nm are due to the LMCT transition as charge transfer from *p*-orbital on the lone-pair of ligands' oxygen atoms to the empty *d*-orbital of the vanadium atoms. The other mainly LMCT and to some extent $\pi \rightarrow \pi^*$ bands appear at about 275 nm for the vanadium complexes are attributed to the oxygen donor atoms bound to V atoms.[12]

The ^1H NMR spectra of the hydrazones H_2L^1 and H_2L^2 exhibit OH(phenolic) resonances at 12.32 and 12.51 ppm, respectively. Signals for one CH proton at 8.66 ppm, and one NH proton at 11.31 ppm for H_2L^1, and signals for one CH=N proton at 8.64 ppm, and one NH proton at 11.27 ppm for H_2L^2. Signals for aromatic protons are found in the 7.69–7.12 ppm range. Signals for methyl protons of H_2L^2 are found at 2.32 ppm.

3. 3. Structure Description of H_2L^1

Molecular structure of H_2L^1 is shown in Figure 1. The molecule adopts *E* configuration about the methylidene group. The distance of the C7–N1 group, 1.266(8) Å, indicates it a typical double bond. The distance of the C8–N2 bond (1.352(9) Å) is shorter, and that of the C8–O2 bond (1.222(7) Å) for the –C(O)–NH– unit is longer than usual, implies the conjugation effects in the hydrazone molecule. The bond lengths and angles in this compound are within normal values.[4a] The two aromatic rings C1–C6 and C9–C14 form a dihedral angle of 20.5(5)°. In the crystal structure of the compound, the molecules

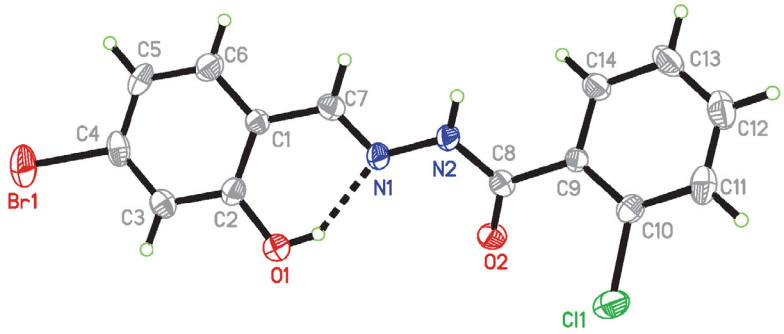


Figure 1. A perspective view of H_2L^1 with the atom labeling scheme. Thermal ellipsoids are drawn at the 30% probability level. Hydrogen bond is shown as a dotted line.

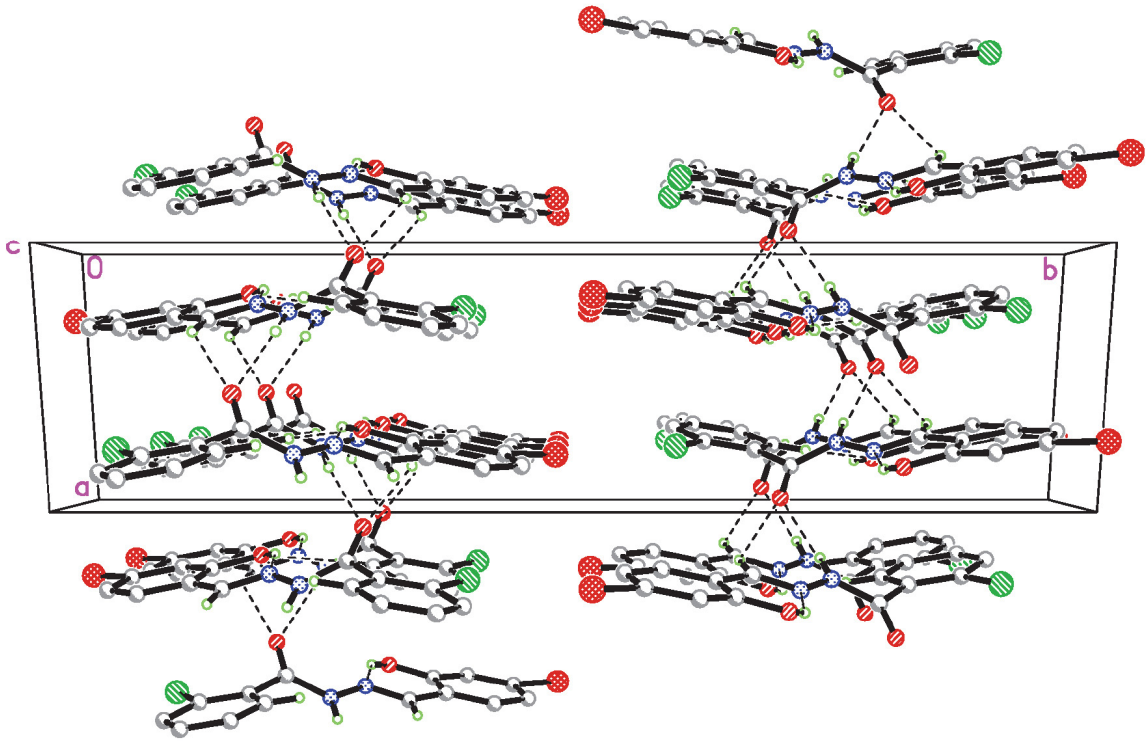


Figure 2. Molecular packing structure of H_2L^1, with hydrogen bonds shown as dotted lines.

are linked through N–H···O and non-classical C–H···O hydrogen bonds (Table 3), to form chains along the *a*-axis direction (Figure 2).

3. 4. Structure Description of the Complexes

Molecular structures of the vanadium complexes **1** and **2** are shown in Figures 3 and 4, respectively. The coordination spheres around the V atoms are best described as distorted octahedral geometry. The hydrazones, act as tridentate ligands, chelate the V atoms in a meridional fashion, generating one five and one six-membered rings with bite angles of 73.6(2)–74.1(2)° and 82.9(2)–83.5(2)°, respectively. This is not uncommon for this type of ligand systems.[13] Each hydrazone ligand lies in a plane with one hydroxylato ligand which lies *trans* to the hydrazone imino nitrogen atom. The oxygen atoms of the methanol ligands *trans* to the oxo oxygen atoms complete the distorted octahedral coordination spheres at rather elongated distances of 2.306(5)–2.329(6) Å, due to the *trans* effects of the oxo groups. This is accompanied by significant displacements of the V atoms of complexes **1** and **2** from the planes defined by the four basal donor atoms toward the apical oxo oxygen atoms by 0.295(3) and 0.299(3) Å, respectively. As

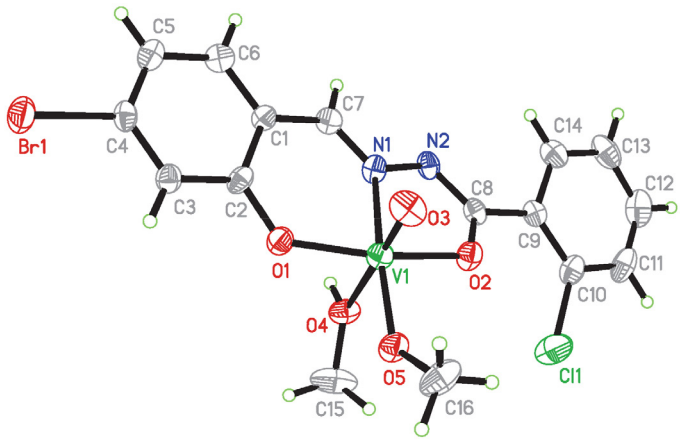


Figure 3. A perspective view of complex **1** with the atom labeling scheme. Thermal ellipsoids are drawn at the 30% probability level.

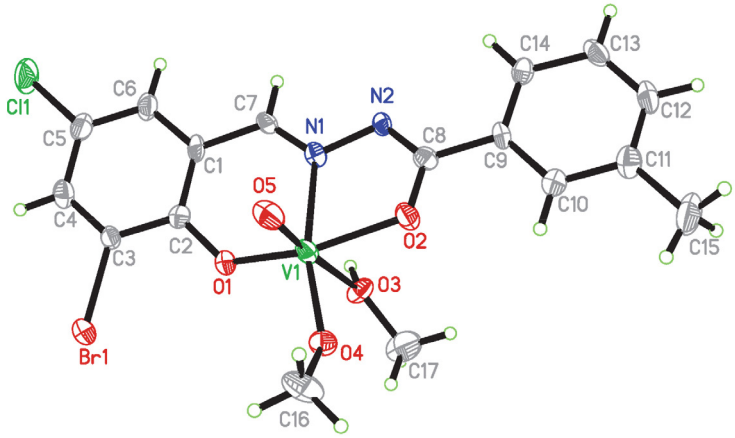


Figure 4. A perspective view of complex **2** with the atom labeling scheme. Thermal ellipsoids are drawn at the 30% probability level.

expected, the hydrazone ligands coordinate in their doubly deprotonated enolate form which is consistent with the observed O2–C8 and N2–C8 bond lengths of 1.28–1.31 Å and 1.29–1.31 Å. This agrees well with reported vanadium complexes with the enolate form of this type of ligands.[14]

In the crystal packing structure of complex **1**, the molecules are linked by hydrogen bonds (Table 3), leading to the formation of dimers (Figure 5). In the crystal packing structure of complex **2**, the molecules are linked by hydrogen bonds (Table 3), leading to the formation of chains along the *c*-axis direction (Figure 6).

3. 5. Antimicrobial Activity

The hydrazone compounds and the vanadium complexes were screened for antibacterial activities against two Gram (+) bacterial strains (*Bacillus subtilis* and *Staphylococcus aureus*) and two Gram (–) bacterial strains (*Escherichia coli* and *Pseudomonas fluorescence*) by MTT method. The MIC (minimum inhibitory concentration, μg mL^{-1}) values of the compounds against four bacteria are listed in Table 4. Penicillin G was used as the standard drug. Both hydrazone compounds show medium activity against *B. subtilis* and *S. aureus*, weak activity against *E. coli*, and no activity against *P. fluorescence*. H_2L^2 has stronger activities against the bacteria than H_2L^1 except for *P. fluorescence*. The vanadium complexes, in general, have stronger activities against the bacteria than the free hydrazones. The complexes have strong activities against *B. subtilis*, *S. aureus* and *E. coli* which are comparable to Penicillin G. Complex **1** has no activity against *P. fluoresence*, while complex **2** has weak activity. Both complexes have no activity on the fungal strains *Candida albicans* and *Aspergillus niger*.

Interestingly, the bromo and chloro-containing hydrazone H_2L^2 is more active than the bromo and methoxy-containing hydrazones *N*'-(3-bromo-2-hydroxybenzylidene)-3-hydroxy-4-methoxybenzohydrazide and *N*'- (3-bromo-2-hydroxybenzylidene)-3,5-dimethoxybenzohydrazide.[7a] Subsequently, the complex **2** with bromo and chloro-containing hydrazone ligand is more active than the vanadium complex with bromo and methoxy-containing hydrazone ligand on *S. aureus* and *P. fluorescence*.[7a]

Table 3. Hydrogen bond distances (Å) and bond angles (°) for the compounds

D–H···*A*	*d*(*D*–H)	*d*(H···*A*)	*d*(*D*···*A*)	Angle (*D*–H···*A*)
H_2L^1				
O1–H1···N1	0.85(1)	1.86(4)	2.608(7)	147(7)
N2–H2···O2^{i}	0.90(1)	1.91(2)	2.790(7)	166(6)
C7–H7···O2^{i}	0.93	2.51	3.198(5)	131(6)
C14–H14···O1^{ii}	0.93	2.45	3.295(5)	150(6)
1				
O3–H3···N2^{iii}	0.85(1)	1.92(3)	2.739(7)	162(10)
C6–H6···O5^{iv}	0.93	2.59	3.446(5)	154(5)
2				
O3–H3···N2^{v}	0.85(1)	1.98(1)	2.842(8)	176(3)
C13–H13···O5^{vi}	0.93	2.56	3.362(3)	145(4)

Symmetry codes: (i) ½ + *x*, ½ – *y*, ½ + *z*; (ii) *x*, *y*, 1 + *z*; (iii) 1 – *x*, –*y*, 1 – *z*; (iv) 1 – *x*, – *y*, 2 – *z*; (v) –*x*, 1 – *y*, 1 – *z*; (vi) –*x*, 1 – *y*, 2 – *z*.

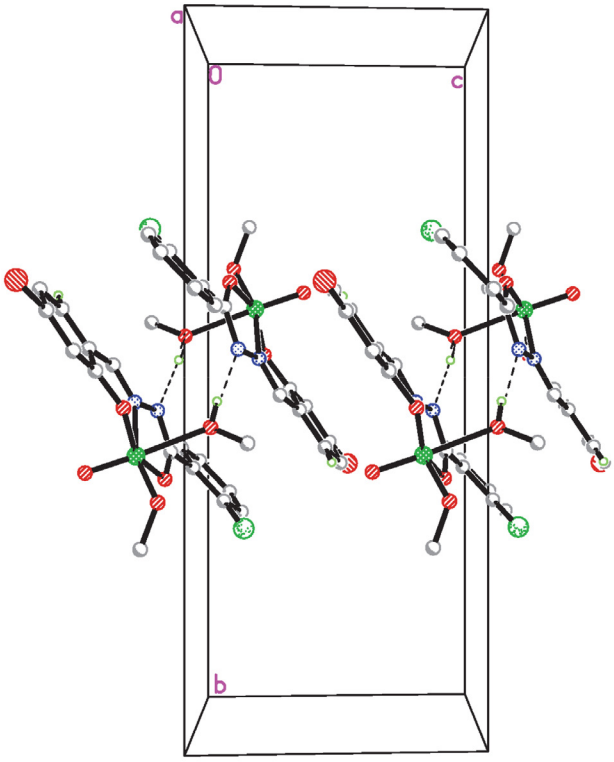


Figure 5. Molecular packing structure of complex **1**, with hydrogen bonds shown as dotted lines.

As compared with the chloro-containing hydrazone 2-chloro-*N*'-(3,5-dichloro-2-hydroxybenzylidene)benzohydrazide,[7c] H_2L^1 is obviously weak for all the bacteria, while H_2L^2 is similar except for *S. aureus*, a little weaker than the reported one. As for the vanadium complexes, complex **1** is similar to the reported vanadium complex with chloro-containing hydrazone ligand, while complex **2** is superior to the reported one against *B. subtilis*, *E. coli* and *P. fluorescence*.[7c] Moreover, when compared with the vanadium complexes with chloro and fluoro-containing hydrazone ligands, both complexes are to some extent have higher MIC values.[7b,15]

When compared with the vanadium complexes with Schiff base ligand 2-(((2-hydroxyethyl)imino)methyl)-6-methylphenol and the pyrone ligands 3-hydroxy2-methyl-4H-pyran-4-one or 2-ethyl-3-hydroxy-4H-pyran-4-one,[16] and the vanadium complexes with the ligands *N*'-(5-chloro-2-hydroxybenzylidene)pivalohydrazide and 3-hydroxy2-methyl-4H-pyran-4-one or 2-ethyl-3-hydroxy-4H-pyran-4-one,[17] the complexes **1** and **2** in this work is weaker for the bacteria *S. aureus*, *E. coli*, and *C. albicans*.[16] The present complexes have higher activities against *B. subtilis*, *S. aureus* and *E. coli*, when compared with the vanadium complex with the ligands *N*'-(3-bromo-2-hydroxybenzylidene)picolinohydrazide and 2-hydroxybenzohydroxamate. Interestingly, when the ligands changed to 2-chloro-*N*'-(2-hydroxy-3-methoxybenzylide-

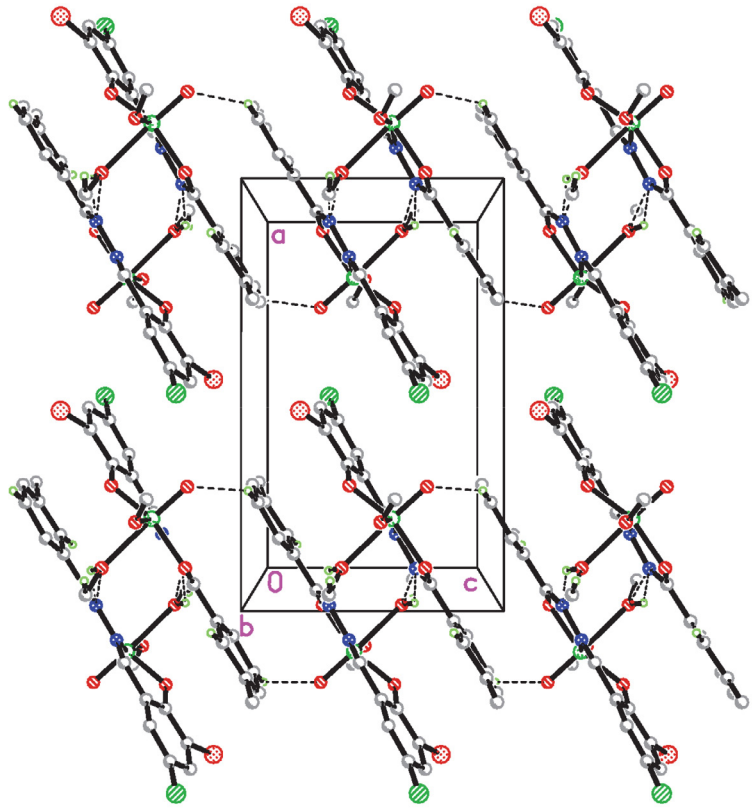


Figure 6. Molecular packing structure of complex **2**, with hydrogen bonds shown as dotted lines.

Table 4. Antimicrobial activities of the compounds with minimum inhibitory concentrations (μg mL^{-1})

Tested material	*B. subtilis*	*S. aureus*	*E. coli*	*P. fluorescence*
H_2L^1	37.5	18.8	75	>150
H_2L^2	9.4	9.4	37.5	>150
1	4.7	9.4	17.5	>150
2	2.3	4.7	9.4	37.5
Penicillin G	2.3	4.7	>150	>150

ne)benzohydrazide and 2-hydroxybenzohydroxamate, the present complexes have higher activities against *B. subtilis* and *E. coli*, while lower activities against *S. aureus*.[18]

3. 6. TGA Analysis

The thermograms of complexes **1** and **2** are shown as Figures 7 and 8, respectively. The decomposition mode of both complexes is similar. The neutral methanol ligands are removed between 80–120 °C, and the deprotonated methanol ligands are removed between 115–120 °C for complex **1** and 130–140 °C for complex **2**. Then, the complexes continue to decompose between 150–510 °C. The residue remained about 510 °C is 17% for complex **1** and 16% for complex **2**, which is in accordance with the expected amount of V_2O_5.

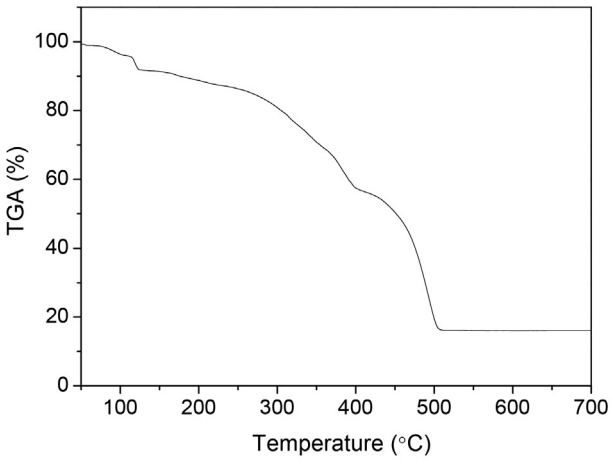


Figure 7. The TGA thermogram of complex **1** in air atmosphere.

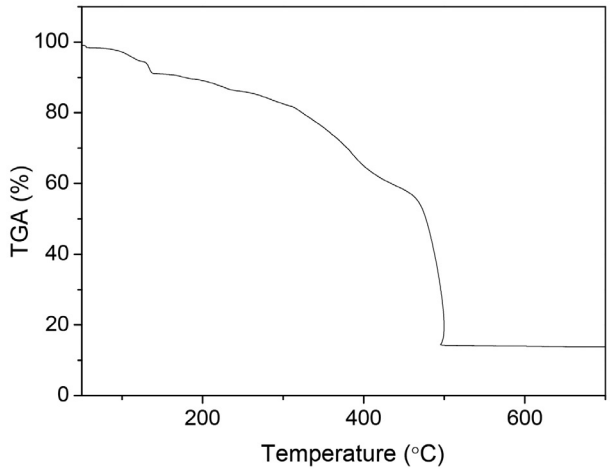


Figure 8. The TGA thermogram of complex **2** in air atmosphere.

Supplementary Data

CCDC 2012695 (H_2L^1), 1891034 (**1**) and 2012696 (**2**) contain the supplementary crystallographic data for the compounds. These data can be obtained free of charge *via* http://www.ccdc.cam.ac.uk/conts/retrieving.html, or from the Cambridge Crystallographic Data Centre, 12 Union Road, Cambridge CB2 1EZ, UK; fax: (+44) 1223-336-033; or e-mail: deposit@ccdc.cam.ac.uk.

4. Acknowledgments

This work was financially supported by K.C. Wong Magna Fund in Ningbo University, Ningbo Public Fund (Project No. 202002N3056) and the State Key Laboratory Development Fund of Structural Chemistry (Project No. 20190028).

5. References

1. (a) K. Pyta, A. Janas, M. Szukowska, P. Pecyna, M. Jaworska, M. Gajecka, F. Bartl, P. Przybylski, *Eur. J. Med. Chem.* **2019**, *167*, 96–104; **DOI:**10.1016/j.ejmech.2019.02.009
(b) R. Fekri, M. Salehi, A. Asadi, M. Kubicki, *Inorg. Chim. Acta* **2019**, *484*, 245–254; **DOI:**10.1016/j.ica.2018.09.022
(c) H. Y. Qian, *Inorg. Nano-Met. Chem.* **2018**, *48*, 461–466; **DOI:**10.1080/24701556.2019.1569689
(d) H. Y. Qian, *Russ. J. Coord. Chem.* **2017**, *43*, 780–786. **DOI:**10.1134/S1070328417110070
2. (a) D. A. Megger, K. Rosowski, C. Radunsky, J. Kosters, B. Sitek, J. Muller, *Dalton Trans.* **2017**, *46*, 4759–4767; **DOI:**10.1039/C6DT04613D
(b) N. R. Palepu, J. R. Premkumar, A. K. Verma, K. Bhattacharjee, S. R. Joshi, S. Forbes, Y. Mozharivskyj, K. M. Rao, *Arabian J. Chem.* **2018**, *11*, 714–728. **DOI:**10.1016/j.arabjc.2015.10.011
3. (a) Y.-C. Liu, H.-L. Wang, S.-F. Tang, Z.-F. Chen, H. Liang,

Anticancer Res. **2014**, *34*, 6034–6035;
(b) A. Erguc, M. D. Altintop, O. Atli, B. Sever, G. Iscan, G. Gormus, A. Ozdemir, *Lett. Drug Des. Discov.* **2018**, *15*, 193–202. **DOI:**10.2174/1570180814666171003145227
4. (a) M. Zhang, D.-M. Xian, H.-H. Li, J.-C. Zhang, Z.-L. You, *Aust. J. Chem.* **2012**, *65*, 343–350; **DOI:**10.1071/CH11424
(b) L. Shi, H.-M. Ge, S.-H. Tan, H.-Q. Li, Y.-C. Song, H.-L. Zhu, R.-X. Tan, *Eur. J. Med. Chem.* **2007**, *42*, 558–564. **DOI:**10.1016/j.ejmech.2006.11.010
5. N. P. Rai, V. K. Narayanaswamy, T. Govender, B. K. Manuprasad, S. Shashikanth, P. N. Arunachalam, *Eur. J. Med. Chem.* **2010**, *45*, 2677–2682. **DOI:**10.1016/j.ejmech.2010.02.021
6. (a) L.-H. Wang, X.-Y. Qiu, S.-J. Liu, *J. Coord. Chem.* **2019**, **DOI:**10.1080/00958972.2019.1590561
(b) X. W. Zhu, *Russ. J. Coord. Chem.* **2018**, *44*, 335–339; **DOI:**10.3103/S1068367418040213
(c) Z. H. Chohan, S. H. Sumrra, M. H. Youssoufi, T. B. Hadda, *Eur. J. Med. Chem.* **2010**, *45*, 2739–2747; **DOI:**10.1016/j.ejmech.2010.02.053
(d) O. Taheri, M. Behzad, A. Ghaffari, M. Kubicki, G. Dutkiewicz, A. Bezaatpour, H. Nazari, A. Khaleghian, A. Mohammadi, M. Salehi, *Transition Met. Chem.* **2014**, *39*, 253–259. **DOI:**10.1007/s11243-014-9798-9
7. (a) C.-L. Zhang, X.-Y. Qiu, S.-J. Liu, *Acta Chim. Slov.* **2019**, *66*, 719–725; **DOI:**10.17344/acsi.2019.5241
(b) L.-Y. He, X.-Y. Qiu, J.-Y. Cheng, S.-J. Liu, S.-M. Wu, *Polyhedron* **2018**, *156*, 105–110; **DOI:**10.1016/j.poly.2018.09.017
(c) S. M. Wu, X. Y. Qiu, J. C. Wang, S. J. Liu, L. Y. He, *Russ. J. Coord. Chem.* **2019**, *45*, 384–390.
8. Bruker, SMART (Version 5.625) and SAINT (Version 6.01). Bruker AXS Inc., Madison, Wisconsin, USA, 2007.
9. G. M. Sheldrick, SADABS. Program for Empirical Absorption Correction of Area Detector, University of Göttingen, Germany, 1996.
10. G. M. Sheldrick, Acta Crystallogr. 2008, A64, 112-122. **DOI:**10.1107/S0108767307043930
11. J. Meletiadis, J. F. G. M. Meis, J. W. Mouton, J. P. Donnelly, P. E. Verweij, *J. Clin. Microbiol.* **2000**, *38*, 2949–2954. **DOI:**10.1128/JCM.38.8.2949-2954.2000
12. A. Sarkar, S. Pal, *Polyhedron* **2007**, *26*, 1205–1210. **DOI:**10.1016/j.poly.2006.10.012
13. (a) D.-L. Peng, *Transit. Met. Chem.* **2016**, *41*, 843–848; **DOI:**10.1007/s11243-016-0086-8
(b) X. W. Zhu, *Russ. J. Coord. Chem.* **2018**, *44*, 421–424. **DOI:**10.1134/S1070328418070084
14. (a) D. L. Peng, *Russ. J. Coord. Chem.* **2017**, *43*, 404–410; **DOI:**10.1134/S1070328417060045
(b) Y. Li, L. Xu, M. Duan, J. Wu, Y. Wang, K. Dong, M. Han, Z. You, *Inorg. Chem. Commun.* **2019**, *105*, 212–216; **DOI:**10.1016/j.inoche.2019.05.011
(c) S. Guo, N. Sun, Y. Ding, A. Li, Y. Jiang, W. Zhai, Z. Li, D. Qu, Z. You, *Z. Anorg. Allg. Chem.* **2018**, *644*, 1172–1176. **DOI:**10.1002/zaac.201800060
15. E.-C. Liu, W. Li, X.-S. Cheng, *Acta Chim. Slov.* **2019**, *66*, 971–977.
16. G.-X. He, L.-W. Xue, Q.-L. Peng, P.-P. Wang, H.-J. Zhang, *Acta Chim. Slov.* **2019**, *66*, 570–575. **DOI:**10.17344/acsi.2018.4868
17. L.-W. Xue, Y.-J. Han, X.-Q. Luo, *Acta Chim. Slov.* **2019**, *66*, 622–628. **DOI:**10.17344/acsi.2019.5039
18. H.-Y. Qian, *Acta Chim. Slov.* **2019**, *66*, 995–1001. **DOI:**10.4149/neo_2019_190112N36

Povzetek

Sintetizirali smo dva vanadijeva(V) kompleksa z bromo in kloro-substituiranima hidrazonoma *N*'-(4-bromo-2-hidroksibenziliden)-2-klorobenzohidrazidom (H_2L^1) in *N*'-(3-bromo-5-kloro-2-hidroksibenziliden)-3-metilbenzohidrazidom (H_2L^2) s formulo $[VOL^1(OCH_3)(CH_3OH)]$ (**1**) in $[VOL^2(OCH_3)(CH_3OH)]$ (**2**) ter ju okarakterizirali z IR, UV-Vis in ^{1}H NMR spektroskopijo. Strukturo H_2L^1 in obeh kompleksov smo določili z monokristalno rentgensko difrakcijo. Oba vanadijeva kompleksa sta enojedrna, kovinski atom je oktaedrično koordiniran s hidrazonskim ligandom, metanolom in metanolatnim ligandom ter okso skupino. Hidrazona in vanadijeva kompleksa smo testirali za antimikrobno delovanje na *Bacillus subtilis*, *Staphylococcus aureus*, *Escherichia coli*, *Pseudomonas fluorescence*, *Candida albicans* in *Aspergillus niger*. Prisotnost bromo in kloro skupin na hidrazonskem ligandu lahko izboljša antimikrobne lastnosti.

Except when otherwise noted, articles in this journal are published under the terms and conditions of the Creative Commons Attribution 4.0 International License

DOI: 10.17344/acsi.2020.6252 *Acta Chim. Slov.* **2020,** *67,* 1290–1300
creative commons

Scientific paper

Four Different Crystalline Products from One Reaction: Unexpected Diversity of Products of the $CuCl_2$ Reaction with *N*-(2-Pyridyl)thiourea

Sara Tomšič, Janez Košmrlj and Andrej Pevec*

Faculty of Chemistry and Chemical Technology, University of Ljubljana, Večna pot 113, 1000 Ljubljana, Slovenia

** Corresponding author: E-mail: andrej.pevec@fkkt.uni-lj.si*

Received: 07-10-2020

Abstract

The reaction of *N*-(2-pyridyl)thiourea with $CuCl_2$ in methanol yields four different crystalline products: yellow dimeric complex, $[Cu_2Cl_2(\mu\text{-}Cl)_2(\mathbf{L})_2]$ (**1**), red polymeric complex, $[Cu_3Cl_8\mathbf{L}_2]_n$ (**2**), orange crystalline product with ionic structure, $\mathbf{L}_2[CuCl_4]$ (**3**), and colourless ionic compound **L**Cl (**4**), where **L** = 2-amino-[1,2,4]thiadiazolo[2,3-*a*]pyridin-4-ium cation as a result of oxidative cyclization of *N*-(2-pyridyl)thiourea. The crystal structures of all these crystalline products have been determined by single-crystal X-ray diffraction analysis. Compound **1** involves a copper(I) ion while in **2** and **3** the copper centre is in the divalent state. ^{1}H NMR spectra for compounds **1**–**3** are identical and confirm deprotonated thioamide groups of *N*-(2-pyridyl)thiourea and the formation of a thiadiazolopyridinium cation in solution. The hydrogen bonding and π–π stacking interactions were investigated in the solid state. In addition, all crystalline products **1**–**4** exhibit also S···Cl bonding interactions which consolidate the complexes into networks. The X-ray diffraction analyses indicate the absence of other crystalline phases in the crude reaction mixture.

Keywords: Cu(II) complex; Cu(I) complex; oxidative cyclization; crystal structure, thiourea

1. Introduction

Thiourea and its derivatives are readily oxidized in both aqueous and non-aqueous solutions by several oxidizing agents including bromine, iodine and copper(II) ions.[1] The reaction of thiourea and its derivatives with copper(II) salts in solution results in a reduction of Cu(II) ions into Cu(I) and the formation of many different stabile polynuclear products.[2–12] The chemistry of thioureas in copper-ion containing solutions is complex due to a variable and frequently uncertain nature of the redox processes involved. A number of copper(I) and even copper(II) complexes have been obtained with different molecular structures.[13] The oxidation and redox kinetics in copper(II) – thioureas systems have been investigated.[14,15]

Nitrogen-heterocyclic thiourea ligands can act as bridging units in some systems through thiourea sulfur and ring nitrogen atoms. Such coordination modes have been encountered especially in platinum group metal complexes.[16–19] The nitrogen-heterocyclic thiourea ligands are also efficient ligands for coordination to a Cu(I) cation producing a variety of monomeric and polymeric structures.[20,21] In addition, thioureas are widely recognized for their ability of hydrogen-bond formation and consequently supramolecular network arrangement.[22] Pyridine-thiourea derivatives also reveal great potential as ionophores for the detection of copper(II) ions in aqueous phase.[23]

Interestingly, treating *N*'-aryl and *N*'-benzoyl functionalized *N*-(2-pyridyl)thiourea derivatives with copper(II) chloride resulted in a variety of coordination compounds where a [1,2,4]thiadiazolo[2,3-*a*]pyridin-4-ium cation was coordinated to the copper centre.[24–26] It has been established that the *N*-(2-pyridyl)thiourea could easily be oxidized by copper(II) into the corresponding [1,2,4]thiadiazolo[2,3-*a*]pyridin-4-ium cation. These types of coordination compounds have been examined *in vitro* for their cytotoxic activity against human cancer cell lines showing promise in anticancer treatment.[26]

Although reported to undergo oxidative cyclisation into 2-amino-[1,2,4]thiadiazolo[2,3-*a*]pyridin-4-ium cation on treatment with sulphuryl chloride,[27,28] or bromine,[27,29–31] to our knowledge the cyclisation of the parent unsubstituted *N*-(2-pyridyl)thiourea with $CuCl_2$ has not been studied yet.

Herein we report that the reaction of *N*-(2-pyridyl)thiourea with $CuCl_2$ in methanol solution affords four dif-

ferent crystalline products: small yellow crystals, $[Cu_2Cl_2(\mu\text{-}Cl)_2(\mathbf{L})_2]$ (**1**), a red polymeric complex, $[Cu_3Cl_8\mathbf{L}_2]_n$ (**2**), a larger orange crystalline product with ionic structure, $\mathbf{L}_2[CuCl_4]$ (**3**) and a colourless ionic compound **L**Cl (**4**) (**L** = 2-amino-[1,2,4]thiadiazolo[2,3-*a*]pyridin-4-ium cation). The 2-amino-[1,2,4]thiadiazolo[2,3-*a*]pyridin-4-ium cation is the result of oxidative cyclization of *N*-(2-pyridyl)thiourea with copper(II). The structures of compounds **1**–**4** were determined by single-crystal X-ray diffraction analysis. The powder X-ray diffraction analysis was performed to analyse multicomponent products in the reaction mixture.

2. Experimental

General Procedure. *N*-(2-Pyridyl)thiourea and other reagents were purchased from commercial sources and were used as received. Proton NMR spectra were recorded at 500 MHz with a Bruker Avance III 500 spectrometer and referenced to $Si(CH_3)_4$ as an internal standard.

Synthesis. *N*-(2-pyridyl)thiourea (100 mg; 0.653 mmol) was dissolved in MeOH (10 mL). A few drops of Et_3N were added, followed by the addition of solid $CuCl_2$ (88 mg; 0.653 mmol). The resulting suspension was stirred for 40 min at room temperature. The undissolved residue was filtered off and the clear green filtrate was kept at room temperature. After 4–5 days, slow evaporation of methanol from the filtrate afforded crystals of **1**–**4**. The relative yields were **1** > **3** > **2** > **4**. Small quantities of each of these compounds were separated from the mixture of products manually under microscope.

X-ray Crystallography. Crystal data and refinement parameters of compounds **1**–**4** are listed in Table 1. The X-ray intensity data were collected on a Nonius Kappa CCD diffractometer equipped with graphite-monochromated Mo Kα radiation (λ = 0.71073 Å) at room temperature. The data were processed using DENZO.[32] The structures were solved by direct methods using SHELXS-2013/1[33] or SIR-2014[34] and refined against F^2 on all data by a full-matrix least-squares procedure with SHELXL-2016/4.[33] All non-hydrogen atoms were refined anisotropically. All hydrogen atoms bonded to carbon were included in the model at geometrically calculated positions and refined using a riding model. The nitrogen bonded hydrogen atoms were located in the difference map and refined with the distance restraints (DFIX) with d(N-H) = 0.86 Å and with $U_{iso}(H) = 1.2U_{eq}(N)$. Finally, the three residual peaks in the structure of compound **2** higher than 1 eÅ^{-3} were observed near to the Cu or Cl atoms, with no chemical meaning.

X-Ray powder diffraction data were collected using a PANalytical X'Pert PRO MPD diffractometer with θ–2θ

Table 1. Crystal data and structure refinement details for **1**–**4**.

	1	**2**	**3**	**4**
formula	$C_{12}H_{12}Cl_4Cu_2N_6S_2$	$C_{12}H_{12}Cl_8Cu_3N_6S_2$	$C_{12}H_{12}Cl_4CuN_6S_2$	$C_6H_6ClN_3S$
Fw (g mol^{-1})	573.28	778.62	509.74	187.65
crystal size (mm)	0.10 × 0.08 × 0.05	0.10 × 0.05 × 0.03	0.25 × 0.20 × 0.05	0.40 × 0.08 × 0.05
crystal color	yellow	red	orange	colorless
crystal system	monoclinic	monoclinic	triclinic	triclinic
space group	*C* 2/*c*	*C* 2/*c*	*P* –1	*P* –1
a (Å)	17.1791(9)	14.8897(4)	8.5710(2)	5.2892(2)
b (Å)	7.1000(5)	13.1658(3)	10.4873(4)	7.4109(5)
c (Å)	15.5496(8)	12.0204(3)	11.9667(5)	10.2184(6)
α (°)	90	90	110.638(2)	81.224(3)
β (°)	95.548(4)	94.174(2)	106.838(2)	80.666(3)
γ (°)	90	90	93.453(2)	82.732(3)
V (Å3)	1887.72(19)	2350.17(10)	947.51(6)	388.48(4)
Z	4	4	2	2
calcd density (g cm^{-3})	2.017	2.201	1.787	1.604
F(000)	1136	1524	510	192
no. of collected reflns	4034	5130	6643	2807
no. of independent reflns	2127	2655	4219	1753
R_{int}	0.0320	0.0208	0.0222	0.0191
no. of reflns observed	1535	2156	3257	1403
no. of parameters	124	149	238	106
$R[I > 2\sigma(I)]^a$	0.0440	0.0446	0.0354	0.0314
wR_2 (all data)^b	0.1025	0.1252	0.0812	0.0832
Goof , S^c	1.095	1.045	1.067	1.053
Largest diff. peak/hole (e Å^{-3})	+0.42/–0.52	+2.36/–0.691	+0.34/–0.35	+0.22/–0.26

[a] $R = \Sigma||F_o| - |F_c||/\Sigma|F_o|$. [b] $wR_2 = \{\Sigma[w(F_o^2 - F_c^2)^2]/\Sigma[w(F_o^2)^2]\}^{1/2}$. [c] $S = \{\Sigma[w(F_o^2 - F_c^2)^2]/(n-p)\}^{1/2}$ where n is the number of reflections and p is the total number of parameters refined.

reflection geometry, primary side Johansson type monochromator and Cu $K\alpha_1$ radiation (λ = 1.54059 Å). The ambient temperature XRD spectrum of a sample was acquired from 2θ angles of 5° to 80° in steps of 0.034° with integration time of 100 seconds using a 128 rtms channel detector. Simulated powder diffraction pattern were calculated from single crystal structural data by Mercury[35] program.

3. Results and Discussion

Synthetic Aspects. The reaction between equimolar amounts of *N*-(2-pyridyl)thiourea and $CuCl_2$ was performed in methanol solution in the presence of a small quantity of Et_3N. Four different crystalline products were obtained after evaporation of solvent from the clear green solution. Figure 1 shows a photography of the crystalline products: yellow (**1**), red (**2**), orange (**3**) and colourless crystals (**4**). Samples of each type could be manually collected and characterized by ^{1}H NMR spectroscopy and X-ray diffraction analyses. Small quantities of an amorphous green deposit were also found at the bottom of the vial but we are unable to characterize it.

From the crystal structure analyses it was evident that in all cases the *N*-(2-pyridyl)thiourea starting compound underwent oxidative cyclization into a 2-amino-[1,2,4]thiadiazolo[2,3-*a*]pyridin-4-ium cation (**L**) as shown in Scheme 1. A part of $CuCl_2$, added to the reaction

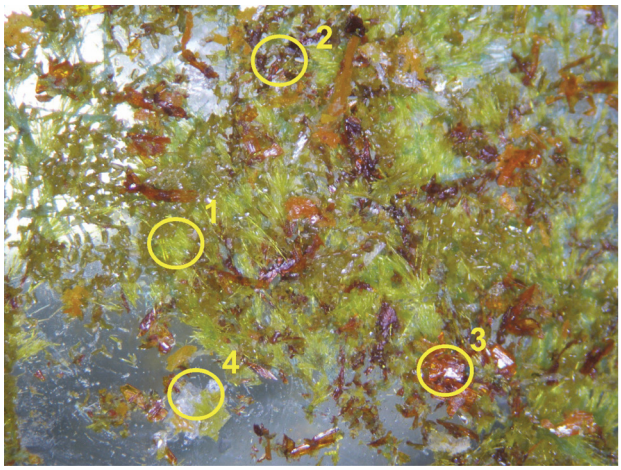
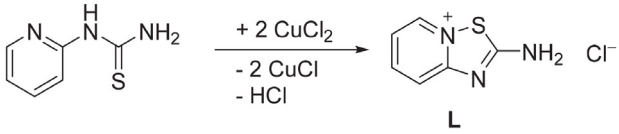


Figure 1. Photography of the bottom of vial containing the products of reaction between *N*-(2-pyridyl)thiourea and $CuCl_2$: yellow (**1**), red (**2**), orange (**3**) and colourless crystals (**4**).



Scheme 1. Oxidative cyclization of *N*-(2-pyridyl)thiourea with $CuCl_2$ forming 2-amino-[1,2,4]thiadiazolo[2,3-*a*]pyridin-4-ium cation (**L**).

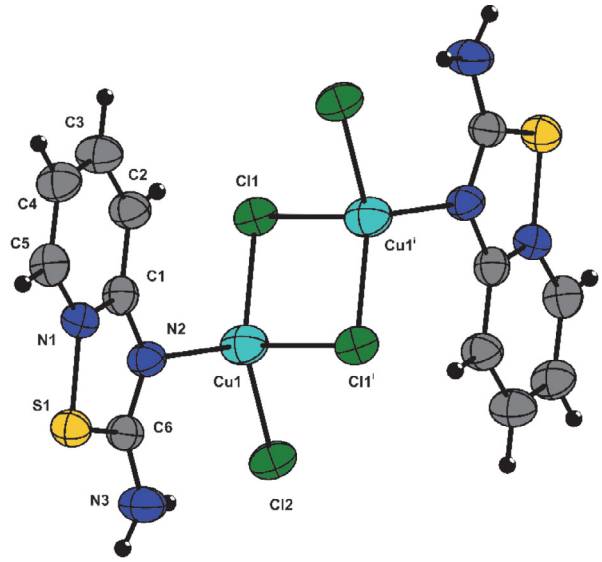


Figure 2. Molecular structure of **1** showing the atom-labeling scheme. The ellipsoids are shown at a probability level of 50%. Symmetry code: (i) –x+1/2, –y+3/2, –z+1.

Table 2. Selected bond lengths (Å) and angles (°) of compounds **1**–**4**.[a]

1			
Cu1–Cl1	2.2837(12)	Cl1–Cu1–Cl2	116.92(4)
Cu1–Cl1^i	2.5352(13)	Cl1–Cu1–Cl1^i	104.50(4)
Cu1–Cl2	2.3072(12)	Cl1–Cu1–N2	116.26(10)
Cu1–N2	2.069(3)	Cl2–Cu1–N2	115.66(10)
N1–S1	1.731(3)	Cu1–Cl1–Cu1^i	75.50(4)
S1–C6	1.762(4)	N1–S1–C6	86.92(18)
2			
Cu1–Cl1	2.2799(9)	Cl1–Cu1–Cl2	91.16(4)
Cu1–Cl2	2.2985(9)	Cl1–Cu1–Cl3	173.28(3)
Cu1–Cl3	2.2931(9)	Cl1–Cu1–Cl4	91.22(4)
Cu1–Cl4	2.3076(9)	Cl1–Cu1–Cl5	85.11(3)
Cu1–Cl5	2.946(1)	Cl1–Cu1–N2	95.52(8)
Cu1–N2	2.546(3)	Cl1–Cu2–Cl1^{ii}	180.00(4)
Cu2–Cl1	3.005(1)	Cl1–Cu2–Cl4^{ii}	105.35(3)
Cu2–Cl4	2.3290(9)	Cu1–Cl1–Cu2	74.47(3)
Cu2–Cl5	2.2672(9)	Cu1–Cl4–Cu2	88.97(3)
N1–S1	1.710(3)	Cu1–Cl5–Cu2	75.87(3)
S1–C6	1.756(4)	N1–S1–C6	88.21(17)
3			
Cu1–Cl1	2.2932(8)	Cl1–Cu1–Cl2	99.32(3)
Cu1–Cl2	2.2184(8)	Cl1–Cu1–Cl3	122.87(3)
Cu1–Cl3	2.2567(7)	Cl1–Cu1–Cl4	99.55(3)
Cu1–Cl4	2.2300(8)	Cl2–Cu1–Cl3	98.65(3)
N1–S1	1.720(2)	Cl2–Cu1–Cl4	139.35(3)
S1–C6	1.761(3)	N1–S1–C6	86.95(12)
4			
N1–S1	1.7293(15)	N1–S1–C6	86.38(8)
S1–C6	1.7632(17)	N3–C6–S1	121.23(14)

[a] Symmetry transformations used to generate equivalent atoms: (i) –x+1/2, –y+3/2, –z+1; (ii) –x+1/2, –y+1/2, –z.

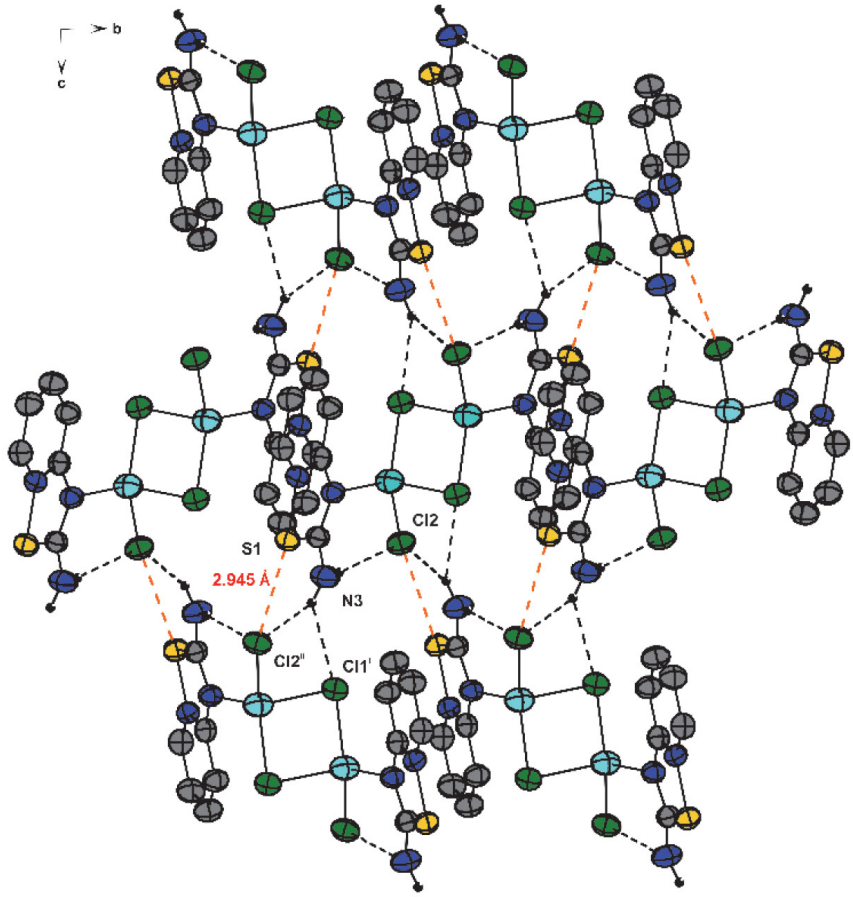


Figure 3. Layer formation in **1** through N–H···Cl hydrogen bonds and S···Cl contacts. The hydrogen atoms on aromatic rings have been removed for clarity. The ellipsoids are shown at a probability level of 50%. Symmetry codes: (i) x, –y+1, *z*+1/2; (ii) –x+1/2, y–1/2, –z+3/2.

Table 3. Hydrogen bonding geometry for **1**, **2**, **3** and **4**.

D – H ··· A	d(D – H)/ Å	d(H ··· A)/ Å	d(D ··· A)/ Å	<(DHA)/ °	Symmetry transformation for acceptors
1					
N3–H2N···Cl1	0.86(2)	2.78(5)	3.258(4)	116(4)	x, –y+1, z+1/2
N3–H1N···Cl2	0.86(2)	2.57(3)	3.391(4)	159(5)	
N3–H2N···Cl2	0.86(2)	2.40(3)	3.160(4)	148(5)	–x+1/2, y–1/2, –z+3/2
2					
N3–H1N···Cl1	0.848(19)	2.64(3)	3.398(4)	150(5)	
N3–H2N···Cl1	0.85(2)	2.63(4)	3.273(4)	134(5)	x, –y, z+1/2
N3–H2N···Cl5	0.85(2)	2.82(4)	3.533(4)	142(5)	x, –y, z+1/2
3					
N3–H1N···N5	0.855(18)	2.265(18)	3.119(3)	176(3)	
N3–H2N···Cl4	0.861(18)	2.48(2)	3.250(2)	149(3)	
N6–H3N···Cl3	0.849(18)	2.416(19)	3.254(3)	169(3)	
N6–H4N···Cl1	0.853(18)	2.47(2)	3.234(3)	149(3)	–x+1, –y+1, –z+2
4					
N3–H1N···Cl1	0.865(16)	2.27(2)	3.0319(18)	147(2)	
N3–H2N···N2	0.860(16)	2.286(18)	3.123(2)	164(2)	–x+2, –y+1, –z+2

mixture was reduced into copper(I) during oxidative cyclization and got involved into the coordination. Triethylamine assisted deprotonation of the thiamine group and neutralized the reaction mixture.

X-ray analysis of complex 1. The molecular structure of **1** shows the dinuclear complex to be a bis-chlorido-bridged copper(I) compound (Fig. 2 and Fig. S1). Selected bond lengths and angles are summarized in Table 2. The coordination polyhedron of each copper atom in the structure of complex **1** is a distorted tetrahedron. Each copper atom is coordinated by ligand **L**, one terminal and two bridging chlorine atoms. One bridging Cu–Cl bonding distance (2.284 Å) is shorter whereas the other (2.535 Å) is longer as compared to the terminal Cu–Cl bonding distance (2.307 Å). The Cu–N bond distance of 2.069 Å is slightly longer than the corresponding Cu(II)–N bond distance in similar compounds (from 1.988 to 1.996 Å).[26] The Cu···Cu separation of 2.957 Å suggest a narrow Cu–Cl–Cu angle in **1**. Discrete dinuclear units are connected into a 2D network parallel to the *bc* plane by N–H···Cl hydrogen bonds (Fig. 3, Table 3) and by S···Cl interactions of 2.945 Å. The 2D layers are then π–π stacked with a centroid-to-centroid separation distance between two pyridine rings of 3.731 Å into 3D array (Fig. 4).

X-ray analysis of complex 2. The structure of **2** features a linear homonuclear Cu(II) chloride polymer in which the $Cu_3Cl_8\mathbf{L}_2$ is the repeating unit (Fig. 5 and Fig. S2). Selected bond lengths and angles are given in Table 2. All chlorine atoms in these infinite chains are in the bridging positions. The coordination geometry around all copper atoms can be described as a distorted octahedron (Fig. 5). One type of copper atoms is coordinated by six chlorine atoms whereas the other is surrounded by five chlorine atoms and one **L** ligand. The Cu–N distance to the ligand **L** is 2.546 Å and is significantly longer than in the case of complex **1.** The Cu–Cl distances are in the range from normal 2.267 Å to very long Cu···Cl interaction of 3.005 Å. The structures with such elongated octahedra and very long Cu···Cl interaction can be found in the literature.[36] The elongated Cu···Cl and Cu···N interactions likely result from Jahn-Teller distortion. Two different Cu···Cu separations of 3.25 Å and 3.36 Å are longer than in compound **1** where copper is in +1 oxidation state. All the chlorido bridged copper atoms form a *zig-zag* chain, with the angles between the neighboring Cu atoms of 139° and 180°. The whole structure is stabilized by the N–H···Cl hydrogen bonding interactions, π–π stacking (3.878 Å) and by S···Cl interactions of 3.112 Å constructing a 3D network (Fig. 6, Table 3).

X-ray analysis of compound 3. The asymmetric unit of **3** consists of one $[CuCl_4]^{2-}$ anion and two **L** cations (Fig. S3). The packing of the structural units is depicted in Fig. 7. The coordination environment of the copper atom is tetrahedral with Cu–Cl distances ranging from 2.218 Å to 2.293 Å (Table 2), which is typical for tetrahedral $[CuCl_4]^{2-}$ ions. The cationic ligand **L** does not coordinate to the Cu atom in the structure of compound **3**. Four cations and two anions are connected by N–H···Cl and N–H···N hydrogen bonds (Table 3) and also by S···Cl inter-

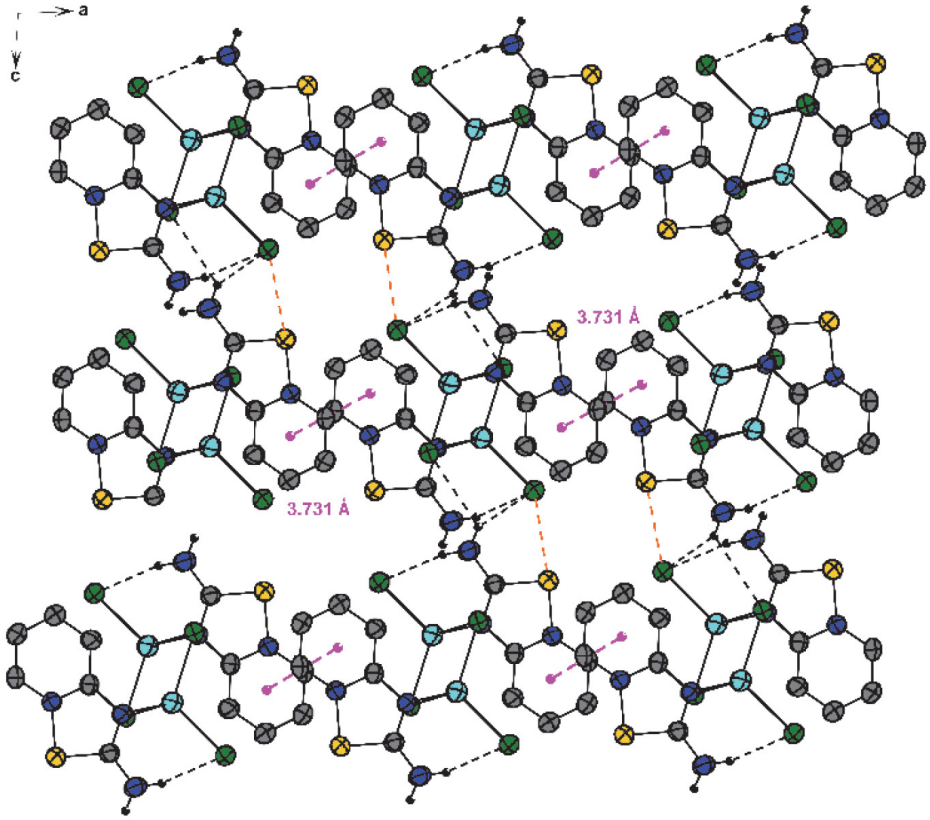


Figure 4. Fragment of the crystal packing of **1** with π–π stacking between pyridine rings. The ellipsoids are shown at a probability level of 50%.

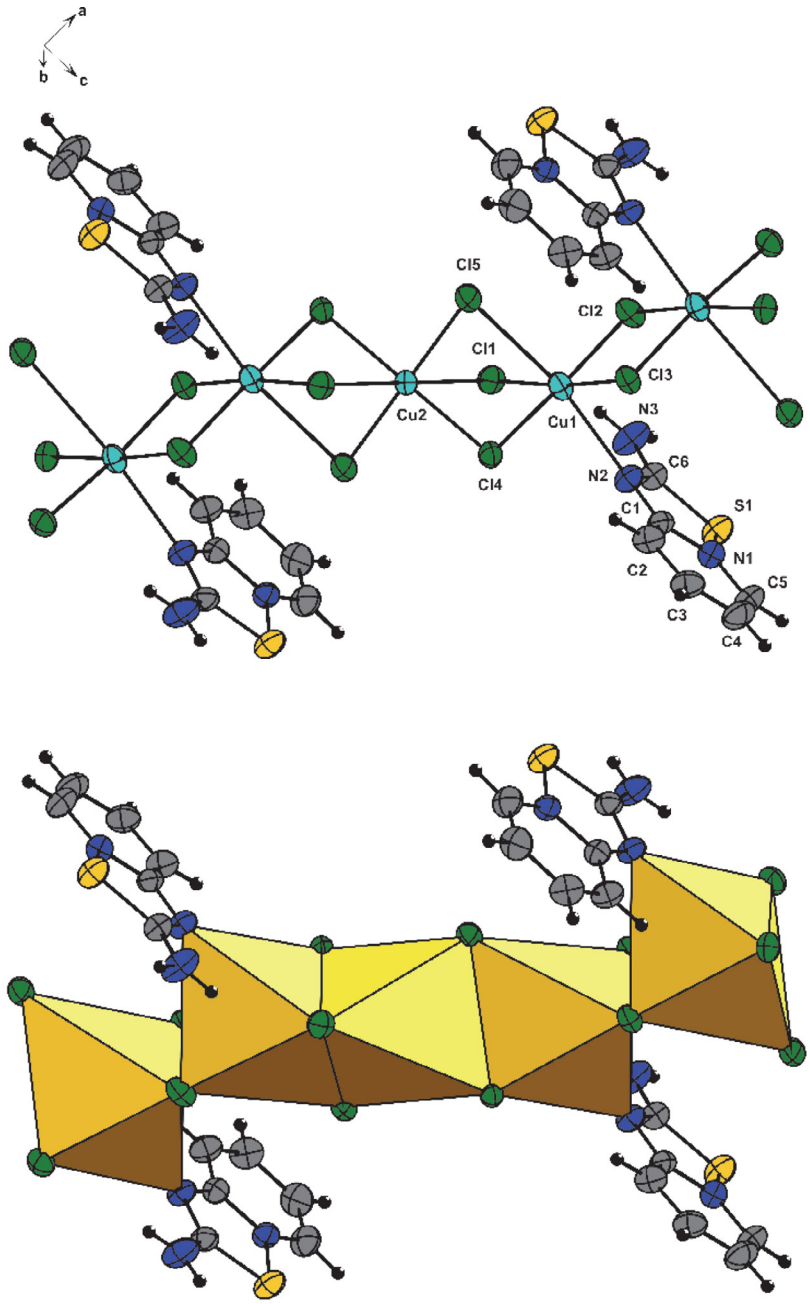


Figure 5. Molecular structure of **2** showing the atom-labeling scheme (above) and distorted octahedra representation (below). The ellipsoids are shown at a probability level of 50%.

actions into a discrete unit in the crystal structure. The S···Cl interaction distances are of two types, 3.029 and 3.113 Å, respectively. These units are then connected by π–π stacking interactions between the fused thiadiazole rings into chains along the *c*-axis with an interring distance of 3.673 Å (Fig. 8).

X-ray analysis of compound 4. The colorless crystals are an ionic phase without copper incorporated into the structure (Table 2 and Fig. S4). The reaction of formation of this ionic compound **4** is depicted in Scheme 1. Two cationic ligands **L** are connected by N–H···N hydrogen bonds into dimeric species (Fig. 9). The chloride anion is acceptor of a N–H···Cl hydrogen bond from the amino group of the ligand **L** (Table 3). These dimeric species are also stabilized by S···Cl interaction of 2.868 Å. In addition, the chloride anion is involved in other weak C–H···Cl hydrogen bonding interactions to form the 2D network in the crystal structure.

NMR spectra. The ^{1}H NMR spectra of compounds **1**, **2** and **3** recorded in DMSO-d_6 solutions (Figures S5–S7) are nearly identical indicating ligand **L** dissociation from the copper center in the solution. In comparison to the

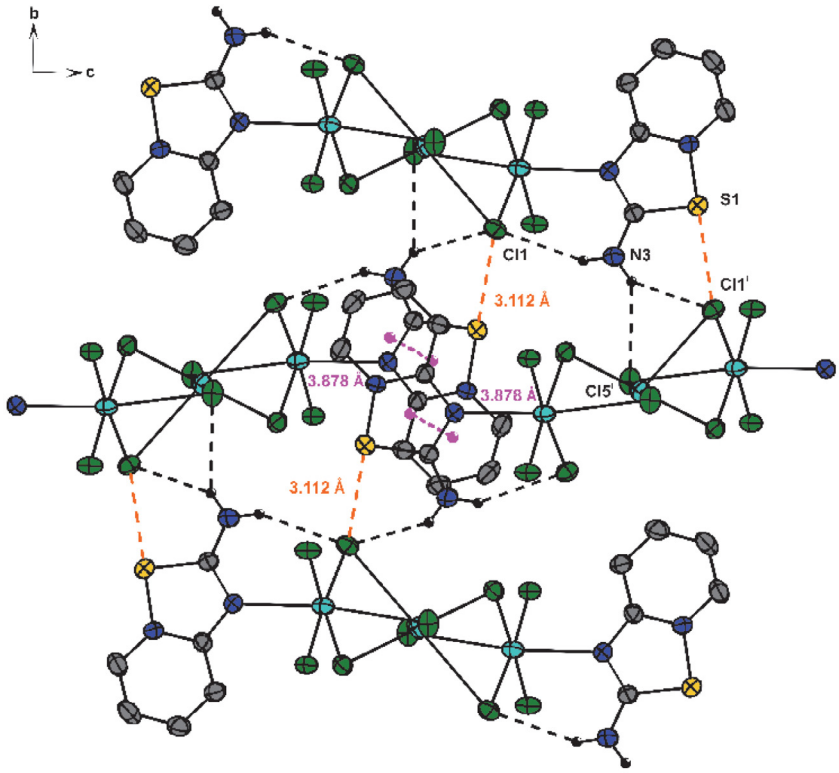


Figure 6. Fragment of the crystal packing in **2** with N–H···Cl hydrogen bonds, π–π stacking and S···Cl contacts. The hydrogen atoms on aromatic rings have been removed for clarity. The ellipsoids are shown at a probability level of 50%. Symmetry code: (i) x, –y, z+1/2.

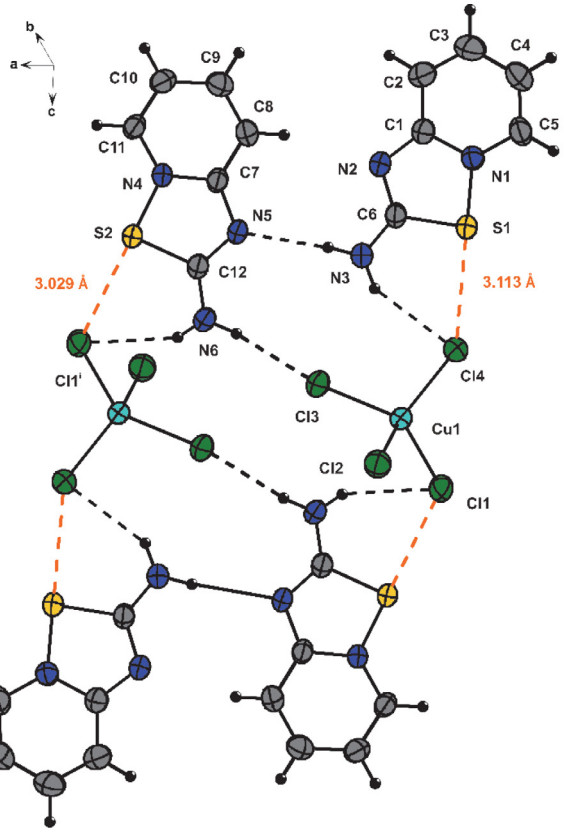


Figure 7. Fragment of crystal packing and the atom-labeling scheme of **3** with N–H···Cl and N–H···N hydrogen bonds and S···Cl interactions. The ellipsoids are shown at a probability level of 50%. Symmetry code: (i) –x+1, –y+1, –z+2.

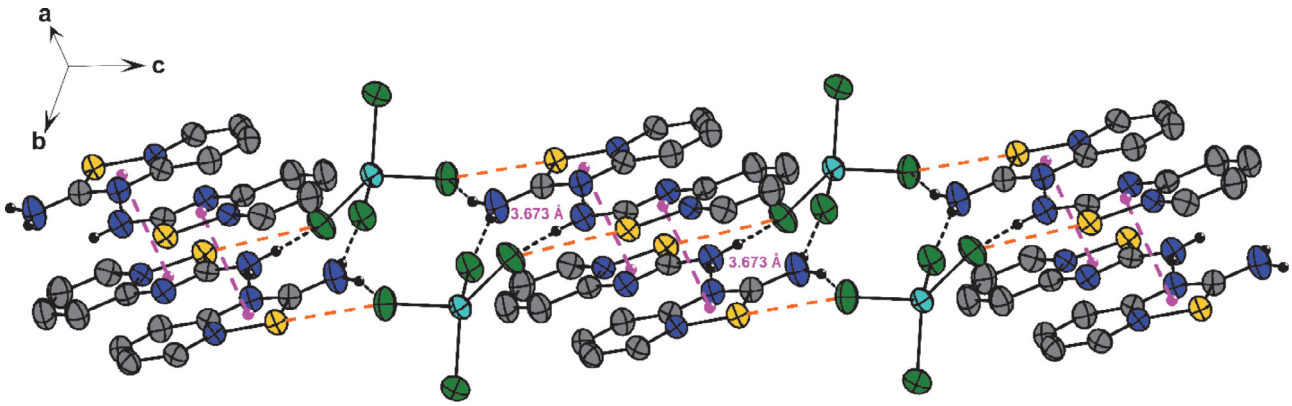


Figure 8. Fragment of crystal packing of 3 with π–π stacking between thiadiazole rings. The ellipsoids are shown at a probability level of 50%.

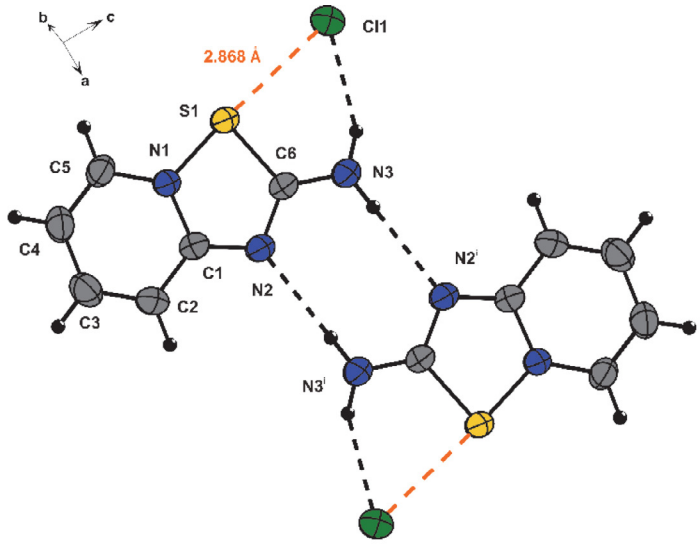


Figure 9. Fragment of crystal packing and the atom-labeling scheme of **3** with N–H···Cl and N–H···N hydrogen bonds and S···Cl interactions. The ellipsoids are shown at a probability level of 50%. Symmetry code: (i) –x+2, –y+1, –z+2.

starting *N*-(2-pyridyl)thiourea (Figure S8), the spectra of compounds **1**–**3** lack broad N–H resonance at δ 8.90 ppm (Fig. 10). The presence of 2-amino-[1,2,4]thiadiazolo[2,3-*a*]pyridin-4-ium cation is confirmed by a significant downfield shift of the electron-deficient fused pyridine protons resonating at δ 9.05 (d), 8.06 (dd), 7.70 (d) 7.33 (dd) ppm as compared to the *N*-(2-pyridyl)thiourea (δ 8.24 (d), 7.77 (dd), 7.16 (d), 7.05 (dd) ppm) and upfield shift for amino NH_2 hydrogen atoms (from 10.59 (s), 10.53 (s) ppm to 9.70 (s), 9.48 (s) ppm). The ^{1}H NMR chemical shifs of ligand **L** are in agreement with those for the substituted [1,2,4]thiadiazolo[2,3-*a*]pyridin-4-ium cations reported in the literature.[25,26]

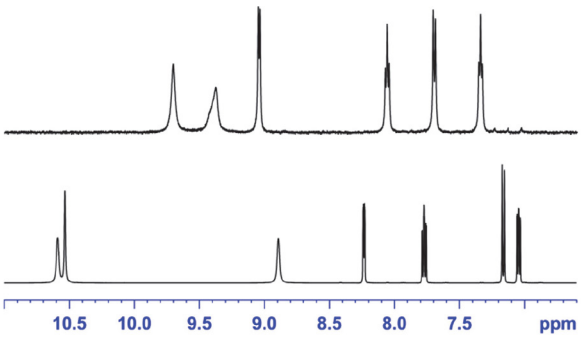


Figure 10. Selected parts of ^{1}H NMR spectra of compound **2** (above) and *N*-(2-pyridyl)thiourea (below).

Powder diffraction X-ray analysis. The product of the reaction was characterized by X-ray powder diffraction. There is clear evidence that the sample is a mixture of compounds **1**–**4** (Fig. 11). No other crystalline phases were additionally present since all diffraction peaks in the powder pattern of the sample can be contributed to compounds **1**–**4**.

4. Conclusion

In summary, four different crystalline complexes have been found as products of the reaction between

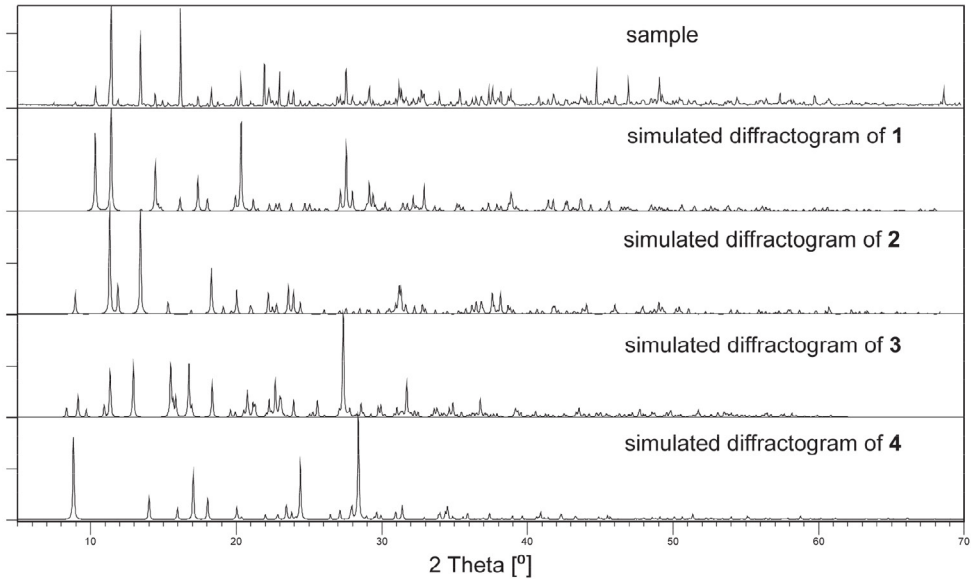


Figure 11. Comparison of the measured powder diffraction pattern of the reaction product and the simulated diffraction patterns of **1**–**4**. Intensities of diffracted x-rays are given in arbitrary units.

N-(2-pyridyl)thiourea and $CuCl_2$. Oxidative cyclization of *N*-(2-pyridyl)thiourea occurred with copper(II) chloride as an oxidant affording thiadiazolopyridinium cation as planar ligand. The complexes consist of a dimeric dinuclear unit (**1**), polymeric chains (**2**) and ionic (**3**) compounds. Copper(I) ions, which are a product of reduction of Cu(II) to Cu(I) and concomitant oxidation of *N*-(2-pyridyl) thiourea, are incorporated in complex **1**. Complexes **2** and **3** contain copper(II) while the ionic compound **4** contains a cationic ligand **L** with chlorine counter ion. The crystal structure determinations have established the existence of N–H···Cl hydrogen bonding interactions in all crystal structures. The remarkable feature of the **1**–**4** compounds is that there are S···Cl interactions involved in the crystal packing. Intermolecular or interionic S···Cl contacts with distances from 2.87 to 3.11 **Å** are significantly shorter than the corresponding van der Waals radii sum of 3.65 **Å**.[37] The short S···Cl contacts are now widely interpreted as chalcogen bonds.[38–41] The X-ray diffraction analysis compared the experimental powder diffraction pattern of the product of the reaction with the simulated diffraction patterns for all compounds **1**–**4** obtained from the single-crystal structure analysis.

Supplementary Material

The Supporting Information is available: ORTEP view of compounds **1**–**4**, ^{1}H NMR spectra of compunds **1**–**3** and *N*-(2-pyridyl)thiourea.

CCDC 1812471–1812474 contain the supplementary crystallographic data for this paper. This data can be obtained free of charge via www.ccdc.cam.ac.uk/data_request/cif, or by emailing data_request@ccdc.cam.ac.uk, or by contacting The Cambridge Crystallographic Data Centre, 12 Union Road, Cambridge CB2 1EZ, UK; fax: +44 1223 336033.

Acknowledgements

This work was supported by the Slovenian Research Agency (Grants: P1-0175 and P1-0230). Authors also thank to Dr. Marta Počkaj for her extremely helpful comments on powder diffraction analysis.

5. References

1. E. W. Ainscough, A. M. Brodie, *Coord. Chem. Rev.* **1978**, *27*, 59–86. **DOI:**10.1016/S0010-8545(00)80353-7
2. R. G. Vranka, E. L. Amma, *J. Am. Chem. Soc.* **1966**, *88*, 4270–4271. **DOI:**10.1021/ja00970a036
3. A. G. Gash, E. H. Griffith, W. A. Spofford, III, E. L. Amma, *J. Chem. Soc., Chem. Commun.* **1973**, 256–257. **DOI:**10.1039/c39730000256
4. I. F. Taylor, Jr., M. S. Weininger, E. L. Amma, *Inorg. Chem.* **1974**, *13*, 2835–2842. **DOI:**10.1021/ic50142a014
5. E. H. Griffith, G. W. Hunt, E. L. Amma, *J. Chem. Soc., Chem. Commun.* **1976**, 432–433. **DOI:**10.1039/C39760000432
6. J. P. Declercq, R. Kamara, C. Moreaux, J. M. Dereppe, G. Germain, M. Van Meerssche, *Acta Cryst.* **1978**, *B34*, 1036–1037. **DOI:**10.1107/S0567740878004793
7. R. C. Bott, G. A. Bowmaker, C. A. Davis, G. A. Hope, B. E. Jones, *Inorg. Chem.* **1998**, *37*, 651–657. **DOI:**10.1021/ic970910q
8. O. E. Piro, R. C. V. Piatti, A. E. Bolzán, R. C. Salvarezza, A. J. Arvia, *Acta Cryst.* **2000**, *B56*, 993–997. **DOI:**10.1107/S0108768100008028
9. P. Bombicz, I. Mutikainen, M. Krunks, T. Leskelä, J. Madarász,

L. Niinistö, *Inorg. Chim. Acta* **2004**, *357*, 513–525. **DOI:**10.1016/j.ica.2003.08.019
10. S. Athimoolam, J. Kumar, V. Ramakrishnan, R. K. Rajaram, *Acta Cryst.* **2005**, *E61*, m2014–m2017. **DOI:**10.1107/S1600536805028588
11. G. A. Bowmaker, J. V. Hanna, C. Pakawatchai, B. W. Skelton, Y. Thanyasirikul, A. H. White, *Inorg. Chem.* **2009**, *48*, 350–368. **DOI:**10.1021/ic801310r
12. H. Zouihri, *Acta Cryst.* **2012**, *E68*, m260–m261. **DOI:**10.1107/S1600536812004448
13. E. A. H. Griffith, W. A. Spofford, III, E. L. Amma, *Inorg. Chem.* **1978**, *17*, 1913–1917. **DOI:**10.1021/ic50185a043
14. D. A. Zatko, B. Kratochvil, *Anal. Chem.* **1968**, *40*, 2120–2123. **DOI:**10.1021/ac50158a031
15. C. J. Doona, D. M. Stanbury, *Inorg. Chem.* **1996**, *35*, 3210–3216. **DOI:**10.1021/ic9502077
16. M. L. Soriano, J. T. Lenthall, K. M. Anderson, S. J. Smith, J. W. Steed, *Chem. Eur. J.* **2010**, *16*, 10818–10831. **DOI:**10.1002/chem.201001354
17. J. G. Małecki, J. Nycz, *Polyhedron* **2013**, *55*, 49–56. **DOI:**10.1016/j.poly.2013.02.056
18. M. Kalidasan, R. Nagarajaprakash, S. Forbes, Y. Mozharivskyj, K. M. Rao, *Z. Anorg. Allg. Chem.* **2015**, *641*, 715–723. **DOI:**10.1002/zaac.201400491
19. M. Kalidasan, R. Nagarajaprakash, K. M. Rao, *Transition Met. Chem.* **2015**, *40*, 531–539. **DOI:**10.1007/s11243-015-9946-x
20. Y. Fan, H. Lu, H. Hou, Z. Zhou, Q. Zhao, L. Zhang, F. Cheng, *J. Coord. Chem.* **2000**, *50*, 65–72. **DOI:**10.1080/00958970008054925
21. A. Saxena, E. C. Dugan, J. Liaw, M. D. Dembo, R. D. Pike, *Polyhedron* **2009**, *28*, 4017–4031. **DOI:**10.1016/j.poly.2009.08.023
22. A. Saxena, R. D. Pike, *J. Chem. Crystallogr.* **2007**, *37*, 755–764. **DOI:**10.1007/s10870-007-9246-1
23. W. M. Khairul, H. M. Zuki, M. F. A. Hasan, A. I. Daud, *Procedia Chem.* **2016**, *20*, 105–114. **DOI:**10.1016/j.proche.2016.07.019
24. D.-J. Che, G. Li, Z. Yu, D.-P. Zou, C.-X. Du, *Inorg. Chem. Commun.* **2000**, *3*, 537–540. **DOI:**10.1016/S1387-7003(00)00115-5
25. G. Li, D.-J. Che, Z.-F. Li, Y. Zhu, D.-P. Zou, *New J. Chem.* **2002**, *26*, 1629–1633. **DOI:**10.1039/B206257G
26. F. Adhami, M. Safavi, M. Ehsani, S. K. Ardestani, F. Emmerling, F. Simyari, *Daton Trans.* **2014**, *43*, 7945–7957. **DOI:**10.1039/C3DT52905C
27. R. L. N. Harris, *Aust. J. Chem.* **1972**, *25*, 993–1001. **DOI:**10.1071/CH9720985
28. A. Castro, A. Martinez, *J. Heterocyclic. Chem.* **1999**, *36*, 991–995. **DOI:**10.1002/jhet.5570360427
29. B. Koren, B. Stanovnik, M. Tisler, *Org. Prep. Proced. Int.* **1975**, *7*, 55–59. **DOI:**10.1080/00304947509355570
30. I. Leban, *Acta Cryst.* **1976**, *B32*, 1601–1604. **DOI:**10.1107/S0567740876005980
31. G. Barnikow, J. Bödeker, *J. Prakt. Chem.* **1971**, *313*, 1148–1154. **DOI:**10.1002/prac.19713130622
32. Z. Otwinowski, W. Minor, *Methods Enzymol.* **1997**, *276*, 307–326. **DOI:**10.1016/S0076-6879(97)76066-X
33. G. M. Sheldrick, *Acta. Crystallogr.* **2015**, *C71*, 3–8. **DOI:**10.1107/S0108767307043930
34. M. C. Burla, R. Caliandro, B. Carrozzini, G. L. Cascarano, C. Cuocci, C. Giacovazzo, M. Mallamo, A. Mazzone, G. Polidori, *J. Appl. Cryst.* **2015**, *48*, 306–309. **DOI:**10.1107/S1600576715001132
35. C. F. Macrae, I. Sovago, S. J. Cottrell, P. T. A. Galek, P. McCabe, E. Pidcock, M. Platings, G. P. Shields, J. S. Stevens, M. Towler, P. A. Wood, *J. Appl. Cryst.* **2020**, *53*, 226–235. **DOI:**10.1107/S1600576719014092
36. Y. Fujii, Z. Wang, R. D. Willett, W. Zhang, C. P. Landee, *Inorg. Chem.* **1995**, *34*, 2870–2874. **DOI:**10.1021/ic00115a013
37. L. Pauling, *The Nature of the Chemical Bond*; Cornell University Press, Ithaca, 1960.
38. D. J. Pascoe, K. B. Ling, S. L. Cockroft, *J. Am. Chem. Soc.* **2017**, *139*, 15160–15167. **DOI:**10.1021/jacs.7b08511
39. K. T. Mahmudov, M. N. Kopylovich, M. F. C. Guedes da Silva, A. J. L. Pombeiro, *Dalton Trans.* **2017**, *46*, 10121–10138. **DOI:**10.1039/C7DT01685A
40. E. S. Yandanova, D. M. Ivanov, M. L. Kuznetsov, A. G. Starikov, G. L. Starova, V. Yu. Kukushkin, *Cryst. Growth Des.* **2016**, *16*, 2979–2987. **DOI:**10.1021/acs.cgd.6b00346
41. W. Wang, B. Ji, Y. Zhang, *J. Phys. Chem. A* **2009**, *113*, 8132–8135. **DOI:**10.1021/jp904128b

Povzetek

Pri reakciji med *N*-(2-piridil)tiosečnino in $CuCl_2$ v metanolu smo dobili štiri različne kristalinične produkte: rumene dimerne kristale, $[Cu_2Cl_2(\mu\text{-}Cl)_2(\mathbf{L})_2]$ (**1**), rdeč polimerni kompleks, $[Cu_3Cl_8\mathbf{L}_2]_n$ (**2**), oranžni kristalinični product z ionsko zgradbo, $\mathbf{L}_2[CuCl_4]$ (**3**), in brezbarvno ionsko spojino, **L**Cl (**4**). Pri tem je **L** = 2-amino-[1,2,4]tiadiazolo[2,3-*a*]piridin-4-ijev kation, ki je nastal v raztopini kot produkt oksidativne ciklizacije *N*-(2-piridil)tiosečnine. Kristalne strukture vseh kristaliničnih produktov so bile določene s pomočjo rentgenske strukturne analize. V spojini **1** je baker(I) ion, medtem ko je v spojinah **2** in **3** baker kolt centralni ion v oksidacijskem stanju +2. ^{1}H NMR spektri spojin **1**–**3** so identični in potrjujejo deprotonacijo tioamidne skupine *N*-(2-piridil)tiosečnine ter tvorbo tiadiazolopiridinijevega kationa v raztopini. V kristalnih strukturah so bile proučene tudi vodikove vezi in π–π interakcije. Poleg teh interakcij pa spojine **1**–**4** vsebujejo tudi S···Cl interakcije, ki povezujejo komplekse v trodimenzionalne tvorbe. Primerjava izračunanih rentgenskih praškovnih difraktogramov s difraktogramom produkta po reakciji nakazuje na odsotnost drugih kristaliničnih primesi.

Except when otherwise noted, articles in this journal are published under the terms and conditions of the Creative Commons Attribution 4.0 International License

Scientific paper

Syntheses, Crystal Structures and Antimicrobial Property of Schiff Base Copper(II) Complexes

Shun-Feng Yu, Xiao-Yang Qiu* and Shu-Juan Liu*

College of Science and Technology, Ningbo University, Ningbo 315212, P. R. China

** Corresponding author: E-mail: xiaoyang_qiu@126.com (Xiao-Yang Qiu), lsj_578@163.com (Shu-Juan Liu)*

Received: 08-06-2020

Abstract

Four new copper(II) complexes, $[CuL^1(\mu_{1,1}\text{-}N_3)]_n$ (**1**), $[CuL^1(\mu_{1,3}\text{-}NCS)]_n$ (**2**), $[Cu(HL^2)_2](SCN)_2$ (**3**) and $[Cu(L^2)_2]$ (**4**), where L^1 and L^2 are 2-((2-(dimethylamino)ethylimino)methyl-4,6-difluorophenolate and 2,4-difluoro-6-((3-morpholinopropylimino)methyl)phenolate, respectively, and HL^2 is 2-((2-(dimethylammonio)ethylimino)methyl-4,6-difluorophenolate, were synthesized and characterized by elemental analysis, IR and UV-vis spectroscopy. The structures for the complexes were further confirmed by single crystal X-ray structure determination. Complexes **1** and **2** are polymeric copper(II) complexes, with the Cu atoms in square pyramidal coordination. Complexes **3** and **4** are mononuclear copper(II) complexes, with the Cu atoms in square planar coordination. The complexes were assayed for their antimicrobial properties.

Keywords: Schiff base; copper complex; crystal structure; antimicrobial property

1. Introduction

Schiff base compounds and their metal complexes have attracted much attention due to their interesting biological aspects like antibacterial,[1] antifungal,[2] and antitumor.[3] It has been proved that the compounds with electron-withdrawing substituent groups can enhance their antimicrobial ability.[4] Rai *et al.* reported some compounds with fluoro, chloro, bromo, and iodo-substituted groups, and their remarkable antimicrobial property.[5] Schiff base complexes of copper have potential antibacterial property.[6] Recently, our research group has reported some Schiff base complexes with biological properties.[7] In pursuit of new Schiff base complexes with potential antimicrobial property, in this work, four new copper(II) complexes, $[CuL^1(\mu_{1,1}\text{-}N_3)]_n$ (**1**), $[CuL^1(\mu_{1,3}\text{-}NCS)]_n$ (**2**), $[Cu(HL^2)_2](SCN)_2$ (**3**) and $[Cu(L^2)_2]$ (**4**), where L^1 and L^2 are 2-((2-(dimethylamino)ethylimino)methyl-4,6-diluorophenolate and 2,4-difluoro-6-((3-morpholinopropylimino)methyl) phenolate, respectively, and HL^2 is 2-((2-(dimethylammonio)ethylimino)methyl-4,6-diluorophenolate, and their antimicrobial properties are present.

2. Experimental

2. 1. Materials and Methods

3,5-Difluorosalicylaldehyde, *N,N*-dimethylethane-1,2-diamine, *N*-(3-aminopropyl)morpholine, copper bromide, ammonium thiocyanate and sodium azide were obtained from Sigma-Aldrich. All other chemicals were commercial obtained from Xiya Chemical Co. Ltd. Elemental analyses of C, H and N were carried out in a Perkin-Elmer automated model 2400 Series II CHNS/O analyzer. The molar conductivity was determined using DDS-11A conductor device. FT-IR spectra were obtained on a Perkin-Elmer 377 FT-IR spectrometer with samples prepared as KBr pellets. UV-Vis spectra were obtained on a Lambda 35 spectrometer. Single crystal structural X-ray diffraction was carried out on a Bruker APEX II CCD diffractometer.

Caution! Because of their explosive character, sodium azide and the complexes containing azide ligand should be handled with care and in very low amounts.

2. 2. Synthesis of Complex 1

3,5-Difluorosalicylaldehyde (0.10 mmol, 16 mg), *N,N*-dimethylethane-1,2-diamine (0.10 mmol, 8.8 mg), sodium azide (0.10 mmol, 6.5 mg) and copper bromide (0.10 mmol, 22 mg) were mixed in methanol (15 mL) to give a clear blue solution. Block blue single crystals of the complex, suitable for X-ray diffraction, were grown from the solution upon slowly evaporation within five days. The crystals were isolated by filtration. Yield 37%. Anal. calc. for $C_{11}H_{13}CuF_2N_5O$: C, 39.70; H, 3.94; N, 21.04; found: C, 39.57; H, 4.03; N, 20.89%. IR data (cm^{-1}): 2045 (s), 1637

(s), 1461 (s), 1255 (m). UV-Vis data (MeOH, λ_{max}, nm): 215, 265, 376, 572. Λ_M (10^{-3} M in methanol): 45 Ω^{-1} cm^2 mol^{-1}.

2. 3. Synthesis of Complex 2

The complex was prepared with similar method as that described for complex **1**, but with sodium azide replaced with ammonium thiocyanate (0.10 mmol, 7.6 mg). Block blue single crystals of the complex, suitable for X-ray diffraction, were grown from the solution upon slowly evaporation within a week. The crystals were isolated by filtration. Yield 41%. Anal. calc. for $C_{12}H_{13}CuF_2N_3OS$: C, 41.31; H, 3.76; N, 12.05; found: C, 41.13; H, 3.92; N, 12.21%. IR data (cm^{-1}): 2094 (s), 1636 (s), 1462 (s), 1257 (m). UV-Vis data (MeOH, λ_{max}, nm): 215, 265, 380, 575. Λ_M (10^{-3} M in methanol): 42 Ω^{-1} cm^2 mol^{-1}.

2. 4. Synthesis of Complex 3

3,5-Difluorosalicylaldehyde (0.10 mmol, 16 mg), *N*-(3-aminopropyl)morpholine (0.10 mmol, 14 mg), ammonium thiocyanate (0.10 mmol, 7.6 mg) and copper bromide (0.10 mmol, 22 mg) were mixed in methanol (15 mL) to give a clear blue solution. Block blue single crystals of the complex, suitable for X-ray diffraction, were grown from the solution upon slowly evaporation within three days. The crystals were isolated by filtration. Yield 27%. Anal. calc. for $C_{30}H_{36}CuF_4N_6O_4S_2$: C, 48.15; H, 4.85; N, 11.23; found: C, 48.30; H, 4.92; N, 11.11%. IR data (cm^{-1}): 2056 (s), 1626 (s), 1480 (m), 1265 (m). UV-Vis data (MeOH, λ_{max}, nm): 210, 270, 362, 587. Λ_M (10^{-3} M in methanol): 182 Ω^{-1} cm^2 mol^{-1}.

2. 5. Synthesis of Complex 4

The complex was prepared with similar method as that described for complex **3**, but with ammonium thiocyanate replaced with sodium azide (0.10 mmol, 6.5 mg). Block blue single crystals of the complex, suitable for X-ray diffraction, were grown from the solution upon slowly evaporation within a week. The crystals were isolated by filtration. Yield 39%. Anal. calc. for $C_{28}H_{34}CuF_4N_4O_4$: C, 53.37; H, 5.44; N, 8.89; found: C, 53.23; H, 5.52; N, 8.75%. IR data (cm^{-1}): 1628 (s), 1472 (s), 1268 (m). UV-Vis data (MeOH, λ_{max}, nm): 210, 270, 360, 595. Λ_M (10^{-3} M in methanol): 36 Ω^{-1} cm^2 mol^{-1}.

2. 6. X-ray Crystallography

X-ray diffraction was carried out at a Bruker APEX II CCD area diffractometer equipped with MoKα radiation (λ = 0.71073 Å). The collected data were reduced with SAINT,[8] and multi-scan absorption correction was performed using SADABS.[9] The structures of the complexes were solved by direct method, and refined against F^2 by

Table 1. Crystallographic and refinement data for the complexes

Complex	1	2	3	4
Formula	$C_{11}H_{13}CuF_2N_5O$	$C_{12}H_{13}CuF_2N_3OS$	$C_{30}H_{36}CuF_4N_6O_4S_2$	$C_{28}H_{34}CuF_4N_4O_4$
Formula weight	332.80	348.85	748.31	630.13
T (K)	298(2)	298(2)	298(2)	298(2)
Crystal system	Monoclinic	Monoclinic	Triclinic	Triclinic
Space group	$P2_1/c$	$P2_1/c$	P-1	P-1
a (Å)	10.074(1)	16.352(1)	6.4118(8)	4.731(1)
b (Å)	6.531(1)	7.563(1)	7.465(1)	11.399(1)
c (Å)	20.322(1)	11.761(1)	17.532(1)	13.749(1)
α (°)	90	90	93.867(1)	68.109(1)
β (°)	101.559(1)	103.849(1)	100.024(1)	81.436(1)
γ (°)	90	90	90.778(1)	84.849(1)
V (Å^3)	1310.0(3)	1412.2(3)	824.2(2)	679.9(2)
Z	4	4	1	1
D_{calc} (g cm^{-3})	1.687	1.641	1.508	1.539
μ (Mo Kα) (mm^{-1})	1.694	1.714	0.857	0.873
F(000)	676	708	387	327
Measured reflections	7376	8002	4867	10251
Unique reflections	2429	2600	3040	2529
Observed reflections ($I \geq 2\sigma(I)$)	1790	1625	2396	1913
Parameters	183	183	214	187
Restraints	0	0	0	0
GOOF	1.005	1.001	1.129	1.000
R_1, wR_2 [$I \geq 2\sigma(I)$][a]	0.0320, 0.0667	0.0581, 0.1471	0.0491, 0.1290	0.0502, 0.1261
R_1, wR_2 (all data)[a]	0.0552, 0.0736	0.0981, 0.1822	0.0714, 0.1689	0.0719, 0.1381

[a] $R_1 = \Sigma||F_o| - |F_c||/\Sigma|F_o|$, $wR_2 = \{\Sigma[w(F_o^2 - F_c^2)^2]/\Sigma[w(F_o^2)^2]\}^{1/2}$

full-matrix least-squares method using SHELXTL.[10] All of the non-hydrogen atoms were refined anisotropically. The hydrogen atoms were placed in calculated positions and constrained to ride on their parent atoms. The crystallographic data and refinement parameters for the complexes are listed in Table 1. Selected bond lengths and angles are listed in Table 2.

Table 2. Selected bond distances (Å) and angles (°) for the complexes

1			
Cu1–O1	1.9224(17)	Cu1–N1	1.963(2)
Cu1–N2	2.075(2)	Cu1–N3	1.986(2)
O1–Cu1–N1	92.61(8)	O1–Cu1–N3	89.49(8)
N1–Cu1–N3	170.79(11)	O1–Cu1–N2	176.46(8)
N1–Cu1–N2	83.98(9)	N3–Cu1–N2	93.74(9)
2			
Cu1–O1	1.898(4)	Cu1–N1	1.933(5)
Cu1–N2	2.076(6)	Cu1–N3	1.944(4)
O1–Cu1–N3	90.9(2)	O1–Cu1–N1	92.1(2)
N3–Cu1–N1	168.9(2)	O1–Cu1–N2	171.5(2)
N3–Cu1–N2	91.1(2)	N1–Cu1–N2	84.4(2)
3			
Cu1–O1	1.892(3)	Cu1–N1	2.013(3)
O1–Cu1–O1A	180	O1–Cu1–N1	92.28(12)
O1–Cu1–N1A	87.72(12)	N1–Cu1–N1A	180
4			
Cu1–O1	1.875(2)	Cu1–N1	2.007(3)
O1–Cu1–O1A	180	O1–Cu1–N1A	88.06(10)
O1–Cu1–N1	91.94(10)	N1–Cu1–N1A	180

Symmetry code for A: 1 – *x*, 1 – *y*, 1 – *z*.

2. 7. Antimicrobial Assay

The antibacterial property of the complexes was tested against *Bacillus subtilis*, *Staphylococcus aureus*, *Escherichia coli*, and *Pseudomonas fluorescence* using MH (Mueller–Hinton) medium. The antifungal activities of the compounds were tested against *Candida albicans* and *Aspergillus niger* using RPMI-1640 medium. The MIC values of the tested compounds were determined by a colorimetric method using the dye MTT.[11] A stock solution of the compound (150 μg mL^{-1}) in DMSO was prepared and graded quantities (75 μg mL^{-1}, 37.5 μg mL^{-1}, 18.8 μg mL^{-1}, 9.4 μg mL^{-1}, 4.7 μg mL^{-1}, 2.3 μg mL^{-1}, 1.2 μg mL^{-1}, 0.59 μg mL^{-1}) were incorporated in specified quantity of the corresponding sterilized liquid medium. A specified quantity of the medium containing the compound was poured into micro-titration plates. Suspension of the microorganism was prepared to contain approximately 1.0×10^5 cfu mL^{-1} and applied to microtitration plates with serially diluted compounds in DMSO to be tested and incubated at 37 °C for 24 h and 48 h for bacteria and fungi, respectively. Then the MIC values were visually determined on each of the microtitration plates, 50 μL of PBS (phosphate buffered saline 0.01 mol L^{-1}, pH = 7.4) containing 2 mg of MTT mL^{-1} was added to each well. Incubation was continued at room temperature for 4–5 h. The content of each well was removed and 100 μL of isopropanol containing 5% 1 mol L^{-1} HCl was added to extract the dye. After 12 h of incubation at room temperature, the optical density was measured with a microplate reader at 550 nm.

3. Results and Discussion

3. 1. Synthesis and Characterization

The complexes were readily prepared by the reaction of equimolar quantities of 3,5-difluorosalicylaldehyde, *N,N*-dimethylethane-1,2-diamine or *N*-(3-aminopropyl)morpholine, sodium azide or ammonium thiocyanate, and copper bromide in methanol. Single crystals of the complexes were obtained by slow evaporation of their methanolic solution. The azide and thiocyanate coordinate to the Cu atoms in complexes **1** and **2**, respectively. However, the thiocyanate acts as a counteranion in complex **3**, and the azide is absent in complex **4**. Without sodium azide, complex **4** can also be obtained by the reaction of equimolar quantities of 3,5-difluorosalicylaldehyde, *N*-(3-aminopropyl)morpholine, and copper bromide in methanol. Elemental analyses of the complexes are in accordance with the molecular structures determined by the single crystal X-ray analysis. Molar conductivity for 10^{-3} mol L^{-1} sample/methanol solutions for ionic electrolytes at 25 °C indicates the non-electrolytic nature of complexes **1**, **2** and **4**, and 1:2 electrolytic nature of complex.[12]

3. 2. Spectroscopic Studies

The typical and strong absorptions at 1626–1637 cm^{-1} of the complexes are generated by the vibrations of the C=N bonds, indicating the formation of the Schiff bases from the condensation reaction of the 3,5-difluorosalicylaldehyde and the amines during the coordination. The intense absorption at 2045 cm^{-1} for complex **1** is attributed to the stretching vibration of the azide,[13] and those at 2094 cm^{-1} for complex **2** and 2056 cm^{-1} for complex **3** are assigned to the stretching vibrations of CN bond in thiocyanate. The difference of the absorption bands of the thiocyanate groups, indicates different modes in the complexes. The thiocyanate in complex **2** coordinates to the Cu atom, while that in complex **3** is free.[14]

In the UV-Vis spectra of the complexes, the bands at 360–380 nm are attributed to the azomethine chromophore $\pi \rightarrow \pi^*$ transition.[15] The bands at higher energies (210–215 and 265–270 nm) are associated with the benzene $\pi \rightarrow \pi^*$ transition.[15] The weak and less well-defined broad bands found at 570–600 nm are assigned to the *d–d* transitions.[16]

3. 3. Structure Description of Complex 1

Molecular structure of the end-on azido bridged polymeric copper complex **1** is shown in Figure 1. The asymmetric unit of the complex contains a [$CuL^1(N_3)$] unit. The Cu atom is coordinated in a square pyramidal geometry, with the phenolate O1, imino N1, amino N2 atoms of the Schiff base ligand L^1, and the azido N3 atom defining the basal plane, and with the azido N3A atom located at the apical position. The Schiff base ligand, acts as a tridentate ligand, chelate the Cu atom by generating one five and one six-membered rings with bite angles of 83.98(9)° and 92.61(8)°, respectively. The displacement of the Cu atom from the plane defined by the four basal donor atoms toward the apical azido N atom by 0.087(2) Å. The azide ligand bridges Cu atoms with an end-on bridging mode, generating a Cu···Cu distance of 4.156(3) Å. The bond lengths and angles in the square pyramidal coordination are similar to those in the reported azido bridged Schiff base copper complexes.[17] In the crystal structure of the complex, the [CuL^1] units are linked by the azide bridges, to form one-dimensional chains along the *b* axis (Figure 2).

3. 4. Structure Description of Complex 2

Molecular structure of the end-to-end thiocyanato bridged polymeric copper complex **2** is shown in Figure 3.

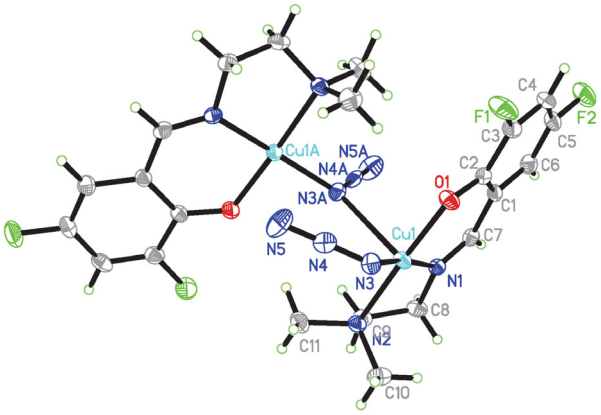


Figure 1. A perspective view of complex **1** with the atom labeling scheme. Thermal ellipsoids are drawn at the 30% probability level.

The asymmetric unit of the complex contains a [CuL^1(NCS)] unit. The Cu atom is coordinated in a square pyramidal geometry, with the phenolate O1, imino N1, amino N2 atoms of the Schiff base ligand L^1, and the thio-

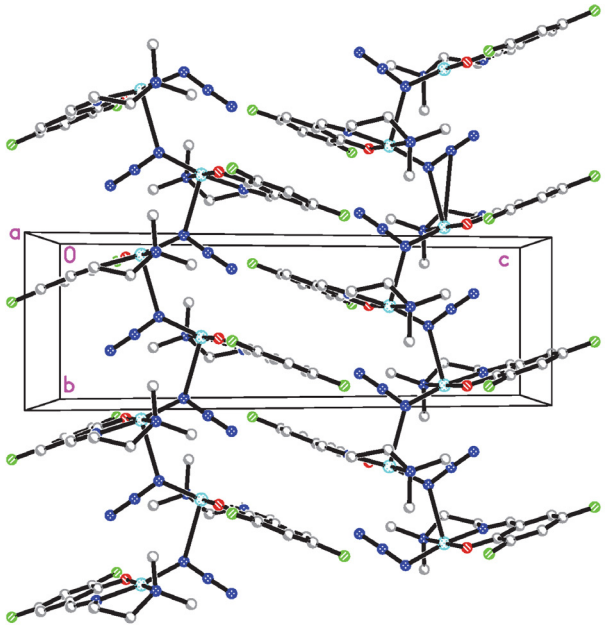


Figure 2. Molecular packing structure of complex **1**, viewed along the *b* axis.

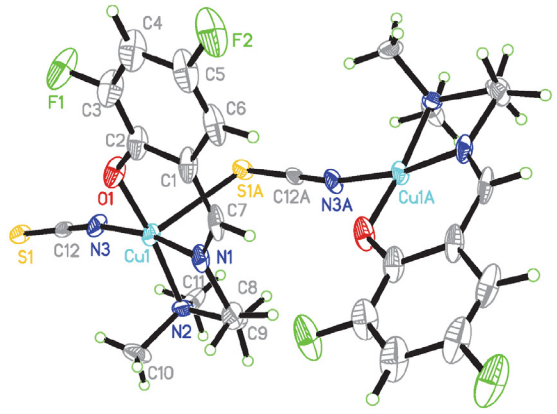


Figure 3. A perspective view of complex **3** with the atom labeling scheme. Thermal ellipsoids are drawn at the 30% probability level.

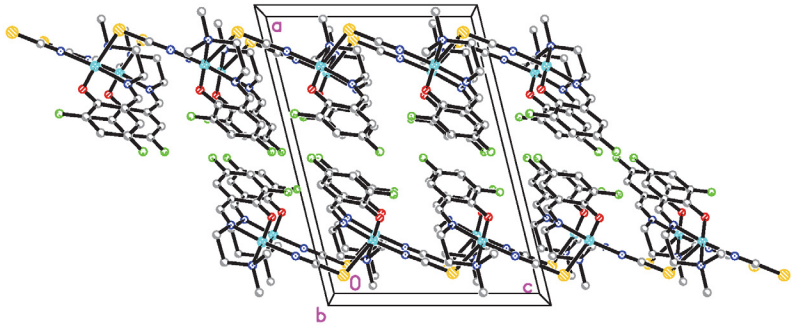


Figure 4. Molecular packing structure of complex **2**, viewed along the *c* axis.

cyanate N3 atom defining the basal plane, and with the thiocyanato S1A atom located at the apical position. The Schiff base ligand, acts as a tridentate ligand, chelate the Cu atom by generating one five and one six-membered rings with bite angles of 84.4(2)° and 92.1(2)°, respectively. The displacement of the Cu atom from the plane defined by the four basal donor atoms toward the apical thiocyanato S atom by 0.160(2) Å. The thiocyanate ligand bridges Cu atoms with an end-to-end bridging mode, generating a Cu···Cu distance of 6.077(4) Å. The bond lengths and angles in the square pyramidal coordination are similar to those in the reported thiocyanate bridged Schiff base copper complexes.[18] In the crystal structure of the complex, the [CuL^1] units are linked by the thiocyanate bridges, to form one-dimensional chains along the *c* axis (Figure 4).

3. 5. Structure Description of Complex 3

Molecular structure of the mononuclear copper complex **3** is shown in Figure 5. The complex contains a [Cu(HL^2)$_2$]$^{2+}$ cation and two thiocyanate anions. The molecule possesses crystallographic inversion center symmetry. The Cu atom, located at the center, is coordinated in a square planar geometry by the phenolate O1 and O1A and imino N1 and N1A atoms. The Schiff base ligand, acts as a bidentate ligand, chelate the Cu atom by generating one six-membered ring with bite angle of 92.3(1)°. The morpholine N atom is protonated, and forms a hydrogen bond with the thiocyanate anion (N2–H2···N3: N2–H2 = 0.91 Å, H2···N3 = 1.92 Å, N2···N3 = 2.806(7) Å, N2–H2···N3 = 165(3)°). The bond lengths and angles in the square planar coordination are similar to those in the reported Schiff base copper complexes.[19] In the crystal structure of the complex, the molecules are stack along the *a* axis *via* weak π···π interactions (Figure 6).

3. 6. Structure Description of Complex 4

Molecular structure of the mononuclear copper complex **4** is shown in Figure 7. The complex contains a [Cu(L^2)$_2$] molecule. The molecule possesses crystallographic inversion center symmetry. The Cu atom, located at the center, is coordinated in a square planar geometry by the phenolate O1 and O1A and imino N1 and N1A atoms. The Schiff base ligand, acts as a bidentate ligand, chelate the Cu atom by generating one six-membered ring with bite angle of 88.1(1)°. The bond lengths and angles in the square planar coordination are similar to those in the reported Schiff base copper complexes.[19] In the crystal structure of the complex, the molecules are stack along the *a* axis *via* weak π···π interactions (Figure 8).

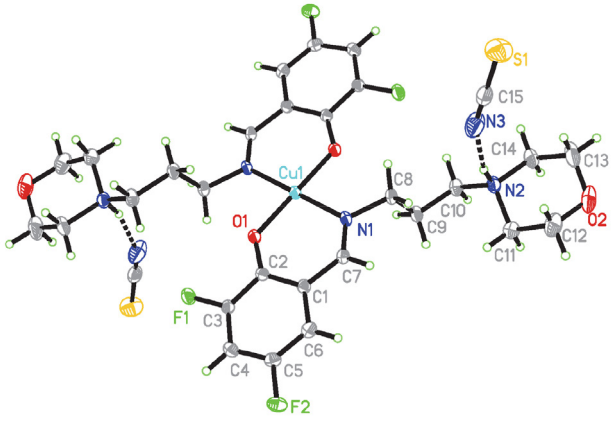


Figure 5. A perspective view of complex **3** with the atom labeling scheme. Thermal ellipsoids are drawn at the 30% probability level. Hydrogen bonds are shown as dashed lines.

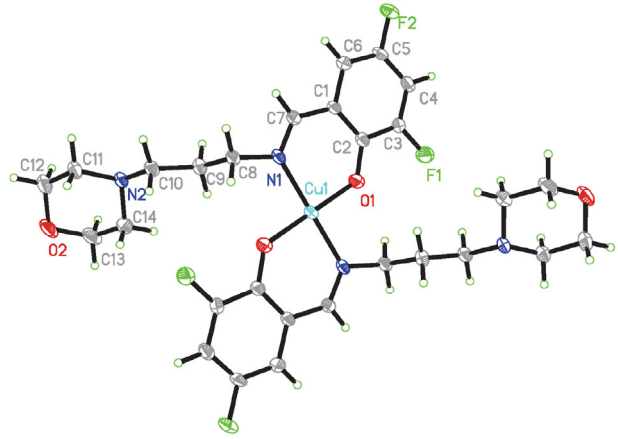


Figure 7. A perspective view of complex **4** with the atom labeling scheme. Thermal ellipsoids are drawn at the 30% probability level.

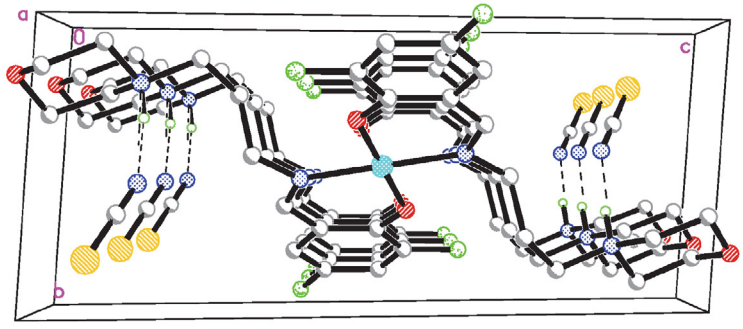


Figure 6. Molecular packing structure of complex **3**, viewed along the *a* axis. Hydrogen bonds are shown as dashed lines.

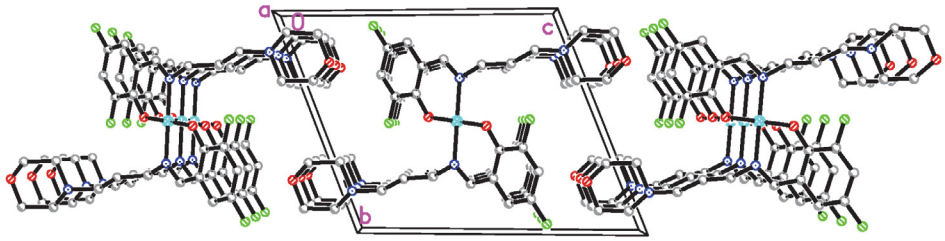


Figure 8. Molecular packing structure of complex **4**, viewed along the *a* axis.

Table 3. Antimicrobial activities of the complexes with minimum inhibitory concentrations (μg mL^{-1})

Tested material	*B. subtilis*	*S. aureus*	*E. coli*	*P. fluorescence*
1	2.3	9.4	4.7	37.5
2	2.3	9.4	4.7	37.5
3	1.2	2.3	9.4	75
4	1.2	2.3	9.4	75
Penicillin G	2.3	4.7	>150	> 150

3. 7. Antimicrobial Activity

The complexes were screened for antibacterial activities against two Gram (+) bacterial strains (*Bacillus subtilis* and *Staphylococcus aureus*) and two Gram (–) bacterial strains (*Escherichia coli* and *Pseudomonas fluorescence*) by MTT method. The MIC (minimum inhibitory concentration, μg mL^{-1}) values of the compounds against four bacteria are listed in Table 3. Penicillin G was used as the standard drug. Interestingly, complex **1** has the same activities against all the bacteria as complex **2**. And, complex **3** has the same activities against all the bacteria as complex **4**. Thus, the azide and thiocyanate ligands or anions in the complexes do not have obvious influence on the antibacterial activity. Complexes **1** and **2** show strong activity against *B. subtilis* and *E. coli*, and medium activity against *S. aureus* and *P. fluorescence*. Complexes **3** and **4** show strong activity against *B. subtilis* and *S. aureus*, medium activity against *E. coli*, and weak activity against *P. fluorescence*. The complexes have strong or similar activities against *B. subtilis*, *S. aureus* and *E. coli* which comparable to Penicillin G. However, all the complexes have no activity on the fungal strains *Candida albicans* and *Aspergillus niger*. The antimicrobial activities of the complexes are comparable to the copper complex derived from 2-hydroxy-5-methylbenzaldehyde oxime.[20]

4. Conclusion

In summary, an end-on azide bridged polymeric copper(II) complex, an end-to-end thiocyanate bridged polymeric copper(II) complex, and two mononuclear copper(II) complexes derived from the Schiff bases 2-((2-(dimethylamino)ethylimino)methyl-4,6-diluorophenol and 2,4-difluoro-6-((3-morpholinopropylimino)methyl)phenol were obtained. The Cu atoms in the polymeric complexes are in square pyramidal geometry, and those in the mononuclear complexes are in square planar geometry. One compound has ionic structure ($[Cu(HL^2)_2]^{2+}$ cation, two thiocyanate anions) in others the molecules are present. The results of the conductivity measurements are in agreement with that determined by the single crystal X-ray analysis. The complexes have strong activities against the bacteria *B. subtilis*, *S. aureus* and *E. coli*.

Supplementary Data

CCDC 2021453–2021456 (**1**–**4**) contain the supplementary crystallographic data for the compounds. These data can be obtained free of charge *via* http://www.ccdc.cam.ac.uk/conts/retrieving.html, or from the Cambridge Crystallographic Data Centre, 12 Union Road, Cambridge CB2 1EZ, UK; fax: (+44) 1223-336-033; or e-mail: deposit@ccdc.cam.ac.uk.

Acknowledgments

This work was financially supported by K.C. Wong Magna Fund in Ningbo University, Ningbo Public Fund (Project No. 202002N3056), and the State Key Laboratory Development Fund of Structural Chemistry (Project No. 20190028).

5. References

1. (a) M. H. Esfahani, M. Behzad, *J. Coord. Chem.* **2020**, *73*, 154–163; **DOI:**10.1080/00958972.2020.1725492

(b) K.-C. Gan, K.-M. Sim, T.-M. Lim, K.-C. Teo, *Lett. Org. Chem.* **2020**, *17*, 191-198; **DOI:**10.2174/1570178616666190724114741
(c) S. Mandal, T. Sen, U. Mandal, D. Bhunia, C. Rizzoli, D. Bandyopadhyay, *J. Coord. Chem.* **2019**, *72*, 3614-3624; **DOI:**10.1080/00958972.2019.1704275
(d) I. P. Ejidike, P. A. Ajibade, *Rev. Inorg. Chem.* **2015**, *35*, 191-224. **DOI:**10.1515/revic-2015-0007

2. (a) P.-L. Lam, K. K.-H. Lee, S. H.-L. Kok, R. Gambari, K.-H. Lam, C.-L. Ho, X. Ma, Y.-H. Lo, W.-Y. Wong, Q.-C. Dong, Z.-X. Bian, C.-H. Chui, *RSC Advances* **2016**, *6*, 104575-104581; **DOI:**10.1039/C6RA20186E
(b) R. K. Mohapatra, A. K. Sarangi, M. Azam, M. M. El-ajaily, M. Kudrat-E-Zahan, S. B. Patjoshi, D. C. Dash, *J. Mol. Struct.* **2019**, *1179*, 65-75; **DOI:**10.1016/j.molstruc.2018.10.070
(c) M. A. Malik, S. A. Lone, P. Gull, O. A. Dar, M. Y. Wani, A. Ahmad, A. A. Hashimi, *Med. Chem.* **2019**, *15*, 648-658. **DOI:**10.2174/1573406415666181203115957
3. (a) N. R. Palepu, S. L. Nongbri, J. R. Premkumar, A. K. Verma, K. Bhattacharjee, S. R. Joshi, S. Forbes, Y. Mozharivskyj, R. Thounaojam, K. Aguan, M. R. Kollipara, *J. Biol. Inorg. Chem.* **2015**, *20*, 619-638; **DOI:**10.1007/s00775-015-1249-3
(b) D. A. Sabbah, F. Al-Tarawneh, W. H. Talib, K. Sweidan, S. K. Bardaweel, E. Al-Shalabi, H. A. Zhong, G. Abu Sheikha, R. Abu Khalaf, M. S. Mubarak, *Med. Chem.* **2018**, *14*, 695-708; **DOI:**10.2174/1573406414666180412160142
(c) A. S. Hassan, H. M. Awad, A. A. Magd-El-Din, T. S. Hafez, *Med. Chem. Res.* **2018**, *27*, 915-927; **DOI:**10.1007/s00044-017-2113-5
(d) K. Venkateswarlu, N. Ganji, S. Daravath, K. Kanneboina, K. Rangan, Shivaraj, *Polyhedron* **2019**, *171*, 86-97. **DOI:**10.1016/j.poly.2019.06.048
4. (a) M. Zhang, D.-M. Xian, H.-H. Li, J.-C. Zhang, Z.-L. You, *Aust. J. Chem.* **2012**, *65*, 343-350; **DOI:**10.1071/CH11424
(b) L. Shi, H.-M. Ge, S.-H. Tan, H.-Q. Li, Y.-C. Song, H.-L. Zhu, R.-X. Tan, *Eur. J. Med. Chem.* **2007**, *42*, 558-564. **DOI:**10.1016/j.ejmech.2006.11.010
5. N. P. Rai, V. K. Narayanaswamy, T. Govender, B. K. Manuprasad, S. Shashikanth, P. N. Arunachalam, *Eur. J. Med. Chem.* **2010**, *45*, 2677-2682. **DOI:**10.1016/j.ejmech.2010.02.021
6. (a) M. Ghosh, M. Layek, M. Fleck, R. Saha, D. Bandyopadhyay, *Polyhedron* **2015**, *85*, 312-319; **DOI:**10.1016/j.poly.2014.08.014
(b) N. Imani, M. Behzad, H. A. Rudbari, G. Bruno, H. S. Jahromi, A. Khaleghian, *J. Coord. Chem.* **2015**, *68*, 2296-2306; **DOI:**10.1080/00958972.2015.1051476
(c) M. Honarkar Ashna, M. Behzad, M. Salehi, *J. Coord. Chem.* **2016**, *69*, 190-198; **DOI:**10.1080/00958972.2015.1117073
(d) N. Mahlooji, M. Behzad, H. A. Rudbari, G. Bruno, B. Ghanbari, *Inorg. Chim. Acta* **2016**, *445*, 124-128. **DOI:**10.1016/j.ica.2016.02.040
7. (a) C.-L. Zhang, X.-Y. Qiu, S.-J. Liu, *Acta Chim. Slov.* **2019**, *66*, 719-725; **DOI:**10.17344/acsi.2019.5241
(b) L.-Y. He, X.-Y. Qiu, J.-Y. Cheng, S.-J. Liu, S.-M. Wu, *Polyhedron* **2018**, *156*, 105-110; **DOI:**10.1016/j.poly.2018.09.017
(c) S. M. Wu, X. Y. Qiu, J. C. Wang, S. J. Liu, L. Y. He, *Russ. J. Coord. Chem.* **2019**, *45*, 384-390.
8. Bruker, SMART (Version 5.625) and SAINT (Version 6.01). Bruker AXS Inc., Madison, Wisconsin, USA, 2007.
9. G. M. Sheldrick, SADABS. Program for Empirical Absorption Correction of Area Detector, University of Göttingen, Germany, 1996.
10. G. M. Sheldrick, SHELXTL V5.1 Software Reference Manual, Bruker AXS, Inc., Madison, Wisconsin, USA, 1997.
11. J. Meletiadis, J. F. G. M. Meis, J. W. Mouton, J. P. Donnelly, P. E. Verweij, *J. Clin. Microbiol.* **2000**, *38*, 2949-2954. **DOI:**10.1128/JCM.38.8.2949-2954.2000
12. (a) W. J. Geary, *Coord. Chem. Rev.* **1971**, *7*, 81-122; **DOI:**10.1016/S0010-8545(00)80009-0
(b) G. S. Girolami, T. B. Rauchfuss, R. J. Angelici, Synthesis and technique in inorganic chemistry, a laboratory manual, 3rd edition, University Science Books, Sausalito, **1999**, 254.
13. (a) S. S. Massoud, F. A. Mautner, *Inorg. Chim. Acta* **2005**, *358*, 3334-3340; **DOI:**10.1016/j.ica.2005.05.007
(b) A. D. Khalaji, H. Stoekli-Evans, *Polyhedron* **2009**, *28*, 3769-3773. **DOI:**10.1016/j.poly.2009.07.068
14. (a) H. Grove, M. Julve, F. Lloret, P. E. Kruger, K. W. Tornroos, J. Sletten, *Inorg. Chim. Acta* **2001**, *325*, 115-124; **DOI:**10.1016/S0020-1693(01)00642-9
(b) S. Basak, S. Sen, S. Banerjee, S. Mitra, G. Rosair, M. T. Garland Rodriguez, *Polyhedron* **2007**, *26*, 5104-5112. **DOI:**10.1016/j.poly.2007.07.025
15. Y.-M. Zhou, X.-R. Ye, F.-B. Xin, X.-Q. Xin, *Transition Met. Chem.* **1999**, *24*, 118-120. **DOI:**10.1023/A:1006989707001
16. A. Ray, D. Sadhukhan, G. M. Rosair, C. J. Gomez-Garcia, S. Mitra, *Polyhedron* **2009**, *28*, 3542-3550. **DOI:**10.1016/j.poly.2009.07.017
17. (a) P. Bhowmik, A. Bhattacharyya, K. Harms, S. Sproules, S. Chattopadhyay, *Polyhedron* **2015**, *85*, 221-231; **DOI:**10.1016/j.poly.2014.08.021
(b) S. Jana, B. K. Shaw, P. Bhowmik, K. Harms, M. G. B. Drew, S. Chattopadhyay, S. K. Saha, *Inorg. Chem.* **2014**, *53*, 8723-8734; **DOI:**10.1021/ic501353g
(c) P. Mukherjee, M. G. B. Drew, A. Ghosh, *Eur. J. Inorg. Chem.* **2008**, 3372-3381; **DOI:**10.1002/ejic.200800186
(d) R. Vafazadeh, A. Kazemi-nasab, A. C. Willis, *Acta Chim. Slov.* **2019**, *66*, 1010-1018. **DOI:**10.17344/acsi.2019.5333
18. (a) P. Bhowmik, S. Chattopadhyay, M. G. B. Drew, A. Ghosh, *Inorg. Chim. Acta* **2013**, *395*, 24-32; **DOI:**10.1016/j.ica.2012.10.020
(b) Z.-L. You, D.-M. Xian, M. Zhang, *CrystEngComm* **2012**, *14*, 7133-7136; **DOI:**10.1039/c2ce26201k
(c) X.-Y. Qiu, W.-S. Liu, H.-L. Zhu, *Z. Anorg. Allg. Chem.* **2007**, *633*, 1480-1484; **DOI:**10.1002/zaac.200700132
(d) H. Zhao, X.-P. Tan, Q.-A. Peng, C.-Z. Shi, Y.-F. Zhao, Y.-M. Cui, *Acta Chim. Slov.* **2020**, *67*, 638-643. **DOI:**10.17344/acsi.2019.5644
19. (a) C. Senol, Z. Hayvali, H. Dal, T. Hokelek, *J. Mol. Struct.* **2011**, *997*, 53-59; **DOI:**10.1016/j.molstruc.2011.04.037

(b) M. E. Bluhm, M. Ciesielski, H. Gorls, O. Walter, M. Doring, *Inorg. Chem.* **2003**, *42*, 8878–8885;
DOI:10.1021/ic034773a
(c) P. A. N. Reddy, M. Nethaji, A. R. Chakravarty, *Inorg. Chem. Commun.* **2003**, *6*, 698–701;
DOI:10.1016/S1387-7003(03)00090-X
(d) M. Iqbal, A. Mushtaq, S. Ali, M. Sohail, P. A. Anderson, *Acta Chim. Slov.* **2018**, *65*, 989–997.
DOI:10.17344/acsi.2018.4695
20. Y.-L. Sang, X.-S. Lin, *Acta Chim. Slov.* **2019**, *66*, 168–172.

Povzetek

Sintetizirali smo štiri nove bakrove(II) komplekse, $[CuL^1(\mu_{1,1}\text{-}N_3)]_n$ (**1**), $[CuL^1(\mu_{1,3}\text{-}NCS)]_n$ (**2**), $[Cu(HL^2)_2](SCN)_2$ (**3**) in $[Cu(L^2)_2]$ (**4**), kjer sta L^1 in L^2 2-((2-(dimetilamino)etilimino)metil-4,6-difluorofenolat in 2,4-difluoro-6-((3-morfolinopropilimino)metil)fenolat, HL^2 pa je 2-((2-(dimetilammonio)etilimino)metil-4,6-difluorofenolat. Okarakterizirali smo jih z elementno analizo ter IR in UV-vis spektroskopijo. Strukture kompleksov smo potrdili z monokristalno rentgensko difrakcijo. Kompleksa **1** in **2** sta polimerna bakrova(II) kompleksa s kvadratno piramidalno geometrijo okoli Cu atoma. Kompleksa **3** in **4** sta enojedrna bakrova(II) kompleksa s kvadratno planarno geometrijo okoli Cu atoma. Kompleksom smo določili antimikrobne lastnosti.

Except when otherwise noted, articles in this journal are published under the terms and conditions of the Creative Commons Attribution 4.0 International License

AUTHOR INDEX

Acta Chimica Slovenica
Year 2020, Vol. 67 No. 1–4

Abbasi Muhammad Athar....403
Abboushi Eman Kh.....530
Abdel-Motaal Marwa....560
Abdelwahab Amal....83
Abdi Maryam....476
Abdollahi Mahsa....866
Absalan Ghodratollah....415
Abu-Melhab Sraa....167
Agostinho Alexandre....778
Ahmed Neven....757
Akçeşme Faruk Berat....1202
Akhgar Mohammadreza....246
Akhond Morteza....415
Akhondi Maryam....537
Aktaş Aydın....830
Akyıl Saniye....1250
Alanzy Asmaa L.....560
Ali Enas Shabaan....396
Ali Gazunfor....195
Alzein Mazen....55
Amani Ali Mohammad....469
Amarray Amina....1180
Aqil Mohamed....1180
Ara Tabassum....195
Ardjmand Mehdi....469
Arjmand Omid....469
Arshad Muhammad Nadeem....785
Asem Medhat....560
Asiri Abdullah Mohamed....785
Atalay Rengul Cetin....70
Avramescu Viorel....469
Aydar Sevda....729
Aydogan Feray....1014
Aytan-Goze Elif....842
Azzi Mohammed....1180
Babanly Dunya Mahammad....799
Babanly Mahammad Baba....799
Bahrami Mohammad Javad....710
Banožić Marija....778
Basha Mubarak Ali Muhamath....235
Bayraktepe Dilek Eskiköy....729
Bedenk Jure....885
Berman-Mendoza Dainet....319
Beşli Nail.... 1202, 1262
Bešter-Rogač Marija....1, 270, 977
Bhatt Bhupesh S.....957
Bi Ye....860
Bibi Ayesha....785
Blazhev Gavazov Kiril....151
Brahmi Younes....1180
Bren Urban....1163
Brezeanu Mihai....469
Buiu Octavian....469
Bumbac Marius....469
Burvalova Anezka....522
Cai Ya-Jun....896
Cao Tong....916
Castillo Santos J.....319
Castillo Santos Jesús....1196
Cavas Levent....15
Çaylak Osman....375
Celepci Duygu Barut....830
Chaban Ihor G.....1035
Chaban Taras.... 970, 1035
Chandrasekaran Muthukumaran....602
Chebotarev Alexander....1118
Chen Chen....189
Chen Wei....860
Chen Wen-Tong.... 622, 1111
Cheng Chil-Hung....1124
Chorilli Marlus....1273
Cobianu Cornel....469
Couto Nilton....985
Cui Yong-Ming.... 638, 644, 896
Daflon Gremião Maria Palmira....1273
Dahbi Mouad....1180
Dalay Meltem Conk....1250
Dangroo Nisar A.....195
Danish Muhammad....785
Daryasari Ameneh Porgham....748
De Leon Aned....1196
Demirel Zeliha....1250
Deng Tong-Tong....1155
Deschamps Eleonora....985
Devetak Iztok....904
Ding Li-Hong....822
Divarova Vidka....594
Djeukoua Sorel Kamal Dimo....203
Dodevska Totka....1216
Dolinar Marko....S49, S98
Dou Yong....916
Doungmo Giscard....203
Du Xiu-Li....822
Dubovyi Vitaliy....1118
Duliban Jerzy....221
Dumbravescu Nicolae....469
Eikani Mohmmad Hasan....469
Ekom Steve Endeguele....203
El Ghachtouli Sanae....1180
El Henawee Magda....757

El Khair Afaf Abou....757
Elçi Latif....375
El-Hadidya Sherihan A.....167
El-Saadaney Ahmed Mohamed....1024
El-Sayed Elsherbiny Hamdy....1024
Enache Mirela....629
Encheva Elzhana....1082
Erdoğan Ayşegül....1250
Ertekin Figen Kaymak....1250
Evgenevich Baulin Vladimir....246
Fabjan Teja....885
Fadda Ahmed Ali....1024
Faganeli Jadran....985, S91
Fallah Armin....1092
Falnoga Ingrid....985
Fang Xiao-Niu....507
Fang Zhijie....812
Farahi Mahnaz....866
Fayez Yasmin Mohamed....396
Fedorchuk Andrii....1148
Fedyshyn Orest....970
Filik Hayati....729
Fondjo Emmanuel Sopbué....203
Fošnarič Miha....674
Fouladgar Masoud....701
Frost Carminita....764
Furtula Boris....312
Gavarić Aleksandra....778
Georgiev Hristov Danail....151
Ghadermazi Mohammad....476
Ghazanfari Dadkhoda....276
Gholtash Jamileh Etemad....866
Glažar Saša A.....904
Gołębiewski W. Marek....325
Golshani Zahra....710
Golubović Jelena....445
González Diaz Yudith....1239
Goreshnik Evgeny....1148
Gryshchouk Galyna....105
Gucma Mirosław....325
Guncheva Maya....253
Guney Gurkan....551
Guo Jin....507
Guven Ebru Bilget....70
Hadjmohammadi Mohammad Reza....1092
Hadzhiev Dobrin....1216
Haghighat Majid Hamouni....1072
Hajare Ashok Ananda....283
Hajkova Pavlina....47
Hammoudeh Ayman Y.....530
Han Yong-Jun....159, 853
Hao Xiaoyun....916
Hassan Mubashir....403
Hassan Nagiba Yehia....396
Hegazy Mohammad....462
Himi Mohammed Ait....1180
Höl Ayşen....375
Hoppe Heinrich....764
Hosseini Seyyed Mohammad Ali....710
Hosten Eric....764
Hota Sidhartha Sankar....179
Hou Jin-Long....860
Huang Rui-Rui....822
Huang Xin....462
Huang Yudong....462
Hussien Emad Mohamed....757
Idakieva Krassimira....253
Iglič Aleš....674
Ignjatović Janko....445
İlter Işıl....1250
Isaacs Michelle....764
Issa Yousry M.....1053
Ivanova-Kolcheva Vanina....609
Ivanovich Kovalenko Sergey....586
Jaafar Nur Farhana....361
Jaćimović Radojko....985
Jakić Miće....651
Jamalizadeh Effat....537
Jamil Waqas....260
Jiang You-Xin....644
Jokić Stela....778
Kafka Stanislav....421
Karami Bahador....866
Karkhut Andriy....934
Kenawy Sayed H.....96
Keskin Elif....1014
Khai Michael Ling Nguang....570
Khairuddean Melati....361
Khairulin Andrei....934
Khajuria Heena....119
Khaless Khaoula....1180
Khalifeh Reza....1044
Khalil Ahmed M.....96
Khalili Dariush....1044
Khan Khalid Mohammad....260
Khanye Setshaba D.....764
Killedar Suresh....1100
Kimmel Roman....421
Kirboga Semra....137
Klochkova Anastasiia....1118
Knez Željko....1172
Koç Mehmet....1250
Koc Ziya Erdem....551
Koçyiğit-Kaymakçıoğlu Bedia....1139
Kolenc Zala....1163
Koler Amadeja....349
Konstantinova Toncheva Galya....151
Konstantinovich Karandashev Vasilii....246
Kopp Josef....522
Kostiv Oksana....23
Korkuna Olha....23
Rydchuk Petro....23
Košak Urban....940
Košir Iztok J.....720
Košir Iztok Jože....1163
Košmrlj Janez....270, 421, 1290
Kotnik Pirš Ana....666
Krajnc Peter....349

Kralj Cigić Irena....993
Kralj-Iglič Veronika....674
Krause Jason....764
Kravchenko Iryna....934
Krawczyk Maria....325
Krivec Uroš....666
Kshash Abdullah Hussein....113
Kshash Abdullah Hussein....739
Kucukdumlu Asligul....70
Kučić Grgić Dajana....651
Kuiate Jules Roger....203
Kulanthasamy Rasappan....602
Kumar Manesh....119
Kumar Sanjay....1172
Kumer Kristina....885
Kytova Dina....487
Lahuri Azizul Hakim....570
Lakshmipathy Mangaleshwaran....602
Lazarova Yanna....1216
Lei Yan....927
Leitgeb Maja....1172
Lekova Vanya....594
Leon Ained de....319
Li Dacheng....916
Li Fuxiang....336
Li Jia....507
Li Li-Jie....1155
Li Yueyun....916
Lin Xue-Song....581
Liu Huan-Yu....130
Liu Qiao-Ru....159
Liu Qingyun....916
Liu Shu-Juan....1281, 1301
Lobb Kevin....764
Lubczak Renata....221
Luo Xiao-Qiang....159, 853
Lv Zhiping....336
Ma Jian-Ping....822
Mahmoud Amal M.....530
Malej Alenka....S91
Maljurić Nevena....445
Mallick Subrata....179, 1227
Manhi Fatma M.....83
Mansimova Shabnam Hamlet....799
Mansoor Seyed Jamaledin....36
Abbasitabar Fatemeh....36
Mansouri Zahra....516
Marfur Nor Amira....361
Marintsova Nataliia....934
Mashadiyeva Leyla Farhad....799
Matias Ana....778
Matiichuk Yulia E.....1035
Matiychuk Vasyl....970
Matiychuk Vasyl S.....1035
Matoušek Jindřich....47
Medoš Žiga....270
Memon Saima Qayyum....260
Memon Zunaira....260
Menezes Maria Ângela de B. C.....985
Mesarec Luka....674
Michalczyk Alicja Katarzyna....325
Milanova Maria....1082
Milićević David....421
Mishra Satyaki Aparajit....1227
Mitrasinovic
Petar M.....386, 683, 876, 949
Moghadam Tahereh Tohidi....304
Moghaddam-Manesh
Mohammadreza....276
Mohamed Samah Abd ELSabour....396
Mohammadinejad Fatemeh....710
Mohammad-Khah Ali....1072
Mohareb Rafat M.....83
Moradi-Shoeili Zeinab....476
Moslavac Tihomir....778
Mykolayovych Antypenko Oleksii....586
Mys'kiv Marian....1148
Nadaf Sameer....1100
Nandi Souvik....1227
Naqvi Tahira....195
Nazir Majid....403
Nektegayev Ihor A.....1035
Nesterkina Mariia....934
Nicolescu Cristina Mihaela....469
Nikolaevich Turanov Alexander....246
Nordin Norazzizi....361, 570
Noreen Nadia....785
Novak Petr....522
Novikov Volodymyr....934
Oancea Petruta....629
Obeidat Safwan M.....530
Ocelić Bulatović Vesna....651
Ochoa-Landín Ramón....1196
Ocvirk Miha....720
Odame Felix....764
Ogurtsov Volodymyr V.....1035
Oleksiv Lesia....970
Oliveira Eloy Josimar....1273
Öner Mualla....137
Osredkar Joško....885
Otašević Biljana....445
Pan Fei....896
Pandey Jitendra K.....1172
Pandya Juhee G.....957
Patel Mohan N.....957
Pathak Chandramani....957
Patsay Ihor....105
Pattnaik Satyanarayan....179
Pavlin Jerneja....904
Pavlović Nika....778
Peña-García Jorge....1202
Peng Qi-An....638, 644, 896
Pérez-Sánchez Horacio....1202
Perner Jakub....47
Petkova Milcheva Nikolina....151
Petković Miloš....445
Pevec Andrej....421, 1290
Pinar Pınar Talay....212
Pineda-Leon Horacio Antolín....1196
Pintar Albin....1082

Polat Sevgi 842
Polish Nataliia 934
Popović Ljiljana 778
Potočnik Tanja 1163
Powar Trupti Ashok 283
Prochazka Vit 522
Pulko Irena 349
Qin Jie 822
Qin Lan 916
Qiu Xiao-Yang 1281, 1301
Racheva Petya 594
Rafi Mohammad 1124
Raheem Shabnam 195
Rahim Afidah Abdul 570
Ramírez-Bon Rafael 319
Ranjbar Bijan 304
Ranjbar Salumeh 748
Rastegar Najme 1044
Ravnikar Matjaž 445
Raza Hussain 403
Raza Muhammad Asam 785
Redžepović Izudin 312
Rehman Aziz-ur- 403
Rehman Zia-ur- 403
Rijavec Tjaša 993
Rishikesan Saranya 235
Rizvi Masood Ahmad 195
Rojas Vargas Armando 1239
Rojas-Hernández Armando G. 319
Rydchuk Petro 970
S Gobec tanislav 940
Penič Samo 674
Sabory-García Rafael A. 319
Sahoo Rudra Narayan 1227
Saleh Hanaa 757
Salem Maissa Yacoub 396
Salimian Mani 304
Samiey Babak 1124
Samon Muhammad Kashif 260
Sang Ya-Li 581
Savodnik Nika 445
Sayan Perviz 842
Sayed Yasien 764
Şenturk İlknur 55
Seo Sung-Yum 403
Serban Bogdan Catalin 469
Shah Syed Adnan Ali 403
Shamili Sriramoju 1061
Sheikh Haq Nawaz 119
Sheikh Haq Nawaz 119
Sheikhhosseini Enayatollah 276
Sheikhian Leila 415
Shi Cong-Zhong 638
Shojaei Abdollah Fallah 476
Shtemenko Alexander 487
Shtemenko Nataliia 487
Shterev Ivan 1216
Shyyka Olga Ya 1035
Siddiqui Sabahat Zahra 403
Siéwé Désire André 203
Simon Peter F. W. 203
Singh Rajinder 119
Slapničar Miha 904
Slyvka Yurii 1148
Slipkan Anastasiia 487
Smerdel Snježana 435
Snigur Denys 1118
Sodan Nilgün Elyas 375
Soleimani Mojtaba 748
Sousa Araujo Victor Hugo 1273
Srinivas Avula 1061
Stanislavovich Kazunin Maxim 586
Stechynska Emilia 105
Stojnova Kirila 594
Stoyanova Elena 253
Stoyanova Maria 609
Strlič Matija 993
Sun Cheng-Bin 860
Sun Wei-Dong 581
Sun Zi-Qiang 1281
Sunitha Malladi 1061
Swain Rakesh 1227
Sygellou Labrini 609
Šarac Bojan 977
Šlejkovec Zdenka 985
Štanfel Urša 270
Štrukelj Borut 445
Tagiyev Dilqam Babir 799
Taha Muhammad 260
Taloub Nadia 462
Tamokou Jean-de-Dieu 203
Tan Xiang-Peng 638, 644
Tan Yao 1233
Tashi Lobzang 119
Toader Ana Maria 629
Todinova Svetla 253
Tok Fatih 1139
Tompa Valerija 904
Tomšič Sara 1290
Torres-Duarte Angel Roberto 1196
Trebušak Podkrajšek Katarina 666
Trujillo Nieves María Elena 1239
Tshentu Zenixole 764
Tsopmo Appolinnaire 203
Tsvetkov Martin 1082
Tuncbilek Meral 70
Turkmen Ceylan 15
Tymoshuk Oleksandr 970
Urankar Damijana 421
Uysal Saban 551
Vafazadeh Rasoul 516
Vaidya Foram U. 957
Valentynivna Shishkina Svetlana 586
Varma Reena R. 957
Vasić Katja 1172
Vasylechko Volodymyr 105
Vidović Senka 778
Virant Miha 270
Virant-Klun Irma 885
Vladić Jelena 778

Vladimirovich Baulin Dmitriy 246
Von Zuben Eliete de Souza 1273
Vrba Vlastimil.....522
Vrtačnik-Bokal Eda.....885
Walters Mallory E.....203
Wang Fu-Ming.....1155
Wang Lin 812
Wang Pu.....927
Wang Si-Huan.....644
Wang Yi-Di.....644
Willis Anthony C.....516
Wu Guangyu 462
Wu Hong-Yuan.....860
Wu Yuan-Yuan.....896
Xie Long-Yan 822
Xie Ting 822
Xie Zhen-Ping.....507
Xu Xin-Lan.....1281
Xue Jianwei.....336
Xue Ling.....336
Xue Ling-Wei 159, 189, 853
Yancheva Denitsa 253
Yanev Pavel.....594
Yang Lu 916
Yang Luo-Ju.....130
Yang Qiwen 927
Yang Wei-Chun.....189
Yazan Zehra.....729
Ye Ya-Fang.....130
Yenmis Guven.....1262
Yi Xiu-Guang.....507
Yin Yi-Shu 130
Yolacan Cigdem.....1014
You Zhong-Lu.....1155
Yu Shun-Feng..... 1281, 1301
Yu Shun-Feng.....1301
Yurievich Voskoboynik Oleksii 586
Yusibov Yusif Amirali 799
Yusupovich Tsivadze Aslan 246
Zandi Mehdi Shahidi 710
Zang Guo-Wei 1155
Zayed Muhammad 462
Zayed Sayed I. M. 1053
Zejnilagić Hajrić Meliha.....435
Żelechowski Krzysztof.....325
Zhang Daopeng 916
Zhang Tong 336
Zhao Gan-Qing.....189
Zhao Hui.....638
Zhao Long 822
Zhao Yi-Fei.....638
Zheng Kai 822
Zhou Pei.....462
Zhou Zhen.....916
Zou Xiao-Ling.....130
Žener Boštjan.....270

DRUŠTVENE VESTI IN DRUGE AKTIVNOSTI
SOCIETY NEWS, ANNOUNCEMENTS, ACTIVITIES

Vsebina

Obalni ekosistemi na prehodu: Primerjalna analiza severnega Jadrana in Zaliva Chesapeake S91
Obiski Rosalind Franklin v Sloveniji S98
Koledar važnejših znanstvenih srečanj s področja kemije, kemijske tehnologije in kemijskega inženirstva S106
Navodila za avtorje S110

Contents

Coastal Ecosystems in Transition: A Comparative Analysis of the Northern Adriatic and Chesapeake Bay S91
Visits of Rosalind Franklin in Slovenia S98
Scientific meetings – chemistry, chemical technology and chemical engineering S106
Instructions for authors S110

Obalni ekosistemi na prehodu: Primerjalna analiza severnega Jadrana in Zaliva Chesapeake

Jadran Faganeli,* Alenka Malej*

Morska biološka postaja, Nacionalni inštitut za biologijo, Fornače 41, 6330 Piran, Slovenija

** Corresponding author: E-mail: jadran.faganeli@nib.si, Tel.: +386 5 9232911*
alenka.malej@nib.si, Tel.: +386 5 9232903

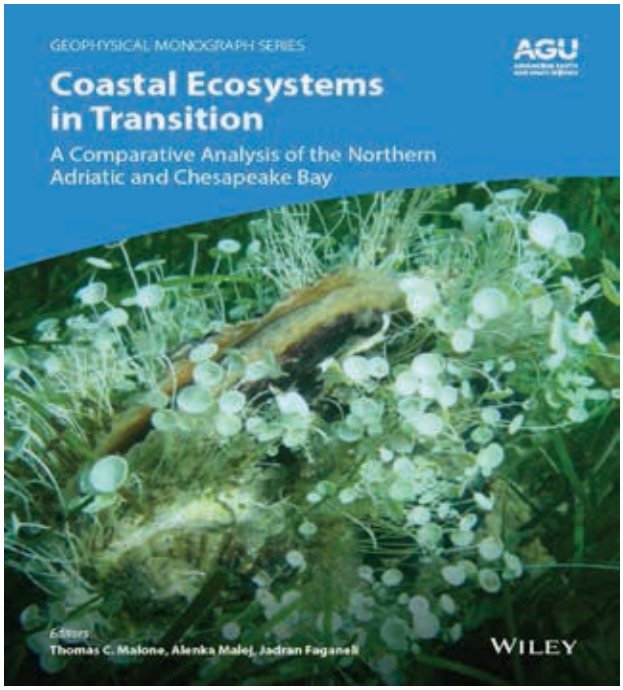
Received: 08-12-2020

Izvleček

Predstavljena je vsebina knjige v tisku pri založbi AGU-Wiley z naslovom »Obalni ekosistemi na prehodu: Primerjalna analiza severnega Jadrana in Zaliva Chesapeake« urednikov T. Maloneja, A. Malej in J. Faganelija. Knjiga prinaša primerjavo ekosistemov severnega Jadrana in Zaliva Chesapeake (vzhodna obala ZDA) in širi znanje o antropogenih vplivih na obalne ekosisteme, kjer je koncentrirano tako prebivalstvo kot izkoriščanje naravnih virov. Ponovni pregled obeh ekosistemov je omogočil, da smo ocenili spremembe v zadnjih 20 letih, še posebej lokalne vplive v okviru globalnih podnebnih sprememb ter uspešnost posegov za upravljanje in zmanjšanje antropogenih vplivov na obalne ekosisteme.

Ključne besede: obalno morje, severni Jadran, Chesapeake Bay, antropogeni vplivi

Knjiga v tisku pri založbi AGU-Wiley z naslovom »Obalni ekosistemi na prehodu: Primerjalna analiza severnega Jadrana in Zaliva Chesapeake«[1] (ISBN 9781119543589) posodablja in razširja naše znanje o učinkih človekovih dejavnosti na obalne ekosisteme, kjer je koncentrirano tako prebivalstvo kot izkoriščanje naravnih virov (slika 1). Knjiga je posvečena 50-letnici delovanja Morske biološke postaje NIB v Piranu in podaja novo analizo obeh ekosistemov, ki so bili predstavljeni leta 1999 v objavljeni knjigi »Ekosistemi na prehodu kopno-morje: Od porečja do morja«.[2] Ponovni pregled je omogočil, da smo ocenili spremembe v zadnjih 20 letih, učinke lokalnih vplivov v luči globalnih podnebnih sprememb in zlasti uspešnost posegov za upravljanje in zmanjšanje antropogenih vplivov na ekosisteme. Knjiga obsega **11 poglavij** slovenskih, ameriških, italijanskih in hrvaških avtorjev (v oklepaju), ki vključujejo: **uvodne besede o ogroženih obalnih ekosistemih** (T. Malone, A. Malej, J. Faganeli), **rečne pritoke** (Q. Zhang, S. Cozzi, C. Palinkas, M. Giani), **tokovanje in podnebne spremembe** (W.V. Boicurt, M. Ličer, M. Li, M. Vodopivec, V. Malačič), **fitoplankton** (M.J. Brush, P. Mozetič, J. France', F. Bernardi Aubry, T. Djakovac, J. Faganeli, L. Harris, M. Niesen), **zooplankton** (J. Pierson, E. Camatti, R. Hood, T. Kogovšek, D. Lučić, V. Tirelli, A. Malej), **vlogo mikrobov** (V. Turk, S. Malkin, M. Celussi, T. Tinta, J. Cram, F. Malfatti, F. Chen), **evtrofikacijo, pomanjkanje kisika in »kisanje« morja** (M. Brush, M. Giani, C. Totti, J. Testa, J. Faganeli, N. Ogrinc, M. Kemp, S. Fonda Umani), **sklopitev pelagiala in bentosa** z vidika kroženja organskega ogljika ($C_{org.}$), dušika (N), fosforja



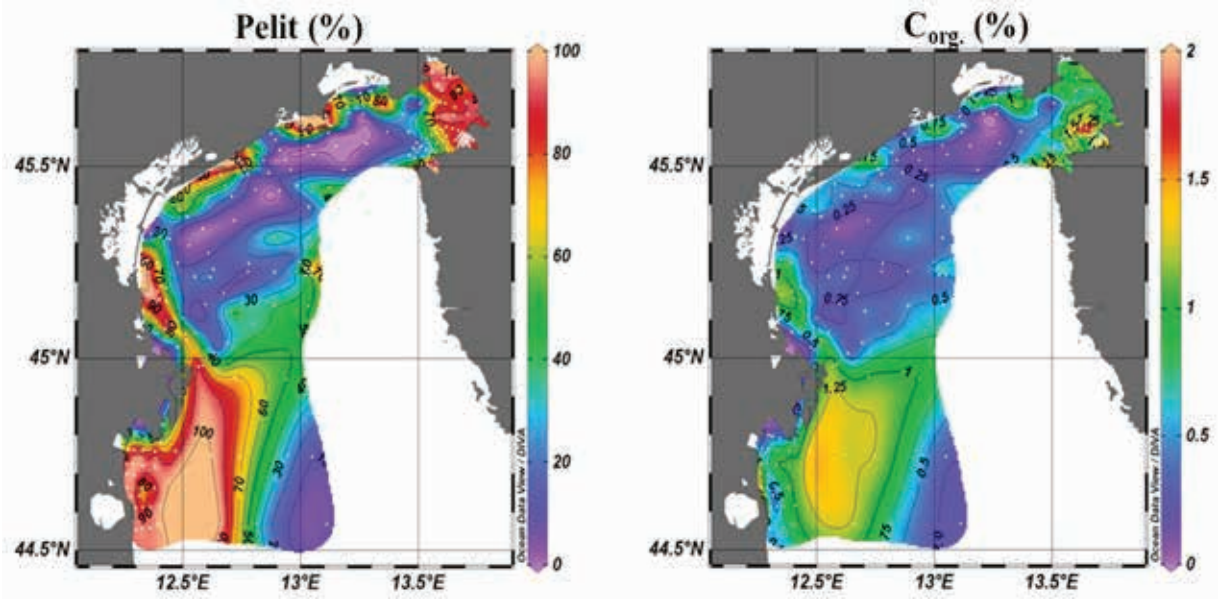
Slika 1: Naslovnica knjige

(P) in silicija (Si) (J.M. Testa, J. Faganeli, M. Giani, M.J. Brush, C. de Vittor, S. Covelli, W.R. Boynton, W.M. Kemp, N. Kovač, R. Woodland), **ključne habitate in tujerodne vrste** (C. Palinkas, M. Mistri, L. Staver, L. Lipej, P. Kružić, J. Court Stevenson, M. Tamburri, C. Munari, M. Orlando Bonaca), **ribištvo** (V.S. Kenneddy, L. Bolognini, J. Dulčić, R.J. Woodland, M.J. Wilberg, L.A. Harris) in **zaključke o upravljanju ekosistemov** in prognozah v prihodnosti (A. Malej, J. Faganeli, T. Malone). Knjiga je lahko, glede na vsebino, učbenik o severnem Jadranu.

Ključni ekološki dejavniki v severnem Jadranu in Zalivu Chesapeake

Veliki **rečni vnosi** s hranili in suspendiranimi snovmi so pomembni dejavniki, ki vplivajo na delovanje ekosistemov severnega Jadrana (SJ) in Zaliva Chesapeake (CB). Oba ekosistema z različnimi geomorfološkimi lastnostmi, ki se odražajo v večji površini in globini SJ ter plitvejšem in razpotegnjenem CB, sta podvržena podobnim letnim vnosom z rečnimi pritoki in padavinami. Pad, glavni rečni vnos v SJ, se izliva kot dvodimenzionalni linijski izvor v severozahodnem delu, v CB pa je glavni pritok Susquehanna lociran na skrajnem severu zaliva. Letni režim rečnih pritokov v CB je unimodalen s pomladnim vrhom, medtem ko je v SJ bimodalen s pomladnim in jesenskim vrhom. V obeh ekosistemih imajo vnosi velik presežek N glede na P. Rečna suspendirana snov se v SJ akumulira s hitrostjo 2–6 cm letno ob zahodni obali, predvsem ob izlivu Pada. Hitrost akumulacije je precej nižja (0,4–1 mm letno) v vzhodnem delu SJ in Tržaškem zalivu. Pas najbolj aktivne sedimentacije ob ustju Pada vsebuje večjo frakcijo pelita (gline in melj, <63 μm). Drobni pesek se deponira v obalnem pasu, temu pa sledi na odprtem morju področje reliktnega peska. Danes je v večini globljega SJ akumulacija mala ali pa je sploh ni in holocenski obalni pesek predstavlja večino recentnega sedimenta. V vzhodnem delu SJ je recentna sedimentacija delcev kopenskega izvora in avtohtonega skeletnega materiala prisotna le vzdolž zahodne istrske obale. Pozitivna korelacija med pelitom in vsebnostjo $C_{org.}$ v zahodnem delu SJ odraža vpliv rečnega vnosa organske snovi in avtohtone fitoplanktonske produkcije na akumulacijo $C_{org.}$ v sedimentu (slika 2). Sedimentacija v CB, na katero vpliva velikost in vrsta delcev, znaša 1,3 cm letno, toda veliki dotoki rek, povezani s tropskimi nevihtami povzročajo večjo sedimentacijo (4 cm letno) v par tednih. Peščena komponenta se praviloma akumulira v plitvem oligohalinem delu zaliva. Sediment globljega oligo- in mezohalinega dela zaliva je pretežno sestavljen iz pelita. Plitvi prag ob glavnem kanalu v zalivu vsebuje precej več peska, kar kaže, da je akumulirani pelit v globljem predelu manj podvržen resuspenziji. V zgornjem delu CB sedimentira pretežno rečni $C_{org.}$, v osrednjem zaliva pa $C_{org.}$ fitoplanktonskega izvora. Njuna vsebnost se nato zmanjšuje proti odprtemu delu zaliva.

V SJ se v odsotnosti vetrov vzpostavlja ciklonalno **tokovanje**, kot posledica vzgona in vrtenja Zemlje, kar pospešuje advekcijski tok vod Pada proti jugu (zahodnojadranski mejni tok WAC). Vetrovi spremenijo opisani vzorec. Vetrovi, ki pospešujejo tonjenje vode v zahodnem delu SJ (zimska burja) lokalizirajo izliv reke v zahodni del in pospešijo tok (WAC) v smeri juga. Nasprotno, vetrovi, ki prispevajo k dviganju vode (poletni jugo) potiskajo padske vode nižje slanosti proti severu in vzhodu, kar vpliva na večji zadrževalni čas hranil v SJ in s tem evtrofikacijo. Izjemoma lahko taka situacija tudi spremeni smer WAC. Klimatske spremembe bodo povečale jakost juga in s tem podvrženost SJ evtrofikaciji. Tokovanje v CB je ob odsotnosti vetrov posledica vzgona v delno razslojenem

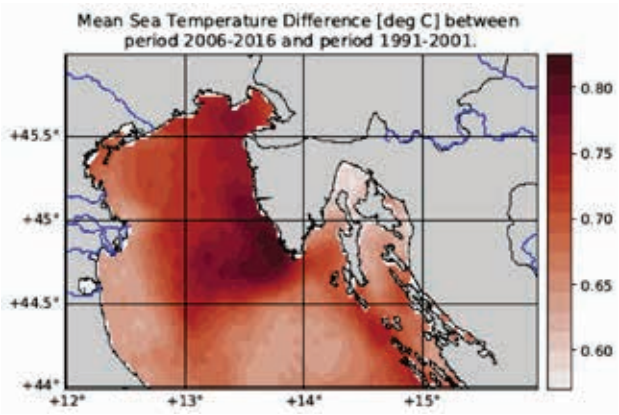


Slika 2: Porazdelitev zrnavosti (pelit <63 μm) in vsebnosti $C_{org.}$ v površinskih sedimentih severnega Jadrana[3]

estuariju s tokom površinske vode v smeri proti morju in pridnenem toku v nasprotni smeri, proti kopnemu. Tropske nevihte (tornadi) spremenijo to gibanje s potiskanjem slane vode iz kontinentalne police v zaliv in posledično višanje morske gladine. Ko tropske nevihte preidejo na kopno, lokalne nevihte v zalivu uravnavajo slanost in gibanje vodnih mas (vzvodno ali nizvodno v odvisnosti od nevihte) z vertikalnim mešanjem in longitudinalnim transportom vodne mase. V obeh primerih povečanje padavin v porečju zaliva lahko vodi do večjega vnosa hranil antropogenega izvora s kopnega in evtrofikacije. Predvideno naraščanje tropskih neviht bo tako ogrozilo okoljevarstvene ukrepe in vplivalo na povečanje evtrofikacije v CB.

Tako v SJ kot v CB največji delež primarne produkcije prispeva **fitoplankton**. V obeh ekosistemih fitoplankton kaže izrazito sezonsko spremenljivost biomase in produktivnosti, velika so tudi medletna nihanja. Med hranili, ki omejujejo rast, je v SJ praviloma najpomembnejši P, medtem ko v CB poleg P v poletnem času rast omejuje tudi N. Kljub primerljivemu vnosu hranil v SJ in CB sta v slednjem biomasa in produkcija bistveno višja. Koncentracije klorofila *a* so v SJ praviloma nižje od 5 mg m^{-3} v primerjavi z razponom 5 – 15 mg m^{-3} v CB. Podobno je tudi letna primarna produkcija v CB (350 – 660 g C m^{-2}) skoraj štirikrat višja kot v SJ (80 – 150 g C m^{-2}). Zato CB opredeljujemo kot evtrofen do hipertrofen ekosistem, medtem ko je SJ klasificiran kot oligotrofen do evtrofen. Primerjava rečnih vnosov z volumnom obeh morskih ekosistemov kaže, da ima SJ mnogo večji morski volumen. Poleg tega je za razmere v SJ pomemben tudi dotok oligotrofnih južnojadranskih vod ob vzhodni obali.

Vrstna pestrost **zooplanktona** je v SJ višja kot v CB, kjer prevladuje nekaj zelo številnih vrst. V obeh ekosistemih diverziteta raste z naraščanjem slanosti. V SJ in CB so najpomembnejša skupina zooplanktona ceponožni raki (Copepoda). V CB njihova številčnost dolgoročno upada, nižanje pa je povezano z večanjem plenilskega pritiska želatinoznega planktona, predvsem rebrač. Dodaten pritisk za kopepode predstavlja hipoksija, ki v CB zavzema



Slika 3: Razlika v satelitsko izmerjeni povprečni površinski temperaturi morja med obdobjema 2006–2016 in 1991–2001[4]

velike prostorske razsežnosti in se tudi časovno podaljšuje. V SJ se v povezavi z višanjem temperature morja (slika 3) zmanjšuje število hladnoljubnih vrst.

V obeh ekosistemih v zadnjih desetletjih narašča številčnost želatinoznega planktona, v CB rebrač, v SJ pa klobučnjakov in od leta 2016 dalje tudi invazivne tujerodne rebrače *Mnemiopsis leidyi*. Te spremembe v sestavi planktona vplivajo tudi na številčnost in prehranjenost pelaških rib, saj povečano število želatinoznih plenilcev znižuje količino hrane za ribe.

Pikofitoplankton, heterotrofne bakterije in arheje, nanoflagelati in mikrozooplankton sestavljajo **mikrobni prehranjevalni splet**, ki ima prevladujoč vpliv na kroženje hranil v morju. V letnem poteku pikofitoplanktona je v obeh ekosistemih viden poletni vrh in zimski dol, toda razpon številčnosti je večji v CB (10^2–10^6 celic/ml) v primerjavi s SJ (10^3–10^5 celic/ml). Na hitrost heterotrofne bakterijske aktivnosti v obeh ekosistemih jeseni, pozimi in na pomlad vpliva predvsem temperatura, poleti pa, ko bakteriofagi omejujejo bakterijsko številčnost, prisotnost povišane koncentracije raztopljene makromolekularne (koloidne) organske snovi. Številčnost heterotrofnih bakterij in virusov sledi številčnosti pikofitoplanktona. Čeprav je razpon bakterijske produkcije v obeh ekosistemih približno enak (0,2–280 mg C m^{-3} $leto^{-1}$), je bakterijska številčnost v CB za red velikosti večja. Opisano kaže, da je pretvorbena hitrost bakterioplanktona večja v SJ; razlika odseva tudi visoko razmerje virusi/bakterije v SJ v primerjavi z CB.

V **sklopitvi pelagiala in bentosa**, z vidika kroženja organskega C ter N, P (tabela 1) in Si, je razvidno, da zelo mali del suspendirane organske snovi (avtohtone kot rezultat neto primarne produkcije in alohtone z rečnimi pritoki) sedimentira v SJ (19 %) v primerjavi z CB (83 %). To kaže, da se v SJ večina organske snovi, nastale v primarni produkciji, razgradi v vodnem stolpu in izvozi proti jugu. Opisano je v skladu z večjo pretvorbeno hitrostjo bakterioplanktona in manjšo bentoško respiracijo v SJ, čeprav je bentoška respiracija sedimentirane organske snovi, ki vključuje tudi oksidacijo reduciranih kemijskih zvrsti Mn^{2+}, Fe^{2+}, S^{2-} nastalih z anaerobno razgradnjo organske snovi, v obeh ekosistemih približno enaka (90 %). Mala produkcija (10 %) raztopljenega anorganskega C z raztapljanjem karbonatov v sedimentih SJ poteka v poletnem obdobju. Tudi sproščanje regeneriranega N s sedimenta v vodni stolp je v obeh ekosistemih približno enako. Denitrifikacija je nekoliko večja v sedimentih CB, kjer tudi večji delež N (45 %) ostaja trajno deponiran (»pokopan«) v sedimentu v primerjavi s SJ (23 %). Sproščena hranila se v SJ uporabljajo predvsem v bentoški primarni produkciji mikroalg, ki obsega približno 25 % celotne (bentoške in pelaške) produkcije. Denitrifikacija in trajno deponirani P v sedimentu skupaj z rečnimi pritoki, osiromašenimi s P razložijo, zakaj je P omejujoči dejavnik primarne produkcije v SJ.

Ključni **bentoški habitati** v morskih ekosistemih SJ in CB vključujejo grebene ostrig (CB) in koralne grebene

Tabela 1: Primerjava med masnima bilancama $C_{org.}$, N in P severnem Jadranu (SJ) in zalivu Chesapeake (CB) (mol m^{-2} $leto^{-1}$), *depozicija korigirana glede na resuspenzijo,**področja z aktivno sedimentacijo[3]

Habitat	Proces	C_{org}		N		P	
		SJ	CB	SJ	CB	SJ	CB
Pelagial	Rečni vnos	6,5	4,1	0,7	0,9	0,03	0,02
	Rečni vnos DOC	3,2	0,8				
	NPP	8,4	45				
	Asimilacija			1,27	8,27	0,08	0,49
	Respiracija planktona	11,5	38				
Bentos	Depozicija*	3,4	18	0,40	2,3	0,02	0,11
	Produkcija MPB	2,3	0,8				
	Asimilacija			0,34	0,12	0,02	0,01
	Recikliranje			0,18	0,33	0,01	0,05
	Denitrifikacija			0,30	0,53		
	Respiracija	4,9	17				
	Trajna depozicija**	1,1	3,4	0,09	1,02	0,01	0,10
	Razlike	–0,4	–	0,3	–	0,01	–

(SJ), podvodno vegetacijo (alge in trave), obalna mokrišča in lagune. Grebeni ostrig in koral, podvodni travniki in razrast alg (slika 4) sodijo med ekosistemske gradnike, ki zagotavljajo številčnost in pestrost z njimi povezanih komercialnih in nekomercialnih organizmov. Najpomembnejši vzroki za degradacijo bentoških habitatov v obeh morskih sistemih so antropogeno preoblikovanje obalne črte in širjenje urbane infrastrukture, vnosi hranil in tujerodnih vrst, povečan pomorski promet, dvigovanje sedimentov, prelov in podnebne spremembe. Verjetno je, da se bo večina teh pritiskov ohranila tudi v bodoče in tako ogrožala za ljudi pomembne ekosistemske usluge, kot so zaščita obale in kontrola erozije, ribištvo, biotska pestrost, ohranjanje kakovosti morja.

Oba ekosistema podpirata ekonomsko pomembno **ribiško dejavnost** in pri nekaterih vrstah se kažejo znaki prelova. V SJ je število ribjih vrst v celoti višje in tudi ulov vključuje večje število vrst kot v CB. V obeh ekosistemih je pomemben ulov male pelaške ribe: v SJ *Engraulis encrasicolus*, *Sardina pilchardus*, *Sprattus sprattus*, v CB pa *Brevoortia tyrranus*. Med demerzalnimi ribami so v SJ najpomembnejše *Merluccius merluccius*, *Mullus barbatus*, *Solea solea* in *Sparus aurata*, v CB pa *Micropogonias undulates*, *Leiostomus xanthurus* in *Paralichthys dentatus*. Med nevretenčarji v SJ lovijo več vrst rakov in mehkužcev, medtem ko je v CB lov osredotočen na posamezno vrsto rakov (*Callinectes sapidus*) in školjk (*Crassostrea virginica*). Medtem ko je skupni ulov v SJ zrasel od 140000 t na leto v obdobju 1992 – 2002 na 180000 ton leta 2016, je v istem obdobju v CB upadel od 350000 na okoli 200000 t na leto. Na enoto fitoplanktonske produkcije je ulov v SJ približno 1,5 krat višji kot v CB.



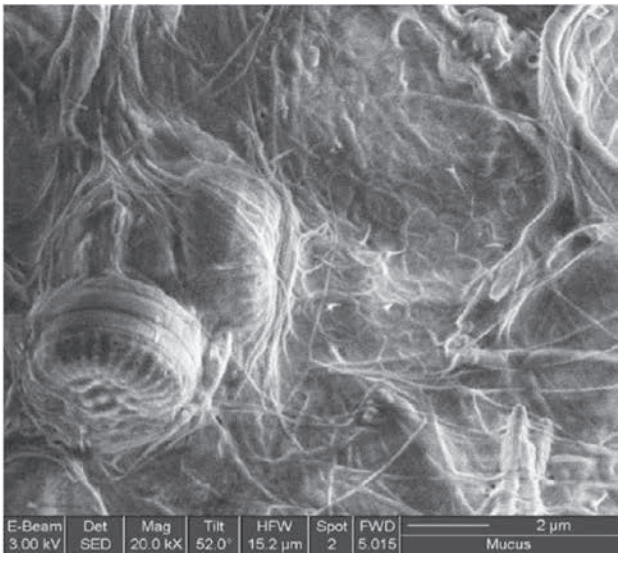
Slika 4: Podvodni »gozdički« cistozir so pomembni ekosistemski gradniki (Foto: B. Mavrič)

Antropogeni vplivi na ekologijo in ekosistemske storitve so znatni v obeh sistemih. Kot indikatorje stanja ekosistemov uporabljamo prostorsko razsežnost ključnih habitatov (podvodni travniki, školjčni in koralni grebeni, mokrišča), fitoplanktonktonsko produkcijo, številčnost zooplanktona, številčnost morskih virov – rib, školjk, rakov, številčnost filtratorjev, prostorsko razsežnost hipoksij in anoksij, pogostost škodljivih cvetenj fitoplanktona, številčnost želatinoznega planktona, zakisanost, površinsko temperaturo, nivo gladine morja. Med pritiski imajo najširši negativen učinek na stanje ekosistemov in ekosistemskih storitev vnosi hranil in podnebne spremembe (tabela 2).

Evtrofikacija, katere posledice so izgube habitatov, zmanjšanja evfotske globine v vodnem stolpu, daljši časovni in večji prostorski obseg hipoksij in anoksij ter pojavljanje škodljivih cvetenj mikroalg, je v SJ in CB najpomembnejši dejavnik, ki vpliva na izkoriščanje obeh ekosistemov. Rečni vnosi N (CB) in P (SJ) antropogenega izvora so najpomembnejši vzroki evtrofikacije in z njo povezanih destruktivnih procesov v ekosistemih. V obeh ekosistemih je dolgoročno dokumentirana »kulturna« evtrofikacija kot posledica vnosa hranil, z vidnim pospeškom po 2. svetovni

Tabela 2: Vpliv vrednosti indikatorjev stanja ekosistemov na izboljšanje (+) oz. poslabšanje (↓) ekosistemskih storitev. **Indikatorji stanja**: Hab = stanje habitatov; NPP = neto primarna produkcija; Zoo = številčnost zooplanktona; MV = živi morski viri; F = številčnost filtratorjev; Hyp = časovna in prostorska razsežnost hipoksij/anoksij; Tox = pogostost pojavov škodljivih cvetenj fitoplanktona; Žel = številčnost želatinoznih organizmov (meduze, rebrače); Kis = kisanje morja; T^0 = površinska temperatura; GM = gladina morja **Ekosistemske storitve**: (1) ribolov (ribe, mehkužci, raki); (2) vzdrževanje kakovosti morja (kroženje hranil, prehranjevanje filtratorjev, stabilizacija morskega dna); (3) odpornost obale (stabilizacija obale, manjšanje erozije, zadrževanje poplav); (4) podpora biotski pestrosti (biološko strukturirani habitati, različne vrste, reprodukcija, zaščita pred predatorji); (5) sekvestracija ogljika (kontrola ogljika v atmosferi in vpliv na podnebne razmere); (6) estetska vrednost (turizem, rekreacija, kultura); prirejeno po Malone in sod.[5]

Ekosistemske storitve	**Indikatorji stanja ekosistemov**										
	Hab	**NPP**	**Zoo**	**MV**	**F**	**Hyp**	**Tox**	**Žel**	**Kis**	**T^0**	**GM**
1.Ribolov	+	+	+	+	+	↓	↓	↓	↓	↓	
2.Kakovost morja	+				+	↓	↓		↓	↓	
3.Odpornost obale	+					↓					↓
4.Pestrost organiz.	+	+	+	+	+	↓	↓	↓	↓	↓	
5.Sekvestracija C	+	+				↓				↓	
6.Estetska vrednost	+					↓	↓				



Slika 5: Posnetek makroagregatov iz Tržaškega zaliva z vkleščeno diatomejo z elekronsko vrstično mikroskopijo[6]

vojni, vendar je bolj evtrofen CB. SJ je evtrofen le ob izlivih rek ob severni in zahodni obali. V SJ so bolj prisotni toksični fitoplanktonski rodovi, med katerini so *Lingulodinium*, *Prorocentrum*, *Dinophysis* in *Alexandrium* prisotni tudi v CB. Le v SJ smo beležili edinstven sezonski pojav sluzi (lipidnih in heteropolisharidnih makroagregatov) kot posledica akumulacije koloidne organske snovi pozno pomladi (slika 5), Sedimentacija sluzi je povzročila lokalno pomanjkanje kisika pri dnu, hipoksijo in celo anoksijo s posledičnim pomorom bentoških organizmov.

Zaradi zmanjšanja vnosa antropogenih hranil v zadnjih desetletjih (po 1985), P v SJ in N v CB, se je evtrofikacija obeh ekosistemov zmanjšala, vendar v celoti ne dosega končnega cilja kvalitete vod, zapisanega v smernicah evropskih direktiv (EU Water Framework Directive, Marine Strategy Directive) in programa za Zaliv Chesapeake (Chesapeake Bay Program).[7,8] Upravljalski posegi so vplivali na znižanje koncentracij P v SJ in N v CB, a ostaja problem povečanja koncentracije celotnega N v vodah SJ in celotnega P v CB. Z nadaljevanjem asanacijskih in restavracijskih posegov je pomembno dokumentirati izboljšanje stanja in razumenti, kako na spremembe ekosistemov vplivajo drugi antropogeni pritiski vključno s klimatskimi spremembami, ribištvom in izkoriščanjem obalnega področja. Padec pH, **»kisanje« morja,** je posebno v estuarijih lahko posledica evtrofikacije. SJ je danes ponor CO_2 z letnim tokom –1.2 to –3 mol C m^{-2}, istega reda velikosti kot v severozahodnem Sredozemlju. Nanj vplivajo predvsem temperatura in vetrovi, manj poraba fitoplanktona. Ocenjeni 25-letni (1983–2008) padec pH v vodah SJ je 0,003, podobno kot v širšem Sredozemlju. Izračunani Revellov faktor (»pufranost«) za SJ je približno 10, kar kaže, da je puferska kapaciteta visoka in da SJ ni podvržen »kisanju«. Celotna alkalnost je visoka (2,6–2,7 mmol l^{-1}), na zgornji meji v Sredozemlju, takoj za Egejskim morjem, predvsem zaradi vnosa karbonata z alpskimi in kraškimi rekami. Približno 60 % vnosa alkalnosti prispeva Pad (~3 mmol l^{-1}) in ta pada z naraščajočo slanostjo. Vode SJ so prenasičene glede na kalcit (Ω_{Ca}) in aragonit (Ω_{Ar}) v celem letu, vendar je v obdobju gostotne stratifikacije vodnega stolpa nasičenost precej nižja v sloju pri dnu zaradi remineralizacijskih procesov v sedimentu. CB je ponor CO_2 in šibek izvor alkalnosti z nizko pufersko kapaciteto. Vzrok je mešanje rečne in morske vode ter produkcija CO_2 z anaerobnimi redoks reakcijami (dihanja), ki danes presega vnos atmosferskga CO_2. Alkalnost narašča v smeri morja (s slanostjo) in z globino. 15-letni padec pH v odprtem delu zaliva znaša 0,11, do naraščanja v osrednjem (0,12) in zgornjem (0,16) delu zaliva pa prihaja zaradi dolgoročnega porasta pH reke Susquehanna. V pridnenih vodah je

trend podoben, kar ne kaže na »kisanje« zaradi razgradnje organske snovi.

Povečanje temperature površinske plasti morja in s tem povečanje vertikalne temperaturne in gostotne stratifikacije zaradi **podnebnih sprememb** in zvečanje jakosti vetrov, spremembe padavin (povečanje v porečju CB in zmanjšanje v SJ) in zvišanje morske gladine (približno enako v obeh ekosistemih) spreminjajo sistem tokovanja in mešanja vodnih mas ter valovanja. Vse te spremembe vplivajo na razmere v obeh ekosistemih in njihovo izkoriščanje. V SJ in v porečju bi zmanjšana količina letnih padavin pospešila oligotrofikacijo[9], v CB pa v povezavi s povišano temperaturo povečan prostorski in časovni obseg hipoksij v pridnenem sloju kljub zmanjšanemu vnosu hranil.[10] Zvišanje temperature v obeh ekosistemih bo pospešilo rast toploljubnih (termofilnih) vrst. Morska trava *Zostera marina* je tako prisotna na svojem južnem robu v obeh ekosistemih in toplejše poletne vode so lahko vzrok za zmanjšano številčnost oziroma pomembno regresijo vrste. Povečanje temperature oziroma ekstremni temperaturni pojavi lahko pospešijo odmiranje koralnih grebenov v SJ. Povišana temperatura bo spremenila sukcesije hladno- in toploljubnih vrst z daljšim poletnim obdobjem in večjo prisotnostjo vrst kot so npr. *Chrysaora spp.*, *Mnemiopsis leidyi*. Zaradi povišane temperature v CB ni več prisoten hladnoljuben kopepod *Acartia hudsonica*. Povišana temperatura bo verjetno pospešila pretok snovi v mikrobnem spletu v primerjavi z metazojskim, kar ima negativne posledice za prehrano rib. Dvig gladine morja in ekstremni vremenski pojavi bodo povečali nevarnost poplav in erozije. Slana močvirja bodo poplavljena. Organizmi v CB bodo bolj podvržen »kisanju« kot v SJ, saj ima slednji zaradi manjših časovnih in prostorskih razsežnosti hipoksij ter vnosa karbonata alpskih rek, visoko pufersko kapaciteto. Kljub prenasičenosti glede na kalcit in aragonit, pa v prihodnosti lahko pričakujemo vplive »kisanja« tudi v SJ, saj karbonatni organizmi potrebujejo visok indeks nasičenja.

Sinergije

Tako CB kot tudi SJ sta v celoletnem časovnem obdobju avtotrofna sistema, v katerih je primarna produkcija višja kot respiracija. V CB ekosistemu se suspendirani C pretaka na kontinentalno polico, medtem ko fitoplanktonska produkcija v povezavi s tvorbo goste jadranske vode v severnem Jadranu pospešuje prenos ogljika v Sredozemsko morje in s tem prispeva k nižanju atmosferskega CO_2.[11] Zaradi podnebnih sprememb in višanja temperature bo predvidoma tvorba goste vode v SJ zmanjšana in s tem se bo znižala tudi sekvestracija atmosferskega CO_2.

Dvig temperature skupaj z ribolovnim pritiskom spreminja sestavo ribje združbe od prevlade velikih vrst, ki spolno dozorijo pozno in imajo maloštevilno potomstva, v združbo z majhnimi vrstami in zgodnjo spolno zrelostjo ter številnim potomstvom, katerih mesto je nižje v prehranjevalnem spletu. Podnebne spremembe s segrevanjem morja negativno vplivajo na hladnoljubne, borealne ribe (*Sprattus sprattus*, *Merlangius merlangus*), ki so v severnem Jadranu bolj razširjene kot v preostalem delu Sredozemskega morja. Po drugi strani je večja številčnost komercionalno pomembne kozice *Penaeus kerathurus* povezana s segrevanjem Jadranskega morja.

Izguba pomembnih habitatov v obeh sistemih je povezana s pridnenim pomanjkanjem kisika (hipoksija, anoksija) in z antropogeno degradacijo okolja. V obeh sistemih se sezonska hipoksija razvije v poletnem in zgodnjejesenskem obdobju. V CB hipoksija zajame celotno mezohalino območje, medtem ko je v SJ tako prostorsko kot tudi časovno manj predvidljiva. Pomanjkanje kisika ob dnu pomembno vpliva na ključne habitate v obeh ekosistemih. Naraščajoči vnosi hranil v oba sistema so v preteklih obdobjih (1945–1985) povzročili propad ali zmanjšanje pomembnih habitatov: grebenov ostrig v CB, koralnih grebenov in travnikov ter pokrovnosti makroalg v SJ. Izgubo pomembnih habitatov so še poslabšale gradnje številnih obalnih infastruktur, dvig temperature in invazije tujerodnih organizmov. Pozitiven znak je, da se v ključnih habitatih po zmanjšanju antropogenih pritiskov razmere izboljšujejo.

Monitoring in modeliranje

Glede na opisane antropogene pritiske je za trajnostni razvoj nujen pristop ekosistemskega upravljanja (EKOU), ki upošteva socialno-ekonomski razvoj in dinamiko ekosistemov[5]. Ekonomske dejavnosti, ki potekajo v mreži socialnih interakcij, so tako omejene z razpoložljivostjo ekosistemskih storitev. EKOU potencialno zagotavlja stroškovno učinkovite rešitve za doseganje pogosto konfliktnih ciljev socialno-ekonomskega razvoja in trajnostne rabe okolja. Temelj trajnostnega socialno-ekonomskega razvoja in rabe ekosistemskih storitev je dobro stanje ekosistemov. Zato je za učinkovit EKOU nujno spremljanje (monitoring) ekosistemov s primernimi časovnimi presledki in v zadostni prostorski razsežnosti ter redna analiza in poročanje o stanju.[5]

Napredek v znanstvenem razumevanju obalnih ekosistemov in predvidljivost sprememb stanja sta ključna tudi za ugotavljanje sposobnosti ekosistemov SJ in CB za trajnostne ekosistemske storitve. Pri tem sta ključna monitoring obeh sistemov in modeliranje procesov. Za EKOU je potrebna integralna ocena stanja (IEA) v kateri so vključeni državljani, predstavniki industrij, znanstveniki, upravljavci virov, politiki[12], ki zagotovijo:

(1) soglasje o prioritetnih ekoloških, socialnih in ekonomskih ciljih, ki pomagajo opredeliti usmeritve politikov in upravljavcev,
(2) opredelitev antropogenih pritiskov na ekosisteme ter stanje ekosistemov na osnovi indikatorjev, oceno stanja in trendov ekosistemskih storitev glede na dogo-

vorjene cilje (tj. doseganje ekosistemskih storitev na želenem nivoju),
(3) opredelitev naravnih in antropogenih (ekoloških, socialnih, ekonomskih) vzrokov in posledic ugotovljenih trendov stanja ekosistemov in ekosistemskih storitev,
(4) predvidevanja sprememb v stanju ekosistemov in ekosistemskih storitvah glede na opredeljene dejavnosti,
(5) rutinsko preverjanje učinkovitosti ukrepov v rednih časovnih presledkih in v povezavi z opredeljenimi cilji,
(6) identifikacijo ključnih pomanjkljivosti v znanju in razpoložljivih podatkih ter modelih, ki so nujni za izboljšanje integralne ocene stanja.

Danes je zmožnost modeliranih napovedi tokovanja in mešanja vodnih mas omejena z nezanesljivostjo regionalnih napovedi sprememb padavin, rečnih pritokov in vetrov. Izboljšane napovedi fizikalnih sprememb in stanja ekosistemov zahteva v regionalnem okviru vzdržno in zelo pogosto sinoptično merjenje in modeliranje sprememb gradientov atmosferskega tlaka, tokov toplote in CO_2 med atmosfero in morjem, ekstremnih vetrov (burje, juga, tropskih neviht), okoljskih lastnosti ekosistema (temperature, slanosti, hranil, kisika, vertikalnega mešanja, prostorske porazdelitve habitatov, gostote invazivnih vrst) in gostote in porazdelitve ključnih skupin organizmov (fitoplanktona, kopepodov, želatinoznega zooplanktona, ključnih predatorjev in izbranih ribjih populacij). Uporabo podobnega pristopa načrtujemo tudi v prihodnjem primerjalnem prikazu izvora in porazdelitve onesnaževal (kovin, radionuklidov, organskih onesnaževal, plastike, termičnega onesnaževanja, hrupa) v SJ in CB.

Literatura

1. T. C. Malone, A. Malej, J. Faganeli (Ed.): Coastal Ecosystems in Transition: A Comparative Analysis of the Northern Adriatic and Chesapeake Bay, AGU Wiley, New Jersey, **2021**.
2. T. C, Malone, A. Malej, L. W. Harding, N. Smodlaka, R. E. Turner (Ed.): Ecosystems at the Land-Sea Margin: Watershed to the Coastal Sea, AGU, Washington DC, **1999**. **DOI:**10.1029/CE055
3. J.M. Testa, J. Faganeli, M. Giani, M. J. Brush, C. De Vittor, W. R. Boynton, S. Covelli, W. M. Kemp, N. Kovač, R. Woodland, in: T. C. Malone, A. Malej, J. Faganeli (Ed.): Coastal Ecosystems in Transition: A Comparative Analysis of the Northern Adriatic and Chesapeake Bay, AGU Wiley, New Jersey, **2021**.
4. A. Malej, D. Lučić, M. Ličer, T. Kogovšek, P. Lučić, in: Ocean Sciences Meeting, San Diego, Ca., **2020,** https://agu.confex.com/agu/osm20/meetingapp.cgi/Paper/645896.
5. T.C. Malone, P.M. DiGiacomo, E. Gonçalves, A.H. Knap, L. Talaue-McManus, S. de Mora, *Mar. Policy,* **2014**, 43, 262–272. **DOI:**10.1016/j.marpol.2013.06.008
6. V. Turk, V. Flander-Putrle, A. Malej, in: ASLO 2005 Summer Meeting: A pilgrimage through global aquatic sciences, Santiago de Compostela, Spain, **2005,** www.aslo.org/santiago2005.
7. M. Herrmann, S. Doney, T. Ezer, K. Gedan, P. Morefield, B. Muhling, D. Pirhalla. S. Shaw, Scientific and Technical Advisory Committee review of the Chesapeake Bay Program partnership's climate change assessment framework and programmatic integration and response efforts. STAC Publication Number 18-001, Edgewater, MD., **2018**.
8. N.Voulvoulis, K.D. Arpon, T. Giakoumis, *Sci. Tot. Environ.,* **2017,** 575, 358–366. **DOI:**10.1007/s12237-009-9191-7
9. P. Mozetič, C. Solidoro, G. Cossarini, G. Socal, R. Precali, J. Francé, F. Bianchi, C. De Vittor, N. Smodlaka, S. Fonda Umani, *Estuar. Coasts,* **2010,** 33, 362–375.
10. C. R. Pyke, R. G. Najjar, M. B. Adams, D. Breitburg, C. Herschner, R. Howarth, M. Kemp, M. Mulholland, M. Paolisso, D. Secor, K. Sellner, D. Wardrop, R. Wood, Climate Change and the Chesapeake Bay: State-of-the-Science Review and Recommendations. Technical Advisory Committee (STAC) Publication #08-004, Annapolis, MD., **2008**.
11. G. Cossarini, S. Querin, C. Solidoro, *Ecol.Model.,* **2015,** 118–134. **DOI:**10.1016/j.ecolmodel.2015.07.024
12. P. S. Levin, M. J. Fogarty, S. A. Murawski, D. Fluharty, *PLoS Biol.,* **2009,** 7(1), e1000014. **DOI:**10.1371/journal.pbio.1000014

Abstract

A new book in press entitled Coastal Ecosystems in Transition: A Comparative Analysis of the Northern Adriatic and Chesapeake Bay (AGU Wiley, New Jersey) edited by T.C. Malone, A. Malej and J. Faganeli is presented. This book reports the comparison of ecosystems of the northern Adriatric and the Chesapeake Bay. It enlarges our knowledge of anthropogenic pressures on coastal ecosystems where is concentrated the majority of the population and the exploitation of natural resources. The revisited ecosystems permitted to evaluate changes, particularly local, over the last twenty years in the context of global climate changes and to evaluate the success of management efforts and reduction of anthropogenic pressures on coastal ecosystems.

Except when otherwise noted, articles in this journal are published under the terms and conditions of the Creative Commons Attribution 4.0 International License

DOI: 10.17344/acsi.2020.6474 *Acta Chim. Slov.* **2020,** *67,* S98–S105
creative commons

Obiski Rosalind Franklin v Sloveniji

Marko Dolinar

Univerza v Ljubljani, Fakulteta za kemijo in kemijsko tehnologijo, Katedra za biokemijo, Večna pot 113, 1000 Ljubljana, Slovenija

** Corresponding author: E-mail: marko.dolinar@fkkt.uni-lj.si*

Received: 30-10-2020

Povzetek

Ob 100-letnici rojstva znane kristalografinje Rosalind Franklin (1920-1958) članek opisuje njene stike s slovenskimi in hrvaškimi kemiki v letih 1952-1955, predvsem z Dušanom Hadžijem in Katarino Kranjc. Ugotovil sem, da je najbolj znana planinska fotografija Rosalind Franklin nastala v Julijskih Alpah verjetno leta 1952 in ne na Norveškem konec 30-tih let, kot je veljalo doslej. Na Triglav pa se je vzpela julija 1954 ali septembra 1955 in ne leta 1952, kot piše v njeni biografiji.

Ključne besede: kristalografija; Dušan Hadži; Rosalind Franklin; Ajdovska deklica

1. Uvod

Znana britanska kristalografinja Rosalind Elsie Franklin je bila rojena 25. julija 1920. Svetovno slavo si je prislužila z raziskavami strukture molekule DNA. Danes je jasno, da so njene rentgenske uklonske slike hidratirane molekule DNA, predvsem »fotografija 51«, ki sta jo posnela z doktorandom Raymondom Goslingom leta 1952, ključno pripomogle, da sta James Watson in Francis Crick leta 1953 objavila zasnovo zgradbe DNA[1]. Povsem v senci tega članka je ostal članek Franklinove in Goslinga v isti številki revije Nature, v katerem sta opisala obstoj dveh oblik DNA, A in B, v odvisnosti od hidratacije, osnovno vijačno zasnovo oblike B in njene dimenzije[2]. Podobno se je zgodilo s tretjim člankom v isti številki revije Nature, katerega vodilni avtor je bil Maurice Wilkins[3]. Z zgodovinske razdalje se zdi pomembna razlika med avtorji: Watson, Crick in Wilkins so leta 1962 dobili Nobelovo nagrado, Franklinova pa ne. Racionalno stališče je, da je ni mogla dobiti, ker je leta 1958 umrla. Nekateri pa menijo, da je tudi če bi bila živa, ne bi dobila, ker je bila kot samosvoja ženska zapostavljena, in ker si nagrade ne morejo deliti več kot trije prejemniki, bi tretji prejemnik v vsakem primeru bil Wilkins, ne Rosalind Franklin[4].

2. Rosalind Franklin, Dušan Hadži in gore

Na začetku svoje poklicne poti je Rosalind Franklin raziskovala strukturo premoga[5]. Med 2. svetovno vojno in kmalu po njej je bilo namreč razumevanje premoga strateško pomembno, zato je država podpirala tovrstne raziskave. To pa je bila skupna tema s slovenskimi kemiki v času po drugi svetovni vojni.

Januarja 1951 je Franklinova začela delati na King's Collegeu v Londonu, kjer so ji namenili raziskovanje strukture DNA, čeprav dotlej ni delala na bioloških molekulah. Zaposlili so jo zaradi dobrega poznavanja tehnike rentgenske spektroskopije, ki jo je v Franciji uporabljala pri ugotavljanju strukture različnih ogljikovih spojin (predvsem amorfnih polimerov) ter raziskavah mehanizma kristalizacije v trdni fazi. Kot je zapisal Jure Zupan v glasilu Kemijskega inštituta Dogodki[6], je leta 1951 Dušan Hadži, ki se je v tistem času izpopolnjeval v Cambridgeu, obiskal King's College[i]. Kot navaja Zupan, naj bi Hadži takrat Franklinovo, ki je bila ljubiteljica gora, povabil v Slovenijo.

Rosalind Franklin se je vabilu naslednje leto odzvala[ii]

i V Zupanovem članku je naveden obisk King's Collegea junija 1951, vendar je na osnovi Hadžijevega osebnega dnevnika mogoče reči, da je šel na King's College prav zaradi srečanja z Rosalind Franklin (»v sredo sem šel v London k Miss Franklin«), s katero se je sestal 23. maja 1951. Na King's Collegeu je bil sicer že 7. aprila, a ker je bila sobota, tam ni bilo nikogar.

ii O poti v Jugoslavijo leta 1952 je Rosalind Franklin v pismu z dne 1. marca 1952 prijateljici Anne Sayre zapisala: *Nadejam se prijetnega potovanja to pomlad, čeprav sem že nekoliko živčna, saj že nekaj časa nisem dobila nobenih novic [glede tega]. Vprašali so me, če bi sprejela povabilo na pogovor o problemih raziskovalnega laboratorija, ki se ukvarja s premogom v Jugoslaviji! Kraj se imenuje Ljubljana, a so mi ponudili tudi pot v Beograd in Zagreb in mogoče v Alpe. Dogovorili smo se za maj, ker je to čas, ko je vreme najboljše za razprave o premogu, a doslej uradnega povabila še nisem dobila.*

in obiskala Ljubljano, kjer je imela predavanje[iii] na Kemijskem inštitutu, o čemer obstaja kratka navedba v letopisu Slovenske akademije znanosti in umetnosti (SAZU)[7]. O obisku v Ljubljani je na kratko pisal tudi časopis Slovenski poročevalec[8] 14. maja 1952:

Te dni se mudi v Ljubljani dr. Rosalind E. Franklin, predavateljica na King's College v Londonu. Našo državo je obiskala na vabilo Kemičnega inštituta Slovenske akademije znanosti in umetnosti, kjer bo imela razgovore z našimi strokovnjaki za koks. Franklinova dela na problemih okrog fine strukture premoga in koksa in je doslej dosegla na tem področju zelo dragocene rezultate. V Ljubljani bo tudi predavala v okviru Slovenskega kemijskega društva. Obiskala bo tudi Zagreb in Beograd.

Jenifer Glynn je v biografiji z naslovom My sister Rosalind Franklin[9] navedla, da naj bi predavanju sledil izlet na Triglav. V knjigi navaja, kako je Rosalind doživela hribovski izlet v Julijce, verjetno v pismu domačim[iv]:

Šli smo na pohod za tri dni in pol v resne hribe, Julijske Alpe, kjer smo spali v planinskih kočah in se povzpeli na Triglav, najvišjo goro v Jugoslaviji (pribl. 9500 čevljev). Čudovito je bilo biti ponovno med gorskimi vršaci, *prvič po petih letih. Vračali smo se skozi »dolino Sedmerih jezer«, ki je narodni park zaradi botaničnih in zooloških posebnosti. Še nikoli nisem videla tako čudovite preproge alpskih cvetic – tako zgoraj, v skalah in na meliščih, kot spodaj, v dolini, so bile dosti bolj raznolike in pisane kot sem jih videla v Franciji ali Italiji.*

Kot navaja avtorica biografije, je Rosalind Franklin takrat prišla v Ljubljano, kjer je predavala, potem pa najprej odšla na Bled, v vilo ob jezeru. Oče njenega kolega (zelo verjetno gre za Dušana Hadžija) je imel visok položaj v Slovenski akademiji[v]. To mu je omogočalo, da so tri generacije njegove družine in prijatelji tam preživljali počitnice. Družba na Bledu je Rosalind Franklin ugajala in je bila navdušena nad tem, da tu »živijo tako civilizirano, čeprav so skoraj brez denarja«. Iz Slovenije naj bi odpotovala v Kotor v Črno goro.

Zupanov prispevek v Dogodkih sicer kot letnico vzpona na Triglav navaja 1954. Podatek izvira iz pogovora, ki ga je imel Jure Zupan z Dušanom Hadžijem, ko je bil ta star že 95 let, tako da ni mogoče povsem izključiti, da se je glede letnice zmotil. Gotovo pa drži, da sta se Dušan Hadži in Rosalind Franklin osebno poznala in sta šla skupaj tudi na Triglav.

3. Fotografija z »Norveške«

Delo in življenje Rosalind Franklin sta zelo dobro obdelana in arhivi hranijo veliko dokumentacije iz časa njenega aktivnega raziskovalnega dela. Na spletu je dostopnih le malo fotografij, ki prikazujejo Rosalind Franklin v gorah, čeprav jih je pogosto obiskovala. Ena od najbolj znanih fotografij Rosalind Franklin, hrani jo ameriška National Library of Medicine, jo prikazuje, kako sedi na



Slika 1: Fotografija Rosalind Franklin, ki je v arhivu The National Library of Medicine's Profiles in Science označena kot »*Rosalind Franklin mountain climbing in Norway*« (NLM ID: 101584586X127, https://profiles.nlm.nih.gov/spotlight/kr/catalog/nlm:nlmuid-101584586X127-img) z letnico 1940 in pripisom »avtor neznan«. Fotografijo je arhivu posredovala sestra Rosalind Franklin, Jenifer Glynn, objavljena pa je v več biografijah. V tisti, ki jo je napisala Glynnova, je označena kot »*Rosalind in mountains on a family holiday in Norway, 1937 or 1939*«. Kot je razvidno iz primerjave s sliko 2, gre za enako ozadje in je bila torej fotografija posneta pod vrhom prelaza Vršič. Obraz Ajdovske deklice je točno nad glavo Rosalind Franklin. Fotografijo je najverjetneje posnel Dušan Hadži sredi maja leta 1952.

iii V arhivu Slovenskega kemijskega društva vabila ali kakšnega drugega dokumenta o tem predavanju ne hranijo, čeprav je bilo predavanje – glede na navedbo v Slovenskem poročevalcu – organizirano tudi kot del društvenih aktivnosti. Tako žal ni mogoče ugotoviti, katerega dne točno je potekalo predavanje v Ljubljani. Tudi v letopisu SAZU datum ni naveden.

iv Churchill Archives Centre, Churchill College, Cambridge hrani mapo s počitniškimi pismi in razglednicami Rosalind Franklin. V navedbi vsebine so omenjena sporočila iz Jugoslavije iz leta 1952 (nič pa iz naslednjih let). Gradivo je nedostopno do leta 2034. Zelo verjetno je Jenifer Glynn (sestra Rosalind Franklin) imela dostop do celotne korespondence svoje sestre z domačimi.

v Jovan Hadži je bil v času obiska Rosalind Franklin v SAZU tajnik 4. razreda, ki je pokrival naravoslovne in medicinske vede.

obcestnem kamnu, v ozadju pa so skalnati gorski vrhovi (slika 1). To fotografijo je v arhiv posredovala Jenifer Glynn, objavila pa jo je tudi v biografiji[9] iz leta 2012 in pri tem navedla, da je bila posneta med družinskim dopustom leta 1937 ali 1939 na Norveškem. Tako je tudi označena v ameriškem arhivu (»cca 1940«, avtor neznan). Vendarle pa natančen pogled razkriva strukturo kamnine, ki je ne bi pričakovali na Norveškem, pač pa prej v Alpah. Še več, na fotografiji so vidna drevesa, ki so zelo verjetno macesni, areal rasti macesna pa je omejen na alpsko področje. Še podrobnejša preučitev skalnih struktur pokaže, da gre za severno steno Prisojnika s ceste na Vršič. Nad glavo Rosalind Franklin je namreč jasno viden značilen obraz Ajdovske deklice, prav tako pa ustreza oblika stene z značilnimi tremi stožci, kot je razvidno iz fotografije na sliki 2.



Slika 2: Fotografija Ajdovske deklice v severozahodni steni Prisojnika, posneta pri Erjavčevem domu pod prelazom Vršič. Fotografiral Rok Kočar 29. julija 2008. Posnetek je z mesta, ki je, sodeč po perspektivi, samo nekoliko nižje od kraja, kjer je bila posneta fotografija Rosalind Franklin.

Glede na to, da je v življenjepisu avtorice Jenifer Glynn omenjena samo pot na Triglav leta 1952, ne pa tudi pot na Vršič, je možnih več ugibanj, kdaj in v kakšnih okoliščinah je nastala fotografija. Možno je, da je šlo za krajši izlet leta 1952, ki v biografiji ni posebej omenjen, druga možnost pa bi bila, da je bila Franklinova v Sloveniji večkrat.

Vendar pa je biografijo, ki jo je napisala Jenifer Glynn, treba jemati z zadržkom. Glede na to, da se je zmotila pri fotografiji svoje sestre tako glede kraja nastanka kot glede letnice (in to za več kot 10 let), bi bilo možno tudi, da se je zmotila glede letnice pohoda na Triglav. O nezanesljivosti avtorice govori tudi to, da je Nobelovo nagrado za strukturo DNA v članku[10], objavljenem leta 2008 v časopisu Notes & Records of the Royal Society, umestila v leto 1959, čeprav so jo podelili šele leta 1962. Konec koncev je bila Jenifer Glynn, čeprav 9 let mlajša od svoje sestre Rosalind, v času izida biografije stara že 83 let. Po drugi strani pa je ista fotografija vključena tudi v brošuro[11], ki je bila verjetno natisnjena v le nekaj izvodih, in jo je napisala mama Rosalind Franklin, Muriel Franklin[vi] (1894-1976), leta 1963 ali nekaj let kasneje. Kaže torej, da je bila fotografija napačno označena že v družinskem arhivu. Glede na vse ostale podatke je mogoče skoraj zagotovo reči, da je avtor fotografije Dušan Hadži.

4. Drugi obisk v Ljubljani

Iz članka[12] Anne Piper (1920-2017), ki je izšel leta 1998 v ugledni reviji Trends in Biochemical Sciences, je razvidno, da je bila Rosalind Franklin v Ljubljani tudi leta 1953, ko se je tu za en dan ustavila na poti v Atene. Iz Grčije je pot nadaljevala v Izrael, kjer si je ogledala vse dele nove države[vii], saj jo je kot Judinjo zelo zanimala. Kot piše Anne Piper, ki je bila Rosalindina prijateljica in na tem potovanju do Aten tudi sopotnica, sta se v Ljubljani srečali s kolegom Dušanom (zapisano napačno: *Duysan*). Ta je Piperjevi rekel, da je Rosalind človek, ki ga navdaja z življenjsko energijo (angl.: *she makes my clockwork tick*). Citat je bil kasneje objavljen tudi v biografijah, ki sta jih napisali Jenifer Glynn[9] in Brenda Maddox[13], le da brez imena tistega, ki je besede izrekel.

Dušan Hadži (1921–2019) je bil samo eno leto mlajši od Rosalind Franklin. Njuna skupna točka je bilo raziskovalno delo v Franciji (Hadži 3 mesece v letu 1950[viii], in sicer v Rennesu in Parizu, kjer se je uvajal v infrardečo spektroskopijo, Franklinova od februarja 1947 do konca leta 1950 v Parizu, kjer se je ukvarjala z rentgensko spektroskopijo). Hadži je oktobra 1950 prišel za 9 mesecev v Cambridge k Normanu Sheppardu (1921–2015), ki je takrat zaradi odsotnosti svojega mentorja, prof. Gordona Sutherlanda, prevzel delo z IR-spektrometri. Njegov laboratorij je namreč IR-spektroskopijo uporabljal tudi za

vi Muriel Franklin je bila v času pisanja spominov na hčerko stara med 70 in 80 let. V poznih letih svojega življenja je napisala podobno delo o svojem možu Ellisu. En izvod brošure o Rosalind Franklin hrani ameriška knjižnica Linda Hall Library v Kansas Cityju (https://www.lindahall.org/rosalind-franklin/). Opis knjige je na spletni strani antikvariata Alembic Rare Books (https://alembicrarebooks.com/blogs/alembic-rare-books-blog/a-rare-biographical-sketch-of-rosalind-franklin-by-her-mother).

vii Obisk v Izraelu je bil avgusta 1953, saj je v notesniku Rosalind Franklin »Visit to Weizmann Institute« prvi (in edini datirani) vpis od 17.8.1953.

viii Iz Hadžijevega poročila[15] o izpopolnjevanju v tujini je razvidno, da je bil v Franciji od 1. maja do 1. avgusta in sicer prvo polovico časa pri dr. Renéju Freymanu v Rennesu na Faculté des Sciences, Laboratoire de Physique, nato pa pri dr. Pierru Barchewitzu v Parizu na univerzitetnem Laboratoire de Physique (Annexe de la Sorbonne). V Veliki Britaniji je bil od začetka oktobra 1950 do konca junija 1951 na University of Cambridge, Department of Colloid Science.

analizo premogov[14], kar je bila Hadžijeva doktorska tema. Tudi Franklinova je bila na nek način nova v Veliki Britaniji, saj je po štirih letih dela v Franciji prišla na King's College v London, a je študirala v Cambridgeu (1938–1941) in je premog raziskovala v letih 1942–1946, ko je bila zaposlena v okviru Britanskega združenja za raziskave uporabe premoga (British Coal Utilisation Research Association, BCURA).

Kot je razvidno iz poročila[15] Dušana Hadžija, objavljenega v Letopisu SAZU za 1950 in 1951, je med izpopolnjevanjem v Parizu med drugim obiskal Laboratoire Central des Services Chimiques de l'Etat (kjer je bila zaposlena Franklinova), med izpopolnjevanjem v Cambridgeu pa je obiskal laboratorije British Coal Utilisation Research Association[ix] (kjer je Franklinova pred odhodom v Francijo raziskovala premog, na osnovi česar je tudi doktorirala). Lahko, da gre za naključje, lahko pa je pri organizaciji obiskov pomagala Rosalind Franklin.

Zanimivo je, da je biografinja Rosalind Franklin, Anne Sayre (1923–1998), ob pisanju knjige[16] »Rosalind Franklin and DNA« podatke o Franklinovi iskala pri številnih ljudeh, ki so jo poznali, med drugim tudi pri Dušanu Hadžiju, ki mu je pisala aprila 1970. Vendar pa ji ta kljub prijazni prošnji ni poslal nobenih informacij. V dobro urejenem arhivu A. Sayre[17] je namreč samo avtoričino pismo Hadžiju, njegovega odgovora pa v mapi ni, niti ni v biografiji nobenih vsebin, ki bi kazale na to, da je avtorici posredoval kakšne podatke.

5. Rosalind Franklin in Katarina Kranjc

Bistveno več podatkov o Rosalind Franklin je Sayreova dobila od hrvaške fizičarke Katarine Kranjc (1915-1989), ki je pri raziskavah trdne snovi pogosto uporabljala rentgensko difrakcijo[18, 19]. Katarina Kranjc je bila prva ženska, ki je v Jugoslaviji doktorirala iz fizike (leta 1954 na zagrebški univerzi)[18]. V svojem pismu je navedla, da sta se z Rosalind Franklin prvič srečali leta 1952, ko je z vlakom prispela iz Ljubljane v Zagreb, kjer je predavala o strukturi premoga. Kranjčeva se spominja, da je bila Rosalind Franklin v Ljubljani nekaj dalj časa kot v Zagrebu (kjer je bila verjetno tri dni[x]) in da je šla na izlet v gore (ni pa prepričana, če ni to bilo morda naslednje leto[xi]). Postali sta prijateljici in avgusta leta 1955[xii] je Rosalind Franklin približno dva tedna preživela s Katarino Kranjc, njeno mamo, bratom in njegovo ženo v Kotorju v Črni gori, kjer je bil brat zdravnik. Takrat se je med drugim povzpela tudi na Lovčen.

Kranjčeva se v svojem pismu Anne Sayre ni mogla natančno spomniti, ali je Rosalind Franklin leta 1955 iz Zagreba šla v Ljubljano in slovenske hribe ali nekam v Italijo, da zato na morju ni mogla ostati dalj, čeprav so jo poskušali pregovoriti. Pripoved Katarine Kranjc se zdi bistveno bolj verodostojna in pravilno datirana kot navedba[9] Jenifer Glynn, da je bila Franklinova v Kotorju leta 1952. Možno bi torej bilo, da je bila Rosalind Franklin v Sloveniji tudi po dopustu v Kotorju, torej leta 1955.

V eni od kasnejših biografij Rosalind Franklin[13] – napisala jo je leta 2002 Brenda Maddox (1932–2019) – je razpored obiskov v Sloveniji in drugih delih takratne Jugoslavije nekoliko drugačen kot v biografiji Jenifer Glynn[9]. Maja leta 1952 naj bi bila v Zagrebu, Beogradu, v Julijskih Alpah (dva dni hoje, ena nočitev v koči)[xiii] in en teden v Dalmaciji[xiv] (Dubrovnik, Split, Korčula [zapisano napačno: *Kricula*]), nato pa se je preko Benetk in Pariza vrnila v London[xv]. V Ljubljano je torej prišla le nekaj dni

ix BCURA je obiskal 4. junija 1951 in ves dan porabil za pogovore s tamkajšnjimi raziskovalci. V dnevniku navaja, da je bil obisk zelo prijeten in koristen.

x Rosalind Franklin je v pismu, napisanem 2. junija 1952, zapisala, da je bila v Zagrebu dva dni (prim. opombi (m) in (o)).

xi Za leto 1953 drugi viri omenjajo samo kratek postanek Rosalind Franklin v Ljubljani in nobenih pohodov v gore, tako da je zelo verjetno gorski izlet, ki ga je spomnila Katarina Kranjc, bil leta 1952.

xii Katarina Kranjc bi se težko zmotila v letnici, saj je bila julija 1954 na kongresu v Parizu, kjer se je ponovno srečala s Franklinovo, dopust v Kotorju pa je datirala v leto 1955. Če bi bilo istega leta kot pariški kongres, bi se gotovo morala spomniti. Poleg tega je o obisku v Jugoslaviji leta 1955 Rosalind Franklin na kratko pisala Anne in Davidu Sayre 8. maja 1956:

Prejšnje poletje sem imela lep dopust v Jugoslaviji, z jugoslovanskimi prijatelji, in še posebej mi je bilo všeč, da sem obiskala nekaj malega Črne Gore.

xiii Anne Sayre v biografiji[16] »Rosalind Franklin and DNA« v opombah navaja (na str. 209), da ji je Rosalind Franklin pisala z ladje med Splitom in Reko dne 2. junija 1952 (gl. tudi opombo (o)). Takrat je bila v Jugoslaviji en mesec (str. 141). Iz kopije pisma, ki sem ga pridobil, je razvidno, da je bila »v Ljubljani« en teden in da je bila od tega dva dni v gorah, peljali pa so jo tudi v Postojnsko jamo. Potem je bila dva dni v Zagrebu in pet dni v Beogradu. Glede na to, da omenja dva dni v gorah, to ni mogel biti vzpon na Triglav, ki je omenjen v biografiji njene sestre Jenifer Glynn in naj bi trajal tri dni in pol.

xiv Niti Drago Grdinić niti Katarina Kranjc nista omenila nadaljevanja potovanja Rosalind Franklin v Split in Dubrovnik. To je nekoliko nenavadno, saj bi pričakovali, da so ga organizirali Hrvati. Vendar ni izključeno, da je pri organizaciji sodeloval Jovan Hadži, ki se je v zgodnjih letih precej ukvarjal z morsko biologijo in je sodeloval tudi pri nastajanju biološko-oceanografskega inštituta v Splitu (http://www.sazu.si/clani/jovan-hadzi), ki ga je Franklinova obiskala.

xv Rosalind Franklin je v pismu Anne Sayre z dne 2. junija 1952 dokaj natančno opisala svoje potovanje in vtise. V nasprotju z zapisom v biografiji avtorice Brende Maddox je iz pisma razvidno, da Franklinovi Zagreb sploh ni bil všeč. Iz Beograda se je preko Sarajeva z vlakom odpeljala v Dub-

po tem, ko sta z doktorandom Raymondom Goslingom (1926-2015) posnela znamenito »fotografijo 51« (kar je bilo v prvih dneh[xvi] maja 1952). V biografiji piše, da ji Beograd ji ni bil všeč (»nobene stalnice ni, nihče ne ve, ali sodi na vzhod ali na zahod«), Zagreb pa (»po dveh dneh v Zagrebu lahko do konca življenja na eno miljo prepoznam Hrvata«) (prim. opombo (o)). Predvsem jo je na poti po takratni Jugoslaviji navdušila visoka raven raziskovalnega dela, prijazni ljudje in enkratna pokrajina, včasih pa jo je motilo politično spreobračanje, kot navaja Maddoxova.

6. Na Triglavu leta 1952, 1954 ali 1955?

V isti biografiji je omenjen tudi kratek obisk Ljubljane leta 1953 ter pohod na Triglav leta 1954[xvii]. Vendar pa je podatek o letnici vzpona na Triglav dobila avtorica od Dušana Hadžija, kot je razvidno iz opomb na koncu knjige. Žal je v biografiji napaka, saj je predavanje v Zagrebu omenjeno tako maja leta 1952 kot maja 1954, obakrat z enakim naslovom (Nekateri vidiki ultrastrukture premogov in koksov). V svojem pismu biografinji Anne Sayre 11. maja 1970 je Drago Grdenić (1919–2018), soustanovitelj zagrebške šole strukturne kemije, sicer pa tudi član Slovenske akademije znanosti in umetnosti[21,22], omenil samo eno predavanje s tem naslovom, in sicer tisto 20. maja 1952[xviii], ki se ga je spomnila tudi Katarina Kranjc. Organizirala sta ga Hrvaško kemijsko društvo in Hrvaško fizikalno društvo. Bilo je dobro obiskano in v času, ko so bili tuji predavatelji redki, zelo lepo sprejeto. Predavanje z enakim naslovom je imela 22. maja tudi v Beogradu pod okriljem Srbskega kemijskega društva, objavljeno pa je bilo v srbskem prevodu in angleškem izvirniku leto kasneje v Glasniku hemiskog društva[23].

Če primerjamo podatek Katarine Kranjc, da je bila s Franklinovo leta 1955 na Jadranu 10-14 dni, pred tem pa sta bili na poti iz Zagreba še en dan na Plitvicah, in poda-

rovnik (tam je bila 29.5., kot je razvidno iz datuma pisma Adrienne Weil, v katerem najavlja svoj prihod v Pariz). Od tam je šla za en dan na Korčulo in bila potem dva dni v Splitu, naredila pa je tudi izlet v Trogir. Z Reke se je vračala tako, da je bila še eno noč v Ljubljani, potem pa je šla preko Benetk (1 noč) v Pariz (2 dni, prihod 6. junija, povratek v London 8. junija), tako da naj bi potovanje v celoti trajalo malo več kot en mesec – kar pomeni, da se je odpravila na pot že okrog 5. maja, a ni jasno, kaj je počela prvih približno pet dni potovanja. Glede na to, da je bila v hribih samo dva dni in to okrog 10. maja, je praktično nemogoče, da bi takrat opazila toliko cvetja v dolini triglavskih jezer, kot jih omenja v biografiji Jenifer Glynn.

V pismu navaja med drugim naslednje:

Ljubljana je čudovito mesto. Dokaj spominja na Grenoble, samo da je manjše in lepše. So očarljivi in omikani ljudje, polni svežega, mladega entuziazma. In njihovi znanstveni dosežki so res impresivni – veliki inštituti rastejo skoraj kot v Stockholmu in v njih dela nekaj res dobrih ljudi. Izredno si želijo vsakršnih možnosti za stike z zahodom.

Sledila sta dva dneva v Zagrebu, ki mi je bil precej manj všeč. Zagreb, namesto da bi si zadal, da doseže nekaj novega, se ponaša samo s tradicijo, ki gre kakšnih 70 let nazaj. Zdel se mi je kot kakšen tretjerazreden zaostal Pariz. In ljudje so prav strašljivo pusti – po dveh dneh v Zagrebu mislim, da bom do konca življenja na eno miljo razdalje prepoznala nekoga, ki je Hrvat.

Potem 5 dni v Beogradu. Pomilovanja vreden kraj, kjer ni nič stalnega in nihče ne ve, ali pripada vzhodu ali zahodu. Srbi nimajo tiste kulture kot Slovenci, vendar sem pri njih opazila več svežine Ljubljane kot zadušljivosti Zagreba. Povsod so me sprejeli z izjemno prijaznostjo in ljudje so si zelo želeli pogovarjati se o vsem mogočem.

Večino časa ni bilo sonca, tako da sem se odločila to nadoknaditi z enotedenskim dopustom na obali. Tako sem šla z vlakom skozi Sarajevo v Dubrovnik. V Sarajevu sem se ustavila samo za dve uri, ker je bilo vreme še slabo, a je bilo dovolj, da sem naredila krog po mestu, ki me je razočaralo. Dubrovnik je bil seveda krasen. Imela sem priporočilno pismo za direktorja zgodovinskega inštituta, ki si je vzel ves dan, da mi je razkazal mesto.

xvi Glede datuma posnetka je v virih več različnih podatkov, največkrat omenjajo 1. maj. Glede na to, da je zajem slike trajal več kot 90 ur, kot se spominja Gosling[20], je možno, da se je snemanje začelo še pred 1. majem. Kot piše v sicer dokaj podrobni biografiji Brende Maddox[13], je bila Rosalind Franklin med snemanjem uklonske slike, 1. maja, na konferenci o strukturi proteinov, ki jo je organizirala Royal Society.

xvii Teoretično bi bilo možno, da je bila Rosalind Franklin res v Julijcih leta 1954, in to pred obiskom ZDA (na pot je odšla točno 20. avgusta). Glede na omembo gorske flore v Dolini sedmerih jezer (v sestrini biografiji) bi bil najprimernejši čas sicer sredi julija. Za to poletje je iz korespondence razvidno, da je bila v pisarni 2. junija (pismo L.I. Rebhunu), 3.6. (pismi P. Emmettu in J.W. Gartlandu), 4.6. (pismo T. Eddinger), 9.6. (pismo L. Meyxerju), 11.6. (pismo W.G. Parksu), 14.6. (pismo B.E. Warrenu), 23.6. (pismi P. Emmettu in B. Lewisu), 30.6. (pismi L. Paulingu in J.W. Gartlandu), 5.7. (glede na odgovor G.W. Brindleya od 19.7.), 6.7. (pismo W.M. Stanleyu), 12.7. (pismo P. Kaesbergu), 19.7. (pismi W.M. Stanleyu in F.H. Winslowu), 9.8. (pisma P. Kaesbergu, F.H. Winslowu, A. Wood, g. Madanu, J.W. Gartlandu), 13.8. (pismo prof. Chargaffu). Glede na korespondenco je torej en teden (za manj bi bilo nesmiselno oditi na pot, glede na to, da je vožnja z vlakom v eno smer trajala nekaj več kot en dan) bilo samo med 14. in 23.6. (8 dni) ali pa po kristalografskem kongresu v Parizu (21.-28.7.), kjer je predavala o strukturi virusa mozaika tobaka. To bi pomenilo, da je bila leta 1954 na dopustu okvirno od 29.7. do 8.8., na vsak način pa pred odhodom v ZDA.

xviii V svojih spominih[27] na znanstveno in strokovno delo je leta 2000 Drago Grženić obisk Rosalind Franklin sicer datiral v leto 1953, enako v intervjuju[28], ki ga je dal za časopis Jutarnji list leta 2016. Vendar je v prvem članku ob omembi Rosalind Franklin tudi napaka, saj navaja, da je doktorirala na Sorboni. V resnici je doktorirala na univerzi v Cambridgeu in je v Pariz (a ne na Sorbono) odšla šele dve leti po doktoratu. Podatek iz pisma, trideset let pred objavo članka, se zdi bistveno bolj verodostojen.

tek iz biografije Brende Maddox, da si je Rosalind Franklin poleti 1955 privoščila en mesec dopusta v Jugoslaviji (potem pa je odšla še na kolesarski izlet v Normandijo), bi bilo mogoče, da se je tega leta spet oglasila tudi v Ljubljani oz. v slovenskih gorah, kar je kot možnost nakazala Kranjčeva.

Tako torej ostaja nekaj dvoma, ali je bila Franklinova na Triglavu res leta 1954 (kot je trdil Dušan Hadži), ali morda leto kasneje, zelo verjetno pa je, da je bila na Vršiču leta 1952[xix]. Leta 1954 je bila Rosalind Franklin od 20. avgusta dalje na turneji po ZDA, kjer je predavala o strukturi premoga, pa tudi o novejših raziskavah zgradbe virusa mozaika tobaka. Vrnila se je šele 20. oktobra, Dušan Hadži pa je omenil[6], da sta šla na Triglav *po vrnitvi* Rosalind Franklin iz ZDA, *poleti* 1954. Če bi šla v gore šele oktobra, gotovo ne bi videla toliko alpskega cvetja, kot ga je omenila v pismu domačim.

V citatu, navedenem v biografiji Jenifer Glynn, je podatek, da je bila Franklinova, ko je šla na Triglav, v gorah »prvič po petih letih«. Kot je razvidno iz drugih biografij, je bila Rosalind Franklin v Savojskih Alpah poleti 1947, v italijanskih Alpah nad Aosto leta 1949, znana pa je njena fotografija iz zavetišča Cabane des Evettes[xx], ki jo je posnel njen prijatelj Vittorio Luzatti (1923-2016) avgusta[xxi] leta 1950 (https://www.npg.org.uk/collections/search/portrait/ mw56561/Rosalind-Franklin). Tako bi torej 5 let od zadnjega hribolazenja lahko bilo leta 1955, zagotovo pa ne leta 1952.

Bolj negotovo je, kdaj je bila Rosalind Franklin na Bledu. Glede na to, da je v biografiji Jenifer Glynn (za leto 1952) navedeno, da so v počitniški hiši Akademije letovale tri generacije (zelo verjetno Jovan Hadži, sin Dušan in vnuk Aleksander, ki pa se je rodil maja 1953), je mogoče sklepati, da na Bledu ni bila leta 1952, pač kasneje. Dodaten argument, ki kaže, da na Bledu ni bila leta 1952, je, da je SAZU pridobil vilo Epos na Bledu šele 8. maja 1952, po prevzemu pa so jo dalj časa prenavljali iz zasebne vile v počitniški dom[xxii]. Ker je v biografiji bivanje na Bledu združeno z vzponom na Triglav, je torej tudi ta vzpon moral biti leta 1954 ali 1955.

7. Hadžijevo vabilo na dopust v Slovenijo

V arhivih [Correspondence and Working Notes, str. 39] je ohranjeno pismo Dušana Hadžija, ki ga je poslal Rosalind Franklin 10. junija 1954. Najprej se ji zahvaljuje za poslani čaj, potem pa jo prosi za korekture in komentarje na članek[25], ki ga je napisal o kemijski strukturi grafitnega oksida (v soavtorstvu Aleksandra Novaka je bil objavljen 1955 v reviji Transactions of the Faraday Society). Proti koncu pisma ji predlaga dopust v Sloveniji[xxiii], ki bi ga lahko izvedla tako, kot to baje naredijo nekateri nemški biologi: pridejo v Slovenijo, zberejo nekaj vzorcev in jih opišejo, potem pa to objavijo kot članek, za kar dobijo 15 000 dinarjev honorarja za 10 strani. Piše, da bi Rosalind Franklin lahko na podoben način objavila kaj o našem koksu in ob tem imela še dopust. V zaključku Hadži omenja, da gre z družino za dva tedna na Bled, ki mu ni všeč, a mora iti, ker bo dopust koristil sinovemu zdravju.

Leta 1955 je bila Rosalind Franklin 28. julija še v Londonu[xxiv], nato pa se je udeležila 3. kongresa biokemije, ki je potekal v Bruslju med 1. in 6. avgustom. Sledil je enomesečni dopust[xxv], za katerega je vnaprej načrtovala

xix Da je bila fotografija posneta sredi maja, je posredno mogoče sklepati iz krošenj macesnov, ki imajo še kratke iglice. Krošnje postanejo na Vršiču bolj polne konec maja. Čeprav je bila zima 1951/52 znana kot zelo snežena, snega v visokogorju ni bilo nič več kot druga leta, februarskemu sneženju pa je sledilo suho in kasneje tudi dokaj toplo vreme v drugi polovici marca in predvsem v prvi polovici aprila[24]. Zato kljub hudi zimi ozelenitev macesnov najverjetneje ni kasnila.
Glede na to, da je Rosalind Franklin oblečena v srajco s kratkimi rokavi in da je bila fotografija posneta na nadmorski višini približno 1550 m, je bil verjetno dan precej topel. Ob upoštevanju, da je imela predavanje v Zagrebu (kjer je bila 2-3 dni) 20. maja, je bila v Sloveniji (kjer je bila okvirno en teden) najverjetneje med 10. in 18. majem. V tem obdobju je bil v Julijcih najtoplejši dan 11.5., ko je meteorološka postaja v Ratečah zabeležila najvišjo dnevno temperaturo 22,4 °C, vendar so bile ta dan nevihte, kar je nekoliko ohladilo ozračje (12. maja v Ratečah največ 17,9 °C, 13. maja pa je bila najvišja temperatura 16 °C, a je bilo vreme lepše in podobno je ostalo tudi naslednje dni). Vremenski podatki so iz arhiva Agencije Republike Slovenije za okolje. Podatki za Kranjsko Goro so podobni. Na Vršiču bi pričakovali za okrog 4 °C nižjo temperaturo kot v Kranjski Gori, tako da ni mogoče povsem izključiti izleta 11. maja, lahko pa je bil tudi v naslednjih dneh. Glede na novico v Slovenskem poročevalcu od 14.5., da predavanje šele bo, bi lahko sklepali, da je bil izletu namenjen prvi del obiska, predavanje pa bi lahko bilo 15. ali 16.5. (četrtek oz. petek).

xx Tako je zavetišče poimenovano v albumu, a gre verjetno za Refuge des Evettes na nadmorski višini 2594 m. Prvotno kamnito kočo je leta 1940 požgala francoska vojska, po vojni pa so naredili novo, leseno. Zrcalni izsek fotografije Rosalind Franklin iz te koče je na naslovnici biografije, ki jo je napisala Anne Sayre.

xxi V britanski National Portrait Gallery je fotografija z oznako NPG x76912 datirana z »julij 1950«, vendar Brenda Maddox v biografiji navaja vzpone z Vittoriom Luzattijem in njegovo ženo Denise v Visoki Savoji avgusta tega leta.

xxii Informacija g. Zorana Mezgeca, SAZU.

xxiii Glede na to, da je vabilo iz junija 1954, se je Rosalind Franklin bodisi zelo na hitro odločila za obisk v juliju 1954, ali pa je prava letnica, ko je šla na Triglav, 1955. Ni pa nujno, da je bil vzpon na Triglav povezan z vabilom Dušana Hadžija iz leta 1954.

xxiv V arhivih je ohranjeno kratko pismo dr. McDonaglu, poslano 28. julija 1955 iz Londona.

xxv Pismo A. Golda z UC Berkeley glede rastlinskih virusov, ki jih je Franklinova želela preučevati, je v London prispe-

daljši obisk pri svoji zagrebški prijateljici. Glede na to, da je bila na Jadranu dva tedna, je preostala dva tedna očitno izrabila nekje drugje, vprašanje pa je, ali je (enotedenski) kolesarski izlet po Normandiji, ki ga v biografiji omenja Brenda Maddox, bil v okviru enomesečnega dopusta ali nekoliko kasneje – tako bi se zapis namreč dalo razumeti.

Če sledimo navedbi Dušana Hadžija, da sta šla z Rosalind Franklin na Triglav[xxvi] *po njenem obisku* ZDA, je treba omeniti, da je Franklinova obiskala Združene države tudi eno leto kasneje in bi torej teoretično lahko bil vzpon na Triglav leta 1956. V ZDA se je odpravila junija 1956 in ostala dva meseca, do 23. avgusta. Vendar po povratku ni bilo več časa za planinske izlete, saj je zbolela za rakom in bila jeseni 1956 prvič operirana. Zdravljenje se je nadaljevalo še z eno operacijo in s kemoterapijo, ki pa ni bila uspešna. Umrla je 16. aprila 1958.

Ko so Nobelovo nagrado za kemijo leta 1962 dobili James Watson, Francis Crick in Maurice Wilkins, je bila Rosalind Franklin v veliki meri pozabljena. Šele leta 1968, z objavo Watsonove knjige Dvojna vijačnica[26], v kateri je opisal odkrivanje strukture DNA, je postalo jasno, da je bila za določitev strukture v veliki meri pomembna »fotografija 51«. Do slike sta s Francisom Crickom prišla posredno, preko Wilkinsa, brez vednosti Rosalind Franklin, nato pa sta dobila še interno delovno poročilo, v katerem so bili navedeni njeni preliminarni rezultati. Ti utrinki iz obdobja odkrivanja strukture DNA so razkrili, kako težko se je bilo raziskovalki njenega kova uveljaviti v prevladujoče moškem svetu raziskovalcev v petdesetih letih prejšnjega stoletja.

Zahvala

Zahvaljujem se za povratne informacije, ki so mi jih posredovali Miha Pavšič (Univerza v Ljubljani), Tomasz Pospieszny (Univerza v Poznanu) in Zoran Mezgec (Slovenska akademija znanosti in umetnosti), Juretu Zupanu (Kemijski inštitut) pa za nekatere zanimive podatke o Dušanu Hadžiju, ki je bil njegov mentor pri magistrski in doktorski nalogi. Zupanov prispevek v Dogodkih je bil vzpodbuda za pričujoči članek. Hvala tudi Sanu Hadžiju za utrinke iz družinske zgodovine in dostop do osebnega dnevnika Dušana Hadžija. Še posebej se zahvaljujem Jeffu Karru, arhivarju Ameriškega mikrobiološkega društva (American Society for Microbiology), za dostop do biografskih gradiv Anne Sayre. Roku Kočarju se zahvaljujem za dovoljenje za objavo njegove fotografije Ajdovske deklice, ki je sicer prvotno bila objavljena na portalu kam.si.

Viri

1. J. D. Watson, F. H. C. Crick, Molecular structure of nucleic acids; a structure for deoxyribose nucleic acid. *Nature* **1953**, *171*, 737–738. **DOI:**10.1038/171737a0
2. R. E. Franklin, R. G. Gosling, Molecular configuration in sodium thymonucleate. *Nature* **1953**, *171*, 740–741. **DOI:**10.1038/171740a0
3. M. H. F. Wilkins, A. R. Stokes, H. R. Wilson, Molecular structure of deoxypentose nucleic acids. *Nature* **1953**, *171*, 738–740. **DOI:**10.1038/171738a0
4. M. Lawler, Rosalind Franklin still doesn't get the recognition she deserves for her DNA discovery. *The Conversation*, 28. april **2018**. Dostopno na: https://theconversation.com/rosalind-franklin-still-doesnt-get-the-recognition-she-deserves-for-her-dna-discovery-95536 (datum dostopa 5. 2. 2020).
5. P. J. F. Harris, Rosalind Franklin's work on coal, carbon, and graphite. *Interdisciplinary Science Reviews* **2001**, *26*, 204–210. **DOI:**10.1179/030801801679467
6. J. Zupan, Rosalind E. Franklin sta v Slovenijo privabila ljubezen do gora in premog. *Dogodki, interno glasilo Kemijskega inštituta* **2020**, *3*, 5.
7. Milko Kos (ur.), Letopis Slovenske akademije znanosti in umetnosti, peta knjiga, 1952-1953. Ljubljana: SAZU **1954**, str. 190.
8. Obisk angleške znanstvenice. *Slovenski poročevalec* **1952**, *113*, 2.
9. Jenifer Glynn, My sister Rosalind Franklin. Oxford: Oxford University Press, **2012**. **DOI:**10.1016/S0140-6736(12)60452-8
10. J. Glynn, Rosalind Franklin: 50 years on, *Notes and Records of the Royal Society* **2008**, *62*, 253–255. **DOI:**10.1098/rsnr.2007.0052
11. M. Franklin, Rosalind, samozaložba, **1963** (?). Hrani Linda Hall Library, Kansas City, Missouri, ZDA.
12. A. Piper, Light on a dark lady, *Trends in Biochemical Sciences* **1998**, *23*, 151–154. **DOI:**10.1016/S0968-0004(98)01194-3
13. B. Maddox, Rosalind Franklin: The dark lady of DNA. London: Harper Collins, **2002**.
14. N. Sheppard, In honour of professor Dusan Hadzi's 60th birthday. *Croatica Chemica Acta* **1982**, *55*, 1–5.
15. D. Hadži, Poročilo o delu v Franciji in Angliji, v: Milko Kos (ur.), Letopis Slovenske akademije znanosti in umetnosti, četrta knjiga, 1950-1951. Ljubljana: SAZU 1952, str. 231–233.
16. A. Sayre, Rosalind Franklin and DNA. New York: W.W. Norton, **1975**.

lo 9.8., a so ga preusmerili na privatni naslov Katarine Kranjc v Zagrebu, kamor je prišlo 11.8.1955. V arhivih je shranjeno pismo Rosalind Franklin dr. A. Sieglu z UC Los Angeles z dne 6. septembra 1955. V njem se zahvaljuje za novo pošiljko virusnega izolata in sporoča, da se je ravnokar vrnila z dopusta in da z novim materialom ni izvedla še nobenega poskusa. V dopisu L.D. Butlerju z Bakteriološkega oddelka Medicinske fakultete Sv. Jurija v Londonu je v odgovoru na pismo, poslano 2. septembra, 4. oktobra zapisala, da je njegovo pismo prispelo, ko je bila na dopustu. Torej je bila Franklinova na dopustu od konca kongresa 6. avgusta do največ 5. septembra.

xxvi Žal vpisne knjige z vrha Triglava za obdobje 1952-1955 niso ohranjene, prav tako ne vpisne knjige planinskih koč v Triglavskem pogorju.

17. Anne Sayre Collection of Rosalind Franklin Materials: https://lib.guides.umbc.edu/c.php?g=836720&p=6572944 (Box 4)
18. M. M. Julian, Women in crystallography, v: G. Kass-Simon, P. Farnes (ured.), Women of science: Righting the record. Bloomington: Indiana University Press, **1990**, 335–383.
19. R. Krog, Kranjc, Katarina. Hrvatski biografski leksikon, **2013**. Zagreb: Leksikografski zavod Miroslav Krleža. Dostopno na: http://hbl.lzmk.hr/clanak.aspx?id=10852 (datum ogleda 11. 2. 2020)
20. N. Attar, Raymond Gosling: the man who crystallized genes, *Genome Biology* **2013**, *14*, 402. **DOI:**10.1186/gb-2013-14-4-402
21. Drago Grdenić, http://www.sazu.si/clani/drago-grdenic, april 2013 (datum ogleda 10. 2. 2020)
22. B. Kaitner, U uspomen: Professor emeritus Drago Grdenić, *Kemija u industriji: Časopis kemičara i kemijskih inženjera Hrvatske* **2018**, *67*, 454–455.
23. R. Franklin, Neki pogledi na ultrafinu strukturu uglja i koksa / Some aspects of the ultra-fine structure of coals and cokes, *Glasnik Hemiskog društva Beograd = Bulletin de la Société chimique Belgrade* **1953**, *18*, 203–212.
24. I. Gams, Snežni plazovi v Sloveniji v zimah 1950-1954, *Geografski zbornik* **1955**, *3,* 115–214, str. 175.
25. D. Hadži, A. Novak, Infra-red spectra of graphitic oxide, *Transactions of the Faraday Society* **1955**, *51*, 1614–1620. **DOI:**10.1039/TF9555101614
26. J. D. Watson, The double helix. New York: Atheneum, **1968**.
27. D. Grženić, Mojih pedeset godina kemije. Kemija u industriji **2000**, 49, 317-337, str. 326.
28. T. Rudež, Drago Grdenič, najstariji hrvatski akademik - Nevjerojatna životna priča posljednjeg živućeg osnivača Instituta Ruđer Bošković: »Ja mislim da više nema nijednog živog moga vršnjaka‘. Jutarnji list, 14. februar **2016**. Dostopno na https://www.jutarnji.hr/vijesti/najstariji-hrvatski-akademik-nevjerojatna-zivotna-prica-posljednjeg-zivuceg-osnivaca-instituta-ruder-boskovic-ja-mislim-da-vise-nema-nijednog-zivog-moga-vrsnjaka-99313 (datum dostopa 22. 6. 2020).

Abstract

The world-renowned structural chemist and biochemist Rosalind Franklin (1920-1958) maintained contacts with Slovenian and Croatian chemists and visited both countries on several occasions. On the basis of biographies and archived correspondence, this article summarises her visits to Slovenia and other parts of the former Yugoslavia. Interestingly, I discovered that the most famous mountaineering photograph of Rosalind Franklin was not taken on her family vacation in Norway in the late 1930s as generally believed, but on the Vršič Pass in Julian Alps, as the vegetation and rock structure, especially the so-called Heathen Maiden in the northwest face of Mount Prisojnik, show. It is likely that the photo was taken by her Slovenian colleague Dušan Hadži, probably in May 1952, so the photo was obviously wrongly labelled in the Franklin family archives. In addition, her mountaineering trip to Mt. Triglav and her stay at Lake Bled could not have happened in 1952 as mentioned in her biography, but rather in 1954 or 1955.

Keywords: Rosalind Franklin, Dušan Hadži, mountaineering, Slovenia, Julian Alps

KOLEDAR VAŽNEJŠIH ZNANSTVENIH SREČANJ S PODROČJA KEMIJE IN KEMIJSKE TEHNOLOGIJE

SCIENTIFIC MEETINGS – CHEMISTRY AND CHEMICAL ENGINEERING

2021

February 2021

15 – 17	1ST GREENERING INTERNATIONAL CONFERENCE Lisbon, Portugal
Information:	https://greenering.eu/general-information.html

March 2021

15 – 18	CHISA 2021 VIRTUALLY – 24TH INTERNATIONAL CONGRESS OF CHEMICAL AND PROCESS ENGINEERING Online
Information:	https://virtually.chisa.cz/
17 – 19	7TH INTERNATIONAL CONGRESS ENGINEERING, ENVIRONMENT AND MATERIALS IN PROCESSING INDUSTRY Sarajevo, Bosnia and Herzegovina
Information:	https://eem.tfzv.ues.rs.ba/

May 2021

16 – 19	POLYMERS 2021: NEW TRENDS IN POLYMER SCIENCE: HEALTH OF THE PLANET, HEALTH OF THE PEOPLE Turin, Italy
Information:	http://polymers2021.sciforum.net
16 – 20	48TH WORLD POLYMER CONGRESS – MACRO2020+ Jeju Island, Korea, Republic Of
Information:	http://www.macro2020.org

June 2021

6 – 9	31ST EUROPEAN SYMPOSIUM ON COMPUTER AIDED PROCESS ENGINEERING Istanbul, Turkey
Information:	https://www.escape31.org/
7 – 9	EUROPEAN FOOD CHEMISTRY CONGRESS XXI – EUROFOODCHEM XXI Belgrade, Serbia
Information:	http://horizon2020foodentwin.rs/sr/eurofoodchemxxi/
9 – 11	5TH INTERNATIONAL CONFERENCE ON CONTAMINATED LAND, ECOLOGICAL ASSESSMENT AND REMEDIATION – CLEAR London, United Kingdom
Information:	http://clear2020.mdx.ac.uk/

9 – 11	ENERSTOCK 2021 Ljubljana, Slovenia
Information:	https://enerstock2021.org/
13 – 17	12TH EUROPEAN SYMPOSIUM ON ELECTROCHEMICAL ENGINEEING Leeuwarden, The Netherlands
Information:	http://www.electrochemical-engineering.eu/2021/
27 – 30	17TH EUROPEAN CONFERENCE ON MIXING Porto, Portugal
Information:	http://mixing17.eu/
27 – Jul. 2	44TH INTERNATIONAL CONFERENCE ON COORDINATION CHEMISTRY Rimini, Italy
Information:	https://www.iccc2021.com
29 – Jul. 2	26TH INTERNATIONAL SYMPOSIUM ON SEPARATION SCIENCES - ISSS 2021 Ljubljana, Slovenia
Information:	https://isss2020.si/

July 2021

3 – 8	2021 FEBS CONGRESS Ljubljana, Slovenia
Information:	https://2021.febscongress.org/
7 – 9	9TH EUROPEAN VARIETY IN UNIVERSITY CHEMISTRY EDUCATION – EUROVARIETY 2021 Ljubljana, Slovenia
Information:	http://www.eurovariety2021.si/
18 – 22	84TH PRAGUE MEETING ON MACROMOLECULES – FRONTIERS OF POLYMER COLLOIDS Prague, Czech Republic
Information:	https://www.imc.cas.cz/sympo/84pmm
19 – 23	SECOND INTERNATIONAL CONFERENCE ON NONCOVALENT INTERACTIONS 2021 – ICNI2021 Strasbourg, France
Information:	http://icni2021.unistra.fr/
25 – 30	12TH TRIENNIAL CONGRESS OF THE WORLD ASSOCIATION OF THEORETICAL AND COMPUTATIONAL CHEMISTS Vancouver, Canada
Information:	https://watoc2020.ca/

August 2021

13 – 20	IUPAC WORLD CHEMISTRY CONGRESS 2021 Montréal, Québec Canada
Information:	http://iupac2021.org
15 – 18	18TH EUROPEAN CONFERENCE ON SOLID STATE CHEMISTRY – ECSSC2021 Dejvice, Prague
Information:	http://www.ecssc18.com/
29 – Sept. 1	GDCH SCIENCE FORUM CHEMISTRY 2021 – WIFO 2021 München, Germany
Information:	https://en.wifo2021.de/
29 – Sept. 2	XXIV EUROPEAN CONFERENCE ON ORGANOMETALLIC CHEMISTRY – EUCOMC XXIV Madrid, Spain
Information:	https://congresosalcala.fgua.es/eucomc2021

29 – Sept. 3	15TH EUROPEAN CONGRESS ON CATALYSIS Prague, Czech Republic
Information:	https://www.europacat2021.cz/
30 – Sept. 2	21ST INTERNATIONAL SYMPOSIUM ON INDUSTRIAL CRYSTALLIZATION Potsdam, Germany
Information:	https://dechema.de/ISIC_21.html

September 2021

22 – 24	ANNUAL MEETING OF THE SLOVENIAN CHEMICAL SOCIETY 2021 Portorož-Portorose, Slovenia
Information:	https://skd2020.chem-soc.si/
26 – 29	5TH EUCHEMS CONFERENCE ON GREEN AND SUSTAINABLE CHEMISTRY – EUGSC-5 Thessaloniki, Greece
Information:	https://www.euchems.eu/events/5th-euchems-conference-on-green-and-sustainable-chemistry-eugsc-5/

Oktober 2021

21 – 22	2021 EUCHEMS GENERAL ASSEMBLY (GA) Larnaca, Cyprus
Information:	https://www.euchems.eu/events/2021-euchems-general-assembly-ga/
22 – 23	2021 EUCHEMS PROFESSIONAL NETWORKS (PNS) ANNUAL MEETING Larnaca, Cyprus
Information:	https://www.euchems.eu/events/2021-euchems-professional-networks-pns-annual-meeting/

November 2021

6 – 9	2ND CARBON DIOXIDE CONVERSION CATALYSIS CONFERENCE – CDCC-2 Lisbon, Portugal
Information:	https://www.fusion-conferences.com/conference/104#
7 – 11	31TH INTERNATIONAL SYMPOSIUM ON THE CHEMISTRY OF NATURAL PRODUCTS AND 11TH INTERNATIONAL CONGRESS ON BIODIVERSITY (ISCNP31 & ICOB11) Naples, Italy
Information:	https://www.iscnp31-icob11.org/index.php

Acta Chimica Slovenica

Author Guidelines

Submissions

Submission to ACSi is made with the implicit understanding that neither the manuscript nor the essence of its content has been published in whole or in part and that it is not being considered for publication elsewhere. All the listed authors should have agreed on the content and the corresponding (submitting) author is responsible for having ensured that this agreement has been reached. The acceptance of an article is based entirely on its scientific merit, as judged by peer review. There are no page charges for publishing articles in ACSi. The authors are asked to read the Author Guidelines carefully to gain an overview and assess if their manuscript is suitable for ACSi.

Additional information

- Citing spectral and analytical data
- Depositing X-ray data

Submission material

Typical submission consists of:

- full manuscript (PDF file, with title, authors, abstract, keywords, figures and tables embedded, and references)
- supplementary files
  - ***Full manuscript*** (original Word file)
  - ***Statement of novelty*** (Word file)
  - ***List of suggested reviewers*** (Word file)
  - ***ZIP file containing graphics*** (figures, illustrations, images, photographs)
  - ***Graphical abstract*** (single graphics file)
  - ***Proposed cover picture*** (optional, single graphics file)
  - ***Appendices*** (optional, Word files, graphics files)

Incomplete or not properly prepared submissions will be rejected.

Submission process

Before submission, authors should go through the checklist at the bottom of the page and prepare for submission.

Submission process consists of 5 steps.

Step 1: Starting the submission

- Choose one of the journal sections.
- Confirm all the requirements of the ***checklist.***
- Additional plain text comments for the editor can be provided in the relevant text field.

Step 2: Upload submission

- Upload full manuscript in the form of a Word file (with title, authors, abstract, keywords, figures and tables embedded, and references).

Step 3: Enter metadata

- First name, last name, contact email and affiliation for all authors, in relevant order, must be provided. Corresponding author has to be selected. Full postal address and phone number of the corresponding author has to be provided.
- ***Title and abstract*** must be provided in plain text.
- Keywords must be provided (max. 6, separated by semicolons).
- Data about contributors and supporting agencies may be entered.
- ***References*** in plain text must be provided in the relevant text filed.

Step 4: Upload supplementary files

- Original Word file (original of the PDF uploaded in the step 2)
- ***Statement of novelty*** in a Word file must be uploaded
- All ***graphics*** have to be uploaded in a single ZIP file. Graphics should be named Figure 1.jpg, Figure 2.eps, etc.
- ***Graphical abstract image*** must be uploaded separately
- ***Proposed cover picture*** (optional) should be uploaded separately.
- Any additional ***appendices*** (optional) to the paper may be uploaded. Appendices may be published as a supplementary material to the paper, if accepted.
- For each uploaded file the author is asked for additional metadata which may be provided. Depending of the type of the file please provide the relevant title (Statement of novelty, List of suggested reviewers, Figures, Graphical abstract, Proposed cover picture, Appendix).

Step 5: Confirmation

- Final confirmation is required.

Article Types

Feature Articles are contributions that are written on editor's invitation. They should be clear and concise summaries of the most recent activity of the author and his/her research group written with the broad scope of ACSi in mind. They are intended to be general overviews of the authors' subfield of research but should be written in a way that engages and informs scientists in other areas. They should contain the following (see also general directions for article structure in ACSi below): (1) an introduction that acquaints readers with the authors' research field and outlines the important questions to which answers are being sought; (2) interesting, new, and recent contributions of the author(s) to the field; and (3) a summary that presents possible future directions. Manuscripts normally should not exceed 40 pages of one column format (letter size 12, 33 lines per page). Generally, experts in a field who have made important contribution to a specific topic in recent years will be invited by an editor to contribute such an **Invited Feature Article**. Individuals may, however, send a proposal (one-page maximum) for an Invited Feature Article to the Editor-in-Chief for consideration.

Scientific articles should report significant and innovative achievements in chemistry and related sciences and should exhibit a high level of originality. They

should have the following structure:

1. Title (max. 150 characters),
2. Authors and affiliations,
3. Abstract (max. 1000 characters),
4. Keywords (max. 6),
5. Introduction,
6. Experimental,
7. Results and Discussion,
8. Conclusions,
9. Acknowledgements,
10. References.

The sections should be arranged in the sequence generally accepted for publications in the respective fields and should be successively numbered.

Short communications generally follow the same order of sections as Scientific articles, but should be short (max. 2500 words) and report a significant aspect of research work meriting separate publication. Editors may decide that a Scientific paper is categorized as a Short Communication if its length is short.

Technical articles report applications of an already described innovation. Typically, technical articles are not based on new experiments.

Preparation of Submissions

Text of the submitted articles must be prepared with Microsoft Word. Normal style set to single column, 1.5 line spacing, and 12 pt Times New Roman font is recommended. Line numbering (continuous, for the whole document) must be enabled to simplify the reviewing process. For any other format, please consult the editor. Articles should be written in English. Correct spelling and grammar are the sole responsibility of the author(s). Papers should be written in a concise and succinct manner. The authors shall respect the ISO 80000 standard [1], and IUPAC Green Book [2] rules on the names and symbols of quantities and units. The Système International d'Unités (SI) must be used for all dimensional quantities.

Graphics (figures, graphs, illustrations, digital images, photographs) should be inserted in the text where appropriate. The captions should be self-explanatory. Lettering should be readable (suggested 8 point Arial font) with equal size in all figures. Use common programs such as MS Excel or similar to prepare figures (graphs) and ChemDraw to prepare structures in their final size. Width of graphs in the manuscript should be 8 cm. Only in special cases (in case of numerous data, visibility issues) graphs can be 17 cm wide. All graphs in the manuscript should be inserted in relevant places and **aligned left**. The same graphs should be provided separately as images of appropriate resolution (see below) and submitted together in a ZIP file (Graphics ZIP). Please do not submit figures as a Word file. In **graphs**, only the graph area determined by both axes should be in the frame, while a frame around the whole graph should be omitted. The graph area should be white. The legend should be inside the graph area. The style of all graphs should be the same. **Figures and illustrations** should be of sufficient quality for the printed version, i.e. 300 dpi minimum. **Digital images and photographs** should be of high quality (minimum 250 dpi resolution). On submission, figures should be of good enough resolution to be assessed by the referees, ideally as JPEGs. High-resolution figures (in JPEG, TIFF, or EPS format) might be required if the paper is accepted for publication.

Tables should be prepared in the Word file of the paper as usual Word tables. The captions should appear above the table and should be self-explanatory.

References should be numbered and ordered sequentially as they appear in the text, likewise methods, tables, figure captions. When cited in the text, reference numbers should be superscripted, following punctuation marks. It is the sole responsibility of authors to cite articles that have been submitted to a journal or were in print at the time of submission to ACSi. Formatting of references to published work should follow the journal style; please also consult a recent issue:

1. J. W. Smith, A. G. White, *Acta Chim. Slov.* **2008**, *55*, 1055–1059.
2. M. F. Kemmere, T. F. Keurentjes, in: S. P. Nunes, K. V. Peinemann (Ed.): Membrane Technology in the Chemical Industry, Wiley-VCH, Weinheim, Germany, **2008**, pp. 229–255.
3. J. Levec, Arrangement and process for oxidizing an aqueous medium, US Patent Number 5,928,521, date of patent July 27, **1999**.
4. L. A. Bursill, J. M. Thomas, in: R. Sersale, C. Collela, R. Aiello (Eds.), Recent Progress Report and Discussions: 5th International Zeolite Conference, Naples, Italy, 1980, Gianini, Naples, **1981**, pp. 25–30.
5. J. Szegezdi, F. Csizmadia, Prediction of dissociation constant using microconstants, http://www. chemaxon.com/conf/Prediction_of_dissociation _constant_using_microco nstants.pdf, (assessed: March 31, 2008)

Titles of journals should be abbreviated according to Chemical Abstracts Service Source Index (CASSI).

Special Notes

- Complete characterization, **including crystal structure**, should be given when the synthesis of new compounds in crystal form is reported.
- Numerical **data should be reported with the number of significant digits corresponding to the magnitude** of experimental uncertainty.
- **The SI system of units and IUPAC recommendations** for nomenclature, symbols and abbreviations should be followed closely. Additionally, the authors should follow the general guidelines when citing spectral and analytical data, and depositing crystallographic data.
- **Characters** should be correctly represented throughout the manuscript: for example, 1 (one) and l (ell), 0 (zero) and O (oh), x (ex), D7 (times sign), B0 (degree sign). Use Symbol font for all Greek letters and mathematical symbols.
- The rules and recommendations of the **IUBMB** and the **International Union of Pure and Applied Chemistry (IUPAC)** should be used for abbreviation of chemical names, nomenclature of chemical compounds, enzyme nomenclature, isotopic compounds, optically active isomers, and spectroscopic data.
- **A conflict of interest** occurs when an individual (author, reviewer, editor) or its organization is involved in multiple interests, one of which could possibly corrupt the motivation for an act in the

other. Financial relationships are the most easily identifiable conflicts of interest, while conflicts can occur also as personal relationships, academic competition, etc. **The Editors** will make effort to ensure that conflicts of interest will not compromise the evaluation process; potential editors and reviewers will be asked to exempt themselves from review process when such conflict of interest exists. When the manuscript is submitted for publication, **the authors** are expected to disclose any relationships that might pose potential conflict of interest with respect to results reported in that manuscript. In the Acknowledgement section the source of funding support should be mentioned. The statement of disclosure must be provided as Comments to Editor during the submission process.

- **Published statement of Informed Consent.** Research described in papers submitted to ACSi must adhere to the principles of the Declaration of Helsinki (***http://www.wma.net/e/policy/b3.htm***). These studies must be approved by an appropriate institutional review board or committee, and informed consent must be obtained from subjects. The Methods section of the paper must include: 1) a statement of protocol approval from an institutional review board or committee and 2), a statement that informed consent was obtained from the human subjects or their representatives.
- **Published Statement of Human and Animal Rights.**When reporting experiments on human subjects, authors should indicate whether the procedures followed were in accordance with the ethical standards of the responsible committee on human experimentation (institutional and national) and with the Helsinki Declaration of 1975, as revised in 2008. If doubt exists whether the research was conducted in accordance with the Helsinki Declaration, the authors must explain the rationale for their approach and demonstrate that the institutional review body explicitly approved the doubtful aspects of the study. When reporting experiments on animals, authors should indicate whether the institutional and national guide for the care and use of laboratory animals was followed.
- To avoid conflict of interest between authors and referees we expect that not more than one referee is from the same country as the corresponding author(s), however, not from the same institution.
- Contributions authored by **Slovenian scientists** are evaluated by non-Slovenian referees.
- Papers describing **microwave-assisted reactions** performed in domestic microwave ovens are not considered for publication in *Acta Chimica Slovenica.*
- *Manuscripts that are **not prepared and submitted** in accord with the instructions for authors are not considered for publication.*

Appendices

Authors are encouraged to make use of supporting information for publication, which is supplementary material (appendices) that is submitted at the same time as the manuscript. It is made available on the Journal's web site and is linked to the article in the Journal's Web edition. The use of supporting information is particularly appropriate for presenting additional graphs, spectra, tables and discussion and is more likely to be of interest to specialists than to general readers. When preparing supporting information, authors should keep in mind that the supporting information files will not be edited by the editorial staff. In addition, the files should be not too large (upper limit 10 MB) and should be provided in common widely known file formats to be accessible to readers without difficulty. All files of supplementary materials are loaded separately during the submission process as supplementary files.

Proposed Cover Picture and Graphical Abstract Image

Graphical content: an ideally full-colour illustration of resolution 300 dpi from the manuscript must be proposed with the submission. Graphical abstract pictures are printed in size 6.5 x 4 cm (hence minimal resolution of 770 x 470 pixels). Cover picture is printed in size 11 x 9.5 cm (hence minimal resolution of 1300 x 1130 pixels)

Authors are encouraged to submit illustrations as candidates for the journal Cover Picture*. The illustration must be related to the subject matter of the paper. Usually both proposed cover picture and graphical abstract are the same, but authors may provide different pictures as well.

* The authors will be asked to contribute to the costs of the cover picture production.

Statement of novelty

Statement of novelty is provided in a Word file and submitted as a supplementary file in step 4 of submission process. Authors should in no more than 100 words emphasize the scientific novelty of the presented research. Do not repeat for this purpose the content of your abstract.

List of suggested reviewers

List of suggested reviewers is a Word file submitted as a supplementary file in step 4 of submission process. Authors should propose the names, full affiliation (department, institution, city and country) and e-mail addresses of three potential referees. Field of expertise and at least two references relevant to the scientific field of the submitted manuscript must be provided for each of the suggested reviewers. The referees should be knowledgeable about the subject but have no close connection with any of the authors. In addition, referees should be from institutions other than (and preferably countries other than) those of any of the authors.

How to Submit

Users registered in the role of author can start submission by choosing USER HOME link on the top of the page, then choosing the role of the Author and follow the relevant link for starting the submission process.

Prior to submission we strongly recommend that you familiarize yourself with the ACSi style by browsing the journal, particularly if you have not submitted to the ACSi before or recently.

Correspondence

All correspondence with the ACSi editor regarding the paper goes through this web site and emails. Emails are sent and recorded in the web site database. In the correspondence with the editorial office please provide ID number of your manuscript. All emails you receive from the system contain relevant links. **Please do not answer the emails directly but use the embedded links in the emails for carrying out relevant actions.** Alternatively, you can carry out all the actions and correspondence through the online system by logging in and selecting relevant options.

Proofs

Proofs will be dispatched via e-mail and corrections should be returned to the editor by e-mail as quickly as possible, normally within 48 hours of receipt. Typing errors should be corrected; other changes of contents will be treated as new submissions.

Submission Preparation Checklist

As part of the submission process, authors are required to check off their submission's compliance with all of the following items, and submissions may be returned to authors that do not adhere to these guidelines.

1. The submission has not been previously published, nor is it under consideration for publication in any other journal (or an explanation has been provided in Comments to the Editor).
2. All the listed authors have agreed on the content and the corresponding (submitting) author is responsible for having ensured that this agreement has been reached.
3. The submission files are in the correct format: manuscript is created in MS Word but will be **submitted in PDF** (for reviewers) as well as in original MS Word format (as a supplementary file for technical editing); diagrams and graphs are created in Excel and saved in one of the file formats: TIFF, EPS or JPG; illustrations are also saved in one of these formats. The preferred position of graphic files in a document is to embed them close to the place where they are mentioned in the text (See ***Author guidelines*** for details).
4. The manuscript has been examined for spelling and grammar (spell checked).
5. The ***title*** (maximum 150 characters) briefly explains the contents of the manuscript.
6. Full names (first and last) of all authors together with the affiliation address are provided. Name of author(s) denoted as the corresponding author(s), together with their e-mail address, full postal address and telephone/fax numbers are given.
7. The ***abstract*** states the objective and conclusions of the research concisely in no more than 150 words.
8. Keywords (minimum three, maximum six) are provided.
9. ***Statement of novelty*** (maximum 100 words) clearly explaining new findings reported in the manuscript should be prepared as a separate Word file.
10. The text adheres to the stylistic and bibliographic requirements outlined in the ***Author guidelines***.
11. Text in normal style is set to single column, 1.5 line spacing, and 12 pt. Times New Roman font is recommended. All tables, figures and illustrations have appropriate captions and are placed within the text at the appropriate points.
12. Mathematical and chemical equations are provided in separate lines and numbered (Arabic numbers) consecutively in parenthesis at the end of the line. All equation numbers are (if necessary) appropriately included in the text. Corresponding numbers are checked.
13. Tables, Figures, illustrations, are prepared in correct format and resolution (see ***Author guidelines***).
14. The lettering used in the figures and graphs do not vary greatly in size. The recommended lettering size is 8 point Arial.
15. Separate files for each figure and illustration are prepared. The names (numbers) of the separate files are the same as they appear in the text. All the figure files are packed for uploading in a single ZIP file.
16. Authors have read ***special notes*** and have accordingly prepared their manuscript (if necessary).
17. References in the text and in the References are correctly cited. (see ***Author guidelines***). All references mentioned in the Reference list are cited in the text, and vice versa.
18. Permission has been obtained for use of copyrighted material from other sources (including the Web).
19. The names, full affiliation (department, institution, city and country), e-mail addresses and references of three potential referees from institutions other than (and preferably countries other than) those of any of the authors are prepared in the word file. At least two relevant references (important papers with high impact factor, head positions of departments, labs, research groups, etc.) for each suggested reviewer must be provided.
20. Full-colour illustration or graph from the manuscript is proposed for graphical abstract.
21. ***Appendices*** (if appropriate) as supplementary material are prepared and will be submitted at the same time as the manuscript.

Privacy Statement

The names and email addresses entered in this journal site will be used exclusively for the stated purposes of this journal and will not be made available for any other purpose or to any other party.

ISSN: 1580-3155

Koristni naslovi

Slovensko kemijsko društvo
www.chem-soc.si
e-mail: chem.soc@ki.si

Wessex Institute of Technology
www.wessex.ac.uk

SETAC
www.setac.org

European Water Association
http://www.ewa-online.eu/

European Science Foundation
www.esf.org

European Federation of Chemical Engineering
https://efce.info/

International Union of Pure and Applied Chemistry
https://iupac.org/

Novice europske zveze kemijskih društev EuChemS najdete na:

Brussels News Updates
http://www.euchems.eu/newsletters/

Sistemi za čisto in ultračisto vodo

Kvaliteta vode 1 do 3*

***v skladu s standardom ISO 3696 in ustreznimi ASTM ter CLSI**

DONAU LAB Ljubljana
Member of LPPgroup

Donau Lab d.o.o., Ljubljana
Tbilisijska 85
SI-1000 Ljubljana
www.donaulab.si
office-si@donaulab.com



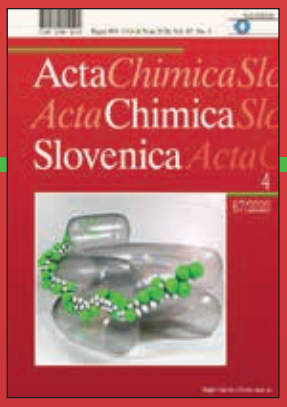


Že od
3.214€ +DDV
(B30 Trace s 25 L Pro rezerv.
Slika je simbolična)

adrona

Acta Chimica Slovenica

Acta Chimica Slovenica



Year 2020, Vol. 67, No. 4

An iconic PVC object from the collection of MNAM, Centre Pompidou. The Blow Inflatable Armchair was designed in 1967 by Paolo Lomazzi, Donato D'Urbino and Jonathan De Pas. Design objects like this, representing the creativity of the 20th Century, are at risk of rapid degradation and loss. Reproduced with permission of MNAM, Centre Pompidou, Paris, France (see page 993).











